www.jresm.org

Research on Engineering Structures and Materials

Volume 11
Issue 2
April 2025

P-ISSN: 2148-9807 E-ISSN: 2149-4088

The International Journal of **Research on Engineering Structures and Materials (RESM**) is a peer-reviewed open access journal (p-ISSN: 2148-9807; o-ISSN: 2149-4088) published by MIM Research Group. It is published in February, April, June, August, October, and December.

The main objective of RESM is to provide an International academic platform for researchers to share scientific results related to all aspects of mechanical, civil, and material engineering areas.

RESM aims the publication of original research articles, reviews, short communications technical reports, and letters to the editor on the latest developments in the related fields.

All expenditures for the publication of the manuscripts are most kindly reimbursed by *MIM Research Group*. Thus, authors do not need to pay for publishing their studies in the journal.

The scope of the journal covers (but not limited to) behavior of structures, machines and mechanical systems, vibration, impact loadings and structural dynamics, mechanics of materials (elasticity, plasticity, fracture mechanics), material science (structure and properties of concrete, metals, ceramics, composites, plastics, wood, etc.,), nano-materials performances of new and existing buildings and other structural systems, design of buildings and other structural systems, seismic behavior of buildings and other structural systems, repair and strengthening of structural systems, case studies and failure of structural systems, safety and reliability in structural and material engineering, use of new and innovative materials and techniques in energy systems and mechanical aspects of biological systems (biomechanics and biomimetics).

The topics covered in JRESM include:

- Structural Engineering
- Mechanical Engineering
- Material Engineering
- Earthquake Engineering
- Nano-technology
- Energy Systems (Focus on Renewable)
- Biomechanics and Biomimetics
- Environment (Material and Engineering System Related Issues)
- Computer Engineering and Data Science (Material and Engineering System-Related Issues)

Abstracting and Indexing
Please visit http://www.jresm.org for more information.

Graphics and Design

Mehmet Yılmaz myilmaz@jresm.net

RESEARCH on ENGINEERING STRUCTURES & MATERIALS

Research Group

RESEARCH on ENGINEERING STRUCTURES & MATERIALS

Editorial Board

Editorial Office

Publishing Manager		
Mehmet Yılmaz	MIM Research Group	Türkiye
Language Editors		
Gaye Kuru	Uşak University	Türkiye
Mete Çal	MIM Research Group	Türkiye

Advisory Board Members		
Abdelhalim Bensaada	University of Yahia Fares of Medea	Algeria
Abdellah Douadi	Ferhat Abbas University of Setif 1	Algeria
Abdel-Nasser Sharkawy	Faculty of Engineering, South Valley University	Egypt
Abdul Haseeb Wani	Presidency University, Bengaluru	India
Abrham Gebre	Addis Ababa University	Ethiopia
Alaa M. Rashad	Housing & Building National Research Center (HBRC)	Egypt
Aleksandar Ašonja	University Business Academy	Serbia
Ameer Baiee	University of Babylon	Iraq
Amirreza Sadeghi	University of Birjand	Iran
Andi Yusra	Universitas Teuku Umar	Indonesian
Anthony N. Papathanassiou	National and Kapodistrian University of Athens	Greece
Arunkumar K	Mangalam College of Engineering	India
Ary A. Hoyos-Montilla	Construction School at Universidad Nacional de Colombia	Colombia
Ashhad Imam	National Institute of Technology Jamshedpur	India
Ayoub Souileh	University Mohammed V	Morocco
Azzura Ismail	Universiti Tun Hussein Onn Malaysia	Malaysia
Berrin Ikizler	Ege University	Türkiye
Bilge Demir	Karabuk University	Türkiye
Cagri Yardimci	Usak University	Türkiye
Caroline S. Sobhy	Fayoum University	Egypt
Catur Harsito	Universitas Sebelas Maret	Indonesia
Chau-Khun Ma	Universiti Teknologi	Malaysia
Christopher Fapohunda	Federal University Oye-Ekiti	Nigeria
Daniel Cruze	Mohamed Sathak A J College of Engineering	India
Deep Tripathi	University of Sherbrooke	Canada
Dr Neeraj Sn	Visvesvaraya Technological University	India
Dr. Jayalalitha Subbaiah	SASTRA Deemed University	India

Elavenil S	Vellore Institute of Technology	India
Ercan Isik	Bitlis Eren University	Türkiye
Erion Bukaci	Polytechnic University of Tirana	Albania
Fatih Ahmet Senel	Süleyman Demirel University	Türkiye
Fokruddin Ahmad	Washington State University	USA
Ghasan Fahim Huseien	Universiti Teknologi Malaysia	Malaysia
Gökhan Gece	Bursa Teknik Üniversitesi	Türkiye
Gururaj Hatti	KLS VDIT	India
Gustavo Bosel Wally	Federal University of Rio Grande do Sul	Brazil
Gür Emre Güraksın	Afyon Kocatepe University	Türkiye
Halit Cetiner	Isparta University	Türkiye
Hamid Saberi	University of Eyvanekey	Iran
Hamoon Fathi	Islamic Azad University	Iran
Hasan ULUS	Selcuk University	Türkiye
Hayri B. Ozmen	Usak University	Türkiye
Hossein Jarrahi	University of Birjand	Iran
Hüsnügül Yilmaz Atay	Izmir Katip Celebi University	Türkiye
J. Paulo Davim	University of Aveiro	Portugal
Jesús Castro	Universitat Politecnica de Catalunya	Spain
Kabiru Mustapha	Kwara State University	Nigeria
Kaplan Kaplan	Kocaeli University	Türkiye
Kourosh Mehdizadeh	Islamic Azad University	Iran
Lavanya Prabha	SRM Easwari Engineering College	India
Lawrence Zahemen Tuleun	University of Ilorin	Nigeria
Leonid Dvorkin	National University of Water and Environmental Engineering	Ukraine
Lomesh Mahajan	Dr. Babasaheb Ambedkar Technological University	India
Luiz Rocha	Federal University of Rio Grande do Sul	Brazil
Lyamine Briki	University of Batna2	Algeria
Madhulika Sinha	National Institute of Technology	India

Maheswaran Muthiah	Kalasalingam Academy of Research and Education	India
Majid Pouraminian	Islamic Azad University	Iran
Mehdi Panji	Islamic Azad University	Iran
Mehmet Kaya	Bozok University	Türkiye
Melika Mahmoodabadi	Islamic Azad University	Iran
Mevlüt Gürbüz	Ondokuz Mayıs University	Türkiye
Mihir Mishra	Texas A&M University	USA
Mohammad Afrazi	Tarbiat Modares University	Iran
Mohammad Lesani	University of Tehran	Iran
Mohammad .I Al Biajawi	Universiti Malaysia Pahang Al-Sultan Abdullah	Malaysia
Mohammad Hossein Razmkhah	Semnan University	Iran
Mohammad Naeim Moradi	Amirkabir University of Technology	Iran
Mohammadreza Baghoolizadeh	Shahrekord University	Iran
Mohd Syahrul Hisyam Mohd Sani	Universiti Teknologi MARA (UiTM)	Malaysia
Mohsen Hajizamani	Graduate University of Advanced Technology	Iran
Motahhareh Nezafat Tabalvandani	Islamic Azad University	Iran
Mukaila Anifowose	Federal Polytechnic Offa	Nigeria
Mutluhan Akin	Nevşehir Hacı Bektaş Veli University	Türkiye
N.L.N. Kiran Kumar	Sri Venkateswara University	India
N.Venkata Sairam Kumar Namepalli	R.V.R & J.C College of Engineering	India
Nahida Nazim Musayeva	Azerbaijan National Academy of Sciences	Azerbaijan
Naveen S	National Institute of Technology, Raipur	India
Nermin Demirkol	Kocaeli University	Türkiye
Nhlanhla Nyembe	University of the Witwatersrand	South Africa
Ola Mazen Makki	University of Al-Qadisiyah	Iraq
Oladimeji Olatunji Ojo	Federal University of Technology Akure	Nigeria
Oleg V. Devitsky	Federal Research Centre Southern Scientific Centre of the Russian Academy of Sciences	Russia

Oleksii Hrechanyi	Zaporizhzhia National University,	Ukraine
Orhan Gülcan	General Electric Aerospace	Türkiye
Oritonda Muribwathoho	Cape Peninsula University of Technology	South Africa
P. Manoj Kumar	KPR Institute of Engineering and Technology	India
Partheeban Pachaivannan	Chennai Institute of Technology	India
Qasim M. Shakir	University of Kufa	Iraq
Rayeh Nasr Al-Dala'ien	Universiti Tenaga Nasional	Malaysia
Royal Madan	Chandigarh University	India
S. Ali Faghidian	Islamic Azad University	Iran
Saeid Foroughi	Selçuk University	Türkiye
Saman Saadatfar	Islamic Azad University	Iran
Sangeetha Palanivelu	SSN College of Engineering	India
Sastri M V S S	Vasavi College of Engineering	India
Serdar Gungor	Bilecik Şeyh Edebali University	Türkiye
Serkan Elcin	Pamukkale University	Türkiye
Seymur Bashirzade	Azerbaijan University	Azerbaijan
Shahazadi Begum	Baba Institute of Technology and Sciences	India
Shahrul Niza Mokhatar	Universiti Tun Hussein Onn Malaysia	Malaysia
Shaise K. John	College of Engineering Trivandrum	India
Shashi Prakash Dwivedi	G. L. Bajaj Institute of Technology & Management	India
Shoulong Zhang	Harbour Engineering Research Institute Co. Ltd.	China
Srinivasan Anandhan	National Institute of Technology Karnataka	India
Sumanth Ratna Kandavalli	New York University	USA
Talha Taskanat	Erciyes University	Türkiye
Tasnia Ahmed	Military Institute of Science and Technology (MIST)	Bangladesh
Toufik Sebbagh	University of Skikda	Algeria
Upendra K. Mallela	Aerospace Vertical, Largy Services Limited	India
Victor Rizov	University of Architecture	Bulgaria
Vijayasarathy Rathanasalam	ATRIA Institute of Technology	India

Vinicius Pepe	University Ritter dos Reis	Brazil
Waleed A Abbas	University of Technology	Iraq
Xiaojian Wang	Xinjiang University	China
Yuvaraj K	K.S.Rangasamy College of Technology	India
Zafer Kaya	Dumlupınar University	Türkiye
Zainorizuan Mohd Jaini	Universiti Tun Hussein Onn Malaysia	Malaysia

In This Issue

Research on Engineering Structures & Materials
MIM Research Group Publications
P-ISSN: 2148-9807
E-ISSN: 2149-4088
http://www.jresm.org

ABSTRACTING / INDEXING

The international journal of Research on Engineering Structures and Materials (RESM) is currently Abstracted/Indexed by Asos Indeks, CiteFactor, Cosmos, CrossRef, Directory of Research Journal Indexing, Engineering Journals (ProQuest), EZB Electronic Journal Library, Global Impact Factor, Google Scholar, International Institute of Organized Research (I2OR), International Scientific Indexing (ISI), Materials Science & Engineering Database (ProQuest), Open Academic Journals Index, Publication Forum, Research BibleScientific Indexing Service, Root Indexing, Scopus, Ulakbim TR Index (Tubitak), Universal Impact Factor and under evaluation by many other respected indexes.

Check web site for current indexing info, www.jresm.org

Research on Engineering Structures & Materials
www.jresm.org
Research Group

Research Article

Enhancing sustainability and performance in alkali-activated mortars with recycled rubber aggregates subjected to varied curing methods

Abdelhafid Benammar[a], Ammar Noui[b], Abdelatif Benouadah[c],Nabil Maafi[d], Oussama Kessal[e], Meriem Dridi[f], Ahmed Abderraouf Belkadi[g]

Department of Civil Engineering, Faculty of Sciences and Technology, University Mohamed El Bachir El Ibrahimi of Bordj Bou Arreridj, ElAnasser, 34030, Algeria

Article Info

Article history:

Received 26 Feb 2024
Accepted 30 June 2024

Keywords:

Alkali-activated;
Rubberized mortars;
Curing methods;
ANOVA analysis

Abstract

Rubber waste represents a significant waste stream that can be used as a substitute for natural aggregates in concrete. The main objective of this innovative study is to evaluate the effectiveness of alkali-activated mortars (AAM) incorporating recycled rubber aggregates in the development of an environmentally friendly construction material. Different replacement rates of sand with rubber particles (10%, 20%, and 30% by volume) are analysed. Rubberized alkali-activated mortars (RAAM) were produced using a combination of 10 M sodium hydroxide (NaOH) and a Na_2SiO_3/NaOH ratio of 3. Additionally, the influence of three curing methods on the properties of RAAM is also examined: air drying, curing in a climate chamber, or in an oven. The properties of RAAM were evaluated through tests including the flow table test, density test, water absorption test, and compressive strength test. Furthermore, the study also assessed the cost-effectiveness and environmental impact of RAAM. This variable study is complemented by an ANOVA parametric analysis. The results show a decrease in the compressive strength and flowability of AAM proportionally to the increase in R content. Experimental and statistical analysis reveal that curing in an oven at 60°C significantly optimizes compressive strength by approximately 50.52%. It is worth noting that this curing method of RAAM has demonstrated superior economic and environmental benefits compared to OPC mortar. The study highlights the strong potential of RAAM cured at 60°C or in a humid chamber, combining mechanical performance with reduced CO_2 emissions, as a sustainable and eco-friendly solution to replace traditional concrete.

1. Introduction

Geopolymers (GP) are increasingly attracting interest as a new class of sustainable construction materials, are subject to extensive research and practical applications [1, 2]. Contrary to ordinary Portland cement, which is estimated to contribute approximately 8% of global CO_2 emissions [3, 4], GPs are synthesized from aluminosilicate sources such as fly ash, slag, clay minerals, siliceous sand, or recycled aggregates, which are available locally [5, 6]. Their excellent mechanical strengths, durability, fire resistance, and low carbon footprint position them as next-generation binders in line with sustainable construction principles [7-9].

*Corresponding author: nabil.maafi@univ-bba.dz
[a]orcid.org/0009-0001-5271-9928; [b]orcid.org/0009-0005-6325-7131; [c] orcid.org/0000-0001-5326-4470; [d]orcid.org/0009-0005-0956-8908; [e]orcid.org/0000-0002-3669-6164; [f]orcid.org/0009-0008-7569-2036; [g]orcid.org/0009-0002-5978-9774
DOI: http://dx.doi.org/10.17515/resm2024.192ma0226rs

In parallel with the rise of geopolymers, waste production has continued to grow due to industrial development in recent decades. Among them, rubber waste represents a significant problem. It is estimated that around 1 billion tires reach the end of their lifespan every year, and this figure could reach 5 billion per year by 2030 [10, 11]. These huge volumes of non-biodegradable waste take up considerable space and pose environmental risks. The incorporation of alternative materials to replace natural aggregates in concrete could help reduce pressure on resources, as these aggregates account for 70% of the composition of concrete[12-14].

The incorporation of rubber in geopolymers presents a trade-off between decreasing mechanical performance and improving ductility [15]. Several studies in the literature have looked at the properties of geopolymers incorporating rubber aggregates Zhao, J., et al [16] as well as Qaidi, S.M., et al. [17] have shown that an increase in rubber content leads to a decrease in volumetric weight, as well as compressive, tensile, and flexural strengths of the material. Quantitatively, the presence of 10% rubber causes a 32% decrease in compressive strength. Researchers investigated the partial replacement of sand with crumb rubber (up to 20%) in fly ash-based geopolymer concrete. This substitution, according to Park et al.[18] led to a 35% decrease in compressive strength. However, the increased rubber content also enhanced the material's ductility. Similarly, Athira et al [19], partially substituted fines with rubber particles (0% to 20%) in fly ash and slag-based geopolymers, resulting in improved energy absorption at the expense of mechanical strength. Valente et al [20], highlighted enhanced interfacial compatibility between rubber aggregates and alkali-activated geopolymers, leading to improved porosity, flexural and toughness properties, albeit with compressive strengths consistently lower than equivalent Portland concretes. Parmender Gill et al . [21] demonstrated that geopolymer specimens with crumb rubber substitution exhibit up to a 17% reduction in compressive strength. Additionally, adding of Ordinary Portland cement improves microstructural integrity, but exposure to acid results in surface disintegration. Furthermore, optimal reinforcement with glass fibers reduces acid permeability, while the addition of steel fibers enhances both compressive and flexural strength. Abdullah et al.[22] studied the effects of incorporating rice husk ash (RHA) on the characteristics of lightweight geopolymer concrete, along with the addition of waste tire aggregates (WTA). The inclusion of WTA also resulted in a decrease reduction in density and compressive strength, with a further decrease in the thermal conductivity coefficient when WTA replaced 50% of the pumice aggregate.

In addition, various curing methods are commonly used for GPC, including ambient temperature curing, autoclave or steam curing, oven curing, and water curing. These processes aim to create the necessary conditions for the geopolymerization reaction, and to promote the development of the desired properties of the concrete [23, 24]. Liu et al. [25] have shown that GGBS content is crucial for mechanical properties, with better performance under thermal curing conditions. Accurate prediction models have been established for compressive strength. Specimens under optimal curing conditions exhibited a dense microstructure and characteristic hydrated gels.

Previous work by Luhar,S et al. [26], has demonstrated the effectiveness of high temperature curing (from 60 to 90°C) for a period ranging from 24 to 72 hours in improving the strength of GPs. Additionally, Park, Y., et al. [18], have highlighted the effectiveness of steam curing (in an autoclave) of GPs at a temperature of 46°C for 7 days. The study conducted by Rajendran and Akasi [27] revealed that oven curing is about 56% more effective than steam curing in terms of enhancing the strength of geopolymer concrete. Furthermore, Luhar, S. et al. [28], have indicated that a curing duration of 48 hours provides optimal compressive strength performance of rubber GPCs.

Expanding the study on the integration of rubber aggregates from used tires into AAM matrices represents a significant advancement towards more sustainable construction. This innovative approach aims to reduce environmental impact by incorporating recycled materials while enhancing concrete properties. What makes this study unique is the incorporation of recycled rubber fractions into AAMs, with the goal of designing concrete mixes that use a low carbon binder while improving characteristics such as lightness, mechanical strength, thermal and acoustic insulation, as well as durability. Based on previous research, a significant gap has been identified: the absence of studies investigating the synergistic effect between the presence of tire waste and the curing mode on AAM properties.

In this study, thoroughly investigate the effects of different proportions of rubber aggregates partially substituting mineral sand at volume fraction of (0%, 10%, 20%, and 30%) on the fresh and hardened properties of slag-based AAM. It also considers the impact of different curing modes, including air curing, chamber curing, or oven curing. The objective of this research is to mitigate the potential strength reduction in rubber-substituted AAMs while employing eco-friendly and cost-effective curing methods. To assess the correlation between the different parameters studied, an analysis of variance (ANOVA) was conducted using JMP software[29]. By conducting a comprehensive analysis of fundamental mechanics and bonding interactions, this research aims to facilitate wider adoption of oven-cured rubber-substituted AAM composites as alternatives to ordinary Portland cement concretes. The complete set of experimental data allows for a quantitative how these critical parameters influence on key performance measures of recycled rubber-substituted AAM composites.

2. Materials and Methods

2.1. Materials

In this study, Ground Granulated Blast Furnace Slag (GGBS) was used as precursor in the production of alkali-activated mortars (AAM). The GGBS was sourced from the El Hadjar steel complex located in Annaba, Algeria. The microstructures of GGBS were analyzed using the X-ray diffraction (XRD) technique, and the resulting phases are illustrated in Fig.1. As shown in Fig. 1, the calcite compounds with an amorphous structure demonstrate significant peaks. According to a previous study [30], the incorporation of GGBS was found to have a positive effect on the formation of calcium silicate hydrate (CSH) gel.

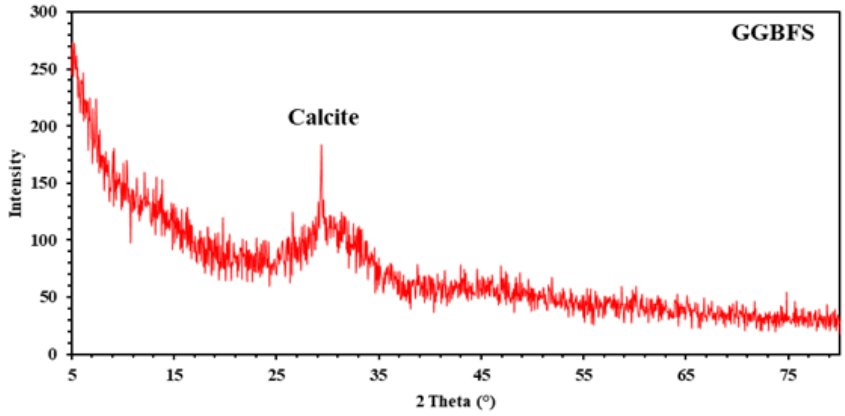

Fig. 1. X-ray diffraction of GGBS

This gel plays a crucial role in filling voids within the concrete matrix, thereby increasing the concrete's density. Figure 2 displays the particle size distribution and SEM image of GGBS. Its physical properties and chemical composition are detailed in Tables 1 and 2, respectively.

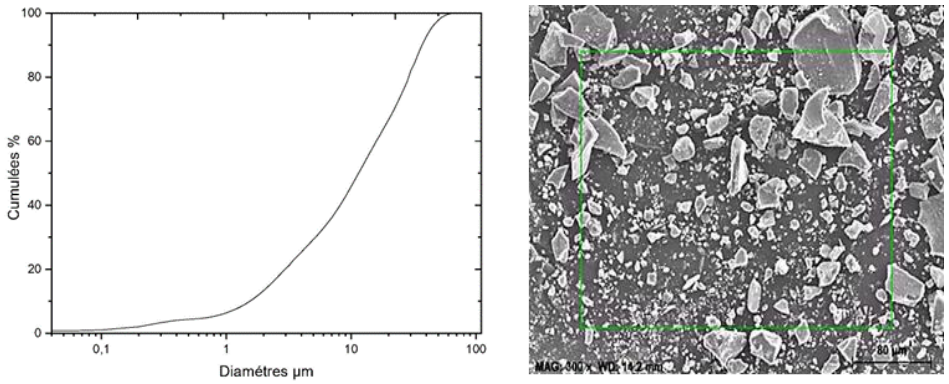

(a) (b)

Fig. 2. (a) Particle size distribution measured by laser granulometry and(b) SEM image of GGBS

Table 1. Physical properties of sand GGBS and rubber particles

Properties	Sand	GGBS	R
Absolute density (g/cm^3)	2.6	3.08	0.93
Fineness Modulus	2.2	_	_
Water Absorption (%)	2.7	_	0.7
Apparent density (g/cm^3)	1.7	1.4	0.6
Blaine surface area (m^2/kg)	_	4155	_

Table 2. Chemical compositions of GGBS.

Specimens	SiO_2	AL_2O_3	F_2O_3	CaO	MgO	SO_3	K_2O	Na_2O	LOI
GGBS	35.34	7.52	6.75	38.50	3.28	0.43	0.59	0.2	1.03

For the preparation of geopolymer AAM, two different activators, namely sodium hydroxide (NaOH), with 99% of purity and sodium silicate (Na_2SiO_3) were commonly used as alkali activators. A 10 M NaOH solution was prepared by dissolving pellets in tap water and allowing them to rest for 24 hours before casting.

(a) (b) (c)

(d) (e)

Fig. 3. Materials used in this study: (a) GGBS, (b)rubber, (c) river sand, (d) Na_2SiO_3 solution and (e) Solid NaOH

Additionally, a commercial Na_2SiO_3 solution was utilized in the process. The activators employed in this study are illustrated in Figure 3, and their properties are detailed in Table 3.

Table 3. Properties of activators

	Density (g/cm^3)	SiO_2 (wt%)	Na_2O (wt%)	H_2O (wt%)
NaOH powder	2.14	—	—	—
Na_2SiO_3 solution	1.53	29.8	14.43	55.77

The investigation employed two types of aggregates: natural river sand and rubber particles. The river sand had a fineness modulus of 2.2 and was dried prior to use. Fig.4 illustrates the particle size distribution within the sand sample. The rubber particles, sourced from discarded tires, had a size of 3 mm (as shown in Fig. 4). Table 1 provides the physical characteristics of these aggregates, while Figure 4 visually represents the aggregates used in the study.

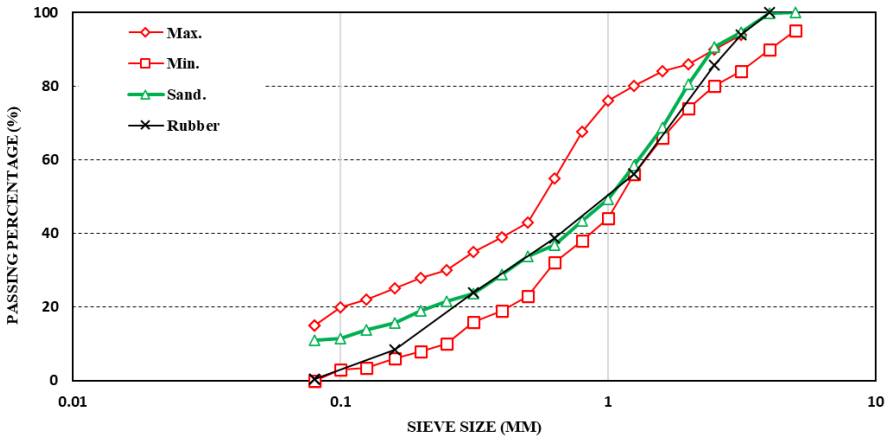

Fig. 4. Particle size distribution of natural sand and rubber

2.2. Rubber Treatment and Preparation of AAM Samples

Based on previous studies[31, 32], the activator solution was prepared by combining a 10M NaOH solution with Na_2SiO_3. The mixing process was carried out for 5-7 minutes. This activator solution was then kept at room temperature until the final mixing process. Furthermore, to evaluate the impact of rubber particles on the performance of AAM, sand was substituted with waste rubber particles at volume ratios of 0%, 10%, 20%, and 30%. The pretreatment of rubber particles involved washing them with tap water and then treating them with a NaOH solution. The rubber particles were initially rinsed with water to remove any impurities adhering to their surfaces. Subsequently, the particles were air dried for 48 hours at room temperature. After drying, the rubber particles were immersed in 5% NaOH solution at a temperature of 25°C for 24 hours. This NaOH treatment has been reported in a previous study to enhance the adhesion between rubber and other concrete ingredients [33]. Following the NaOH treatment, the rubber particles were washed multiple times to remove any remaining traces of NaOH from their surfaces. Finally, the pretreated rubber particles were dried at room temperature (60°C) for 48 hours. This pretreatment setup has been utilized in a previous study [34] and has demonstrated its effectiveness in achieving the desired results. Fig. 5 illustrates an organizational chart summarizing the processing steps for the different pretreatment methods of rubber particles.

The solid particles (GGBS, sand and rubber particle) were mixed for 3 minutes to ensure a higher level of homogeneity in the AAM. Subsequently, the activator solution was mixed with the solid particles for 2 minutes, blending the alkali solution and binder portion. Table 4 summarized the detailed compositions of all the mixes.

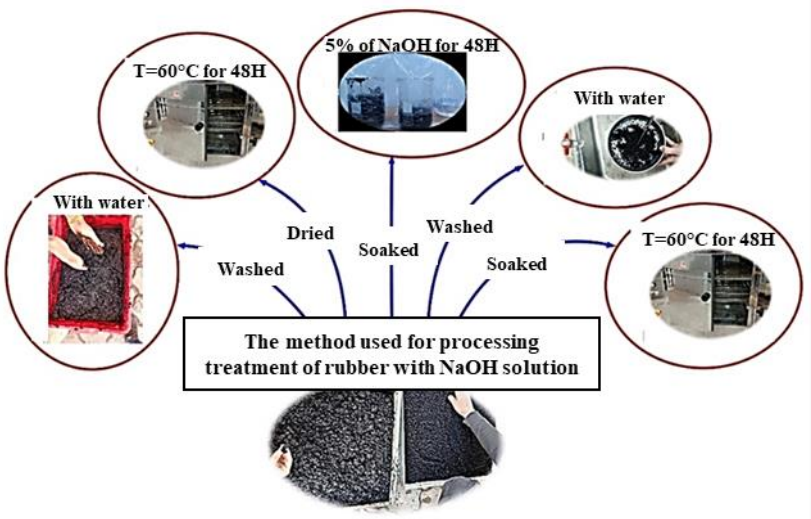

Fig. 5. The method used for processing treatment of rubber particles

The fresh mixtures obtained were poured into 25 mm cube molds in two separate layers, and each layer was compacted by applying 25 drops from a jolting table to remove air voids. After that, the specimens were subjected to three different curing modes. In the first curing mode (CM01), the molds containing the AAM samples are placed in an open-air chamber with an ambient temperature of 20°C and a relative humidity of 50% for 24 H. For the second curing method (CM02), the molded specimens were placed in an oven and maintained at a temperature of 60°C for a duration of 24 H.

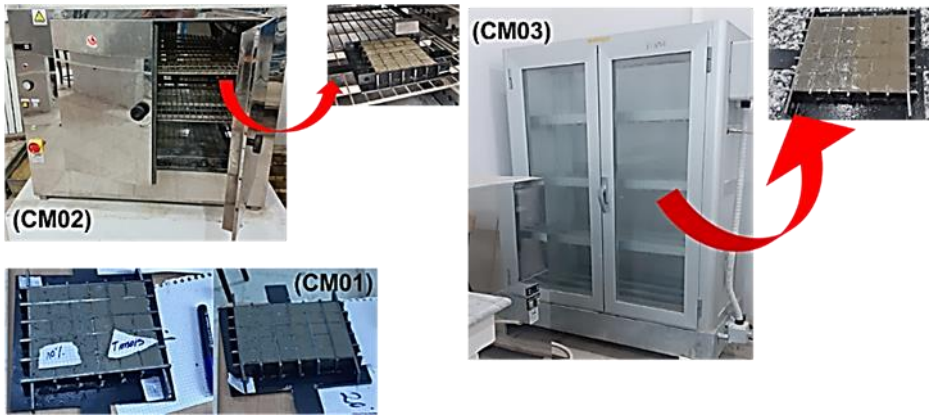

Fig. 6. Curing methods used for 24h, (CM01) an open-air chamber cured, (CM02) oven cured (CM 03) a humid room cured

In the third curing mode (CM03), the molded specimens were transferred to a humid room with a relative humidity (H) of 90% and an ambient temperature of 20°C. They were kept in this environment for 24 H. After curing method, the AAM were de-molded and placed in the laboratory at 20°C chambre until the testing age. Fig.6 shows the different curing methods employed in this study.

Table 4. Mixture proportions of AAM

Mix proportions (unit weight: Kg/m^3)					
Mixture	GGBS	Sand	Rubber	NaOH	Na_2SiO_3
CAAM	149	372	---	22	67
AAM-10R	149	335	13	22	67
AAM-20R	149	298	26	22	67
AAM-30R	149	261	39	22	67

Note: CAAM control Alkali-Activated Mortars without rubber, AAM-10R: Alkali-Activated Mortars with 10% rubber, AAM-20R: Alkali-Activated Mortars with 20% rubber, AAM-30R: Alkali-Activated Mortars with 30% rubber.

2.3. Experimental Procedure

2.3.1 Fluidity Test

To evaluate the workability of fresh AAM mixtures, a jolting table test was conducted following ASTM C1437 [35]. A cone-shaped container (dimensions in Fig.7a) was placed on the table and filled with the mixture. The mixture was then jolted 25 times, and its diameter was measured at two perpendicular points. The final result was reported as the average of these measurements.

2.3.2 Density

According to ASTM C642-13 [36], following the demolding process, the hardened density of AAM was determined using Equation (1):

$$\rho_r = \frac{m_r}{v_t} \quad (1)$$

Equation 1 defines hardened density (ρ_r) as the ratio of a hardened specimen's mass (m_r) to its total volume (V_t). This volume is calculated by multiplying the length, width, and height of the cubic specimens. To ensure accuracy, each specimen's side length was measured six times at different locations and averaged. The AAM's final density is calculated by averaging the hardened densities of all six specimens.

2.3.3 Compressive Strength

According to the NF EN 196-1 standard [37], the compressive strength of AAM was measured using 25 mm size cubes. The testing was carried out using a hydraulic compression testing machine with a maximum capacity of 3000 kN, as depicted in Fig.7b.

2.3.4 Total Water Absorption

According to the EN 1015-18 standard [38], the water absorption test was conducted for all AAM and RAAM specimens. The aim of this test is to measure the water absorbed by the mortars over a 24-hour period. Water absorption is a vital factor for assessing and predicting the durability of building materials. [15] To determine the total water absorption of AAM, three cubes from each series were subjected to oven drying at a temperature of 85°C for 24 hours until a constant mass was achieved.

(a)

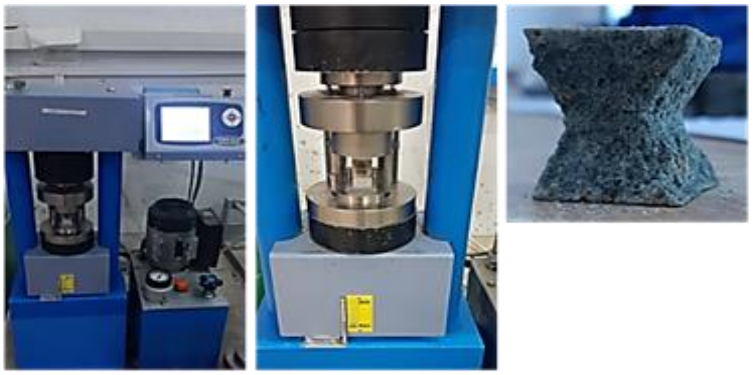

(b)

Fig. 7. Test equipment used, (a) flow test, (b) compression testing machine

The weight of the cubes after drying, recorded as the initial weight, was then compared to the saturated surface dry weight obtained after the AAM cubes were soaked in water for 24 hours or more at atmospheric pressure. The water absorption of the specimens was reported as the percentage increase in weight. The choice of an 85°C drying temperature was made to avoid potential disruptions in the microstructure of the AAM specimens and to ensure accurate water absorption values.

3. Results and Discussions

Table 5 presents a comprehensive summary of all the experimental findings. It is worth noting that the recorded errors for each composition did not exceed 3%. This indicates that the modeling of the responses, specifically the compressive strengths at 28 days (CS_{28}), was successful, as the errors remained within an acceptable range.

Table 5. The experimental results

Curing methods	Mixture	R (g)	Flow table (mm)	Fresh Density (Kg/m^3)	Hardened Density (Kg/m^3)	CS_{28} (MPa)	WA (%)
CM01	CAAM01	0	195	2341	2387	35.36	7.361
	AAM-10R	50.92	179.5	2272	2354	30.32	7.77
	AAM-20R	101.84	172	2176	2238	23.07	8.15
	AAM-30R	152.76	155	2129	2156	17.78	9.13
CM02	CAAM 02	0	195	2341	2403	53.24	6.42
	AAM-10R	50.92	179.5	2272	2370	39.74	7.34
	AAM-20R	101.84	172	2176	2322	34.60	7.86
	AAM-30R	152.76	155	2129	2173	23.72	8.29
CM03	CAAM 03	0	195	2341	2395	44.95	7.03
	AAM-10R	50.92	179.5	2272	2367	38.96	7.43
	AAM-20R	101.84	172	2176	2309	32.98	8.24
	AAM-30R	152.76	155	2129	2212	27.15	8.57

3.1. Flow Table Test Results

In order to determine the workability of various AAM mixes, flow table tests were conducted in compliance with the ASTM C1437 23 [35] standard. The flowability test results are shown in Fig.8. The CAAM exhibited the highest level of flowability among all the mixes, with a maximum measurement of 195 mm.

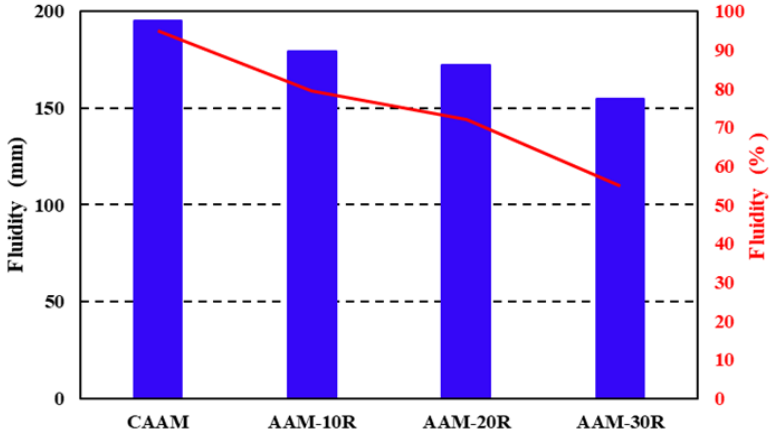

Fig. 8. Effects of rubber content on RAAM fluidity

The results showed the impact of rubber content on the fluidity of the rubber alkali-activate mortar (RAAM). It can be observed that as the rubber content increases, the fluidity of the RAAM decreases. When the rubber replacement levels are increased to 10%, 20%, and 30%, the fluidities of the RAAM mixtures decrease by 8%, 12%, and 20%, respectively, compared to the CAAM. This finding aligns with previous research on RAAM [9, 39, 40], which has shown that incorporating rubber particles can notably affect the

fluidity of geopolymer mixtures. As the rubber content increases, the fluidity decreases, reinforcing the understanding of the connection between rubber content and fluidity in geopolymer systems. The decrease in workability observed when incorporating rubber in AAM can be attributed to several factors. Firstly, the rough surface of rubber particles increases friction between the rubber particles and the other components of the AAM, resulting in reduced workability [41]; Secondly, the hydrophobic nature of rubber particles leads to increased air entrapment, further decreasing the flow resistance of the mixture. This can contribute to the reduction in workability of RAAM. Lower workability is also attributed to reduced friction, hindered flow of large rubber particles, and the texture of small rubber aggregates [41]. The low density of rubber particles may further contribute to the decrease in workability. Furthermore, incorporating waste rubber aggregates as aggregates in lightweight geopolymer concrete diminishes workability, consequently increasing the proportion of trapped air bubbles [42]. However, it is interesting to note that the rubber content has a lesser impact on the fluidity of RAAM. This implies that pretreatment with NaOH might have enhanced the interface performance of the rubber, thereby offsetting the adverse impacts of increased rubber content on fluidity [43]. The improved interface performance could be attributed to the hydrophilic nature of the rubber particles, which can serve as a standard for assessing the enhancement of rubber-cementitious materials [44]. Overall, the workability of all the AAM mixes fell within the acceptable range for their application in construction practices.

3.2. Density

Table 5 and Figure 9 illustrate the impact of rubber content on the fresh and hardened densities of the AAM specimens. The findings indicate that the addition of rubber particles in AAM leads to a decrease in its fresh density, and this reduction becomes progressively more pronounced with higher rubber content.

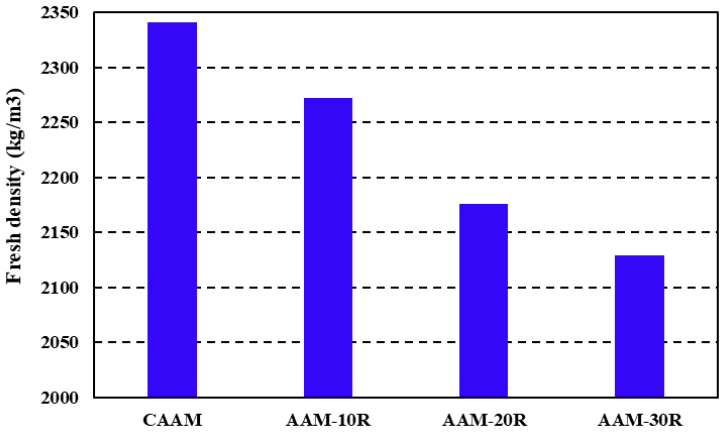

Fig. 9. Fresh AAM density of various mixes

As shown in Fig. 9, the fresh density of the RAAM ranged from 2272 Kg/m^3 to 2138 Kg/m^3, while the hardened RAAM densities for CM01, CM02 and CM03 varied from 2354-2156 Kg/m^3, 2370-2173 Kg/m^3 and 2367-2212 Kg/m^3 respectively (see table 5) , and were slightly lower than that of the control mix (without rubber), which is consistent with an earlier study [45, 46]. For example, the fresh densities of the AAM with 10%, 20%, and 15% rubber were reduced by 2.9%, 7.4%, and 10.0%, respectively, in comparison to those without rubber. Using 30 % R decreases the hardened density of AAM to about 212, 230 and 183 Kg/m^3 for CM01, CM02 and CM03, respectively. This reduction in density

contributes to improved thermal and sound properties of the composite. It is widely acknowledged that rubber has a lower density compared to river sand [42]. The average specific gravity of rubber particles is approximately 0.93, which is 2.6 times lower than that of sand. Additionally, rubber particles serve as solid hydrophobic air-entraining agents [47], meaning they introduce more air into the alkali-activated mixture.

3.3. Relationship Between 28-Day Compressive Strength and Water Absorption

Linear regression analysis was employed to investigate the correlation between the 28-day compressive strength and water absorption of AAM. The results of this analysis are presented in Fig.10. Linear regression is a statistical technique used to establish the relationship between two variables. By fitting a linear equation to the data, it becomes easier to comprehend the impact of different parameters. The linear equations developed in this study provide basic insights into the influence of various factors.

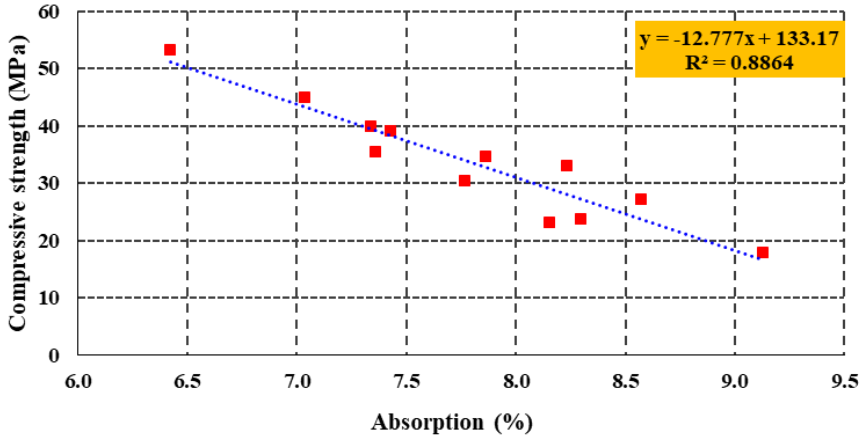

Fig. 10. Relationship between 28-day compressive strength and water absorption of various mixes

The average correlation value (R^2) for the linear fitting curve of compressive strength and water absorption was approximately 0.88, indicating a strong correlation between the variables. The positive slope observed in the graph indicates a direct relationship between compressive strength and water absorption, implying that as water absorption increases, the compressive strength tends to increase as well. This finding aligns with the theory that reducing the presence of pores enhances the resistance of cementitious materials. Notably, Kirgiz et al. [48] also reported similar results, further validating this theory.

3.4. Statistical Analysis Results

Various designs, as described by Dean et al. [49] and Lawson [50], can be employed to investigate the relationships between factors and responses. In the experimental program, the focus was on evaluating the compressive strength and water absorption of AAM, while also studying the impact of curing methods and the incorporation of crumb rubber on these properties[51, 52]. The analysis of these factors was carried out using the "JMP 16" software [53].

3.4.1 Analysis and Outcomes of The Variance Within The Model

The ANOVA analysis presented in Figs 11 and 12 partitions the overall variability of the dependent variables, namely compressive strength, and water absorption, into two components: one attributed to the regression and the other to deviations around the fitted

model. The R-squared statistic (RSq), calculated by comparing the model sum of squares to the total corrected sum of squares, indicates that the model explains approximately 98% and 96% of the variability in compressive strength and water absorption, respectively.

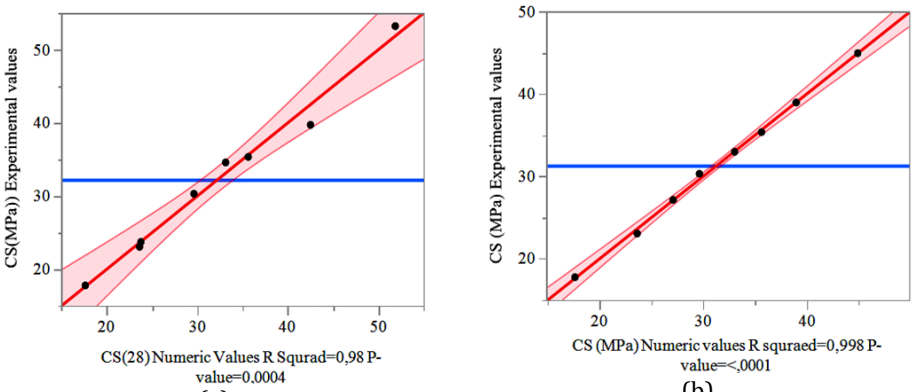

(a) (b)

Fig. 11. Compressive Strength Actual by Predicted Plot for AAM cured in oven (CM02) and cured in a humid room (CM03)

The mean squared error (EMSE) serves as an estimate of the variance of the deviations around the model, obtaining values of 0.222 to 3.134 and 0.04617 to 0.05229 for compressive strength and water absorption, respectively. The fact that the P value is less than 0.0004 for both compressive strength and water absorption demonstrates that the model is statistically significant, indicating a meaningful relationship between the predictors and responses.

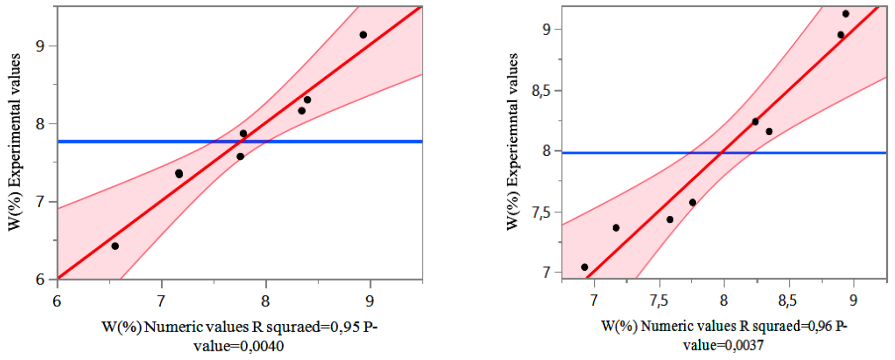

(a) (b)

Fig. 12. Water absorptions at 28 days, actual by Predicted Plot (a) for AAM cured in oven (CM02) and (b) for AAM cured in a humid room (CM03)

Table 6 presents the ANOVA analysis for all modeled responses. The Fisher test, based on the Fisher test distribution, allows us to evaluate the statistical significance of these models, indicating their overall importance. In this study, the Frisher rations for both curing modes CM02 and CM03 are 0001 and 0.0004 for CS_{28}, 0.0004 and 0.0040 for WA respectively. With a 90% confidence interval, signifying a notable level of significance. The probability values (P-values) exceeding the F-statistic (Prob. > F) were all below 5% for every model, suggesting the presence of at least one factor with a statistically significant impact in each model. This suggests that the effect factors considered in the models have a notable impact on the responses.

Table 6. ANOVA (Analysis of Variance) for the derived models

	Source	Degree of freedom	Sum of squares	Mean square	F -ratio
CS_{28}	Model	3	531.83018	177.277	798.8634
	Error	4	0.88764	0.222	Prob. > F
	Total	7	532.71782		<.0001*
CS_{28}	Model	3	869.45871	289.820	92.4891
	Error	4	12.53422	3.134	Prob. > F
	Total	7	881.99293		0.0004*
WA	Model	3	3.9250779	1.30836	28.3367
	Error	4	0.1846873	0.04617	Prob. > F
	Total	7	4.1097653		0.0037*
WA	Modèle	3	4.2770621	1.42569	27.2663
	Erreur	4	0.2091502	0.05229	Prob. > F
	Total	7	4.4862123		0.0040*

According to the Table 7, it is clear that the contributions of each factor, rubber particle (R %), relative humidity (H%), and temperature (T °C), along with their interactions, to the responses are significant. The significance of each coefficient was assessed using the criterion $P \leq 0.05$, and it was observed that the effects of the factors R %, H%, T°C, and their interactions on the responses are highly significant.

Table 7. Effect test

	Model term	Estimation	Standard Error	t ratio	Prob. > |t|
CS_{28} CM02	Intercepts	31.320875	0.166354	188.28	<.0001*
	R (%)	-8.95425	0.223188	-40.12	<.0001*
	H (%)	4.68675	0.166354	28.17	<.0001*
	R (%)×H (%)	0.047025	0.223188	0.21	0.8434
CS_{28} CM03	Intercepts	32.230063	0.62594	51.49	<.0001*
	R (%)	-11.52769	0.839786	-13.73	0.0002*
	T(°C)	5.5959375	0.62594	8.94	0.0009*
	R (%)×T(°C)	-2.526412	0.839786	-3.01	0.0396*
WA CM02	Constante	7.983825	0.07597	105.09	<.0001*
	R(%)(0.30)	0.93369	0.101925	9.16	0.0008*
	H(%)(50.90)	-0.069925	0.07597	-0.92	0.4094
	R(%)*H(%)	0.05064	0.101925	0.50	0.6454
WA CM03	Constante	7.7674125	0.080845	96.08	<.0001*
	R(%)(0.30)	0.9023925	0.108465	8.32	0.0011*
	T(°C)(20.60)	-0.286413	0.080845	-3.54	0.0240*
	R(%)*T(°C)	0.0192075	0.108465	0.18	0.8680

3.4.2 Expression for predicting the values of compressive strength and water absorption

Based on the conducted statistical analysis, the following prediction expressions, represented by Eqs. (2)-(5), were derived to estimate the values of compressive strength

and water absorption in relation to the rubber incorporated (R%) and curing methods (oven cured (CM02) and a humid room cured (CM03)).
The compressive strength of, which were cured in CM02, can be described with the following expression:

$$CS(28\ days) = 32.23 - 11.527.\left(\frac{R(\%)-15}{15}\right) + 5.595.\left(\frac{T(C)-40}{20}\right) - .5264.\left(\frac{R(\%)-15}{15}\right).\left(\frac{T(C)-40}{20}\right) \quad (2)$$

The compressive strength of AAM, which were oven cured CM03, can be described with the following expression:

$$CS(28\ days) = 31.32 - 8.954.\left(\frac{R(\%)-15}{15}\right) + 4.686.\left(\frac{H(\%)-70}{20}\right) + 0.047.\left(\frac{R(\%)-15}{15}\right).\left(\frac{H(\%)-70}{20}\right) \quad (3)$$

The expression for water absorption (%) of AAM cured in CM02 can be given as follows:

$$W(\%) = 7.767 + 0.9023.\left(\frac{R(\%)-15}{15}\right) - 0.286.\left(\frac{T(C)-40}{20}\right) + 0.0192.\left(\frac{R(\%)-15}{15}\right).\left(\frac{T(C)-40}{20}\right) \quad (4)$$

The expression for water absorption (%) of AAM cured in CM03 can be given as follows:

$$W(\%) = 7.983 + 0.9336.\left(\frac{R(\%)-15}{15}\right) - 0.0699.\left(\frac{H(\%)-70}{20}\right) + 0.0506.\left(\frac{R(\%)-15}{15}\right).\left(\frac{H(\%)-70}{20}\right) \quad (5)$$

3.4.3 Compressive Strength Results Analysis

The different types of graphs from the analysis of the results of the compressive strength (CS) at 28 days, taking into account the factors of rubber particles content (%) and curing methods are presented in Fig 13, 14, 15 and 16. The compressive strength is assessed by the average force of three cubic samples (Table 5). For the control samples using the CM01 curing method, a maximum compressive strength (CS) of 35.37 MPa was observed at 28 days. With the partial substitution of sand by rubber particles, a significant decrease in the CS of AAMs was observed. AAM-10R displayed a reduced strength of 14%, this is equivalent to. 30.32 MPa, compared to CM01. Similarly, AAM-20R and AAM-30R recorded respective strength losses of 34% (23.07 MPa) and 49% (17.78 MPa). The CS of the samples subjected to CM02 and CM03 curing methods was measured at 53.24 MPa and 44.95 MPa respectively. The results of partial substitution of sand by rubber particles in AAMs showed a downward trend in CS, similar to that observed with CM01. For CM02, AAM-10R revealed a 25% strength reduction, reaching 39.74 MPa, while for CM03, the reduction was 13%, 38.96 MPa. In addition, AAM-20R and AAM-30R showed more pronounced strength decreases: For CM02, the losses were 35% and 55%, while for CM03, they were 26% and 39%. These results reveal clear trends regarding the impact of sand substitution by rubber particles on the compressive strength of AAMs. It is evident that the integration of rubber negatively affects compressive strength, regardless of the curing method used (CM01, CM02, or CM03). This loss of performance varies according to the percentage of substitution and the curing method. Moreover, this decrease in load bearing capacity can be attributed to crucial factors such as reduced density and elasticity of rubber, increased porosity due to trapped air, and hydrophobicity of rubber, all of which contribute to decreased compressive strength [54] [55] [28].

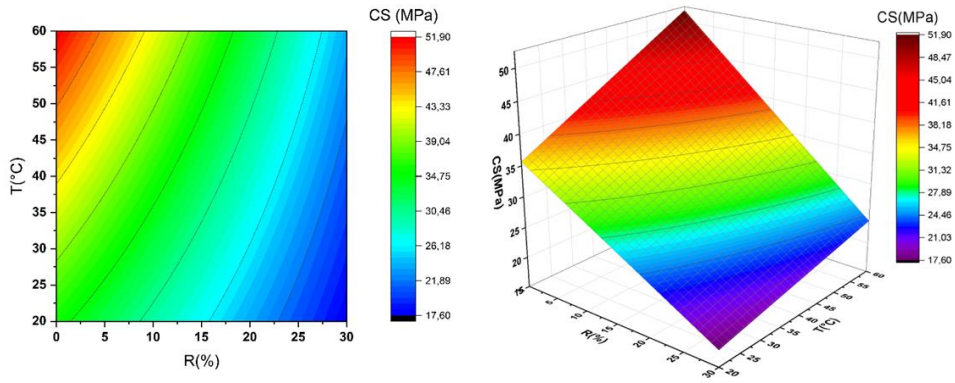

Fig. 13. Iso-response analysis of 28-Day compressive strength in RAAM CM02 subjected to oven curing

Re-focusing the analysis on the impact of curing methods, makes it clear that they are key in optimizing the CS strength of AAMs. Specimens treated with the CM02 method, oven-cured at 60°C without adding rubber particles, demonstrated a marked improvement in CS compared to other techniques. After 28 days, CM02 shows a significant increase in CS of 50.52% compared to CM01 and 18.44% compared to CM03. These data highlight the effectiveness of 60°C curing without rubber particles to increase the strength of AAM samples, this observation is in total agreement with the work of Mustafa Al Bakri et al. [56] who identified 60°C as the optimal curing temperature for geopolymer specimens. Their research also reveals that geopolymers cured at high temperatures suffer from a lack of moisture necessary for optimal strength development. Liu et al. demonstrated the significance of GGBS content in influencing mechanical properties, particularly showing improved performance under thermal curing conditions. They developed precise prediction models for compressive strength. Specimens cured optimally displayed a dense microstructure and distinctive hydrated gels. In a study by Joseph and Mathew [57], geopolymer concrete specimens were cured at different temperatures, ranging from 30 °C to 100 °C. The results showed that the compressive strength of the concrete increased significantly with higher curing temperatures.

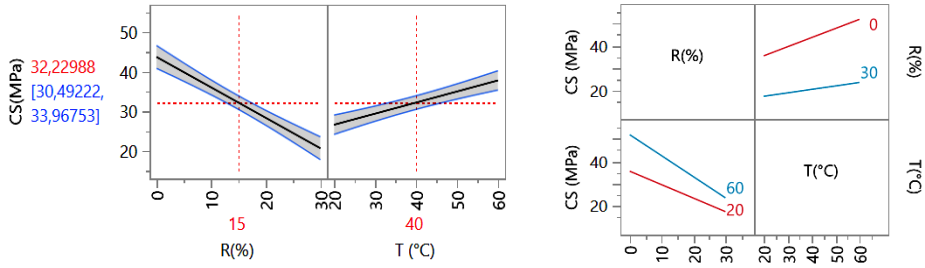

(a) (b)

Fig. 14. (a) Main effects plot (b) interaction plot of the 28-day compressive strengths for AAMR oven cured CM02

Figures 14 and 16 present the main effects plots on the 28-day CS response of AAM, taking into account factors of rubber particles content (%), T (°C) and H (%). Analysis of the data presented in Table 7, together with the graphical visualizations in Fig14a and 16a, reveals the complex dynamics governing the 28-day CS of AAMs. The negative influence of rubber

percentage on CS is highlighted by negative coefficients of -11.52769 for CM02 and -8.95425 for CM03, underscoring an inverse proportional effect between CS and amount of R incorporated.

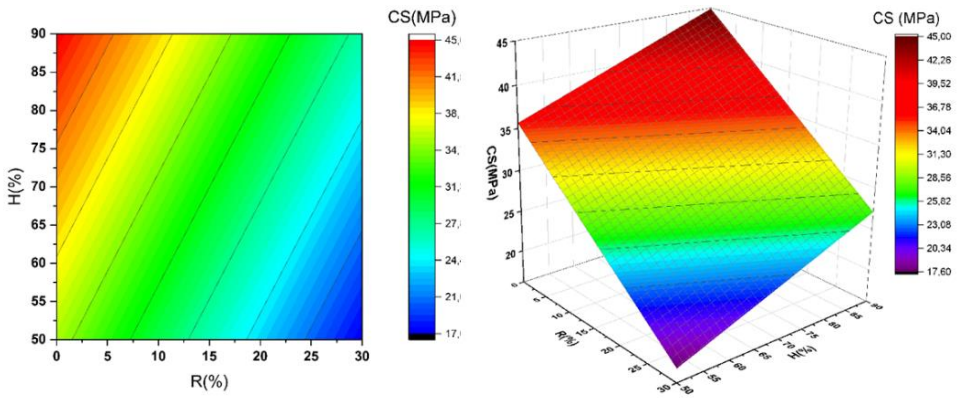

Fig. 15. Iso-response curves and surfaces illustrate the variations in 28-day compressive strengths for AAMR cured in a humidity room CM03

In parallel, a positive coefficient of +5.599375 for curing temperature (T in °C) indicates that increasing temperature promotes improvement in CS, up to an optimal point. This synergy is illustrated in Figure 14a for oven-cured AAM CM02, where rising T causes an increase in CS, while addition of rubber particles decreases it, a relationship that is graphically supported by the trends observed in the 14b interaction plot.

Figure 16a exposes the effects of rubber particles (%) and humidity (H%) on chamber-cured AAMs CM03. The decreasing CS with increasing rubber particles (%) is clearly visible in the downward curve of the plot. However, the 16b interaction plot reveals that the interaction between rubber particles (%) and H (%) does not have a pronounced impact on CS, deduced from the near-parallelism of the curves.

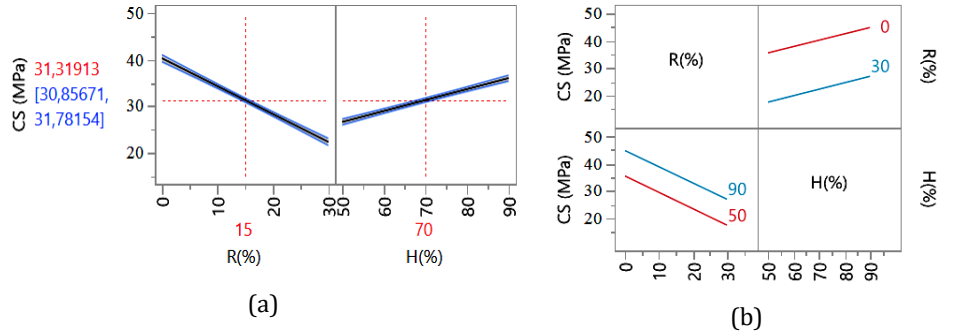

Fig. 16. Main (a) and Interactive (b) Drivers of AAMR Compressive Strength in Humidity Room CM03 (28-Day Analysis)

3.4.4 Water Absorption Results Analysis

The water absorption responses of AAM for CM02 and CM03 curing methods are illustrated in Figures 17, 18, 19 and 20. Figures 17 and 19 illustrate the response surface curves and isometric plots of the 28-day water absorption (WA) of AAM as a function of the sand substitution rate by rubber particles, for the different curing methods studied.

Analysis of the data shows an upward trend in water absorption as the rubber proportion rises from 10% to 30%, regardless of the curing method used, oven-cured CM02 or chamber-cured CM03. Specifically, for CM02, water absorption increases from 7.34% to 8.29%, and for CM03, it rises from 7.43% to 8.57%, revealing a direct and proportional relationship between the increase in rubber particles content and the material's WA after 28 days.

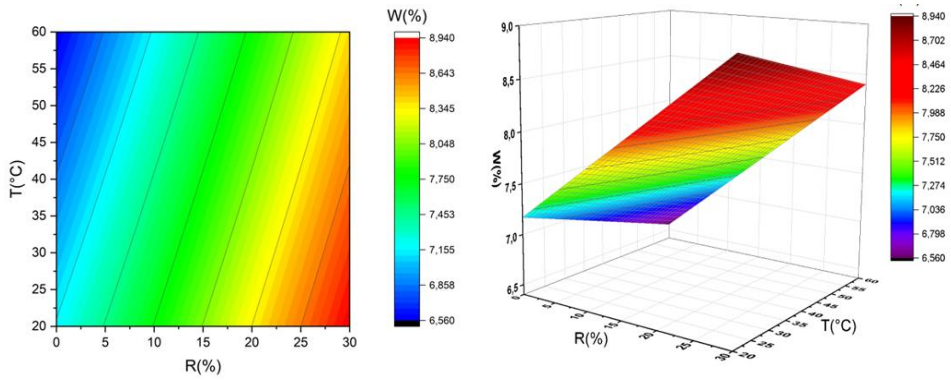

Fig. 17. Mapping the influence of process parameters on AAMR water absorption (28 Days) using iso-response analysis

According to Dehdezi et al. [58], weak bonding between the geopolymer and the rubber particles creates a poor interfacial transition zone (ITZ). This weak zone, in turn, increases the number of apparent pores in the material. These observations are validated by the coefficients presented in Table 7 and defined by Equations (4 and 5). The coefficients for rubber particles (%) are positive, with (+0.90) for CM02 and (+0.93) for CM03, confirming a positive correlation between the amount of rubber and the observed WA.

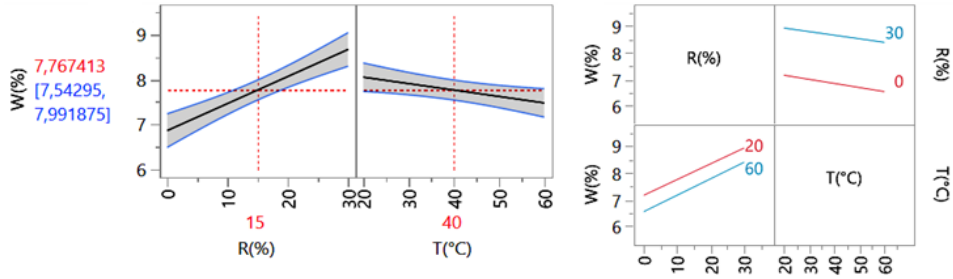

(a) (b)

Fig. 18. AAMR Water Absorption (28-Day): Main (a) & Interaction Effects (b) (Oven Cured CM02)

The coefficients for temperature (T °C) and humidity (H %) are (-0.28) and (-0.08) respectively, indicating an inverse relationship between these parameters and water absorption suggesting that increases in temperature and humidity help reduce WA. This result highlights the overriding influence of rubber particle replacement rate and curing conditions on the hygral behavior of AAMs.

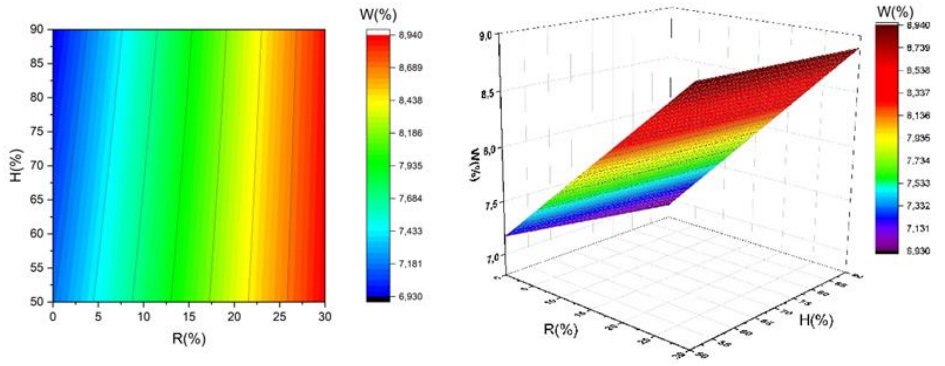

Fig. 19. Iso-response Modeling of AAMR water Absorption in Humidity Room CM03

Figures 18b and 20b present detailed interaction plots of the dynamics governing the 28-day WA of different AAM mixes. In oven-cured CM02 samples, the interaction plots display parallel behavior between the rubber particles content factor (%) and temperature (T°C), indicating an absence of marked synergy between these variables on water absorption. In contrast, the interactions in chamber-cured CM03 samples exhibit crossing curves, revealing a significant interdependence between the rubber particles content factor (%) and humidity (H%). This difference suggests that curing conditions significantly influence AAMs. Conversely, analysis of the results for AAM without rubber particles exposes a reduction in capillary absorption for the compositions subjected to CM02 curing with a respective decrease of 18% and 9% compared to the control compositions CM01 and CM02.

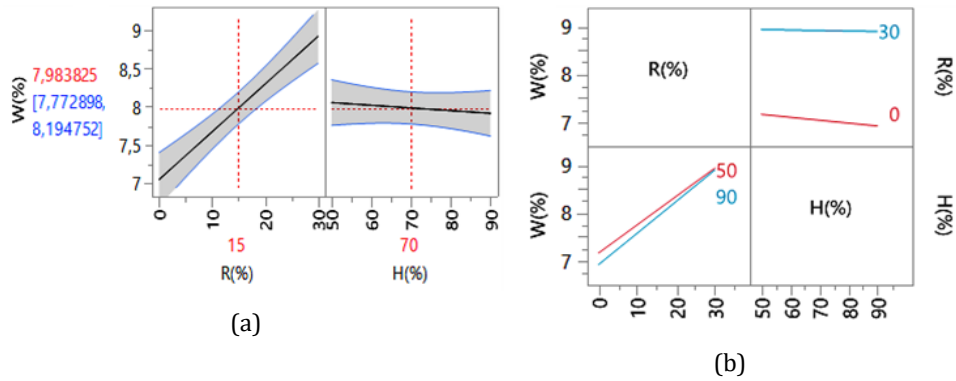

Fig. 20. Main (a) and interactive (b) drivers of RAAM water absorption in oven-cured CM02 (28-Day Analysis)

3.5. Economic and Ecological Analyses

In this section, we offer an assessment of the carbon dioxide emissions and conduct a financial analysis for the AAM blends formulated in this research. The aim is to assess the environmental and economic implications of substituting rubber particles with natural sand in the AAM compositions, which are subjected to various curing techniques. To quantify the RAAM's cost-effectiveness and environmental footprint, we employed two indices developed by Ma [59] (Equations 6 and 7).

$$C_P = \frac{Cost}{fc28} \quad (6)$$

The cost-efficiency and environmental impact are calculated using a formula that considers the cost per unit of strength (C/$MPa), the total material cost per cubic meter (Cost), and the material's 28-day compressive strength (σ). The cost-efficiency and environmental impact are calculated using a formula that considers the cost per unit of strength (C/$MPa), the total material cost per cubic meter (Cost), and the material's 28-day compressive strength (σ).

$$E_P = \frac{embodied\ CO_2}{fc28} \quad (7)$$

Embodied CO_2 per MPa (Ep ($kg/Mpa.m^3$)) and total embodied CO_2 (($kgCO_2$)/(kg)) were calculated for the AAM, considering its 28-day compressive strength (fc28) and local raw material costs in Algeria. These calculations also incorporated the embodied CO_2 data for the raw materials sourced from relevant research [16, 59, 60]. The findings from these calculations are detailed in Table 8.

Figure 21a and Table 9 present the calculated CP values for the AAM subjected to various curing conditions. Notably, the CP values for each AAM mixture exceed those of Ordinary Portland Cement (OPC). When comparing AAM mixtures without rubber, it's evident that the CP values of CAAM01 and CAAM03 are nearly double that of OPC, while CAAM02 and OPC exhibit only a slight difference in CP values. Additionally, incorporating rubber into RAAM results in an elevated CP value. This can be attributed to two primary factors: firstly, the adverse impact of rubber on the compressive strength of the mixture, and secondly, the higher cost associated with using rubber compared to natural aggregate. These factors collectively contribute to the observed increase in the CP of the RAAM.

Table 8. Cost and embodied CO_2 of raw materials

Materials	Reel study Cost ($\$ / kg$)	embodied CO_2 ($kgCO_2/kg$)	
GGBS	0.035	0.067	[61]
Sand	0.029	0.005	[16]
Cement	0.12	0.830	[62]
Rubber	0.67	0.004	[59]
NaOH powder	4.06	1.915	[63, 64]
Na_2SiO_3 solution	0.56	0.650	[64, 65]
Water	0.00372	0.001	[16]
Energy	($\$ / kwh$)	($kgCO_2$/kWh)	
Heating	0.28	1.08	[60]

Regarding the impact of curing methods on the CP values of RAAM, it was noted that the humidity curing method (CM03) demonstrated significant economic efficiency. This suggests that CM03 could be a viable option for real-world application in engineering projects, especially when compared to the preparation methods evaluated by CM02, which require more thermal energy (refer to Table 8). The E_P values for different RAAM mixtures are depicted in Fig. 21b. It is clear that AAM exhibits a higher level of environmental friendliness compared to OPC. While adding rubber increased the material's embodied CO_2 per MPa (Ep), its inherently lower CO_2 intensity per unit mass compared to natural aggregate could offer an environmental benefit.

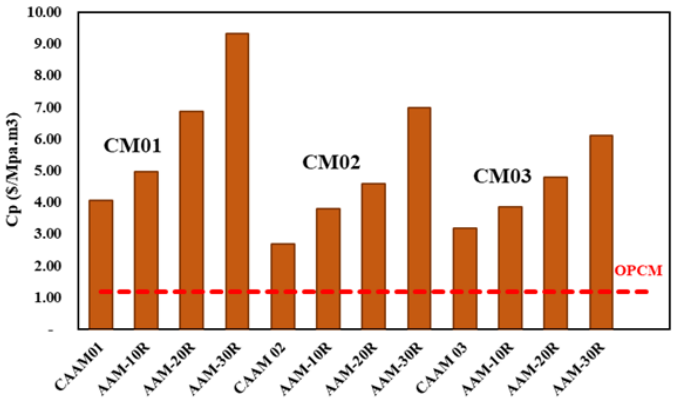

(a)

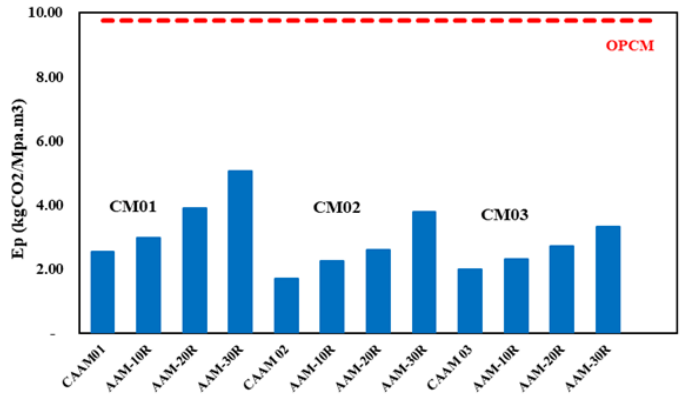

(b)

Fig. 21. (a) Cost efficiency and (b) environmental impact of curing methods on the AAM

Table 9. AAM cost efficiency and environmental impact

Curing methods	Mix	Compressive strength (MPa)	Cp ($/Mpa. m^3)	Ep ($kgCO_2$/ Mpa. m^3)
	CAAM01	35.37	4.04	2.56
	AAM-10R	30.32	4.96	2.98
CM01	AAM-20R	23.07	6.85	3.91
	AAM-30R	17.78	9.32	5.06
	CAAM 02	53.24	2.68	1.70
	AAM-10R	39.74	3.79	2.27
CM02	AAM-20R	34.60	4.57	2.60
	AAM-30R	23.72	6.99	3.79
	CAAM 03	44.95	3.18	2.01
	AAM-10R	38.96	3.86	2.32
CM03	AAM-20R	32.98	4.79	2.73
	AAM-30R	27.15	6.11	3.31
	OPCM	30.00	2.19	9.75

However, this advantage was offset by the decrease in compressive strength caused by the rubber, leading to a negative impact on the RAAM's overall ecological index. In addition, incorporating rubber particles into the RAAM mixture led to an increase in the E_P value, indicating higher embodied CO_2 emissions. It is important to note that rubber has a lower carbon footprint when compared to natural aggregates. However, the reduction in compressive strength resulting from the use of rubber had an adverse effect on the ecological index of the RAAM, affecting its overall ecological performance. A significant finding emerged from the study, revealing that the E_P of RAAM was lower than that of OPCM. This discrepancy can be predominantly attributed to the substantial CO_2 emissions generated during cement production. This discovery highlights the imperative need to promote the advancement and application of RAAM as a strategy to mitigate environmental impacts, particularly by reducing embodied CO_2 emissions.

In terms of the influence of curing methods on the E_P values of RAAM, it was observed that the humidity curing method (CM03) exhibited notable economic efficiency. This indicates that CM03 holds promise for practical implementation in engineering projects, given the currently available preparation methods compared by CM02, which require more thermal energy (see Table 8). In terms of evaluating the embodied environmental impact, CM03 is identified as the most favorable choice for producing a cleaner AAM. It is subsequently followed by CM01, with CM02 being the least preferable option in terms of their respective environmental impacts. A comprehensive analysis of economics and environmental sustainability highlights CM03 as the preferred curing approach for RAAM. Furthermore, incorporating 5% rubber content proves ideal, meeting strength demands while unlocking significant economic and ecological benefits.

3.6 Synthesis of Discussion

The study provides a comprehensive analysis of the effects of rubber content on the properties of alkali-activated mortar (AAM), covering flowability, density, compressive strength, and water absorption. The results reveal that increasing rubber content decreases the flowability of AAM, with a reduction ranging from 8% to 20% in the flowability of RAAM mixes compared to CAAM. This decrease is attributed to increased friction between rubber particles and AAM components, increased air entrainment due to the hydrophobic nature of rubber, and lower density of rubber particles. However, pre-treatment with NaOH appears to enhance interface performance, mitigating the adverse effects of rubber content on flowability. Additionally, incorporating rubber reduces both fresh and hardened densities of AAM, with reductions of 2.9% to 10% in fresh density and 183 Kg/m^3 to 230 Kg/m^3 in hardened density for 30% rubber substitution levels. Curing methods significantly influence compressive strength, with higher curing temperatures generally favouring increased strength. However, a curing temperature of 60°C appears optimal for compressive strength development, with an increase of 50.52% compared to other curing methods. Furthermore, water absorption increases with higher rubber content, with increases from 7.34% to 8.29% for oven curing and from 7.43% to 8.57% for chamber curing. Economic and ecological analyses reveal that incorporating rubber increases costs and environmental footprint compared to natural sand, with a notable increase in costs per unit of compressive strength and carbon footprint. In summary, this study provides valuable insights for informed decision-making in construction practices, considering both performance and sustainability considerations.

4. Conclusions

Based on this study, it is concluded that:

- The results show a gradual decrease in compressive strength with increasing rubber particles content, indicating a negative correlation between rubber content and compressive strength.
- Curing methods have a significant impact on AAM properties, with 60°C oven curing (CM02) markedly improves compressive strength compared to other conditions.
- Flowability tests reveal that adding rubber particles reduces the flowability of AAM mixes, with decreases of up to 20%, highlighting the marked influence of rubber on the workability of the materials.
- The incorporation of rubber particles reduces the density of AAMs, thereby helping to improve the thermal and acoustic properties of the composite, while exhibiting a significantly lower average specific density than that of sand.
- A strong correlation ($R^2 \approx 0.88$) between 28-day compressive strength and water absorption was identified, suggesting that reduced porosity enhance the strength of cementitious materials. ANOVA analyses confirm the significant importance of the established models, with P values less than 0.05, indicating a significant relationship between predictors and responses.
- The incorporation of rubber increases the water absorption of AAMs in proportion to the substitution rate regardless of the curing method. In contrast, the absorption of control samples without rubber decreases with CM02 heat curing by about 18%.
- Economic and ecological analysis highlights that CM02 curing presents notable economic efficiency, suggesting significant practical application potential, in addition to being identified as the most favorable choice for producing environmentally cleaner AAM.

These experimental results highlight that the integrating rubber into AAM materials significantly influences their physical and mechanical properties. Although the addition of rubber decreases compressive strength and flowability, it enhances the thermal and acoustic performance of the composite. Moreover, this research sheds light on the considerable impact of the MA02 curing method at 60°C on AAM properties. This approach stands out markedly by its significant enhancement of AAM compressive strength, outperforming results obtained with other methods. The economic and ecological analysis underscores the efficiency of 60°C oven curing offering a promising pathway for the production of a more environmentally friendly and economically viable material.

5. Limitations of the Current Study

While the study sheds light on the impact of rubber content on various properties of alkali-activated mortar (AAM), it has several limitations. Firstly, its findings may not be widely applicable beyond the specific experimental conditions and materials used. Additionally, the focus on short-term analysis up to 28 days limits insights into long-term performance and durability. The study's emphasis on rubber content overlooks other factors that could influence AAM properties, such as the type of activator, precursor nature, etc. Recognizing these limitations underscores the need for further research to address these gaps and provide a more holistic evaluation of AAM's performance and applicability.

6. Future Recommendations

The study highlights the effects of rubber content on alkali-activated mortar (AAM) properties, but it has limitations. It primarily focuses on short-term analysis and overlooks other factors like the type of activator and curing conditions. Future research should explore long-term performance, optimize rubber incorporation methods, conduct field

trials, compare AAM with conventional materials, and expand economic and environmental assessments. These efforts will enhance understanding and optimize the use of rubber-incorporated AAM in construction for sustainable infrastructure development.

Acknowledgement

The authors gratefully acknowledge the Civil Engineering Laboratory at the University of Bordj Bou Arreridj and its staff for enabling the experimental work carried out in this study.

References

[1] Luukkonen, T., et al., One-part alkali-activated materials: A review. Cement and Concrete Research, 2018. 103: p. 21-34. https://doi.org/10.1016/j.cemconres.2017.10.001

[2] Jain, A. and S. Marathe, Soft computing modeling on air-cured slag-fly ash-glass powder-based alkali activated masonry elements developed using different industrial waste aggregates. Asian Journal of Civil Engineering, 2023: p. 1-13. https://doi.org/10.1007/s42107-023-00584-7

[3] Amran, Y.M., et al., Clean production and properties of geopolymer concrete; A review. Journal of Cleaner Production, 2020. 251: p. 119679. https://doi.org/10.1016/j.jclepro.2019.119679

[4] Singh, N., M. Kumar, and S. Rai, Geopolymer cement and concrete: Properties. Materials Today: Proceedings, 2020. 29: p. 743-748. https://doi.org/10.1016/j.matpr.2020.04.513

[5] Hills, T., N. Florin, and P.S. Fennell, Decarbonising the cement sector: a bottom-up model for optimising carbon capture application in the UK. Journal of Cleaner Production, 2016. 139: p. 1351-1361. https://doi.org/10.1016/j.jclepro.2016.08.129

[6] Nakkeeran, G. and L. Krishnaraj, Developing lightweight concrete bricks by replacing fine aggregate with vermiculite: A regression analysis prediction approach. Asian Journal of Civil Engineering, 2023: p. 1-9. https://doi.org/10.1007/s42107-023-00586-5

[7] De Azevedo, A.R., et al., Use of glass polishing waste in the development of ecological ceramic roof tiles by the geopolymerization process. International Journal of Applied Ceramic Technology, 2020. 17(6): p. 2649-2658. https://doi.org/10.1111/ijac.13585

[8] Diaz-Loya, E.I., E.N. Allouche, and S. Vaidya, Mechanical properties of fly-ash-based geopolymer concrete. ACI materials journal, 2011. 108(3): p. 300.

[9] Hossain, F.Z., et al., Mechanical properties of recycled aggregate concrete containing crumb rubber and polypropylene fiber. Construction and Building Materials, 2019. 225: p. 983-996. https://doi.org/10.1016/j.conbuildmat.2019.07.245

[10] Sofi, A., Effect of waste tyre rubber on mechanical and durability properties of concrete–A review. Ain Shams Engineering Journal, 2018. 9(4): p. 2691-2700. https://doi.org/10.1016/j.asej.2017.08.007

[11] Association, U.T.M., US scrap tire management summary. US Tire Manufacturers Association: Washington, DC, USA, 2018.

[12] Long, W.-J., et al., Sustainable use of recycled crumb rubbers in eco-friendly alkali activated slag mortar: Dynamic mechanical properties. Journal of cleaner production, 2018. 204: p. 1004-1015. https://doi.org/10.1016/j.jclepro.2018.08.306

[13] Ameri, F., et al., Partial replacement of copper slag with treated crumb rubber aggregates in alkali-activated slag mortar. Construction and Building Materials, 2020. 256: p. 119468. https://doi.org/10.1016/j.conbuildmat.2020.119468

[14] Ameur Belmouhoub, Assia Abdelouahed, and Ammar Noui, Experimental and factorial design of the mechanical and physical properties of concrete containing waste rubber Powder. Res. Eng. Struct. Mater.2023. http://dx.doi.org/10.17515/resm2023.54me0810rs
[15] Chiker, T., et al., Sodium sulfate and alternative combined sulfate/chloride action on ordinary and self-consolidating PLC-based concretes. Construction and Building Materials, 2016. 106: p. 342-348. https://doi.org/10.1016/j.conbuildmat.2015.12.123
[16] Zhao, J., et al., Workability, compressive strength, and microstructures of one-part rubberized geopolymer mortar. Journal of Building Engineering, 2023. 68: p. 106088. https://doi.org/10.1016/j.jobe.2023.106088
[17] Qaidi, S.M., et al., Rubberized geopolymer composites: A comprehensive review. Ceramics International,2022.48(17):p.24234-24259. https://doi.org/10.1016/j.ceramint.2022.06.123
[18] Park, Y., et al., Compressive strength of fly ash-based geopolymer concrete with crumb rubber partially replacing sand. Construction and Building Materials, 2016. 118: p. 43-51. https://doi.org/10.1016/j.conbuildmat.2016.05.001
[19] Athira, V., et al., Influence of different curing methods on mechanical and durability properties of alkali activated binders. Construction and Building Materials, 2021. 299: p. 123963. https://doi.org/10.1016/j.conbuildmat.2021.123963
[20] Valente, M., et al., Reducing the emission of climate-altering substances in cementitious materials: A comparison between alkali-activated materials and Portland cement-based composites incorporating recycled tire rubber. Journal of Cleaner Production, 2022. 333: p. 130013. https://doi.org/10.1016/j.jclepro.2021.130013
[21] Gill, P., et al., Effects of various additives on the crumb rubber integrated geopolymer concrete.CleanerMaterials,2023.8:p.100181. https://doi.org/10.1016/j.clema.2023.100181
[22] Zeyad, A.M., et al., Impact of rice husk ash on physico-mechanical, durability and microstructural features of rubberized lightweight geopolymer composite. Construction andBuildingMaterials,2024.427:p.136265. https://doi.org/10.1016/j.conbuildmat.2024.136265
[23] Haruna, S., et al., Effect of paste aggregate ratio and curing methods on the performance of one-part alkali-activated concrete. Construction and Building Materials, 2020. 261: p. 120024. https://doi.org/10.1016/j.conbuildmat.2020.120024
[24] Trincal, V., et al., Effect of drying temperature on the properties of alkali-activated binders-recommendations for sample preconditioning. Cement and Concrete Research, 2022. 151: p. 106617. https://doi.org/10.1016/j.cemconres.2021.106617
[25] Liu, J., et al., Study the Mechanical Properties of Geopolymer under Different Curing Conditions. Minerals, 2023. 13(5): p. 690. https://doi.org/10.3390/min13050690
[26] Luhar, S., S. Chaudhary, and U. Dave, Effect of different parameters on the compressive strength of rubberized geopolymer concrete. Multi-Disciplinary Sustainable Engineering: Current and Future Trends, 2016: p. 77-86.
[27] Rajendran, M. and M. Akasi, Performance of crumb rubber and nano fly ash based ferro-geopolymer panels under impact load. KSCE Journal of civil engineering, 2020. 24: p. 1810-1820. https://doi.org/10.1007/s12205-020-0854-z
[28] Luhar, S., S. Chaudhary, and I. Luhar, Thermal resistance of fly ash based rubberized geopolymer concrete. Journal of Building Engineering, 2018. 19: p. 420-428. https://doi.org/10.1016/j.jobe.2018.05.025
[29] Kaveh, A. and N. Khavaninzadeh. Efficient training of two ANNs using four meta-heuristic algorithms for predicting the FRP strength. in Structures. 2023. Elsevier. https://doi.org/10.1016/j.istruc.2023.03.178
[30] Narasimha Reddy, P. and J. Ahmed Naqash, Experimental study on TGA, XRD and SEM analysis of concrete with ultra-fine slag. International Journal of Engineering, 2019. 32(5): p. 679-684. https://doi.org/10.5829/ije.2019.32.05b.09

[31] Rathee, M., A. Misra, and J. Kolleboyina, Study of mechanical properties of geopolymer mortar prepared with fly ash and GGBS. Materials Today: Proceedings, 2023. 93: p. 377-386. https://doi.org/10.1016/j.matpr.2023.07.360
[32] Zhang, H.-Y., J.-C. Liu, and B. Wu, Mechanical properties and reaction mechanism of one-part geopolymer mortars. Construction and Building Materials, 2021. 273: p. 121973. https://doi.org/10.1016/j.conbuildmat.2020.121973
[33] Pham, T.M., et al., Durability characteristics of lightweight rubberized concrete. Construction and Building Materials, 2019. 224: p. 584-599. https://doi.org/10.1016/j.conbuildmat.2019.07.048
[34] advanced drying technique. Agriculture and Agricultural Science Procedia, 2014. 2: p. 26-32. https://doi.org/10.1016/j.aaspro.2014.11.005
[35] C1437, A., Standard Test Method for Flow of Hydraulic Cement Mortar. ASTM International, 1999: p. ASTM C1437-01.
[36] C642-13, A., Standard Test Method for Density, Absorption, and Voids in Hardened Concrete. ASTM International, 2013.
[37] Standard, E., Methods of testing cement-Part 1: Determination of strength. Turkish Standards Institute, Ankara, Turkey, 2009.
[38] EN.1015-18, Methods of Test for Mortar for Masonry: Determination of Water Absorption Coefficient Due to Capillary Action of Hardened Mortar 2002.
[39] Hamidi, F., A. Valizadeh, and F. Aslani. The effect of scoria, perlite and crumb rubber aggregates on the fresh and mechanical properties of geopolymer concrete. in Structures. 2022. Elsevier. https://doi.org/10.1016/j.istruc.2022.02.031
[40] Pham, T.M., Y.Y. Lim, and M. Malekzadeh, Effect of pre-treatment methods of crumb rubber on strength, permeability and acid attack resistance of rubberised geopolymer concrete. Journal of Building Engineering, 2021. 41: p. 102448. https://doi.org/10.1016/j.jobe.2021.102448
[41] Sheraz, M., et al., Fresh and hardened properties of waste rubber tires based concrete: a state art of review. SN Applied Sciences, 2023. 5(4): p. 119. https://doi.org/10.1007/s42452-023-05336-5
[42] Wongsa, A., et al., Mechanical and thermal properties of lightweight geopolymer mortar incorporating crumb rubber. Journal of Cleaner Production, 2018. 195: p. 1069-1080. https://doi.org/10.1016/j.jclepro.2018.06.003
[43] Abd-Elaty, M.A.A., M.F. Ghazy, and O.H. Khalifa, Mechanical and Impact Properties of Fibrous Rubberized Geopolymer Concrete. Mansoura Engineering Journal, 2023. 48(4): p. 5. https://doi.org/10.58491/2735-4202.3054
[44] Zhai, S., et al., Effect of modified rubber powder on the mechanical properties of cement-based materials. Journal of Materials Research and Technology, 2022. 19: p. 4141-4153. https://doi.org/10.1016/j.jmrt.2022.06.070
[45] Nematollahi, B., J. Sanjayan, and F.U.A. Shaikh, Synthesis of heat and ambient cured one-part geopolymer mixes with different grades of sodium silicate. Ceramics International, 2015. 41(4): p. 5696-5704. https://doi.org/10.1016/j.ceramint.2014.12.154
[46] Lương, Q.-H., et al., Effects of crumb rubber particles on mechanical properties and sustainability of ultra-high-ductile slag-based composites. Construction and Building Materials, 2021. 272: p. 121959. https://doi.org/10.1016/j.conbuildmat.2020.121959
[47] Ali, I.M., A.S. Naje, and M.S. Nasr, Eco-friendly chopped tire rubber as reinforcements in fly ash based geopolymer concrete. Glob. Nest J., 2020. 22: p. 342-7. https://doi.org/10.30955/gnj.003192
[48] Kirgiz, M.S., Advancements in mechanical and physical properties for marble powder–cement composites strengthened by nanostructured graphite particles. Mechanics of Materials, 2016. 92: p. 223-234. https://doi.org/10.1016/j.mechmat.2015.09.013
[49] Dean, A. and D. Voss, Design and analysis of experiments. 1999: Springer. https://doi.org/10.1007/0-387-22634-6_15

[50] Lawson, J., Design and Analysis of Experiments with R. Vol. 115. 2014: CRC press.
[51] Kaveh, A., Applications of metaheuristic optimization algorithms in civil engineering. 2017: Springer.
[52] Khanzadi, M., et al., Optimization of building components with sustainability aspects in BIM environment: Optimization of building components with sustainability aspects in BIM environment. Periodica Polytechnica Civil Engineering, 2019. 63(1): p. 93-103. https://doi.org/10.3311/PPci.12551
[53] Goupy, J. and L. Creighton, Introduction to design of experiments with JMP examples. 2007: SAS publishing. https://doi.org/10.1145/3289402.3289534
[54] Xie, J., et al., Effects of the addition of silica fume and rubber particles on the compressive behaviour of recycled aggregate concrete with steel fibres. Journal of Cleaner Production, 2018. 197: p. 656-667. https://doi.org/10.1016/j.jclepro.2018.06.237
[55] Yahya, Z., et al. Durability of fly ash based geopolymer concrete infilled with rubber crumb in seawater exposure. in IOP Conference Series: Materials Science and Engineering. 2018. IOP Publishing. https://doi.org/ 10.1088/1757-899X/374/1/012069
[56] Al Bakria, A.M., et al., The effect of curing temperature on physical and chemical properties of geopolymers. Physics Procedia, 2011. 22: p. 286-291. https://doi.org/10.1016/j.phpro.2011.11.045
[57] Mathew, G. and B. Joseph, Flexural behaviour of geopolymer concrete beams exposed to elevated temperatures. Journal of Building Engineering, 2018. 15: p. 311-317. https://doi.org/10.1016/j.jobe.2017.09.009
[58] Dehdezi, P.K., S. Erdem, and M.A. Blankson, Physico-mechanical, microstructural and dynamic properties of newly developed artificial fly ash based lightweight aggregate–Rubber concrete composite. Composites Part B: Engineering, 2015. 79: p. 451-455. https://doi.org/10.1016/j.compositesb.2015.05.005
[59] Ma, C., et al., Preparation of cleaner one-part geopolymer by investigating different types of commercial sodium metasilicate in China. Journal of Cleaner Production, 2018. 201: p. 636-647. https://doi.org/10.1016/j.jclepro.2018.08.060
[60] Samarakoon, M., et al., Properties of one-part fly ash/slag-based binders activated by thermally-treated waste glass/NaOH blends: A comparative study. Cement and Concrete Composites, 2020. 112: p. 103679. https://doi.org/10.1016/j.cemconcomp.2020.103679
[61] Ma, C., et al., Properties and characterization of green one-part geopolymer activated by composite activators. Journal of Cleaner Production, 2019. 220: p. 188-199. https://doi.org/10.1016/j.jclepro.2019.02.159
[62] Chiaia, B., et al., Eco-mechanical index for structural concrete. Construction and Building Materials, 2014. 67: p. 386-392. https://doi.org/10.1016/j.conbuildmat.2013.12.090
[63] Maddalena, R., J.J. Roberts, and A. Hamilton, Can Portland cement be replaced by low-carbon alternative materials? A study on the thermal properties and carbon emissions of innovative cements. Journal of Cleaner Production, 2018. 186: p. 933-942. https://doi.org/10.1016/j.jclepro.2018.02.138
[64] Perez-Cortes, P. and J.I. Escalante-Garcia, Alkali activated metakaolin with high limestone contents–Statistical modeling of strength and environmental and cost analyses. Cement and Concrete Composites, 2020. 106: p. 103450. https://doi.org/10.1016/j.cemconcomp.2019.103450
[65] Jiang, M., et al., Comparative life cycle assessment of conventional, glass powder, and alkali-activated slag concrete and mortar. Journal of Infrastructure Systems, 2014. 20(4): p. 04014020. https://doi.org/10.1061/(ASCE)IS.1943-555X.0000211

Research on Engineering Structures & Materials
www.jresm.org
Research Group

Research Article

Improving early strength and durability of eco-friendly mortars: Investigating the influence of limestone filler fineness and blast furnace slag combination

Ammar Noui[1, a], Ahmed Abderraouf Belkadi[1,b], Leila Zeghichi[2,c], Oussama Kessal[1,d], Mohammed Sallah Bouglada[3,e], Yacine Achour[1,f], João Castro Gomes[4,g]

[1]*Department of Civil Engineering Faculty of Sciences and Technology University Mohamed El Bachir El Ibrahimi of Bordj Bou Arreridj ElAnasser 34030 Algeria*
[2]*Department of Civil Engineering and Hydraulic Mohamed Khider University Biskra Algeria*
[3]*Department of Civil Engineering Batna 2 University Algeria*
[4]*C-MADE Centre of Materials and Building Technologies Covilhã UBI University Portugal*

Article Info

Article history:

Received 07 Apr 2024
Accepted 01 July 2024

Keywords:

Blast furnace slag;
Limestone filler;
Ternary mortars;
Carbonation;
Chemical attack;
Durability

Abstract

This study investigates eco-friendly approaches for enhancing the early mechanical strength and durability of mortars utilizing slag. a byproduct of the steel industry. Mortars incorporating slag often exhibit inferior strength and durability compared to those made with cement. The objective is to ameliorate these properties through the incorporation of limestone filler (LF) and granulated ground blast furnace slag (BFS) at varying proportions. either independently or in combination. The physical properties (gas permeability). mechanical properties (compressive and flexural strength at 2. 7. 28. 365. 1095 days). and durability (HCL chemical attack and carbonation) of the resultant mortars were assessed. along with their microstructure using scanning electron microscopy and mercury porosimeter. Experimental findings indicate that the inclusion of LF enhances the initial strength of ternary mortars containing 10-17.5% LF and 10-25% BFS. while subsequent hydration of BFS yields mortars with comparable or superior compressive strength and resistance to chemical attack (HCL) relative to the reference mortar after 365 days.

1. Introduction

The chemical production process of Portland cement, which involves the use of clinker. accounts for 60-65% of CO_2 emissions during its manufacture [1,2]. Moreover. the clinkering process exerts a significant impact on natural sources of raw materials. which are depleting at an alarming rate [3]. Various strategies have been proposed to mitigate anthropogenic CO_2 emissions linked to clinker production by 5-8%. Among the technological solutions suggested. substituting clinker with industrial or natural waste shows promise in reducing total CO_2 emissions by approximately 37% [3,4].

Blast furnace slag (BFS) isn't just an add-on in concrete production; it's a sustainability champion. By incorporating BFS. concrete gains improved workability for easier placement. reduced heat of hydration to minimize cracking. enhanced long-term strength for lasting structures. and all while significantly lowering greenhouse gas emissions thanks to its partial replacement of clinker in cement [5-8]. However. a significant drawback of

*Corresponding author: ahmedabderraouf.belkadi@univ-bba.dz
[a] orcid.org/0009-0005-6325-7131; [b] orcid.org/0009-0002-5978-9774; [c]orcid.org/0000-0003-2886-0339; [d]orcid.org/0000-0002-3669-6164; [e]orcid.org/0000-0001-9455-8686 [f] orcid.org/0000-0003-4249-5884; [g]orcid.org/0000-0002-2694-5462
DOI: http://dx.doi.org/10.17515/resm2024.226ma0407rs

incorporating slag into Portland cement is its poor early-age strength. particularly evident at high replacement levels. attributed to the slow hydration kinetics of this cementitious additive [9-11]. To mitigate this limitation. numerous studies have been undertaken to expedite the hydration processes of slag within cementitious solutions [12,13]. Bougara et al. [12]. suggest that the activation of hydration mechanisms at an early stage can be achieved through physical. thermal. or chemical means. Additionally. limestone filler (LF) has emerged as a recent addition to binary cementitious systems incorporating BFS [14,15]. Ternary mortars comprising LF and BFS demonstrate a superior cost-effectiveness ratio and reduced environmental footprint compared to slag-based materials [16]. leading to enhanced hydration levels attributed to the dilution effect within the cement paste containing slag [17].

The primary drawback of incorporating slag into Portland cement is the poor early-age strength. especially noticeable at high replacement levels. owing to the slow development of hydration in this cementitious addition[9-11].To mitigate this issue. various studies have endeavored to expedite the hydration reactions of slag within cement solutions. Bougara et al. [12]report that the activation of hydration processes at an early age can occur through physical. thermal. or chemical means. activation of hydration processes at an early age being physical. thermal or chemical [13]. The incorporation of limestone filler (LF) into binary blends containing blast furnace slag (BFS) is a recent innovation. This development has led to ternary mortars with LF and BFS boasting a more favorable cost-effectiveness ratio and a reduced environmental footprint compared to traditional slag-based materials [14,15] [16]. This leads to improved hydration levels due to the dilution effect in the cement paste containing slag [17] [18].Berodier et al. [19]note that the rate of substitution and the fineness of the mineral addition introduced depend on this mechanism. Moreover. the presence of limestone in Portland cement leads to the formation of carboaluminate due to reactions between C_3A and $CaCO_3$. However. this production is limited to ages below 3 days because of the complete consumption of C_3A. In contrast. in ternary mortars containing limestone and a source of aluminosilicate. the aluminate-carbonate reaction persists at later ages. For instance. mixtures based on fly ash and limestone exhibit carboaluminates present up to 90 days [20,21]. as do mixtures of metakaolin-limestone [22]. This results in an increase in compactness and mechanical strength due to the stabilization of ettringite, which causes an expansion in the volume of hydrates. thereby enhancing hydration levels [23,24] [17]. This study builds upon prior research investigating the properties of ternary composites combining ordinary Portland cement (OPC). LF. BFS. Previous studies have shown that these composites offer promising benefits. Gao et al. [25] found that incorporating 10% LF enhances the early-age compressive strength of BFS concrete while reducing CO_2 emissions and production costs. Similarly. Carraco et al. [26]demonstrated that. within the LF-BFS-OPC ternary mixture. LF and BFS contribute to increased early and later compressive strength. respectively.

Building on this concept. Menéndez et al. [27] developed a model to identify the ideal ternary mix for maximum strength and minimal porosity. Their model predicted a mortar containing 10% limestone and 10% slag for peak early-age compressive strength. Conversely. for later stages. the optimal mix shifted to an Ordinary Portland Cement (OPC) blend with 35% Blast Furnace Slag (BFS) and 7.5% Limestone Filler (LF) to achieve superior physical and mechanical properties. Deboucha et al. [9]studied how limestone and slag influence the chemical reactions in which water is absorbed by ternary cements. Their findings revealed that the degree of hydration is dependent on both the replacement level of these additives and the water-to-binder ratio employed.

Yu et al. [28] suggested that LF and BFS have the potential to enhance cement hydration and homogenize mixtures. thereby reducing pores. particularly in regions near aggregates

due to their filling effect and nucleation sites. when used in fabricating ternary composites. Xuan et al. [29] found that limestone filler (LF) and slag (BFS) work together to enhance a certain process (synergistic effect). while Adu-Amankwah et al. [17] noted that these same ternary blends (OPC-LF-BFS) have a low aluminum to silicon ratio (Al/Si). Arora et al. [30] established a linear function correlating monocarbonate formation with carbonate consumption.

Line with previous research. Bouaskeret et al. [14] reported that incorporating limestone filler (LF) between 10% and 20% effectively hinders the development of endogenous shrinkage and prevents initial cracking in cement-blast furnace slag (BFS) systems. Similarly. Itimet et al. [31]hey discovered that adding up to 15% limestone filler (LF) with the right amount of slag (BFS) can lessen the concrete's shrinkage caused by water loss. Investigating the impact of limestone fineness. Briki et al. [32]found that replacing 20% of clinker with finer limestone (BSS = 4.21 m^2/g) resulted in comparable strength to OPC up to 7 days. This improvement is attributed to enhanced cement hydration. which compensates for the dilution effect of limestone.

However. despite these prior studies. there remains a significant gap in research regarding ternary mortars. For instance. microscopic analyses to comprehend macroscopic phenomena must be undertaken. Therefore. an exhaustive investigation was imperative to elucidate the impacts of dilution and nucleation in ternary mixtures (OPC-LF-BFS). Additionally. the effects of Blaine specific surface area (BSS) of slag and limestone on ternary composites have not been thoroughly explored based on previous research. According to the authors of this study. no research was found on the long-term mechanical behavior (365 and 1095 days) of ternary mortars (OPC-LF-BFS). Consequently. the durability of ternary cement-limestone-slag mortars has seldom been examined.

To address these existing research gaps. this study scrutinizes the microstructural. mechanical properties. and durability of OPC-LF-BFS ternary mortars. Various experimental tests were conducted to evaluate compression and bending resistance (at ages of 2. 7. 28. 365. and 1095 days). employing scanning electron microscopy (SEM). mercury porosimetry (MIP). gauze permeability. carbonation. and chemical attack (HCl).

The principal findings of this study are as follows: firstly. the properties of the ternary mixture were analyzed using both macroscopic and microscopic tests. Secondly. the experimental results delineated the effects of limestone and slag fineness and substitution rate. Thirdly. the durability of OPC-LF-BFS ternary mortars was assessed through immersion in 1.5% HCl solution. carbonation testing. and gauze permeability analysis.

2. Materials and Methods

2.1. Materials

In experimental tests. Portland clinker sourced from the Ain-El-Kébira cement plant (Sétif-Algeria) was ground to a fineness of 350 m^2/kg. Gypsum. obtained from natural rock quarries near the same cement plant. with a 3% content rate. was utilized. with a hydrated calcium sulphate ($CaSO_4 \bullet 2H_2O$) level of 76.4%. Granulated blast furnace slag (BFS) from El HADJAR. consisting of spherical grains with a particle size class of 0/5 mm. and limestone fillers (LF) from limestone rock deposits. were also ground to various Blaine-specific surface areas (BSS). The particle size distributions of the raw materials are depicted in Fig. 1. illustrating that limestone and slag contained a higher volume of fine particles compared to clinker.

Chemical compositions. determined by X-ray fluorescence (XRF) analysis. and physical properties (Blaine-specific surface and density) of OPC. LF. and BFS are presented in Tables 1 and 2. respectively.

Table 1. Chemical compositions of all powders used (wt. %)

	Clinker	Gypsum	Slag	Limestone filler
CaO	63.73	22.5	43.2	45.85
SiO_2	21.42	3.8	41.1	12.74
Al_2O_3	4.58	0.5	7	1.65
Fe_2O_3	4.96	0.1	2.8	0.58
MgO	1.43	0.58	4.7	0.73
Na_2O	0.24	-	0.6	-
K_2O	0.32	-	0.32	0.24
SO_3	0.72	32.84	0.25	0.11
L.O.I	2.62	39.09	-	37.54

Table 2. The Blaine specific surface area (BSS) and density of all powders

	Clinker	Gypsum	Slag	Limestone filler
BSS1 (m^2/kg)	350	350	350	350
BSS2(m^2/kg)	-	-	550	550
Absolute density (kg/m^3)	3200	2340	2800	2600
Apparent density(kg/m^3)	1300	980	1000	1030

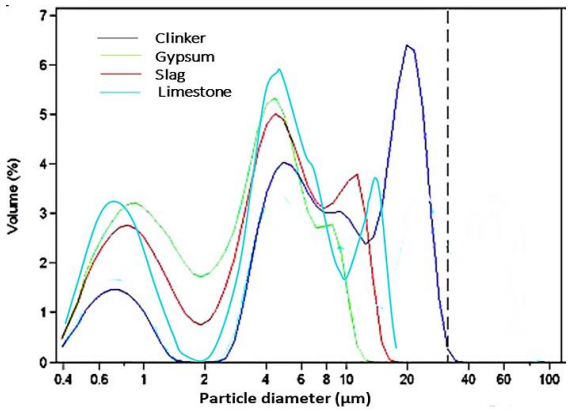

Fig. 1. Particle size analysis of clinker. slag and limestone

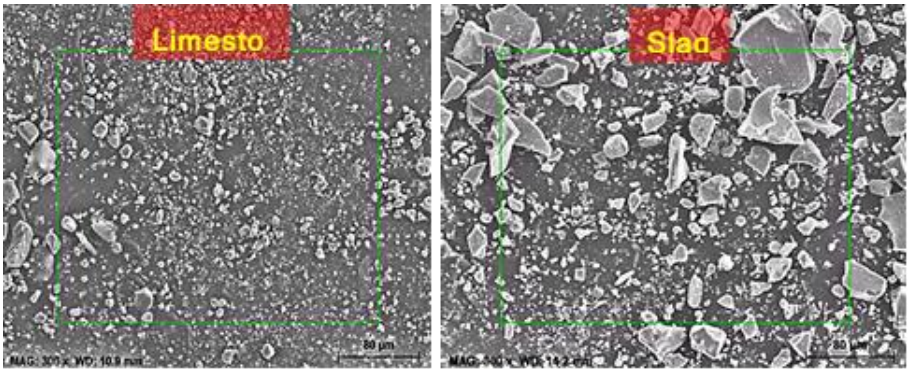

Fig. 2. SEM images of the raw materials

Additionally. standardized siliceous sand (0/3). meeting EN196-1 [33] standards. was employed. Fig. 2 showcases the particle morphologies of blast furnace slag and limestone filler powders. Coarse BFS particles larger than 10 µm exhibit a crushed gravel appearance with a uniform shape. a highly compact morphological structure. and a smooth surface.

2.2. Preparation of Mixtures

This study adhered to EN 196-1 standard [33] for mortar preparation. incorporating limestone filler (LF) and granulated blast furnace slag (BFS) as partial cement replacements (up to 35% by weight) in various combinations with differing fineness (refer to Table 3). A fixed water-to-binder ratio of 0.50 and sand-to-cement ratio of 3:1 were maintained for all mixtures. After casting in molds for 24 hours. the mortars were cured by immersion in water at a controlled temperature (23°C ± 2°C). The specific composition details for each mixture are provided in Table 3.

Table 3. Mixtures proportions

	Mixture (ID) Labels	Clinker (%)	Gypsum (%)	BFS (%)	LF (%)	W/L
1	0S-0L	97	3	-	0.5	0.5
2	3S-0L	62	3	-	0.5	0.5
3	0S-35L	62	3	35	0.5	0.5
4	10S1-25L1	62	3	10	25	0.5
5	10S2-25L1	62	3	10	25	0.5
6	10S1-25L2	62	3	10	25	0.5
7	10S2-25L2	62	3	10	25	0.5
8	17S1-17L1	62	3	17.5	17.5	0.5
9	17S1-17L2	62	3	17.5	17.5	0.5
10	17S2-17L1	62	3	17.5	17.5	0.5
11	17S2-17L2	62	3	17.5	17.5	0.5
12	25S1-10L1	62	3	10	25	0.5
13	25S1-10L2	62	3	10	25	0.5
14	25S2-10L1	62	3	10	25	0.5
15	25S2-10L2	62	3	10	25	0.5

2.3. Experimental Tests

Table 4 shows the experimental tests used in this study. their fields of application and measurement times.

Table 4. Experimental methods and fields of applications

Method	Test sample	Test time
Compressive strength	All samples (Mixtures from 1 to 15)	2. 7. 28. 365 and 1095 days
Flexural strength	All samples (Mixtures from 1 to 15)	2. 7. 28. 365 and 1095 days
Permeability	Mixtures (Mixtures1.2.3 and 8)	28 Days
Carbonation	Mixtures (Mixtures1.2.3 and 8)	28 Days+15 Days (in the carbonation chamber)
SEM	Mixtures (5. 9.11. 13 and 14)	365 Days
MIP	Mixtures (1.2.3. 5. 9.11. 13 and 14)	365 Days
Chemical attacks (1.5 % HCL)	All samples (Mixtures from 1 to 15)	200 Days

2.3.1. Compressive and Flexural Strength

The compression and flexural strength tests were conducted using an apparatus with a maximum capacity of 3000 KN. These mechanical properties were determined in accordance with standard [33]. The molds used had dimensions of 40 × 40 × 160 mm. Four samples of each mixture were tested at 2. 7. 28. 365. and 1095 days after casting. The average strength value was used to represent the ultimate flexural and compressive strength for each mixture.

2.3.2. Scanning Electron Microscope (SEM)

To better understand the macrostructural phenomena. a microstructural analysis of various mixtures was performed after 365 days using a Hitachi S-3400N scanning electron microscope (SEM).

2.3.3. Mercury Porosimeter

Mercury intrusion porosimeter (MIP) is a technique employed in this study to analyze the pore size distribution within the mortar samples [34,35]. An Autopore IV-Micromeritics mercury porosimeter was used. capable of applying high pressures (up to 414 MPa) to force mercury into pores as small as 3.6 nanometers and as large as 360 micrometers. By analyzing the pressure required for mercury intrusion. researchers can determine the distribution of pore sizes within the mortars.

2.3.4. Oxygen Permeability

The O2 oxygen permeability method. which evaluates gas penetration resistance and transfer properties in cementitious mortars. was employed. After drying in a 105°C oven until constant weight was achieved (48 hours). 11 cm diameter and 5 cm thick specimens were laterally sealed and vertically confined to ensure unidirectional radial oxygen flow. Intrinsic permeability (Kint) was then calculated from apparent permeability (Ka) measurements at three absolute pressures (2. 3. and 4 bar) using the inverse of the average pressure (refer to equation 1 for details).

$$Ka = 2Q * P_{atm} * L * \frac{\mu}{P_2 - P_{atm2}} * A \quad (1)$$

Where Q is the volume flow at the inlet (cm3/s). μ is the dynamic viscosity of oxygen at 20°C±2°C equal to 2.0210−5 Pa. P is the absolute pressure at l input (bar). Patm is the atmospheric pressure (bar). L is the thickness of the sample (m) and A the section (m^2).

The Klinkenberg approach [36] was employed to isolate the intrinsic permeability. representing only the viscous flow of the permeating fluid. This value is determined through linear regression of various apparent permeability values in relation to the inverse of the average pressure (calculated as the mean between atmospheric pressure and gas inlet pressure) [37] [38]. It is defined as follows:

$$K = K_{int}(1 + \frac{\beta}{P_{moy}}) \quad (2)$$

$$P_{moy} = (P_0 + P_{atm})/2 \quad (3)$$

With β: the Klinkenberg coefficient. P0: atmospheric pressure and β. Kint is the slope of the Klinkenberg line.

2.3.5. Accelerated Carbonation

To assess CO_2 penetration resistance. an accelerated carbonation test based on the NF P18-458 458 standard [39] was conducted. After 28 days of water curing. cylindrical mortar

specimens (110 x 220 mm) were sectioned into four discs (approximately 5 cm thick). To ensure unidirectional carbonation. all sides except the sawn face were sealed with self-adhesive aluminum foil. Following a 14-day drying period at 60°C. one quarter of the specimens were placed in a dedicated chamber maintained at 4% CO_2. 65% ± 5% relative humidity. and 20°C for a month.

2.3.6. Chemical Attack

Following 24 hours in molds. mortar samples were cured in water for 28 days. They were then conditioned in a controlled environment (50% relative humidity. 20°C) until reaching constant weight before immersion in a 1.5% hydrochloric acid (HCl) solution for 200 days. This process simulates chemical attack. and the samples were subsequently evaluated for physical and mechanical properties to assess their durability.

3. Results and Discussion

3.1. Compressive Strength

The results of the evolution of the compressive strength of mortars formulated with slag and limestone in the short and long term were presented in Fig. 3a and 3b. respectively. At the two-day mark. the 0S-0L blend exhibited superior compressive strength compared to other mixtures. This can be attributed primarily to the dilution effect caused by the inclusion of limestone filler and slag [7,40]. Consequently. the compressive strength of 0S-35L exceeded that of 35S-0L by 19%. attributed to LF acting as nucleation sites. facilitating additional C–S–H formation and enhancing cement hydration kinetics [5,41]. Moreover. LF was noted to fill voids. increasing mixture compactness and altering reaction rates at early stages [42]. However. the combination and fineness of LF and BFS had minimal effect on compressive strength at this early stage.

Thermogravimetric analysis revealed that calcite consumption increased over time. particularly after 28 and 90 days. indicating slower calcite reaction kinetics with aluminates from slag to form hemi/monocarboaluminates [9] [30]. Although comparable compressive strengths were observed for 35S-0L and 0S-35L after 7 days. a remarkable increase in strength was noted in blends containing LF and BFS additions. For instance. mortars like 10S1-25L1. 17S1-17L1. 17S1-17L2. and 25S1-10L2 exhibited substantial increases in strength compared to 35S-0L and 0S-35L [30].

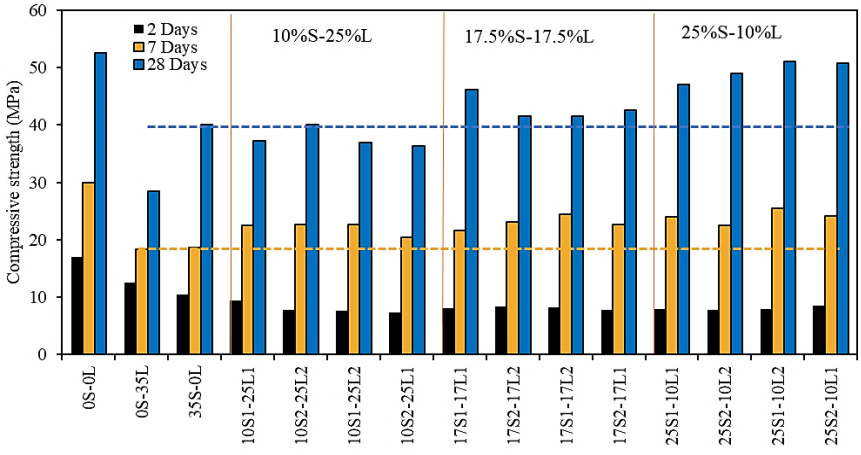

(a)

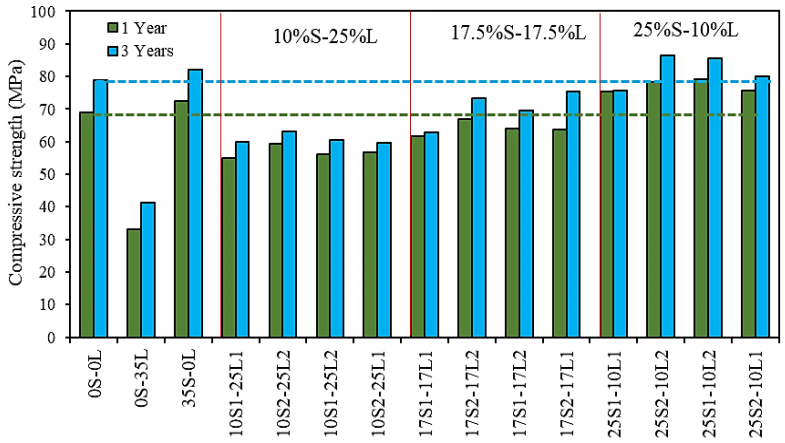

(b)

Fig. 3. The compressive strength of various mixtures in (a) the short-term and (b)long-term

This increase was attributed to the formation of hemi/monocarboaluminate. preventing ettringite transformation into monosulphate and resulting in higher total hydrate volume and hydration reaction rates [21]. However. the compressive strength of mortar with these additions was slightly lower compared to the control (0S-0L). indicating that while hemi/monocarboaluminate formation offset the dilution effect. it couldn't fully compensate for the decline in cement hydrates[43]. Additionally. LF with a higher specific surface caused higher resistance. and finely ground limestone was found to improve hydration and compensate for dilution caused by clinker reduction [32].

After 28 days. while the compressive strength of 35S-0L was significantly higher than that of 0S-35L. it remained lower than that of 0S-0L by 30.9%. Ternary blends with high slag content showed notable strength increases over 35S-0L and 0S-35L due to various factors such as nucleation of C-S-H. ettringite stabilization. and carboaluminate formation. However. the presence of LF with a high-rate induced performance decreases due to dilution. Compared to 35S-0L. certain composites like 25S1-10L1. 25S2-10L2. 25S1-10L2. and 25S2-10L1 showed increased strength. while slight decreases were observed compared to 0S-0L. Moreover. the higher fineness of additions. particularly LF. led to better performance. contributing to capillary pore filling and mortar property improvement. While ternary mixtures with low BFS content showed lower resistance compared to 0S-0L and other ternary composites after one and three years. 35S-0L exhibited higher strength compared to 0S-0L controls. Overall. the study highlights the importance of material fineness in short and long-term reactions. emphasizing the necessity of alumina sources for carboaluminates formation and the optimal LF content for improved mortar strength. Furthermore. an increase of 14% in compressive strength at the one-year mark was observed with the addition of 25% BFS and 10% LF to cementitious mortars. This underscores the significance of maintaining carboaluminate formation for extended periods. as observed in mixtures containing limestone and aluminosilicate sources [42]. The presence of AFm phases was linked to calcite and reactive aluminates from limestone and slag. potentially explaining the lower long-term resistance of certain mixtures [44]. Studies suggest that using an ideal limestone content ensures the utilization of all active alumina from pozzolans in ternary binders [45]. In this study. 10% LF was

deemed optimal. highlighting the importance of balanced material compositions for optimal mortar performance.

In summary. the fineness of materials significantly influences the reactions in ternary mixtures in both short and long terms. particularly for limestone fillers. Maintaining the formation of carboaluminates for up to three years requires adequate alumina sources in the ternary mixtures. Adding 25% slag (BFS) and 10% limestone filler (LF) boosted the mortar's compressive strength by 14% after one year. This highlights the importance of precisely formulated compositions for achieving superior mortar performance.

3.2. Flexural Strength

The flexural strength of mortars containing various additions at different ages (2. 7. 28. 365. and 1095 days) is illustrated in Figure 4(a) and (b). Similar to the compressive strength trend. flexural strength development varied across ages for different mixtures.

- At early ages (2 days). 0S-35L containing LF exhibited the highest flexural strength. likely due to improved packing and reduced capillary porosity [41].
- By 7 days. ternary blends showed similar flexural strength to the control mortar (0S-0L) and surpassed the strength of 35S-0L (BFS only). The enhanced strength is ascribed to the combined effects of limestone filler (LF) promoting nucleation and the early formation of Hemicarboaluminates (HC). which contribute to a stronger structure.
- Interestingly. long-term (1 and 3 years) results showed a greater increase in flexural strength compared to compressive strength for ternary blends with a low LF content (25% BFS. 10% LF). This suggests that carboaluminates formed in these mixtures are more effective in improving flexural strength than compressive strength [46]. This translates to stronger and more robust carboaluminate particles that contribute significantly to the enhanced mechanical performance of these eco-friendly mortars.

Overall, the flexural strength results support the findings from compressive strength analysis. highlighting the benefits of incorporating both BFS and LF in cementitious mortars. particularly at a 25% BFS and 10% LF ratio. The improved packing by LF and the formation of carboaluminates play a crucial role in strengthening these mortars over time.

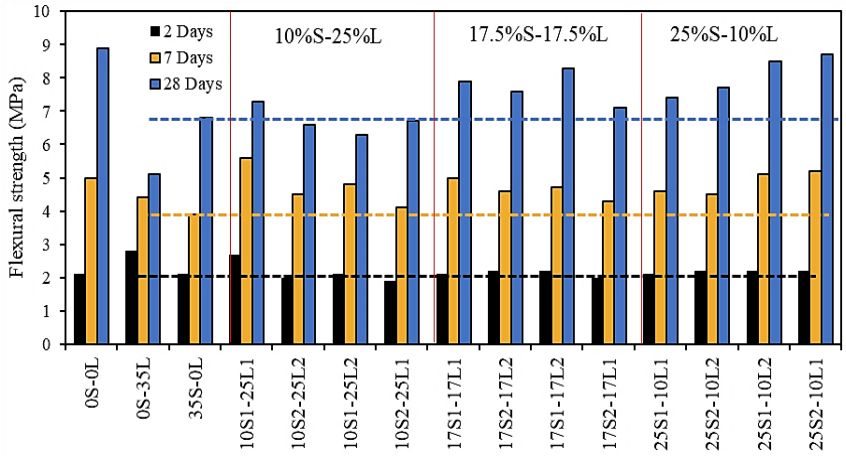

(a)

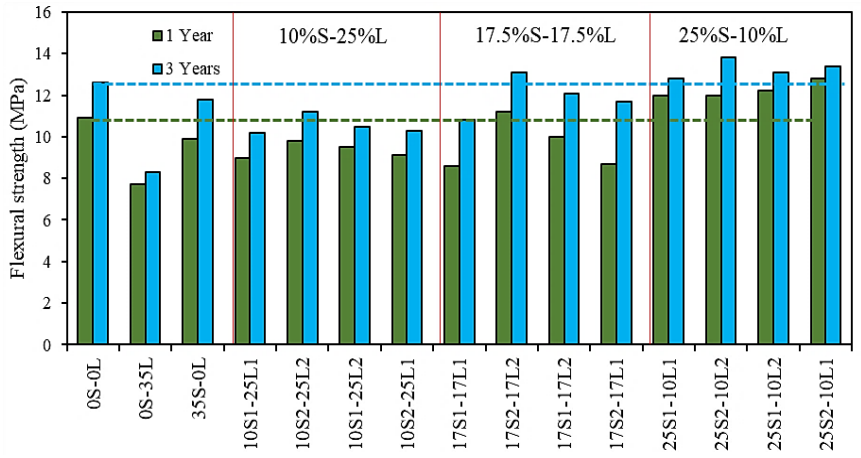

(b)

Fig. 4. Flexural strength of different mixtures in (a) the short-term and (b) long-term

3.3. Compressive vs. Flexural Strength Correlation

Figure 5 examines how well a mortar's compressive strength (resistance to crushing) translates to its flexural strength (resistance to bending) across the different mixture combinations. The results show a strong positive correlation (R^2 = 0.97). indicating that compressive strength generally increases along with flexural strength. Interestingly. the data points for early ages (2 and 7 days) are tightly clustered. while those for later ages (28 days. 1 year. and 3 years) are more dispersed.

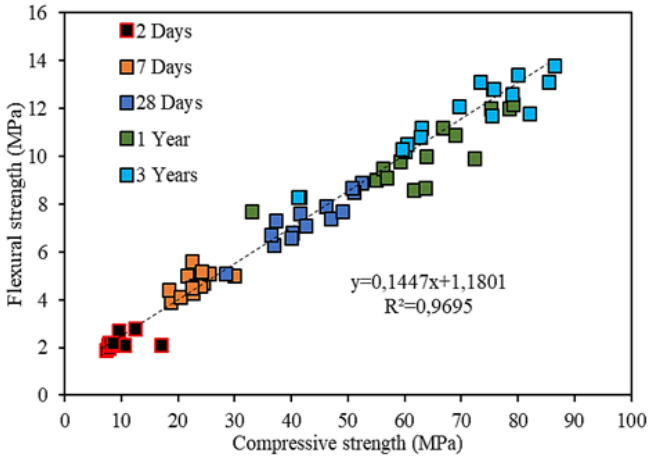

Fig. 5. Relationship between compressive and flexural strength

This suggests that at early ages. the variations in compressive and flexural strength between mixtures are relatively small. However. as the mixtures age and the effects of their composition and fineness become more pronounced. the mechanical properties diverge. leading to a wider spread of data points in the long term.

3.4. Mercury Porosity

To better understand the mechanical behavior of the different mortars studied. the pore size distribution was evaluated using a mercury porosimeter. Fig. 6 shows the results

obtained at 365 days. It can be seen that the 0S-0L mixture has a large number of pores with dimensions ranging between 0.02-0.4 µm. Additionally. for the same mixture. there is a wide distribution of pores between 0.2 and 2 µm. which corresponds to a high number of capillary pores. The 0S-35L mortar presents peaks between the ranges of 0.02-0.1 µm and 0.2-2 µm. indicating a considerable number of pores with these diameters.

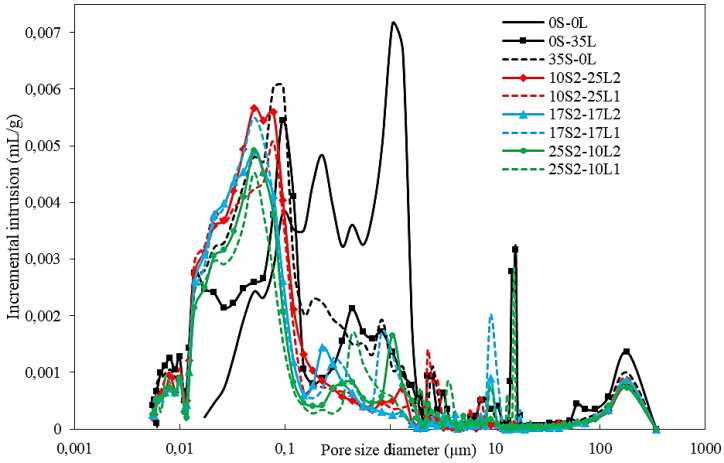

Fig. 6. Pore size variation in different mortars after one year

However, the 35S-0L binary composite shows fine pores varying between 0.01 µm and 0.1 µm. which is a result of the pozzolanic reaction of long-term slag producing a large volume of C-S-H that fills voids and capillary pores [47]. Additionally. the pore distribution of all mortars based on ternary types of cement is better compared to those based on binary binders or cement alone. as they evolve significantly towards fine pores. For example. the composites 25S2-10L1 and 25S2-10L2 reveal peaks between 0.01 and 0.03 µm with a total mercury intrusion of around 0.045 ml/g. indicating good compactness and homogeneity of these mixtures. Moreover. the decrease in pore size in the ternary mortars 25S2-10L1. 25S2-10L2 and 17S2-17L2 results in high mechanical performances (see Fig. 3). This is due to the phenomena of nucleation of C-S-H on CaO surfaces. the stabilization of ettringite. and the formation of carboaluminates of the clinker phase the ternary composite. These results were confirmed by Hadj Sadok et al. [7,48]. which showed at 90 days a finer pore size distribution for mixtures containing slag and calcined sediment (15 %).

3.5. Accelerated Carbonation and Gas Permeability

The physical and chemical characteristics of building materials significantly influence their durability. Figure 7 explores how these properties affect transport phenomena. specifically focusing on accelerated carbonation and gas permeability. for the different mortar mixtures at 28 days of age. Figure 7 explores the relationship between material properties and transport phenomena (permeability and carbonation) for the different mortar mixtures at 28 days.

- **Permeability:** The binary mixture with 35% LF (0S-35L) exhibited the lowest gas permeability (1.01×10^{-17} m^2) compared to other mixtures. This aligns with findings by Tsivilis et al. [49] and Panesar et al. [50] who attributed reduced permeability to LF's pore-filling effect. Conversely. the 35S-0L mortar (high BFS) showed higher permeability due to the slow hydration of BFS at early ages. creating more pores [9,11,51]. Interestingly. the ternary blend (17S1-17L1) demonstrated a significant permeability reduction compared to 35S-0L. Suggesting a beneficial interaction

between LF and BFS. This improvement in pore structure is likely due to the combined effects of pore filling by LF and nucleation sites provided by both BFS and LF. as suggested by Yu et al. [28] and Xuan et al. [29].

- **Carbonation:** The 0S-35L mortar displayed the lowest carbonation depth (0.25 cm). likely due to its denser microstructure achieved through LF addition. Conversely. the 35S-0L blend showed higher carbonation depths. which aligns with findings by Gruyaert et al. [52]due to its higher porosityThe mixture combining limestone filler and slag (17S1-17L1) resisted carbonation better than the one without (35S-0L). This improvement may be due to the formation of particles within the mixture (carboaluminates) that fill in tiny gaps and make the structure denser.
- The limited number of mixtures tested (four) due to travel constraints restricts broader conclusions. Further research is recommended to investigate the impact of varying BFS and LF contents and fineness on permeability and carbonation in ternary mixtures at later ages.

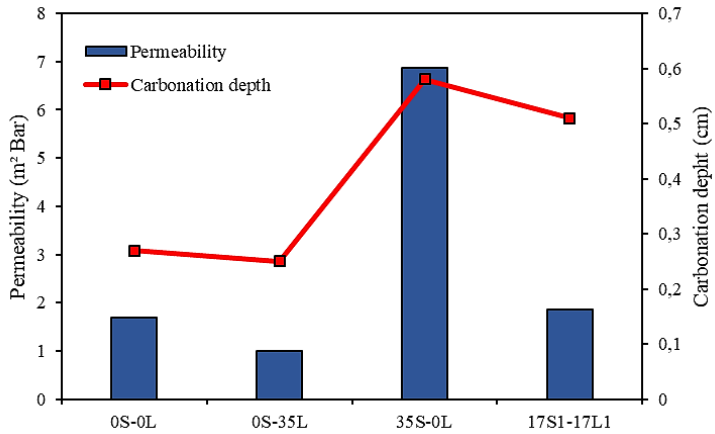

Fig. 7. Permeability and depth of carbonation of different mortars at 28 days

3.6. Scanned Electron Microscope (SEM)

The fig. 8 shows the results of the morphological analysis of hydrates after 365 days. The control paste's portlandite formed into a dense hexagonal crystal [53]. The hydration products. appearing as needles and flakes. were identified as AFt and Ms. respectively. Additionally. some capillary pores were discernible in the control mixture (0S-0L). These findings align with the results from the mercury porosimeter test in section 3.4. Conversely. the ternary mortars mainly exhibit the initial hydration phase.

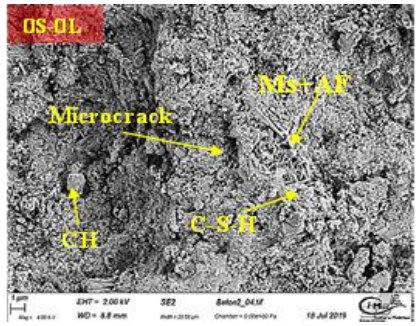

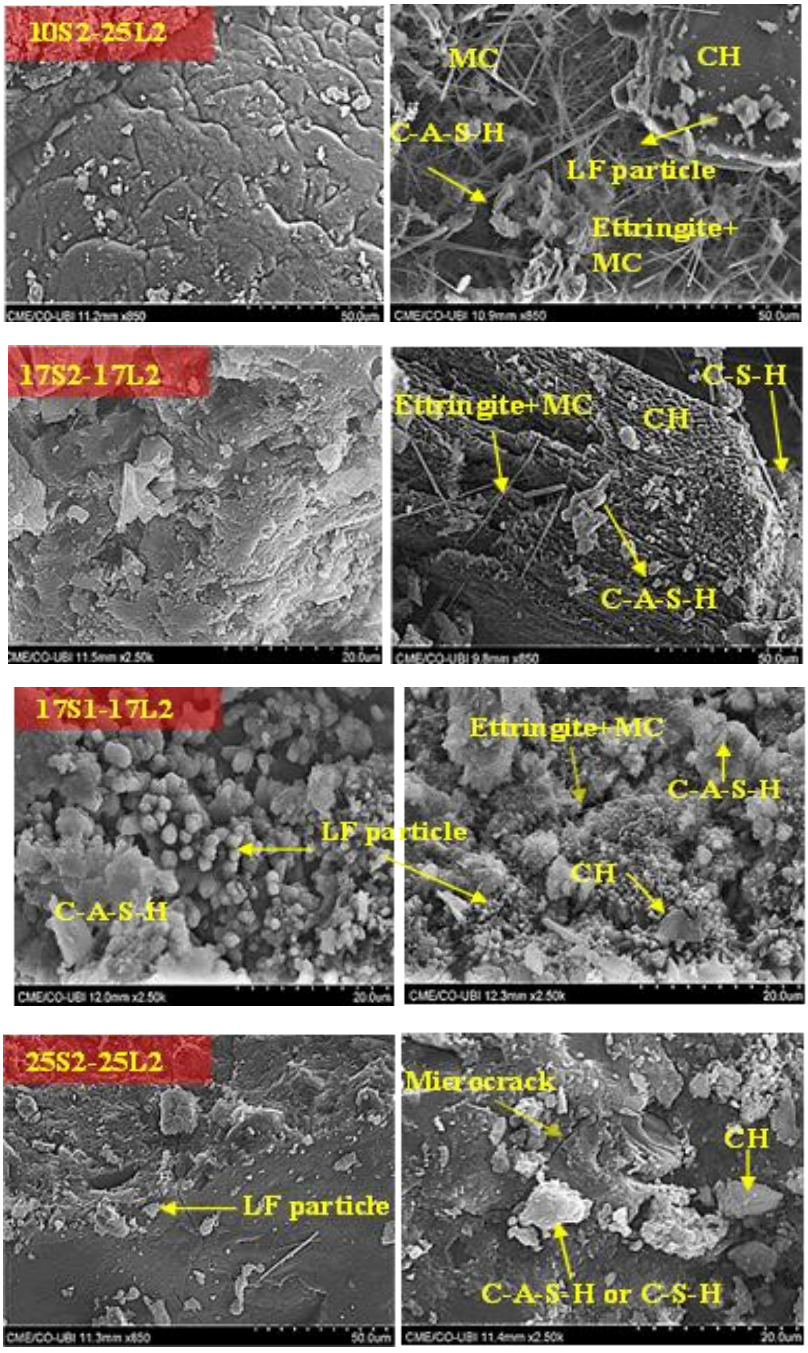
10S2-25L2
MC
CH
C-A-S-H
LF particle
Ettringite+
MC
17S2-17L2
Ettringite+MC
CH
C-S-H
C-A-S-H
17S1-17L2
LF particle
C-A-S-H
Ettringite+MC
C-A-S-H
CH
25S2-25L2
LF particle
Microcrack
CH
C-A-S-H or C-S-H

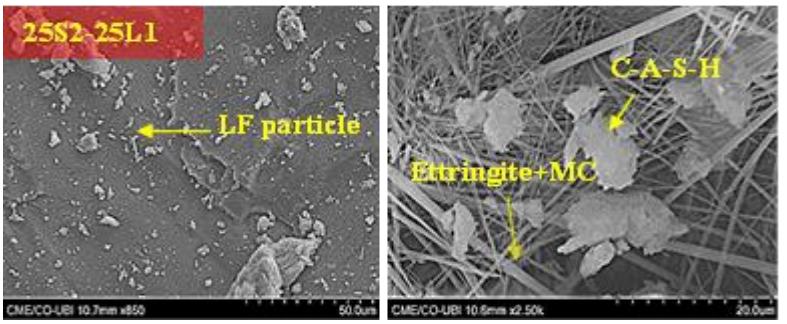

Fig. 8. The microstructures of various types of mortars

Despite the low clinker content in the ternary mixture. there are more hydrates present (C-(A)-S-H gel). It is also noted that Ms manifests as plates in the mixture without additives (0S-0L). while the introduction of LF and BFS alters these particles into Hc and Mc. The presence of C-A-S-H in the capillary pores significantly impacts transfer properties. Crystalline phases such as CO-AFm in needle-shaped form [54] (observed in mixture 25S2-25L1) effectively occupy capillary voids. The C-A-S-H resulting from the pozzolanic reaction can also play a significant role in masking the limestone dilution effect. The mortar 25S2-25L1 exhibits the highest compactness. correlating with the highest compressive strength. However. microcracks were observed on samples 25S2-25L2. According to Khalifa et al. [55]. the high substitution rate and fineness of slag induce some microcracks due to the accelerated hydration rate of the composite.

3.7. Hydrochloric Acid Attack

In Fig. 9a and b. it can be observed that the loss of compressive strength and mass after 200 days of various mortars immersed in aggressive media (HCL (1.5 %)) is shown. The behavior of all mortars varies according to the nature of the aggressive medium. Concerning hydrochloric acid resistance. a significant 78% decrease in compressive strength is observed after 200 days of HCl exposure in the 35S1-0L1 composite [56]. This reduced resistance is attributed to the presence of a high number of pores at the age of 28 days. resulting in lower resistance to ionic penetration and compromising the stability of hydrated phases. Additionally. significant strength decreases of 75% and 68% are also observed in mortars 0S-0L and 0S1-35L1. respectively [57]. This is believed to be due to the sufficient amount of portlandite present in the OPC and LF. leading to the formation of gypsum. which is known to be expansive. Mass loss corroborates the compressive strength results. However. all ternary mortars exhibit a notable improvement in resistance against hydrochloric acid (HCl) attack compared to 35S1-0L and OPC. Mixtures 10S2-25L2. 17S1-17L1. and 25S1-10L2 show respective strength decreases of 50%. 42%. and 46% after 200 days in HCl. resulting in an approximately 85% increase in resistance to HCl attack for ternary mixtures.

The addition of pozzolanic materials with limestone is identified as a potential solution to improve sulfate resistance. as observed by Boubekeur et al. Furthermore. the effect of fineness is noted. with higher Blaine specific surface (BSS) area resulting in a slight improvement in HCl resistance. Mixtures 10S2-25L2 and 25S2-10L2 show strength increases of 14% and 17% over 10S1-25L1 and 25S1-10L1. respectively. This is attributed to the accelerated hydration process. leading to a denser and more compact porous structure. as noted by Sia et al. Microstructural analysis reveals that the Si/Al-rich residues generated at the surface by the pozzolanic behavior of BFS effectively inhibit corrosion by acting as a barrier to chemical attack [58] [59].

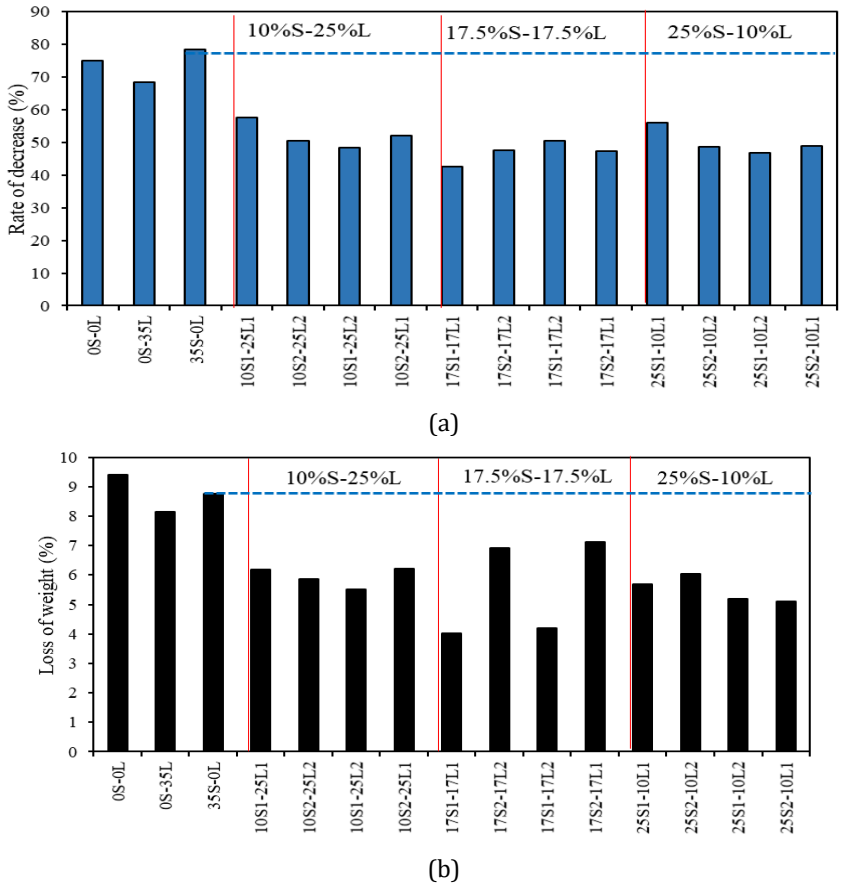

Fig. 9. Illustrates the percentage decrease in both compressive strength (a) and weight loss (b) for different mortar specimens

5. Environmental Assessment

The environmental analysis of the materials used in this study focuses on the energy consumption during the grinding process of each powder and the corresponding CO_2 emissions. These analyses are crucial for assessing the sustainability and environmental impact of the cementitious materials employed. The energy required to grind the various powders (clinker. gypsum. LF. and slag) was calculated based on Bond's third theory of comminution[60]. According to Bond's law. the energy consumption for grinding is proportional to the new surface area generated. which can be expressed as:

$$E = 10 * Wi \left(\frac{1}{\sqrt{P80}} - \frac{1}{\sqrt{F80}}\right) \quad (4)$$

Where; E is the energy consumption (kWh/ton); Wi is the Bond work index (kWh/ton); P80 is the 80% passing size of the product (μm); F80 is the 80% passing size of the feed (μm).

Using this equation. the energy consumption for grinding 1 ton of each powder was calculated basing on the SME Handbook for Mineral Processing [61]. Table 6 summarizes the energy consumption values for clinker. gypsum. LF. and slag. The energy consumption

values were converted to CO_2 emissions using the grid emissions factor specific to Algeria. which is 0.73 $kgCO_2/kWh$ [62]. The CO_2 emissions for grinding each powder were calculated using the following formula:

$$CO_2 \text{ emissions (kg } CO_2\text{/ton)} = \text{Energy consumption (kWh/ton)} \times 0.73 \quad (5)$$

Table 5. Energy consumption and Carbone emission for grinding 1 ton

	Wi (kWh/ton)	P80 (µm)	F80 (µm)	E (kWh/ton)	CO_2 emissions (kg/ton)
Clinker	13.6	32	5000	22.12	16.15
Gypsum	7.42	36	3000	11.01	8.04
Slag S1	13.4	14.6	3000	32.62	23.81
Slag S2	13.4	10.23	3000	39.45	28.80
LF L1	11.22	16.8	3000	25.33	18.49
LF L2	11.22	11.25	3000	31.40	22.92

Fig. 10 illustrates the CO_2 emissions and the embodied CO_2 parameters. which represents the ratio of CO_2 emissions to the compressive strength after one year. for various mixtures. providing a clear visual representation of their environmental efficiency. The results of the energy consumption and the Carbone emissions for grinding 1 ton of each powder are also illustrated in Table 5. The analysis reveals that the grinding process for each material results in different levels of energy consumption and CO_2 emissions. Slag and LF grinding is typically the most energy-intensive process. resulting in the highest CO_2 emissions. Conversely. clinker and gypsum require less energy to grind. resulting in lower CO_2 emissions. However. when considering the embodied CO_2 parameter. which represents the ratio of CO_2 emissions to the compressive strength of the mixtures after one year. a more nuanced picture emerges.

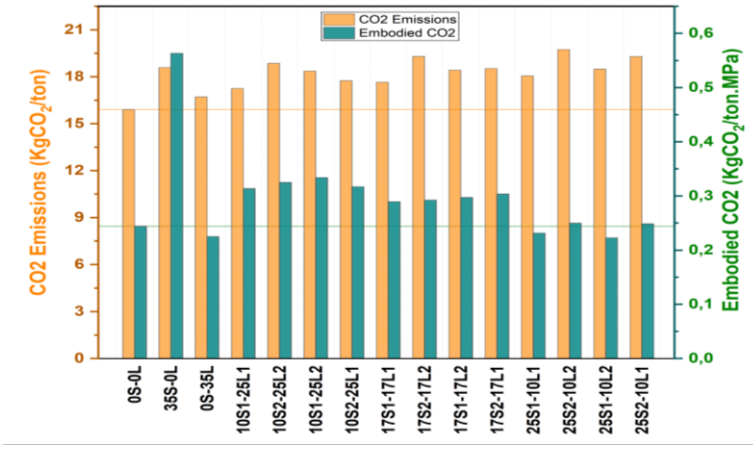

Fig. 10. CO_2 emissions and embodied CO_2 parameter results of each mixture

Mixtures such as 35S-0L exhibit the highest embodied CO_2 values due to the significant CO_2 emissions associated with high slag content and their low strength. On the other hand. mixtures incorporating higher proportions of LF and slag. such as 0S-35L and 25S1-10L2. demonstrate the lowest embodied CO_2 values. This indicates that substituting clinker with LF and slag not only reduces CO_2 emissions but also enhances environmental efficiency by

improving compressive strength relative to the carbon footprint. For instance. the mixture 25S1-10L2. with an embodied CO_2 value of 0.22 $kgCO_2$/ton.MPa. represents the best environmental efficiency among the tested mixtures. achieving a balance between lower emissions and robust structural performance.

4. Conclusion

This study assessed various mortars containing different proportions of limestone filler (LF) and blast furnace slag (BFS) powder. commonly used as cementitious materials. The findings yielded the following conclusions:

- Ternary mortars containing limestone filler (LF) and slag (BFS) exhibited significantly higher compressive strength compared to mortar with only 35% slag. After 7 days of curing. the ternary mortars showed a remarkable 62% increase in strength. and this improvement remained substantial at 31% after 28 days. Additionally. the compressive strength of ternary mortars was found to be 8.23-14% higher than that of OPC-0L-0S after 365 days.
- The fineness of materials significantly influenced the reaction of ternary mixtures (LF+BFS) in both short-term and long-term scenarios. particularly concerning limestone fillers.
- Adequate amounts of alumina sources (BFS) were necessary in ternary mixtures to ensure the formation of carboaluminates for up to 3 years.
- There were consistent variations in flexural and compressive strength. with a perfect linear relationship (R2 = 0.97) observed through correlation analysis.
- Ternary mixtures exhibited a dense. compact. and less porous microstructure. as evidenced by SEM and mercury porosity tests. attributed to the presence of C-A-S-H and carboaluminate.
- The inclusion of LF with BFS in cementitious composites (17S1-17L1) improved resistance to CO_2 diffusion by 80% compared to mixtures with only 35% BFS. resulting in a permeability decrease of over 100% at 28 days for 17S1-17L1 compared to 35S-0L. These findings were consistent with mercury porosimeter tests.
- The cement mixture containing 35% slag exhibited a significant decrease in compressive strength after 200 days in 1.5% hydrochloric acid compared to all other mixtures. However. all ternary mixtures demonstrated substantial improvement in acid resistance. ranging from 45-80%.
- The optimal mix in terms of mechanical performance and durability was found to be 25S1-10L. with an optimal LF content of 10%.

In conclusion. the development of eco-efficient materials with high performance and reduced cement content (substituted with a combination of slag and limestone filler) did not compromise long-term strength and durability against carbonation and hydrochloric acid attack. On the contrary. depending on the added fines. it significantly enhanced durability performance. ensuring longer-lasting constructions made with concrete containing such mortar formulations.

Acknowledgments

The authors express their sincere gratitude to the laboratory staff at the University of Bordj Bou Arreridj and the C-MADE Covilhã laboratory at UBI University for their support.

References

[1] Soldado E, Antunes A, Costa H, et al. Durability of mortar matrices of low-cement concrete with specific additions. Construction and Building Materials. 2021;309:125060. https://doi.org/10.1016/j.conbuildmat.2021.125060
[2] Mahasenan N, Smith S, Humphreys K, editors. The cement industry and global climate change: current and potential future cement industry CO2 emissions. Greenhouse gas control technologies-6th international conference; 2003: Elsevier. https://doi.org/10.1016/B978-008044276-1/50157-4
[3] Fennis SA, Walraven JC, Den Uijl JA. The use of particle packing models to design ecological concrete. Heron. 2009;54(2/3.
[4] Schneider M, Romer M, Tschudin M, et al. Celitement: a sustainable prospect for the cement industry. Cem Concr Res. 2011;41:642-650. https://doi.org/10.1016/j.cemconres.2011.03.019
[5] Sadok AH, Courard L. Chloride diffusion and oxygen permeability of mortars with low active blast furnace slag. Construction and Building Materials. 2018;181:319-324. https://doi.org/10.1016/j.conbuildmat.2018.06.036
[6] Chidiac S, Panesar D. Evolution of mechanical properties of concrete containing ground granulated blast furnace slag and effects on the scaling resistance test at 28 days. Cement and Concrete Composites. 2008;30(2):63-71. https://doi.org/10.1016/j.cemconcomp.2007.09.003
[7] Hadj Sadok R, Maherzi W, Benzerzour M, et al. Mechanical properties and microstructure of low carbon binders manufactured from calcined canal sediments and ground granulated blast furnace slag (GGBS). Sustainability. 2021;13(16):9057. https://doi.org/10.3390/su13169057
[8] Deboucha W, Sebaibi N, El Mendili Y, et al. Reactivity effect of calcium carbonate on the formation of carboaluminate phases in ground granulated blast furnace slag blended cements. Sustainability. 2021;13(11):6504. https://doi.org/10.3390/su13116504
[9] Deboucha W, Leklou N, Khelidj A. Combination effect of limestone filler and slag on hydration reactions in ternary cements. European Journal of Environmental and Civil Engineering. 2022;26(9):3931-3946. https://doi.org/10.1080/19648189.2020.1825233
[10] Najm O, El-Hassan H, El-Dieb A. Ladle slag characteristics and use in mortar and concrete: A comprehensive review. Journal of Cleaner Production. 2021;288:125584. https://doi.org/10.1016/j.jclepro.2020.125584
[11] Salvador RP, Rambo DA, Bueno RM, et al. On the use of blast-furnace slag in sprayed concrete applications. Construction and Building Materials. 2019;218:543-555. https://doi.org/10.1016/j.conbuildmat.2019.05.132
[12] Bougara A, Lynsdale C, Ezziane K. Activation of Algerian slag in mortars. Construction and Building Materials. 2009;23(1):542-547. https://doi.org/10.1016/j.conbuildmat.2007.10.012
[13] Kumar S, Kumar R, Bandopadhyay A, et al. Mechanical activation of granulated blast furnace slag and its effect on the properties and structure of portland slag cement. Cement and Concrete Composites. 2008;30(8):679-685. https://doi.org/10.1016/j.cemconcomp.2008.05.005
[14] Bouasker M, Khalifa NEH, Mounanga P, et al. Early-age deformation and autogenous cracking risk of slag-limestone filler-cement blended binders. Construction and Building Materials. 2014;55:158-167. https://doi.org/10.1016/j.conbuildmat.2014.01.037
[15] Celik K, Hay R, Hargis CW, et al. Effect of volcanic ash pozzolan or limestone replacement on hydration of Portland cement. Construction and Building Materials. 2019;197:803-812. https://doi.org/10.1016/j.conbuildmat.2018.11.193

[16] Dhandapani Y, Santhanam M. Investigation on the microstructure-related characteristics to elucidate performance of composite cement with limestone-calcined clay combination. Cement and Concrete Research. 2020;129:105959. https://doi.org/10.1016/j.cemconres.2019.105959
[17] Adu-Amankwah S, Zajac M, Stabler C, et al. Influence of limestone on the hydration of ternary slag cements. Cement and Concrete Research. 2017;100:96-109. https://doi.org/10.1016/j.cemconres.2017.05.013
[18] Bullard JW, Jennings HM, Livingston RA, et al. Mechanisms of cement hydration. Cement and Concrete Research. 2011;41(12):1208-1223. https://doi.org/10.1016/j.cemconres.2010.09.011
[19] Berodier E, Scrivener K. Understanding the Filler Effect on the Nucleation and Growth of C-S-H. Journal of the American Ceramic Society. 2014;97(12):3764-3773. https://doi.org/10.1111/jace.13177
[20] De Weerdt K, Kjellsen K, Sellevold E, et al. Synergy between fly ash and limestone powder in ternary cements. Cement and Concrete Composites. 2011;33(1):30-38. https://doi.org/10.1016/j.cemconcomp.2010.09.006
[21] Vickers NJ. Animal communication: when I'm calling you, will you answer too? Current Biology. 2017;27(14). https://doi.org/10.1016/j.cub.2017.05.064
[22] Antoni M, Rossen J. Cement Substitution by a Combination of Metakaolin and Limestone. Cement and Concrete Research. 2012;42(12):1579-1589. https://doi.org/10.1016/j.cemconres.2012.09.006
[23] Adu-Amankwah S, Black L, Skocek J, et al. Effect of sulfate additions on hydration and performance of ternary slag-limestone composite cements. Construction and Building Materials. 2018;164:451-462. https://doi.org/10.1016/j.conbuildmat.2017.12.165
[24] Matschei T, Lothenbach B, Glasser F. The AFm phase in Portland cement. Cement and Concrete Research. 2007;37(2):118-130. https://doi.org/10.1016/j.cemconres.2006.10.010
[25] Gao T, Dai T, Shen L, et al. Benefits of using steel slag in cement clinker production for environmental conservation and economic revenue generation. Journal of Cleaner Production. 2021;282:124538. https://doi.org/10.1016/j.jclepro.2020.124538
[26] Carrasco-Maldonado F, Spörl R, Fleiger K, et al. Oxy-fuel combustion technology for cement production-state of the art research and technology development. International Journal of Greenhouse Gas Control. 2016;45:189-199. https://doi.org/10.1016/j.ijggc.2015.12.014
[27] Menéndez G, Bonavetti V, Irassar E. Strength development of ternary blended cement with limestone filler and blast-furnace slag. Cement and Concrete Composites. 2003;25(1):61-67. https://doi.org/10.1016/S0958-9465(01)00056-7
[28] Yu L, Wang Q, Wu K, et al. Identification of multi-scale homogeneity of blended cement concrete: Macro performance, micro and meso structure. Journal of Thermal Analysis and Calorimetry. 2022:1-12.
[29] Xuan M-Y, Han Y, Wang X-Y. The hydration, mechanical, autogenous shrinkage, durability, and sustainability properties of cement-limestone-slag ternary composites. Sustainability. 2021;13(4):1881. https://doi.org/10.3390/su13041881
[30] Arora A, Sant G, Neithalath N. Ternary blends containing slag and interground/blended limestone: Hydration, strength, and pore structure. Construction and Building Materials. 2016;102:113-124. https://doi.org/10.1016/j.conbuildmat.2015.10.179
[31] Itim A, Ezziane K, Kadri E-H. Compressive strength and shrinkage of mortar containing various amounts of mineral additions. Construction and Building Materials. 2011;25(8):3603-3609. https://doi.org/10.1016/j.conbuildmat.2011.03.055
[32] Briki Y, Zajac M, Haha MB, et al. Impact of limestone fineness on cement hydration at early age. Cement and Concrete Research. 2021;147:106515. https://doi.org/10.1016/j.cemconres.2021.106515

[33] EN-196-1. Methods of testing cement-Part 1: Determination of strength. Quality and Standards Authority of Ethiopia, ES. 2005:1176-1.
[34] Ibáñez-Gosálvez J, Real-Herraiz T, Ortega JM. Microstructure, durability and mechanical properties of mortars prepared using ternary binders with addition of slag, fly ash and limestone. Applied Sciences. 2021;11(14):6388. https://doi.org/10.3390/app11146388
[35] Horpibulsuk S, Rachan R, Chinkulkijniwat A, et al. Analysis of strength development in cement-stabilized silty clay from microstructural considerations. Construction and Building Materials. 2010;24(10):2011-2021. https://doi.org/10.1016/j.conbuildmat.2010.03.011
[36] Klinkenberg L. The permeability of porous media to liquids and gases. Am Petrol Inst, Drilling and Production Practice. 1941;2:200-213.
[37] Perraton D. La perméabilité aux gaz des bétons hydrauliques. Toulouse; 1992.
[38] Rozière E. Etude de la durabilité des bétons par une approche performantielle. Nantes; 2007.
[39] P18-458 X. Tests for Hardened Concrete-Accelerated Carbonation Test-Measurement of the Thickness of Carbonated Concrete. AFNOR: Paris, France; 2008.
[40] Benkaddour M, Aoual FK, Semcha A. Durabilité des mortiers à base de pouzzolane naturelle et de pouzzolane artificielle. Nature & Technology. 2009;(1):63.
[41] Dubois V, Abriak NE, Zentar R, et al. The use of marine sediments as a pavement base material. Waste Management. 2009;29(2):774-782. https://doi.org/10.1016/j.wasman.2008.05.004
[42] Dhandapani Y, Santhanam M, Kaladharan G, et al. Towards ternary binders involving limestone additions-A review. Cement and Concrete Research. 2021;143:106396. https://doi.org/10.1016/j.cemconres.2021.106396
[43] Ballim Y, Graham PC. The effects of supplementary cementing materials in modifying the heat of hydration of concrete. Materials and Structures. 2009;42(6):803-811. https://doi.org/10.1617/s11527-008-9425-3
[44] Avet F, Scrivener K. Investigation of the calcined kaolinite content on the hydration of Limestone Calcined Clay Cement (LC3). Cement and Concrete Research. 2018;107:124-135. https://doi.org/10.1016/j.cemconres.2018.02.016
[45] Federico L, Chidiac S. Waste glass as a supplementary cementitious material in concrete-critical review of treatment methods. Cement and Concrete Composites. 2009;31(8):606-610. https://doi.org/10.1016/j.cemconcomp.2009.02.001
[46] Aoual-Benslafa FK, Kerdal D, Ameur M, et al. Durability of mortars made with dredged sediments. Procedia Engineering. 2015;118:240-250. https://doi.org/10.1016/j.proeng.2015.08.423
[47] Manmohan D, Mehta P. Influence of pozzolanic, slag, and chemical admixtures on pore size distribution and permeability of hardened cement pastes. Cement, Concrete and Aggregates. 1981;3(1):63-67. https://doi.org/10.1520/CCA10203J
[48] Hadj-sadok A, Kenai S, Courard L, et al. Microstructure and durability of mortars modified with medium active blast furnace slag. Construction and Building Materials. 2011;25(2):1018-1025. https://doi.org/10.1016/j.conbuildmat.2010.06.077
[49] Tsivilis S, Tsantilas J, Kakali G, et al. The permeability of Portland limestone cement concrete. Cement and Concrete Research. 2003;33(9):1465-1471. https://doi.org/10.1016/S0008-8846(03)00092-9
[50] Panesar DK, Zhang R. Performance comparison of cement replacing materials in concrete: Limestone fillers and supplementary cementing materials-A review. Construction and Building Materials. 2020;251:118866. https://doi.org/10.1016/j.conbuildmat.2020.118866
[51] Carrasco M, Menéndez G, Bonavetti V, et al. Strength optimization of "tailor-made cement" with limestone filler and blast furnace slag. Cement and Concrete Research. 2005;35(7):1324-1331. https://doi.org/10.1016/j.cemconres.2004.09.023

[52] Gruyaert E, Van den Heede P, De Belie N. Carbonation of slag concrete: Effect of the cement replacement level and curing on the carbonation coefficient-Effect of carbonation on the pore structure. Cement and Concrete Composites. 2013;35(1):39-48. https://doi.org/10.1016/j.cemconcomp.2012.08.024
[53] L'Hôpital E, Lothenbach B, Le Saout G, et al. Incorporation of aluminium in calcium-silicate-hydrates. Cement and Concrete Research. 2015;75:91-103. https://doi.org/10.1016/j.cemconres.2015.04.007
[54] Matschei T, Lothenbach B. Thermodynamic properties of Portland cement hydrates in the system CaO-Al2O3-SiO2-CaSO4-CaCO3-H2O. Cement and Concrete Research. 2007;37(10). https://doi.org/10.1016/j.cemconres.2007.06.002
[55] Khalifa NEH, Bouasker M, Mounanga P, et al. Physicochemical study of cementitious materials based on binary and ternary binders. Chemistry and Materials Research. 2013;4:24.
[56] Santhanam M, Cohen MD, Olek J. Effects of gypsum formation on the performance of cement mortars during external sulfate attack. Cement and Concrete Research. 2003;33(3):325-332. https://doi.org/10.1016/S0008-8846(02)00955-9
[57] Makhloufi Z, Kadri E, Bouhicha M, et al. Resistance of limestone mortars with quaternary binders to sulfuric acid solution. Construction and Building Materials. 2012;26(1):497-504. https://doi.org/10.1016/j.conbuildmat.2011.06.050
[58] Boubekeur T, Boulekbache B, Aoudjane K, et al. Prediction of the durability performance of ternary cement containing limestone powder and ground granulated blast furnace slag. Construction and Building Materials. 2019;209:215-221. https://doi.org/10.1016/j.conbuildmat.2019.03.120
[59] Siad H, Lachemi M, Sahmaran M, et al. Effect of glass powder on sulfuric acid resistance of cementitious materials. Construction and Building Materials. 2016;113:163-173. https://doi.org/10.1016/j.conbuildmat.2016.03.049
[60] Bond FC. Crushing and grinding calculations, Part I. Br Chem Eng. 1961;6:378-385.
[61] Weiss NL. SME mineral processing handbook. New York: Society of Mining Engineers; 1985.
[62] Belkadi AA, Kessal O, Berkouche A, et al. Experimental investigation into the potential of recycled concrete and waste glass powders for improving the sustainability and performance of cement mortars properties. Sustainable Energy Technologies and Assessments. 2024;64:103710. https://doi.org/10.1016/j.seta.2024.103710

Research on Engineering Structures & Materials
www.jresm.org
Research Group

Research Article

Impact of supplementary cementitious materials on life cycle cost of high-strength concrete in coastal environments

Ashok D. Chavan[1,a], V. K. Rattan[2,b], Y. S. Patil[3,c]

[1]*Department of Civil Engineering, GNA University, Phagwara, Punjab, India*
[2]*GNA University, Phagwara, Punjab, India*
[3]*Department of Civil Engineering, S.H. Jondhale Engineering College, Thane, Maharashtra, India*

Article Info

Article history:

Received 04 Apr 2024
Accepted 28 June 2024

Keywords:

Life cycle cost analysis; Quaternary blended concrete; Supplementary cementitious materials; Life-365; Sustainable construction

Abstract

This research investigates the application of Life Cycle Cost (LCC) analysis in the construction industry, focusing on reinforced concrete structures. LCC analysis goes beyond initial building costs, encompassing all expenses throughout a structure's service life. Among various service life prediction models, Life-365 and DURACON are noteworthy. Life-365, a specialized computer program, predicts the life cycle cost of reinforced concrete exposed to chlorides. This paper presents a case study using Life-365 to compare the LCC of two concrete mixes, TM1 and TM2, in Mumbai, a location with conditions conducive to chloride exposure. The study uses average monthly temperatures and location-specific input parameters to evaluate the LCC of M70-grade concrete mixes with different compositions, including Fly Ash, GGBS, and Micro Silica as partial cement replacements. Results indicate that quaternary blended M70 grade concrete, incorporating supplementary cementitious materials (SCMs), not only enhance durability but also offers economic benefits, reducing overall life cycle costs. These findings provide valuable insights for engineers and decision-makers, promoting durable, cost-effective, and sustainable concrete structures.

1. Introduction

Uncontrolled urban development poses significant challenges in both developing nations like India and developed countries globally. Unplanned expansions frequently lack adequate infrastructure, resulting in substantial maintenance, rehabilitation, and reconstruction costs that often exceed initial estimates. Addressing this issue necessitates the integration of all life-cycle costs (LCC) into the structural analysis [1]. The primary objective of this research is to apply Life Cycle Cost (LCC) analysis to reinforced concrete structures, particularly focusing on the use of quaternary blended concrete mixes. By employing Life-365 software, the study aims to compare the LCC of different concrete compositions and provide insights into their economic and durability performance.

The study investigates the comprehensive costs associated with reinforced concrete structures exposed to chlorides, including initial construction and long-term maintenance expenses [2].The research utilizes Life-365, a specialized service life prediction model, to analyse the economic viability and durability of concrete mixes in chloride-exposed environments [3].A comparative analysis between two trial mixes, TM1 and TM2, is conducted to determine the most cost-effective and durable option for M70 grade concrete in a coastal setting like Mumbai [4]. Despite the extensive use of LCC analysis across various fields, its application in the construction industry, particularly in predicting the

*Corresponding author: adchavan2020@gmail.com
[a] orcid.org/0009-0003-2702-2138; [b] orcid.org/0000-0002-9819-9403; [c] orcid.org/0009-0006-7224-1606
DOI: http://dx.doi.org/10.17515/resm2024.232st0404rs

long-term costs and performance of reinforced concrete with supplementary cementitious materials (SCMs), remains limited [5]. Existing literature lacks comprehensive studies that integrate LCC analysis with service life prediction models like Life-365, particularly for high-performance concrete mixes in chloride-rich environments [6]. This study addresses this gap by providing a detailed analysis of the economic and durability benefits of quaternary blended concrete, incorporating Fly Ash, GGBS, and Micro Silica [7].

The contemporary application of LCC analysis provides a holistic assessment of costs from initial construction to the end of a structure's service life [8]. This approach is increasingly important for optimizing construction costs while reducing energy expenses through innovative solutions. Unlike traditional emphasis on architectural and structural design, modern LCC analysis extends to operational costs over a structure's lifespan, facilitated by advancements in computer technology [9]. The concept of limit state design, incorporating ultimate strength and serviceability limits, further underscores the safety and longevity of structures [10]. LCC terminology varies globally, with terms such as 'Life Cycle Cost,' 'Cost in Use,' 'Whole Life Costing' (WLC), and 'Whole Life Appraisal' (WLA) being used interchangeably [11]. Despite these differences, the core principle remains the same: a holistic examination of a building's entire life cycle. This paper adopts LCC as equivalent to WLC, acknowledging the comprehensive approach necessary for accurate cost analysis [12].

While minimizing initial construction costs is a common objective, this study emphasizes that achieving the lowest cost does not guarantee optimal performance over a structure's lifetime [13]. Higher initial costs may, in fact, reduce total life cycle costs by enhancing durability and reducing long-term maintenance needs [14]. This research underscores the importance of demonstrating to clients the relationship between design choices and lifetime costs, incorporating energy analyses early in the design phase to ensure sustainable and cost-effective construction solutions [15].

2. Literature Review

The concept of LCC originated in the mid-1960s with the U.S. Department of Defence, later evolving with contributions from institutions such as the Royal Institution of Chartered Surveyors and the British Ministry of Industries. Flanagan and Norman's work in 1983 introduced data collection methods, while subsequent studies, including those by Abraham and Dickson, considered disposal costs in LCC [8, 9]. In 1992, British standards formally accepted the LCC concept, defining it as a technique enabling comparative cost assessments over a specified period, considering all relevant economic factors. Internationally, the Common European Methodology for Life Cycle Costing project by Davis Longdon addressed LCC, yet despite its advantages, LCC's utilization remains limited in the construction industry due to incomplete understanding among professionals [10]. Buyers often prioritize purchase costs without considering structural design, building architecture, and energy systems, neglecting future operation and maintenance costs. Recognition of life cycle costs, encompassing construction costs and subsequent expenses, allows for more effective decision-making [15, 16].

Service life prediction becomes crucial for LCC analysis, with models like fib (Model Code) and ISO being commonly used. In seismic zones, LCC incorporates earthquake-related damages, influencing future building ownership costs. Researchers like Takahashi et al. and Frangopol and Liu have explored seismic risk costs in LCC, considering both initial and expected damage costs [17,18,19,20]. Studies on LCC extend beyond traditional structures, with Frangopol and Liu analyzing bridges, and Kappos and Dimitrapoulos evaluating the feasibility of strengthening reinforced concrete buildings. Notably, Oberg emphasizes the substantial and enduring investments in buildings, both financially and in terms of

resources [21,22]. In regions with cold climates, indoor design gains prominence for property buyers spending a significant portion of their time indoors. Despite this, reports by Bakis et al. and Flanagan and Jewell highlight the limited application of LCC, revealing that maintenance and other expenses can triple the initial capital cost of construction over a building's first 25 years [04, 23]. Kotaji et al. stress the importance of demonstrating the relationship between design choices and lifetime costs for effective decision-making [24].

Consideration of all aspects is imperative during structural design to ensure the fulfilment of functions throughout the designed service life. While predicting the service life for shorter periods, such as 20 to 50 years, is feasible, determining service life for extended durations, like 100 or 150 years, presents a significant challenge [25].

Service life design involves predicting the behaviour of a structure over an extended period. While current service life models are adequately predictive, challenges arise due to variations in construction quality across different sites. The prevalent use of prescriptive designs in many countries poses a significant problem for quality assessment and service life prediction. Thus, there is a pressing need to adopt a performance-based approach for accurate prediction of service life [26]. For structures in mild or non-aggressive environments, a minimalist approach may be sufficient. However, site engineers should pay attention to good construction practices, including optimal mix design, compaction, and curing, to ensure adequate durability.

A performance-based approach is implemented following ISO – 13823. This standard, based on the limit-state method, covers various service life design approaches. The fib Model Code (2010) [27] adopts the methodology outlined in ISO-13823, offering advantages over current simplistic approaches.

3.Materials and Method

3.1. Concrete Mix Design Trials: TM1 and TM2 Composition Analysis

In this study, M70 Grade concrete mix design trials are conducted and designated as TM1 and TM2. Trial Mix 1 (TM1) is formulated with a primary component of Ordinary Portland Cement (OPC), constituting 90% of its composition. This OPC is sourced from Ambuja, a renowned provider of 53 Grade cement. Unlike TM2 and subsequent trial mixes, TM1 does not incorporate Ground Granulated Blast Furnace Slag (GGBS) in its composition, making it solely reliant on OPC for its binding properties. Additionally, TM1 does not include Micro Silica or any other supplementary cementitious materials apart from a minor inclusion of Pulverized Fly Ash (PFA) at a ratio of 10%. This PFA is sourced from Adani-Dahanu. Moreover, TM1 utilizes a Super Plasticizer, specifically Sika Viscocrete 5210 N, at a proportion of 0.8% to enhance its workability and reduce water content, thereby potentially improving its overall strength and durability

In contrast, Trial Mix 2 (TM2) exhibits a different composition, aimed at exploring alternative materials and proportions for enhanced concrete properties. TM2 incorporates a lower percentage of OPC, accounting for 57% of its composition, still sourced from Ambuja 53 Grade Cement. However, TM2 introduces GGBS, sourced from JSW and certified for quality, constituting 25% of the mix. This addition of GGBS aims to improve the long-term durability and strength characteristics of the concrete. Moreover, TM2 includes 8% Micro Silica, further enhancing its strength and reducing permeability. Similar to TM1, TM2 also includes 10% PFA sourced from Adani-Dahanu, providing additional benefits in terms of sustainability and durability. Finally, both TM1 and TM2 utilize the same Super Plasticizer, Sika Viscocrete 5210 N, at a consistent ratio of 0.8%, ensuring uniformity in workability and strength enhancement across the trial mixes.

3.2. Manufacturing Cost of Concrete:

- **Material Costs:** The primary components of concrete—cement aggregates, water, and admixtures—contributed to the manufacturing cost. The prices of these materials are taken in to account for determining the initial manufacturing cost (All costs in INR). The initial cost of production is taken as an input value for calculating the Life Cycle cost over 70 years.
- **Equipment and Energy Costs:** The use of machinery, transportation equipment, and energy resources during the manufacturing process contributed to the overall cost. The total manufacturing cost of 1 m3 concrete for TM1(Control sample) & TM2.

Table 1. Comparison of production cost of M70-Grade concrete mix TM1 and TM2 for 1m^3

Material	Rates (Rs.)	Unit
Cement	7.1	Per Kg.
Fly Ash	3	Per Kg.
Metal	1000	Per MT
Cr. sand	1100	Per MT
SikaViscocrete 5210 NS Admixture	151	Per Kg.
Micro silica	28.50	Per Kg.
GGBS	4.14	Per Kg.
water	0.190	Per Kg.
Diesel	104.8	Per Lit

Grade/ Mix	Material in Kgs.									A	B	C	D	E	F	Prod. cost (E+F)
										Total Mater. Cost	Wastage on (A) Cost 2%	Mater. + wastage A+B	Op. & Plant cost + Profit	Total Cost (C+D)	GST on E 18%	(Rs.)
TM1 M-70	475.0	0.00	145	460	590	615	6.0	50	147							
Cont.Sam.	3372	0.00	435	460	590	676	910	1425	28	7869	157.3	8026	950	8976	1615	10593
TM2 M-70	237.5	237	145	460	590	615	3.8	50	147							
(50:50)	1686	983	435	460	590	676	365	1425	28	6649	132.9	6782	950	7732	1391	9124

3.3. Life Cycle Cost Analysis Using Life-365 ver.2.2.3

Life-365 serves as both a Service Life Prediction Model and a Computer Program designed for predicting the Service Life and Life-Cycle Cost of reinforced concrete exposed to chlorides. Initiated in 1998 by the ACI's Strategic Development Council (SDC), a consortium including representatives from various entities developed Life-365 for service life prediction and life-cycle cost analysis (LCCA).

Life-365 predicts the start of corrosion and the time required for corrosion to reach a level necessitating repair. It estimates initial construction costs, predicted repair costs, and costs over the entire design life of a structure. The required inputs include geographic location, construction type, depth of clear concrete cover to the reinforcement, and details of corrosion protection strategies used. The analysis done by Life-365 involves predicting

the initiation period of corrosion (ti), the propagation period of corrosion (tp), and the time of the first repair (tr), which is the sum of these two periods (tr = ti + tp). A repair schedule is then calculated for the entire design life after the initial repair of the structure. Estimation of Life-Cycle Cost (LCC) is based on the initial concrete costs, corrosion protection system costs, and future repair costs.

The total life cycle cost is the sum of initial construction costs and discounted future repair costs over the service life of a structure. The initial cost of construction includes the cost of concrete, reinforcing steel, and the cost of surface protection membrane or sealer used, if any. Future repair costs are calculated using software, considering present worth along with the discount rate provided by the user. Life-365 expresses these costs on the unit area of the structure. While the current version has limitations and makes several assumptions to address complex phenomena, the software allows users to run user-defined scenarios by making minor changes to selected values. However, uncertainties in concrete material properties, structural geometry, boundary conditions, and project costs are not fully addressed. Users are encouraged to input data based on exposure conditions and project-specific economic factors.

Life-365 calculates the initiation period using the Fickian diffusion model (One or two-dimensional). Default corrosion propagation times are provided for different types of reinforcement. ASTM E 917 -05, 'Standard practice for measuring Life cycle costs of building and building systems,' is followed in Life-365v2.0, initially setting the design life at 75 years. The most recent model, Life 365v 2.2, allows users to insert the value of Chloride diffusion (Cs) obtained from testing specimens on-site using the ASTM C1556 method of testing, which is similar to NT Build 443 [28].

3.4 Data Gathering Procedure

- **Geographic Location:** Data includes average monthly temperatures, humidity levels, and chloride exposure conditions specific to the structure's location.
- **Concrete Composition:** Details on the mix design, including the proportions of OPC, GGBS, Micro Silica, PFA, and any other supplementary cementitious materials.
- **Exposure Conditions:** Information on the environmental conditions the structure will face, such as chloride concentration from seawater or deicing salts.
- **Economic Factors:** Cost inputs for materials, labour, maintenance, and repair activities, as well as discount rates for future cost calculations.

3.5 Standardization Followed

Life-365 adheres to several international and industry standards to ensure the reliability and accuracy of its predictions:

- **ASTM Standards**: Life-365 follows ASTM E917-05 for measuring life cycle costs of building and building systems. This standard provides a methodology for cost estimation, ensuring consistency and comparability in LCC analysis.
- **ISO Standards:** The software incorporates methodologies aligned with ISO 15686-5, which focuses on building and construction asset management and service life planning.
- **Testing Methods:** For input parameters such as chloride diffusion, the software utilizes data from standardized testing methods like ASTM C1556 and NT Build 443, which measure chloride penetration in concrete.

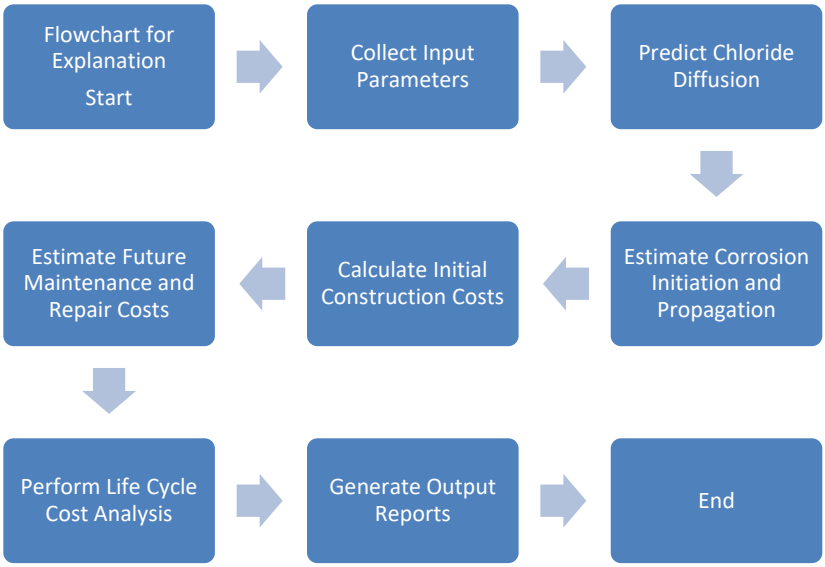

Flow Chart 1. The flow chart above explains how the software works

- **Input Parameters:** The software begins with the collection of various input parameters essential for accurate predictions. These parameters include the geographic location of the structure, which influences environmental exposure conditions; the specific composition of the concrete mix, including any supplementary materials; and economic factors such as material costs and maintenance schedules.
- **Service Life Prediction:** Life-365 uses these inputs to predict chloride diffusion into the concrete over time, estimate the time until corrosion initiation, and determine the propagation period until significant damage occurs. This step involves complex modelling of chloride ingress and the resulting deterioration processes.
- **Life Cycle Cost Analysis:** The software calculates initial construction costs based on the concrete composition and other materials used. It then estimates future costs for maintenance and repairs, considering the predicted timing and extent of corrosion-related damage. These costs are discounted to present value to facilitate a comprehensive cost-benefit analysis over the structure's expected service life.
- **Output Results:** Finally, Life-365 generates detailed reports that include predicted service life, total life cycle costs, and recommendations for cost-effective and durable concrete mix designs. These results provide valuable insights for engineers and decision-makers, helping them to select materials and design strategies that optimize both economic and performance outcomes.

4. Results and Discussions

4.1 Life Cycle Cost of Concrete

The decision-making between manufacturing and life cycle costs hinges on project-specific requirements and constraints. While short-term projects may prioritize minimizing manufacturing costs, long-term projects benefit from life cycle cost analysis. Recognizing that decisions made during manufacturing have far-reaching implications, a holistic approach considers factors like energy efficiency, environmental impact, and maintenance

requirements. This report utilizes Life-365 software for a case study, comparing TM1 and TM2 composite mixes over their entire life cycle.

4.2 Average Monthly Temperatures

Life-365 facilitates the analysis of chloride migration's impact on the structure's entire life and the effects of temperature variation on durability. Using Mumbai as a study location, average monthly temperatures are input into the software to assess the life cycle cost of M70-grade concrete mixes. The study employs Life-365 to analyze the impact of temperature variations on life cycle costs, considering different compositions with supplementary materials.

The M70 grade concrete mixes were designed with a base mix containing 450 kg/m^3 of Ordinary Portland cement (OPC), fine and coarse aggregates, and water. Different trial mixes are formulated, incorporating supplementary cementitious materials using Fly Ash, Ground Granulated Blast Furnace Slag (GGBS), and Micro Silica as partial cement replacement with different proportions. The water-cement ratio is maintained at 0.22 for all mixes. Life-365 software, a comprehensive life-cycle cost analysis tool, is employed to assess the impact of average monthly temperatures on the life-cycle cost of the concrete structure. The software is given inputs on material costs, maintenance, repair, and replacement costs. The average monthly temperatures as input to the software as shown below:

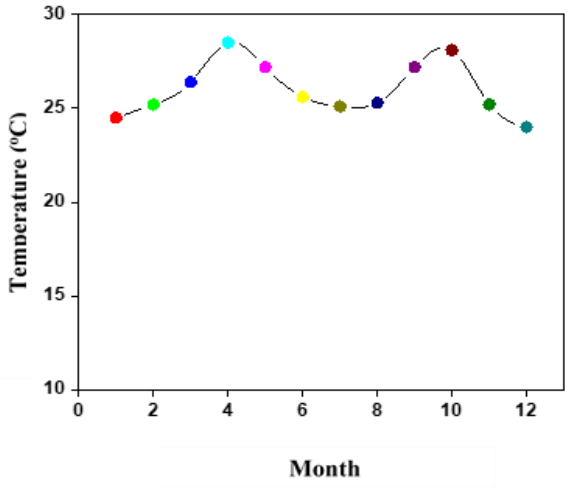

Fig. 1. Shows that the change in average temperature for the period of 12 months

4.3 Cumulative Current Costs

Cumulative current cost graphs visually represent the accumulation of costs over time in life cycle cost analysis. "Life 365" generates these graphs, illustrating cost evolution throughout a project's life cycle. The graph allows stakeholders to understand cost trends over time. For comparison, a cumulative current cost graph is plotted for TM1 and TM2, providing a clear representation of their life cycle costs.

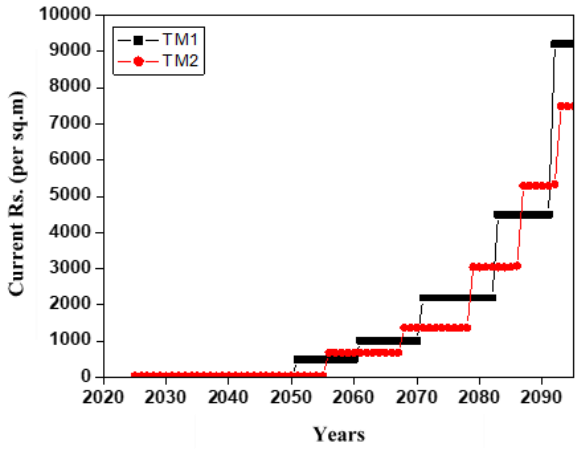

Fig. 2. Shows the cumulative current cost against age of structure in number of years

4.4 Cumulative Present Value

This section assesses the durability of quaternary blended M70 grade concrete, focusing on Cumulative Present Cost. Utilizing Life-365, the study compares two trial mixes over 70 years, incorporating supplementary cementitious materials. Fig. 3 summarizes the cumulative present cost analysis, indicating a positive impact on economic sustainability due to the addition of Fly Ash, GGBS, and Micro Silica in Trial Mix 1 compared to Trial Mix 2.

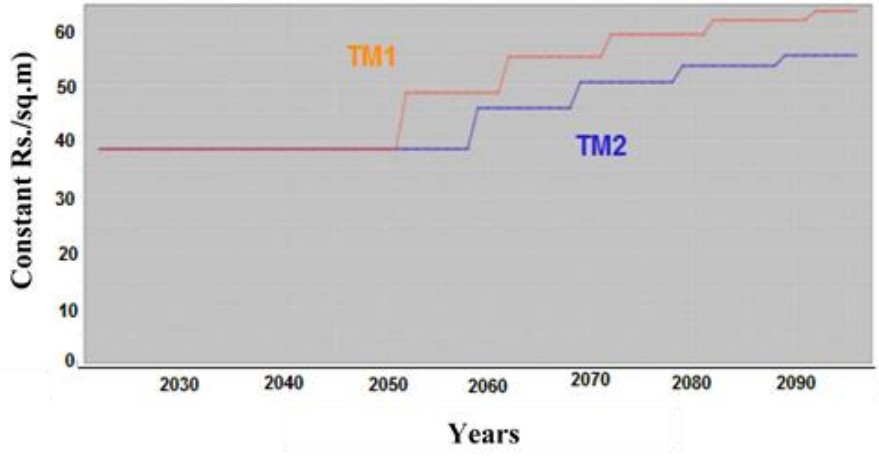

Fig. 3. Shows the cumulative constant cost

Trial Mix 1, which is a control mix, demonstrated a 26.31 % reduction in cumulative present cost compared to Trial Mix 2 when observed at 40 years' age of structure. It is also observed that in Trial Mix 1, the cumulative present cost started increasing at the age of 32 years whereas the same started at 38 years in the case of Trial Mix 2. It is further to be noted that at the end of the life, the cumulative present cost of Trial Mix 1 is 15.68% more than that of Trial Mix 2. This suggests that the addition of Fly Ash, GGBS, and Micro Silica positively influenced the economic sustainability of M70 grade concrete over the 70 years.

4.5 Current Costs

This section focuses on the Current Cost analysis for quaternary blended M70 grade concrete. Figure 4 depicts the outcomes of the current cost analysis for TM1 and TM2, emphasizing the positive influence of supplementary materials on economic sustainability over the total life of the structure.

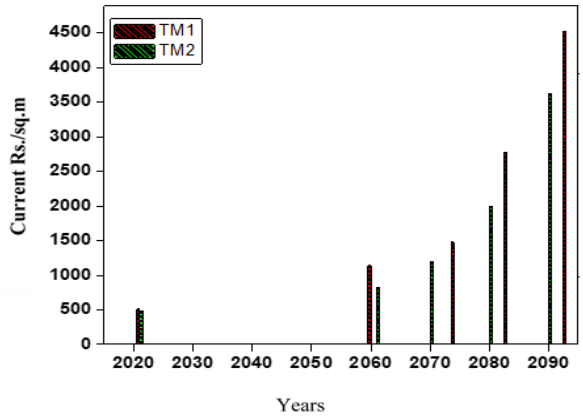

Fig. 4 shows the current cost

It is also observed that in Trial Mix 1, the current cost started adding its value at the age of 32 years whereas the same is started at 40 years in the case of Trial Mix 2. It is further to be noted that at the end of its life current cost of Trial Mix 1 is 24.32 % more than that of Trial Mix 2. This suggests that the addition of Fly Ash, GGBS, and Micro Silica positively influenced the economic sustainability of M70 grade concrete over the total life of the structure i.e. 70-year period [29].

4.6 Diffusivity Versus Time

Employing Life-365, the study analyses diffusivity over 70 years for two trial mixes. Figure 5 illustrates the results, showing that Trial Mix 1, incorporating Fly Ash and GGBS, reduces diffusivity.

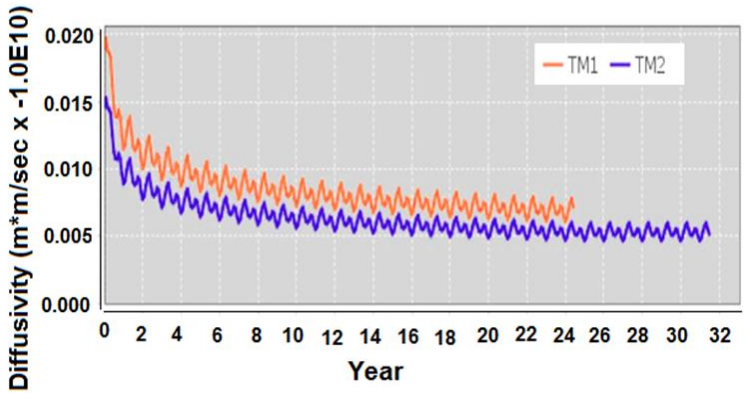

Fig. 5. Shows the change in diffusivity as a function of time

Trial Mix 1, which included Fly Ash and GGBS, demonstrated a 15% reduction in diffusivity compared to the control mix over 70 years. This suggests that the addition of Fly Ash and

GGBS had a positive impact on reducing the diffusion of harmful substances in M70-grade concrete, contributing to enhanced durability. Trial Mix 2, incorporating Fly Ash, GGBS, Silica Fume, and OPC, showed a further 10% reduction in diffusivity compared to Trial Mix 1.

4.7 Comparison of Initiation and Propagation of Chloride Penetration:

The study employed Life-365 software to scrutinize the initiation and propagation of chloride penetration over 70 years for two trial mixes incorporating supplementary materials. Graph 6 visually represents the outcomes of this analysis.

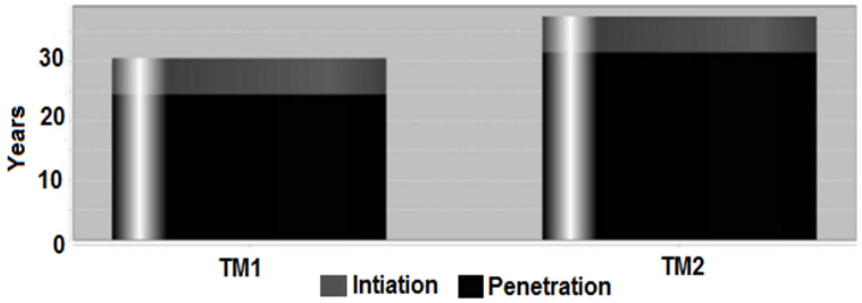

Fig. 6. shows the initiation of chloride penetration

Figure 6 indicates that Trial Mix 2 displayed a delayed initiation of chloride penetration compared to Trial Mix 1, emphasizing the enhanced resistance to chloride ion initiation. Furthermore, the propagation of chloride penetration in Trial Mix 2 exhibited a significantly slower pace than in Trial Mix 1, underscoring the effectiveness of the quaternary blend in preventing chloride ingress [30].

4.8 Chloride Concentration (% Weight) vs. Time in Years at a Depth of 60 mm

The study, utilizing Life-365 software, examined Chloride Concentration (% Weight) vs. Time at a depth of 60 mm over 70 years for two trial mixes with different compositions. The graphical representation of the chloride concentration analysis is presented below.

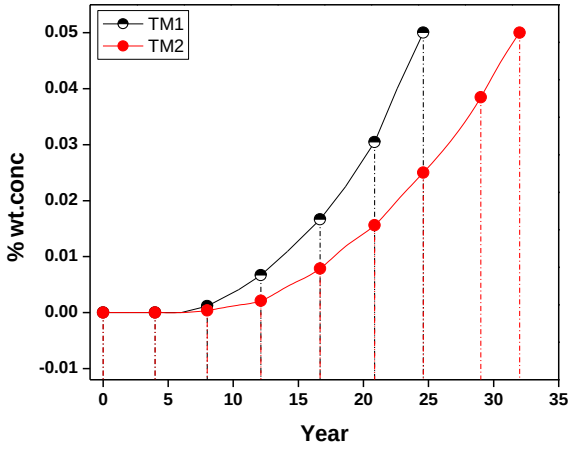

Fig. 7. Shows the effect of chloride concentration as a function of time at the depth of 60 mm

Figure 7 illustrates that Trial Mix 2 exhibited a considerably slower increase in chloride concentration compared to both the control mix and Trial Mix 1. This suggests that the additional inclusion of PFA, GGBS, and Silica Fume enhanced resistance to chloride penetration in Trial Mix 2, highlighting the effectiveness of the quaternary blend [31].

4.9 Life Cycle Cost Comparison Between Two Alternatives

The life cycle cost comparison analysis results for the two trial mixes are summarized and graphically presented in figure 8.

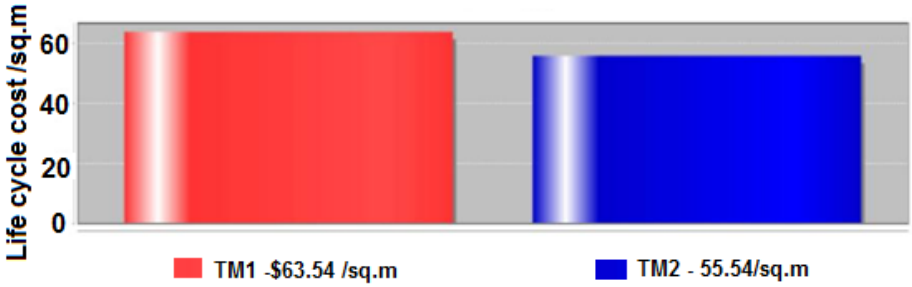

Fig. 8. Shows the comparison of life cycle cost

Figure 8 reveals that Trial Mix 2, incorporating PFA, GGBS, and Silica Fume, achieved a further 10% reduction in life cycle costs per square meter compared to Trial Mix 1. This underscores the cumulative positive impact of supplementary materials in Trial Mix 2, contributing to extended service life and reduced overall costs [32].

4.10 Surface Concentration of Chloride (% Weight) vs. Time in Years

The study utilized Life-365 software to analyse the surface concentration of chloride over 70 years for two trial mixes. The outcomes of the surface concentration of chloride analysis for the two trial mixes are presented graphically below.

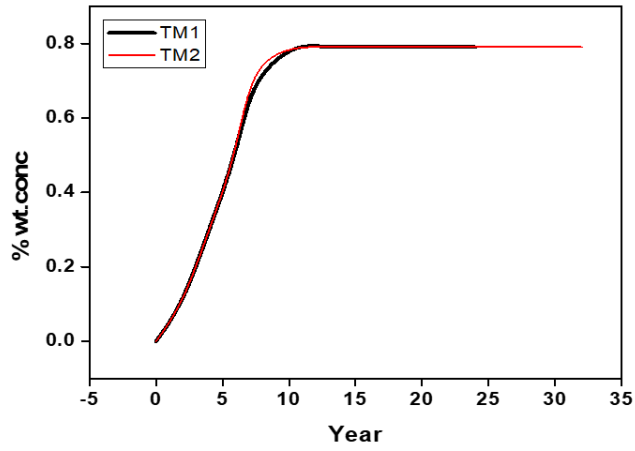

Fig. 9. Shows the surface concentration of chloride as a function of time

Figure 9 demonstrates that Trial Mix 2 exhibited an even slower increase in surface chloride concentration compared to Trial Mix 1. This suggests that the additional inclusion of PFA, GGBS, and Silica Fume further improved the resistance to chloride penetration at the concrete surface, highlighting the effectiveness of the quaternary blend [33].

4.11 Constant Cost Incurred in the Life of a Structure

The study, utilizing Life-365 software, analysed constant costs per square meter over 75 years for two trial mixes. The outcomes of the constant cost analysis for the two trial mixes are summarized and presented graphically below.

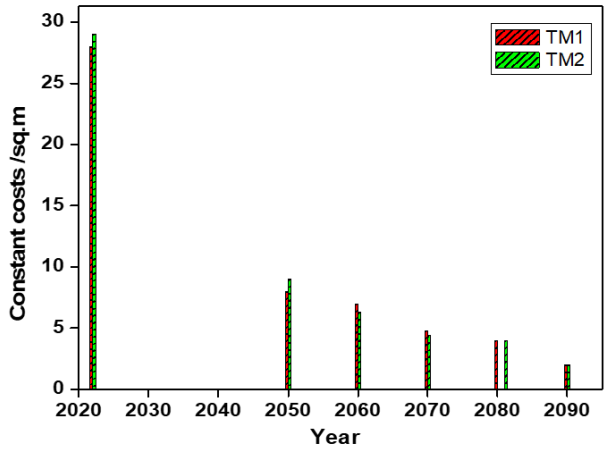

Fig. 10. Shows the constant cost as a function of time

5. Limitation of the Work

5.1 Dependence on Assumptions and Approximations

The Life-365 software relies on several assumptions and approximations for predicting chloride ingress, corrosion initiation, and life cycle costs. These assumptions may not always accurately represent real-world conditions, leading to potential discrepancies between predicted and actual performance.

5.2 Data Quality and Availability

The accuracy of Life-365's predictions heavily depends on the quality and completeness of the input data. In cases where precise data on environmental conditions, material properties, and economic factors are unavailable or unreliable, the software's outputs may be compromised.

5.3 Simplification of Complex Processes

While Life-365 models the essential aspects of chloride-induced corrosion and concrete deterioration, it simplifies many complex processes. Factors such as varying environmental conditions, load-induced stresses, and interactions between different degradation mechanisms are not fully accounted for, which can affect the robustness of the predictions.

5.4 Geographic and Climatic Variability

The software's performance may vary significantly based on geographic and climatic conditions. While it includes generalized environmental data, local variations in temperature, humidity, and chloride exposure may not be precisely captured, potentially leading to inaccuracies in service life predictions.

5.5 Limited Consideration of Non-Chloride Aggressors

Life-365 primarily focuses on chloride-induced corrosion and does not comprehensively address other potential aggressors such as carbonation, sulfate attack, or alkali-silica reaction. Structures exposed to multiple or combined deterioration mechanisms may require additional analysis beyond the capabilities of Life-365.

5.6 Economic Factor Variability

The economic analysis within Life-365 assumes static costs for materials, labor, maintenance, and repairs. However, these costs can fluctuate due to market conditions, inflation, and regional economic factors, potentially affecting the accuracy of the life cycle cost analysis.

5.7 User Expertise and Interpretation

The effectiveness of Life-365 depends on the expertise of the user. Incorrect input data, improper calibration of the model, or misinterpretation of the results can lead to suboptimal decision-making. Training and experience are essential to maximize the software's potential benefits.

5.8 Software Limitations and Updates

As with any software, Life-365 is subject to limitations in its algorithms and computational capabilities. Additionally, the need for regular updates to incorporate the latest research findings, standards, and technological advancements can be a challenge. Users must ensure they are using the most current version of the software.

5.9 Scope of Applicability

The study primarily focuses on quaternary blended M70 grade concrete. While the findings provide valuable insights for this specific mix design, the applicability of the results to other concrete grades or mix designs with different proportions or supplementary materials may be limited.

5.10 Site-Specific Variability

The performance of concrete structures can vary significantly based on site-specific factors such as construction practices, workmanship quality, and on-site environmental conditions. These factors are not fully captured in the software's predictions, potentially affecting the real-world applicability of the study's conclusions.

These limitations highlight the need for cautious interpretation and application of the study's findings. While Life-365 provides a valuable framework for life cycle cost analysis, supplementary analyses and considerations are necessary to ensure comprehensive and accurate assessments for concrete infrastructure projects.

6. Conclusions

The contemporary construction industry is progressively prioritizing the integration of cost optimization and energy-efficient strategies. This necessitates a comprehensive approach that encompasses both the initial acquisition costs and the long-term service life costs of structures. Life Cycle Cost (LCC) analysis emerges as a crucial tool in this endeavour, providing a holistic framework to evaluate the economic feasibility and sustainability of construction materials and methodologies.

In this study, we conducted a detailed LCC analysis using Life-365 software, focusing on two specific concrete mix design trials: TM1 and TM2, both designed for M70 grade concrete. TM1 consists predominantly of Ordinary Portland Cement (OPC), while TM2

incorporates supplementary cementitious materials such as Ground Granulated Blast Furnace Slag (GGBS) and Micro Silica, reflecting a quaternary blended composition. Our objective was to not only compare their immediate performance but also project their long-term economic and durability implications.

The findings from the Life-365 analysis indicate significant differences in the long-term cost efficiency and durability between TM1 and TM2. TM2 demonstrated a substantial reduction in life cycle costs due to its enhanced resistance to chloride penetration, leading to extended service life and lower maintenance requirements. This underscores the economic advantages of incorporating supplementary materials in concrete mixes, which enhance durability and reduce the frequency and cost of repairs over the structure's lifespan.

One of the critical insights from this study is the necessity of making informed adjustments and considerations when using predictive tools like Life-365. While the software provides valuable approximations, the accuracy of its prediction's hinges on the precise calibration of input parameters based on site-specific conditions and material properties.

Furthermore, the study highlights the broader implications of LCC analysis for sustainable construction. By demonstrating the long-term cost savings and durability benefits of quaternary blended concrete, we provide a compelling case for the adoption of such materials in construction projects, particularly in environments exposed to aggressive conditions like chloride ingress.

For engineers and decision-makers, these insights are invaluable. They emphasize the importance of looking beyond initial construction costs and considering the total cost of ownership over the structure's life. This approach not only promotes economic efficiency but also aligns with the principles of sustainable development by minimizing resource consumption and environmental impact over the long term.

In conclusion, our study reinforces the critical role of LCC analysis in guiding sustainable construction practices. By integrating economic and durability assessments, we can make more informed decisions that ensure the construction of cost-effective, durable, and environmentally friendly infrastructure. The adoption of quaternary blended concrete, as evidenced by the superior performance of TM2, represents a significant step forward in achieving these goals.

References

[1] Durairaj SK, Ong SK, Nee AYC, Tan RBH. The valuation of Life Cycle Cost Analysis Methodologies. Corporate Environmental Strategy. 2002;9:30-9. https://doi.org/10.1016/S1066-7938(01)00141-5

[2] Hooton RD. Canadian use of ground granulated blast-furnace slag as a supplementary cementing material for enhanced performance of concrete. Canadian Journal of Civil Engineering. 2000;27(4):754-60. https://doi.org/10.1139/l00-014

[3] Dave N, Misra AK, Srivastava A, Sharma AK, Kaushik SK. Study on quaternary concrete micro-structure, strength, durability considering the influence of multi-factors. Construction and Building Materials. 2017;139:447-57. https://doi.org/10.1016/j.conbuildmat.2017.02.068

[4] Jeong Y, Park H, Jun Y, Jeong JH, Oh JE. Microstructural verification of the strength performance of ternary blended cement systems with high volumes of fly ash and GGBFS. Construction and Building Materials. 2015;95:96-107. https://doi.org/10.1016/j.conbuildmat.2015.07.158

[5] Golewski GL. Concrete Composites Based on Quaternary Blended Cements with a Reduced Width of Initial Microcracks. Applied Sciences. 2023;13(12):7338. https://doi.org/10.3390/app13127338
[6] Hashemmoniri S, Fatemi A. Optimization of Lightweight Foamed Concrete Using Fly Ash Based on Mechanical Properties. Innovative Infrastructure Solutions. 2023;8:59-68. https://doi.org/10.1007/s41062-022-01016-2
[7] Manatkar PA, Koratkar VJ, Lonkar YN, Parmar KS, Sonawane DA, Thombare RR. Life Cycle Cost Analysis of Commercial Building (Collector Office Pune) with Sustainability Approach. International Journal for Research in Applied Science & Engineering Technology (IJRASET). 2018;6(VI). https://doi.org/10.22214/ijraset.2018.6078
[8] Abraham DM, Dickinson RJ. Disposal costs for environmentally regulated facilities: LCC approach. Journal of Construction Engineering and Management. 1998;124(2):146-54. https://doi.org/10.1061/(ASCE)0733-9364(1998)124:2(146)
[9] Reis JML, Chianelli-Junior R, Cardoso JL, Marinho FJV. Effect of Recycled PET in the Fracture Mechanics of Polymer Mortar. Construction and Building Materials. 2011;25:2799-804. https://doi.org/10.1016/j.conbuildmat.2010.12.056
[10] Sterner E. Life-cycle costing and its use in the Swedish building sector. Building Research and Information. 2000;28(5/6):387-93. https://doi.org/10.1080/096132100418537
[11] Clift M, Bourke K. Study on whole life costing. DETR Report No. CR 366/98; 1999.
[12] Larsson N, Clark J. Incremental costs within the design process for energy-efficient buildings. Building Research and Information. 2000;28(5/6):411-6. https://doi.org/10.1080/096132100418573
[13] Cole RJ, Sterner E. Reconciling theory and practice of life-cycle costing. Building Research and Information. 2000;28(5/6):368-75. https://doi.org/10.1080/096132100418519
[14] Flanagan R, Kendell A, Norman G, Robinson GD. Life cycle costing and risk management. Construction Management and Economics. 1987;5:53-71. https://doi.org/10.1080/01446193.1987.10462093
[15] Jakob M. Marginal costs and co-benefits of energy efficiency investments. The case of the Swiss residential sector. Energy Policy. 2006;34:172-87. https://doi.org/10.1016/j.enpol.2004.08.039
[16] Kovacic I, Zoller V. Building life cycle optimization tools for early design phases. Energy. 2015;92:409-19. https://doi.org/10.1016/j.energy.2015.03.027
[17] Chen S, Wang H, Guan J, Yao X, Li L. Determination Method and Prediction Model of Fracture and Strength of Recycled Aggregate Concrete at Different Curing Ages. Construction and Building Materials. 2022;343:128070. https://doi.org/10.1016/j.conbuildmat.2022.128070
[18] Zhang MH. Microstructure, Crack Propagation, and Mechanical Properties of Cement Pastes Containing High Volumes of Fly Ashes. Cement and Concrete Research. 1995;25:1165-78. https://doi.org/10.1016/0008-8846(95)00109-P
[19] Frangopol DM, Bruhwiler E, Faber MH, Adey B, editors. Life-cycle performance of deteriorating structures: assessment, design, and management. Reston, VA: ASCE/SEI; p. 229-36.
[20] Takahashi Y, Der Kiureghian A, Ang AH-S. Life-cycle cost analysis based on a renewal model of earthquake occurrences. Earthquake Engineering and Structural Dynamics. 2004;33:859-80. https://doi.org/10.1002/eqe.383
[21] Frangopol DM, Liu M. Maintenance and management of civil infrastructure based on condition, safety, optimization, and life-cycle cost. Structure and Infrastructure Engineering. 2007;3(1):29-41. https://doi.org/10.1080/15732470500253164
[22] Kappos AJ, Dimitrakopoulos EG. Feasibility of pre-earthquake strengthening of buildings based on cost-benefit and life cycle cost analysis, with the aid of fragility

curves. Natural Hazards. 2008;45(1):33-53. https://doi.org/10.1007/s11069-007-9155-9
[23] Flanagan R, Jewell C. A Practical Approach to Whole Life Appraisal for Construction. Whole Life Appraisal for Construction; p. 129-48.
[24] Yuan B, Wang H, Jin D, Chen W. C-S-H Seeds Accelerate Early Age Hydration of Carbonate-Activated Slag and the Underlying Mechanism. Materials. 2023;16:1394. https://doi.org/10.3390/ma16041394
[25] Alexander MG. Durability and service life prediction for concrete structures - developments and challenges. MATEC Web of Conferences. 2018;149:01006. https://doi.org/10.1051/matecconf/201714901006
[26] International Organization for Standardization. ISO 13823-1 General Principles on the design of structures for durability. Geneva: ISO; 2008.
[27] Alyousef R, Abbass W, Aslam F, Gillani SAA. Characterization of High-Performance Concrete using Limestone Powder and Supplementary Fillers in Binary and Ternary Blends under Different Curing Regimes. Case Studies in Construction Materials. 2023;18. https://doi.org/10.1016/j.cscm.2023.e02058
[28] Suchorab Z, Franus M, Barnat-Hunek D. Properties of Fibrous Concrete Made with Plastic Fibers from E-Waste. Materials. 2020;13:2414. https://doi.org/10.3390/ma13102414
[29] Aghajanian A, Cimentada A, Fayyaz M, Brand AS, Thomasa C. ITZ Microanalysis of Cement-Based Building Materials with Incorporation of Siderurgical Aggregates. Journal of Building Engineering. 2023;67:106008. https://doi.org/10.1016/j.jobe.2023.106008
[30] Juenger MCG, Snellings R, Bernal SA. Supplementary Cementitious Materials: New Sources, Characterization, and Performance Insights. Cement and Concrete Research. 2019;122:257-73. https://doi.org/10.1016/j.cemconres.2019.05.008
[31] Pacewska B, Wilińska I. Usage of Supplementary Cementitious Materials: Advantages and Limitations: Part I. C-S-H, C-A-S-H and Other Products Formed in Different Binding Mixtures. Journal of Thermal Analysis and Calorimetry. 2020;142:371-93. https://doi.org/10.1007/s10973-020-09907-1
[32] Menéndez G, Bonavetti V, Irassar EF. Strength development of ternary blended cement with limestone filler and blast-furnace slag. Cement and Concrete Composites. 2003;25:61-7. https://doi.org/10.1016/S0958-9465(01)00056-7
[33] Liu F, Zou Y, Wang B, Yuan X. The Effect of Stray Current on Calcium Leaching of Cement-Based Materials. Materials. 2022;15:2279. https://doi.org/10.3390/ma15062279

Research on Engineering Structures & Materials
www.jresm.org
MIM Research Group

Research Article

Investigating the constraint role in *J-CTOD* relationship for compact tension (CT) specimen

Nagaraj Ekabote[a]

School of Mechanical Engineering, KLE Technological University, Hubli, India

Article Info

Article history:

Received 19 Apr 2024
Accepted 03 July 2024

Keywords:

CTOD;
J-integral;
Constraint factor (m);
ASTM 1820;
45^0 intercept method

Abstract

The Crack Tip Opening Displacement (CTOD or δ) estimation from J-integral (J) defined by ASTM 1820 considers the CTOD dependency on material properties, and the constraint factor (m). The m in Compact Tension (CT) specimen is based on yield to tensile strength ratio (σ_{ys}/σ_{ut}) without taking into account of in-plane dimensions as in Single Edge Notch Bending (SENB). Hence, an attempt is made to understand the effect of crack length to specimen width (a/W), specimen thickness to specimen width (B/W) for different σ_{ys}/σ_{ut} on CTOD using CT specimen. A new method of estimating the CTOD from FE analysis is demonstrated and validated with 45^0-intercept method. It has been found that the ASTM 1820 based CTOD (δ_{ASTM}) assessed values under-estimate the actual CTOD present in the CT specimen. The variation in a/W and B/W doesn't affect the J-CTOD relationship as stated by ASTM 1820. However, the CTOD measured by FE analysis (δ_{FE}) are consistently higher than the δ_{ASTM}. Therefore, an effort is made to correct the constraint factor, m based on present FE analysis by considering the effect of σ_{ys}/σ_{ut}. The proposed corrected constraint factor, m_{FE}, can be employed in fracture applications that generally need both the J-integral and the CTOD.

1. Introduction

Stress intensity factor (K_I) and *J*-integral (*J*) are the common fracture parameters used to determine the crack behavior in elastic and elastic-plastic materials, respectively. The K_I (stress-based parameter) and *J* (energy-based parameter) are determined using the applied load, Crack Mouth Opening Displacement (*CMOD*), and crack length (*a*) increment. Similarly, Crack Tip Opening Displacement (*CTOD*) is the oldest fracture toughness parameter used for fracture assessment of pipelines, pressure vessels, and oil and gas industries [1, 2]. *CTOD* is the displacement-based parameter, and its direct relation with micro mechanisms of dislocations among the grains to characterize the material is an advantage over other fracture toughness parameters [3, 4]. However, unlike K_I and *J* evaluation, the acceptance of *CTOD* is deprived, owing to its distinct estimation methods adopted by different standards. The under and over-estimation of actual *CTOD* by these standards led to restricting the *CTOD* application as a characterizing fracture parameter.

CTOD, refers to the displacement of the original crack tip in the direction of the applied force. The Plastic Hinge Method (PHM) and *J*-based *CTOD* techniques were adopted by different standard bodies for critical *CTOD* measurement (δ_{IC}). *CTOD* measurements derived from PHM-based technique were accepted by the Japan Welding Engineering Society (JWES) and British Standard Institution (BSI) standards. The literature [1, 5-7] revealed the PHM-based measured *CTOD*'s vulnerability towards the specimen's geometry

Corresponding author: nagaraj_ekbote@kletech.ac.in, ekabotenagaraj@gmail.com
[a]orcid.org/0000-0002-5711-7416
DOI: http://dx.doi.org/10.17515/resm2024.251me0419rs

and material property. The researchers [5-7] recommended modifying the PHM-based *CTOD* equation accounting for various specimen geometry and material properties. Experimental *CTOD* values validated these modifications in the equations of the *CTOD*. However, the standard bodies have yet to recommend these modified equations for the critical *CTOD* measurement. Also, the applicability of the modified equations other than Single Edge Notch Bending (SENB) must be verified. Previous studies [6-10] have documented the precise experimental determination of *CTOD* via the digital image correlation (DIC) technique and the silica replica method. However, the time and effort required to measure *CTOD* using these techniques limit its applicability as a fracture parameter.

ASTM 1820 [11] recommends the *CTOD* estimation using experimentally evaluated *J* as shown in Equation (1). In Equation (1), the σ_Y represents the effective yield strength and m is the constraint parameter. The dependency of m on specimen type and geometry is also acknowledged in Equation (1) for SENB and Compact Tension (CT) specimens. According to ASTM 1820, the m depends on σ_{ys} (yield stress) and σ_{ut} (ultimate stress) along with geometrical constants A_0, A_1, A_2, and A_3. These geometrical constants A_0, A_1, A_2, and A_3 are crack length (a) dependent in SENB but independent in the CT specimen. As per our best knowledge, there is no justification in literature or standards for the non-inclusiveness of the a/W effect on *CTOD* in CT specimen. However, the in-plane constraint variation due to crack length to specimen width (a/W) in the case of CT for other fracture toughness parameters (K_I and J) was well evidenced in the literature [8, 12, 13]. Similarly, the effect of specimen thickness to width (B/W) on fracture toughness and constraint variation [12-15] was reported. Hence, it is essential to investigate the role of specimen geometry variations on *CTOD* using CT specimen.

$$\delta = \frac{J}{m\,\sigma_Y} \tag{1}$$

Where;

$$m = A_0 - A_1 * \left(\frac{\sigma_{ys}}{\sigma_{ut}}\right) + A_2 * \left(\frac{\sigma_{ys}}{\sigma_{ut}}\right)^2 - A_3 * \left(\frac{\sigma_{ys}}{\sigma_{ut}}\right)^3 \tag{2}$$

For SENB;

$$A_0 = 3.18 - 0.22 * \left(\frac{a}{W}\right) \tag{3}$$

$$A_1 = 4.32 - 2.23 * \left(\frac{a}{W}\right) \tag{4}$$

$$A_2 = 4.44 - 2.29 * \left(\frac{a}{W}\right) \tag{5}$$

$$A_3 = 2.05 - 1.06 * \left(\frac{a}{W}\right) \tag{6}$$

For CT;

$$A0 = 3.62,\ A1 = 4.21,\ A2 = 4.33,\ and\ A3 = 2.00 \tag{7}$$

Equation (1) was derived from extensive Finite Element (FE) analysis using 45^0-intercept method to measure the *CTOD* [11] and is applicable for $\sigma_{ys}/\ \sigma_{ut} \geq 0.5$. Kodancha & Kudari [16] re-evaluated the *J-CTOD* relationship using FE based 45^0 -intercept method and PHM

for CT and SENB. It has been concluded that d_n (=1/m) factor strongly depends on the *CTOD* estimation technique. Also, the influence of specimen type, applied load, and material on *CTOD* was reported. Similarly, Kittur et al. [17] also noticed the d_n factor and a/W influence on the magnitude of *CTOD* measured as per ASTM 1290 (now this standard is withdrawn) on CT specimen. Further, M. Graba [18] proposed the d_n equation, accounting for the effect of strain hardening, a/W, and applied load on SENB specimen. Tagawa et al. [19] reported that the *CTOD* from ASTM 1290 was 60% lower in SENB compared to the *CTOD* measured from BS 7448 for low σ_{ys}/σ_{ut} steels. Similarly, Kawabata et al. [20] found out the ASTM 1820 based *CTOD* estimation values were 15% lower compared to experimentally estimated *CTOD* in SENB. The effect of σ_{ys}/σ_{ut} on *CTOD* was considered in a newly proposed *CTOD* estimation method to minimize the difference with experimentally measured *CTOD*. Savioli et al. [21] presented the new equations for estimating *CTOD* and *J* in CT specimen with center-line crack welds. The results revealed the dependency of *CTOD* on a/W, strain hardening of the alloy, and strength mismatch ratio. Khor et al. [5] witnessed the inconsistency in *CTOD* values estimated from different standards over a range of σ_{ys}/σ_{ut} in SENB specimen. Kayamori and Kawabata [22] claimed that the *J*-based *CTOD* estimation is more effective in considering the a/W and σ_{ys}/σ_{ut} compared to PHM while using CT specimen.

In the literature [1, 5-7], the researchers and practicing engineers preferred PHM-based *CTOD* estimation over *J*-based *CTOD*. However, the *CTOD* measurement from *the J*-based method is favored at high-temperature applications due to non-dependency on *CMOD* measurement. Also, most *CTOD* measurement techniques were revised to suit SENB rather than CT specimen. In specific applications (like aircraft wings and spars), the CT specimen is appropriate for fracture toughness evaluation and involves extreme temperature variations [23-25]. It is essential to establish a unique and well-accepted relationship between *CTOD* and other popular fracture parameters for the widespread usage of *CTOD* in most applications [1, 5-7, 26]. Overall, the suitability of the *CTOD* estimation method is vital but complex, and hence, a more inclusive and accurate *CTOD* estimation method is essential. This study aims to reassess the implications of a/W, B/W, and σ_{ys}/σ_{ut} on *J*-based *CTOD*, as specified in ASTM 1820, for CT specimens. Further, these implications on the *J*-based *CTOD* equation will be considered for effective constraint inclusiveness.

2. Specimen and Material Details

The three different strain-hardening steels ranging between $0.45 < \sigma_{ys}/\sigma_{ut} > 1$ have been selected from the work of Khor et al. [5, 7]. The chosen steels have σ_{ys}/σ_{ut} of 0.93, 0.72, and 0.48 and are designated further as ST01, ST02, and ST03, respectively. The chosen steel grades will be used to assess the efficiency of the *J*-based *CTOD* equation developed from ASTM 1820, across a wider spectrum of strain hardening. The essential properties of these steel materials are given in Table 1. Typically, a low strain hardening steel have strain hardening exponent (n) less than 0.1, higher σ_{ys}/σ_{ut}, and lower % elongation. The Poisson's ratio (υ) and Elastic modulus (E) are the linear elastic properties.

Table 1. Drill pipe dimensions and properties [4]

Steel category	σ_{ys} (MPa)	σ_{ut} (MPa)	σ_{ys}/σ_{ut}	E (GPa)	υ
ST01	850	914	0.93	217	0.29
ST02	421	585	0.72	205	
ST03	286	595	0.48	205	

Figure 1 displays the typical CT specimen involved for *J* and *CTOD* investigation. The CT specimen has a width (*W*) of 25.4 mm, and the remaining parameters are determined according to the relationship specified in Fig. 1.

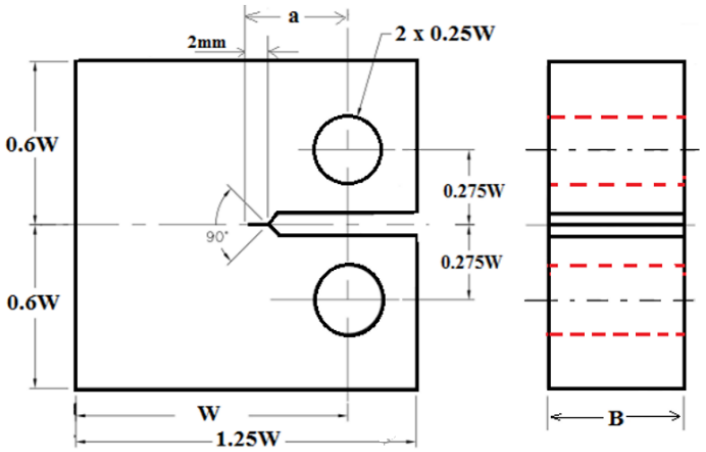

Fig. 1. Standard CT Specimen

To investigate the *a/W*, and *B/W* impact on *J* and *CTOD* fracture parameters, the CT specimens with varied crack length and specimen thicknesses were considered. The *a/W* is varied as 0.45, 0.5, and 0.7, within specified range as per ASTM 1820. Similarly, the thin, standard, and thick specimen effect is considered by varying the *B/W* as 0.25, 0.5, and 1 respectively. The 3-dimensional CT specimens representing the low, medium, and high strain hardening properties, with specimen geometry variations in terms of *a/W* and *B/W* are modelled in ABAQUS software. The 3D models are further processed for elastic-plastic fracture analysis and the details of FE analysis are discussed in further section.

3. Finite Element Analysis

3.1. Meshing and Boundary Conditions

A 3-dimensional non-linear fracture investigation was conducted utilizing ABAQUS 6.14 software. A 3-D half-symmetry CT specimen model was used for analyses. Linear elastic properties (E and υ), and stress-strain post-yield values were input parameters in non-linear fracture analyses. The procedure to input the material properties and stress-strain values into the ABAQUS software was documented in the ABAQUS manual and adopted similarly to the work of Kudari et al. [16]. The symmetrical boundary condition at the un-cracked ligament (*W-a*) and the tensile load along the *y*-direction at the hole was applied, as shown in Fig. 2.

Three-dimensional models with varied *a/W*, *B/W,* and σ_{ys}/σ_{ut} were used in the analyses. 20-noded hexahedral elements with reduced integration (C3D20R) were used for meshing. Near crack area, smaller size elements were utilized to ensure accurate measurement of *CTOD*. The center nodes of the crack adjacent C3D20R elements were advanced in the direction of crack [16, 25]. The movement of these crack adjacent center nodes ensured the natural crack characteristics. Small element size meshes around the crack and relatively coarse mesh far from the crack were utilized for non-linear fracture analysis. The mesh quality was finalized based on converging *J* values and a uniform plasticity distribution around the crack front. Around twenty thousand elements were typically used

for a 3-D symmetric model of $a/W = B/W = 0.5$, of which about 12,000 elements situated at crack surroundings and is shown in Fig. 2.

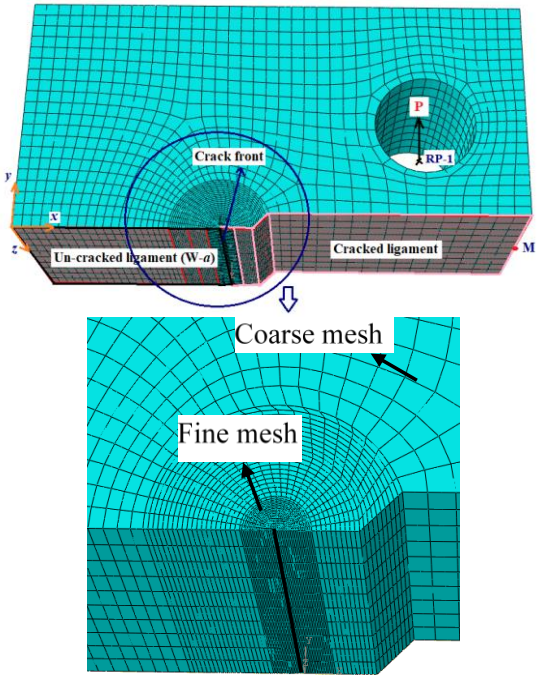

Fig. 2. Three-Dimensional half symmetrical CT model with boundary conditions

3.2. *J*-Integral Extraction and Validation

The direct extraction of *J* values is done from ABAQUS and are similar to the procedure of Kudari et al. [16]. The extracted *J* values are non-linear concerning the load applied. The *CMOD* is the *y*-displacement at the mouth grooves measured through a clip gauge in the fracture toughness experiment. In FE analysis, the *CMOD* can be measured along the loading direction at the mouth groove (point M in Fig. 2). The present non-linear fracture analysis methodology is verified with the Kudari et al. [16] results. The *CMOD* vs. *J* are plotted in Fig. 3 for the CT specimen made of Interstitial Free steel. For a thin specimen, with a/W = 0.5 and W = 20 mm the *J* values are extracted from ABAQUS and used to compare with the Kudari et al. [16] results as plotted in Fig. 3. From Fig. 3, it is confirmed that the results validate the current elastic-plastic fracture procedure, since they significantly coincide with the findings of Kudari et al. [16].

3.3. *CTOD* Extraction and Validation

Similarly, *CTOD* are measured by using 45^0-intercept method (also known as 90^0-intercept method). In this method, along the cracked ligament nodes the displacement in *y*-direction is measured. A typical *y*-displacement of nodes considered along specimen center and surface in the cracked ligament area is shown in Fig. 4. It has been reported that the specimen crack center point possesses the larger *y*-displacement value compare to specimen surface [5, 25]. The measured displacements along the cracked ligament from specimen crack center point are plotted and is shown in Fig. 5. From the origin of the graph, a 45^0 line will be drawn (dotted line in Fig. 5), which will intercept with the *y*-displacement curve (pink line in Fig. 5). The vertical (*y*-direction) distance from the intercept point to

the *x*-axis is termed as *CTOD*/2 as per 45^0-intercept method. Comprehensive FE analysis yields the *J*-based *CTOD*, Equation (1), where the *CTOD* is measured using the 45^0-intercept approach.

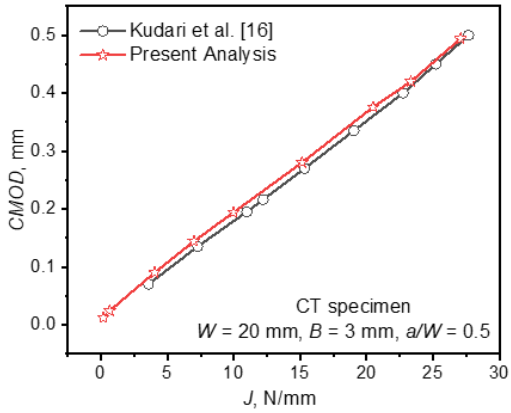

Fig. 3. *J* vs. *CMOD* for thin CT specimen

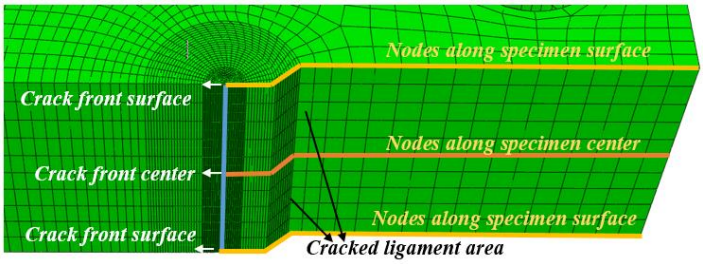

Fig. 4. *J* vs. Cracked ligament area at center and surface

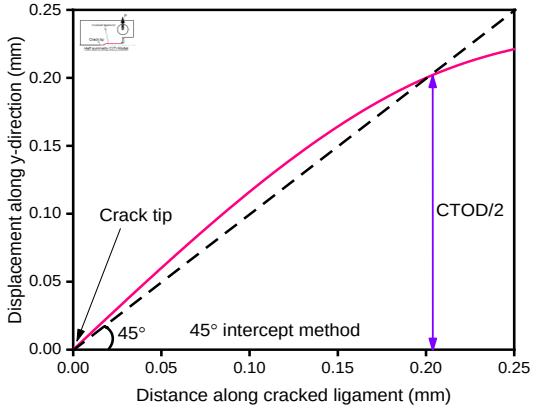

Fig. 5. *CTOD* measurement by 45^0-intercept method

The major limitation of the 45^0-intercept method is its incapability to measure the *CTOD* at lower load magnitudes. Therefore, the *CTOD* at lower loads may be obtained by using Equation (1), which was derived by extrapolating the *CTOD* values. To assess *CTOD* at lower loads, a new *CTOD* estimation approach based on FE analysis is helpful in updating

the value of the constraint parameter in Equation (1). The new technique for measuring the FE-based *CTOD*, its validity and accuracy are discussed in the following section.

3.4. δ_{FE} technique

The $CTOD/2$ value in the δ_{FE} technique is determined by taking the y-displacement of first nearest node from crack front along the cracked ligament direction. Fig. 6 (a) shows the chosen first nearest node along the cracked ligament in the unloaded half-symmetry CT model. For any applied load, the corresponding y-displacement of this chosen node will result in the $CTOD/2$ value as shown in Fig. 6 (b). The proposed δ_{FE} technique seems to be simpler and can be measured directly at chosen single node at cracked ligament.

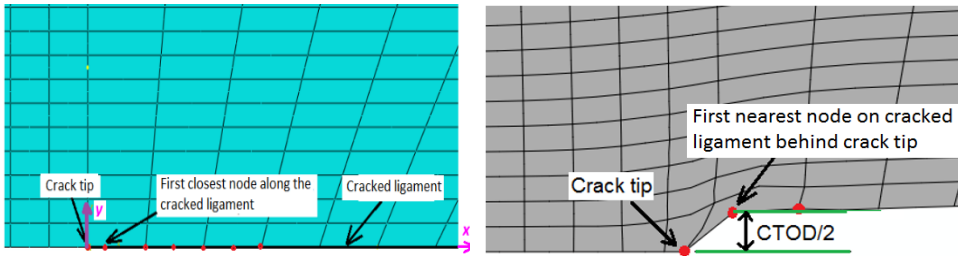

(a) (b)

Fig. 6. *CTOD* measurement by δ_{FE} technique (a) before loading (b) after loading

The accuracy of δ_{FE} technique is measured by comparing with the *CTOD* obtained from 45^0-intercept method (δ_{45}). Fig. 7 shows the *CTOD* measured by the δ_{FE} and δ_{45} techniques with respect to applied stress ratio (applied stress / yield stress = $\sigma_{appl}/\sigma_{ys}$). The nature of *CTOD* variation are non-linear and similar to the J variations. The δ_{FE} technique accurately measured the *CTOD* as similar to the δ_{45} technique for both standard and thick specimens. The δ_{45} technique unable to measure the $CTOD < 0.4$ mm, making it less suitable for lower applied loads. However, δ_{FE} technique accounts the lower *CTOD* values at lower applied loads and *CTOD* measurement is simpler.

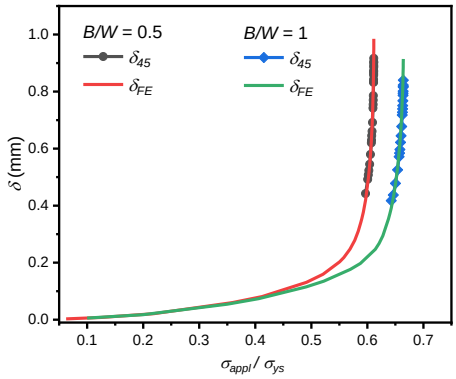

Fig. 7. Comparison of δ_{FE} and δ_{45} techniques

The quality and type of mesh influence on the proposed δ_{FE} technique is verified by introducing the various mesh refinements along the sharp crack front. A fine mesh at crack with up to 0.05 mm gap between crack tip and the first node along the ligament resulted *CTOD* identical (within 2% error) to δ_{45}. As the gap between first node and tip increases more than 0.05 mm, the difference widens for δ_{FE} and δ_{45}. A minimum of 0.05 mm gap may

not result the identical *CTOD* as δ_{45} for some other fracture specimen and mesh quality. Hence, in the absence of comprehensive results on other fracture specimens, one must conduct an extensive FE analysis to define the gap between crack tip and first node. The finer and refined mesh quality near the crack is important in achieving the better *CTOD* value. Also, the smaller elements near the crack ensures the better plasticity distribution. However, the effectiveness of the proposed δ_{FE} technique for blunted cracks used for ductile materials need to be verified. The satisfactory validation depicted in Fig. 7 justifies the adoption of the proposed δ_{FE} technique for subsequent discussions and analysis.

4. Results and Discussions

In this section, the influence of geometry (*a/W*, and *B/W*) and $\sigma_{ys}/\ \sigma_{ut}$ *on J-CTOD* relationship are analyzed. *CTOD* measured from ASTM 1820 will be represented as δ_{ASTM} in further discussions. Both δ_{FE} and δ_{ASTM} are used to analyze the *J-CTOD* relationship.

4.1. δ_{FE} technique

The half-symmetrical CT specimens with *a/W* varying as 0.45, 0.5 and 0.7 are modelled. The standard thickness of *B/W* = 0.5 and the material properties of ST01, ST02, and ST03 are employed in FE analysis. The estimated *CTOD* values as per ASTM 1820 and proposed δ_{FE} technique are shown in Fig. 8. J/σ_Y along the *x*-direction and estimated *CTOD* values along *y*-direction are considered to verify the relation between *J-CTOD*. It has been observed from Fig. 8, that the *a/W* variation has nullifying effect on *CTOD* values measured by both methods for different steel materials considered in the study. However, the δ_{FE} measured values are consistently higher compared to δ_{ASTM} and considered to be improved represented magnitudes of *CTOD* (as validated in Fig. 3). The similar trend of underestimating the actual *CTOD* by δ_{ASTM} compared to PHM are earlier reported [18-20].

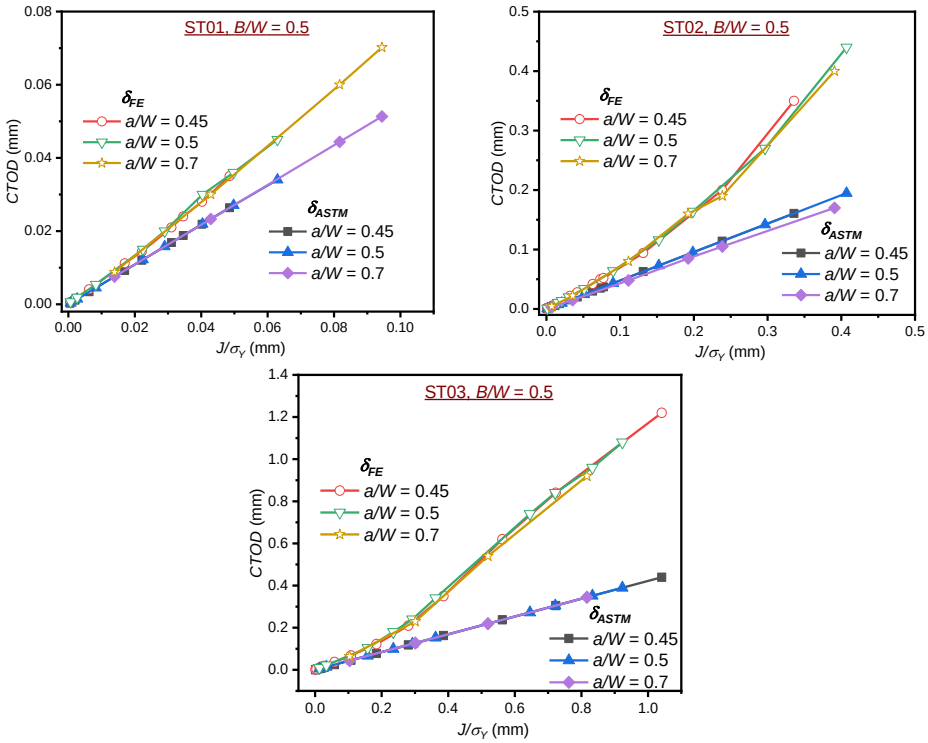

Fig. 8. Effect of *a/W* on *CTOD*

Similarly, the effect of *B/W* on *J-CTOD* relationship is considered and plotted in Fig. 9. Thin, standard, and thick CT specimens are analyzed for standard *a/W* of 0.5. δ_{ASTM} values are unaltered by the varied specimen thickness indicating the effective *J-CTOD* relationship. As similar to Fig. 8, here also the δ_{FE} magnitudes are higher compared to δ_{ASTM} values. The *J* estimation procedure as per ASTM 1820 already imbibes the *a/W* and *B/W* effect and hence a strong relationship is witnessed between *J-CTOD* through unaltered curves for both δ_{ASTM} and δ_{FE}. However, the conservative δ_{ASTM} values shows its incapability to measure the actual constraint near the crack. This major limitation of δ_{ASTM} resulted in almost non-usage of *J*-based *CTOD* in fracture toughness assessments. The enhanced δ_{FE} values over δ_{ASTM} for all *a/W* and *B/W*, signifies a modification required in *J-CTOD* relationship for CT specimen. Hence, the improvised measurement technique to find *CTOD* through FE analysis may enhance the usage of *J*-based *CTOD*.

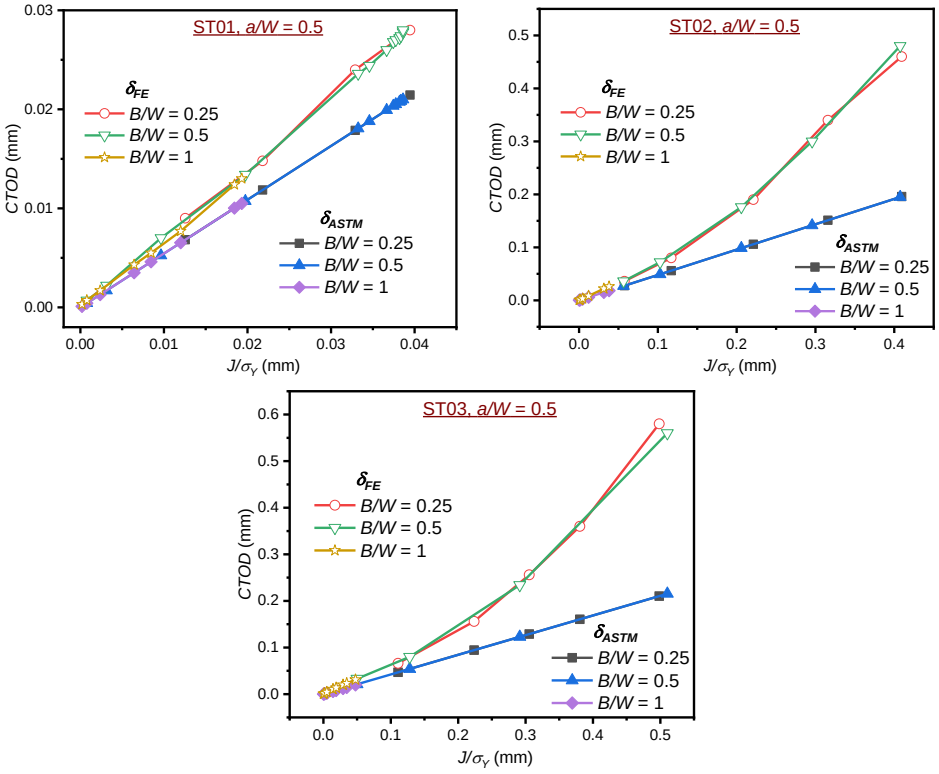

Fig. 9. Effect of *B/W* on *CTOD*

4.2. Effect of σ_{ys}/σ_{ut}

The varied strain hardening of the steel is represented in terms of σ_{ys}/σ_{ut} in the present analysis. Fig. 10 shows the estimated *CTOD* through FE analysis and ASTM 1820 for different strain-hardened steels at *a/W* = *B/W* = 0.5. Here also, the δ_{FE} values are higher over the δ_{ASTM} owing to the conservative constraint factor, *m*. The effect of σ_{ys}/σ_{ut} accounted through constraint factor, *m* equation for CT specimen in ASTM 1820. The higher magnitudes of δ_{FE} specify the better constraint measurement and can be acknowledged through the corrected constraint factor, m_{FE}. A distinction between δ_{ASTM} and δ_{FE} can be made by modifying the constraint factor, *m*, while maintaining the same format of Equation (1). By conducting an in-depth finite element analysis, the influence *a/W*, *B/W*, and σ_{ys}/σ_{ut} is adequately accounted in *J*-based *CTOD* estimation.

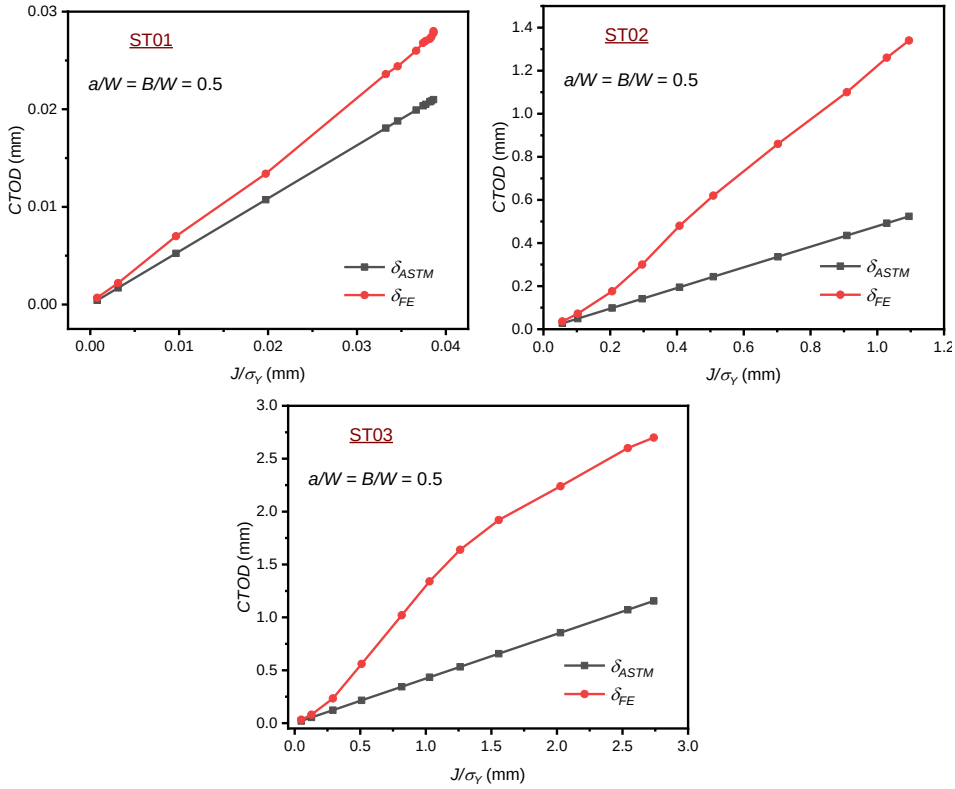

Fig. 10. *CTOD* for different strain hardening materials

The goal is to attain the identical *CTOD* value from PHM and *J*-based *CTOD* methods for a given loading. The reported literature favors the PHM-based standards over *J*-based *CTOD* due to their accuracy with the experimental *CTOD* assessments. However, the unique and recognized relationship among the other fracture toughness parameters is essential for wide acceptance and increased applicability. The interchangeability between fracture toughness parameters, *J* and *CTOD*, provides a strong understanding of non-linear fracture behavior through a constraint perspective. Hence, an attempt is made to extract the slope between J/σ_Y vs. *CTOD* for FE measured values in terms of the constraint factor, *m,* as shown in Fig. 11. The slope is further used to define the corrected constraint factor, m_{FE}, for the actual crack tip/front constraint measurement.

In Fig. 11, the constraint factor, *m,* decreased with increasing σ_{ys}/σ_{ut} and has been defined in ASTM 1820 through the constants A_0, A_1, A_2, and A_3. The cubic polynomial measures the constraint variation due to alteration in σ_{ys}/σ_{ut}. However, the variation of constraint factor, *m,* is linear and has been represented using the straight line as seen in Fig. 11. A cubic equation usage for linear variation of the constraint indicates overestimation and leads to errors. In the present FE analysis, the *m* value increased with an increase in σ_{ys}/σ_{ut}, and also shown the exponential variation with respect to σ_{ys}/σ_{ut}. The extensive FE analysis represented the improved crack constraint measurement resulting in corrected constraint factor, m_{FE} behavior. Thus, an effort is directed to define corrected values of constants A_0, A_1, A_2, and A_3 in the *m* equation. Based on the present FE analysis, the corrected values of constants are A_0 = -2.015, A_1 = -14.750, A_2 = -25.217, *and* A_3 = -14.298.

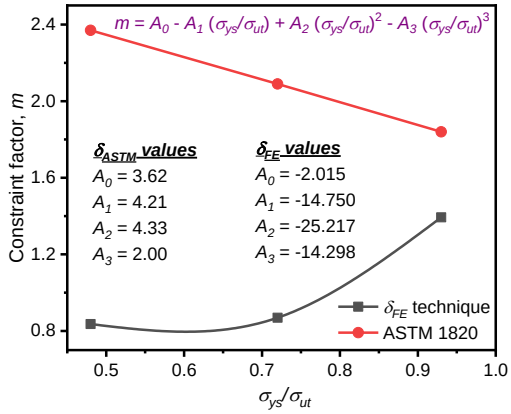

Fig. 11 Constraint factor, m as per ASTM 1820 and FE analysis

Equation (2) may be used to represent the corrected constraint factor, m_{FE}, based on newly suggested constants. The *CTOD* estimated from Equation (2) yielded sufficient accuracy (less than 2% error) compared to δ_{FE}. Equation (8) can be applied to B/W of 0.25 to 1, a/W of 0.45 to 0.7, and $\sigma_{ys}/\sigma_{ut} > 0.45$ to estimate *CTOD* between 0.01 and 1.5 mm. The variations in in-plane (a/W) and out-of-plane (B/W) dimensions align with the ASTM 1820 specified range. Therefore, the applicability of the proposed m_{FE} to different fracture assessments will boost the much-needed correction in ASTM 1820.

$$m_{FE} = -2.015 + 14.750\left(\frac{\sigma_{ys}}{\sigma_{ut}}\right) - 25.217\left(\frac{\sigma_{ys}}{\sigma_{ut}}\right)^2 + 14.298\left(\frac{\sigma_{ys}}{\sigma_{ut}}\right)^3 \quad (8)$$

The PHM based *CTOD* measurement is adopted by European and Japanese fracture toughness related standards. WES 1108 standard utilized the modified PHM to define *CTOD* measurement and is prevalent among the fracture mechanics applications [1, 7]. Unlike δ_{ASTM}, the *CTOD* measured from PHM not related to *J*-integral for its determination. The improvement in determining *CTOD* from corrected constraint factor, m_{FE} is verified for AA2050-T84 alloy having $\sigma_{ys}/\sigma_{ut} = 0.84$. CT specimen is used to understand the fracture behaviour of the aircraft spars and ribs made of AA2050-T84 alloy [23, 25]. Fig. 12 shows the *CTOD* values determined by WES 1108 (shown as $\delta_{\text{WES 1108}}$), ASTM 1820 (shown as $\delta_{\text{ASTM 1820}}$), and proposed δ_{FE} for $a/W = B/W = 0.5$. In the absence of an experimentally measured *CTOD* from DIC or silica replica method, Fig. 12 is useful in justifying the usefulness of δ_{FE}. The *CTOD* determined by ASTM 1820 are the least values due to improper constraint measurement between *J* and *CTOD*. Similarly, the *CTOD* derived by WES 1108 are higher and most *CTOD* based fracture assessment rely on this procedure. The gap between the $\delta_{\text{WES 1108}}$ and $\delta_{\text{ASTM 1820}}$ is larger and therefore the scarce usage of *CTOD* based fracture assessment witnessed in the field. However, the reduced gap between $\delta_{\text{WES 1108}}$ and δ_{FE} will help to relook of both *CTOD* measuring techniques to find efficient way to determine *CTOD* in future. Owing to the proper and efficient FE simulations accounted through corrected constraint factor, m_{FE}, the ASTM may need to re-examine the *J-CTOD* relationship for correction. In the literature, neither the PHM approach nor the *J*-based method can claim to be the correct method for quantifying the true *CTOD* of a CT specimen. However, typical data show that PHM-based *CTOD* measurement tends to overestimate the *CTOD* magnitude [19]. As seen in Fig. 12, the δ_{FE} values appear to be an improved assessment of the constraint at the crack over $\delta_{\text{ASTM 1820}}$. Thus, the suggested corrected constraint factor, m_{FE}, can be used in fracture applications that typically need both the *J*-integral and *CTOD.*

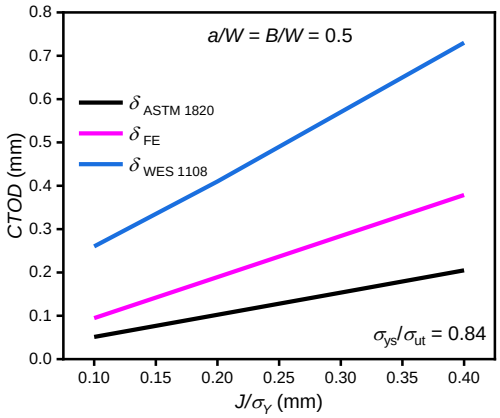

Fig. 12. J/σ_Y vs. *CTOD* by different *CTOD* measuring methods

5. Conclusion

This work primarily addresses the scarce usage of ASTM 1820 recommended *J*-based *CTOD* in fracture toughness assessments of CT specimens. Literature study revealed that the *J*-based *CTOD* equation underestimates the actual *CTOD*. Furthermore, according to ASTM 1820, the constraint at the fracture is determined using a constraint factor, *m*, with the CT specimen's dependence being solely on σ_{ys}/σ_{ut}. The present analysis studies the influence of geometrical variations and σ_{ys}/σ_{ut} on constraint parameter, *m*. The limitation of the 45^0-intercept method and its implications on constraint measurement is addressed by a novel *CTOD* measuring technique, δ_{FE}. The role of geometrical variations is considered by varying *a/W* and *B/W* of the CT specimen within the specified ASTM 1820 recommended range. The varied strain hardening of the material represented in terms of σ_{ys}/σ_{ut} are used to assess the constraint at crack tip/front by in-depth FE analysis. Based on the current research, the following findings may be made.

- A novel *CTOD* measuring technique, δ_{FE} is proposed and validated to measure the lower *CTOD* values. As per our present observations, the proposed δ_{FE} technique seemed simpler and precise for fine mesh quality along the cracked ligament. However, the applicability of the δ_{FE} technique on blunted cracks in the case of ductile material needs to be verified.
- The *J* estimation procedure as per ASTM 1820 already imbibes the *a/W* and *B/W* effect, and hence, a strong relationship is witnessed between *J-CTOD* through unaltered curves for both δ_{ASTM} and δ_{FE}. However, the δ_{FE} magnitudes are consistently higher compared to δ_{ASTM}.
- Improvement in the constraint assessment noticed through δ_{FE} based corrected constraint factor, m_{FE}, with the same *J-CTOD* relation. The proposed corrected constraint factor, m_{FE}, uses the identical cubic polynomial equation as described for constraint factor, *m*, with modified constants as A_0 = -2.015, A_1 = -14.750, A_2 = -25.217, *and* A_3 = -14.298.
- The gap between *J*-based *CTOD* and PHM based *CTOD* can be minimized by using corrected constraint factor, m_{FE}. Hence, the usage of *J*-based *CTOD* can fit the applications demanding both *J*-integral and *CTOD*.
- The corrected constraint factor, m_{FE}, represented through Equation (2), applies to varied crack lengths (*a/W*) between 0.4 to 0.7 for thin, standard, and thick CT specimens with $\sigma_{ys}/\sigma_{ut} > 0.45$ to estimate *CTOD* up to 1.5 mm. Authors believe that

the present work may lead to relooking constraint factor, *m,* for CT specimens by ASTM in future days for better *CTOD*-based fracture toughness assessments.

Acknowledgement

Author thanks the KLE Technological University, Hubballi, for the financial support under the "Capacity Building Project" grants.

References

[1] Khor W. A CTOD equation based on the rigid rotational factor with the consideration of crack tip blunting due to strain hardening for SEN (B). Fatigue & Fracture of Engineering Materials & Structures. 2019 Jul;42(7):1622-30. https://doi.org/10.1111/ffe.13005

[2] Wells AA. Crack opening displacements from elastic-plastic analyses of externally notched tension bars. Engineering Fracture Mechanics. 1969 Apr 1;1(3):399-410. https://doi.org/10.1016/0013-7944(69)90001-0

[3] Ritchie, Robert O., and Dong Liu. Introduction to fracture mechanics. Elsevier, 2021. https://doi.org/10.1016/B978-0-323-89822-5.00008-6

[4] Subramanian, R. Harihara, Subbaiah Arunkumar, Sreekumar Jithin, and Ravi Kiran Bollineni. A critical assessment of J-integral and CTOD as fracture parameters. In Advances in Interdisciplinary Engineering: Select Proceedings of FLAME 2018,429-438. https://doi.org/10.1007/978-981-13-6577-5_41

[5] Khor WL, Moore P, Pisarski H, Brown C. Comparison of methods to determine CTOD for SENB specimens in different strain hardening steels. Fatigue & Fracture of Engineering Materials & Structures. 2018 Mar;41(3):551-64. https://doi.org/10.1111/ffe.12718

[6] Moore, Philippa L., and Wee Liam Khor. The effect of material strain hardening on the determination of CTOD R-curves using SENB specimens. In International Pipeline Conference, vol. 51883, p. V003T05A004. American Society of Mechanical Engineers, 2018. https://doi.org/10.1115/IPC2018-78278

[7] Khor, W., P. L. Moore, H. G. Pisarski, and C. J. Brown. Determination of the rigid rotation plastic hinge point in SENB specimens in different strain hardening steels. In Journal of Physics: Conference Series,IOP Publishin. 2018; 1106(1) 012015. https://doi.org/10.1088/1742-6596/1106/1/012015

[8] Zhu XK, Joyce JA. Review of fracture toughness (G, K, J, CTOD, CTOA) testing and standardization. Engineering fracture mechanics. 2012 May 1;85:1-46. https://doi.org/10.1016/j.engfracmech.2012.02.001

[9] Newman Jr JC, James MA, Zerbst U. A review of the CTOA/CTOD fracture criterion. Engineering Fracture Mechanics. 2003 Feb 1;70(3-4):371-85. https://doi.org/10.1016/S0013-7944(02)00125-X

[10] Vasco-Olmo JM, Diaz Garrido FA, Antunes FV, James MN. Plastic CTOD as fatigue crack growth characterising parameter in 2024-T3 and 7050-T6 aluminium alloys using DIC. Fatigue & Fracture of Engineering Materials & Structures. 2020 Aug;43(8):1719-30.0. https://doi.org/10.1111/ffe.13210

[11] Standard, A.S.T.M., 1820. Standard Test Method for Measurement of Fracture Toughness, West Conshohocken, USA, 2013.

[12] Gupta M, Alderliesten RC, Benedictus R. A review of T-stress and its effects in fracture mechanics. Engineering Fracture Mechanics. 2015 Jan 1;134:218-41. https://doi.org/10.1016/j.engfracmech.2014.10.013

[13] Garcia-Manrique J, Camas D, Gonzalez-Herrera A. Study of the stress intensity factor analysis through thickness: methodological aspects. Fatigue & Fracture of Engineering Materials & Structures. 2017 Aug;40(8):1295-308. https://doi.org/10.1111/ffe.12574

[14] Ekabote, Nagaraj, Krishnaraja G. Kodancha, and S. K. Kudari. Suitability of Standard Fracture Test Specimens for Low Constraint Conditions. In IOP Conference Series: Materials Science and Engineering, vol. 1123, no. 1, p. 012033. IOP Publishing, 2021. https://doi.org/10.1088/1757-899X/1123/1/012033
[15] Meshii T, Tanaka T. Experimental T33-stress formulation of test specimen thickness effect on fracture toughness in the transition temperature region. Engineering Fracture Mechanics. 2010 Mar 1;77(5):867-77. https://doi.org/10.1016/j.engfracmech.2010.01.014
[16] Kudari SK, Kodancha KG. On the relationship between J-integral and CTOD for CT and SENB specimens. Frattura ed Integrità Strutturale. 2008;2(6):3-10. https://doi.org/10.3221/IGF-ESIS.06.01
[17] Kittur, Md Ibrahim, Krishnaraja G. Kodancha, and C. R. Rajashekar. Study of Constraint Issues in Elasto-Plastic Fracture Analysis Using Experimental and Finite Element Simulation. In Turbo Expo: Power for Land, Sea, and Air, vol. 50923, p. V07AT31A009. American Society of Mechanical Engineers, 2017. https://doi.org/10.1115/GT2017-63871
[18] Graba M. Numerical analysis of the influence of in-plane constraints on the crack tip opening displacement for SEN (B) specimens under predominantly plane strain conditions. International Journal of Applied Mechanics and Engineering. 2016 Dec;21(4):849-66. https://doi.org/10.1515/ijame-2016-0050
[19] Tagawa T, Kayamori Y, Ohata M, Handa T, Kawabata T, Yamashita Y, Tsutsumi K, Yoshinari H, Aihara S, Hagihara Y. Comparison of CTOD standards: BS 7448-Part 1 and revised ASTM E1290. Engineering Fracture Mechanics. 2010 Jan 1;77(2):327-36. https://doi.org/10.1016/j.engfracmech.2009.02.009
[20] Kawabata T, Tagawa T, Sakimoto T, Kayamori Y, Ohata M, Yamashita Y, Tamura EI, Yoshinari H, Aihara S, Minami F, Mimura H. Proposal for a new CTOD calculation formula. Engineering Fracture Mechanics. 2016 Jul 1;159:16-34. https://doi.org/10.1016/j.engfracmech.2016.03.019
[21] Savioli RG, Ruggieri C. J and CTOD estimation formulas for C (T) fracture specimens including effects of weld strength overmatch. International journal of fracture. 2013 Jan;179:109-27. https://doi.org/10.1007/s10704-012-9781-4
[22] Kayamori Y, Kawabata T. Evaluation of rotational deformation in compact specimens for CTOD fracture toughness testing. Procedia Structural Integrity. Jan 1;5: 286-93, 2017. https://doi.org/10.1016/j.prostr.2017.07.135
[23] Ekabote, Nagaraj, and Krishnaraja G. Kodancha. Temperature and test specimen thickness (TST) effect on tensile and fracture behavior of AA2050-T84 alloy. Materials Today: Proceedings 59, 673-678, 2022. https://doi.org/10.1016/j.matpr.2021.12.202
[24] Deshpande, Piyush K., Nagaraj Ekabote, and Krishnaraja G. Kodancha. Numerical elastic fracture analysis of SENT test specimen subjected to non-linear loading. Materials Today: Proceedings 2023. https://doi.org/10.1016/j.matpr.2023.09.060
[25] Kodancha K, Ekabote N, Revankar PP. Elastic-plastic fracture analysis of anisotropy effect on AA2050-T84 alloy at different temperatures: A numerical study. Frattura ed Integrità Strutturale. 2022;16(59):78-88. https://doi.org/10.3221/IGF-ESIS.59.06
[26] Antunes FV, Simões R, Branco R, Prates P. Effect of numerical parameters on plastic CTOD. Frattura ed Integrità Strutturale. 2017;11(41):149-56. https://doi.org/10.3221/IGF-ESIS.41.21

Research on Engineering Structures & Materials
www.jresm.org
Research Group

Research Article

Evaluation of self-compacting concrete for concrete repair applications

Billel Rebai [*,1,a], Hachemi Benaddi[1,b], Tidjani Messas[1], Mohamed Salhi[2,c]

[1]*Civil Engineering Department, Abbes Laghrour University, BP. 1252, Khenchela 4004, Algeria*
[2]*Civil Engineering Department, University of Relizane, Algeria*

Article Info

Article history:

Received 23 April 2024
Accepted 25 June 2024

Keywords:

Self-compacting concrete;
Concrete repairs;
Mechanical properties;
Bond strength;
Mineral additives;
Limestone fillers;
Blast furnace slag;
Silica fume;
Adhesion tests

Abstract

This study investigates the suitability of utilizing Self-Compacting Concrete (SCC) as a repair material for concrete structures. Various SCC mixtures were formulated with different compositions, including 100% cement, 30% limestone fillers, 40% blast furnace slag, and 10% silica fume. The fresh properties, such as fluidity, deformability, and stability, were evaluated to optimize the SCC mixtures for repair applications. The mechanical properties, including compressive strength, tensile strength, and elastic modulus, were assessed and compared to vibrated ordinary concrete (VOC). Additionally, the bond strength between the SCC repair material and the existing concrete substrate was investigated using simulated repair specimens subjected to indirect tensile bond and splitting tensile bond tests. The results demonstrated the superior mechanical performance of SCC compared to VOC, with higher compressive and tensile strengths. Furthermore, the incorporation of mineral additives, such as limestone fillers, slag, and silica fume, enhanced the mechanical properties and bond strength of the SCC mixtures. The study highlights the potential advantages of using SCC over VOC for concrete repair applications, offering improved mechanical performance and adhesion characteristics.

1. Introduction

Achieving a robust and durable bond between repair materials and existing concrete substrates is a pivotal challenge in concrete repair and rehabilitation projects. The field of civil engineering has seen extensive research efforts aimed at optimizing various aspects of the concrete repair process, such as bonding durability [1], thin repairs [2], experimental methodologies and modeling techniques [3, 27], and hydraulic and mechanical interactions [4]. Specialized tests have been developed to assess substrate cohesion [5] and quantify adhesion [6, 28], emphasizing the importance of proper surface preparation [7].

Compatibility between repair materials and the existing concrete matrix is crucial to prevent future issues like cracking and debonding [8]. Selecting appropriate repair materials depends on factors such as the extent of damage, prevailing load conditions, and environmental influences [9]. For reinforced concrete structures, repair interventions must restore structural integrity and ensure long-term durability [10]. A strong repair-substrate bond involves both mechanical interlocking and chemical bonding mechanisms between the old and new concrete layers [11]. Additionally, meticulous curing practices are essential to achieve the desired strength and performance characteristics [12].

*Corresponding author: billel.rebai@univ-khenchela.dz
[a]orcid.org/0000-0003-3739-2784; [b]orcid.org/0000-0002-2792-6159; [c]orcid.org/0000-0001-9285-9442
DOI: http://dx.doi.org/10.17515/resm2024.255st0423rs

The adhesion between repair materials and substrates involves a complex interplay of chemical bonding and mechanical interlocking mechanisms [6]. Various solutions, including dry/wet shotcrete, formwork, and self-compacting concrete (SCC), offer promising avenues for enhancing adhesion in repair and reinforcement scenarios. Adhesion assessment typically involves subjecting specimens to tension, flexion, and/or shear stresses [13, 14]. Bond tests are crucial for quantifying the adhesion of repair systems to concrete substrates, employing direct or indirect tensile stress generation methodologies [29].

This study investigates the potential of utilizing Self-Compacting Concrete (SCC) as a repair material for concrete structures. The research focuses on formulating and characterizing various SCC mixtures with compositions including 100% cement, 30% limestone fillers, 40% blast furnace slag, and 10% silica fume. The fresh and hardened properties of these SCC mixtures are evaluated and compared to vibrated ordinary concrete (VOC). Additionally, the study assesses the bond strength between the SCC repair material and the existing concrete substrate using simulated repair specimens.

Recent research has demonstrated the suitability of SCC for concrete repair applications due to its excellent fluidity, stability, and bond strength [15, 30]. Studies have explored different SCC mix designs for repair overlays, incorporating steel fibers for enhanced strength [16]. The development of self-healing concrete technology offers a solution to micro-cracks in concrete structures, with Bacillus Subtilis bacteria proving effective in promoting self-recovery of cracks [17]. Evaluating the long-term durability of self-healing concrete is crucial, focusing on resistance to fatigue, creep, and corrosion, alongside mechanical properties assessments [18].

Furthermore, recycled self-compacting concrete, which utilizes recycled aggregates, presents challenges such as reduced flowability and strength but offers benefits like internal curing effects to reduce shrinkage [21]. Lightweight self-compacting concrete has also shown promise in civil engineering applications, achieving densities below 1000 kg/m^3 while maintaining strength and durability, making it a viable option for repair work [24]. The use of self-healing technology with SCC has been explored to control moisture ingress and enhance durability in repair mortars, demonstrating a reduction in sorptivity coefficients and improved autonomous healing efficiency, beneficial for concrete repair applications in terms of longevity and performance [25].

Overall, the combination of SCC's properties, lightweight characteristics, and self-healing capabilities makes it a compelling choice for concrete repair applications, offering enhanced durability and longevity [26]. This study aims to contribute to the existing body of knowledge by evaluating the performance of SCC as a repair material and investigating its bond strength with existing concrete substrates.

2. Materials Used

2.1. Cement

The cement used in all mixtures is CEM I/42.5 grade from the GIGA group of the Ain-Touta cement plant, located in Algeria. The physical characteristics of this cement include an absolute density of 3.1, an apparent density of 1.13, and a Blaine specific surface of 3917 cm2/g. The normal consistency of the cement is 27.2% H2O, with a start time of 2 hours and 12 minutes and an end time of 3 hours and 8 minutes. The hot expansion of the cement is 0.50 mm.

2.2. Sand

The sand used in this study is a local silica sand with a granular class of 0/5 mm, extracted from Oued Ittel, located 85 km south of Biskra, Algeria. This approach is supported by several studies, such as those conducted by de Larrard (1999) and Fennis et al. (2009) [30], which demonstrate the improved mechanical properties and durability of concrete when using gap-graded aggregates. The sand's properties, including absolute density, apparent density, fineness modulus, and visual sand equivalent, were determined according to the standard testing methods [31]. The values obtained for the sand's absolute density, apparent density, fineness modulus, and visual sand equivalent were 2.56, 1.54, 2.54, and 78.32, respectively.

The measurements were performed as follows:

- Absolute density: The sand sample was oven-dried at 105°C for 24 hours, cooled to room temperature, and then immersed in water for 24 hours. The saturated surface-dry (SSD) condition was achieved by removing the surface moisture using a dry cloth. The SSD sand was weighed in air and water, and the absolute density was calculated using the formula specified in ASTM C128.
- Apparent density: The sand sample was oven-dried at 105°C for 24 hours and cooled to room temperature. The dry sand was placed in a cylindrical container of known volume, and the mass of the sand was measured. The apparent density was calculated by dividing the mass of the sand by the volume of the container.
- Fineness modulus: The sand sample was oven-dried at 105°C for 24 hours and cooled to room temperature. The dry sand was sieved through a series of standard sieves (4.75 mm, 2.36 mm, 1.18 mm, 0.60 mm, 0.30 mm, and 0.15 mm), and the cumulative percentage retained on each sieve was calculated. The fineness modulus was determined by adding the cumulative percentages retained on each sieve and dividing the sum by 100.
- Visual sand equivalent: The sand sample was placed in a graduated cylinder with a flocculating solution, agitated, and allowed to settle for 20 minutes. The height of the sand and clay layers was measured, and the sand equivalent value was calculated by dividing the height of the sand layer by the total height of the sand and clay layers, expressed as a percentage.

The values obtained for the sand's absolute density, apparent density, fineness modulus, and visual sand equivalent were 2.56, 1.54, 2.54, and 78.32, respectively.

2.3. Gravel

The physical properties of the crushed limestone gravel from the Ain-Touta deposit in the Batna province of Algeria were determined according to relevant testing standards. The absolute density and absorption coefficient were measured as per ASTM C127 [31], while the apparent density and porosity were determined using ASTM C29/C29M [31]. The Los Angeles coefficient, which assesses the resistance to abrasion and impact, was evaluated following ASTM C131/C131M [31].

The use of gap-graded gravel sizes (7/15 and 15/25) in concrete mixture design is a common practice that offers several advantages. The combination of smaller and larger gravel sizes helps to optimize the packing density by minimizing void spaces between particles, resulting in a denser and more compact concrete matrix [30]. The smaller gravel size (7/15) enhances the workability and filling ability of self-compacting concrete (SCC) by reducing interparticle friction and facilitating mixture movement [32]. On the other hand, the larger gravel size (15/25) is typically used in conventional vibrated concrete to improve interlocking and load transfer between particles, leading to higher strength and stability [33].

The physical characteristics of the gravel were determined for two size ranges: Gravel 15/25 and Gravel 7/15. The absolute density values were found to be 2.62 and 2.61, respectively, while the apparent density values were 1.255 and 1.283. The absorption coefficient values were 0.64 and 0.60, and the porosity values were 0.96 and 0.56. The Los Angeles coefficient was found to be 26 for both gravel sizes, indicating a satisfactory level of durability [34].

2.4. Limestone Fillers

The crushed limestone rock used in this study is sourced from the quarries of Ain-Touta, Algeria. The laboratory analysis of the limestone filler revealed an absolute density of 2.76, an apparent density of 1.09, and a specific surface area of 3070 cm2/g. The absolute density was determined using the pycnometer method, as described in ASTM C128 [31], which involves measuring the displacement of a liquid (usually water) by a known mass of the material. The apparent density was measured using the ASTM C29/C29M standard [31], which involves filling a container of known volume with the material and determining its mass. The specific surface area was determined using the Blaine air permeability method, as outlined in ASTM C204 [31], which measures the time required for a fixed volume of air to pass through a compacted bed of the material.

The incorporation of limestone fillers in self-compacting concrete (SCC) mixtures has been shown to improve various properties of the concrete. Limestone fillers contribute to the workability and cohesiveness of the mixture by increasing the paste volume and improving the particle packing density [34]. The increased packing density results in a reduction of the water demand for a given workability [35]. Additionally, the fine limestone particles act as nucleation sites for the formation of hydration products, leading to an enhancement in the mechanical properties of the concrete [36].

2.5. Blast Furnace Slag

It is a granulated and ground blast furnace slag product from the El-Hadjar steel complex in Annaba, Eastern Algeria. Its physical characteristics are as follows: absolute density = 2.73, apparent density = 1.08, and specific surface area = 3000 cm2/g. The absolute density was determined using the pycnometer method, as described in ASTM C188 [31], while the apparent density was measured using the ASTM C29/C29M standard [31]. The specific surface area was determined using the Blaine air permeability method, as outlined in ASTM C204 [31]. The chemical composition of the blast furnace slag, with its respective proportions in percentage, is as follows: SiO2 (40.8%), CaO (43.0%), MgO (6.4%), Al2O3 (5.2%), MnO (3.0%), S (0.8%), and Fe2O3 (0.5%).

The use of blast furnace slag as a partial replacement for cement in self-compacting concrete (SCC) mixtures can improve various properties of the concrete. Blast furnace slag exhibits pozzolanic properties, reacting with calcium hydroxide produced during cement hydration to form additional calcium silicate hydrates, contributing to strength development over time [38]. The incorporation of slag in SCC mixtures can enhance the workability and cohesiveness of the mixture, as the slag particles act as a filler material, improving the particle packing density and reducing the water demand [36]. Furthermore, the use of slag in concrete can improve the durability characteristics, such as resistance to chloride ingress and sulfate attack, due to the refined pore structure and reduced permeability of the concrete matrix [39].

2.6. Silica Fume

It is a silica fume designated by the name "MEDAPLAST HP," a gray powder-based micro silica from the "GRANITEX" company. Its physical characteristics are: absolute density = 1.87, apparent density = 0.5, and specific surface area = 20470 cm2/g.

The absolute density was determined using the pycnometer method, as described in ASTM C188 [31], while the apparent density was measured using the ASTM C29/C29M standard [31]. The specific surface area was determined using the Brunauer–Emmett–Teller (BET) surface area analysis method, as outlined in ASTM C1069 [31].

Silica fume is a highly reactive pozzolanic material that can significantly improve the mechanical properties, durability, and impermeability of concrete when used as a partial replacement for cement [40, 41]. The ultrafine nature of silica fume particles contributes to the enhancement of the interfacial transition zone between the cement paste and aggregate, resulting in a denser and more homogeneous microstructure [42]. The high pozzolanic reactivity of silica fume leads to the formation of additional calcium silicate hydrates, which improve the strength and durability characteristics of the concrete [43].

2.7. Chemical Admixture (Superplasticizer)

The chemical admixture used is the superplasticizer "MEDAFLOW30," produced by the company "GRANITEX." It is in liquid form with light brown color and is based on Polycarboxylates, with a density of 1.07, chlorine content lower than 0.1g*/l,* dry extract of 30%, and pH ranging from 6 to 6.5, according to the manufacturer.

2.8. Mixing Water

The mixing water used complies with the requirements of standard ASTM C1602 [31]. It is potable water from the tap of the public network in the city of Biskra, ensuring the water is free from impurities that could potentially affect the properties of the concrete.

3. Methodology

3.1. Mixes and Formulations

Based on the guidelines provided by [19], several preliminary formulations were conducted to optimize and characterize a 100% cement self-compacting concrete (SCC) that meets the criteria and recommendations for fresh state properties according to [20], with a water-to-cement ratio (W/C) of 0.4 and paste-to-volume ratio (S/paste) of 0.7. Then, a portion of cement was replaced by various mineral additions (30% limestone fillers, 40% blast furnace slag, and 10% silica fume) to obtain four self-compacting concrete mixtures.

The incorporation of mineral additions, such as limestone fillers, blast furnace slag, and silica fume, can significantly enhance the water efficiency of concrete mixtures. These mineral additions contribute to the improvement of water efficiency through different mechanisms. Limestone fillers act as a filler material, improving the particle packing density and reducing the water demand for a given workability [8]. The fine limestone particles can fill the voids between cement and aggregate particles, resulting in a denser and more cohesive mixture.

Blast furnace slag exhibits pozzolanic properties, reacting with calcium hydroxide produced during cement hydration to form additional calcium silicate hydrates [9]. This pozzolanic reaction consumes part of the water, reducing the effective water-to-binder ratio and improving the water efficiency of the mixture. Silica fume, with its ultrafine particle size and high pozzolanic reactivity, can significantly improve the particle packing density and contribute to the formation of additional calcium silicate hydrates [10]. The improved particle packing and pozzolanic reaction led to a reduction in water demand and enhanced water efficiency. By optimizing the combination and proportions of these mineral additions, it is possible to achieve self-compacting concrete mixtures with improved water efficiency, leading to better workability, cohesiveness, and mechanical properties while reducing the water demand and potential for segregation or bleeding [11, 12].

For the vibrated ordinary concrete (VOC), the Dreux-Gorisse method was used in this study [21]. The procedure before studying the adhesion involves two groups of tests. Initially, a self-compacting concrete was formulated and characterized after several preliminary tests, meeting the guidelines of [19] and the fresh state recommendations of AFGC [20]. To determine the mechanical performance of the different concretes, compression behavior characterization tests were carried out in accordance with the norm (NFP 18-406), on cubic specimens with dimensions of (10x10x10 cm^3), cured in water. The compressive strength fcj results at 7,14, 28 and 90 days represent the average of three samples. The testing machine used for uniaxial cube crushing is a hydraulic press with a maximum capacity of 1500 kN in compression. The expression of the results is given by the relation:

$$fcj = \frac{F}{S} \tag{1}$$

Where F is the maximum load and S is the compression surface of the specimen [21]. For flexural tensile tests, tests were conducted on prismatic specimens with dimensions of (10x10x40 cm^3), cured in water, following the norm (NFP 18-406). The tensile strength ft28 obtained at 28 days is the average of results from three samples. The apparatus used is a bending hydraulic press with a maximum capacity of 150 kN in shear. The expression of the results for expressing the flexural tensile strength is given by the relation:

$$ftj = 1.8\frac{F}{a^2} \tag{2}$$

Where F is the rupture load and a is the side of the base in mm. Regarding the elastic modulus at 28 days, it is determined on cylindrical specimens of (16x32 cm^2), cured in water, and equipped with a single-sensor axial extensometer to measure longitudinal deformations of the sample under increasing loads up to a maximum stress equal to:

$$\sigma_c = 0.6 f_{cj} \tag{3}$$

From the equation:

$$\sigma c = Ec\varepsilon c \tag{4}$$

It is possible, according to R. Dupan [22], to plot the curve:

$$\sigma_c = f(\varepsilon_c) \tag{5}$$

For σ ranging from 0 to $0.6f_c$. On this curve, the slope of the tangent at the origin (tangent modulus) and the slope of the line passing through the origin and the coordinate point εc and 0.6fc (secant modulus) can be measured, with:

$$E = 0.6\frac{fc}{\varepsilon c} \tag{6}$$

The evaluation of adhesion between the old and new concrete was conducted through repair simulations. Prismatic specimens with dimensions of 10x10x10 cm^3 and cylindrical specimens with dimensions of 16x32 cm^2 were prepared using ordinary concrete. After 28 days of curing, these specimens were subjected to flexural tensile tests (for prisms) and splitting tensile tests (for cylinders) to obtain half-specimens with exposed aggregates, resulting in rougher surfaces.

Before applying the repair, the rough surfaces of the half-specimens (prismatic and cylindrical) were moistened for 24 hours to achieve the Saturated Surface Dry (SSD) condition. Subsequently, the half-specimens were placed in suitable molds, and the repair concrete (self-compacting concrete, SCC) and the vibrated ordinary concrete (VOC) as a

reference were poured to obtain composite specimens after demolding. The composite specimens consisted of two parts bonded at the interface: the first part formed the base concrete or substrate, and the second part formed the repair concrete or new concrete (Figure 1). This setup allowed for the evaluation of the adhesion between the old (substrate) and new (repair) concrete.

(a) (b)

Fig. 1. The Composite specimens (a) old concrete, (b) repair

Finally, these specimens were kept in water to determine the adhesion between the old and new concrete, we conducted two tests: before being subjected to the crushing tests at the age of 28 days to evaluate the adhesion strength between the old and new concrete.

3.1.1. The First Method (Indirect Tensile Bond Test)

This involves subjecting the composite prismatic specimens to the indirect tensile bond test, which is inspired by the CRD C85 standard. The procedure entails applying a compressive load parallel to the repair interface between the existing concrete and the repair concrete. The bond stress in this method is estimated by the ratio of the load at failure to the surface area, and the whole is adjusted by a correction factor estimated at 0.98.

3.1.2. The Second Method (Splitting Tensile Bond Test)

The cylindrical (composite) specimens are subjected to the splitting tensile bond test to evaluate the quality of adhesion between the old and new concrete. With this method, the bond stress is only that of splitting tensile stress, which will be calculated using the following formula:

$$ftj = 2P/\pi DL \quad (7)$$

Where: P is the maximum compressive load causing the cylinder to split when subjected to tensile stress along the vertical diametral plane; D and L are the diameter and length of the cylinder.

4. Results and Discussion

4.1. Formulation and characterization of fresh SCC

For the formulation of our SCC, we initially focused on optimizing the gravel volume. Five SCC samples with gravel doses ranging from *250 l to 350 l* in increments of 25 *l* were prepared. All mixtures had sand/paste ratios (S/Pt) of 0.6 and water-to-cement ratios

(W/C) of 0.4, along with a superplasticizer content of 0.8%. The results obtained in the fresh state, as shown in Figure 2.a, indicate that increasing the gravel volume considerably reduces the fluidity of the SCC. This reduction can reach 73.68% when the gravel volume increases from 250 *l* to 350 *l*.

This phenomenon is attributed to the insufficient cement paste content due to the increased volume of gravel. In fact, the gravel particles tend to come into contact with each other, leading to increased frictional forces between them, thereby restricting the flow of the SCC. This observation aligns with previous studies on SCC [23, 24]. Similarly, the increase in gravel volume has a negative effect on the filling capacity of the SCC (H2/HI ratio) as shown in Figure 2.b. When the gravel volume reaches 350 *l*, the gravel particles shear and touch, resulting in the formation of clusters against the reinforcements, thus blocking the material. Regarding stability, Figure 2.c shows that the segregation index decreases as the gravel volume increases, even reaching almost zero with a volume of 350 *l*. This decrease is due to the reduction in the volume of cement paste caused by the increased gravel volume, leading to a decrease in the segregation index. Therefore, the increase in gravel volume has a significant impact on the properties in the fresh state and the characterization of the SCC.

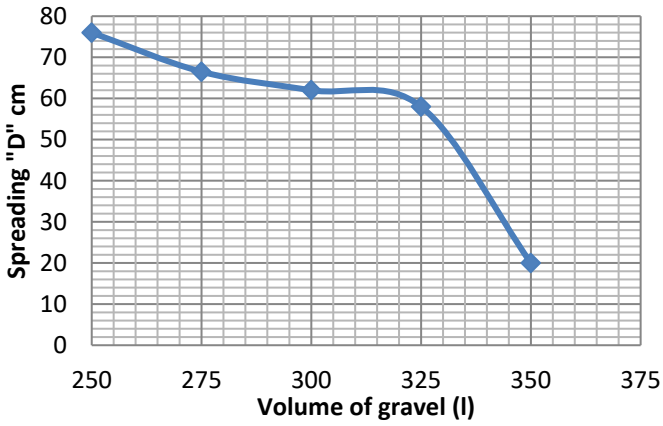

(a)

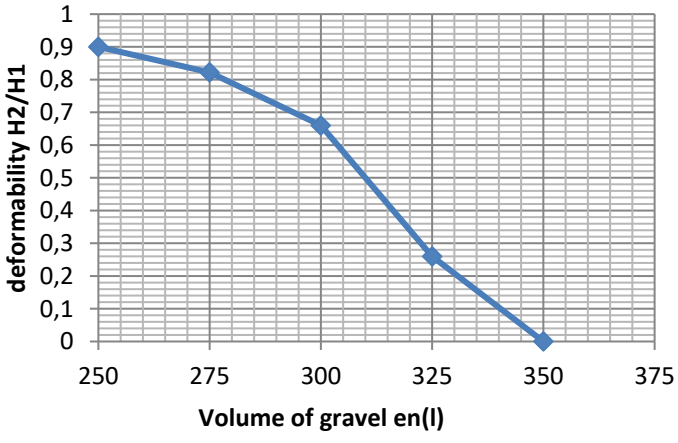

(b)

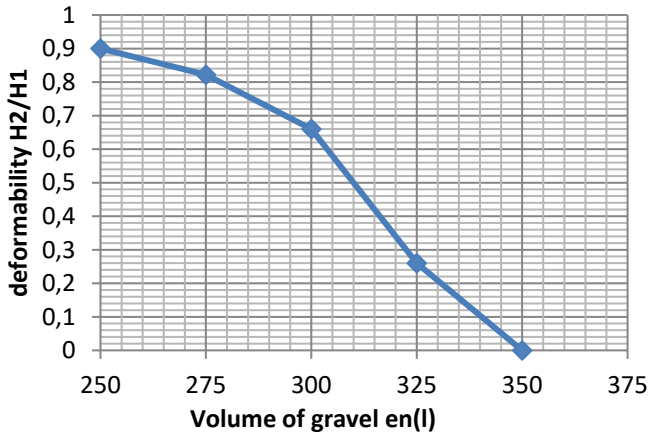

(c)

Fig. 2. Effect of gravel volume on fresh scc properties (a) effect of gravel on fluidity b:effect of gravel deformability, and c: effect of gravel on stability

A gravel dosage of 275 l was identified as the most appropriate to meet the performance criteria while ensuring good adhesion between the mortar and the gravel. To optimize the superplasticizer dosage, nine SCC samples were prepared with a fixed gravel volume of 275 l and W/C ratio of 0.4. The percentages of superplasticizer were varied from 0.8% to 1.2% with an increment of 0.2%, and the S/Pt ratio was varied from 0.6 to 0.8 with an increment of 0.1. The effect of the superplasticizer on the rheological properties is well illustrated in Figure 3 where the increase in spread diameter is directly related to the progressive increase in the superplasticizer dosage. For example, at an S/Pt ratio of 0.6, the spread diameter increases from 66.5 cm to 90 cm when the superplasticizer dosage increases from 0.8% to 1.2% (Figure 3 a). This improvement in fluidity is attributed to the action of long-chain molecules of the superplasticizer, which cause deflocculation of cement particles and lubricate the paste. Additionally, the increase in superplasticizer dosage leads to a higher filling capacity of the mixtures, as shown in Figure 3.b, since deformability is closely linked to fluidity.

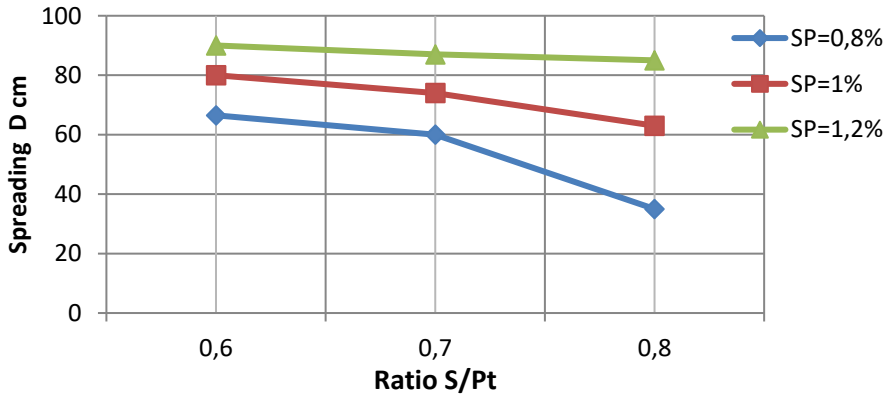

(a)

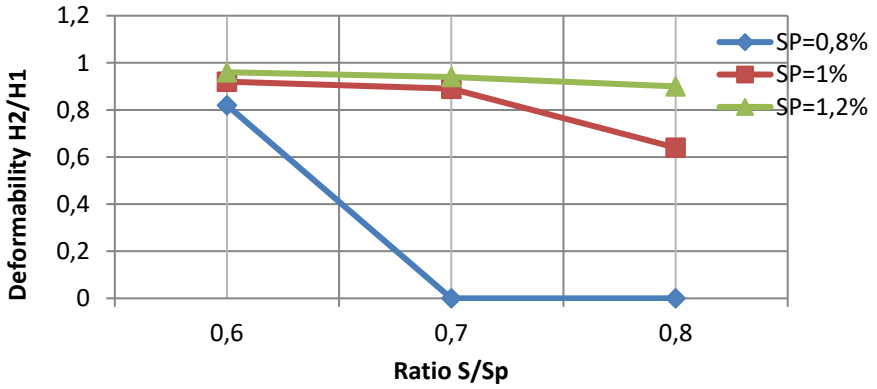

(b)

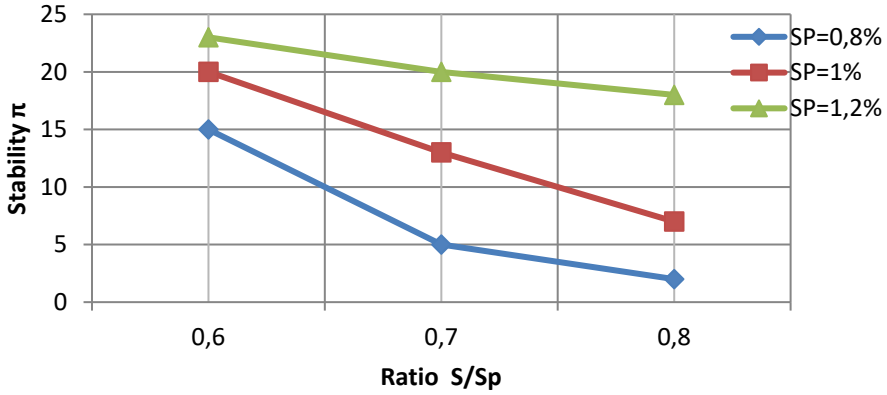

(c)

Fig. 3. Effect of superplasticizer dosage on fresh SCC properties (a) effect of superplasticizer on fluidity, (b) effect of superplasticizer on filling rate (deformability), and (c) effect of superplasticizer on segregation rate (stability)

However, we observed that the increase in superplasticizer dosage also causes a loss of stability, as illustrated in Figure 3.c. The segregation index increases significantly when the superplasticizer dosage goes from 0.8% to 1.2%, which could be problematic for the mechanical properties of the SCC. These results indicate that a dosage of 1% of superplasticizer with an S/Pt ratio of 0.7 provides good fluidity and meets the requirements of self-compacting concrete (SCC). After optimizing the required gravel volume and superplasticizer percentage, the study focused on optimizing the volumetric ratios of S/Pt (sand/paste) and W/C (water/cement) using nine SCC mixtures while keeping the superplasticizer dosage and gravel volume constant. The effect of the S/Pt and W/C ratios on the fluidity of the mixtures is illustrated in Figure 4.

It is observed that for a given W/C ratio, an increase in the S/Pt ratio leads to a decrease in the spread diameter (Figure 4.a). This decrease is attributed to a reduction in the volume of cement paste, which is crucial for ensuring good compatibility of the SCC. Similarly, for all S/Pt ratios, an increase in the W/C ratio improves fluidity, primarily due to the excess water content that reduces internal shear stresses. Regarding the effect of the S/Pt and

W/C ratios on the filling capacity of the mixtures (Figure 4.b), it is observed that the filling rates decrease as the S/Pt ratio increases. To facilitate the passage of SCC through heavily reinforced formwork, the volume of cement paste needs to be adjusted accordingly. This result is consistent with the findings of other researchers [25]. Regarding stability (Figure 4.c), an increase in the S/Pt ratio can reduce the segregation index, while an increase in the W/C ratio can directly influence the segregation rate. An increase in the W/C ratio improves fluidity and deformability but affects stability, whereas an increase in the S/Pt ratio reduces spread diameter and deformability but improves stability. Among all the tested mixtures, only one was considered truly self-compacting, meeting the requirements of the French Association of Civil Engineering (AFGC) [20], with an S/Pt ratio of 0.7, anW/C ratio of 0.4, a superplasticizer dosage of 1%, and a gravel volume of 275 l. These results are in line with those reported in the literature by other researchers [25, 26]. The formulation of SCC with a high cement content can lead to high costs and issues related to heat of hydration. The use of mineral additives can be a solution to improve these properties while reducing the cement quantity. In this study, we analyze the effect of limestone fillers, slag, and silica fume on the workability of SCC. The effect of limestone fillers on the fluidity of SCC is significant (Figure 5.a), with an increase in the spread diameter from 74 cm to 77 cm for a dosage of 30% limestone fillers. This can be explained by the fine nature of limestone fillers, which can fill the gaps between the coarse cement particles and release the trapped water between them.

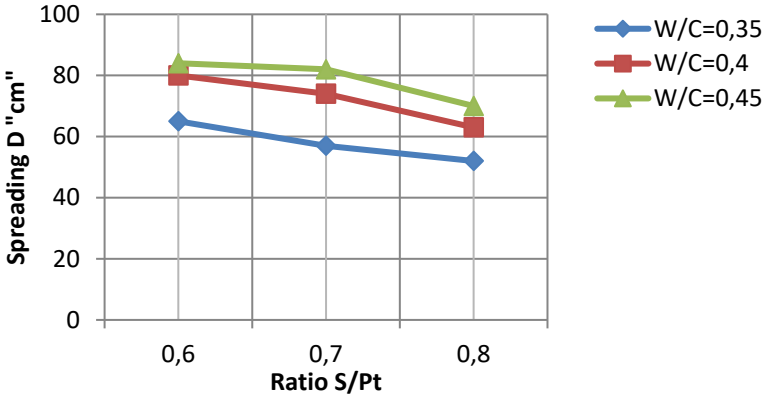

(a)

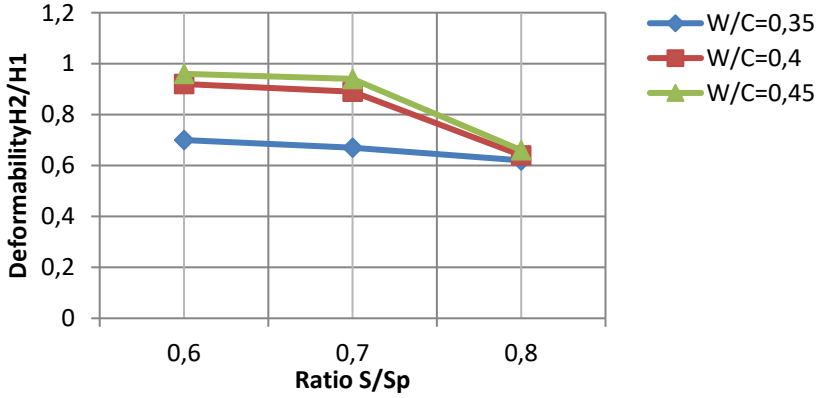

(b)

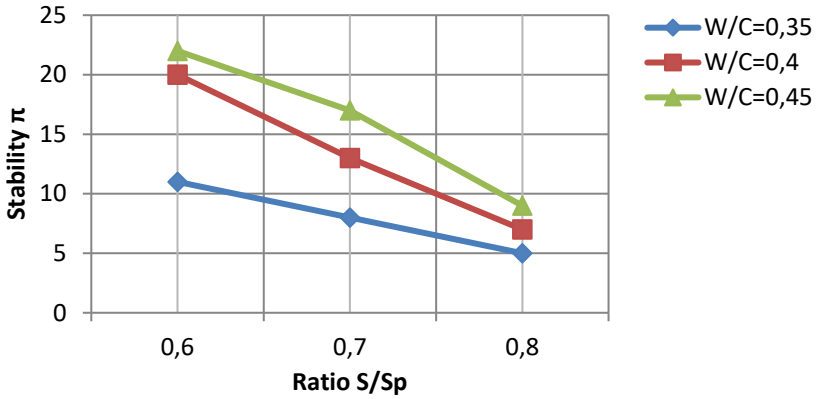

(c)

Fig. 4. Effect of sand/paste ratio (S/P) on fresh SCC properties (a) effect of sand/paste ratio(s/p) on fluidity, (b) effect of sand/paste ratio(s/p) on filling rate (deformability), and (c) effect of sand/paste ratio(s/p) on segregation rate (stability)

On the other hand, slag tends to decrease the spread diameter of SCC, requiring an increase in the dosage of superplasticizer (SP) to maintain its self-placing ability. Silica fume also shows a similar effect, with a decrease in spread diameter and an increased demand for SP to ensure good workability. The deformability of SCC is directly related to its fluidity. Limestone fillers improve deformability, with a filling rate (H2/H1) increasing from 0.89 to 0.95 for a dosage of 30% limestone fillers. For mixtures containing slag or silica fume, an increase in SP dosage is necessary to enhance deformability and achieve a filling rate of 0.78 and 0.82, respectively, as shown in Figure 5.b. Figure 5.c illustrates that the incorporation of limestone fillers and slag improves the stability of SCC, reducing the segregation index from 13% to 10% and 4.5%, respectively.

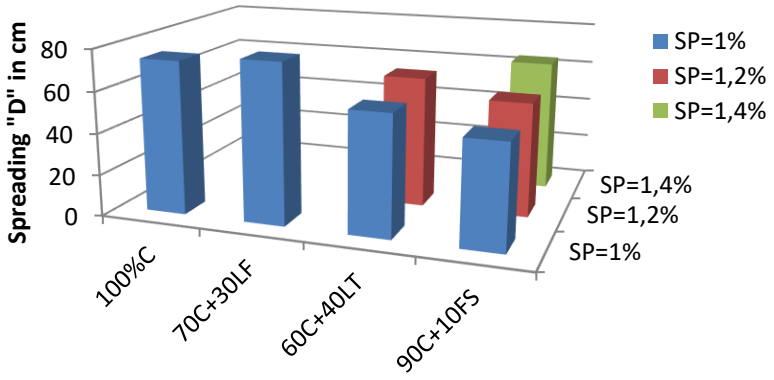

(a)

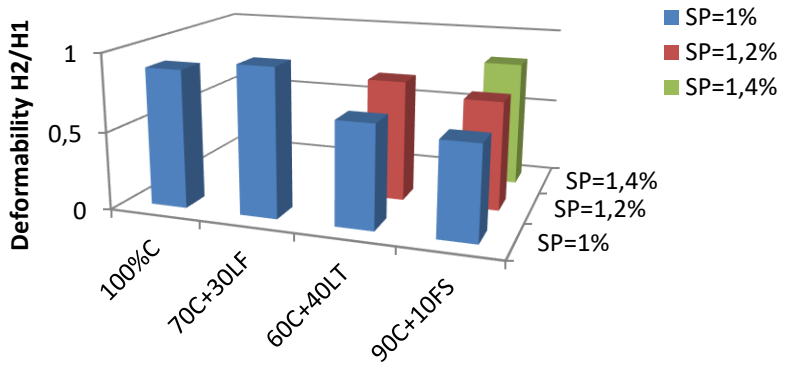

(b)

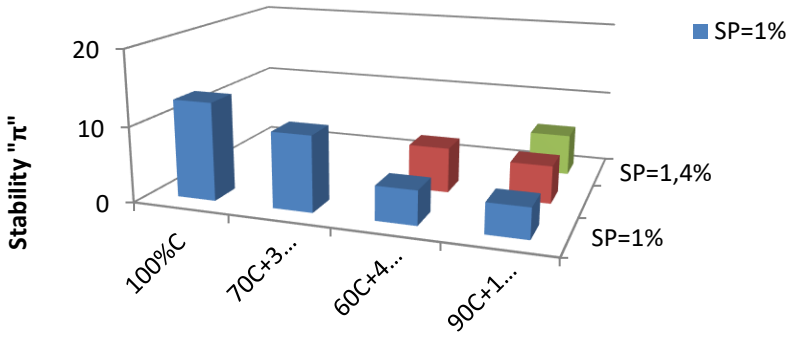

(c)

Fig. 5. Effect of mineral additives on fresh SCC properties (a) effect of mineral additions on fluidity, (b) effect of mineral additions on filling rate (deformability), and (c) effect of mineral additions on segregation rate (stability)

Table 1. presents the compositions of several optimized concrete mixtures, while Table 2 displays the results of fresh state tests conducted on various Self-Compacting Concretes (SCC). Silica fume also exhibits a positive effect on stability, with a segregation rate of only 5.5% for a dosage of 1.4% SP. The use of mineral additives in the formulation of Self-Compacting Concrete (SCC) allows for the improvement of its rheological and mechanical properties.

Table 1. Compositions of various formulated concretes

N°	Designation	Gravel 7/15	Gravel 3/8	Sand	Cement	Addition	Water	SP
		Kg/m³	Kg/m³	Kg/m³	Kg/m³	Kg/m³	l/m³	%
01	SCC100%C	720.5	00	742.67	574.74	00	229.89	1
02	SCC30%LF	720.5	00	742.89	388.75	166.6	222.14	1
03	SCC40%BFS	720.5	00	740.18	335.30	223.53	223.53	1.2
04	SCC10%SF	720.5	00	737.59	501.39	55.71	222.84	1.4
05	VOC	851	261	630	400	00	200	00

Limestone fillers enhance fluidity and deformability, while slag and silica fume improve stability and mechanical strengths. Optimizing the dosage of superplasticizer is essential to maintain the self-placing ability of SCC while benefiting from the advantages of mineral additives.

Table 2. Results of fresh state tests for different self-compacting concretes (SCC)

N°	Designation	Slump flow D in (cm)	Deformability H2/H1	Stability π
01	SCC100%C	74	0.89	13
02	SCC30%LF	77	0.95	10
03	SCC40%BFS	63	0.78	6
04	SCC0%SF	64	0.82	5.5

4.2. Study of Mechanical Properties of Different Optimized Concrete Mixtures in The Hardened State

The evolution of compressive strength at different ages is well illustrated in Figure 6, where we observe that at early ages, all mixtures except those containing slag, develop higher strengths than vibrated ordinary concrete. For example, the 100% cement SCC recorded 32MPa at 14 days, which represents 82% of the strength of ordinary concrete at 28 days (39MPa). Similarly, the 10% silica fume SCC developed a strength of 45MPa at 14 days, representing 115.38% of that of ordinary concrete at 28 days. Concrete mixes based on slag (SCC 40% BFS) exhibit lower strengths at 14 days compared to ordinary concrete, partly because slag does not have enough time at 14 days to contribute to strength development, and also due to the lower cement content in slag-based concrete. At long term (90 days), it is observed that all self-compacting concretes, regardless of the substitution type, recorded higher strengths than ordinary concrete. For instance, the 100% cement SCC showed a strength of 58MPa compared to 47MPa for ordinary concrete, the SCC30% LF developed a strength of 46MPa, and the SCC10%SF marked a strength of 70MPa. Similarly, the slag-based SCC (40%) at long term showed a strength of 52MPa, surpassing the 47MPa of ordinary concrete at 90 days due to its pozzolanic property. Regarding the evolution of tensile strength, according to Figure 7, all SCCs developed slightly higher tensile strengths at the age of 28 days compared to ordinary concrete.

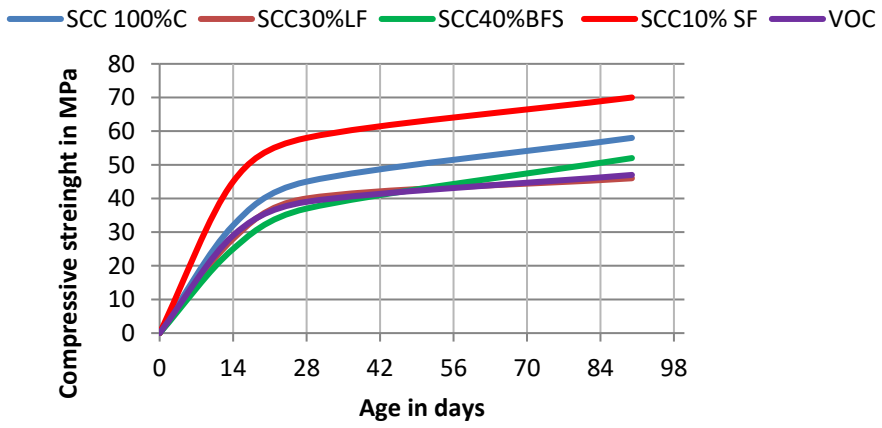

Fig. 6. Evolution of compressive strength over

Specifically, the SCC100% cement showed a tensile strength of 3.3MPa, the SCC30% LF 3MPa, and the SCC10%SF 4.2MPa, while vibrate ordinary concrete had a tensile strength of 3MPa. However, the SCC 40% BFS recorded a tensile strength of 2.9MPa, which can be attributed to the fact that the 40% substitution is at its maximum, and at 28 days, this mixture containing slag has not yet developed its mechanical properties. The highest result was obtained for the SCC10% BFS (4.2MPa), indicating the homogeneity and proper distribution of aggregates in the binder paste.

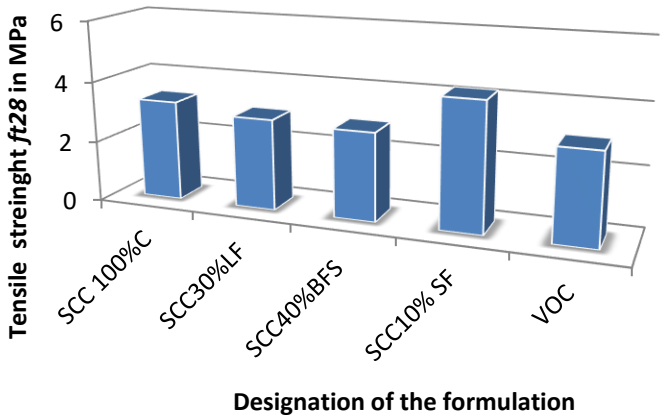

Fig. 7. Tensile strength at 28 days of different concretes

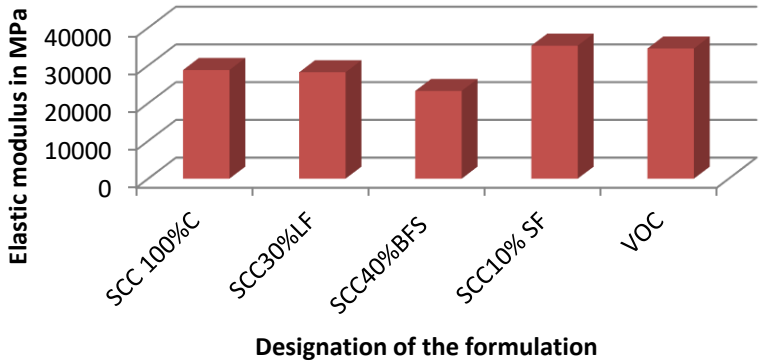

Fig. 8. Elastic modulus at 28 days of different concretes

This homogeneity is ensured by the presence of the superplasticizer, which disperses the cement grain stacking and silica fume particles. Regarding the elastic modulus, which is generally affected by the gravel content, SCCs are likely to be more deformable than ordinary concrete. As shown in Figure 8, the elastic modulus of SCC is consistently lower than that of ordinary concrete. For example, at 28 days, the elastic modulus is 28800MPa for 100% cement SCC, 28200MPa for SCC 30% LF, 23250MPa for SCC40%BFS and 34500MPa for vibrated ordinary concrete. These results are confirmed by AFGC and have also been found by several researchers [4], [24] and [27]. On the other hand, the SCC10%SF

yielded an elastic modulus of 35250MPa, higher than that of ordinary concrete, which can be attributed to its higher compressive strength as well.

4.3. Evaluation of The Bond Strength Between Old and New Concrete

The first observation we made during the evaluation of bond strength is that the test on prismatic specimens yields higher results compared to the splitting tensile test on cylindrical specimens. As shown in Figure 9, the bond strength for 100% cement SCC is 2.64MPa for the test on prisms, compared to 1.92 MPa on cylinders. Similarly, the 30% LF SCC recorded 1.96MPa on prisms and 1.74MPa on cylinders, and the SCC40% BFS showed 1.52MPa on prisms and 1.36MPa on cylinders.

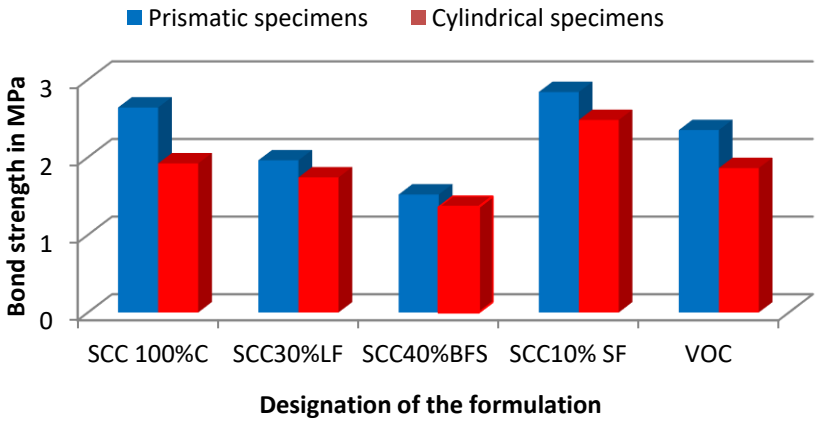

Fig. 9. Bond strength for different repair mixes

The second observation is that the bond strengths of all SCCs generally follow the trend of tensile strength. It can be noted that the 10% FS mixture offers the best bond strength in both the prism and cylindrical tests (2.84MPa and 2.48MPa) compared to 2.35MPa and 1.86MPa for ordinary concrete, respectively. This result is confirmed by Soneibi [25]. The lowest result compared to ordinary concrete was found for the SCC30% LF with 1.96 MPa on prisms and 1.74 MPa on cylinders, but it was even lower for the SCC40%BFS with 1.52MPa on prisms and 1.36MPa on cylinders. This can be attributed to the low cement content in this mixture (335.5kg/m^3) and the low specific surface area of the slag used (3070cm^2/g).

5. Conclusion

This comprehensive study evaluated the potential of utilizing Self-Compacting Concrete (SCC) as an effective repair material for concrete structures. Through a systematic approach, various SCC mixtures were formulated with different compositions, including 100% cement, 30% limestone fillers, 40% blast furnace slag, and 10% silica fume. The primary objective was to optimize the fresh properties, such as fluidity, deformability, and stability, to ensure compliance with the requirements for self-compacting concrete in repair applications.

The mechanical properties of the optimized SCC mixtures were extensively characterized and compared to those of vibrated ordinary concrete (VOC). Remarkably, all SCC mixtures exhibited higher compressive strengths than VOC at later ages, with the 10% silica fume SCC outperforming the others by achieving the highest compressive strength. This

superior performance can be attributed to the pozzolanic activity of silica fume, which contributed to the formation of additional calcium silicate hydrates, resulting in a denser and stronger concrete matrix. Furthermore, the tensile strengths of the SCC mixtures were evaluated at 28 days, and all mixtures demonstrated slightly higher values compared to VOC. Once again, the 10% silica fume SCC emerged as the top performer, exhibiting the highest tensile strength among all mixtures. This can be attributed to the improved interfacial transition zone between the cement paste and aggregates, as well as the homogeneous distribution of silica fume particles within the concrete matrix.

A crucial aspect of this study was the assessment of the bond strength between the SCC repair material and the existing concrete substrate. Simulated repair specimens were subjected to indirect tensile bond and splitting tensile bond tests to quantify the adhesion between the old and new concrete interfaces. The results revealed that the SCC mixtures generally exhibited higher bond strengths compared to VOC, with the 10% silica fume SCC demonstrating the best bond strength performance. This superior adhesion can be attributed to the improved microstructure and reduced porosity of the SCC mixtures, leading to enhanced mechanical interlocking and chemical bonding mechanisms at the repair interface. The incorporation of mineral additives, such as limestone fillers, blast furnace slag, and silica fume, played a pivotal role in influencing the fresh and hardened properties of the SCC mixtures. Limestone fillers contributed to improved fluidity, deformability, and stability by enhancing the particle packing density and reducing the water demand. On the other hand, blast furnace slag and silica fume exhibited positive effects on mechanical strengths and bond strength, albeit with a slight reduction in workability due to their higher water demand.

Overall, this study highlights the promising potential of using SCC as a superior repair material for concrete structures. The superior mechanical performance, enhanced bond strength, and the ability to incorporate mineral additives make SCC an attractive choice for concrete repair applications. The improved durability and longevity offered by SCC can lead to more sustainable and cost-effective repair solutions, ultimately extending the service life of concrete structures and reducing the need for frequent repairs or replacements.

References

[1] Srinath D, Ramesh G, Ramya D, Krishna BV. WITHDRAWN: Mechanical properties of sustainable concrete by using RHA and hydrated lime. 2021. https://doi.org/10.1016/j.matpr.2021.02.785

[2] Bissonnette B. Le fluage en traction: un aspect important de la problematique des reparations minces en beton. Université Laval; 1997.

[3] Billel R. Contribution to study the effect of (Reuss, LRVE, Tamura) models on the axial and shear stress of sandwich FGM plate (Ti-6A1-4V/ZrO2) subjected on linear and nonlinear thermal loads. AIMS Materials Science. 2023;10(1). https://www.aimspress.com/article/doi/10.3934/matersci.2023002

[4] Molez L. Comportement des réparations structurales en béton: couplage des effets hydriques et mécaniques [Doctoral dissertation]. École normale supérieure de Cachan-ENS Cachan; Université Laval; 2003.

[5] Courard L, Bissonnette B. Essai dérivé de l'essai d'adhérence pour la caractérisation de la cohésion superficielle des supports en béton dans les travaux de réparation: analyse des paramètres d'essai. Materials and Structures. 2004;37(269). https://hdl.handle.net/2268/17594

[6] Bissonnette B, Courard L, Jolin M, Thomassin M, Vaysburd A, Garbacz A, von Fay K. Adhérence des réparations en béton: évaluation et facteurs d'influence. In: Journées scientifiques du (RF)B. 2014. https://hdl.handle.net/2268/171851

[7] Bissonnette B, Vaysburd AM, von Fay KF. Best practices for preparing concrete surfaces prior to repairs and overlays. No. MERL 12-17. 2012. http://www.usbr.gov/research/projects/download_product.cfm?id=446
[8] Morgan DR. Compatibility of concrete repair materials and systems. Construction and building materials. 1996;10(1):57-67. https://doi.org/10.1016/0950-0618(95)00060-7
[9] Luković M, Ye G, Van Breugel K. Reliable concrete repair-a critical review. In: Proc. of international conference Structural Faults & Repair; 2012.
[10] Jumaat MZ, Kabir MH, Obaydullah M. A review of the repair of reinforced concrete beams. Journal of Applied Science Research. 2006;2(6):317-326. http://eprints.um.edu.my/id/eprint/6103
[11] Manawadu A, Qiao P, Wen H. Characterization of substrate-to-overlay interface bond in concrete repairs: a review. Construction and Building Materials. 2023;373:130828. https://doi.org/10.1016/j.conbuildmat.2023.130828
[12] Page CL, Ngala VT, Page MM. Corrosion inhibitors in concrete repair systems. Magazine of Concrete Research. 2000;52(1):25-37. https://doi.org/10.1680/macr.2000.52.1.25
[13] Kuhlmann LA. Test method for measuring the bond strength of latex-modified concrete and mortar. Materials Journal. 1990;87(4):387-394.
[14] Espeche AD, León J. Estimation of bond strength envelopes for old-to-new concrete interfaces based on a cylinder splitting test. Construction and building materials. 2011;25(3):1222-1235. https://doi.org/10.1016/j.conbuildmat.2010.09.032
[15] Le HT, Müller M, Siewert K, Ludwig H-M. The mix design for self-compacting high performance concrete containing various mineral admixtures. Materials and Design. 2015;72:51-62. https://doi.org/10.1016/j.matdes.2015.01.006
[16] Belmokretar K, Ayed K, Kerdal DE, Leklou N, Mouli M. New Repair Material for Ordinary Concrete Substrates: Investigating Self-Compacting Sand Concrete and Its Interaction with Roughness of the Substrate Surface. Journal of Materials in Civil Engineering. 2023;35(9):05023004. https://doi.org/10.1061/JMCEE7.MTENG-15348
[17] Arasteh Khoshbin O, Madandoust R, Ranjbar MM. Evaluation of pull-off strength for steel fibre reinforced self-compacting concrete repair overlays. European Journal of Environmental and Civil Engineering. 2023;27(16):4613-4628. https://doi.org/10.1080/19648189.2023.2194953
[18] Setiawan ES, Sriwahyuni Y, Kartika N. Analisis Efektivitas Kemampuan Pulih Mandiri Micro Crack pada Self-Healing Concrete. Rekayasa Sipil. 2023;17(2):169-178. https://doi.org/10.21776/ub.rekayasasipil.2023.017.02.8
[19] Pandey S, Umale S, More S, Kale NK. Study of the Long-Term Durability of Self-Healing Concrete. International Journal of Advanced Research in Science, Communication and Technology. 2023.
[20] EFNARC. Specifications and Guidelines for the use of specialist products for Mechanized Tunnelling (TBM) in Soft Ground and Hard Rock. Recommendation of European federation of producers and contractors of specialist products for structures; 2005.
[21] Association française de génie civil. Recommandations pour l'emploi des bétons auto-plaçants: recommendations for use of self-compacting concrete. AFGC; 2008.
[22] Ramesh G, Srinath D, Ramya D, Krishna BV. WITHDRAWN: Repair, rehabilitation and retrofitting of reinforced concrete structures by using non-destructive testing methods. 2021. https://doi.org/10.1016/j.matpr.2021.02.778
[23] Adhikary SK, Ashish DK, Sharma H, Patel J, Rudžionis Ž, Al-Ajamee M, et al. Lightweight self-compacting concrete: A review. Resources, Conservation & Recycling Advances. 2022;15:200107. https://doi.org/10.1016/j.rcradv.2022.200107

[24] Rahman SK, Al-Ameri R. Marine Geopolymer Concrete—A Hybrid Curable Self-Compacting Sustainable Concrete for Marine Applications. Applied Sciences. 2022;12(6):3116. https://doi.org/10.3390/app12063116
[25] Ramesh G. Self-Compacting Concrete: A Review. Indian Journal of Structure Engineering (IJSE). 2021;1(2):9-12. https://www.ijse.latticescipub.com/portfolio-item/a1303051121/
[26] Rajendrana D, Christopher CG, Muthu MS. Self-compacting concrete made with partial replacement of lime stone and quarry dust powder. Res. Eng. Struct. Mater. 2022;8:633-642. http://dx.doi.org/10.17515/resm2022.346ma1001tn
[27] Alghamri R, Rengaraju S, Al-Tabbaa A. Large-scale laboratory trials of smart aggregates for self-healing in concrete under different curing regimes. Cement and Concrete Composites. 2023;136:104864. https://doi.org/10.1016/j.cemconcomp.2022.104864
[28] Nécira B, Abadou Y. Properties of self-compacting mortar made with various mineralogical sources different types of sands and fillers. World Journal of Engineering. 2021;18(6):861-869. https://doi.org/10.1108/WJE-10-2020-0483
[29] Memiş S. Performance Characteristics and Cost Optimization of Self-Compacting Concrete with Industrial Waste Additives to be Used in Agricultural Buildings. Turkish Journal of Agriculture-Food Science and Technology. 2021;9(1):89-97. https://doi.org/10.24925/turjaf.v9i1.89-97.3731
[30] De Larrard F. Concrete mixture proportioning: a scientific approach. CRC Press; 1999.
[31] ASTM International. ASTM C131/C131M - Standard Test Method for Resistance to Degradation of Small-Size Coarse Aggregate by Abrasion and Impact in the Los Angeles Machine. West Conshohocken, PA; 2020.
[32] Okamura H, Ouchi M. Self-compacting concrete. Journal of advanced concrete technology. 2003;1(1):5-15. https://doi.org/10.3151/jact.1.5
[33] Neville AM, Brooks JJ. Concrete Technology. 2nd ed. Pearson Education Limited; 2010.
[34] Mehta PK, Monteiro PJM. Concrete: Microstructure, Properties, and Materials. 4th ed. McGraw-Hill Education; 2014.
[35] Uysal M, Yilmaz K. Effect of mineral admixtures on properties of self-compacting concrete. Cement and Concrete composites. 2011;33(7):771-776. https://doi.org/10.1016/j.cemconcomp.2011.04.005
[36] Ghezal A, Khayat KH. Optimizing self-consolidating concrete with limestone filler by using statistical factorial design methods. Materials Journal. 2002;99(3):264-272. https://www.concrete.org/publications/acimaterialsjournal.aspx
[37] Ye G, Liu X, De Schutter G, Poppe AM, Taerwe L. Influence of limestone powder used as filler in SCC on hydration and microstructure of cement pastes. Cement and Concrete Composites. 2007;29(2):94-102. https://doi.org/10.1016/j.cemconcomp.2006.09.003
[38] Oner AD, Akyuz S. An experimental study on optimum usage of GGBS for the compressive strength of concrete. Cement and concrete composites. 2007;29(6):505-514. https://doi.org/10.1016/j.cemconcomp.2007.01.001
[39] Kou SC, Poon CS. Properties of self-compacting concrete prepared with recycled glass aggregate. Cement and Concrete Composites. 2009;31(2):107-113. https://doi.org/10.1016/j.cemconcomp.2008.12.002
[40] Bache HH. Densified cement ultra-fine particle-based materials; 1981.
[41] Neville AM. Properties of concrete. Vol. 4. London: Longman; 1995.
[42] Goldman A, Bentur A. The influence of microfillers on enhancement of concrete strength. Cement and concrete research. 1993;23(4):962-972. https://doi.org/10.1016/0008-8846(93)90050-I
[43] Mouli M, Khelafi H. Performance characteristics of lightweight aggregate concrete containing natural pozzolan. Building and environment. 2008;43(1):31-36. https://doi.org/10.1016/j.buildenv.2006.11.038

Research on Engineering Structures & Materials
www.jresm.org
Research Group

Research Article

Influence of the ground motion directionality on the global ductility of 3D RC structures

Marco Breccolotti*,a, Mattia Puccib

Department of Civil and Environmental Engineering, University of Perugia, via G. Duranti, 93, Perugia, Italy

Article Info

Article history:

Received 14 May 2024
Accepted 03 July 2024

Keywords:

Global ductility;
Framed RC buildings;
Seismic action;
Directionality

Abstract

This study examines the influence of ground motion directionality on global ductility μ_s of framed reinforced concrete structures. Suitable values of angle of attack θ, longitudinal reinforcement ratio ρ_l, dimensionless axial stress υ and mechanical ratio of transverse reinforcement ω_{wd} were assumed. Detailed nonlinear modeling was adopted to reproduce the behavior of reinforced concrete elements in the plastic field considering, also, the confinement effect on concrete mechanical properties. Nonlinear static simulations were carried out with the capabilities of the OpenSees code to evaluate the capacity curves and the corresponding global ductility. The results show that plastic hinges develop on the columns for the combined effect of bending moments transmitted by the beams framing into the same joint for values of the angle θ equal to 30° and 45°. Consequently, the formation of soft-storey mechanisms significantly reduces the global ductility μ_s. A design formula is proposed to avoid such collapse mechanism for framed reinforced concrete structures in ductility class high.

1. Introduction

It is known that one of the most relevant actions that can affect reinforced concrete (RC) framed structures is represented by the seismic action. In the last decades, scientific research has made great advances both on the characterization of the seismic action, on the definition of building structural response and on the optimal exploitation of the materials used in the construction. However, the complexity of this problem still leaves unresolved some aspects that could jeopardize buildings structural safety. Among these aspects can be included the effect of seismic action directionality on the global ductility of framed 3D RC structures.

One of the first researches on this topic was conducted by Park and Paulay [1]. The authors observed that seismic loading applied along an axis different from the principal ones of a building will require column strengths considerably greater than that required for the principal directions. Similar comments were raised decades later by Wilson et al. [2]. Their research demonstrated that the way of combining 100% of horizontal action in one direction plus 30% of the seismic action in the perpendicular direction can underestimate the building seismic demand. The authors also showed that a combination according to the square root of the sum of the squares rule of two 100% seismic actions with respect to any user defined orthogonal axes, provides a structural design which has suitable resistance to seismic motions from all directions.

In the last years several investigations have been carried out to analyze the behavior of 3D frame structures subjected to generally oriented seismic action. Magliulo et al. [3]

*Corresponding author: marco.breccolotti@unipg.it
[a] orcid.org/0000-0003-1008-9769; [b] orcid.org/0009-0006-3345-1643
DOI: http://dx.doi.org/10.17515/resm2024.286st0514rs

highlighted how the response of a structural system is significantly influenced by the direction of the earthquake comparing the behavior of regular and irregular buildings subjected to bidirectional seismic actions. According to their findings, a critical angle of the seismic action can modify the displacement demand up to 15% and the rotation of the plastic hinges up to 30%.

Two irregular structures, located in Portugal, with 6 floors above ground and 3 underground floors have been studied by Mosleh et al. [4]. The design of the structural elements was carried out considering national and international regulations, including Eurocode 2 [5]. The assessment of the seismic capacity of both structures was carried out by means of non-linear analysis:

- initially pushover simulations were developed for the main directions of each building;
- subsequently integrated through a series of dynamic simulations that included different artificial accelerograms applied to the base of the structures.

The results of the analysis in terms of maximum displacements of the control points were compared with some international guidelines [6, 7]. The study underlined the importance, during the phase of dimensioning and verification of the structural elements, of understanding the effect of biaxial stresses on columns behavior and the influence of axial load variation as a function of the relative position of the element with respect to the system.

Hosseinpour and Abdelnaby [8] carried out a series of analysis on two eight-story framed RC buildings, one regular and the other one irregular in elevation. Seismic sequences were used in irregular buildings along directions corresponding to significantly different global performances due to variations in stiffness, resistance, and ductility. Studies on vertical irregular buildings have been also performed by Shojaei and Behnam [9] who observed that structures with story irregularities sustain more damage than regular structures.

Subsequently, Garcìa et al. [10] evaluated the response of three-dimensional steel buildings of different heights under the action of multiple seismic actions. The investigation was conducted through the application of base accelerations with 5 angles of incidence, respectively of 0°, 22.5°,45°, 67.5° and 90°. The results of their analyses showed that the angle of incidence influences the interstory drift demands also for steel moment-resisting buildings.

Dang et al. [11] carried out experimental investigations to study the behavior of RC columns with controlled failure modes subjected to uniaxial/biaxial loading. Based on tests results, the authors observed that biaxial loading degrades column deformation capacity, and that this reduction can be even more severe for combination of biaxial loading and high axial force. Similar results were also observed by Breccolotti et al. [12].

Recently, Valenzuela-Beltran et al. [13] presented an in-depth analysis of the parameters that influence the seismic response of reinforced concrete buildings, such as: the global ductility level of the buildings, the post-failure stiffness ratio, the structural resistance and the number of stories of the structure. In this regard, the analyses were carried out on three structures of 6, 9 and 12 floors, each of which provided for different levels of ductility capacity (low, medium, and high). The results of their investigation allowed to notice that the magnitude of residual drift demands (RIDD) was close to 1%, making these buildings prone to suffer large permanent deformations.

The importance of the problem is evidenced by recent publications on the subject such as that of Zhang and Tao [14] who proposed an iterative method to prevent the soft story failure mode and that by Karki, Oinam and Sahoo [15] and Esfandiari, Zangeneh and

Esfandiar [16] who evaluated several strengthening techniques for RC moment resisting frames.

This work aims at further analyze the suitability of current design procedures provided by structural design codes to deal with relevant seismic biaxial loadings on framed 3D structures and ductility capacity of RC columns. Numerical investigations developed through OpenSees software were developed for this purpose. Finally, a simply additional equation to enforce the strong column – weak beam condition also for general biaxial bending in RC columns is proposed. Future studies will be conducted to assess the influence of stiffness and strength degradation resulting from repeated biaxial earthquake loading as already addressed by Abdelnaby and Elnashai [17] for planar frames.

2. Seismic Design of Framed RC Buildings

The effect of seismic force directionality is considered in design codes by specific combination rules. A complete state-of-the-art review on this topic has been published by Wang et al. [18]. For instance, EN 1998 [19] and ASCE-SEI [20] assume that the orthogonal seismic effects can be simulated by means of combination of two orthogonal response spectra, or through a pair of ground movement recordings, where one of these components is taken at its 100% value and the other one is scaled to a 30% value. While this approach provides a conservatory evaluation of the loading intensity, it doesn't consider possible performances changes of the structural system due to a different direction of the resulting loading system. In the next paragraph the main parameters that can be used to describe such performances, namely material, local and global ductility, are briefly recalled.

2.1. Material, local and global ductility

The intrinsic ductility is the property of the material to develop deformations while maintaining a constant or slightly variable level of stress. It is defined, starting from the σ – ε stress-strain diagram obtained through tensile or compression tests, using the following formula:

$$\mu_\varepsilon = \frac{\varepsilon_u}{\varepsilon_y} = 1 + \frac{\varepsilon_p}{\varepsilon_y} \tag{1}$$

where ε_y is the deformation at the elastic limit, ε_u the ultimate deformation and ε_p is the strain excursion in the plastic field. With reference to RC structures, an extremely ductile behaviour can be assumed for the reinforcing steel while concrete exhibits a very fragile stress-strain relationship. Nevertheless, the ductility of the concrete can be improved with the introduction of longitudinal and transverse reinforcements in the structural elements. This behavior, known as confinement, can be responsible of an increase in the concrete ultimate strain that can reach values up to 2% [21]. Local ductility is the property of a section to develop localized plastic deformations without a significant reduction in the load bearing capacity. With reference to flexural ductility, it can be determined for a generic section from the moment-curvature diagram using the following formula:

$$\mu_\theta = \frac{\theta_u}{\theta_y} = 1 + \frac{\theta_p}{\theta_y} \tag{2}$$

where θ_y is the curvature at the elastic limit, θ_u is the curvature at the ultimate limit and θ_p is the curvature excursion in the plastic field. To calculate the bending ductility, it is necessary to determine the couples $(M_y; \theta_y)$ and $(M_u; \theta_u)$ respectively in the elastic and plastic range. In general, the parameters that influence the flexural ductility of a RC section are:

- concrete compressive strength: as the resistance of the material increases, local ductility increases too;
- concrete confinement: concrete confined by longitudinal and transverse reinforcement is characterized by ultimate strain greater than the value 0.0035, usually assumed by the standards for unconfined concrete, with a corresponding increase in the local ductility of the section;
- reinforcement ratios: an increase in the reinforcement in the compressed zone determines an increase in ductility of the section; conversely, an increase in the reinforcement in the tensile zone reduces the value of ductility;
- tensile strength and yield strength of steel: the use of more resistant steels or steels with higher yield values leads to a reduction in section ductility;
- axial load: as the normal stress acting on the structural element increases, there is a progressive ductility reduction.

This latter aspect is very relevant for determining the actual ductility of the structural elements, especially for the columns which are subjected to high compressive stresses as well as to biaxial bending. The global ductility is the property of the structure as a whole of developing plastic deformations under seismic action without relevant lessening of the load-bearing capacity. In this case the ductility is evaluated observing force-displacement diagrams with the following formula:

$$\mu_s = \frac{s_u}{s_y} = 1 + \frac{s_p}{s_y} \tag{3}$$

where s_y is the displacement at the elastic limit, s_u is the displacement limit and s_p is the displacement excursion in the plastic field of a point assumed as reference for the entire structure (e.g. centre of the top floor of the building). Global ductility is highly influenced by the type of collapse mechanism. In a framed RC structure at ultimate state, two different collapse mechanisms can occur:

- type L mechanism: the formation of plastic hinges occurs at beams ends.
- type H mechanism: the formation of plastic hinges occurs in the columns just below or just above the joints.

With the former mechanism, higher values of the global ductility are generally met. Conversely, the latter mechanism is often responsible for very low global ductility values.

3. Organization of The Study and Method of Investigation

In order to evaluate the influence of bidirectional actions on the global ductility of framed RC structures, two FE models were analyzed with the software OpenSees [22]. Detailed information on the two case studies is provided in the next paragraphs. The dimensions of beams and columns of these structures were assumed based on experience from projects with similar dimensions and loads. This assumption is not relevant for the purposes of the research work. In fact, the results of the following parametric investigations have been analyzed in terms of several dimensionless parameters whose range of use is defined by structural codes. Both models were subjected to nonlinear static analysis (pushover) with different directions of the seismic action. The columns have been assumed perfectly fixed into the foundation even if it is known that soil-foundation-structure interaction can play a relevant role in the seismic performance of buildings [23]. Parametric investigations were carried out assuming different values of the parameters that mostly influence the structural behavior [24]. Finally, global ductility values were extracted from the bi-linearized force-displacement curves.

3.1. One-Story Building

Model T1 represents a typical yet simple precast RC structure frequently found in low-rise commercial buildings in central Italy. It has a square plan of 10.0 m side, a single floor above ground with a height of 8.0 m and hinged connections between beams and columns in both directions. This structure can be considered as representative of low-rise commercial and industrial RC buildings. A perspective view of the structure with its main dimensions is shown in Fig. 1. The columns have a cross section of 600×600 mm while the beams have dimensions of 400×800 mm. The use of concrete C45/55 is foreseen for both structural elements The roof has an infinitely rigid behavior in its plan. Steel B450C is used for the longitudinal and transverse reinforcements whose arrangement is shown in Fig. 1.

3.2. Two-Story Building

Model T2 represents a typical residential low-rise cast on site RC building frequently found in low-rise residential buildings in central Italy. It has a rectangular plan 5.0×6.0 m, is made up of two floors above ground with a total height of 6.60 m with continuity connections between beams and columns at each level in both directions. A perspective view of the structure is shown in Fig. 1. The columns have a cross-sectional dimension of 400×400 mm while the beams have cross sections of 400×600 mm. Both floors have an infinitely rigid behavior. Concrete class C25/30 is used for beams and columns and B450C steel is used for longitudinal and transverse reinforcements. The arrangement of steel rebars in the columns and in the beams is shown in Fig. 1.

4. Mechanical Properties of Materials

In order to carefully analyze the seismic behavior of the investigated structures, nonlinear behaviors were assumed for concretes and steel. Their mechanical properties are described in the following. Two different concrete materials have been used in the fiber modelling of every cross-section, one for the concrete cover and one for the concrete core. The FE models assume perfect bonding between steel and concrete, thus neglecting the influence of relative slip between the two materials [25] and ignore joint damage and nonlinearity that may also contribute to the deflection of the structure [26].

4.1. Concrete

It is known that concrete stress-strain relationship plays a non-negligible role in the ductility properties of RC elements [27]. For these reasons, the *Concrete02 Linear Tension Softening* material has been chosen from the OpenSees library to describe the concrete behavior. It models uniaxial concrete material objects with tensile strength and linear tension softening with the following stress-strain relationship proposed by Kent and Park [28], subsequently modified by Park et al. [29]:

$$\frac{\sigma_c}{f_{cd}} = \begin{cases} -\left[2\frac{\varepsilon_c}{\varepsilon_{c1}} - \left(\frac{\varepsilon_c}{\varepsilon_{c1}}\right)^2\right] & for\ 0 \le |\varepsilon_c| \le |\varepsilon_{c1}| \\ -[1 - Z(\varepsilon_c - \varepsilon_{c1})] & for\ |\varepsilon_{c1}| < |\varepsilon_c| \le |\varepsilon_{c,lim}| \end{cases} \tag{4}$$

$$Z = \frac{0.5}{\varepsilon_{50u} - \varepsilon_{c1}} \tag{5}$$

and where σ_c is the concrete stress, f_{cd} is the design concrete compressive strength, ε_c is the concrete strain, ε_{c1} is the concrete strain at peak strength, ε_{50u} is the strain corresponding to half-peak stress and $\varepsilon_{c,lim}$ is the ultimate concrete strain. The constitutive law and the parameters for modelling confined and unconfined concrete are reported, respectively, in Fig. 2 and Table 1.

The effect of confinement in the concrete columns was considered according to the provision of EN 1992 [5]. In detail, the mechanical design properties of the concrete, in terms of stresses and deformations, have been increased to consider the effect of confinement produced by the longitudinal and transverse reinforcements (stirrups or ties). Although it is known that the effect of confinement also produces effects in the ductility of the beams [30], it has been neglected in the present study.

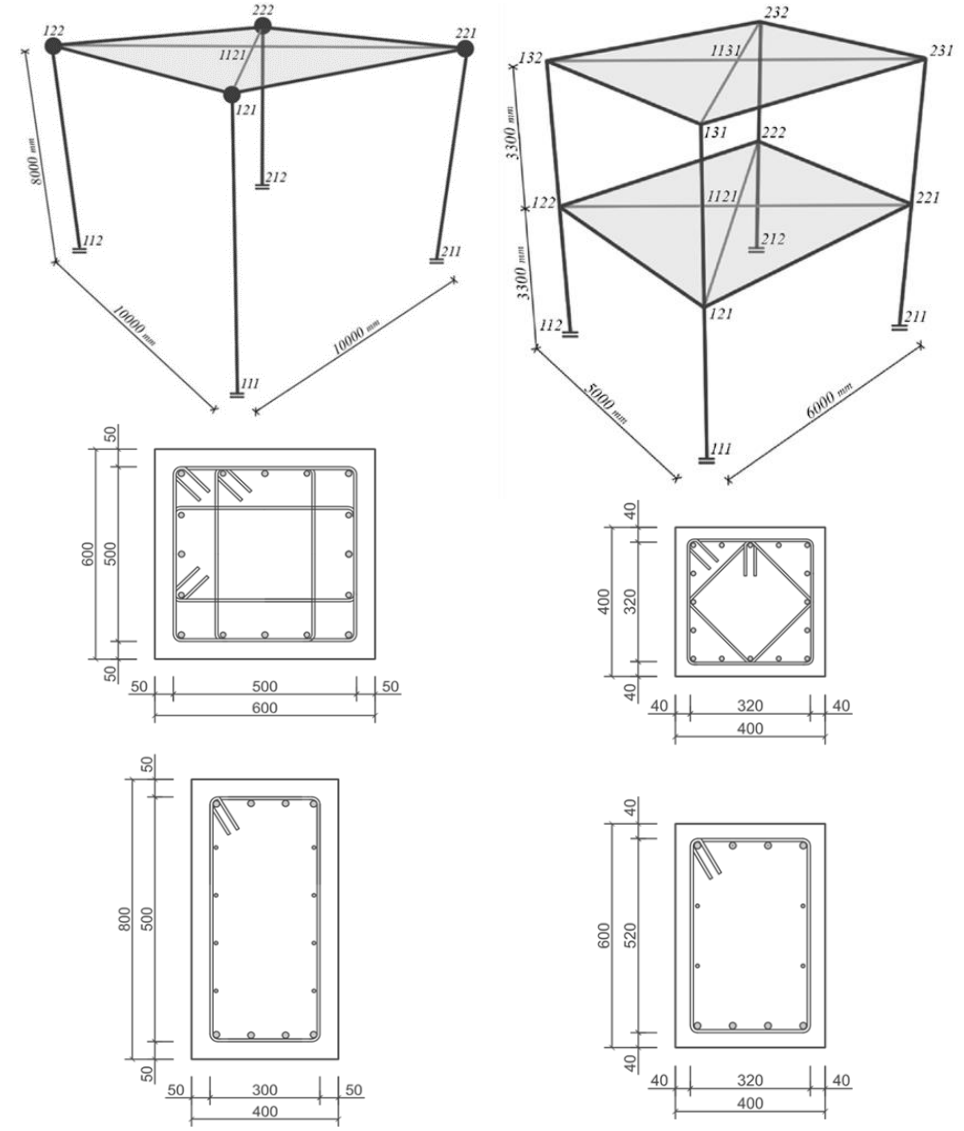

(a) (b)

Fig. 1. Perspective view with main dimensions, cross sections and reinforcements of columns and beams (from top to bottom) for (a) model T1 and (b) model T2

In the absence of specific analyses involving the use of analytical models of proven validity, the characteristic strength $f_{ck,c}$ and deformations ($\varepsilon_{c2,c}$ and $\varepsilon_{cu2,c}$) of the confined concrete can be evaluated according to the following relationships provided by Eurocode 2 [5]:

$$f_{ck,c} = \begin{cases} f_{ck} \cdot \left(1.0 + 5.0 \cdot \frac{\sigma_2}{f_{ck}}\right) & for\ \sigma_2 \leq 0.05\ f_{ck} \\ f_{ck} \cdot \left(1.125 + 2.5 \cdot \frac{\sigma_2}{f_{ck}}\right) & for\ \sigma_2 > 0.05\ f_{ck} \end{cases} \quad (6)$$

$$\varepsilon_{c2,c} = \varepsilon_{c2} \cdot \left(\frac{f_{ck,c}}{f_{ck}}\right)^2 \quad (7)$$

$$\varepsilon_{cu2,c} = \varepsilon_{cu} + 0.2 \cdot \frac{\sigma_2}{f_{ck}} \quad (8)$$

where f_{ck} is the concrete compressive strength measured on standard cylinders, σ_2 is the effective lateral confinement pressure; ε_{c2} and ε_{cu} are, respectively, equal to 0.0020 and 0.0035. The effective confinement pressure was determined as $\sigma_2 = \alpha \cdot \sigma_l$ being σ_l the confinement pressure exerted by the transverse reinforcement and α an efficiency coefficient defined as the ratio between the volume $V_{c,eff}$ of effectively confined concrete and the volume V_c of the concrete element. For the rectangular sections of this investigation, the lateral pressure was evaluated, for each main direction, taking into consideration the equilibrium equations in correspondence with the yield stress of the transverse reinforcement, with the following relations:

$$\sigma_{l,x} = \frac{A_{st,x} \cdot f_{yk,st}}{b_y \cdot s} \quad (9)$$

$$\sigma_{l,y} = \frac{A_{st,y} \cdot f_{yk,st}}{b_x \cdot s} \quad (10)$$

where $A_{st,x}$ and $A_{st,y}$ are the areas of the transverse reinforcement in the direction parallel to the main directions X and Y, respectively; b_x and b_y are the dimensions, with reference to the average line of the stirrups, of the confined core in the two corresponding directions; s is the stirrups pitch and $f_{yk,st}$ is the tensile characteristic strength of steel. Once the values of $\sigma_{l,x}$ and $\sigma_{l,y}$ are known, the equivalent lateral pressure can be calculated as $\sigma_l = \sigma_{l,x} \cdot \sigma_{l,y}$. The confinement efficiency coefficient α is a combination of two coefficients, $\alpha = \alpha_n \cdot \alpha_s$, where α_n is a term relating to the arrangement of the transverse reinforcement in the plane of the section and α_s is a term relating to the spacing of the stirrups. For rectangular sections, these two coefficients are equal to:

$$\alpha_n = 1 - \sum_{i=1}^{n} \frac{b_i}{6 \cdot b_x \cdot b_y} \quad (11)$$

$$\alpha_s = \left[1 - \frac{s}{2 \cdot b_x}\right] \cdot \left[1 - \frac{s}{2 \cdot b_y}\right] \quad (12)$$

being n the total number of longitudinal bars laterally contained by stirrups or ties and b_i the distance between two consecutive contained bars. Finally, the design resistance $f_{cd,c}$ is given by:

$$f_{cd,c} = \frac{\alpha_{cc} \cdot f_{ck,c}}{\gamma_c} \quad (13)$$

where α_{cc} considers the long-term effect on concrete strength and γ_c is the concrete partial safety coefficient.

4.2. Steel

Reinforcement steel has been modeled with the Hysteretic material, also present in the OpenSees library. A strain hardening behavior was modelled by identifying pairs of stress-

strain values as foreseen by EN 1992 [5]. The constitutive law and the parameters used for steel modelling in both case studies are shown, respectively, in Fig. 3 and Table 2.

5. Parametric Investigations

Models T1 and T2 described in chapter 3 were used to perform parametric investigations in which, by varying several geometric and mechanical parameters, 1260 analyses were obtained for each model. To speed up the control and the synthesis of such a great amount of data, the output text files produced by OpenSees were post-processed through an automatic procedure in a MATLAB environment. The following parameters were investigated for both T1 and T2 models:

- angle of application of horizontal forces θ;
- longitudinal reinforcement ratio ρ_l;
- dimensionless axial stress v;
- mechanical ratio of transverse reinforcement ω_{wd}.

The investigated ranges of these parameters are described in the following paragraphs. The values of these factors used in the parametric analyses are listed in Table 3. Every combination of 4 values of the different parameters has been considered in the analysis for a total number of possible combination equal to 4 x 7 x 9 x 5 = 1260.

Table 1. Concrete mechanical parameters for models T1 and T2

Model	$matTag	$fpc	$epsc0	$fpcu	$epscu	$lambda	$ft	$Ets
		[MPa]		[MPa]			[MPa]	[GPa]
T1	IDConcCover	45.0	0.002	9.0	0.0035	0.1	3.80	70
	IDConcCore	$f_{ck,c}$	$\varepsilon_{c2,c}$	0.2 $f_{ck,c}$	$\varepsilon_{cu2,c}$	0.1	0.3 $f_{ck,c}^{2/3}$	70
T2	IDConcCover	25.0	0.002	5.0	0.0035	0.1	2.55	70
	IDConcCore	$f_{ck,c}$	$\varepsilon_{c2,c}$	0.2 $f_{ck,c}$	$\varepsilon_{cu2,c}$	0.1	0.3 $f_{ck,c}^{2/3}$	70

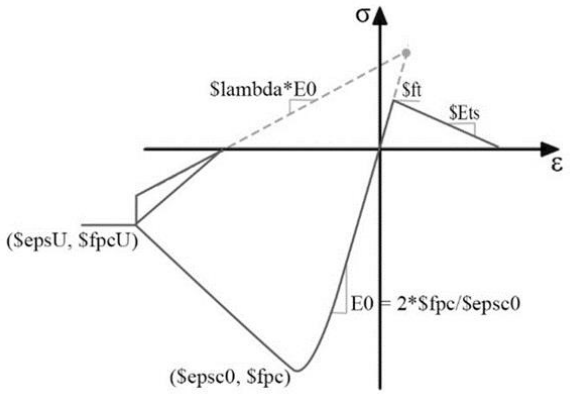

Fig. 2. Hysteretic Stress-Strain Relation for Concrete02 materials

Table 2. Reinforcing steel mechanical parameters

$matTag	$e1p	$sp1	$e2p	$s2p	$e3p	$s3p
		[N/mm^2]		[N/mm^2]		[N/mm^2]
IDSteel	0.00195	450	0.675	540	0.068	0

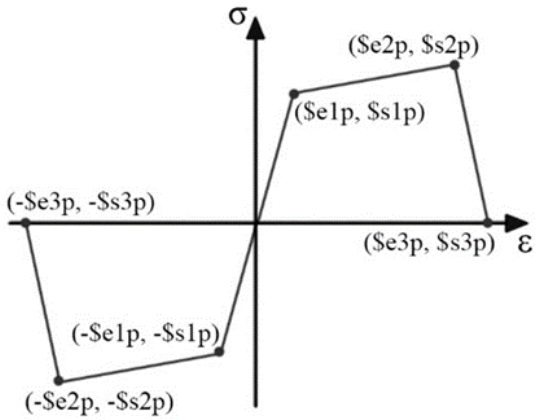

Fig. 3. Hysteretic Stress-Strain Relation for steel rebars

5.1. Angle of Application of Horizontal Forces

Both analyzed models, globally symmetrical with respect to the main axes, have square section columns, with dimensions respectively equal to 600×600 mm and 400×400 mm. The arrangements of the longitudinal reinforcements are also symmetrical with respect to the same main axes. For these reasons, the investigations can be limited to horizontal forces having inclinations θ between 0° and 45°. Intermediate values were chosen every 15°. The lateral force profiles F_i have been determined in proportion to the fundamental mode of vibration. The load values applied along the two directions were obtained based on a decomposition of the force F_i for the i − th floor according to the sine and cosine functions. For instance, with reference to the analysis carried out with an application angle of 15°, the forces along the X direction, $F_{i,x}$ results equal to 0.96 F_i while that along the Y direction, $F_{i,y}$, results equal to 0.25 F_i.

5.2. Longitudinal Reinforcement Ratio

The longitudinal reinforcement ratio is defined as:

$$\rho_l = \frac{\sum A_{si} \cdot n_{bi}}{A_c} \tag{14}$$

where A_{si} is the area of a single rebar, n_{bi} is the number of bars evenly distributed on the cross section and A_c is the total area of concrete. Taking into consideration the provisions of current standards [5], the variability of this parameter was defined in the range $0.01 \leq \rho_l \leq 0.04$ with increments for the intermediate steps of 0.005. The parametric investigations for the longitudinal reinforcement ratio were planned without taking into consideration the commercially available diameters of the reinforcing bars. In each column a total number of rebars n_{bi} equal to 16 was assumed. The rebar diameter and area A_{si} were defined to satisfy the value of the longitudinal reinforcement ratio ρ_l established for the parametric investigation.

5.3. Dimensionless Axial Stress

As well known, the presence of a relevant axial stress is responsible, with the remaining other parameters being unchanged, of a considerable reduction in the local ductility of the elements and, consequently, in the global ductility of the structure. The influence of the axial stress is better investigated referring to the dimensionless axial stress v, defined by the following relationship:

$$v = \frac{N_{Ed}}{B \cdot H \cdot f_{cd}} \tag{15}$$

where N_{Ed} is the axial force acting on the considered cross-section of the element, B and H are its geometric dimensions and f_{cd} is the concrete compressive design strength. To avoid brittle behaviors, structural standards generally put limits on the maximum values of the dimensionless axial stress v. For instance, the current Italian standard [31] requires that the maximum axial load for RC columns in ductility class "A" (high) and "B" (medium) must not exceed, respectively, 55% and 65% of the maximum compression capacity of the section of concrete only. For these reasons, the range of values $0.10 \leq v \leq 0.50$ have been considered in both models with increments between two consecutive values of 0.05. The value of v equal to $0.10 \div 0.15$ corresponds, approximately, to the dimensionless axial stress acting on the columns of ordinary buildings with geometry like that of the analyzed models. To obtain such values of the dimensionless axial stress, suitable uniformly distributed loads were applied to the beam elements of the floor decks.

5.4. Mechanical Ratio of Transverse Reinforcement

A further parameter that influences the local ductility of structural elements is the mechanical ratio of transverse reinforcement. For the reasons listed in par. 4.1, it is expected an increase in the local ductility of the element as the transverse reinforcement increases, all other conditions being equal. The effect of the transverse reinforcement was fictitiously considered by suitably modifying the constitutive relationship of confined concrete, keeping that of the concrete cover unchanged. The mechanical transverse reinforcement ratio is defined as:

$$\omega_{wd} = \frac{\left(V_{st,y} + V_{st,z}\right) \cdot f_{yd}}{V_c \cdot f_{cd}} \tag{16}$$

where $V_{st,y}$ and $V_{st,z}$ are, respectively, the volume of the stirrups along the y and z directions and V_c is the volume of the confined concrete core. According to current standards [19], at the ends of all primary columns, the value of ω_{wd} must be no less than 0.08. Consequently, the values investigated in the parametric analysis were chosen in the range $0.16 \leq \omega_{wd} \leq 0.32$ with intermediate increments equal to 0.04. To consider this parameter in the analysis, for each model and for each value of ω_{wd}, the spacing of the stirrups was properly determined. The values of the parameters α_n and α_s are subsequently calculated to evaluate the confinement coefficient α.

Table 3. Values of the investigated parameters used in the analyses

Parameter	Value								
	1	2	3	4	5	6	7	8	9
Angle Of Application of Horizontal Forces Θ	0°	15°	30°	45°					
Longitudinal Reinforcement Ratio P_L	0.010	0.015	0.020	0.025	0.030	0.035	0.040		
Dimensionless Axial Stress V	0.1	0.15	0.20	0.25	0.30	0.35	0.40	0.45	0.50
Mechanical Ratio of Transverse Reinforcement	0.16	0.20	0.24	0.28	0.32				

Finally, considering the geometric characteristics of the sections, the values of the stresses $\sigma_{l,x}$ and $\sigma_{l,y}$, necessary for the determination of the effective confinement pressure σ_2, were calculated according to the formulas shown in par. 4.1. The values of the confinement pressures thus obtained are summed up in Tables 4 and 5, respectively for models T1 and T2.

Table 4. Effective confinement pressures for model T1

ω_{wd}	s [mm]	α_n	α_s	α	$\sigma_{l,x}$ [MPa]	$\sigma_{l,y}$ [MPa]	σ_l [MPa]	σ_2 [MPa]
0.16	155	0.875	0.714	0.624	1.159	1.159	1.159	0.724
0.20	124	0.875	0.767	0.671	1.449	1.449	1.449	0.972
0.24	104	0.875	0.804	0.703	1.739	1.739	1.739	1.223
0.28	89	0.875	0.830	0.727	2.029	2.029	2.029	1.474
0.32	78	0.875	0.851	0.744	2.318	2.318	2.318	1.726

Table 5. Effective confinement pressures for model T2

ω_{wd}	s [mm]	α_n	α_s	α	$\sigma_{l,x}$ [MPa]	$\sigma_{l,y}$ [MPa]	σ_l [MPa]	σ_2 [MPa]
0.16	108	0.781	0.692	0.540	1.306	1.306	1.306	0.706
0.20	86	0.781	0.749	0.585	1.633	1.633	1.633	0.955
0.24	72	0.781	0.788	0.615	1.960	1.960	1.960	1.206
0.28	62	0.781	0.817	0.638	2.286	2.286	2.286	1.458
0.32	54	0.781	0.839	0.655	2.613	2.613	2.613	1.711

Table 6. Mechanical parameters for confined concrete of model T1

ω_{wd}	σ_2 [MPa]	$f_{ck,c}$ [MPa]	$\varepsilon_{c2,c}$	$\varepsilon_{cu,c}$	k_1	k_2	k_3
0.16	0.724	48.620	0.002	0.007	1.080	1.167	1.919
0.20	0.972	49.860	0.003	0.008	1.108	1.228	2.235
0.24	1.223	51.110	0.003	0.009	1.136	1.290	2.553
0.28	1.474	52.370	0.003	0.010	1.164	1.354	2.872
0.32	1.726	53.630	0.003	0.011	1.192	1.420	3.192

Table 7. Mechanical parameters for confined concrete of model T2

ω_{wd}	σ_2 [MPa]	$f_{ck,c}$ [MPa]	$\varepsilon_{c2,c}$	$\varepsilon_{cu,c}$	k_1	k_2	k_3
0.16	0.706	28.530	0.003	0.009	1.141	1.302	2.613
0.20	0.955	29.770	0.003	0.011	1.191	1.418	3.182
0.24	1.206	31.030	0.003	0.013	1.241	1.540	3.756
0.28	1.458	32.290	0.003	0.015	1.292	1.668	4.333
0.32	1.711	33.550	0.004	0.017	1.342	1.801	4.911

At this point, once the effective confinement pressures σ_2 are known, it is possible to calculate the parameters necessary for the mechanical characterization of the confined concrete. However, the determination of the characteristic strengths $f_{ck,c}$ and of the strains $\varepsilon_{c2,c}$ and $\varepsilon_{cu2,c}$ of the confined concrete is not sufficient for the purposes of the parametric analysis. In order to simplify the procedure, the following coefficients, $k_1 = f_{ck,c}/f_{ck}$, $k_2 = \varepsilon_{c2,c}/\varepsilon_{c2}$ and $k_3 = \varepsilon_{cu,c}/\varepsilon_{cu}$ have been used in the analysis with f_{ck} respectively equal to 45 MPa and 25 MPa for T1 and T2 models. Tables 6 and 7 show the values obtained for these parameters as the mechanical transverse reinforcement ratio ω_{wd} varies.

6. FE Analyses

As already mentioned, the structural behavior of the two models was analyzed for each different combination of the investigated parameters with the capabilities of the OpenSees software. In order to reduce the approximation errors, especially those related with the definition of the length and behavior of the plastic hinges, diffused plasticity models were implemented through the nonlinear beam column elements.

After having defined the formulations characterizing beams and columns, the cross-sections were discretized into a finite number of fibers for each control point. The fibers model allowed to accurately describe the behavior of structural elements under different load conditions through the determination of the stress-strain states on each single fiber. Therefore, if the number of fibers with which the cross-section is discretized is sufficiently large, the distribution of mechanical non-linearities can be accurately modelled even in a markedly inelastic field.

6.1. Modelling Details

The main assumptions made in the analysis were as follows:

- the control points for the pushover analysis were located at the center of gravity of the last rigid floor;
- a Corotational transformation was adopted for the beams (i.e. an exact geometric transformation of the element stiffnesses from the local to the global system) to follow the excursion in the plastic field of the elements during the execution of the nonlinear analysis;
- P-Delta effects were considered for column elements being the building subjected to relevant lateral displacements;
- the normalized eigenvector values calculated by modal analysis were used to define the shape of lateral force profile to be applied to the models.

6.2. Results of Pushover Simulations

The main results of each analysis can be synthesized with a capacity curve (i.e. a force-displacement curve). In fact, it provides the necessary information for the subsequent determination of global ductility μ_s. Each analysis provided reactions and displacements of the control point in the two main directions X and Y. To allow the comparison of results, base shears V_i and displacements s_i were calculated for each analysis by means of vectors summation. Once the base shear and the displacement for each step or i-th increment are known, the curve of real capacity V-s can be obtained.

6.3. Bilinearization of Capacity Curves

For real systems, the capacity curves generally show similar trends characterized by a first straight branch, corresponding to the linear behavior of the structure, followed by a non-linear path corresponding to the plastic response. To synthesize and compare the seismic behavior of different structures, the curves obtained through nonlinear static analysis must be simplified through linearization. This procedure is briefly recalled in the following.

In literature there are several criterions for linearizing the capacity curves, but different criteria can also provide significantly different results starting from the same input values. The approximation of the curve is the more accurate the smaller the distance, point by point, between the linearized curve and the original one.

Below, reference will be made to the following characteristic points:

- point corresponding to the first yielding of any reinforcement within the structural system with coordinates (x_{sy}, y_{sy});

- point at which the maximum base shear is reached, with coordinates (x_{max}, y_{max});
- point at which the collapse conditions are conventionally assumed to occur, with coordinates (x_{su}, y_{su}).

The main procedures for identifying the displacement at the elastic limit in a linearized capacity curve have been summarized by Park and include:

- the exact identification of the point corresponding to the first yielding of any reinforcement within the structural system;
- the intersection between the straight-line tangent to the curve in the origin and the tangent line to the capacity curve at its maximum value;
- the intersection between the straight-line passing through the origin of the system and the point of the curve corresponding to a value of 75% of the maximum base shear and the straight-line tangent to the capacity curve at its maximum value;
- the definition of a bi-linear curve obtained through the equality of the subtended area with that of the capacity curve of the structure.

Among these different possibilities, a mixed strategy between methods c and d was chosen in this investigation. In detail, the stiffness of the initial elastic branch was calculated according to method c). It was, thus, imposed the passage of this line through the point (s_y, $V_y = 0.75 \cdot V_{max}$). The ultimate displacement, of coordinates (s_u, V_u), is identified assuming $V_u = 0.85 \cdot V_{max}$.

The perfectly plastic branch was determined according to method d). Thus, the value of the yielding plateau was determined imposing the equivalence between the area subtended by the bilinear curve up to the displacement value s_u and the area subtended by the real pushover curve up to the collapse point (s_u, V_u). It can be demonstrated that, imposing this area equivalence, the yielding plateau $V_{y,bil}$ of the bilinear curve results equal to:

$$V_{y,bil} = \frac{V_y}{s_y}\left(s_u - \sqrt{s_u^2 - 2\frac{s_y}{V_y}A_{push}}\right) \tag{17}$$

Correspondingly, the yielding displacement $s_{y,bil}$ in the bilinear curve is:

$$s_{y,bil} = s_y \frac{V_{y,bil}}{V_y} \tag{18}$$

Finally, the global ductility of the structure μ_s was calculated accordingly to Eq. (3).

7. Results of Parametric Investigations

The 1260 global ductility values obtained for models T1 and T2 are shown in Figs. 4 and 5, respectively. In these figures the ductility values are reported on the vertical axis. In the other two axes are reported the angle of attack of the seismic action θ and the longitudinal reinforcement ratio ρ_l. Different colors are used to distinguish between different values of dimensionless axial stress v. Different shades of the same color represent different values of the mechanical ratio of transverse reinforcement ω_{wd}. From these figures is it clearly observable the negative influence that an angle of attack different from 0° has on the values of the global ductility μ_s.

But it is, indeed, very difficult the observation in these figures of trends and features different from the principal ones. Further observations can be made in different graphs. For instance, in Fig. 6 are shown the results of models T1 and T2 obtained for a constant value of the transverse reinforcement mechanical ratio ω_{wd} equal to 0.28. Each image is relative to a different value of the longitudinal reinforcement ratio ρ_l (from 0.010 at the top to 0.040 at the bottom). The reading and interpretation of the results is facilitated by

the introduction of trend lines, relative to the same value of the dimensionless axial stress v (from 0.10 depicted with light green to 0.50 represented with dark blu) that connect ductility values obtained for different values of the angle of attack of the seismic action θ (from 0° to 45°).

7.1. Comments on The Obtained Results

The results obtained in terms of global ductility μ_s for model T1 are like those found for the local ductility in another publication [12]. This can be ascribed to the presence of a single global collapse mechanism corresponding to that already identified at the section level. In fact, whatever the direction of the seismic actions, the plasticization in the structural elements is concentrated at the base sections of the columns. Therefore, the angle of application of the seismic action does not determine a variation of the collapse mechanism but at most a reduction of the global ductility values, the latter being function of strength and ductility capacities of the individual columns. Conversely, the parametric analyses carried out for model T2 allow to highlight how the application of bidirectional actions on more complex structures can determine different global behaviors. In fact, the analysis conducted on the two-story model reveal that the development of plastic deformations in the structure is influenced not only by the geometric and mechanical characteristics of the structural elements but also by the angle of application of the horizontal forces.

For low values of the ratio ρ_l (0.01 and 0.015), model T2 behaves according to the soft-story mechanism (type "H") with low global ductility values, regardless of the angle of application of the horizontal force profiles. This result was expected since in these conditions a configuration with strong beam - weak column is obtained, contradicting the basic condition of "Capacity Design":

$$\sum_{i=1}^{n_c} M_{c,Rd,i} \geq \gamma_{Rd} \cdot \sum_{j=1}^{n_b} M_{b,Rd,j} \tag{19}$$

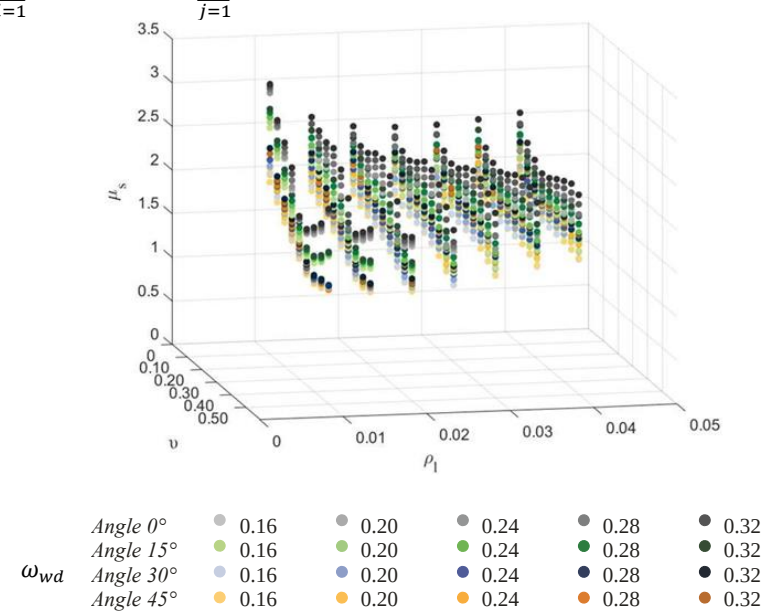

Fig. 4. Complete plot of displacement ductility factors for model T1

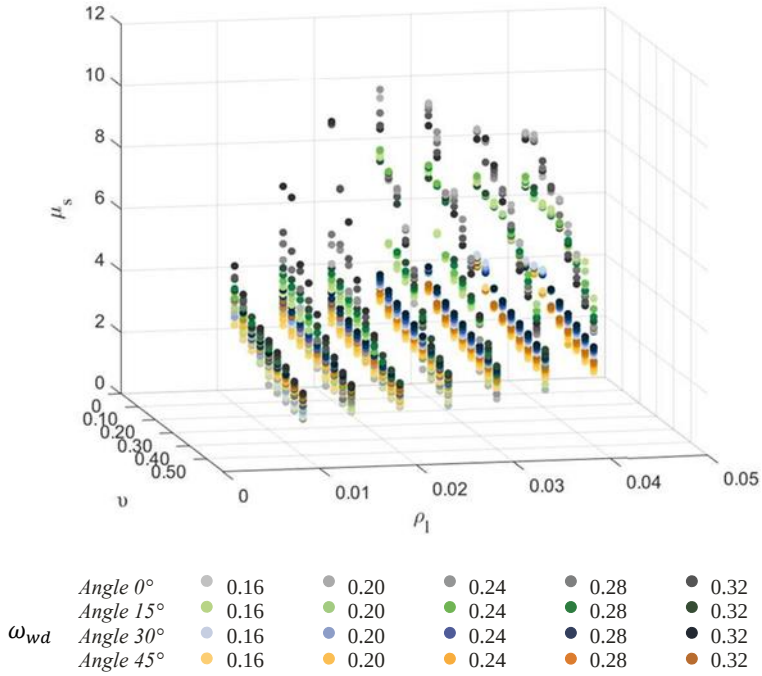

Fig. 5. Complete plot of displacement ductility factors for model T2

where γ_{Rd} is the model uncertainty factor for the design value of resistances, also known as overstrength factor, $M_{c,Rd,i}$ is the bending capacity of the column and $M_{b,Rd,j}$ is the bending capacity of the beams framing into the joint. As the longitudinal reinforcement in the columns increases with unchanged other conditions (mechanical ratio of transverse reinforcement and dimensionless axial stress), an increase in the resisting capacities is obtained. Nevertheless, the transition from the strong beam - weak column mechanism to the strong column - weak beam configuration can be observed only for small values (θ = 0° and 15°) of the angle of attack. To better understand the physical reasons that determine a decrease in displacement ductility, the progression of the plastic hinges during the analysis was observed. For ease of simplicity, only the configuration of the model at the moment of reaching the displacement corresponding to s_u is considered.

The parametric survey highlights how some angles of application of lateral forces can facilitate the activation of collapse mechanisms other than those commonly expected during the design phase, with consequent effects on the displacement ductility values. The capacity curves shown in Fig. 7, as examples of effective and linearized capacity curves, were obtained by varying the angle of application of the lateral forces θ and the longitudinal reinforcement ratio ρ_l, while the mechanical ratio of the transverse reinforcement ω_{wd} and the dimensionless axial stress ν were kept constant. In the upper part of the figure are shown four images, each one for a different angle of attack θ. In a single image, 7 couples of curves are shown for different values of the longitudinal reinforcement ratio ρ_l. The results obtained by varying the angle θ highlight a decrease in ductility values when the lateral forces are not parallel to one of the main axes of the structural system. In fact, the range of values obtained in the case of θ = 0° is between 4.00 and 9.15, depending on the longitudinal reinforcement ratio ρ_l. This range of values is maintained unchanged, albeit with some reductions not exceeding 10%, for an application angle of 15°.

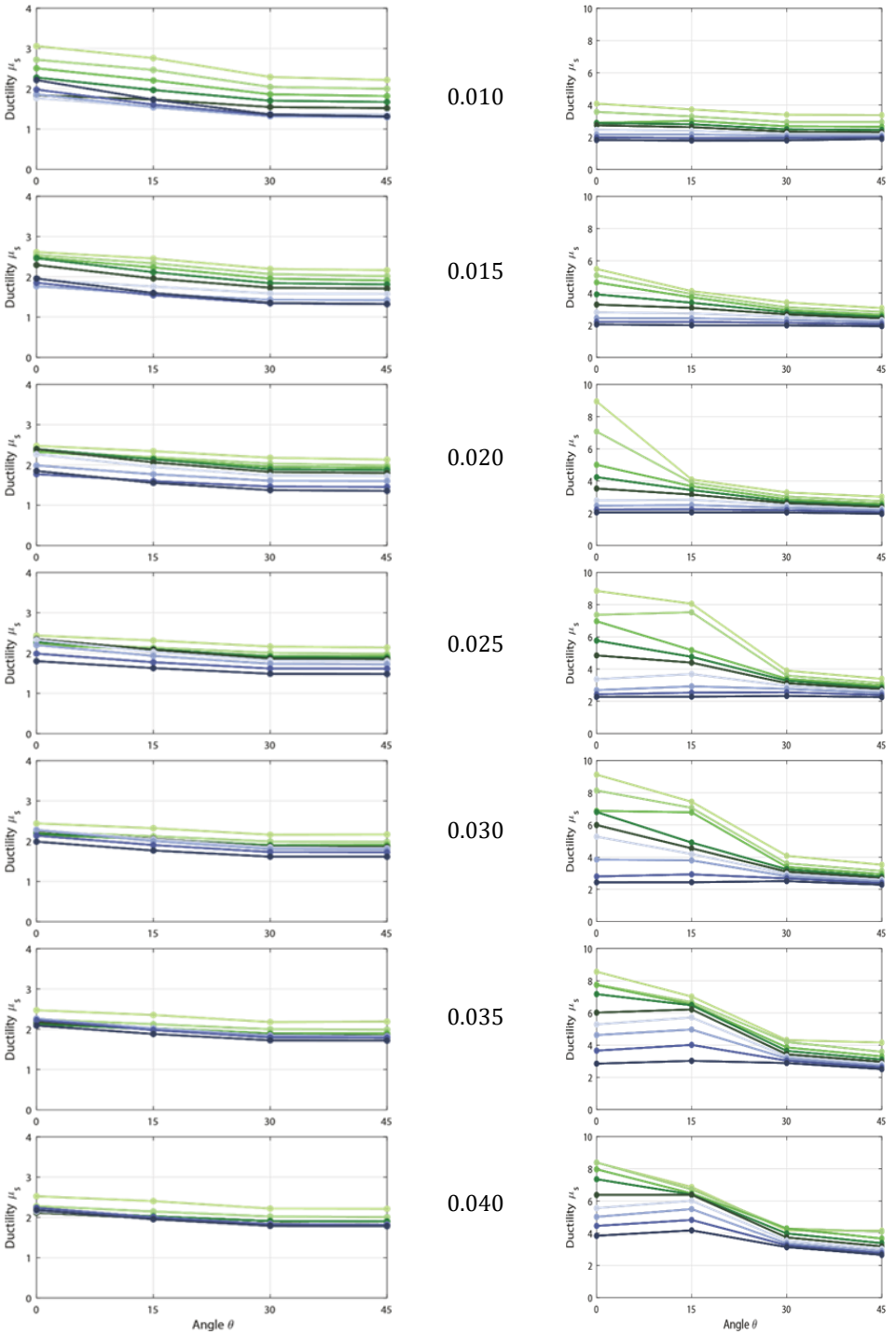

(a) Model T1 (b) Model T2

Fig. 6. Ductility values μ_s obtained for ω_{wd}=0.28 and different values of ρ_l (from 0.010 at the top to 0.040 at the bottom) and v (from 0.10 depicted with light green to 0.50 represented with dark blu) for model T1 (a) and model T2 (b)

Conversely, the capacity curves obtained for the remaining angles show global ductility values never higher than 4.50, with ultimate displacements reached by the control point of less than 200 mm. Similarly, the influence of the angle of attack of the seismic forces on the ductility can be highlighted, in the same figure, considering the development of plastic hinges on the structural elements when the displacement s_u is reached. In the lower part of the figure, in fact, are shown 24 images of model T2, one for each combination of the 4 θ and 7 ρ_l values of the previous mentioned capacity curves. In each image:

- the formation of the plastic hinges in correspondence with the elements is highlighted in green for the beams and red for the columns;
- the type "L" collapse mechanism is indicated with a light grey background and the type "H" one with a dark grey background.

Consistently with the capacity curves, the reduction of ductility values as the angle θ increases is conditioned by the mechanism developed during the excursion in the plastic phase. In fact, for angles between 30° and 45° the dominant collapse mechanism is the "H" type, with plasticization in the columns of the first floor and low values of μ_s. The occurrence of this mechanism can be identified in the images shown in the lower part of Fig. 7 characterized by a dark gray background. In these images it is possible to notice the presence of two plastic hinges (red circles) at the ends of all the columns of the first floor, a configuration which corresponds precisely to the "H" type mechanism. This can happen despite the following combinations of seismic actions required from the structural codes, also for non-linear static analysis:

$$E = \begin{cases} E_{Edx} + 0.3E_{Edy} \\ 0.3E_{Edx} + E_{Edy} \end{cases} \tag{20}$$

where E_{Edx} represents the action effects due to the application of the seismic action along the chosen horizontal axis X of the structure and E_{Edy} represents the action effects due to the application of the same seismic action along the orthogonal horizontal axis Y of the structure. While providing for the simultaneous presence of seismic actions on two orthogonal directions, these combinations could not be sufficient to cover all cases to which constructions could be subjected during an earthquake. In fact, the combination rule of Eq. (20) allows to consider only seismic action with inclination in the range ±15° respect the mail directions. Although these combinations introduce a seismic intensity slightly higher (104.4%) than the effective one (100%), it is not sure that it reproduces the most demanding condition for the system: any floor mechanisms that are activated by different directions of application of the seismic action are ignored by regulatory provisions. Recalling the content of par. 5.1, since the relationship $F_{i,x} > F_{i,y}$ remains such for the entire analysis, the first yielding will occur in correspondence of beams positioned along the X direction, while the beams located in the Y direction will remain in the elastic range without undergoing yielding.

The final positions of the structural model evaluated at the end of each analysis (achievement of the displacement s_u) are shown in the left image of Fig. 8. In the same figure, in its right part, are shown the trajectories of the control point of the system with their corresponding X and Y displacements. For the reasons described above, if plasticization occurs in the beams, the structure tends to deform almost completely along the direction for which a reduction in stiffness is obtained. This effect is particularly evident for analysis carried out with application angles between 15° and 30°: the dominant displacements along X direction confirm how the structure has developed a post-elastic mechanism with plasticization at the end sections of the beams. In some cases, it is also evident a sudden increase of the displacement in the Y direction. This occurs when plastic hinges appear in the columns.

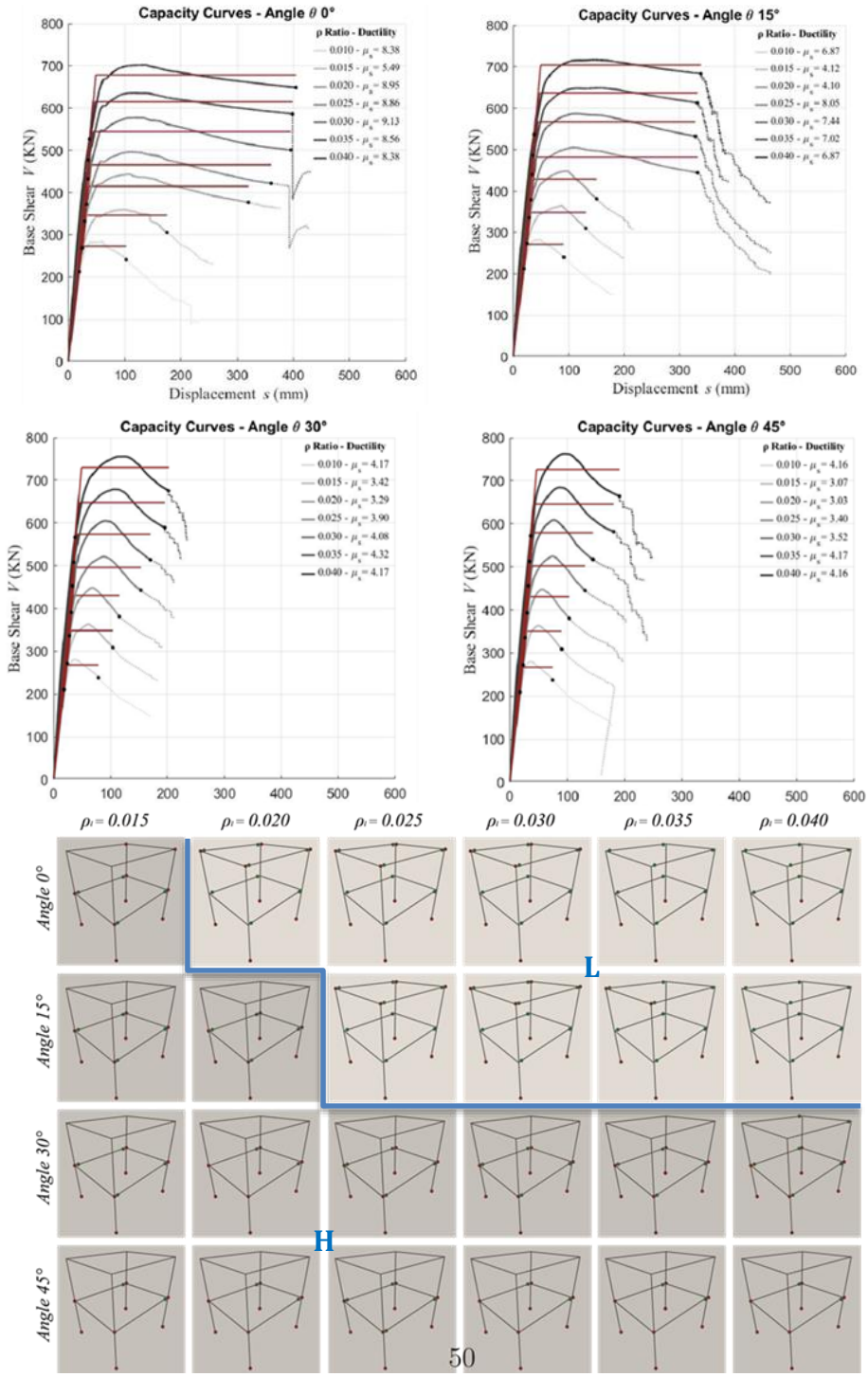

Fig. 7. Failure mechanisms in model T2 for different values of longitudinal reinforcement ratio and angles of attack. Red and green dots: plastic hinges in columns and beams, respectively. Dark and light grey background: "H" and "L" mechanism, respectively

7.2. Main Outcomes and Proposal for Behavior Improvements

The main outcomes of this investigation can be resumed as follows:

- for high values of the angle of attack (θ equal to 30° and 45°) a relevant reduction of the global ductility μ_s can be observed;
- for high values of the angle of attack (θ equal to 30° and 45°) collapses occur according to a soft-story mechanism. The rule relating to the hierarchy of bending resistances applied separately at the node in the two main directions may no longer be sufficient when dealing with seismic actions having direction very different from the principal directions of the system.

The first observation derives by the reduction of flexural strength for biaxially loaded rectangular or square columns when the vector moment is inclined respect the principal axis of the section [32]. An improvement to this behavior can be achieved by simply moving some of the rebars placed along the sides of the column section towards the vertexes of the section itself. This is shown, for instance, in Fig. 9 (left) for the column of model T2. This modified distribution, without reducing the concrete confinement and the flexural resistance towards the bending moments along the principal axes, allows obtaining greater resistance and ductility against biaxial bending loadings. The positive effect of this expedient in the distribution of the reinforcing bars can be noted in the comparison between the capacity curves show in Fig. 10. For a standard rebars distribution the maximum ductility value μ_s is equal to 3.75. It raises up to 4.25 (+13.3 %) for the modified distribution without affecting the behavior of the section for axially loaded column in one direction only and without cost increase.

Nevertheless, this simple trick is not always sufficient for a relevant improvement of the seismic behavior. Such drawback can be ascribed to the inadequacy of the control laws of Eq. (19) for both principal directions to guarantee the capacity design for seismic actions having directions different from the principal axis of the section. In these cases, especially for structures designed assuming a ductility class high (DCH) according to EN 1998 [19], it would be recommended also checking the following condition:

$$\sum_{i=1}^{n_c} M_{c,Rd,i,45°} \geq \gamma_{Rd} \cdot \sqrt{\left(\sum_{i=1}^{n_{cx}} M_{b,Rd,i,x}\right)^2 + \left(\sum_{j=1}^{n_{cy}} M_{b,Rd,j,y}\right)^2} \tag{20}$$

where $M_{c,Rd,i,45°}$ is the minimum resisting bending moment of the column along a direction inclined of ±45° respect one of the principal directions, $M_{b,Rd,i,x}$ and $M_{b,Rd,j,y}$ are the bending strengths of beams in the x and y principal directions, respectively.

This condition requires that the resisting moment of the columns should be greater than the vector combination of the resisting moments of the beams converging in the joint. The effects of this provision have been checked on model T2 where the dimensions of the columns have been increased to 500×500 mm (Fig. 9, right) in order to satisfy Eq. (20) without varying the longitudinal reinforcement ratio ρ_l values. The results show that the ductility increase is evident starting from values of ρ_l equal to 0.02 for which a ductility value of 5.93 is achieved (Fig. 11). This value corresponds to an increase of +58.1% compared to the maximum ductility value obtained in the case of the 400×400 mm column with standard reinforcement pattern.

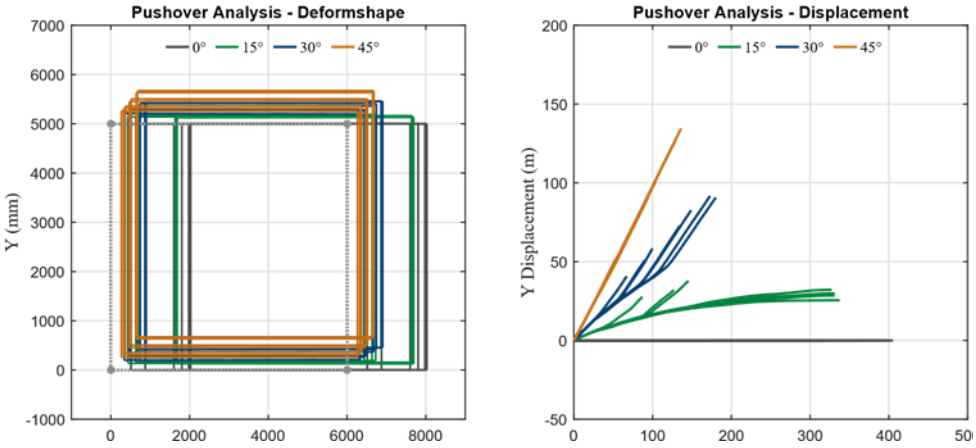

Fig. 8. Planar positions (left) and displacements of the control point (right) at the end of pushover analysis for model T2

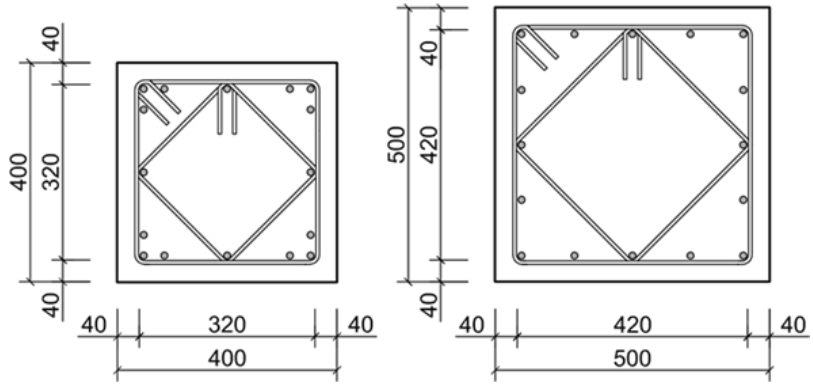

Fig. 9. Section 400×400 mm with improved steel rebars distribution (left) and section 500×500 mm satisfying Eq. (21)

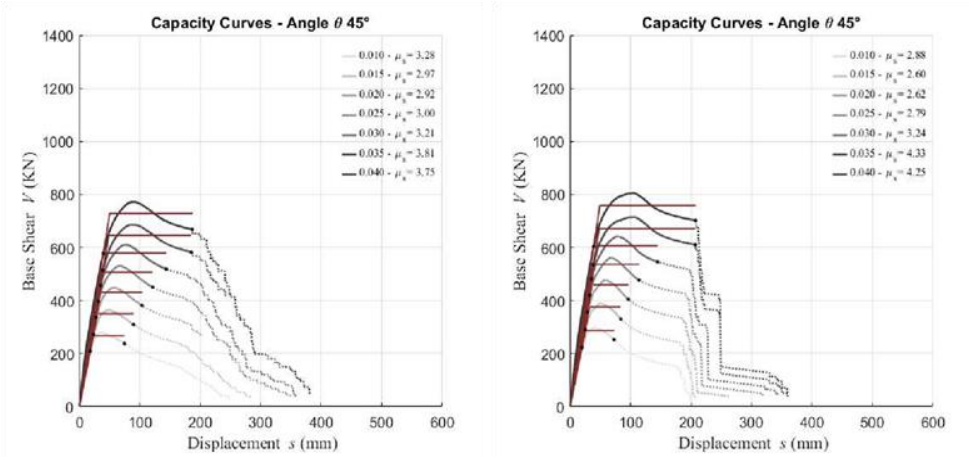

Fig. 10. Comparison between several capacity curves for a model T2 400×400 mm columns section with rebars position according to Fig. 1 (left) and Fig. 9 (right)

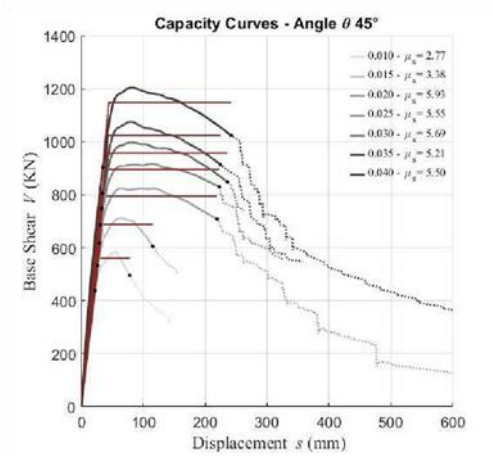

Fig. 11. Capacity curves of model T2 with 500×500 mm cross section columns

Although the design formula has been validated on low-rise buildings, its validity can be extended to three-dimensional beam-column nodes also belonging to medium and high-rise RC buildings. Referring to the second observation, the design rule set out in Eq. (20) will prevent collapses with "H" type mechanism for any direction of the seismic action, with consequent improvement of the ductility values.

8. Conclusions

This work investigates the nonlinear behaviors of two framed RC structures subjected to seismic actions characterized by different propagation directions. The results, obtained through a parametric investigation conducted using OpenSees and Matlab, allow to highlight how the global (displacement) ductility is strongly influenced by the direction of the earthquake, as already observed for the local (curvature) ductility. Structural standards generally require the simultaneous presence of both horizontal components of the seismic action, one at its full value (100%) and the other at a reduced percentage (30%). Nevertheless, this provision does not make available any indication for the evaluation of the critical angle of the seismic action for which the lowest ductility value would be obtained. The results of this investigations also show that as the angle of attack increases, the framed 3D RC structures start to be affected by unwanted collapse mechanisms, such as soft story mechanisms, due to the reduction of the local ductility capacities of the columns. In particular, it was possible to observe that, while for angles of attack of the seismic action of 0° and 15° the prevailing collapse mode is the "L" type, for angles of attack of 30° and 45° the prevailing collapse mode becomes the "H" type. This mechanism, which significantly reduce the excursion in the plastic field, may not be avoided through the application of the simplified procedure provided by current design standards. To overcome this drawback, especially for DCH structures, a further condition to be checked after having defined the longitudinal reinforcements of beams and columns framing into the same joint, has been proposed. It can avoid the formation of a plastic hinge in the columns under the combined effect of the bending moments transmitted to the joints by the beams lying along two perpendicular axes for any direction of the seismic action.

References

[1] Park R, Paulay T. Ductile reinforced concrete frames - Some comments of the Special provision for seismic design of ACI 318-71 and on Capacity design. Bull N Z Natl Soc Earthq Eng. 1975;8(1):70-91. https://doi.org/10.5459/bnzsee.8.1.70-90

[2] Wilson EL, Suharwardy I, Habibullah A. A clarification of the orthogonal effects in a three-dimensional seismic analysis. Earthquake Spectra. 1995;11(4):659-66. https://doi.org/10.1193/1.1585831
[3] Magliulo G, Maddaloni G, Petrone C. Influence of earthquake direction on the seismic response of irregular plan RC frame buildings. Earthq Eng Eng Vib. 2014;13(2):243-56. https://doi.org/10.1007/s11803-014-0227-z
[4] Mosleh A, Rodrigues H, Varum H, Costa A, Arêde A. Seismic behavior of RC building structures designed according to current codes. Structures. 2016;7:1-13. https://doi.org/10.1016/j.istruc.2016.04.001
[5] CEN. EN 1992-1-1:2004, Eurocode 2: Design of concrete structures - Part 1-1: General rules and rules for buildings. European Committee for Standardization; 2004.
[6] FEMA. FEMA 356 Prestandard and commentary for the seismic rehabilitation of buildings. Federal Emergency Management Agency; 2000.
[7] ATC. ATC-40 Seismic Evaluation and Retrofit of Concrete Building. Redwood City, CA: Applied Technology Council; 1996.
[8] Hosseinpour F, Abdelnaby A. Effect of different aspects of multiple earthquakes on the nonlinear behavior of RC structures. Soil Dyn Earthq Eng. 2017;92:706-25. https://doi.org/10.1016/j.soildyn.2016.11.006
[9] Shojaei F, Behnam B. Seismic vulnerability assessment of low-rise irregular reinforced concrete structures using cumulative damage index. Adv Constr Concr. 2017;5(4):407-22.
[10] Ruiz-García J, Yaghmaei-Sabegh S, Bojórquez E. Three-dimensional response of steel moment-resisting buildings under seismic sequences. Eng Struct. 2018;175:399-414. https://doi.org/10.1016/j.engstruct.2018.08.050
[11] Dang H, Lee K, Han S, Kim S. Experimental assessment of the effects of biaxial bending moment and axial force on reinforced concrete corner columns. Struct Concr. 2018;19(4):1063-78. https://doi.org/10.1002/suco.201700211
[12] Breccolotti M, Materazzi A, Regnicoli Benitez B. Curvature ductility of biaxially loaded reinforced concrete short columns. Eng Struct. 2019;200:109669. https://doi.org/10.1016/j.engstruct.2019.109669
[13] Valenzuela-Beltrán RS, Bojórquez E, Chávez R, Bojórquez J, Llanes-Tizoc M. Ground motion selection for the evaluation of residual inter-story drifts in moment-resisting reinforced concrete frame buildings. Soil Dyn Earthq Eng. 2020;136:106217. https://doi.org/10.1016/j.soildyn.2020.106217
[14] Zhang C, Tao M-X. Strong-column-weak-beam criterion for reinforced concrete frames subjected to biaxial seismic excitation. Eng Struct. 2021;241:112481. https://doi.org/10.1016/j.engstruct.2021.112481
[15] Karki P, Oinam RM, Sahoo DR. Evaluation of seismic strengthening techniques for non-ductile soft-story RC frame. Adv Constr Concr. 2020;9(4):423-35.
[16] Esfandiari J, Zangeneh E, Esfandiar S. Experimental and numerical investigation on RC moment-resisting frames retrofitted with NSD yielding dampers. Adv Constr Concr. 2022;13(4):339-47. https://doi.org/10.1007/s40996-021-00773-x
[17] Abdelnaby A, Elnashai A. Numerical modeling and analysis of RC frames subjected to multiple earthquakes. Earthq Struct. 2015;9(5):957-81. https://doi.org/10.12989/eas.2015.9.5.957
[18] Wang J, Burton HV, Dai K. Combination rules used to account for orthogonal seismic effects: State-of-the-art review. J Struct Eng. 2019;145(11):03119001. https://doi.org/10.1061/(ASCE)ST.1943-541X.0002420
[19] CEN. EN 1998-1-1:2004, Eurocode 8: Design of structures for earthquake resistance - Part 1: General rules, seismic actions and rules for buildings. European Committee for Standardization; 2004.
[20] ASCE. ASCE/SEI 7-16: Minimum design loads and associated criteria for buildings and other structures. Reston, VA: American Society of Civil Engineers; 2017.

[21] Dabiri H, Kaviani A, Kheyroddin A. Influence of reinforcement on the performance of non-seismically detailed RC beam-column joints. J Build Eng. 2020;31:101333. https://doi.org/10.1016/j.jobe.2020.101333
[22] McKenna F, Scott M, Fenves G. Nonlinear finite-element analysis software architecture using object composition. J Comput Civ Eng. 2010;24(1):95-107. https://doi.org/10.1061/(ASCE)CP.1943-5487.0000002
[23] Nguyen QV, Fatahi B, Hokmabadi AS. The effects of foundation size on the seismic performance of buildings considering the soil-foundation-structure interaction. Struct Eng Mech. 2016;58(6):1045-75. https://doi.org/10.12989/sem.2016.58.6.1045
[24] Belkacem MA, Bechtoula H, Bourahla N, Belkacem AA. Effect of axial load and transverse reinforcements on the seismic performance of reinforced concrete columns. Front Struct Civ Eng. 2019;13(4):831-51. https://doi.org/10.1007/s11709-018-0513-3
[25] Ahmad N, Masoudi M, Salawdeh S. Cyclic response and modelling of special moment resisting beams exhibiting fixed-end rotation. Bull Earthq Eng. 2021;19:203-40. https://doi.org/10.1007/s10518-020-00987-w
[26] Ahmad N, Shahzad A, Rizwan M, Khan A, Ali S, Ashraf M, et al. Seismic Performance Assessment of Non-Compliant SMRF-Reinforced Concrete Frame: Shake-Table Test Study. J Earthq Eng. 2019;23(3):444-62. https://doi.org/10.1080/13632469.2017.1326426
[27] Chen M, Ho J. Combined strain gradient and concrete strength effects on flexural strength and ductility design of RC columns. Comput Concr. 2015;15(4):607-42. https://doi.org/10.12989/cac.2015.15.4.607
[28] Kent D, Park R. Flexural members with confined concrete. J Struct Div. 1971;97(7):1969-90. https://doi.org/10.1061/JSDEAG.0002957
[29] Park R, Priestley M, Gill W. Ductility of square-confined concrete columns. J Struct Div. 1982;108(4):929-50. https://doi.org/10.1061/JSDEAG.0005933
[30] Chen X, Bai Z, Au F. Effect of confinement on flexural ductility design of concrete beams. Comput Concr. 2017;20(2):129-43.
[31] C.S.LL.PP. Aggiornamento delle norme tecniche per le costruzioni. 2018.
[32] Papanikolaou V, Sextos A. Design charts for rectangular R/C columns under biaxial bending: A historical review toward a Eurocode-2 compliant update. Eng Struct. 2016;115:196-206. https://doi.org/10.1016/j.engstruct.2016.02.033

Research on Engineering Structures & Materials
www.jresm.org
Research Group

Technical Note

Optimal positioning and distribution of magnetorheological damper

Chandan K[1,a], Daniel C*[1,2,b], Anuroop P[2,c], S. Vivekananda Sharma[1,3,d], Arunraj E[1,e], Hemalatha G[1,f]

[1]*Department of Civil Engineering, Karunya Institute of Technology and Sciences, Coimbatore, India*
[2]*Department of Civil Engineering, Hindustan Institute of Technology and Science, Chennai, India*
[3]*Department of Civil Engineering, National Institute of Technology Meghalaya, Shillong, India*

Article Info

Article history:

Received 30 Jan 2024
Accepted 10 July 2024

Keywords:

Magnetorheological (MR) damper;
MR damper placement;
Semi-Active control;
Equation of motion

Abstract

During seismic events, devices are used to disperse energy in buildings, reducing structural damage and preventing collapse. One such device is the magnetically polarizable particle damper, consisting of a hydraulic cylinder filled with magnetically responsive particles in fluid. Recent research optimized damper placement and distribution using detailed mathematical modeling and mode shapes covering over 95% of the building's mass. Researchers identified critical damper positions by correlating these models with maximum force functions in the equations of motion. The study proposed a positioning strategy to reduce costs associated with damper installation in typical building practices. The number of dampers required varied with applied loads: 20kN, 30kN, 90kN, and up to 200kN. For instance, under 20kN and 30kN loads, optimal distribution included assigning 8 dampers to the ground, first, second floors, decreasing to 4 on floors three and four, and 2 on the fifth floor, totaling 14 and 20 dampers, respectively. Optimization values for these loads were calculated at 17.71. Dealing with a 90kN load required 44 dampers, distributed as 8 on lower levels, 4 on the third floor, and 8 each on floors four and five. Remarkably, while 20kN and 30kN damper counts reduced, 24 were added for 90kN, yielding an optimization score of 45.84. For a 200kN load, 17 dampers were strategically allocated, with specific placements adjusted per floor, achieving an efficiency score of 49.616. This underscores the effectiveness of the chosen damper arrangement in bolstering structural resilience against seismic forces.

1. Introduction

Studies pertaining to earthquakes are essential for comprehending seismic hazards, which aids in determining the possible threats to life and property. This research covers a wide range of topics, including ground motion prediction, fault line detection, and seismicity patterns. They offer insightful information on the probability and severity of earthquakes in particular areas [1]. Building designs that can survive seismic pressures and resilient infrastructure are made possible by research in earthquake engineering. This covers developments in material science, structural engineering, and retrofitting methods meant to reduce mortality and damage during seismic occurrences. Significant material losses, such as collapsing structures, occur in areas vulnerable to strong earthquakes, a problem that contemporary engineering finds difficult to address. [2-4]. This is a more comprehensive illustration of how magneto-rheological dampers are used in civil

*Corresponding author: danielckarunya@gmail.com
[a]orcid.org/0009-0001-1496-0681; [b]orcid.org/0000-0002-4024-4742; [c] orcid.org/ 0009-0002-0986-4537; [d]orcid.org/0000-0003-4923-621X; [e]orcid.org/0000-0001-7067-3786; [f] orcid.org/0000-0001-7067-3786
DOI: http://dx.doi.org/10.17515/resm2024.168ma0130tn

engineering to reduce the seismic response of buildings during earthquakes. As electromagnetically controlled shock absorbers, MR dampers enhance safety by reducing unanticipated displacements to guarantee livable circumstances. [5-8]. The development of control devices with practical applications has been the focus of major efforts throughout the past few decades. For their capacity to absorb energy and lessen structural reactions in buildings and bridges, passive devices such as base isolation, metallic yield dampers, friction dampers, visco-elastic dampers, viscous dampers, tuned mass dampers, and tuned liquid dampers have been the subject of much research. Although these devices produced good results, they showed limits when it came to changing patterns and loads. [8-12]. Variable orifice dampers, variable stiffness devices, and electro-rheological and magneto-rheological fluid dampers are examples of semi-active devices that provide more adaptability and dependability than their passive equivalents. Magneto-Rheological (MR) fluid damper as shown in Fig. 1. One proposed semi-active control device that shows promise is the magnetorheological damper. It is controlled by a magnetic field, usually produced by an electromagnet, and includes magnetorheological fluid [13–17]. With this configuration, the power of the electromagnet may be continuously adjusted to change the damping properties of the shock absorber. However, due to financial limitations, it is not feasible to place MR dampers at every joint due to their high cost, which is impacted by different fluid characteristics. Therefore, in order to achieve cost-effective distribution, it is imperative to optimize their placement throughout multiple levels. [18-20].

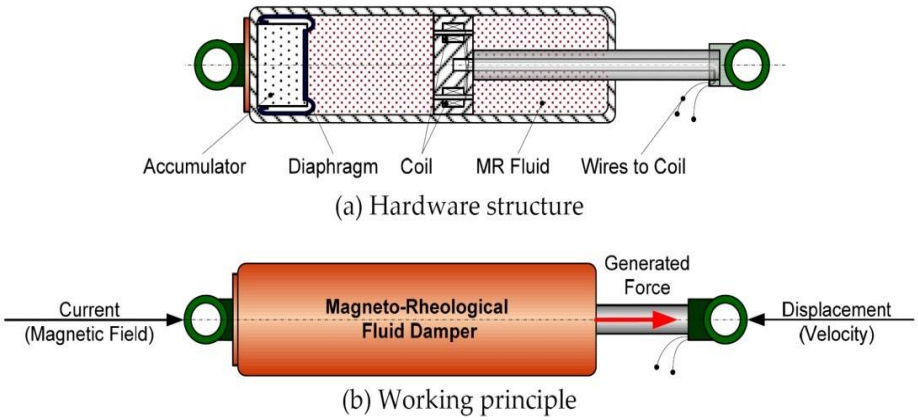

Fig. 1. Magneto rheological damper and its principle [21]

In this work, the forces acting on the joints of the structure are analyzed, and a methodical approach to positioning the MR damper for maximum damper efficiency is proposed. A magnetorheological (MR) damper's hardware normally consists of components as shown in Fig 1: The MR damper's internal components are contained and shielded by the outside shell. To endure mechanical loads, it is usually composed of steel or other robust materials. Within a cylinder that contains MR fluid is a piston assembly that moves. The piston aids in regulating the MR fluid flow via the damper. One part that keeps MR fluid in reserve under pressure is the accumulator. In the accumulator, the diaphragm divides the gas or air from the MR fluid. It guarantees that the MR fluid stays under pressure and keeps gas or air from combining with the fluid. The cylinder is surrounded by an electromagnetic coil. The coil creates a magnetic field that changes the viscosity of the MR fluid when an electric current is supplied to it. A suspension of magnetic particles with a size of microns suspended in a carrier fluid, such silicone or oil, is known as an MR fluid. The MR fluid's viscosity varies in response to a magnetic field, enabling modification of its damping properties. The electromagnetic coil is connected to a power supply and control device via

electrical connections. These cables provide the coil with the electricity it needs to create the magnetic field that regulates the MR fluid's damping characteristics. The study consists of the process that entails calculating the general equation of motion to fully represent each floor's natural displacement, and then utilizing matrix methods to validate the findings to assure correctness. The analytical approach incorporates many methodologies, such as benchmarking to IS1893:2002 criteria for base shear and load distribution, determining the point of contra flexure, and considering external force function impacts based on seismic loading. The modal mass distribution of MR dampers is established by extensive mathematical modeling and modal mass computations. This modal mass ensures effective damper use throughout the structure by acting as a criterion for load breakdown and damper distribution. Motivated by energy conservation concepts like the transmission of energy between colliding metallic balls, an algorithm is designed to strategically install dampers, mainly along extreme columns. To further inform the distribution strategy, participation variables are considered to evaluate the role that mass plays in the structure's responsiveness to external influences. Project advances show optimization under various conditions; higher efficiency is shown in situations with several damper versions. Thorough mapping and data processing offer a thorough picture of damper distribution on every floor, guaranteeing implementation feasibility and economy.

2. Methodology

The goal of this research is to fully represent the general equation of motion mathematically in order to comprehend the natural displacement of each floor. This entails employing matrix techniques to validate the correctness of the displacement, velocity, and acceleration solutions. Correlating mode shapes and examining force functions at maximum boundary circumstances are used to reduce the number of dampers. The emphasis is on utilizing MATLAB calculations, which are provided in an MS-Excel sheet, to identify crucial places for the placement of dampers and to build an optimal distribution plan across floors. The goal of MS-Excel's data analysis and charting is to make fieldwork more efficient. A benchmark building is used in the research for these inquiries is shown in Fig. 2.

3. Methods for Analysis

The displacement or frequency of seismic loads on the structure affects how far the point of contra flexure is from the highest floor. Only when ground acceleration is greater than natural frequency does structural deformation occur; the external forces that have the greatest effect are sinusoidal and are referred to as the force function [22]. The main positioning restriction is determined by using IS1893:2002 [25] to determine base shear and load distribution. This entails determining how shear is distributed throughout floors. Positioning recommendations are verified at several joints and locations with varying lateral seismic stresses. The mode forms covering more than 95% of mass are identified and examined for association with the equation of motion's maximum boundary conditions. This determines the best location for dampers across floors.

The analyzed data is shown to show the relationship between the modal mass of each floor and the capabilities of different dampers. An Excel document has a detailed record of the joint placement. The maximum modal mass and base shear are given priority in this technique, which serves as a constraint for the placement and distribution of dampers. Since a structure might have an endless number of mode forms, it is not realistic to study them all; thus, it is important to choose one by thorough mathematical modeling that encompasses over 95% of the mass. This entails using an exponential function as the force function and a sine to solve the general equation of motion.

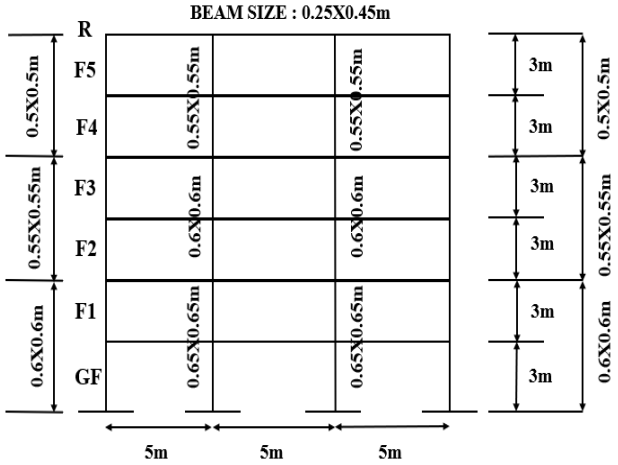

Fig. 2. Benchmark G+5 building

The specific integral and complementary function are two components of the mathematical method that equally contribute to the result. In order to properly address non-trivialities, a quadratic characteristic equation of degree 2 and order 1 is used in this specific integral.

- Case1: Applying excessive sufficiency to a linear equation of degree 1 and order 1 causes mathematical uncertainty, as the solution might not satisfy all equations on separate levels.
- Case 2: If a third-degree polynomial were taken into account, the equation would need to be solved with at least three floor loads. This would limit the equation's application to six-story buildings and render it inappropriate for structures with fewer floors, which is outside the purview of our study.

Therefore, based on the justification provided, it was determined that the second-degree equation, which has degree 1 and order 1, is more appropriate for the current situation and is used to solve the current problem. The left-hand linear differential equation can be used to obtain the expression's complementary function.

$$(m * D^2 + c * D + k) * x = 0 \tag{1}$$

must be resolved by taking into account each disparity with regard to ‘x’ as ‘D’ where ‘m' represents the mass, 'c' represents the damping coefficient, 'k' represents the stiffness, 'D' represents the differential operator, and 'x' represents the displacement and solving it for its solution i.e.

$$\frac{-b \pm \sqrt{b^2 - (4 * a * c)}}{2 * a} \tag{2}$$

after which the obtained values of D can be retraced by integrating and solve the obtained solution for 2 different constants (since the degree of the differential equation is 2).

3.1 Mode Shape

The mode shape which contains more than 95% involvement of the mass of the given structure then that mode can be used for analysis and can proceed for further mathematical modelling, and the mode is generally assumed as most probable mode. since

for a given structure there will be infinite number of modes due to non-triviality of the particular integral of the solution since all the mode shapes cannot be analyzed for it is identified as the cumbersome job, so in order to analyze all the mode shapes of the structure a mode that contains more than ninety-five percent of the mass involvement is found out and taken for obtaining the same for further proceedings

3.2 Equation of Motion

The terms involved are mass(m), damping(c), stiffness(k), displacement or lateral deflection(x), velocity ($\dot{x}$), acceleration ($\ddot{x}$), force function (f(t)), here the force function is taken as the combination of sine function followed by exponential function. Reason for sine function is among all the earthquake data available the trigonometric function involving sine or cosine was found to give the worst results for its wave form of intensified load pattern, so it's chosen for this case [23].

$$m\ddot{x} + c\dot{x} + kx = f(t) \tag{3}$$

This is general equation of motion that is used here for all the six slabs of the structure, in fact this is not an equation it's an expression because the right-hand side had the force function involved. It was generally termed to be equation since mostly in all the calculations involved only the complementary function part of the solution was considered as the complete solution. There is the case where the complete solution i.e. complementary solution as well as force function is also used as its significance is elucidated in the following subheadings.

3.3 Complementary Function

This is one part of the solution which generally contributes 50% of the solution to the given problem depending on the degree of uncertainty involved in the problem. If no ambiguity was identified for available unknowns and chosen knowns of the problem, then complementary function of the solution is assumed to be the complete solution i.e. if no trace of non-triviality. Since our case of problem involves almost a due uncertainty it is mandatory to consider the integral to sum up to the existing complementary function. Roots:

$$r_{1,2} = \frac{-c}{m} \pm \sqrt{\frac{c^2}{4m^2} - \frac{k}{m}} \tag{4}$$

General solution:

$$x = p * e^{r_1 t} + q * e^{r_2 t} \tag{5}$$

Modified solution

$$x=A*\sin(\omega t) + B*\cos(\omega t) \tag{6}$$

Since imaginary function involved in the above roots. Final complementary function (C.F):

$$x=A*\sin^{fo}(\omega t) + B*\cos^{fo}(\omega t) \tag{7}$$

complementary function gives the information on the roots obtained for given equation of motion considering only the left-hand side equating to zero to assume it for quadratic nature of the equation. since the roots are equated to the differential function (D) of the existing equation it has to be solved to obtain the 'x' value for different time periods, after which the constant must be solved for extreme boundary conditions (time taken for highest amplitude (1st amplitude generally taken) of the structure). since

$$e^{ix} = p * cos(\omega t) + i * sin(\omega t) \tag{8}$$

in the root's 'r' will be imaginary, if the equation was evaluated for zero damping, temporarily it was considered as zero (after which analyzed for 5% of damping force i.e. 0.05) in this case to avoid the uncertainty for obtaining the solution, after putting the E7 in the E5 the solution was modifies as shown in the E6. since the modified solution i.e. E6 contains a greater number of unknowns than the available knowns it triggers the uncertainty of the problem to solve.

3.4 Particular Integral

This part of the solution contributes to almost fifty percent of the complete solution which contains the solvation of the force function for differential terms in the denominator. The differential terms include the skeletal part of the left-hand side of the expression i.e. only the differential inclusion of the LHS is taken to the denominator of the integral. Since both the terms of consideration in the force function are empirical in nature i.e. ambiguous in nature it needs the solvation by differential chain rule by justifiable choosing of the first and second term. After evaluation as per the above procedure the final integral was identified as,

$$\frac{e^{-t}sin(\omega t)}{mD^2 + k} \tag{9}$$

In the above-mentioned expression D is not a variable but it is a differential form with respect to 'x', which again must be solved for different variables for different floors which has been tabulated in

3.5 Characteristic Equation

Characteristic equation is generally adopted when there is ambiguity in solvation of the linear differential equation depending on the number of unknowns and available or chosen knowns.

The choice of this characteristic equation comes to play when the uncertainty in the solvation arises, here in this case in the part of solution i.e. complementary function the equation E6 is identified as ambiguous for its mismatch of the knowns and unknowns, so

$$p * \mu^2 + q * \mu + r = 0 \tag{10}$$

This equation is found suitable for this problem and here p, q, r are the constants which are taken for calculation convenience only which don't have any practical significance. Since it was assumed of degree 2 and order 1 it needs at least 2 floor loads to obtain the solution. Which means the equation is solved initially for first 2 floor loads, after that 2nd and 3rd, after that 3rd and 4th, and so on so that the equation was validated for all the floor loads of the given benchmark building. This solvation will trigger 5% of error/ambiguity which could be neglected or ignores for its miniature measure.

3.6 Obtained Mode Shape

After a compressive evaluation and solvation of the equation of motion we arrive to an empirical value of the lateral deflection or displacement which gives the values for plotting the mode shape. This node was selected as since this mode is thought to be the most likely, it comprises almost 95% of the mass of the structure that is being analyzed.

It is not feasible to analyze all mode forms due to the non-triviality of the integral solution. Thus, the analytical process is streamlined by concentrating on the mode with

considerable mass engagement. The solution is tabulated in Table 1. The mode shape has been plotted for floor distance along y axis and the values of the empirical solution along x- axis the schematic representation is shown in Fig. 3.

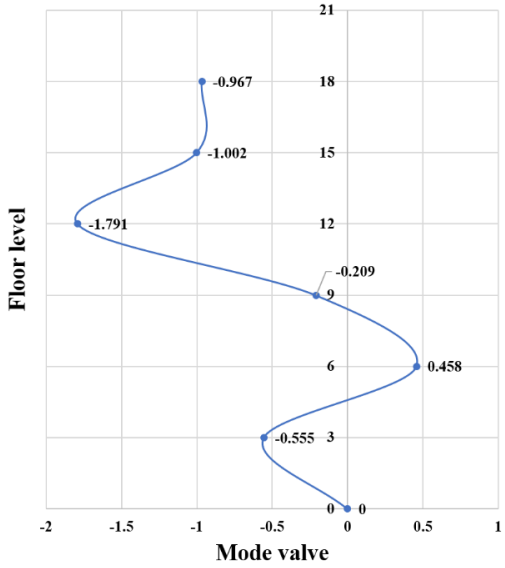

Fig. 3. Mode shape

Table 1. Solution for the displacement

Solution	
S1	S2
-0.555	0.458
-0.209	-1.791
-1.002	-0.967

3.7 Proposal for Positioning

When there are quantification constraints of the MR Damper, i.e. These are available at different capacity there might arrive a situation where the damper capacity may not arrive to meet the criteria for positioning in a structure. In such case this kind of positioning makes a crucial play and it also identified that the reduction of the displacement at substantial measures i.e. It was identified that this kind of positioning is 23% more efficient than the conventional practice of positioning. Since the final damping force was breakdown to availability of the dampers this kind of positioning found to be elemental. The following Fig. 4 represents the efficient positioning of dampers.

3.8 Constraints for Different Cases

Keeping in view the type of energy dissipation from the damper this kind of positioning was restricted for heavy heat dissipation. That is if the chances of heat dissipation were found at very heavy levels this is restricted by some other parameter like placing the different capacity dampers to ameliorate the worst possible effect of physical damage to the equipment. Despite the type of energy dissipation there is possibility of physical demolishment of the damper by itself, if the load acting on the damper exceeds its capacity, in such case a combination of dampers of different capacity must take with practical justification and ensure the avoidance of structure cracking. So, this kind of positioning

was restricted if there is unequal mitigation of energy dissipation between them, and some of the configuration flaws are also contribute for restricting this kind of positioning.

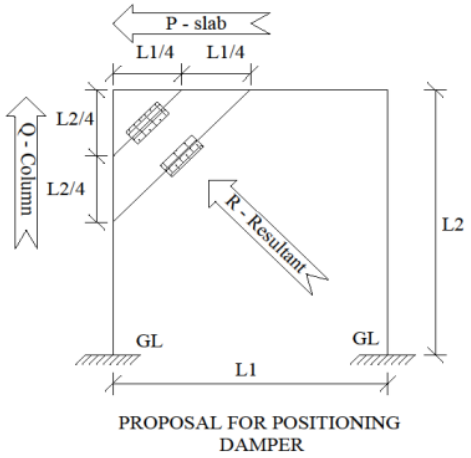

Fig. 4. Schematic representation of proposed positioning

3.9 Elements of Structure Involved

The proposed positioning involves the load acting due to the slab normal to the surface of the slab. It's not only the load due the self-weight of the beam and slab's but it includes the impulse force due to the earthquake loading (both lateral and normal to the plane of the structure) and the cumulative increase in the normal load due to variation in the beam and column size across the different locations of the structure. The contribution of the column i.e. the load acting due to the succeeding column along that joint and the upward or downward thrust due to the oscillations of the structure for different intensified earthquake loadings. Among these two the percentage share of the elements (beams & columns) mentioned changes depending on the direction of the earthquake loading, natural frequency, natural time and mode shape of the structure.

3.10 Load Contribution by the Elements (P&Q)

Let the load contributed by the slab and beams be assumed as 'P', the component P contains both static and dynamic load and combination of both as an external aggressive load (earthquake load). The static load includes the self-weight, dead load due to the existing things on that slab. The dynamic load includes the increasing the load with respect to time frame, it may be external or internal loading our case deals with the external loading i.e. earthquake loading which was assumed to have sine wave form. Due to this dynamic loading, there is chance of impulse force acting on the different slabs the ultimately damages the extreme columns of the structure depending on the oscillation of the structure. The 2nd elemental force that contributes to this kind of positioning was the thrust due to the column which is multi directional. The factors that are involved for producing the thrust include the natural frequency of the structure, time period, intensity of the external earthquake loading, column sizes at different storeys and symmetry of the structure. The thrust is produced due to lateral movement of the structure due to the external aggressive force impacting on the structure.

3.11 Resultant Force Vector and Its Validation

The force due to slab and beams will contribute to the P force acting is impulsive in nature when external aggressive force act on the structure, there will be no issue when there is no

external force acting on the structure. When there is coincidence of these two elemental forces the worst effect on the extreme columns were felt and observed as well. This could become the criteria for positioning to take the load due to its elemental force contribution. Since the direction and magnitudes of the two forces was identified to be measurable the vector notation was assumed to ease the calculations. So resultant vector was formed which is a virtual force vector that is obtained by calculating through vector algebra which can be given as 'R'.

$$R = \sqrt{P^2 + Q^2 + 2 * P * Q * cos\theta} \tag{11}$$

The resultant vector has nothing to contribute in practicality but it is used only for calculation purposes, if the external aggressive force acting on the structure in the direction of the resultant force the load can be spitted for P & Q by maintaining the proportionality for beams and columns.

3.12 Validation

This kind of positioning is not required at all the joints of the structure, its only required where the load acting at joint does not match with the capacity of the damper. So due to the mismatch of the load and capacity of the damper the load has been breakdown to the availability of the dampers, and they are placed keeping in mind the restrictions. This is also used where the worst point of affect was found, it was generally identified where the coincidence of the sine wave form and the exponential function occurs. As per the obtained mode shape the points are located depending on the empirical values achieved as a measure of the intensity of the force function. So, if the damper was placed/positioned, the loads taken by the pistons on both sides can be analyzed easily and the capacity of the damper required at that point is estimated as well

3.13 Exceptional Case and Practical Convenience

Since assumed earthquake have harmonic profile of motion there might be a case where the direction P & Q are in the opposite direction at the resultant can be obtained by taking the divergence of the force vector with respect to that point. Practical convenience: This not only reduces the displacements by substantial measure but also creates the spatial environment and aesthetic visual ambience when compared to the conventional practice of positioning.

4. Distribution of MR Dampers

4.1 Modal Mass and Its Significance for This Case

The mode shape which is obtained by this comprehensive mathematical modelling and its modal mass was evaluated by the formula.

$$[M]_k = \frac{[\sum(w_i * \varphi_{ik})]^2}{g * \sum(w_i * \varphi_{ik}{}^2)} \tag{13}$$

The mass for each slab was found out and compared with the normal mass by inclusion of the participation factor to it, which eventually results in an average of 96.42% mass involvement which conveys that our mode shape calculated was as per the objective mentioned. This modal mass is used as a criterion for distribution of the dampers along each floor and it also used as the criteria for load break down to allot the dampers of different damping capacity.

4.2 Development of a Simple Algorithm

The distribution of dampers across each joint is found uneconomical and through this algorithm no dampers are placed at the middle columns, only extreme columns are targeted through this algorithm. This algorithm finds its root from the concept of collisions (both elastic & inelastic). Assume a series of metallic balls when a single metallic ball is strike along the line of series of balls the force with which the 1st ball hits will be divides into number of balls taken into consideration. Immediately after hitting the 1st ball the energy will be conserved i.e. law of conservation of mass as well as law of conservation of energy was satisfied as of this case. So the as mentioned in the point 'c' the energy was transferred to the corresponding ball by the above laws by maintaining the proportionality with respect to the applied force on the initial ball. In this case of distribution of dampers, it was used to place all the dampers only along the extremely located columns at each and every floor on different constraints the last but one series of the extremity was used at certain cases only. Here the force is the external aggressive force i.e. earthquake loading, and the conservation of energy takes place between the columns with beams as median between them and the laws are sufficiently satisfied.

4.3 Participation Factor and Its Significance

For real systems there is often mass participating in the forcing function (such as the mass of ground in an earthquake) and mass participating in inertia effects (the mass of the structure itself, Meq). The modal participation factor is a comparison of these two masses. In this case the modal participation factor is given by p_k

$$p_k = \frac{[\sum w_i * \varphi_{ik}]^2}{\sum w_i * \varphi_{ik}{}^2} \tag{14}$$

In the above formula W with its suffix, I is generally taken as load due to each floor and'φ_ik' is the term stating the empirical solution of the mode shape.

4.4 Comprehensive Charting and Detailing

The technique was then used to transfer the load to the column endpoints after determining the modal mass for different slab loadings. The 90kN, 30kN, and 20kN-rated damper holes on each column at the extremities corresponded to the modal mass breakdown for the available capacities. Charts were used to record the distribution of loads among the various types of dampers according to their capabilities.

4.5 Project Developments

- Case 1: An optimization of 17.71% is obtained by using only 20kN and 30kN dampers. Base shear and seismic response estimates for the six-story benchmark structure are the parameters taken into consideration.
- Case 2: An optimization of 45.84% was obtained by doing a breakdown for three damper variants: 90kN, 30kN, and 20kN. Here, the six-story, three-bay benchmark building's modal mass and seismic response are among the variables that were taken into consideration.

- Case 3: By using 200kN dampers alone for analysis, efficiency was raised by almost 4%, yielding an optimization value of 49.66%. Similarly, a cost decrease of around 82.86% was calculated, contingent on damper costs.

4.6 Finalized Distribution

Following the determination of the load distribution breakdown to the structure's extreme columns, charts were created for each floor and joint in both the XZ and YZ directions. Because the benchmark building is symmetrical in both directions, it was sufficient to track one route and replicate the other. These charts, which are numbered 1 through 13, list the different types and quantities of dampers utilized each level. To make purchasing and actual use easier, the number of each damper variety was also tallied. Lastly, the percentage of cost reduction was mentioned, which was in line with the main goal of the project.

4.7 Detailing Along Each Floor Was Tabulated in XZ & YZ Directions

A thorough schematic showing the distribution and placement of dampers on each level, together with their precise locations, is given in Charts Nos. 1 through 10. The YZ direction needs the same number of dampers as the XZ direction because of the structural symmetry that has been noticed. The positioning need, where each chart shows whether the suggested damper placement is customary (No. 1) or essential (No. 2) at different places inside the structure, depends on this alignment.

5. Result and Discussion

Table 2 shows the details of the G+6 Benchmark building. Fundamental natural time period (Ta), zone factor (Z), importance factor (I), response reduction factor (R), Sa/g, horizontal seismic coefficient (Ah) is obtained from IS 1893 part 1 2016. Calculation of Base Shear and Load Distribution along each floor is shown in Table 3. The Table 3 gives details regarding each storey's net load, height, and seismic weight inside the structure. The seismic weight multiplied by the height is computed. The base shear and load distribution of the structure may be ascertained using the seismic weight and height of each story.

Table 2. Details of the G+6 Benchmark building

Height Of Structure (h)	18
Base Dimension (d)	5
Fundamental Natural Time Period (Ta)	0.724
Zone Factor (Z)	0.16
Importance Factor (I)	1.5
Response Reduction Factor (R)	3
Sa/g	1.879
Horizontal Seismic Coefficient (Ah)	0.075
Total Seismic Weight 'W'(KN)	31218
Design Base Shear (Vb)	2341.35
Height Of Gf In (m)	3
Sum (W*H)	190419.75

The mode comprising more than 95% of the mass may be found by analyzing the mode forms of the structure using the net load of each storey. Determining the worst point of effect of the load impulse and improving damper location depend heavily on the mode shape involving more than 95% of the mass. Fig.5 shows an illustration of the load distribution laterally over a structure is provided by a lateral load distribution curve. The force or pressure applied to the structure in a horizontal direction, as during an earthquake, is referred to in this context as the lateral load.

The distribution of the load at the building's various levels or floors is shown by the curve. It aids in comprehending the variance in load distribution and may be applied to ascertain

the best location and arrangement of dampers to regulate the building's seismic reaction. Researchers can install dampers where greater control is needed and reduce the number of dampers in regions with lesser load distribution by evaluating the curve to determine which floors or levels have concentrated and distributed loads.

Through an evaluation of the efficiency score derived from the optimization process, the curve can also shed light on the efficacy of the chosen damper configuration. The shear distribution details, and stiffness calculation is shown in Fig. 6 and Table 4. The distribution of forces acting perpendicular to the floor planes is known as the shear distribution. Understanding the building's response to seismic forces and how those forces are dispersed throughout the structure requires knowledge of this information. The best location and arrangement of magnetic resonance dampers (MR dampers), which are control devices used to lessen vibration and absorb energy during an earthquake, may be determined with the aid of the shear distribution. Researchers can determine which floors or parts of the structure encounter higher shear forces and may need more dampers for successful control by examining the shear distribution. Together with further computations and studies, the shear distribution information shown in Fig. 6 may be utilized to establish the best location and quantity of dampers for regulating the building's seismic reaction. In Table 4 varying columns have varying stiffness values; higher values indicate more resistance to deformation. The width and depth of the columns have an impact on how rigid they are as well. The total stiffness of the interior and exterior columns is considered in the net stiffness. All things considered, the chart offers details regarding the stiffness and sizes of various columns, which may be helpful in comprehending the building's structural characteristics. The seismic weight of building is calculated by adding full amount of dead load and imposed load of 25% as per IS 1893 (part 1): 2016. While computing the seismic weight of each floor, the weight of columns and walls in any storey shall be equally distributed to the floors above and below the storey. The net load on each floor is calculated by the difference between lateral shear force (Q) and the loads on the prior floor. The lateral shear force (Q) at each floor is calculated by an equation as per IS 1893 (part 1): 2016

$$Q_i = v_B \frac{w_i h_i^2}{\sum w_j h_j^2} \tag{15}$$

Table 3. Design calculation excel for G+6 Benchmark building

Seismic Weight (W) In kN		Height Of Storeys (H) In m		W*H (kNm)	Q (Kn)	Net Load (kN)
GF	7348.5	GF	0	0	0	2341.352
F1	6972	H1	3	20916	257.178	2341.352
F2	5751.75	H2	6	34510.5	424.332	2084.174
F3	4247.25	H3	9	38225.25	470.008	1659.842
F4	3417.75	H4	12	41013	504.285	1189.834
F5	2299.5	H5	15	34492.5	424.111	685.549
R	1181.25	H6	18	21262.5	261.438	261.438

Table 4. Stiffness calculations

Floors	Ext Column Dimension		Int Column Dimension		Moment Of Inertia		Stiffness		
	Breadth (m)	Depth (m)	Breadth (m)	Depth (m)	Ext I (N/m)	Int I (N/m)	Ext K (N/m)	Int K (N/m)	Net K (N/m)
F1	0.6	0.6	0.65	0.65	0.011	0.015	122.223	166.667	2311.112

F2	0.6	0.6	0.65	0.65	0.011	0.015	15.27778	20.8334	288.8895
F3	0.55	0.55	0.6	0.6	0.008	0.011	3.29219	4.5268	62.552
F4	0.55	0.55	0.6	0.6	0.008	0.011	1.38889	1.9098	26.3896
F5	0.5	0.5	0.55	0.55	0.006	0.008	0.53334	0.7112	9.9564
R	0.5	0.5	0.55	0.55	0.006	0.008	0.30865	0.4116	5.762

Table 5. Characteristics

Young's modulus	25000
Total number of external columns	8
Total number of internal columns	8
Characteristic compressive strength	25

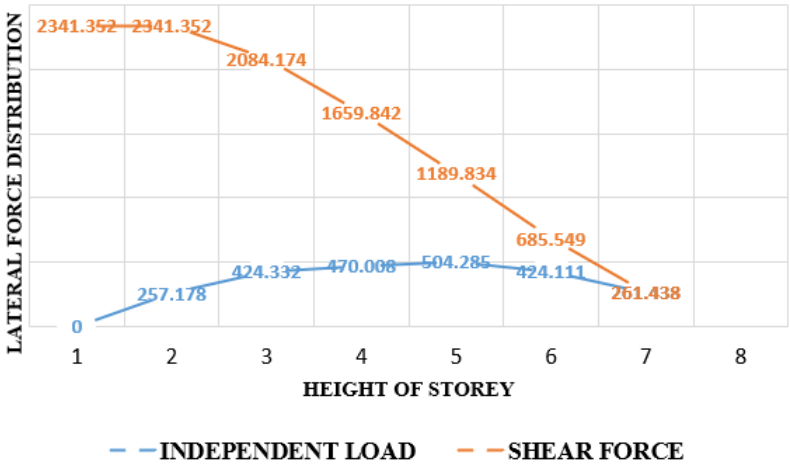

Fig 5. Lateral load distribution curve

General equation of motion:

$$m * xm * \ddot{x} + c * \dot{x} + k * x = e^{-t} * \tag{16}$$

Formula Used:

$$K = \frac{12*E*I}{l^3} \quad k_{NET} = \sum_{i=1}^{16} K_i \tag{17}$$

Complementary function:

$$r_{1,2} = \frac{-c}{m} \pm \sqrt{\frac{c^2}{4 \times m^2} - \frac{k}{m}} \tag{18}$$

$$x = p \times e^{r_1 t} + q \times e^{r_2 t} \tag{19}$$

Integral:

$$\frac{e^{-t} \times \sin(\omega t)}{m \times D^2 + k} \tag{20}$$

Modified complimentary function

Solution for this case of problem

$$x = A \times \sin(\omega t) + B \times \cos(\omega t) \tag{21}$$

5.1 Result of Case 1: When 20kN,30kN Load Damper Is Used

Table 6 lists how many dampers are needed at each floor for the specified loads of 20 and 30 kN. There are eight dampers needed for each of the first, second, and ground floors. Each of the third and fourth levels needs four dampers. Two dampers are needed for the fifth story. Based on Table 7 a 20 kN load is applied to a total of 14 dampers.

Table 6. The required quantity of dampers for each floor

Required Number of Dampers	
GROUND FLOOR	8
FLOOR 1	8
FLOOR 2	8
FLOOR 3	4
FLOOR 4	4
FLOOR 5	2
TOTAL	34

A load of 30kN is applied to a total of 20 dampers. Using a total of 14 dampers allows for the best possible damper location and distribution for the specified load of 20 kN and 30 kN. This distribution lessens structural damage during an earthquake and helps regulate the building's seismic reaction. The distribution places the greatest number of dampers on the ground level, first floor, and second floor, and the lowest number on the fifth story.

Table 7. Total number of 20 & 30kN dampers

Distribution Of Dampers at Different Floors		
FLOORS	20 kN	30 kN
GF	0	8
F1	0	8
F2	4	4
F3	0	4
F4	4	0
F5	2	0
TOTAL	10	24

5.2 Result of Case 2: When 20 kN, 30 kN and 90 kN Load Damper Is Used

The load capacity affects how dampers are distributed. The number of dampers needed for the first, second, and ground floors is the same for all load capacities. Compared to the other levels, the third floor needs less dampers to support the 30kN load. For all load capacities, the same number of dampers are needed on the fourth and fifth floors. Regardless of the load capacity, the building has a total of 44 dampers.

Table 8. The required quantity of dampers for each floor

Required Number of Dampers	
GROUND FLOOR	8
FLOOR 1	8
FLOOR 2	8
FLOOR 3	4
FLOOR 4	8
FLOOR 5	8
TOTAL	44

Table 9. Total quantity of 20 kN, 30 kN & 90 kN dampers @ different floors

Distribution of Dampers at Different Floors			
	90 kN	20 kN	30 kN
GF	8	0	0
F1	8	0	0
F2	4	4	0
F3	4	0	0
F4	0	0	8
F5	0	8	0
TOTAL	24	12	8

5.3 Result of Case 3: When Using A 200kN Load Damper

The number of dampers required at each floor for the 200 kN prescribed loads is listed in Table 10. Eight dampers are required for the ground levels, four dampers are required for the first floor, and no dampers are required for the second story. Two dampers are required for each of the third and fourth tiers. It takes one damper to cover the fifth storey. There is a total of 17, 200 kN dampers dispersed over many floors.

Table 10. Required number of dampers at different floors

Required Number of Dampers	
GROUND FLOOR	8
FLOOR 1	4
FLOOR 2	0
FLOOR 3	2
FLOOR 4	2
FLOOR 5	1
TOTAL	17

5.4 Non-linear Time History Analysis

The most accurate method for representing the behavior of a structure under seismic stresses is thought to be nonlinear time history analysis. In order to account for the nonlinear properties of the support system, this technique entails methodically integrating the equations of motion of the system. It calculates the displacements, peak accelerations, and forces of the system for each time step and determines their maximum values during seismic occurrences. To accomplish accurate earthquake effect simulations, SAP2000 V19 software was used to perform nonlinear time history analysis on the building models.

Three grid lines each in the x and z directions and six grid lines in the y direction make up the grid system used in SAP2000's structural design. These grid lines are spaced five meters apart in the x and z directions and three meters apart in the y direction. The material parameters are defined in accordance with Indian norms; 25 kN/m^3 of density, 20,000 MPa of modulus of elasticity (E), 0.2 Poisson's ratio, 1E-05 (1/°C) coefficient of thermal expansion (α), and 25 MPa of compressive strength were chosen for the concrete. For reinforcing bars, the minimum yield strength (Fy) is 420 MPa, the minimum tensile strength (Fu) is 550 MPa, the predicted yield stress (Fyc) is 420 MPa, and the Young's modulus (E) is 200,000 MPa. The coefficient of thermal expansion (α) is 1.2E-05 (1/°C). 16d longitudinal bar sizes and 8d confinement bar sizes are used to define columns and beams. In accordance, section attributes are assigned, and 0.18 meters is the membrane and bending thickness. Diaphragm limitations are applied and joint constraints are fixed. Using El Centro earthquake data for the load case type and scaling by 9.81E-3, a time history function is created. Dead loads are defined as mass sources, and the output time step size is fixed at 0.005 seconds. Two-way distribution of uniform area loads of 10 kN/m^2 is applied to the frames. Frames are allocated element loads, and load cases are prepared for evaluation. The inter-story drift during the El Centro earthquake was found to exceed the allowable limit in all structures, according to the study results. The permissible maximum for inter-story drift is 0.004 times the storey height, under IS 1893 part 1 (2002). The maximum permissible inter-story drift value for a structure with a storey height of eighteen meters is determined by this:

$$\Delta = 0.004 \times h = 0.004 \times 3 = 0.012m \tag{22}$$

The results of the investigation show that during the El Centro earthquake, the inter-story drift in every building surpassed the allowable limit. The maximum permitted inter-story drift, under IS 1893 part 1 (2002), is 0.004 times the height of each storey. This rule establishes the maximum amount of inter-story drift for a structure with eighteen-meter-tall storeys.

6. Conclusion

By using this mathematical modeling, the complementary function and particular integral's complexity were addressed, leading to a solution with over 90% confidence. Accuracy and project scope may be varied for higher storeys, improving damper distribution efficiency, by varying the degree and order of the characteristic equation. By reducing displacements substantially (23% more effectively than standard approaches), the suggested positioning strategy improved space usage and attractiveness. Moreover, this decreased deflection, especially for P and Q intensities, demonstrating the efficacy of the dampers. As to IS 1893 (part 1) 2002, the maximum allowable inter-storey drift is 0.012 meters, or 0.004 times the storey height. To make sure drift stayed within this bound, dampers were positioned strategically. The worst-case impact analysis (mode shape and force function correlation) was used to determine the ideal damper placements and amounts. To handle the stress on extreme columns, only 20kN (14#) and 30kN (20#) dampers were utilized, depending on availability. To limit seismic response, the study proposes a methodical approach for determining the best location and distribution of magnetorheological (MR) dampers in a benchmark 6-story structure. To identify the worst location for damper positioning, the authors provide a mathematical modelling technique that makes use of the maximal force function and mode shape. This method aids in lowering the price of damper allocation in construction projects. The optimum damper distribution for several load scenarios, including 20kN, 30kN, 90kN, and 200kN, is provided in this study. There are 17 dampers utilized overall for a 200kN load, with the distribution differing throughout floors. An efficiency score of 49.616 from the

optimization process illustrates how effective the chosen damper configuration is. The practicality of the suggested damper placement—which, in contrast to traditional methods, not only minimizes displacements but also produces an aesthetically pleasing spatial environment—is also covered in the study. The precise standards or selection process for the benchmark building, as well as the seismic reaction factors taken into consideration for optimization, are not covered in this work. The financial ramifications of the damper placement and distribution are not thoroughly examined in the article. The cost reduction based on the optimization outcomes is only mentioned in general terms. The suggested damper location may not work in real-world situations due to practical restrictions, installation requirements, or possible conflicts with other building systems. These issues are not covered in the article. Future research in seismic response control may find great use for the methodical approach to damper installation and distribution that is presented in this study. Future studies can build on and enhance the mathematical modelling technique employed in this study, which involves mode shape and maximal force function, to increase the precision and effectiveness of damper optimization. Future research on comparable benchmark buildings or structures might utilize the optimal damper distribution results from this study as a guide since they offer information on the quantity and positioning of dampers needed for efficient seismic response management.

References

[1] Stein RS. The role of stress transfer in earthquake occurrence. Nature. 1999;402(6762):605-609. https://doi.org/10.1038/45144

[2] De Silva CW. An algorithm for the optimal design of passive vibration controllers for flexible systems. J Sound Vib. 1981;75(4):495-502. https://doi.org/10.1016/0022-460X(81)90437-5

[3] Ibidapo-Obe O. Optimal actuators placements for the active control of flexible structures. J Math Anal Appl. 1985;105(1):12-25. https://doi.org/10.1016/0022-247X(85)90094-0

[4] Zhang RH, Soong TT. Seismic design of viscoelastic dampers for structural applications. J Struct Eng. 1992;118(5):1375-1392. https://doi.org/10.1061/(ASCE)0733-9445(1992)118:5(1375)

[5] Milman MH, Chu CC. Optimization methods for passive damper placement and tuning. J Guid Control Dyn. 1994;17(4):848-856. https://doi.org/10.2514/3.21275

[6] Peng Y, Zhang Z. Optimal MR Damper-Based Semiactive Control Scheme for Strengthening Seismic Capacity and Structural Reliability. J Eng Mech. 2020;146(6). https://doi.org/10.1061/(ASCE)EM.1943-7889.0001768

[7] Elias S, Matsagar V. Seismic response control of steel benchmark building with a tuned mass damper. Asian J Civ Eng. 2020;21(2):267-280. https://doi.org/10.1007/s42107-019-00206-1

[8] Takewaki I, Uetani K. Optimal damper placement for building structures including surface ground amplification. Soil Dyn Earthq Eng. 1999;18(5):363-371. https://doi.org/10.1016/S0267-7261(99)00007-X

[9] Shukla AK, Datta TK. Optimal use of viscoelastic dampers in building frames for seismic force. J Struct Eng. 1999;125(4):401-409. https://doi.org/10.1061/(ASCE)0733-9445(1999)125:4(401)

[10] Singh MP, Moreschi LM. Optimal placement of dampers for passive response control. Earthq Eng Struct Dyn. 2002;31(4):955-976. https://doi.org/10.1002/eqe.132

[11] Lopez Garcia D, Soong TT. Efficiency of a simple approach to damper allocation in MDOF structures. J Struct Control. 2002;9(1):19-30. https://doi.org/10.1002/stc.3

[12] Villarreal K, Wilson C, Abdullah M. Effects of MR damper placement on structure vibration parameters. In: Proceedings of the 2004 Earthquake Engineering Symposium for Young Researchers. 2004 July. 279;5-8.

[13] Bharti SD, Dumne SM, Shrimali MK. Seismic response analysis of adjacent buildings connected with MR dampers. Eng Struct. 2010;32(8):2122-2133. https://doi.org/10.1016/j.engstruct.2010.03.015
[14] Cha YJ, Agrawal AK, Phillips BM, Spencer Jr BF. Direct performance-based design with 200 kN MR dampers using multi-objective cost effective optimization for steel MRFs. Eng Struct. 2014;71:60-72. https://doi.org/10.1016/j.engstruct.2014.04.023
[15] Uz ME, Hadi MN. Optimal design of semi-active control for adjacent buildings connected by MR damper based on integrated fuzzy logic and multi-objective genetic algorithm. Eng Struct. 2014;69:135-148. https://doi.org/10.1016/j.engstruct.2014.03.006
[16] Cetin S, Zergeroglu E, Sivrioglu S, Yuksek I. A new semiactive nonlinear adaptive controller for structures using MR damper: design and experimental validation. Nonlinear Dyn. 2011;66(4):731-743. https://doi.org/10.1007/s11071-011-9946-0
[17] Wang H, Li A, Jiao C, Spencer BF. Damper placement for seismic control of super-long-span suspension bridges based on the first-order optimization method. Sci China Technol Sci. 2010;53(7):2008-2014. https://doi.org/10.1007/s11431-010-4009-1
[18] Kori JG, Jangid RS. Semi-active MR dampers for seismic control of structures. Bull N Z Soc Earthq Eng. 2009;42(3):157-166. https://doi.org/10.5459/bnzsee.42.3.157-166
[19] Cha YJ, Agrawal AK, Friedman A, Phillips B, Ahn R, Dong B, Dyke SJ, Spencer BF, Ricles J, Christenson R. Performance validations of semiactive controllers on large-scale moment-resisting frame equipped with 200-kN MR damper using real-time hybrid simulations. J Struct Eng. 2014;140(10). https://doi.org/10.1061/(ASCE)ST.1943-541X.0000982
[20] Aydin E. Optimal damper placement based on base moment in steel building frames. J Constr Steel Res. 2012;79:216-225. https://doi.org/10.1016/j.jcsr.2012.07.011
[21] Soto MG, Adeli H. Placement of Control Devices for Passive, Semi-Active, and Active Vibration Control of Structures. Scientia Iranica. 2013;20(6):1567-1578.
[22] Truong DQ, Ahn KK. MR fluid damper and its application to force sensorless damping control system. In: Smart Actuation and Sensing Systems-Recent Advances and Future Challenges. 2012;83-425.
[23] Cruze D, Hemalatha G, Jebadurai SVS, Sarala L, Tensing D, Christy SJE. A review on the magnetorheological fluid, damper and its applications for seismic mitigation. Civil Eng J. 2018;4(12):3058-3074. https://doi.org/10.28991/cej-03091220
[24] Daniel C, Hemalatha G, Sarala L, Tensing D, Sundar Manoharan S. Magnetorheological Fluid with Nano Fe3O4 for Performance Enhancement of MR Damper for Seismic Resistance of Steel Structures. In: Key Eng Mater. 2018;763:975-982. https://doi.org/10.4028/www.scientific.net/KEM.763.975
[25] IS 1893 : 1962. Recommendations for earthquake resistant design of structures.

Research on Engineering Structures & Materials
www.jresm.org
Research Group

Research Article

Study the effects of TiB_2 reinforcement on the AA-2014 matrix fabricated by friction stir processing

Jitendra Kumar[a], Vipin Kumar Sharma*[,b], Ajay Partap Singh[c]

Department of Mechanical Engineering, IIMT University, Meerut, India

Article Info

Article history:

Received 09 Mar 2024
Accepted 11 July 2024

Keywords:

Friction stir processing;
TIB_2;
Aluminum alloy;
Hardness;
Ultimate tensile strength;
Microstructure analysis

Abstract

This study explores the impact of TiB_2 nanoparticles on the microstructure, microhardness, and tensile properties of AA-2014 surface composite manufactured through Friction Stir Processing (FSP). A series of experiments were conducted with varying FSP parameters, and the findings were compared with the base metal. Microstructure studies revealed optimal bonding between TiB_2 and the AA-2014 substrate at 1200 rpm, surpassing results from 900 and 1600 rpm. However, microstructural analysis unveiled agglomeration of particles and void formation on the composite surface. Microhardness values indicated a substantial increase from 88 HV (AA-2014) to 138 HV (AA-2014/3%TiB_2 @1200rpm), attributed to the presence of TiB_2 nanoparticles and FSP-induced modifications. Ultimate Tensile Strength (UTS) values exhibited a noteworthy improvement from 290 MPa (AA-2014) to 465 MPa (AA-2014/3%TiB_2 @1200rpm), emphasizing the positive influence of uniform TiB_2 dispersion achieved during FSP. The study underscores the effectiveness of TiB_2 reinforcement and FSP in enhancing the mechanical properties of AA-2014 surface composite, despite observed microstructural features.

1. Introduction

Aluminum alloys have emerged as a superior choice over steel in various industries due to their remarkable strength-to-weight ratio [1]. This characteristic makes aluminum alloys particularly desirable in the aircraft and automotive sectors [2]. In aircraft construction, the utilization of high-strength structural components is essential for ensuring both performance and safety [3]. The 2000 series of aluminum alloys, in particular, has found extensive use in this domain [4]. One of the primary advantages of aluminum alloys, especially those in the 2000 series, is their ability to reduce weight without compromising strength. This weight reduction has a significant impact on fuel efficiency in aircraft, ultimately leading to increased payload capacity [5]. The 2xxx series alloys, such as AA 2014, have become integral in the aerospace industry for achieving these goals [6]. The ongoing trend in favor of aluminum can be attributed to its diverse set of qualities. Not only does it exhibit impressive strength, but it also possesses corrosion resistance, a crucial factor in ensuring the longevity and durability of aircraft [7]. The reduced maintenance and repair costs associated with corrosion-resistant materials further contribute to the economic viability of aluminum alloys in aviation. The various applications of aluminum extend beyond its use in aircraft. The material's reflective, electrically conductive, non-magnetic, non-sparking, and non-combustible properties make it suitable for a wide range of purposes [8]. These characteristics have led to its incorporation in the construction of structural beams, which are vital for the overall integrity of various engineering structures [9]. A notable example of aluminum's versatility is evident in the construction of fuel tanks

*Corresponding author: vipinkumarsharma_me@iimtindia.net
[a] orcid.org/0009-0000-0325-1049, [b]orcid.org/0000-0001-5464-8644; [c] orcid.org/0000-0002-7234-4043
DOI: http://dx.doi.org/10.17515/resm2024.212ma0309rs

and booster rockets for both aircraft and space shuttles [10]. The demand for lightweight yet durable materials in these critical components aligns perfectly with the properties offered by aluminum alloys [11]. The lightweight materials not only aid in the efficiency of vehicles but also elevate their general performance and dependability. In the realm of ground transportation, aluminum alloys play a crucial role in the construction of vehicles such as dump trucks, tank trucks, and trailer trucks [12]. The need for robust materials that can withstand the rigors of transportation and hauling is met by aluminum alloys. This usage extends to various industries where the reliability and durability of vehicles are paramount. Within the spectrum of aluminum alloys, the AA 2014 alloy stands out, particularly for its mechanical properties. This alloy is partially composed of copper as its major alloying ingredient, contributing to its strength and other desirable characteristics. In the context of construction, especially in aerospace applications, AA 2014 has become the preferred choice due to its well-balanced properties [13]. Taking the exploration of aluminum alloys further, a recent study involved the use of AA-2014 alloy as a matrix material, reinforced with TiB_2 particles through friction stir processing. This innovative approach aims to enhance the material's mechanical properties and performance in specific applications. The incorporation of reinforcing particles, such as TiB_2, opens up new possibilities for tailoring the properties of aluminum alloys to meet the evolving demands of various industries. In conclusion, the widespread adoption of aluminum alloys, particularly in the 2xxx series, signifies a paradigm shift in material choices for industries where strength, weight, and durability are critical factors [14]. The continuous upward trend in aluminum utilization is justified by its unique combination of properties, including corrosion resistance, non-toxicity, heat conduction, and recyclability [15]. As technology advances, the incorporation of reinforcing particles in aluminum alloys, as demonstrated in the AA-2014 alloy study, showcases the commitment to pushing the boundaries of material science for improved performance and efficiency in construction applications [16]. Whether soaring through the skies or navigating the highways, aluminum alloys have firmly established themselves as indispensable materials in modern engineering and construction [17].

The objective of the study was to investigate the effects of incorporating TiB_2 nanoparticles into AA-2014 aluminum alloy through friction stir processing (FSP) on the bonding quality, microhardness, and ultimate tensile strength (UTS) of the resulting surface composite. The study aimed to assess the optimal processing parameters for achieving good bonding between TiB_2 and the AA-2014 substrate, as well as to analyze the influence of TiB_2 reinforcement on the mechanical properties of the composite material.

2. Materials and Method

2.1. Materials

The choice of aluminum alloys AA-2014 and TiB_2 reinforcement for friction stir processing is driven by their exceptional versatility, making them highly suitable for a diverse range of industries. These alloys have applications in aerospace, automotive, construction, and various other sectors due to their unique combination of properties. The decision to employ friction stir processing reflects the ongoing effort to enhance the mechanical properties of these materials for specific applications. To gain insight into the composition of the chosen alloys, spectrometric analytical equipment was employed.

Table 1. Chemical composition of the AA-2014

Elements	Al	Si	Ti	Cr	Mn	Fe	Cu	Zn	Mg
Wt.%	86.0	0.75	0.23	0.05	0.82	0.30	4.18	0.83	0.83

The resulting chemical composition values are presented in Tables 1 and 2 for AA-2014 and TiB_2 reinforcement, respectively. These nominal values provide a comprehensive understanding of the elemental makeup of each material, laying the foundation for further discussions on their properties and potential applications.

Table 2. Chemical Composition of TiB_2

Reinforcement TiB_2	Ti	B
Composition	39.78	60.22

2.2. FSP Processing

Friction Stir Processing (FSP) is a specialized technique used to modify the microstructure and properties of metals, particularly aluminum alloys like AA2014 T6. It involves several distinct steps, each carefully orchestrated to achieve desired material properties and structure [18]. The step by step for FSP process is mentioned below:

- Step 1: The process begins with the spindle strategically positioned at the center of the machine. The spindle is then set to rotate at a specific speed, measured in revolutions per minute (rpm). This rotation of the spindle is a crucial initial step in preparing for the subsequent stages of FSP.

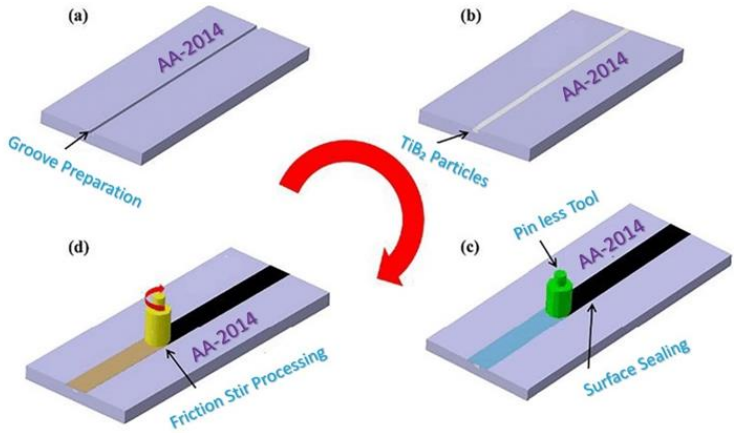

Fig. 1.FSP representation in graphical form

- Step 2: Simultaneously, the machine table undergoes a progressive vertical elevation. This upward movement continues until the tool insert penetrates the surfaces of the aluminum alloy plates by a precise depth, typically around 0.1 mm. This controlled penetration depth is critical as it sets the stage for the material interaction and stirring process [19].

- Step 3: Once the penetration depth is achieved, the spindle remains stationary, spinning in place for a specified duration, typically around 30 seconds. This dwell time serves the purpose of warming the plates in preparation for the welding process. Controlled heating at this stage optimizes the material for subsequent stirring and processing steps [20].
- Step 4: The core of the FSP process lies in the plate mixing procedure, which occurs during this stage. The machine table advances at a defined linear speed, measured in millimeters per minute (mm/min). This movement induces the welding process,

where the rotating tool stirs and mixes the material within its vicinity. The stirring action is crucial for achieving a homogeneous structure and desirable material properties [21].

- Step 5: The combination of the rotational motion of the spindle and the linear movement of the machine table results in a dynamic stirring effect. This intricate process is precisely controlled to ensure uniformity and consistency in the stirred material. The stirring action facilitates the redistribution of alloying elements and the refinement of grain structure, leading to improved mechanical properties [22].
- Step 6: As the machine table progresses and the stirring reaches the specified length of the weld, the retracting step commences. At this point, the forward movement of the tool halts, and it is systematically removed from the sample. This controlled retraction leaves a characteristic hole at the end of the weld. The retracting step is critical as it finalizes the stirring action and shapes the processed material [23].
- Step 7: The hole left at the end of the weld is a consequence of the tool's retraction and serves as a visual marker of the processed region. It provides a clear indication of the extent and location of the FSP treatment [24].
- The FSP process involves a sequence of precisely controlled steps aimed at modifying the microstructure and properties of aluminum alloys through mechanical mixing and stirring. Each step plays a crucial role in achieving the desired material properties and structural characteristics. Table 3 shows the sample nomenclature, processing parameters, and compositions of each specimen.

Table 3. Processing parameters of FSP

Samples Nomenclature	Rotation rate (RPM)	Composition
BM (AA-2014)	1000	100% AA-2014
FSPed-1	900	97%AA-2014- 3%TiB_2
FSPed-2	1200	97%AA-2014- 3%TiB_2
FSPed-3	1600	97%AA-2014- 3%TiB_2

3. Characterization

3.1. Tensile Test

The mechanical characteristics of the treated zone, after heat treatment, were systematically explored through a series of nine experiments. The objective was to assess the impact of heat treatment on these mechanical properties.

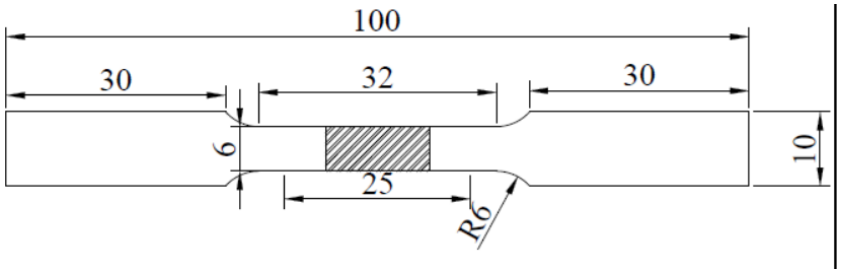

Fig. 2. ASTM Standard E8 for tensile test specimens

The tensile test specimens, crucial for evaluating these properties, were meticulously crafted using CNC wire cut technology. The geometry of these specimens (Figure 2) adhered to the specifications outlined in the ASTM standard E8/E8M-09, specifically designed for sub-size specimens [25].

3.2. Microhardness Testing

The Vickers hardness test, a key method for assessing material hardness, was conducted using a computerized microhardness tester (Melkorp, Model AHT-1000). This modern testing apparatus ensures precision and accuracy in measuring hardness values. The measurements were performed as per ASTM standards, a widely recognized set of guidelines that ensures consistency and comparability of test results [26]. The testing was conducted at several central locations throughout the treated zone, providing a comprehensive understanding of the hardness distribution within the material. This approach allows for the identification of variations in hardness across different regions of the treated zone, providing valuable insights into the impact of the treatment on the material's mechanical properties.

4. Result and Discussions

4.1. Microhardness Evaluation

The microhardness measurements depicted in Figure 3 provide valuable insights into the effects of Friction Stir Processing (FSP) on specimens treated with and without TiB_2 particles at various rotational speeds (900 rpm, 1200 rpm, and 1600 rpm). At a constant traversal speed of 40 mm/min, the figure reveals a trend were increasing the rotational speed often leads to higher microhardness values. This phenomenon is attributed to enhanced dynamic recrystallization; a consequence of the intensified stirring motion induced by the instrument's pin. The microhardness values generally exhibit an upward trend as the rotational speed increases. This suggests that higher rotational speeds contribute to increased hardness in the treated specimens. The intensified stirring motion at elevated speeds is responsible for this effect. Interestingly, the specimens treated with a rotational speed of 1200 rpm demonstrate the highest microhardness values (138 HV) compared to those processed at 1600 rpm and 900 rpm. This highlights an optimal rotational speed for achieving the desired hardness characteristics. Within the stirred zone, the specimen treated at 1200 rpm stands out for having a homogeneous distribution of TiB_2 particles. This results in a uniform scattering of reinforcement throughout the material, contributing to enhanced hardness properties.

The observed increase in microhardness with higher rotational speeds aligns with the concept of dynamic recrystallization. The intensified stirring motion at elevated speeds promotes more effective grain refinement and strengthening mechanisms, leading to enhanced hardness. The optimal microhardness values at 1200 rpm suggest that there is a balance between stirring efficiency and potential material properties. This could be attributed to an ideal combination of heat input, plastic deformation, and particle distribution achieved at this rotational speed.

The homogeneous distribution of TiB_2 particles in the specimen treated at 1200 rpm is crucial. A uniform scattering of reinforcement particles contributes to consistent strengthening effects across the material, resulting in a more homogenously hardened structure. In conclusion, Figure 3 illustrates the influence of rotational speed on microhardness in FSP-treated specimens, emphasizing the importance of finding an optimal speed for achieving desired material properties. The homogenous distribution of reinforcement particles further demonstrates the significance of process parameters in tailoring the mechanical characteristics of FSP-treated materials.

The comparative analysis of the microhardness values from this study with other research reveals significant insights into the performance of Friction Stir Processing (FSP) on Al-based alloys. The highest microhardness value in this study, achieved at 1200 rpm with TiB_2 particle reinforcement, is 138 HV. This is substantially higher than the base material

(Al-2014 alloy) which has a hardness of 98 HV. When compared to other studies, such as Gaoqiu Sun et al. on Al7050-TiB_2 (92 HV) [27], and Rajiv Panda et al. on Al2024-TiB_2 (109 HV) [28], the microhardness values from this study indicate a superior improvement in hardness due to the optimal FSP conditions.

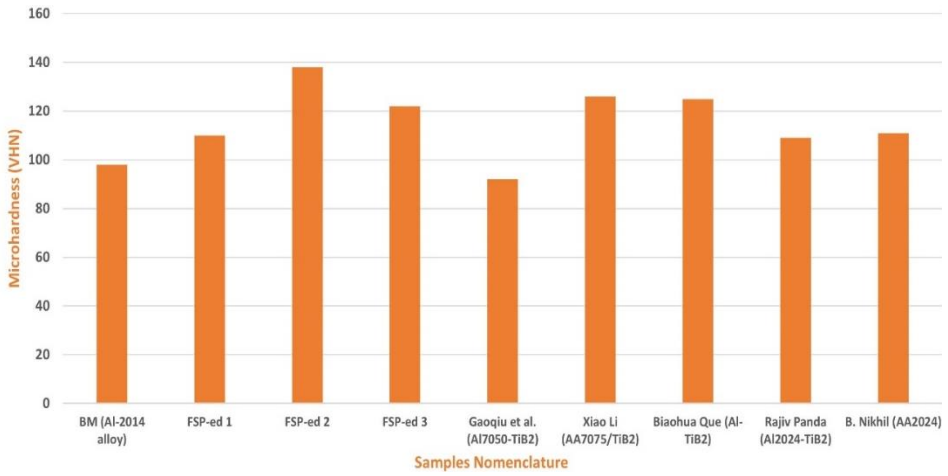

Fig. 3. Hardness values of different FSP-ed specimens

Xiao Li et al. research on AA7075/TiB_2 shows a microhardness of 126 HV [29], and Biaohua Que et al. study on Al-TiB_2 reports 124.9 HV [30], both of which are lower than the 138 HV achieved in the present study. Additionally, B. Nikhil et al. work on AA2024 reveals a microhardness of 111 HV [31], further emphasizing the significant enhancement observed in this study. The superior microhardness at 1200 rpm in this study is attributed to a combination of optimal heat input, plastic deformation, and a homogeneous distribution of TiB_2 particles, which collectively contribute to effective grain refinement and strengthening mechanisms. This comparative analysis underscores the effectiveness of the FSP parameters used in this study, particularly the rotational speed, in achieving enhanced mechanical properties in Al-based alloys reinforced with TiB_2 particles.

4.2. Tensile Strength

The tensile strength characteristics of different specimens (Figure 4) are derived from the base material (BM), which has an initial tensile strength of 290 MPa. The subsequent specimens, FSPed-1, FSPed-2, and FSPed-3, undergo Friction Stir Processing (FSP), resulting in varied tensile strength improvements. Base Material (BM) represents the unprocessed AA-2014 material without any reinforcement or FSP treatment. The tensile strength for base material was noted as 290 MPa. The specimen FSPed-1 after FSP treatment involves mixing and recrystallizing the base material, leading to a significant tensile strength improvement from 290 MPa to 360 MPa. The addition of TiB_2 particles, coupled with the stirring process, likely contributes to increased dislocation density and refined grain size in the microstructure, resulting in improved strength. Further processing enhances the tensile strength compared to FSPed-1, FSPed-2 has tensile strength of 465 MPa. Additional FSP treatment might cause more homogenization of TiB_2 particles in the matrix, leading to further strengthening. FSPed-3 exhibits the highest tensile strength (405 MPa) among the specimens. Continued processing may have caused even more refinement of the microstructure and further dispersion and alignment of TiB_2 particles, resulting in the highest tensile strength. The progressive increase in tensile strength from FSPed-1 to FSPed-3 indicates the cumulative effect of multiple FSP

treatments on the mechanical properties of the material. The addition of TiB_2 particles and the stirring process during FSP play crucial roles in enhancing dislocation density, refining grain size, and promoting homogenization, leading to improved tensile strength. The highest tensile strength in FSPed-2 suggests that continued processing results in further microstructural refinement and better dispersion and alignment of TiB_2 particles, contributing to the material's strength.

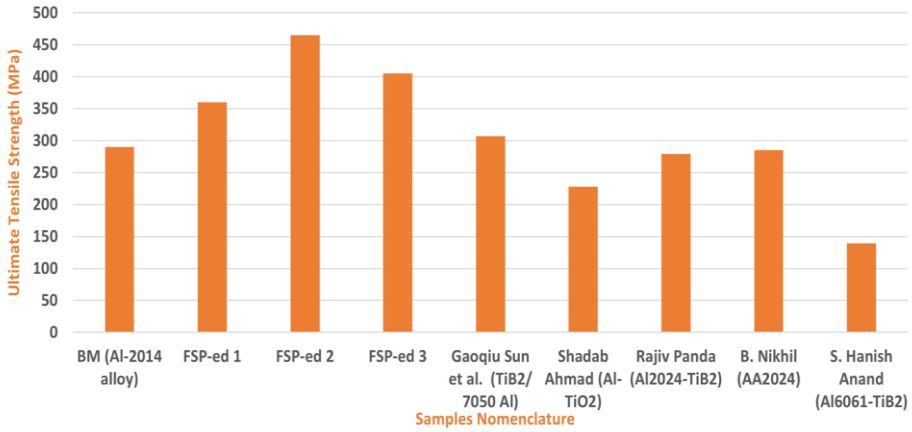

Fig. 4. UTS values of different FSP-ed specimens

Comparatively, the tensile strengths reported in other studies also provide insights into the effectiveness of different reinforcement particles and base materials. Gaoqiu Sun et al. achieved a tensile strength of 307 MPa with TiB_2/7050 Al [27], which is notable but lower than the FSPed-2 and FSPed-3 specimens from this study. Shadab Ahmad et al. work on Al-TiO_2 reported a tensile strength of 228 MPa [32], indicating that TiO_2 reinforcement, while beneficial, may not be as effective as TiB_2 in enhancing tensile strength. Rajiv Panda et al. study on Al2024-TiB_2 shows a tensile strength of 279 MPa [28], and B. Nikhil et al. work on AA2024 reports a tensile strength of 285 MPa [31]. Both values are lower than those achieved in the present study, suggesting that the specific FSP conditions and the base material (AA-2014) used in this research might be more conducive to tensile strength improvement. S. Hanish Anand et al. research on Al6061-TiB_2 reports a tensile strength of 139 MPa [33], which is the lowest among the studies considered. This further emphasizes the superior tensile strength achieved through the optimized FSP conditions and TiB_2 reinforcement in the current study.

4.3. Microstructure Analysis

The microstructure analysis is crucial in understanding the distribution and arrangement of TiB_2 nanoparticles within the AA-2014 alloy, providing insights into how these factors influence the material's mechanical properties. The base material, representing unprocessed AA-2014, serves as the control in this study. The FSPed-2 specimen, reinforced with 3% TiB_2 nanoparticles, showcases a significant improvement in the dispersion of these reinforcing particles within the AA-2014 matrix. The enhanced dispersion of TiB_2 nanoparticles in the FSPed-2 specimen is a key contributor to its improved mechanical properties. This is because a more uniform distribution of TiB_2 particles leads to better interfacial bonding between the matrix and the nanoparticles. Such improved bonding facilitates effective load transfer from the softer aluminum matrix to the harder TiB_2 particles, thereby enhancing the overall strength and hardness of the material. Additionally, the fine and uniform dispersion of TiB_2 particles helps in refining

the grain structure of the aluminum matrix. This grain refinement is a result of dynamic recrystallization promoted by the FSP process, which further contributes to the enhancement of mechanical properties such as tensile strength and hardness.

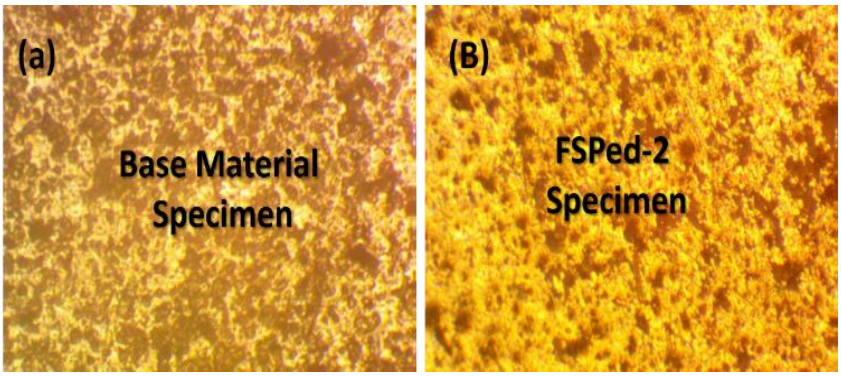

Fig. 5. Microstructure of BM and FSPed-2 specimens

In Figure 5, the mechanical properties of the FSPed-2 specimen, including tensile strength and hardness, are compared to those of the base material. The tensile strength of the FSPed-2 specimen shows a marked increase, attributed to the better dispersion of TiB_2 nanoparticles. This uniform distribution not only strengthens the material but also improves its ductility by preventing the formation of weak points that could lead to fracture. The hardness of the FSPed-2 specimen is also significantly higher than that of the base material, which can be explained by the Hall-Petch effect, where the fine grain structure and the presence of hard particles hinder the movement of dislocations, thereby increasing the material's resistance to deformation. The interaction between the TiB_2 nanoparticles and the aluminum matrix is a critical aspect of the material's enhanced properties. Previous research has shown that TiB_2 particles serve as effective barriers to dislocation movement, contributing to the strengthening of the material through mechanisms such as Orowan strengthening, where the dislocations bypass the nanoparticles, and grain boundary strengthening, where the fine grains enhance the yield strength of the material. Yihong Wu et al. revealed that the deagglomeration and dispersion of TiB_2 particles improve both the strength and ductility of the particulate-reinforced aluminum matrix composite. The uniform distribution of precipitates and the elimination of agglomerated TiB_2 bumps and residual Al3Ti blocks are crucial for these improvements [34]. Santha Rao et al. observed that the microstructural analysis sheds light on the intricate mechanisms during the FSP process. The uniform distribution of filler particles in the stir zone contributes to improved mechanical properties and signifies the effectiveness of the welding conditions, particularly at higher rotational speeds. The nuanced interplay between mixing, distribution of filler particles, recrystallization, and grain refinement underscores the complexity of the microstructural evolution in the fabrication of composites [35].

5. Conclusion

The fabrication of AA-2014 TiB_2 surface composite using the FSP process has been accomplished. This composite has numerous industrial applications, particularly in the automotive, aerospace, and construction sectors, owing to its enhanced mechanical properties and durability. The investigation into the effect of TiB_2 particles on the microstructure, microhardness, and tensile behavior of AA-2014 surface composite fabricated by Friction Stir Processing (FSP) has yielded significant conclusions.

- The optimal bonding of TiB_2 with the AA-2014 substrate was consistently observed at 1200 rpm, as evidenced by good bonding compared to both the base metal and FSP-ed specimens processed at 900 and 1600 rpm. This optimal bonding at 1200 rpm is critical as it ensures the effective integration of TiB_2 particles within the AA-2014 matrix, enhancing the overall properties of the composite.
- Microhardness values for AA-2014 and AA-2014/3%TiB_2 @1200rpm surface composite were measured at 88 HV and 138 HV, respectively. The significant increase in hardness value is attributed to the presence of TiB_2 nanoparticles and the modifications induced by the FSP process. The incorporation of TiB_2 particles into the AA-2014 matrix results in a harder surface, which is indicative of enhanced strength and resistance to deformation, showcasing the effectiveness of the TiB_2 reinforcement.
- Ultimate tensile strength (UTS) values for AA-2014 and AA-2014/3%TiB_2 @1200rpm surface composite were found to be 290 MPa and 465 MPa, respectively. The substantial increase in UTS is linked to the uniform dispersion of TiB_2 nanoparticles within the matrix material (AA-2014 alloy) during the FSP process. This uniform dispersion of TiB_2 particles not only enhances the load-bearing capacity of the composite but also improves its overall tensile behavior.

The addition of TiB_2 particles and the optimal processing parameters of FSP at 1200 rpm significantly improve the microhardness and tensile strength of the AA-2014 alloy. The enhanced properties are attributed to the uniform dispersion and strong bonding of TiB_2 particles within the matrix, resulting in a surface composite with superior mechanical properties compared to the unreinforced AA-2014 alloy and those processed at different rpm settings. These findings underscore the potential of TiB_2-reinforced AA-2014 composites for applications necessitating high strength and hardness.

Nomenclature

FSP	Friction Stir Processing	BM	Base Material
AMMCs	Aluminum metal matrix composites	AA-2014	Aluminum 2014 Alloy
AS	Advanced Side	TiB_2	Titanium Diboride
RS	Retreating Side	TiO_2	Titanium Dioxide
TMAZ	Thermo-Mechanically Affected Zone	UTS	Ultimate Tensile Strength
HAZ	Heat Affected Zone	VHN	Vickers Hardness

References

[1] Vipin S, Sharma K. A review of recent research on rare earth particulate composite materials and structures with their applications. Trans Indian Inst Met. 2021. https://doi.org/10.1007/s12666-021-02338-y

[2] Sharma VK, Kumar V, Joshi RS. Experimental investigation on effect of RE oxides addition on tribological and mechanical properties of Al-6063 based hybrid composites. Mater Res Express. 2019;6(8). https://doi.org/10.1088/2053-1591/ab2504

[3] Kumar D, Angra S, Singh S. Synthesis and characterization of DOE-based stir-cast hybrid aluminum composite reinforced with graphene nanoplatelets and cerium oxide. 2023. https://doi.org/10.1108/AEAT-04-2023-0104

[4] Kumar S, Kumar R, Goyal KK, Sharma N. Experimental study on tensile strength of Al2024/SiC/FA/Graphite hybrid MMC prepared by stir casting. Mater Today Proc. 2022;395-399. https://doi.org/10.1016/j.matpr.2022.03.306

[5] Alderliesten R, Open Textbook Library. Introduction to aerospace structures and materials. 2018. https://doi.org/10.5074/T.2018.003

[6] Srivastava AK, Maurya NK, Maurya M, Dwivedi SP, Saxena A. Effect of multiple passes on microstructural and mechanical properties of surface composite Al 2024/SiC produced by friction stir processing. Ann Chim Sci Mat. 2020;44(6):421-426. https://doi.org/10.18280/acsm.440608
[7] Kumar D, Angra S, Singh S. Investigation of corrosion behavior of stir-cast hybrid aluminum composite reinforced with CeO2 and GNPs nanoparticles. 2023;59(6):1210-1218. https://doi.org/10.1134/S2070205123701186
[8] Iranshahi F, Nasiri MB, Warchomicka FG. Investigation of the degradation rate of electron beam processed and friction stir processed biocompatible ZKX50 magnesium alloy. J Magnes Alloy. 2022;10(3):707-720. https://doi.org/10.1016/j.jma.2021.08.016
[9] You X, et al. A review of research on aluminum alloy materials in structural engineering. Dev Built Environ. 2024;17(September 2023):100319. doi:10.1016/j.dibe.2023.100319. https://doi.org/10.1016/j.dibe.2023.100319
[10] Lorusso M, Aversa A, Marchese G, Calignano F, Manfredi D, Pavese M. Understanding friction and wear behavior at the nanoscale of aluminum matrix composites produced by laser powder bed fusion. Adv Eng Mater. 2020;22(2):1-12. https://doi.org/10.1002/adem.201900815
[11] Kale SS, Raja VS, Bakare AK. Enhancing the environmentally assisted cracking resistance of aircraft quality Al alloy of type AA7075 stiffened with polymer matrix composite using cerium chloride inhibitor. Trans Indian Inst Met. 2018;71(12):3021-3027. https://doi.org/10.1007/s12666-018-1403-z
[12] Abraham CB, Nathan VB, Jaipaul SR, Nijesh D, Manoj M, Navaneeth S. Basalt fibre reinforced aluminium matrix composites - a review. Mater Today Proc. 2020;21:380-383. https://doi.org/10.1016/j.matpr.2019.06.135
[13] Chak V, Chattopadhyay H, Dora TL. A review on fabrication methods, reinforcements and mechanical properties of aluminum matrix composites. J Manuf Process. 2020;56(May):1059-1074. https://doi.org/10.1016/j.jmapro.2020.05.042
[14] Partheeban CMA, Rajendran M, Vettivel SC, Suresh S, Moorthi NSV. Mechanical behavior and failure analysis using online acoustic emission on nano-graphite reinforced Al6061-10TiB2 hybrid composite using powder metallurgy. Mater Sci Eng A. 2015;632:1-13. https://doi.org/10.1016/j.msea.2015.02.064
[15] Paper R. Lignocellulosic abaca fibre-reinforced thermoplastic composites as future sustainable structural materials: a bibliometric analysis and literature review. 2024.
[16] Kumar S, Alok N, Sisir S. Impact of process parameters on solid particle erosion behavior of waste marble dust-filled polyester composites. Arab J Sci Eng. 2021;46(8):7197-7209. https://doi.org/10.1007/s13369-020-05175-1
[17] Kalhapure M, Dighe P. Impact of silicon content on mechanical properties of aluminum alloys. Int J Sci Res (IJSR). 2013;14(6):2319-7064.
[18] Khiyavi BA, Aghchai AJ, Arbabtafti M, Kazem M, Givi B. Effect of friction stir processing on mechanical properties of surface composite of Cu reinforced with Cr particles. 2014;829:851-856. https://doi.org/10.4028/www.scientific.net/AMR.829.851
[19] Raja R, et al. Development of Al-Mg2Si alloy hybrid surface composites by friction stir processing: mechanical, wear, and microstructure evaluation. Mater. 2023;16:4131. https://doi.org/10.3390/ma16114131
[20] Ajenifuja E, Odetola P, Popoola API, Popoola O. Spark plasma sintering and structural analysis of nickel-titanium/coconut shell powder metal matrix composites. Int J Adv Manuf Technol. 2020;108(11-12):3465-3473. https://doi.org/10.1007/s00170-020-05634-x
[21] Siddesh Kumar NM, Sadashiva M, Monica J, Praveen Kumar S. Investigation on corrosion behaviour of hybrid aluminium metal matrix composite welded by friction stir welding. Mater Today Proc. 2021;52:2339-2344. https://doi.org/10.1016/j.matpr.2022.01.362

[22] Singh S, Pal K. Influence of texture evolution on mechanical and damping properties of SiC/Li2ZrO3/Al composite through friction stir processing. J Eng Mater Technol Trans ASME. 2020;142(2):1-9. https://doi.org/10.1115/1.4045495
[23] Kumar S, Kumar A, Vanitha C. Corrosion behaviour of Al 7075/TiC composites processed through friction stir processing. Mater Today Proc. 2019;15:21-29. https://doi.org/10.1016/j.matpr.2019.05.019
[24] Zhang Z, Wu Q. Numerical studies of tool diameter on strain rates, temperature rises and grain sizes in friction stir welding. J Mech Sci Technol. 2015;29(10):4121-4128. https://doi.org/10.1007/s12206-015-0906-3
[25] Xia J, Lewandowski JJ, Willard MA. Tension and fatigue behavior of Al-2124A/SiC-particulate metal matrix composites. Mater Sci Eng A. 2020;770(June 2019):138518. https://doi.org/10.1016/j.msea.2019.138518
[26] Venkatesan SP, Muthuswamy G, Shyam Sundar R, Ganesan S, Hemanandh J. Investigation of mechanical properties of aluminum metal matrix composites with nanomaterial reinforcement. Mater Today Proc. 2022;62:572-582. https://doi.org/10.1016/j.matpr.2022.03.594
[27] Sun G, Zhao G, Shao L, Li X, Deng Y. Particle dispersion and mechanical properties enhancement of in-situ TiB2/7050 Al matrix composite via additive friction stir deposition. Mater Lett. 2024;357(November 2023):135790. https://doi.org/10.1016/j.matlet.2023.135790
[28] Panda R, Gupta RK, Mandal A, Chakravarthy P. Processing, microstructure evolution, and heat treatment response of AA2024 and its metal matrix composites of in situ TiB2 dispersoids. J Mater Eng Perform. 2024. https://doi.org/10.1007/s11665-024-09344-3
[29] Li X, et al. Exceptional strength and wear resistance in an AA7075/TiB2 composite fabricated via friction consolidation. Mater Des. 2024;242(March):113006. https://doi.org/10.1016/j.matdes.2024.113006
[30] Que B, Chen L, Chen Y, Qian L, Zhao G, Zhang C. Fabrication of Al/Al-TiB2 laminate composites via hot press sintering process: an insight into the mechanical properties and fracture behavior. J Manuf Process. 2024;109(July 2023):53-64. https://doi.org/10.1016/j.jmapro.2023.11.040
[31] Nikhil B, Govindan P. Effect of tool probe geometry on the material flow and mechanical behaviour of dissimilar AA2024/AA7075 friction stir welded joints. Int J Interact Des Manuf (IJIDeM). 2024;18(3):1645-1664. https://doi.org/10.1007/s12008-023-01717-7
[32] Ahmad S, et al. Experimental studies on mechanical properties of Al-7075/TiO2 metal matrix composite and its tribological behaviour. J Mater Res Technol. 2024;30(May):8539-8552. https://doi.org/10.1016/j.jmrt.2024.05.227
[33] Anand SH, Sathishkumar NVB. Microstructural, mechanical and tribological analysis of TiB2 ceramic-reinforced Al6061 aluminium alloy composites. Arab J Sci Eng. 2024;49(2):1827-1842. https://doi.org/10.1007/s13369-023-07978-4
[34] Wu Y, Li L, Kang H, Guo E, Li J, Du G. Agglomerating behavior of in-situ TiB2 particles and strength-ductility synergetic improvement of in-situ TiB2p/7075Al composites through ultrasound vibration. Mater Charact. 2024;208(September 2023):113652. https://doi.org/10.1016/j.matchar.2024.113652
[35] Dakarapu SR, Chinta ND, Reddy S, Avinash K, Shaik K, Chakravarthy P. Optimization of process parameters for improvement of joint strength of dissimilar aluminum alloys by friction stir welding with an activated flux of titanium diboride. Int J Interact Des Manuf (IJIDeM). 2024. https://doi.org/10.1007/s12008-024-01787-1

Research on Engineering Structures & Materials
www.jresm.org
Research Group

Research Article

Phenomenological failure criteria analysis of a composite bolted joint under multi-axial loading using the finite element method

Manuela Karla Ribeiro Mathias[*,a], Bruno Mikio Fujiwara Marques[b]

Mechanical Engineering, Instituto Federal de Educação, Ciência e Tecnologia de São Paulo, IFSP, São José dos Campos, São Paulo, Brazil

Article Info

Article history:

Received 11 Apr 2024
Accepted 12 July 2024

Keywords:

Composites;
Bolted joints;
Failure criteria;
Hashin;
LaRC04;
Puck

Abstract

Carbon Fiber Reinforced Polymer Composites (CFRP) are commonly used in various sectors due to their excellent properties. However, they present complex failure modes, particularly in bolted joints, which are widely used in the aeronautical industry due to their ease of assembly and disassembly. Phenomenological failure criteria can be used to evaluate failure modes analytically and reduce the number of experimental tests. It is important to determine the criterion that best reflects reality. The Hashin, Puck, and LaRC04 failure criteria were evaluated using a finite element method software - FEMAP 2021.2 educational version - through simulation. Numerical simulations were conducted on a 2D model of a carbon/epoxy composite bolted joint under multiaxial loads, following ASTM D5661 dimensions. The failure criteria were compared to determine the most appropriate one for this type of component. Among the evaluated criteria, the Hashin criterion showed an intermediate level, while the Puck criterion was the most conservative and the LaRC04 criterion was the least conservative. It is recommended to use the Hashin criterion for general analyses. For analyses that require a detailed examination of compression failure modes, it is recommended to use the LaRC04 criterion. The Puck criterion is suggested for more conservative analyses.

1. Introduction

Carbon fiber reinforced polymer composites (CFRP) are widely used in the industrial sector due to their excellent properties, such as outstanding strength, high stiffness, and low weight [1, 2]. A notable example can be observed in the aerospace industry, where the Boeing 787 Dreamliner is composed of approximately 50% composite materials. As a result, the aircraft's weight is reduced, which consequently enhances its fuel efficiency [3, 4]. Moreover, these materials represent 40% of modern aircraft with a variety of applications, including interiors, engine blades, fuselage, wings, rotors, brackets, and others [1,4]. However, the failure modes for composite materials are complex due to the anisotropy and heterogeneity of the material, which depend on various factors such as the combination of fiber and matrix properties, the orientation of the fibers, and the number of plies in the component. As a result, they can present various types of damage mechanisms, such as delamination, fiber breakage, pull-out, matrix cracking, and other mechanisms, which makes it a challenge to identify the start of the failure [5, 6].

Therefore, it is necessary to take great care when manufacturing composite parts, especially bolted joints. Due to their ease of assembly and disassembly, bolted joints are crucial components in the aeronautical industry. However, despite this, more than 70% of

*Corresponding author: manuela.k@aluno.ifsp.edu.br
[a] orcid.org/0009-0005-2120-6918; [b] orcid.org/0000-0002-2367-9410
DOI: http://dx.doi.org/10.17515/resm2024.225me0411rs

structural failures occur at the joints [7,8]. In addition to the complexity of composite materials, the hole in their structure generates stress concentration in this region, making the components more susceptible to failures [7]. Thus, among the factors that can influence the failure mode of these components are the preload, the clearance of the screw hole, the type of screw head, and the geometric relationships between the hole diameter, width, thickness, and distance from the edge [9,10].

Generally, these components can fail in three main ways, varying based on the dimensions of the laminate: net-tension, shear-out, and bearing [10]. Net-tension and shear-out failures are the most catastrophic failure modes. While net-tension failure occurs at a low value for the ratio between the width of the plate to the diameter of the hole and a high value for the ratio between the distance from the hole to the edge of the joint by the diameter of the hole, shear-out failure occurs for reasons inverse to net tension, i.e., a high value between the width by the diameter and low value between the edge distance by the diameter [10]. However, unlike other failure modes, bearing failure produces a progressive failure. This failure is initiated by the compressive force applied to the inside of the hole by the bolt shank and a small value of the width-to-diameter ratio [9]. Due to the progressive failure behavior of bearing, bolted joints are designed to fail in this mode [7].

It is important to note that the application of torque is directly related to the resulting tension in the bolts and plates. Therefore, it is crucial to consider torque when studying bolted joints [7]. Torque generates a preload in the bolt, which aims to restrict the hole region and enable the transfer of external loads between plates through fixation [11]. The torque value should be defined based on the bolt strength, the material of the clamped parts and the type of installation so that the preload increases the strength of the bolted joint. Otherwise, if the torque is not properly applied, it could cause premature failure of the composite component due to the low resistance to out-of-plane stresses of these materials [7,9,10].

Furthermore, due to the wide range of factors that influence the failure modes of these components, the number of experimental tests has increased considerably, making material analysis costly, time-consuming, and analytically challenging [5,8]. This is particularly evident in the aerospace industry, due to the considerable costs and labor associated with the composites applied to this sector and the tools used in their production [3]. However, with increasingly powerful computers and the evolution of numerical modeling, simulation in software such as those using the finite element method (FEM) significantly reduces the number of tests, proving to be a cost-effective alternative when experimentally validated [2,3].

In conjunction with FEM simulation models, failure criteria for composite materials can be used to identify and predict the modes and onset of failure in the component being analyzed [5]. These criteria can be classified into macroscopic and microscopic aspects, with the macroscopic group being the most widely used due to their ease of application [12,13]. Within this group, there is a further classification grouping the criteria as follows [5,14]:

- Criteria that neglect the interactions between the different stress components, such as the maximum stress criterion and the maximum strain criterion.
- Criteria that include total stress interaction and have only one inequality, so they do not predict the initial failure mode, such as the Hoffman, Tsai-Wu, and Tsai-Hill criteria.
- Phenomenological criteria address the physical aspects of fracture and distinguish between different failure modes, such as the Hashin, Puck, and LaRC04 criteria.

The criteria in the third group, which deal with phenomenological models, are the closest to reality. Therefore, the study of these criteria is crucial for enhancing numerical analysis with accurate and realistic failure modes, especially in the industry, such as aircraft components, where the mechanical qualities are high and safety is of main concern. As the majority of commercial finite element software only provides the most traditional criteria, including Hashin, Tsai-Wu, Tsai-Hill, a limited number of studies have demonstrated the implementation of the Puck criterion used in the aeronautical sector [1,15]. Consequently, in addition to incorporating new criteria into the software, it is essential to validate them through experimental tests and identify the criterion that most closely aligns with reality for each component and specific conditions, with aim of reducing costs, time, materials and tests [1,13].

Good results using phenomenological criteria can be found in the literature. Zheng et al. [12] conducted a comparative study of failure criteria for predicting the onset of failure, concluding that the Hashin criterion provides reasonable results in a good execution time while the Puck and LaRC03 criteria offer more accurate results but with a longer execution time. Kober and Kühhorn [16] used the Tsai-Hill, Puck, and LaRC04 criteria to analyze, determining that the Puck criterion generates more realistic results. On the other hand, the LaRC04 criterion achieves results like the Puck criteria but from a mechanical point of view of the fracture. Marques et al. [13] carried out a comparative analysis between various criteria such as Hashin, Puck, Tsai-Hill, Tsai-Wu, Hoffman, and maximum stress, resulting in coherent results, but with an advantage for the Puck criterion due to the distinction between fiber and inter-fiber failure modes.

It is clear from the literature that the Puck criterion correlates well with experimental results, making it a reference for others [16]. The World-Wide Failure Exercise (WWFE) identified this criterion as one of the most effective in failure assessment [5]. In addition, several studies analyzing the results of FEM simulations of failure criteria for composite models compared to experimental results are available in the literature [1,15,17-20]. These studies present models with satisfactory results compared to their experimental tests.

In this context, a comparative analysis is proposed between the Hashin, Puck, and LaRC04 criteria, applied to a 2D model of a carbon/epoxy CFRP bolted joint in the FEMAP 2021.2 educational version software to determine the one best suits to this type of component. The model is a simple shear, two plates, and a bolt, subjected to multiaxial loads and dimensions according to ASTM D5961 [21].

2. Failure Criteria

The failure criteria employed in this study were consulted from the literature [5,13,15, 16,22], leading to the creation of Tables 1, 2, and 4, encompassing the equations for each criterion. In addition, some failure criteria depend on other constants and equations that may vary depending on the material and specimen analyzed.

In the equations, σ_1, σ_2, and σ_3 are the normal stresses in the principal axes of the specimen, τ_{12}, τ_{13} and τ_{23} are the in-plane and out-of-plane shear stresses, Xt and Xc are the longitudinal tensile and compressive strengths, Yt and Yc are the transverse tensile and compressive strengths, S_{12}, S_{13} and S_{23} are the in-plane and out-of-plane shear strengths, ε_1 is the normal strain, γ_{12} is the in-plane shear strain, m is the stress magnification factor, ε_{1t} and ε_{1c} are the longitudinal strain in tension and compression respectively.

Moreover, the failure modes are categorized as follows: fiber failure in tension (FFT), fiber failure in compression (FFC), matrix failure in tension (FMT), matrix failure in

compression (FMC), inter-fiber failure in transverse tension (IFF-A), inter-fiber failure in in-plane shearing (IFF-B), and inter-fiber failure in large transverse compression (IFF-C).

2.1. Hashin Criterion

Table 1. Hashin criterion equations [5,13]

FFT	$\left(\frac{\sigma_1}{X_t}\right)^2 + \frac{({\tau_{12}}^2 + {\tau_{13}}^2)}{S_{12}} = 1$	(1)
FFC	$-\left(\frac{\sigma_1}{X_c}\right) = 1$	(2)
FMT	$\frac{(\sigma_2 + \sigma_3)^2}{{Y_t}^2} + \frac{({\tau_{23}}^2 - \sigma_2\sigma_3)}{{S_{23}}^2} + \frac{({\tau_{23}}^2 + {\tau_{13}}^2)}{{S_{12}}^2} = 1 \text{ for } \sigma_2 + \sigma_3 > 0$	(3)
FMC	$\frac{1}{Y_c}\left[\left(\frac{Y_c}{2S_{23}}\right)^2 - 1\right](\sigma_2 + \sigma_3) + \frac{(\sigma_2 + \sigma_3)^2}{{Y_t}^2} + \frac{({\tau_{23}}^2 - \sigma_2\sigma_3)}{{S_{23}}^2} + \frac{({\tau_{23}}^2 + {\tau_{13}}^2)}{{S_{12}}^2} = 1$ for $\sigma_2 + \sigma_3 < 0$	(4)

2.2. Puck Criterion

Puck [23] determined the value of the inclination parameters (for further details, see [23]), and the parameters for CFRP materials are presented in Table 3. It should be noted that the parameter $P_{\perp\perp}^{-}$ exhibits a specified variation set at 0.30. Another constant, defined by the Puck criterion is the stress magnification factor (m), which accounts for the mismatch of elastic properties between the fiber and the matrix. For CFRP materials, its value is 1.1 [13].

Table 2. Puck criterion equations [13,15]

FFT	$\frac{1}{\varepsilon_{1t}}\left(\varepsilon_1 + \frac{\nu_{f12}}{E_{f1}} m\sigma_2\right) = 1 \text{ for } \left(\varepsilon_1 + \frac{\nu_{f12}}{E_{f1}} m\sigma_2\right) \geq 0$	(5)
FFC	$\frac{1}{\varepsilon_{1c}}\left\|\left(\varepsilon_1 + \frac{\nu_{f12}}{E_{f1}} m\sigma_2\right)\right\| + (10\gamma_{12})^2 = 1 \text{ for } \left(\varepsilon_1 + \frac{\nu_{f12}}{E_{f1}} m\sigma_2\right) < 0 \text{ and } \sigma_1 < 0$	(6)
IFF-A	$\sqrt{\left(\frac{\tau_{12}}{S_{12}}\right)^2 + \left(1 - P_{\perp\parallel}^{+}\frac{Y_t}{S_{12}}\right)^2\left(\frac{\sigma_2}{Y_t}\right)^2} + P_{\perp\parallel}^{+}\frac{\sigma_2}{S_{12}} + \frac{\sigma_1}{\sigma_{1D}} = 1 \text{ for } \sigma_2 \geq 0$	(7)
IFF-B	$\frac{1}{S_{12}}\left(\sqrt{(\tau_{12})^2 + \left(P_{\perp\parallel}^{-}\sigma_2\right)^2} + \left(P_{\perp\parallel}^{-}\sigma_2\right)^2\right) + \frac{\sigma_1}{\sigma_{1D}} = 1$ for $\sigma_2 < 0$ and $0 \leq \left\|\frac{\sigma_2}{\tau_{12}}\right\| \leq \frac{R_{\perp\perp}^{A}}{\lvert\tau_{12c}\rvert}$	(8)
IFF-C	$\left(\left[\left(\frac{\tau_{12}}{2(1 + P_{\perp\perp}^{-}S_{12})}\right)^2 + \left(\frac{\sigma_2}{Y_c}\right)^2\right].\frac{Y_c}{-\sigma_2}\right) = 1 \text{ for } \sigma_2 < 0 \text{ and } 0 \leq \left\|\frac{\tau_{12}}{\sigma_2}\right\| \leq \frac{\lvert\tau_{12c}\rvert}{R_{\perp\perp}^{A}}$	(9)

The longitudinal linear degradation index (σ_{1D}) is obtained experimentally, but as experimental tests will not be conducted, it will not be possible to obtain the linear degradation index, so two situations will be evaluated: the linear degradation index having a numerical value equal to the longitudinal stress (σ_1), with the ratio between the

unknowns being equal to one; and the linear degradation index being significantly greater than the stress, with this ratio tending to zero.

Table 3. Inclination parameters [13]

Parameter	Value
$P_{\perp\perp}^{-}$	0.25 – 0.30
$P_{\perp\parallel}^{-}$	0.30
$P_{\perp\parallel}^{+}$	0.35

The longitudinal strain in tension (ε_{1t}) and compression (ε_{1c}) can be calculated as follows:

$$\varepsilon_{1t} = \frac{Y_t}{E_1} \tag{10}$$

$$\varepsilon_{1c} = \frac{Y_c}{E_1} \tag{11}$$

The terms $R_{\perp\perp}^{A}$ and τ_{12c} represent, respectively, the in-plane failure strength due to transverse or shear stress and the shear stress at the critical point where the transition between Mode B and Mode C occurs [15]. They can be calculated from the following equations [15]:

$$R_{\perp\perp}^{A} = \frac{S_{12}}{2P_{\perp\perp}^{-}}\left(\sqrt{1 + 2P_{\perp\parallel}^{-}\frac{Y_c}{S_{12}}} - 1\right) \tag{12}$$

$$\tau_{12c} = S_{12}\sqrt{1 + 2P_{\perp\perp}^{-}} \tag{13}$$

2.3. LaRC04 Criterion

Table 4. LaRC04 criterion equations [16,22]

FFT	$\frac{\sigma_1}{X_t} = 1$ for $\sigma_1 \geq 0$	(14)
FFC	$\left(\frac{\tau_{1m2m}}{S_{12is} - \eta^L \sigma_{2m2m}}\right)^2 = 1$ for $\sigma_1 < 0$ and $\sigma_{2m2m} < 0$	(15)
FFC[1]	$(1-g)\frac{\sigma_{2m2m}}{Y_{tis}} + g\left(\frac{\sigma_{2m2m}}{Y_{tis}}\right)^2 + \frac{\triangle_{23}^{0}\,\tau_{2m3\psi}^{2} + \chi(\gamma_{1m2m})}{\chi\left(\gamma_{\frac{12}{is}}^{u}\right)} = 1$ for $\sigma_1 < 0$ and $\sigma_{2m2m} \geq 0$	(16)
FMT	$(1-g)\frac{\sigma_2}{Y_{tis}} + g\left(\frac{\sigma_2}{Y_{tis}}\right)^2 + \frac{\triangle_{23}^{0}\,\tau_{23}{}^{2} + \chi(\gamma_{12})}{\chi\left(\gamma_{12/is}^{u}\right)} = 1$ for $\sigma_2 \geq 0$	(17)
FMC	$\left(\frac{\tau^T}{S^T - \eta^T \sigma_n}\right)^2 + \left(\frac{\tau^L}{S_{12is} - \eta^L \sigma_n}\right) = 1$ for $\sigma_2 < 0$ and $\sigma_1 \geq -Y_c$	(18)
FMC[2]	$\left(\frac{\tau^{Tm}}{S^T - \eta^T \sigma_n^m}\right)^2 + \left(\frac{\tau^{Lm}}{S_{12is} - \eta^L \sigma_n^m}\right) = 1$ for $\sigma_2 < 0$ and $\sigma_1 < -Y_c$	(19)

[1] Tensile failure of the matrix under longitudinal compression (with eventual fiber-kinking).

[2] Failure of the matrix under biaxial compression.

For the LaRC04 criterion, it is necessary to make some considerations regarding the behavior and dimensions of the specimen. According to Dvorak and Laws [22], the transition between a thin and thick ply is between 0.7 mm, about 5 or 6 plies. Therefore, for the analysis, it was assumed that the specimen has a thick ply and is subjected to linear shear behavior. Knowing the laminate thickness, the transverse tensile strength (Y_{tis}) and the in-plane shear strength (S_{12is}) under the in-situ effect are calculated from the following equations [22]:

$$S_{12is} = \sqrt{2}S_{12} \tag{20}$$

$$Y_{tis} = 1.12\sqrt{2}Y_t \tag{21}$$

Additionally, for matrix failure under tension, the toughness ratio (g) was calculated using the Equation (14):

$$g = \frac{\triangle_{22}^{0} Y_{tis}^{2}}{\chi\left(\gamma_{12/is}^{u}\right)} \tag{22}$$

Thus:

$$\triangle_{22}^{0} = 2\left(\frac{1}{E_2} - \frac{\nu_{12}^{2}}{E_1}\right) \tag{23}$$

$$\chi\left(\gamma_{\frac{12}{is}}^{u}\right) = \frac{S_{12/is}^{2}}{G_{12}} \tag{24}$$

The fracture angle (α) can be analytically calculated, so it was considered equal to 0º according to Pinho et al. [22], and the angle of fracture under uniaxial compression (α_o) based on experimental tests is generally equal to 53 ± 2º for composite materials, being defined as 53º for the application of the equations. These angles are applied to calculate some of the unknowns used in the equations of the LaRC04 criterion and are presented in more detail in Pinho et al. [22].

3. Failure Criteria Code

For the application of failure criteria in the FEMAP 2021.2 software – educational version - it was necessary to write the equations according to the software's programming. To achieve this, we used the guidelines described in the Function Reference document, accessed from the Help Topics option in FEMAP [25].

Table 5. Coding example: Hashin criterion - tensile fiber failure

Format	Written
Equation	$\left(\frac{\sigma_1}{X_t}\right)^2 + \frac{(\tau_{12}{}^2 + \tau_{13}{}^2)}{S_{12}} = 1$
Coded[1]	(SQR(VEC(!case;O1;!i)/Xt))+(((SQR(VEC(!case;T12;!i)))+(SQR(VEC(!case;T13;!i))))/SQR(S12))
Coded with properties (First Ply)	(SQR(VEC(!case;1000020;!i)/1006))+(((SQR(VEC(!case;1000023;!i)))+(SQR(VEC(!case;1000025;!i))))/SQR(68.1))

[1] O1=σ_1; τ_{12}=T12; τ_{13}=T13.

Initially, the properties of the composite material have been defined as parameters to make it possible to apply the coded equations to different materials. In addition, the stresses and strains were defined as vectors, because as they are associated with the model tested by the software, it is necessary to know the positions of the vectors for each of the stresses and strains generated by the software in post-processing. The parameters for vector

positions and property values were substituted into the software. An example of the coding of the equations is in Table 5. The mechanical properties used in the analysis are of a carbon/epoxy CFRP material produced by Gurit, SE 84LV RC416T [26] and are detailed in Table 6.

Table 6. Material and carbon fiber properties [13, 27]

Property	Value
Longitudinal modulus, E1 (GPa)	59.1
Transverse modulus, E2 (GPa)	58.9
Transverse modulus, E3 (GPa)	3.9
In-plane shear modulus, G12 (GPa)	4.2
Out-of-plane shear modulus, G13 (GPa)	4.2
Out-of-plane shear modulus, G23 (GPa)	22.7
Longitudinal tensile strength, XT (MPa)	1006
Transverse tensile strength, YT (MPa)	858
Longitudinal compressive strength, XC (MPa)	649
Transverse compressive strength, YC (MPa)	659
In-plane shear strength, S12 (MPa)	68.1
In-plane shear strength, S13 (MPa)	55.8
Major Poisson's ratio, ν12	0.037
Elastic modulus of the fiber, Ef1 (GPa)	231
Major Poisson's ratio of the fiber, νf12	0.28

The bolted joint was dimensioned according to the specifications of the ASTM D5961 standard, considering a simple two-piece shear test specimen without a fixing bracket [21]. The specimen was defined as having a thickness of 2.58 mm, divided into six plies of 0.43 mm each, and oriented $[0º/45º/90º]_S$. The dimensions are shown in Table 7 and illustrated in Fig. 1.

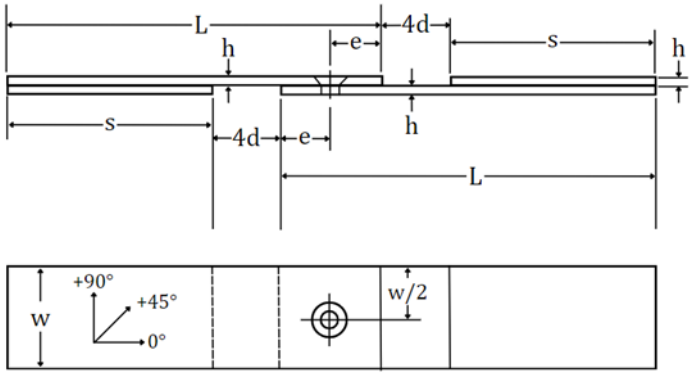

Fig. 1. Dimensions of the specimen [21]

Table 7. Dimensions of the specimen (mm) [21]

Hole diameter [d]	Length [L]	Width [w]	Edge distance [e]	Tab length [s]
6.35	135	36	18	75

The hole diameter was determined based on the NAS6204-4 standard [28]. According to the same standard, the bolt material was defined as AISI 4340 steels, and the mechanical properties of the material are in Table 8. To simulate the contact region, a washer with an outer diameter of 12.70 mm was used, following the NAS1149F0416P standard [29].

Table 8. AISI 4340 Steel property [30]

Property	Value
E1 (GPa)	210
ν12	0.28

To conduct the simulation, it was developed a 2D model of the bolted joint using FEMAP. The specimen's material was specified as 2D orthotropic, and the model property was divided into three sections: the left tab, the right tab, and the plate. Although the laminate plate property was defined in all three cases, the tab region, containing twice the number of plies, required specific definition and adjustment to accurately represent the specimen.

The left tab represents the region of the clamped end, while the right tab represents the region subjected to loading. Despite being a 2D model, it is possible to visualize the model considers the thickness of the specimen. Fig. 2 illustrates the model with the colors according to each property, and Table 9 shows the properties defined for each region of the model.

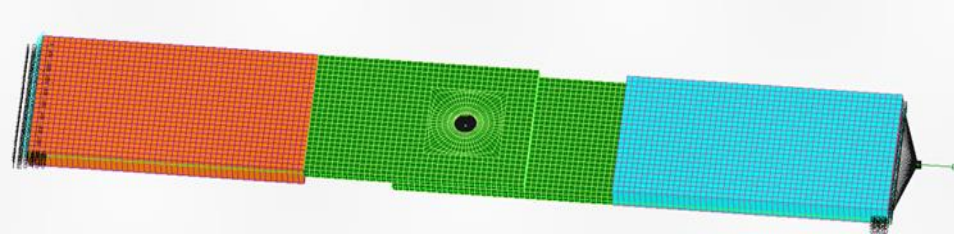

Fig. 2. Specimen model

Table 9. Properties applied to the model

Color	Number of plies	BondSh Allow (Mpa)	Ply configuration
10	6	55,8	0°/45°/90°/90°/45°/0°
14	12	55,8	0°/45°/90°/90°/45°/0°/0°/45°/90°/90°/45°/0°
120	12	55,8	0°/45°/90°/90°/45°/0°/0°/45°/90°/90°/45°/0°

The surface was discretized into 1.5 mm elements, resulting in 4604 elements and 14371 nodes after mesh refinement around the hole. Subsequently, two rigid elements (RBE2) were used to connect all nodes of each plate to a radius of 6.35 mm from the center of the hole to represent the washer in contact with the plates and the bolt. The bolt was represented by a beam element, which connected the RBE2s through the central node of each one.

However, the connections alone are not enough to represent the specimen, and it is necessary to establish a connection between them. The connection was made between the washers to link one plate to another. The connection type was set to contact, and properties were defined as standard by the software, with a coefficient of friction set to 0.3 [27]. Further details of the contact are illustrated in Fig. 3.

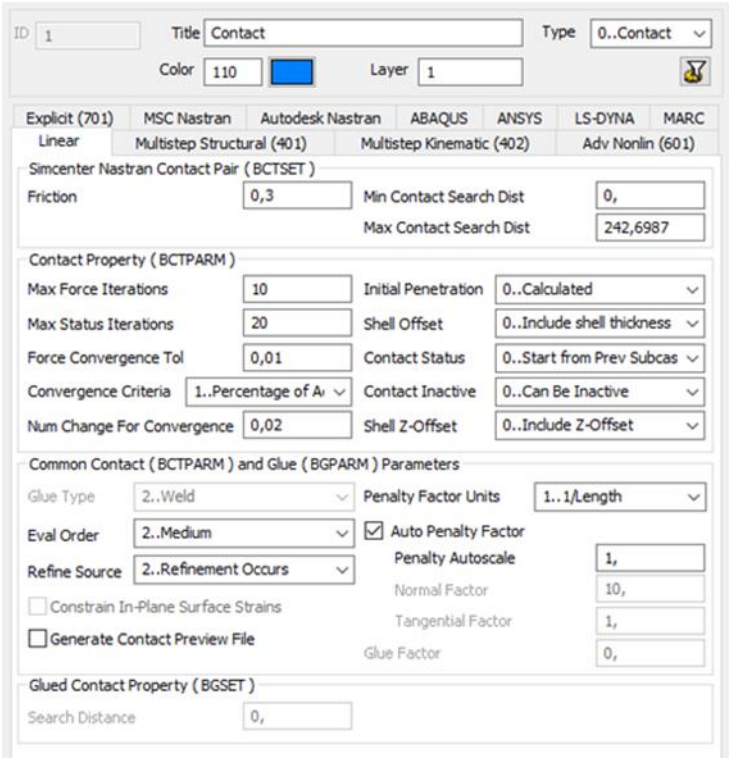

Fig. 3. Contact properties

Loadings were applied to a node outside the part, which transmits the load via an RBE2 to the nodes at the right end of the specimen. Eight loading cases were defined: 8000, 10000, 12000, 14000, 16000, 18000, 20000 and 22000 N. In addition, as the bolted joint is subjected to multiaxial loadings, a preload of 13124N was also applied in all loading cases. In order to calculate the pre-load using Equation (25) [10] the torque is set at 25 N.m and the torque coefficient at 0.3, based on the study by Marques [27], which showed that a torque of 25 N.m increases the mechanical strength of the joint without causing damage to the laminate.

$$F = \frac{T}{k.d} \tag{25}$$

Where F is the preload, k is the torque coefficient, T is the applied torque and d is the bolt diameter [10]. After simulating and adding the failure criteria equations to FEMAP, the failure indexes (FI) analysis was conducted, considering failure in the first ply. For each failure mode of each criterion, the element with the highest failure index in each ply was chosen. Then, the highest failure index among all plies was identified. Using the interpolation technique, loadings that closely approach the onset of failure were determined, with the failure index approaching the value 1. Consequently, the load values and the plies that failed were compared between the criteria to determine the criterion that best suits the behavior observed in the specimen.

4. Results and Discussion

After analyzing the failure index, Tables 10, 11, and 12 were generated, which show the loads at which the onset of failure was observed for each criterion in question, considering the failure of the first ply. In addition, no specific element in the model was considered, but rather the element that achieved the highest failure index, with the data interpolated to obtain a failure index equal to 1. The data was then put together in a line graph, illustrated in Fig. 4, providing a clear visual representation of the results obtained. For criteria with more than one compression failure mode, the lowest failure index was considered in the graphical representation.

Table 10. Hashin criterion - Loadings

Failure modes	Load (N)	Ply
Fiber failure in tension	15761	1
Fiber failure in compression	26032	6
Matrix failure in tension	18252	3
Matrix failure in compression	24904	2

Table 11. Puck criterion - Loadings

Failure modes	Load (N)	Ply
Fiber failure in tension	13839.07	6
Fiber failure in compression	26115.14	6
Inter-fiber failure in transverse tension (Mode A)	$\sigma_{1D} = \sigma_1$: 1000[1] $\sigma_{1D} >>> \sigma_1$: 4103.8	3
Inter-fiber failure in in-plane shearing (Mode B)	$\sigma_{1D} = \sigma_1$: 1000[1] $\sigma_{1D} >>> \sigma_1$: 5400.6	1
Inter-fiber failure in large transverse compression (Mode C)	4134.72	2

[1]Failure occurs at loads less than 1000N

Notably, the failure exhibits similar behavior between the criteria analyzed, such as Hashin and Puck. In plies 1 and 6, oriented at 0 degrees, fiber failure is observed, while in plies 2 and 3, at 45 and 90 degrees, respectively, matrix failure occurs. This is due to the fibers in the 0-degree direction being more resistant and supporting higher loads while in the 45 and 90-degree orientation, the matrix plays a supporting role, as the fibers are less resistant in these directions.

Furthermore, it was observed that tensile failures occur at lower loads compared to compressive failures. This behavior is related to the crushing failure mode of these components, as it generates compression in the region between the end and the edge of the hole. Therefore, as it is a progressive failure mode, it propagates slowly until failure

occurs. As tensile failure is a catastrophic failure mode, it is expected to occur at lower loads than compressive failure. Fig. 5 illustrates the mapping of stresses in the component, allowing precise identification of the areas where each type of failure occurs.

Table 12. LaRC04 criterion – Loadings

Failure modes	Load (N)	Ply
Fiber failure in tension	18229.3	1
Fiber failure in compression	39519.35	6
Fiber failure in compression[1]	46210.36	1
Matrix failure in tension	31037.45	1
Matrix failure in compression	29453.34	1
Matrix failure under biaxial compression	42132.17	1

[1] Tensile failure of the matrix under longitudinal compression (with eventual fiber-kinking);

*For Puck: Inter-fiber failure in transverse tension (Mode A)

** For Puck: Inter-fiber failure in large transverse compression (Mode C)

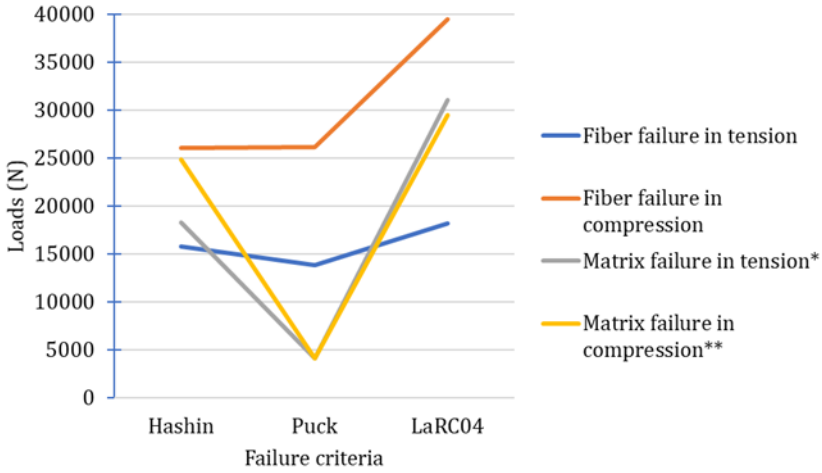

Fig. 4. Failure loads comparison

Similar results with experimental analysis are found in the literature, but it is important to highlight that are some differences due to the mechanical properties, orientations and the analysis method. Montagne et al. [31] studied the main parameters leading to the failure of joints based on an experimental database that included single-shear tests with countersunk head screws on various composite materials. They used Hashin's criterion for fiber failure and, based on the experimental results, found that some specimens failed in the net section, corresponding with Hashin's fiber failure criteria computed in the 0° plies. Additionally, the bearing failure mode was related to fiber failure in compression, delamination, or matrix damage, corresponding to failures in 0º or 45º plies due to fiber compression.

Park, Jeon, and Choi [32] studied the bearing strength of bolted joints in Carbon Fiber Reinforced Plastic (CFRP) with unidirectional weave fabric. They varied the specimen

width-to-hole diameter ratio and the distance between the hole center and specimen end-to-hole diameter ratio. For a width-to-hole diameter ratio of 6 and a distance-to-hole diameter ratio of 3, similar to the present work, the specimens experienced bearing failure.

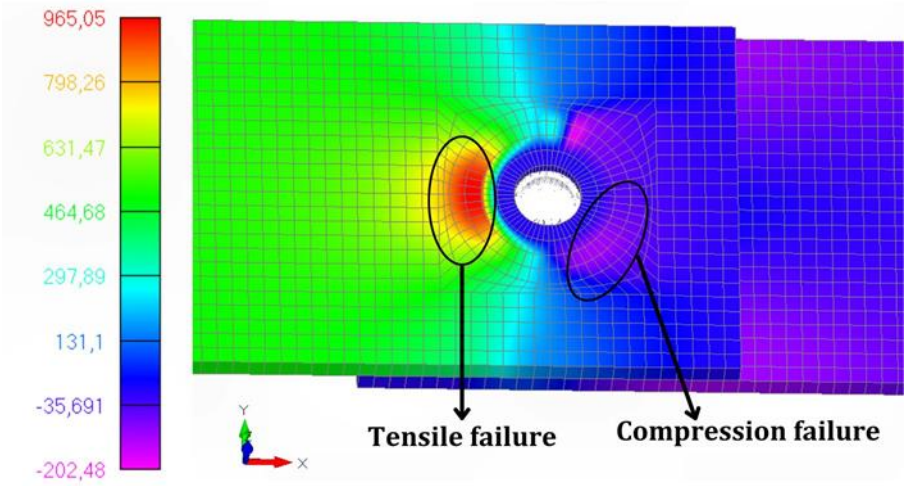

Fig. 5. Longitudinal stress map in ply 1 (0º), 18000 N and T0 model

Marques [27] studied the torque coefficients applicable to bolted joints in single shear overlays with two protruding head screws of carbon fiber reinforced epoxy matrix composite materials. The study examined the effects of different torque values on the laminate and demonstrated the relationship between bolt proof load and preload. Hashin's failure criteria was applied, which revealed interlaminar failure in the matrix, confirming the crushing effect and fiber failure in the longitudinal direction of the specimen due to traction. The results showed good correlation with the experimental tests.

About the criteria, Fig. 4 highlights that the matrix failure index for the Puck criterion occurs at significantly lower loads compared to the other criteria analyzed. Table 11 shows that for mode A and mode B the loads vary based on the value assigned to the linear degradation index, a material parameter that can be experimentally obtained. However, in the absence of experimental tests, the value was considered analytically. In the first case, it assumes that the linear degradation index value equals the longitudinal stress; consequently, the ratio between the parameters is 1. In the second case, the linear degradation index is considered much greater than the longitudinal stress, so the ratio between the parameters tends to be zero.

As a result, it is observed that for mode A, the tensile failure mode, in the first case, failure occurred at loads below 1000 N, while in the second case, failure was recorded at 4103.8 N. This type of failure, originating between the fibers, is associated with delamination between the plies and represents an initial failure mechanism because even with the presence of this mechanism, the component can withstand higher load levels [1, 13].

About mode B and mode C of the Puck criterion, both representing compressive failure mechanisms, Table 11 shows that they achieve a failure index equal to 1 in different plies and loads. In mode B, failure occurs in ply 1 at loads below 1000 N in the first case and at 5400.6 N in the second case. On the other hand, mode C results in failure in ply 2 with a load of 4134.72 N. This difference is due to the failure modes being associated with moderate and large compression, respectively. Thus, the region in which the equations are applied is limited by the ratio between the transverse stress and the in-plane shear stress,

and by the ratio between the strength of the failure plane and the critical transition point between mode B and C, as shown in Equations (8) and (9).

Despite being applied to different regions, modes B and C are characterized by the formation of cracks in the matrix, which propagate to the limits of the fiber, also representing an initial failure mode [1]. In this context, it is expected that both mode A and modes B and C, as they are initial failure mechanisms, will occur at lower loads, although in this case, they resulted in much lower loads than the other criteria.

As for the tensile and compressive fiber failure modes for Puck, the loads are close to the Hashin criterion. Puck is more conservative for tensile fiber failure, while Hashin is more conservative for compressive fiber failure, with a difference of approximately 100 N. Puck's more conservative behavior may be due to its equation, since it considers the failure plane, considering the micro-damage that occurs before the load reaches the material's strength, decreasing the strength of the matrix and increasing the chance of fiber failure [16].

On the other hand, the LaRC04 criterion behaves oppositely to the Puck criterion because failure occurs at much higher loads than the other criterion, especially in calculations involving compression, as shown in Table 12. The LaRC04 criterion considers the in-situ effect in its calculations, i.e., it considers the transverse tensile and shear strengths present in a ply of the laminate, limited by other plies of different fiber orientations [16, 22]. These strengths, as shown by Pinho et al. [22], are significantly higher when compared to unidirectional laminates. Therefore, due to the in-situ effect, it is expected that failure will occur at higher loads due to the greater resistance in the plies.

The in-situ effect is not considered only for tensile fiber failure which presents a more simplified equation, as shown in Equation (14). Fig. 4 shows that the discrepancy between the loads for which the failure index reaches 1 in this mode is smaller compared to the other modes, due to the greater similarity between the equations.

In addition, for the tensile failure of the matrix, the LaRC04 criterion occurs at a very high load and in a ply with a different orientation from the other criteria. For this failure mode, the LaRC04 criterion considers the ply stresses and in-situ strengths. However, it also considers the material's toughness coefficient, which can be obtained experimentally and analytically, based on Equation (22). However, after some comparisons, it was observed that the value calculated analytically is significantly higher than those obtained in the literature [16, 33]. Therefore, the coefficient may have influenced the results, causing the ply and the resulting load to vary.

As for the compressive failure modes, they can be divided into four failure modes, two of which are attributed to the fibers and two to the matrix. When analyzing the fiber failure modes by compression in the LaRC04 criterion, Table 12 shows that fiber failure by compression occurs at lower loads than tensile failure in the matrix under longitudinal compression (with eventual fiber kinking). Both are considered fiber failures, but they do have some differences. Fiber failure due to compression is related to kink-band formation, resulting in the phenomenon of micro buckling, while tensile failure in the matrix under longitudinal compression, with possible fiber kinking, relates two distinct types of failure: tensile failure in the matrix and fiber kinking due to deformation caused by shear in the matrix [22].

Regarding matrix failure, it is observed that matrix compression failure occurs at loadings lower than biaxial matrix compression failure. Biaxial compression failure considers fiber misalignment in its equations, while matrix compression failure considers the fracture plane [16]. Furthermore, biaxial matrix failure is related to fiber failure under

compression, resulting from micro buckling in the matrix and kink-band formation [Pihno21].

Finally, the Hashin criterion shows failure at intermediate loads. While the Puck criterion is associated with failure at low loads and the LaRC04 criterion is associated with failure at high loads. In addition, the Hashin criterion is subdivided into four failure modes, in which the failure is consistent with the orientation of the plies. It is important to note that to apply this criterion, all the material properties used were available, eliminating the need for analytical calculations to obtain them.

Also, it is important to note that, as the Hashin criterion was proposed first, the Puck and LaRC04 criteria that came later were based on some of its concepts [1,22]. Puck and his partners extended the Hashin criterion by dividing inter-fiber and fiber failure modes with the implementation of the fracture angle [1]. On the other hand, in the case of the LaRC04 criterion, the most recent of those discussed, it is developed from the fracture mechanics point of view [16,22].

Regarding failure criteria, several studies in the literature have utilized and compared different approaches. Dogan et al [34] investigated the failure behavior of carbon fiber reinforced pin-jointed composite plates using Hashin and Puck criteria. Compared with the experimental results, the numerical data using the Puck damage criterion showed at least 87% compatibility, while the Hashin damage criterion showed 85% compatibility for a single pin joint. In this case, for a ratio equal to 3 in a single pin, bearing failure, inter-fiber failure in shear, and inter-fiber failure in plane shear occur for Puck, while matrix shear and fiber compression occur for Hashin.

Gao et al [35] studied the strength and failure modes of fastened composite plates under static tensile loading based on experimental bolted joint bearing tests. They compared these results with various progressive damage numerical modeling simulations, considering the effects of damage variables, subroutines, and the Puck, Hashin, LaRC05, and maximum-stress criteria. The LaRC05 and Puck criteria provided more accurate results than the maximum stress and Hashin criteria in predicting matrix failure.

It is important to emphasize that some parameters used can be experimentally obtained for greater accuracy in the results. However, as it is not within the scope of this work to carry out tests on the specimens analyzed, the theoretical values were considered. Therefore, this variation in very high or very low failure index may be related to the considerations made when applying the criterion.

5. Conclusions

The FEMAP 2021.2 Educational Version software was used to perform a computer simulation of a bolted carbon fiber composite specimen, focusing on three failure criteria, Hashin, Puck, and LaRC04, to determine which best represented the specimen analyzed.

Thus, it can be concluded that the analysis based on the failure of the first ply of the bolted joint model was successful, presenting satisfactory and consistent results for the failure indexes of each criterion. With respect to fiber orientations, a variation in failure modes was observed depending on the orientation of each ply, with a greater tendency for fiber failure in the 0º plies, while matrix failure occurred in the 45º and 90º plies.

Additionally, it has been observed that tensile failure occurs at lower loads than compression failure, which aligns with the progressive crushing failure mechanism of these components. In terms of failure criteria, the Puck criterion is more conservative for fiber tensile failure, while the LaRC04 criterion is less conservative. On the other hand, the Hashin criterion is the most conservative for fiber compression failure, while the LaRC04

criterion is the least conservative. It is important to note that these observations are based on the modes of failure for LaRC04. The Puck criterion, which has an initial failure mechanism, exhibits much lower loadings, while the LaRC04 criterion shows significantly higher loadings for both matrix tensile and compression failure.

Therefore, the choice of criterion that best suits this type of component will depend on how conservative and detailed the analysis needs to be. In general, it is recommended to apply the Hashin criterion for the analyses. For analyses that require a more detailed examination of compression failure modes, it is suggested to use the LaRC04 criterion. For more conservative analyses, the use of the Puck criterion is proposed. However, it should be noted that the Puck criterion has shown failures at very low loadings, so it is recommended to verify the results using experimentally obtained parameters.

Acknowledgement

The authors acknowledge the financial support received from the CNPq - National Council for Scientific and Technological Development.

References

[1] El Idrissi H, Seddouki A. Modelling of progressive damage in a notched carbon/epoxy composite laminate subjected to tensile loading using different assessment methods coupled with FEM. Fibers and Polymers. 2022 Nov 1;23(11):3146-62. https://doi.org/10.1007/s12221-022-0019-4

[2] González C, Vilatela JJ, Molina-Aldareguía JM, Lopes CS, LLorca J. Structural composites for multifunctional applications: Current challenges and future trends. Progress in Materials Science. 2017;89:194-251. https://doi.org/10.1016/j.pmatsci.2017.04.005

[3] Cepero-Mejias F, Phadnis VA, Curiel-Sosa JL. Machining induced damage in orthogonal cutting of UD composites: FEA based assessment of Hashin and Puck criteria. Procedia CIRP. 2019;332-7. https://doi.org/10.1016/j.procir.2019.04.241

[4] Borges C, Chícharo A, Araújo A, Silva J, Santos RM. Designing of carbon fiber-reinforced polymer (CFRP) composites for a second-life in the aeronautic industry: strategies towards a more sustainable future. Front Mater.2023;10. https://doi.org/10.3389/fmats.2023.1179270

[5] Nali P, Carrera E. A numerical assessment on two-dimensional failure criteria for composite layered structures. Compos B Eng. 2012;43(2):280-9. https://doi.org/10.1016/j.compositesb.2011.06.018

[6] Parambil NK, Gururaja S. Bridging micro-to-macro scale damage in UD-FRP laminates under tensile loading. Int J Mech Sci. 2019 Jul 1;157-158:184-97. https://doi.org/10.1016/j.ijmecsci.2019.03.039

[7] Olmedo Á, Santiuste C. On the prediction of bolted single-lap composite joints. Compos Struct. 2012 May;94(6):2110-7. https://doi.org/10.1016/j.compstruct.2012.01.016

[8] Li X, Li Y, Li F, Huang Z, Chen H. Failure analysis and experimental study on bolted composite joints based on continuum damage mechanics. Compos Struct. 2023 Jan 1;303. https://doi.org/10.1016/j.compstruct.2022.116274

[9] El-Sisi A, Hassanin A, Alsharari F, Galustanian N, Salim H. Failure behavior of composite bolted joints: review. CivilEng. 2022 Dec 1;3(4):1061-76. https://doi.org/10.3390/civileng3040060

[10] Yoon D, Kim S, Kim J, Doh Y. Study on bearing strength and failure mode of a carbon-epoxy composite laminate for designing bolted joint structures. Compos Struct. 2020 May 1;239. https://doi.org/10.1016/j.compstruct.2020.112023

[11] Hu J, Zhang K, Cheng H, Qi Z. An experimental investigation on interfacial behavior and preload response of composite bolted interference-fit joints under assembly and

thermal conditions. Aerosp Sci Technol. 2020 Aug 1;103. https://doi.org/10.1016/j.ast.2020.105917
[12] Zheng J, Maharaj C, Liu J, Chai H, Liu H, Dear JP. A comparative study on the failure criteria for predicting the damage initiation in fiber-reinforced composites. Mechanics of Composite Materials. 2022 Mar 23;58(1):125-40. https://doi.org/10.1007/s11029-022-10016-3
[13] Marques BMF, Marques TPZ, Silva F de A, Cândido GM, Rezende MC. Failure criteria assessment of carbon/epoxy laminate under tensile loads using finite element method: validation with experimental tests and fractographic analysis. Mechanics of Advanced Materials and Structures. 2023;30(6):1274-83. https://doi.org/10.1080/15376494.2022.2029984
[14] Gu J, Chen P. Some modifications of Hashin's failure criteria for unidirectional composite materials. Compos Struct. 2017 Dec 15;182:143-52. https://doi.org/10.1016/j.compstruct.2017.09.011
[15] Gadade AM, Lal A, Singh BN. Finite element implementation of Puck's failure criterion for failure analysis of laminated plate subjected to biaxial loadings. Aerosp Sci Technol. 2016 Aug 1;55:227-41. https://doi.org/10.1016/j.ast.2016.05.001
[16] Kober M, Kühhorn A. Comparison of different failure criteria for fiber-reinforced plastics in terms of fracture curves for arbitrary stress combinations. Compos Sci Technol. 2012;72(15):1941-51. https://doi.org/10.1016/j.compscitech.2012.08.007
[17] Demiral M, Tanabi H, Sabuncuoglu B. Experimental and numerical investigation of transverse shear behavior of glass-fibre composites with embedded vascular channel. Compos Struct. 2020 Nov 15;252. https://doi.org/10.1016/j.compstruct.2020.112697
[18] Topac OT, Gozluklu B, Gurses E, Coker D. Experimental and computational study of the damage process in CFRP composite beams under low-velocity impact. Compos Part A Appl Sci Manuf. 2017 Jan 1;92:167-82. https://doi.org/10.1016/j.compositesa.2016.06.023
[19] Zhuang W, Zhang H, Wang E, Chen S, Liu Y. A progressive damage model for carbon fiber-reinforced polymer laminates subjected to fastener pull-through failure. Compos Struct. 2023 Dec 15;326. https://doi.org/10.1016/j.compstruct.2023.117623
[20] Gu J, Chen P, Su L, Li K. A theoretical and experimental assessment of 3D macroscopic failure criteria for predicting pure inter-fiber fracture of transversely isotropic UD composites. Compos Struct. 2021 Mar 1;259. https://doi.org/10.1016/j.compstruct.2020.113466
[21] ASTM International. ASTM D5961/D5961M - Standard test method for bearing response of polymer matrix composite laminates. West Conshohocken, PA; 2003.
[22] Pinho ST, Dávila CG, Camanho PP, Iannucci L, Robinson P. Failure models and criteria for FRP under in-plane or three-dimensional stress states including shear non-linearity [Internet]. 2005.
[23] Puck A, Kopp J, Knops M. Guidelines for the determination of the parameters in Puck's action plane strength criterion. Compos Sci Technol [Internet]. 2002;62(3):371-8. https://doi.org/10.1016/S0266-3538(01)00202-0
[24] Puck A, Schürmann H. Failure analysis of FRP laminates by means of physically based phenomenological models. Compos Sci Technol [Internet]. 1998;58(7):1045-67. https://doi.org/10.1016/S0266-3538(96)00140-6
[25] Siemens Digital Industries Software Inc. Simcenter Femap versão educacional 2021.2. 2021. Femap 2021.2 Help: 4.2.4.2 Plane element properties.
[26] Gurit Ltd. SE84LV low temperature cure epoxy prepreg. Wattwill: Gurit; 2017.
[27] Marques BMF. Análise do coeficiente de torque e do pré-carregamento resultante em juntas aparafusadas de compósito polimérico reforçado com fibra de carbono [Tese (Doutorado)]. [Guaratinguetá]: Universidade Estadual Paulista; 2022.

[28] Aerospace Industries Association of America Inc. NAS6203 thru NAS6220: bolt, tension, hex head, close tolerance, alloy steel, short thread, reduced major thread dia., self-locking and non-locking, 160 KSI Ftu. Arlington: AIA; 2013.
[29] Aerospace Industries Association of America Inc. NAS1149 - washer, flat. Arlington: AIA; 2008.
[30] AZoM. AISI 4340 alloy steel (UNS G43400) [Internet]. 2012 [cited 2024 Jan 15].
[31] Montagne B, Lachaud F, Paroissien E, Martini D. Failure analysis of composite bolted joints by an experimental and a numerical approach. In: Proceedings of the 18th European Conference on Composite Materials (ECCM18); 2018 Jun 24-28; Athens, Greece. p. 1-8.
[32] Park SM, Jeon JH, Choi WJ. Study on bearing strength and failure modes of single bolted joint carbon/epoxy composite materials. Polymers (Basel) [Internet]. 2024;16(6). https://doi.org/10.3390/polym16060847
[33] Sebaey TA, Blanco N, Lopes CS, Costa J. Numerical investigation to prevent crack jumping in double cantilever beam tests of multidirectional composite laminates. Compos Sci Technol. 2011 Sep 9;71(13):1587-92. https://doi.org/10.1016/j.compscitech.2011.07.002
[34] Dogan C, Kaman MO, Erdem S, Albayrak M. Comparison of Hashin and Puck criterions for failure behavior of pin loaded composite plates. Materwiss Werksttech [Internet]. 2024 Mar 1;55(3):314-29. https://doi.org/10.1002/mawe.202300104
[35] Gao G, An L, Giannopoulos IK, Han N, Ge E, Hu G. Progressive damage numerical modelling and simulation of aircraft composite bolted joints bearing response. Materials. 2020;13(24). https://doi.org/10.3390/ma13245606

Research on Engineering Structures & Materials
www.jresm.org
Research Group

Research Article

The effects of the quality of recycled aggregates on the mechanical properties of roller compacted concrete

Selma Kaabeche*, [a], Mebarek Belaoura[b,c]

Public Works Laboratory Transport and Environment Engineering LTPiTE, National School of Built and Ground Works Engineering, Algeria

Article Info

Article history:

Received 18 Apr 2024
Accepted 06 July 2024

Keywords:

Roller compacted concrete;
Recycled aggregates;
Water absorption;
Old mortar

Abstract

This study investigates the performance of roller compacted concrete (RCC) made with recycled aggregates derived from crushed demolished concrete with various proportions of natural. The experimental study examines substituting various proportions of natural aggregate (3/8, 8/15, and 15/20) with recycled aggregate. The replacement rates range from 0% to 100% in increments of 25%. Eleven different mixtures have been made by changing the amount of recycled aggregate used, with and without pre-wetting, before being added to concrete. Additionally, 5% of the cement content was substituted with silica fume and slag in each composition. An experiment test was done to see how recycled aggregate-based BCRs' performance changed with the incorporation rate on fresh and hardened concrete's mechanical and physical properties. Physical parameters, including volume masse, vebe time consistency, and mechanical properties such as compression resistance, flexion resistance, and ultrasonic pulse speed, were measured over time. The results found were compared to the control mix made with 100% natural aggregates. Those results show that as the replacement rate increases, the water absorption rate increases with a decrease in mechanical strength. In addition, the pre-wetting treatment did not significantly impact mechanical strength. This can be explained by the characteristics of the recycled aggregate, such as high absorption, low resistance to wear, and low density, which were caused by the residual paste adhered to the recycled aggregate.

1.Introduction

Protecting the environment is absolutely essential to human being. Modern construction standards with several considerations, including environmental awareness, protection of natural resources, and sustainable development. Hence, it is crucial to minimize the use of natural resources and implement effective strategies to manage and recover solid waste. Today, concrete is the most widely used as construction material in the world, 4 to 10 times more than metals and 10 to 30 times more than cardboard or plastic[1] Moreover, aggregates represent the majority of the volume of concrete [2]; As a result, there is a huge demand for aggregates in the construction field. To meet this demand, it is essential to limit the use of natural aggregates and maximize the use of recycled aggregates. The increasing use of natural coarse aggregates is causing ecological disruption. Therefore, the utilization of alternative resources in the construction industry is imperative. Numerous studies have shown a keen interest in this field, whereby environmental preservation has emerged as a significant target, specifically regarding the use of recycled concrete aggregates (RCA) [2].

*Corresponding author: s.kaabeche@enstp.edu.dz
[a]orcid.org/0009-0005-0008-7411 ; [b]orcid.org/0000-0002-1974-6801; [c] orcid.org/0000-0002-3288-2939
DOI: http://dx.doi.org/10.17515/resm2024.249me0418rs

According to the literature, the European Union and the United States of America produced 850 million tons and 530 of deconstruction waste in 2014, respectively [3]. In comparison, the amount of deconstruction waste generated in 2015 reached a staggering 1.5 billion tons in China. [4]. In Algeria, population growth is accompanied by a growing demand for infrastructure to meet these needs. As a result, the number of construction sites in the field of construction is increasing significantly, increasing the amount of inert waste generated, according to a study implemented by the National Waste Agency. The annual production of inert waste from construction field amounted to approximately 11 million tonnes in 2016 [5]. According to a projected scenario, this production is expected to reach an estimated 27 million tonnes by 2035. Various forms of garbage pose significant difficulties at the end of their lifecycle. A significant quantity of concrete waste is generated as a result of the demolition of ancient concrete edifices. The most common way of disposing of concrete waste is by its deposition in landfills, which causes significant environmental impacts and serious hazards to health [6]. Reusing this material offers the potential to preserve natural resources, thereby improving the sustainability of construction projects [7]. One of the techniques used to protect the environment is recycling inert waste in construction by reusing such materials. Utilizing recycled concrete aggregates (RCAs) is considered as the most efficient method of decreasing the worldwide need for natural aggregate. [8]. This approach has two significant advantages. It helps to reduce the accumulation of debris, which is essential mainly since inert waste constitutes a significant portion of solid waste, and contributes to preserving the environment's visual appeal and ecological characteristics. Also, recycling and reusing construction and demolition waste can reduce energy demand and CO2 emissions. [3,7,8]

Recycled aggregates are characterized by a gang of cementitious paste that adheres to the surface. The principal distinction between RCAs and natural aggregates is the adhering mortar and cement paste. The presence of this adhesive layer on the cover leads to a reduction in the mechanical and physical characteristics of aggregates, in particular their density and ability to resist fragmentation, while at the same time increasing their water absorption capacity. Several researchers have confirmed these findings [9-11]. This study investigates the impact of recycled concrete aggregate (RCA) on the mechanical properties of roller-compacted concrete (RCC) mixes. The research covers a variety of RCC mix designs with both natural and RCA materials. RCC is a type of concrete that can withstand a roller's compaction while remaining unhardened.[12]It consists of the same constituents as conventional concrete, in different ratios: cement materials, both fine and coarse aggregates, water, and, if necessary, chemical admixtures.[13,14] It is typically laid by asphalt pavers and compacted using vibratory rollers, and a similar slump cannot measure its workability because it has zero slump. The workability or consistency of this type of concrete is frequently evaluated using a vibrating table test. This test involves measuring the vibratory time, which refers to the period of vibration required to create a mortar ring inside the specimen[15]. Multiple parameters, including aggregate gradation, water content, cement content, additive content, and the presence of admixtures, may impact the consistency of a roller-compacted concrete (RCC) mixture [16,17]. The first use of a non-slump mixture goes back to the 1960s, with the construction of the Alpe Gere dam in Italy and the Manicouagan I dam in Canada. However, it wasn't until 1970 once the subject became more appealing when Raphael presented an edit for the "optimum gravity dam" concept. After a considerable amount of ten years focused on research and development in different countries of the world, dam building with RCC was acknowledged as the most economical approach[12]. RCC mixes usually have a lower cement content than conventional concrete. This considerably reduces problems caused by the heat of cement hydration. In addition to their positive economic impact, these properties also contribute to the reduction of CO_2 emissions and atmospheric pollution. [13,18,19]. The significant growth and widespread application of this particular type of concrete it's due to the

exceptional performance and low cost compared with other types of concrete. According to an economic study, the initial cost of roller compacted concrete RCC pavements is approximately 30% less than that of conventional asphalt pavements and around 10 to 20% lower than the costs of conventional Portland cement concrete pavements [13]. The RCC is now used in many constructions, including dams, heavily trafficked roads, highway borders, city streets, and rural highways. In industrial applications such as wood storage areas, port infrastructure, storage car parks, sheds, and airport corridors. [20-23].

The study involved the use of recycled aggregates obtained from a landfill as a replacement for natural aggregates in the production of roller-compacted concrete. Eleven different formulations have been developed by varying the proportion of recycled aggregates, both with and without treatment, in order to assess the effect, the quality of recycled aggregate Furthermore, adjustments were made to the cement content by incorporating silica fume and slag at a 5% substitution rate. The primary aim of this is present research is to improve the mechanical properties of the concrete. The purpose of these formulations was to evaluate the impact of different quantities of recycled aggregates on the physical and mechanical characteristics of concrete at different levels of replacement.

2.Methodology

2.1. Material

A combination of materials was employed to prepare RCC specimens for this study. These materials included water, cement, natural aggregates (NA), recycled aggregates (RA), a setting retardant, silica fume, and slag. Also, two types of aggregate were employed.

2.1.1. Cement

The present research takes into account the use of Portland cement CEM II/B L 42.5 N, which was obtained from the LAFARGE firm in Algeria. A dosage of 300 kg/m^3 was used in all the mixes. Cement's Blaine surface was 4238 m^2/kg, and its bulk density was 3013 kg/m^3. Table 1 presents the chemical composition.

Table1. Characteristics and composition of the used cement

Fe_2O_3 (%)	SiO_2	Al_2O_3 (%)	SO_3 (%)	MgO (%)	CaO (%)	LOI (%)	K_2O	Free CaO	NaO_2	Vol. masse (g/cm^3)	Specific surface Blaine (cm^2/g)
2.88	17.45	3.99	2.26	1.66	61.51	10.75	00	1.71	0.52	3,01	4238

2.1.2. Mineral Additive

Silica Fume

The silica fume used in the present investigation is a grey powder acquired from microsilica sourced from the GRANITEX firm. Analysis shows that the surface has a mass of 19785 g/cm^2 and a density of 2.23 g/cm^3

Slag

The blast furnace slag used in this research is sourced from the El Hadjar steel plant. The substance has a density of 2.8 g/cm^3 and a Blaine-specific surface area measuring 3600 cm^2/g.

2.1.3. Chemical Admixture

This study used a setting retarder (SR) as a chemical admixture. The SR serves the purpose of reducing water content. It is known as "SIKA PLASTIRETARD" in Algeria. Table 2 provides an overview of the properties associated with this SR.

Table 2. Properties of the chemical admixture used

Density	1,175 ±0,015
PH	8,5 à 10,5
Chloride continent	≤ 0,1%
equivalent sodium oxide	≤ 6,0%
Dry solid content	31±2%

2.1.4. Natural Aggregates

Sand and natural aggregates were extracted from the Ouled Sidi Brahim M'sila quarry. The sand had a diameter of 4 mm. Crushed rock and coarse natural limestone aggregates (NA) varied in size from 4 to 20 millimeters. Figure 1 presents the distribution of particles used for this project: (3/8), (8/15), and (15/20).

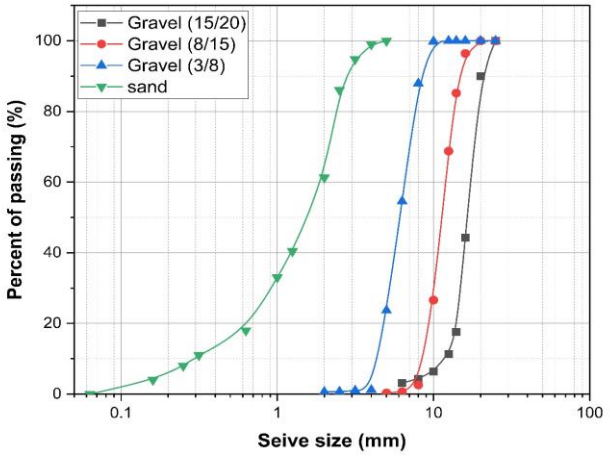

Fig. 1. The granulometric curve of the NA used

2.1.5. Recycled Aggregates

The recycled aggregates came from Algeria's Hamici Zerlada landfill (Fig.2). The aggregates recovered are crushed demolition and deconstruction concrete aggregates that have been recycled. A procedure was implemented to achieve the desired fractions of recycled aggregates by cleaning and washing the recycled waste. The process involved the removal of plastic, glass, and wood contaminants, resulting in a clean material ready for further processing.

Fig. 2. Recycled aggregates recovered from Construction and Demolition Waste (CDW)

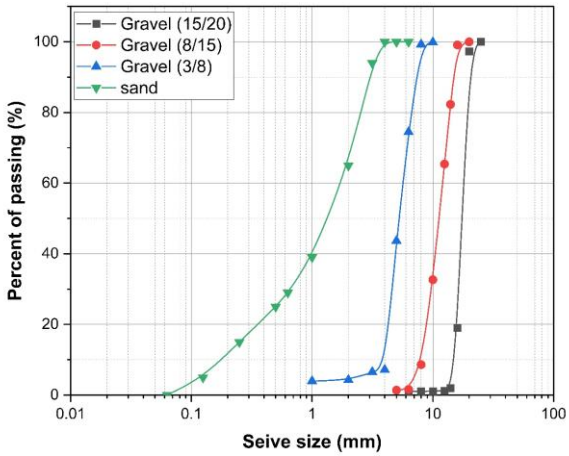

Fig. 3. Particle size distribution curves of the RCA used

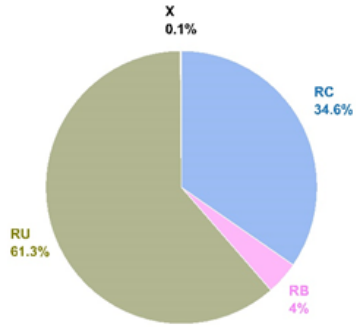

Fig.4. composition of recycled aggregate in accordance with standard EN 933-11

Table 3. Properties of natural and recycled aggregates

Properties	NA			RA			NS	RS	Test method
	3/8	8/15	15/20	3/8	8/15	15/20			
Absolute volumetric mass (kg/m³)	2,73	2,71	2,83	2,72	2,72	2,69	2,72	2,69	EN12697-6
SSD density (g/cm³)	2,65	2,64	2,75	2,50	2,53	2,53	2,64	2,47	EN12697-6
Water absorption (%)	1,65	1,41	1,30	5,43	4,58	3,91	1,78	5,52	EN12697-6
Acid-soluble sulphate content (% SO3)		0.0011			0.9898		-	0.8446	EN 1744-1
% MO		0.7512			2.7272		0.4003	4.9222	EN 1744-1
Sand equivalent	_	_	_	_	_	_	71.43	60,65	EN 933-8
Los-Angeles (%)		29.5			33.83		-	-	EN 1097-2
Micro-Deval (%)		12.96			34.4		-	-	EN 1097-1

Table 4. RCA composition according to EN 933_11

Composition	%
R_c: Concrete masonry units, mortar, and concrete-based materials	35
Ru: Aggregates that have been treated with hydraulic binders include untreated gravel and natural stone.	62
R_b: Clay materials, such as bricks and tiles Masonry made of calcium silicate Aerated concrete that is not floatable	4
X: Other: Cohesive, Miscellaneous: metals (ferrous and non-ferrous)	0,13
R_g: Glass	0

The rubble was then sieved through a 20-mm sieve to eliminate rejected particles. Subsequently, a series of sieves were used to obtain the four desired fractions: sand (0/4), aggregates (3/8), (8/15), and (15/20). However, because of its high capacity for water absorption and less desirable chemical properties, including a high organic material content compared to standard recommendations, it was determined that recycled sand would not be used in this research. The mechanical, chemical, physical, and characteristic properties of these materials are given in Table 3. Table 4 and Figure 4 present the composition of recycled aggregates as described in the standard [24].

2.2.Mix Design

In order to reach the main objectives of this research, a total of eleven mixtures were prepared. Table 4 presents the proportions of each mix investigated in this study. Roller-compacted concrete (RCC) should be between 12% and 16% of its dry mass made up of cementitious materials, according to research that has already been done and best practices for mix design [12, 13, 20, 25] . To carry out this study, a mean of these factors was chosen, and the cementitious material content stayed at 15% throughout all mix proportions. This includes cement and other cementitious materials like slag and silica fume. In this study, the RCC mix had a cement content of 15%.The LCPC laboratory conducted a compaction test on a shake table to determine the relative proportions of the various aggregate classes, aiming to improve the density of the mixture. [26]This experiment test assesses the degree of compactness of a defined granular mass fraction when subjected to a standardized mechanical load within a cylindrical container. After determining the compactness of each class, tests were conducted to determine the maximum compactness of each mixture. These tests assessed the compactness of both recycled and natural granular mixtures. Subsequently, the fractions were quantitatively analyzed and compared to the recommended granular spindle outlined in the standard [25]. This evaluation was carried out to verify whether the mixtures adhered to the specified standards, ensuring optimal compactness. Figure 5 shows the aggregates' granulometry and the upper and lower limits determined by the standard [25] .

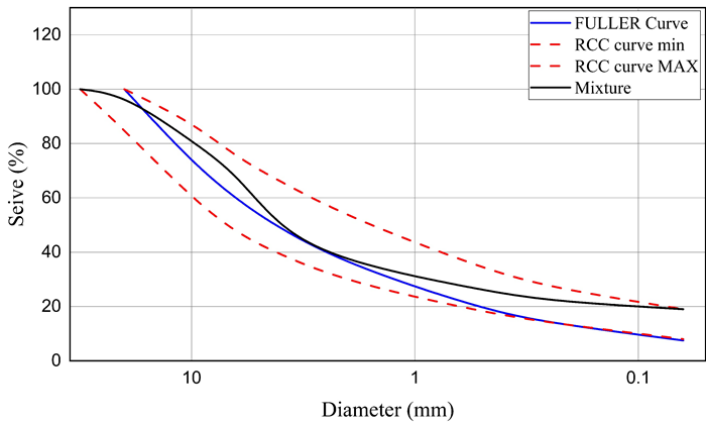

Fig. 5. Mixing curve used for the present research

After estimating the aggregate quantities, the cement dosage was determined to be 300 kg/m³. The water quantity was calculated using the Proctor-modified standard [27]. In general, the cement content of RCC pavement ranges from 8% to 12% [12], [25] .For this study, a cement composition containing 15% of cement was used. The compressive strength test showed that a cement concentration of 300 kg/m³ and an optimal water content of 5.3% reached the best compressive strength for RCC after seven days. Table 5

presents full details about each concrete mix, including the specific composition, proportions, and water/cement (W/C) ratios.

Table. 5. The groupings, titles, proportions, water/cement ratios, and material for each mix

Type of concrete	W/C	NG (%)	RG (%)	NS (%)	Proportions (kg/m³)					
					3/8N	3/8 R	8/15N	8/15R	15/20 N	15/20 R
RCC0	0,46	100	0	986	495	0	356	0	144	0
RCC25	0,48	75	25	986	371	124	267	89	108	36
RCC50	0,50	50	50	986	248	248	178	178	72	72
RCC75	0,53	25	75	986	124	371	89	267	36	108
RCC100	0,54	0	100	986	0	264	0	386	0	259
RCC25SF	0,48	25	75	986	371	124	267	89	108	36
RCC50SF	0,50	50	50	986	248	248	178	178	72	72
RCC25S	0,48	25	75	986	371	124	267	89	108	36
RCC5OS	0,50	50	50	986	248	248	178	178	72	72
RCC25 PREW	0,41	25	75	986	371	124	267	89	108	36
RCC50PREW	0,42	50	50	986	248	248	178	178	72	72

The procedure for mixing the eleven mixtures consisted of using a concrete mixer. The mixtures were divided into three different groups. The first group included five mixtures in which the aggregates were substituted with different proportions of recycled aggregates: 0%, 25%, 50%, 75%, and 100%.

Table. Mixing method

1 minute of mixing	1 minute of mixing	1 minute of mixing	2 minutes of mixing	0 min
Aggregates	Cement	rest	Water + adj	Mix

In the second group of experiments, additional silica fume (SF) and slag (S) were added at a proportion of 5% to replace cement in the concrete mixtures, which contained 25% and 50% recycled aggregates. Finally, the third group was subjected to a preliminary pre-wetting (PREW) treatment of recycled aggregates for 48 hours before being implemented into the mixtures, which contained 25% and 50% recycled aggregate following the mixing protocol described in Table 6. After mixing, as described in the table above, the concrete was placed in the cubic moulds in four layers, while the prismatic moulds received the concrete in two layers.

Fig. 6. The vibrating hammer employed for compacting the RCC specimens

The concrete specimens were made using cubic moulds with dimensions of 150 mm × 150 mm and prismatic moulds of 70 mm × 70 mm × 280 mm. Before its use, the moulds underwent a rigorous cleaning procedure and were then treated with oil to eliminate impurities and mitigate the adhesion of concrete to the interior surfaces of the moulds. Fresh concrete was introduced into cubic, prismatic, and cylindrical moulds, then compacted using an electric vibrating hammer with square, rectangular, and circular plates, according to[28] the cast specimens were retained inside the moulds for 24 hours. Subsequently, the moulds were recovered, and the specimens were subjected to a controlled humidity environment for seven, twenty-eight, and ninety days. Three specimens were used for each test.

3. Results and Discussion

3.1. Vebe Time

Consistency is the main factor in determining the buildability of RCC. Because of its stiff to extremely dry consistency, the standard slump test with an Abrams cone is not applicable to this type of concrete. The vebe test[15] is generally used to evaluate the consistency of an RCC mixture. According to the ASTM C1170 Standard Test, in the case of roller-compacted concrete, workability corresponds to the compaction energy required to consolidate the concrete in its fresh state adequately [29]. The procedure consists of placing the specimen of the RCC in a cylindrical mould fixed on a vibrating table figure 7. An overcharge of 22.7 kg is placed on the top of the material. The vebe time is the time of vibration when a mortar ring is observed around the total perimeter of the surcharge.

Table 7. The mean values of compressive, flexural, ultrasonic pulse and vebe time

Mixtures	Compressive strength (MPa)			Flexural strength (MPa)			Ultrasonic pulse velocity (m/s)		
	7_{days}	28_{days}	90_{days}	7_{days}	28_{days}	90_{days}	7_{days}	28_{days}	90_{days}
RCC_0	46,25	56,47	60,41	8,86	9,46	10,30	4941,15	4970,43	5220,61
RCC_{25}	44,74	53,98	59,94	8,39	8,79	9,58	4865,27	4875,82	5102,63
RCC_{50}	43,17	51,06	53,26	7,47	8,72	8,82	4687,55	4871,36	4852,40
RCC_{75}	38,49	46,58	50,62	7,73	8,80	8,86	4604,99	4737,66	4732,51
RCC_{100}	36,48	40,29	47,39	6,92	7,87	8,64	4592,37	4634,04	4713,5
RCC_{25SF}	41,48	53,29	56,58	8,02	8,75	8,88	4931,10	4904,55	5180,98
RCC_{50SF}	41,53	45,69	57,91	7,90	8,70	8,75	4854,89	4876,3	4988,33
RCC_{25S}	40,71	47,34	57,66	8,23	8,51	8,81	4886,95	4840,77	5025,59
RCC_{50S}	37,20	46,79	57,10	8,09	8,14	8,44	4836,41	4869,53	5021,53
RCC_{25PREW}	44,49	45,69	55,05	8,75	8,94	8,7	4719,821	4928,374	4942,146
RCC_{50PREW}	41,16	45,06	51,64	7,07	7,73	8,63	4607,993	4808,467	4855,437

The table below displays the test results, demonstrating the variation in vebe time with the proportion of recycled aggregate substitution. The objective in designing RCC mixtures is to achieve a blend that provides maximum dry density and suitable consistency (vebe time ranging from 30 to 75 seconds). A few lab tests show that a changed vebe time of 30 to 40 seconds for RCC pavement mixtures, measured with a 50-lb (22.7 kg) extra charge, works much better[19] . To investigate the consistency of roller-compacted concrete (RCC) mixes,

through modified vebe tests, the process is conducted ten minutes after the casting process, following the ASTM C 1170 standard.

Fig. 7. Vebe test Apparatus for evaluating consistency of fresh RCC

The primary objective was to evaluate the impact of recycled aggregate substitution on the consistency of RCC mixes. The test results, as presented in Table 8, revealed that increased recycled aggregate substitution led to higher optimum water contents. Furthermore, it was observed that the vebe times for mixtures with a high substitution of recycled aggregates decreased when compared to the control specimen. This was due to the mixtures having a higher optimum water content. In the context of the vebe test, a decrease in the vebe time reflects a wet consistency of the mixture, while an increase in this parameter indicates a dry or rigid mixture consistency. The comparison of vebe time between the two concrete mixes, RCC_{75} and RCC_{50SF}, shows that water quantity, aggregate gradation, and fine content have a significant impact.

Table 8. The results of Vebe time

Mixes	Vebe time(s)
RCC_0	43
RCC_{25}	42
RCC_{50}	39
RCC_{75}	36
RCC_{100}	31
RCC_{25SF}	43
RCC_{50SF}	40
RCC_{25S}	41
RCC_{50S}	35
RCC_{25PREW}	30
RCC_{50PREW}	28

The vebe time for RCC_{50} is 36 seconds, while for RCC_{50SF}, it is 40 seconds. The difference suggests that the mixture with a greater number of fines takes longer to settle and compact, possibly due to the increased surface area of the fine particles. These results are consistent with the findings obtained by [16], who found a decrease in vebe time with increased water content. Using silica fume in RCC_0 and RCC_{25SF} mixtures resulted in the highest vebe time of 43 seconds. This oddly contrasts with the impact of slag on the consistency properties of RCC mixtures. The addition of silica fume resulted in the mixtures becoming drier, which in turn led to a longer compaction time. This finding suggests that using silica fume in RCC mixtures may pose challenges to fieldwork. This result is based on research by [30], who

observed an improvement in the workability of mixes with 30% pumice substitution, recording an average time of 69 seconds.

In comparison, they recorded an average time of 88 seconds for the C12S10 mix. These findings confirm the observations regarding the use of silica fume. As the substitution of aggregates increases, the vebe time tends to decrease. The RCC_{50PREW} mix has the lowest vebe time of 28 seconds. This reduction may be attributed to the residual water content in the recycled aggregates after pre-wetting them before adding them to the mix. The pre-wetting makes up for the high-water absorption. However, studies have noted that excessive mixing, typically lasting longer than 30 seconds, can lead to segregation in recycled aggregate concrete[31], increased by the compaction vibration from the vibrating hammer. The vibration effect causes the water stored in the aggregates to come out and envelop them, resulting in an excess film of water covering the aggregates. This excess water leads to a higher workability of the concrete, which sets it apart from other mixes and explains the reduction in vebe time. This result aligns with previous research [32], which identified a loss of workability with the increasing substitution of recycled aggregates with the same ration (w/c). The higher water absorption of concrete waste compared to natural aggregates could be the cause of this workability loss.

3.2. Density

It is important to note that RCA may have a lighter specific gravity and may contain adhered old cement mortar, contributing to the reduced density of concrete containing RCA. [33], [34] Researchers suggest that the low specific gravity of recycled concrete aggregates (RCA) may be attributed to the quality of virgin aggregates rather than the quantity of old cement mortar present [35], [36].

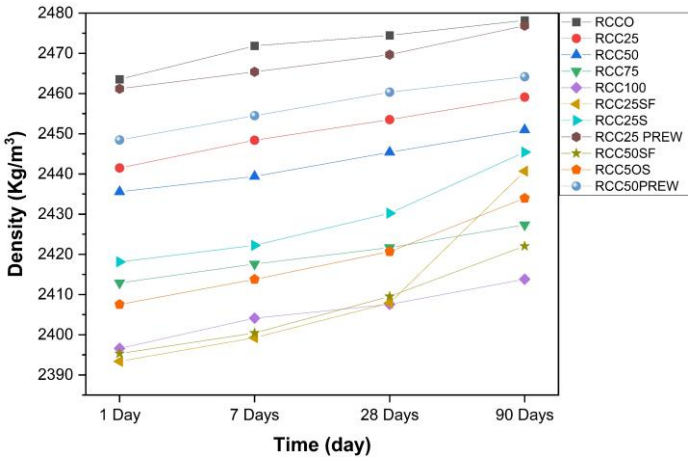

Fig. 8. Variation of the Density according to the rate of substitution of aggregates

During sample preparation, it was observed that integrating recycled aggregates (RA) had a little influence on the wet density. The following figure illustrates the density evolution by substituting recycled aggregates over time. As depicted in Figure 8, the highest density is for the natural aggregate concrete. A decrease of around 3% was observed for the RCC_{100} mix over time, decreasing as the substitution rate increased. A 1% and 2% decrease for the RCC_{25} and RCC_{50} mixes, respectively, was noted. This decrease is attributed to the properties and quantity of the substituted recycled aggregate. The mortar paste adhered to the aggregate makes the density of the aggregate lower than a natural aggregate [37], and this is due to the porosity of the interface between the two materials. However, the

RCC 50_{PREW} mix showed a minor decrease in density due to the pre-wetting process, during which recycled aggregates are saturated before being incorporated into the concrete. The RCC_{25SF} and RCC_{25S} mixes decreased due to the substitution of recycled aggregates and the addition of cementitious materials. Some previous studies on recycled concrete confirm what has been mentioned above. In their study, Maleseva et al. [10] noted a reduction in wet density as the amount of recycled aggregate increased. This effect was observed to be approximately 3% when recycled aggregates entirely replaced natural aggregates. Similar outcomes were reported by [38], indicating a significant reduction in fresh density of approximately 11% due to an increase in the 100% recycled aggregate substitution rate. Furthermore, a decline in the hardened density of approximately 6% was observed in concrete specimens that contained 100% recycled aggregate. Other research developed by Zaetang et al. [39]discovered a 5% decrease in density for concrete substituted with 100% recycled aggregates compared to control concrete. Abraham et al. [40][40] found that as recycled aggregates and fines increased, the fresh density of concrete decreased by approximately 2% and 5%, respectively.

Similarly, the density of hardened concrete dropped by about 5% and 10% for mixtures replaced with 100% recycled granulates without fines and with fines, respectively, after 28 days. Marta Sánchez et al.[37]found that old mortar on recycled aggregates affects concrete density, with increased mortar causing a decrease. Angel Salesa et al.[41] found a 2.54% decrease in SSD for 2nd generation recycled aggregates and 1.45% for RC1, with a 4.03% reduction in dry density compared to control concrete. The above study found that the difference in density depends on the type and amount of aggregate used. The lower specific gravity of the cohesive mortar layer on top of the aggregates causes the density to drop down.

3.3. Compressive Strength

Three groups were tested to evaluate the influence of recycled aggregates (RCA) on the compressive strength of roller-compacted concrete mix (RCC). Ninety-nine cubic specimens with 150 mm x 150 mm dimensions were prepared and subjected to compression testing to assess their resistance at three different periods: seven days, 28 days, and 90 days. These tests were performed according to [42] standards after the curing period, during which the samples were kept in a moist room at 22 °C with a relative humidity of 92%. After the curing period, three samples of each mixture were subjected to testing. The load was applied perpendicular to the surface of the concrete during compaction.

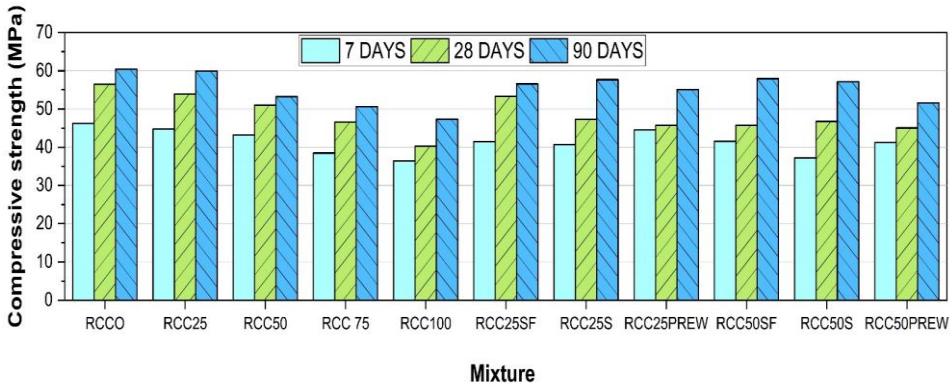

Fig. 9. Compressive strength of Roller-Compacted Concrete (RCC) at various substitution rates

According to the substitution rate, the average 28-day compression resistance losses for RCC mixtures with recycled aggregate compared to RCC mixtures with 100% natural aggregates with a 25% progression were 7%, 10%, 18%, and 29%, respectively. The data from Table 7 and Figure 9 indicates that the mixes with a pre-wetting treatment displayed less favorable results when compared to those without a pre-wetting treatment. A decrease in compressive strength of approximately 12% for the RCC_{50PREW} mixture was observed compared to the untreated RCC_{50} mixture, and a decrease of about 11% for the RCC50S and RCC50SF mixtures compared to RCC_{50}. The higher (w/c) ratio and the inclusion of silica fume and slag in the RCC_{50} mix, which had no impact at the 28-day age, contributed to the latter's strength decrease. It is noteworthy that the inclusion of 5% SF did not affect the compressive strength results of these mixtures. Table 7 presents the compressive strengths of different mixtures after 7, 28, and 90 days of curing. In consideration of the substitution rate, the average 7-day compression resistance losses for RCC mixtures containing 100% natural aggregate until RCC mixtures containing 100% recycled aggregates with a 25% progression were 3%, 7%, 16%, and 22%, respectively. Mixtures containing recycled aggregates, silica fume, and slag exhibit reduced strength due to aggregate substitution and the water-cement ratio(w/c). Experiments tests show that the addition of 5% silica fume and slag has an insignificant effect on strength. It was observed that RCC_{25SF}, RCC_{50SF}, RCC_{25S}, and RCC_{50S} mixes became weaker after 7 and 28 days compared to the reference concrete, indicating a decrease in strength. At seven days, the decreases were 10%, 11%, 12%, and 20%, respectively, while at 28 days, they were approximately 12%, 20%, 16%, and 18%, respectively. Notably, using 5% SF and 5% slag had no significant impact on the compressive strength results. Resistance improved after 90 days of age when mixtures were replaced with silica fume, indicating increased resistance. The decrease amounts to approximately 4% in comparison to the control concrete. The enhancement is due to its high reactivity and pozzolanic qualities, which improve the microstructure of the cement paste and reinforce the link between the aggregates and the cement by closing voids in the concrete [43], [44]. A study by Farshid et al.[30] showed similar results. They showed that replacing 10% of the cement with silica fume (SF) increased the compressive strength of roller-compacted concrete. In contrast, a 5% substitution had no significant effect on strength. Another study [45] documented an increase in the compressive strength of roller-compacted concrete (RCC) with the addition of silica fume (SF). However, another reference [46] reported similar results at a 10% SF cement replacement. For comparative analysis, more research is needed regarding the use of a blend of RCA and slag in the production of RCC. Most existing studies have focused on using RAP or RCA in conjunction with silica fume. The results indicate that a low percentage of slag does not significantly improve resistance. The figure's representation indicates that mixes subjected to a pre-wetting treatment exhibited lower results compared to non-treated mixes.

The RCC_{50PREW} mixture exhibited a 12% reduction in compressive strength compared to the untreated RCC_{50} mixture. Similarly, the RCC_{25PREW} mixture demonstrated an 11% decrease in compressive strength relative to the RCC_{50} mixture. The reduction in strength of recycled concrete aggregates (RCA) can be attributed to various factors, such as the properties of the mortar matrix and the interfacial transition zone (ITZ). The presence of old mortar affects the bond between the aggregate and the new cement in the mix, leading to weakened ITZ behaviour and a subsequent reduction in strength. Additionally, recycled aggregates have high absorption, and the pores in the old mortar weaken the aggregate compared to natural aggregates, resulting in lower density and a higher susceptibility to fragmentation. This ultimately affects the mechanical properties of concrete made with recycled aggregates. When compared to the results of McGinnis et al., who noticed a decrease in strength of around 16 to 26% for substitution rates of 50% and 100%, respectively, similar trends are evident. Other references [34], [47] that reported similar

results attributed the strength loss to variations in humidity, the water-to-cement (W/C) ratio, and the mixing method. These factors all significantly affect compressive strength, causing a substantial decrease after seven days of curing. Vivian et al.[48] attributed the loss in strength to the mixing method, where they observed a 20% improvement in compressive strength using a two-stage mixing approach (TSMA) compared to normal mixing (NMA), which strengthens the interfacial bond. These results are consistent with the findings of [49]. According to the American Concrete Institute (ACI) 325-10R[19], roller-compacted concrete pavements must exhibit a minimum compressive strength of 27.6 MPa after 28 days. According to the data in Table 7, all the mixes achieved the specified limiting level at 28 days.

3.4. Flexural Strength

In order to assess the mechanical properties of a mixture, an experiment test was conducted in accordance with EN standard 12390-5 [50]. The test involved using three prismatic specimens with dimensions of 7x7x28, which were subjected to a three-point bending moment. During the testing process, the force was applied perpendicular to the surface of the compacted specimens. Testing was carried out at three intervals: seven, twenty-eight, and ninety days. The mean of three measurements was calculated for each specimen, and the results are presented in Table 7. The experiment test was implemented to evaluate the performance of the mixtures for flexural strength over time.

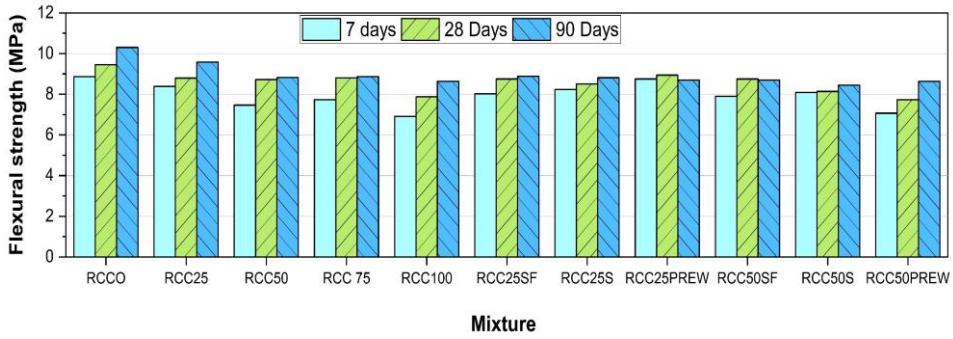

Fig. 10. Flexural strength of Roller-Compacted Concrete (RCC) at various substitution rates

The graphical representation illustrates the flexural strength results of various concrete mixtures. Particularly, the concrete compositions that exhibited the most substantial declines in strength were RCC_{100} and RCC_{50PREW}, with a recorded decrease of 22% and 21%, respectively, compared to the control concrete at seven days of curing. Conversely, the control mixes, namely RCC_0 and the mixtures RCC_{25}, RCC_{25SF}, RCC_{25S}, and RCC_{50PREW}, showed the highest resistance values. Within the first seven days, the reduction in strength was relatively minor, ranging between 3% and 5%. However, RCC_{100} experienced a decline of 17% at the 28 and 90-day marks. It is worth emphasizing that the reduction in strength diminishes over time, with the control concrete exhibiting the maximum strength characteristics among all the mixes. The study's results reveal a close relationship between the concrete's flexural strength and compressive strength, which decreases as recycled aggregates are substituted. However, the decline in strength is comparatively less pronounced than the compressive strength. The concrete mix that included recycled aggregates, identified by RCC100, recorded a 29% reduction in strength compared to the concrete used as a control. A previous study [46] observed a decrease of approximately 36% in flexural strength, which aligns with these findings. In comparison, compressive

strength suffered a decline as high as 70%. According to a study conducted by R.Kumar[51], similar results were found, with a decrease of 20% observed in the mix made with a small recycled granular class, possibly due to the negative impact of cementitious paste on strength. As previously mentioned, a mortar layer attached to the recycled aggregates creates a transition zone (TZ) between the natural aggregates and the cementitious paste, there by influencing the properties of new concrete. The use of recycled aggregates in new concrete results in the creation of a new interface that is directly affected by the moisture content and characteristics of the old concrete. Consequently, the resulting concrete shows a decrease in its overall characteristics and increased water absorption. These findings are compliant with those of earlier studies, such as the ones presented by[28] . Based on the guide for roller-compacted concrete pavements[52] ,the flexural strength of pavement concrete varies between 3.5 and 7 MPa at 28 days. As shown in the figure, the results obtained for the eleven mixes prepared meet the required values, indicating that using recycled aggregates is desirable in pavement concrete.

3.5. Ultrasonic Pulse Velocity

All the concrete samples were subjected to UPV evaluation after being cured for 7, 28, and 90 days. To calculate the velocity of the waves, The distance between the transducers was equivalent to the width of the concrete specimen, which measured 150 mm, was divided by the measured time. Each specimen was examined five times, and the mean values of the results was taken in consideration.

Three cubic samples (150×150×150) mm3 were used for each mixture to determine the ultrasonic pulse velocity. The results for each mixture are the average of three samples at 7, 28, and 90 days. The results of the non-destructive ultrasonic wave propagation test were obtained from the test conducted by EN 12504-4 [53], Figure 1 illustrates the evolution of concrete mixtures' ultrasonic pulse velocity (UPV). It is quite evident from the image that when recycled aggregates substituted natural aggregates, the UPV of concrete mixtures decreased at all test ages.

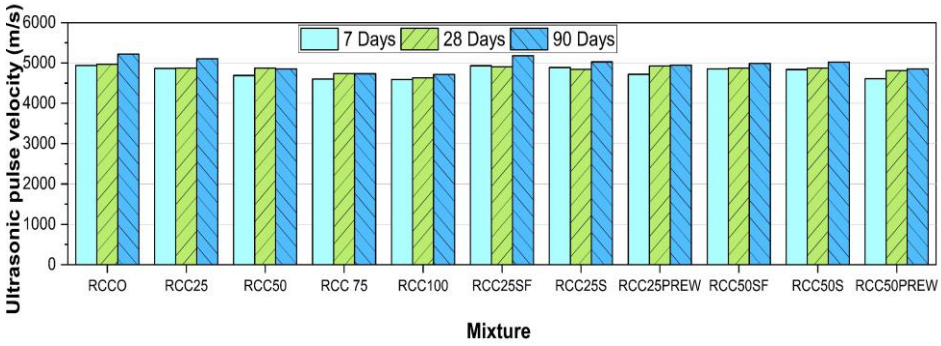

Fig. 11. Progression of UPV with time for RCC mixes

This reduction correlates with the previous mechanical strength findings, in opposition to the results obtained by [54], who noticed a decrease in ultrasonic pulse velocity as strength increased. The results showed a decrease in UPV for concrete with recycled aggregates. The decrease in UPV was significant, with values of 5%, 9%, and 10% for concrete with 50%, 75%, and 100% substitution, respectively, in comparison to the control concrete. However, the decrease was less pronounced for concrete containing silica fume and slag, with a decrease of 3% for RCC_{50S} and RCC_{50SF} mixtures compared to the control concrete. Based on the findings, it has been observed that the ultrasonic pulse velocity (UPV) of

concrete manufactured with recycled aggregate tends to decrease. This can be explained by the fact that recycled aggregate typically has a lower density and greater porosity than natural aggregate. The presence of voids and pores in recycled aggregate leads to a higher degree of attenuation and scattering of ultrasonic waves, thereby reducing UPV values. These findings highlight the need for appropriate selection and processing of recycled aggregates to ensure their compatibility with the desired concrete properties. The velocity of ultrasonic pulses that travel through a solid material depends on the material's thickness and elastic properties.

4. Conclusion

This study has provided empirical evidence supporting using recycled concrete aggregate as a sustainable option for creating new roller-compacted concrete. Its shows that using this method can result in significant reductions in waste production while maintaining similar performance qualities as conventional concrete. The results have potential implications for the construction industry, where the adoption of environmentally friendly techniques is becoming more important. The results obtained from this experimental study led to the following conclusions:

The incorporation of recycled aggregates in concrete is associated with a reduction in its compressive strength. This decrease in strength has been observed to become more pronounced with increased substitution rates However, it is important to note that despite the decrease in strength, the recommended mechanical strengths for roller-compacted concrete were met for all substitution percentages.

- The substitution of aggregates in roller-compacted concrete (RCC) mixes with recycled materials leads to higher optimum waters contents. Additionally, the vebe times tend to decrease as the substitution of aggregates increases, with silica fume mixtures having the longest Vebe times and RCC_{50PREW} mix having the lowest vebe time. This decrease in vebe time is mainly due to the water retained in recycled aggregates and the compaction vibration of the vibrating hammer.
- The moisture content and characteristics of the old concrete have an impact on the new interface that recycled aggregates introduce. This alteration leads to a decrease in the overall characteristics of the concrete.
- Based on the results it has been found that the mechanical properties of concrete remain comparable to those of the control with up to 50% substitution of recycled aggregates. However, beyond this substitution level, there is a noticeable decrease in strength and properties.
- The use of recycled aggregates in concrete production lead to a significant decrease in ultrasonic pulse velocity (UPV), which is mainly due to the lower density and higher porosity of these aggregates compared to natural ones. However, the addition of silica fume and slag can mitigate this decrease to some extent
- Using recycled aggregates in making concrete can result in a gradual reduction in density over time. The RCC0 had the maximum density, and the RCC_{100} had the minimum density, with a 3% decline detected as the substitution rate fell. The drop in density is due to the properties and quantity of the substituted recycled aggregate and the amount of mortar attached to the recycled aggregates used as a substitute.
- The results demonstrate that the flexural strength is comparable to the compressive strength. The study also revealed that the strength of the material decreases with an increase in the substitution of recycled aggregates. However, the drop in strength is less pronounced in flexural strength compared to compressive strength

Based on the positive results obtained from using recycled aggregates in this study, it can be confidently concluded that concrete created with these materials is suitable for practical applications. Utilizing waste by recycling aggregates, rather than using new materials, contributes to the attainment of sustainable development objectives and provides substantial cost reductions in construction. Furthermore, using recycled materials reduces environmental damage and conserves natural resources for subsequent generations.

Acknowledgment

The authors thank the National School of Built and Grounds Works Engineering (ENSTP) for generously funding this research project.

References

[1] Siddique R, Jamal K, Inderpreet K. Use of recycled plastic in concrete: A review Waste management. 2018; 28(10): 1835-1852. https://doi.org/10.1016/j.wasman.2007.09.011
[2] Berredjem L, Arabi N, Molez L. Mechanical and durability properties of concrete based on recycled coarse and fine aggregates produced from demolished concrete. Construction and Building Materials. 2020 Jun;246:118421. https://doi.org/10.1016/j.conbuildmat.2020.118421
[3] Villoria Sáez P, Osmani M. A diagnosis of construction and demolition waste generation and recovery practice in the European Union. Journal of Cleaner Production. 2019 Dec;241:118400. https://doi.org/10.1016/j.jclepro.2019.118400
[4] Ibrahim HA, et al. Hydraulic and strength characteristics of pervious concrete containing a high volume of construction and demolition waste as aggregates. Construction and Building Materials. 2020 Aug;253:119251. https://doi.org/10.1016/j.conbuildmat.2020.119251
[5] Report on the state of waste management in Algeria 2020.
[6] Safiuddin M, Alengaram UJ, Rahman MM, Salam MA, Jumaat MZ. Use of recycled concrete aggregate in concrete: a review. Journal of Civil Engineering and Management. 2013;19(6):796-810. https://doi.org/10.3846/13923730.2013.799093
[7] Behera M, Bhattacharyya S, Minocha A, Deoliya R, Maiti S. Recycled aggregate from C&D waste & its use in concrete-A breakthrough towards sustainability in construction sector: A review. Construction and Building Materials. 2014;68:501-516. https://doi.org/10.1016/j.conbuildmat.2014.07.003
[8] Sereng M, Djerbi A, Metalssi OO, Dangla P, Torrenti JM. Improvement of recycled aggregates properties by means of CO2 uptake. Applied Sciences. 2021;11(14):6571. https://doi.org/10.3390/app11146571
[9] Pedro D, De Brito J, Evangelista L. Influence of the use of recycled concrete aggregates from different sources on structural concrete. Construction and Building Materials. 2014;71:141-151. https://doi.org/10.1016/j.conbuildmat.2014.08.030
[10] Malešev M, Radonjanin V, Marinković S. Recycled concrete as aggregate for structural concrete production. Sustainability. 2010;2(5):1204-1225. https://doi.org/10.3390/su2051204
[11] Berredjem L. Contribution à l'étude des propriétés des mortiers et bétons à base de granulats recyclés et leurs durabilités. 2018.
[12] ACI Committee. Roller-compacted Mass Concrete. American Concrete Institute; 1999.
[13] Modarres A, Hosseini Z. Mechanical properties of roller compacted concrete containing rice husk ash with original and recycled asphalt pavement material. Materials & Design. 2014;64:227-236. https://doi.org/10.1016/j.matdes.2014.07.072
[14] Rambabu D, Sharma SK, Akbar MA. Evaluation of roller compacted concrete for its application as high traffic resisting pavements with fatigue analysis. Construction and

Building Materials. 2023 Oct;401:132977. https://doi.org/10.1016/j.conbuildmat.2023.132977
[15] ASTM C1170/C1170M-08. Standard test method for determining consistency and density of roller-compacted concrete using a vibrating table. 2020.
[16] Chhorn C, Lee SW. Consistency control of roller-compacted concrete for pavement. KSCE Journal of Civil Engineering. 2017;21(5):1757-1763. https://doi.org/10.1007/s12205-016-0820-y
[17] Husein Bayqra S, Mardani-Aghabaglou A, Ramyar K. Physical and mechanical properties of high volume fly ash roller compacted concrete pavement (A laboratory and case study). Construction and Building Materials. 2022 Jan;314:125664. https://doi.org/10.1016/j.conbuildmat.2021.125664
[18] Lopez-Uceda A, Agrela F, Cabrera M, Ayuso J, López M. Mechanical performance of roller compacted concrete with recycled concrete aggregates. Road Materials and Pavement Design. 2018;19(1):36-55. https://doi.org/10.1080/14680629.2016.1232659
[19] Arent WL, et al. State of the art report on roller compacted concrete pavements. ACI Materials Journal. 1994;91(5):509-516. https://doi.org/10.14359/9760
[20] Hossain MS, Ozyildirim HC. Roller Compacted Concrete Pavement in Virginia. In: Airfield and Highway Pavements 2015. 2015. p. 429-440. https://doi.org/10.1061/9780784479216.039
[21] Kim YS. Roller-compacted concrete shoulder construction on interstate highway in Georgia. Transportation research record. 2007;2040(1):71-79. https://doi.org/10.3141/2040-08
[22] Park JY, Lee SW, Han SH, Kim YK. Fatigue behavior of roller-compacted concrete pavement based on full-scale fatigue test. Journal of Testing and Evaluation. 2020;48(4):2895-2907. https://doi.org/10.1520/JTE20170522
[23] Naik TR, Chun YM, Kraus RN, Singh SS, Pennock LLC, Ramme BW. Strength and durability of roller-compacted HVFA concrete pavements. Practice Periodical on Structural Design and Construction. 2001;6(4):154-165. https://doi.org/10.1061/(ASCE)1084-0680(2001)6:4(154)
[24] EN. 933-11 Tests for Geometrical Properties of Aggregates-Part 11: Classification Test for the Constituents of Coarse Recycled Aggregate. London, UK; 2009.
[25] NORME. NF P98-128 Road foundations. Road roller compacted concretes and high performances Cementitious granular material. Definition. Composition. Classification. 2014.
[26] Ledee V, De Larrard F, Sedran T, Brochu F. Essai De Compacité des fractions granulaires à la table à secousses: Mode opératoire. TECHNIQUES ET METHODES DES LABORATOIRES DES PONTS ET CHAUSSEES-METHODE D'ESSAI. 2004;ME 61.
[27] ASTM Committee D-18 on Soil and Rock. Standard Test Methods for Laboratory Compaction Characteristics of Soil Using Modified Effort (56,000 Ft-Lbf/Ft3 (2,700 KN-M/M3)). ASTM international; 2009.
[28] ASTM International. Standard practice for molding roller-compacted concrete in cylinder molds using a Vibrating Hammer, ASTM C1435/C1435M-08. ASTM West Conshohocken, USA; 2008.
[29] Gauthier P, Marchand J. Conception et réalisation de revêtements en béton compacté au rouleau au Québec. Association Béton, Québec (ABQ) Québec. 2004;63-87.
[30] Vahedifard F, Nili M, Meehan CL. Assessing the effects of supplementary cementitious materials on the performance of low-cement roller compacted concrete pavement. Construction and Building Materials. 2010;24(12):2528-2535. https://doi.org/10.1016/j.conbuildmat.2010.06.003
[31] Debieb F, Courard L, Kenai S, Degeimbre R. Mechani cal and durability properties of concrete using contaminated recycled aggregates. Cement and Concrete Composites. 2010;32(6):421-426. https://doi.org/10.1016/j.cemconcomp.2010.03.004

[32] Tavakoli D, Dehkordi RS, Divandari H, de Brito J. Properties of roller-compacted concrete pavement containing waste aggregates and nano SiO2. Construction and Building Materials. 2020;249:118747. https://doi.org/10.1016/j.conbuildmat.2020.118747
[33] Wang B, Yan L, Fu Q, Kasal B. A comprehensive review on recycled aggregate and recycled aggregate concrete. Resources, Conservation and Recycling. 2021;171:105565. https://doi.org/10.1016/j.resconrec.2021.105565
[34] Kisku N, Joshi H, Ansari M, Panda S, Nayak S, Dutta SC. A critical review and assessment for usage of recycled aggregate as sustainable construction material. Construction and Building Materials. 2017;131:721-740. https://doi.org/10.1016/j.conbuildmat.2016.11.029
[35] Younis KH, Pilakoutas K. Strength prediction model and methods for improving recycled aggregate concrete. Construction and Building Materials. 2013;49:688-701. https://doi.org/10.1016/j.conbuildmat.2013.09.003
[36] Duan ZH, Poon CS. Properties of recycled aggregate concrete made with recycled aggregates with different amounts of old adhered mortars. Materials & Design. 2014;58:19-29. https://doi.org/10.1016/j.matdes.2014.01.044
[37] De Juan MS, Gutiérrez PA. Study on the influence of attached mortar content on the properties of recycled concrete aggregate. Construction and Building Materials. 2009;23(2):872-877. https://doi.org/10.1016/j.conbuildmat.2008.04.012
[38] Topcu IB, Şengel S. Properties of concretes produced with waste concrete aggregate. Cement and concrete research. 2004;34(8):1307-1312. https://doi.org/10.1016/j.cemconres.2003.12.019
[39] Zaetang Y, Sata V, Wongsa A, Chindaprasirt P. Properties of pervious concrete containing recycled concrete block aggregate and recycled concrete aggregate. Construction and Building Materials. 2016;111:15-21. https://doi.org/10.1016/j.conbuildmat.2016.02.060
[40] Gebremariam AT, Di Maio F, Vahidi A, Rem P. Innovative technologies for recycling End-of-Life concrete waste in the built environment. Resources, Conservation and Recycling. 2020;163:104911. https://doi.org/10.1016/j.resconrec.2020.104911
[41] Salesa Á, et al. Physico-mechanical properties of multi-recycled concrete from precast concrete industry. Journal of Cleaner Production. 2017;141:248-255. https://doi.org/10.1016/j.jclepro.2016.09.058
[42] EN. 13286-41; Mélanges Traités et Mélanges Non Traités aux Liants Hydrauliques-Partie 41: Méthode D'essai pour la Détermination de la Résistance à la Compression des Mélanges Traités aux Liants Hydrauliques. AFNOR: Paris, France; 2021.
[43] Balapour M, Joshaghani A, Althoey F. Nano-SiO2 contribution to mechanical, durability, fresh and microstructural characteristics of concrete: A review. Construction and Building Materials. 2018;181:27-41. https://doi.org/10.1016/j.conbuildmat.2018.05.266
[44] Zhang P, Wan J, Wang K, Li Q. Influence of nano-SiO2 on properties of fresh and hardened high performance concrete: A state-of-the-art review. Construction and Building Materials. 2017;148:648-658. https://doi.org/10.1016/j.conbuildmat.2017.05.059
[45] Fakhri M. The effect of waste rubber particles and silica fume on the mechanical properties of roller compacted concrete pavement. Journal of cleaner production. 2016;129:521-530. https://doi.org/10.1016/j.jclepro.2016.04.017
[46] Ashteyat A, Obaidat A, Kirgiz M, AlTawallbeh B. Production of roller compacted concrete made of recycled asphalt pavement aggregate and recycled concrete aggregate and silica fume. International Journal of Pavement Research and Technology. 2022;1-16. https://doi.org/10.1007/s42947-021-00068-4

[47] Ferreira L, De Brito J, Barra M. Influence of the pre-saturation of recycled coarse concrete aggregates on concrete properties. Magazine of Concrete Research. 2011;63(8):617-627. https://doi.org/10.1680/macr.2011.63.8.617
[48] Tam VW, Gao X, Tam CM. Microstructural analysis of recycled aggregate concrete produced from two-stage mixing approach. Cement and concrete research. 2005;35(6):1195-1203. https://doi.org/10.1016/j.cemconres.2004.10.025
[49] Salas Montoya A, Chung CW, Mira Rada BE. Interaction Effect of Recycled Aggregate Type, Moisture State, and Mixing Process on the Properties of High-Performance Concretes. Case Studies in Construction Materials. 2023; e02208. https://doi.org/10.1016/j.cscm.2023.e02208
[50] EN 12390-5. Testing hardened concrete-Part 5: Flexural strength of test specimens. European Committee for Standardization; 2009.
[51] Kumar R. Influence of recycled coarse aggregate derived from construction and demolition waste (CDW) on abrasion resistance of pavement concrete. Construction and Building Materials. 2017;142:248-255. https://doi.org/10.1016/j.conbuildmat.2017.03.077
[52] Harrington D, Abdo F, Ceylan H, Adaska W, Hazaree C, Bektas F. Guide for roller-compacted concrete pavements. 2010.
[53] EN 12504-4. Concrete Tests-Part 4: Determination of Ultrasonic Pulsed Wave Velocity. 2012.
[54] Kou S, Poon C. Effect of the quality of parent concrete on the properties of high performance recycled aggregate concrete. Construction and Building Materials. 2015;77:501-508. https://doi.org/10.1016/j.conbuildmat.2014.12.035

Research on Engineering Structures & Materials
www.jresm.org
Research Group

Research Article

Optimization of process parameter of FS-welding of aluminum-lithium alloy (AA8090) by using desirability analysis

Munna Singh Dahiya*[,a], Meenu Gupta[b]

Department of Mechanical Engineering, National Institute of Technology, Kurukshetra, India

Article Info

Article history:

Received 11 May 2024
Accepted 07 Aug 2024

Keywords:

FS-Welding;
Central composite design;
ANOVA;
Response surface methodology

Abstract

This study explores the potential of Friction Stir Welding (FSW) for Aluminum Lithium (AA8090) Alloys, emphasizing the crucial role of experimental investigations in optimizing the FSW process. Using a vertical machine center (VMC) with a customized fixture and tool for FSW, factors like Rotational speed (RS), Tilt angle (TA), and Welding Speed (WS) are considered to enhance ultimate tensile strength (UTS) and % elongation (EL). A regression model based on Response Surface Methodology's Central Composite Design (CCD) is used to analyze UTS and % EL. The effectiveness of welded joints is comparable to the parent metal, with optimal UTS and EL achieved at 1428 rpm rotational speed, 36.4 mm/min welding speed, and 1.5° tilt angle. While significant interaction effects are observed in UTS, none are noted in EL. FSW joint performance is evaluated through microstructural analysis, microhardness distribution and fractography analysis.

1. Introduction

FS-welding is a solid-state joining procedure that has received considerable interest in recent years due to its several advantages over traditional welding techniques, such as increased joint strength, decreased distortion and reduced thermal distortion. In a variety of industries, notably aerospace, automobile, marine and defence the method has been used successfully to combine diverse materials, particularly aluminium alloys. With the continuous development of new materials, it is essential to investigate the feasibility and performance of FS-welding for emerging alloys, such as Aluminum Lithium (AA8090) alloys [1]. The fundamental concept of FSW technique is depicted in Figure 1. It consists of a non-consumable rotating tool having a specially designed tool pin and shoulder. Tool pin is plunged into the faying faces of sheets or plates to be joined thus tool moves in the transverse direction along the length. The purpose of this study is to investigate the viability of friction stir welding (FS-welding) of AA8090 Aluminum Lithium alloy and to conduct a comprehensive experimental investigation of the process parameters, microstructural characterization and mechanical properties of the resulting joints. Utilizing the CCD technique of Surface Methodology (RSM), regression design models for UTS and % elongation (EL) of welded joints are developed [2-7]. In addition, microstructural analysis, microhardness distribution and fractography are performed to evaluate the performance of the FS-welding joints and comprehend the links between the process parameters, microstructure and mechanical properties [8-10].

The experimental setup involves using a vertical machine center (VMC) equipped with a custom fixture and tool specifically designed for the FS-welding process [11-12]. During

*Corresponding author: munna_61900003@nitkkr.ac.in
[a]orcid.org/0000-0003-3269-2630; [b]orcid.org/0000-0002-4025-3374
DOI: http://dx.doi.org/10.17515/resm2024.275ma0511rs

the FS-welding process, the VMC is combined with a control system that manages the RS, WS and axial force providing accurate and reproducible outcomes. The precise design of the experimental procedure ensures a stable and evidenced for the FS-welding procedure, which contributes to the dependability and reproducibility of the obtained results.

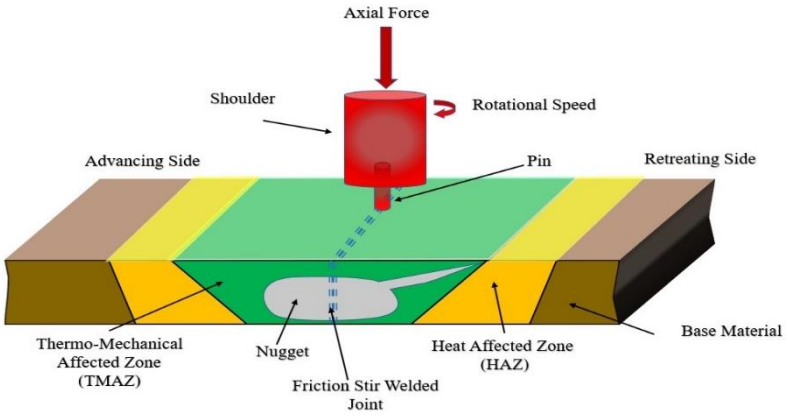

Fig. 1. FS-welding with its components

The outcome of the study discusses the results and focusing on the parametric optimization, microstructural analysis, microhardness distribution, and fractography of the FS-welding joints. Finally, the last part conclusion summarizes the study's conclusions and highlights the implications of the findings for the improvement of FS-welding processes and the potential applications of AA8090 Aluminum Lithium alloys in various industries. Mahto et al. conducted a study to determine the physical parameters of AA 6061-T6 Al-alloy and AISI 304 stainless steel friction stir lap welded joints. The study discovered that faster tool speeds and slower WS led to stronger joints [13]. Verma and Misra studied the FS-welding of dissimilar Al-alloys and found that joint strength is maximized when a stronger Al-alloy is utilized to cover the AS [14]. Verma et al. investigated the temperature distribution during FS-welding of Al-6082 plates using eight L-shaped thermocouples[15]. Verma et al. FS-welding of Al-Mg-Si-Mn alloy (AA6082) for butt joint fabrication[16], while Verma et al. evaluated six different tool pin-geometries for FS-welding of aviation-grade Al-alloy (AA6082) [17]. Verma et al. studied the effects of preheating and water cooling on the properties of friction-stir-welded AA6082 joints[18], and Verma et al. studied FS-welding of aviation grade Al-alloy[19]. Additionally, Verma et al. used a modified vertical milling machine to perform FS-welding on AA7039 plates [20], while Mahto et al. investigated mechanical factors such as ultimate UTS and fractography and the influence of welding and rotating speeds[21]. Raja et al. examined the effect of FS-welding on the microstructure and physical parameters of two Al-alloys with variable hardness levels: AA7475-T651 and AA2219-O.ls [22]. Rajendran et al. investigated the effect of tool TA on the strength of friction stir lap welding of AA2014-T6 Al-alloy[23], while Rajkumar et al. optimized the FS-welding process for dissimilar Al-alloys AA 5052 and AA 6061[24]. Lastly, Mehta and Badheka conducted two studies; one in 2016 [25] to investigate defect development in FS-welding using different tool pin designs and another in 2017 [26] to investigate the dissimilar FS-welding of copper and Al- using nine different tool designs. Overall, these experimental studies prove the potential of FS-welding and highlight the importance of varying process parameters to optimize FS-welding for varied materials and applications. Several studies have used artificial intelligence (AI) techniques, specifically artificial neural networks (ANN) to perfect the FS-welding process and predict the resulting joint properties. Boldsaikhan et al. [27] evaluated the quality of FS-welding

in real-time using feedback signals, achieving high accuracy rates for identifying welds with defects and classifying weld strength. Fratini et al. [28] used an artificial neural network with a finite element design model to forecast the average grain size of FS-welding joints. Both Ghetiya and Patel were present [29] optimized the FS-welding process parameters for an aluminum alloy using an ANN to predict the joint's tensile strength based on input parameters. Wakchaure et al. [30] used Taguchi-based Grey Relational Analysis and ANN to optimize FS-welding parameters, while Alkayem et al. [31] ANN design models were created to predict weld quality based on process characteristics. Kamal Babu et al. [32] ANN and algorithm (GA) techniques were used to optimize FS-welding of cryorolled AA2219 alloy for a defect-free weld junction with optimal strength. Additionally, Masoudi Nejad et al. [33]AA2024-T351's fracture behaviour and fatigue crack propagation rate were explored utilizing ANN to predict the ensuing attributes. Prasanna et al. (2013)[34]examined the impact of heat-treatment techniques and tool pin geometries on FS-welding of AA6061, comparing the mechanical behavior of single-pass and double-pass welded joints. These studies prove the potential of AI techniques to optimize FS-welding and predict resulting joint properties, leading to enhanced quality and cost-effective production. V. Haribalaji et al. perfected the FS-welding process parameters to join dissimilar AA2014 and AA7075 aluminum alloys using the RSM and Taguchi methods. Author found that the WS had a significant influence on the joint strength of the welded alloys [35]. A. Nait Salah et al. perfected the process parameters of FS-welding joints of dissimilar aluminum alloys AA3003 and AA6061 using the RSM. Author found that the RS and WS had a significant effect on the mechanical properties of the welded joints [36]. Sarvaiya and D. Singh proposed a particle swarm optimization algorithm to select the best process parameters in FS-welding/processing. Author found that the proposed algorithm provided a more efficient and accurate optimization process for the selection of the optimal process parameters[37]. M. Simoncini et al. performed an experimental and numerical investigation on forming limit curves of AA6082 aluminum alloy at high strain rates. Author concluded that the forming limit curves of the AA6082 aluminum alloy were significantly influenced by the strain rate[38]. Abd Elnabi et al. investigated the influence of FS-welding parameters on metallurgical and mechanical properties of dissimilar AA5454-AA7075 aluminum alloys. Author concluded that optimizing the FS-welding parameters led to improved mechanical properties and a more refined microstructure[39]. Subramanian et al. used RSM to optimize FS-welding process parameters for dissimilar magnesium alloys. The study showed that optimized parameters significantly improved the weld quality, mechanical properties, and microstructure[40]. Khan) optimized FS-welding of AA6062-T6 alloy, showing that proper selection of process parameters can enhance the mechanical properties of the joint[41]. Haribalaji et al. optimized FS-welding process parameters for joining dissimilar AA2014 and AA7075 aluminum alloys. Author found that optimizing the parameters improved the tensile strength and microstructural characteristics of the joint [42]. The alloys exhibit high strength-to-weight ratios, excellent fatigue properties and reduced density making them suitable for various applications requiring lightweight and high-performance materials. The purpose of this investigation focuses on the benefits of friction stir welding (FS-welding) over conventional welding techniques and stresses the significance of experimental research in enhancing the FS-welding process and the resulting joints.

2. Materials and Methods

2.1. Material

The material used for this study is AA8090 having welding plate's dimensions of 100 mm x 70 mm x 6 mm. Table 1 provides details on the chemical composition and mechanical properties of AA8090.

Table 1. Chemical Composition and mechanical properties of AA8090

Elements	Mg	Si	Li	Zr	Fe	Cu	Zn	Ti	Al
Percentage	0.95	0.20	2.30	0.12	0.33	1.3	0.25	0.10	Bal

Density	Young's Modulus	Poisson's Ratio	Tensile Strength	% Elongation	Hardness (HV)	Shear Strength
2.54 g/cc	77 GPa	0.3	450Mpa	7	158	270Mpa

2.2. Experimental Setup

The present study involves the use of a vertical machine center (VMC) to conduct the FS-welding process and Specifications of Vertical Milling Center (VMC) shown in Table 2. A fixture and tool are specifically designed for this purpose, as shown in Figure 2.

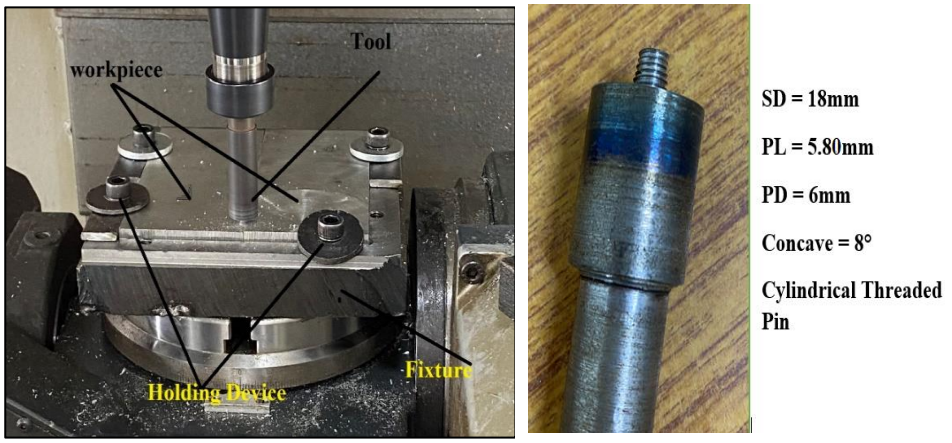

Fig. 2. Fixture and tool used in the FS-welding process

The fixture is designed to firmly hold the workpiece during the FS-welding process, while the tool generates the necessary heat to melt the material and join the workpiece. The tool is mounted on the spindle of the VMC, while the fixture is attached with bed of machine. The VMC is equipped with a control system to regulate the RS, WS and TA applied during the FS-welding process.

Table 2. Specifications of vertical milling center (VMC)

Specifications	Values
Company	MAXMILL++(Vertical Milling Center)
Control system	Siemens 828D
Rpm range	100-8000rpm
Motor capacity	7kw
Programmable feed rate	0-10m/min
X-Axis Travel(Longitudinal Travel)	600mm
Y-Axis Travel(Latitudinal Travel)	450mm
Z-Axis Travel(Vertical Travel)	500mm

2.3. Experiment Design and Procedure

This study uses the design of experiment (DOE) approach, specifically response surface methodology (RSM) to optimize FS-welding process parameters. RSM is a mathematical practice introduced by Box and Wilson in 1951, used to analyze and optimize processes. It is particularly useful when multiple variables significantly influence the process's outcomes. Using RSM, the relationship between input variables and outcomes can be expressed, and an experimental matrix can be designed to determine optimal conditions.

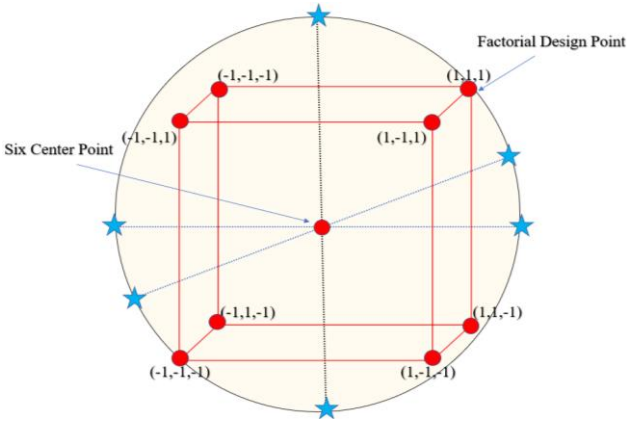

Fig. 3. Design point in CCD

To address the curvature in the response surface, the study adopts a second-order design model with interaction effects. As an economical and precise design technique, central composite design (CCD) is adopted. The experimental matrix is made up of factorial design, star and centre points as well as process variables with varying values of RS, WS and TA. The CCD design is made up of three groups of design points, as shown in Table 3. The CCD approach was used to design a total of 20 tests. Table 5 shows the experimental parameters and matching responses for all 20 studies.

Table 3. Input variables and their values

Symbol	Input Parameter	Units	Level		
			Low	Medium	High
A	RS	rpm	1428	1652	1876
B	WS	mm/min	24.6	36.4	48.2
C	TA	degree	1.1°	1.5°	1.9°

Table 4. Detail of CCD design group

No. of Input Variables (k)	Factorial Points (2k)	Star Points (2k)	Center Points (N)	Total
3	8	6	6	20

Numerous researchers have used a variety of experimental design methods to generate regression equations, but central composite rotatable design (CCD) is regarded as one of the most efficient and accurate design methods. As illustrated in Figure 3, the design incorporates three sets of points, namely factorial design, star, and centre points. As indicated in Table 4, the experiment incorporates three process variables: RS, WS and TA, each with three distinct levels.[2], [4].

Table 5. Experimental design and its results

Exp no.	Coded welding parameters			Value of welded parameters			UTS (MPa)	% Elong. (%)
	RS (rpm) A	WS (mm/min) B	Tilt angle (°)C	RS (rpm) A	WS (mm/min) B	Tilt angle (°)C		
1	-1	1	-1	1428	48.2	1.1	356	7.46
2	0	0	0	1652	36.4	1.5	360	7.23
3	0	-1	0	1652	24.6	1.5	328	5.53
4	1	-1	-1	1876	24.6	1.1	233	3.41
5	0	0	1	1652	36.4	1.9	341	6.73
6	0	0	0	1652	36.4	1.5	371	7.54
7	0	0	0	1652	36.4	1.5	362	6.97
8	1	1	-1	1876	48.2	1.1	316	5.21
9	-1	1	1	1428	48.2	1.9	349	6.88
10	-1	-1	1	1428	24.6	1.9	359	7.31
11	1	1	1	1876	48.2	1.9	333	5.87
12	0	1	0	1652	48.2	1.5	340	6.17
13	1	-1	1	1876	24.6	1.9	281	4.89
14	0	0	-1	1652	36.4	1.1	306	5.79
15	-1	0	0	1428	36.4	1.5	407	8.13
16	0	0	0	1652	36.4	1.5	354	7.27
17	1	0	0	1876	36.4	1.5	343	6.61
18	0	0	0	1652	36.4	1.5	352	7.03
19	0	0	0	1652	36.4	1.5	350	7.05
20	-1	-1	-1	1428	24.6	1.1	353	6.91

2.4. Testing

For the current investigation, rectangular strips of 100×12×6 mm was cut from of the welded sample to use a power hacksaw in order to perform UTS and microhardness testing. Using an end milling on a milling machine, these strips were subsequently turned into tensile specimens in accordance with ASTM E8M-04 and with the orientation of the specimens opposite to the welding direction. Utilizing a servo-controlled universal testing machine, the ultimate tensile and EL of the friction stir-welded joint were measured by UTM (universal testing machine). Figure 4 is a pictorial view of the tensile specimens utilised in the research work.

In this study, rectangular strips measuring 25 mm × 5 mm × 6 mm were cut from the welded plates to prepare the specimens for microstructure analysis. To ensure the surfaces of the specimens were uniform, emery papers with varying grit sizes were used ranging from 200 to 2000. The surfaces were then cloth-polished to make them scratch-free and reflective. Chemical etching with Kroll's reagent was applied to reveal the microstructure and an optical microscope (Conation Technologies) was used to observe and analyze the different welding zones. Figure 5 describes a photographic view of the metallurgical samples. The microstructure analysis is a crucial step for understanding the properties of the welded joint, as it provides essential information about the grain structure, phase composition and other significant characteristics of the material.

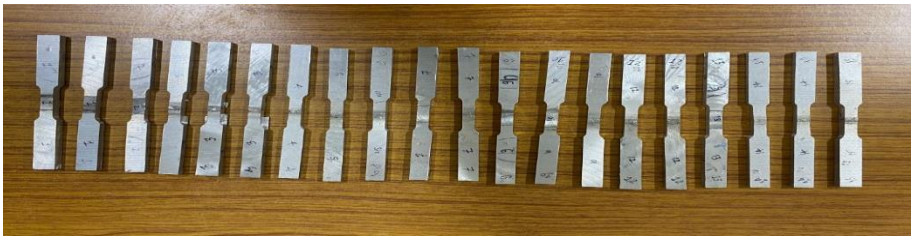

Fig. 4. Photographic representation of tensile specimens

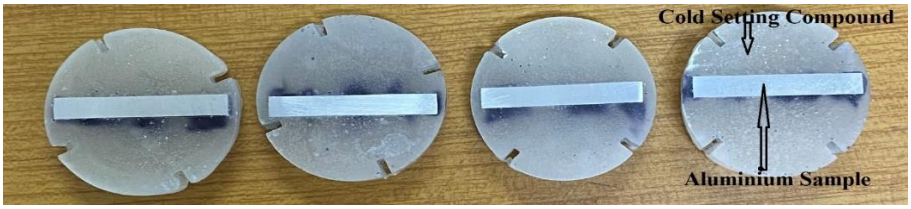

Fig. 5.Photographic depiction of (microstructure and microhardness) samples

The use of emery papers and cloth polishing helps to ensure that the surfaces of the specimens are free from scratches and other surface defects that may affect the accuracy of the analysis. The optical microscope and Kroll's reagent provide a powerful combination of tools for visualizing and analyzing the microstructure of the material.

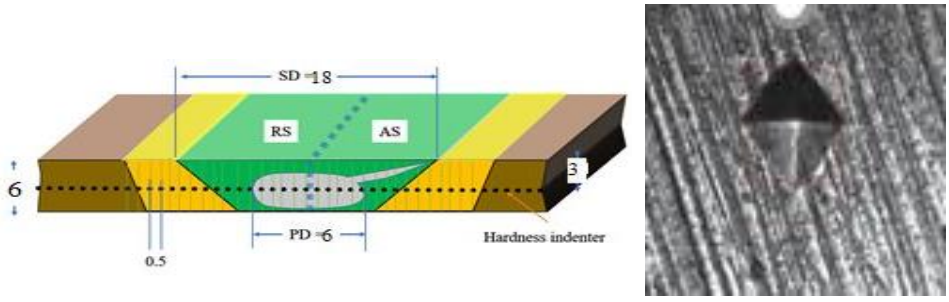

(a) (b)

Fig. 6. The impression of the indenter on the surface of the specimen (a) Schematics diagram of different location for measuring microhardness and (b)Impression indentation

Microhardness testing is a vital method for assessing the mechanical properties and hardness of materials particularly at small scales. The precise Vickers indenter allows accurate measurements providing insights into strength, toughness and other critical properties. Proper sample preparation is crucial to obtain reliable results, as surface defects can affect microhardness measurements. In this study, rectangular strips measuring 25 mm × 5 mm × 6 mm cut from welded plates and prepared with emery sheets of differing grits. Cloth-polishing ensured reflective and scratch-free surfaces. A Vickers microhardness tester analyzed the specimens at a 100 g load yielding precise microhardness measurements. Figures 6(a) and (b) depict the indenter imprint and microhardness distribution points, respectively.

3. Experimental Result and Analysis

The sufficiency test is essential for ensuring the precision and dependability of the design model system. Variables such as sum of the squares (SS), lack-of-fit test and design model descriptive statistic can be used to evaluate the design model's fit. These testing and evaluations are simplified by statistical software.

Table 6. ANOVA for UTS

Independent variable	SS	df	MS	F-value	P-value	
Model (Prototype)	23836.86	9	2648.54	39.69	< 0.0001	Significant
A-RS	10112.40	1	10112.40	151.53	< 0.0001	
B-WS	1960.00	1	1960.00	29.37	0.0003	
C-TA	980.10	1	980.10	14.69	0.0033	
AB	2520.50	1	2520.50	37.77	0.0001	
AC	544.50	1	544.50	8.16	0.0171	
BC	242.00	1	242.00	3.63	0.0860	
A^2	1007.05	1	1007.05	15.09	0.0030	
B^2	1314.55	1	1314.55	19.70	0.0013	
C^2	2880.36	1	2880.36	43.16	< 0.0001	
Residual	667.34	10	66.73			
Lack of Fit	362.50	5	72.50	1.19	0.4269	not significant
Residual error	304.83	5	60.97			
Cor Total	24504.20	19				

Table 7. ANOVA for % elongation

Independent variable	SS	df	MS	F-value	P-value	
Model (Prototype)	22.49	9	2.50	28.22	< 0.0001	significant
A-RS	11.45	1	11.45	129.26	< 0.0001	
B-WS	1.25	1	1.25	14.15	0.0037	
C-TA	0.8410	1	0.8410	9.49	0.0116	
AB	0.8844	1	0.8844	9.99	0.0102	
AC	0.6728	1	0.6728	7.60	0.0203	
BC	0.4050	1	0.4050	4.57	0.0582	
A^2	0.7064	1	0.7064	7.97	0.0180	
B^2	2.82	1	2.82	31.87	0.0002	
C^2	1.00	1	1.00	11.30	0.0072	
Residual	0.8858	10	0.0886			
Lack of Fit	0.6621	5	0.1324	2.96	0.1294	not significant
Residual error	0.2237	5	0.0447			
Cor Total	23.38	19				

In this study, Design-Expert software was used to analyze experimental outcomes and assess design model adequacy. Sum of squares, lack-of-fit test and design model summary statistics were considered. Results indicate that the quadratic design model is suitable for both UTS and EL. Insignificant terms were identified and removed through backward

elimination to enhance design model adequacy. Pooled ANOVA results after elimination are presented in Tables 8 and 9 for UTS and EL, respectively. The adequacy check confirms the design model's suitability for predicting responses across different input parameter combinations.

Table 8. Pooled ANOVA for UTS

Independent variable	SS	df	MS	F-value	P-value		% Contribution
Model (Prototype)	23594.86	8	2949.36	35.68	< 0.0001	significant	
A-RS	10112.40	1	10112.40	122.33	< 0.0001		42.85
B-WS	1960.00	1	1960.00	23.71	0.0005		8.30
C-TA	980.10	1	980.10	11.86	0.0055		4.15
AB	2520.50	1	2520.50	30.49	0.0002		10.68
AC	544.50	1	544.50	6.59	0.0262		2.30
A^2	1007.05	1	1007.05	12.18	0.0051		4.26
B^2	1314.55	1	1314.55	15.90	0.0021		5.57
C^2	2880.36	1	2880.36	34.84	0.0001		12.20
Residual	909.34	11	82.67				3.80
Lack of Fit	604.50	6	100.75	1.65	0.2990	not significant	2.56
Residual error	304.83	5	60.97				1.29
CorTotal	24504.20	19					

Table 9. Pooled ANOVA for % elongation

Independent variable	SS	df	MS	F-value	P-value		% Contribution
Model (Prototype)	22.09	8	2.76	23.53	< 0.0001	significant	
A-RS	11.45	1	11.45	97.57	< 0.0001		51.83
B-WS	1.25	1	1.25	10.68	0.0075		5.65
C-TA	0.8410	1	0.8410	7.17	0.0215		3.80
AB	0.8844	1	0.8844	7.54	0.0190		4.00
AC	0.6728	1	0.6728	5.73	0.0356		3.04
A^2	0.7064	1	0.7064	6.02	0.0320		3.19
B^2	2.82	1	2.82	24.06	0.0005		12.76
C^2	1.00	1	1.00	8.53	0.0139		4.52
Residual	1.29	11	0.1173				5.63
Lack of Fit	1.07	6	0.1778	3.98	0.0757	not significant	4.85
Residual error	0.2237	5	0.0447				1.01
Cor Total	23.38	19					

Table 10. Fit statistics data for UTS, and % elongation

	S.D.	Mean	CV (%)	R^2	Adjusted R^2	Predicted R^2	Adeq. Precision
UTS	9.09	339.70	2.68	0.9629	0.9359	0.8159	27.4999
EL	0.3426	6.50	5.27	0.9448	0.9046	0.7125	21.8585

By dividing the mean square value for the design models by the mean square values of the residuals, the F- value of the design model is calculated. The F- value test is used to look at the relationship between the residual variance and the variance in the design model. The percentage will be close to one if the variances are almost equal, suggesting that the model of design may not have a big impact on the outcomes. The developed design models for UTS and % elongation (EL) have F-values of 35.68 and 23.53%, each with a P-value of less than 0.01. The developed design model has a substantial impact on the outcomes if the Prob > F value is below 0.05, which is the degree of confidence used in this study to determine whether the design model is adequate. The most important terms in the design model for UTS are A, B, C, AB, AC, A^2, B^2 and C^2, whereas the most important terms in the design model for EL are A, B, C, AB, AC, A^2, B^2 and C^2. By dividing each term's sum of square by the sum of squares for the design model, the proportional contribution made by each design modeling term is determined.

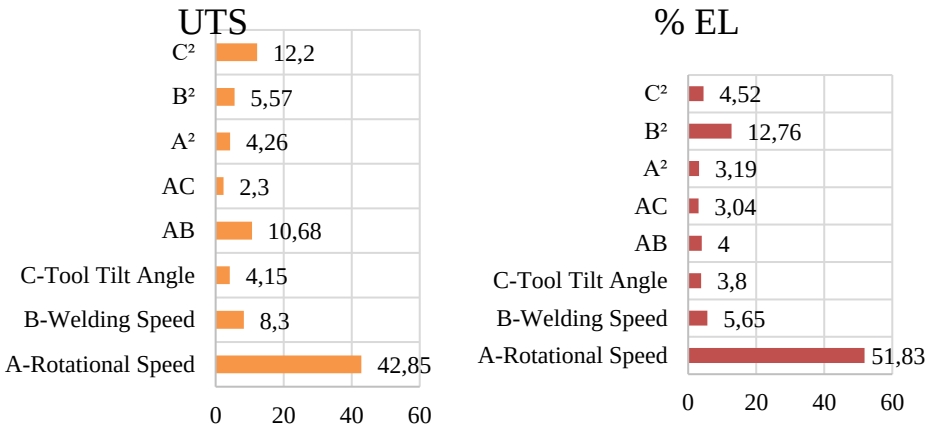

Fig. 7. Contributions of various significant terms for both design models

The contributions of different important variables for both design models are shown in Figure 7 which reveals that RS provides 42.85% for UTS and 51.83% for EL. The design model component is not significant if the p-value is higher than 0.05. According to Tables 8 and 9 the lack of fit F-value for UTS and EL are 1.65 and 3.98, accordingly, indicating a negligible joint with pure error. Noise may be to blame for the lack of fit probability for UTS and EL which are 0.2990 and 0.0757, respectively. The designed models are suitable due to this negligible lack of fit. According to Table 10 the determination coefficients (R^2) for UTS and EL are 96.29% and 94.48%, respectively. A closer fit between the response designing model and the experimental data is shown by higher R^2 values. Less fluctuation between experimental and predicted outcomes can be seen in R^2 values that are closer to 1. R^2 values alone however, should not be taken into account as sufficient for the suitability of the established design model. Therefore, other properties such as for design model adequacy, adjusted R^2, predicted R^2 and adequate precision are also taken into account. Both the predicted R^2 (71.25) and adjusted R^2 (90.46%) for EL and the predicted R^2 (81.59%) and adjusted R^2 (93.59%) for UTS show a high degree of agreement. A signal-to-noise ratio (S/N) value greater than 4 is typically needed to achieve adequate precision.

For UTS and % elongation (EL), the appropriate precision values in this investigation were found to be 27.49 and 21.85, respectively. The generated design models can be used to direct the design space and forecast values for both responses thanks to these high values, which imply adequate signal strength. Both design models' R^2 and adequate precision values highlight how important they are for fitting and forecasting experimental data.

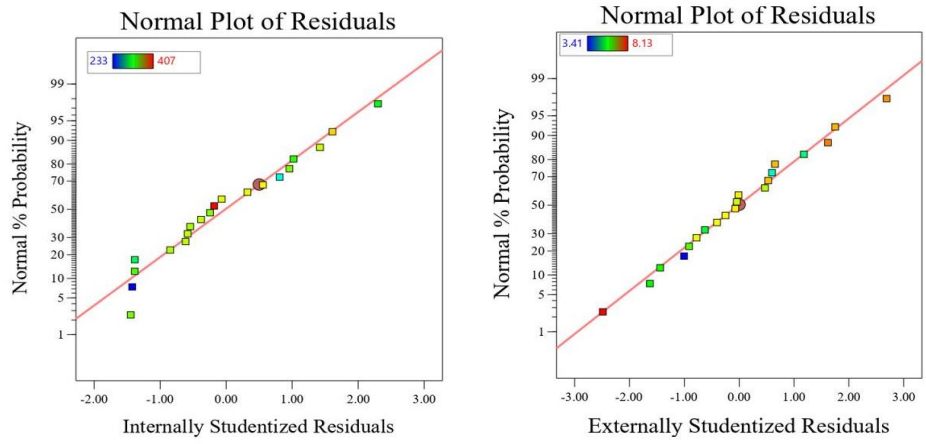

(a)

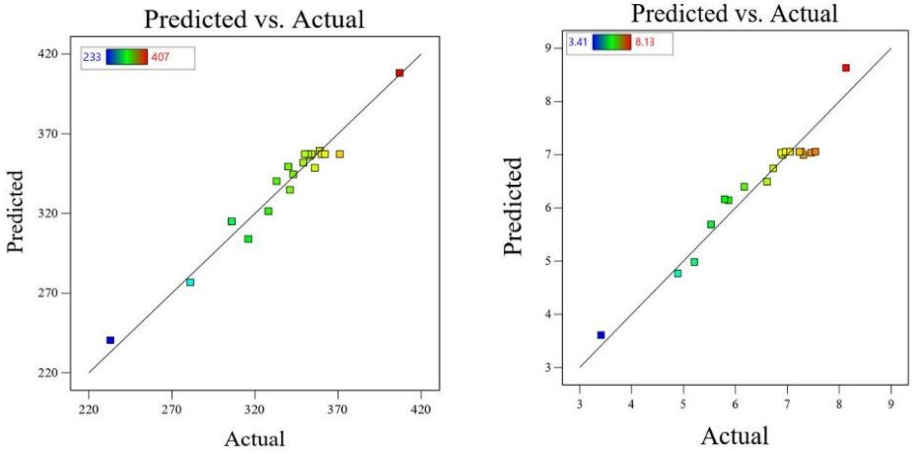

(b)

Fig. 8. Diagnostics plots of UTS and EL (a) normal probability curve (b) predicted vs. actual

$$UTS = +1521.11387 - 1.78461A + 1.52384B + 479.4588C + 0.00671AB + 0.092076AC + 0.000381A^2 - 0.157021B^2 - 202.27273C^2 \quad (1)$$

$$EL = +37.79353 - 0.047584A + 0.351918B + 6.68778C + 0.000126AB + 0.003237AC + 0.000010A^2 - 0.007277B^2 - 3.76989C^2 \quad (2)$$

The normal probability curve for residuals is shown in Figure 8(a), and it shows that for both UTS and EL, residuals are aligned with a straight line and fall within 3 limits. Figure 8(b) shows that for UTS and EL, the predicted values from the design model agree with the experimental values, supporting the validity of the findings from the ANOVA tables. Figures 8 meet the requirements for error normalcy and predictive potential. The regression designs for UTS and EL are shown in equations (1) and (2), respectively.

3.1. Effect of Welding Parameters on UTS

A regression analysis model for UTS is presented in this paper emphasizing the importance of first- and second-order variables as well as the relationship between the tools RS and TA. These terms are significant in the following order: A, B, C, AB, AC, A^2, B^2, and C^2. Variations in joint characteristics occur throughout the FS-welding process due to temperature cycles, cooling speeds and plastic deformation. These modifications also have an impact on the creation, growth, and dissolution of reinforcing precipitates in the NZ.

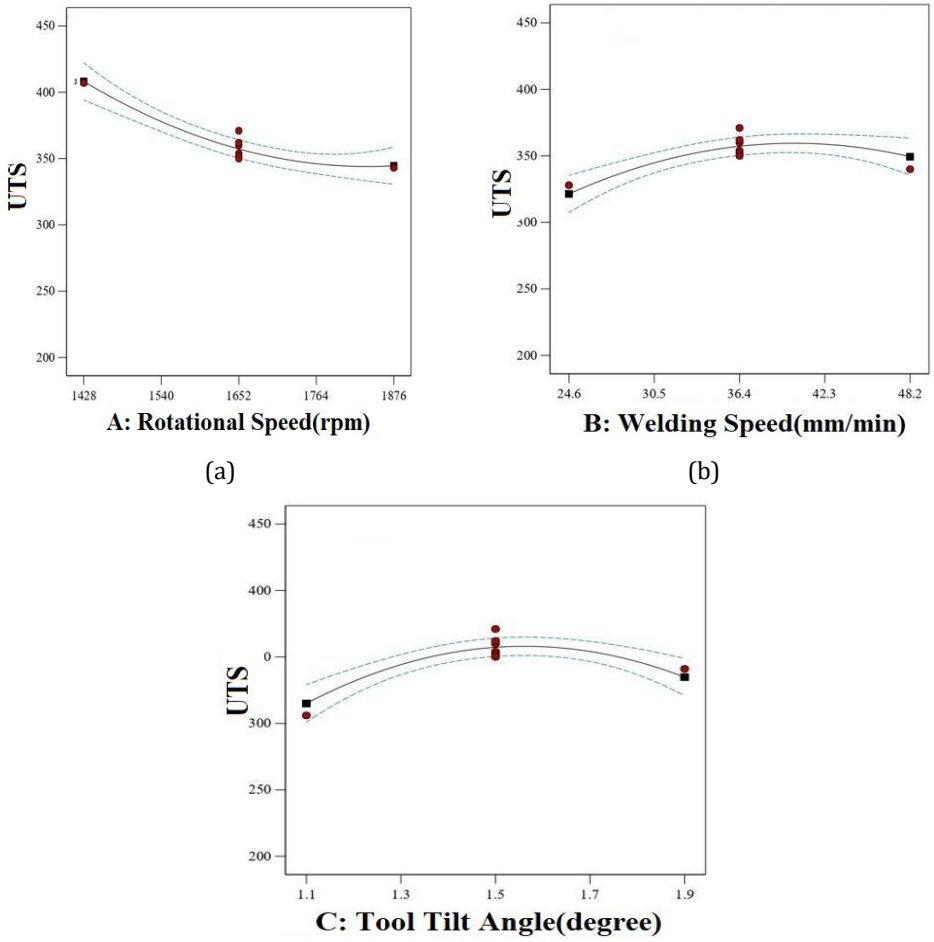

Fig. 9. Performance of overall factors in UTS (a) rotation speed vs UTS, (b) WS vs UTS and (c) tool TA vs UTS

These precipitates dissolve in Aluminium Lithium (AA8090) Alloys during FS-welding mechanical stirring, but the HAZ has a coarser structure. In order to regulate the degree of coarsening, which is controlled by the rate of cooling and thermal cycles throughout the FS-welding process, proper control of temperature is essential.

The Figure 9 highlights the individual effects of process parameters on UTS. Figure 9 (a) describes that UTS decreases significantly when RS increases from 1428 rpm to 1876 rpm. This phenomenon observed by other researchers in precipitation-hardening alloys can be

attributed to the increased heat input resulting from the higher RS [23]. The subsequent turbulence in the NZ causes material to rise to the workpiece's upper surface as flashes, which then creates tunnel defects in the NZ. Out of the 20 experiments conducted in the study only two joint presented tunnel defects all of which were fabricated at the higher RS of 1876 rpm. The tunnel defects contributed to a reduced tensile strength[43], [44]. Figure 9 (b) describes the relationship between WS and UTS showing a minimum UTS at lower WS a sharp increase up to a WS of 36.4 mm/min and a subsequent decline as WS continues to increase.

3.2. Interaction Effects on UTS

3.2.1. RS and WS

Figure 10 depicts how RS and WS affect the UTS of friction stir welded joints with a TA of 1.5°. Maximum joint efficiency is 450 MPa (90%) with low RS and moderate WS measured as the joint's UTS divided by the parent metal's UTS.

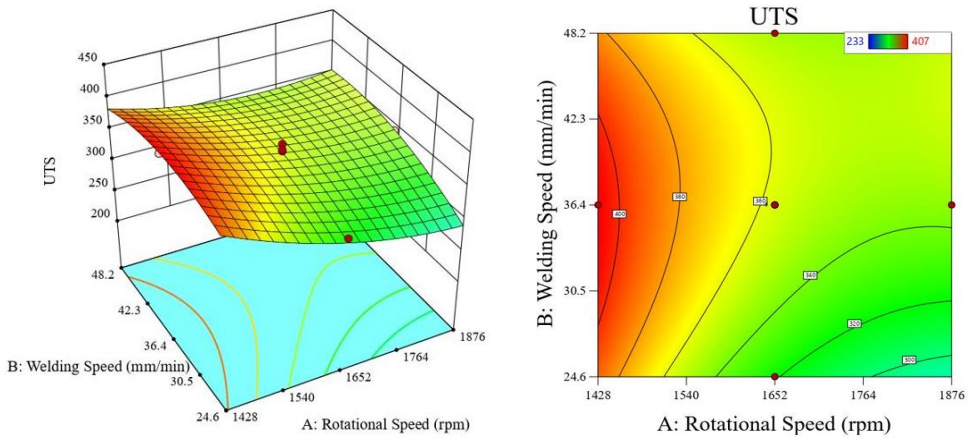

(a) (b)

Fig.e 10. (a) Three-dimensional response and (b) contour plot for UTS

The heat cycle in FS-welding processes is greatly influenced by RS and WS. Changes in both parameters cause the heat intake to rise, which causes the cooling rate to fall. Joint strength for heat-treatable alloys depends on the melting of hardening precipitates [25]. Solid-state diffusion, that is dependent on temperature and time, is the basis for this dissolution procedure. The solid-state diffusion process takes less time with increased WS and heat input. While the area with joint efficiency greater than 85% is significantly larger the region with joint efficiency exceeding the parent metal is very tiny. A minimum area is one whose joint efficiency is less than 85%. Joint efficiency of more than 80% can be attained at all RS as illustrated in Figure 10(b) provided that the WS is properly selected.

UTS levels below 300 MPa are produced by the procedure when RS is high and WS is low as shown in Figure 10(b). Overheating slows down cooling, extending the holding period required for metallurgical changes. Therefore, RS should be decreased and WS should be moderate in order to get better tensile strength values.

$$UTS = +1521.11387 - 1.78461A + 1.52384B + 479.4588C + 0.00671AB + 0.092076AC + 0.000381A^2 - 0.157021B^2 - 202.27273C^2 \quad (3)$$

The coefficients for term A^2 are larger than those for term B^2, showing that RS is of greater importance than WS, and Equation 5 shows the coded factor values of UTS. The interaction between RS and WS is denoted by the word AB. Equation 5 shows that when the RS has been set to a value of "-1" and the WS to level "0", this interaction is helpful in boosting joint strength. Joint efficiency falls off when the WS has been set to a value of "-1" and the RS is at level "1".

3.2.2. RS and Tilt Angle

Figure 11 depicts the effects of TA and RS at a WS of 36.4 mm/min. The procedure's temperature cycle, stirring manage and movement of materials are all considerably influenced by RS and TA. Minimum RS and moderate TA result in maximum joint efficiency. Heat input rises at higher RS causing a material flow to become more turbulent. Additionally, a decreased TA leads in less plunge force being used throughout the procedure. As a result, incorrect material flow and extrusion of material on the outermost layer due to higher speed of rotation and lower TA result in the production of tunnel defects.

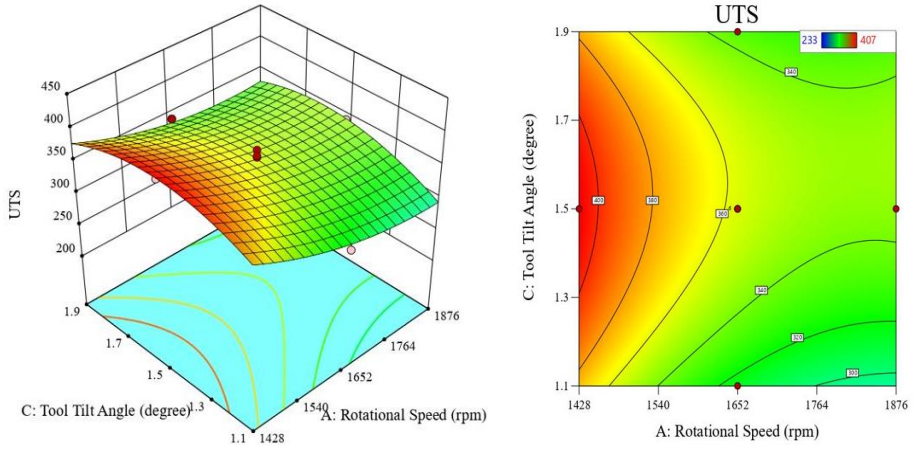

Fig. 11. (a) Three-dimensional response and (b) contour plot for UTS

In the area where the TA fluctuates between 1.3° and 1.7° and the RS varies between 1428 rpm and 1540 rpm, joint efficiency exceeding 86% is attained. Equation 5 shows that RS has a greater impact than TA because the coefficient of A^2 is higher than the coefficient of C^2. The relationship between RS and TA is denoted by the term AC. According to Equation 5 UTS is seen to rise when RS is set to level "-1" and TA is set to level "0". RS at level "1" and WS at level "-1" result in a reduction in joint efficiency.

3.3. Impact of Welding Parameters on EL

The developed design model for EL shows significant first-order and second-order terms, while the interaction between process parameters is insignificant. The design model includes square terms, resulting in curvature plots as shown in Figure 12. Figure 12(a) shows a dramatic decrease in EL as RS rises, which is ascribed to material flow turbulence at faster speeds which causes tunnel defect development in the NZ. In contrast as shown in Figure 12(b) EL steadily rises with WS up to 36.4 mm/min because there is less heat input and less precipitation disintegration. Above 36.4 mm/min EL declines as a result of a greater WS which results in irregular material flow, inadequate heat input, incorrect mixing and cavity development. The effect of TA on EL is shown in Figure 12(c) where EL increases gradually up to 1.5° before declining. This indicates that the tool loses its ability

to effectively manage and keep molten metal under the shoulder above a particular TA limit. Improper stirring causes material to move incorrectly, extrude as flashes onto the working surface and diminish EL.

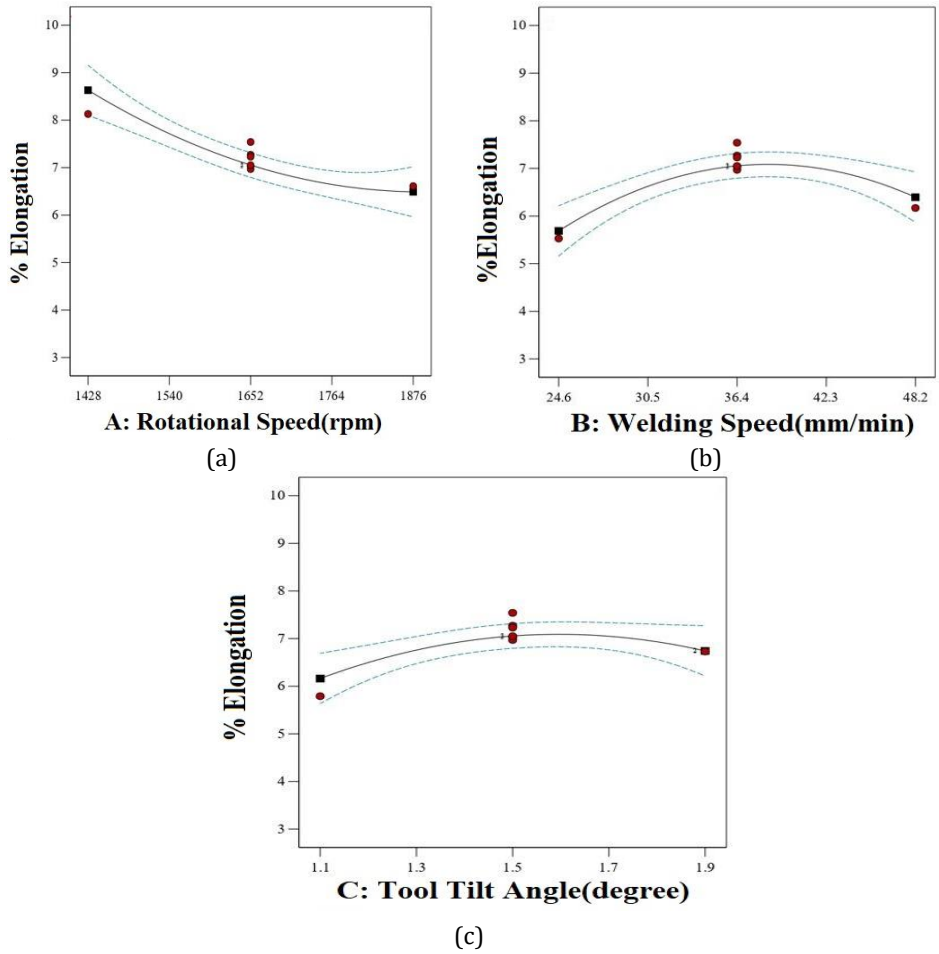

Fig. 12. Performance of overall factors in EL Rotation speed vs EL (a) rotation speed vs UTS, (b) WS vs UTS and (c) tool TA vs UTS

4. Microstructure Analysis

Microstructure analysis was conducted to examine the morphology of the FS weld with maximum strength obtained in experiment no. 15 at (1428rpm,36.4mm/min,1.5°) , medium strength ibtained in experiment no. 3 at (1652rpm, 24.6mm/min,1.5°) lowest strength obtained at experiment no. 4 at (1876rpm,24.6mm/min,1.1°). The microstructure revealed the presence of three distinct zones, including the NZ , TMAZ , and HAZ [2] as shown in Figure 13. In contrast to the FS-welding procedure, it was discovered that the parent metal (PM) had huge, elongated grains. In contrast to TMAZ and HAZ, dynamic recrystallization in the NZ during FS-welding led to the development of fine equiaxed grains [36–37]. Material strengthening is due to the combined effect of dislocations multiplication, secondary phases and the development of finer grains when the density of dislocations reaches a critical value. Furthermore, the HAZ's grains resembled those of the

parent metal since it was heated without undergoing any plastic deformation. Because of mechanical deformation in the TMAZ, the zone's grain sizes were smaller than those of the HAZ Lowest strength. The microstructural study provided insightful information about the structure of the FS weld and the effect of FS welding on the welded joint's microstructure.

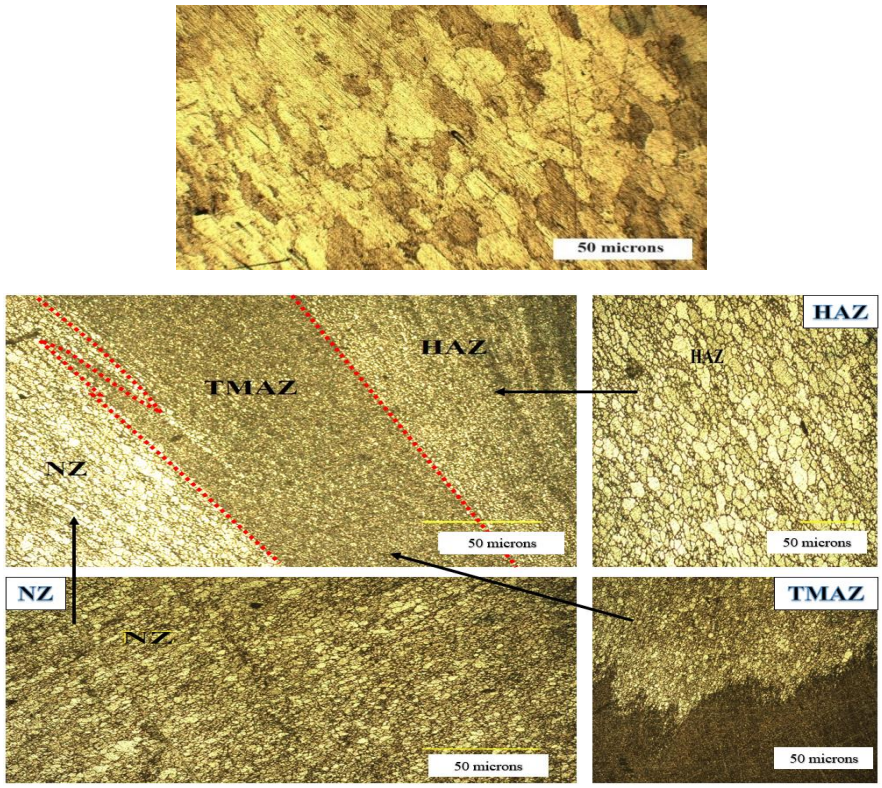

Fig. 13.Microstructural morphology of FS-welding joint

5. Microhardness Distribution

As shown in Figure 14, a microhardness test was carried out with an angle of 0.5 mm for each reading in order to explore the NZ. The base metal was found to have a microhardness of 158 HV. The distribution of microhardness with regard to the process parameters is shown in Figure 14. It was discovered that the NZ's microhardness, which ranged from 103 HV to 118 HV, was lower than that of the parent metal. The dislocation density, size of grains, coarsening, and dissolving of second phase particles were blamed for the decline in microhardness in the NZ. In addition to plastic deformation, the heat cycle variation throughout the process has an impact on the dissolving of strengthening precipitates in alloys from the 8xxx series. Figure 14(a) shows that the NZ's microhardness reduced from 118 HV to 103 HV while its RS increased from 1428 rpm to 1876 rpm. In contrast, the NZ's greatest microhardness was discovered at an average WS of 36.4 mm/min, while the NZ's minimum microhardness was discovered at a WS of 24.6 mm/min. These outcomes matched the tensile strength findings shown in Table 5. As seen in Figures 14(a) and 14(b), applied to the advancing side than the retreating side, the degree of microhardness on the strengthening precipitates were more easily dissolved as a result of the increased heat input brought on by an increase the rotational speed and a decrease Welding Speed. This

resulted in reduced microhardness in the NZ. Of all the constructed joints on the RS, the TMAZ had the highest microhardness. This was due to decreased second phase particle coarsening and dissolution which Sharma et al. [38] also reported. Because more heat was advancing side was lower [39]. This led to the discovery of an asymmetrical microhardness gradient on either side of the centerline. When FS-welding AA7075 Evik et al. [28] noted the similar asymmetrical microhardness distribution. The TMAZ received more intense temperatures than the HAZ, which led to a greater quantity of the second phase particles dissolving, and was therefore determined to have a higher microhardness than the NZ and HAZ. The formation of new nuclei during the process' natural aging can be aided by the breakdown of strengthening precipitates, and the work-hardening effect may also be a factor in the TMAZ's increased microhardness.

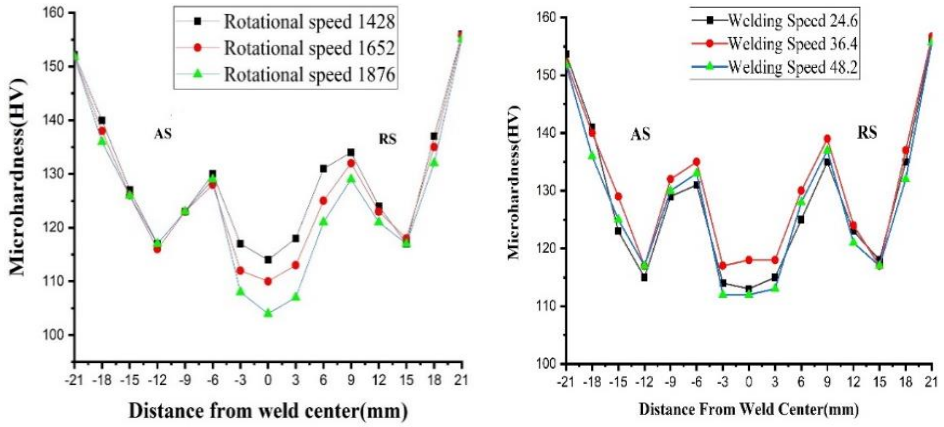

Fig. 14.Microhardness Profile at different a) RS and b) WS

6. Fractography Analysis

As shown in Figure 15 the fractured area of the parent metal, the high strength and the low strength specimens were examined using the fractography analysis. According to the macro fracture the entire artificial joint was shear cracked at an angle of 45 degrees to the tensile axis. On the surfaces of the parent metal and the manufactured joint tiny and big dimples were visible indicating ductile fracture. Small, deep dimples with ripped edges could be seen on the fracture surface of the specimen with lower tensile strength which suggests reduced ductility.

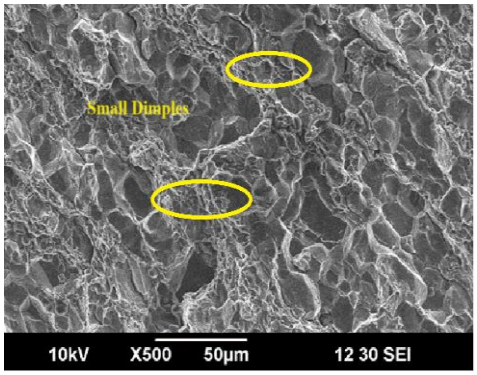

(a)

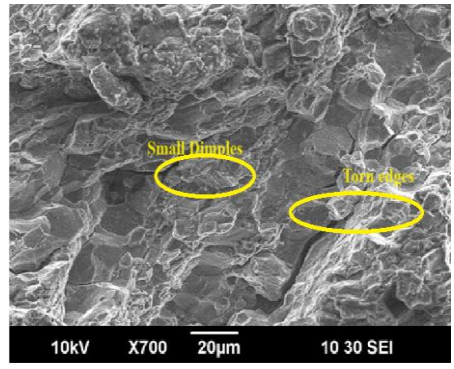

(b)

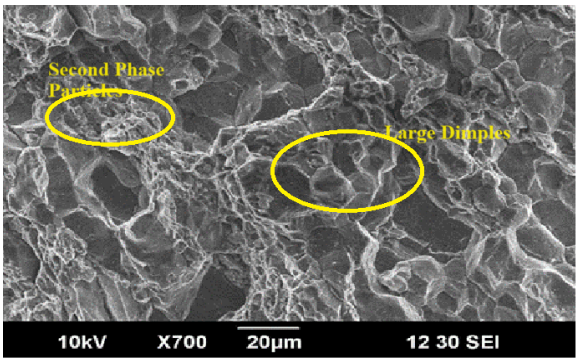

(c)

Fig. 15. (a) Tensile specimens of the parent metal (b) the highest strength specimen and (c) the lowest strength specimen

The fracture surface of the joint with higher tensile strength on the other hand revealed wider and shallower dimples, indicating adequate material mixing and greater plastic deformation throughout the process without any flaws. Similar to how the parent metal's fracture surface showed huge dimples which suggested excellent ductility.

6.1 Analysis of Fracture Location

Figure 16 show the failure locations of the fractured aluminium joints. The table shows that the fractured phenomena are observed in different area of welded portion nugget zone, thermos-mechanically heat effected zone and heat affected zone. Mostly failure of FSW joints in the NZ is a common phenomenon.

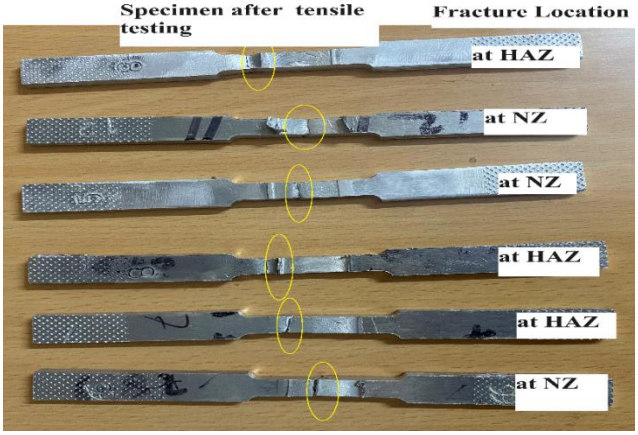

Fig. 16. Tensile specimens of welding aluminium alloys and failure locations

In this research found that mostly fractured at NZ, and others are HAZ. Moreover, it has been shown that HAZ fracture tends to occur on the side of relatively softer materials. The reason is grain coarsening at HAZ as a consequence of high temperature transmission throughout the process. For better understanding SEM is used for fracture failure.

7. Optimization

7.1. Numerical optimization

UTS and EL are the quantitative parameters used in this study to evaluate the efficiency of the FS-welding procedure. The lowest RS, moderate WS and TA together with the maximum UTS are obtained. UTS and % EL are reduced when RS, TA and WS are increased. Higher values in both replies can only be attained with optimal process settings. The ideal UTS and % EL process parameters are chosen using the desirability function.

Harrington first proposed the desirability function approach in 1965 [31–33] and Derinder and Suich later modified it in 1980 [34]. There are several different desirability functions such as target, smaller-the-better and larger-the-better. Equation 3 specifies that the larger-the-better functional is applied to both replies in the current investigation. To calculate the combined desirability function, use equation 4.

$$d_i = \begin{cases} 0 & y_i \le y_{i*} \\ \left[\dfrac{y_i - y_{i*}}{y_i' - y_{i*}}\right]^t, & y_{i*} < y_i < y_i' \\ 1, & y_i \ge y_i' \end{cases} \quad (4)$$

$$D = (d_1 x d_2 x d_3 \dots x d_m)^{\frac{1}{m}} \quad (5)$$

$$D = (d_1^{w1} x d_2^{w2} x d_3^{w3} x \dots x d_n^{wm})^{1/m} \quad (6)$$

Deringer added weight values to the results in 1994, as shown in Equation 6, to further express the desirability function. Where w is the weight given to the m-th response, m is the overall amount of options, and D stands for the combined desirability. Desirability scales from 0 to 1. Response are less capable as desirability values get closer to 0, whereas Response are more capable as desirability values get closer to 1.

Table 11. Range of input parameters and responses for desirability

Name	Goal	Lower Limit	Upper Limit	Importance
A:Rotational Speed	is in range	1428	1876	3
B:Welding Speed	is in range	24.6	48.2	3
C:Tilt Angle	is in range	1.1	1.9	3
UTS	Maximize	233	407	3
% elongation	Maximize	3.41	8.13	3

Table 12. FS-welding process parameters for highest desirability value

No.	RS	WS	TA	UTS	% Elongation	Desirability
1	1430.477	36.194	1.510	407.488	8.607	1.000
2	1428.036	37.199	1.467	407.466	8.624	1.000
3	1428.000	36.400	1.500	408.182	8.631	1.000
4	1430.120	36.423	1.507	407.534	8.611	1.000
5	1428.676	36.410	1.492	407.919	8.625	1.000

The current study's goal is to determine the ideal input parameter values for the FS-welding process in order to maximize desirability [35]. Table 11 lists the limited values of the process parameters used in this study and describes the ideal values at which the highest level of desirability is attained. The overall desirability plot for both the individual

and combined process variables is shown in Figure 17. The ramp function's plots in Figure 18 show the values of the process variables needed to achieve high desirability.

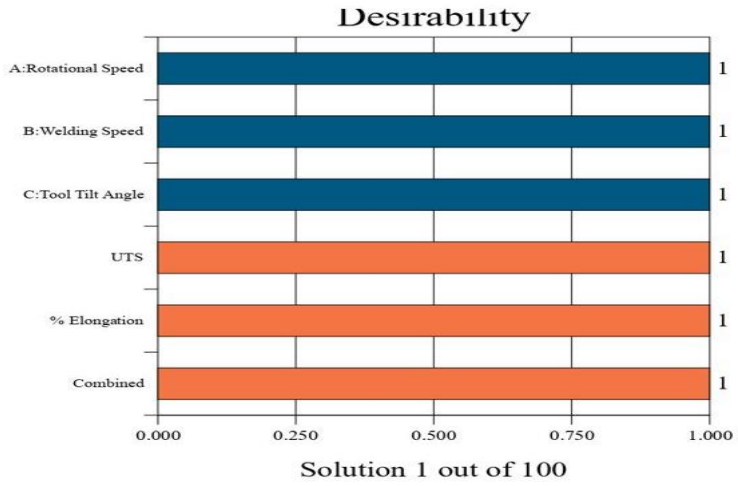

Fig.17. Desirability of process variables and outcomes overall

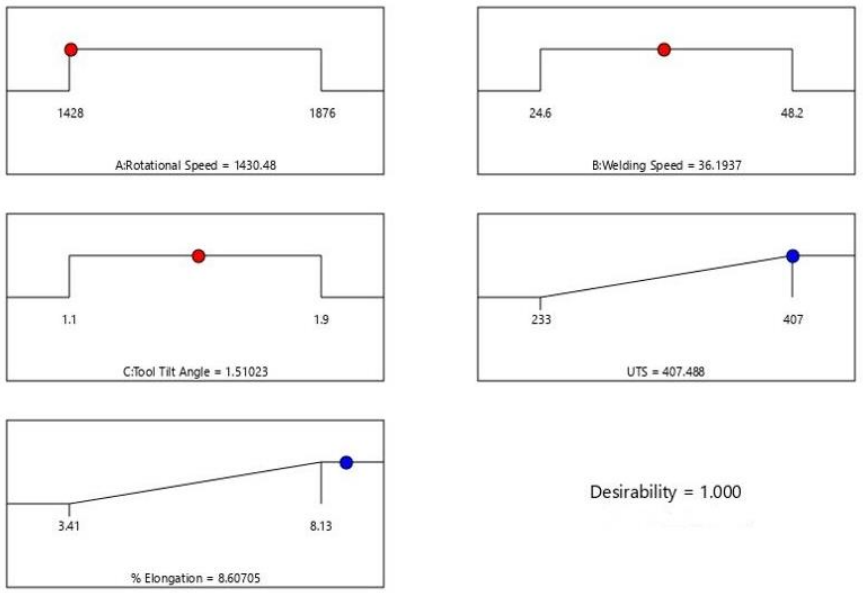

Fig. 18. Ramp diagram of optimized input and output responses of JOINTS

As shown in Figure 19, the desirable index of 1 was attained at the ideal process settings. The WS and TA exhibited negative effects before and after 36.91mm/min and 1.51°respectively while the decrease in RS had a beneficial impact on the desirability function. The multi-response optimization's greatest desirability function values were attained at RS 1430.47 rpm, TA 1.51° and WS 36.19 mm/min table13. presents the findings of the validation experiment carried out to establish the ideal circumstance for maximal desirability. The experimental results were in line with what was expected.

Table 13. Confirmation experiments result

RS (rpm)	WS (mm/min)	TA (degree)	UTS (MPa) Predicted	UTS (MPa) Actual	EL Predicted	EL actual
1430.47	36.19	1.51	407.48	407	8.60	8.13

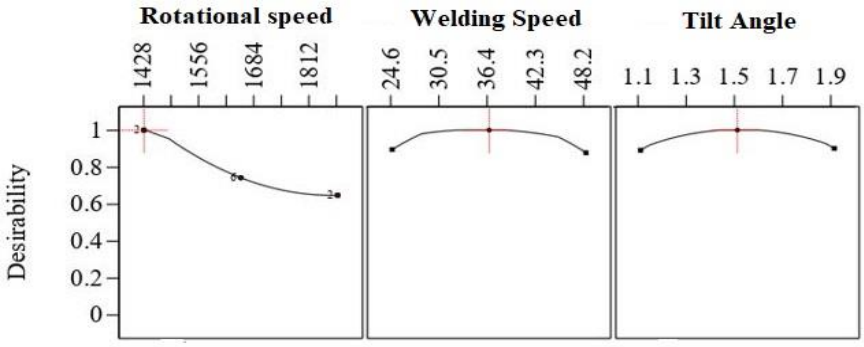

Fig. 19. Overall desirability curve for process parameters

8. Conclusion

The statistical design models for UTS and EL in the current study were created using CCD-RSM. It was discovered that CCD-RSM was used to create these models, which were shown to be substantial and quadratic in nature. According to the regression design models, RS (rotational speed) was the most important variable for both responses and each input variable was thought to be the least effective parameter. This was the case even though RS was not the sole factor that was taken into account. All components, with the exception of WS and TA were found to interact significantly for UTS, but there was no proof that this interaction was substantial for EL. The maximum joint strength that could be achieved was 407 MPa. The maximum joint strength was found where RS was least and WS was medium level in the 3D interaction plot of RS and WS for UTS, which can be attributed to sufficient heat input during the process. The fact that this location was situated in the middle of the plot provided additional support for this conclusion. The 3D interaction plot between RS and TA for UTS similarly showed that the region where RS was reduced to its lower limit while TA was modest was where the best joint strength was reached. For the UTS, this was true. We were able to get the perfect conditions for achieving the maximum UTS and EL at an RS of 1430.47 rpm, WS of 36.19 mm/min and a TA (tilt angle) of 1.51°. The maximum EL of 10.57% that we were able to get was higher than that of the parent metal. The grains in the parent metal and the HAZ were found to be relatively big and elongated, whereas the grains in the NZ were found to be fine due to mechanical stirring. The microhardness of the TMAZ was discovered to be higher than typical due to the intense heat. This resulted in more second phase particles dissolving, which could result in the production of additional nuclei during the subsequent natural aging process. Furthermore, it was shown that the increased microhardness in the TMAZ was a result of the work hardening effect. Finally, the presence of dimples on the fracture surfaces of all the samples allowed ductile fracture to be recognized.

References

[1] Yang Y, Zhang J, Li W, Zhuang W, Jiang H, Wu X, et al. Research progress on the microstructure and mechanical properties of friction stir welded Al-Li alloy joints. J Manuf Process. 2022;82(May):230-44. https://doi.org/10.1016/j.jmapro.2022.07.067

[2] Seetharaman R, Seeman M, Kanagarajan D, Sivaraj P, Saravanan I. A statistical evaluation of the corrosion behaviour of friction stir welded AA2024 aluminium alloy. Mater Today Proc. 2020;22:673-80. https://doi.org/10.1016/j.matpr.2019.09.066

[3] Nosrati HG, Yazdani NM, Khoran M. Double-sided friction stir welding of AA 2024-T6 joints: Mathematical design modeling and optimization. CIRP J Manuf Sci Technol. 2022;36(2022):1-11. https://doi.org/10.1016/j.cirpj.2021.10.010

[4] Palanivel R, Mathews PK, Murugan N, Dinaharan I. Prediction and optimization of wear resistance of friction stir welded dissimilar aluminum alloy. Procedia Eng. 2012;38:578-84. https://doi.org/10.1016/j.proeng.2012.06.072

[5] Elatharasan G, Kumar VSS. An experimental analysis and optimization of process parameter on friction stir welding of AA 6061-T6 aluminum alloy using RSM. Procedia Eng. 2013;64:1227-34. https://doi.org/10.1016/j.proeng.2013.09.202

[6] Rambabu G, Naik DB, Rao CHV, Rao KS, Reddy GM. Optimization of friction stir welding parameters for improved corrosion resistance of AA2219 aluminum alloy joints. Def Technol. 2015;11(4):330-7. https://doi.org/10.1016/j.dt.2015.05.003

[7] Elatharasan G, Kumar VSS. Modelling and optimization of friction stir welding parameters for dissimilar aluminium alloys using RSM. Procedia Eng. 2012;38:3477-81. https://doi.org/10.1016/j.proeng.2012.06.401

[8] Bruce AR, Kumar PP, Arul K, Kumar PM, Kumar SL, Aravindh. Experimental characteristics and optimization of friction stir welded AA5052-AA6061 using RSM technique. Mater Today Proc. 2022;59:1379-87. https://doi.org/10.1016/j.matpr.2021.12.099

[9] Qin Q, Zhao H, Li J, Zhang Y, Su X. Microstructure and mechanical properties of friction stir processed Al−Mg2Si alloys. Trans Nonferrous Met Soc China. 2020;30(9):2355-68. https://doi.org/10.1016/S1003-6326(20)65384-5

[10] Liu Z, Zhang H, Hou Z, Feng H, Dong P, Liaw PK. Microstructural origins of mechanical and electrochemical heterogeneities of friction stir welded heat-treatable aluminum alloy. Mater Today Commun. 2020;24(May):101229. https://doi.org/10.1016/j.mtcomm.2020.101229

[11] Sharma HK, Bhatt K, Shah K, Joshi U. Experimental analysis of friction stir welding of dissimilar alloys AA6061 and Mg AZ31 using circular butt joint geometry. Procedia Technol. 2016;23:566-72. https://doi.org/10.1016/j.protcy.2016.03.064

[12] Özel C. Research of production times and cutting of the spur gears by end mill in CNC milling machine. Int J Adv Manuf Technol. 2011;54(1-4):203-13. https://doi.org/10.1007/s00170-010-2943-5

[13] Mahto RP, Bhoje R, Pal SK, Joshi HS, Das S. A study on mechanical properties in friction stir lap welding of AA 6061-T6 and AISI 304. Mater Sci Eng A. 2016;652:136-44. https://doi.org/10.1016/j.msea.2015.11.064

[14] Verma S, Misra JP. Experimental investigation on friction stir welding of dissimilar aluminium alloys. Proc Inst Mech Eng Part E J Process Mech Eng. 2021;235(5):1545-54. https://doi.org/10.1177/09544089211008694

[15] Verma S, Meenu, Misra JP. Study on temperature distribution during friction stir welding of 6082 aluminum alloy. Mater Today Proc. 2017;4(2):1350-6. https://doi.org/10.1016/j.matpr.2017.01.156

[16] Verma S, Misra JP, Gupta M. Study of temperature distribution and parametric optimization during FS-welding of AA6082 using statistical approaches. SAE Int J Mater Manuf. 2019;12(1):73-82. https://doi.org/10.4271/05-12-01-0005

[17] Verma S, Gupta M, Misra JP. Effect of pin-profiles on thermal cycle, mechanical and metallurgical properties of friction stir-welded aviation-grade aluminum alloy. Proc Inst Mech Eng Part B J Eng Manuf. 2019;233(11):2183-95. https://doi.org/10.1177/0954405419832109
[18] Verma S, Gupta M, Misra JP. Effect of preheating and water cooling on the performance of friction-stir-welded aviation-grade aluminum alloy joints. J Mater Eng Perform. 2019;28(7):4209-20. https://doi.org/10.1007/s11665-019-04183-z
[19] Verma S, Gupta M, Misra JP. Study of thermal cycle, mechanical, and metallurgical properties of friction stir welded aviation grade aluminum alloy. Proc Inst Mech Eng Part:G J.Aerosp Eng. 2019;233(11):4202-13. https://doi.org/10.1177/0954410018816601
[20] Verma S, Misra JP, Gupta M. Procedure to find out the optimal ranges of process parameters for friction stir welding. Proc Inst Mech Eng Part L J Mater Des Appl. 2021;235(5):1172-80. https://doi.org/10.1177/1464420721993145
[21] Mahto RP, Kumar R, Pal SK, Panda SK. A comprehensive study on force, temperature, mechanical properties and micro-structural characterizations in friction stir lap welding of dissimilar materials (AA6061-T6 & AISI304). J Manuf Process. 2018;31:624-39. https://doi.org/10.1016/j.jmapro.2017.12.017
[22] Raja R, Parthiban A, Jeyakumar S, Radha Krishnan B. Investigation of mechanical properties of friction stir welding aluminium alloy AA7475-T651 and AA2219-O. Mater Today Proc. 2022;60:1421-3. https://doi.org/10.1016/j.matpr.2021.10.439
[23] Rajendran C, Srinivasan K, Balasubramanian V, Balaji H, Selvaraj P. Effect of tool TA on strength and microstructural characteristics of friction stir welded lap joints of AA2014-T6 aluminum alloy. Trans Nonferrous Met Soc China. 2019;29(9):1824-35. https://doi.org/10.1016/S1003-6326(19)65090-9
[24] RajKumar V, VenkateshKannan M, Sadeesh P, Arivazhagan N, Devendranath Ramkumar K. Studies on effect of tool design and welding parameters on the friction stir welding of dissimilar aluminium alloys AA 5052 - AA 6061. Procedia Eng. 2014;75:93-7. https://doi.org/10.1016/j.proeng.2013.11.019
[25] Mehta KP, Badheka VJ. Effects of tool pin design on formation of defects in dissimilar friction stir welding. Procedia Technol. 2016;23:513-8. https://doi.org/10.1016/j.protcy.2016.03.057
[26] Mehta KP, Badheka VJ. Influence of tool pin design on properties of dissimilar copper to aluminum friction stir welding. Trans Nonferrous Met Soc China. 2017;27(1):36-54. https://doi.org/10.1016/S1003-6326(17)60005-0
[27] Boldsaikhan E, Corwin E, Logar A, Arbegast W. Neural network evaluation of weld quality using FS-welding feedback data. 2006.
[28] Fratini L, Buffa G, Palmeri D. Using a neural network for predicting the average grain size in friction stir welding processes. Comput Struct. 2009;87:1166-74. https://doi.org/10.1016/j.compstruc.2009.04.008
[29] Ghetiya ND, Patel KM. Prediction of wear behaviour and optimization of process parameters of AA7075-T6 hybrid composite using Taguchi coupled ANN approach. Measurement. 2018;127:185-97.
[30] Wakchaure KN, Thakur AG, Gadakh V, Kumar A. Multi-Objective Optimization of Friction Stir Welding of Aluminium Alloy 6082-T6 Using Hybrid Taguchi-Grey Relation Analysis-ANN Method. Mater Today Proc. 2018;5(2):7150-9. https://doi.org/10.1016/j.matpr.2017.11.380
[31] Alkayem NF, Parida B, Pal S. Optimization of friction stir welding process parameters using soft computing techniques. Soft Comput. 2017;21(23):7083-98. https://doi.org/10.1007/s00500-016-2251-6
[32] Babu KK, Rao CR, Reddy GM, et al. Parameter optimization of friction stir welding of cryorolled AA2219 alloy using artificial neural network design modeling with genetic

algorithm. Int J Adv Manuf Technol. 2018;94(9-12):3117-29. https://doi.org/10.1007/s00170-017-0897-6
[33] Masoudi Nejad R, Sina N, Ghahremani Moghadam D, Branco R, Macek W, Berto F. Artificial neural network based fatigue life assessment of friction stir welding AA2024-T351 aluminum alloy and multi-objective optimization of welding parameters. Int J Fatigue. 2022;160:106840. https://doi.org/10.1016/j.ijfatigue.2022.106840
[34] Prasanna P, Penchalayya CH, Rao DA. Effect of tool pin profiles and heat treatment process in the friction stir welding of AA 6061 aluminium alloy. Am J Eng Res. 2013;2(1):7-15.
[35] Haribalaji V, Sampath, Asif MM. Optimization of friction stir welding process to join dissimilar AA2014 and AA7075 aluminum alloys. Mater Today Proc. 2021;50:2227-34. https://doi.org/10.1016/j.matpr.2021.09.499
[36] Nait Salah A, Mehdi H, Mehmood A, Hashmi AW, Malla C, Kumar R. Optimization of process parameters of friction stir welded joints of dissimilar aluminum alloys AA3003 and AA6061 by RSM. Mater Today Proc. 2022;56:1675-83. https://doi.org/10.1016/j.matpr.2021.10.288
[37] Sarvaiya J, Singh D. Selection of the optimal process parameters in friction stir welding/processing using particle swarm optimization algorithm. Mater Today Proc. 2022;62:896-901. https://doi.org/10.1016/j.matpr.2022.04.062
[38] Simoncini M, Forcellese A, Mancini E, Chiappini G, Sasso M. Experimental and numerical investigation on forming limit curves of AA6082 aluminum alloy at high strain rates. Int J Adv Manuf Technol. 2021;112(7-8):1973-91. https://doi.org/10.1007/s00170-020-06448-7
[39] Abd Elnabi MM, Elshalakany AB, Abdel-Mottaleb MM, Osman TA, El Mokadem A. Influence of friction stir welding parameters on metallurgical and mechanical properties of dissimilar AA5454-AA7075 aluminum alloys. J Mater Res Technol. 2019;8(2):1684-93. https://doi.org/10.1016/j.jmrt.2018.10.015
[40] Subramanian M, Sathishkumar N, Sasthrigal JS, Arunkumar N, Hariharan V. Optimization of process parameters in friction stir welded dissimilar magnesium alloys using RSM. Mater Today Proc. 2019;46:9736-46. https://doi.org/10.1016/j.matpr.2020.09.049
[41] Khan N. Optimization of friction stir welding of AA6062-T6 alloy. Mater Today Proc. 2018;29:448-55. https://doi.org/10.1016/j.matpr.2020.07.298
[42] Haribalaji V, Boopathi S, Asif MM. Optimization of friction stir welding process to join dissimilar AA2014 and AA7075 aluminum alloys. Mater Today Proc. 2021;50:2227-34. https://doi.org/10.1016/j.matpr.2021.09.499
[43] Kumar SR, Rao VS, Pranesh RV. Effect of Welding Parameters on Macro and Microstructure of Friction Stir Welded Dissimilar Butt Joints between AA7075-T651 and AA6061-T651 Alloys. Procedia Mater Sci. 2014;5:1726-35. https://doi.org/10.1016/j.mspro.2014.07.362
[44] Heirani F, Abbasi A, Ardestani M. Effects of processing parameters on microstructure and mechanical behaviors of underwater friction stir welding of Al5083 alloy. J Manuf Process. 2017;25:77-84. https://doi.org/10.1016/j.jmapro.2016.11.002

Research on Engineering Structures & Materials
www.jresm.org
Research Group

Research Article

Optimization of stir casting parameters for the tensile behavior of nano Al_2O_3 and ZrO_2 reinforced Al-Mg-Si alloy metal composites

Annapoorna K[1,2,a], Shobha R[2,b], Bharath V[1,*,c], Rajanna S[3,d], Manjunath Vatnalmath[4,e] Madeva Nagaral[5,f], V Auradi[4,e], C G Shivaprasad[6,g]

[1]*Dept. of Mechanical Eng., RNS Institute of Technology, Visvesvaraya Technological University, India*
[2]*Dept. of Industrial Eng. and Management, Ramaiah Institute of Technology, Bengaluru, Karnataka, India*
[3]*Dept. of Mechanical Eng., Government Engineering College, Mosale Hosahalli, India*
[4]*Dept. of Mechanical Eng., Siddaganga Institute of Tech., Visvesvaraya Technological University, India*
[5]*Aircraft Research and Design Centre, Hindustan Aeronautics Limited, Bangalore 560037, Karnataka, India*
[6]*Hindustan Management Academy, Hindustan Aeronautics Limited, Bangalore 560037, Karnataka, India*

Article Info

Article history:

Received 18 May 2024
Accepted 07 Aug 2024

Keywords:

Stir casting;
Nano Al_2O_3 and ZrO_2;
Taguchi technique;
Tensile behavior;
Fractography

Abstract

Stir casting is a frequently used method in the metallurgical process of casting aluminium composites. The microstructure and performance of the composites are influenced by the stirring casting parameters. The majority of research conducted in this area focused on producing composites using stir casting parameters that were predetermined, without utilizing an optimization method. This work aims to optimize the stir casting parameters for the manufacturing of Al-Mg-Si (Al6061) alloy reinforced with hybrid nano Al_2O_3 and nano ZrO_2 in order to enhance its performance. The Taguchi optimization technique was employed to analyze the important effects of stir casting parameters on the ultimate tensile strength of a hybrid metal matrix composite. The composites were produced by the ultrasonic aided stir casting method, employing a set of process parameters determined by the Taguchi L16 orthogonal array. The S/N (Signal to Noise ratio) and Regression model were utilized to determine the optimal values and assess the influence of process parameters on the tensile qualities. The Minitab 21 software was utilized to perform simultaneous optimization of the attributes. The findings indicated that the composition of the nano reinforcement, stirring temperature, stirring speed, and stirring time all had a substantial impact on improving the UTS (Ultimate Tensile Strength) of the material.

1. Introduction

In recent years, the modern in service performance demands the materials with a bundle of properties, which are difficult to achieve using monolithic materials [1, 2]. New generation hybrid nano metal matrix composites have been satisfying the recent demand of advance engineering. For several years, researchers have been investigating the mechanical properties of light metal matrix composite materials that incorporate ceramic particles as reinforcements due to their exceptional performance. Aluminium matrix composites, which are strengthened by ceramic particles, have become increasingly popular in the military, aerospace, and electrical industries because of their improved mechanical properties [3, 4]. Ongoing research is being conducted to enhance the characteristics of metal matrix composites in the domains of automotive, aerospace,

*Corresponding author: bharathv88@gmail.com
[a]orcid.org/0000-0003-2543-4801; [b]orcid.org/0000-0003-0210-3540; [c]orcid.org/0000-0001-6765-4728; [d]orcid.org/0000-0001-9209-5104; [e]orcid.org/0000-0003-3138-9453; [f]orcid.org/0000-0002-8248-7603; [g]orcid.org/0000-0001-6549-6340
DOI: http://dx.doi.org/10.17515/resm2024.292ma0518rs

electrical, and marine sectors. Aluminium 6061 is a metal alloy that possesses a low density, high ductility, good corrosion resistance, and is relatively inexpensive [5]. It finds uses in engineering fields such as automotive and aerospace, where mechanical features like high tensile strength and high wear resistance are crucial. Aluminium alloys possess low hardness and exhibit less wear resistance, hence restricting their use. The incorporation of rigid ceramic reinforcing particles into aluminium and its alloys results in the formation of a composite material with a discontinuous metal matrix. This composite exhibits almost isotropic properties [6, 7]. There is a lack of study on Aluminium metal matrix composites that are strengthened by hybrid nano particles. Alumina is a highly utilized engineering ceramic material because of its exceptional elastic modulus, wear resistance, and resistance to chemical corrosion [8, 9]. Zirconia possesses several distinctive characteristics, including high toughness that contributes to its strong mechanical strength, exceptional resistance to crack propagation, outstanding thermal resistance, and low thermal conductivity at elevated temperatures. These features have been demonstrated to surpass those of other ceramics [10, 11]. There is an increasing global interest in the production of HMMC's (Hybrid Metal Matrix Composites). HMMC materials comprise a combination of the qualities of their reinforcements and have enhanced mechanical and tribological capabilities. Hence, the incorporation of a hard nanostructure material such as Al_2O_3 into a ZrO_2 matrix with high toughness appears to be a very promising approach for creating a superior composite reinforcement and enhancing the overall mechanical properties of the composite [12, 13].

The literature review reveals that numerous research studies have been published on the use of nano particles as reinforcement in aluminium metal matrix composites. However, there is a limitation of works specifically focused on the use of hybrid nano particle reinforcement and also there is a limited research on the impact of weight fraction, stirring speed, stirring time, and temperature when using Alumina and Zirconia as reinforcement. In addition, there is a scarcity of research that investigate the combined impact of various process factors, such as percent weight fraction, stirring speed, and stirring duration [14]. Stir casting is a widely acknowledged and commercially utilized manufacturing process for Metal Matrix Composites (MMCs). It is considered a potential route for mass production [15, 16]. The process of combining reinforcement and matrix is a crucial step to achieve a uniform dispersion of reinforcing particles within the matrix. Stir casting provides enhanced bonding between the matrix and particles by incorporating the stirring movement of particles into the molten material. In order to thoroughly investigate the impact of different process parameters, the Taguchi design is utilized [17]. This design methodology provides an effective and methodical approach by reducing the number of tests while encompassing a broad variety of parameter combinations [18, 19]. It allows for the investigation of factors like stirring speed, stirring time, temperature, and nano particle composition simultaneously [20]. This study aims to create a new material by incorporating nano alumina and zirconia as reinforcements into an aluminium metal matrix composite. The goal is to enhance the mechanical properties of the material and improve the distribution and wettability of the reinforcing particles. To achieve this, a two-stage mixing process combined with preheating of the reinforcing particles is being utilized. The study will also examine how different stir casting parameters, including as stirring speed, time, temperature, and weight percentage of reinforcement, affect the final tensile strength of the Al/Alumina/Zirconia HMMC's. This will be done using Taguchi DOE [21]. The ANOVA, or Analysis of Variance, is employed to examine the collective impact of the aforementioned parameters, including their interactions.

2. Experimental Details

2.1 Reinforcement Materials and Matrix

Al6061 aluminium metal was used as the base for this study, and nano Al_2O_3 and nano ZrO2 were used to make it stronger. An Energy Dispersive X-ray Analysis (EDAX) machine was used to check the chemical compositions make-up of the raw material. The chemical make-up of the Al6061 metal is shown in Table 1.

Table 1. displays the precise chemical composition of the Al6061 alloy

Constituent	Mg	Si	Ti	Cr	Mn	Fe	Cu	Zn	Al
Wt. %	0.81	0.62	0.1	0.13	0.11	0.35	0.2	0.12	Balance

Table 2. displays the characteristics of the matrix and reinforcing material

Material	Density (gm/cc)	Melting point(deg C)	Modulus of Elasticity (GPa)	Brinell Hardness	Poisons Ratio	Tensile Strength (MPa)
Al6061	2.7	585	68.9	30-33	0.33	110-182
Al_2O_3	3.98	2072	370	450-500	0.21	650-660
ZrO2	5.68	2715	94.5	130-145	0.34	300-330

2.2 Composite Fabrication

The stir casting process is a vital technique used to manufacture metal matrix composites (MMCs) that have improved characteristics. This experiment focuses on investigating the effects of varying parameters (stirring speed, stirring time, temperature), Composition (nano Zirconia and nano Alumina) on the properties of Al6061-based composites. The Taguchi L16 orthogonal array design was employed for an efficient experimental setup. This method allows for studying multiple factors with minimal experimentation. The array consists of 16 distinct combinations of components being studied, as displayed in Table 4, in order to optimize the variables of stirring time, speed, and temperature and wt. % of reinforcement. The hybrid metal matrix composite is fabricated using Al6061 Alloy with a chemical composition outlined in Table 1. The reinforcement materials employed were nano alumina (n-Al_2O_3) and nano zirconia (n-ZrO_2), with an average particle size ranging from 50 to 90 nanometers. Figure 1 and 2 depict the stir casting experimental setup (Manufacturer: Swamequip) that was utilized for producing Metal Matrix Composites (MMCs). The setup comprises an electrical induction furnace, a crucible, a stirring apparatus, thermocouples, a weighing scale, a digital timer, and an ultrasonic vibrator.

Al6061 ingots were placed inside the induction furnace and melted until it reaches the desired molten state at the temperature (700, 725, 750, 775°C) a degassing agent was added into molten Al6061 to remove the slag. Preheat the nano ZrO2 (0.50, 0.75, 1.00 and 1.25 wt %) and nano Al_2O_3 (0.50, 0.75, 1.00 & 1.25 wt.%) particles at 250 deg C to eliminate any moisture and ensure uniform dispersion during stirring. At 1.25 wt. %, the particle-matrix interface is optimized, allowing for effective load transfer between the reinforcements and the matrix, leading to improved mechanical properties. A stainless-steel stirrer coupled with electric motor was immersed into the molten aluminum alloy.

A fixed amount of preheated n-Al_2O_3 powder and n-ZrO_2 powder was introduced into the mixture while stirring at varying speeds (400, 450, 500, 550 RPM) for different durations (6, 8, 10, and 12 minutes) to create a swirling motion. An ultrasonic vibrator was then

applied for 5 minutes, followed by an additional 5 minutes of stirring. The frequency of Ultrasonic vibrator used is 20 KHz and power is 2500 watts. Finally pour the melt into the preheated (400 deg C) mould, allow the cast material to cool and solidify inside the mould before removing it for further analysis. Taguchi L16 orthogonal array design was used to create 16 unique combinations of stirring speed, stirring time, temperature, and $ZrO2/Al_2O_3$ composition.

Fig. 1. Stir casting machine

Fig. 2. Stirring of molten metal

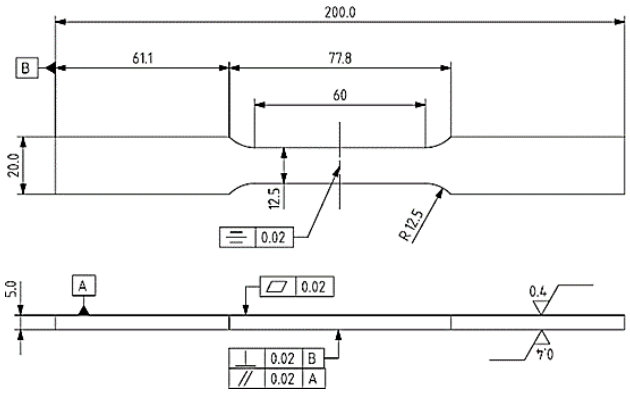

Fig. 3. Tensile specimen specification

The tensile specimens were prepared according to the ASTM E8-22 standard [22, 23]. The specimens were manufactured according to the procedure depicted in Figure 3. The tensile test was conducted using a servo hydraulic universal testing machine (Make: BISS) with a load capability of 25KN.The testing machine is equipped with a load cell to measure the applied force and an extensometer to measure the deformation. The load and displacement data is converted into stress-strain values, which are subsequently used to calculate mechanical properties (i.e., such as Young's modulus, yield stress, and UTS).

3. Results and Discussion

Table 3 displays the experimental design and the associated levels for the different parameters examined in the study. Five criteria were taken into account, with each factor having four levels. The five factors and their respective levels were systematically varied

to investigate their individual and combined effects on the properties of the fabricated material. Such a design allows for a comprehensive exploration of the parameter space and facilitates the identification of optimal conditions for desired material properties.

The Table 4 provides a detailed overview of the experimental runs conducted, along with the corresponding values of the factors and the resultant UTS of the fabricated material. Each row represents a distinct experimental run, while the columns depict the weight percentage of reinforcement, stirring time, stirring speed and temperature respectively. Each combination of factor levels resulted in a unique set of ultimate tensile strength and S/N ratio, as reflected in table 4. The table provides a comprehensive dataset that enables the analysis of the effects of individual factors as well as their interactions on the UTS of the material. These experimental data are valuable for optimizing the fabrication process to achieve desired mechanical properties and overall performance characteristics of the material.

Table 3. Design of Factors for Stir Casting Process

Factor	Levels	Values
Zirconia	4	0.50, 0.75, 1.00, 1.25
Alumina	4	0.50, 0.75, 1.00, 1.25
Temperature	4	700, 725, 750, 775
Speed	4	400, 450, 500, 550
Time	4	6, 8, 10, 12

Table 4. Design matrix and experimental observations

Runs	ZrO_2	Al_2O_3	Time	Speed	Temperature	UTS	S/N Ratio
1	0.50	0.50	6	400	700	149.3	43.48
2	0.50	0.75	8	450	725	155.2	43.82
3	0.50	1.00	10	500	750	170	44.61
4	0.50	1.25	12	550	775	167.1	44.46
5	0.75	0.50	8	500	775	165.5	44.38
6	0.75	0.75	6	550	750	168	44.51
7	0.75	1.00	12	400	725	169.7	44.59
8	0.75	1.25	10	450	700	167	44.45
9	1.00	0.50	10	550	725	172.1	44.72
10	1.00	0.75	12	500	700	171	44.66
11	1.00	1.00	6	450	775	183.7	45.28
12	1.00	1.25	8	400	750	184.9	45.34
13	1.25	0.50	12	450	750	173	44.76
14	1.25	0.75	10	400	775	174.3	44.83
15	1.25	1.00	8	550	700	177	44.96
16	1.25	1.25	6	500	725	180.5	45.13

The stress-strain relationship of the composites that were created with varying weight fractions is displayed in Figure 4. Because the presence of nano-alumina and nano-ZrO_2 reinforcing particles inhibits the matrix material's ability to flow plastically, the weight fraction of n-Al_2O_{3p} and n- ZrO2 increased while the fracture strain and ductility of the resulting composites dropped gradually.

The findings from Tables 5 and 6 illustrate the responses concerning the S/N ratio and means, respectively. These tables collectively identify key factors significantly influencing the UTS of the composite material under investigation. Notably, among the five parameters analyzed, ZrO_2, Al_2O_3 percentage and temperature emerges as particularly noteworthy, as indicated by its high delta value. Following this, stirring speed, and stirring time also exhibit notable impacts on the UTS behavior of the Al6061 composite with ZrO_2 and Al_2O_3 content. This influence can be attributed to the enhancement of composite strength facilitated by the inclusion of ZrO_2 and Al_2O_3 nanoparticles in the matrix. These nanoparticles play a crucial role in refining the grain structure of the composite, thereby contributing to the observed improvement in mechanical properties.

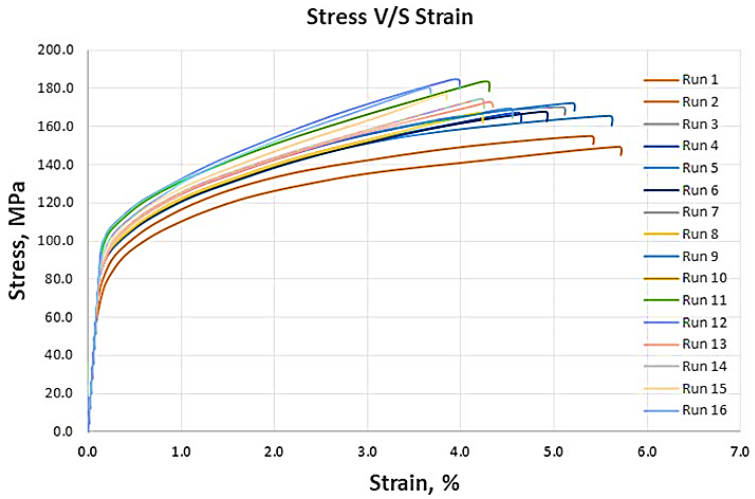

Fig. 4. Stress-strain curve of the produced composites at different runs

Table 5 displays the response table for signal to noise ratios

Level	ZrO_2	Al_2O_3	Time	Speed	Temperature
1	44.09	44.33	44.6	44.56	44.39
2	44.48	44.45	44.62	44.58	44.56
3	45	44.86	44.65	44.69	44.8
4	44.92	44.85	44.62	44.66	44.74
Delta	0.91	0.53	0.05	0.13	0.41
Rank	1	2	5	4	3

Figures 5 and 6 display the primary effect graphs, illustrating the impact of different settings on the S/N ratio and data means, respectively. After careful investigation, it has been determined that the ideal conditions for producing the highest ultimate tensile strength (UTS) are as follows: a composition consisting of 1% weight percent, a melt temperature of 750°C, a stirring speed of 500 RPM, and a stirring period of 10 minutes.

Notably, the UTS demonstrates its highest values at a moderate stirring speed of 500 RPM, with a decrease in tensile properties observed upon further increases in stirring speed. Additionally, it is observed that a moderate stirring time yields superior tensile

strength, whereas an excessive increase in stirring time leads to a reduction in tensile strength.

Table 6. displays the response table for means

Level	ZrO_2	Al_2O_3	Time	Speed	Temperature
1	160.4	165	170.4	169.6	166.1
2	167.6	167.1	170.7	169.7	169.4
3	177.9	175.1	170.9	171.8	174
4	176.2	174.9	170.2	171.1	172.6
Delta	17.5	10.1	0.7	2.2	7.9
Rank	1	2	5	4	3

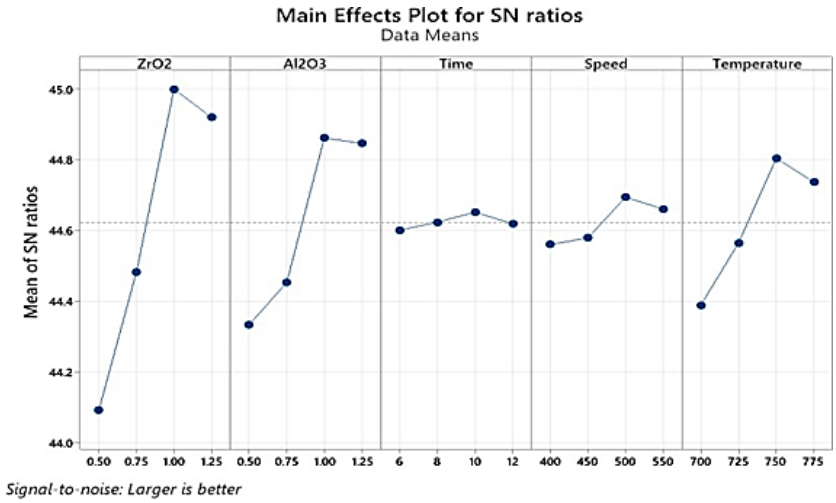

Fig. 5. Main effects plot for S/N ratios

Fig. 7 illustrates the interaction plot concerning tensile strength, revealing notable interactions primarily among filler percentage followed by temperature, stirring speed, and stirring time. Among these factors, ZrO2 and Al_2O_3 emerge as the most influential and highly interacting parameter affecting ultimate tensile strength (UTS). Specifically, the interaction between stirring speed and stirring time indicates a pattern wherein an increase in stirring time initially boosts strength before exhibiting a subsequent decline.
The observed enhancement in strength when the filler content increases by 1% can be ascribed to mechanisms such as particle reinforcement and grain refining. Moreover, the increase in stirring speed first improves the strength of the composite, but then it decreases. Appropriate stirring speeds are essential for achieving a uniform dispersion of reinforcement inside the matrix. The contour plots in Figure 8 depict the correlation between the process parameters and ultimate tensile strength (UTS) in relation to the weight percentage (wt %) of ZrO2.

The weight percentage of ZrO2 is a crucial factor that can impact the ultimate tensile strength (UTS). Experimental evidence demonstrates that increasing temperatures, while decreasing the weight percentage of ZrO2 and increasing the weight percentage of Al_2O_3, lead to increased ultimate tensile strength (UTS). On the other hand, low stirring time and high ZrO_2 wt % yield maximum UTS, however high stirring speed and high ZrO_2 wt % can

also yield the highest UTS. Likewise, Fig. 12 shows the contour plots of UTS relative to wt % of Al_2O_3. It is evident that the low stirring time, stirring speed and wt % of Al_2O_3 increases the UTS. Additionally, the low wt% of Al_2O_3 with high temperature also attains maximum UTS.

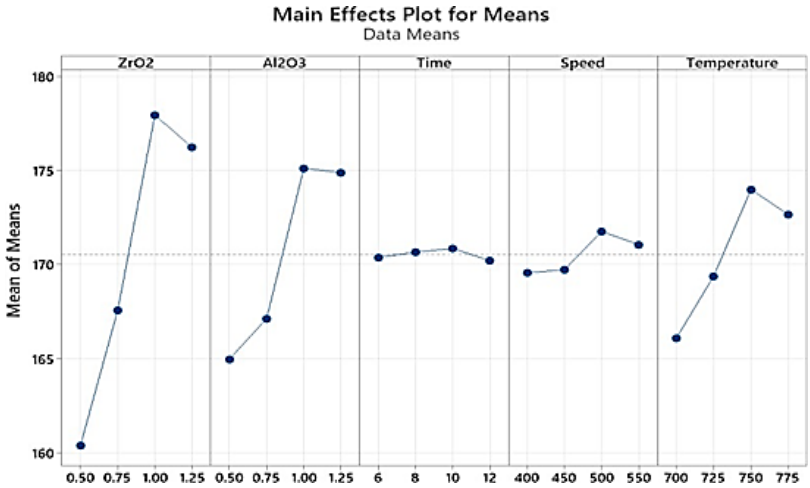

Fig. 6. Main effects plot for means

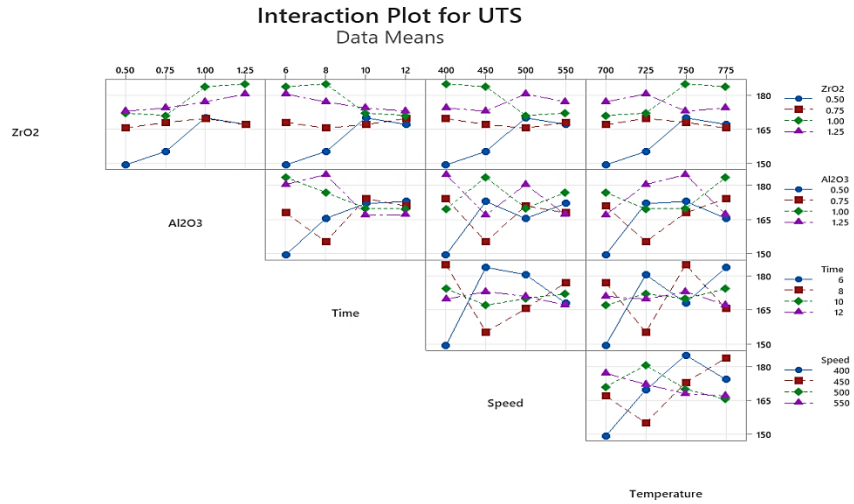

Fig. 7. Interaction plot for UTS of Al6061/ZrO_2/ Al_2O_3

ANOVA Table 7 summarizes regression analysis results to determine how factors affected the dependent variable. ZrO2, Al2O3, Time, Speed, and Temperature are considered. The regression model is significant with an F-value of 10.35 and a p-value of 0.001. The p-values for ZrO2, Al_2O_3, and temperature are 0.000, 0.004, and 0.038, respectively. These low p-values indicate a substantial relationship with UTS, as they are all below the threshold of 0.05. The high p-values of 0.975 and 0.537 for stirring duration and speed indicate that they do not affect the dependent variable.

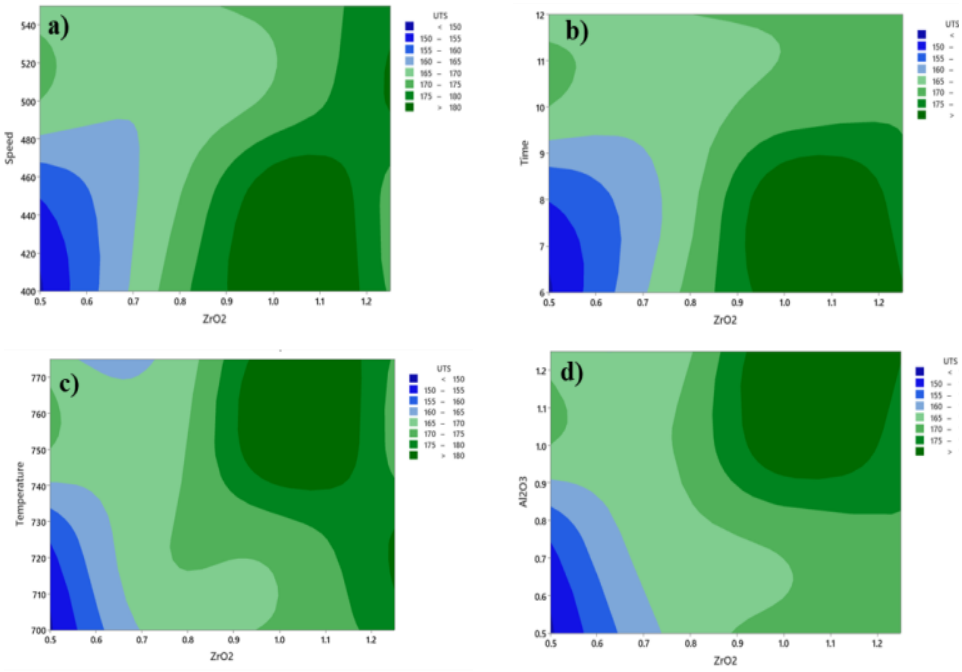

Fig. 8. Contour plots of UTS for various process parameters with respect to wt% of ZrO_2

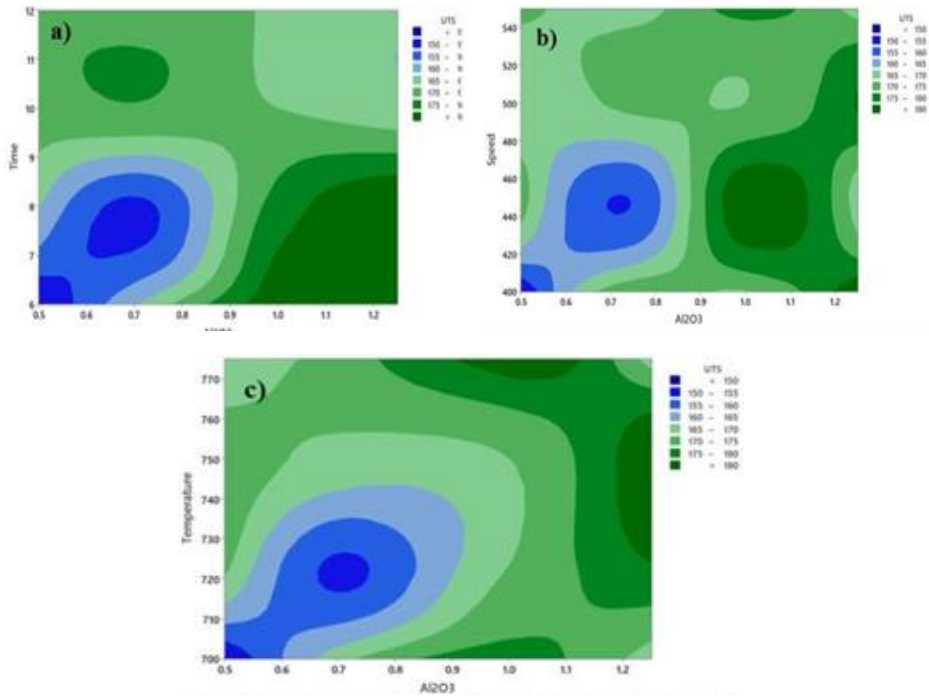

Fig. 9. Contour plots of UTS with various process parameters with respect to wt.% of Al_2O_3

Table 7. Summary of Analysis of Variance

Source	DF	Adj SS	Adj MS	F-Value	P-Value
Regression	5	1078.35	215.67	10.35	0.001
ZrO_2	1	667.59	667.59	32.02	0.000
Al_2O_3	1	283.88	283.881	13.62	0.004
Time	1	0.02	0.021	0	0.975
Speed	1	8.52	8.515	0.41	0.537
Temperature	1	118.34	118.341	5.68	0.038
Error	10	208.48	20.848		
Total	15	1286.82			

- Regression Equation

UTS= 59.3 + 23.11 ZrO2 + 15.07 Al_2O_3 - 0.016 Time + 0.0130 Speed + 0.0973 Temperature

Regression equation is a mathematical representation of the relationship between the predictor variables (ZrO_2, Al_2O_3, Time, Speed, and Temperature) and the response variable (UTS). It can be used to predict the Ultimate Tensile Strength for given values of the predictor variables.

- Model Summary

These data provide a comprehensive understanding of the regression model's accuracy and predictive capabilities. The regression's standard error, shown as S, is precisely 4.566. The provided value is the standard deviation of the residuals, which indicates the average difference between the actual values and the expected values. An R-squared value of 83.80% shows that the model successfully explains a substantial portion of the variability seen in the dependent variable (ZrO_2, Al_2O_3, Time, Speed, and Temperature). Overall, the high R-squared value shows that the model fits the data well.

Table 8. Model summary

S	R-sq	R-sq(adj)	R-sq(pred)
4.566	83.80%	75.70%	51.15%

3.1 Outcome of Taguchi and ANOVA Analysis

Table 4 summarizes the average UTS of the runs. The Ultimate tensile strength for Al6061/Al_2O_3/ZrO_2 composite was higher when compared to base alloy. Figures 5 and 6 demonstrate that the combination of 1 weight % of ZrO2 and 1 weight % of Al_2O_3 exhibits the highest Ultimate tensile strength when subjected to a melt temperature of 750 deg C, speed of 500 RPM, and time of 10 minutes. The quality qualities are assessed by converting the experimental values into S/N ratio. An analysis has been conducted on the impact of parameters such as composition, melt temperature, stirring speed, and stirring time on the ultimate tensile strength. This analysis was performed utilizing a signal-to-noise response table. The signal-to-noise ratio (S/N ratio) is a single value that represents the level of variation in a set of iterations. Table 5 provides the ranking of process parameters for Ultimate tensile strength based on the signal to noise ratio achieved for different parameter values. The control factors have been found to be statistically significant in influencing the signal to noise ratio. It has been noted that the composition is the most influential parameter in improving the Ultimate tensile strength, followed by the Melt temperature, speed, and time of stirring. Figure 10 depicts the graphical representation of the impact of process parameters. The experimental data was analyzed utilizing the signal-

to-noise ratio approach to ascertain the optimal conditions that result in an augmentation of the ultimate tensile strength. According to Figure 8, the highest Ultimate tensile strength is achieved at a melt temperature of 750 deg C, speed of stirring is 500 RPM, and duration of 10 minutes when the composition includes 1 weight % of ZrO_2 and 1 weight % of Al_2O_3. Therefore, the most effective configuration of the control variables to enhance the Ultimate tensile strength of HMMC has been determined. Furthermore, the literature survey clearly indicates that these process parameters are quite similar to the optimized parameters [24].

3.2 Confirmation Test

After conducting Taguchi and ANOVA analyses to optimize the fabrication process of Al6061- based composites with nano ZrO_2 and nano Al_2O_3, it is essential to validate the results by performing confirmation tests. These tests provide assurance that the identified optimal parameter settings indeed lead to the desired material properties and consistent performance.

Table 9. Optimized parameters

ZrO_2	Al_2O_3	Time	Speed	Temperature
1	1	10	500	750

The main goal of the confirmation test is to verify the outcomes of the Taguchi and ANOVA analyses. By implementing the optimized parameter combinations, as determined by these analyses, we aim to assess whether the predicted improvements in mechanical properties are reproducible and consistent.

Table 10. Predicted and Experimental Values

S/N Ratio	Predicted UTS	Experimental UTS	Deviation
45.5162	187.52	195.21	4.1%

3.3 SEM/EDAX Analysis of Produced Composites

SEM and EDAX plot indicate the presence of peaks associated with n-Al_2O_3, n-ZrO2, base alloy, and Al6061/1% n-ZrO_2/1% n-Al_2O_3 is depicted in Figures 10, 11, 12 and 14, respectively.

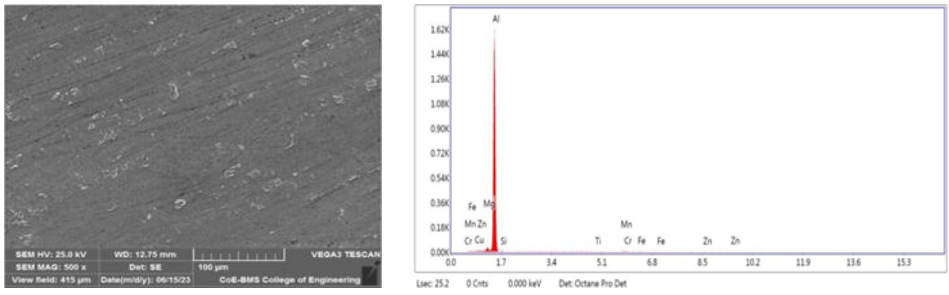

Fig. 10. SEM and EDS Spectrum of Al6061

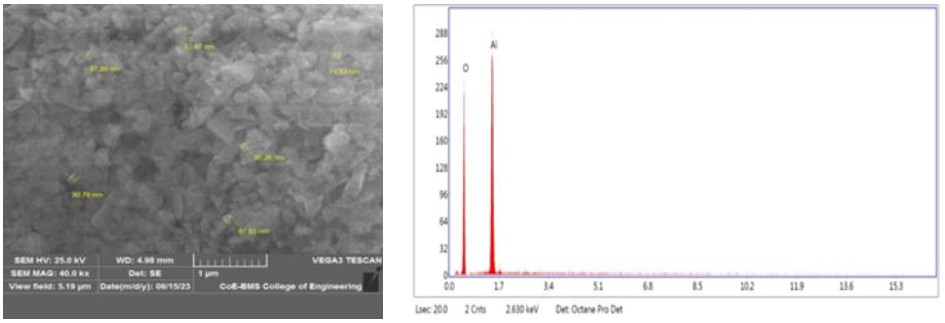

Fig. 11. SEM and EDS Spectrum of n-Al_2O_3

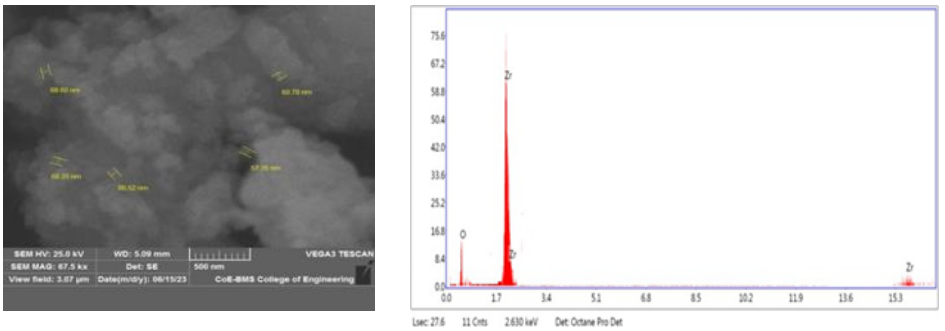

Fig. 12. EDS Spectrum of n-ZrO_2

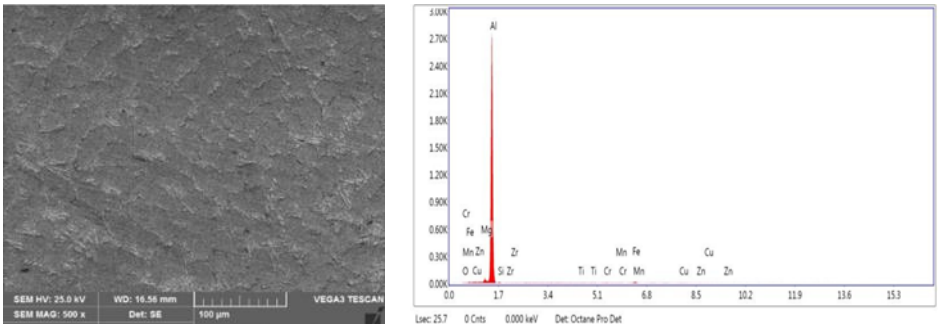

Fig. 13. EDS Spectrum of Al6061/1%ZrO_2/1%Al_2O_3

Table 11. Chemical composition of Al6061/1%ZrO_2/1%Al_2O_3

Elements	Mg	Si	Ti	Cr	Mn	Fe	Cu	Zn	O	Zr	Al
Percentage	0.84	0.72	0.12	0.2	0.09	0.34	0.3	0.16	0.52	0.91	Balance

3.4 Fracture Behavior

An essential procedure for identifying the cause of material failure involves analyzing the broken surface of the alloys and their composites. When examining fractography, it is crucial to bear in mind two fundamental aspects. Firstly, a ductile material that does not exhibit the formation of small dimples, such as a structural pattern, in the fractured regions. Furthermore, when examining SEM pictures of a failed material, one may notice

trans-granular or intergranular fragmentations in the event of fractures occurring. Figure 14 (a-e) shows the fractured surfaces of the Al6061 alloy and Al6061-0.5, 0.75, 1, and 1.25 wt. % n- Al_2O_3 and n-ZrO2 particles in their as-cast state. The base matrix exhibited a smooth and consistent surface with shallow and evenly distributed depressions, indicating a fracture that is capable of being stretched without breaking. This can be observed in Figure 14a. On the other hand, the composite material displayed a distribution of depressions in two directions. This means that the larger depressions absorbed the reinforcing particles, while the smaller depressions were caused by the breaking down of the stretchable matrix. Furthermore, the scanning electron microscope (SEM) analysis of the damaged composite surface (Fig. 14b and Fig. 14d) revealed the presence of fine cracks on the n- Al_2O_{3p} and n-ZrO_2 particles, as well as partial separation between the matrix and reinforcement, and even fracture of the matrix itself. Typically, the fracture surfaces displayed smooth particles, suggesting that the particles were broken rather than detached, and that these composites are mainly distinguished by their robust interfacial connections. The fracture surfaces in the Al6061 matrix showed both large and relatively smaller depressions in the composites reinforced with 1.25 and 1.25 wt % n- Al_2O_{3p}/n-ZrO_2 (Figure 14 e). These findings indicate that the failure was caused by the expansion, combination, and eventual collapse of flexible empty spaces. The addition of n- Al_2O_{3p}/n-ZrO_2 resulted in a change in the fracture behavior of the Al6061 matrix. It shifted from being ductile to brittle, and then to an intermediate ductile mode [25]. The n-Al_2O_3 particle displays small depressions, as well as a matrix and a fine crack.

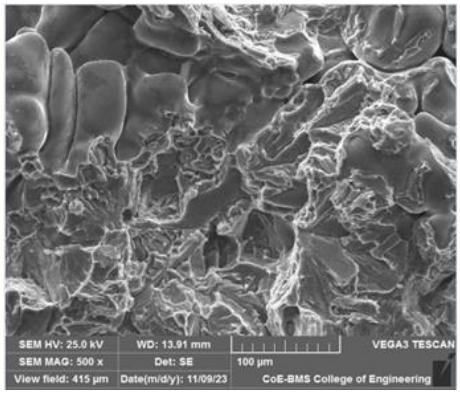

(a)

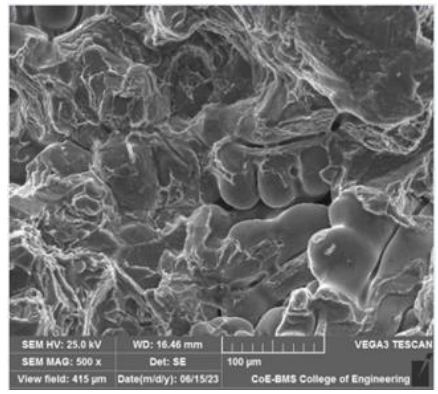

(b)

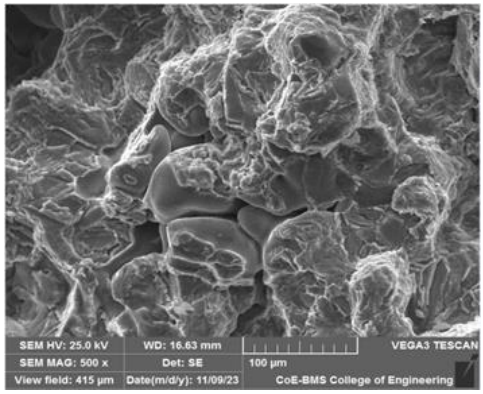

(c)

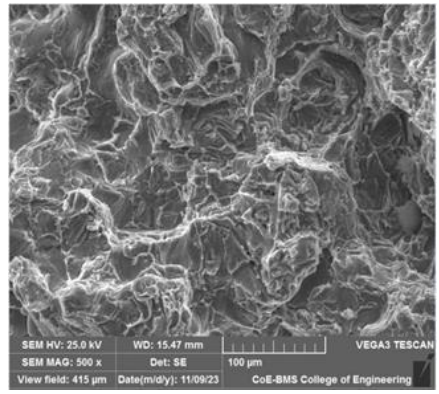

(d)

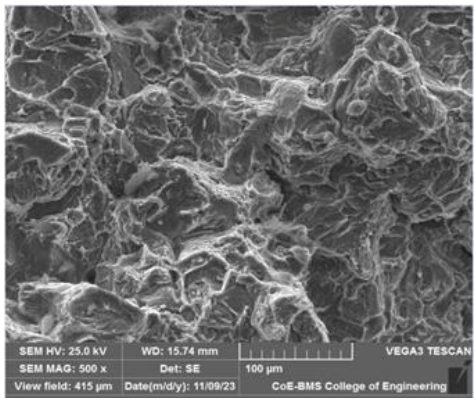

(e)

Fig. 14. (a-e) Fractography of images of (a) Al6061 and (b) Al6061-0.5 wt. % of n-Al_2O_{3p} and n-ZrO_2 (c) Al6061-0.75 wt. % of n- Al_2O_{3p} and n-ZrO_2 and (d) Al6061-1 wt. % of n-Al_2O_{3p} and n-ZrO_2 (e) Al6061-1.25 wt. % of n-Al_2O_{3p} and n-ZrO_2

4. Conclusion

The present experiment produced 16 stir-cast composite samples. Through optimization techniques, the ultimate tensile strength results of Al6061 with ZrO_2 and Al_2O_3 filler content were obtained. The experimental findings are summarized as follows:

- Scanning electron microscopy (SEM) analysis revealed that the ZrO_2 and Al_2O_3 components were evenly distributed throughout the aluminium matrix. Energy-dispersive X-ray spectroscopy (EDS) confirmed ZrO_2 and Al_2O_3 particles in composite materials.
- Among the parameters studied, filler content (ZrO_2 and Al_2O_3) and temperature emerged as the most significant factors influencing the output response (UTS), in contrast to stirring speed and stirring time which exhibited comparatively lesser significance.
- The most effective parameters (i.e., a temperature of 750 deg C, a speed of 500 RPM, and a time of stirring is 10 minutes) determined through stir casting to achieve improved ultimate tensile strength are 1 wt.% ZrO_2, 1 wt.% Al_2O_3
- The interaction plot concerning tensile strength, revealing notable interactions primarily among filler percentage followed by stirring speed, temperature, and stirring time. Among these factors, ZrO_2 and Al_2O_3 emerge as the most influential and highly interacting parameter affecting ultimate tensile strength.
- The control factors have been found to be statistically significant in influencing the signal to noise ratio. It has been noted that the composition is the most influential parameter in improving the Ultimate tensile strength, followed by the Melt temperature, and stirring time and speed.
- The primary objective of the confirmation test is to validate the findings of the Taguchi and ANOVA analyses. The confirmation tests served to corroborate the results obtained.
- Fractography analysis using a SEM was conducted to examine the surfaces that had undergone tensile rupture. This analysis indicated distinct fracture mechanisms between the base alloy Al6061 and the resultant composites. As cast Al6061 alloy exhibits purely ductile mode of fracture, further with the inclusion of particles like ZrO_2 and Al_2O_3, the combined brittle and ductile fracture mode has been observed.

References

[1] Ramanathan A, Krishnan PK, Muraliraja R. A review on the production of metal matrix composites through stir casting-Furnace design, properties, challenges, and research opportunities. Journal of Manufacturing processes. 2019 Jun 1;42:213-45. https://doi.org/10.1016/j.jmapro.2019.04.017

[2] Pazhouhanfar Y, Eghbali B. Microstructural characterization and mechanical properties of TiB2 reinforced Al6061 matrix composites produced using stir casting process. Materials Science and Engineering: A. 2018 Jan 5;710:172-80. https://doi.org/10.1016/j.msea.2017.10.087

[3] Jadhav PR, Sridhar BR, Nagaral M, Harti JI. Evaluation of mechanical properties of B4C and graphite particulates reinforced A356 alloy hybrid composites. Materials Today: Proceedings. 2017 Jan 1;4(9):9972-6. https://doi.org/10.1016/j.matpr.2017.06.304

[4] Boppana SB, Dayanand S, Murthy BV, Nagaral M, Telagu A, Kumar V, Auradi V. Development and mechanical characterisation of Al6061-Al_2O_3-graphene hybrid metal matrix composites. Journal of Composites Science. 2021 Jun 10;5(6):155. https://doi.org/10.3390/jcs5060155

[5] Matti S, Shivakumar BP, Shashidhar S, Nagaral M. Dry sliding wear behavior of mica, fly ash and red mud particles reinforced Al7075 alloy hybrid metal matrix composites. Indian Journal of Science and Technology. 2021 Feb 2;14(4):310-8. https://doi.org/10.17485/IJST/v14i4.2081

[6] Kumar GV, Venkatesh Chowdary G, Surya Vamsi M, Jayarami Reddy K, Nagaral M, Naresh K. Effects of addition of titanium diboride and graphite particulate reinforcements on physical, mechanical and tribological properties of Al6061 alloy based hybrid metal matrix composites. Advances in materials and processing technologies. 2022 Apr 3;8(2):2259-76. https://doi.org/10.1080/2374068X.2021.1904370

[7] Bharath V, Auradi V, Nagaral M, Boppana SB. Experimental investigations on mechanical and wear behaviour of 2014Al-Al_2O_3 Composites. Journal of Bio-and Tribo-Corrosion. 2020 Jun;6:1-0. https://doi.org/10.1007/s40735-020-00341-2

[8] Nagaral M, Auradi V, Parashivamurthy KI, Kori SA, Shivananda BK. Synthesis and characterization of Al6061-SiC-graphite composites fabricated by liquid metallurgy. Materials Today: Proceedings. 2018 Jan 1;5(1):2836-43. https://doi.org/10.1016/j.matpr.2018.01.073

[9] Kumar HV, Kempaiah UN, Nagaral M, Revanna K. Investigations on mechanical behaviour of micro B4C particles reinforced Al6061 alloy metal composites. Indian J. Sci. Technol.. 2021 Jun 29;14(22):1855-63. https://doi.org/10.17485/IJST/v14i22.736

[10] Prasad GP, Chittappa HC, Nagaral M, Auradi V. Influence of B4C reinforcement particles with varying sizes on the tensile failure and fractography of LM29 alloy composites. Journal of Failure Analysis and Prevention. 2020 Dec;20(6):2078-86. https://doi.org/10.1007/s11668-020-01021-6

[11] Shetty RP, Mahesh TS, Ali Z, Veeresha G, Nagaral M. Studies on mechanical behaviour and tensile fractography of boron carbide particles reinforced Al8081 alloy advanced metal composites. Materials Today: Proceedings. 2022 Jan 1;52:2115-20. https://doi.org/10.1016/j.matpr.2021.12.397

[12] Hanizam H, Salleh MS, Omar MZ, Sulong AB. Optimisation of mechanical stir casting parameters for fabrication of carbon nanotubes-aluminium alloy composite through Taguchi method. Journal of Materials Research and Technology. 2019 Apr 1;8(2):2223-31. https://doi.org/10.1016/j.jmrt.2019.02.008

[13] Chandrasekhar GL, Vijayakumar Y, Nagaral M, Anilkumar C. Microstructural Evaluation and Mechanical Behaviour of Nano B4C Reinforced Al7475 Alloy Metal

Composites. International Journal of Vehicle Structures & Systems (IJVSS). 2021 Dec 1;13(5). https://doi.org/10.4273/ijvss.13.5.24

[14] Kumar VA, Anil MP, Rajesh GL, Hiremath V, Auradi V. Tensile and compression behaviour of boron carbide reinforced 6061Al MMC's processed through conventional melt stirring. Materials Today: Proceedings. 2018 Jan 1;5(8):16141-5. https://doi.org/10.1016/j.matpr.2018.05.100

[15] Siva MM, Rajesh R, Pugazhendhi S, Sivapragash M. Effect of Microstructure and Hardness Properties of Al2011 based Composites for Titanium Di Boride using Stir Casting Method. International Journal of Mechanical and Production Engineering Research and Development (IJMPERD). 2017 Mar;7(2):187-200.

[16] Venkataraman V, Nagaral M. Mechanical characterization and wear behavior of aerospace alloy AA2124 and micro B4C reinforced metal composites. Journal of Metals, Materials and Minerals. 2020;30(4):97-105. https://doi.org/10.55713/jmmm.v30i4.641

[17] Kumar HV, Kempaiah UN, Nagaral M, Auradi V. Impact, tensile and fatigue failure analysis of boron carbide particles reinforced Al-Mg-Si (Al6061) alloy composites. Journal of Failure Analysis and Prevention. 2021 Dec;21(6):2177-89. https://doi.org/10.1007/s11668-021-01265-w

[18] Priyankar D, Ali Z, Nagaral M, Rathnakumar P, Muthuraman V, Umar MD. Microstructure and evolution of mechanical properties of Cu-Sn alloy with graphite and nano zirconium oxide particulates. Materials Today: Proceedings. 2022 Jan 1;52:296-300. https://doi.org/10.1016/j.matpr.2021.08.300

[19] Bharath V, Auradi V, Kumar GV, Nagaral M, Chavali M, Helal M, Sami R, Aljuraide NI, Hu JW, Galal AM. Microstructural evolution, tensile failure, fatigue behavior and wear properties of Al_2O_3 reinforced Al2014 alloy T6 heat treated metal composites. Materials. 2022 Jun 15;15(12):4244. https://doi.org/10.3390/ma15124244

[20] Krishna Prasad S, Dayanand S, Rajesh M, Nagaral M, Auradi V, Selvaraj R. Preparation and mechanical characterization of TiC particles reinforced Al7075 alloy composites. Advances in Materials Science and Engineering. 2022;2022(1):7105189. https://doi.org/10.1155/2022/7105189

[21] Nie CZ, Gu JJ, Liu JL, Zhang D. Production of boron carbide reinforced 2024 aluminum matrix composites by mechanical alloying. Materials Transactions. 2007 May 1;48(5):990-5. https://doi.org/10.2320/matertrans.48.990

[22] Satheesh M, Pugazhvadivu M. Investigation on physical and mechanical properties of Al6061-Silicon Carbide (SiC)/Coconut shell ash (CSA) hybrid composites. Physica B: Condensed Matter. 2019 Nov 1;572:70-5. https://doi.org/10.1016/j.physb.2019.07.058

[23] Balaraj V, Kori N, Nagaral M, Auradi V. Microstructural evolution and mechanical characterization of micro Al_2O_3 particles reinforced Al6061 alloy metal composites. Materials Today: Proceedings. 2021 Jan 1;47:5959-65. https://doi.org/10.1016/j.matpr.2021.04.500

[24] Venkataraman V, Nagaral M. Mechanical characterization and wear behavior of aerospace alloy AA2124 and micro B4C reinforced metal composites. Journal of Metals, Materials and Minerals. 2020;30(4):97-105. https://doi.org/10.55713/jmmm.v30i4.641

[25] Prasad L, Kumar N, Yadav A, Kumar A, Kumar V, Winczek J. In situ formation of ZrB2 and its influence on wear and mechanical properties of ADC12 alloy mixed matrix composites. Materials. 2021 Apr 23;14(9):2141. https://doi.org/10.3390/ma14092141

Research on Engineering Structures & Materials
www.jresm.org
MIM Research Group

Review Article

Influence of palm oil fuel ash as agricultural waste on the environment and strength of geopolymer concrete

Khamees N Abdulhaleem[1,a], Hussein M. Hamada[*2,b], Ali Majdi[3,c], Salim T. Yousif[4,d]

[1]*Civil Engineering Department, University of Kirkuk, Kirkuk, Iraq*
[2]*Al-Qalam University college, Kirkuk 36001, Iraq*
[3]*Dept. of Building and Construction Techniques, Al Mustaqbal University College, 51001 Hilla, Babylon, Iraq*
[4]*Dept. of Civil Engineering, College of Engineering, Nawroz University, Kurdistan, Iraq*

Article Info

Article history:

Received 02 June 2024
Accepted 01 Aug 2024

Keywords:

Palm oil fuel ash;
Geopolymer;
Agriculture waste;
Strength;
Sustainability;
Environment effect;
Durability

Abstract

The utilization of agricultural waste in concrete has gained important attention owing to its potential to improve sustainability and reduce environmental impact. Palm oil fuel ash (POFA), a by-product of the palm oil industry, is one of the agricultural waste materials that has shown promise as a supplementary cementitious material (SCM) in geopolymer concrete (GPC). This paper presents a comprehensive review of the influence of POFA on the environment and strength properties of GPC. The review highlights the chemical composition and physical properties of POFA, its environmental impact, and the challenges and potential strategies for its sustainable utilization. The main factors affecting the strength enhancement or reduction in GPC containing POFA are discussed, including the optimal replacement level and curing condition. The results reveal that the silica oxide in POFA ranges between 55.7% and 69.02%, depending on the POFA source and treatment conditions. The increase in POFA replacement from 0 to 20% led to an increase in the compressive strength of GPC from 28.1 to 30.1 MPa, while in another case the compressive strength decreased from 24 to 18.5 MPa for the same replacement level. There is no specific optimum replacement level. However, the low replacement levels between 0 and 20, are the best. The review also summarizes experimental studies evaluating the effect of POFA on GPC strength. In general, the review provides valuable insights into the use of POFA in GPC and suggests future research directions to enhance its utilization and sustainability in the construction industry.

1. Introduction

Geopolymer concrete (GPC) is a type of concrete that is produced by reacting aluminosilicate materials like slag and fly ash with alkaline activators, like sodium silicate (Na_2SiO_3) and sodium hydroxide (NaOH) [1]. Unlike normal cement concrete, which relies on calcium silicate hydrates (CSH) for strength, GPC forms a three-dimensional aluminosilicate polymer network, as shown in Figure 1. This chemical reaction, known as geopolymerization, results in a binder that can provide comparable or even superior mechanical properties to Portland cement-based concrete [2]. Reducing carbon dioxide (CO_2) emissions compared to Portland cement concrete is one of the significant advantages achieved by GPC [3]. The production of Ordinary Portland cement (OPC) required in huge amounts to produce conventional cement concrete, constitutes a major source of CO_2 emissions due to the high-temperature calcination of limestone in kilns [4]. In contrast, GPC can be produced at much lower temperatures, leading to a significant reduction in CO_2

*Corresponding author: enghu76@gmail.com
[a] orcid.org/0000-0001-9049-227X; [b] orcid.org/0000-0001-9911-8639; [c] orcid.org/0000-0003-0528-6696; [d] orcid.org/0000-0002-3047-822X
DOI: http://dx.doi.org/10.17515/resm2024.306ma0602rv

emissions [5]. Mortar and concrete are used in construction and infrastructure projects, which consume huge amounts of materials and most of these materials are extracted as virgin materials and generate greenhouse gasses in the atmosphere. For instance, cement alone is responsible for the generation of more than 7% of the global CO_2 emissions that mainly contribute in climate change [6]. Additionally, GPC offers several other sustainability benefits. It can utilize industrial by-products and waste materials as precursors, reducing the consumption of natural resources and minimizing the accumulation of waste in open areas [8]. This is associated with the philosophies of the circular economy, where materials are reused or recycled to minimize environmental impact. GPC also exhibits excellent durability and resistance to harsh environments, leading to longer service life and reduced maintenance requirements compared to traditional concrete [9]. Overall, GPC represents a promising alternative to Portland cement concrete, offering improved sustainability, reduced environmental impact, and comparable or superior performance [10]. Incorporating agricultural waste materials, like palm oil fuel ash (POFA), into GPC further enhances its environmental identification by reducing waste generation and supporting the efficient use of resources [11].

The use of agricultural waste like POFA in GPC production is important due to its environmental and economic advantages. Agricultural activities produce large amounts of waste, presenting disposal challenges and environmental risks [12]. Incorporating these wastes into concrete can address these challenges and support sustainable development. Using agricultural waste in GPC production reduces waste disposal costs and turns waste into a valuable construction resource [13]. Moreover, POFA enhances GPC performance by containing pozzolanic materials that react with calcium hydroxide to form additional cementitious compounds [14]. This improves concrete strength, durability, and chemical resistance, while also reducing the risk of thermal cracking. Even though conducting numerous studies about the use of POFA in the GPC. For instance, Liu et al. [15] used POFA instead of fly ash in different replacement levels in the production of lightweight GPC. They used Oil palm shell (OPS) as one of the palm oil wastes as aggregate to obtain low lightweight GPC. They used POFA in 0, 10, 20, 40, and 100% as fly ash replacement with two alkaline solutions to binder ratios of 0.35 and 0.55. They found that the maximum compressive strength of GPC was 30 MPa achieved due to the use of 20% POFA as a fly ash replacement.

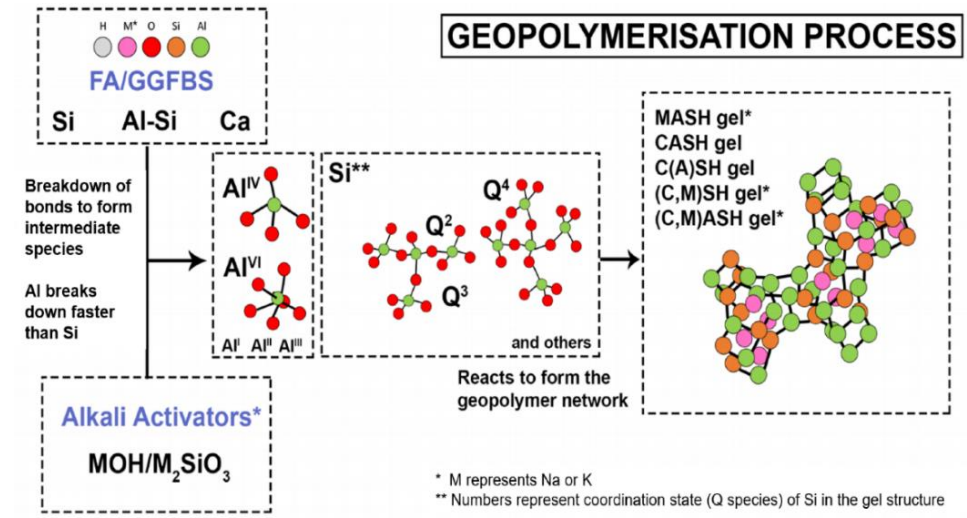

Fig. 1. Geopolymer model with different Si/Al molars [7]

Huseien et al. [16] investigated the effect of different calcium content and curing temperatures on the properties of geopolymer mortars (GPM) comprising agricultural and industrial wastes, such as POFA, GGBS, and fly ash. They detected that the GPM strengths and the reaction products depended significantly on the composition's nature, curing temperatures, and activators. However, there is no study conducted as a review paper discussed the effect of POFA on the environment and strength development. Therefore, this paper reviews the impact of POFA, as agricultural waste, on the strength of GPC and the environment. It highlights the environmental benefits of using agricultural waste in GPC production and emphasizes the significance of POFA in improving the strength of GPC and reducing waste disposal costs. The review aims to provide insights into the effects of POFA on GPC strength, offering valuable information for researchers and academics in sustainable construction.

2. Palm Oil Fuel Ash (POFA) as Agricultural Waste

2.1 Overview of Palm Oil Production and The Generation of POFA

Palm oil is one of the most widely produced and consumed vegetable oils globally, with its production primarily concentrated in tropical regions, particularly Malaysia, Indonesia, Thailand, and Nigeria [17]. As reported by Al-Sabaeei et al. [18], palm oil trees are one of the economic sources in terms of production of huge amounts of oil, palm oil includes crude and kernel oil palm producing 54% of total oil, as shown in Figure 2.

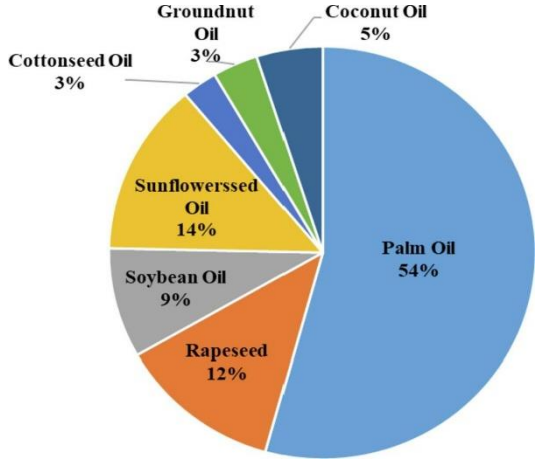

Fig. 2. Capacity per hectare proportion of main corps oil generated in 2018 [18]

The palm oil industry generates a substantial quantity of effluent waste and biomass residue; which can be considered a significant source of greenhouse gases. Therefore, numerous studies have been conducted to investigate the potential use of waste generated from the palm oil industry in different applications. Palm oil fuel ash (POFA) is one of the by-products generated during the production of palm oil. POFA is obtained from the combustion of palm oil biomass, including empty fruit bunches, palm kernel shells, and palm oil mill effluent, in boiler furnaces to generate electricity and steam for palm oil mills [19], as shown in Figure 3 [20]. POFA is a finely divided, pozzolanic material that contains high amounts of silica (SiO_2) and alumina (Al_2O_3), along with other minor constituents [21]. Its chemical composition and pozzolanic properties make it suitable for use as a supplementary cementitious material (SCM) in concrete and GPC production.

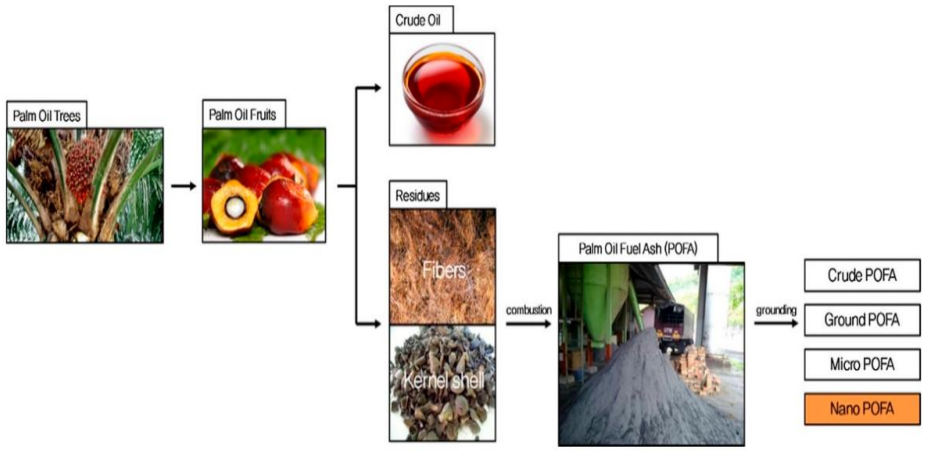

Fig. 3. Production of POFA [20]

2.2 Chemical Composition and Properties of POFA

POFA is a by-product of the combustion of palm oil biomass, mainly generated in palm oil mills. The chemical composition of POFA can vary depending on several factors, including the type of palm oil biomass burned, combustion conditions, post-combustion treatment, and others [22]. As reported by Demirboga and Farhan [23], the chemical composition of POFA has a significant impact on the strength and workability of concrete. The chemical composition of POFA is affected by the source of raw materials, heating temperature, particle fineness, and production process. These factors can affect directly or indirectly on the classification of pozzolanic of POFA, to produce either class C pozzolan [24] or Class F pozzolan [25]. Thanks to the reviewer for the insightful comment. Finer particles of POFA have a larger surface area, which can increase the pozzolanic activity. The chemical composition of POFA is usually classified as Class C Pozzolan due to containing higher amounts of calcium oxide (CaO), more than 10%, or Class F Pozzolan due to having lower calcium oxide content, less than 10%.

Table 1. Chemical composition of POFA

References	SiO_2	Al_2O_3	Fe_2O_3	CaO	MgO	K_2O	Na_2O	SO_3	LOI
Salami et al. [29]	66.91	6.44	5.72	5.56	3.13	5.20	0.19	0.33	2.3
Hamada et al. [30]	67.5	4. 2	8.12	3.97	2.72	8.45	0.115	0.535	1.48
Tangchirapat et al. [31]	65.3	2.5	1.9	6.4	3.0	5.7	0.3	0.4	10.0
Kroehong et al. [32]	55.7	0.9	2.0	12.5	5.1	11.9	1.0	2.9	4.7
Bashar et al. [33]	67.72	3.71	4.71	5.57	4.04	7.67	0.16	1.07	6.2
Alsubari et al. [34]	69.02	3.9	4.33	5.01	5.18	6.9	0.18	0.41	1.8
Liu et al. [35]	63.4	5.5	4.2	4.3	3.7	6.3	---	0.9	6.0
Olivia et al. [36]	64.3	4.36	3.41	7.92	4.58	5.57	---	0.04	4.97
Mijarsh et al. [37]	61.33	7.018	5.11	8.20	4.69	6.50	0.123	0.27	2.53
Yusuf et al. [38]	60.42	4.26	3.34	11.0	5.31	5.03	0.18	0.45	2.55

Generally, POFA contains a significant amount of silica, typically ranging from 40% to 70%, and alumina content ranging from 20% to 30%. Other constituents found in POFA include iron oxide (Fe2O3), calcium oxide (CaO), magnesium oxide (MgO), potassium oxide (K2O), and sodium oxide (Na2O), among others. Table 1 shows the chemical composition of POFA.

The pozzolanic properties of POFA are attributed to its amorphous silica content, which reacts with calcium hydroxide (Ca(OH)2) in the existence of water to produce further calcium silicate hydrate (C-S-H) gel [26]. This reaction enhances the durability and strength of concrete by filling in voids and improving the overall microstructure [27]. In addition to its chemical composition, POFA also possesses certain physical properties that influence its suitability for use in concrete. POFA is typically a fine powder with a specific surface area ranging from 1230 m2/kg to 7670 m2/kg, making it highly reactive when mixed with alkaline activators in concrete [28]. Its particle size distribution, density, and color can also vary depending on the combustion process and post-combustion treatment.

As shown in Table 1, the silica oxide recorded the highest value among other POFA components, it was ranging between 55.7% and 69.02%. The study investigated different content of SiO2 of POFA on the strength of GPC. The chemical composition of POFA differs from one study to another, and this difference depends on the sources, treatment conditions, and other factors. The differences in the chemical composition of POFA mainly affect the strength of concrete and GPC [39]. For instance, Khankhaje et al. [40] reported that POFA is rich in SiO2 content with slight amounts of magnesium and calcium. Therefore, the existence of large amounts of silica content affects the pozzolanic activity essential to produce further calcium-silicate-hydrate (C–S–H) gels, thus increasing the GPC strength. Liu et al. [35] stated that the sum of silica, alumina, and Iron is 73.1%, which means that the POFA produced has a high pozzolanic activity and can be used to enhance the GPC strength. Overall, the chemical composition of POFA is various and depends on numerous factors. The use of POFA especially with high silica and alumina oxide can enhance concrete properties.

2.3 Physical Properties of POFA

The physical properties of POFA have mainly contributed to enhancing GPC properties. The fine particle size of POFA as micro and nanoparticles has affected the strength and durability of GPC. The physical properties of POFA are influenced by several factors such as the burning temperature and source of palm oil waste [28, 41], for instance, the color of POFA is converted from grey into darker, if it includes a high quantity of unburned carbon; and converted into grey after exposing to further burning [42]. For instance, Khalid et al. [43], reported that the POFA exposed to the milling process can produce further fineness of POFA. Awal and Shehu [44] detected that the specific surface area of treated POFA was 4930 cm^2/g and the amount of POFA retained on the 45 mm sieve was 10.5%. Table 2 shows the physical properties of POFA that have been examined by the previous studies.

Table 2. Physical properties of POFA

References	Specific gravity	Specific surface area m^2/g	Median particle size μm
Lim et al. [45]	2.56	7.205	1.10
Shehu and Awal [46]	2.42	---	2.89
Hossain et al. [47]	---	1.230	13.37
Kroehong et al. [48]	2.36	670	15.6
Zeyad et al. [49]	2.59	7.67	2.06
Sumesh et al. [50]	2.1	509	19.4
Hamada et al. [51]	2.52	1962	1.0
Yusuf et al. [52]	2.6	13.4	1.07

As shown in Table 2, the specific gravity of POFA ranges from 2.1 to 2.6 and the particle size of POFA ranges from 1.0 to 19.4 μm. These physical properties are affected by several factors as mentioned above. These properties also affect the properties of GPC, especially

the fine particle size POFA has a higher influence than that of a larger one. For instance, Elbasir et al. [53] investigated the effect of different particle sizes of POFA on the strength of alkaline-activated mortars (AAM). They found that the high strength of AAM has been achieved due to the addition of POFA with greater fineness. This result can be attributed to the production of extra N–A–S–H and C–S–H in the AAM which used POFA with higher fineness.

2.4 Environmental Impact of POFA Disposal and the Need for Sustainable Utilization

The disposal of POFA into landfills and open areas leads to numerous environmental issues. Inappropriate disposal practices can lead to soil contamination, air pollution, and groundwater pollution [54]. POFA comprises trace elements and fine particles that can cause risks to environment issues and human health if not appropriately managed. Furthermore, the accumulation of POFA in landfills can contribute to the generation of leachate, a liquid that can contain harmful chemicals and pollutants [55]. Leachate has the potential to contaminate surface water and groundwater, posing risks to aquatic ecosystems and human populations. Given these environmental concerns, there is a growing need for sustainable utilization of POFA. By incorporating POFA into concrete production, it is possible to mitigate the environmental impact of its disposal while also providing a value-added application for the waste material. The green use of POFA in GPC production offers several environmental benefits. Firstly, it reduces the need for landfill space, helping to alleviate the pressure on waste disposal facilities. Secondly, it reduces the demand for natural resources, such as limestone and clay, which are used in the production of traditional cement. This contributes to the conservation of natural resources and helps to minimize the environmental impact of cement production [56]. Moreover, the use of POFA in concrete production can help reduce greenhouse gas emissions [42]. The production of Portland cement, the key component of conventional concrete, is a major source of CO_2 emissions [57]. By partially replacing cement with POFA, which requires lower energy inputs for production, the overall carbon footprint of the concrete is reduced.

3. Influence of POFA on the Strength of GPC

3.1 Experimental Studies Evaluating the Effect of POFA on GPC Strength

Numerous experimental studies have been conducted to investigate the influence of POFA on the strength properties of GPC [15, 58, 59]. These studies have demonstrated that the incorporation of POFA can lead to both enhancements and reductions in the strength of GPC, depending on various factors such as the replacement level of POFA, curing conditions, and activator composition. For instance, Isa et al. [60] conducted an experimental study on the influence of POFA and granulated blast furnace slag (GGBS) on the strength of GPC. They observed that the addition of GGBS and POFA in geopolymer mortar (GPM) enhances and increases the 28 days-compressive and flexural strengths up to 28.17 and 4.48 MPa, respectively. The compressive strength increased by 73.3% due to the addition of 40% GGBS as a POFA replacement. Huseien et al. [61] assessed the influence of POFA with fly ash and GGBS on the strength of GPM. They used POFA in different replacement levels to replace fly ash and slag. The bond strength performance of the mortars was assessed in terms of slant shear, flexural, and splitting tensile strengths. They observed that the addition of POFA and fly ash in the GPM led to a significant reduction in the CaO: Al_2O_3 and CaO: SiO_2 ratios, consequently reducing the strength performance and geopolymerization process. The compressive strength of GPC increased by 17% due to the addition of 10% POFA and 20% fly ash with 70% GGBS.

.

Table 3. Influence of POFA on the compressive, flexural, and splitting tensile strengths of GPC.

References	Aluminosilicate used	POFA % by weight	Compressive strength MPa	Flexural strength MPa	Splitting tensile strength MPa
Liu et al. [15]	Fly ash	0	28.1	3.55	2.12
		10	28.4	3.70	2.13
		20	30.1	3.74	2.41
		40	16.4	3.11	1.62
		100	10.0	1.95	1.27
Huseien et al. [63]	Slag	30	70	10.2	5.5
		40	70	9.0	4.7
		50	55	7.5	4.7
		60	45	5.5	3.1
		70	31	3.5	2.5
Alnahhal et al. [64]	Fly ash	0	3.8		
		10	5.5		
		20	6.1		
		30	5.9		
Fauzi [65]	Fly ash	0	24		
		5	23		
		10	23		
		15	21.5		
		20	18.5		
Hawa et al. [66]	Metakaolin	0	75		
		5	70		
		10	68		
		15	54		
Chub-Uppakarn et al. [59]	Metakaolin	0	47		
		10	18		
		20	37		
		40	18		
Karim et al. [67]	fly ash and rice husk ash	0	23.1		
		20	12.9		
		30	20.5		
		35	14.9		
		40	5.9		
Liu et al. [68]	Fly ash	0	28.1	3.55	2.12
		10	28.4	3.70	2.13
		20	30.1	3.74	2.41
		40	16.4	3.11	1.62
		100	10	1.95	1.27

The variability in the effects of POFA on GPC strength can be attributed to several factors. The pozzolanic reactivity of POFA, which depends on its chemical composition and fineness, plays a crucial role in determining its impact on concrete strength [62]. Additionally, the curing conditions, activator type, and mix proportion can also influence

the strength development of GPC containing POFA [14, 60]. For instance, Chub-uppakarn et al. [59] examined the influence of metakaolin (MK) and POFA on the GPM. They partially replace MK with POFA to show the effect of POFA on the strength of GPM. They found that the replace 10% MK by POFA led to an increase in the 28 days-compressive strength by 22.08 %. This increase in strength was attributed to the improvement in the geopolymerization process, thus increasing the compressive strength. Table 3 shows the influence of POFA on the compressive, flexural, and splitting tensile strength of GPCAs shown in Table 3, the use of POFA as a binder material in the production of GPC mostly decreases the strength of GPC. At the same time, some studies proved that the use of POFA as a binder material enhances the strength of GPC, and this enhancement depends on numerous factors like fineness, particle size, materials sources, and chemical composition. Numerous researchers used treated POFA to get better performance when used in the production of GPC. For instance, Mijarsh et al. [37] reported that the use of treated POFA in the GPC mix can increase the compressive strength of GPC at 1, 2, and 7 days up to 42.64, 45.55, and 47.27 MPa. This increase is significantly affected by the treatment methods of POFA. Therefore, the treatment of POFA before incorporation into the GPC mixture is a significant issue to consider. Alnahhal et al. [64] reported that the addition of POFA into fly ash-based geopolymer foamed concrete (GPFC) can increase the compressive strength, as shown in Figure 4.

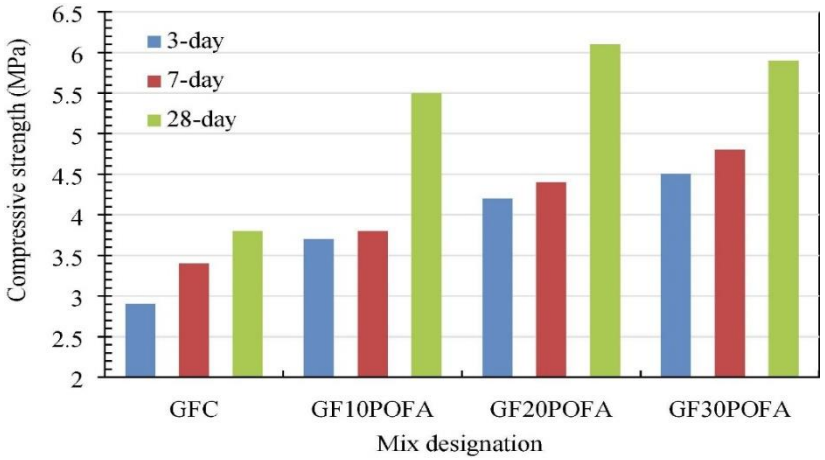

Fig. 4. Improvement of compressive strength for GPFC due to the addition of POFA [64]

3.2 Factors affecting the strength enhancement or reduction.

As mentioned before, the strength of GPC containing POFA can be influenced by various factors, including the chemical composition of POFA, its fineness, the replacement level of cement with POFA, curing conditions, and activator composition. Determining these factors is essential for optimizing the mix design and achieving the desired strength properties. Table 4 shows the important factors effecting the strength enhancement or reduction.

In general, the factors abovementioned in Table 4 interact in complex ways to influence the strength properties of GPC containing POFA. Optimizing these factors through careful mix design and curing practices is essential for maximizing the strength enhancement potential of POFA in GPC. As reported by Elbasir et al. [53], the physical properties of POFA like fineness and particle size also have a significant effect on the strength of GPC.

Table 4. Factors effecting the strength of GPC.

No.	Factors	Effect on strength
1	Chemical Composition of POFA	The chemical composition of POFA, particularly its silica oxide (SiO_2) and alumina oxide (Al_2O_3) content, plays a crucial role in determining its pozzolanic reactivity. POFA with higher silica and alumina content is generally more reactive and can contribute to greater strength enhancement in GPC and GPM [14, 61].
2	Fineness of POFA	The fineness of POFA affects its reactivity and its ability to react with the activator solution. Finer particles have a larger surface area, allowing for more effective pozzolanic reactions and potentially leading to higher strength development in GPC [20, 67].
3	Replacement Level of POFA	The compressive strength of GPC significantly affected by the replacement levels of POFA. Further POFA percentage might leads to reduce the compressive strength up to the lowest value, and this reduction is might be due to incomplete pozzolanic reactions [59].
4	Curing Conditions	The curing conditions, including temperature, humidity, and duration, can influence the rate and extent of pozzolanic reactions between POFA and the activator solution. Optimum curing conditions are essential for achieving the desired strength properties in GPC [67, 69].
5	Activator Composition	The composition of the activator solution, including the type and concentration of alkali activators, can affect the pozzolanic reactivity of POFA. Different activator compositions may lead to varying degrees of strength enhancement or reduction in GPC [14, 69].
	Mix Design	The overall mix design, including the proportions of POFA, aggregate, and other ingredients, can impact the strength properties of GPC. A well-balanced mix design is essential for achieving the desired strength and durability [59].

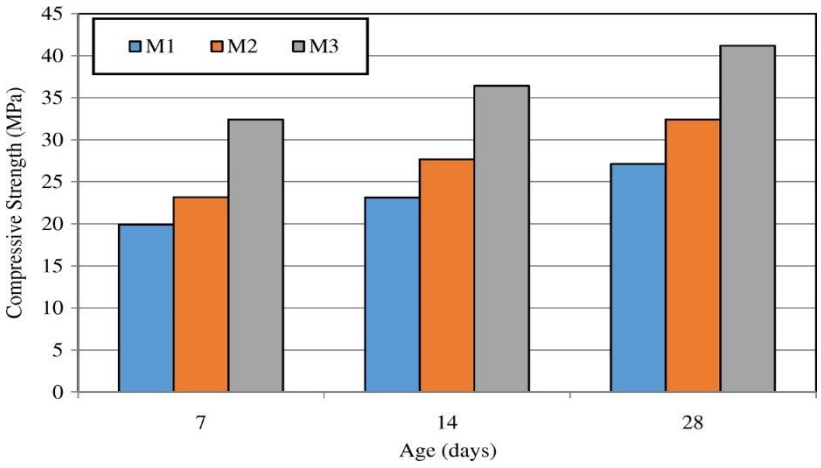

Fig. 5. Compressive strength of POFA based-GPC [53]

For example, the utilization of three distinct particle fineness levels results in varying compressive strengths, as depicted in Figure 5. M1, M2, and M3 represent the specifically treated POFA (t-POFA), fine POFA (f-POFA), and ultrafine POFA (u-POFA), respectively. These three types of POFA have particle sizes of 2.79 μm, 2.04 μm, and 1.1 μm, respectively.

4. Challenges in Addition POFA in GPC

Despite its potential benefits, the addition of POFA in GPC poses several challenges that need to be addressed for successful implementation. These challenges can be summarized in Table 5.

Table 5. Challenges in the use of POFA as a source material in the production of GPC.

No.	Challenges	Results
1	Variability in POFA properties	POFA properties, such as chemical composition and physical properties including, silica oxide content, particle size, fineness, and pozzolanic reactivity, can vary depending on factors such as source, combustion process, and post-treatment [70]. This flexibility can affect the consistency and performance of GPC, thus involving careful characterization and selection of POFA in the production of GPC.
2	Optimum replacement level	Identify the optimum replacement level of POFA in the concrete mix is one of the challenges which effect the performance of GPC. However, the use of high replacement levels of POFA can reduce the environmental issues but reducing strength of GPC. Therefore, finding the best balance of POFA content and strength required is critical.
3	Compatibility with Activators	POFA may show various reactivity with alkali activators compared to other SCMs normally used in GPC, like slag or fly ash. Confirming compatibility between activators and POFA is crucial for getting the desired strength and durability properties.
4	Curing requirements	GPC containing POFA may have specific curing requirements, such as continued curing durations or elevated temperatures, to enhance optimum strength. Meeting these curing requirements can be challenging in practical construction applications and may require special curing facilities.
5	Long-term performance	The long-term performance of GPC containing POFA, including durability and resistance to environmental factors is affected by numerous factors. Confirming the long-term durability of concrete structures incorporating POFA requires careful consideration of factors like maintenance requirements, exposure conditions, and material aging.

Addressing these challenges requires collaboration between industry stakeholders, researchers, and regulatory bodies to determine guidelines, standards, and best practices for the sustainable applications of POFA in GPC. Generally, the use of POFA in the production of GPC in vast quantities depends on finding suitable solutions for the challenges above-mentioned.

5. Future Directions to Use POFA in GPC

There are some potential strategies that should be applied to maximize use of POFA in GPC mixtures, which can be summarized in Table 6.

Table 6. Potential strategies to enhance the use of POFA in GPC.

No.	Strategies	Strategies that should be conduct
1	Optimization of POFA properties	Implement further studies to optimize the properties of POFA, such as its fineness, chemical composition, and pozzolanic reactivity, can enhance its suitability for use in GPC.
2	Blending with other SCMs	Blending POFA with other SCMs, such as fly ash or slag, can enhance the performance of GPC.
3	Use of chemical additives	Incorporating chemical additives, such as silica fume or metakaolin, can enhance the reactivity of POFA and improve its performance in GPC.
4	Optimization of mix design	Conducting detailed mix design studies to optimize the proportions of POFA, activators, and other ingredients in GPC can improve its performance.
5	Development of standardized guidelines	Developing standardized guidelines and best practices for the use of POFA in GPC can facilitate its widespread adoption.
6	Innovative applications	Discovering advanced techniques and applications for additional POFA in GPC, such as high-performance concrete, precast elements, or 3D printing, can expand its potential use and value.
7	Collaboration and knowledge sharing	Encouraging collaboration between researchers, industry stakeholders, and government agencies can promote knowledge sharing and technology transfer related to the use of POFA in GPC.

Adoption of the strategies abovementioned in Table 6, can maximize the use of POFA in GPC, thus enhancing sustainability, reducing environmental impact, and increasing economic value in GPC. Also, the compressive, flexural, and splitting tensile strengths of GPC containing POFA can be improved when obtaining the optimal mix design with suitable additives and curing conditions.

5. Conclusions and Recommendations

This study shows the effect of POFA as agriculture waste and high silica content on the environment and the strength of GPC. The main results can be summarized in the following points:

- The addition of an appropriate replacement level of POFA in GPC can increase compressive, flexural, and splitting tensile strengths. However, this increase is associated with the pozzolanic reactivity of POFA. While the addition of a high volume of POFA decreases the strength of GPC.
- The optimum content and proportion of POFA varies depending on factors like POFA properties, curing conditions, and mix design. While low replacement levels 10% to 20%, have been found to increase strength. The increase in POFA replacement from 0 to 20% led to an increase in the compressive strength of GPC from 28.1 to 30.1 MPa, while in another case the compressive strength decreased from 24 to 18.5 MPa for the same replacement level.
- The properties of POFA, such as its chemical composition, fineness, and pozzolanic reactivity, significantly influence its impact on concrete strength. POFA with higher silica and alumina content and finer particle size tends to exhibit greater strength enhancement in GPC.

- Optimum curing conditions, including temperature, humidity, and duration, are crucial for achieving the desired strength properties in GPC containing POFA. Proper curing can promote the complete hydration of cementitious compounds and enhance the strength development of the concrete.
- Despite the potential benefits of using POFA in GPC, various challenges need to be addressed, such as variability in POFA properties, compatibility with activators, and long-term performance.

In conclusion, the utilization of POFA as agricultural waste in GPC offers a sustainable solution to waste management and contributes to the reduction of environmental impact in the construction industry. By optimizing mix design, addressing challenges, and promoting knowledge sharing, POFA can be effectively utilized to enhance the strength and sustainability of GPC.

References

[1] Wu X, Shen Y, Hu L. Performance of geopolymer concrete activated by sodium silicate and silica fume activator. Case Stud Constr Mater. 2022;17. https://doi.org/10.1016/j.cscm.2022.e01513

[2] Fan C, Wang B, Ai H, Qi Y, Liu Z. A comparative study on solidification/stabilization characteristics of coal fly ash-based geopolymer and Portland cement on heavy metals in MSWI fly ash. J Clean Prod. 2021;319:128790. https://doi.org/10.1016/j.jclepro.2021.128790

[3] Das S, Saha P, Jena SP, Panda P. Geopolymer concrete: Sustainable green concrete for reduced greenhouse gas emission-A review. Mater Today Proc. 2022;60:62-71. https://doi.org/10.1016/j.matpr.2021.11.588

[4] Nilimaa J. Smart materials and technologies for sustainable concrete construction. Dev Built Environ. 2023;100177. https://doi.org/10.1016/j.dibe.2023.100177

[5] Amran YM, Alyousef R, Alabduljabbar H, El-Zeadani M. Clean production and properties of geopolymer concrete; A review. J Clean Prod. 2020;251:119679. https://doi.org/10.1016/j.jclepro.2019.119679

[6] Shah IH, Miller SA, Jiang D, Myers RJ. Cement substitution with secondary materials can reduce annual global CO2 emissions by up to 1.3 gigatons. Nat Commun. 2022;13:5758. https://doi.org/10.1038/s41467-022-33289-7

[7] Wong V, Jervis W, Fishburn B, Numata T, Joe W, Rawal A, et al. Long-term strength evolution in ambient-cured solid-activator geopolymer compositions. Minerals. 2021;11:143. https://doi.org/10.3390/min11020143

[8] Tahir MFM, Abdullah MMA, Abd Rahim SZ, Hasan MRM, Saafi M, Jaya RP, et al. Potential of industrial By-Products based geopolymer for rigid concrete pavement application. Constr Build Mater. 2022;344:128190. https://doi.org/10.1016/j.conbuildmat.2022.128190

[9] Luhar S, Luhar I, Gupta R. Durability performance evaluation of green geopolymer concrete. Eur J Environ Civ Eng. 2022;26:4297-4345. https://doi.org/10.1080/19648189.2020.1847691

[10] Beskopylny AN, Stel'makh SA, Shcherban' EM, Mailyan LR, Meskhi B, El'shaeva D, et al. Developing environmentally sustainable and cost-effective geopolymer concrete with improved characteristics. Sustainability. 2021;13:13607. https://doi.org/10.3390/su132413607

[11] Pradhan P, Dwibedy S, Pradhan M, Panda S, Panigrahi SK. Durability characteristics of geopolymer concrete-Progress and perspectives. J Build Eng. 2022;59:105100. https://doi.org/10.1016/j.jobe.2022.105100

[12] Gontard N, Sonesson U, Birkved M, Majone M, Bolzonella D, Celli A, et al. A research challenge vision regarding management of agricultural waste in a circular bio-based

economy. Crit Rev Environ Sci Technol. 2018;48:614-654. https://doi.org/10.1080/10643389.2018.1471957
[13] Raju GK, Nagaraju TV, Jagadeep K, Rao MV, Varma VC. Waste-to-energy agricultural wastes in development of sustainable geopolymer concrete. Mater Today Proc. 2023.
[14] Kwek SY, Awang H, Cheah CB. Influence of liquid-to-solid and alkaline activator (Sodium silicate to sodium hydroxide) ratios on fresh and hardened properties of alkali-activated palm oil fuel ash geopolymer. Materials. 2021;14:4253. https://doi.org/10.3390/ma14154253
[15] Liu MYJ, Chua CP, Alengaram UJ, Jumaat MZ. Utilization of palm oil fuel ash as binder in lightweight oil palm shell geopolymer concrete. Adv Mater Sci Eng. 2014;2014:610274. https://doi.org/10.1155/2014/610274
[16] Huseien GF, Mirza J, Ismail M, Hussin MW. Influence of different curing temperatures and alkali activators on properties of GBFS geopolymer mortars containing fly ash and palm-oil fuel ash. Constr Build Mater. 2016;125:1229-1240. https://doi.org/10.1016/j.conbuildmat.2016.08.153
[17] Paterson RRM. Longitudinal trends of future climate change and oil palm growth: empirical evidence for tropical Africa. Environ Sci Pollut Res Int. 2021;28:21193-21203. https://doi.org/10.1007/s11356-020-12072-5
[18] Al-Sabaeei AM, Al-Fakih A, Noura S, Yaghoubi E, Alaloul W, Al-Mansob RA, et al. Utilization of palm oil and its by-products in bio-asphalt and bio-concrete mixtures: A review. Constr Build Mater. 2022;337:127552. https://doi.org/10.1016/j.conbuildmat.2022.127552
[19] Hamada HM, Al-Attar A, Shi J, Yahaya F, Al Jawahery MS, Yousif ST. Optimization of sustainable concrete characteristics incorporating palm oil clinker and nano-palm oil fuel ash using response surface methodology. Powder Technol. 2023;413:118054. https://doi.org/10.1016/j.powtec.2022.118054
[20] Amran M, Lee YH, Fediuk R, Murali G, Mosaberpanah MA, Ozbakkaloglu T, et al. Palm oil fuel ash-based eco-friendly concrete composite: A critical review of the long-term properties. Materials. 2021;14:7074. https://doi.org/10.3390/ma14227074
[21] Katte AR, Mwero J, Gibigaye M, Koteng DO. Recycling palm oil wastes for the production of a pozzolanic cement replacement material for concrete. Results Eng. 2023;17:100903. https://doi.org/10.1016/j.rineng.2023.100903
[22] Ayub M, Othman MHD, Khan IU, Hubadillah SK, Kurniawan TA, Ismail AF, et al. Promoting sustainable cleaner production paradigms in palm oil fuel ash as an eco-friendly cementitious material: A critical analysis. J Clean Prod. 2021;295:126296. https://doi.org/10.1016/j.jclepro.2021.126296
[23] Demirboga R, Farhan KZ. Palm oil fuel ash (POFA). In: Sustainable Concrete Made with Ashes and Dust from Different Sources. Elsevier; 2022. p. 279-330. https://doi.org/10.1016/B978-0-12-824050-2.00006-1
[24] Ahmad M, Omar R, Malek M, Noor NM, Thiruselvam S. Compressive strength of palm oil fuel ash concrete. In: Proceedings of the international conference on construction and building technology. Kuala Lumpur, Malaysia; 2008. p. 16-20.
[25] Karim M, Zain M, Jamil M, Lai F. Fabrication of a non-cement binder using slag, palm oil fuel ash and rice husk ash with sodium hydroxide. Constr Build Mater. 2013;49:894-902. https://doi.org/10.1016/j.conbuildmat.2013.08.077
[26] Kwek SY, Awang H, Cheah CB, Mohamad H. Development of sintered aggregate derived from POFA and silt for lightweight concrete. J Build Eng. 2022;49:104039. https://doi.org/10.1016/j.jobe.2022.104039
[27] Zeyad AM, Johari MAM, Alharbi YR, Abadel AA, Amran YM, Tayeh BA, et al. Influence of steam curing regimes on the properties of ultrafine POFA-based high-strength green concrete. J Build Eng. 2021;38:102204. https://doi.org/10.1016/j.jobe.2021.102204
[28] Hamada HM, Thomas BS, Yahaya FM, Muthusamy K, Yang J, Abdalla JA, et al. Sustainable use of palm oil fuel ash as a supplementary cementitious material: A

comprehensive review. J Build Eng. 2021;40:102286. https://doi.org/10.1016/j.jobe.2021.102286
[29] Salami BA, Johari MAM, Ahmad ZA, Maslehuddin M. Impact of added water and superplasticizer on early compressive strength of selected mixtures of palm oil fuel ash-based engineered geopolymer composites. Constr Build Mater. 2016;109:198-206. https://doi.org/10.1016/j.conbuildmat.2016.01.033
[30] Hamada HM, Alya'a A, Yahaya FM, Muthusamy K, Tayeh BA, Humada AM. Effect of high-volume ultrafine palm oil fuel ash on the engineering and transport properties of concrete. Case Stud Constr Mater. 2020;12. https://doi.org/10.1016/j.cscm.2019.e00318
[31] Tangchirapat W, Jaturapitakkul C, Chindaprasirt P. Use of palm oil fuel ash as a supplementary cementitious material for producing high-strength concrete. Constr Build Mater. 2009;23:2641-2646. https://doi.org/10.1016/j.conbuildmat.2009.01.008
[32] Kroehong W, Sinsiri T, Jaturapitakkul C, Chindaprasirt P. Effect of palm oil fuel ash fineness on the microstructure of blended cement paste. Constr Build Mater. 2011;25:4095-4104. https://doi.org/10.1016/j.conbuildmat.2011.04.062
[33] Bashar II, Alengaram UJ, Jumaat MZ, Islam A, Santhi H, Sharmin A. Engineering properties and fracture behaviour of high volume palm oil fuel ash based fibre reinforced geopolymer concrete. Constr Build Mater. 2016;111:286-297. https://doi.org/10.1016/j.conbuildmat.2016.02.022
[34] Alsubari B, Shafigh P, Jumaat MZ. Development of self-consolidating high strength concrete incorporating treated palm oil fuel ash. Materials. 2015;8:2154-2173. https://doi.org/10.3390/ma8052154
[35] Liu MYJ, Alengaram UJ, Santhanam M, Jumaat MZ, Mo KH. Microstructural investigations of palm oil fuel ash and fly ash based binders in lightweight aggregate foamed geopolymer concrete. Constr Build Mater. 2016;120:112-122. https://doi.org/10.1016/j.conbuildmat.2016.05.076
[36] Olivia M, Pradana T, Sitompul IR. Properties of plain and blended cement concrete immersed in acidic peat water canal. Procedia Eng. 2017;171:557-563. https://doi.org/10.1016/j.proeng.2017.01.372
[37] Mijarsh M, Johari MM, Ahmad Z. Synthesis of geopolymer from large amounts of treated palm oil fuel ash: Application of the Taguchi method in investigating the main parameters affecting compressive strength. Construction and Building Materials. 2014;52:473-81. https://doi.org/10.1016/j.conbuildmat.2013.11.039
[38] Yusuf MO, Johari MAM, Ahmad ZA, Maslehuddin M. Effects of addition of Al(OH)3 on the strength of alkaline activated ground blast furnace slag-ultrafine palm oil fuel ash (AAGU) based binder. Construction and Building Materials. 2014;50:361-7. https://doi.org/10.1016/j.conbuildmat.2013.09.054
[39] Kabir S, Alengaram UJ, Jumaat MZ, Sharmin A, Islam A. Influence of molarity and chemical composition on the development of compressive strength in POFA based geopolymer mortar. Advances in Materials Science and Engineering. 2015;2015. https://doi.org/10.1155/2015/647071
[40] Khankhaje E, Hussin MW, Mirza J, Rafieizonooz M, Salim MR, Siong HC, et al. On blended cement and geopolymer concretes containing palm oil fuel ash. Materials & Design. 2016;89:385-98. https://doi.org/10.1016/j.matdes.2015.09.140
[41] Liew Y, Doh S, Chin S. A comprehensive review on the impact of micro and nano palm oil fuel ash in cementitious material. Materials Today: Proceedings. 2023. https://doi.org/10.1016/j.matpr.2023.10.037
[42] Hamada H, Abed F, Alattar A, Yahaya F, Tayeh B, Aisheh YIA. Influence of palm oil fuel ash on the high strength and ultra-high performance concrete: A comprehensive review. Engineering Science and Technology, an International Journal. 2023;45:101492. https://doi.org/10.1016/j.jestch.2023.101492

[43] Khalid NHA, Hussin MW, Mirza J, Ariffin NF, Ismail MA, Lee HS, et al. Palm oil fuel ash as potential green micro-filler in polymer concrete. Construction and Building Materials. 2016;102:950-60. https://doi.org/10.1016/j.conbuildmat.2015.11.038
[44] Balakrishnan B, Awal A, Shehu I. Influence of high volume fly ash in controlling heat of hydration of concrete. Measurement. 2013;3:932-6.
[45] Lim NHAS, Ismail MA, Lee HS, Hussin MW, Sam ARM, Samadi M. The effects of high volume nano palm oil fuel ash on microstructure properties and hydration temperature of mortar. Construction and Building Materials. 2015;93:29-34. https://doi.org/10.1016/j.conbuildmat.2015.05.107
[46] Shehu I, Awal AA. Mechanical properties of concrete incorporating high volume palm oil fuel ash. Advanced Materials Research. 2012;599:537-40. https://doi.org/10.4028/www.scientific.net/AMR.599.537
[47] Hossain M, Karim M, Elahi M, Islam M, Zain M. Long-term durability properties of alkali-activated binders containing slag, fly ash, palm oil fuel ash and rice husk ash. Construction and Building Materials. 2020;251:119094. https://doi.org/10.1016/j.conbuildmat.2020.119094
[48] Kroehong W, Damrongwiriyanupap N, Sinsiri T, Jaturapitakkul C. The effect of palm oil fuel ash as a supplementary cementitious material on chloride penetration and microstructure of blended cement paste. Arabian Journal for Science and Engineering. 2016;41:4799-808. https://doi.org/10.1007/s13369-016-2143-1
[49] Zeyad AM, Johari MM, Tayeh BA, Yusuf MO. Efficiency of treated and untreated palm oil fuel ash as a supplementary binder on engineering and fluid transport properties of high-strength concrete. Construction and Building Materials. 2016;125:1066-79. https://doi.org/10.1016/j.conbuildmat.2016.08.065
[50] Sumesh M, Alengaram UJ, Jumaat MZ, Mo KH. Microstructural and strength characteristics of high-strength mortar using nontraditional supplementary cementitious materials. Journal of Materials in Civil Engineering. 2019;31:04019017. https://doi.org/10.1061/(ASCE)MT.1943-5533.0002626
[51] Hamada HM, Yahaya FM, Muthusamy K, Jokhio GA, Humada AM. Fresh and hardened properties of palm oil clinker lightweight aggregate concrete incorporating Nano-palm oil fuel ash. Construction and Building Materials. 2019;214:344-54. https://doi.org/10.1016/j.conbuildmat.2019.04.101
[52] Yusuf MO, Johari MAM, Ahmad ZA, Maslehuddin M. Effects of H2O/Na2O molar ratio on the strength of alkaline activated ground blast furnace slag-ultrafine palm oil fuel ash based concrete. Materials & Design (1980-2015). 2014;56:158-64. https://doi.org/10.1016/j.matdes.2013.09.078
[53] Elbasir OM, Johari MAM, Ahmad ZA. Effect of fineness of palm oil fuel ash on compressive strength and microstructure of alkaline activated mortar. European Journal of Environmental and Civil Engineering. 2019;23:136-52. https://doi.org/10.1080/19648189.2016.1271362
[54] Mujedu KA, Ab-Kadir MA, Ismail M. A review on self-compacting concrete incorporating palm oil fuel ash as a cement replacement. Construction and Building Materials. 2020;258:119541. https://doi.org/10.1016/j.conbuildmat.2020.119541
[55] Abuabdou SM, Bashir MJ, Aun NC, Sethupathi S, Yong WL. Development of a novel polyvinylidene fluoride membrane integrated with palm oil fuel ash for stabilized landfill leachate treatment. Journal of Cleaner Production. 2021;311:127677. https://doi.org/10.1016/j.jclepro.2021.127677
[56] Hamada HM, Jokhio GA, Yahaya FM, Humada AM, Gul Y. The present state of the use of palm oil fuel ash (POFA) in concrete. Construction and Building Materials. 2018;175:26-40. https://doi.org/10.1016/j.conbuildmat.2018.03.227
[57] Alsalman A, Assi LN, Kareem RS, Carter K, Ziehl P. Energy and CO2 emission assessments of alkali-activated concrete and Ordinary Portland Cement concrete: A

comparative analysis of different grades of concrete. Cleaner Environmental Systems. 2021;3:100047. https://doi.org/10.1016/j.cesys.2021.100047
[58] Salih MA, Ali AAA, Farzadnia N. Characterization of mechanical and microstructural properties of palm oil fuel ash geopolymer cement paste. Construction and Building Materials. 2014;65:592-603. https://doi.org/10.1016/j.conbuildmat.2014.05.031
[59] Chub-Uppakarn T, Chompoorat T, Thepumong T, Sae-Long W, Khamplod A, Chaiprapat S. Influence of partial substitution of metakaolin by palm oil fuel ash and alumina waste ash on compressive strength and microstructure in metakaolin-based geopolymer mortar. Case Studies in Construction Materials. 2023;19 https://doi.org/10.1016/j.cscm.2023.e02519
[60] Isa MN, Awang H. Characteristics of palm oil fuel ash geopolymer mortar activated with wood ash lye cured at ambient temperature. Journal of Building Engineering. 2023;66:105851. https://doi.org/10.1016/j.jobe.2023.105851
[61] Huseien GF, Hussein ZJ, Kubba Z, Nikolaevich BM, Mirza J. Improved Bond Strength Performance of Geopolymer Mortars: Role of High Volume Ground Blast Furnace Slag, Fly Ash, and Palm Oil Fuel Ash Incorporation. Minerals. 2023;13:1096. https://doi.org/10.3390/min13081096
[62] Olutoge FA, Kolade AS. Investigation of Compressive Strength of Slag-based Geopolymer Concrete Incorporated with Palm Oil Fuel Ash. West Indian Journal of Engineering. 2023;45. https://doi.org/10.47412/ZGIJ9698
[63] Huseien GF, Ismail M, Tahir MM, Mirza J, Khalid NHA, Asaad MA, et al. Synergism between palm oil fuel ash and slag: Production of environmental-friendly alkali activated mortars with enhanced properties. Construction and Building Materials. 2018;170:235-44. https://doi.org/10.1016/j.conbuildmat.2018.03.031
[64] Alnahhal AM, Alengaram UJ, Yusoff S, Darvish P, Srinivas K, Sumesh M. Engineering performance of sustainable geopolymer foamed and non-foamed concretes. Construction and Building Materials. 2022;316:125601. https://doi.org/10.1016/j.conbuildmat.2021.125601
[65] Fauzi A. Effect of POFA as a replacement material on fly ash based geopolymer mortar. IOP Conference Series: Materials Science and Engineering. 2020;012012. https://doi.org/10.1088/1757-899X/854/1/012012
[66] Hawa A, Tonnayopas D, Prachasaree W, Taneerananon P. Investigating the effects of oil palm ash in metakaolin based geopolymer. Ceramics-Silikaty. 2013;57:319-27. https://doi.org/10.1155/2013/857586
[67] Karim MR, Hossain MM, Elahi MMA, Zain MFM. Effects of source materials, fineness and curing methods on the strength development of alkali-activated binder. Journal of Building Engineering. 2020;29:101147. https://doi.org/10.1016/j.jobe.2019.101147
[68] Liu MYJ, Chua CP, Alengaram UJ, Jumaat MZ. Utilization of palm oil fuel ash as binder in lightweight oil palm shell geopolymer concrete. Advances in Materials Science and Engineering. 2014;2014:610274. https://doi.org/10.1155/2014/610274
[69] Kubba Z, Huseien GF, Sam ARM, Shah KW, Asaad MA, Ismail M, et al. Impact of curing temperatures and alkaline activators on compressive strength and porosity of ternary blended geopolymer mortars. Case Studies in Construction Materials. 2018;9. https://doi.org/10.1016/j.cscm.2018.e00205
[70] Oyehan TA, Salami BA, Badmus SO, Saleh TA. Technological trends in activation and modification of palm oil fuel ash for advanced water and wastewater treatment-A review. Sustainable Chemistry and Pharmacy. 2022;29:100754. https://doi.org/10.1016/j.scp.2022.100754

Research on Engineering Structures & Materials
www.jresm.org
Research Group

Research Article

Assessing recycled asphalt pavement: Impact of waste cooking oil and waste engine oil as rejuvenators on mechanical properties

Kavitha Madhu*,[a], Arya Raj J[b], Niranjini Shibu[c], Viswa G[d]

Department of Civil Engineering, TKM College of Engineering, Kollam 691005, Kerala, India

Article Info

Article history:

Received 25 Mar 2024
Accepted 02 Aug 2024

Keywords:

Recycled asphalt pavement (RAP);
Aging of RAP;
Performance characteristics;
Physical properties of bitumen;
Optimal rejuvenator content;
Marshall stability;
Asphalt mixtures

Abstract

Sustainable pavement construction is an extensively researched subject within the field of pavement engineering. Due to its environmental and commercial advantages, the construction of pavements utilizing recycled asphalt pavement (RAP) is progressively gaining popularity worldwide. Owing to the aging process, binder extracted from RAP is inherently harder than virgin binder and requires rejuvenation for application in high RAP blends. This paper investigates the performance characteristics of Waste Cooking Oil (WCO) and Waste Engine Oil (WEO) as rejuvenators in RAP-incorporated asphalt mixtures to assess their suitability for pavement use. The optimal rejuvenator content is determined based on the performance of physical properties. The study indicates that asphalt mixes rejuvenated with Waste Cooking Oil (WCO) demonstrate higher Marshall Stability values compared to mixes rejuvenated with Waste Engine Oil (WEO) at both 30% and 60% Recycled Asphalt Pavement (RAP) levels. Additionally, mixes incorporating WCO exhibit increased flow values. Furthermore, WCO outperforms WEO in Tensile Strength Ratio (TSR) at 30% RAP, with a slight decrease at 60% RAP. Results from Marshall and Indirect Tensile Strength (ITS) tests suggest that both WEO and WCO are effective rejuvenators, playing a critical role in aligning the properties of RAP-inclusive asphalt mixes with those of virgin mixes.

1. Introduction

The rapid expansion of global infrastructure, particularly within the transportation sector, has significantly increased the demand for construction materials, leading to the depletion of natural resources, especially in developing countries. As a result, the adoption of environmentally sustainable construction practices has become imperative. One such practice is the reuse of existing pavement layers, known as recycled or reclaimed asphalt pavement (RAP), which allows for the effective reutilization of both binders and aggregates. However, the extent to which RAP materials can be reused remains an important area of research that requires further investigation.

It is essential to employ sustainable road construction practices and find alternatives to virgin materials [1]. People are becoming more aware of the need for sustainable pavements, and this puts pressure on the pavement construction industry to use recycled materials [2]. Recycled asphalt pavements (RAPs) are constructed using milled materials from existing pavement layers [3]. Using RAP is becoming more popular because of its environmental and economic feasibility [4]. People have been using RAP in asphalt mixes

*Corresponding author: kavithamadhu@tkmce.ac.in
[a]orcid.org/0000-0002-0253-1230; [b]orcid.org/0009-0006-4135-6929; [c]orcid.org/0009-0004-8188-1424; [d]orcid.org/0009-0002-3587-6283
DOI: http://dx.doi.org/10.17515/resm2024.218me0325rs

as it is considered to be a cheaper alternative compared to virgin binder and aggregates [5]. But, the strength and performance criteria of RAP mixtures need to be investigated.

Scientific studies also show that RAP material, including aged asphalt and aggregates, improves the mechanical aspects, performance, and longevity of asphalt pavements. Depending on the construction mode and technical features, asphalt pavement recycling systems may be classified as central plant hot recycling (CPHR), hot in-place recycling (HIR), central plant cold recycling (CPCR), and cold in-place recycling (CIR) [6]. Hot in-place recycling (HIR) uses reclaimed asphalt pavement (RAP), a non-renewable resource, in its entirety. When combined with RAP, HIR requires just 10%–20% virgin materials and an insignificant quantity of rejuvenator [7]. Cold recycling of asphalt pavement is a more cost-effective maintenance method than hot recycling since it minimizes carbon emissions, eases the pressure on the construction material supply, and lowers the cost of paving rehabilitation. As loading frequency increased under dry conditions, permanent strain decreased, and among the four temperatures, the highest permanent strain was measured at the lowest loading frequency [8]. In the cold recycling process, fresh materials are mixed with reclaimed asphalt pavement (RAP), which is produced by cold milling the asphalt layer, to create a cold recycled mixture (CRM), which is subsequently inserted into the rebuilt pavement layer [9].

The incorporation of RAP into conventional asphalt pavements emulates a bigger leap toward the realization of sustainable pavement construction. It upholds the 3R concept of sustainability: Reduce, Reuse, and Recycle. As a petroleum-derived organic material, asphalt ages during the building (short-term aging) and service (long-term aging) processes [3]. The main advantage with RAP binder is its higher stiffness compared to virgin binder. To make RAP binder applicable for construction purposes, rejuvenators are added which rejuvenate the physical and chemical properties. Through oxidation, the maltenes component in asphalt changes to the more viscous asphaltenes component during aging. Asphaltenes with a greater molecular weight prefer to form a colloidal suspension with maltenes with a lower molecular weight. The viscosity of asphalt materials is mostly due to asphaltenes. Aging causes a rise in asphaltenes, resulting in high stiffness and a low creep rate [4]. Rejuvenators may be used to restore some of the mechanical properties of RAP binder. They restore the natural asphaltene-maltene ratio in aged binder and replace volatiles, and disperse oils while improving adhesion. The optimum quantity of rejuvenator to be added depends on the type and condition of the aged bitumen [10].

In terms of physical properties such as penetration, softening point, ductility, striping, and viscosity, researchers identified major differences between virgin and rejuvenated RAP binders [11]. When used appropriately and optimally, rejuvenators can assist in reversing the indications of aging and regulating its short-term and long-term aging. Understanding the role of aged binder as well as the influence of rejuvenators is critical for selecting the most ecologically and economically beneficial solution [12]. Rejuvenators are divided into two types: rejuvenating and softening agents [10]. Based on chemical composition, rejuvenators can also be broadly classified as bio-based and petroleum-based rejuvenators [13]. Commercial rejuvenators and bio-based oils contain volatile compounds in their chemical composition and are highly vulnerable to aging even though they possess a number of advantages. The presence of volatile components in waste oils like waste cooking oil (WCO) and waste engine oil (WEO) is significantly lower than that of fresh bio-oils since WCO and WEO survive high temperatures throughout the manufacturing process [14]. The addition of a suitable waste oil dosage can improve the conventional physical properties of RAP, and it will reduce the chances of other chemical reactions. Excessive waste oil addition will lead to an undesirable reduction in the viscosity of the asphalt [15].

Waste engine oil (WEO) is extracted from vehicles during normal oil changes at vehicle repairs. It has a comparable molecular structure, physical, and chemical qualities as petroleum asphalt [16]. Also, WEO becomes a common modifier in the asphalt industry due to ease of availability and efficiency [17]. WCO is used in a variety of products, including biodiesel, yellow grease, animal feed, and soaps. The issue with WEO and WCO is that the majority of them are illegally thrown into rivers and landfills, producing pollution and environmental issues, while only minor amounts are legitimately collected and processed. Thus, the use of WEO and WCO also adds to the concept of sustainability.

Understanding the role of Recycled Asphalt Pavement (RAP) binder, along with the influence of rejuvenators, is crucial for selecting the most ecologically and economically beneficial solution [12]. Numerous studies have evaluated the effects of rejuvenators on asphalt mixtures. Moisture can exacerbate existing pavement issues, underscoring the need to consider affordable and long-lasting asphalt mixtures [18]. It is important to comprehend the drainage and strength characteristics of the aggregate base course [19]. RAP concentration shows no discernible effect on Marshall stability, while the Tensile Strength Ratio (TSR) exhibited a trend that initially increased before eventually falling [15].

Capitão et al. [20] aimed to study cost-effective asphalt mixtures with high RAP content. El-Shorbagy et al. [10] examined the impact of rejuvenators on the mechanical qualities of the mix in direct comparison to a mix without a rejuvenator. It has been demonstrated that a low RAP concentration improves the moisture damage potential of the mixtures while enhancing the tensile strength ratio [21]. The gradation of blends with 80% and 60% RAP is closer to the limits of standard gradation because they contain virgin aggregate. Zhang et al. [22] investigated how the macroscopic mechanical characteristics of asphalt mixes are affected when European rock bitumen (ERB) and used cooking oil (WCO) are combined with asphalt. WCO can significantly enhance the anti-cracking effectiveness of asphalt-related mixtures at relatively lower temperatures [10]. The ERB/WCO composite alteration could improve the Marshall stability performance of the asphalt mixture. Similarly, petroleum-based rejuvenators such as fuel oil, aromatic extracts, naphthenic oil, coke oven gas, and waste engine oil have been subjected to scientific studies to understand their effects on RAP [13].

The overall influence of rejuvenators on Marshall properties varies according to RAP content and rejuvenator type, showing greater values for blends incorporating Waste Engine Oil (WEO). It is expected that the use of WEO for higher percentages of RAP (>30%) can meet the growing need for road construction materials in a more sustainable way [23]. The Indirect Tensile Strength (ITS) of the combination increases and the rejuvenator proportion to be added varies with the RAP content [24]. The addition of WEO to hot mix asphalt (HMA) is shown to have good fatigue resistance, although it has some drawbacks like reduced elastic recovery and rutting resistance [25].

The literature reveals broad gaps in the current understanding of using waste cooking oil (WCO) and waste engine oil (WEO) as rejuvenators in recycled asphalt pavement (RAP) construction. These gaps include a lack of comprehensive comparative analysis between WCO and WEO properties, insufficient details on the methodology for determining optimal rejuvenator content, and a dearth of information on the long-term performance, environmental impact, and comparative effectiveness with other rejuvenators in RAP mixtures. The present study compares the properties of WCO and WEO and investigates its suitability to be used as rejuvenator in RAP construction. The objectives of the study include: (i) Evaluate the performance of waste engine oil (WEO) and waste cooking oil (WCO) as rejuvenators in recycled asphalt pavement (RAP); (ii) Identify the optimal content of WEO and WCO as rejuvenators in RAP to achieve properties similar to VG 30

bitumen; (iii) Assess the stability and flow values of RAP-incorporated asphalt mixtures with the optimum content of WEO and WCO, comparing them to the virgin mix and mixtures without a rejuvenator; (iv) to measure and compare the moisture sensitivity of RAP mixtures with WEO and WCO.

2. Experimental Program Methodology: The Procedures and Protocols

The schematic diagram representing the methodology of the study is shown in Fig. 1. The mechanical parameters of RAP incorporated asphalt mixtures with and without rejuvenators (WEO & WCO) are compared with that of conventional mix.

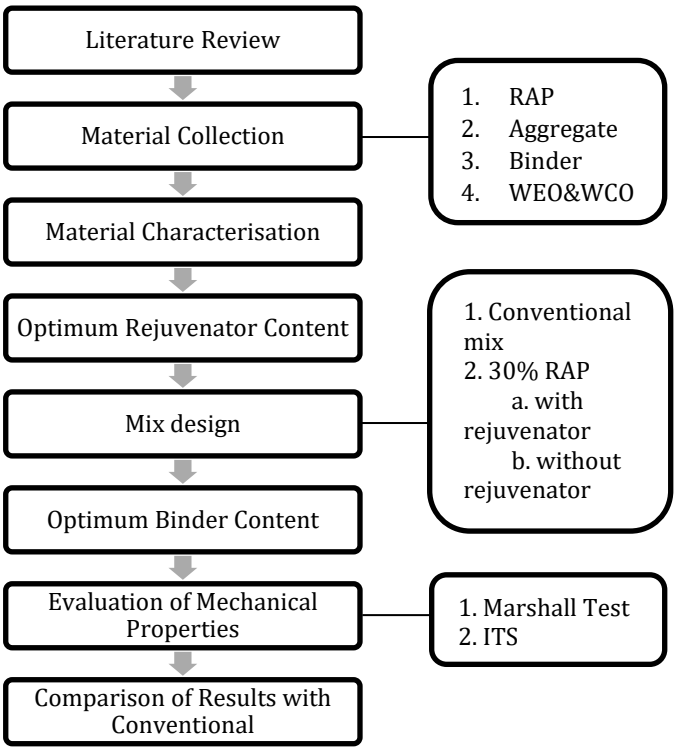

Fig. 1. Study methodology

India experiences an average hot climate. Given the fluctuations in climatic conditions, it is crucial to design pavements that can withstand varying temperatures. The investigation utilized VG 30 (Viscosity Grade) bitumen supplied by Hindustan Colas Ltd. (HINCOL). Recycled Asphalt Pavement (RAP) materials were milled from a 3.5-year-old National Highway pavement in Mangad, part of the Kollam bypass, processed, and shredded.

Aged binder was extracted using a centrifugal extractor with trichloroethylene as a solvent, following ASTM D 2172 -11 [26], and recovered using Abson's apparatus in accordance with ASTM D 1856 – 98A [27]. Given the rising demand for rejuvenators, the study explored the use of waste oils, including Waste Engine Oil (WEO) and Waste Cooking Oil (WCO). WEO, a dark oily liquid, was collected from a local repair garage and used without further treatment as a solvent. The WCO, specifically Palmolein oil, was obtained from various fritter shops (shown in Fig. 2).

(a) (b)

Fig. 2. Rejuvenators used in the study (a) discarded waste cooking oil (WCO) and (b) waste engine oil (weo) collected from automobile workshop

2.1. Experimental Methodology and Design

A laboratory investigation was carried out to assess the basic physical characteristics of materials. The study analysed the physical properties of the virgin binder (VG30), the extracted aged Recycled Asphalt Pavement (RAP) binder, and the aged binder treated with varying percentages (1.5%, 2.5%, 3.5%, 4.5%) of Waste Engine Oil (WEO) and Waste Cooking Oil (WCO). This analysis helped to determine the optimal rejuvenator content as a percentage of the total bitumen weight.

Five asphalt mixtures were prepared for testing, including a virgin mix, a 30% RAP mix, and a 60% RAP mix, both with and without the optimal rejuvenator content by weight of bitumen. The mix design involved determining the ideal binder content based on the volumetric properties of the virgin mix and Marshall stability data. The mechanical properties of these asphalt mixtures were evaluated using the Marshall test and indirect tensile strength (ITS) tests. Additionally, physical properties tests such as softening point, penetration, ductility, viscosity, and specific gravity were conducted.

2.1.1 Penetration Test

The penetration test measures the consistency of bitumen by evaluating its resistance to deformation. Penetration in bituminous materials is defined as the vertical distance, in tenths of millimeters, that a standard needle penetrates under specified conditions—standard temperature (25°C), standard load (100g), and standard time. The examination is conducted in compliance with IS: 1203–1978 [28].

2.1.2 Softening Point Test

The softening point is determined by the temperature at which two bitumen-coated rings soften enough to allow a 9.5mm diameter ball, weighing 3.5g, to drop. This test indicates the material's tendency to flow at elevated temperatures.

2.1.3 Ductility Test

In flexible pavement design, the binder must form a thin, ductile film around the aggregates to enhance overall performance and improve structural interlocking. The ductility test, conducted in accordance with IS: 1208–1978 [29], measures the adhesive properties of asphalt and its capacity to stretch under specific conditions. The ductility of bitumen is defined as the length, in centimeters, to which a standard briquette of bitumen can be stretched before the bitumen thread breaks.

2.1.4 Viscosity Test

The coefficient of viscosity is determined by the relationship between the applied shear stress and the fluid's shear rate. Viscosity, a key property of bitumen, allows it to resist flow, reflecting both its elastic and viscous behaviors. It's important to note that bitumen's viscosity decreases as temperature increases. This test procedure involves measuring apparent viscosity using a rotating viscometer. The test was conducted with a Brookfield Rotational Viscometer in accordance with ASTM D 4402–06 [30].

2.1.5 Marshall Stability Test

To determine the mechanical properties, Marshall stability test and ITS test was deployed.

When a compacted cylindrical specimen of a bituminous mixture is loaded diametrically at a deformation rate of 50 millimeters per minute, its resistance to plastic deformation is assessed. The Marshall mix design method comprises two primary components: (i) density-voids analysis and (ii) stability-flow tests. Marshall stability refers to the maximum load the specimen can withstand at the standard test temperature of 60°C. The flow value represents the specimen's deformation under loading until it reaches the maximum load, measured in units of 0.25 mm. The purpose of this test is to determine the optimal binder content based on the specific aggregate mix and the expected traffic load.

2.1.6 Indirect Tensile Strength Test

Six samples are used to evaluate the change in indirect tensile strength: three are tested dry, while the other three are subjected to water conditioning. For the Indirect Tensile Strength (ITS) test, the specimen is placed between two load strips and loaded radially at a rate of 50 mm per minute. The maximum load at fracture is recorded. This test helps assess the bitumen mix's ability to resist cracking and its overall durability under varying conditions**.**

3. Results and Discussion

Table 1 presents the results of the physical tests performed on the virgin binder, conducted in accordance with IS 73-13 [31] specifications. The test results indicate that the bitumen's physical properties comply with the standards set by the Bureau of Indian Standards (BIS).

Table 1. Physical properties of bitumen

Property	Value Obtained	Required Value	Standards
Ductility (cm)	100	Min 75	IS: 1208-1978
Penetration at 25^0C	48	Min 45	IS: 1203-1978
Softening point (°C)	49	Min 47	IS: 1205-1978
Viscosity (cst)	420	Min 350	IS: 1205-1978 Part II
Specific Gravity	1.01	0.97-1.02	IS: 1202-1978

The results obtained on virgin aggregate physical property testing are shown in Table 2. The tests were carried out under the standards of IS: 2386 Part 1 [32], Part 3 [33], and Part 4 [34]. The test findings show that aggregates' physical characteristics meet BIS requirements. After pre-processing and binder extraction and recovery, the Recycled Asphalt Pavement (RAP) material was tested in the laboratory. The test results, shown in Table 3, reveal that the properties of the RAP materials have deteriorated, particularly highlighting that the characteristics of the aged binder do not meet the standard limits.

Table 2. Physical properties of aggregate

Property	Value Obtained	Required Value	Standards
Aggregate crushing value (%)	35	Less than 30	IS :2386 Part IV
Aggregate impact strength (%)	19	Max 24	IS :2386 Part IV
Combined flakiness and elongation index	28	Max 35	IS :2386 Part I
Specific gravity test (%)	2.65	2.5-3	IS :2386 Part III
Water absorption test (%)	0.87	Max 2%	IS :2386 Part III

Table 3. Physical properties of extracted RAP

Property	Value Obtained
Binder Content (%)	4.8
Impact Strength (%)	16.5
Crushing Strength (%)	28
Softening Point (^{0}C)	72
Penetration(0.1mm) at 25^{0}C	18.5
Ductility (cm)	34
Viscosity at 135^{0}c (cSt)	840

3.1. Optimum Rejuvenator Content

In this paper, the optimal rejuvenator content is determined based on the physical property analysis of recovered Recycled Asphalt Pavement binder (RAPB) supplemented with 1.5%, 2.5%, 3.5%, and 4.5% of Waste Engine Oil (WEO) and Waste Cooking Oil (WCO). These analyses encompassed ductility tests, softening point tests, penetration tests, and Brookfield viscosity tests. Subsequently, the results obtained from all the RAP binder blends with the rejuvenator were compared to those of fresh binder. The findings are presented in Table 4. The two most crucial tests employed are the penetration and softening point tests. As bitumen is presumed to be stiff and capable of forming mixtures less susceptible to deflections and cracking from fatigue at elevated temperatures, bitumen with a higher softening point is preferred.

Fig. 3(a) shows the effect of combining Waste Cooking Oil (WCO) and Waste Engine Oil (WEO) on the softening point of bitumen samples. The addition of WEO and WCO to the Recycled Asphalt Pavement (RAP) binder resulted in a decrease in the softening point temperature, which is below the minimum required threshold of 47°C. Specifically, the softening point of the RAP binder dropped to 50°C with 4.5% WEO and 49.5°C with 2.5% WCO, approaching the softening point of the VG30 grade binder. However, higher concentrations of WCO in the RAP blend led to a further decrease in the softening point, reaching levels deemed unacceptable.

Table 4. Physical properties of rejuvenated RAP binders

Property	RAPB+ 1.5%		RAPB+ 2.5%		RAPB+ 3.5%		RAPB+ 4.5%	
	WEO	WCO	WEO	WCO	WEO	WCO	WEO	WCO
Softening Point (°C)	62	55	58	49.5	54.5	44.5	50	44.2
Penetration at 25°C	38	42	46.5	48.4	52	52.65	55	56.6
Ductility (cm)	48	53	72	88	87	92	100	100
Brookfield Viscosity (cSt) at 135°C	840	525	684	440	460	400	418	395

Fig. 3(b) illustrates the penetration test results for bitumen treated with various ratios of WCO and WEO. The RAP binder had a penetration value of 18.5mm, which is below the standard value compared to the virgin VG30 binder. The penetration value increased with higher amounts of rejuvenator, reflecting a reduction in the asphaltene-to-maltene ratio. The optimal rejuvenator proportions were found to be approximately 4.5% for WEO and 2.5% for WCO, achieving a target penetration value of 48 (0.1mm) at 25°C. Similar trends were observed in ductility tests, as shown in Fig. 3(c), where the ductility values of the aged binder matched those of VG30 at WEO and WCO contents of 4.5% and 2.5%, respectively.

Fig. 3(d) presents the viscosity measurements of the RAP binder. The viscosity of rejuvenated aged binders containing WEO and WCO was significantly lower than that of VG30, measured at 840 cSt at 135°C. The reduction in viscosity indicates improved fluidity, allowing the RAP binder to coat aggregates effectively. Adding 4.5% WEO or 2.5% WCO as rejuvenators enabled the RAP binder to achieve physical properties comparable to the virgin VG30 binder, maintaining the desired level of workability for the rehabilitation procedure.

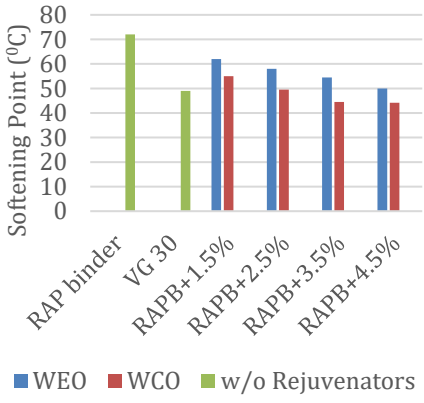

(a) Softening point

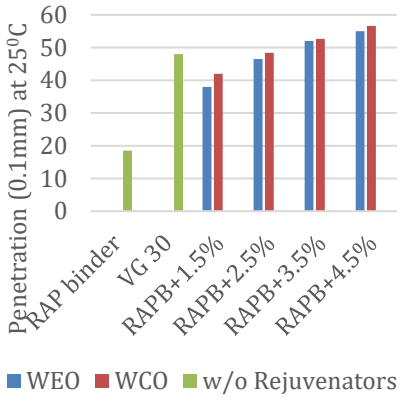

(b) Penetration (0.1mm) at 25° C

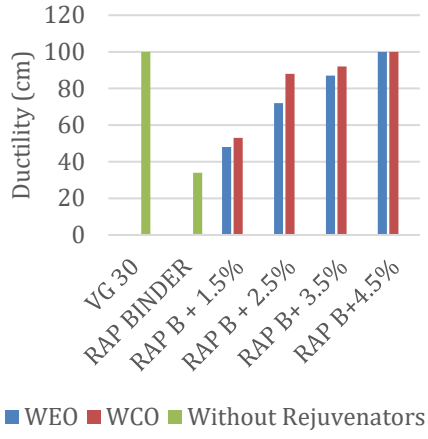

(c) Ductility (cm)

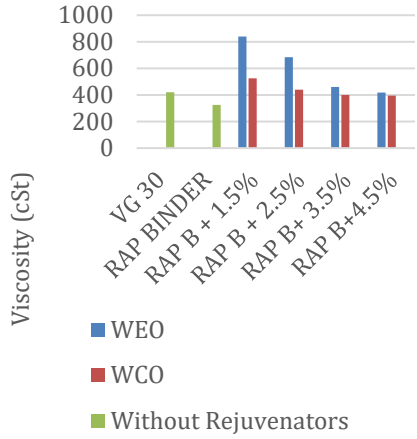

(d) Viscosity (cSt)

Fig. 3. Physical property values of VG30 and RAP binder with varying values of WEO and WCO %

3.2. Marshall Stability and Flow Test

To evaluate the volumetric properties of standard bituminous mixes, Marshall samples were prepared with bitumen contents of 5%, 5.5%, and 6%. These samples followed the bituminous concrete Grade II gradation specified in MoRTH – 5th revision [35]. As shown in Fig.s 4(a) through 4(f), the optimal bitumen content for the asphalt mix was determined to be 5.5%, which achieved the lowest VMA, highest specific gravity, maximum stability, and 4% air voids. The primary aim of this research was to examine the impact of adding a rejuvenator on the mechanical properties of the mix compared to a mix without a rejuvenator.

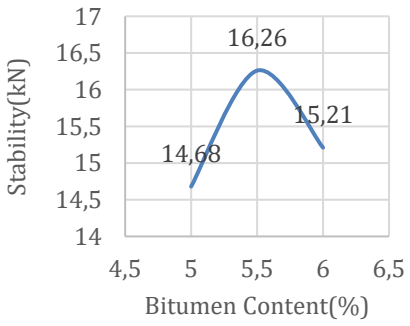

(a) Stability Vs Bitumen Content

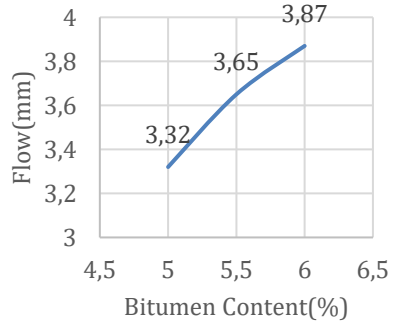

(b) Flow Vs Bitumen Content

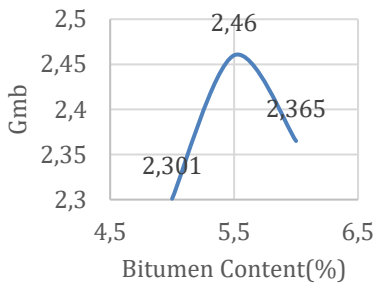

(c) Gmb Vs Bitumen Content

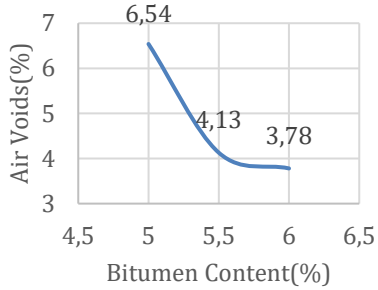

(d) Air Voids Vs Bitumen Content

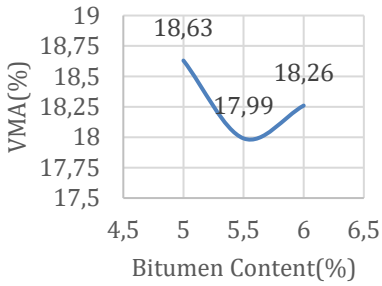

(e) VMA Vs Bitumen Content

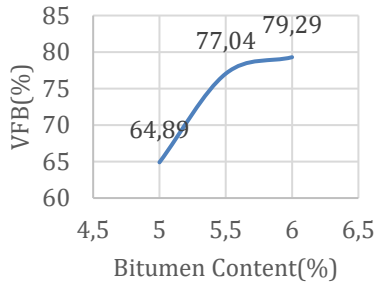

(f) VFB Vs Bitumen Content

Fig. 4. Volumetric properties of virgin mix

Marshall tests for stability and flow were conducted on seven mixtures: a virgin mix, 30% Recycled Asphalt Pavement (RAP), 30% RAP with 4.5% Waste Engine Oil (WEO), 30% RAP with 2.5% Waste Cooking Oil (WCO), 60% RAP, 60% RAP with 4.5% WEO, and 60% RAP with 2.5% WCO, all prepared according to the Asphalt Institute MS-2 specifications. The results of these Marshall tests are summarized in Table 5. Fig. 4 shows that the stability value and bulk specific gravity increase, peaking at a bitumen content of 5.5%, after which they decline. The flow values also increase with higher bitumen content, reaching up to 3.87 mm at 6% bitumen content. Air voids decrease as bitumen content rises, since more bitumen fills the voids within the mixture. Given that maintaining air voids at 4% is a critical criterion for laboratory asphalt mixes, the optimal binder content is identified based on this requirement.

For the Volumetric Mix Analysis (VMA), the binder content of 5.5% results in a low peak VMA value of 17.99%, which then increases. This occurs because bitumen, having a lower specific gravity than aggregates, displaces and separates them. The Voids in the Binder (VFB) is a measure used in mix design to ensure proper asphalt thickness. If VFB is too low or too high, the mix may become unstable. Based on these observations, the optimal bitumen content for the asphalt mix is determined to be 5.5%, which provides maximum stability, highest specific gravity, 4% air voids, and the lowest VMA.

Table 5. Marshall test results of examined mixtures

Examined Mixtures	Virgin Mix	30% RAP	30% RAP + 4.5% WEO	30% RAP + 2.5% WCO	60% RAP	60% RAP + 4.5% WEO	60% RAP + 2.5% WCO
Marshall Stability (kN)	16.26	26.78	17.08	18.31	31.22	22.59	23.85
Flow Value (mm)	3.32	2.18	3.34	3.73	2.56	3.30	3.66

The main objective of this research was to assess how the addition of a rejuvenator influences the mechanical characteristics of the mix compared to a mix without a rejuvenator. According to MoRTH specifications, the minimum stability value for bituminous concrete should be 9 kN. Fig. 5(a) demonstrates that all tested mixtures meet this standard. The inclusion of Recycled Asphalt Pavement (RAP) positively affects stability values, with higher RAP content leading to significant improvements in stability, thereby enhancing rutting resistance and load-bearing capacity. This improvement in Marshall stability can be attributed to the stiffening effect of the RAP.

However, adding Waste Engine Oil (WEO) and Waste Cooking Oil (WCO) to RAP mixtures reduces the stiffness and softening point temperature of the RAP binder, which in turn lowers the stability values. Despite this, the stability of rejuvenated asphalt mixtures approaches that of the virgin mix, indicating that the rejuvenator effectively restores stability.

Fig. 5(b) shows that the flow values follow a similar trend to the stability results. An increase in RAP percentage leads to a decrease in flow characteristics, but this effect is countered by the addition of WEO and WCO rejuvenators, resulting in flow values comparable to those of the virgin mix. Notably, the use of WEO aligns more closely with the virgin mix results.

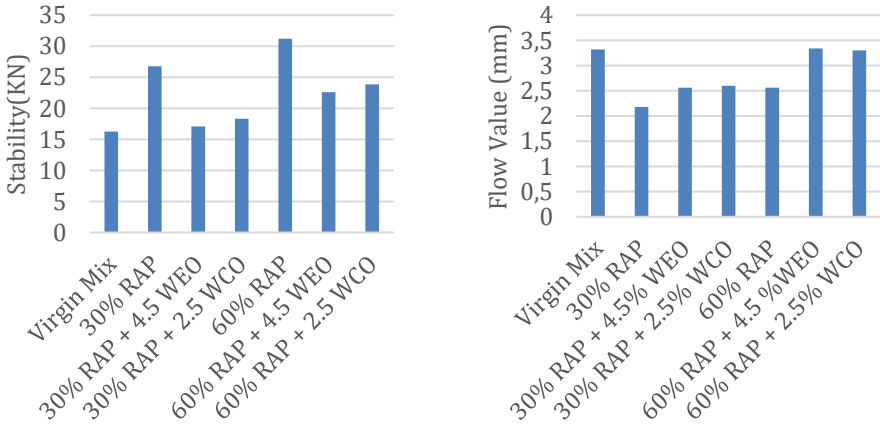

(a) Stability (b) Flow Value

Fig. 5. Results of Marshall test for examined asphalt mixtures

3.3. Indirect Tensile Strength Test

The Indirect Tensile Strength (ITS) test, conducted following AASHTO T 283 standards, was used to evaluate the moisture susceptibility of various mixtures. The test results are shown in Table 6. Fig. 6(a) presents the ITS values for both unconditioned and conditioned samples. Using the ITS values from the seven mixes described earlier, the Tensile Strength Ratio (TSR) was calculated and is illustrated in Fig. 6(b). These results aid in assessing the moisture susceptibility of the mixes.

Table 6. ITS test results of examined mixtures

Examined Mixtures	Virgin Mix	30% RAP	30% RAP + 4.5% WEO	30% RAP + 2.5% WCO	60% RAP	60% RAP + 4.5% WEO	60% RAP + 2.5% WCO
Unconditioned Strength (MPa)	0.643	0.715	0.654	0.642	0.748	0.674	0.541
Conditioned Strength (MPa)	0.532	0.612	0.543	0.537	0.650	0.558	0.650
TSR (%)	82.73	85.59	83.03	83.64	86.9	82.79	83.23

The test results show that increasing the concentration of Recycled Asphalt Pavement (RAP) in the mixtures improves the Indirect Tensile Strength (ITS). This enhancement is due to reduced strain and stress concentrations in bituminous mixtures with higher RAP content, attributed to the stiff binder of RAP and the additional binder in the mix. However, mixtures containing Waste Engine Oil (WEO) and Waste Cooking Oil (WCO) exhibit lower ITS values, as these additives negatively affect the indirect tensile strength. This is expected, as WEO significantly reduces the stiffness of the RAP binder, leading to decreased tensile strength.

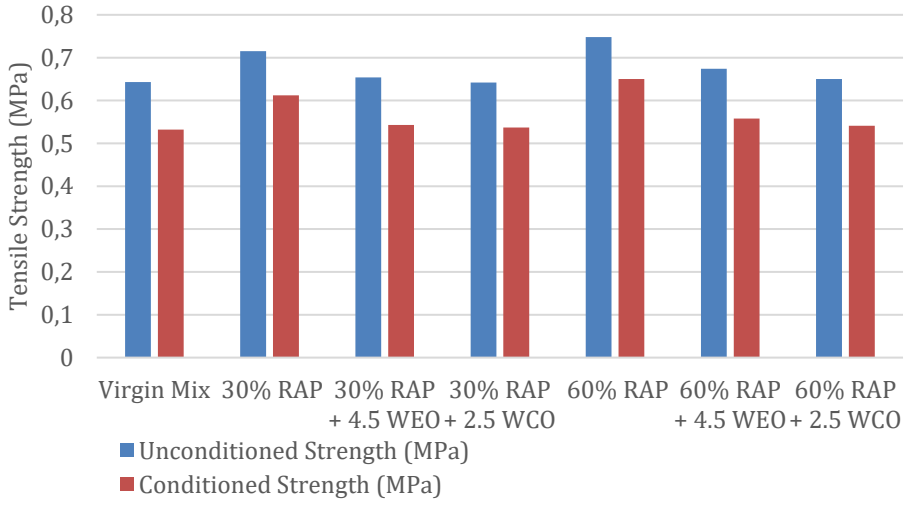

Fig. 6(a). ITS of dry and wet conditioned mixtures under examination

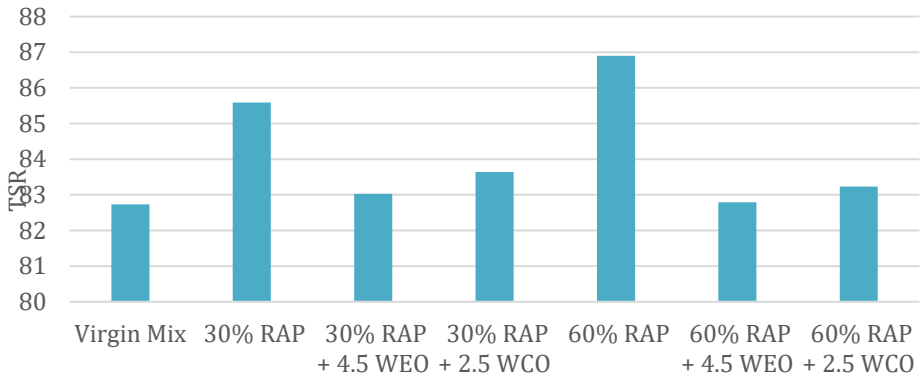

Fig. 6(b). TSR of mixtures under examination

All mixes achieved a minimum Tensile Strength Ratio (TSR) of 80%, as required by AASHTO T283. The highest TSR was observed in the mix containing 60% RAP, followed by mixes with 30% RAP, 30% RAP with 2.5% WCO, 60% RAP with 2.5% WCO, 30% RAP with 4.5% WEO, 60% RAP with 4.5% WEO, and the Virgin Mix. The TSRs of rejuvenated mixes and the virgin mix are nearly identical. This suggests that including RAP improves the tensile strength ratio, indicating better moisture susceptibility. This improvement may be linked to the strong binder coating on RAP aggregates, which reduces water penetration into the aggregate-bitumen interface and minimizes adverse effects on mechanical properties. Although the 60% RAP mix meets standard requirements, its lower TSR compared to the control mix is likely due to its increased surface roughness.

3.4. Comparison of Performance of WEO and WCO

The Marshall Stability values are higher for mixtures containing Waste Cooking Oil (WCO), with a peak of 18.31 kN, compared to 17.08 kN for Waste Engine Oil (WEO) in asphalt mixtures with 30% Recycled Asphalt Pavement (RAP). This trend continues with 60% RAP, where the stability value is 23.85 kN for WCO and 22.59 kN for WEO. In terms of Flow values, mixes with WCO exhibit higher values than those with WEO at the same RAP content. When compared to the virgin mix, the performance of WEO is more closely aligned.

The Tensile Strength Ratio (TSR) is higher for mixtures with WCO compared to those with WEO for 30% RAP content, though TSR values decline slightly for 60% RAP content. Based on the results from the Marshall stability and Indirect Tensile Strength (ITS) tests, both WEO and WCO are effective rejuvenators, successfully aligning the properties of RAP-containing asphalt mixtures with those of virgin mixtures.

4. Conclusion

This study evaluates the effectiveness of Waste Engine Oil (WEO) and Waste Cooking Oil (WCO) as rejuvenators for improving the quality of Recycled Asphalt Pavement (RAP). The findings indicate that under aged conditions, both WEO and WCO increase penetration values and decrease softening point temperatures as their concentrations rise, compared to VG30 bitumen. Adding 2.5% WCO or 4.5% WEO to RAP binder yields properties similar to VG30, with WCO demonstrating a more pronounced effect than WEO.

Asphalt mixtures with optimal rejuvenator content of WEO and WCO show stability and flow values comparable to those of virgin mixes, unlike RAP mixtures without rejuvenators. All tested mixtures meet the AASHTO T283 minimum Tensile Strength Ratio (TSR) of 80%, indicating excellent moisture resistance. For 60% RAP, the stability values were 23.85 kN for WCO and 22.59 kN for WEO, with WCO also showing higher Flow values than WEO. In comparison, WEO results were closer to those of the virgin mix.

In practical terms, the study demonstrates that the identified rejuvenator contents effectively improve the mechanical performance of RAP mixtures, making the use of WEO and WCO a viable and environmentally friendly approach for enhancing asphalt pavement quality. This research supports the use of waste oils in asphalt recycling, contributing to more sustainable and resilient road construction practices.

Some limitations of the study include the potential impairment of asphalt mixture properties due to excessive use of Waste Engine Oil (WEO) and Waste Cooking Oil (WCO), which could reduce durability and increase susceptibility to rutting and cracking. Additionally, maintaining the desired performance standards of the asphalt requires precise balancing of rejuvenator proportions.

Based on the study's findings, several recommendations are proposed. It is advisable to use dynamic shear rheometers and bending beam rheometers to assess the performance of the bitumen at both high and low temperatures, which will help determine the temperature sensitivity of the binder. Additionally, conducting chemical analyses, such as Fourier Transform Infrared Spectroscopy (FTIR), Atomic Force Microscopy (AFM), X-ray Diffraction (XRD), and Gas Chromatography-Mass Spectrometry (GC-MS), can provide detailed insights into the chemical properties of the bitumen. Furthermore, performing a life cycle cost analysis on aged asphalt modified with WCO and WEO should be considered before field application to evaluate its economic feasibility and long-term benefits.

References

[1] Ali B, Li P, Khan D, Hasan MR, Khan WA. Investigation into the effect of waste engine oil and vegetable oil recycling agents on the performance of laboratory-aged bitumen. Budownictwo i Architektura. 2024 Mar 29;23(1):033-54. https://doi.org/10.35784/bud-arch.5500

[2] Al-Qadi IL, Elseifi M, Carpenter SH. Reclaimed asphalt pavement-a literature review. FHWA-ICT-07-001. 2007.

[3] Behnood A. Application of rejuvenators to improve the rheological and mechanical properties of asphalt binders and mixtures: A review. Journal of cleaner production. 2019 Sep 10;231171-82. https://doi.org/10.1016/j.jclepro.2019.05.209

[4] Cao W, Wang A, Yu D, Liu S, Hou W. Establishment and implementation of an asphalt pavement recycling decision system based on the analytic hierarchy process. Resources, Conservation and Recycling. 2019 Oct 1;149:738-49. https://doi.org/10.1016/j.resconrec.2019.06.028

[5] Capitão S, Picado-Santos L, Almeida A, Mendes F. Assessment of aged and unaged hot and warm asphalt concrete containing high reclaimed asphalt pavement rate rejuvenated with waste cooking oil. Construction and Building Materials. 2023 Oct 12; 400:132801. https://doi.org/10.1016/j.conbuildmat.2023.132801

[6] Çolak MA, Zorlu E, Çodur MY, Baş Fİ, Yalçın Ö, Kuşkapan E. Investigation of Physical and Chemical Properties of Bitumen Modified with Waste Vegetable Oil and Waste Agricultural Ash for Use in Flexible Pavements. Coatings. 2023 Oct 31;13(11):1866. https://doi.org/10.3390/coatings13111866

[7] Devulapalli L, Kothandaraman S, Sarang G. Effect of rejuvenating agents on stone matrix asphalt mixtures incorporating RAP. Construction and Building Materials. 2020 Sep 10; 254:119298. https://doi.org/10.1016/j.conbuildmat.2020.119298
[8] Dinh BH, Park DW, Le TH. Effect of rejuvenators on the crack healing performance of recycled asphalt pavement by induction heating. Construction and building materials. 2018 Mar 10; 164:246-54. https://doi.org/10.1016/j.conbuildmat.2017.12.193
[9] El-Shorbagy AM, El-Badawy SM, Gabr AR. Investigation of waste oils as rejuvenators of aged bitumen for sustainable pavement. Construction and Building Materials. 2019 Sep 30;220: 228-37. https://doi.org/10.1016/j.conbuildmat.2019.05.180
[10] Elkashef M, Williams RC. Improving fatigue and low temperature performance of 100% RAP mixtures using a soybean-derived rejuvenator. Construction and Building Materials. 2017 Oct 1;151: 345-52. https://doi.org/10.1016/j.conbuildmat.2017.06.099
[11] Elkashef M, Williams RC, Cochran E. Investigation of fatigue and thermal cracking behavior of rejuvenated reclaimed asphalt pavement binders and mixtures. International Journal of Fatigue. 2018 Mar 1; 108:90-5. https://doi.org/10.1016/j.ijfatigue.2017.11.013
[12] Eltwati A, Mohamed A, Hainin MR, Jusli E, Enieb M. Rejuvenation of aged asphalt binders by waste engine oil and SBS blend: Physical, chemical, and rheological properties of binders and mechanical evaluations of mixtures. Construction and Building Materials. 2022 Sep 5;346: 128441. https://doi.org/10.1016/j.conbuildmat.2022.128441
[13] Han D, Liu G, Xi Y, Zhao Y. Research on long-term strength formation and performance evolution with curing in cold recycled asphalt mixture. Case Studies in Construction Materials. 2023 Jul 1; 18:e01757. https://doi.org/10.1016/j.cscm.2022.e01757
[14] Huang B, Shu X, Vukosavljevic D. Laboratory investigation of cracking resistance of hot-mix asphalt field mixtures containing screened reclaimed asphalt pavement. Journal of Materials in Civil Engineering. 2011 Nov 1;23(11):1535-43. https://doi.org/10.1061/(ASCE)MT.1943-5533.0000223
[15] Jameel MS, Khan AH, ur Rehman Z, Tarar MA. Evaluation of performance characteristics of asphalt mixtures modified with renewable oils and reclaimed asphalt pavement (RAP). Construction and Building Materials. 2023 Apr 24; 375:130925. https://doi.org/10.1016/j.conbuildmat.2023.130925
[16] Jahanbakhsh H, Karimi MM, Naseri H, Nejad FM. Sustainable asphalt concrete containing high reclaimed asphalt pavements and recycling agents: Performance assessment, cost analysis, and environmental impact. Journal of Cleaner Production. 2020 Jan 20; 244:118837. https://doi.org/10.1016/j.jclepro.2019.118837
[17] Joni HH, Al-Rubaee RH, Al-zerkani MA. Rejuvenation of aged asphalt binder extracted from reclaimed asphalt pavement using waste vegetable and engine oils. Case Studies in Construction Materials. 2019 Dec 1;11:e00279. https://doi.org/10.1016/j.cscm.2019.e00279
[18] Karati S, Karmakar S, Roy TK. Moisture effect analysis on bituminous mix containing reclaimed asphalt pavement material by durability index. Journal of Materials in Civil Engineering. 2022 Mar 1;34(3):04021482. https://doi.org/10.1061/(ASCE)MT.1943-5533.0004120
[19] Khodaii A, Moghadas Nejad F, Forough SA, Saleh Ahari A. Investigating the effects of loading frequency and temperature on moisture sensitivity of SBS-modified asphalt mixtures. Journal of materials in civil engineering. 2014 May 1;26(5):897-903. https://doi.org/10.1061/(ASCE)MT.1943-5533.0000875
[20] Kumar V, Aggarwal P. Characteristics of Waste Oil-rejuvenated RAP Bitumen: An Experimental Study. Jordan Journal of Civil Engineering. 2023 Jul 1;17(3). https://doi.org/10.14525/JJCE.v17i3.07

[21] Li H, Zhang F, Feng Z, Li W, Zou X. Study on waste engine oil and waste cooking oil on performance improvement of aged asphalt and application in reclaimed asphalt mixture. Construction and Building Materials. 2021 Mar 22;276 :122138. https://doi.org/10.1016/j.conbuildmat.2020.122138
[22] Liu S, Peng A, Wu J, Zhou SB. Waste engine oil influences on chemical and rheological properties of different asphalt binders. Construction and Building Materials. 2018 Dec 10;191: 1210-20. https://doi.org/10.1016/j.conbuildmat.2018.10.126
[23] Mamun AA, Al-Abdul Wahhab HI. Evaluation of Waste Engine Oil-Rejuvenated Asphalt Concrete Mixtures with High RAP Content. Advances in Materials Science and Engineering. 2018;2018(1):7386256. https://doi.org/10.1155/2018/7386256
[24] Pan Y, Han D, Yang T, Tang D, Huang Y, Tang N, Zhao Y. Field observations and laboratory evaluations of asphalt pavement maintenance using hot in-place recycling. Construction and Building Materials. 2021 Feb 15;271:121864. https://doi.org/10.1016/j.conbuildmat.2020.121864
[25] Podolsky JH, Sotoodeh-Nia Z, Huisman T, Williams RC, Cochran EW. Practical Approach to Mix Design with High Binder and Aggregate Replacement in Iowa using Fractionation. Transportation Research Record. 2019 Oct;2673(10):571-8. https://doi.org/10.1177/0361198119834303
[26] Singh D, Chitragar SF, Ashish PK. Comparison of moisture and fracture damage resistance of hot and warm asphalt mixes containing reclaimed pavement materials. Construction and Building Materials. 2017 Dec 30;157:1145-53. https://doi.org/10.1016/j.conbuildmat.2017.09.176
[27 Taherkhani H, Noorian F. Comparing the effects of waste engine and cooking oil on the properties of asphalt concrete containing reclaimed asphalt pavement (RAP). Road Materials and Pavement Design. 2020 Jul 3;21(5):1238-57. https://doi.org/10.1080/14680629.2018.1546220
[28] Taziani EA, Toraldo E, Crispino M, Giustozzi F. Application of rejuvenators and virgin bitumen to restore physical and rheological properties of RAP binder. Australian Journal of Civil Engineering. 2017 Jul 3;15(2):73-9. https://doi.org/10.1080/14488353.2017.1383580
[29] Wu S, Muhunthan B. Evaluation of the effects of waste engine oil on the rheological properties of asphalt binders. Journal of Materials in Civil Engineering. 2018 Mar 1;30(3):06017020. https://doi.org/10.1061/(ASCE)MT.1943-5533.0002189
[30] Yan K, Li Y, Long Z, You L, Wang M, Zhang M, Diab A. Mechanical behaviors of asphalt mixtures modified with European rock bitumen and waste cooking oil. Construction and Building Materials. 2022 Feb 14;319:125909. https://doi.org/10.1016/j.conbuildmat.2021.125909
[31] Yaro NS, Sutanto MH, Baloo L, Habib NZ, Usman A, Yousafzai AK, Ahmad A, Birniwa AH, Jagaba AH, Noor A. A comprehensive overview of the utilization of recycled waste materials and technologies in asphalt pavements: Towards environmental and sustainable low-carbon roads. Processes. 2023 Jul 13;11(7):2095. https://doi.org/10.3390/pr11072095
[32] Prabakaran B, Yasin MH. An Assessment of Performance of Compression Ignition Engine Fueled with Recycled Waste Engine Oil Waste Cooking Oil and Waste Plastic Oil as Fuel. SAE Technical Paper; 2024 Apr 9.
[33] Zhang Z, Han S, Han X, Dong S, Yao T. Performance changes of hot recycled asphalt mixture in different layers under coupling of multiple aging factors. Construction and Building Materials. 2021 Feb 1;269:121343. https://doi.org/10.1016/j.conbuildmat.2020.121343
[34] Zhu H, Xu G, Gong M, Yang J. Recycling long-term-aged asphalts using bio-binder/plasticizer-based rejuvenator. Construction and building materials. 2017 Aug 30;147:117-29. https://doi.org/10.1016/j.conbuildmat.2017.04.066

Research on Engineering Structures & Materials
www.jresm.org
Research Group

Research Article

Influence of hybrid basalt fibre with varied length on the mechanical properties of normal and high strength concrete

Jisa Johnson[a,*], Eswari S.[b], Saravanan R.[c]

Dept. of Civil Engineering, Puducherry Technological University, Puducherry, India

Article Info

Article history:

Received 13 Apr 2024
Accepted 24 Aug 2024

Keywords:

Hybrid basalt fibre;
Mechanical properties;
Fibre reinforced concrete;
Flexural strength;
High strength concrete

Abstract

Hybrid fibre-reinforced concrete combines different types of fibres or fibres of varying lengths to maximize their individual advantages, which can potentially lead to a synergistic enhancement in overall performance. The main aim of this study is to explore the feasibility of integrating a hybrid fibre system to enhance the efficiency and properties of basalt fibre-reinforced concrete. Specifically, the research focuses on evaluating the mechanical characteristics of basalt hybrid fibre-reinforced concrete across two concrete grades: normal strength M30 and high strength M60. Basalt fibres of 12 mm and 30 mm lengths are used to hybridize the concrete, with a total fibre volume fraction of 1.5%. By incorporating both short and long basalt fibres into the concrete matrix, this study aims to assess how these variations impact essential properties such as workability, compressive strength, flexural strength, and Modulus of Elasticity (MOE). The hybrid mix, comprising 25% of 12 mm fibres and 75% of 30 mm fibres at a volume content of 1.5%, demonstrates enhanced mechanical properties across all concrete grades. The addition of basalt fibres, particularly those with higher proportions of longer fibres, results in a decrease in workability. Notably, hybridizing fibres have no discernible effect on compressive strength or MOE in both concrete grades. From the results it was observed that the flexural strength of the optimal hybrid mixes is significantly higher, surpassing conventional concrete by 39% and 54.35% for M30 and M60 grades of concrete, respectively.

1. Introduction

Civil engineering encompasses construction, maintenance, planning, and rehabilitation activities aimed at improving the built environment for humanity. It entails redesigning and reshaping daily life via innovative infrastructure projects. Concrete, a versatile material, is widely used in the construction industry due to its ability to be cast into various shapes and its good workability. It plays a crucial role in numerous infrastructure projects, providing durability, strength, and longevity to structures ranging from foundations to skyscrapers and highways to airports.

On the other side, concrete possesses several undesirable traits such as brittleness, limited impact resistance, and high weight. While traditional concrete exhibits strength primarily in compression, it lacks resilience in tension; as a result, there is a necessity to enhance the tensile capacity of concrete [1-3]. New types of concrete, including High Performance Concrete (HPC), High Strength Concrete (HSC), Ultra High-Performance Concrete (UHPC), Fibre Reinforced Concrete (FRC), and Fibre Reinforced High Strength Concrete (FRHSC), offer enhanced characteristics such as increased strength, long-term mechanical properties, toughness, durability, low permeability, high modulus of elasticity and

*Corresponding author: jisajohnson@ptuniv.edu.in
[a] orcid.org/0009-0006-3292-4541; [b] orcid.org/0000-0002-3709-5432; [c] orcid.org/0009-0002-5893-0561
DOI: http://dx.doi.org/10.17515/resm2024.239me0413rs

resilience. HSC integrates mineral admixtures like blast furnace slag, metakaolin, silica fume, fly ash and chemical admixtures such as superplasticizers. Integrating metakaolin as an additional cementitious material enhances both the mechanical properties and durability of concrete. Concrete mixtures incorporating metakaolin exhibit superior flexural and compressive strengths, along with increased resilience against adverse environmental factors such as sulphate and acid attacks. This substitution of some cement with metakaolin not only promotes sustainability but also reduces environmental impact. In applications demanding high-performance and high-strength concrete, the inclusion of metakaolin alters pore structure, chloride diffusivity, and other microstructural properties, thereby enhancing overall performance and longevity [4-8].

However, HSC suffers from brittleness and crack development. To address these shortcomings, fibres can be incorporated into concrete, resulting in FRC with improved tensile strength, ductility, toughness, and durability properties [9]. FRC can be produced by integrating various types of fibres, including steel, cellulose, asbestos, polypropylene, glass, polyvinyl alcohol, basalt, carbon, and aramid fibres [10]. Basalt fibre is increasingly favored in construction for its exceptional qualities. Its high tensile strength makes it perfect for reinforcing concrete, while its resistance to corrosion, chemical and biological damage ensures durability in harsh conditions. With low thermal conductivity and excellent fire resistance, it minimizes heat loss and is suitable for fire-resistant structures. Its low water absorption prevents damage from freeze-thaw cycles, and its resilience to weathering and UV radiation suits outdoor use. Additionally, its high modulus of elasticity enhances concrete stiffness and reduces cracking [11]. As a sustainable material derived from volcanic rock, basalt fibre production demands minimal energy [12,13].

In concrete applications, the percentage of basalt fibres typically ranges from around 0.1% to 3% by volume of concrete. However, the exact percentage deemed "optimum" can vary based on factors such as the desired increase in flexural strength, compressive strength, durability, and tensile strength. Similarly, the length of basalt fibres can vary depending on the composite materials' intended properties. According to research, the utilization of basalt fibres as reinforcement in composite materials, particularly in concrete and polymer mortars, offers significant potential for enhancing mechanical properties such as tensile strength, flexural strength, durability and the long-term performance of concrete, leading to increased resistance to cracking [3,14], abrasion, and environmental degradation. However, the workability of the concrete is reduced when basalt fibre is added to the plain concrete, especially long length fibres [15-17]. Certain studies have noticed that the compressive strength of basalt fibre reinforced concrete shows enhancement with lower amounts of basalt fibres, whereas higher dosages do not lead to further improvement in compressive strength [18-21].

In Hybrid Fibre-Reinforced Concrete (HFRC), the combination of two or more distinct fibre kinds allows for the creation of a composite material. This composite leverages the unique mechanical and physical properties of each type of fibre, resulting in improved overall performance. Additionally, the interaction between these different fibres can lead to a synergistic response, further enhancing the mechanical and physical characteristics of the concrete. By carefully selecting and combining various fibre types, HFRC offers the opportunity to optimize performance and achieve superior results compared to single-fibre reinforcement [22].

The hybridization of concrete can be achieved by using fibres of different moduli or combining the same fibres of different lengths (short and long fibres). Short fibres are typically utilized to improve attributes such as impact resistance and crack control. Their shorter length allows for more uniform dispersion within the concrete matrix, effectively bridging microcracks and mitigating crack propagation. On the other hand, longer fibres,

primarily contribute to enhancing tensile and flexural strength. Their greater length enables them to span larger distances within the concrete, providing reinforcement against applied forces and improving the overall structural integrity. Recent studies have demonstrated the superiority of hybrid basalt fibre-reinforced concrete over formulations using single basalt fibres alone. This hybrid approach has shown remarkable performance improvements in various aspects, including compressive strength, flexural strength, tensile strength, and fracture resistance. The integration of a hybrid fibre system allows for a more comprehensive reinforcement strategy, addressing multiple structural requirements simultaneously [23-25]. Overall, the adoption of hybrid basalt fibre-reinforced concrete represents a promising advancement in construction materials, offering enhanced durability, resilience, and sustainability for a wide range of infrastructure projects.

The present research work is significant as it tackles two major concerns in the field of construction materials. The first concern is to explore the potential of using a hybrid fibre system to enhance the performance of basalt FRC. Traditional concrete, although strong in compression, lacks tensile strength and is susceptible to cracking. The goal of this study is to use the synergistic benefits of different types of fibres to improve the overall mechanical properties by combining a hybrid system of basalt fibres of different lengths. This approach could result in the creation of more resilient concrete structures.

The second concern is to examine the specific enhancements brought about by hybrid fibre reinforcement in concrete. Studies have demonstrated that incorporating basalt fibres leads to better performance compared to plain concrete. However, there is a need for further research to evaluate the specific impact of hybridizing short and long basalt fibres on the mechanical properties of both normal and high-strength concrete. This involves a detailed analysis of how the combination of fibres affects key performance metrics such as workability, compressive strength, flexural strength, and MOE. By investigating these parameters, the research seeks to identify the optimal fibre proportions and configurations that offer the best balance between improved mechanical properties and practical considerations like ease of mixing and application. Understanding these mechanical behaviors is crucial for determining whether hybrid fibre-reinforced concrete can offer superior performance over conventional concrete in structural applications. The findings from this study could provide valuable insights for the construction industry, paving the way for the adoption of hybrid fibre-reinforced concrete in a variety of applications and ultimately leading to stronger, more durable, and more cost-effective infrastructure.

1.1 Research Significance

In recent years, basalt fibres have gained increasing attention and application in the construction industry, leading to several advancements. Currently, two primary methods are employed for fibre mixing: (a) using fibres with different properties and (b) using fibres of the same type but in varying lengths. Numerous studies have investigated the effects of discrete basalt fibres on the fresh and mechanical properties of concrete. While researchers have explored the combination of basalt fibre with various types of cement, cementitious materials, and hybrid fibres, the hybridization of the basalt fibre with different lengths and contents remains largely unexamined. Therefore, the primary goal of the current study is to assess the impact of single and hybrid basalt fibre lengths on the workability and mechanical properties of normal and high strength concrete. Short fibres are more efficient in controlling micro-cracks propagation, while long fibres bridge macro-cracks [25]. The current study also attempted to develop meaningful and reliable models to predict the compressive strength and the flexural strength of concrete using Response Surface Methodology. The experimental investigation was carried out on M30 and M60

grade concrete utilising 12mm and 30 mm basalt fibres and a hybrid mix of the two lengths at 1.5% fibre content.

2. Experimental Work and Procedure

2.1 Materials

Ordinary Portland Cement (OPC) 53 grade conforming to IS: 12269-2013, was utilized for both normal and high-strength concrete. Metakaolin was incorporated as the binder material along with cement for high-strength concrete. The chemical constitution of cement and metakaolin provided by the manufacturers is given in Table 1.

Table 1. Chemical composition of cement and metakaolin

Chemical components	SiO_2	Al_2O_3	Fe_2O_3	TiO_2	CaO	MgO	Na_2O	K_2O	Loss on ignition	Insoluble Residue
OPC 53 grade cement (%)	19.56	4.10	6.08	-	60.75	1.50	0.35		1.65	6.55
Metakaolin (%)	52	46	0.6	0.65	0.09	0.03	0.10	0.03	0.50	-

High-quality locally available manufactured sand (M sand) conforming to Zone II standards is used as fine aggregate in both normal and high-strength concrete. For coarse aggregates, a maximum size of 20 mm is used in normal concrete, while a maximum size of 10 mm is utilized in high-strength concrete. Various laboratory tests were conducted on the fine and coarse aggregates to assess their different physical properties, all of which adhered to the specifications outlined in IS: 383 – 2016.

This research aims to enhance the flexural performance of basalt fibre reinforced concrete by combining fibres with varying lengths i.e., hybridization obtained using short and long length fibres. For this hybridization, basalt fibres measuring 12 mm and 30 mm in length were employed. The properties of basalt fibre given by the manufacturer are presented in Table 2.

Table 2. Properties of basalt fibres

Fibre	Length (mm)	Density (kg/m^3)	Tensile Strength (MPa)	Elastic Modulus (GPa)	Elongation (%)
Basalt	12	2750	3500-4500	95-115	2.4-3.0
Basalt	30	2750	3500-4500	95-115	2.4-3.0

2.2 Mix Proportions

In this study, concrete grades M30 and M60, representing normal strength and high strength concrete, respectively, were formulated in accordance with the guidelines outlined in IS 10262:2019, and details are given in Table 3.

The total fibre volume fraction was 1.5%, and proportions of basalt fibres were determined based on the pilot study and literature review [26, 27]. The proportions of basalt fibre are given in Table 4.

Superplasticizers utilized in M30 and M60 concrete mixes were "Classic Superflow – SP" and "Classic Superflow-PC," respectively. The former is a brown liquid based on Naphthalene formaldehyde condensates, while the latter is a yellowish-brown liquid based on Polycarboxylate condensates.

Table 3. Design mix details

Grade of concrete	Cement (kg/m^3)	Metakaolin (kg/m^3)	Water (lit/m^3)	Coarse aggregate (kg/m^3)	Fine aggregate (kg/m^3)
M30	420	-	168	1210	665
M60	444	49.3	138	1100	777

Table 4. Proportion of basalt fibres

Mix Designation	Fibre volume fraction (%)	Basalt fibre content (%)	
		12mm	30mm
HBFO	0	0	0
HBF1	1.5	100	0
HBF2	1.5	75	25
HBF3	1.5	50	50
HBF4	1.5	25	75
HBF5	1.5	0	100

2.3 Casting and Testing of Specimens

The concrete mixes were prepared using a tilting drum mixer equipped with revolving star blades. To prevent absorption, the interior of the drum was initially rinsed with water. The preparation process involved mixing fine and coarse aggregates, cement, mineral admixtures, and basalt fibres in the tilting drum mixer. Dry mixing was carried out for one minute, followed by the addition of water mixed with superplasticizers. Subsequently, mixing was continued for four minutes to achieve a homogeneous mixture. Standard moulds were prepared, oiled, and positioned on a vibration table set at a low speed while the concrete was poured. Firm steel moulds were utilized for retaining the freshly mixed concrete, and a table vibrator was used to compact it. After a 24-hour curing period, the specimens were demolded, and each one was labelled with the date of casting and the mix used. The specimens were put in the curing tank, and all the tests were done after 28 days of curing. The tests conducted are explained in the following sections.

2.3.1 Slump Cone Test

In the slump test, the freshly mixed concrete was placed in four layers, with each layer being tamped 25 times using a standard rod. Subsequently, the surface of the concrete was levelled. After raising the cone vertically, the difference in height between the concrete sample and the mould was measured. This test assesses the consistency and flowability of the concrete, which are crucial properties for ensuring proper placement and

consolidation of the concrete within the formwork. The test was conducted in accordance with IS 1199:1959 specifications, and the test set up is shown in Fig.1(a).

2.3.2 Compressive Strength Test

The primary test frequently carried out on hardened concrete entails testing cubical specimens with dimensions of 150 mm × 150 mm × 150 mm in a Compression Testing Machine (CTM) with a capacity of 3000 kN. The test was conducted at a loading rate of 14 N/mm^2 per minute in accordance with IS: 516-1959 specifications. Compressive strength is found by dividing the ultimate load by the area of loading zone, typically after 28 days of curing. The strength of concrete is influenced by the proportions of its constituent materials. The water-cement ratio plays a crucial role in determining concrete strength, with lower ratios typically resulting in higher compressive strength. Fig. 1b illustrates a compression test being performed on a cube specimen.

2.3.3 Flexural Strength Test

The bending strength of concrete is estimated through a flexural test, which assesses the load at which cracking occurs. This test measures its ability to endure bending failure. The flexural strength of conventional concrete was determined using a two-point loading method. A plain concrete beam specimen measuring 100 mm × 100 mm × 500 mm was utilized for the test in accordance with IS: 516-1959. The specimen was positioned on steel rollers resting on the bed of the testing machine, spaced at a distance of 400 mm center to center. Two 38 mm diameter rollers were positioned at one-third points of the supporting span, spaced at 133 mm intervals. The load was applied at a rate of 1.8 kN per minute, and the maximum load at which the specimen failed under flexure was recorded. The average flexural strength of three samples of each mix was mentioned as the Modulus of Rupture (MOR). The flexural strength test was conducted after 28 days of curing. Fig.1c depicts the arrangement for the flexural strength test.

2.3.4 Modulus of Elasticity Test

The MOE was determined by subjecting cylindrical specimens to uniaxial compression, as outlined in IS 516-1959. The test involved measuring deformations using a dial gauge fixed between gauge lengths of 200 mm, as depicted in Fig. 1d. Cylindrical specimens with a standard size of 300 mm in height and 150 mm in diameter were placed on a CTM of 3000 kN capacity, ensuring uniform loading without eccentricity.

(a) (b) (c) (d)

Fig. 1. Test set-up a) slump cone test b) compressive strength test c) flexural strength test d) MOE test apparatus

The load was applied until the cylinder failed, and the target load and deflection were recorded. Deflection readings were converted to strain by calculating the change in length. Stress was calculated by dividing the applied load by the cylinder's cross-sectional area. A series of readings were taken, and stress-strain graphs were plotted. The MOE was obtained from the slope of the stress-strain graph, providing a measure of the material's stiffness.

3. Results and Discussion

3.1 Workability

The slump cone test with respect to IS 1199-1959 standards was conducted for all the basalt hybrid mixes and the values for M30 and M60 grades are reported in Table 5. The test was done for investigating the impact of basalt fibres on workability of the concrete.

The observed slump values are lower than those of conventional concrete. It's widely acknowledged that the addition of any fiber type typically decreases slump values, a trend consistently documented across various studies. A portion of the cement paste was employed to cover the basalt fibres as they were included in the mixture, leaving less paste for workability [28, 29].

It is easy to note that the inclusion of 30 mm length basalt fibre in cement concrete compromised the workability of the concrete compared to the 12 mm length basalt fibre. The concrete mix containing only 30 mm fibres exhibited the lowest slump values, measuring 40 mm for the M30 grade and 30 mm for the M60 grade. During the concrete mixing process, the higher volume fraction of fibres led to noticeable clustering of fibres, significantly reducing workability. This issue was particularly pronounced in mixes containing 30 mm fibres compared to those with 12 mm fibres due to their greater length. Incorporating 30 mm basalt fibres made it exceedingly difficult to achieve a uniform concrete mixture during mixing. The 30 mm basalt fibres have a greater surface area than 12 mm basalt fibres, which results in the high water absorption of 30 mm basalt fibres and hence low workability. The slump decreased with increasing fibre length due to the greater specific surface area, rough surface, and high coefficient of friction [18, 30]. The workability can be increased by the use of appropriate dosage of super plasticizers. In this study, the dosage of super plasticizers has been found out from trial and errors.

3.2 Compressive Strength (f_c)

The compressive strength values of different concrete mixes after 28 days of water curing were obtained by testing cubes of side 15 cm in the CTM and results were presented in Table 5. The results are presented in graphical form in Fig. 3. The accompanying graph depicts the f_c values of concrete cubes with varying proportions of basalt fibres (12 mm and 30 mm). Introducing basalt fibres into the concrete mix had a negligible impact on its compressive strength. The most significant enhancement in compressive strength, amounting to 1.29% and 4.48% for M30 and M60, respectively was observed when the concrete mix comprised 75% basalt fibres 30 mm and 25% basalt fibres 12 mm. An insignificant decrease of 3.63% in compressive strength was observed for normal grade concrete with only 12 mm basalt fibres, and a 6.22% decrease was noted for normal grade concrete with only 30 mm fibres, compared to conventional concrete specimens. Similarly, for high-strength grade concrete, a 2.81% decrease in compressive strength was observed with only 12 mm basalt fibres and a 5.231% decrease with only 30 mm fibres, when compared to conventional concrete specimens. This trend aligns with previous studies [21, 31], potentially due to the bunching effect of the fibres, compaction issues, and an increase in poor interface regions within the matrix [28, 32, 33]. Conversely, the compressive

strength of M30 and M60 concrete reinforced with a hybrid of 12 mm and 30 mm basalt fibres at a volume content of 1.5% was higher than that of conventional concrete specimens. The compressive strength of the hybrid fibre concrete HBF4 mix showed an insignificant increase of 1.29% for M30 and 4.48% for M60, compared to conventional concrete. Hybrid fibre concrete mixes HBF2, HBF3, and HBF4 demonstrated better compressive strength than single-length fibre-reinforced specimens for both M30 and M60 grades. The variation in the average cube compressive strengths of normal and high-strength hybrid basalt fibre-reinforced concrete was within ±5% when compared to conventional concrete. These results align with the findings from previous literature [28, 33, 34].

The compressive strength of mixes containing 30 mm fibres is lower than that of mixes incorporating 12 mm basalt fibres for the same fibre volume. This discrepancy in strength can be ascribed to the greater length and higher volume content of long fibres in the concrete mixture, which may result in inadequate dispersion of fibres throughout the concrete matrix, which elevates the likelihood of pore concentration within the matrix and fosters the creation of a feeble interface between the fibres and the matrix, consequently leading to diminished compressive strengths when subjected to compressive forces [18]. The conventional concrete specimens experienced failure primarily through the crushing of the concrete under the applied load. In contrast, the cubes containing hybrid basalt fibre concrete failed differently, as fissures formed on their surfaces. This indicates the effectiveness of the adhesion between the basalt fibre and concrete. Fig. 2a illustrates the failure mode observed in hybrid basalt fibre concrete. Additionally, some of the M60 cube samples failed by splitting along one or more planes, which occurs when the tensile strength of the concrete is surpassed, resulting in cracks propagating perpendicular to the direction of loading.

3.3 Flexural Strength

The flexural strength of concrete refers to its ability to resist failure under bending forces. Four point bending tests were conducted on a beam specimen of 10cm x 10cm cross section and 50cm length. The failed specimens are shown in Fig. 2b. The results for the test are given in Table 5. The results are presented in graphical form in Fig. 4.

The flexural strength or MOR values showed an increase in the range of 24.2% to 39.6% for M30 and 14.35% to 54.35% for M60 grade concrete mixes when compared to conventional concrete mixes. Addition of basalt fibres particularly boosted the flexural strength, unlike the compressive strength.

According to Loh et al., [32] the flexural strength of normal strength concrete mixes with 12 mm basalt fibres increased by approximately 39.6% at a fibre volume content of 1.5% compared to conventional concrete. Similarly, Shoaib et al., [15] reported a 56% increase in flexural strength for normal strength concrete using 43 mm long basalt fibres at the same volume content. For high-strength concrete, Ayub et al., [31] observed a 43.5% increase in flexural strength with 25 mm basalt fibres at a volume content of 2%. In the current study, the M30 concrete mix containing only 12 mm basalt fibres exhibited 24.2% higher MOR values than conventional concrete, while the M60 mix showed a 14.35% increase. Additionally, the M30 mix with only 30 mm basalt fibres demonstrated a 27% higher MOR, and the M60 mix showed a 38.55% increase compared to conventional concrete. The present study's findings align well with previous research, confirming that basalt fibres, especially when used in optimal lengths and volumes, can markedly improve the mechanical properties of concrete. Concrete mixes with longer fibres demonstrated better MOR values than those with shorter fibres, regardless of the concrete grade. These findings are consistent with the previous studies [31, 35].

The MOR values for M30 concrete HBF2, HBF3, and HBF4 mixes were 34.6%, 35.2%, and 39.6% higher than conventional concrete, respectively. For the M60 mixes, the values were 20.8%, 41.45%, and 54.35% higher. The results from the flexural strength tests indicate that the hybridization of different basalt fibre length specimens demonstrates superior performance compared to conventional and single basalt fibre reinforced concrete mixes [34]. This enhancement may be attributed to the crack bridging properties inherent in the incorporated fibres. Short fibres are more effective in regulating micro-cracks proliferation, while long fibres bridge macro cracks. During the test, the conventional concrete mix experienced an abrupt brittle failure when a fracture formed, causing the beam to split into two separate pieces. In contrast, the fibre-reinforced specimen with single length and hybrid length basalt fibres exhibited ductile failure mechanisms. The crack was formed at the bottom, which then propagated towards the top of the specimen. Additionally, there was a delay observed in the propagation of cracks. The bridging function of the fibres successfully impeded the rapid propagation of fractures and longer fibres show a stronger anchorage and bridging effect [35].

The hybrid fibre concrete mixes, with 25% and 75% basalt 12 mm and 30 mm fibres respectively exhibited superior values for modulus of rupture compared to conventional concrete mixes for both M30 and M60 grades. Despite the lower flexural strength values observed for the concrete mix containing only 30 mm fibres when compared to optimum hybrid mix, it was surprising that the beam specimen did not split into two separate parts. The data suggests that as the proportion of 30 mm fibres increases, there is a significant rise in flexural strength values, indicating that longer fibres are more effective in bridging macro cracks. However, the lower flexural strength of concrete mix with 30 mm fibres only may be due to the poor fibre dispersion in the mix. The same trend was noted for both normal and high strength concrete.

3.4 Modulus of Elasticity

There wasn't a considerable increase in the MOE values with the addition of basalt fibres. Studies indicate that even with higher fibre volumes, the enhancement of MOE for both normal and high-strength concrete grades remains minimal. This is in line with the observation/s of a few investigators [36, 37].

(a) (b) (c)

Fig. 2. Failed specimens after testing a) prisms b) cube c) cylinder

The results are shown in graphical form in Fig. 5. The correlation between the MOE and compressive strength of concrete has been reported by many researchers. Given the absence of improvement in compressive strength values, it's reasonable to conclude that

the change in MOE values is very minimal. The failed cylindrical specimen is shown in Fig. 2c.

Table 5. Mechanical properties for M30 and M60 grade of concrete

Specimen ID	M30				M60			
	Slump (mm)	f_c (MPa)	MOR (MPa)	MOE (GPa)	Slump (mm)	f_c (MPa)	MOR (MPa)	MOE (GPa)
HBF0	70	38.60	5.00	26.60	97	69.20	6.20	33.40
HBF1	64	37.26	6.21	27.53	75	67.25	7.09	36.05
HBF2	60	37.80	6.73	27.64	68	70.08	7.49	36.42
HBF3	56	38.21	6.76	27.90	62	71.26	8.77	36.81
HBF4	50	39.10	6.98	28.31	55	72.31	9.57	37.15
HBF5	40	36.20	6.35	28.12	30	65.58	8.59	36.86

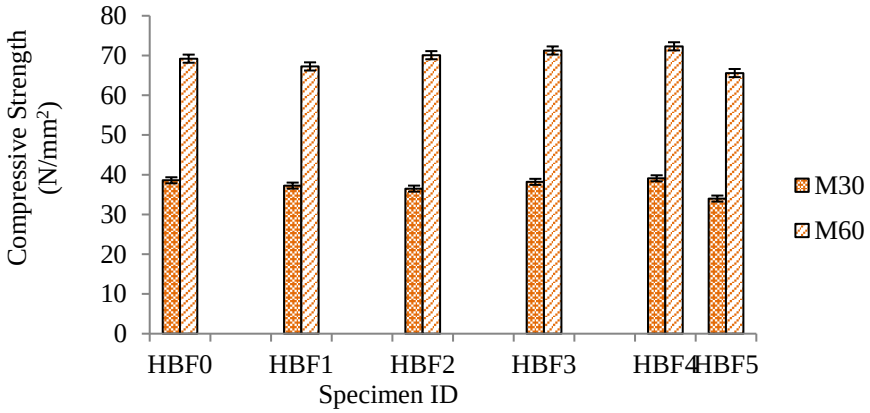

Fig. 3. Compressive strength of hybrid mixes

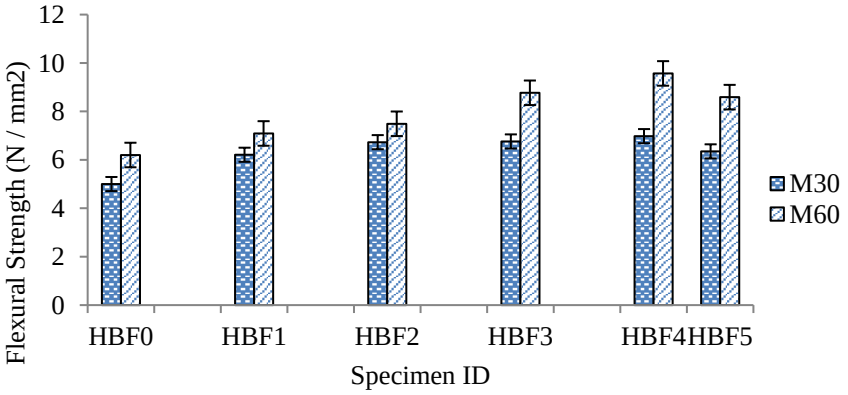

Fig. 4. Flexural strength/ MOR of hybrid mixes

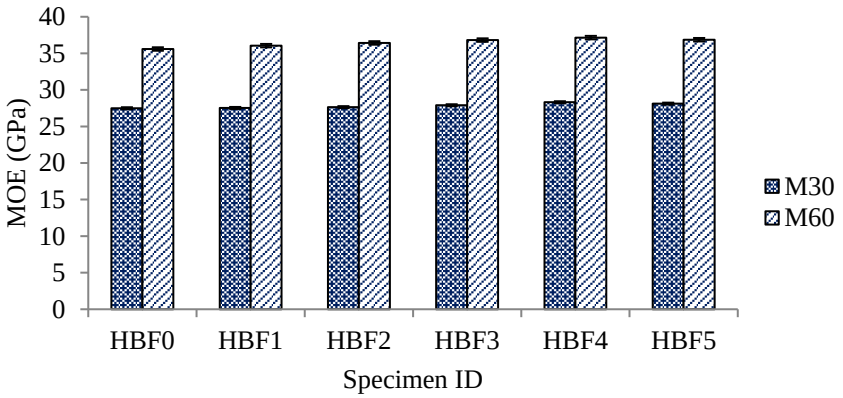

Fig. 5. MOE of hybrid mixes

3.5 Microstructural Characteristics

The Scanning Electron Microscopy (SEM) images of the optimum hybrid mixes are shown in Fig. 6. Both images depict the presence of voids within the concrete matrix, with M60 exhibiting a denser matrix compared to the other. The strong adhesion between the basalt fibres and the concrete matrix is evident from the fibre-concrete interphase observed in the images. Additionally, the basalt fibres were visibly embedded within the concrete matrix in both images. The images clearly display the slip trace of basalt fibres that have been pulled out from the concrete matrix. This phenomenon indicates that the fibres have been pulled out without rupturing, which contributes to increased energy dissipation during the post-cracking process. As a result, this behavior enhances the tensile strength of basalt hybrid fibre-reinforced concrete. The presence of slip traces suggests strong adhesion between the basalt fibres and the concrete matrix, allowing for effective load transfer and improved mechanical properties, particularly in tension [9].

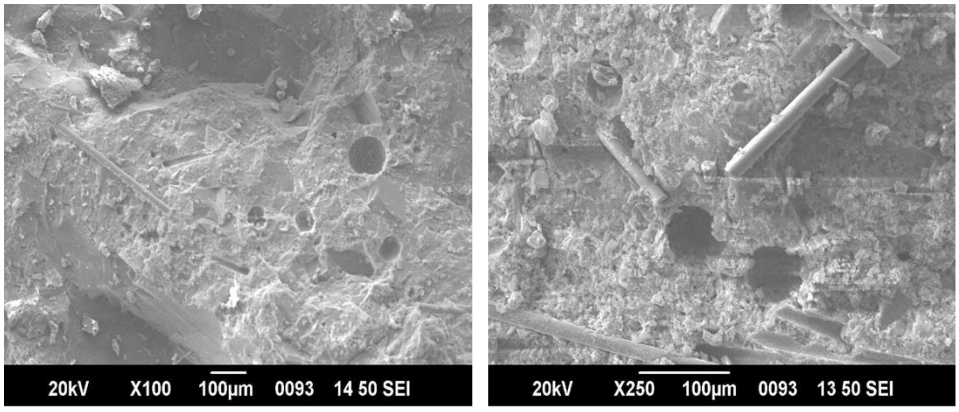

(a) (b)

Fig. 6. SEM images of optimal hybrid mix HBF4 a) M30 b) M60

3.6 Statistical Analysis

In this section, a detailed descriptive statistical analysis was carried out on the selected parameters from the gathered dataset. To further analyze the data, Response Surface Methodology (RSM) was employed to develop predictive models. RSM is a sophisticated statistical technique used to explore the relationships between several input variables (also known as factors) and one or more response variables (output factors) [38]. This method helps in understanding the interaction effects of these input variables on the output and in constructing an ideal mathematical model that can predict the desired outcomes with high accuracy. The core concept of RSM is that the input variables can be visualized as the vertices of a geometric shape, typically a cuboid in multi-dimensional space. By analyzing how the response variable changes as the input variables are varied, RSM creates contour plots—lines that connect points of equal response. These contour lines, when analyzed collectively, provide a clear understanding of how different combinations of input variables influence the output**.** The RSM model can be represented using the mathematical expression given in Eq.1[39].

$$Y = \beta_0 + \sum_{i=1}^{n} \beta_i X_i + \sum_{i=1}^{n} \beta_{ii} X_i^2 + \sum_{i<j}^{n} \beta_{ij} X_i X_j \ldots + e(X_i, X_j, \ldots \ldots, X_n) \quad (1)$$

where, X_i and Y denote independent factors and response, β_0 is the intercept, β_i , β_{ii} and β_{ij} are model coefficients that characterize the linear, squared and interaction effect of the model, respectively. A commercially available software with statistical design and analysis tool pack was used to develop the RSM models [45].

In this study, the selected input parameters include the water-to-binder ratio (w/b) and the amounts of basalt fibres of different lengths, specifically shorter length 12 mm and a longer length 30 mm, which are denoted as bfs and bfl respectively. The response variables being analyzed are the compressive strength (cs) and flexural strength (fs) of the concrete. The corresponding regression equations for cs and fs derived using RSM are provided in Eq. 2 and Eq. 3, respectively. The coefficients of determination R^2 values for these equations are 0.99 for cs and 0.95 for fs. This high R^2 value indicates an excellent fit, meaning the model is highly accurate in predicting the compressive strength and flexural strength based on the input parameters. The residual plots for cs and fs are plotted in Fig. 7 and Fig. 8 respectively.

$$cs = 142.18 - 259.6\ w/b + 2.1\ bfs - 1.15\ bfl - 1.84\ bfs*bfs - 2.2\ w/b*bfs - 1.5\ w/b*bfl \quad (2)$$

$$fs = 9.41 - 11.21\ w/b + 4.43\ bfs + 3.72\ bfl - 3.27\ bfs*bfs + 3.14\ w/b*bfs - 6.97\ w/b*bfl \quad (3)$$

By applying RSM, the study aims to develop a predictive model that can accurately estimate these mechanical properties based on the variations in the selected input parameters, thereby providing valuable insights for optimizing the composition of basalt fibre-reinforced concrete.

The accuracy of the prediction model was validated by comparing its predicted values for both compressive strength and flexural strength with experimental data from previous studies and is shown in graphical form in Fig. 9 and Fig. 10 respectively. The comparison revealed that all estimated values fell within ±6% and ±3.4% for compressive strength and flexural strength, respectively compared to the experimental results, indicating a high level of agreement and validating the model's performance.

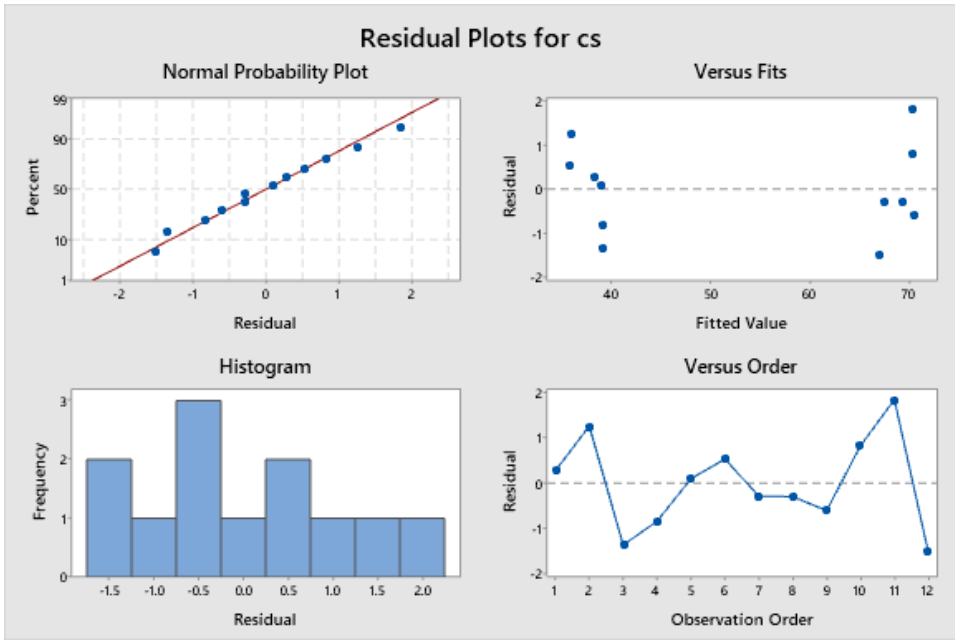

Fig. 7. Residual plot for cs

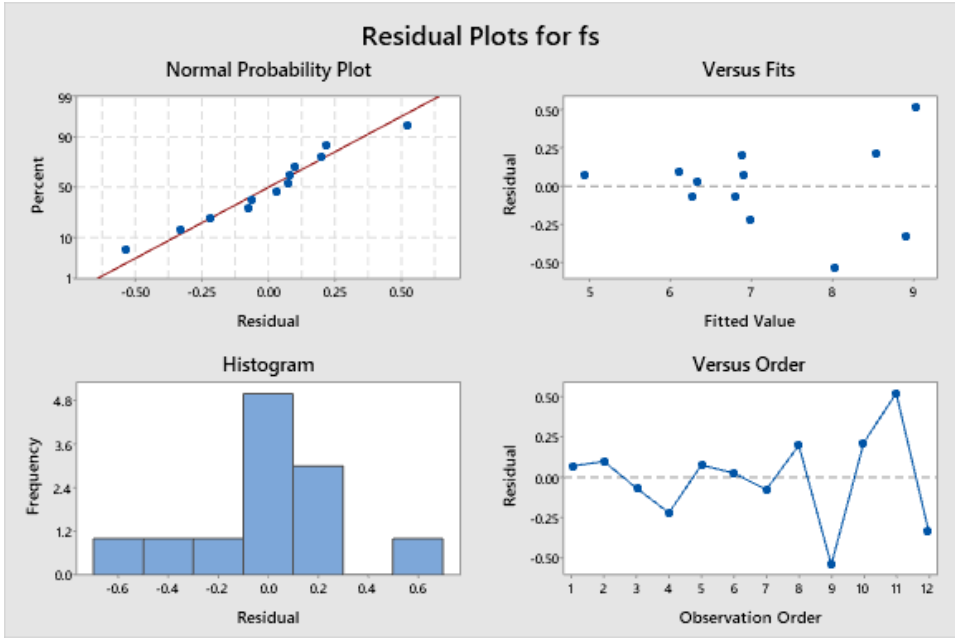

Fig. 8. Residual plot for fs

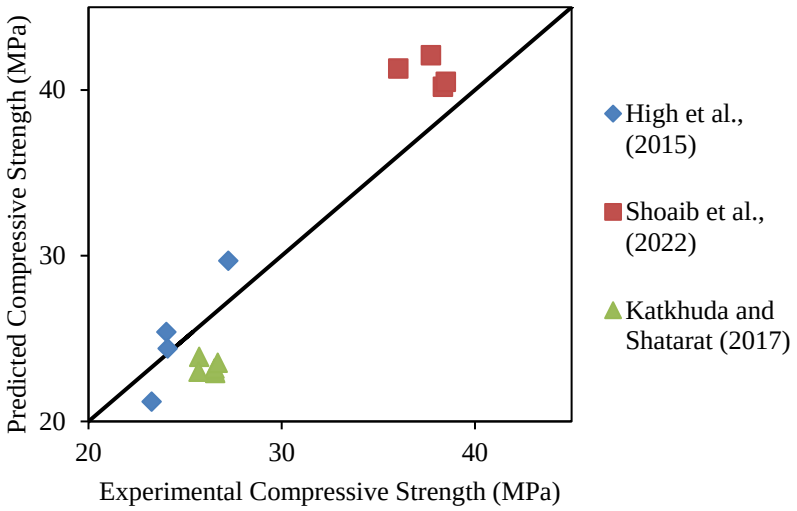

Fig.9. Comparison between compressive strength results of earlier researchers [13,15,29] and the predicted values by RSM model

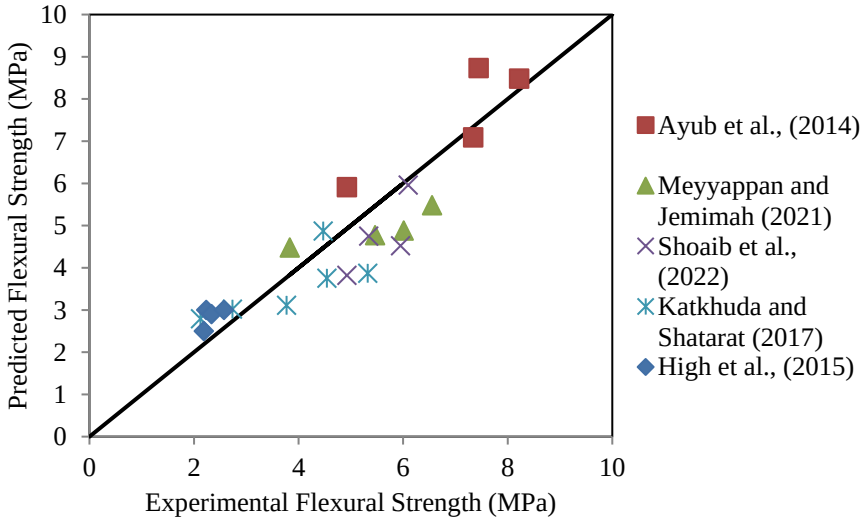

Fig.10. Comparison between flexural strength results of earlier researchers [13,15,29,31,33] and the predicted values by RSM model

4. Conclusions

The inclusion of fibres and pozzolanic materials helps in maximizing the mechanical and chemical attributes of concrete. In the present study, the influence of hybrid basalt fibre lengths on the workability and mechanical properties of normal and high-strength reinforced concrete were examined. Basalt fibres, measuring 12 mm and 30 mm in length and constituting 1.5% of the concrete volume, were integrated into the mixture. Various parameters were investigated; including workability assessed using the slump cone test, as well as compressive strength, flexural strength and MOE. Furthermore, SEM analysis

was performed to examine the microstructural characteristics of basalt FRC. Based on the results obtained from lab experiments and discussions, the following conclusions are drawn,

- The hybrid fibre volume fraction of 1.5% with 25-75 basalt fibre 12 mm-30 mm combination (HBF4) significantly improves the general performance.
- Slump values decreased for hybrid mixes in comparison to conventional concrete, with a notable decrease observed in workability with the inclusion of 30 mm fibres. The slump decreased with increasing fibre length due to the greater specific surface area, rough surface, and high coefficient of friction. Specifically, in high strength concrete, there was a maximum reduction in slump value.
- The inclusion of basalt fibres did not lead to a significant enhancement in compressive strength values. However, the compressive strength of different length hybrid fibre reinforced specimens is better than that of single length fibre reinforced specimens for the same basalt fibre content.
- The maximum flexural strength in the HBF4 mix was found to be 39% and 54.35% higher than the control specimens for normal and high-strength concrete, respectively. This improvement could be attributed to the crack-bridging properties of the incorporated fibres.
- All the hybrid mixes showed no notable improvement in the Modulus of Elasticity (MOE) of the concrete.

Therefore, the positive results obtained from the enhanced properties of hybrid basalt fibre-reinforced concrete (FRC) utilizing 12 mm and 30 mm basalt fibres in both normal and high-strength concrete indicate its potential utility in structural applications.

5. Scope for Future Work

For future research on basalt hybrid FRC, it is essential to evaluate its ductility performance. This involves assessing the material's ability to undergo significant plastic deformation before failure, which is crucial for structures subject to dynamic loads and seismic activity. Studies should focus on how different fibre combinations influence ductility using tensile and bending tests to measure strain capacity and energy absorption. Additionally, investigating the failure modes of basalt hybrid FRC will provide insights into its structural integrity and weaknesses. A thorough study of crack patterns under various loading conditions is necessary to understand its stress response, including examining the spacing, width, distribution, and progression of cracks over time. Evaluating the long-term durability of basalt hybrid FRC, including resistance to environmental factors such as freeze-thaw cycles, chemical exposure, and UV radiation, will help determine its suitability for various applications. Research should also explore optimizing fibre proportions and lengths to balance workability, mechanical properties, and cost-effectiveness, potentially experimenting with fibre types and lengths beyond those used in current study.

Acknowledgement

The author would like to express gratitude for the financial support from All India Council for Technical Education (AICTE) and technical support from Sophisticated Test & Instrumentation Centre (STIC) India.

References

[1] Qsymah A, Sangi A, Al-Sayyab A, Al-Balushi A, Al-Mahruqi H, Al-Abri A. Thermal properties, microstructure analysis, and environmental benefits of basalt fiber reinforced concrete. J Eng Fibers Fabr. 2023;18. https://doi.org/10.1177/15589250221146547

[2] Amin M, Elsakhawy Y, Abu el-Hassan K, Abdelsalam BA. Behavior evaluation of sustainable high strength geopolymer concrete based on fly ash, metakaolin, and slag. Case Stud Constr Mater. 2022;16. https://doi.org/10.1016/j.cscm.2022.e00976
[3] Zhou H, Jia B, Huang H, Mou Y. Experimental study on basic mechanical properties of basalt fiber reinforced concrete. Materials. 2020;13. https://doi.org/10.3390/ma13061362
[4] Wild S, Khatib JM, Jones A. Relative strength, pozzolanic activity and cement hydration in superplasticised metakaolin concrete. Cem Concr Res. 1996;26:1537-1544. https://doi.org/10.1016/0008-8846(96)00148- 2
[5] Poon CS, Kou SC, Lam L. Compressive strength, chloride diffusivity and pore structure of high performance metakaolin and silica fume concrete. Constr Build Mater. 2006;20:858-865. https://doi.org/10.1016/j.conbuildmat.2005.07.001
[6] Viswanadha Varma D, Rama Rao GV, Markandeya Raju P, Pavan Kumar M. Compressive strength and durability of Metakaolin blended concrete exposed to acid and sulphate attack. IOP Conf Ser Mater Sci Eng. 2021;1025(1). https://doi.org/10.1088/1757-899X/1025/1/012004
[7] Gowram I, BM, Sudhir M, Mohan MK, Jain D. Efficacy of natural zeolite and metakaolin as partial alternatives to cement in fresh and hardened high strength concrete. Adv Mater Sci Eng. 2021;2021:1-10. https://doi.org/10.1155/2021/4090389
[8] Dubey M, Deo SV, Ramtekkar G. Evaluating properties of high performance concrete containing metakaolin as cementitious material. Int Rev Appl Sci Eng. 2022;13:257-262. https://doi.org/10.1556/1848.2021.00359
[9] ACI Committee 544. State-of-the-Art report on fibre reinforced concrete. Concr Int Des Constr. 1983;9-30.
[10] Sagar B, Sivakumar MVN. Compressive properties and analytical modelling for stress-strain curves of polyvinyl alcohol fiber reinforced concrete. Constr Build Mater. 2021;291. https://doi.org/10.1016/j.conbuildmat.2021.123192
[11] Wang Y, Kang AH, Wu ZG, Xiao P, Gong YF, Sun HF. Investigation of the basalt fiber type and content on performances of cement mortar and concrete. Constr Build Mater. 2023;408. https://doi.org/10.1016/j.conbuildmat.2023.133720
[12] Dhand V, Mittal G, Rhee KY, Park SJ, Hui D. A short review on basalt fiber reinforced polymer composites. Compos Part B Eng. 2015;73:166-180. https://doi.org/10.1016/j.compositesb.2014.12.011
[13] High C, Seliem HM, El-Safty A, Rizkalla SH. Use of basalt fibers for concrete structures. Constr Build Mater. 2015;96:37-46. https://doi.org/10.1016/j.conbuildmat.2015.07.138
[14] Cakir F. Evaluation of mechanical properties of chopped glass/basalt fibers reinforced polymer mortars. Case Stud Constr Mater. 2021;15. https://doi.org/10.1016/j.cscm.2021.e00612
[15] Shoaib S, El-Maaddawy T, El-Hassan H, El-Ariss B, Alsalami M. Workability and flexural strength of concrete reinforced with basalt macro-fibers. Proc Int Struct Eng Constr. 2022;9. https://doi.org/10.14455/ISEC.2022.9(1).MAT-32
[16] Branston J, Das S, Kenno SY, Taylor C. Mechanical behaviour of basalt fibre reinforced concrete. Constr Build Mater. 2016;124:878-886. https://doi.org/10.1016/j.conbuildmat.2016.08.009
[17] Kumar KS, Ravande K. Influence of different lengths and volumes of basalt fibre on mechanical properties of concrete. Civ Eng Archit. 2023;11:613-628. https://doi.org/10.13189/cea.2023.110207
[18] Wang X, He J, Mosallam AS, Li C, Xin H. The effects of fiber length and volume on material properties and crack resistance of basalt fiber reinforced concrete (BFRC). Adv Mater Sci Eng. 2019;2019:1-17. https://doi.org/10.1155/2019/7520549

[19] AL-Kharabsheh BN, Al-Masri M, AL-Majali A, AL-Momani Z, AL-Bis B. Basalt fibers reinforced concrete: strength and failure modes. Materials. 2022;15:1-24. https://doi.org/10.3390/ma15207350
[20] Ramesh B, Eswari S. Mechanical behaviour of basalt fibre reinforced concrete: An experimental study. Mater Today Proc. 2021;43:2317-2322. https://doi.org/10.1016/j.matpr.2021.01.071
[21] Jalasutram S, Sahoo DR, Matsagar V. Experimental investigation of the mechanical properties of basalt fiber-reinforced concrete. Struct Concr. 2017;18:292-302. https://doi.org/10.1002/suco.201500216
[22] Di Prisco M, Plizzari G, Vandewalle L. Fibre reinforced concrete: new design perspectives. Mater Struct. 2009;42:1261-1281. https://doi.org/10.1617/s11527-009-9529-4
[23] Khan M, Cao M, Xie C, Ali M. Efficiency of basalt fiber length and content on mechanical and microstructural properties of hybrid fiber concrete. Fatigue Fract Eng Mater Struct. 2021;44:2135-2152. https://doi.org/10.1111/ffe.13483
[24] Khan M, Cao M, Xie C, Ali M. Hybrid fiber concrete with different basalt fiber length and content. Struct Concr. 2021;23:346-364. https://doi.org/10.1002/suco.202000472
[25] Heweidak M, Kafle B, Al-Ameri R. Influence of hybrid basalt fibres' length on fresh and mechanical properties of self-compacted ambient-cured geopolymer concrete. J Compos Sci. 2022;6. https://doi.org/10.3390/jcs6100292
[26] Smarzewski P, Barnat-Hunek D. Property assessment of hybrid fiber-reinforced ultra-high-performance concrete. Int J Civ Eng. 2017;16(6):593-606. https://doi.org/10.1007/s40999-017-0145-3
[27] Sivakumar A, Santhanam M. Mechanical properties of high strength concrete reinforced with metallic and non-metallic fibres. Cem Concr Compos. 2007;29(8):603-608. https://doi.org/10.1016/j.cemconcomp.2007.03.006
[28] Chen B, Liu J. Contribution of hybrid fibers on the properties of the high-strength lightweight concrete having good workability. Cem Concr Res. 2005;35(5):913-917. https://doi.org/10.1016/j.cemconres.2004.07.035
[29] Katkhuda H, Shatarat N. Improving the mechanical properties of recycled concrete aggregate using chopped basalt fibers and acid treatment. Constr Build Mater. 2017;140:328-335. https://doi.org/10.1016/j.conbuildmat.2017.02.128
[30] Ma J, Qiu X, Cheng L, Wang Y. Experimental research on the fundamental mechanical properties of presoaked basalt fiber concrete. In: Ye L, Feng P, Yue Q, editors. Advances in FRP composites in civil engineering. Berlin, Heidelberg: Springer; 2011. p. 85-88. https://doi.org/10.1007/978-3-642-17487-2_16
[31] Ayub T, Shafiq N, Nuruddin MF. Effect of chopped basalt fibers on the mechanical properties and microstructure of high performance fiber reinforced concrete. Adv Mater Sci Eng. 2014;2014:1-14. https://doi.org/10.1155/2014/587686
[32] Loh ZP, Mo KH, Tan CG, Yeo SH. Mechanical characteristics and flexural behaviour of fibre-reinforced cementitious composite containing PVA and basalt fibres. Sādhanā. 2019;44. https://doi.org/10.1007/s12046-019-1072-6
[33] Meyyappan P, Carmichael MJ. Studies on strength properties of basalt fibre reinforced concrete. Mater Today Proc. 2021;43:2105-2108. https://doi.org/10.1016/j.matpr.2020.11.890
[34] Khan M, Cao M. Effect of hybrid basalt fibre length and content on properties of cementitious composites. Mag Concr Res. 2021;73(10):487-498. https://doi.org/10.1680/jmacr.19.00226
[35] Jiang C, Fan K, Wu F, Chen D. Experimental study on the mechanical properties and microstructure of chopped basalt fibre reinforced concrete. Mater Eng. 2014;58:187-193. https://doi.org/10.1016/j.matdes.2014.01.056

[36] Ayub T, Shafiq N, Nuruddin MF. Mechanical properties of high-performance concrete reinforced with basalt fibers. Procedia Eng. 2014;77:131-139. https://doi.org/10.1016/j.proeng.2014.07.029
[37] Arslan ME. Effects of basalt and glass chopped fibers addition on fracture energy and mechanical properties of ordinary concrete: CMOD measurement. Constr Build Mater. 2016;114:383-391. https://doi.org/10.1016/j.conbuildmat.2016.03.176
[38] Ma H, Sun Z, Ma G. Research on compressive strength of manufactured sand concrete based on response surface methodology (RSM). Appl Sci. 2022;12(7). https://doi.org/10.3390/app12073506
[39] Sankar B, Ramadoss P. Modelling the compressive strength of high-performance concrete containing metakaolin using distinctive statistical techniques. Results Control Optim. 2023;12. https://doi.org/10.1016/j.rico.2023.100241
[40] Bureau of Indian Standards. Coarse and fine aggregates for concrete specification. IS: 383-2016. New Delhi: Bureau of Indian Standards; 2016.
[41] Bureau of Indian Standards. Concrete mix proportioning - guidelines. IS: 10262-2019. New Delhi: Bureau of Indian Standards; 2019.
[42] Bureau of Indian Standards. Methods of test for strength of concrete. IS: 516-2004. New Delhi: Bureau of Indian Standards; 2004.
[43] Bureau of Indian Standards. Methods of sampling and analysis of concrete. IS: 1199-1959. New Delhi: Bureau of Indian Standards; 1959.
[44] Bureau of Indian Standards. Ordinary Portland cement, 53 grade - specification. IS: 12269-2013. New Delhi: Bureau of Indian Standards; 2013.
[45] Minitab Inc. Minitab Statistical Software Version 21.4.2. State College, PA: Minitab Inc.; 2021.

Research on Engineering Structures & Materials
www.jresm.org
Research Group

Research Article

An experimental study on strength of concrete having calcium carbonate as a partial replacement material to cement and natural river sand

Konala Harish[a], L.N.K. Sai Madupu[*,b], S.V. Satyanarayana[c]

Department of Civil Engineering, R.V.R & J.C College of Engineering, Guntur, India

Article Info

Article history:

Received 16 Apr 2024
Accepted 27 Aug 2024

Keywords:

Calcium carbonate powder;
Calcium carbonate sand;
Compressive strength;
Flexural strength;
Split tensile strength

Abstract

Limestone is a sedimentary rock mainly composed of calcium carbonate mineral. Limestone is quarried abundantly in and around Piduguralla region, Andhra Pradesh, India. Good quality limestone is used to manufacture cement. Calcium oxide is used as white wash which is obtained by heating calcium carbonate. Limestone, as fine powder or as coarse grains is also used as base for paint. In this research, the calcium carbonate mineral in the form of limestone procured from Piduguralla region is used in concrete in two different forms i.e as powder form and as sand form. The cement was partially replaced with the calcium carbonate powder when the calcium carbonate is used as fine powder. The natural river sand was partially/fully replaced with calcium carbonate sand when the calcium carbonate is used as sand (coarser) form. Experiments on cube, cylinder and beam specimens are conducted using Universal Testing Machine to establish compression strength, split tensile strength and flexural strength of concrete having calcium carbonate. The test results support the usage of calcium carbonate in concrete to enhance the strength of concrete. Up to thirty percent cement can be replaced with calcium carbonate powder without adversely affecting the strength of concrete. Natural river sand can be partially/fully replaced with calcium carbonate sand which in turn increases the strength of concrete, but the optimum percentage of replacement is fifty percent of natural sand.

1. Introduction

India is the most populous country in the world and hence the infrastructural development works are increasing year by year which in turn increases the demand for concrete. Cement is the essential component in concrete. To protect the environment from greenhouse gases released during the cement production, an alternative to cement is necessary. An estimation of about 52.3% of worldwide CO_2 will be released from the cement industries of India by 2070 [11]. These consequences made the engineers to focus on changing the present way of preparing the concrete or mortar mix by replacing the cement with suitable other materials for getting economical and long-lasting concrete. If the cement is partially replaced with other suitable material without affecting the strength of concrete, then the consumption of cement can be reduced, which in turn prevent the environmental damage. The waste materials which are released from different industries as by-products are the probable alternatives for cement. These untreated waste materials such as fly ash, rice husk ash, silica fume, granite waste, blast furnace slag, marble powder etc., are released from industries and dumped into environment may cause hazardous

[*]Corresponding author: mlnkrishnasai@rvrjc.ac.in
[a]orcid.org/0009-0004-4441-6128; [b]orcid.org/0000-0001-5164-498X; [c]orcid.org/0000-0001-6197-1837
DOI: http://dx.doi.org/10.17515/resm2024.242ma0416rs

environment. Hence, they can be used for producing concrete. Also, a large amount of river sand is used as fine aggregate for preparing concrete and mortar leading to exploitation of river sand in an uncontrolled manner causing shortage of it. Due to this heavy demand in construction industries, natural river sand also requires immediate substitution. Hence researchers are showing interest on waste materials. Apart from the by-products of various industries, mined calcium carbonate can also be used as alternative material for cement and natural sand. The mined calcium carbonate boulders are crushed into granular or powder form which is used as a raw material for cement manufacturing and as base in paints. From many years the CCP is used as a building material, as a constituent of cement and as an aggregate for roads in construction industries. It is also used as a filler material in paints and plastics. The calcined calcium carbonate is used as whitewashing the walls. Calcium carbonate can cut down the acidic nature by maintaining the alkalinity and hence used to defuse the acidic content in soil and water. It has the capability of removing Sulfur dioxide and Nitrogen dioxide emissions from fossil fuels.

Jingliang Xia *et al* concluded that at lower dosage of Calcium carbonate powder can decrease the drying shrinkage of white High Strength Concrete (HSC) and at higher dosage can increase the workability, whiteness and mechanical properties and decrease the impermeability and carbonation resistance of white HSC [1]. Dhanendra Kumar *et al* determined that in Strain Hardening Cementitious Composites depending upon the increase in weight ratio of slag (substitute to fly ash in normal SHCC) to cement the compressive strength decreased and depending upon the increase in volume ratio of calcium carbonate powder (substitute to silica sand in normal SHCC) to solids the compressive strength improved by minimizing the cement content [2]. Ali Heidari *et al* have replaced silica sand with calcium carbonate in Reactive Powder Concrete decreased cement usage and enhanced flexural, compressive and tensile strengths at certain ratios of sand to cement and trimmed down the water absorption of concrete [3]. Joaquin Abellan-Garcia *et al* found that calcium carbonate increased rheological properties of Ultra High-Performance Concrete and Ultra High-Performance Fibre Reinforced Concrete (FRC) by lessening the requirement of chemical admixtures like superplasticizer which led to the fall of drying shrinkage [4].

Xuejiao Zhu *et al* proved that Calcium Carbonate Precipitating Biomass Powder has the capability of suppressing the corrosion and closing the cracks automatically in structures which are in contact with water [5]. Y.S. Zhang *et al* disclosed that the Microbially induced $CaCO_3$ precipitation can work as a medicine for concrete cracks, and it is environmental friendly with less maintenance [6]. Joaquin Abellan Garcia *et al* declares that by partial replacement of cement and microsilica with micro $CaCO_3$ and waste glass respectively increased the compressive strength, rheological properties of concrete and declined the superplasticizer usage which optimized the cost of Ultra High-Performance Concrete (HPC) [7]. Y. El Hafiane *et al* finalized those mechanical properties of the hardened material increased by calcium carbonate which is used partially as an alternative for calcium aluminate cement on addition of a dispersant [8]. Mingli Cao *et al* investigated that Calcium Carbonate Whiskers in mortar has capability of increasing the compressive strength, prohibiting the cracks in further enlargement and increasing the mortar compactness leading to resistance against abrasion [9].

P.Rashidi Rad *et al* said that the concrete can be long lasting with high mechanical strength, workable and sustainable when mixed with admixtures called calcium carbonate powder and micro silica gel which in turn increased the properties of fresh and hardened concrete [10]. Bhaskar Prakash *et al* conclude that waste marble powder as a sustainable replacement to cement hiked the workability and compressive strength by increasing hydration process [11]. Wenhao Song *et al* studied and stated that by replacing the fine aggregate with modified Waste Marble Powder (WMP) mixed with stearic acid the fresh

mortar fluidity increased along with resistance against corrosion and also condensed water absorption of mortar mix [12]. Ahmed Essam *et al* proved that by partial replacement of cement with waste Marble Powder (MP) gives a denser mixture resulting to decrease in workability, emission of carbon dioxide and calcium hydroxide content leading to higher mechanical strength to get Eco- High-performance concrete [13]. Bing Liu *et al* explored that alkali activated binders prepared with waste marble powder augmented the early compressive and flexural strength but reduction in overall strength [14]. Elyas Asadi Shamsabadi *et al* researched-on waste marble powder usage in concrete mix and identified that by using Machine Learning approach the compressive strength of mix can be measured accurately, and hydration of cement takes place at early age [15].

Ismail Sedat Buyuksagis *et al* determined that there is a raise in bending and compressive strength, water absorption, porosity of mortar mix with higher density when the mortar is mixed with marble powder and this additive can also be used in adhesive mortar [16]. K.I. Syed Ahmed Kabeer *et al* found that for saving water and river sand in cement mortar a waste product released from cutting the marble stones was used which increased the mechanical properties, bond and adhesive strength of mortar in construction projects [17]. Manpreet Singh *et al* disclosed that by substituting the cement with Waste Marble Powder (WMP) the durability and strength of the concrete increased and made the mixture denser which in turn fight against permeability and sorptivity [18]. Kirti Vardhan *et al* declared that on 10% substitution of cement with marble powder increased the workability but on more replacement of material caused a delay in hydration of cement and made the microstructure porous [19]. Valeria Corinaldesi *et al* derived that by replacing the sand with Marble Powder (MP) the compressive strength increased at same workability and due to its filler ability, the strength achieved even at early ages [20]. Kursat Esat Alyamac *et al* investigated that the marble industry waste can be used as a filler material in Self Compacting Concrete and monograms were prepared by conducting tests on fresh and hard mixes for getting economic mix design [21].

Muhammad Junaid Munir *et al* studied that Alkali Silica Reaction (ASR) is controlled by using waste Marble Powder (MP) as a substitute for cement in preparation of mortar mix led to the development of compressive strength and suppression of ASR expansion [22]. Kirti Vardhan *et al* finalized that the resistance against chloride ion penetration, sorptivity, water absorption, workability of concrete mix is declined and enhanced the compressive and split tensile strength of concrete mix by partial substitution of waste marble to fine aggregate making the mix denser [23]. L.G.Li *et al* said that the marble dust can be used as a substitute to cement paste which increased the durability, dimensional stability, mortar impermeability, carbonation resistance, water resistance and reduced shrinkage strain and shrinkage rate [24]. Omar M. Omar *et al* presented that there is an improvement in compressive strength, tensile strength and flexural strength of concrete when fine aggregate is partially substituted with Lime stone Waste and Marble Powder [25]. Abhishek Kumar *et al* have examined that Stone dust can be used as a partial substitution to fine aggregate and concrete is prepared by adding fixed percentage of steel fibres which enhanced the compressive strength and durability up to certain percentage of stone dust substitution [26]. Tao Fu *et al* proved that the use of stone powder in manufactured sand concrete first enhanced the slump, compressive and split tensile strength of concrete and the strengths reduced later [27]. Ashu Singh *et al* determined that the stone powder and ceramic waste materials which are used as sand improved the strength of concrete and reduced the cost of concrete by reducing the usage of aggregates [28]. Mohanad Yaseen Abdulwahid *et al* in his study replaced the coarse aggregate of pervious concrete with stone powder which enhanced the strength, and the rate of strength gain improved along with mechanical properties of concrete with the use of Sand Stone and Marlstone [29]. Er. Farooq Ahmad Parray *et al* explored that the workability of concrete reduced due to

substitution of river sand with fine sized clastic sediment Stone Powder (SP) but there is an improvement in compressive strength, split tensile strength and flexural strength of concrete [30]. Lalit Kumar Gupta *et al* proved that the waste Granite Powder can be used as an alternative to sand in mortar which improved the compressive strength, bond strength, adhesive strength and mortar shrinkage; hence this mortar can be used for plastering and masonry work [31]. Kishan Lal Jain *et al* researched on an area of usage of glass powder as replacement of cement and granite waste as fine aggregate which suppressed the water absorption, permeability and increased durability, resistance against acid attack and sulphate attack [32]. T. Balasubramaniam *et al* concluded that on partial substitution of fine aggregate with both bottom ash and granite powder, the negative effect of using only bottom ash on strength characteristics, porosity, interlocking of particles and fighting against entry of acid or saline water into concrete mix can be reduced [33]. Abhishek Jain *et al* determined that the compressive strength, chloride resistance, carbonation resistance, corrosion resistance was increased, and shrinkage deformation was decreased due to 50% replacement of sand with granite powder waste to form environmentally friendly blended self-compacted concrete compared to fly ash [34]. The calcium carbonate is used in various construction sectors. The available literature is also diversified. The literature available on study of the strength of concrete having calcium carbonate is meagre. Many researchers used silica sand, glass fibres, micro silica gel etc., in addition to calcium carbonate in the concrete. Effect of incorporating only calcium carbonate in normal concrete is not studied previously. In addition, present research by the authors considered the calcium carbonate in powder form as well as in sand form. The objective of the research is to study the strength aspects of concrete having calcium carbonate. The following aspects are considered to achieve the objective of the study.

- Determination of compressive strength, split tensile strength and flexural strength of various concrete mixes having calcium carbonate powder at various percentages ranging from 0 to 50% (0, 10, 20, 30, 40 and 50 percentage of cement).
- Determination of compressive strength, split tensile strength and flexural strength of various concrete mixes having calcium carbonate in coarser (sand) form at various percentages ranging from 0 to 100% (0, 25, 50, 75 and 100 percentage of natural sand).
- Prediction of strength of concrete having calcium carbonate by developing mathematical models.

2. Materials

Ordinary Portland Cement of 53 grade confirming to IS 12269:2013. Natural river sand of Zone III as per IS 383:2016 and having specific gravity of 2.7. Stone aggregate of size 20mm and 10mm confirming to IS 383:2016. Calcium Carbonate Powder (Fig.1a) (limestone in powder form mainly consists of calcite) having specific gravity of 2.7 and Calcium Carbonate Sand (Fig.1b) (lime stone in coarser form mainly consists of calcite) of Zone III as per IS 383:2016 having specific gravity of 2.7.

(a) (b)

Fig. 1. (a) Calcium carbonate powder and (b) calcium carbonate sand

3. Experimental Program

The concrete mixes with calcium carbonate powder are designated as CP and with calcium carbonate sand as CS. Mix without CP and CS i.e control mix are designated as CP0 and CS0 respectively. The concrete mixes having 10%, 20%, 30%, 40% and 50% replacement of cement with calcium carbonate powder are given designation as CP10, CP20, CP30, CP40 and CP50 respectively. Similarly for the mixes where natural river sand replaced at 25%, 50%, 75% and 100% with calcium carbonate sand given signs as CS25, CS50, CS75 and CS100 respectively. The designation of different concrete mixes casted and corresponding mix proportions is shown in Table 1 and 2. The mix proportion is designed as per IS 10262:2019 and corrected according to the requirements by studying trail mixes.

Table 1. Mix proportion of calcium carbonate powder (CP) concrete mixes

Designation	Cement	CP	Fine Aggregate	Coarse Aggregate (20mm)	Coarse Aggregate (10mm)	Water
CP0	1	0	1.53	1.83	1.22	0.42
CP10	0.9	0.089	1.53	1.83	1.22	0.42
CP20	0.8	0.177	1.53	1.83	1.22	0.42
CP30	0.7	0.266	1.53	1.83	1.22	0.42
CP40	0.6	0.354	1.53	1.83	1.22	0.42
CP50	0.5	0.443	1.53	1.83	1.22	0.42

Table 2. Mix proportion of calcium carbonate sand (CS) concrete mixes

Designation	Cement	Fine Aggregate	CS	Coarse Aggregate (20mm)	Coarse Aggregate (10mm)	Water
CS0	1	1.53	0	1.83	1.22	0.42
CS25	1	1.148	0.383	1.83	1.22	0.42
CS50	1	0.765	0.765	1.83	1.22	0.42
CS75	1	0.383	1.148	1.83	1.22	0.42
CS100	1	0	1.53	1.83	1.22	0.42

Concrete mixes were prepared as per the proportion and casted 100mm cube specimens, 100mm x 200mm cylinder specimens and 100mm x 100mm x 500mm beam specimens. The specimens were water immersed and cured till the test day. Strength tests were performed by using a universal testing machine. Compressive test was performed at 7 days and 28 days of curing age. Split tension test and flexure test were performed at 28 days of curing age.

4. Results and Discussion

In this research, the calcium carbonate in powder form was used as partial replacement material to cement. Also, the calcium carbonate in sand form was used as partial replacement material to natural river sand.

4.1 Calcium Carbonate in Powder Form

The compressive strength, split tensile strength and flexural strength values of CP designated concrete are shown in Fig.2. Here fcp is the compressive strength of concrete having calcium carbonate in powder form. fco is the value of compressive strength of concrete in which no calcium carbonate is present i.e compressive strength of control mix. ftp is the split tensile strength of concrete having calcium carbonate in powder form. fto is the value of split tensile strength of concrete in which no calcium carbonate is present i.e split tensile strength of control mix. frp is the flexural strength of concrete having calcium carbonate in powder form. fro is the value of flexural strength of concrete in which no calcium carbonate is present i.e flexural strength of control mix. The ratios of (fcp, ftp, frp) strength of concrete having calcium carbonate powder and corresponding strength of concrete not having calcium carbonate powder (fco, fto, fro) are shown in Table 3.

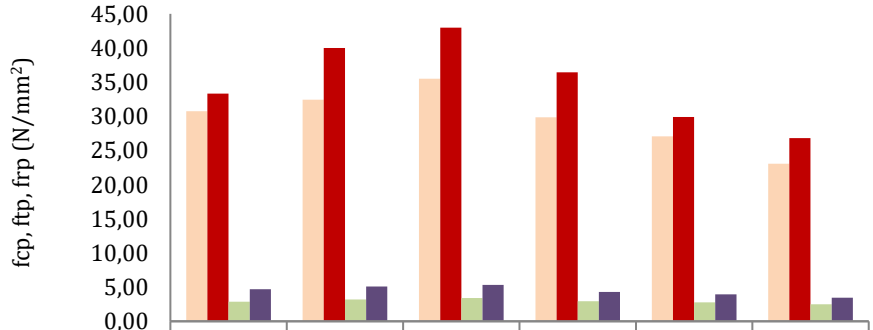

	CP0	CP10	CP20	CP30	CP40	CP50
fcp(7 Days)	30,75	32,43	35,50	29,86	27,06	23,05
fcp(28 Days)	33,33	40,01	42,98	36,45	29,90	26,80
ftp(28 Days)	2,87	3,20	3,40	2,93	2,76	2,49
frp(28 Days)	4,70	5,10	5,33	4,30	3,95	3,44

Fig. 2. Compressive, tensile and flexure strengths of concrete having calcium carbonate powder

Table 3. Ratios of strengths of concrete having CP and corresponding control mix

CP (%)	fcp/fco		ftp/fto	frp/fro
	7 Days	28 Days	28 Days	28 Days
0	1.00	1.00	1.00	1.00
10	1.05	1.20	1.11	1.09
20	1.15	1.29	1.18	1.13
30	0.97	1.09	1.02	0.91
40	0.88	0.90	0.96	0.84
50	0.75	0.80	0.87	0.73

4.1.1 Compressive Strength

After analyzing the test results, as percentage of calcium carbonate powder increases up to 20% the compressive strength of concrete increases. Beyond 20% and up to 50% replacement of cement with calcium carbonate, the compressive strength decreases. The maximum percentage increase in compressive strength at 28 days is 29% which is for CP20 Mix. At 30% replacement level, the compressive strength at 28 days of CP30 mix is almost equal to the CP0 Mix i.e., the mix without calcium carbonate. Therefore, a thirty percent of cement can be replaced with calcium carbonate powder without affecting strength adversely. The same trend is observed for 7 days compressive strength. At 50% replacement level, the decrease in compressive strength at 28 days is 20% than that of control mix (CP0).

4.1.2 Split Tensile Strength

Up to 20% increase in calcium carbonate powder the split tensile strength of concrete increases. Beyond 20% and up to 50% replacement of cement with calcium carbonate, the split tensile strength decreases. The maximum percentage increase in split tensile strength at 28 days is 18% which is for CP20 Mix. At 30% replacement level, the split tensile strength at 28 days of CP30 mix is almost equal to the CP0 Mix i.e., the mix without calcium carbonate. Therefore, a thirty percent of cement can be replaced with calcium carbonate powder without affecting split tensile strength adversely. At 50% replacement level, the decrease in split tensile strength at 28 days is 13% than that of control mix (CP0).

4.1.3 Flexural Strength

As percentage of calcium carbonate powder increases up to 20% the flexural strength of concrete increases. Beyond 20% and up to 50% replacement of cement with calcium carbonate, the flexural strength decreases. The maximum percentage increase in flexural strength at 28 days is 13% which is for CP20 Mix. At 30% replacement level, the flexural strength at 28 days of CP30 mix is equal to or slightly less than the CP0 Mix i.e., the mix without calcium carbonate. Therefore, a thirty percent of cement can be replaced with calcium carbonate powder without affecting strength much adversely. At 50% replacement level, the decrease in compressive strength at 28 days is 27% than that of control mix (CP0).

4.2 Calcium Carbonate in Sand Form

The compressive strength, split tensile strength and flexural strength values of CS designated concrete are shown in Fig.3. Here fcs is the compressive strength of concrete having calcium carbonate in sand form. fco is the value of compressive strength of concrete

in which no calcium carbonate is present i.e compressive strength of control mix. fts is the split tensile strength of concrete having calcium carbonate in sand form. fto is the value of split tensile strength of concrete in which no calcium carbonate is present i.e split tensile strength of control mix. frs is the flexural strength of concrete having calcium carbonate in sand form. fro is the value of flexural strength of concrete in which no calcium carbonate is present i.e flexural strength of control mix. The ratios of (fcs,fts,frs) strength of concrete having calcium carbonate sand and corresponding strength of concrete not having calcium carbonate sand (fco,fto,fro) are shown in Table 4.

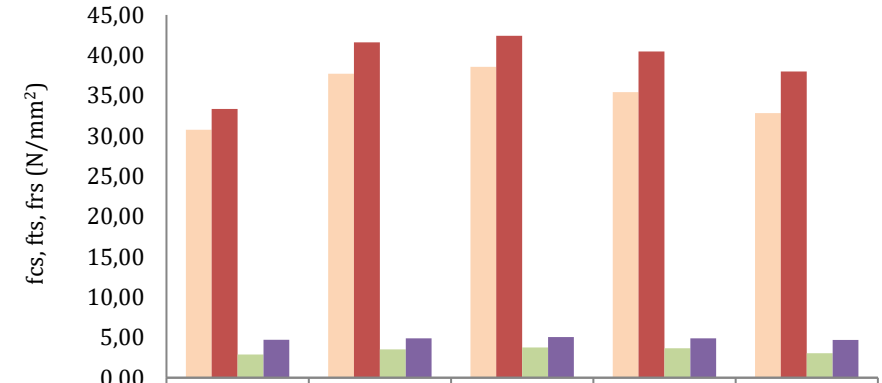

	CS0	CS25	CS50	CS75	CS100
fcs(7 Days)	30,75	37,70	38,56	35,42	32,82
fcs(28 Days)	33,33	41,59	42,41	40,46	37,98
fts(28 Days)	2,87	3,52	3,75	3,65	3,04
frs(28 Days)	4,70	4,88	5,04	4,88	4,69

Fig. 3. Compressive, tensile and flexure strengths of concrete having calcium carbonate sand

Table 4. Ratios of strengths of concrete having cs and corresponding control mix

CS (%)	fcs/fco		fts/fto	frs/fro
	7 Days	28 Days	28 Days	28 Days
0	1.00	1.00	1.00	1.00
25	1.23	1.25	1.23	1.04
50	1.25	1.27	1.31	1.07
75	1.15	1.21	1.27	1.04
100	1.07	1.14	1.06	1.00

4.2.1 Compressive Strength

Addition of calcium carbonate in sand form enhances the compressive strength of all mixes compared to the control mix (CS0). The maximum percentage increase in compressive strength at 28 days is 27% which is for CS50 Mix. Even at 100% replacement level (i.e for CS100), the increase in compressive strength is 14%. Also at 7 days, the compressive

strength of all mixes having calcium carbonate as sand is greater than that of control mix (CS0). With this analysis, natural sand can be partially or even fully can be replaced with calcium carbonate sand without any adverse effect on strength of concrete.

4.2.2 Split Tensile Strength

Addition of calcium carbonate in sand form enhances the split tensile strength of all mixes compared to the control mix (CS0). The maximum percentage increase in split tensile strength at 28 days is 31% which is for CS50 Mix. Therefore, the natural sand can be replaced at 50% level with the calcium carbonate sand with an advantageous gain in split tensile strength.

4.2.3 Flexural Strength

By addition of calcium carbonate in sand form, the flexural strength of all mixes is equal to or slightly greater than that of control mix (CS0). The maximum percentage increase in flexural strength at 28 days is 7% which is for CS50 Mix. From the above analysis it can be understood that the addition of calcium carbonate to the concrete as sand, does not affect the flexural strength of concrete adversely.

4.3 Microstructure Using SEM Images

SEM images of concrete having calcium carbonate as in powder form at various percentage levels are presented in Fig.4. For CP0, CP10, CP20 and CP30 distinct reaction products such as CSH gel, $Ca(OH)_2$ flakes, Ettringite can be seen. For CP40 and CP50 the spread of precipitated calcium carbonate can be visualized along with porous reaction products. For CP20 mix, i.e 20% cement is replaced by calcium carbonate powder, the spread of dense CSH gel can be observed. This can support the experimental test result of maximum strength obtained with CP20 mix.

SEM images of concrete having calcium carbonate as in sand form at various replacement levels (i.e CS25, CS50, CS75 and CS100) are presented in Fig.5. Sand particles are identified on the SEM image and encircled with red colour. The interfacial transition zone is marked with white colour. The alphabets on SEM images i.e CS stands for calcium carbonate sand particle and NS stands for natural sand particle. Natural sand particle can be identified by its glossy finish whereas calcium carbonate sand particle can be identified by its dull finish. Reaction products such as CSH gel can be observed along the periphery of the sand particles. The joint between sand particle and reaction products is called as interfacial transition zone (ITZ).

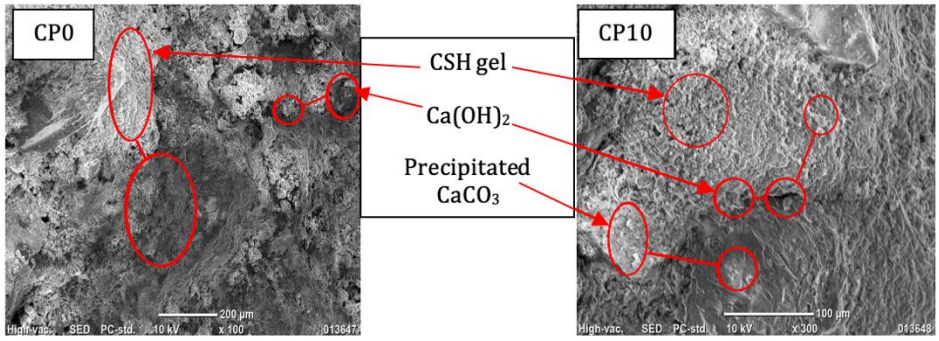

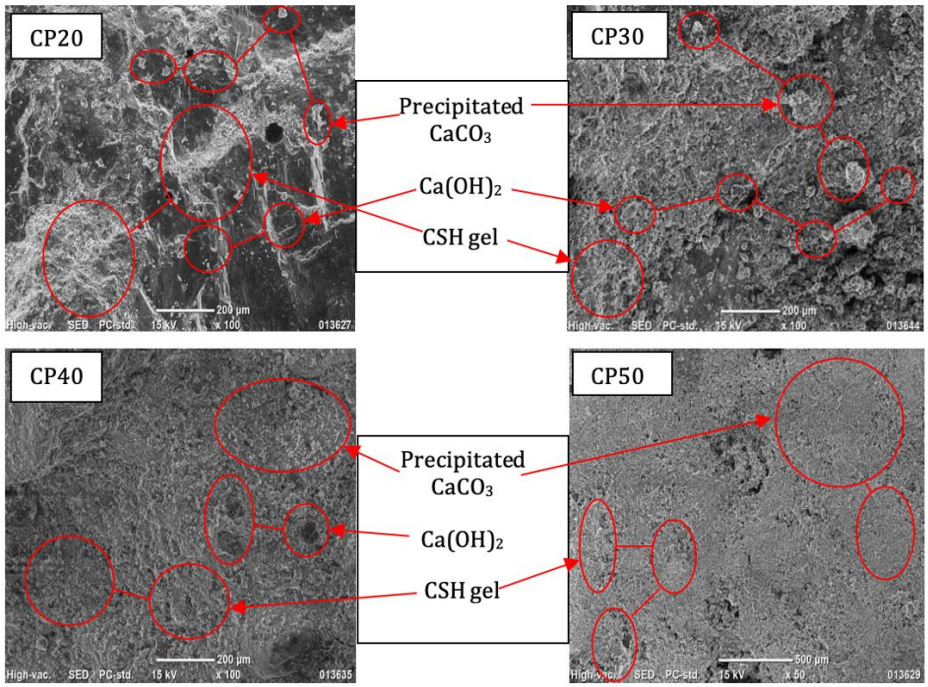

Fig. 4. SEM images of concrete having calcium carbonate as in powder form

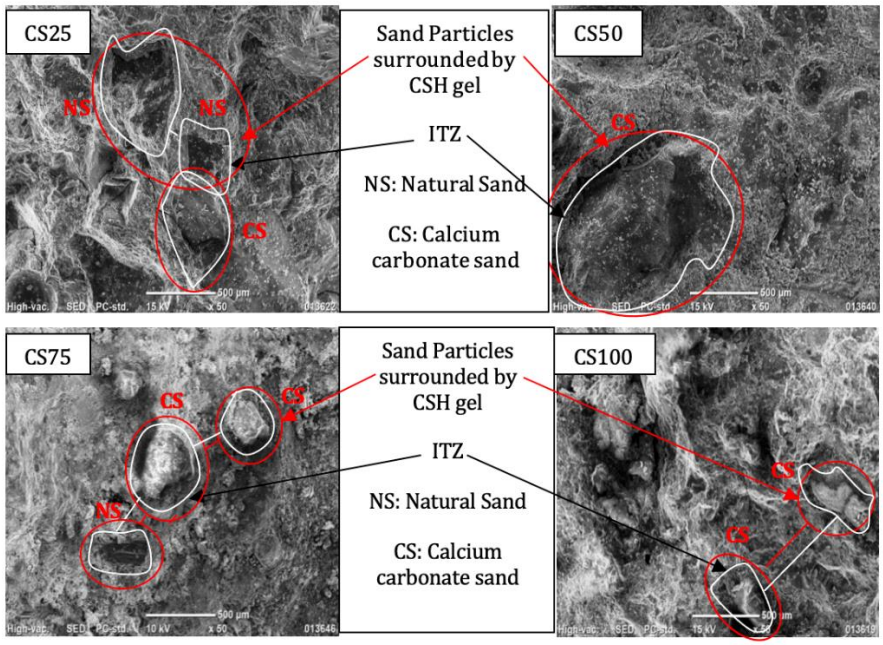

Fig. 5. SEM images of concrete having calcium carbonate as in Sand form

The ITZ region of CS particle can be seen as bright and in white colour which indicates the reaction products of CS particle. The CS particle is reactive and participates in the cement reaction with water producing CSH gel which strengthens the ITZ. This could be the reason for increase in strength of CS25, CS50, CS75 and CS100 mixtures compared with that of CS0 mixture.

4.4 Prediction of Strength

Plots are drawn (Fig.6 and Fig.7) with percentage of calcium carbonate on x-axis and strength ratios (fcp/fco, ftp/fto, frp/fro, fcs/fco, fts/fto, frs/fro) on y-axis. Second order polynomial equations are developed to predict the strength of concrete having calcium carbonate using the above-mentioned plots.

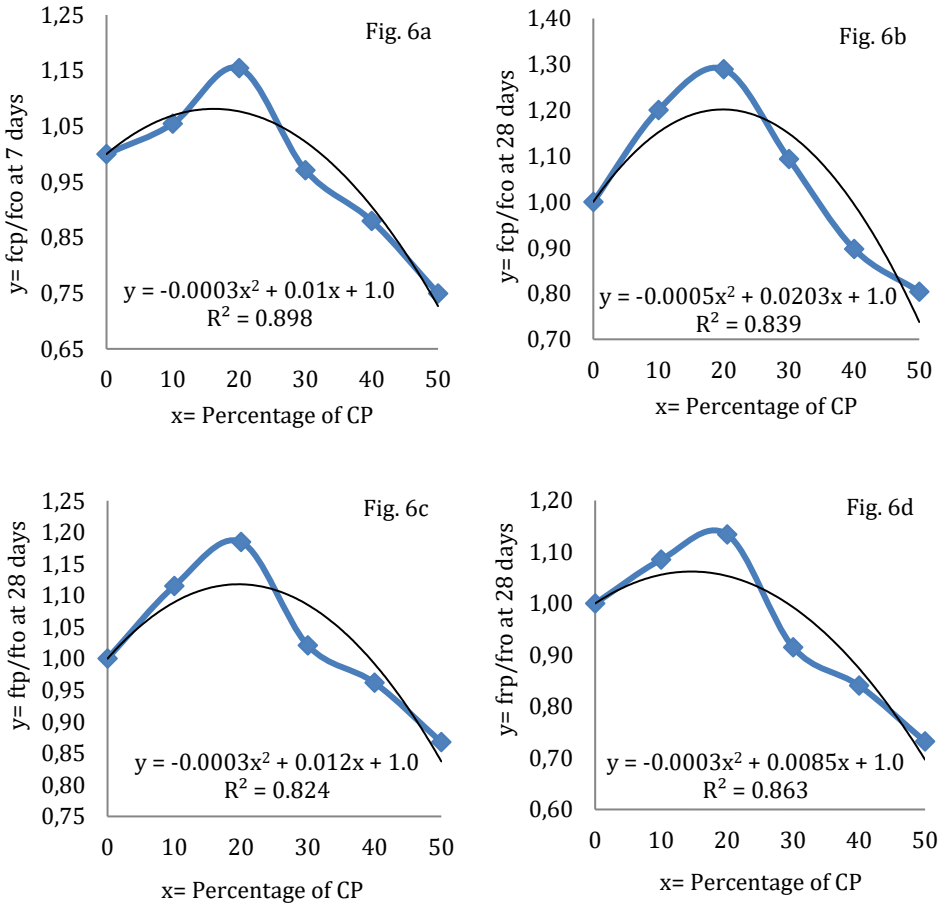

Fig. 6. Plots between percentage of calcium carbonate powder and corresponding strength ratios

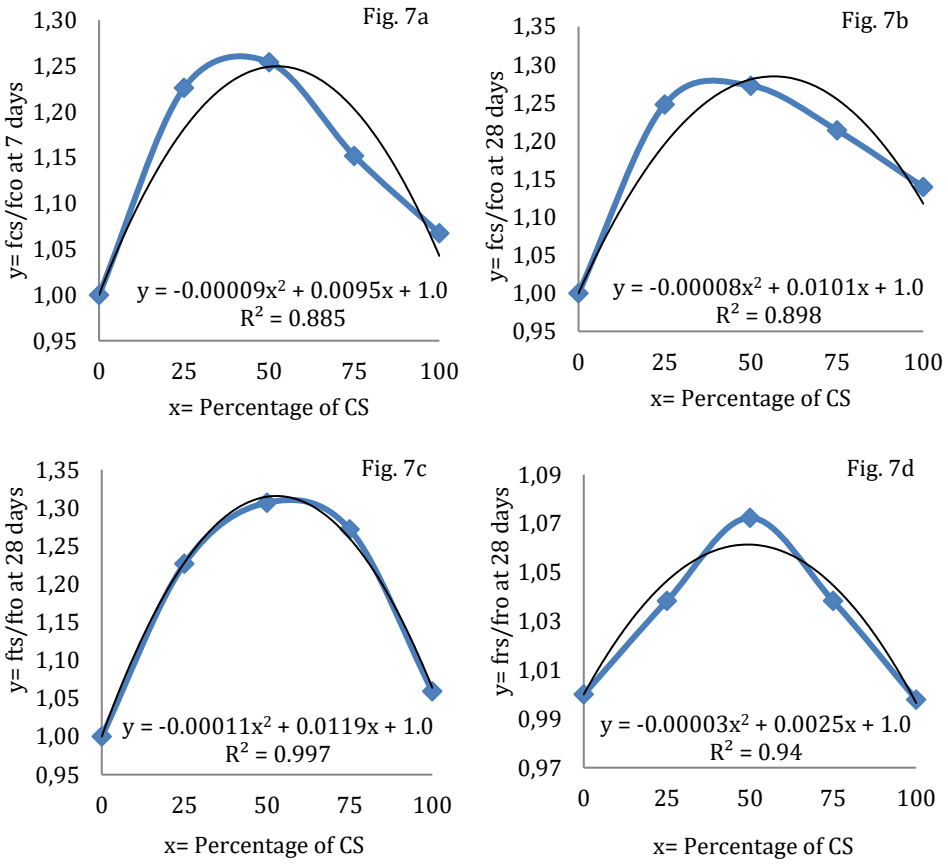

Fig. 7. Plots between percentage of calcium carbonate sand and corresponding strength ratios

Strength values of concrete having calcium carbonate are calculated using the developed expressions and shown in Table 5 and 6. The percentage error in calculating the strength is also shown in Table 5 and 6.

Table 5. Predicted strengths of concrete having calcium carbonate powder and percentage error

CP (%)	Predicted fcp (N/mm²)				Predicted ftp (N/mm²)		Predicted frp (N/mm²)	
	7 Days	Error %	28 Days	Error %	28 Days	Error %	28 Days	Error %
0	30.75	0.00	33.33	0.00	2.87	0.00	4.70	0.00
10	32.90	0.47	38.43	-1.58	3.13	-0.07	4.96	-0.14
20	33.21	-2.29	40.20	-2.78	3.21	-0.19	4.94	-0.40
30	31.67	1.81	38.63	2.18	3.13	0.20	4.63	0.33
40	28.29	1.23	33.73	3.83	2.87	0.11	4.04	0.09
50	23.06	0.01	25.50	-1.30	2.44	-0.05	3.17	-0.27

Table 6. Predicted strengths of concrete having calcium carbonate sand and percentage error

CS (%)	Predicted fcs (N/mm^2)				Predicted fts (N/mm^2)		Predicted frs (N/mm^2)	
	7 Days	Error %	28 Days	Error %	28 Days	Error %	28 Days	Error %
0	30.75	0.00	33.33	0.00	2.87	0.00	4.70	0.00
25	36.32	-1.38	40.08	-1.51	3.53	0.01	4.91	0.03
50	38.44	-0.12	43.50	1.09	3.79	0.04	4.94	-0.11
75	37.09	1.67	43.58	3.12	3.66	0.01	4.79	-0.09
100	32.29	-0.53	40.33	2.35	3.13	0.09	4.47	-0.23

It can be observed that the percentage error is within ±4%, hence the developed expressions can be used to predict the strength of concrete having calcium carbonate after knowing the replacement percentage and the corresponding strength of concrete without having calcium carbonate.

4.4.1 Comparison with Available Literature

The 28th day compressive strengths predicted using the proposed expression are compared with the published experimental results by various researchers (Table 7). The percentage error varies in between 2.55 and 23.50. The variation in percentage error is attributed to the factors such as difference in grade of concrete, mix proportions and interaction of additional materials in the concrete other than those used by the authors.

Table 7. Comparison of predicted 28th day compressive strength with the available literature

Referred Literature	Ali Heidari *et al* [3]			P.Rashidi Rad *et al* [10]		
Percentage of Calcium Carbonate Powder (x)	Experimental 28 Days Compressive Strength	Predicted Compressive Strength using y =-0.0005x^2 + 0.0203x + 1.0	% Error	Experimental 28 Days Compressive Strength	Predicted Compressive Strength using y = -0.0005x^2 + 0.0203x + 1.0	% Error
0.00	130.00	130.00	0.00	39	39.00	0.00
10.00	135.00	149.89	11.03	--	--	--
12.50	--	--	--	42	45.85	9.17
20.00	140.00	156.78	11.99	--	--	--
25.00	--	--	--	45	46.61	3.57
30.00	139.00	150.67	8.40	--	--	--
31.25	--	--	--	52	44.70	-14.04
37.50	--	--	--	43	41.27	-4.03
40.00	135.00	131.56	-2.55	--	--	--
43.75	--	--	--	40	36.31	-9.22
50.00	120.00	99.45	-17.13	39	29.84	-23.50

5. Conclusions

In this research, the calcium carbonate mineral in the form of lime stone is used as alternative material for cement and natural river sand. Following are the conclusions drawn from the study.

- A twenty per cent of the total cement content in the conventional concrete mix can be replaced with calcium carbonate powder advantageously. The maximum increase in compressive strength is 29% than that of concrete mixture without having calcium carbonate powder. Further, a thirty per cent of total cement can be replaced with calcium carbonate powder without affecting strength adversely.
- The maximum percentage increase in split tensile strength at 28 days is 18% which is at 20% replacement level. At 30% replacement level, the split tensile strength at 28 days of CP30 mix is almost equal to that of CP0 Mix i.e., the mix without calcium carbonate.
- The maximum percentage increase in flexural strength at 28 days is 13% which is at 20% replacement level. At 30% replacement level, the flexural strength at 28 days of CP30 mix is equal to or slightly less than that of the CP0 Mix i.e., the mix without calcium carbonate.
- Natural sand can be replaced partially or fully with calcium carbonate sand which enhances the compressive strength of concrete compared with that of the control mix concrete (CS0). The maximum percentage increase in compressive strength at 28 days is 27% which is at 50% replacement level.
- Addition of calcium carbonate in sand form enhances the split tensile strength of concrete compared to that of the control mix (CS0). The maximum percentage increase in split tensile strength at 28 days is 31% which is for CS50 Mix.
- By addition of calcium carbonate in sand form, the flexural strength of all mixes is equal to or slightly greater than that of control mix (CS0). The maximum percentage increase in flexural strength at 28 days is 7% which is for CS50 Mix.
- Expressions are developed to predict the strength of concrete having calcium carbonate.
- In summary, a thirty percent cement can be replaced with calcium carbonate powder without adverse effect on strength as calcium carbonate can be used in concrete as powder form. Similarly, the natural river sand can be partially/fully replaced with calcium carbonate sand (coarser). By using calcium carbonate in concrete, the quantities of cement and sand can be conserved.

Acknowledgement

The authors acknowledge the support and encouragement of the Management & Staff of R.V.R & J.C. College of Engineering, Chowdavaram, Guntur, AP.

References

[1] Xia J, Ke G, Leng F, Wang J, Ren L, Liang H. Effect of industrial-grade heavy calcium carbonate powder on properties of white high-strength concrete. Constr Build Mater. 2023;378:131211. https://doi.org/10.1016/j.conbuildmat.2023.131211

[2] Kumar D, Ravi RR. Development of strain-hardening cementitious composites utilizing slag and calcium carbonate powder. Constr Build Mater. 2021;273:122028. https://doi.org/10.1016/j.conbuildmat.2020.122028

[3] Heidari A, Shourabi FN. Mechanical properties of ultra-high performance concrete based on reactive powder concrete: Effect of sand-to-cement ratio, adding glass fiber and calcium carbonate. Constr Build Mater. 2023;368:130108. https://doi.org/10.1016/j.conbuildmat.2022.130108

[4] Abellan-Garcia J, Khan MI, Abbas YMA, Martínez-Liron V, Carvajal-Munoz JS. The drying shrinkage response of recycled-waste-glass-powder-and calcium-carbonate-based ultrahigh-performance concrete. Constr Build Mater. 2023;379:131163. https://doi.org/10.1016/j.conbuildmat.2023.131163
[5] Zhu X, Sakarika M, Ganigue R, Van Tittelboom K, Ersan YC, Boon N, et al. Production of calcium carbonate-precipitating biomass powder as self-healing additive in concrete and performance evaluation in mortar. Cem Concr Compos. 2023;138:104952. https://doi.org/10.1016/j.cemconcomp.2023.104952
[6] Zhang YS, Liu Y, Sun XD, Zeng W, Xing HP, Lin JZ, et al. Application of microbially induced calcium carbonate precipitation (MICP) technique in concrete crack repair: A review. Constr Build Mater. 2024;411:134313. https://doi.org/10.1016/j.conbuildmat.2023.134313
[7] Abellan-Garcia J, Khan MI, Abbas YMA, Castro-Cabeza A, Carrillo J. Multi-criterion optimization of Low-Cost, Self-compacted and Eco-Friendly Micro-calcium-carbonate- and Waste-glass-flour-based Ultrahigh-Performance concrete. Constr Build Mater. 2023;371:130793. https://doi.org/10.1016/j.conbuildmat.2023.130793
[8] El Hafiane Y, Smith A, Abouliatim Y, Benhammou A, Abourriche A, Nibou L, et al. Substitution of aluminous cement by calcium carbonates in presence of carboxylic acid. Constr Build Mater. 2017;154:711-720. https://doi.org/10.1016/j.conbuildmat.2017.08.023
[9] Cao M, Liu Z, Xie C. Effectiveness of calcium carbonate whiskers in mortar for improving the abrasion resistance. Constr Build Mater. 2021;295:123583. https://doi.org/10.1016/j.conbuildmat.2021.123583
[10] Rashidi Rad P, Haj Sd TA, Darvishvand HR, Ebrahimi M. Technical and Economical Approaches in Application of Micro Silica Gel and Calcium Carbonate Powder in Self-compacting Concrete. Int J Eng Trans A: Basics. 2022;35(04):760-773. https://doi.org/10.5829/IJE.2022.35.04A.16
[11] Prakash B, Saravanan TJ, Kabeer KISA, Bisht K. Exploring the potential of waste marble powder as a sustainable substitute to cement in cement-based composites: A review. Constr Build Mater. 2023;401:132887. https://doi.org/10.1016/j.conbuildmat.2023.132887
[12] Song W, Wang Q, Qu L, Li X, Xu S. Study of water absorption and corrosion resistance of the mortar with waste marble powder. Constr Build Mater. 2022;345:128235. https://doi.org/10.1016/j.conbuildmat.2022.128235
[13] Essam A, Mostafa SA, Khan M, Tahwia AM. Modified particle packing approach for optimizing waste marble powder as a cement substitute in high-performance concrete. Constr Build Mater. 2023;409:133845. https://doi.org/10.1016/j.conbuildmat.2023.133845
[14] Liu B, Geng S, Ye J, Liu X, Lin W, Wu S, et al. A preliminary study on waste marble powder-based alkali-activated binders. Constr Build Mater. 2023;378:131094. https://doi.org/10.1016/j.conbuildmat.2023.131094
[15] Shamsabadi EA, Roshan N, Hadigheh SA, Nehdi ML, Khodabakhshian A, Ghalehnovi M. Machine learning-based compressive strength modelling of concrete incorporating waste marble powder. Constr Build Mater. 2022;324:126592. https://doi.org/10.1016/j.conbuildmat.2022.126592
[16] Buyuksagis IS, Uygunoglu T, Tatar E. Investigation on the usage of waste marble powder in cement-based adhesive mortar. Constr Build Mater. 2017;154:734-742. https://doi.org/10.1016/j.conbuildmat.2017.08.014
[17] Kabeer KISA, Kumar V. Utilization of marble powder as fine aggregate in mortar mixes. Constr Build Mater. 2018;165:321-332. https://doi.org/10.1016/j.conbuildmat.2018.01.061
[18] Singh M, Srivastava A, Bhunia D. Long term strength and durability parameters of hardened concrete on partially replacing cement by dried waste marble powder slurry.

Constr Build Mater. 2019;198:553-569. https://doi.org/10.1016/j.conbuildmat.2018.12.005
[19] Vardhan K, Goyal S, Siddique R, Singh M. Mechanical properties and microstructural analysis of cement mortar incorporating marble powder as partial replacement of cement. Constr Build Mater. 2015;96:615-621. https://doi.org/10.1016/j.conbuildmat.2015.08.071
[20] Corinaldesi V, Moriconi G, Naik TR. Characterization of marble powder for its use in mortar and concrete. Constr Build Mater. 2010;24:113-117. https://doi.org/10.1016/j.conbuildmat.2009.08.013
[21] Alyamac KE, Ince R. A preliminary concrete mix design for SCC with marble powders. Constr Build Mater. 2009;23:1201-1210. https://doi.org/10.1016/j.conbuildmat.2008.08.012
[22] Munir MJ, Kazmi SMS, Wu Y-F. Efficiency of waste marble powder in controlling alkali-silica reaction of concrete: A sustainable approach. Constr Build Mater. 2017;154:590-599. https://doi.org/10.1016/j.conbuildmat.2017.08.002
[23] Vardhan K, Siddique R, Goyal S. Strength, permeation and micro-structural characteristics of concrete incorporating waste marble. Constr Build Mater. 2019;203:45-55. https://doi.org/10.1016/j.conbuildmat.2019.01.079
[24] Li LG, Huang ZH, Tan YP, Kwan AKH, Liu F. Use of marble dust as paste replacement for recycling waste and improving durability and dimensional stability of mortar. Constr Build Mater. 2018;166:423-432. https://doi.org/10.1016/j.conbuildmat.2018.01.154
[25] Omar MO, Abd Elhameed GD, Sherif MA, Mohamadien HA. Influence of limestone waste as partial replacement material for sand and marble powder in concrete properties. HBRC J. 2012;8:193-203. https://doi.org/10.1016/j.hbrcj.2012.10.005
[26] Kumar A, Singh V. Study the effect of stone dust & Steel fibre on strength properties of concrete. Int J Civ Eng Technol (IJCIET). 2019;10(03):2211-2219.
[27] Fu T, Liang JL, Lan YF, Xiao YP, Wei JH. Effect of Stone Powder Content on Mechanical Properties of Manufactured Sand Concrete. Iran J Sci Technol Trans Civ Eng. 2022;46:4255-4264. https://doi.org/10.1007/s40996-022-00882-1
[28] Singh A, Sachan V. Experimental study on the strength of concrete by partial replacement of ceramic waste and stone powder as fine aggregate. IOSR J Mech Civ Eng (IOSR-JMCE). 2022;19(5):30-32.
[29] Abdulwahid MY. Influences of different stone powders on pervious concrete strength. Struct Concr. 2020;2020:1-7. https://doi.org/10.1002/suco.202000095
[30] Parray FA, Rani H, Kaur M. Exploration of Properties of Concrete by Partial Replacement of Fine Aggregate with Clastic Sediment Stone Powder. Int J Eng Res Technol (IJERT). 2020;9(02). https://doi.org/10.17577/IJERTV9IS020173
[31] Gupta LK, Vyas AK. Impact on mechanical properties of cement sand mortar containing waste granite powder. Constr Build Mater. 2018;191:155-164. https://doi.org/10.1016/j.conbuildmat.2018.09.203
[32] Lal KJ, Gaurav S, Gupta LK. Durability performance of waste granite and glass powder added concrete. Constr Build Mater. 2020;252:119075. https://doi.org/10.1016/j.conbuildmat.2020.119075
[33] Balasubramaniam T, Stephen SJ. Influence of industrial wastes on the mechanical and durability characteristics of high strength concrete. Constr Build Mater. 2022;317:126202. https://doi.org/10.1016/j.conbuildmat.2021.126202
[34] Abhishek J, Choudhary S, Gupta R, Chaudhary S, Gautam L. Effect of granite industry waste addition on durability properties of fly ash blended self-compacting concrete. Constr Build Mater. 2022;340:127727. https://doi.org/10.1016/j.conbuildmat.2022.127727

Research on Engineering Structures & Materials
www.jresm.org
MIM Research Group

Review Article

Particleboard from biomass wastes: A review of production techniques, properties, and future trends

Peter P. Ikubanni[*1,a], Adekunle A. Adeleke[2,b], Timothy A. Adekanye[1,c], Oluwasegun J. Aladegboye[3,d], Olayinka O. Agboola[4,e], Bamidele T. Ogunsemi[1,f]

[1]*Department of Mechanical Engineering, Landmark University, Omu-Aran, Nigeria*
[2]*Department of Mechanical Engineering, Nile University of Nigeria, Abuja, Nigeria*
[3]*Department of Civil Engineering, Landmark University, Omu-Aran, Nigeria*
[4]*Department of Mechanical Engineering, Federal University of Technology, Akure, Nigeria*

Article Info

Article history:

Received 02 May 2024
Accepted 29 Aug 2024

Keywords:

Particleboard;
Biomass;
Mechanical properties;
Sustainable environment;
Construction materials

Abstract

The availability of various biomass wastes and the stringent rules against deforestation have led to the increased utilization of waste biomass in particleboard development. These biomass wastes become environmental pollutants when not properly managed. Hence, their utilization in developing particleboards helps attain a sustainable environment, one of the United Nations Sustainable Development Goals. This study reviews some of the production techniques of particleboards from biomass wastes such as rice husk, sawdust, corn cob, sugarcane bagasse, oat hulls, coconut fibers, Areca nuts, rye straw, tomato stalk, hazelnuts, and castor husk. The properties (physical, mechanical, chemical, and thermal) and microstructures of the developed particleboards using a scanning electron microscope were critically reviewed. The density values were used to classify the particleboards into low-density, medium-density, and high-density particleboards. The particleboard's durability, storability, and dimensional stability are determined using the water absorption and thickness swelling values. The modulus of elasticity and modulus of rupture help to determine the quality and applicability of the particleboards following the appropriate standards. Lower thermal conductivity indicates better insulation properties. The challenges and prospects of particleboard production and utilization were stated. The utilization of waste biomass for particleboard production is sustainable to prevent environmental pollution and deforestation.

1. Introduction

Wood is a type of biomass that contains constituents like cellulose, hemicellulose, and lignin content. The various percentages of these constituents determine how structurally stable the wood will be during its utilization as a renewable energy source. The utilization of wood in the world grows on a timely basis to attain developmental needs such as furniture, building construction, and household appliances [1]. The huge impact of deforestation on the abundance of wood particles (wood shavings, sawdust) on the environment cannot be overemphasized. The availability of different sawmills in Nigeria has led to an increase in the wood particles in various sawmills across the nation. The sawdust and wood shavings are most times burnt in the open air; hence, causing environmental pollution and also adding to the depletion of the ozone layer [2]. The wood wastes are sometimes used in cooking, poultry farms, and so on.

*Corresponding author: ikubanni.peter@lmu.edu.ng
[a] orcid.org/0000-0002-2710-1130; [b] orcid.org/0000-0002-0301-7698; [c] orcid.org/0000-0002-7581-8785; [d] orcid.org/0000-0002-3266-9924, [e]orcid.org/0000-0002-8979-7778, [f] orcid.org/0000-0003-0850-2414
DOI: http://dx.doi.org/10.17515/resm2024.265ma0502rv

The all-round development of people can be linked to the correct utilization of available resources. For several decades, one of the important resources used by mankind was wood-based products. However, due to seeking better environmental conditions, coupled with the recycling of environmental wastes and global warming challenges, the utilization of non-wood resources has grown [3]. Non-wood resources including sunflower stalks, pepper stalks, rice straw, wheat straw, rice husks, sugarcane bagasse, cotton stalks, rapeseed, and many more, have found utilization in particleboard production [3 - 7]. For many years, forest products have been used in the production of particleboard. However, due to the reduction in the availability of these raw materials (forest products) with more demand for particleboard products, agricultural-based materials have been the new research focus in this regard because of their built-in insulation, low-cost production, and characteristic sound suppression [8, 9]. Some of the agro-waste (biomass) products that have been used are displayed in Fig. 1.

Fig. 1. Agro-waste utilized for particleboard manufacture (a) Areca nut fiber, (b) Coconut fiber, (c) Rye straw, (d) Sugarcane bagasse, (e) Rice husk, (f) Sawdust, (g) Corncob, (h) Oat hulls

Particleboard is the composition of wood elements with adhesive bonding and is produced under heat and pressure [10, 11]. In the production of particleboard, softwoods, and lower-density hardwoods are commonly utilized. The utilization of lower-density wood helps in the production of lower-density particleboards with the maintenance of their strength and stiffness [8]. Several adhesives have been used in the production of particleboards. For instance, citric acid and tapioca starch were used as adhesives in the particleboard produced using oil palm fronds, oil palm trunks, and empty fruit bunch [12]. The adhesives were utilized at different mixing ratios and the results of the particleboards bonded with the citric acid and tapioca starch showed better properties when compared with particleboards bonded by urea-formaldehyde. It is noteworthy that urea-formaldehyde (UF) is the most commonly utilized adhesive in producing particleboards [6, 9, 11]. Some of the various biomasses with the different adhesives that have been utilized in the

production of particleboards are displayed in Table 1. A typical example of a particleboard is shown in Fig. 2.

Table 1. Particleboard produced from different biomass and adhesives

S/N	Biomass used	Parts utilized for particleboard production	Adhesive used	Ref.
1.	Areca nuts	Fiber	Tapioca adhesive	[13]
2.	Coconuts	Pit and Fiber	UF and green binders (BST00 and BST20)	[14]
3.	Hazelnuts with shell	Shell	Melamine-UF or polyurethane	[15]
4.	Rye	Straw	Polymeric diphenylmethane diisocyanate (pMDI)	[16]
5.	Sugarcane	Bagasse	UF	[11]
6.	Tomatoes	Stalk	UF	[9]
7.	Cashew nuts with shell	Shell	Isocyanate resin, UF resin	[17]
8.	Rice, Wood	Husk, Sawdust	UF and gelatinous starch	[6]
9.	Dates	Palm branches	Vermiculite	[18]

Lee et al. [19] presented the worldwide production quantity of particleboard to have reached 96.01 million m^3 in the year 2020 with a disparity of about 4 million m^3 from the preceding year 2019. Among the world-renowned leading producers of particleboards are China, Italy, Germany, Austria, France, and Poland, as displayed in Fig. 3. Of all the continents in the world, Asia was found to be the largest producer of particleboards while Europe, the Americas, Africa, and Oceania were not left behind. It is also important to state that with 54.43%, the European countries are the largest importers of particleboards.

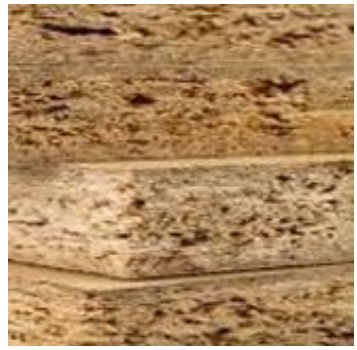

Fig. 2. Typical particleboard

The other percentages are Asia (26.51%), America (15.89%), Africa (2.89%), and Oceania (0.34%) [19]. Concerning the exportation of particleboard, European countries such as Austria, Russia, Germany, France, Belarus, Belgium, and Romania, are among the highest exporters, while Thailand is recognized as the key exporter of particleboard in the year 2020 [19]. The Food and Agriculture Organization (FAO) data for the exportation quantities of particleboards in the year 2022 for some selected countries is presented in Fig. 4.

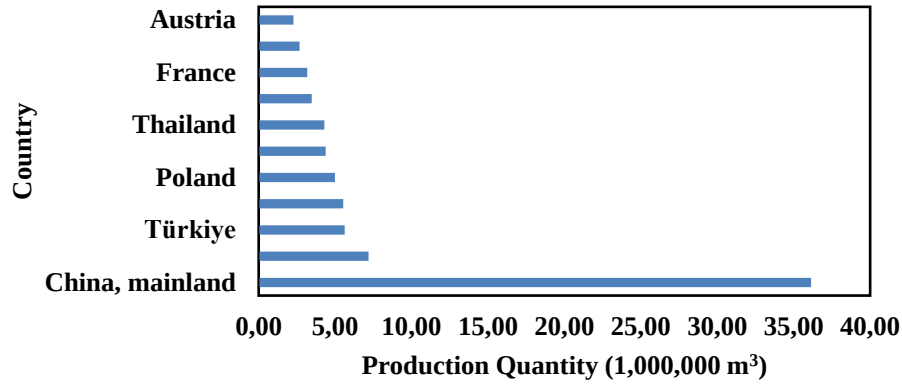

Fig. 3. Particleboard production quantity (m^3) per country in 2022 [20]

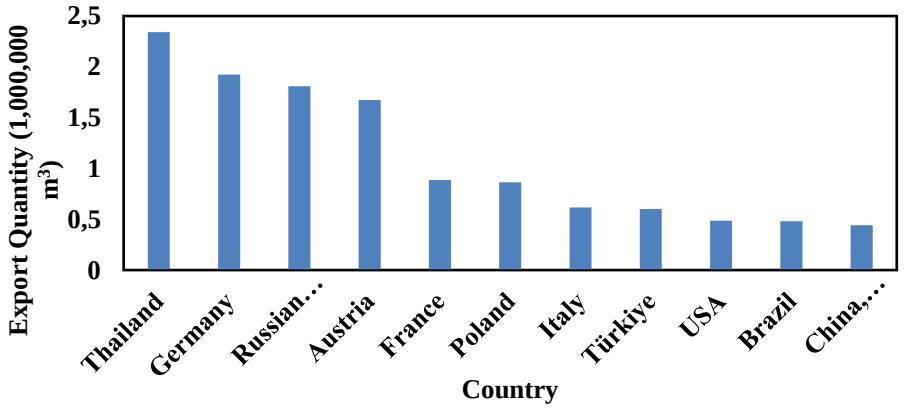

Fig. 4. Particleboard exportation quantity (in m^3) per country in 2022 [20]

The wood-based panel industry has suffered a setback in terms of the supply of wood due to the new legislative rules on wood usage in some countries, growing environmental challenges, and its global demand for wood raw materials. Hence, to replace wood in the production of particleboard due to the challenges earlier mentioned, an alternative search of naturally abundant feedstocks from renewable agricultural residues and wood by-products is a great measure of lowering the adverse environmental effects. The agricultural residues, considered biomass resources, have been greatly exploited and converted into different useful products such as energy utilization as densified biomass [21 – 25], biogas generation [26 – 28], particleboard production [6, 29], and many more. These utilizations have been reported to reduce environmental concerns and enhance environmental pollution control. In this current study, the utilization of agricultural residues for the production of particleboards was the focus and was not for other utilizations earlier mentioned. Hence, the application of agricultural residues in particleboard production should be made economically practicable and profitable. For the profitability of the particleboards made from agricultural residues, the manufactured boards are expected to meet or exceed the required technical standard of usage [19].

Within 5 – 6 years, it has been projected that there will be around a 6.1% increase in the global particleboard market. This is because of the increase in building activities around

the world as well as the target market growth worldwide. Interestingly, due to increased urbanization, many urban settlers have the desire to beautify the interior of their building which could cause a boost in the global particleboard market [19]. The cost of particleboard compared to other wood products including plywood is a driver of the global particleboard market. More so, its extraordinary capability to absorb sound has made it find applications in recording studios and music halls. The aesthetic features of particleboard can be enhanced through coating, painting, or the application of beautiful wallpaper; leading to more demand for particleboards in modern offices and other similar sectors. More innovative and acceptable particleboards from natural fibers are gradually being introduced to the global particleboard market.

The utilization of biomass waste for the production of particleboard is to address and tackle environmental challenges and also to support responsible biomass waste resource management for sustainable ventures. The utilization of biomass wastes in the development of particleboard could result in several advantages. These include the cost-effectiveness of the biomass residue serving as an alternative to traditional wood chips. Production costs of the particleboards are reduced due to the utilization of these alternatives. The usage of biomass waste for particleboard production could also promote a circular economy where resources are efficiently re-used for the production of other sustainable products. Hence, the transformation of waste materials into viable particleboards helps to achieve sustainable urban development. With sustainable urban actualization through the use of waste materials for particleboard development, deforestation is reduced, the natural ecosystem is preserved, affordable housing is achievable, and environmental harm is minimized [19, 30 – 35].

This study focused on the review of the production techniques, properties, and future trends of particleboard from different biomass wastes. The physical, mechanical, chemical, and thermal properties of the particleboards were discussed as well and the internal microstructural arrangement was highlighted. The future trends in particleboard developments for continuous utilization were also discussed.

2. Method of Particleboard Production

Different production methods of particleboards have been employed in different studies. The most commonly used method of producing particleboard is the compression molding. The schematic diagram in Fig. 5 displays the overview of the step-by-step method involved in producing particleboards from various biomass or agro-waste materials using the compression molding technique.

In Fig. 5, the raw materials biomass residues such as sawdust, rice husk, and corncob) are locally sourced. They are sundried for some days to remove moisture inherent in them and sorted to remove unwanted foreign materials. They are screened to the required particle size of between 1 mm and 4 mm. The raw materials are later mixed at the desired mixing ratios or proportions while resins are added as adhesives. The mixtures are properly mixed either manually or mechanically to ensure a homogeneous distribution of the raw materials. Forming and pre-pressing are done by hand-filling the mixture in a created mold and manually pressing the mixture. The final compression can be either done using the hydraulic hot-pressing technique or the compression molding technique. The compressed mixture is allowed to stay for about 4 h before removing from the machine. The panel products are then ready for stacking and further usage [36 – 38].

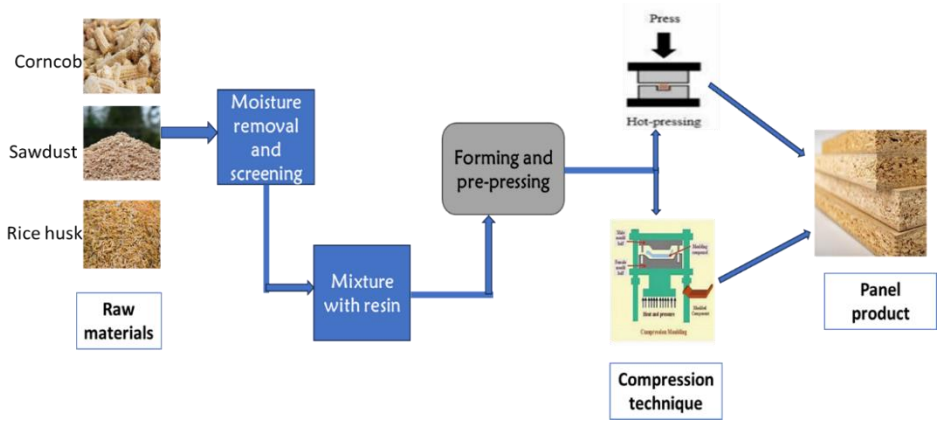

Fig. 5. Schematic presentation of particleboard production

Another method of producing particleboard is the extrusion method. In this method, the raw material particles are blended with bonding agents and other additives. A uniform thickness of the blended mixture is used to form the mat. The mat is then forced through a heated die to form the board. The board is passed through a heating zone to complete the resin curing. After, the board is allowed to cool before cutting to the desired size [39, 40]. In the steam-injection molding method, saturated steam is injected into the mat of particles during pressing. This is done through small holes or channels in the press platens. Through conduction, the steam heats the particles and binder. Through heat and pressure, the binder is cured. After, the steam is vented from the press via a vacuum system. The desired density and thickness are achieved through the continued pressure application to the mat. The board is allowed to cool before removal from the press for finishing operations [41 – 43].

Another technique of producing particleboard is the emulsion-based method. This method is commonly used for the development of particleboards with improved moisture resistance and durability. A water-based polymer (polyvinyl acetate (PVA) or acrylic emulsion) is the typical emulsion-based binding agent that is normally utilized. A stable and durable bond is created when this emulsion-based binding agent is mixed with the biomass particles. Typically, in this method, biomass particles are mixed with polymer emulsion binding and other additives. The blended mixture is used to form a uniform-thickness mat. Then, the mat is pressed to ensure the removal of excess water and achieve the desired density. The board is allowed to cure in a controlled environment (heated room or under ultraviolet light). The board is later cut to size and finishing treatments are applied on it [44, 45].

Studies have revealed the impact of resin contents on the mechanical properties of particleboards. The higher the resin contents in a particleboard, the better the mechanical properties. For instance, the effects of resin content on the mechanical properties of particleboard produced using *Neolamarckia* and *Leucaena* particles were evaluated by Abd Rahman et al. [46]. The resin used for the particleboard production was melamine urea formaldehyde at three different resin contents of 10, 12, and 14%. It was reported that mechanical properties such as internal bonding (IB), modulus of elasticity (MOE), and modulus of rupture (MOR) increased with an increase in resin content. The increase in MOE and MOR due to resin content increase could be linked to the increase in surface contact between the particle and the resin; thereby resulting in improved bonding properties. Ashori and Nourbakhsh [47] also reported an increase in mechanical properties of the particleboards produced using UF resin contents of 9, 10, and 11%. This

implies that the resin-wood polymerization produced better properties at 11% resin addition. Also, using phenol-formaldehyde in the production of particleboards from oil palm fronds, the MOR, MOE, and IB values increased with increased resin contents from 9 to 11% [48]. Table 2 highlights some of the methods used by different studies. The methods of compression molding and hot-pressing machines were common in the study. However, various pressing pressure, temperature, and time were employed in the studies.

Table 2. Particleboard production method

S/N	Method of production	Ref.
1.	Three-layer composition board was produced using a hot-press machine at 160°C temperature for 5 min and a pressure of 3 N/mm^2.	[36]
2.	Urea formaldehyde was synthesized and added to a constant weight of the sawdust, and thoroughly mixed using an electric mixer. The mixture was molded using a compression molding machine at a pressure of 10 tonnes and a temperature of 150°C for 15 minutes.	[37]
3.	Binderless particleboards were produced at different pressing temperatures (180, 200, and 220°C), pressing times (15, 30, and 45 min), and pressure between 4 and 6 MPa. The particles were hand-formed into a particle mat using a forming box. After, the particleboards were hot-pressed and water-cooled.	[49]
4.	The pre-treated feedstock (wood chip) was mixed with adhesive and placed in a mat-forming box. Pre-pressing at 0.78 N/mm^2 of the particleboards was done using a manual pressing machine. Then, a hydraulic press was used to press the box for 8 minutes at 1.23 × 10^6 N/mm^2 to produce the board.	][50]
5.	Leather shavings and waste papers were manually mixed at varied blend ratios using polyester resin as a binder and 2% methyl ethyl peroxide as a catalyst to produce a single-layer particleboard. A modified compression molding method was utilized by employing a hydraulic press of 50 kN load. Curing of the particleboard was done at room temperature for 4 h.	[51]
6.	12% UF resin content was used to adhere the particles together and were manually formed into a mat in a frame. Hot-pressing process using open hydraulic laboratory press using pressure of 2.5 N/mm^2, temperature of 180°C, and pressing time 20 s/mm.	[34]
7.	Corncob-sawdust particleboard was made from homogeneously mixed particles with adhesives. It was placed in a mold and compressed using a hydraulic compressing machine for 10 min. It was then oven-dried for 1 h at 80°C and allowed to cool. The panel was then removed from the mold and re-placed in the oven for 3 h at 130°C. The panel was allowed to cool before stacking.	[38]

3. Physical and Mechanical Properties of Particleboards

3.1 Density of Particleboard

The density of particleboards is determined to properly classify the boards into low-density, medium-density, and high-density boards [6]. It is usually evaluated using the ratio of mass (kg) and volume (m^3). It is a measure of how compact the particleboard is considering its particle. The particleboard's density depends on the wood's density, the adhesive used, and the applied pressure during compaction [52]. The density of the particleboards produced using plantain pseudostem, cocoa stem and pod, and Ceiba sawdust with either cassava or urea-formaldehyde (UF) were obtained to be classified as medium-density particleboards according to ANSI A208.1 standard [53]. Particleboards are classified as medium-density when the density is between 400 and 800 kg/m^3. The range of density values of particleboards with cassava starch adhesive was between 497 and 598 kg/m^3 while that of UF adhesive was from 421 to 557 kg/m^3 [52]. It can be deduced that there is more compaction of the particles of the raw materials of the board when cassava starch is used. The higher density when cassava starch was used could be due to the cassava adhesive properties which create strong bonds between the biomass particles leading to a denser structure. In addition, during the curing of the particleboard, cassava starch displays self-expansion properties. During the curing, the adhesive expands to effectively fill the gaps between the wood particles. Hence, the particleboard density is enhanced with this self-expansion property. It was, however, revealed that the high bulk density of cocoa pod over other raw materials like cocoa stem, plantain pseudostem, and Ceiba sawdust gave its particleboard superior density over other particleboards produced.

Table 3 presents the density of particleboards made from different materials and adhesives. The density values for the particleboards produced in the study of Iswanto et al. [36] ranged from 0.53 to 0.61 g/cm^3 which was less than 0.75 g/cm^3 target value. The density of the boards attained the JIS standard (0.40 – 0.90 g/cm^3) [54]. 8% isocyanate resin was used as the binder. Srichan and Raongjant [55] produced particleboards from bamboo shoot sheaths. The adhesive used in the production was diphenylmethane diisocyanate (MDI) resins. The obtained density values at 0.6 mm and 0.5 mm particle sizes varied from 554 to 836 kg/m^3, and 475 to 889 kg/m^3, respectively. In cement-bonded particleboard produced by Odeyemi et al. [56], all the boards produced met the minimum requirement as stipulated by ISO 8335, IS14276, and JIS A 5908 standards [54, 57, 58], which are respectively 1000, 1250, and 800 kg/m^3. The value of density of the particleboards ranged from 1281.10 to 1766.40 kg/m^3. The particleboards produced are classified as high-density particleboards. The presence of cement in the composition caused the density of the particleboards to be high, unlike those particleboards produced with cement as seen in some studies [6]. It is paramount to optimize the process involved to achieve an optimum density that would be useful in achieving the desired utilization.

3.2 Water absorption and Thickness swelling

A water absorption test is important to determine the hydrophilic or hydrophobic tendency of the particleboard. It is usually done after 2 and 24 h of water immersion. Water absorption has a direct link with thickness swelling. Thickness swelling occurs when the particleboard has absorbed water. The durability of the particleboard during storage can be assessed through a water absorption test.

In a study by Hartono et al. [78], elephant dung and wood shavings in the ratios of 100/0, 90/10, 80/20, 70/30, 60/40, and 50/50 (%w/w) were the materials used in the production of the particleboards after pre-treatment. The adhesive used was 7% isocyanate resin. The range of values for water absorption of the particleboard produced ranged from 58.32% (50/50 ratio) to 67.74% (100/0 ratio). These values indicate the

lowest and highest water absorption, respectively. Water absorption in the particleboard produced reduced when wood shavings increased in the mix proportion. The low density of the particles of elephant dung led to higher water absorption. Particleboard's water absorption is affected by the size of the particles of the raw materials. Smaller particle sizes could lead to a larger surface area/contact area. However, the thickness swelling (TS) value significantly decreased with the increase of the wood shavings proportion. The value of TS ranged from 20.69% (100/0 ratio) to 36.5% (50/50 ratio). The reduction of TS value with increased wood shaving over elephant dung was linked to higher specific gravity possessed by the wood shaving than the elephant dung.

According to Odeyemi et al. [56], the dimensional stability of particleboards is mostly revealed by water absorption (WA) and thickness swelling. With the IS 14276 standard [58], the maximum WA recommended value should be 13% and 25% at 2 h and 24 h of immersion, respectively. From the study of Odeyemi et al. [56], WA was increased due to an increase in sawdust and cement percentage, whereas WA reduced with an increased percentage of periwinkle shell. Just like the WA, TS increased with a percentage increase in cement and sawdust while a reduction of TS was observed when periwinkle shell increased. The recommended standard TS as stipulated by ANSI A 208.1 standard is 8% [53]. This value was fulfilled by all samples produced.

In Ghana, Mitchual et al. [52] used four biomass residues (plantain pseudostem, cocoa stem and pod, and ceiba sawdust) for particleboard development using two different adhesives (UF and cassava starch). The particle size of the materials was within 0.5 to 1.5 mm. The WA properties were evaluated at 2 and 24 h of water immersion using ASTM D1037-06a standard. At 2 h immersion, the plantain pseudostem gave the least WA of 9.86% (with cassava starch adhesive) and 7.77% (with UF adhesives), while the highest WA was from cocoa pods with 22.41% (with cassava starch adhesive) and 14.98% (with UF adhesive). It was reported that the higher WA property of cocoa pod and ceiba particleboards could be associated with the high content of silica and decreased lignin present in the materials. When UF and cassava starch were used as adhesives in the production of particleboards, lower and better WA was achieved [52]. This could be linked to the hydrophilic nature of cassava starch which tends to absorb water [79].

Particleboards produced using cassava starch adhesive gave significantly higher but worse TS values than the particleboards produced using UF. For instance, at 2 h immersion, TS for Ceiba particleboard with cassava starch adhesive was 5.83% while that of UF adhesive was 3.91%. At 24 h immersion, TS for Ceiba particleboard with cassava starch adhesive was 17.27% while that of UF adhesive was 13.22%. The TS values were reduced from 2 to 24 h immersion for all the biomass residues and adhesives used. This worse phenomenon was attributed to the higher hydrogen polymer chains in the cassava resulting in higher water absorption with higher thickness swelling [80]. Ultimately, the commercialization of particleboard requires the appropriate WA standard. It was documented that WA of 35% at 24 h water immersion was recommended by ANSI A208.1 standard, while 8% and 15% of WA at 2 and 24 h immersion respectively is recommended by EN 312 (2005) standard [81]. Some of the previous results obtained for WA and TS of some particleboards produced are displayed in Table 4.

It can be deduced that WA and TS at 2 h immersion when castor husk and pine wood were used in particleboard development ranged from 77.7 to 43.6% and 20 to 10%, respectively while 117.4 to 76.8% and 33.4 to 19.2% were obtained for WA and TS at 24 h immersion, respectively [59]. When bamboo and *Pinus oocarpa* were utilized in particleboard production at 2 and 24 h immersion, WA was respectively 82 – 65% and 92 – 74% while TS was respectively 18.2 – 14.2% and 22 – 16% [64]. From Table 4, it can be deduced that WA and TS are greatly influenced by the type and proportion of the raw materials, the

adhesive type, and the production processes used. The time-dependent behaviour of the particleboards helps to provide insights into the behaviour of the particleboard under different moisture conditions. Higher WA indicates lower durability and resistance to moisture. Also, higher TS indicates lower dimensional stability and potential delamination [38, 82]. However, the stability of particleboards could be improved against water through the utilization of water-repellent substances [83, 84].

Table 4. Water absorption and thickness swelling of various particleboards used

Materials for particleboards	WA (%)		TS (%)		Ref.
	2h	24h	2h	24h	
Castor husk and Pinewood	77.6 – 43.6	117.4 – 76.8	20 – 10	33.4 – 19.2	[59]
Mauritia flexuosa and *Eucalyptus spp.* Wood	47.3– 89.6	65.47 – 109.97	10.53 – 19.53	19.74 – 24.13	[60]
Cotton wastes and Eucalyptus wood	120.7 – 138.9	138.84 – 151.97	11.34 – 23.93	14.17 – 27.45	[61]
Sugarcane bagasse and Eucalyptus wood	16.1 – 45.7	30.5 – 73.6	7.9 – 15.8	13.5 – 16.2	[62]
Coffee parchment and Eucalyptus wood	120.54 – 84.72	138.08 – 109.44	11.78 – 6.38	12.95 – 9.83	[63]
Bamboo and *Pinus oocarpa*	82.0 – 65.0	92.0 – 74.0	18.2 – 14.2	22.0 – 16.0	[64]
Jupati and Eucalyptus wood	NA	53.79 – 95.77	NA	16.89 – 24.92	[65]
Sugarcane bagasse and Eucalyptus wood	5.8	20.0	5.6	20.1	[66]
Oat Hulls and Eucalyptus grandis	5.2 – 6.8	NA	4.2 – 5.5	NA	[67]
Hevea brasiliensis and *Pinus oocarpa*	125.52 – 73.24	139.58 – 99.74	22.82- 10.14	28.48 – 12.75	[68]
European Black Pinewood and Licorice root	48.25 – 39.07	59.26 – 54.90	17.12 – 13.25	20.19 – 17.65	[69]
Soybean pods and Eucalyptus wood	116.08 – 151.48	121.5 – 164.03	10.38 – 42.78	15.04 – 53.18	[70]
Sugarcane bagasse in fiber lengths (5 mm and 8 mm)	NA	53.2 – 10.4	NA	42.0 – 14.7	[71]
Angelim, Cambara, Canelao, Cedar and Itauba	19.89 – 40.49	27.86 – 42.64	3.57 – 10.11	7.48 – 11.59	[72]
Peanut Hull and *Pinus oocarpa*	65.05 – 76.71	71.97 – 88.24	15.63 – 26.98	22.46 – 31.12	[73]

Pterocarpus violaceus wood and *Pinus oocarpa* wood	73.4 – 70.1	85.0 – 81.2	17.5 – 19.9	24.4 – 21.4	[74]
Miriti petioles and *Pinus oocarpa* wood	92.01 – 162.63	104.03 – 201.2	15.45 – 38.26	21.3 – 43.89	[75]
Maize cob and *Pinus oocarpa*	54 – 40	70 – 90	25.8 – 18.6	37.5 – 30.0	[76]
Pinus oocarpa wood, Castor hull, and Sugarcane Bagasse	35.1 – 61.0	46.1 – 89.6	7.1 – 12.6	7.3 – 18.4	[77]

*NA- Not Available

3.3 Modulus of elasticity (MOE) and Modulus of rupture (MOR)

The MOE and MOR are some of the mechanical properties required to be determined to ascertain the quality and usefulness of particleboards produced. The maximum load-carrying capacity of a material during bending which is proportional to the maximum moment carried by the material is MOR [52]. MOE and MOR of some particleboards developed are shown in Table 5. The MOE and MOR of particleboards made from *Broussonetia papyrifera* wood were studied. The outcome of the particleboard produced revealed a high-performance board. The optimum MOE and MOR values were 4.9 GPa and 27 MPa at a board density of 1.1 g/cm^3. The varying manufacturing parameters used to obtain the optimum responses were temperature (180, 200, and 220^{o}C), time (15, 30, and 45 min), pressure (4.0-6.0 and 4.5-6.5 MPa), particle size (coarse and fine), and density (0.8, 1.0, 1.1, and 1.2 g/cm^3). A trend of MOE and MOR increment with density increment was reported [49]. Due to the high compaction ratio which caused the intimacy of the particles bonding together, the higher mechanical strength of the board at higher board density was reported [49]. The increase in the particleboard's strength could be attributed to the increased heat conductivity of the board resulting in the degradation of the cellulose and hemicellulose of the biomass particles.

Srichan and Raongjant [55] investigated the physico-mechanical and thermal behaviours of single-layer particleboard produced using bamboo shoot sheaths. Diphenylmethane Diisocyanate adhesive with 7% resin content was used as a binder. The study reported that the denser the board, the more the MOE and MOR. More so, a smaller particle size (0.5 mm) tends to assist in obtaining better MOE and MOR than the 0.6 mm particle size of the bamboo shoot sheaths. As stipulated by JIS standard, the minimum MOE value of 3000 MPa and MOR value of 18 MPa are recommended. The board produced using bamboo shoot sheath particles at 0.5 mm and 0.6 mm size and using diphenylmethane diisocyanate (MDI) resin as adhesive showed lower MOE and MOR values compared to the JIS standard except for one [55]. The reason for the low MOE and MOR can be attributed to the low density of the bamboo shoot sheath. The values of the MOE for all the samples produced were between 250 and 1700 MPa while MOR values were between 3 and 19 MPa. A sample produced using 0.5 mm particle size gave the highest MOR (19 MPa) at 800 kg/m^3 density. This sample has the only MOR that surpasses the JIS standard (MOR $\geq$ 18MPa). Due to the values of the MOE (250 – 1700 MPa) and MOR (3 – 19 MPa) obtained, the produced particleboards were not recommended for structural works but for non-structural works.

To meaningfully recycle waste products from the leather industry, Kibet et al. [51] produced particleboards from leather shavings and waste papers. The resin and catalyst used in the production of the particleboard were unsaturated polyester (UP) and methyl

ethyl ketone peroxide (MEKP), respectively. Two percent (2%) catalyst (methyl ethyl ketone peroxide) was mixed with the resin by mass. The range of values of the MOR was between 11.44 and 20.11 MPa at 50 wt.% and 100 wt.% waste papers, respectively. Effective adhesion observed in the particleboard was linked to lower moisture of the waste papers which resulted in decreased trap voids in the product. Also, the MOE ranged from 4.15 to 5.65 GPa at 100 wt.% leather ratio and 100 wt.% waste paper ratios, respectively. Proper adhesion and compaction of the waste paper particles and the resin were linked to the high value of MOE at 100 wt.% waste papers whereas low density with high moisture content was reported to be responsible for the low MOE recorded for the 100 wt.% leather particles. With the reported results, it can be deduced that the produced wood-leather panel met with the JIS standard for utilization for various applications including the structural and interior of a building.

In 2020, Mitchual et al. [52] investigated the properties of particleboards produced using biomass of cocoa pod, plantain pseudostem, ceiba, and cocoa stem at particulate levels. However, it was reported that particleboards obtained from plantain pseudostem with UF resin gave the highest MOE (2413 MPa) while the cocoa pod-cassava starch adhesive particleboard gave the least MOE (1031 MPa). A comprehensive display of the results is presented in Fig. 6. Aside from the cocoa pod-made particleboards, all the boards produced were acceptable for general utilization and production of furniture since ANSI A208.1 requirements were met. The particleboard with the high MOE was characterized and linked to a comparatively high aspect ratio of the plantain pseudostem which was higher compared to other materials.

As observed in MOE, the range of MOR values was from 4.95 MPa for cocoa pod and 16.54 MPa for plantain pseudostem (Fig. 7). ANSI A208.1 standard was met for the produced particleboards except for cocoa pod-based particleboards when either cassava starch or UF adhesives were used. The standard stipulated that a minimum of 10 MPa MOR must be attained for interior fitments in a building structure. The utilization of UF as an adhesive gave better MOR compared to when cassava starch was used.

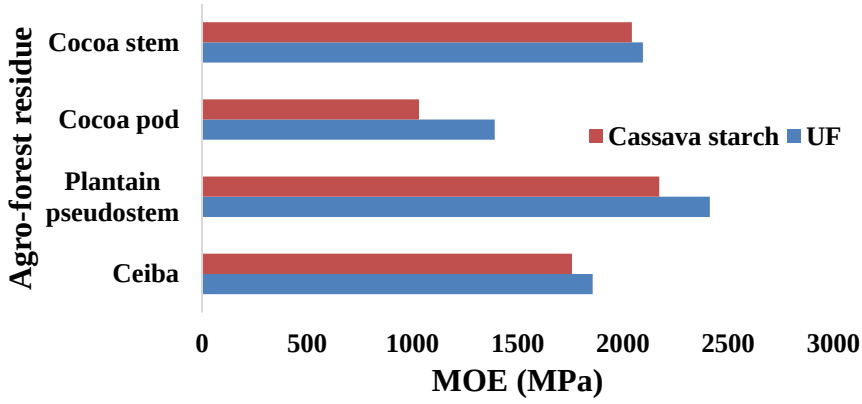

Fig. 6. MOE of different agro-forest residues for particleboard production [52]

Similarly, Hartono et al. [78] characterized the MOE and MOR of various particleboards produced from Elephant dung and wood shavings. From the study, the MOE and MOR values ranged from 1952 to 2573 MPa and 18.6 to 27.4 MPa, respectively. It was revealed that when more wood shaving was added to the mix ratio, higher MOE was obtained. This observation was the same for MOR. The high values of MOE and MOR were attributed to the large dimensions of the wood shavings compared to the elephant dung fibers.

Except for 100 wt.% Elephant dung fiber particleboards, the MOE values of all other fabricated particleboards met with JIS A 5908-2003 standard while all fabricated particleboards met with JIS standard for MOR with 8 MPa required minimum.

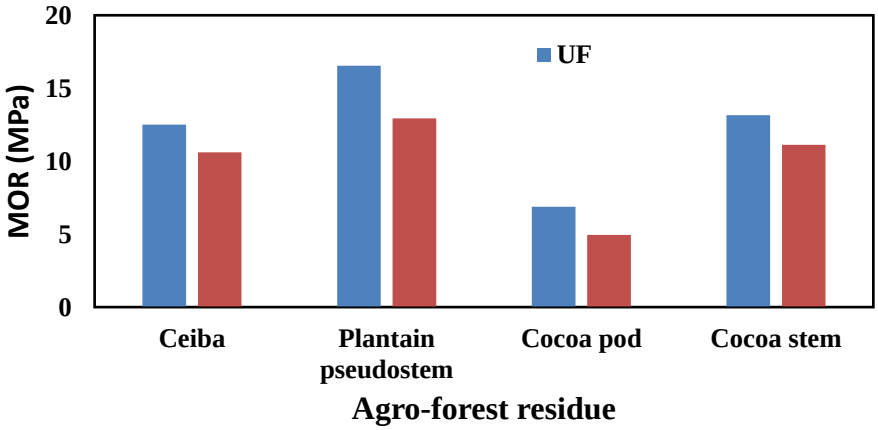

Fig. 7. MOR of different agro-forest residues for particleboard production [52]

Particleboards were produced from walnut wood shavings using UF as adhesive [34]. In the study, the MOE and MOR values were compared with the EN 312 standard under three categories (Type P5, Type P6, and Type P7) [81]. Based on the walnut wood particle substitution range, the produced particleboard with soft particles under standard pressure and at lower resin content satisfied the high requirements of technical standards for construction boards. The type P6 which could be used for heavy-duty load-bearing boards in dry conditions was met. However, the standard P5-type board requirements were satisfied by the remaining boards, which could be useful as load-bearing boards in humid conditions. Other works in this regard are the utilization of Pentung bamboo using sucrose-based for the production of particleboards was investigated [85]. In the investigation, increasing the pressing temperature increased the MOR to some values greater than 13 MPa, which is the JIS A5908 (2003) standard [54]. It was indicated that the raw materials' chemical components influenced the bonding properties of the sucrose-based particleboards. However, improved MOR was observed with samples with ammonium dihydrogen phosphate (ADP) serving as a phosphate catalyst. A similar trend was observed for the MOE values; although, the sucrose-only adhesive-based particleboards fell short of the required 3 GPa MOE values according to the JIS A 5908 (2003) standard.

Table 5. MOE and MOR of various particleboards

Materials for particleboards	MOE (MPa)	MOR (MPa)	Ref.
Castor husk and Pinewood	3111.8 – 2382.8	18.4 – 12.0	[59]
Mauritia flexuosa and *Eucalyptus spp*. Wood	1286.41 - 855.73	10.91 - 6.95	[60]
Cotton wastes and Eucalyptus wood	726.47 - 205.12	8.63 - 3.87	[61]
Sugarcane bagasse and Eucalyptus wood	1707.11 – 2501.97	11.61 – 17.08	[62]
Coffee parchment and Eucalyptus wood	648.62 – 400.73	8.17 – 4.43	[63]
Bamboo and *Pinus oocarpa*	2077.0 – 1636.0	16.7 – 13.9	[64]
Polyol/Pre-polymer and *Pinus spp.*	1479.80 – 2439.60	13.40 - 19.40	[86]
Jupati and Eucalyptus wood	1469.11 – 1084.57	6.66 – 4.75	[65]

Sugarcane bagasse and Eucalyptus wood	2848	22.60	[66]
Oat Hulls and *Eucalyptus grandis*	2349 – 1942	18 – 24	[67]
Hevea brasiliensis and *Pinus oocarpa*	934.75 – 1054.35	5.63 – 9.87	[68]
European Black Pinewood and Licorice root	2142.21– 2582.62 N/mm^2	12.02 – 16.42 N/mm^2	[69]
Soybean pods and Eucalyptus wood	1297.68 – 435.21	7.57 – 2.41	[70]
Sugarcane bagasse in fiber lengths (5 and 8 mm)	2.85 – 1.53	21.20 – 14.9	[71]
Angelim, Cambara, Canelao, Cedar and Itauba	935.62 – 611.90	5.09 – 2.12	[72]
Peanut Hull and *Pinus oocarpa*	1430.91 – 668.35	9.44 – 4.26	[73]
Pterocarpus violaceus wood and *Pinus oocarpa* wood	2653 – 2577	11.6 – 13.3	[74]
Miriti petioles and *Pinus oocarpa* wood	1087.2 – 1273.27	6.45 – 7.36	[75]
Maize cob and *Pinus oocarpa*	1190 – 200	8.0 – 1.0	[76]
Pinus oocarpa wood, Castor hull, and Sugarcane bagasse	2068 – 3111	12.0 – 18.4	[77]

3.4 Internal Bonding Strength, Flexural Strength, Compression Ratio

The internal bonding strength, flexural strength, and compression ratio of particleboards are part of the parameters to be investigated to determine the proper utilization of the products produced. Some various factors affect the IBS values of particleboards. The coating of each particle on the board with the adhesive resin is important for the IBS improvement. For instance, Pedzik et al. [87] increased the walnut wood content with a relatively lower number of particles in the boards, and with UF resin as a binder, better particle coating, as well as higher IBS values, were attained at 50% walnut particles. It was higher with an increased degree of sizing. or. More so, using more resin as an adhesive for the particles was reported to produce improved IBS. The IBS improved with an increased percentage of walnut particles from 0 to 50% and with an increased resin content of between 10 and 12%. The IBS value when 50% of walnut particles were used was around 28% higher than the reference board produced at 1.5 N/mm^2 applied pressure [87]. Modified starch was used as a binder in the production of particleboard from rubberwood with target densities of 0.60, 0.70, and 0.80 g/cm^3. The adhesive used was 15% corn starch-modified with glutardialdehyde. It reported that the IBS increased as the target density increased respectively as 0.62, 0.88, and 1.02 N/mm^2. The analysis revealed that the optimum IBS could be attained at target densities between 0.70 and 0.80 g/cm^3 in which higher panel density could slightly improve the IBS [88].

Another factor that influences the IBS is the board's density. When MDI adhesive was utilized in the production of particleboards using bamboo shoot sheaths, the IBS values were directly proportional to the boards' densities. That is, as the density of the board increased, the IBS value also increased. Unlike the study of Pedzik et al. [34], the effects of the particle size were insignificant on the IBS value. However, the IBS values of the particleboard surpassed the JIS standard of 0.3 MPa which ensured good particleboard development. The high IBS value was linked to the efficient bonding of the particles of the bamboo with the MDI adhesive. The strength of panels increases with increased density; hence, it fulfills the strength requirements for structural materials and building panels [34, 88, 89].

Particleboard was produced using Sumatran elephant dung and wood shavings at different mixed ratios of 100/0, 90/10, 80/20, 70/30, 60/40, and 50/50 (% w/w). The mixed

particle at each ratio was sprayed with 7% isocyanate adhesive. The physical and mechanical properties of the particleboards produced were examined. The IBS values of the particleboards produced in the study of Hartono et al. [78] ranged from 0.16 to 0.34 MPa (100/0 to 50/50 ratio, respectively). The maximum IBS (0.34 MPa) was obtained with the 50/50 ratio of elephant dung fibers and wood shavings while the least IBS (0.16 MPa) was at a 100/0 ratio. These values were reported to have met with the JIS A 5908 (2003) standard [54], which stated that particleboard should have a minimum IBS value of 0.15 MPa. The increase of the wood shavings and decrease of the elephant dung in the ratios was reported to have led to higher internal bond value. The increased density of the particleboards as the wood shavings increased resulted in increased IBS value. Composite boards were developed by Ekpenyong et al. [90] where treated groundnut shell particles (TGP) and untreated groundnut shell particles (UGP) were utilized at 0 to 100% mixture of both raw materials. The binder used was cassava starch at a ratio of 1:3 with the composite mix. The composite mixing ratios of UGP to TGP were 100:0, 75:25, 50:50, 25:75, and 0:100. The least flexural strength value was 1.040 N/mm^2 at 100%UGP:0%TGP and the maximum flexural strength value was 2.255 N/mm^2 at 0%UGP:100%TGP. The study revealed that due to the treatment given to the groundnut shell particles, better and stronger interfacial adhesion was obtained relative to the UGP. Hence, the more the TGP in the composites, the higher the flexural strength. More so, it was reported that the IBS of the TGP was directly proportional to the amount of TGP in the composites. The particleboard produced in the study was suggested to be useful for wall partitioning or ceiling boards.

Particleboard was developed using leather shavings and waste papers at different mix ratios of 100:0, 25:75, 50:50, and 75:25). The resin used was unsaturated polyester while methyl ethyl ketone peroxide was used as a catalyst. The percentage content of resin used was 60, 70, 80, and 90%, which served as the matrix. The mechanical properties of the developed panels were examined. The sample with 100% waste papers gave the highest IBS (13.61 MPa) while the least IBS (5.83 MPa) was obtained at 100% leather waste. As the waste paper content was reduced with increased leather waste content, the IBS value decreased. The waste paper bonded well with the resin compared to the leather waste; leading to improved IBS. Also, at constant particle blend ratios, the IBS decreased from 6.46 MPa (60% resin) to 2.82 MPa (90% resin). It was observed that resin content increase reduced the IBS of particleboards made from leather shavings and waste papers [51]. With further analysis, the IBS reduced as the percentage content of leather shaving increased with reduced waste paper content. Good bonding of the particles of waste papers with the resin used compared to the leather shavings was the reason for the increase in IBS value. The hydrophobic nature of some fibers results in the difficulty of the resin adhesive to chemically react. Hence, it necessitates the hydroxyl group reaction of the resin adhesive [36]. Iswanto et al. [36] investigated the IBS of sandwiched particleboards produced using non-woody biomass of sugar palm fibers, cornstalk, and sugarcane bagasse while bamboo strand was used as reinforcement. The binder used was 8% isocyanate resin. The IBS values ranged between 0.03 and 0.40 N/mm^2. The least IBS value was 0.03 N/mm^2 when sugar palm fibers were used in the core while the maximum IBS value (0.40 N/mm^2) was obtained when sugarcane bagasse was used in the core. The non-absorbent nature of the sugar palm fibers led to the low IBS value. Petung bamboo was used to produce particleboard using sucrose-based adhesive as the binder in the study of Widyorini [85]. The IBS of the particleboards was significantly affected considering the pressing temperature and sucrose-based adhesive. The IBS of the sample produced using only sucrose as the adhesive and pressed at 160^{o}C was the least (0.08 MPa), which indicated that higher pressing temperatures are needed when sucrose only is used as the adhesive. However, the IBS increased from 0.65 to 0.79 MPa when the pressing temperature increased from 180 to 200^{o}C, respectively. Widyorini [85] revealed that many factors could be responsible for bonding mechanisms

which are not limited to adhesive content, utilized raw materials, or pressing time. Table 6 further displays some IBS and compression ratios as obtained from the literature.

Table 6. IBS and FS of various particleboards

Materials for particleboards	IBS (MPa)	CR	Ref.
Castor husk and Pinewood	1.10 – 0.91	1.3 – 2.6	[59]
Mauritia flexuosa and *Eucalyptus spp.* Wood	0.51 – 0.11	1.23 – 1.96	[60]
Cotton wastes and Eucalyptus wood	0.26 – 0.16	1.2 – 1.4	[61]
Sugarcane bagasse and Eucalyptus wood	0.4 – 0.69	1.11 – 6.67	[62]
Coffee parchment and Eucalyptus wood	0.34 – 0.18	1.30 – 1.91	[63]
Bamboo and *Pinus oocarpa*	0.81 – 0.66	1.34 – 2.00	[64]
Jupati and Eucalyptus wood	NA	1.16 – 1.49	[65]
Sugarcane bagasse and Eucalyptus wood	1.18	-	[66]
Oat Hulls and *Eucalyptus grandis*	1.84 – 1.60	1.49 – 3.50	[67]
Hevea brasiliensis and *Pinus oocarpa*	0.14 – 0.56	1.06 – 0.93	[68]
European Black Pinewood and Licorice root	0.33 – 0.55 N/mm^2	1.5	[69]
Soybean pods and Eucalyptus wood	0.48 – 0.07	1.21 – 2.95	[70]
Sugarcane bagasse in fiber lengths (5 and 8 mm)	0.34 – 1.18	NA	[71]
Angelim, Cambara, Canelao, Cedar and Itauba	0.53 – 0.24	0.98 – 1.40	[72]
Peanut Hull and *Pinus oocarpa*	0.54 – 0.22	1.28 -2.57	[73]
Pterocarpus violaceus wood and *Pinus oocarpa* wood	0.93 – 0.66	8.6 – 12.0	[74]
Miriti petioles and *Pinus oocarpa* wood	NA	1.3 – 3.95	[75]
Maize cob and *Pinus oocarpa*	11.0 – 0.3	1.4 – 3.9	[76]
Pinus oocarpa wood, Castor hull, and Sugarcane bagasse	0.35 – 1.09	1.31 – 6.74	[77]

*NA- Not Available

4. Chemical, Thermal, and Microstructural Properties of Particleboards Made from Biomass

The determination of the chemical properties of particleboards produced from different biomass is very important. The use of agricultural wastes for the production of particleboard is limited by the cellulose content of the biomass. The cellulose-ordered structure results in tighter and denser structure particleboards leading to better strength, improved rigidity, and stable dimensions compared with lignocellulosic particleboards [34]. The strength of the particleboards can be improved through various chemical composition interactions. With the improved strength, the particleboards can be utilized in various interior building applications. Unfortunately, limited studies have examined the chemical properties of produced particleboards. Most studies considered the chemical properties of the raw biomass before being used with other biomass and adhesives in the production of the particleboards. They failed to consider the chemical properties of the particleboards after production in which various interactions of the different constituents would have erupted chemical reactions.

Fitri et al. [1] determined the chemical composition of particleboards made from rice straw (50 wt.%) and polypropylene (50 wt.%) using X-ray fluorescence. The study observed that

the major constituents are SiO_2 (35%), K_2O (25%), and CaO (15%). The chemical compositions involved when particleboards were manufactured from sunflower stalks treated with sodium hydroxide were lignin, hemicellulose, and α-cellulose contents, extractive contents, and monosaccharide composition [3]. The study revealed that the treatment of Sunflower stalk particles with alkali has effects on the chemical composition and thermal stability. Thus, the contents of the chemical components like extractive contents, hemicellulose, and lignin were lowered with the rise in NaOH concentrations from 1 to 5%. As a result of the chemical degradation of the particles, there was a reduction of thermal stability as the NaOH concentration increased.

The chemical analysis of the untreated groundnut shell particles (UGP) and treated groundnut shell particles (TGP) for various lignocellulosic constituents were investigated when groundnut shells were used to produce particleboards by Ekpenyong et al. [90]. The cellulose, hemicellulose, and lignin content of the two categories of fibers (UGP and TGP) were analyzed. The analysis for UGP revealed 38.89% cellulose, 27.03% hemicellulose, and 19.61% lignin while TGP showed 45.74% cellulose, 23.52% hemicellulose, and 12.69% lignin. The chemical compositions of UGP and TGP differ because of the alkaline treatment given to the groundnut shell particles (TGP). As reported by [90], the alkaline treatment of fibers increased the cellulose content to 45.74% compared to the untreated fibers (36.89%). A high cellulose content of agro-residues in the production of particleboard has been attributed to giving the particleboard excellent mechanical properties. This makes high cellulose content agro-residues potentially suitable for particleboard production. However, agro-residues with lower cellulose contents have negative effects on the mechanical properties of particleboards [9, 34, 91, 92].

Thermal conductivity analysis is crucial in the determination of the insulation properties of particleboards. This would assist particleboard manufacturers in optimizing production by selecting suitable materials and ensuring compliance with standards and regulations. Particleboards produced from mulberry wood pruning waste with the usage of urea-formaldehyde resin as a binder were characterized by Ferrandez-Villena et al. [93]. The average thermal conductivity values obtained for the particleboards varied between 0.065 and 0.068 W/mK. These values were lower compared to those obtained for other woods such as Date palm (0.083 W/mK), Hemp (0.111 W/mK), and Sisal (0.070 W/mK); but have similar values of 0.065 W/mK with cork panels. The thermal conductivity of the particleboards was not influenced by the particle size of the raw materials. The production of particleboard from papyrus fiber using natural rubber latex as a binder was achieved by Tangjuank and Kumfu [94]. The study investigated the thermal properties of the particleboard produced. The thermal property (conductivity) of the particleboard was 0.029 W/mK, a value lower than that of commercial particleboards at 0.092 W/mK. The value of the thermal insulation obtained showed that the papyrus fiber exhibited good thermal insulation since it has a lower thermal conductivity value compared to the commercial particleboard. Low thermal conductivity is desired to minimize heat transfer and maximize energy efficiency. Hence, lower thermal conductivity is an indication of better insulation properties; thereby, making the material suitable for various applications. Low thermal conductivity of particleboards reduces heat transfer and energy consumption in buildings leading to cost savings and environmental benefits [93, 95].

One of the most important parameters for selecting thermal insulation of particleboards is fire resistance [96]. It is the capability of a material to resist fire and can be considered for interior applications such as ceilings and walls. More so, there is a relationship between thermal conductivity values and the density of the particleboards. Tangjuank [96] observed and reported that the higher-density particleboards of 210 kg/m^3 have the least insulating effect (0.035 W/mK) when pineapple leaves are used in the production of particleboard. This observation was linked to the fact that low-density particleboards are

not well compacted hence they possess a large number of voids filled with air, which serves as one of the poorest conductors. This implies that less heat is being conducted in lower-density boards compared to the higher-density boards. The pineapple leaves particleboards were adjudged excellent thermal insulating materials.

The thermal properties of Sunflower particleboards were investigated by Lenormand et al. [95]. The particleboards were produced without binder. However, the board fabrication was done using a hot hydraulic press. Three particleboard densities (50, 75, and 100 kg/m^3) were desired. It was reported that the thermal conductivity of the materials increased with the density. The least (50 kg/m^3) and densest particleboards (100 kg/m^3) have thermal conductivity values of 38.08 and 42.41 mW/mK, respectively. When density is low, there is increased porosity in the particleboard which could lead to low thermal conductivity. Table 7 displays the density and thermal conductivity values for different biomass materials used in the production of particleboards.

Table 7. Density and thermal conductivity of different particleboards

Particleboard from biomass	Density (kg/m^3)	Thermal conductivity (W/mK)	Ref.
Pineapple leave	210	0.035	[96]
Papyrus fibers	258	0.029	[94]
CCB-treated *Pinus sp.* Wood (100% wood)	0.55 g/cm^3	0.11	[97]
60% wood/40%tire Rubber	0.78 g/cm^3	0.14	[97]
Sunflower	50 – 100	0.038 – 0.042	[98]
Bamboo shoot sheaths	400 – 800	0.066 – 0129	[55]
Spruce	NA	0.062 – 0.091	[99]
Black pine	NA	0.074 – 0.105	[99]
Beech	NA	0.103 – 0.139	[99]
Oak	NA	0.118 – 0.154	[99]
Chestnut	NA	0.087 – 0.120	[99]
Coir fiber	300 – 500	0.120 – 0.169	[100]
Red pine wood and Gypsum	0.845 – 1.333	0.7404 – 0.5021	[101]
Narrow-leaved Cattail fibers	200 – 400	0.0438 – 0.0606	[102]
Norway Spruce residues and coniferous bark	0.232 – 0.291	0.049 – 0.074	[103]
Leave fiber of Camel's foot	528.6 – 538.4	0.0321 – 0.0409	[104]
Bark fiber of Camel's foot	558.3 – 711.8	0.0394 – 0.0434	[104]
Newspaper waste	NA	0.066 – 0.125	[105]

*NA- Not Available

Analyzing the particleboard's morphology is very germane for the examination of the compactness of the raw biomass particles and their interaction with the binders used. It also helps to examine the pores formed in the particleboards produced. During the micrograph analysis of particleboards produced from cocoa pods using starch and urea formaldehyde as adhesives in the study of Mitchual et al. [52], major micropores and loosed particles were observed on some of the samples. The study observed that there was detachment of the particles from the adhesives. The bonding between the adhesives and the particles was reported to be poor owing to the high bulk density and low aspect ratio of the biomass material. However, a contrary observation was reported for some other samples such as Ceiba, cocoa, and plantain pseudostem where the inter-particle spaces of

the particles were filled with adhesives such as UF and cassava starch. Hence, there is better compaction and agglomeration of the particles and adhesives leading to improved mechanical properties.

The overall strength properties of particleboards are dependent on the glue line between the particles [106]. Ulker and Hiziroglu [106] observed in the micrograph that there was a relatively uniform distribution of the starch adhesive leading to improved bonding among the particles. The cross-sectional view of the particleboard produced when glutardialdehyde-modified starch was employed as a binder which showed granulated modified corn starch. The larger the particle size, the more voids in the structure of the particleboards. This was the experience when peach nut shells with glass powder and tea fiber were used in the production of particleboards at particle sizes of 900 µm and 150 µm, respectively, using phenol-formaldehyde as a binder [107]. It was reported that the 900 µm particle size particleboard showed many voids in the structure while the 150 µm particle size particleboard showed no void in the particleboard's structure. This observation supported the water absorption characteristics of the particleboards in which structures with more voids tend to absorb more water which is deleterious to the particleboard when stored. A typical micrograph of particleboard is displayed in Fig. 8.

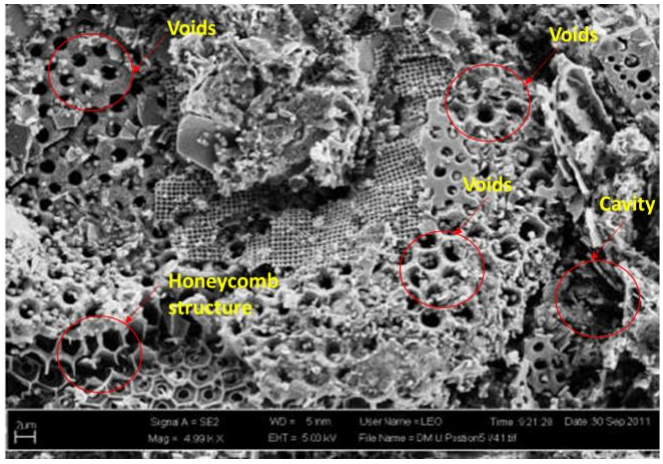

Fig. 8: Micrograph of a particleboard [108]

5. Challenges and Prospects for Future Works on Particleboards

There is a major challenge of inconsistent raw materials supply for the manufacturing of particleboards all over the world. Many producers of particleboards are unyielding in adopting alternative feedstock for their production; rather, they are still seeking the usual raw materials [34, 36, 51]. This kind of issue needs to be tackled appropriately. Manufacturers of particleboards should believe in the utilization of alternative raw materials such as agro-waste materials or biomass. Many developing countries are faced with serious environmental health challenges as a result of the accumulation of various agricultural residues without properly discarding them. Proper waste management and utilization policies especially in the context of agro-residue-based particleboards should be encouraged [19]. Although particleboards from agro-wastes have been greatly researched and have advanced scientifically and technologically, the wider and commercial acceptability of particleboards is limited due to some challenges. The utilization of fresh agro-residue leads to more transportation and storage costs due to its higher moisture content and heaviness [109]. Hence, high moisture content agro-residues are less

compressible during particleboard production. With different processing parameters that have been used by various researchers, it is important to optimize the processing parameters. For instance, the pressing time, temperature, and pressure should be optimized for sufficient compaction/compression ratio and strength [110, 111]. For appropriate bonding, more resins as adhesives are required to cater to the higher volume of agro-residues in the production of particleboards. When fewer resins are used, improper bonding is achieved and the board's final performance is adversely affected [112].

Furthermore, particleboard manufactured using agro-residues is liable to deteriorate in dimension and absorb more water. Hence, the particleboard's water absorption and dimensional stability should be critically examined. This implied that hydrophilic raw materials such as husk, stalk, shell, and straw of various biomass used in the manufacturing of particleboards could be solved by introducing hydrophobic agents (wax) during the fabrication process. Although promising results have been documented on the physical and mechanical properties of agro-based particleboards, wood-based particleboards are of better strength. Therefore, the strength of agro-based particleboards could be increased by introducing woody particles at proper resin dosage and pressing parameters. Further studies are recommended on the critical examination of the fire-resistance characteristics of the particleboard. There is no sufficient information on this aspect. More so, more studies should be done to optimize the manufacturing process of the particleboard. More studies should also be done on the thermal stability of the particleboard by considering the thermal conductivity and insulation of the particleboard.

6. Conclusion

The appropriate utilization of biomass and environmental wastes for a sustainable environment is germane to the reduction of environmental pollutants. Particleboards produced from the recycling of agricultural biomass have been examined in this study. The properties of the particleboards produced with these agro-residues showed similar or superior physico-mechanical properties that met the requirements of different standards for proper utilization for sustainable construction. The density of particleboard depends on the density of the biomass used, the adhesive used, and the compaction pressure applied during production. The density helps to classify particleboards into low-density, medium-density, and high-density boards. The durability and storability of particleboards can be assessed through a water absorption test, which could be influenced by the particle sizes of the biomass used. Also, the quality and usefulness of particleboards were ascertained via the modulus of elasticity and modulus of rupture. The denser the particleboard, the higher the modulus of elasticity and the modulus of rupture. The modulus of elasticity and modulus of rupture are positively influenced to be better with a smaller particle size of the biomass used. Hence, the particle size of the biomass used plays an important role in the determination of the properties of particleboards. The insulation property of particleboards is obtainable through thermal conductivity analysis. Embracing this development could lead to fulfilling the sustainable development goals featuring growth in the economy, protection of the environment from pollution, and social inclusion. With the utilization of these various biomass for the particleboards, the challenge of deforestation is drastically reduced, and more entrepreneurial opportunities are created. Panel production continuation is ensured since agro-waste materials are used as alternative or complementary raw materials. Hence, the production and the products are economical and eco-friendly. Further studies should be considered on the optimization of the processing parameters and critically examining the fire-resistance characteristics.

References

[1] Fitri N, Mursal, Ismail I. Physical and chemical properties of particleboards made from rice straw and plastic waste. IOP Conference Series: Journal of Physics, 2020; 1460: 012146. https://doi.org/10.1088/1742-6596/1460/1/012146

[2] Adeleke AA, Ikubanni PP, Orhadahwe TA, Christopher CT, Akano JM, Agboola OO, Adegoke SO, Balogun AO, Ibikunle RA. Sustainability of multifaceted usage of biomass: A review. Heliyon, 2021a; 7: e08025. https://doi.org/10.1016/j.heliyon.2021.e08025

[3] Guler G. Chemical, physical and mechanical properties of particleboards manufactured from sodium hydroxide-treated sunflower (*Helianthus annus L.*) stalks. Journal of Barlin Faculty of Forestry, 2019; 21(3): 758–770. https://doi.org/10.24011/barofd.588056

[4] Yasina M, Waheed Bhutto A, Bazmi A, Karim S. Efficient utilization of rice-wheat straw to produce value-added composite products. Journal of Environmental Chemical Engineering, 2010; 1: 1–8.

[5] Dukarska D, Czarnecki R, Dziurka D, Mirski R. Construction particleboards made from rapeseed straw glued with hybrid pMDI/PF resin. European Journal of Wood and Wood Product, 2017; 75: 175–184. https://doi.org/10.1007/s00107-016-1143-x

[6] Ikubanni PP, Adeleke AA, Adediran AA, Agboola OO. Physico-mechanical properties of particleboards produced from locally sourced materials. International Journal of Engineering Research in Africa, 2018; 39: 112-118. https://doi.org/10.4028/www.scientific.net/JERA.39.112

[7] Luo P, Yang C, Li M, Wang Y. Manufacture of thin rice straw particleboards bonded with various polymeric methane diphenyl diisocyanate/urea formaldehyde resin mixtures. BioResources, 2020; 15, 935–944. https://doi.org/10.15376/biores.15.1.935-944

[8] Xu Y, Sun XS, Wang D. Chapter 1: Wheat Section 1: Cereals and Soybeans. In: Integrated Processing Technologies for Food and Agricultural By-Products. Edited by Pan, Z., Zhang, R. and Zicari, S.; 2019; p. 3–20.

[9] Taha I, Elkafafy MS, ELMously H. Potential of utilizing tomato stalk as raw material for particleboard. Ain Shams Engineering Journal, 2018; 9(4): 1457–1464. https://doi.org/10.1016/j.asej.2016.10.003

[10] Araújo CKC, Campos CI, Camargo SKCA, Camargo BS. Caracterização mecânica de painéis particulados de média densidade produzidos a partir de resíduos de madeira. Revista Gestão Industrial, 2019; 15(1): 197-211. https://doi.org/10.3895/gi.v15n1.9159

[11] Brito FMS, Junior GB, Surdi PG. Properties of particleboards made from sugarcane bagasse particles. Revista Brasileira de Ciencias Agrarias, 2021; 16(1): 1–7. https://doi.org/10.5039/AGRARIA.V16I1A8783

[12] Zakaria R, Bawon P, Lee SH, Salim S, Lum WC, Al-Edrus SSO, Ibrahim Z. Properties of particleboard from oil palm biomasses bonded with citric acid and tapioca starch. Polymers, 2021; 13(20): 3494. https://doi.org/10.3390/poly13203494

[13] Nurdin H, Hasanuddin H, Kurniawan A. Particleboard made from areca fiber with tapioca adhesive. Journal of Physics: Conference Series, 2020; 1594 (012031). https://doi.org/10.1088/1742-6596/1594/1/012031

[14] Lim JX, Ong TK, Ng CK, Chua IW, Lee YB, Yap ZY, Abu Bakar R. Development of particleboard from green coconut waste. Journal of Physics: Conference Series, 2021; 2120 (012034). https://doi.org/10.1088/1742-6596/1594/1/012031

[15] Barbu MC, Sepperer T, Tudor EM, Petutschnigg A. Walnut and hazelnut shells: untapped industrial resources and their suitability in lignocellulosic composites. Applied Science, 2020; 10: 6340. https://doi.org/10.3390/app10186340

[16] Mirski R, Dziorka D, Banaszak A. Properties of particleboards produced from various lignocellulosic particles. Bioresources, 2018; 13(4): 7758–7765. https://doi.org/10.15376/biores.13.4.7758-7765

[17] Mari E., Villena E. Properties of particleboard from wood wastes and cashew nut shell residue. Philippine Journal of Science, 2016; 145(1): 1-8.
[18] Ghofrani M, Ashori A, Mehrabi R. Mechanical and acoustic properties of particleboards made with date palm branches and vermiculite. Polymer Testing, 2017; 60: 153 –159. https://doi.org/10.1016/j.polymertesting.2017.03.028
[19] Lee SH, Lum WC, Boon JG, Kristak L, Antor P, Pedzik M, Rogozinski T, Taghiyari HR, Lubis MAR, Fatriasari W, Yadav SM, Chotikhun A, Pizzi A. Particleboard from agricultural biomass and recycled wood waste: a review. Journal of Materials Research and Technology, 2022; 20: 4630-4658. https://doi.org/10.1016/j.jmrt.2022.08.166
[20] Food and Agriculture Organization: Forestry production and trade (2023). Available at https://www.fao.org/faostat/en/#data/FO. Accessed 22nd February 2024
[21] Adeleke AA, Odusote JK, Lasode OA, Ikubanni PP, Malathi M, Paswan D. Mild pyrolytic treatment of Gmelina arborea for optimum energetic yields. Cogent Engineering, 2019a; 6: 1-13. https://doi.org/10.1080/23311916.2019.1593073
[22] Adeleke AA, Odusote JK, Lasode OA, Ikubanni PP, Malathi M, Paswan D. Densification of coal fines and mildly torrefied woody biomass into composite fuel using different organic binders. Heliyon, 2019b; 5(7): 1-7. https://doi.org/10.1016/j.heliyon.2019.e02160
[23] Adeleke AA, Odusote JK, Ikubanni PP, Lasode OA, Malathi M, Paswan D. Essential basics on biomass torrefaction, densification and utilization. International Journal of Energy Research, 2021b; 45(2): 1375-1395. https://doi.org/10.1002/er.5884
[24] Ajimotokan HA, Ehindero AO, Ajao KS, Adeleke AA, Ikubanni PP, Shuaib-Babata YL. Combustion Characteristics of fuel briquettes made from charcoal particles and sawdust agglomerates. Scientific African, 2019; 6: 1-9. https://doi.org/10.1016/j.sciaf.2019.e00202
[25] Ikubanni PP, Omololu T, Ofoegbu W, Omoworare O, Adeleke AA, Agboola OO, Olabamiji TS. Performance evaluation of briquette produced from a designed and fabricated piston-type briquetting machine. International Journal of Engineering Research and Technology, 2019; 12(8): 1227 – 1238.
[26] Fajobi MO, Lasode OA, Adeleke AA, Ikubanni PP, Balogun AO. Effect of biomass co-digestion and application of artificial intelligence in biogas production: A review. Energy Sources, Part A: Recovery, Utilization, and Environmental Effects, 2022a; 44(2): 5314-5339. https://doi.org/10.1080/15567036.2022.2085823
[27] Fajobi MO, Lasode OA, Adeleke AA, Ikubanni PP, Balogun AO. Investigation of physicochemical characteristics of some selected lignocellulose biomass. Scientific Reports, 2022b;12: 2918. https://doi.org/10.1038/s41598-022-07061-2
[28] Adegoke SO, Adeleke AA, Ikubanni PP, Nnodim CT, Balogun AO, Falode OA, Adetona S. Energy from biomass and plastic recycling: A review. Cogent Engineering, 2021; 8 (1994106): 1 – 46. https://doi.org/10.1080/23311916.2021.1994106
[29] Ohijeagbon IO, Adeleke AA, Mustapha VT, Olorunmaiye JA, Okokpujie IP, Ikubanni PP. Development and characterization of composite particleboard produced from sawdust and pulverized polypropylene plastic. Case Studies in Construction Materials, 2020; 13(e00365): 1-8. https://doi.org/10.1016/j.cscm.2020.e00365
[30] Mirindi D, Panthi K, Thach TNS, Hunter J. A review of the evolution and performance of particleboard from different types of organic waste and adhesives. EPiC Series in Built Environment, 2024; 5: 740-749.
[31] Baharuddin MNM, Zain NM, Harun WSW, Roslin EN, Ghazali FA, Md Som SN. Development and performance of particleboard from various types of organic waste and adhesives: A review. International Journal of Adhesion and Adhesives, 2023; 124 (103378). https://doi.org/10.1016/j.ijadhadh.2023.103378
[32] Mahieu A, Vivet A, Poilane C, Leblanc N. Performance of particleboards based on annual plant byproducts bound with bio-adhesives. International Journal of Adhesion

and Adhesives, 2021; 107 (102847). https://doi.org/10.1016/j.ijadhadh.2021.102847
[33] Nunes L, Cintura E, Parrcha JL, Fernandes B, Silva V, Faria P. Cement-bonded particleboards with banana pseudostem waste: Physical performance and bio-susceptibility. Infrastructures, 2021; 6(6): 86. https://doi.org/10.3390/infrastructures6060086
[34] Pedzik M, Janiszewska D, Rogozinski T. Alternative lignocellulosic raw materials in particleboard production: A review. Industrial Crops and Products, 2021; 174: 114162. https://doi.org/10.1016/j.indcrop.2021.114162
[35] Betené ADO, Ndiwe B, Krishnan GS, Wedaïna AG, Tchoupmene CM, Djakou CBN, Taoga MM, Betené FE, Atangana A. Processing of tropical agro-industrial waste for particleboard manufacture: Dimensional stability and mechanical performance. Journal of Building Engineering, 2023; 76: 107369. https://doi.org/10.1016/j.jobe.2023.107369
[36] Iswanto AH, Hakim AR, Azhar I, Wirjosentono B, Prabuningrum DS. The physical, mechanical and sound absorption properties of sandwich particleboard (SPb). Journal of Korean Wood Science and Technology, 2020; 48(1): 32-40. https://doi.org/10.5658/WOOD.2020.48.1.32
[37] Ejiogu IK, Odiji MO, Ayejagbara MO, Shekarri TNB, Ibeneme U. Mechanical properties of urea formaldehyde particle board composite. American Journal of Chemical and Biochemical Engineering, 2018; 2: 10-15. https://doi.org/10.11648/j.ajcbe.20180201.12
[38] Akinyemi BA, Afolayan JO, Ogunji OE. Some properties of composite corncob and sawdust particleboards. Construction and Building Materials, 2016; 127: 436-441. https://doi.org/10.1016/j.conbuildmat.2016.10.040
[39] López YM, Paes JB, Rodríguez EM, Gustave D, Gonçalves FG. Wood particleboards reinforced with thermoplastics to improve thickness swelling and mechanical properties. Cerne, 2018; 24(4): 369-378. https://doi.org/10.1590/01047760201824042582
[40] Sun S, Liu L. Manufacturing tubular particleboards via multidimensional-interface extrusion and their physiomechanical properties. BioResources, 2021; 16(1): 1091-1100. https://doi.org/10.15376/biores.16.1.1091-1100
[41] Hata T, Kawai S, Sasaki H. Production of particleboard with steam-injection. Wood Science and Technology, 1990; 24: 65–78. https://doi.org/10.1007/BF00225307
[42] Xu J, Han G, Wong DE, Kawai S. Development of binderless particleboard from kenaf core using steam-injection pressing. Journal of Wood Science, 2003; 49(4): 327-332. https://doi.org/10.1007/s10086-002-0458-7
[43] Li X, Zheng X, Li H. Steam-injection pressing technology of man-made board. Key Engineering Materials, 2011; 474-476: 1351-1355. https://doi.org/10.4028/www.scientific.net/KEM.474-476.1351
[44] Zhang Y, Gu J, Tan H, Di M, Zhu L, Weng X. Straw-based particleboard bonded with composite adhesives. BioResources, 2011; 6(1): 464-476. https://doi.org/10.15376/biores.6.1.464-476
[45] Dhawale P, Vineeth S, Gadhave R, Mahanwar P. Cellulose stabilized polyvinyl acetate emulsion: Review. Open Journal of Organic Polymer Materials, 2021; 11: 51-66. https://doi.org/10.4236/ojopm.2021.112002
[46] Abd Rahman WW, Md Yatim A, Mat Zlan A, Kasim J, Mohd Yunus N. Effects of the resin content and particle size on the properties of particleboard made of *Neolamarckia* and *Leucaena* particles. BioResources, 2019; 14(3): 6079-6087. https://doi.org/10.15376/biores.14.3.6079-6087
[47] Ashori A, Nourbakhsh A. Effect of press cycle time and resin content on physical and mechanical properties of particleboard panels made from the underutilized low-

quality raw materials. Industrial Crops and Products, 2008; 28(2): 225 – 230. https://doi.org/10.1016/j.indcrop.2008.02.015
[48] Yusoff NF, Mohammed Tamat NS, Kasim J. Effects of board density and resin content on the mechanical and physical properties of oil palm frond particleboard. In: Yacob N, Mohamed M, Megat Hanafiah M. (eds) Regional Conference on Science, Technology and Social Sciences (RCSTSS 2014). Springer, Singapore, 2016. https://doi.org/10.1007/978-981-10-0534-3_39
[49] Chen M, Zheng S, Wu I, Xu J. Study on preparation of high-performance binderless board from *Broussonetia papyrifera.* Journal of Wood Science, 2023; 69: 1-14. https://doi.org/10.1186/s10086-023-02092-3
[50] Eyide O, Amenaghawon NA, Modebe LU, Mene JA. Optimization of mechanical properties of bonded particle boards produced from agricultural waste wood chips. Journal of Applied Science and Environmental Management, 2023; 27(4): 733-740.
[51] Kibet T, Tuigong DR, Maube O, Mwasiagi JI. Mechanical properties of particleboard made from leather shavings and waste papers. Cogent Engineering, 2022; 9: 2076350. https://doi.org/10.1080/23311916.2022.2076350
[52] Mitchual SJ, Mensah P, Frimpong-Mensah K, Appiah-Kubi E. Characterization of particleboard produced from residues of plantain pseudostem, cocoa pod and stem and ceiba. Materials Science and Applications, 2020; 11: 817-836. https://doi.org/10.4236/msa.2020.1112054
[53] American National Standards Institute (ANSI), Particle Board Standard ANSI. A208.1-1999, Composite Panel Assoc., Gaithersburg, MD, 1999.
[54] JIS, Japanese Industrial Standard, Particleboards, Japanese Standard Association, Japan, 2003, 5908.
[55] Srichan S, Raongjant W. Characteristics of particleboard manufactured from bamboo shoot sheaths. E3S Web of Conferences, 2020; 187(0301): 1-9. https://doi.org/10.1051/e3sconf/202018703011
[56] Odeyemi SO, Abdulwahab R, Adeniyi AG, Atoyebi OD. Physical and mechanical properties of cement-bonded particleboard produced from African balsam tree (*Populous balsamifera*) and periwinkle shell residues. Results in Engineering, 2020; 6: 100126. https://doi.org/10.1016/j.rineng.2020.100126
[57] ISO 8335, Cement Bonded Particle Board: Board of Portland or Equivalent Cement Reinforced with Fibrous Wood Particles, International Organization for Standardization, Stockhom, 1987.
[58] IS 14276, Indian standard, Cement Bonded Particle Boards Specification, Bureau of Indian Standards (BIS) Division, New Delhi, 1995.
[59] Silva DW, Scatolino MV, do Prado NRT, Mendes RF, Mendes LM. Addition of different proportions of castor husk and pine wood in particleboards. Waste and Biomass Valorization, 2018; 9(1): 139–145. https://doi.org/10.1007/s12649-016-9742-7
[60] Faria LD, Guimarães COJ, Mendes ML, Junior BGJ, Article R. Conventional Low-density Particleboards Produced with Particles from *Mauritia Flexuosa* and *Eucalyptus spp.* Wood. Clean Technologies and Environmental Policy, 2021. https://doi.org/10.21203/rs.3.rs-980174/v1
[61] Scatolino MV, Protásio TP, Souza VM, Farrapo CL., Guimarães Junior JB., Soratto D, Mendes RF, Mendes LM. Does the addition of cotton wastes affect the properties of particleboards? Floresta e Ambiente, 2019; 26(2). https://doi.org/10.1590/2179-8087.030017
[62] Farrapo C, Wisky Silva D. Effect of association of sugarcane bagasse with Eucalyptus wood on the quality of particleboard. Key Engineering Materials, 2016; 668, 341-347. https://doi.org/10.4028/ww.scientific.net/KEM.668.341
[63] Scatolino MV, Costa AO, Guimarães Júnior JB, Protásio TP, Mendes RF, Mendes LM. Madeira de eucalipto e pergaminho de café na produção de aglomerados:

Propriedades físicas e mecânicas. Ciencia e Agrotecnologia, 2017; 41(2): 139–146. https://doi.org/10.1590/1413-70542017412038616
[64] Teodoro R, Raabe J, Silva DW, Mendes RF, Mendes LM, Tonoli GHD. Functionally graded MDP panels using bamboo particles. Key Engineering Materials, 2016; 668: 39–47. https://doi.org/10.4028/www.scientific.net/KEM.668.39
[65] de Araújo Veloso MCR, Lopes FM, Corrêa Furtini AC, da Silva MG, Mendes LM, Guimarães JB. Low-density particleboard properties produced with jupati particles and eucalyptus wood. Revista Brasileirade Ciencias Agrarias, 2020; 15(4). https://doi.org/10.5039/AGRARIA.V15I4A8414
[66] Sartori DL, Cravo JCM, Barrero NG, Fiorelli J, Junior HS, Nakanishi EY. Painel modular em madeira e chapas de partículas de bagaço de cana-de-açúcar para curral de bovinos. Acta Scientiarum-Technology, 2015; 37(1): 3–9. https://doi.org/10.4025/actascitechnol.v37i1.21239
[67] Varanda LD, Do Nascimento MF, Christoforo AL, Silva DAL, Lahr FAR. Oat hulls as addition to high density panels production. Materials Research, 2013; 16(6): 1355–1361. https://doi.org/10.1590/S1516-14392013005000131
[68] Faria DL, Eugênio TMC, Lopes DE, Protásio TP, Mendes LM, Junior, JBG. Particleboards produced with different proportions of *Hevea brasiliensis*: Residual wood valorization in higher value-added products. Ciencia e Agrotecnologia, 2021; 45. https://doi.org/10.1590/1413-7054202145021420
[69] Cengiz G. Production of particleboards from licorice (Glycyrrhiza glabra) and European black pine (Pinus Nigra Arnold) wood particles. Scientific Research and Essays, 2015; 10(7): 273–278. https://doi.org/10.5897/sre2015.6193
[70] Martins EH, Vilela AP, Mendes RF, Mendes LM, Vaz LEVSB, Guimarães Junior JB. (2018). Soybean waste in particleboard production. Ciencia e Agrotecnologia, 2018; 42(2): 186–194. https://doi.org/10.1590/1413-70542018422015817
[71] Fiorelli J, De Lucca Sartori D, Cravo JCM, Savastano H, Rossignolo JA, Do Nascimento MF, Lahr FAR. Sugarcane bagasse and castor oil polyurethane adhesive-based particulate composite. Materials Research, 2013; 16(2): 439–446. https://doi.org/10.1590/S1516-14392013005000004[73]
[72] Longo BL, Da Cunha AB, Rios PD, Terezo RF, De Almeida CCF. Caracterizaçaõ tecnológica de paineís particulados produzidos com resíduos de cinco espécies tropicais. Scientia Forestalis/Forest Sciences, 2015; 43: 907–917. https://doi.org/10.18671/scifor.v43n108.15
[73] Brito FMS, Silva BA, de Carvalho IM, Baúti SB, Mendes LM, Guimarães JB. Technological properties of medium-density particleboards produced with peanut (*Arachis hypogaea*) and *Pinus oocarpa* hulls. Floresta e Ambiente, 2022; 29(2): e20210101. https://doi.org/10.1590/2179-8087-FLORAM-2021-0101
[74] Farrapo CL, Mendes RF, Guimeraes Junior JB, Mendes LM. Utilization of *Pterocarpus violaceus* wood in the particleboard production. Scientia Forestalis, 2014; 42: 329-335.
[75] Furtini ACC, dos Santos CA, de Novais Miranda EH, Villarruel DCV, Gomes DAC, Ferreira GC, da Silva MG, Mendes LM, Guimarães Júnior JB. Using miriti petiole to produce particleboards. Ambiente Construído, 2023; 23(2): 149-162. https://doi.org/10.1590/s1678-86212023000200668
[76] Scatolino MV, Silva DW, Mendes RF, Mendes LM. Uso do sabugo de milho na produção de painéis aglomerados. Ciencia e Agrotecnologia, 2013; 37(4): 330–337. https://doi.org/10.1590/S1413-70542013000400006
[77] Silva DW, Farrapo CL, Mendes RF, Mendes LM, Tonoli GHD, Guimarães JB. Use of castor hull and sugarcane bagasse in particulate composites. Key Engineering Materials, 2016; 668: 381–389. https://doi.org/10.4028/www.scientific.net/KEM.668.381
[78] Hartono R, Dalimunthe AM, Iswanto AH, Herawati E, Sutiawan J, de Azevedo ARG. Mechanical and physical properties of particleboard made from the sumatran

elephant (*Elephas maximus sumatranus*) dung and wood shaving. Polymers 2022; 14: 2237. https://doi.org/10.3390/polym14112237
[79] Salleh KM, Hashim R, Sulaiman O, Hiziroglu S, Wan Nadhari WNA, Abd Karim N, Jumhuri N, Ang LZP. Evaluation of properties of starch-based adhesives and particleboard manufactured from them. Journal of Adhesion Science and Technology, 2014; 29(4): 319-336. https://doi.org/10.1080/01694243.2014.987362
[80] Witono JR, Noordergraaf IW, Heeres HJ, Janssen LPMB. Water absorption, retention and the swelling characteristics of cassava starch grafted with polyacrylic acid. Carbohydrate Polymers, 2014; 103: 325-332. https://doi.org/10.1016/j.carbpol.2013.12.056
[81] EN 312. Particleboards-Specifications. European Committee for Standardization 312, Brussels-Belgium, 2005.
[82] de Melo RR, Muhl M, Stangerlin DM, Alfenas RF, Junior FR. Properties of particleboards submitted to heat treatments. Ciencia Florestal, 2018; 28(2): 776-783. https://doi.org/10.5902/1980509832109
[83] Ferrandez-Garcia A, Ferrandez-Garcia MT, Garcia-Ortuño T, Ferrandez-Villena M. Influence of the density in binderless particleboards made from sorghum. Agronomy, 2022; 12(6): 1387. https://doi.org/10.3390/agronomy12061387
[84] Yilmazer S, Aras U, Kalaycioglu H, Temiz A. Water absorption, thickness swelling and mechanical properties of cement bonded wood composite treated with water repellent. Maderas Ciencia y Tecnologia, 2023; 25: 1-10. https://doi.org/10.4067/s0718-221x2023000100434
[85] Widyorini R. Evaluation of physical and mechanical properties of particleboard made from Petung bamboo using sucrose-based adhesive. BioResources, 2020; 15(3), 5072-5086. https://doi.org/10.15376/biores.15.3.5072-5086
[86] Ferro FS, de Almeida DH, Magalhães de Souza A, Icimoto FH, Christoforo AL, Lahr FAR. Influence of proportion polyol/pre-polymer castor-oil resin components in static bending properties of particleboards produced with Pinus sp. Advanced Materials Research, 2014; 884–885, 667–670. https://doi.org/10.4028/www.scientific.net/AMR.884-885.667
[87] Pedzik M, Auriga R, Kristak L, Antov P, Rogozinksi, T. Physical and mechanical properties of particleboard with addition of walnut (*Juglans regia L.)* wood residues. Materials, 2022; 15: 1280. https://doi.org/10.3390/ma15041280
[88] Amini MHM, Hashim R, Hiziroglu S, Sulaiman NS, Sulaiman O. Properties of particleboard made from rubberwood using modified starch as binder. Composites Part B: Engineering, 2013; 50: 259 – 264. https://doi.org/10.1016/j.compositesb.2013.02.020
[89] Auriga R, Auriga A, Borysiuk P, Wilkowski J, Formalczyk O, Ochmian I. Lignocellolosic biomass from grapevines as raw material for particleboard production. Polymers, 2022; 14: 2483. https://doi.org/10.3390/polym14122483
[90] Ekpenyong NE, Ekong SA, Nathaniel EU, Thomas JE, Okorie US, Robert UW, Akpabio IA, Ekanem NU. Thermal response and mechanical properties of groundnut shells' composite boards. Researchers Journal of Science and Technology, 2023; 2(1): 42-57.
[91] Amilia W, Rusdianto AS, Sofiana W. Characteristics of tobacco stem particleboard in printing load variations and storage time. Journal La Lifesci, 2020; 1: 8–14. https://doi.org/10.37899/journallalifesci.v1i3.115
[92] Fahmy Y, Fahmy TYA, Mobarak F, El-Sakhawy M, Fadl MH. Agricultural residues (Wastes) for manufacture of paper, board, and miscellaneous products: background overview and future prospects. International Journal of ChemTech Research, 2017; 10: 424–448. https://hal.science/hal-01613635
[93] Ferrandez-Villena M, Ferrandez-Garcia A, Garcia-Ortuno T, Ferrandez-Garcia MT. Acoustic and thermal properties of particleboards made from mulberry wood (*Morus*

alba L.) pruning residues. Agronomy, 2022; 12: 1803. https://doi.org/10.2290/agronomy12081803
[94] Tangjuank S, Kumfu S. Particleboards from papyrus fibers as thermal insulation. Journal of Applied Sciences, 2011; 11: 2640–2645. https://doi.org/10.3923/jas.2011.2640.2645
[95] Aladegboye OJ, Oyedepo OJ, Awolola TJ, Oguntayo OD, Babatunde OY, Ilesanmi OT, Ikubanni PP. Physicomechanical and thermal properties of particleboard produced using waste ceramic materials and corncob. Advances in Materials Science and Engineering, 2024; 2024: 8839814. https://doi.org/10.1155/2024/8839814
[96] Tangjuank S. Thermal insulation and physical properties of particleboards from pineapple leaves. International Journal of Physical Sciences, 2011; 6(19): 4528 – 4532.
[97] Da Silva Bertolini M, Christofiro AL, Rocco Lahr FA. Thermal insulation particleboards made with wastes from wood and tire rubber. Key Engineering Materials, 2015; 668: 263–269. https://doi.org/10.4028/www.scientific.net/KEM.668.263
[98] Lenormand H, Gle P, Leblanc N. Investigation of the acoustical and thermal properties of sunflower particleboards. Acta Acustica United with Acustica, 2017; 103: 149 – 157. https://doi.org/10.3813/AAA.919040
[99] Bozikova M, Kotoulek P, Bilcik M, Kubik L, Hlavacova Z, Hlovac P. Thermal properties of wood and wood composites made from wood waste. International Agrophysics, 2021; 35: 251–256. https://doi.org/10.31545/intagr/142472
[100] Kiran MC, Mamatha BS, Anand N, Prakash V, Murthy N. Efficiency of coir particleboard for acoustic and thermal applications. Open Journal of Acoustics, 2019; 9: 39–47. https://doi.org/10.4236/oja.2019.93004
[101] Kaya AI, Yalcm OU, Turker Y. Physical, mechanical, and thermal properties of red pine wood-gypsum particleboard. Bilge International Journal of Science and Technology Research, 2021; 5(2): 139–145. https://doi.org/10.30516/bilgesci.956.352
[102] Luamkanchanaphan T, Chotikaprakham S, Jarusombati S. A study of physical, mechanical and thermal properties of thermal insulation from narrow-leaved cattail fibers. APCBEE Procedia, 2012; 1: 46–52. https://doi.org/10.1016/j.apcbee.2012.03.009
[103] Medved S, Tudor EM, Barbu MC, Young TM. Thermal conductivity of different bio-based insulation materials. Les/Wood, 2021; 70(1): 73–82. https://doi.org/10.26614/les-wood.2021.v70n01a05
[104] Abubakar M, Raji A, Hassan MA. Comparative study of thermal insulation boards from leaf and back fibers of Camel's foot (*Piliostigma thonningri L*). Nigerian Journal of Technology, 2018; 37(1): 108–114. https://doi.org/10.4314/njt.v37i1.14
[105] Theasy Y, Yulianto A, Astuti B. Effect of thickness on thermal conductivity based on waste newspaper particleboard. Journal of Natural Sciences and Mathematics Research, 2017; 210: 210–214. https://doi.org/10.21580/jnsmr.2017.3.1.1696
[106] Ulker O, Hiziroglu S. Some properties of Eastern red cedar (*Juniperus virginiana L.*) particleboard panels made using modified starch as binder. Dryna Industrija, 2020; 71(4): 371 – 377. https://doi.org/10.5552/drvind.2020.1947
[107] Sahin A, Tasdemir HM, Karabulut AF, Guru M. Mechanical and thermal properties of particleboard manufactured from waste peachnut shell with glass powder. Arabian Journal for Science and Engineering, 2017; 42(4): 1559–1568. https://doi.org/10.1007/s13369-017-2427-0
[108] Funk M, Wimmer R, Adamopoulos, S. Diatomaceous earth as an inorganic additive to reduce formaldehyde emission from particleboards. Wood Material Science and Engineering, 2017; 12(2): 92-97. https://doi.org/10.1080/17480272.2015.1040066

[109] Dukarska D, Rogozinski T, Antov P, Kristak L, Kmieciak J. Characterisation of wood particles used in the particleboard production as a function of their moisture content. Materials, 2021; 15(1): 48. https://doi.org/10.3390/ma15010048
[110] Nguyen TT, Redman A, Leggate W, Vandi L, Bailleres H, Heitzmann M. Processing parameters optimization of cotton stalk (*Gossypium hirsutum* L.) particleboards with emulsifiable polymeric isocyanate adhesive. BioResources, 2021; 16(2): 4149-4170.
[111] Zhang B, Hua J, Cai L, Gao Y, Li Y. Optimization of production parameters of particle gluing on internal bonding strength of particleboards using machine learning technology. Journal of Wood Science, 2022, 68: 21. https://doi.org/10.1186/s10086-022-02029-2
[112] Mirindi D. A review of particleboard development and performance using non-toxic and biodegradable adhesives. International Journal of Engineering Trends and Technology, 2024, 72(5): 252 – 260. https://doi.org/10.14445/22315381/IJETT-V7215P126

Research on Engineering Structures & Materials
www.jresm.org
Research Group

Research Article

Mechanical properties of eco-friendly self-compacting concrete made from partially replaced single-use waste plastic and complete recycled coarse aggregate using RSM and ANN methods

Suvidha[1,a], Sumesh Jain[1,b], C. Arvind Kumar[*,2,c]

[1]*Department of Civil Engineering, Om Sterling global University, Hisar, Haryana, India*
[2]*Department of Civil Engineering, Matrusri Engineering College, Hyderabad, Telangana, India*

Article Info

Article history:

Received 07 May 2024
Accepted 21 Aug 2024

Keywords:

Recycled aggregate; Plastic waste; High-density polyethylene; Polypropylene; Response surface Method; Artificial neural network

Abstract

The paper aims to use most of the recycled material from the waste and develop a sustainable Eco-Friendly Self-Compacting Concrete (EF-SCC). Two different plastic wastes, High-Density Polyethylene (HDPE) and Polypropylene (PP), were collected from the dumping yard, thoroughly cleaned, and shredded into the desired shape and size. The plastic was substituted with fine aggregate (FA) in amounts ranging from 5% to 20%, with a 5% rise in each mix. The recycled coarse aggregate was obtained by breaking the concrete cubes, beams, and cylinders available for testing at the concrete technology lab. Totally 4 mixes were prepared for M40 grade EF-SCC to determine the mechanical property at 4 different ages (7, 14, 28 and 56 days). The compressive strength results were then predicted using statistical tools such as RSM and ANN. It is observed that both HDPE and PP have workability in the range of 650mm to 800mm, which is acceptable according to EFNARC 2002. The RSM method yielded 99.69% for PP material, while HDPE had 98.17%. The optimum compressive strength values were achieved at 7.5% of HDPE and 5% of PP material at 28 days and 60 days of curing. The training, validation, Test, and All values of R for M40 grade concrete for HDPE and PP material were 0.9955, 0.9980, 0.9244, 0.9241, and 1, 0.972, 0.802, 0.972 respectively. The flexural strength of EF-SCC showed the best results at 15% replacement. The prediction of actual compressive strength with RSM was more accurate for HDPE material compared to ANN. Recycled aggregate showed positive signs in using waste material in construction industries.

1. Introduction

India is the only country after the USA and European Union to produce the world's largest polymers, and it even creates waste plastic, according to the National Circular Economy Roadmap (NCER). India alone produces 3,500,000 metric tons of waste plastic, out of which only 30% is recycled according to The Economics Times India 2023. Therefore, waste plastic generation in India can be utilized in preparation of concrete with partial replacement of Fine Aggregate (FA) [3, 9 and 42], Coarse Aggregate (CA) [36], or Cement (C) which protect from depleting natural resources and protect the environment.

Substantial work is carried out on ordinary concrete, with the replacement of plastic waste [8], HD- PE [9], PET [10-18], E-Plastic [26], PP [19-24], and PVC [25]. The waste plastic was also used as a replacement for cementitious materials [22], as FA [10-13, 15, 17, 18], and CA [14, 21, 23] as plastic fibres in concrete [24]. Most researchers have worked on partial

*Corresponding author: arvind.cholker@matrusri.edu.in
[a] orcid.org/0009-0009-5993-9948; [b]orcid.org/0009-0009-3818-3977; [c]orcid.org/0000-0003-3980-9088
DOI: http://dx.doi.org/10.17515/resm2024.271me0507rs

replacement of FA/CA from 0% to 100%. Among the waste plastic used worldwide, PP and PET are widely recommended to be used as CA in concrete. Most of the work is carried out on the fresh properties (workability), hardened properties (mechanical properties), durability properties (Acid attack, sulphate attack, RCPT), and thermal properties (temperature variation, thermal conductivity) of concrete. The slump value (workability) of concrete was increased by being replaced partially by PP and PET as plastic waste conventional concrete [10, 14, 21]. The FA, the PET material can improve the workability property, i.e., slump cone test in concrete; this is because the plastic material has low workability and is frictionless [10-11]. It was found that waste plastic (PET), which is round and smooth in shape when replaced with FA in concrete, helps to improve the workability property of ordinary concrete [14]. The partially replacing PP with brick and stone CA, they found that the slump value (workability) of concrete was increased with the percentage increase in PP content regardless of water/cement (W/C) ratios [21].

Nevertheless, an opposite study was observed when PET was partially replaced with concrete. Its workability decreased with PET material increase [13, 15, 18 and 28]. The same material (PET) was used when its rheology was changed; the workability was reduced [13]. When PET was replaced by 20% with FA, it was observed that its workability, slump value, was reduced by 25% [15]. The slump value (workability) of concrete with PET material in concrete was decreased because of its irregular shape and size. The use of PET material to replace FA in concrete and observed the same pattern of reduction in workability because of the surface area of PET material [18 and 28]. The plastics used to replace FA or CA has a more specific gravity (SG) when compared with virgin plastic. Nevertheless, the waste plastics SG is lower than the natural fine and coarse aggregates [14 and 21]. Consequently, plastic waste has negligible weight compared to conventional material and, when replaced with concrete, can reduce the weight on soil strata [14 and 21]. The replacement of PET FA with brick aggregate and found that 10% replacement reduced concrete density by 50%. The heat treatment to PET materials, and when replaced in concrete with FA, a linear reduction in the density was observed [14 and 29]. With a maximum percentage of 15%, the dead weight was reduced by 5.6%. It was also found a linear reduction in density when replaced with PP in concrete. The optimum reduction percentage of 7.4% and 8.4% was observed with a 30% replacement of PP waste plastic with brick and stone aggregate in concrete [21]. The waste plastic material was utilized to prepare self-compacting concrete to consider was light weight concrete [40-41]

Some of the researchers on replacement of Waste Foundry Sand (WFS) with fine aggregate showed interesting facts and figures for M60 grade SCC. The replacement can be till 30% without any changes in the virgin properties of SCC. The waste generated from the foundry is considered as one of the meaningful utilization techniques. It was even observed that treated WFS can reduce the density of concrete and make SCC as lightweight, sustainable and green material [43]. The utilization of waste PET plastic as fiber with replacement of fine aggregate showed that the entire replacements (0.25, 0.5, 0.75, 1.0, and 1.25) % showed decrease in compressive strength after 28 days of curing [44]. He also observed that the correlation coefficient between the porosity and compressive strength is inversely weak relation. The use of fly-ash with PET bottles to improve the flexural and compressive strength of SCC was studied by [6, 34, 35, and 45]. The test results showed that the addition of PET fibers decreased the flowability of SCC. It was observed that fly-ash with PET fiber reduced in its compressive strength but increased the flexural property.

When replaced with FA or CA in concrete, the above waste plastic materials have many advantages and must be cross verified using statistical tools. The Response Surface Methodology (RSM) is a specific approach within the broader Design of Experiments (DOE) framework, used to model and analyze the effects of multiple factors on responses with fewer experiments. This method is usually applied in concrete technology (CT) to predict

the mix proportions and the strength properties of various grades of concrete [2, 27-29]. With the increasing demand in infrastructure and construction industries and models with solid/perfect performance, ANN [32-33] and RSM increasingly handle various civil engineering projects, primarily in material science engineering. ANN has been widely used in many engineering disciplines to counter the drawbacks of empirical formulas and approaches to assess or predict the model with non-linear multivariate interrelationships between concrete's mechanical properties [30].

Table 1. M40 grade eco-friendly self-compacting (EF-SCC) concrete mix proportion

Nomenclature	W/C=0.40					
	Cement (kg/m³)	CA (kg/m³)	FA (kg/m³)	100% RA (Kg)	HDPE	PP
HDPE5	273.5	776.52	60.52	776.52	3.21	-
HDPE10			54.10		6.42	-
HDPE15			44.47		9.63	-
HDPE20			31.63		12.84	-
PP5			60.52			3.21
PP10			54.10			6.42
PP15			44.47			9.63
PP20			31.63			12.84

The present study aims to evaluate the mechanical properties of EF-SCC with partial (5%, 10%, 15% and 20%) replacement of HDPE and PP material and complete replacement of recycled coarse aggregate (RCA). The compressive strength achieved experimentally is cross verified with the Statistical tools such as RSM and ANN methods. We must train a neural network with the Levenberg-Marquadt algorithm (LMA) in MATLAB for the ANN model, a fast method to assess the variables. The Mean squared error (MSE) is the mean squared difference between the outputs and responses, and the regression R-value (R) is the correlation between the output and responses, depicting that both the technique, RSM and ANN, are effective in predicting mechanical properties of concrete. Moreover, both RSM and ANN gave nearly the same values as experimental values, but the RSM model is much more accurate than ANN.

2. Materials

Ordinary Portland cement (OPC) of 43 grade affirming to IS: 8112-1989 was used. All the physical properties of cement were tested according to IS 4031-1988. Locally available river sand (Fine Aggregate -FA) passing through 4.75mm confirming to IS 2386 (part-1)-1963 with a specific gravity of 2.61, Fineness modulus as 2.45%, and dry density as 2400-2900 kg/m3. The Coarse Aggregate (CA) was collected by breaking the available failed concrete cubes, beams, and cylinders at the concrete technology lab. Table: 1 M40 grade eco-friendly self-compacting (EF-SCC) concrete mix proportion. The CA was then cleaned with water and dried in the sun for 24 hours. SG was 2.45, Fineness modulus was 8.35, and dry density was 1750 kg/m3. Waste plastic such as HDPE and PP has achieved a specific gravity of 0.38 and 0.27, nearly 8-10 times less than conventional aggregates. The polycarboxylic ether is a superplasticizer for high performance and long workability retention, eliminating vibration and freeing it from chlorides and alkalis.

3. Methodology

To evaluate the mechanical properties of EF-SC M40 grade, trial mixes were prepared, cast, and the final blend was achieved. The final mix was prepared by Water/Cement (W/C) ratio as 0.40, and the mix proportion is given in Table 1. The slump cone test was performed to check the workability of EF-SCC. The test results achieved experimentally (Mechanical property) were cross verified using statistical toll using the Response Surface Method (RSM) in Minitab and Artificial Neural Network (ANN) in MATLAB.

3.1 Mathematical Model

3.1.1 Response Surface Method (RSM)

The response Surface Method (RSM) gives the relation between the variables, and it uses different outputs to analyze the variables and then design the experiments (DoE). The DoE is used to select the other variables to evaluate and choose the most suitable data with which it can predict the response surface in an examined manner. In the same way, the RSM is used to optimize and adjust all the experimental circumstances, which can yield the best results/responses [33]. The RSM is a mathematical model/technique widely used in research and industries to optimize, refine, and grow any product/variable. It is the best technique to determine the effect of various variables with non-dependent variables and their fundamental interactions. The below Eq (1) gives y responses with £ responses for the above method (RSM).

$$y = f \neg (£1, £2, £3 \ldots £k) \; + \; £ \tag{1}$$

The parameters to input are £1, £2, £3, and £k, and the result is y. Similarly, f represents the response function with a mathematical error. Instead of employing a linear polynomial, the model validated the input variable data with a second polynomial order, as stated in Eq (2).

$$y = \beta_0 + \sum_{i=k}^{k} \beta_i \mathcal{L}_i + \sum_{i=k}^{k} \beta_{ii} \mathcal{L}_{ii}^2 + \sum_{i=1}^{k} \sum_{j=1.j\neq 1}^{k} \beta_{ij} \mathcal{L}_i \mathcal{L}_j + \in \tag{2}$$

y = response, β = coefficient, £ = factor, and ε = error. βo, βi, βii, and βij are regression coefficients for intercept, linear, quadratic, and interaction terms, respectively. £i and £j are input variables.

3.1.2 Artificial Neural Network (ANN) – MATLAB

ANN is a statistical model used to assess concrete's mechanical properties, consisting of input, hidden, and output layers. This method was a valuable tool in predicting the correct output variables. The ANN model's primary advantage is finding the exact model for nonlinear equations with different inputs. Moreover, the ANN method is widely used because it addresses discrepant and undependable data [37, 38]. In the ANN application, there are a lot of basic units to handle, which are bugged together in a complicated network. These units have many interconnections known as neurons. The interconnection between neurons is communicated with other neurons. These multiple neurons are multiplied with different weights, added together to make a single output, and then applied to the activation function using Eq (3). Table 2 lists the various % substitute levels for HDPE and PP material in the EF-SCC.

$$z = f(\sum i = 0 - n \; wixi) + d \tag{3}$$

Table 2. Different levels of variables

Variables	Min (%)	Max (%)
HDPE	0	20
PP	0	20

3.1.3. Comparison Parameters

Using different statistical models like R, R^2, RMSE, MAE and MAPE, which are implemented in RSM and ANN models [39]. The error that occurs in RSM and ANN calculations will be performed by below Eqs (4)–(6).

$$RSME = \sqrt{\frac{\sum_i^n (y-x)^2}{n}} \tag{4}$$

$$MAE = \frac{1}{n}\sum_i^n [y-x] \tag{5}$$

$$MAPE = \sum_i^n [y-x]^*100 \tag{6}$$

Here, x=accurate data, y=forecast data, and n=number of samples. The above equations are taken from [39]. R-squared (R^2, Eq. 7) measures how well an independent variable or variables in a statistical model explain for fluctuations in the dependent variable. It has a value from 0 to 1, with 1 indicating a perfect fit between the model and the data. R^2 is a statistical metric that measures how well an independent variable in a regression model explains the variation in a dependent variable. When it comes to investing, R^2 is typically defined as the percentage of a fund's or security's price swings that can be explained by changes in a benchmark index. When a security's movements (or any other dependent variable) are completely explained by changes in the index or any other relevant independent variable, the R^2 value is 100%.

$$R2 = 1 - \frac{unexplained\ Variation}{Total\ Variation} \tag{7}$$

4. Results and Discussion

The current article focuses on the use of recycled coarse aggregate and waste plastic in the construction sector to improve the mechanical characteristics of EF-SCC. The greatest amount of plastic trash should be used in the development of various infrastructure projects to reduce the increase of plastic garbage at dumping yards, therefore protecting the environment. Similarly, recycled aggregate from building and demolition debris will be considered best practice in the construction business.

4.1 Workability

The workability test was performed on freshly mixed concrete of various compositions to know the flowability of the concrete (EFNARC) 2002). The findings show whether concrete workable is as it's a self-compacting concrete compacted with the help of its self-weight. The below results are taken when 100% replacement of RCA was used instead of natural coarse aggregate with various percentage replacement of HDPE and PP.

4.1.1 Slump Flow Test

The 5% HDPE and PP flowability are 678mm and 680mm, respectively, which is suitable according to EFNARC 2002. It is observed from Fig. 1a that if the % of HDPE and PP material increased from 5% to 20%, its flowability also increased in the flow table test. The pattern was slightly changed when the NA was replaced entirely with RA. It was observed that till 15%, the spread of concrete was increased in both HDPE and PP material, but for 20%, there was a forceful decrease in the flow of concrete [Fig. 1b].

The optimum percentage of 15% was recommended in both natural and recycled aggregate. The slump value of concrete was reduced with the % increase of PP in concrete [16]. The same pattern was observed in natural aggregate after 15% replacement, but the trend was linearly increasing in recycled aggregate. The post-consumer plastic in concrete as a replacement with CA, and they found a zero (0) slump for concrete with plastic when compared with conventional concrete (CC) [1 and 5]. The portion of the FA with PET waste plastic, they saw that the drop in the concrete rose by 22 cm when 75% of the PET material was replaced [4 and 7].

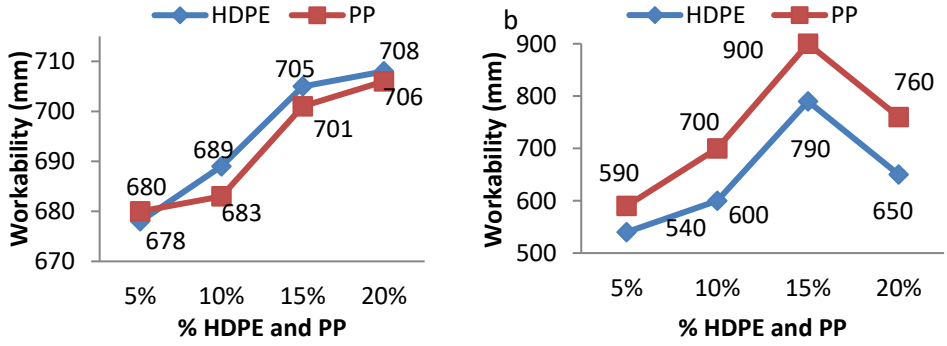

Fig. 1. J-ring Test a) 100% RA b) 100% NA

When FA was substituted for PET waste aggregate in concrete, the slump value rose by 16 cm. According to the current J-ring test findings, recycled coarse aggregate performed better than NA [14]. Given that the curve from Fig. 1a depicts a linear rise in slump value, the percentage of waste plastic made of HDPE and PP may be raised beyond 20%. However, as seen in Fig. 1b, the pattern for natural coarse aggregate has reached an ideal proportion of 15% for both the materials of HDPE and PP.

4.2 Compressive Strength (CS)

The compressive strength (CS) of EF-SCC was cast with distinct percentages of HDPE, and the PP material was partially substituted with FA. All the EF-SCC specimens were tested at 4 different ages, i.e., 7, 14, 28 and 56 days. It was found that there was a linear enhance in CS for all the percentage replacements for both recycled CA and Natural CA. For 7 and 14 days, the results are satisfactory when utilizing recycled aggregate. However, as Fig. 2 illustrates, after 28 and 56 days, the strength of the PP material increased when compared with HDPE. Maximum CS for HDPE at 15% FA replacement is 32.2 MPa, while for PP material at 5% partial FA replacement after 7 days, it is 33 MPa. With a 15% substitution, the HDPE material's strength was almost identical to that of CC, but its CS was lower. The highest CS of 39 MPa and 39.58 MPa for HDPE and PP was noted when the curing period was extended to 14 days respectively. After 28 days, the recycled aggregate (RA) replaced the coarse aggregate (CA) to determine the CS. Fig. 2 shows that RA may provide strengths

of 40 MPa to 45 MPa when combined with 10% HDPE and 15% PP, respectively. Compared to PP, HDPE material displayed 4.5% more, but 4% less than PP. The utmost CS of concrete is 48 MPa when PP is replaced with 15% and 46 MPa when HDPE is replaced with 15%.

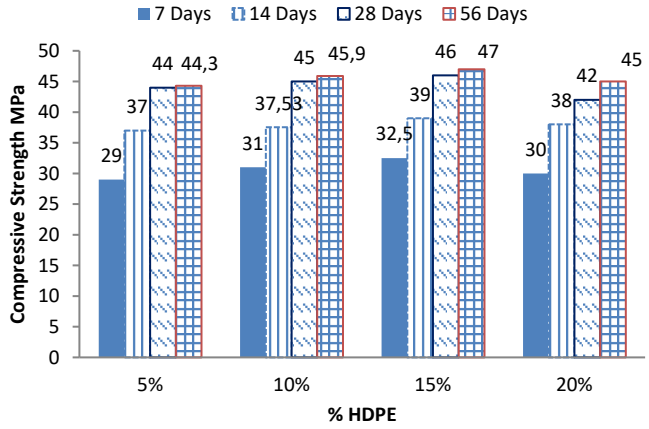

(a)

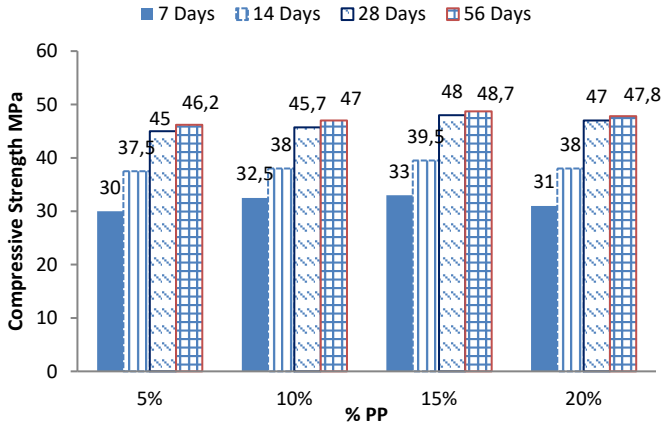

(b)

Fig. 2. Compressive strength for M40 grade SCC with complete recycled Aggregate

a) HDPE b) PP

The maximum compressive test for the M40 grade is 40.10 MPa; nevertheless, the final CS test is raised. The initial CS test is not increased by 5% in three days by replacing PP with fine aggregate. Fine aggregate is substituted for PP material in amounts of 5%, 10%, 15%, and 20%, and the CS test is conducted for three, seven, fourteen, and twenty-eight days. For three, seven, and fourteen days, 15% of the PP was substituted with fine aggregate, and the highest CS test result remained at 40 MPa. With the substitution of 20% PP with fine aggregate, the CS test is enhanced in 3 days, 7 days, 14 days, and 28 days. The maximum CS test is 47 MPa in 28 days. The results from a few researchers showed that replacing FA with plastic waste can reduce the mechanical properties of concrete. It was observed that several researchers have conducted the same experiments and stated that the axial CS decreased with the incorporation of such polymeric waste material in concrete

[11, 37, 39-45]. It is advised that in RA and NA concrete, the CS of both HDPE and PP materials increased by up to 15%, after which the strength decreased. Using RA in concrete that contains HDPE and PP is sustainable because none of the ingredients have a negative environmental impact. The use of the RA, HDPE, and PP in the IS code is encouraged to regulate the usage of Plastic Waste (PW) and Construction and Demolition (C & D) trash in landfills.

4.2.1 Response Surface Method (RSM)

The RSM method was used to analyze the influence of different variables, such as HDPE and PP material, to predict the CS of EF-SCC M40 grade concrete. The CS equation for HDPE (Ƒcs28 of HDPE) was generated and given in Eq (8) for PP material in Eq (9). The residual plots of CS for both HDPE and PP material are shown in Fig. 3.

The Table 3 provided is a summary of the Response Surface Methodology (RSM) analysis for EF-SCC of M40 grade, considering two different materials: HDPE and PP. The standard deviation (S), R-Square (R-sq), R-Square (Adjusted) (R-sq(adj)) and R-- Square (Prepaid) (R-sq(pred)) is given in Table 3. The regression analysis using the RSM method for PP material gave 99.69%, whereas 98.17% was for HDPE materials. The deviation value for HDPE material is >1, and for PP material is <1.

$$Ƒcs28\ of\ PP = 361 + 8.2X1 + 193X2 - 1.48X3 + 0.89X4 - 0.0137X1 * X1 + 0.30X1 * X2 - 0.0256X1 * X3 - 0.0004X1 * X4 \quad (8)$$

$$Ƒcs28\ of\ PP = 361 + 8.2\,X1 + 193.0X2 - 1.48X3 + 0.898X4 - 0.013732X1 * X1 + 0.30\,X1 * X2 - 0.0256X1 * X3 - 0.0004X1 * X4 \quad (9)$$

X1= Days; X2= Percentage of HDPE; X3=Cement; X4= Fine Aggregate

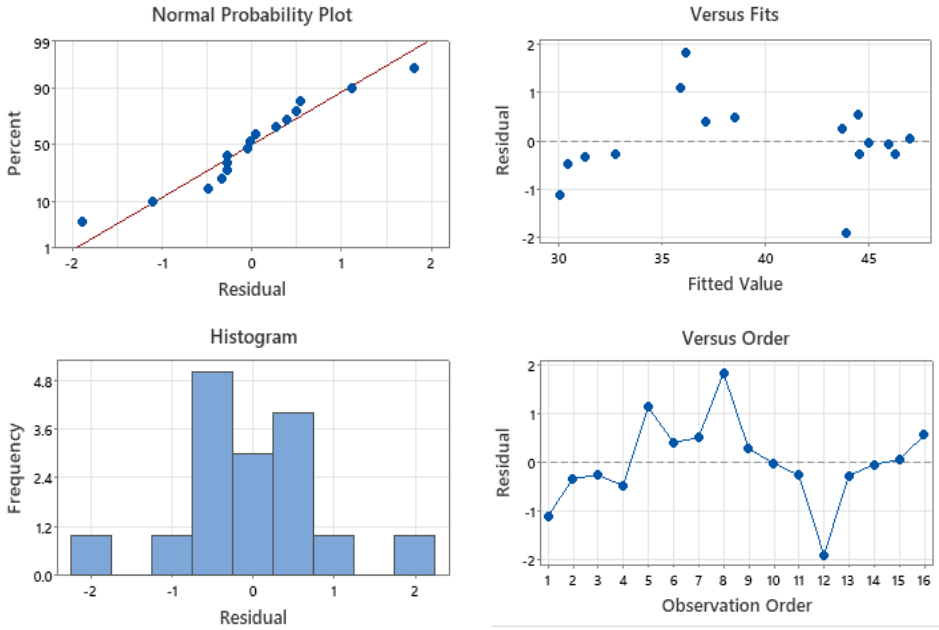

(a)

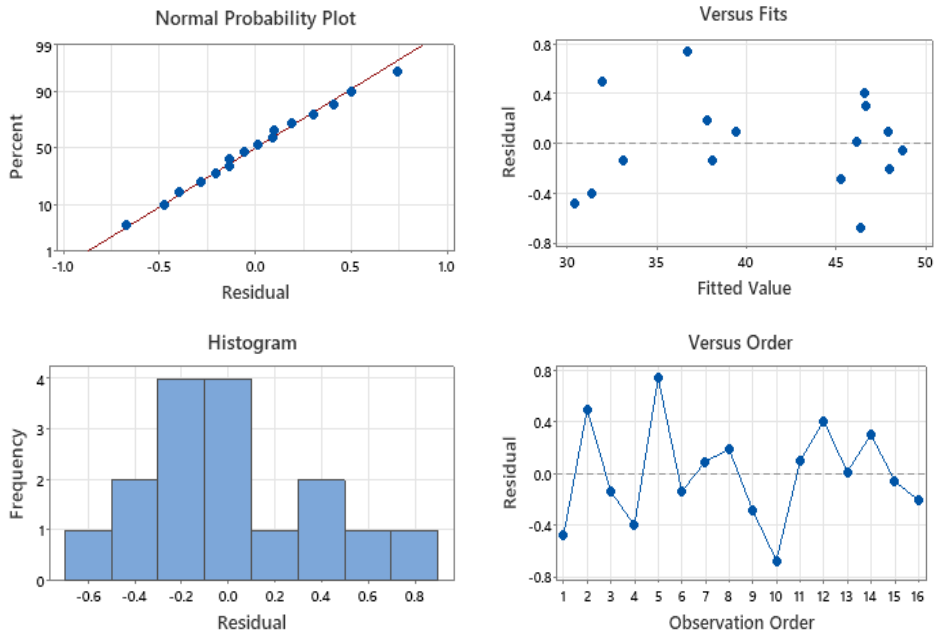

(b)

Fig. 3. Residual Plots of Compressive strength for a) HDPE and b) PP using RSM

Table 3. Summary of RSM for EF-SCC M40 grade

Material	S	R-sq	R-sq(adj)	R-sq(pred)
HDPE	1.23466	98.17%	96.08%	86.84%
PP	0.550001	99.69%	99.33%	96.54%

4.2.2 Lack of Fit (p-value) and Pareto Analysis

The importance of doing progression is assisted by the p-value. The values given in the F-value test should be minimum, which is the p-value of the given model. If the variable of the progression "P" lies in the range of 0.00<P<0.005, then it is treated as considerable, and if it lies > 0.005, then it is insignificant. According to Table 4, the values of X1=0.000, X2, X3, and X4 are more significant than 0.005 for HDPE material, and the values of X1=0.000, X2= 0.004, X3, and X4 are more substantial than 0.005 for PP material which clearly indicates that the curing days plays an essential role in achieving the strength.

The Pareto chart from Fig. 4 indicates that the days of curing (A) the concrete is the most critical parameter, followed by the percentage of HDPE and PP percentage replacement in EF-SCC. The cement(C), which acts as a binding agent to FA and CA, has been proven to achieve the CS of concrete for both HDPE and PP materials. The Pareto chart of HDPE material for EF-SC M40 grade concrete showed that the standard effect for HDPE material is 13 and for PP material is 32. The statistical tool from Mintab (RSM) and Matlab (ANN) methods calculated the CS of EF-SC M40 grade concrete, as shown in Table 4. The below predicted RSM values gave much more accurate HDPE material values for all the percentages when compared with ANN. The values of experimented CS for 15% replacement of HDPE gave -0.82%, 1.26%, -0.58% and 0.09% for 7, 14, 28 and 56 days of curing respectively.

Table 4. Analysis of variance of RSM model for M40 grade concrete

Source	Compressive Strength					
	HDPE			PP		
	DF	F-value	p-value	DF	F-value	p-value
Model	8	47.00	0.000	8	280.67	0.000
Linear	4	46.09	0.000	4	283.16	0.000
X1	1	154.10	0.000	1	1002.55	0.000
X2	1	4.80	0.065	1	17.00	0.004
X3	1	1.53	0.257	1	7.20	0.031
X4	1	5.31	0.055	1	16.53	0.005
Square	1	97.45	0.000	1	580.94	0.000
X1* X1	1	97.45	0.000	1	580.94	0.000
2-Way Interaction	3	0.03	0.992	3	1.18	0.383
X1* X2	1	0.01	0.940	1	0.01	0.908
X1* X3	1	0.01	0.915	1	0.34	0.576
X1* X4	1	0.00	0.957	1	0.00	0.973

X1= Days; X2= Percentage of HDPE; X3=Cement; X4= Fine Aggregate

The only predicted value of ANN for 15% at 28 days was -0.82%, nearly tending to zero, but other values are also.The values of RSM and ANN for PP material showed nearly zero value for 11 activities out of 16 activities. When the RSM was evaluated for 7 days at 15%, the value was -0.41% when compared with conventional concrete; at 14 days for 10%, 15%, and 20%, replacement with FA gave -0.35 %, 0.24%, and 0.50%, respectively, at 28 days only 10% replacement showed -1.46% but remaining percentages of PP gave nearly zero percentage deviation. As the days of curing increased to 56 days, all the percentages of PP showed zero percentage deviation. For the ANN method, the pattern, when compared with RSM, was different; initially, for 7 days of curing, the percentage deviation was nearly zero, but as the age increased to 56 days, the percentage deviation was 4.78% when compared with conventional concrete.

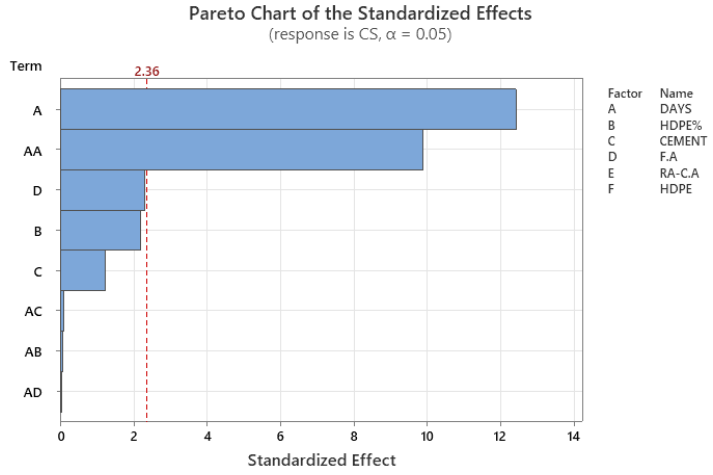

(a)

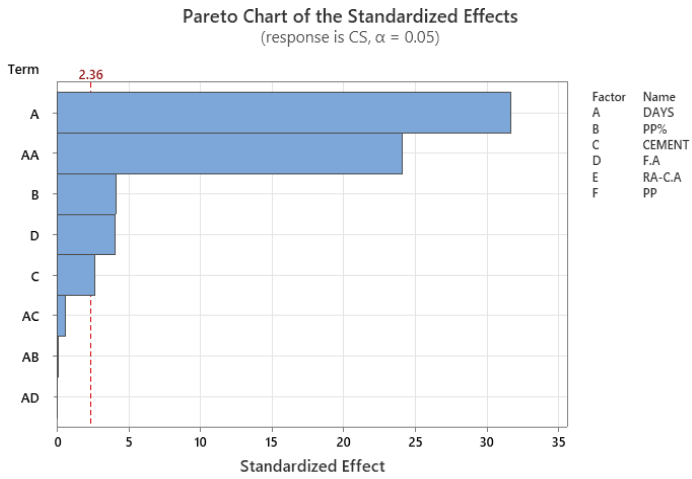

(b)

Fig. 4. Pareto Chart of a) HDPE b) PP

4.2.3 Surface Plot Analysis and Optimization of Progression Variables

The influence of HDPE and PP materials on the CS of M40-grade concrete is depicted in 3D surface plots in Fig. 5. It shows that the material with 7.5% HDPE and 5% PP had reached the ideal CS values after 28 days, and the same pattern was still visible after 60 days of curing.

When HDPE and PP increased from 7.5% to 5%, the CS was reduced. It was observed that PP material gave more strength than HDPE, and the same was even observed in the 3D surface plot graph. These could be the future fine aggregate materials in construction industries to reduce the usage of natural river sand. Some of the research findings of SCC materials are eggshells [23; 24-26], Flyash [27-28], GGBS [24, 29] and Pumice [30] has replaced plastic waste with cement and validated with RSM and ANN. It was discovered that poor bonds have formed in concrete, resulting in low strength and damaging the surface e texture by [31].

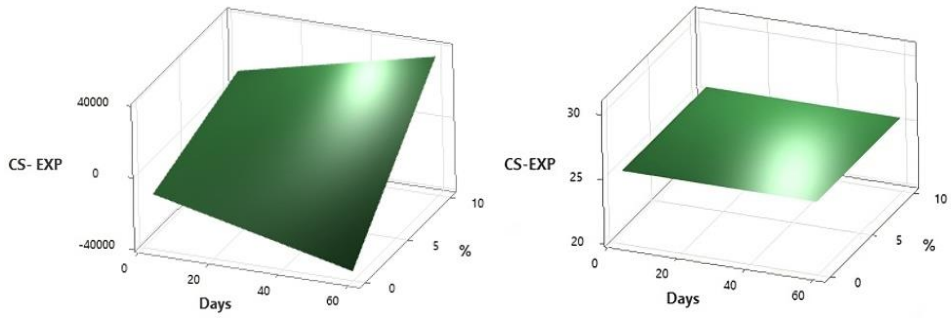

(a) (b)

Fig. 5. 3D Surface plot of a) HDPE b) PP

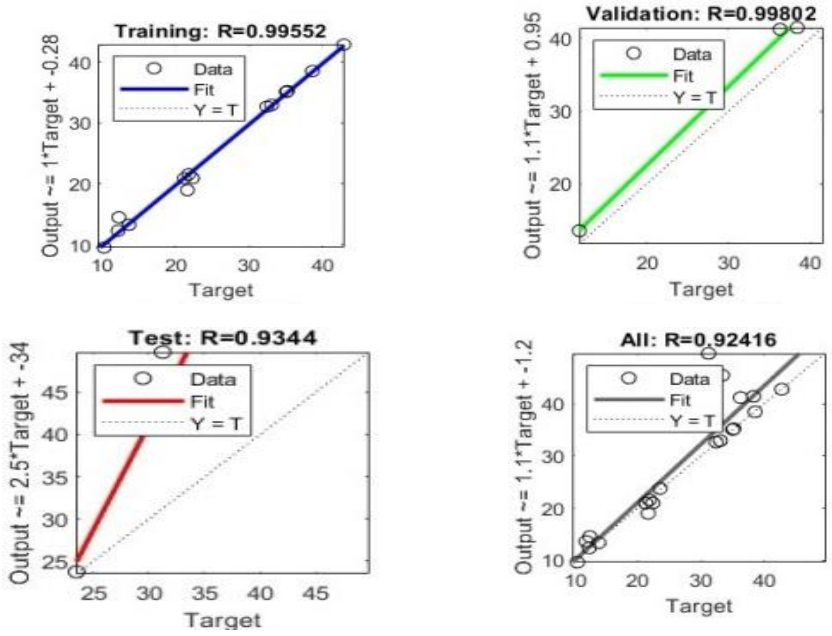

(a)

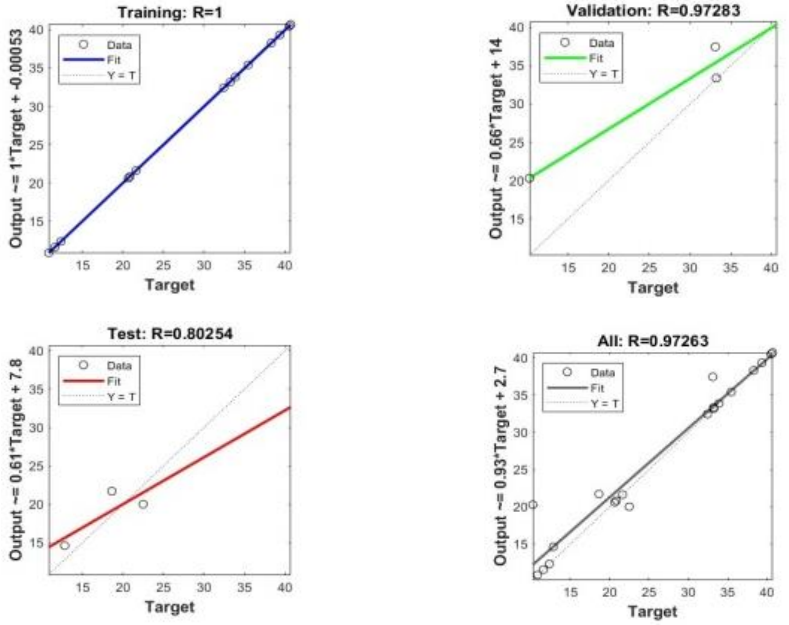

(b)

Fig. 6a. Determination of training, validation, Test, and all values of R for a) HDPE b) PP material in M40 concrete

4.2.4 ANN Model

To predict the CS of M40-grade concrete, we must train a neural network using the Levenberg-Marquadt algorithm (LMA), which is a fast method for assessing variables. The Mean squared error (MSE) is the mean squared difference between the outputs and responses, and the regression R-value (R) is the correlation between the output and responses, depicting that both the technique, RSM and ANN, are effective in predicting mechanical properties of concrete. For every day that concrete would cure—that is, for 3, 7, 28, and 60 —the ANN technique made predictions. 30%of the model, which was trained to predict the CS of the samples, is reserved for testing and validation. The HDPE and PP waste plastic were considered as the parameters, CS is the output layer, with 2 hidden layers as 10 neurons were picked out to make the ANN model as shown in Fig. 6b. The effects of training and validation, Test, and All are presented in Fig. 6a. The training, validation, Test, and All values of R for M40 grade concrete for HDPE and PP material are 0.9955, 0.9980, 0.9244, 0.9241 and 1, 0.972, 0.802, 0.972 respectively, where R represents linear correlation coefficient. The above results of the R-value show that the trained ANN model is in good relationship with the experimental values.

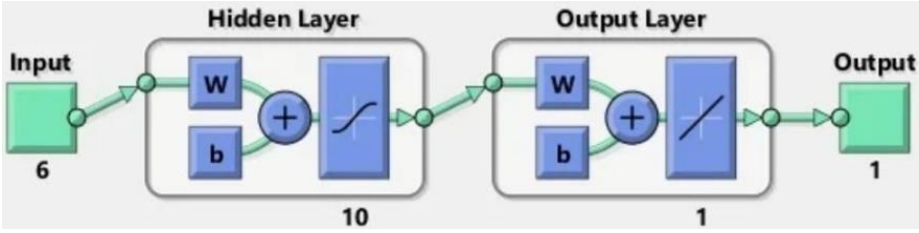

Fig. 6b. The schematic layout of ANN model developed in Matlab

By utilizing Matlab to compare the actual experimental data with the anticipated data, the competence results obtained from the ANN model were ascertained by coefficient determination. A well-fitting model could be shown in the expected CS values of M40-grade concrete containing HDPE and PP. An R-value greater than 0.9 demonstrated a positive connection between the projected and actual CS values. Furthermore, when trained with an ANN model, the tested CS value produced projected results that were quite close to the measured values. The actual, ANN, and RSM projected strengths are shown in Table 5. The present research has several practical applications in civil and infrastructure engineering. To design the mix proportion and any model, such preliminary designs are required to make a product performance based on the optimum percentage replacement of any such materials with cement or FA [32]. To protect the environment from CO_2 emission while cement manufacturing can be reduced by partially replacing waste plastic by regulating the minimum mechanical performance of SCC. For such a study, statistical tools to predict the mechanical properties are helpful and much required. Such tools are useful in civil engineering projects to regulate psychoanalysis's budget and financial feasibility. There are many statistical tools to predict the CS of concrete, but the ANN model is much faster, and it is less expensive when compared with the theoretical experimentation [33]

4.3 Flexural Strength

Following IS 516-1959, the flexural strength of EF-SCC concrete was tested. Fig. 7 shows the 100x100x500mm beams tested on several days and with varying amounts of HDPE and PP. At 15% replacement of HDPE in concrete, the maximum flexural strength of 5.1 MPa was recorded, which is 0.8 MPa stronger than PP after 7 days. The flexural strength of the remaining HDPE replacement 5%, 10%, and 20% was inferior to that of PP. In concrete, the HDPE material demonstrated 4.6 MPa and 4.75 MPa at 5% and 10% replacement, or

0.15 MPa and 0.18 MPa after seven days. A few researchers used plastic aggregates to perform and publish their findings on Flexural strength [34–38]. The flexural strength increased when PET waste plastic was included at low partial replacement levels; the pattern changed when PET material was added in high doses [34]. As seen in Fig. 7, the flexural strength was almost identical after 28 and 56 days. It has been shown that the flexural strength of PP material rose by 1.4 MPa and 1.7 MPa for 28 and 56 days, respectively, as the curing period increased. The flexural strength of concrete was lowered by 0.5 MPa when 20% of PP material was added, but it increased to 1.4 MPa when 15% of PP material was substituted in the concrete. Fig. 7 illustrates how the RA concrete graph steadily climbed as the number of days it took to cure, in contrast to the inconsistent NA concrete graph.

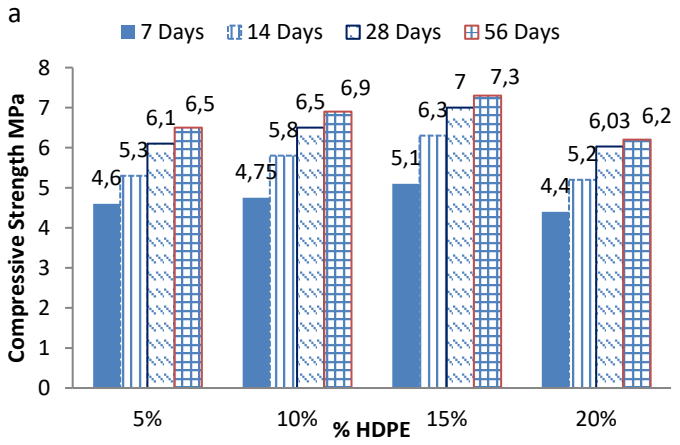

(a)

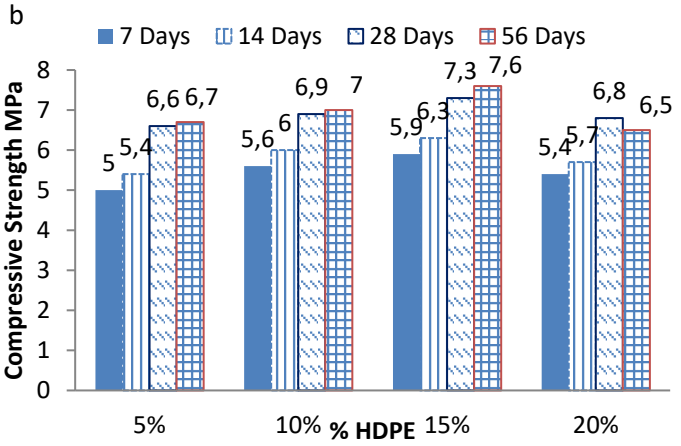

(b)

Fig. 7. Flexural strength of M40 grade concrete with a) HDPE and b) PP material

The flexural strength test increases the % of HDPE and the number of days. For the 7 days, the flexural strength test is increased by replacing 20% HDPE. For the 28 days replaced HDPE with 20%, the maximum flexural strength test is 6.50 MPa. The flexural strength of concrete with PP is partially replacement with fine aggregate. In replacement of 20% PP,

the flexural strength is increased by 0.10 MPa in 3 days, and for 7 days, with replacement of 20%, the flexural strength is decreased by 0.90 MPa. It was observed in Fig. 7 the flexural strength test is increased by 20%, and replacement for 28 days is increased, compared to 10%, and PP is increased by 0.20 MPa. It is observed from Fig. 7 that 100% of the RA used to prepare concrete with 15% HDPE and 15% PP material for flexural strength achieved more strength than the NA concrete mix. According to [35] showed the same pattern as in our study, but the concrete has improved by 10% replacement with plastic waste. According to the [39] experiment, the high PP material dosage showed a drastic reduction in flexural strength. A similar study conducted by [36] partially replaced with e-plastic showed that the flexural strength was below the value of conventional concrete. When 20% of plastic waste was replaced with FA, the maximum reduction was achieved after 28 days of curing. According to [40] has concluded that the waste plastic showed an increase in flexural strength of SCC up to 1.75% replacement by volume.

4.4 Split Tensile Strength

Fig. 8 displays the split tensile strength pattern for 7, 14, 28, and 56 days [34, 36, 41]. According to a related study, the split tensile strength may increase up to a specific optimal proportion of plastic waste, but the strength sharply decreases [34, 36]. At 15% replacement of HDPE in concrete, the maximum flexural strength of 0.91 MPa was recorded, 0.02 MPa less than PP after 7 days

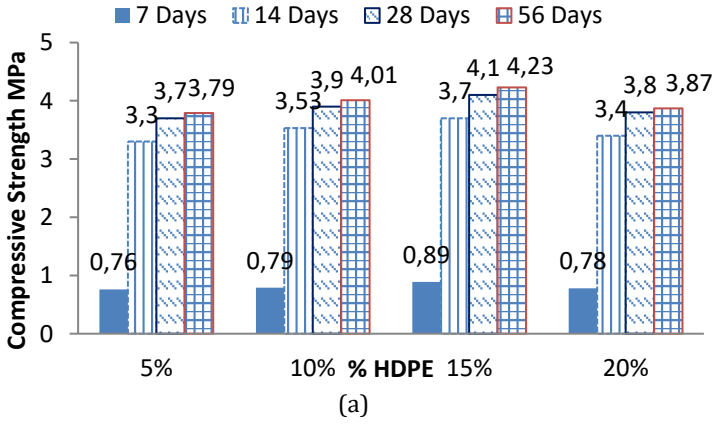

(a)

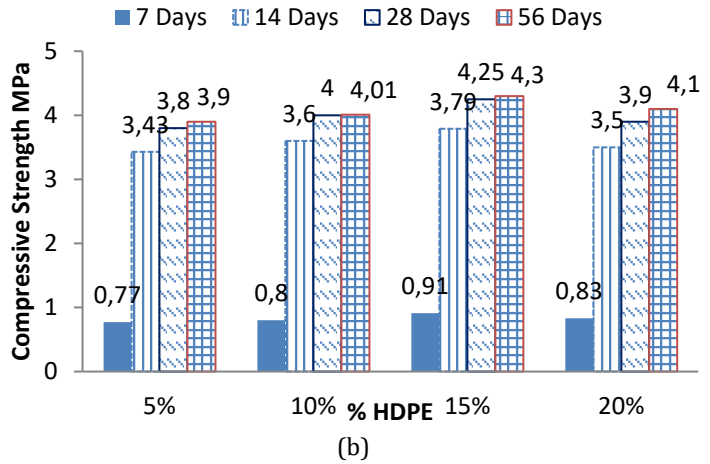

(b)

Fig. 8. Split tensile strength test a) HDPE and b) PP

. The flexural strength of the remaining HDPE replacement 5%, 10%, and 20% was inferior to that of PP. In concrete, the HDPE material demonstrated 0.76 MPa and 0.79 MPa at 5% and 10% replacement, or 0.25 MPa and 0.22 MPa after 7 days. As seen in Fig. 8, the tensile strength for 28 and 56 days was almost identical. The maximum strength for 15% PP material is 3.35 MPa for 28 days and 3.4 MPa for 56 days, respectively. The tensile strength of concrete was lowered by 0.35 MPa when 20% of PP material was added, but it increased to 0.35 MPa when 15% of PP material was substituted in the concrete. According to [9], PET material's substantial tensile properties can improve the tensile property by up to 10% in replacement of waste plastic compared to other concrete materials.

Compared to 100% RA, the 100% NA concrete has good results even with fewer days of curing. It is observed that the maximum strength for 15% HDPE and PP material is 4.23MPa and 4.3MPa for 28 days, respectively, more than RA concrete at 28 days. It is observed from Fig. 8 that 100% of the RA used to prepare concrete with 15% HDPE and 15% PP material for tensile strength achieved more strength than other mixes. According to [36], after 28 days of curing for 20% partial replacement of waste plastic has received maximum tensile strength. When the partial replacement was increased to 30%, it showed a drastic reduction. According to [42], the strength was reduced by 1.5% and 11% for 10% and 20% partial replacement of high-impact polystyrene (HIPS).

4.5 Prediction of RSM and ANN with actual Experimental for Compressive Strength

The experimentally tested values of EF-SCC cubes for CS, when predicted with RSM and ANN methods, are given in Table 5. When expected with ANN and RSM, the CS experimental (CS-EXP) for HDPE showed that the RSM method gave much more accurate results than ANN. The maximum percentage variation in prediction for RSM was positive 4.7% at 20% for 14 days of curing; similarly, the negative maximum percentage variation was 4.49 for 20% replacement but at 28 days. When ANN was analyzed, it showed a maximum percentage variation of -23.65% at 20% of HDPE at 7 days, similarly +14.64% for 5% replacement at 28 days of curing.

The RSM and ANN method was even predicted for PP material with different percentages at different days of curing. Both methods showed the same results as those that were tested. After 28 days of curing, the maximum CS of 48MPa was achieved with 15% replacement, and when it was predicted with RSM, it showed 0.199% variation, and ANN showed - 0.05% variation, a negligible percentage error. The CS achieved suitable mechanical properties even after being partially replaced by 15% with FA in EF-SCC. The recycled aggregate also showed a positive sign in using such waste material in construction industries.

Table 5. Actual and predicted compressive strength of M40 grade SCC using RSM and ANN method

Days (X1)	% (X2)	F.A. (X4)	HDPE/PP (Kg/m^3)	CS- EXP (HDPE)	ANN	RSM	CS-Exp (PP)	ANN	RSM
7	5%	60.52	3.21	29	28.16	30.10	30	29.92	30.47
7	10%	54.1	6.42	31	30.27	31.33	32.5	32.12	31.99
7	15%	44.47	9.63	32.5	31.38	32.76	33	32.98	33.13
7	20%	31.63	12.84	30	37.09	30.47	31	31.28	31.39
14	5%	60.52	3.21	37	30.24	35.88	37.5	34.20	36.75
14	10%	54.1	6.42	37.53	33.72	37.13	38	37.77	38.13
14	15%	44.47	9.63	39	38.09	38.50	39.5	39.42	39.40

14	20%	31.63	12.84	38	39.8	36.18	38	37.18	37.80
28	5%	60.52	3.21	44	37.55	43.73	45	44.55	45.28
28	10%	54.1	6.42	45	43.73	45.01	45.7	45.63	46.37
28	15%	44.47	9.63	46	46.38	46.27	48	48.02	47.90
28	20%	31.63	12.84	42	44.76	43.88	47	46.83	46.58
56	5%	60.52	3.21	44.3	44.77	44.57	46.2	46.12	46.18
56	10%	54.1	6.42	45.9	44.65	45.94	47	44.75	46.69
56	15%	44.47	9.63	47	49.38	46.95	48.7	48.87	48.75
56	20%	31.63	12.84	45	48.01	44.44	47.8	48.82	48.00

CS-EXP (HDPE) = Compressive strength –Experimented for HDPE material; CS-EXP (PP)= Compressive strength –Experimented for PP material; RSM= Response Surface Method; ANN= Artificial Neural Network.

5. Conclusion

The present study ascertains the optimum percentage of HDPE and PP material in workability and mechanical properties of EF-SCC, which was experimentally and statistically evaluated.

- In the slump flow table test, it was found that waste plastic made of HDPE and PP with 20% replacement exhibited 708 mm and 702 mm, respectively. These results fall inside the permitted ranges specified by EFNARC (2002), which is 650 mm to 800 mm.
- The highest compressive strengths of 47 MPa and 48.7 MPa were attained by replacing 15% of the HDPE and PP in the EF-SCC.
- It is recommended that in RA and NA concrete, the compressive strength of both HDPE and PP materials should grow to 15% in replacement, after which the strength should decline.
- For PP materials, the RSM technique regression analysis yielded a result of 99.69%, whereas for HDPE materials, the result was 98.17%.
- With a few exceptions, the P-value from the Pareto analysis revealed values between 0 and 0.005.
- It is evident from Fig. 5 that the material at 7.5% HDPE and 5% PP reached the ideal compressive strength values after 28 days. Surface plot analysis revealed the similar pattern during 60 days of curing.
- For M40 grade concrete for HDPE and PP material, the training, validation, test, and all values of R are, respectively, 0.9955, 0.9980, 0.9244, 0.9241, and 1, 0.972, 0.802, 0.972. R stands for linear correlation coefficient.
- For both materials, the EF-SCC's flexural strength demonstrated the greatest results at 15% replacement.
- In the split tensile test, the NA performed better than the RA. In the split tensile test, a similar pattern to that of flexural strength was noted, with the greatest results for both materials coming at 15% replacement.
- The prediction values of the RSM and ANN techniques for PP material were considerably more accurate; 11 out of 16 values indicated the same projected value. • The prediction of real compressive strength using RSM offered correct results for HDPE material compared with ANN.
- The utilization of such waste material in the building industry appeared to be beneficial for recycled aggregate as well.

6. Further Studies

It is recommended that microstructural properties be conducted in different thermal properties and that different waste plastics are used in various types and other grades of concrete.

Reference

[1] Ghaly AM, Gill MS. Compression and deformation performance of concrete containing post-consumer plastics. J Mater Civ Eng. 2004;16(4):289-96. https://doi.org/10.1061/(ASCE)0899-1561(2004)16:4(289)
[2] Naik TR, Singh SS, Huber CO, Brodersen BS. Use of post-consumer waste plastics in cement-based composites. Cem Concr Res. 1996;26(10):1489-92. https://doi.org/10.1016/0008-8846(96)00135-4
[3] Choi YW, Moon DJ, Kim YJ, Lachemi M. Characteristics of mortar and concrete containing fine aggregate manufactured from recycled waste polyethylene terephthalate bottles. Constr Build Mater. 2009;23(8):2829-35. https://doi.org/10.1016/j.conbuildmat.2009.02.036
[4] Choi YW, Moon DJ, Chung JS, Cho SK. Effects of waste PET bottles aggregate on the properties of concrete. Cem Concr Res. 2005;35(4):776-81. https://doi.org/10.1016/j.cemconres.2004.05.014
[5] Marzouk OY, Dheilly RM, Queneudec M. Valorization of post-consumer waste plastic in cementitious concrete composites. Waste Manag. 2007;27(2):310-8. https://doi.org/10.1016/j.wasman.2006.03.012
[6] Albano C, Camacho N, Hernández M, Matheus A, Gutiérrez A. Influence of content and particle size of waste PET bottles on concrete behavior at different w/c ratios. Waste Manag. 2009;29(10):2707-16. https://doi.org/10.1016/j.wasman.2009.05.007
[7] Islam MJ, Meherier MS, Islam AKMR. Effects of waste PET as coarse aggregate on the fresh and harden properties of concrete. Constr Build Mater. 2016;125:946-51. https://doi.org/10.1016/j.conbuildmat.2016.08.128
[8] Batayneh M, Marie I, Asi I. Use of selected waste materials in concrete mixes. Waste Manag. 2007;27(12):1870-6. https://doi.org/10.1016/j.wasman.2006.07.026
[9] da Luz Garcia M, Oliveira MR, Silva TN, Castro ACM. Performance of mortars with PET. J Mater Cycles Waste Manag. 2021;23(2):699-706. https://doi.org/10.1007/s10163-020-01160-w
[10] Frigione M. Recycling of PET bottles as fine aggregate in concrete. Waste Manag. 2010;30(6):1101-6. https://doi.org/10.1016/j.wasman.2010.01.030
[11] Umasabor RI, Daniel SC. The effect of using polyethylene terephthalate as an additive on the flexural and compressive strength of concrete. Heliyon. 2020;6(8). https://doi.org/10.1016/j.heliyon.2020.e04700
[12] Kim SB, Yi NH, Kim HY, Kim JHJ, Song YC. Material and structural performance evaluation of recycled PET fiber reinforced concrete. Cem Concr Compos. 2010;32(3):232-40. https://doi.org/10.1016/j.cemconcomp.2009.11.002
[13] Kayali O, Haque MN, Zhu B. Some characteristics of high strength fiber reinforced lightweight aggregate concrete. Cem Concr Compos. 2003;25(2):207-13. https://doi.org/10.1016/S0958-9465(02)00016-1
[14] Islam MJ, Shahjalal M. Effect of polypropylene plastic on concrete properties as a partial replacement of stone and brick aggregate. Case Stud Constr Mater. 2021;15. https://doi.org/10.1016/j.cscm.2021.e00627
[15] Sjah J, Chandra J, Rastandi JI. The effect of usage of crushed polypropylene plastic waste in mechanical properties of concrete. Int J Civ Eng Technol. 2018;9(7):1495-505.
[16] Ozbakkaloglu T, Gu L, Gholampour A. Short-term mechanical properties of concrete containing recycled polypropylene coarse aggregates under ambient and elevated

temperature. J Mater Civ Eng. 2017;29(10). https://doi.org/10.1061/(ASCE)MT.1943-5533.0002046
[17] Yang S, Yue X, Liu X, Tong Y. Properties of self-compacting lightweight concrete containing recycled plastic particles. Constr Build Mater. 2015;84:444-53. https://doi.org/10.1016/j.conbuildmat.2015.03.038
[18] Kou SC, Lee G, Poon CS, Lai WL. Properties of lightweight aggregate concrete prepared with PVC granules derived from scraped PVC pipes. Waste Manag. 2009;29(2):621-8. https://doi.org/10.1016/j.wasman.2008.06.014
[19] Senthil Kumar K, Baskar K. Recycling of E-plastic waste as a construction material in developing countries. J Mater Cycles Waste Manag. 2015;17(4):718-24. https://doi.org/10.1007/s10163-014-0303-5
[20] Yin S, Tuladhar R, Sheehan M, Combe M, Collister T. A life cycle assessment of recycled polypropylene fibre in concrete footpaths. J Clean Prod. 2016;112:2231-42. https://doi.org/10.1016/j.jclepro.2015.09.073
[21] Dawood AO, Al-Khazraji H, Falih RS. Physical and mechanical properties of concrete containing PET wastes as a partial replacement for fine aggregates. Case Stud Constr Mater. 2021;14. https://doi.org/10.1016/j.cscm.2020.e00482
[22] Saikia N, de Brito J. Mechanical properties and abrasion behaviour of concrete containing shredded PET bottle waste as a partial substitution of natural aggregate. Constr Build Mater. 2014;52:236-44. https://doi.org/10.1016/j.conbuildmat.2013.11.049
[23] Yerramala S. Properties of concrete with eggshell powder as cement replacement. Indian Concr J. 2014;88:94-105.
[24] Ofuyatan MO, Adeniyi AG, Ijie D, Ighalo JO, Oluwafemi J. Development of high-performance self-compacting concrete using eggshell powder and blast furnace slag as partial cement replacement. Constr Build Mater. 2020;256:119403. https://doi.org/10.1016/j.conbuildmat.2020.119403
[25] Ofuyatan MO, Edeki SO. Dataset on predictive compressive strength model for self-compacting concrete. Data Brief. 2018;17:801-6. https://doi.org/10.1016/j.dib.2018.02.008
[26] Ofuyatan MO, Edeki SO. Dataset on the durability behavior of palm oil fuel ash self compacting concrete. Data Brief. 2018;19:853-8. https://doi.org/10.1016/j.dib.2018.05.121
[27] Rantung D, Supit SWM, Nicolaas S. Effects of different size of fly ash as cement replacement on self-compacting concrete properties. J Sustain Eng Proc Ser. 2019;1(2):180-6. https://doi.org/10.35793/joseps.v1i2.25
[28] Iqbal S, Ali A, Holschemacher K, Ribakov Y, Bier TA. Effect of fly ash on properties of self-compacting high strength lightweight concrete. Period Polytech Civ Eng. 2017;61:81-7. https://doi.org/10.3311/PPci.8171
[29] Guo Z, Jiang T, Zhang J, Kong X, Chen C, Lehman DE. Mechanical and durability properties of sustainable self-compacting concrete with recycled concrete aggregate and fly ash. Constr Build Mater. 2020;231:117115. https://doi.org/10.1016/j.conbuildmat.2019.117115
[30] Ardalan RB, Joshaghani A, Hooton RD. Workability retention and compressive strength of self-compacting concrete incorporating pumice powder and silica fume. Constr Build Mater. 2017;134:116-22. https://doi.org/10.1016/j.conbuildmat.2016.12.090
[31] Cheng E, Sun X. Effects of wood-surface roughness, adhesive viscosity and processing pressure on adhesion strength of protein adhesive. J Adhes Sci Technol. 2006;20(9):997-1017. https://doi.org/10.1163/156856106777657779
[32] Adeniyi AG, Igwegbe CA, Ighalo JO. ANN Modelling of the adsorption of herbicides and pesticides based on sorbate-sorbent interphase. Chem Africa. 2021;4(2):443-9. https://doi.org/10.1007/s42250-020-00220-w

[33] Ighalo JO, Adelodun AA, Adeniyi AG, Igwegbe CA. Modelling the effect of sorbate-sorbent interphase on the adsorption of pesticides and herbicides by historical data design. Iranica J Energy Environ. 2020;11:253-9. https://doi.org/10.5829/IJEE.2020.11.04.02
[34] Azhdarpour AM, Nikoudel MR, Taheri M. The effect of using polyethylene terephthalate particles on physical and strength-related properties of concrete: A laboratory evaluation. Constr Build Mater. 2016;109:55-62. https://doi.org/10.1016/j.conbuildmat.2016.01.056
[35] Pirzada RA, Kalra T, Laherwal FA. Experimental study on use of waste plastic as coarse aggregate in concrete with admixture superplasticizer polycarboxylate ether. Int Res J Eng Technol. 2018;5(03):558-63.
[36] Manjunath BTA. Partial replacement of E-plastic waste as coarse-aggregate in concrete. Procedia Environ Sci. 2016;35:731-9. https://doi.org/10.1016/j.proenv.2016.07.079
[37] Bulut HA, Şahin R. A study on mechanical properties of polymer concrete containing electronic plastic waste. Compos Struct. 2017;178:50-62. https://doi.org/10.1016/j.compstruct.2017.06.058
[38] Sadrmomtazi A, Dolati-Milehsara S, Lotfi-Omran O, Sadeghi-Nik A. The combined effects of waste Polyethylene Terephthalate (PET) particles and pozzolanic materials on the properties of self-compacting concrete. J Clean Prod. 2016;112:2363-73. https://doi.org/10.1016/j.jclepro.2015.09.107
[39] Záleská M, Pavlíková M, Pokorný J, Jankovský O, Pavlík Z, Černý R. Structural, mechanical and hygrothermal properties of lightweight concrete based on the application of waste plastics. Constr Build Mater. 2018;180:1-11. https://doi.org/10.1016/j.conbuildmat.2018.05.250
[40] Al-Hadithi AI, Hilal NN. The possibility of enhancing some properties of self-compacting concrete by adding waste plastic fibers. J Build Eng. 2016;8:20-8. https://doi.org/10.1016/j.jobe.2016.06.011
[41] Kou SC, Lee G, Poon CS, Lai WL. Properties of lightweight aggregate concrete prepared with PVC granules derived from scraped PVC pipes. Waste Manag. 2009;29:621-8. https://doi.org/10.1016/j.wasman.2008.06.014
[42] Wang R, Meyer C. Performance of cement mortar made with recycled high impact polystyrene. Cem Concr Compos. 2012;34:975-81. https://doi.org/10.1016/j.cemconcomp.2012.06.014
[43] Thorneycroft J, Orr J, Savoikar P, Ball RJ. Performance of structural concrete with recycled plastic waste as a partial replacement for sand. Constr Build Mater. 2018;161:63-9. https://doi.org/10.1016/j.conbuildmat.2017.11.127
[44] Arulrajah A, Yaghoubi E, Wong Y, Horpibulsuk S. Recycled plastic granules and demolition wastes as construction materials: Resilient moduli and strength characteristics. Constr Build Mater. 2017;147:639-47. https://doi.org/10.1016/j.conbuildmat.2017.04.178
[45] Kalantarov AI, Prosanov IV, Kadomtseva YV, Vinogradova OV. Using waste polyethylene as a substitute for sand in the production of polymer concrete. Inorg Mater Appl Res. 2021;12:182-6.

Research on Engineering Structures & Materials
www.jresm.org
Research Group

Research Article

Fracture behavior of concrete made with sintered fly ash lightweight coarse aggregate in comparison to normal weight concrete

Brijesh Singh[1,*,a], Shamsher Bahadur Singh[2,b], Sudhirkumar V. Barai[2,c], P. N. Ojha[3,d], Rohit Kumar[3,e]

[1]*Birla Institute of Technology & Sciences Pilani, Pilani & Group Manager at National Council for Cement and Building Materials, Ballabgarh, India*
[2]*Department of Civil Engineering, Birla Institute of Technology and Sciences Pilani, Pilani, India*
[3]*National Council for Cement and Building Materials, Ballabgarh, India*

Article Info

Article history:

Received 07 June 2024
Accepted 19 Aug 2024

Keywords:

Sintered fly ash lightweight aggregate; Normal weight concrete; Lightweight concrete; Fracture energy; Load-CMOD; Load-deflection; Stress intensity factor; Characteristic length

Abstract

Sintered fly ash lightweight aggregate based concrete has been reported to give mechanical and durability properties similar to conventional concrete. But concrete made up of lightweight aggregate possesses lower stiffness and shear strength resulting into a brittle mode of failure due to crack propagating directly inside aggregate which is weak in nature. The study presents findings from the experimental investigation of fracture behavior of concrete made with sintered fly ash lightweight coarse aggregate in comparison to normal weight concrete (NWC) at w/b ratio of 0.5, 0.4 and 0.3. The mixes have been tested for compressive and split tensile strength for both concrete types. On notched beams of size 100x 100 x 500 mm, a three-point bend test has been carried out for both lightweight and normal weight concrete to evaluate fracture parameters. The results of split tensile strength test indicated that the split tensile to compressive strength ratio lies in the range of 5-8% for lightweight concrete and this ratio lies between 5-10% for normal weight concrete. The study indicates comparable fracture behavior for both lightweight and normal weight concrete. The non-linear ascending and descending branches in load vs deflection curve of concrete with sintered fly ash lightweight coarse aggregate can be linked with the non-linearity in tensile type stress-strain behavior and formation of the fracture zone in front of the initial notch. The modulus of elasticity of lightweight concrete is significantly lower than normal concrete. The modulus of elasticity, area under the load deflection curve, tensile strength, fracture behavior etc. needs to be considered appropriately in the non-linear analysis of lightweight concrete.

1. Introduction

Sintered fly ash lightweight concrete nowadays is getting used in construction industry because of its reduced dead load, improved durability performance, better thermal and sound insulation along with improved fire resistance [1-2]. Apart from this lower water permeability, lower chloride ion penetration and better corrosion resistance of lightweight concrete (LWC) makes it more durable as compared to normal concrete. The density of structural lightweight aggregate concrete generally varies from 1100 to 1900 kg/m^3 having minimum compressive strength of 17 MPa [3]. Sintered fly ash lightweight aggregate is mainly produced from fly ash through sintering process [1-2]. LWC has improved mechanical, durability and thermal properties but one drawback or limitation of

*Corresponding author: brijeshsehwagiitr96@gmail.com
[a] orcid.org/0000-0002-6512-1968; [b]orcid.org/0000-0001-6847-0701; [c]orcid.org/0000-0001-5100-0607; [d]0000-0003-1754-4488; [e]orcid.org/0009-0000-6167-375X
DOI: http://dx.doi.org/10.17515/resm2024.310me0607rs

any concrete is its non-ductile (brittle) behavior and low crack resistance. This brittle behavior of concrete limits flexural load carrying capacity and can be extremely critical in earthquakes [3-7]. Due to the brittle nature, concrete structures are bound to undergo cracking under flexural loads and can fail suddenly without showing any signs of warning. The fracture performance of normal concrete has been investigated deeply in the past four to five decades resulting in thorough understanding and development of numerical models related to fracture behavior [5]. The numerous non-linear fracture mechanics models have been developed and are being used such as the fictitious crack model by Hillerborg et al. [6]. the crack band model by Bazant et al. [7] and the two-parameter model by Jenq and Shah [8]. These models have been successfully used in the analysis of non-linear behavior of concrete structures. The estimation of brittleness and ductility of concrete can be quantified through its fracture properties [9-11]. RILEM [12-13] gives a three-point bend test procedure on a notched beam to evaluate the fracture properties for concrete. Fracture energy is key fracture parameters used to compare or analyze the concrete cracking resistance and toughness. RILEM defines fracture energy as the quantum of energy needed to develop a crack with unit area. Other than fracture energy, other indicators of fracture behavior are initial load compliance, stress intensity factor, energy release rate, toughness and characteristic length. Fracture toughness can be expressed as ability of brittle material such as concrete to withstand crack formation under loading. The energy release rate is defined as energy transformation rate during propagation of fracture in concrete.

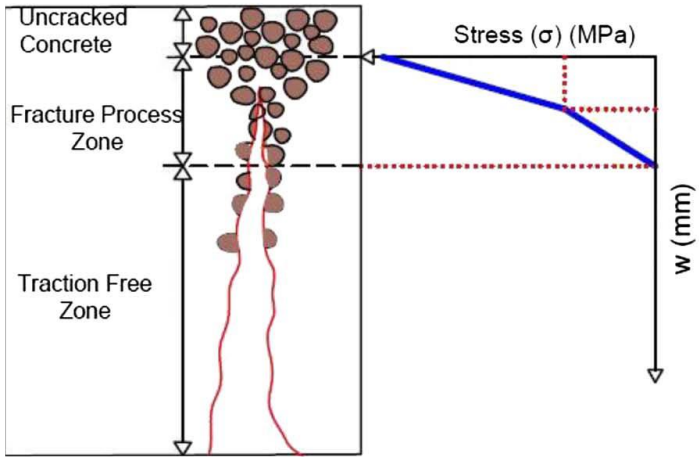

Fig. 1. Stress-crack width response of structural lightweight aggregate concrete [14]

Characteristic length of concrete is indicator of its brittleness and is inversely proportional to characteristic length [9]. In the LWC, there exists three fracture zones (a) traction free zone, (b) fracture process zone, (c) un-cracked zone (Figure-1) [14]. The traction across the coherent surface goes up to maximum load and thereafter drastically reaches to zero as per the multilinear stress-crack width model (Figure-1) [14]. Trivedi et al. [15] studied three approaches for determining fracture behavior of concrete such as Bi-linear approximation, RILEM procedure, and energy release rate to evaluate the fracture energy independent of size and observed similar results suggesting that either of three approaches are applicable. Study done by Murthy et al. [16] on tension softening relation and fracture energy for nano concrete highlighted that notch/depth has a major influence when RILEM method is used for fracture energy determination. Studies on the effect of silica fume as supplementary cementitious materials in normal weight concrete along with distribution of various sizes of aggregate on its fracture behavior are reported by Gil et al. [17] wherein an optimum dose of silica fume for fracture toughness and peak strength has

been reported. According to Siregar et al. [18], ductility of high-strength concrete is affected by the w/b and size of aggregate wherein the aggregate strength decides peak fracture energy.

The study of literature has indicated that numerous studies are carried out on the performance of structural grade lightweight concrete using natural or artificial lightweight aggregate and has evaluated its mechanical and durability performance. However, studies on fracture performance of sintered fly ash lightweight aggregate based concrete is scanty. The comparison of fracture energy and related parameters of plain lightweight concrete with sintered fly ash lightweight coarse aggregate in comparison to normal weight concrete with natural coarse aggregate is not available in the literature. The current study also investigates the water absorption potential for dry state sintered fly ash lightweight aggregate from cement matrix. The paper presents a simplified mix design procedure for lightweight concrete produced from commercially available sintered fly ash lightweight aggregate. The findings of the study will highlight modulus of elasticity, load vs deflection behavior, tensile properties, fracture phenomena, brittleness, crack propagation etc. of LWC compared to normal concrete which would help in non-linear analysis of critical structures such as buildings in high seismic zones, dams, nuclear structures etc. where unstable and sudden crack propagation could lead to disaster. The study findings will also promote enhancement in adoption of sintered fly ash lightweight coarse aggregate in concrete in construction industry leading to conservation of natural resources and production of sustainable concrete.

The study presents findings from the experimental results of fracture behavior of concrete made with sintered fly ash lightweight coarse aggregate in comparison to normal weight concrete (NWC). The w/b ratio adopted for concrete mix preparation has been 0.5, 0.4 and 0.3 wherein (a) three mixes has been prepared with sintered fly ash lightweight coarse aggregate and (b) three mixes has been prepared with natural granite coarse aggregate. The 28-day cube compressive and split tensile strength are determined as procedure given in IS code [19]. The three mixes have shown compressive strength of 39.25, 51.52 and 58.73 MPa for concrete made with sintered fly ash lightweight coarse aggregate. The three mixes have shown compressive strength of 43.35, 55.72 and 68.93 MPa for concrete made with natural granite coarse aggregate. The fracture energy is calculated as per RILEM procedure. Fracture performance has been evaluated at 28-day by determining modulus of elasticity, fracture energy, initial load compliance, energy release rate, stress intensity factor and characteristic length

2. Materials

In this study for production of normal weight concrete, OPC cement (43 Grade), coarse and fine aggregates, silica fume, superplasticizer and water are used. In the study, crushed fine aggregate that conforms with Zone II of IS: 383-2016 [20] has been used as fine aggregate and coarse aggregate having maximum nominal size of 20 mm has been used. Figure 2(a) displays the fine aggregate, while Figure 2(b) displays the coarse aggregate. Table 1 displays the physical characteristics of both coarse and fine aggregate.

The mechanical characteristics of sintered fly ash coarse aggregate is presented in Table-2. The sintered fly ash lightweight aggregate is brown in color as shown in Figure-3 and has black core. The microstructure of sintered fly ash lightweight aggregate has been shown in Figure-4. The samples of sintered fly ash lightweight aggregate (LWA) (two fractions 8-16 mm and 4-8 mm) have been used as coarse aggregate. The chemical composition of sintered fly ash lightweight aggregate, OPC cement 43 grade (as per IS: 269 [21]) and silica fume is given in Table-3. The fineness of OPC cement is 320 m^2/kg and silica fume is 22000 m^2/kg.

(a) (b)

Fig. 2. (a) Fine aggregate (stone dust) and (b) Coarse aggregate (granite)

(a) (b)

Fig. 3. (a) Sintered fly ash lightweight aggregate, Fraction: 4-8 mmand (b) Sintered fly ash lightweight aggregate, fraction: 8-16 mm

Table 1. Aggregates properties

Property		Granite		Sintered Fly ash Lightweight Aggregate		Fine Aggregate
		20 mm	10 mm	8-16 mm	4-8 mm	
Specific gravity		2.82	2.81	1.49	1.47	2.65
Water absorption (%)		0.3	0.3	17.93	17.50	0.59
Sieve Analysis Cumulative Percentage Passing (%)	20mm	97	100	100	100	100
	10 mm	2	66	30	100	100
	4.75	0	2	0	13	99
	2.36	0	0	0	2	89
	1.18	0	0	0	0	64
	600 µ	0	0	0	0	43
	300 µ	0	0	0	0	26
	150 µ	0	0	0	0	14
	Pan	0	0	00	0	0

For preparation of concrete mixes for LWC, the fine aggregate (crushed stone) used in study conforms to IS: 383-2016. Also, for LWC crushed fine aggregate that conforms with Zone II of IS: 383-2016 [20] has been used as fine aggregate The polycarboxylic type chemical admixture conforming to Indian Standard IS:9103[22] has been used for all mixes.

Fig. 4. Microstructure of sintered fly ash lightweight aggregate (10 μm and 1.5x)

Table 2. Mechanical properties of sintered fly ash lightweight aggregate used in study

Fraction	LWA designation	Specific gravity	Water absorption at 24 hours (%)	Loose bulk density (kg/m^3)	Crushing Strength (N/mm^2)	10 % Fines (Ton)
4-8 mm	LWA-I	1.47	17.50	813	8.80	-
8-16 mm	LWA-II	1.49	17.93	849	7.70	3.60

Table 3. Chemical composition of sintered fly ash lightweight aggregate and OPC cement

Component	CaO (%)	SiO_2 (%)	Al_2O_3 (%)	Fe_2O_3 (%)	SO_3 (%)	MgO (%)	Na_2O Equivalent (%)	Loss of Ignition
Sintered fly ash lightweight aggregate	2.45	62.50	25.85	4.19	0.29	0.53	0.77	1.48
Cement OPC 43 grade	59.60	21.22	7.19	4.25	2.50	1.90	1.05	1.94
Silica fume	-	95.02	-	0.80	-	-	-	1.16

3. Concrete Mix Design and Details of Specimen

3.1. Concrete Mix Design

3.1.1 Normal Concrete Mix Design

The w/b ratio adopted for concrete mix preparation has been 0.5, 0.4 and 0.3 wherein (a) three mixes has been prepared with sintered fly ash lightweight coarse aggregate and (b) three mixes has been prepared with natural granite coarse aggregate. The slump has been kept in between 75 -100 mm. The mix design for normal weight concrete has been done in accordance with procedure given in IS: 10262-2019 [23]. The details of concrete mix are given in Table-4.

Table 4. Mix design details for normal weight concrete

w/b	Total Cementitious Content [Cement + Silica Fume (SF)] (Kg/m^3)	Water Content (Kg/m^3)	Admixture % by weight of Cement	Fine Aggregate (Kg/m^3)	Coarse Aggregate 20 mm (Kg/m^3)	Coarse Aggregate 10 mm (Kg/m^3)	28-Day strength of concrete (N/mm^2)
0.50	340 (316+24)	170	0.50	660	775	516	43.35
0.40	425 (382+43)	170	0.80	580	775	515	55.72
0.30	566 (481+85)	170	1.00	493	742	495	68.93

3.1.2 Lightweight Concrete (LWC) Mix Design

The sintered fly ash lightweight aggregate is porous in nature with very high-water absorption as compared to conventional natural aggregate. When lightweight aggregate is added in dry condition with water correction equal to water absorption of aggregate, it leads to segregation of mix in fresh state as well increase in net free water to cement ratio leading to reduction in strength in hardened state. Secondly, the direct correction of water absorption does not take into account the effect of cement paste and in actual condition it is the cement paste and not water alone which dictates the water absorption potential of lightweight aggregates. This problem can be tackled by use of lightweight aggregate in dry state condition with appropriate correction in water absorption taking into account the effect of cement paste for given water cement ratio of concrete mix.

The mix design for LWC with sintered fly ash lightweight coarse aggregate has been done in accordance with procedure given in Indian Standard IS: 10262-2019 [23] and curve has been developed for water absorption correction of aggregate. The sintered fly ash lightweight aggregate is highly porous and its water absorption is about 18 percent. In the present study, the combined aggregate grading given in IS: 9142-2018 [24] has been adopted. The absorption potential of sintered fly ash lightweight aggregate has been determined in the study wherein moisture content of lightweight aggregates have been known. Initially the moisture content and initial weight of the aggregate have been recorded. The mortar pastes of w/b 0.7 has been prepared and placed in container. Twenty-five aggregates have been first placed in a cement paste present in the container for each period of 5, 15, 30, 45 and 60 minutes to decide optimum absorption period (soaking period). After the specified period of absorption, the lightweight aggregates have been removed from the cement paste and the excess cement paste attached to the outer surface of aggregates has been separated with help of nylon brush. The removal time of excess paste has been kept not more than one minutes to not absorb the water trapped in the aggregate particles which takes part in further hydration of cement paste. Thereafter, weight of aggregates has been measured. After this the aggregates have been placed inside an oven for period of 48 hours at a temperature of 105°C. Finally, dry weight of aggregate has been determined and aggregate absorption values have been determined. The total absorption by the lightweight coarse aggregate in terms of percentage is calculated as difference of mass of aggregate after 45 minutes of soaking and initial mass of aggregate before soaking divided by initial mass of aggregate before soaking multiplied by 100. The total water absorption by the lightweight coarse aggregate in terms of percentage is calculated as difference of mass of aggregate after 45 minutes of soaking and dry mass of aggregate after oven drying divided by dry mass of aggregate after oven drying multiplied by 100. The difference between the percentage of total absorption by the lightweight coarse aggregate and total water absorption by the lightweight coarse aggregate is termed as total paste absorption potential of lightweight coarse aggregate.

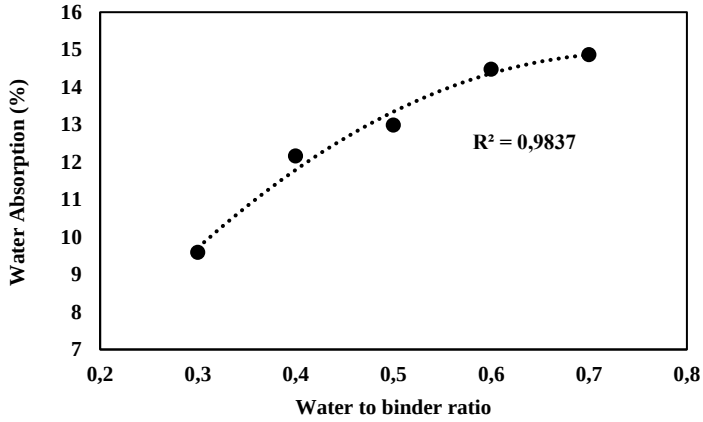

Fig. 5. Relationship between water absorption of sintered fly ash lightweight aggregate with water to cement ratio for 45 minutes absorption period

The water absorption values at w/b 0.70 for absorption period of 5, 15, 30, 45 and 60 minutes have been 12.84. 13.84, 14.36, 14.86, 14.90, respectively. Based on this study, 45 minutes absorption period for sintered fly ash lightweight aggregate has been considered in this study as the absorption capacity of the aggregates beyond this period has been almost negligible. Thereafter, this exercise has been repeated for mortar paste of w/b ratio of 0.3, 0.4, 0.5 and 0.6. Thereafter, correlation has been developed between sintered fly ash lightweight aggregate water absorption potential and different w/b ratios. The correlation developed is presented in Figure-5 for absorption period of 45 minutes. The correlation developed is to be used in water absorption correction of sintered fly ash lightweight aggregate used as coarse aggregate in concrete mix preparation. The brief of mix design procedure developed for production of concrete with sintered fly ash lightweight aggregate is given below:

- Step 1: Deciding w/b - w/b is main strength deciding factor for any concrete mix with all types of aggregate.
- Step 2: Fixing the quantity of water for mix-The quantity of water (kg/m^3) is decided based on the workability requirements of mix for specific situation. The free water content for sintered fly ash lightweight aggregate may be kept in range of 160 kg /m^3 to 210 kg/m^3. The guidance on free water content is taken here from ACI 211.
- Step 3: Determining cement content-The cement content (kg/m^3) is determined by dividing free water content by water to cement ratio.
- Step 4: Determining coarse and fine aggregates-The present method considers coarse aggregate (sintered fly ash lightweight aggregate) and fine aggregate based on the procedure given in IS: 10262-2019. An absolute volume approach is adopted in beginning for determining the quantity of total aggregate. Two fractions (8-16 mm and 4-8 mm) of sintered fly ash lightweight coarse aggregate has been used for mix proportioning. The coarse aggregate of both fractions has been combined in 60 % coarse aggregate 8-16 mm fraction and 40 % coarse aggregate 4-8 mm fraction. The combined aggregate grading meets the requirement of standard aggregate grading curve limit as per IS: 9142-2018. The water absorption correction for both fractions of sintered fly ash lightweight coarse aggregate and fine aggregate has been done. To consider the absorbed water by aggregate at the time of mixing of concrete, relationship between water absorption of sintered fly ash lightweight

aggregate with water to cement ratio given in Figure-5 has been adopted for calculating additional water requirements for lightweight aggregate in dry state condition.

- Step 5: Water absorption correction-The mass of compensated water required is determined as given below:
  - ⇒ Mass of additional water for coarse aggregate= Weight of coarse aggregate* water absorption potential of aggregate at the time of mixing
  - ⇒ Mass of extra water for coarse aggregate 8-16 mm= Weight of coarse aggregate 8-16 mm*total water absorption of aggregate related to chosen w/b
  - ⇒ Mass of extra water for coarse aggregate 4-8 mm Weight of coarse aggregate 4-8 mm*total water absorption of aggregate related to chosen w/b
- Step 6: Modification in concrete mix proportion-Whenever the compressive strength and workability requirements are not achieved, then proper modifications need to be done in concrete mixes along with dose of admixture until desired workability and strength properties of LWC has been achieved.

The mix design details of LWC have been given in Table-5. A 60 kg batch of concrete has been prepared for each concrete mix. Firstly, in the pan mixer both the fractions of lightweight coarse aggregate, fine aggregate and cement has been mixed to obtain homogenous mix and thereafter 80 percent water has been added and mixing has been done for period of 2-3 minutes. After that the remaining 20 percent water along with admixture has been added and mixing has been continued for another 2-3 minutes. It is to be noted that the initial mixing period is critical for sintered fly ash lightweight aggregate due to its absorption characteristics. Adjustment has been made in mixing water as a correction for aggregate water absorption.

Table 5. Concrete mix design of LWC

w/b	Total Cementitious Content [Cement + Silica Fume (SF)] (Kg/m^3)	Total water including aggregate water absorption correction (kg/m^3)	Admixture % by weight of Cement	Fine Aggregate (Kg/m^3)	Coarse Aggregate 10 mm (Kg/m^3)	Coarse Aggregate 20 mm (Kg/m^3)	28-Day strength of concrete (N/mm^2)
0.50	340 (316+24)	260	0.60	708	252	390	39.25
0.40	425 (382+43)	254	0.70	646	250	385	51.52
0.30	566 (481+85)	234	0.80	573	246	371	58.73

The molds have been cleaned properly and concrete cube has been compacted on vibration table wherein each of three layers have been properly compacted. The concrete cubes have been demoulded after 24-hours. The environmental conditions of laboratory have been 27±2°C temperature and 65% or more relative humidity. The concrete cube specimen has been tested in surface dried saturated condition. The concrete has been developed to maintain a slump in between 75-100 mm.

3.2. Details of Specimen

The concrete specimens of different size have been prepared for various tests discussed hereunder as per the standards and literature. The 28-day cube compressive strength has been determined as per procedure given in IS:516-2021 on cube size of 150 mm x 150 mm x 150 mm. The concrete cylinders of size 150 mm diameter and 300 mm height were cast for evaluating split tensile strength of concrete as per IS: 516-2021. For fracture study at 28-day age as per literature and RILEM procedure, the three point bend test has been performed on 100mm x 100mm x 500mm size concrete beam with notch depth as 35mm

(Figure-6). Table 6 gives details of specimens and Figure 5 displays the cast samples with molds.

Fig. 5 Concrete cubes, cylinders, and beams in molds

Fig. 6. Notched beam sample

Table 6. Details of specimen and tests performed

S. No.	Specimen	Dimension(mm)	Tests
1	Concrete Cubes	150 x150 x 150	Compressive strength at 28-day age
2	Concrete Cylinders	150 Diameter x 300 height	Split Tensile strength at 28-day age
3	Concrete Beams	100 x 100 x 500	3–Point bend test for fracture study

4. Experimental Method

The procedure adopted for determining fracture parameters are discussed in this section. The investigation includes compressive and split tensile strength and fracture parameter on notched beams using 3-point bend test.

4.1. 28-day Compressive and Split Tensile Strength Test

The 28-day cube compressive strength and 28–day split tensile strength has been determined as per IS: 516. These tests have been carried out on three specimens in a compression testing machine of capacity 3000 kN and the average value has been presented.

4.2. Study on Fracture Behavior Using Three-Point Bending Test

On notched beams of size 100 x 100 x 500 mm, a three point bend test has been carried out for both lightweight and normal weight concrete. The plot of Load vs CMOD (Crack Mouth Opening Displacement) and Load vs deflection have been used for determining the fracture behaviour of both types of concrete using various standards and RILEM recommendations. Fracture performance has been evaluated by determining modulus of elasticity, fracture energy, initial load compliance, energy release rate, stress intensity factor and characteristic length. In Figure-7 & Figure-8(a), the three point bend test diagram and in Figure 8 the test set up in laboratory has been shown. The 100mm x 100mm x 500mm size beam with a notch depth of 35mm has been created in middle of beam and clear span has been kept as 400 mm.

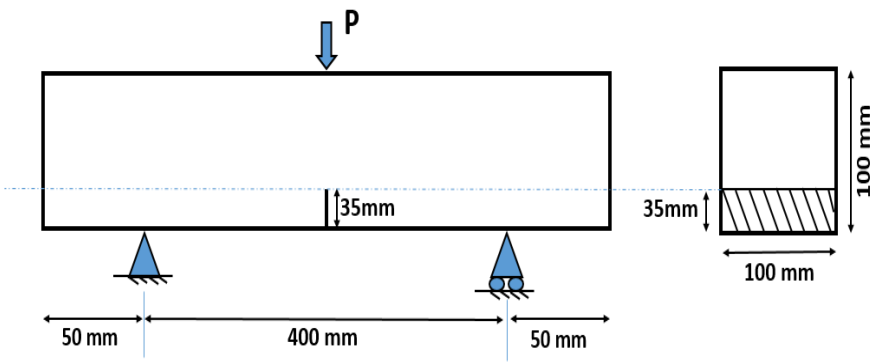

Fig. 7. Three-point bend test diagram

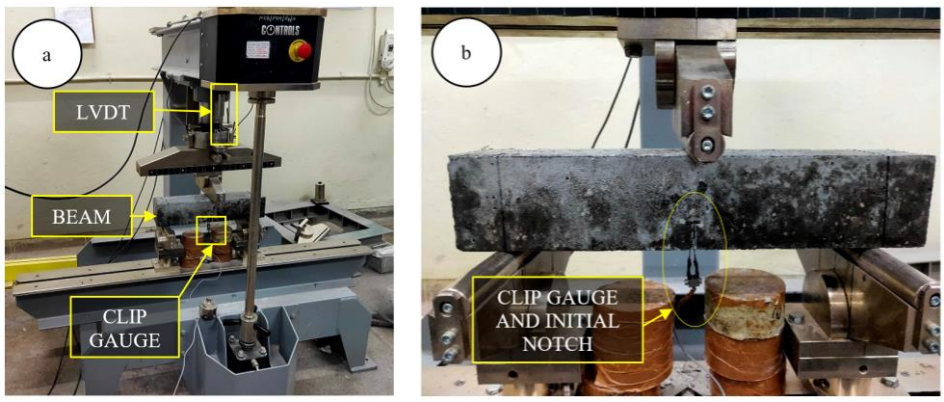

Fig. 8. (a) Typical setup for three-point bend test and (b) CMOD measurement using clip gauge

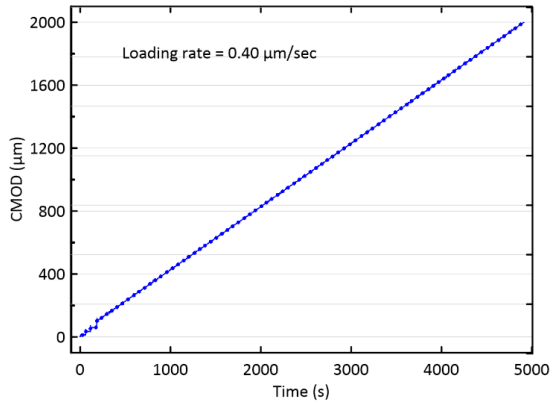

Fig. 9. Crack Mouth Opening Displacement (CMOD) vs time plot for the test

The load on beam specimen has been given through a displacement mode operated machine of 30T capacity. The mid-point beam delfection has been recoded using Crack Mouth Opening Displacement (CMOD) and Linear Variable Displacement Transducer (LVDT). The clip gauge using two nos. steel type knife edges have been placed at the bottom

of the beam for CMOD measurement as shown in Figure 8(b). Eighteen concrete beams have been evaluted for fracture performance study and out of which for each mix given in Table 4 and Table 5, the three beam specimens have been tested. The plot of CMOD vs time is shown in Figure-9. The test has been conducted in displacement operated mode in machine and loading rate for CMOD has been maintained at 0.40μm/s. The experiment continued to the point of failure of beam or to point where CMOD has been 1000 μm.

5. Test Results and Discussions

5.1. 28-day Compressive and Split Tensile Strength Test

Table 7 shows the results of the 28-day cube compressive strength and split tensile strength. The three mixes have shown compressive strength of 39.25, 51.52 and 58.73 MPa for LWC made with sintered fly ash lightweight coarse aggregate. The three mixes have shown compressive strength of 43.35, 55.72 and 68.93 MPa for normal weight concrete (NWC) made with natural granite coarse aggregate. From the results it is seen that split tensile to compressive strength ratio lies in between 5-8% for LWC. Whereas in the case of conventional concrete this ratio lies between 5-10%.

Fig. 10. Fractured LWC after split tensile test

Table 7. 28-day cube compressive strength and split tensile strength

w/b ratio	Type	28-day strength (MPa)	
		Cube Strength	Split Tensile Strength
0.50	LWC	39.25	2.26
0.40	LWC	51.52	3.08
0.30	LWC	58.73	3.20
0.50	NWC	43.35	3.76
0.40	NWC	55.72	3.90
0.30	NWC	68.93	4.42

This indicates that the tensile strength to compressive strength ratio of LWC is almost comparable to normal concrete [25]. The results indicate that the split tensile strength of both concrete types improves with reduction in w/b ratio. The observation of spitted surface of specimen indicates that the fracture path gets transferred through the aggregates in LWC (Figure-10). In case of LWC, it can be inferred that the bond between the cement paste matrix and the sintered fly ash lightweight aggregates are higher than the strength of aggregate. Because of low crushing strength of sintered fly ash lightweight

aggregate compared to natural aggregate, the LWC could not give similar split tensile strength for similar w/b ratio.

5.2 Load-CMOD and Load-Deflection Behavior

This section discusses the study of load-deflection and load-CMOD behavior of LWC and NWC for w/b ratio of 0.5, 0.4, 0.3 in Figures 11, 12 and 13, respectively. These graphs are used for the subsequent calculation of fracture parameters till the point of failure. The failure point is represented by sudden change in deflection without increase in load in load-deflection curve or sudden change in deflection without increase in load-CMOD curve. The comparison of load-CMOD and load-deflection behavior of LWC and NWC for all three concrete mixes indicates that ascending branches of load–deflection and load-CMOD curves of concrete with sintered fly ash lightweight coarse aggregate are similar to normal weight concrete. The non-linear ascending and descending branches in flexural curves of concrete with sintered fly ash lightweight coarse aggregate can be linked with the non-linearity in tensile mode stress-strain behavior and formation of the process zone of fracture in front of the initial notch. The significant difference in elastic modulus of aggregate and cement paste in LWC system with w/b ratio of 0.3 gives further non-linearity in load-CMOD curves and load–deflection of concrete with sintered fly ash lightweight coarse aggregate.

In LWC with w/b 0.3, larger fracture process zone gets developed before the peak because of weaker aggregate to paste bond. The exact reason behind the flat flexural curves in LWC compared to normal weight concrete is not fully understood and one of the reasons can be tortuous crack path in LWC compared to normal concrete. The hard out shell of sintered fly ash lightweight aggregate also provides some crack resistance because of which more crack formation gets diverted to aggregate-cement paste bond than across aggregates particularly for high strength LWC.

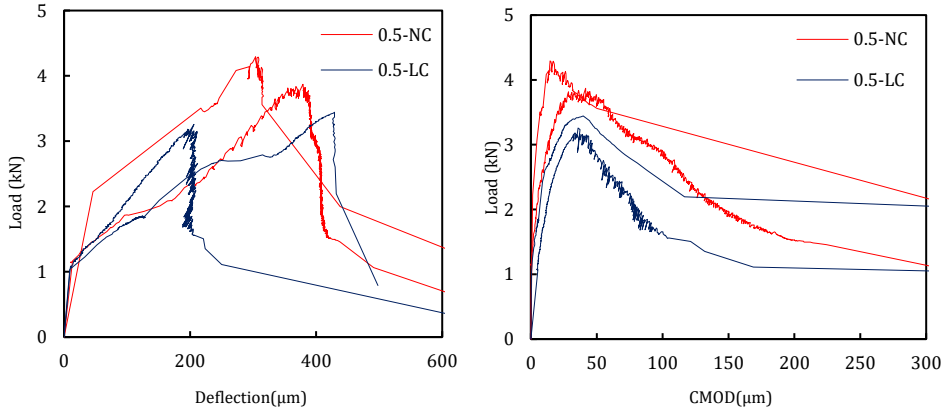

(a) (b)

Fig. 11. w/b ratio 0.5 (a) Load Vs deflection curve and (b) Load Vs CMOD curve

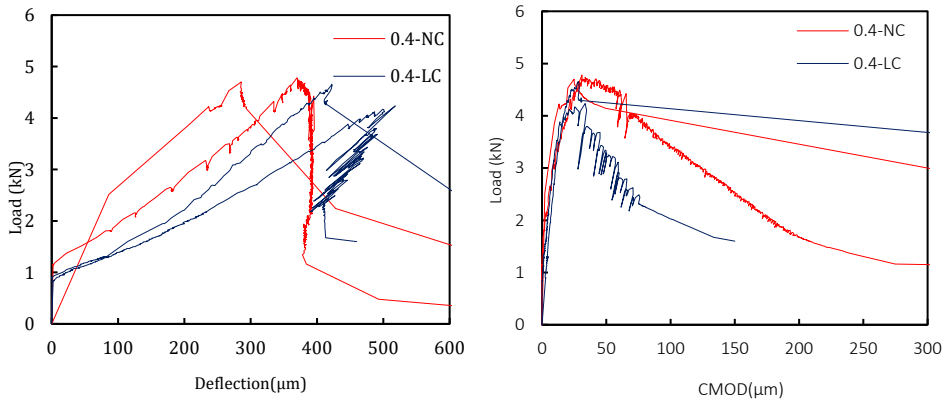

(a) (b)

Fig. 12. w/b ratio 0.4 (a) Load Vs deflection curve and (b) Load Vs CMOD curve

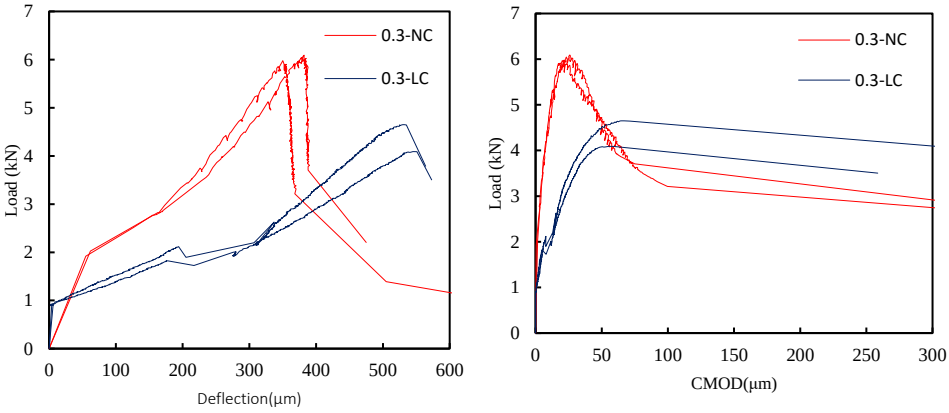

(a) (b)

Fig. 13. w/b ratio 0.30 (a) Load Vs deflection curve and (b) Load Vs CMOD curve

5.3 Fracture Energy

Fracture energy can be termed as the quantum of energy needed to develop a crack with unit area, it is denoted by G_f. It is a critical parameter that is used to examine and assess concrete crack resistance, brittleness and toughness. Fracture energy is calculated by the formula from RILEM 50 [12] given in (1);

$$G_f(N/m) = (W_o + mg\delta_o)/A_{lig} \quad (1)$$

where,

G_f = Fracture energy

W_o = Area below the load-deflection plot as shown in Figure 14.

m = beam mass between the support along with mass of loading arrangement which is not attached to machine

g = Acceleration due to gravity, i.e., 9.81 m/s^2.

δ_o = Deflection of the specimen at failure

A_{lig} = Area of the ligament

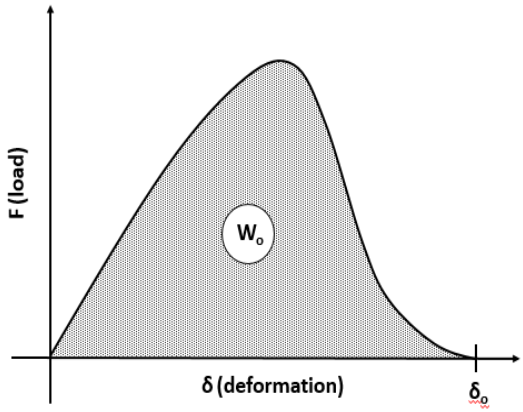

Fig. 14. Area within load and mid-point deflection plot of beam [27]

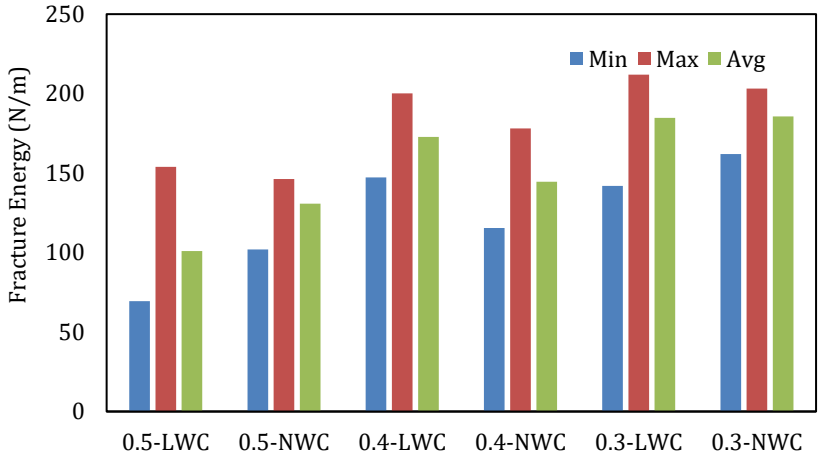

Fig. 15. Fracture energy for w/b ratio of 0.47, 0.36 and 0.20

The comparison of fracture energy of the mix of LWC and NWC at different w/b ratio is presented in Figure 15. The fracture energy in case of NWC increases with increase in strength or with decrease in w/b ratio. The same pattern for fracture energy is observed for LWC. It is also observed that fracture energy for LWC and NWC for w/b ratio 0.3 is comparable but for LWC and NWC for w/b ratio 0.4 and 0.5 the difference is in tune of 19-30%. The difference in fracture energy of LWC and NWC is getting reduced with decrease in w/b ratio. In LWC with w/b ratio 0.3 having compressive strength up to 58 MPa, the difference in the elastic modulus of cement paste and lightweight aggregate is less and the paste–aggregate bond improves. Along with this the improved interfacial transition zone provides better crack resistance compared to LWC with w/b 0.5 or w/b 0.4 leading to similar fracture energy for w/b ratio 0.3. The fracture energy of both LWC and NWC for respective w/b ratio depends upon the type of aggregate and bond of the cement paste–aggregate matrix. In the lightweight concrete, uniform stress distribution happens due to similar moduli of aggregate and cement paste causing simultaneously reduction in stress concentration. The failure of lightweight concrete

happens in brittle manner once fracture initiates due to inferior aggregate interlocking mechanism. The past studies [14-15] has reported that fracture in lightweight aggregate is bound to happen through the aggregate but in case of sintered fly ash lightweight aggregate based concrete, the fracture is happening around the aggregate. The reason behind this phenomenon can be attributed to development of large stress at interface of lightweight aggregate and cement matrix due to incompatibility of elastic modulus of both aggregate and cement matrix. This fact can also be linked with improved interfacial transition zone in case of sintered fly ash lightweight aggregate based concrete due to internal curing and prolonged hydration.

5.4 Modulus of Elasticity (MOE) and Initial Compliance

Initial compliance represented by C_i, is defined as the inverse of the slope of the initial linear portion of the load versus CMOD curve. Equation (2), as given by [12], is used to get the MOE for the concrete beams with midpoint notch using the Ci.

$$E\ (MPa) = 6S\ \frac{\alpha V_1(\alpha)}{C_i d b^2} \tag{2}$$

Where $\alpha = a/d$, a= initial notch depth, d= beam depth. The computation of the slope of the load-CMOD curve's initial straight segment is displayed in Figure 13. Equation (3) provided by Tada et al. [25] is used to determine V1(α) as follows:

$$V_1(\alpha) = 0.76 - 2.28\alpha + 3.87\alpha^2 - 2.04\alpha^3 + \frac{0.66}{(1-\alpha)^2} \tag{3}$$

Table 8 presents the value of MOE as obtained from initial compliance by using equation 2. It can be observed that load-CMOD compliance method for MOE gives higher result than the actual as the strength of concrete increases. The MOE by this method is not accurate and reliable, therefore MOE as per empirical equation by Arora et al. [26] for normal weight concrete and IS: 9142-2018 for LWC is used for calculation of subsequent parameters in the study.

Table 8. Modulus of elasticity and initial compliance of concrete

w/ b ratio	Cube compressive strength (MPa)	Initial compliance Ci (10^{-9} m/N)	Modulus of elasticity (GPa) [CMOD test]	Modulus of elasticity (GPa) [As per Arora et al. For NWC [26] / IS: 9142-2018 for LWC [24]]
0.5-NWC	43.35	5.12	31.33	30.98
0.5-LWC	39.25	6.87	23.35	18.79
0.4-NWC	55.72	4.48	35.79	33.43
0.4-LWC	51.52	3.92	40.90	21.53
0.3-NWC	68.93	3.56	45.37	35.60
0.3-LWC	58.73	5.0	32.10	23.33

The compliance method proposed by RILEM is tedious, difficult, and sensitive to various test parameters. It requires a high degree of measurement sensitivity in mechanical bend tests, in the order of {10-^{9}} meters. Compliance is a function of the initial slope, which can vary slightly based on individual graph analyses. Even a little deviation in measuring the initial level slope in load-CMOD curve significantly affects the MOE. Figure 16 shows the best-fit curve for calculating the initial slope of the load-CMOD curve for different w/b ratios of the mix. From this study, it is evident that this method for determining MOE should not be preferred and is limited to use for comparative analysis only. Other well-known standard empirical methods should be used for MOE calculations.

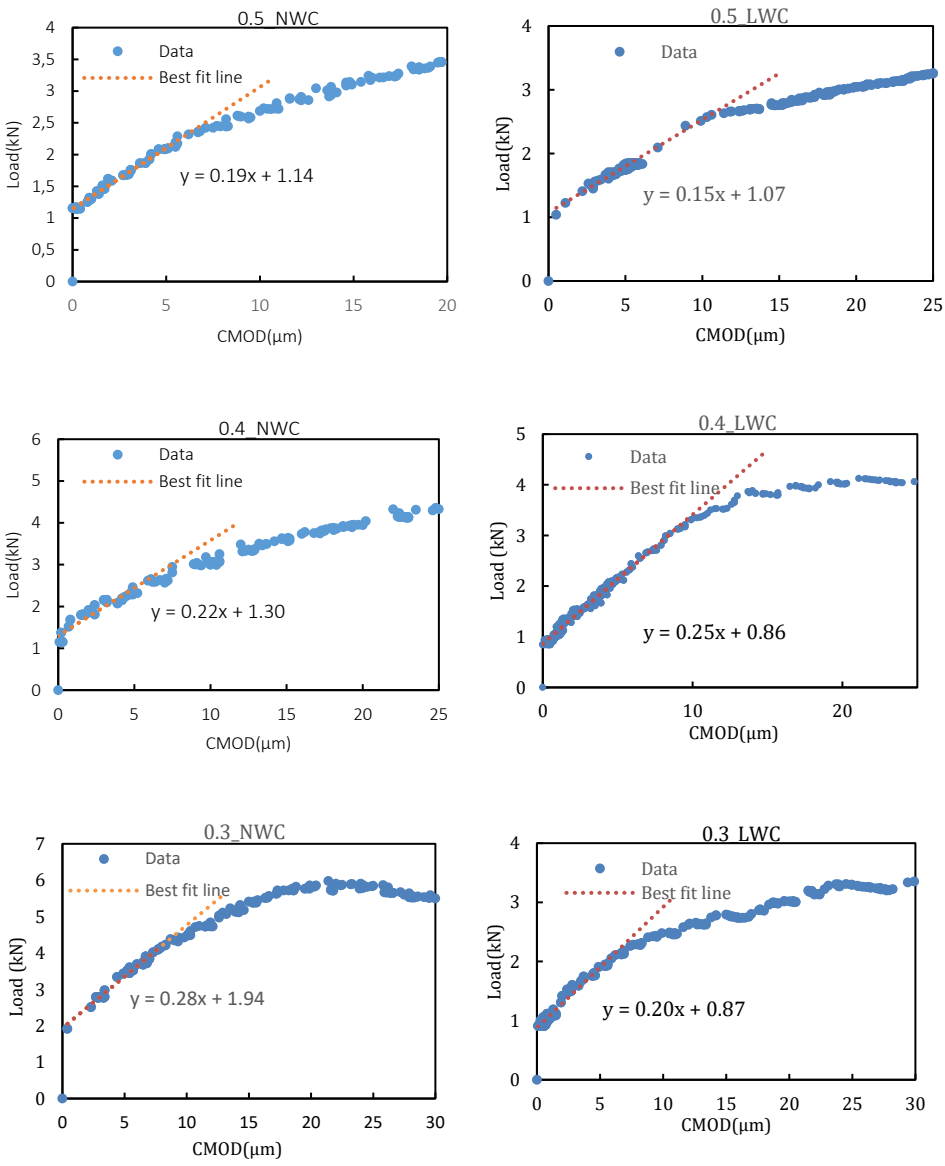

Fig. 16. Initial compliance calculation from Load-CMOD curves

5.5 Stress Intensity Factor

The stress intensity factor (K_{IC}) is defined as stress measurement adjacent to the crack. It represents the state of stress and crack propagation rate in the neighborhood of the crack or notch tip. The specimen with higher (K_{IC}) shows higher stress distribution near the crack representing less brittle the material. According to RILEM [12], the stress intensity factor can be computed using equation (4) as follows:

$$K_{IC}\,(MPa\sqrt{m}) = 3(P_{Nmax} + 0.5W)\frac{S\sqrt{\pi a}}{2d^2 b}f(\alpha) \tag{4}$$

Where P_{Nmax} = peak load beam with midpoint notch in N,

W = Total weight of the beam between the supports

S = span of the beam in m

α = a/d = 0.35

f(α) = Correction related to geometry for bending load.

For calculation of f(α) Finite Element Method is required for varying property of material, size and notch depth [27]. But in the present study equation (5) is used for comparative analysis because of simplicity and wide acceptance of this:

$$f(\alpha) = \frac{1.99 - \alpha(1-\alpha)(2.15 - 3.9\alpha + 2.7\alpha^2)}{\sqrt{\pi}(1+2\alpha)(1-\alpha)^{3/2}} \quad (5)$$

The stress intensity factor test results are shown in Figure 17. The graph shows that the average stress intensity factor for LWC is comparable than the NWC for a w/b ratio of 0.3, 04, and 0.5. The increase in w/b ratio increases the K_{IC} for NWC, almost comparable behavior can be seen with LWC. Also, it can be seen that K_{IC} increases with increase in compressive strength of the concrete because formation of initial cracks depends upon the tensile strength of the beam.

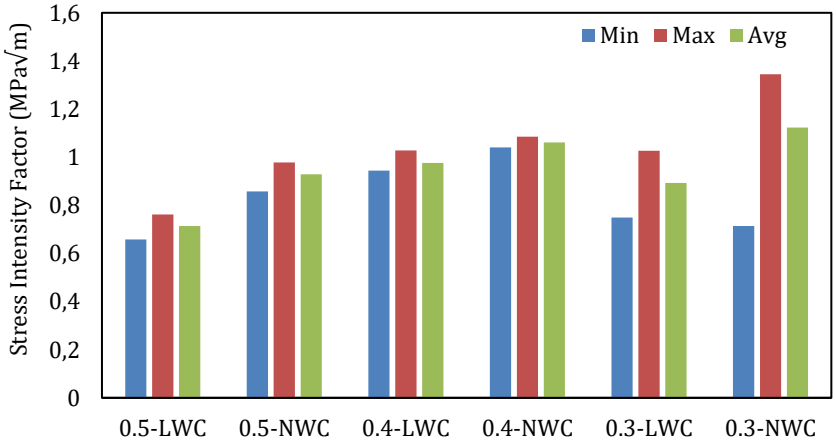

Fig. 17. Stress intensity factor

5.6 Critical Energy Release Rate

The critical energy release rate, GIC is defined as rate of change of energy when new fracture surface is created. It quantifies the energy change associated with crack growth. It can be numerically termed as the reduction in total energy potential per increase in surface area of fracture. It is important parameter to predict fracture toughness and crack growth behavior. The equation given by RILEM [12, 27] and mentioned below in equation (6) is adopted for calculation of GIC:

$$G_{IC}(N/m) = \frac{{K_{IC}}^2}{E} \quad (6)$$

Figure 18 shows the energy release rate of the LWC and NWC mix at w/b ratio of 0.5, 0.4 and 0.3. The graph clearly shows the slight increase in energy release rate in case of LWC

as compared to NWC for given w/b ratio. It means that for LWC the strain energy release with formation of new crack will be higher than NWC. From the figure, it can be noted that there is no definite trend in energy release rate with increase in compressive strength of both NWC and LWC.

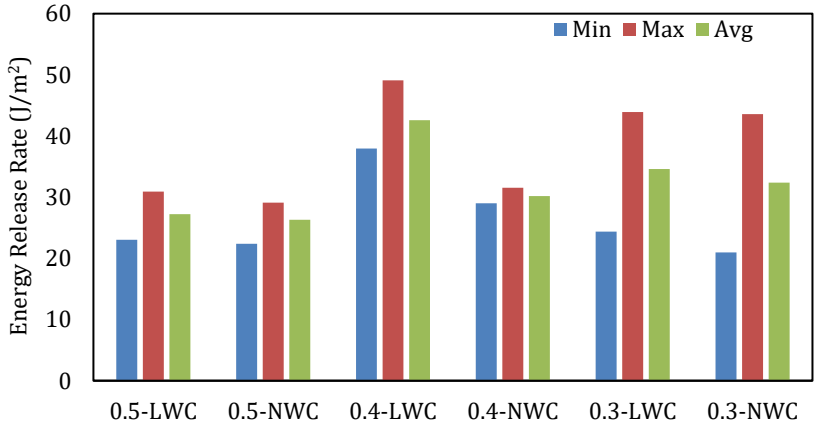

Fig. 18 Energy release rate

5.7 Characteristic Length of Concrete

Characteristic length is inherent property of material which indicates smallest possible width of a zone where damage occurs in a non-local continuum model [26]. It indicates the smallest possible spacing of fracture in discrete fracture model. It is calculated to understand and compare the brittleness of two different materials. The lesser the characteristic length, the lesser the spacing of fracture due to easier crack propagation and more brittle the material. It helps to predict how materials will behave when they start to break. The following formula (7) from [27] can be used to compute it. Here E is elastic modulus, G_f is fracture energy, and f_{st} is split tensile strength.

$$L_{ch}(mm) = \frac{EG_f}{{f_{st}}^2} \tag{7}$$

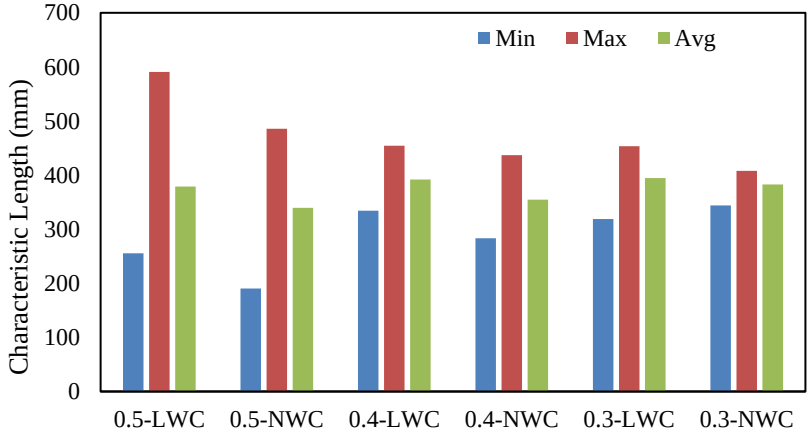

Fig. 19. Characteristic length

Figure 19 shows the characteristic length results, and it can be analyzed from the figure that as the compressive strength increases for NWC there is similar characteristic length. The same trend is observed in case of LWC. At a given water binder ratio, the characteristic length of LWC and NWC are comparable for lower w/b of 0.4 and 0.3 and does not show any significant variation in characteristic length. This indicates that fracture behavior of both LWC and NWC are comparable.

6. Conclusions

Based on the comparison of fracture energy and other fracture parameters adopting the three-point bend test with midpoint loading for plain lightweight concrete with sintered fly ash lightweight coarse aggregate in comparison to normal weight concrete, followings conclusions are drawn:

- Split tensile strength tests shows that lightweight concrete exhibits a split tensile to compressive strength ratio between 5% to 8%, while this ratio ranges from 5% to 10% for normal weight concrete. The modulus of elasticity in case of lightweight concrete is about 60-70% of modulus of elasticity of normal weight concrete.
- The comparison of load-CMOD and load deflection behavior of LWC and NWC indicates that ascending portion of load–deflection and load-CMOD plot of LWC is similar to normal weight concrete. The non-linear ascending and descending branches in flexural curves of lightweight concrete can be correlated with the non-linearity in tensile mode stress-strain behavior and formation of the process zone of fracture in front of the initial notch.
- It can be observed that load-CMOD compliance method for modulus of elasticity gives higher result than the actual as the strength of concrete increases. The modulus of elasticity by initial compliance method is not accurate and reliable. The initial tangent modulus of elasticity as per Indian Standard is used for calculation of subsequent parameters in the study. This compliance method is proposed by RILEM is tedious, difficult and sensitive to test parameters.
- The fracture energy in case of NWC increases with increase in strength or with decrease in w/b ratio. The same trend for fracture energy is observed for LWC. The difference in fracture energy of LWC and NWC is getting reduced with decrease in w/b ratio due to less difference in the elastic modulus of cement paste and lightweight aggregate, improvement in paste–aggregate bond and better interfacial transition zone providing more crack resistance. The stress intensity factor and characteristic length of LWC is comparable to NWC. No definite trend has been noted in energy release rate for both NWC and LWC with increase in compressive strength.
- The modulus of elasticity of LWC is significantly lower than normal concrete. The modulus of elasticity, area under the load deflection curve, tensile strength, fracture behavior etc. needs to be considered appropriately in the non-linear analysis of concrete depending upon type of application such as building, dams, bridges, nuclear structures etc. to compare or analyze the concrete cracking resistance, energy absorption capacity and toughness to estimate the safe period left before unstable and dangerous crack propagation.

References

[1] Singh B, Singh SB, Barai SV. Performance of concrete made using sintered fly ash lightweight aggregate: A review. Indian Concr J. 2023;97(7):41-59.
[2] Ojha PN, Singh B, Behera AK. Sintered fly ash lightweight aggregate: Its properties and performance in structural concrete. Indian Concr J. 2021;95(6):20-30.

[3] Bate SCC. Guide for structural lightweight aggregate concrete: Report of ACI committee 213. Int. J Cem Compos Light Concr. 1979;1(1):5-6. https://doi.org/10.1016/0262-5075(79)90004-6
[4] Bhosale AB, Prakash SS. Crack propagation analysis of synthetic versus steel versus hybrid fibre reinforced concrete beams using digital image correlation technique. Int J Concr Struct Mater. 2020;14(1):1-22. https://doi.org/10.1186/s40069-020-00427-8
[5] Cusatisa G, Cedolin L. Two-scale study of concrete fracturing behavior. Eng Fract Mech. 2007;74(1-2):3-17. https://doi.org/10.1016/j.engfracmech.2006.01.021
[6] Hillerborg A, Modeer M, Peterson PE. Analysis of crack formation and crack growth in concrete by means fracture mechanics and finite elements. Cem Concr Res. 1976;6(6):773-782. https://doi.org/10.1016/0008-8846(76)90007-7
[7] Bazant ZP, Oh BH. Crack band theory for fracture of concrete. Mater Struct. 1983;16(3):155-178. https://doi.org/10.1007/BF02486267
[8] Jenq YS, Shah SP. Two parameter fracture model for concrete. J Eng Mech. 1983;111(10):1227-1241. https://doi.org/10.1061/(ASCE)0733-9399(1985)111:10(1227)
[9] Zhang MH, Gjorv OE. Mechanical properties of high strength lightweight concrete. ACI Mater J. 1991;88(3):240-247. https://doi.org/10.14359/1839
[10] Patel V, Singh B, Arora VV. Study on fracture behaviour of high strength concrete including effect of steel fiber. Indian Concr J. 2020;94(4):1-9.
[11] Ojha PN, Singh B, Singh A, Patel V, Arora VV. Experimental study on creep and shrinkage behaviour of high strength concrete. Indian Concr J. 2021;95(2):30-42.
[12] RILEM TC-50 FMC. Determination of the fracture energy of mortar and concrete by means of three-point bend tests on notched beams. Mater Struct. 1985;18:285-290. https://doi.org/10.1007/BF02472918
[13] Shah SP. Determination of fracture parameters (KIcs and CTODc) of plain concrete using three-point bend tests. Mater Struct. 1990;23(6):457-460. https://doi.org/10.1007/BF02472029
[14] Sahoo S, Lakavath C, Suriya SS. Experimental and analytical studies on fracture behavior of fiber-reinforced structural lightweight aggregate concrete. J Mater Civ Eng. 2021;33(5). https://doi.org/10.1061/(ASCE)MT.1943-5533.0003680
[15] Trivedi N, Singh RK, Jayant C. A comparative study on three approaches to investigate size independent fracture energy of concrete. Eng Fract Mech. 2015;138:49-62. https://doi.org/10.1016/j.engfracmech.2015.03.021
[16] Murthy AR, Ganesh P, Kumar SS, Iyer NR. Fracture energy and tension softening relation for nano-modified concrete. Struct Eng Mech. 2000;54(6):1201-1216. https://doi.org/10.12989/sem.2015.54.6.1201
[17] Gil DM, Golewski GL. Effect of silica fume and siliceous fly ash addition on the fracture toughness of plain concrete in mode I. IOP Conf Ser Mater Sci Eng. 2018. https://doi.org/10.1088/1757-899X/416/1/012065
[18] Siregar APN, Rafiq MI, Mulheron M. Experimental investigation of the effects of aggregate size distribution on the fracture behaviour of high strength concrete. Constr Build Mater. 2017;150:252-259. https://doi.org/10.1016/j.conbuildmat.2017.05.142
[19] IS 516 (Part 1/Sec 1). Hardened concrete: Methods of test part 1, testing of strength of hardened concrete, section 1: compressive, flexural and split tensile strength. Bureau of Indian Standards, New Delhi; 2021.
[20] IS 383. Coarse and fine aggregate for concrete: Specification. Bureau of Indian Standards, Delhi, India; 2016.
[21] IS 269. Ordinary portland cement: Specification. Bureau of Indian Standards, Delhi, India; 2015.
[22] IS 9103:1999. Concrete admixtures: Specification. Bureau of Indian Standards, Delhi, India; 1999.

[23] IS 10262. Concrete mix proportioning: Guidelines. Bureau of Indian Standards, Delhi, India; 2019.
[24] IS 9142 (Part 2). Artificial lightweight aggregate for concrete: Specification Part 2-Sintered fly ash coarse aggregate. Bureau of Indian Standards, Delhi, India; 2018.
[25] Arora VV, Singh B, Jain S. Experimental studies on short term mechanical properties of high strength concrete. Indian Concr J. 2016;90(10):65-75.
[26] Arora VV, Singh B, Patel V, Trivedi A. Evaluation of modulus of elasticity for normal and high strength concrete with granite and calc-granulite aggregate. Struct Concr. 2021;22(S1). https://doi.org/10.1002/suco.202000023
[27] Ojha PN, Singh P, Singh B, Singh A, Mittal P. Fracture behavior of plain and fiber-reinforced high strength concrete containing high strength steel fiber. Res Eng Struct Mater. 2022. http://dx.doi.org/10.17515/resm2022.377ma1228

Research on Engineering Structures & Materials
www.jresm.org
Research Group

Research Article

Influence of melon shell ash reinforcement on the mechanical and microstructural characteristics of recycled aluminium matrix composites

Olatunji P Abolusoro[*,1,2,a], Moshibudi Caroline Khoathane[1,b], Washington Mhike[1,c]

[1]*Dept. of Chemical, Metallurgical and Materials Eng., Tshwane University of Technology, South Africa*
[2]*Dept. of Mechanical and Mechatronics Engineering, Landmark University, Omu-Aran, Nigeria*

Article Info

Article history:

Received 14 June 2024
Accepted 15 Aug 2024

Keywords:

Melon shell ash;
Aluminum cans;
Composite;
Microstructure;
Mechanical properties

Abstract

This study produced a composite using melon shell ash as reinforcement on recycled Aluminium waste cans matrix. The melon shell particulate additions to the matrix were done in wt.% of 0, 10, 5, 15 and 20. The mechanical behaviour of the composite demonstrates that the tensile values increased as the particulate addition increased to 15% wt. to reach a maximum of 113MPa but dropped at the 20% addition. The impact energy on the other hand increases marginally at 5% particulate addition and increases slightly higher with the addition of reinforcement of 10% wt to attain a maximum value of 77J. However, a further increase in the melon shell ash to 15% wt and 20% wt reduced the impact energy. The hardness values of the composites at all the % wt. additions were generally higher than that of the unreinforced Aluminium with the peak hardness value of 57.2BHN obtained at 10% wt. addition. The density of the composites decreases as the % wt. of the melon shell ash particles increases. The improved mechanical properties and lower density of the composites achieved in this study are significant factors in developing strong and lightweight engineering materials for industrial applications.

1. Introduction

Aluminum alloy is a lightweight, malleable, durable and corrosion-resistant metal. It is highly recyclable and has found wide uses in automobile, construction, building, food and beverage industries [1]. As a result of the expansion in the use of Aluminum alloys, there is a need for improvement in some of its properties through modification of its constituent elements. One of the ways this has been achieved is through the reinforcement of the aluminum matrix with suitable substances to form composites [2–4]. The use of Aluminum composites has expanded tremendously as a result of the increase in demand for efficient, lightweight and low-cost materials for industrial applications. Aluminum matrix composites (AMC) have gained wide attention from scientists and researchers own to their simpler production methods, economic feasibility and homogenous structure of the particulate reinforcements. AMC also demonstrate higher stiffness, low density and thermal expansion coefficient, good wear resistance and specific strength [5, 6] Reports have shown that the type and fractions of reinforcements on the Aluminum composites influenced the behavior of the composites. Significant improvements have been achieved in aluminum composites through the introduction of little ceramic-containing particulates such as, Titanium carbide (TiC), Boron carbide (B_4C), Silicon carbide (SiC), and Silica oxides (SiO_2) [7–13]. However, the economic and environmental challenges involved in the

*Corresponding author: abolusoroop@tut.ac.za
[a] orcid.org/0000-0003-1493-3445; [b] orcid.org/0000-0002-5328-2721; [c] orcid.org/0000-0003-4670-1171
DOI: http://dx.doi.org/10.17515/resm2024.320me0614rs

production of these ceramics have led to the exploration of the potential of agricultural waste-based reinforcements [14, 15] Agricultural waste emanates from remnants of crops after the edible parts have been consumed. The abundance and availability of these wastes coupled with low cost and sustainability have endeared them to researchers as reinforcement materials [16,17]. In addition, Agrowastes are usually dumped indiscriminately in the open land giving rise to environmental pollution. Ashes from Agrowastes such as rice husk, groundnut shells, sugar cane bagasse, palm kernel shells, coconut shells and melon shells have been utilized as reinforcement materials in Aluminium matrix composites as a result of their constituents [16], [18–21] Rice husk ash (RHA) possess high percentages of Silicon oxides together with other compounds such as MgO, Fe_2O_3 and Al_2O_3 [22–25]. Tensile strength, toughness, and hardness improvement have been reported in RHA and mica as reinforcement in A7075 matrix composites [26]. SiC extracted from RHA has also been utilized as reinforcement [27, 28]. Joharudin et al [29]. reinforced recycled A7075 chip with silica extracted from RHA. His result showed improvement in the hardness values of the composites. Coconut shell ash (CSA) is another agro-waste that has found application as reinforcement in composite production. It has also been reported to contain SiO_2, MgO, Fe_2O_3 and Al_2O_3 [30]. The addition of CSA as reinforcement to the aluminum matrix of A6082 has been reported to enhance the properties of the composites [30]. Using the stir casting method, Kaladgi et al [31] reinforced 6061 with coconut shell microparticles and Al_2O_3. His result revealed a boost in the hardness and tensile strength of the composites as the percentage of reinforcements increased. Bello et al [32] utilized coconut shell microparticles to reinforce Aluminum alloy using the compo-casting method. An increase in tensile properties was observed due to appreciable interfacial adhesion between the aluminum matrix and the particulate reinforcement. Palm kernel shell ash (PKA) is also an agricultural waste which contains abundant siliceous materials. SiO_2 is a major constituent of PKA mostly up to 40%. Other constituents present include metallic oxides such as aluminum oxide, magnesium oxide, Potassium oxides, and calcium oxide [33, 34]. The addition of PKA as reinforcement on the aluminum matrix was found to improve the wear resistance and the mechanical behavior of the developed composites [35]. Sugar cane bagasse (SCB), a waste from sugar cane has also been explored for reinforcement purposes. The main constituents are cellulose, hemicellulose, wax lignin and ash [36, 37]. The presence of these elements makes SCB a suitable reinforcement fibre material for the development of composites with outstanding physical and chemical characteristics [38, 39]. Chandla et al [40] employed bagasse ash to reinforce the aluminum alloy 6061 matrices via stir casting technique and observed an increase in the hardness and tensile strength of the composite as the bagasse ash content increased. Ashes from other agricultural wastes and organic materials such as Aloe vera, pine leaf and lemon grass have equally been explored as reinforcement materials on Aluminum alloy matrix [41–43]. The potential of melon shell ash as reinforcement on aluminum matrix has also been explored [44, 45]. A study by Abdulwahab et al [46] on an Al-Si-Mg matrix reinforced with melon shell ash revealed improvement in the mechanical property of the Al-Si-Mg alloy up to a maximum of 20% wt addition of the melon reinforcement. However, better thermal conductivity was achieved in the composite with the 5%wt addition of reinforcement than the other proportions (10 wt%, 15 wt%, and 20 wt%). Suleiman et al [47] also employed melon shell ash as a reinforcement on the Al-Si alloy matrix. Their result showed that the hardness and the tensile strength of the composite increased while the impact energy and the percentage elongation decreased. From the foregoing literature review, it is evident that studies on the use of agricultural waste as reinforcement on recycled aluminum alloys are scarce in the literature. Although there has been reported use of melon shell ash reinforcement on a certain grade of aluminum alloy (Al-12%Si), however, research on the use of melon shell ash to develop composites with other aluminum grades and especially aluminum waste cans has not been reported. Therefore, this study focuses on developing and exploring the potential of

recycled aluminium waste cans matrix reinforced with melon shell ash for lightweight engineering applications in automobiles.

This study attempts to reduce the challenges posed by the indiscriminate disposal of agricultural and aluminium wastes and its environmental consequences. Most agro wastes and waste aluminium cans especially in developing countries are usually burnt or buried. This method of disposal constitutes a health risk for both plants and animals. The utilization of the melon ash and the aluminium waste cans to produce composites will help in turning the wastes into useful engineering materials that will help minimize the risk involved in the improper disposal of the wastes thereby promoting good health and a safe environment which is vital to the attainment of the Sustainable Development Goals (SDG) 3 which is good health and well-being. The impact of composite production also extends beyond this goal, with implications for other SDGs such as SDG 12 (responsible consumption and production), SDG 9 (Industry, innovation and infrastructure) and SDG 2 (Zero hunger) as more production of the crops will be encouraged thereby making more food available for consumption as a result of the innovative use of the wastes from the crops.

In this research, the aluminium waste cans were recycled as the matrix material while the melon shell ash was used as the reinforcement via the stir casting technique. The main objectives of the study include burning the melon shell and investigating the chemical compositions of the produced ash, production of the composites via stir casting method, and characterization of the composites to obtain the mechanical properties and the microstructures.

2. Materials and Methods

2.1. Preparation of The Melon Shell Ash

The melon shell (Figure 1) was sourced from a market in Omu-Aran, Kwara state, Nigeria. They were thoroughly washed to eliminate dirt, sun-dried and then burnt into ashes and sieved with a 38 μm sieve size. Figure 2.

2.2. Aluminum Waste Cans Preparation

The Aluminum waste cans were picked from different dumping sites in Omu-Aran, Kwara state, Nigeria. Figure 3. A compositional analysis was carried out on the Aluminum alloy using the theoretical density of 2.7 g/cm3. Table 1.

Table 1. Aluminum waste cans chemical composition (weight %) [2]

Element	Fe	Mn	Ti	K	Si	Cu	Zn	Mg	Cr	Al	Others
% Wt	0.431	0.388	0.006	0.013	0.59	0.074	0.194	2.143	0.008	96.043	0.11

2.3 Analysis of The Produced Melon Shell Ash

X-ray fluorescent (XRF) was employed for the elemental analysis of the melon shell ash. The analysis was carried out using the Thermo Fisher ARL PERFORM'X Sequential XRF equipment with Uniquant software. Table 2.

Table 2. Melon shell ash composition

Oxides	SiO_2	K_2O	SO_3	P_2O_5	FeO_3	TiO_5	Al_2O_3	MnO
Weight %	75.11	4,59	0.62	9,77	1,31	0.16	2,67	0.457
Oxides	CaO	ZnO	BaO	Na_2O	MgO	V_2O_5	LiO	ZrO_2
Weight %	2,12	0.476	0.089	0.53	0.36	0.006	1,42	0.01

Fig. 1. Melon shell

Fig. 2. Melon shell ash

Fig. 3. Waste Aluminium cans

Fig. 4. Sand mould with the composites

2.4 Composite Production

The aluminium cans were crushed and weighed on a weighing scale before being loaded into a mild steel container and charged into the blast furnace, which was preheated to 500 degrees Celsius. The furnace temperature was raised to 800^{o}C, which is higher than the melting point of the aluminium waste cans, which is about 660^{o}C The charged Aluminium was left for about forty-five minutes in the furnace and stirred at 450 rpm to allow proper and complete melting. Following this, the molten aluminium was removed from the furnace and the impurities/ slag were separated from the molten Aluminium. The prepared melon shell ash powder was introduced into the molten metal as the reinforcement in percentage by weight to produce the composites. The mixture was stirred for 1 minute, returned to the furnace, and left for about 15 minutes. After this, the molten composite was removed from the furnace, gently poured into the prepared sand mould (Figure 4) and left to cool naturally. The composite rods (Figure 5) were removed from the sand mould after 24 hours. The reinforcement was added in percentage by weight according to Table 3 to produce five distinct combinations. The samples without reinforcement were the control samples i.e. 0% wt. The percentage weight additions were selected based on literature reports on related studies [2, 22, 46, 47].

Table 3. Various % wt additions of melon shell ash to the Aluminium matrix

S/N	Al alloy (% wt.)	Melon ash (% wt.)
1	100	0
2	95	5
3	90	10
4	85	15
5	80	20

2.5. Characterization

2.5.1. Mechanical Properties

Three specimens were machined into B557M ASTM standard [48] for each percentage reinforcement used (Figure 6). The mean values of the ultimate tensile strength were recorded. The tensile strength was carried out using the INSTRON universal testing machine. The Brinell hardness testing was performed following ASTM E10-18 2017 [49] using a universal testing machine with an indenter of 10mm at 500kgf for 10s. About five indentations were made on each sample and the average was evaluated. Two impact test samples cut to ASTM standard E23 of the year 2007 [50] were evaluated for all the composites. The test was performed on the notched rectangular samples of dimensions 75 x 10 mm using the Avery-Denison Universal Impact-Testing Machine. The impact strength measured in joules (J) was recorded for the test specimens.

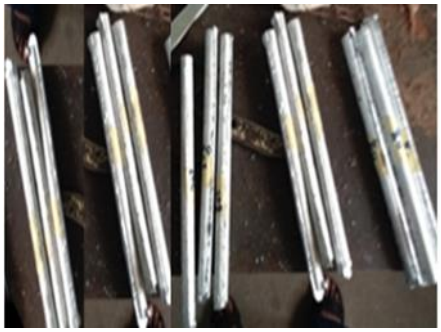

Fig. 5. The composites before machining

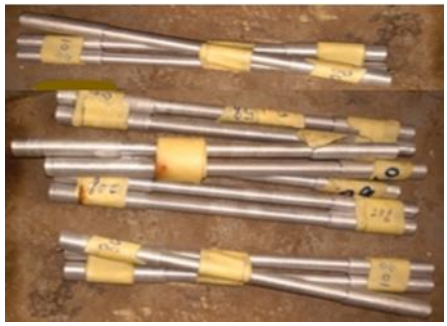

Fig. 6. Tensile samples

2.5.2 Density

The density of the composites was measured using Archimedes's principle and equation 1 [2].

$$\rho c = \left(\frac{Wc}{Wc - Ww} \right) \times \rho w \tag{1}$$

Where; ρc = density of the composite; ρw = density of water at room temperature (1000kg/m^3 or 1g/cm^3); *W*c = weight of composite in air and *W*w = weight of composite immersed in water

2.5.3 Surface Morphology Examination

Samples of 6mm each were cut from the composites, mounted, grinded, polished, and etched with Weck's reagent for the microstructural study. This was performed with an optical microscope set at a magnification of 50. Three samples at different percentage

reinforcement additions i.e., 0% wt, 5% wt, and 15% wt. were selected for SEM and EDS analysis based on their mechanical behavior.

2.6 Challenges

The main challenge encountered during the composite preparation was the melted aluminum cans carrying lots of impurities and slags which increases the melting time of the aluminum in the furnace. Frequent efforts were made to remove the slags on the molten aluminum before adding the reinforcements. The thermal instability resulting from the temperature difference between the sand mould and the molten composites causes sparking of the molten metal during pouring. However, preheating the mould before pouring the molten metal was helpful. The limitation of the stir casting method which includes particle agglomeration at higher volumes of reinforcement additions was another challenge. The stirring time at the higher percentages of reinforcement additions was increased for more even distributions of the melon shell ash.

3. Results and Discussion

3.1 Tensile Test

The tensile result as shown in Figure 7 indicates that the melon shell ash particulate addition has a significant influence on the tensile properties of the Aluminum alloy. At 5% weight addition of the melon shell ash to the Aluminum matrix, the tensile strength increases by 7.5% and increases by 16.1% at 10% weight addition. The highest tensile strength of 113MPa was obtained at the 20% weight addition of the melon shell ash reinforcement representing about 23.7% increase from the unreinforced alloy. However, at 20% reinforcement addition to the matrix, the ultimate tensile strength decreases.

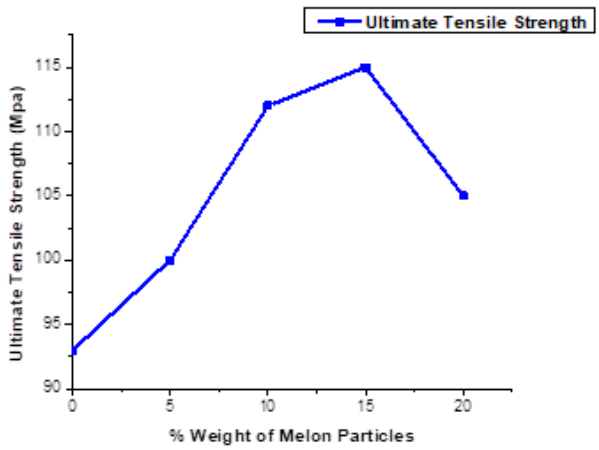

Fig. 7. Ultimate tensile strength of the composites at different weight additions

The increase in tensile strength of the composites up to the 15% weight addition of the melon shell ash could be ascribed to the ability of the melon shell ash particulates to act as a hindrance to dislocations when subjected to loading during the tensile test. The high silicon content of the melon ash which has been known to promote grain boundary strength and other hard compounds such as Fe_2O_3, Al_2O_3, MgO, TiO_2 and CaO present in the melon shell ash have played a significant role in the strength improvement of the composites [46, 47]. The decrease in the composite strength at 20% weight addition could be due to the influence of the segregation of the oxide particles which weakens the strengthening precipitates of the composites [47].

3.2 Hardness

The hardness values of all the composites at different percentage weight additions (Figure 8) were significantly greater than that of the unreinforced Aluminum. The hardness value increased from 48.5 HBN for unreinforced Aluminum to 55.5 BHN at 5% wt melon shell ash addition. This value further increased to 57.2 at 10% wt particulate addition to give the maximum value. Thereafter, the hardness value dropped at 15% wt and reduced a bit further at 20% wt addition. The uniform dispersion of the melon ash particles along the grain boundaries of the composites, as observed in the microstructures, improved its resistance to plastic deformation thereby impacting hardness to the composites. The decrease in hardness values as observed at 15% wt. and 20% wt. melon shell ash additions could be attributed to the increase in the weight of the melon shell ash in the Aluminum matrix which advanced the coarsening of the precipitates and weakened the intermetal-particulate bonding of the composites [2, 34, 44].

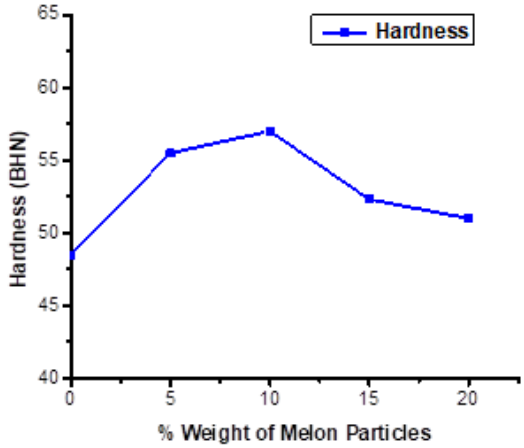

Fig. 8. The hardness of the composites at different weight additions

3.3 Impact

The impact test results vary across the different percentage compositions of the reinforcement (Figure 9). At 5% particulate addition, a marginal increase in impact toughness from that of the Aluminum matrix was observed. Further addition of reinforcement to 10% increases the impact energy slightly higher. However, as the addition of the particulate reinforcement increases further, the impact energy reduces. The highest impact energy of 77J obtained at 10% represents a moderate addition of reinforcements. At this stage, the melon shell ash blends with the Aluminum matrix to enhance interfacial adhesion and maximum absorption of energy with adequate toughness and strength to tolerate the impact force [2, 46]. The impact energy reduces as the melon shell ash addition increases to 15% wt and reduces further at 20% wt. This could be linked to the high volume of melon shell ash present in the composite which could lead to segregation by the ductile Aluminum matrix making it prone to crack propagation. Also, the thermal differences set up between the melon shell ash particles and the Aluminum matrix generate elastic stresses which put the melon shell ash into compression and the matrix into tension, consequently advancing the brittleness which probably lowers the impact strength and could also be responsible for the lower hardness and tensile strength trend observed at the 20% wt addition [51].

Generally, all the mechanical properties of the composite were observed to decrease at the highest percentage of reinforcement. In addition to the explanations already given on this in sections 3.1, 3.2, and 3.3, one of the factors that could be responsible for the lower mechanical properties at this weight fraction addition is the agglomeration of the reinforcements as evidenced in the microstructures in Figures 11 (c) and (d). The clustering of the melon shell particles could lead to stress concentration and nonuniformity in the reinforcement orientation, thereby initiating cracks and failures that could lower the composite strength. Also, insufficient matrix material due to the high volume of reinforcements could lead to reinforcement wetting, causing a reduction in the mechanical properties. Another possible factor is the thermal expansion mismatch resulting from differences in the thermal expansion coefficients of the aluminum matrix and the high volume of melon shell ash which could induce internal stresses in the composite, reducing the mechanical properties.

The factors given above as possible causes of the observed reduction in the mechanical properties of the composites at the 20% wt. could be mitigated by optimizing the melon shell ash processing to enhance the fibre quality. Interfacial modification of the melon shell ash to improve bonding with the Aluminum matrix at higher percentages of weight addition may also be helpful. Other natural fibres could be incorporated into the melon shell ash to form a hybrid reinforcement. However, the compatibility of such hybrid reinforcement with the matrix must be ascertained.

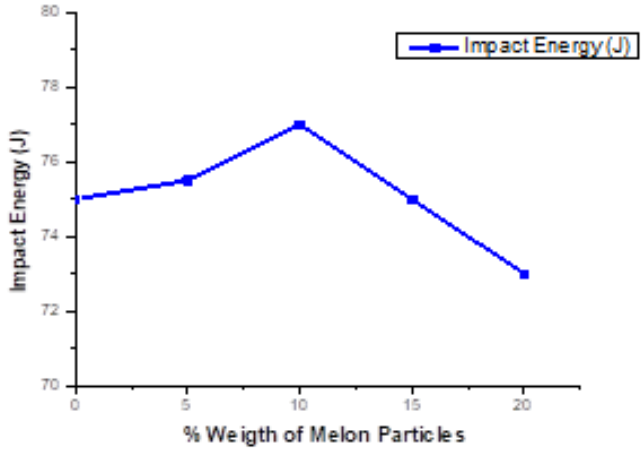

Fig. 9. Impact toughness of the composites at different weight additions

3.4 Density

The densities of the composites, as shown in Figure 10 decreased as the % weight addition of the melon ash increased. The density of the control sample i.e., the unreinforced aluminum is 2.8 g/cm^3. This density decreases to 2.49 g/cm^3 at 20% wt. The implication of this is that the greater the weight of the reinforcement, the lower the weight of the composites. This could be ascribed to the lower density of the melon ash in comparison to that of the Aluminum. This led to the reduction in the weight of the composites' matrix-reinforcement particles, thereby lowering the composites' density [2, 22]. The reduction in the density of the composites observed at all the different % wt additions of the melon

ash revealed that Aluminium lightweight composites are achievable with considerable additions of melon shell ash as reinforcement.

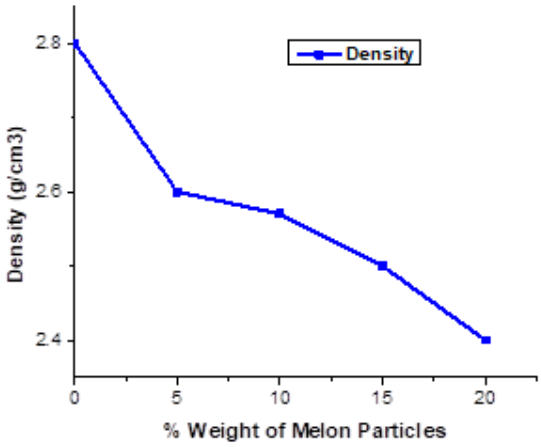

Fig. 10. Density variation of the composites at different weight additions

3.5 Surface Morphology Examination

Optical microstructures of the composites at different % wt reinforcements are presented in Figures 11 a, b, c and d while Figure 11 e is the microstructure of the unreinforced Aluminum alloy. The microstructures generally revealed uniform spread of the melon ash in the aluminum matrix. This further attests to the effectiveness of the stir casting method employed for the composite production, despite a tiny micropore that could be spotted at a point in Figure 11 (b). The melon shell ash particulates were considerably spread along the grain boundaries of all the microstructures although slight clustering of the ash particles could be noticed at some point in some of the samples. Figure 11 (c). Particulate agglomeration could be observed at some points in the composite at the highest reinforcement volume of 20% wt. Figure 11 (d). The homogenous distribution of the melon ash reinforcement in all the composite structures is accountable for the good result in the mechanical behavior of the composites. The structural Modification due to the addition of the reinforcement as evidenced in the microstructure, promotes strong interfacial bonding within the aluminum grain boundaries. This impact strength to the composites and enhanced its resistance to deformations thereby improving the mechanical properties as recorded in the tensile, impact and hardness results obtained from the composites [2, 34, 44]. However, slight agglomeration and non-uniformity in the dispersion of the melon ash particles at higher volumes of reinforcement caused the observed drop in the mechanical strength of the composites.

The SEM and EDS analysis presented in Figures 12 a, b and c for 0% wt, 5%wt. and 15%wt. melon shell ash addition respectively show distinct features. These features emanate from the mixing of the melon shell ash with the Aluminum matrix. The EDS at the 5% wt. composition of reinforcement as shown in Figure 12 (b) reveals the presence of O, Mn, and Mg among others which are key components of the melon shell ash.

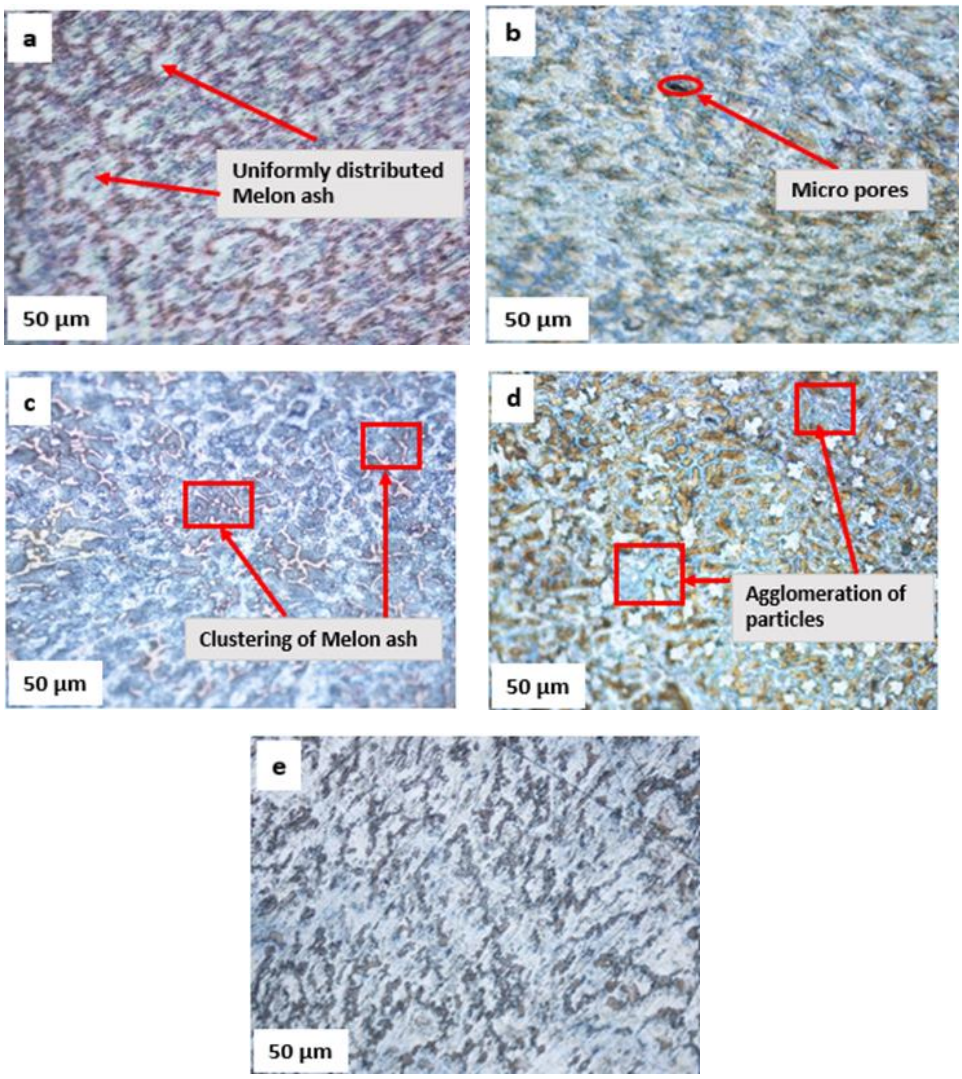

Fig. 11. Microstructures of the composites (a) 5% wt. (b) 10% wt (c) 15% wt (d) 20% wt (e) 0% wt

However, at the 15% wt addition of the melon shell ash, the percentage compositions of the elements changed with silicon having the highest composition after Aluminum. The high-volume addition of the melon shell ash to the aluminum matrix increased the silicon content of the composite since SiO_2 is the major component of the melon shell ash as given in Table 2. The addition of Si to metals has been reported to impart strength to it [46, 47]. This also explains the improvement in the mechanical behavior of the composites as compared with the unreinforced Aluminum alloys.

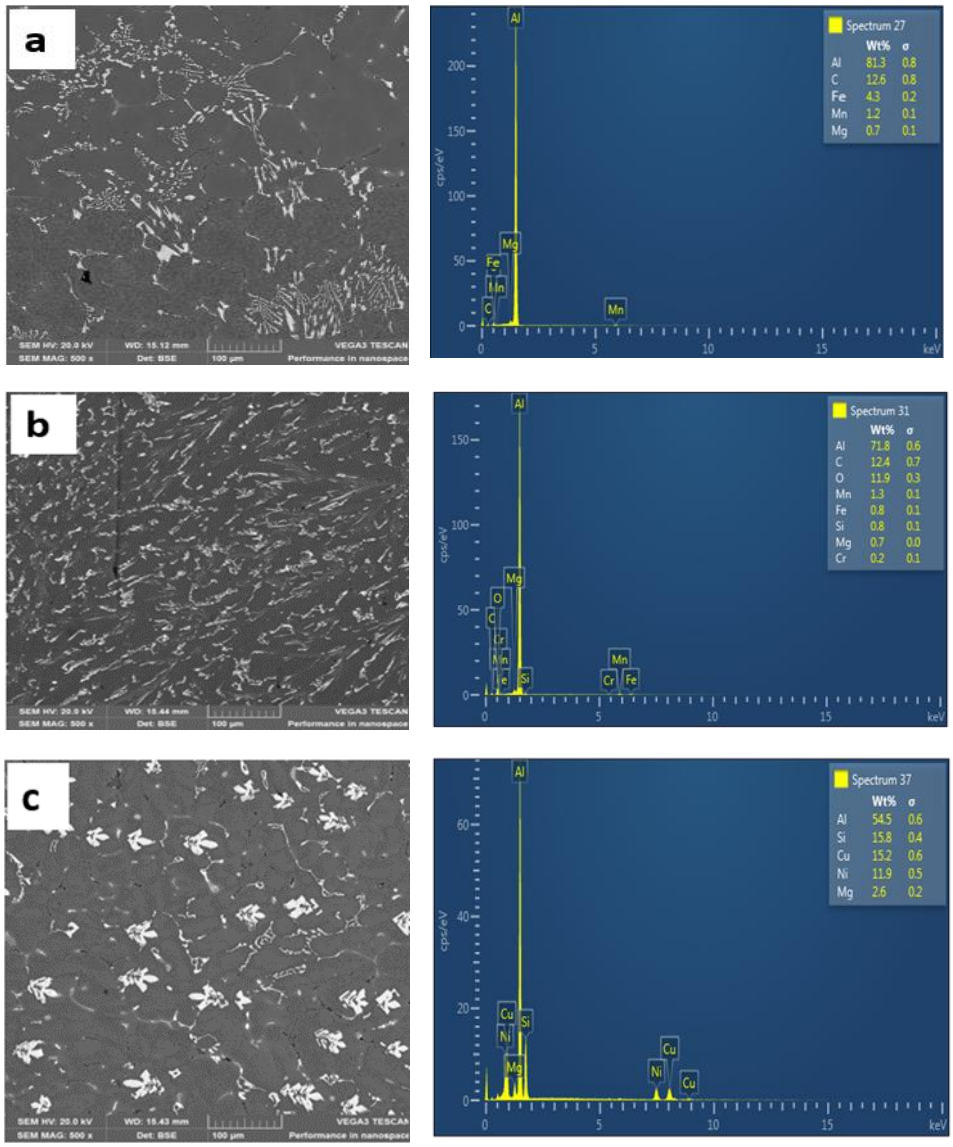

Fig. 12. SEM images and EDS analysis of the Aluminium matrix and the composites (a) 0% wt. (b) 5% wt. (c) 15% wt.

4. Conclusions

Recycled aluminium waste cans have been reinforced with melon shell ash to produce composites. The conclusions that could be drawn from the mechanical and microstructural characterizations carried out on the composites are as follows:

- Melon shell ash reinforcement could be successfully incorporated into a recycled aluminium waste cans matrix through the stir casting method.
- There is an enhancement in the ultimate tensile strength (UTS) of the composites over the unreinforced aluminium. The UTS increases as the percentage

reinforcement increases up to 15% wt particulate addition but drops a little at 20% wt addition. The maximum UTS of 113 MPa was obtained at 15%wt. addition representing about 23.7% increase above the unreinforced alloy. This improvement in the tensile behavior could be linked to the homogenous dispersion of the melon ash particulates in the Aluminum matrix which act as a barrier to dislocations during the tensile test. The high presence of silicon and other hard compounds in the melon ash also contributed to the observed high tensile strength [46,47]. Segregations of oxide particles occurred at 20% addition which declined the strengthening precipitates of the composites leading to the observed reduction in the tensile strength at that 20% [47].

- There was an improvement in the impact energy up to the 10% wt. reinforcement. However, the toughness energy dropped at 15% wt. and dropped further at 20% wt addition. The highest impact energy of 77J was obtained at 10% wt. At this point, there was an enhancement in the interfacial adhesion between the matrix and the melon which promotes energy absorption with considerable toughness and strength to withstand the impact force [2, 47].
- The hardness values of the composites at all the % wt additions were generally higher than that of the unreinforced Aluminum. The maximum hardness was obtained at 10% wt. addition. The uniform distribution of the melon shell ash along the grain boundaries of the composites promotes its resistance to plastic deformation leading to the rise in hardness of the composites [2, 44].
- The microstructures demonstrate that melon ash particles were homogeneously distributed in all the composites although little clustering and particle agglomeration were noticed at higher % wt. reinforcement.
- Additions of the different weight fractions of the melon ash particles lower the density of the composites. This is evident from the fact that the density of the ash was lower than that of the Aluminum. This implies that lightweight Aluminum composites can be achieved with moderate additions of melon ash to the matrix.
- Generally, the produced composite possesses better mechanical properties and lower density than the unreinforced alloys. These two factors achieved in this study are very significant to Engineering materials design and selection making this study a significant contribution towards the quest for lighter-weight engineering materials with uncompromising strength.
- The enhanced mechanical properties and the reduced density of the composites have numerous potential applications in the development of lightweight engineering materials in industries such as aerospace, automobile, marine, medical, construction, sports, and energy. Many industries today are utilizing composite materials own to their benefits, especially their low weight and high strength ability. The aerospace and automobile industries are taking these advantages to produce lighter parts with high strength. The weight savings and dimensional stability offered by composite materials have reduced fuel consumption and enhanced the performance and efficiency of aircraft and automobile engines. Although carbon fibre-reinforced composites and polymer matrix composites have gained wide uses in the aerospace and automobile industries, the availability of materials, ease and cheaper production, and sustainability of melon shell ash reinforced composites could also be of tremendous advantage to the industries. The sports industries have also leveraged the merits of composites in the production of many sports equipment such as bicycles, tennis rackets, and golf clubs to ease sporting. Aluminum-melon shell ash composite does not produce any harmful emissions, this could also enhance its potential uses in the manufacturing of sport equipment. In the marine industries, lightweight composites have found applications in making boats, hulls, and propellers. Glass, carbon, and vinyl fibre-

reinforced composites with epoxy resin matrix are some of the common composites in marine applications. These composites are expected to have good strength, durability, and corrosion resistance ability. Since aluminum generally offers considerable resistance to corrosion the presence of an optimized quantity of melon shell ash as reinforcement in the aluminum matrix may likely not reduce its corrosion resistance when used in the marine environment. Composites such as natural and synthetic fibre-reinforced polymers, metal matrix composites, and carbon fibre-reinforced composites have also been utilized in building development, bridge components, long-span roofs, water storage tanks etc. Properties such as high strength-to-stiffness ratio, low density and low stress are some of the requirements for the composites employed in the construction industries. The aluminum-melon shell ash composites possess some of these qualities making it a viable option for the construction industries. The low density and the improved strength-to-weight ratios achieved in this study are desirable material properties for lightweight applications in many industries especially where cheaper, durable, available and sustainable composite materials are required.

5. Future Perspectives

The mechanical behavior of the composites produced from the melon shell ash has shown that the properties can be controlled by varying the percentage composition of the reinforcements. This study suggests and encourages further exploration of the potential of other agricultural wastes in the environment in the field of materials, manufacturing and production engineering. In the future, agro wastes possess the potential to replace some hazardous and environmentally unfriendly reinforcements such as asbestos fibre employed in automobiles. Although the stir casting technique has been extensively utilized for composite production, however, its deficiencies such as non-uniform distributions of reinforcements and wettability call for explorations of other techniques such as compo casting, friction stir casting and powder metallurgy. Future research works could also encompass the optimization of both the composite production processes and the agro-waste composition in the metal matrix.

Acknowledgement

The authors acknowledged the following from the Department of Mechanical Engineering, Landmark University for their assistance during the composite preparations. J.I. Agaja, G.O. Omebije, M.A. Johnson, M.J. Fayose, C. Ezeobuka, A. D. Adeshina, C.C.Ekwijuru, O. Olanrewaju, K. Ekande, P.Okonkwo , J. Ogbonna and O. Kuforiji.

References

[1] Shoag MD and Rahman MF. IOP Conf. Ser. Earth Environ. Sci. 943 012028 (2021). Using Recycling Aluminum Cans as Composite Materials Aluminum Fiber Using Recycling Aluminum Cans as Composite Materials Aluminum Fiber. 2021; 943 012028. https://doi.org/10.1088/1755-1315/943/1/012028

[2] Omoniyi P, Adekunle A, Ibitoye S, Olorunpomi O, Abolusoro O. Mechanical and microstructural evaluation of aluminium matrix composite reinforced with wood particles. Journal of King Saud University - Engineering Sciences. 2022; 34:445-450. https://doi.org/10.1016/j.jksues.2021.01.006

[3] Omoniyi P, Abolusoro O, Olorunpomi O, Ajiboye T, Adewuyi O, Aransiola O, Akinlabi E Corrosion Properties of Aluminum Alloy Reinforced with Wood Particles. Journal of Composites Science. 2022;2022, 6(7):189. https://doi.org/10.3390/jcs6070189

[4] Abolusoro OP, Akinlabi ET. Wear and corrosion behaviour of friction stir welded aluminium alloys- An overview. International Journal of Mechanical and Production Engineering Research and Development. 2019; 9:967-982.
[5] Parveez B, Maleque A. Influence of agro-based reinforcements on the properties of aluminum matrix composites: a systematic review. J Mater Sci. 2021; 56:16195-16222. https://doi.org/10.1007/s10853-021-06305-2
[6] Ramanathan A, Krishnan P.K, Muraliraja R. A review on the production of metal matrix composites through stir casting-Furnace design, properties, challenges, and research opportunities. J. Manuf Processes. 2019;.42:213-245. https://doi.org/10.1016/j.jmapro.2019.04.017
[7] Baisane VP, Sable YS, Dhobe MM, Sonawane PM. Recent development and challenges in processing of ceramics reinforced Al matrix composite through stir casting process. Int J Eng Appl Sci. 2015; 2:2394-3661
[8] Ikubanni PP, Oki M, Adeleke AA. A review of ceramic/bio-based hybrid rein-forced aluminum matrix composites. Cogent Eng. 2020; 7:1-19
[9] Senthilvelan T, Gopalakannan S, Vishnuvarthan S, Keerthivaran K. Fabrication and characterization of SiC, Al2O3 and B4C reinforced Al-Zn-Mg-Cu alloy (AA 7075) metal matrix composites: a study. Adv Mater Res. 2013; 622:1295-1299. https://doi.org/10.4028/www.scientific.net/AMR.622-623.1295
[10] Bandil K, Vashisth H, Kumar S, Verma L, Jamwal A, Kumar D, Singh N, Sadasivuni KK, Gupta P. Microstructural, mechanical and corrosion behaviour of Al-Si alloy reinforced with SiC metal matrix composite. 2019; 53:4215-4223. https://doi.org/10.1177/0021998319856679
[11] Karthikeyan A, Nallusamy S. Investigation on mechanical properties and wear behavior of Al-Si-SiC-graphite composite using SEM and EDAX. In: IOP Conference Series: Materials Science and Engineering, IOP Publishing. 2017; p 012281. https://doi.org/10.1088/1757-899X/225/1/012281
[12] Alaneme KK, Aluko AO. Production and age-hardening behaviour of borax premixed SiC reinforced Al-Mg-Si alloy composites developed by double stir-casting technique. West Indian J Eng. 2012; 34:2
[13] Dwivedi SP, Sharma S, Mishra RK. Microstructure and mechanical behavior of A356/SiC/Fly-ash hybrid composites produced by electromagnetic stir casting. J Braz Soc Mech Sci Eng. 2019; 37:57-67. https://doi.org/10.1007/s40430-014-0138-y
[14] Osunmakinde L, Asafa TB, Agboola PO, Durowoju MO. Development of aluminum composite reinforced with selected agricultural residues. Discov Mater. 2023; 3:33. https://doi.org/10.1007/s43939-023-00069-z
[15] Abolusoro OP, Orah AM, Yusuf AS, Ayandotun WB, Ibrahim W (2023) Investigation of the Energy Capabilities of Selected Agricultural Wastes in a Fluidized-Bed Combustor. In: 2023 International Conference on Science, Engineering and Business for Sustainable Development Goals, SEB-SDG 2023. Institute of Electrical and Electronics Engineers Inc. 2023. https://doi.org/10.1109/SEB-SDG57117.2023.10124555
[16]Taylor P. Development of metal-matrix composites from industrial/agricultural waste materials and their derivatives. Crit Rev Environ Sci Technol. 2016; 46:143-208. https://doi.org/10.1080/10643389.2015.1077067
[17] Kandpal BC, Johri N, Kumar N, Srivastava A. Effect of industrial/ agricultural waste materials as reinforcement on properties of metal matrix composites. In: Materials Today: Proceedings. Elsevier Ltd, 2021; pp 10736-10740. https://doi.org/10.1016/j.matpr.2021.01.575
[18] Kulkarni PP, Siddeswarappa B, Kumar KSH. A survey on effect of agro-waste ash as reinforcement on aluminum base metal matrix composites. Open J Compos Mater. 2019; 9:12-26

[19] Joseph OO, Babremu KO. Agricultural waste as a reinforcement particulate for Al metal matrix composites (AMMCs). Rev MDPI Fibers. 2019; 7:7-33. https://doi.org/10.3390/fib7040033
[20] Saravanan SD, Kumar MS. Effect of mechanical properties on rice husk ash reinforced aluminum alloy (AlSi10Mg) matrix composites. Proc Eng. 2013; 64:1505-1513. https://doi.org/10.1016/j.proeng.2013.09.232
[21] Olorunmota RT, Ofuya TI, Idoko JE, Ogundeji BA. Effect of rice husk and melon shell wastes as possible grain protectants in cowpea storage. J Adv Biol Biotechnol. 2017; 1-9. https://doi.org/10.9734/JABB/2017/37114
[22] Usman AM, Raji A, Waziri N, Hassan MA. Aluminium alloy - rice husk ash composites production and analysis. Leonardo Electron J Pract Technol. 2014; 25:84-98.
[23] De SC, Khosrow R. Rice Husk Ash as a supplementary raw material for the production of cellulose-cement composites with improved performance. Waste Biomass Valor. 2010; 1:241-249. https://doi.org/10.1007/s12649-010-9017-7
[24] Tiwari S, Pradhan MK. Effect of rice husk ash on properties of Al-alloys. A[review. In: Mater Today Proc. 2017; pp 486-495. https://doi.org/10.1016/j.matpr.2017.01.049
[25] Dinaharan I, Kalaiselvan K, Murugan N. Influence of rice husk ash particles on microstructure and tensile behaviour of AA6061 Al matrix composites produced using friction stir processing. Comp Commun. 2017; 3:42-46. https://doi.org/10.1016/j.coco.2017.02.001
[26] Sathiesh Kumar N. Fabrication and characterization of Al7075 / RHA /Mica composite by squeeze casting. Mater Today Proc. 2020. https://doi.org/10.1016/j.matpr.2020.05.769
[27] Bakar RA, Yahya R, Gan SN. Production of high purity amorphous silica from rice husk. Procedia Chem. 2016; 19:189-195. https://doi.org/10.1016/j.proche.2016.03.092
[28] Verma N, Vettivel SC. Characterization and experimental analysis of boron carbide and rice husk ash reinforced AA7075 aluminium alloy hybrid composite. J Alloys Compd 2018; 741:981-998. https://doi.org/10.1016/j.jallcom.2018.01.185
[29] Joharudin NFM, Latif NA, Mustapa MS, Badarulzaman NA, Mahmod MF. Effect of burning temperature on rice husk silica as reinforcement of recycled aluminium chip AA7075. J Adv Res Fluid Mech Therm Sci. 2020; 68. https://doi.org/10.37934/arfmts.68.1.125132
[30] Ravi Kumar K, Pridhar T, Sree Balaji VS. Mechanical properties and characterization of zirconium oxide (ZrO2) and coconut shell ash(CSA) reinforced aluminium (Al 6082) matrix hybrid composite. J Alloys Compd. 2018; 756:171-179 . https://doi.org/10.1016/j.jallcom.2018.06.177
[31] Kaladgi ARR, Rehman KF, Afzal A, Baig MA, Soudagar MEM, Bhattacharyya S. Fabrication characteristics and mechanical behaviour of aluminium alloy reinforced with Al2O3 and coconut shell particles synthesized by stir casting. IOP Conf Ser Mater Sci Eng. 2021; 1057:12017. https://doi.org/10.1088/1757-899X/1057/1/012017
[32] Bello SA, Raheem IA, Raji NK. Study of tensile properties, fractography and morphology of aluminium (1xxx)/coconut shell microparticle composites. J King Saud Univ - Eng Sci. 2017; 29:269-277. https://doi.org/10.1016/j.jksues.2015.10.001
[33] Zainudin NF, Lee KT, Kamaruddin AH, Bhatia S, Mohamed AR. Study of adsorbent prepared from oil palm ash (OPA) for flue gas desulfurization. Sep Purif Technol. 2005; 45:50-60. https://doi.org/10.1016/j.seppur.2005.02.008
[34] Aigbodion VS, Ezema IC. Multifunctional A365 alloy/PKSAnp composites: microstructure and mechanical properties. Defense Technol. 2020; 16:731-736. https://doi.org/10.1016/j.dt.2019.05.017
[35] Hashimah N, Mohamad B. The utilization of Palm Oil Fuel Ash in Aluminium Metal Matrix Composites. Materials. 2019
[36] Sn W. Sugarcane bagasse: how easy is it to measure it's constituents? . Proc S Afr Sug Technol Ass. 2008; 81:266-273

[37] Thirugnanasambandham T, Chandradass J. Fabrication and Characteristization of Bagasse Ash Particle (BAP) Reinforced Magnesium (AZ91E) Alloy Composite by Vacuum Stir Casting. In: IOP Conf. Ser. Mater. Sci. Eng. 2020; 993 012133. https://doi.org/10.1088/1757-899X/993/1/012133
[38] Usman AM, Raji A, Hassan MA, Waziri NH. A comparative study on the properties of Al-7%Si-rice husk ash and Al-7%Si-bagasse ash composites produced by stir casting. Int J Eng Sci. 2014; 3:1-7
[39] Kamble A, Kulkarni SG. Microstructural examination of bagasse ash reinforced waste aluminium alloy matrix composite. AIP Conf Proc. 2019; 2105. 1-8. https://doi.org/10.1063/1.5100696
[40] Chandla NK, Yashpal, Kant S, Goud MM, Jawalkar CS. Experimental analysis and mechanical characterization of Al 6061/alumina/bagasse ash hybrid reinforced metal matrix composite using vacuum-assisted stir casting method. J Compos Mater. 2020; 54:4283-4297. https://doi.org/10.1177/0021998320929417
[41] Tyagi L, Butola R, Jha AK. Mechanical and tribological properties of AA7075-T6 metal matrix composite reinforced with ceramic particles and aloevera ash via Friction stir processing. Mater Res Express. 2020; 7:1-13. https://doi.org/10.1088/2053-1591/ab9c5e
[42] Jose J, Christy TV, Peter PE, Feby JA, George AJ, Joseph J, Chandra RG, Benjie NM. Manufacture and characterization of a novel agro-waste based low cost metal matrix composite (MMC) by compocasting. Mater Res Express. 2018; 5:1-32. https://doi.org/10.1088/2053-1591/aac803
[43] Gupta MK. Effects of tool pin profile and feed rate on wear performance of pine leaf ash / Al composite prepared by friction stir processing. J Adhes Sci Technol. 2020. https://doi.org/10.1080/01694243.2020.1800290
[44] Nagpal Y, Sharma P, Sharma R. A Study on Characterization of Green Metal Matrix Composites Reinforced with Melon Shell Ash Particulates. In: Lecture Notes on Multidisciplinary Industrial Engineering. Springer Nature, 2022; pp 141-152. https://doi.org/10.1007/978-3-030-73495-4_10
[45] Aigbodion VS, Atuanya CU. Improving the properties of epoxy/melon shell bio-composites: effect weight percentage and form of melon shell particles. Polymer Bulletin. 2016; 73:3305-3317. https://doi.org/10.1007/s00289-016-1657-8
[46] Abdulwahab M, Umaru OB, Bawa MA, Jibo HA. Microstructural and thermal study of Al-Si-Mg/melon shell ash particulate composite. Results Phys. 2017; 7:947-954. https://doi.org/10.1016/j.rinp.2017.02.016
[47] Suleiman IY, Salihu SA, Mohammed TA. Investigation of mechanical, microstructure, and wear behaviors of Al-12%Si/reinforced with melon shell ash particulates. International Journal of Advanced Manufacturing Technology. 2018; 97:4137-4144. https://doi.org/10.1007/s00170-018-2157-9
[48] ASTM International, B557-15 standard test methods for tension testing wrought and cast Aluminium. ASTM Int. 2015; 1-16. https://doi.org/10.1520/B0557- 15.2
[49] ASTM E10-18 2017. Standard Test Method for Brinell Hardness of Metallic Materials.
[50] ASTM International Standard E23 of the year 2007. Test Methods for Notched Bar Impact Testing of Metallic Materials.
[51] Hamouda AMS, Sulaiman S, Vijayaram TR, Sayuti M, Ahmad MHM (2007) Processing and characterization of particulate reinforced aluminium silicon matrix composite. Journal of achievements in materials and manufacturing engineering 2:11-16

Research on Engineering Structures & Materials
www.jresm.org
Research Group

Research Article

Evaluation of bentonite suitability as a binder on the physico-mechanical and thermal properties of insulating bricks produced from quartz deposit

Ogundipe O. B.[1,*,a], Ikubanni P.P.[2,3,b], Adebayo R.A.[4,c], Abolarinwa B.O.[2,d], Dike C.P.[5,e], Lawal S.O.[2,f], Ajewole J.B.[2,g], Oladimeji S.O.[2,h]

[1] *Dept. of Mechanical Engineering, Redeemer's University, Ede, Nigeria*
[2] *Dept. of Mechanical Engineering, Landmark University, Omu-Aran, Nigeria*
[3] *Dept. Mechatronics Engineering, Bowen University, Iwo, Nigeria*
[4] *Dept. of Research and Development, National Engineering Development Institute, Anambra State, Nigeria*
[5] *The Federal Polytechnic Offa, Offa, Kwara State*

Article Info

Article history:

Received 28 June 2024
Accepted 29 Aug 2024

Keywords:

Quartz;
Bentonite;
Bonding material;
Insulating bricks;
High temperature

Abstract

The study developed insulating refractory bricks from quartz with varied percentages of bentonite as a binder was subjected to physico-mechanical and thermal investigations. The produced bricks were dried and then sintered at 1200°C. To examine the refractory performance of the material, analyses were done on the bulk density, apparent porosity, shrinkage test, loss on ignition (LOI), cold crushing strength (CCS), water absorption (WA), and microstructural examination using scanning electron microscope and energy dispersive X-ray spectroscopy (SEM-EDS). The tested bricks' average apparent porosity of 43, 46, and 48%; water absorption of 0.98, 1.70, and 1.86%; bulk density of 1644, 1516, and 1324 kg/m^3; shrinkage value of 1.71, 0.20, and 0.66%; cold crushing strength of 2.165, 1.381, and 1.088 MPa; loss on ignition of 0.98, 1.70, and 1.86%; and refractoriness of 1571.68, 1568.53, and 1565.39 ^{0}C were obtained for varying the percentage of the bentonite to 5, 10, and 15%, respectively. These results were within the range of values considered typical for refractories suggesting their suitability for high temperature applications. Additionally, the microstructural examination demonstrated homogeneity and the distribution of silicon throughout the brick structure. These denote consistent qualities and good thermal and mechanical capabilities. Meanwhile, the bonding materials were observed to significantly affect the refractory bricks produced.

1. Introduction

Refractory materials (RMs) have shown exponential growth in industrial applications over time, which can be attributed to the rising need for high-temperature materials [1-3]. The exponential growth in industrial applications of refractory materials (RMs) over time can be attributed to the increasing demand for high-temperature materials. This demand arises from various industries where RMs are essential, such as pyrometallurgy, where they are used in furnaces, kilns, incinerators, and other high-temperature environments. RMs exhibit properties like thermomechanical stability, resistance to thermal decomposition, pressure loads, physical wear, and chemical attack, making them indispensable in these applications [1-3].

*Corresponding author: benshogo@gmail.com
[a]orcid.org/0009-0002-1880-2581; [b]orcid.org/0000-0002-2710-1130; [c]orcid.org/0009-0005-0779-0070; [d]orcid.org/0009-0009-6106-4992; [e]orcid.org/0009-0007-8808-7401; [f]orcid.org/0000-0002-5776-7654; [g]orcid.org/0009-0007-1517-4889; [h]orcid.org/0009-0000-5010-5730
DOI: http://dx.doi.org/10.17515/resm2024.333me0628rs

Meanwhile, bentonite, a clay mineral renowned for its unique properties such as high-water absorption capacity, swelling ability, plasticity, and thixotropy, plays a significant role in various industrial applications. Its properties make it an excellent binder in the production of building materials like bricks and ceramics [4]. In recent researches, bentonite has been reported to improve sintering mechanism when used as the bonding material [5,6]. Also, the high thermal stability of bentonite is another favorable property. Apart, from the resistance to high temperature, the chemical composition and the content of Montmorillonite of bentonite makes it favorably sorted after for binding in high temperature applications [7-9].

Due to the properties of RMs, they are vastly used in the process of the pyrometallurgical field as part of the structure constituents (pre-eminently inlays) in incinerators, furnaces, ovens, kilns, as well as areas of operation where thermo-mechanical durability is of primary concern for example fire or combustion indicator mechanism for rocket take off supports and re-entry temperature shield used in spacecraft [10, 11]. The predominant of RMs are non-metallic, polyphase, and inorganic materials that also exhibit permeability, non-homogeneity, and polycrystallinity. Hence, these materials are naturally composed of elements like aluminum (Al), silicon (Si), zirconium (Zr), magnesium (Mg), and others, either as oxides or non-oxides. They could be described as consisting of bonding agent phases, additives, and heat resistance composite minerals. Additionally, some metals with melting points higher than 1850 °C, such as tungsten (W), which has a fusion or melting point of 3422 °C, and niobium (Nb), which has a liquefaction phase with 2477 °C, are also regarded as RMs [10 - 12]. The bonding material to be used for the binding of RMs during production needs to also exhibit excellent thermal properties. However, several studies have explored the mineralogical and thermal properties of bentonite, highlighting that it has stable thermal properties [13, 14].

Generally speaking, RMs are materials that retain their mechanical integrity, dimensional stability, and chemical identity when subjected to elevated heat above 538 °C and are mechanically resilient to thermal decomposition, applied force, mechanical deterioration, or chemical degradation such as corrosion [11, 15]. Insulating materials consist primarily of a binder phase, a thermally stable mineral aggregate, and additives. They are non-metallic inorganic materials. Insulating bricks are made to withstand a variety of abrasive and corrosive particles, liquids, or gases as well as exposure to extremely high temperatures [16]. The primary fundamental materials utilized in manufacturing the refractories include silicon oxides SiO_2, calcium (Ca), magnesium (Mg), aluminum (Al), and zirconium (Zr) as well as other non-oxide compounds including borides, nitrides, carbides, silicate, and graphite [17]. Due to the industrial applications of refractories, mechanical strength is critical to be able to resist thermal shock and deformation when in use. Dense refractory materials, such as fireclay and high-alumina bricks, are used for their high mechanical strength. In this light, there are basic requirements a material should meet before it can be used as refractory material [18-20]. Meanwhile, the strength of most refractory materials is extremely reliant on the bonding agent [21], binders are very critical for the production of refractory.

Overall, refractory materials are essential for many high-temperature industrial processes and are however required to perform the following basic functions: act as a thermal insulation; act as a chemical barrier that prevents corrosion; and provide mechanical stability [23]. As demand for these materials continues to grow, the development of new, innovative refractory materials is likely to hold a crucial role in the future of high-temperature manufacturing. In a bid to develop a stable refractory brick, the study investigated the effect of the selected bonding material on the physical, mechanical, and thermal stability of the produced bricks. The microstructural examination of the bricks produced was carried out using scanning electron microscopy with energy-dispersive X-

ray spectroscopy (SEM/EDS). This study is important to enable the selection of the bonding materials and the proportion that enhances overall efficiency in high-temperature industrial applications.

2. Materials and Methods

2.1 Materials

Quartz rock specimens were dug from the extraction sites using the appropriate crude instruments. Figure 1 (a) and (b) presented the as-collected quartz and the milled bentonite powder, respectively. Also, the functions and sources of the specimens utilized for manufacturing the refractories are presented in Table 1.

(a) (b)

Fig. 1. Image of materials used (a) quartz (b) bentonite

Table 1. Materials

S/N	Material	Source	Use
1	Quartzite	Ijero-Ekiti, Ekiti State, Nigeria	Production of refractory bricks
2	Bentonite	Sango, Ogun State, Nigeria	Binding material
3	Distilled Water	-	For mixing the refractory and binder

2.2 Methods

The collected rock samples were cleaned and sunbaked for 3 days to reduce humidity level for easy grinding of the rock samples [23]. The dried samples were then mechanically grinded into fine powders in a lab ball mill (Model 48-D0500/D and Serial No. 14002201). The fined particles were heated at 110 °C for 1 h in an oven to ensure that the unbounded moisture content had completely evaporated [23]. The pictorial illustration of the entire process followed while producing the refractory bricks is presented in Fig 2.

Table 2. Materials composition

	Materials and Percentage Composition	
S/N	Quartzite (wt. %)	Bentonite (wt %)
1	95	5
2	90	10
3	85	15

The process of turning the rock element's fine grains into a uniform mouldable mixture served as the first step in making refractory (insulating) bricks. This was accomplished by including 5, 10, and 15% bentonite as shown in Table 2 in succession as binder, and 8% water. The 8% water was adopted based on the study of [24], stating it to be the ideal amount required for best plasticity. The binder application is done to increase pre-fired or raw strength and serve as an addictive [25]. The slurry was then automatically homogenized by rapidly stirring in a clockwise manner with a ceramic blunger until a uniform plastic paste was achieved. The resulting paste was then put into the steel plate-made mould with dimensions 50 x 50 x 50 mm as shown in Figure 3. With the firing temperature reaching 1200 °C, the green samples were fired using an oven at 100 °C for 10 min. The refractory bricks were maintained at 1200 °C for 8 hr, after which a 24-hour cooling occurred within the furnace [23]. Diverse evaluations were carried out to establish insulating bricks' technical or mechanical characteristics and heat durability.

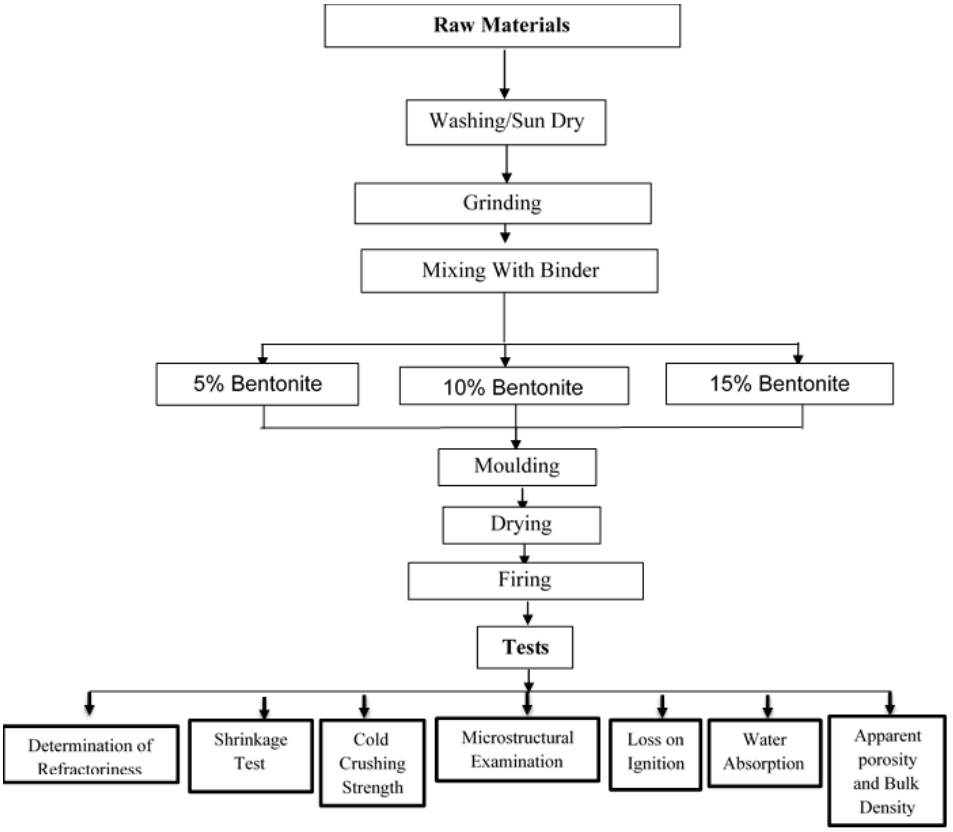

Fig. 2. Schematic representation of the method

Fig. 3. Produced refractory brick

2.2.1 Apparent Porosity of The Bricks

By immersing the brick in a water bath, the permeability of the refractory material produced was ascertained. The bath was kept at 100 °C and the immersion time was set to 24 h. Each brick sample's apparent porosity was assessed in accordance with [26] specification. Apparent porosity was therefore calculated using Eq. (1):

$$Apparent\ porosity\ (p_a) = \frac{w_{sww} - w_{da}}{w_{sww} - w_{sw}} \times 100 \quad (1)$$

where w_{sww}, w_{da}, and w_{sw} are saturated mass of the immersed sample in water, dry mass of the sample in ambient air, and mass of the sample immersed in water, respectively.

2.2.2 Brick Bulk Density Measurement

The bulk density of each refractory bricks was determined using the Eq. (2):

$$Bulk\ Density\ (B_d) = \frac{mass\ of\ material}{volume\ of\ material} \quad (2)$$

2.2.3 Shrinkage Test for the Bricks

The shrinkage analysis is essential for measuring the change in volume that occurs as the water content of refractory bricks fluctuates during manufacturing. To assess the shrinkage of the bricks, a diagonal line labeled as l_1 is drawn across each test sample. Sequentially, samples were exerted to a temperature of 1000 °C in the furnace. After firing, another line, designated as l_2, is depicted through the bias of the fired samples to establish their ultimate dimension. As a result, the material's linear shrinkage was calculated using Eq. (3) from the ASTM C596 - 18 specification [27].

$$Lineear\ Shrinkage = \frac{l_1 - l_2}{l_1} \times\ 100\% \quad (3)$$

2.2.4 Cold Crushing Strength (CCS) Test of the Bricks

The cold crushing strength test is a standard method utilized to establish the strength of bricks mechanically, refractory composites, and other similar products at room temperature varying two experiments per sample. It measures how materials endure a compression force excluding any deformation or failure experience. The CCS test is important for evaluating the quality and durability of bricks. It is the ultimate loading per unit area which a refractory material will exclude under specific conditions at ambient temperature before failing. Typically, cold crushing strength is utilized to assess the

toughness of refractory materials mechanically using universal testing device (Testometric M500-50AT), the CCS of each brick was calculated in compliance with standard [28].

2.2.5 Loss on Ignition Test of the Bricks

Before subjecting a sample to heating, any residual moisture from drying needs to be eliminated. The Loss on Ignition (LOI) analysis is a common method employed to evaluate organic and inorganic composition content in bricks, refractory materials, and other similar products. It measures the percentage of weight loss experienced by a sample when subjected to high temperatures, typically in the range of 800-1000°C. The LOI test is essential for assessing the quality, purity, and composition of bricks. It signifies the variation in material mass before and in the aftermath of ignition.

In this study, LOI is the mass decrease using an overall mass of refractory bricks produced, represented in percentage. As a result, each brick's weight loss was estimated as the difference between their pre- and post-firing weights, and as a result, the LOI at 1200 °C was computed using Eq. (4) as per the [29] test standards.

$$LOI = \frac{W_1 - W_2}{W_1} \times 100 \quad (4)$$

where W_1 is the brick sample's initial mass before firing. Brick sample's ultimate mass W_2 following firing. Lost On Ignition of bricks produced was calculated utilizing the [29] test analyses.

2.2.6 Water Absorption Test of the Bricks

Water Absorption (WA) tests are frequently performed to assess the porosity and permeability characteristics of refractory materials. This test entails quantifying the quantity of water absorbed by a sample of the refractory material within a designated timeframe. Water absorption evaluation was executed by subjecting the ignited evaluation materials to boiling at 100 °C time interval of 24 h, then additional immersion into water was carried out in 4 h. Water absorption was determined by calculating the mass disparity of the produced material prior to and following immersion, utilizing Eq. (5) as outlined in ASTM C20-00-15 [26].

$$WA = \frac{W_s - W_d}{W_d} \times 100 \quad (5)$$

where soaked weight after boiling at 100 °C is W_S and dry weight is W_d

2.2.7 Determination of the Refractoriness of the Bricks

A sample's capacity to tolerate high heat exposure without significantly deforming is evaluated by its refractoriness. Moreover, the fusibility measurement of a refractory material reveals where the material starts to lose rigidity. Shuen's method was used in this study to assess the refractoriness of the sample bricks [30]. The amounts of alumina and other oxides in the refractory brick were measured engaging Shuen's formula to assess the thermal stability of the material. The brick materials were chemically evaluated via (XRF) X-ray fluorescence spectroscopy to achieve this. Eq. (6) was then used to determine the refractoriness of bricks:

$$K = \frac{360 + Al_2O_3 - RO}{0.2280} \quad (6)$$

where refractoriness (°C) is represented by K, Al_2O_3 represents the refractory's alumina composition, and the total of the sample's other oxides except SiO_2 is represented by RO.

2.2.8 Microstructural Examination of the Bricks

Microstructural examination in bricks involves analysis of the internal structure, composition, and morphology of the brick material at a microscopic level. This examination provides valuable intuitions into the superiority, properties, and concert of the refractory bricks. Using scanning electron microscopy (SEM) coupled with energy dispersive spectroscopy (SEM-EDS) using model of Phenom Prox having a voltage of 15 kV, the framework morphology of refractory bricks produced was investigated. Before using SEM analysis, the evaluated materials were sputter-coated and placed on stubs made of aluminium. An energy dispersive detector that can distinguish between different X-ray energies was used to evaluate the X-ray emissions. After each element present was intensified using the EDS scan, the virtual representations were recorded, and the molar concentration in % was computed.

3. Results and Discussion

3.1 Apparent Porosity

The variation in the amount of bentonite used as a binder has an influence on the apparent porosity of refractory bricks. Highly porous brick does not crack because of the pores present. Because of this, depending on the specific service situation(s), Porosity level is a compromise. that are considered. Brick sample's APV, or apparent porosity values, are 43, 46, and 48% with respect to the 5%, 10%, and 15% of bentonite as a binder (Figure 4). From this outcome, it is observed that apparent porosity increases linearly with-respect to the upsurge in Bentonite Binder Content (BBC) for the quartz. A refractory Brick Sample (RBS) with a maximum apparent porosity parameter (APP) of 48% was noted in Q15 RBS and the lowest APP of 43% was observed for the Q5 RBS. The increase and decrease in APPs of RBSs via the addition of binders have been attributed to the particle packing factor of the binders. Binders with closely packed particles usually reduce the APPs of RBSs due to an equivalent elevation of the binding or bonding forces among the material elements, which lowers the number of voids inside of them. On the contrary, binders with loosely packed particles usually increase the APCs of RBSs due to poor adhesive strength between the particles thereby facilitating the presence of more [31].

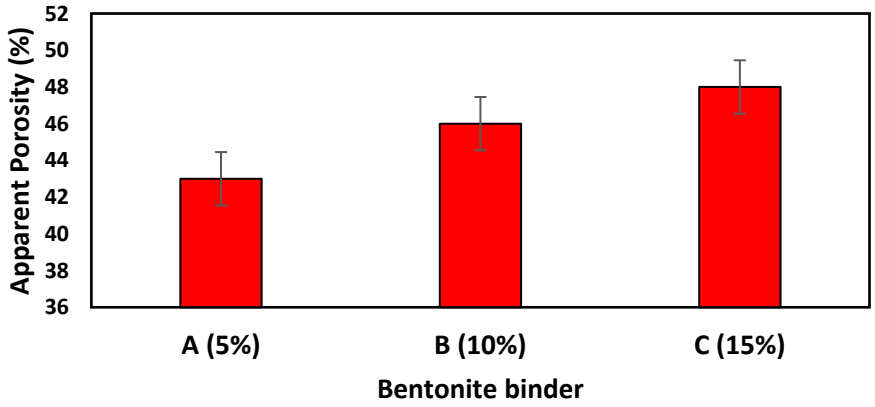

Fig. 4. Apparent porosity of refractory brick at diverse bentonite proportion

An equivalent observation was recorded when [32] studied the constancy of steel waste as heat-resistance material utilizing boric acid and bentonite as bonding agents. This is also

comparable to what was reported by [31] in their study on the ceramics potential of Dabagi clay deposits. The experimental APPs in RBS are more complex than the suitable APPs (20-30%) when compared to standard siliceous fireclay. To address the problem, studies have suggested using bonding agents with densely packed particles in the refractory bricks samples hence applying the proper heat-time processing [33]. In a related investigation, sawdust was used as an addition, and the resulting apparent porosity parameters were 30.230, 39.50, 45.450, and 46.150%, correspondingly. Between 5 and 20% of the sawdust additive composition, comparing the control sample showed a development in apparent porosity parameters at an average of 200 percent. A direct relationship between porosity value and additive composition was established in the study. These outcomes reveal APPs of some burnt bricks solely depend on the amount of binders used, having a proportion enhancement in permeability vacillating from 104 to 199 percent in compositions of rice chaff additions of 5 to 20 percent [34].

3.2 Bulk Density

The bulk density provides a comprehensive indication of the produced bricks quality. Advanced bulk density with minimal porosity in refractories is generally considered to have a higher grade. A higher bulk density increases the volume's stability, thermal capacity, and slag resilience to infiltration [35]. As shown in Figure 5, the average sample's bulk density was determined to be 1644, 1516, and 1324 kg/m^3 with respect to the addition of bentonite as a binder of 5, 10, and 15%. From the result, it can be observed that an increase in the amount of BBC is unfavorable to the quartz sample. Meanwhile, [36] estimated that the bulk density of fireclay refractories should be 1910 kg/m^3. The bulk density parameters acquired in this research were minimal compared to the stipulated amount. The decrease in bulk density with increasing BBC may indicate a potential compromise in the quality of the quartz refractory bricks. However, the observed values are within the range reported for refractory clay, indicating that they still fall within acceptable limits for this type of material. Additional evaluation and deliberation in other properties might be introduced to wholly assess some quality and suitability of the refractory bricks. However, according to [37-39] the result is quite near to the range of 1700.0 to 2300.0 kg/m^3 for refractories mud. In the studies of [39, 40], Egbahieme clay with a comparable composition was reported to have a similar value of 1640 kg/m^3.

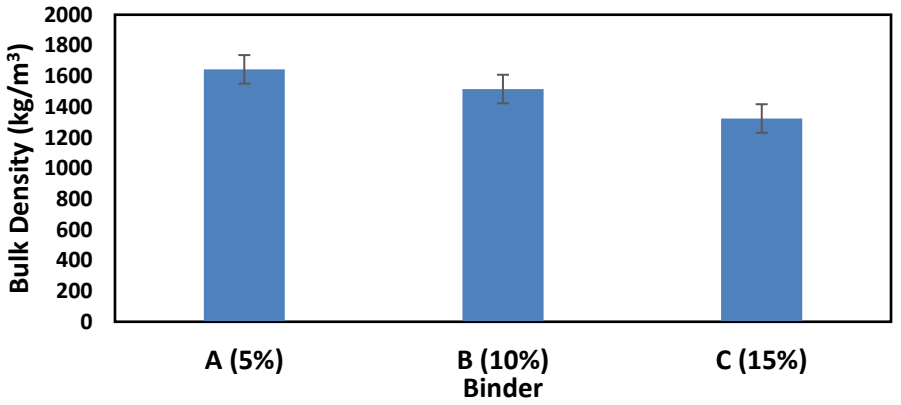

Fig. 5. Bulk density of the refractory brick at different bentonite percentage

3.3 Linear Firing Shrinkage

Linear firing shrinkage tends to modify the direct magnitude of the refractory brick samples during which it has undergone firing. In a thermal treatment furnace, a low shrinkage value is preferable for refractory bricks application [41]. The linear shrinkage values (LSV) obtained in this study were 1.71, 0.20, and 0.66% for 5, 10, and 15% of bentonite (binder), respectively. From the result, it can be observed that the effect of the BBC is significant for the quartz RBS. The highest LSV of 1.71% was observed for the Q5 RBS while the lowest LSV was observed for the Q10. As displayed in Figure 6, the overall RBSs exhibited LSVs between 0.2 and 1.71%, which were minimal compared to LSVs in the range of 4.0 – 10.0% in studies recommended for fireclays [42]. Nonetheless, other investigators claim that values less than 4% would be appropriate and that lower LSVs are preferable. [32, 44]. According to these studies, LSVs below 4% are tolerable, and lower LSVs are preferable. This suggests that the RBSs that are created would be less prone to volumetric shrinking. Furthermore, as the bentonite bonding agent confers proportional durability in Refractory Bricks Samples it does not contract as much as the specimens of rock do with temperature-time response, the minimal LSVs considering the RBSs can be linked to this property. [32] made a similar discovery. [44] additionally ascribed grog, which makes up 90% of their brick composition, having improved thermal stability and anti-shrinkage properties due to the low LSV (1.01%) ratio recorded for Ozanagogo clay.

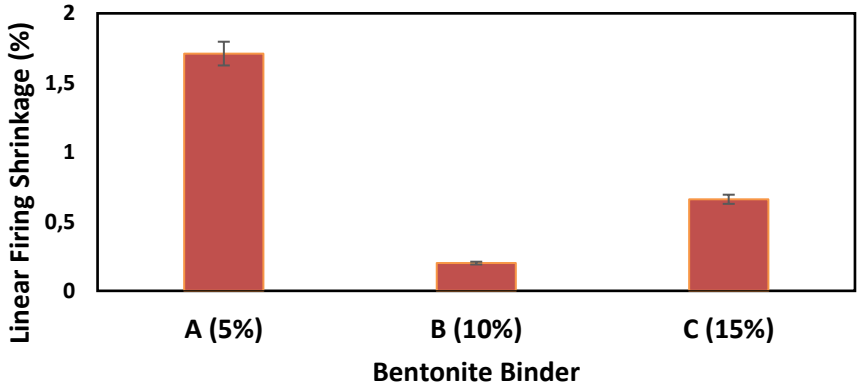

Fig. 6. Linear firing shrinkage of the refractory brick at different bentonite percentages

3.4 Cold Crushing Strength

From the result displayed in Figure 7, it can be deduced that the higher the proportion of the bonding agent, the lower the Cold Crushing Strength (CCS). The compressive stress at peak when 5%, 10%, and 15% binder was used on quarts sample is 2.165, 1.3805, and 1.0875 MPa, respectively. The highest stress that a brick can sustain before failing is 2.165 MPa for Q5 (i.e. 5% of binder to quartz sample), which is the CCS for the RBS. This number is within the range of 0.9810- 6.8670 MPa, for conventional compressive strength values as reported by [44]. The significant porosity of the brick sample can be attributed to the low strength of the bricks. Figure 8 is the image of the bricks that has undergone compression strength testing.

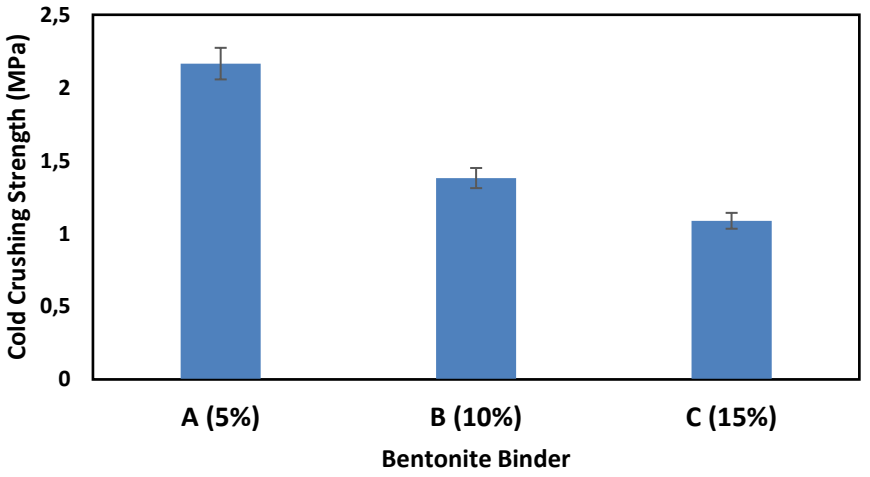

Fig. 7. Cold crushing strength of the refractory brick with different bentonite percentage

Fig. 8. Image of a failed Refractory Bricks under cold crushing strength test

3.5 Loss on Ignition Result

Shrinkage and porosity values are impacted by loss on ignition (LOI), which implies loss of organic solvent materials during firing. The results of the LOI in this study were comparable to research by [45]. The RBSs in this study had LOI values of 0.98, 1.70, and 1.86% for 5%, 10%, and 15% of bentonite (binder), respectively. This displays the maximum quantity of moisture that RBS can contain or the percentages of sample mass loss [23]. According to the minimal LOI ratio discovered during experimentation, RBS does not include much in the way of organic and/or hydrated components.

From the result (Table 3), observations showed that the highest LOI value was attained by the RBS with 15% bentonite while the lowest LOI value was attained by the RBS with 5% bentonite. However, with respect to bentonite wt. %; for the quartz-based RBS, the LOI values increased with an increase in bentonite wt. %.

3.6 Water Absorption (WA)

The quantity of water that a brick sample can absorb is determined by its water absorption (WA). The durability property of refractory bricks is ascertained via the water absorption test. According to Table 3, the RBS's WA on approximation is 2.43, 4.22, and 4.93% with respect to 5%, 10%, and 15% of the binding material, which is minimal when related to the research of [46]. The type of refractory and circumstances used to determine a precise effect of WA on refractory materials, though [47]. Refractories' WA is a crucial component since it has an impact on the material's toughness, longevity, and thermal shock resistance. A refractory becomes more porous and more vulnerable to mutilation in heat cycling and some stressors as its water intake increases. Lower water absorption, on the other hand, results in a refractory that is denser and stronger and can endure greater temperatures and harsher conditions. With less water penetration in refractory bricks, the durability of the bricks is enhanced as well as their capacity to resist the natural environment [41]. According to [48], WA lesser to 1 percent is regarded as having minimal absorption, whilst WA above 6% is regarded as having strong absorption. A clear correlation exists between perceived porosity and the absorption of water in the refractory bricks [41]. In this study, the increase in bentonite percentage tends to increase the WA value.

3.7 Refractoriness

Table 4 contains the refractory material's chemical compositions determined using the XRF. RMs with higher SiO_2 have content higher than 46.51 wt.% and can tolerate comparatively at high temperatures [49]. Also, Al_2O_3 content in refractories is reported to have a straight relationship with the refractoriness of the material in a way in which the higher the Al_2O_3 content, the higher the refractoriness [49].

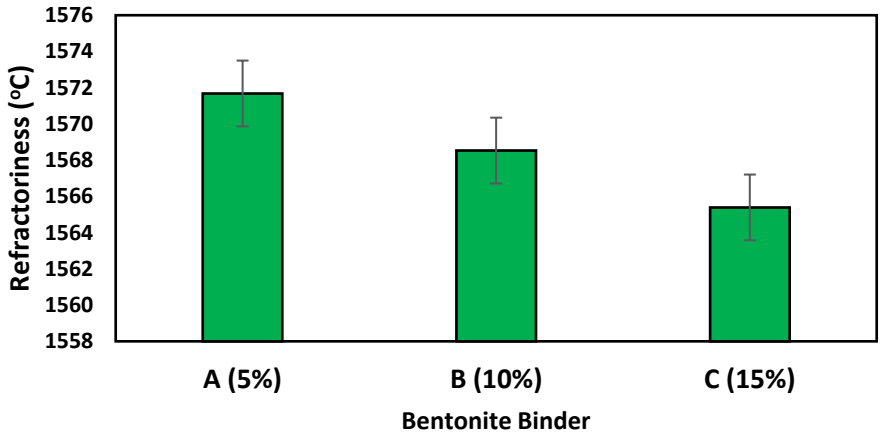

Fig. 9. Refractoriness of the refractory brick at different bentonite percentages

Refractory bricks must be able to tolerate high temperatures without melting, breaking, or degrading for these industrial applications to function well and last a long time. Refractoriness refers to a material's capacity to resist high temperatures without significantly altering its physical or chemical composition. As reflected in Figure 9 and Table 3, the RBS's refractoriness was determined to be 1571.68, 1568.53, and 1565.39 °C with the addition of bentonite at 5%, 10%, and 15% respectively, which is comparable to the 1550 °C that [50] determined for Egyptian magnesite. According to [51-53], the permissible range of refractoriness is often above 1,300 °C.

The summary of the properties obtained from the samples compared with an international standard (ASTM) is displayed in Table 3. Also, to determine the effect of the varied percentage of bentonite on the produced bricks, One-way Analysis of Variance (ANOVA) of the results at 5% significant level was calculated and presented in Table 4. Based on the p-values from the statistical analysis, the result statistically revealed that varying the composition of the binder has a significant effect on the refractoriness, cold crushing strength, water absorption, loss on ignition, and bulk density. Meanwhile, it is statistically insignificant in the apparent porosity and linear firing shrinkage. As presented in Table 5, adding bentonite to refractory bricks significantly affects their chemical composition. Table 4 indicates that bentonite is rich in SiO_2, which is one of the contents that gives the bentonite bonding strength [14].

Table 3. Refractory mechanical characteristic of refractory brick

Properties	Refractory Bricks Sample			International Standard (ASTM)
	5% Binder	10% Binder	15% Binder	
Apparent Porosity (%)	43	46	48	20–30
Bulk Density (kg/m^3)	1644	1516	1324	300 to 3200
Water Absorption (%)	2.43	4.22	4.93	1 to 10
Loss on Ignition (%)	0.980	1.70	1.86	0.5-3
Linear Firing Shrinkage (%)	1.710	0.20	0.66	0.3-2.5
Cold Crushing Strength (MPa)	2.165	1.3805	1.0875	0.981–6.867
Refractoriness (^{o}C)	1571.68	1568.53	1565.39	> 1300

Table 4. One-Way ANOVA of the Brick

(a) Apparent Porosity

Source	Degree of Freedom	Sum of Squares	Mean Square	F-Value	P-Value (0.05)
Samples	2	818.7	409.3	1.58	0.280

(b) Bulk Density at varied bentonite

Source	Degree of Freedom	Sum of Squares	Mean Square	F-Value	p-Value (0.05)
Samples	2	298443	149221	8.42	0.018

(c) Water Absorption

Source	Degree of Freedom	Sum of Squares	Mean Square	F-Value	p-Value (0.05)
Samples	2	934.8	467.42	22.86	0.002

(d) Loss on Ignition

Source	Degree of Freedom	Sum of Squares	Mean Square	F-Value	p-Value (0.05)
Samples	2	20.855	10.428	8.26	0.019

(e) Linear Firing Shrinkage

Source	Degree of Freedom	Sum of Squares	Mean Square	F-Value	p-Value (0.05)
Samples	2	0.7040	0.3520	1.74	0.253

(f) Compressive stress

Source	Degree of Freedom	Sum of Squares	Mean Square	F-Value	p-Value (0.05)
Samples	2	20.855	10.428	8.26	0.019

(g) Refractoriness

Source	Degree of Freedom	Sum of Squares	Mean Square	F-Value	p-Value (0.05)
Samples	2	24756.5	12378.3	294.11	0.000

However, it can be observed that higher bentonite content decreases SiO_2 content while it increases Al_2O_3, Fe_2O_3, and other oxides, enhancing the mechanical strength, thermal stability, and chemical resistance of the bricks. The increased Al_2O_3 content enhances refractory performance at high temperatures by improving mechanical strength and thermal stability while higher fluxing agents like Fe_2O_3 and K_2O tend to influence the melting behaviour and thermal expansion properties of the bricks which in turn enhances the brick's toughness. Also, increased Fe_2O_3 as well as increased CaO, TiO_2, and V_2O_5 influence the resistance to chemical attacks and abrasion. Meanwhile, lowered SO_3 and Cr_2O_3 lower the risk of chemical attack and corrosion attack, respectively. The chemical changes suggest that bricks with higher bentonite content may perform better in harsh thermal and mechanical environments, making them more suitable for high-stress applications.

Table 5. Chemical composition of refractory bricks samples gotten from XRF

Element Type	Conc (wt.%) at 5% Bentonite	Conc (wt.%) at 10% Bentonite	Conc (wt.%) at 15% Bentonite
SiO_2	92.16	90.01	87.86
Al_2O_3	3.09	3.81	4.52
Fe_2O_3	2.53	3.73	4.93
CaO	0.31	0.31	0.31
K_2O	0.22	0.29	0.36
SO_3	0.53	0.50	0.49
TiO_2	0.15	0.31	0.46
V_2O_5	0.02	0.03	0.04
Cr_2O_3	0.09	0.08	0.08
ZrO_2	0.01	0.02	0.03
MnO	0.03	0.03	0.04
Others	0.86	0.88	0.88

3.8 Morphological Analysis of the Samples using SEM/EDS

Figure 10 shows the SEM images of the quartz bricks and Figures 11 – 13 show the EDS analysis of the samples based on the 5, 10, and 15% bonding agents, respectively. The RBS's microtextural organization is made up of numerous ring layers (rims), which are signs of reactions taking place. The brick's inner portion, which is a holdover from initial brick production, which encircled by two rims, one on each that is made up of various complicated matrixes with needle-like silicon crystallization. Elements such as silicon have the highest weight concentrations of 88.38, 78.49, and 80.45% in the EDS analysis for the 5, 10, and 15% bentonite concentrations respectively which is comparable to concentrations of the chemical element in the refractory brick. The high concentration of silicon indicates a predominant presence of SiO_2 with the inclusion of other minor oxides such as Al_2O_3, PbO, P_2O_5, Fe_2O_3, and so on. Based on this analysis, high silica concentrations indicate enhanced thermal stability in all three binding proportions. Alumina on the other

hand increases the overall strength of the refractory brick produced and it also constitutes heat retention and dissipation during the heating process. Alumina traces are found in all the binding proportions but have higher concentrations as the bentonite binding proportion increases. Iron, carbon, oxygen, and titanium, reduced the melting point of the bricks and improved the overall stability and durability of the refractory bricks as appropriate with the same ratio with percentages of binders used. The overall strength of the refractory bricks is influenced due to silicon's concentration and dispersion inside the bricks [54].

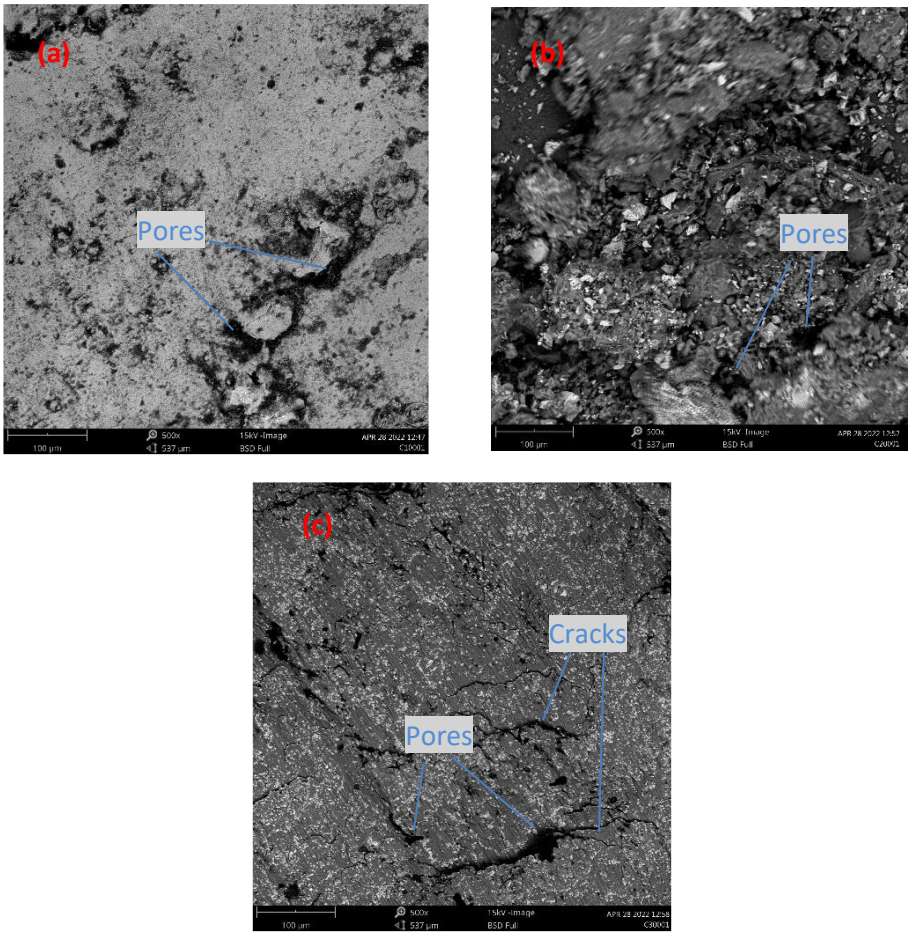

Fig. 9. SEM images of quartz brick at (a) 5% (b) 10% and (c) 15% binding proportion

The morphological analysis and other analyzed results have proved that the produced refractories are mechanically and thermally stable and suitable for applications in high-temperature industrial processes. Meanwhile, the materials utilized are relatively available and inexpensive, particularly bentonite compared to other materials used for bonding in the refractory industry [55, 56]. Additionally, bentonite has been reported to be non-toxic and biodegradable, making it an eco-friendly option for the refractory industry [56-58]. This is in tandem with the outcome of the chemical and morphological analysis of all the produced bricks as they proved to be chemically inert under natural and thermal conditions. Furthermore, the durability of the produced refractories suggests longer lifespan and reusability moreover, used refractory materials containing bentonite

are often recycled [59]. Overall, in addition to the good thermal stability of the refractories, cost-effectiveness, good environmental impact and waste management are other favourable properties provided for utilization in high-temperature industrial processes.

Element Symbol	Element Name	Weight Conc.
Si	Silicon	88.38
Ag	Silver	2.21
Cl	Chlorine	1.72
K	Potassium	1.04
Ca	Calcium	0.92
O	Oxygen	0.89
Al	Aluminium	0.77
S	Sulfur	0.76
N	Nitrogen	0.73
C	Carbon	0.71
Fe	Iron	0.68
P	Phosphorus	0.43
Ti	Titanium	0.30
Mg	Magnesium	0.24
Na	Sodium	0.23
Zn	Zinc	0.00

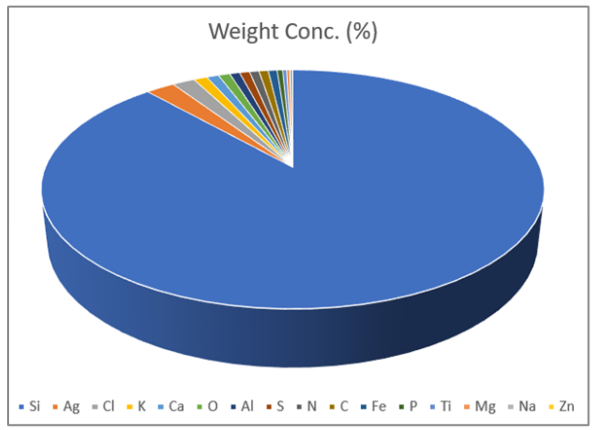

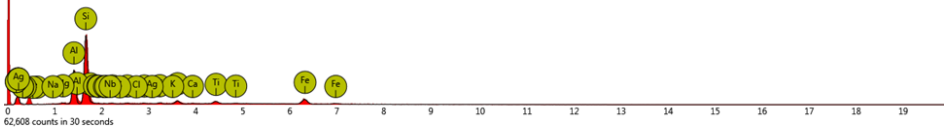

Fig. 10. EDS analysis of quartz brick at 5% binding proportion

Element Symbol	Element Name	Weight Conc.
Si	Silicon	78.49
O	Oxygen	9.75
Pb	Lead	4.65
S	Sulfur	1.97
Al	Aluminium	1.56
N	Nitrogen	1.10
C	Carbon	0.83
F	Fluorine	0.44
Cl	Chlorine	0.40
P	Phosphorus	0.35
K	Potassium	0.24
Ca	Calcium	0.22

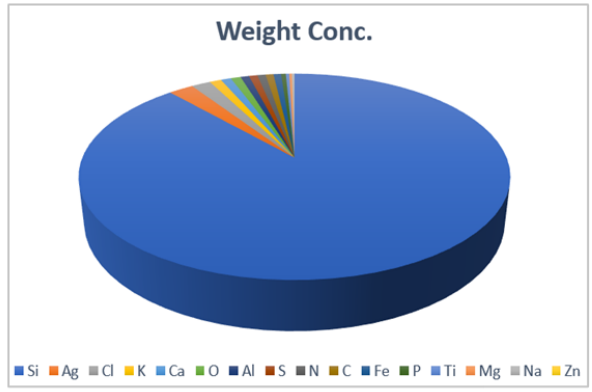

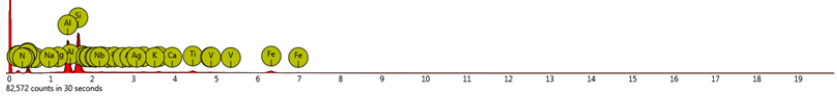

Fig. 11. EDS evaluation of quartz brick at 10% binding proportion

Element Symbol	Element Name	Weight Conc.
Si	Silicon	80.45
P	Phosphorus	6.76
Nb	Niobium	1.89
Ca	Calcium	1.89
Ag	Silver	1.64
S	Sulfur	1.39
Al	Aluminium	1.20
Fe	Iron	1.06
Na	Sodium	0.88
Mg	Magnesium	0.73
C	Carbon	0.73
Cl	Chlorine	0.62
K	Potassium	0.50
V	Vanadium	0.24
Ti	Titanium	0.00

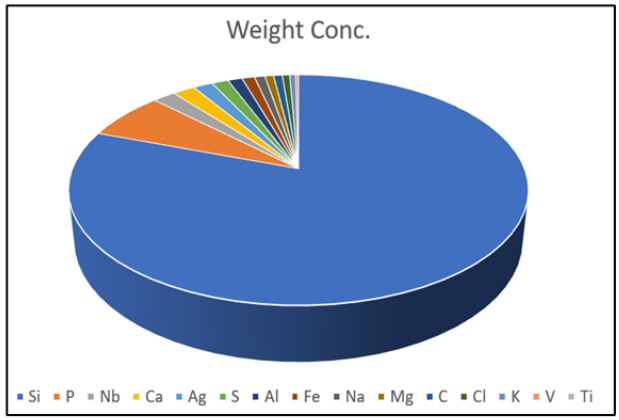

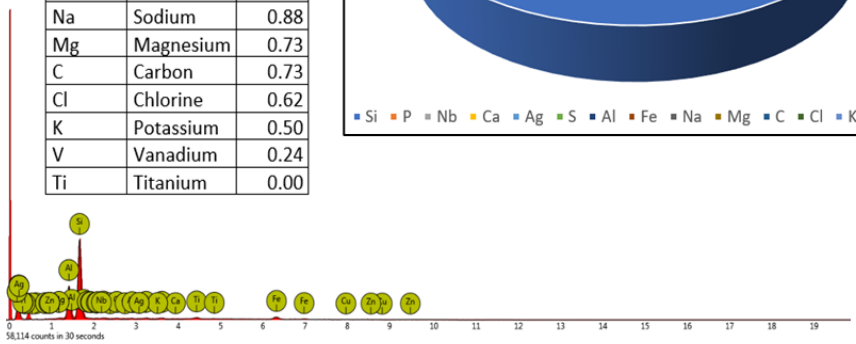

Fig. 12. EDS analysis of quartz brick at 15% binding proportion

4. Conclusions

The effect of developing refractory bricks using three different percentages of bentonite as binder has been examined. The study's measurements of bulk density (1644, 1516, and 1324 kg/m^3) and porosity (43, 46, and 48%) reveal crucial details regarding the sample's packing and compactness as refractory materials. The bricks produced were within the permitted range for refractory materials, according to both results. This shows that using bentonite as a binder enhances the mechanical durability of the produced bricks. The dimensional stability encompassed with the thermal expansion behaviour of quartz brick was significantly improved by the linear firing shrinkage and loss on ignition measurement. According to the findings, these refractory materials' linear firing shrinkage was within an acceptable range of the required percentage. According to the study, high cold crushing strengths are necessary to guarantee the mechanical veracity of refractory materials underneath pressure and it shows that the materials may show potential in being an elevated temperatures option for industrial refractory material furnaces. Additionally, the study's findings regarding water absorption indicated that the refractory bricks have a low water absorption rate. The brick's refractoriness supported this assertion since the uniformity of the significant silicon content and the brick structure content presented in micrographs indicate that they have a high potential to resist thermal shock. The outcome of the study showed that the material combination could be a viable choice for high-temperature industrial applications. Statistically, increasing the binding proportion of bentonite has significant effects on the refractory bricks. The mechanical strengths and thermal strength of the bricks were slightly reduced with increased concentration of bentonite some of which were proved significant by the statistical analysis even though the values are still within the acceptable ranges of good refractory materials. However, improved chemical composition was noticed with increased percentage of bentonite which indicates chemical durability and resistance to slag attack. The study affirmed that the refractory bricks produced in the range of bentonite percentages utilized are suitable

where high thermal stability is required. However, while the thermal and chemical properties of the bricks improved with an increasing percentage of bentonite, some properties such as bulk density, water absorption, crushing strength, and refractoriness are unfavourable. Though their values are still within the accepted range for standard refractories, there is a need to look into optimizing the optimum percentage that will balance both the properties that are affected positively and the ones affected negatively.

References

[1] Jongs LS, Jock AA, Ekanem OE, Jauro A. Investigating the industrial potentials of some selected Nigerian clay deposits. Journal of Minerals and Materials Characterization and Engineering. 2018;6:569-586. https://doi.org/10.4236/jmmce.2018.66041

[2] Adeoti M, Dahunsi O, Awopetu OO, Aramide F, Alabi O, Johnson O, Abdulkarim A. Suitability of selected Nigerian clays for foundry crucibles production. Procedia Manufacturing. 2019;35:1316-1323. https://doi.org/10.1016/j.promfg.2019.05.023

[3] Thethwayo B, Steenkamp J. A review of carbon-based refractory materials and their applications. Journal of the Southern African Institute of Mining and Metallurgy. 2020;120: 641-650. https://doi.org/10.17159/2411-9717/1011/2020

[4] Kumari N, Mohan C. Basics of clay minerals and their characteristic properties. IntechOpen. 2021;24:1-29. https://doi.org/10.5772/intechopen.97672

[5] Lohmeier L, Thaler C, Harris C, Wollenberg R, Schröder HW, Braeuer AS. Use of Bentonite and Organic Binders in the Briquetting of Particulate Residues from the Midrex Process for Improving the Thermal Stability and Reducibility of the Briquettes. Steel Research International. 2021; 92:1-11. https://doi.org/10.1002/srin.202100210

[6] Forsmo SPE, Apelqvist AJ, Björkman BMT, Samskog PO. Binding mechanisms in wet iron ore green pellets with a bentonite binder. Powder Technology 2006;16:147-158 https://doi.org/10.1016/j.powtec.2006.08.008

[7] Kamińska J, Puzio S, Angrecki M, Stachowicz M. The Effect of the Addition of Bentonite Clay to Traditional Sand Mixtures on the Surface Quality of Iron Castings. Journal of Ecological Engineering 2020; 21(1):160-167. https://doi.org/10.12911/22998993/112505

[8] Kanan T, Sre AV, Syed OB, Krishan DY, Samitinjay SB, Swapnil S. Application of Bentonite Clay as a Binding Material. Design Engineering 2021;9:9111-9131

[9] Jelinek P, Dobosz SM, Beno J. Major-Gabrys K. The Behavior of Bentonite Binders for the Elevated and High Temperatures. Archives of Metallurgy and Materials. 2014;59(3): 1041-1044. https://doi.org/10.2478/amm-2014-0175

[10] Lee S. Types of Refractory Materials and Their Applications [Internet]. 2015 [Accessed June 16, 2021]. Available form: https://www.Linkedin.Com/Pulse/Types-Refractory-Materials-Applications-Le-Sylvia.

[11] Sarkar R. Refractory Technology: Fundamentals and Applications. (1st ed). Boca Raton CRC Press; 2016. https://doi.org/10.1201/9781315368054

[12] Jastrzębska I, Szczerba J. Design, Manufacturing and Properties of Refractory Materials. Materials. 2024;17(7):1673. https://doi.org/10.3390/ma17071673

[13] Krajewski PK, Suchy JS, Grzegorz P, Krajewski WK. High temperature thermal properties of bentonite foundry sand. Archives of Foundry Engineering. 2015;15:47-50. https://doi.org/10.1515/afe-2015-0036

[14] Adeleke AA, Odusote JK, Ikubanni PP, Olabisi AS, Nzerem P. Briquetting of subbituminous coal and torrefied biomass using bentonite as inorganic binder. Scientific Report. 2022;12:1-11. https://doi.org/10.1038/s41598-022-12685-5

[15] Fleuriault C, Grogan J, White J. Refractory materials for metallurgical uses. The Journal of The Minerals Metals & Materials Society. 2018;70:2420-2421. https://doi.org/10.1007/s11837-018-3096-5

[16] Abu-Jdayil B, Mourad AH, Hittini W, Hassan M, Hameedi S. Traditional, state-of-the-art and renewable thermal building insulation materials: An overview. Construction and Building Materials. 2019;214;709-735. https://doi.org/10.1016/j.conbuildmat.2019.04.102
[17] Ariyajinno N, Thiansem S. Characterization and properties of cordierite–mullite refractories from raw materials and Narathiwat clay (in Thailand). Materials Today: Proceedings. 2018;5:13948-13953. https://doi.org/10.1016/j.matpr.2018.02.045
[18] Barsoum MW. Fundamentals of Ceramics. New York, NY: Taylor & Francis; 2017.
[19] Mangal R. Refractories for iron and steel making: the current state of the art. Journal of the American Ceramic Society. 2018;101(11):4859-4887.
[20] Kumaravel M, Eynolghozzat Y, Gussone J, Yan F, Lordejani AA, Haubrich J, Requena G, Berglund IS, Guagliano M, Bagherifard S. Elucidating the challenges in the development and deployment of refractory complex concentrated alloys for additive manufacturing. Additive Manufacturing. 2024; 89: 104286. https://doi.org/10.1016/j.addma.2024.104286
[21] Montgomery R. Heat-resisting and refractory concretes. Advanced Concrete Technology. 2003;3(4):1-10. https://doi.org/10.1016/B978-075065686-3/50290-1
[22] Wang Y, Song GJ, Shen P, He JZ, Zhang DX, Fu JX. Reaction mechanism between Al2O3–MgO refractory materials and rare earth high-carbon heavy rail steel. Journal of Iron and Steel Research International. 2024;3:1-11. https://doi.org/10.1007/s42243-023-01147-5
[23] Osarenmwinda J, Abel CP. Performance evaluation of refractory bricks produced from locally sourced clay materials. Journal of Applied Sciences and Environmental Management. 2014;18:151-157.
[24] Nnuka E, Agbo U. Evaluation of the refractory characteristics of Otukpo clay deposits. NSE Technical Transaction. 2000;35:34-36.
[25] Moorkah HI, Abolarin M.S. Investigation of the properties of locally available dolomite for refractory applications, Nigerian Journal of Technology. 2005;24(1):79-86.
[26] ASTM C20-00. Standard test methods for apparent porosity, water absorption, apparent specific gravity, and bulk density of burned refractory brick and shapes by boiling water. ASTM International, West Conshohocken, PA, 2015, www.astm.org.
[27] ASTM C596. Standard test method for drying shrinkage of mortar containing hydraulic cement. ASTM International, West Conshohocken, PA, 2018, www.astm.org.
[28] ASTM C133. Standard test methods for cold crushing strength and modulus of rupture of refractories. ASTM International, West Conshohocken, PA, 2021, www.astm.org.
[29] ASTM D7348. Standard test methods for loss on ignition (LOI) of solid combustion residues. ASTM International, West Conshohocken, PA, 2013, www.astm.org.
[30] Odewole OP, Alemaka EM. Development of aluminosilicate refractory crucibles from the optimum mix of Awo quartz and Ikere Ekiti clays ATBU. Journal of Science, Technology & Education. 2019;7(2):331-340.
[31] Abubakar I, Yauri UB, Faruq UZ, Noma SS, Sharif N. Characterization of Dabagi clay deposit for its ceramics potential. African Journal of Environmental Science and Technology. 2014;8(8):455-459. https://doi.org/10.5897/AJEST2014.1741
[32] Obidiegwu MU, Nwanonenyi SC, Eze IO, Egbuna IC. The effect of walnut shell powder on the properties of polypropylene filled composite. The International Asian Research Journal. 2014;2(1):22-29.
[33] Nwajagu CO. Foundry Theory and Practical (A bridged Edition) Enugu: Olico Publications; 2005. P. 59-76.
[34] Safeer A, Yaseen I, Raz M. Effects of coal and wheat husk additives on the physical, thermal and mechanical properties of clay brick. Boletin De La Societad Espannola De Ceramica. 2017;56:131-138. https://doi.org/10.1016/j.bsecv.2017.02.001

[35] Kipsanai JJ, Namango SS, Muumbo AM. A study of selected Kenyan anthill clays for the production of refractory materials. International Journal of Scientific and Research Publications. 2017;7(9):169–179.
[36] Krishnamurthy N. Metal–Crucible Interactions. CRC Press (1st ed.). 2022. https://doi.org/10.1201/9780429345562
[37] Abuh MA, Abia-Bassey N, Udeinya TC, Nwannewuihe HU, Abong AA, and Akpomie K. G. Industrial potentials of Adiabo clay in Calabar municipal of Cross River State, South-South Nigeria. Pacific Journal Science Technology. 2014;15(1):63-75.
[38] Oyelaran OA. Physico-chemical characterization of "Namu" clay for industrial use. Khon Khaen University Engineering Journal (KKU). 2014;41(3):283-290.
[39] Ojonimi IT, Aponbiede O, Asuke F. Geochemical and refractory properties of Egbahieme clay in Kogi State Nigeria. Journal of Raw Materials Research. 2018;10(4):1-13.
[40] Borisade SG, Oyelaran OA, Sanusi OM, Madueke CI. Assessing the ceramic suitability of Obe clay reinforced with rice husk ash. Adeleke University Journal of Engineering and Technology. 2021;4(2):68-76.
[41] Samad A, Baidya S, Akhtar US, Ahmed KS, Roy SC, Islam S. Manufacture of refractory brick from locally available red clay blended with white portland cement and its performance evaluation. International Journal of Geomate. 2021;20(80):105–112. https://doi.org/10.21660/2021.80.j2033
[42] Babalola BJ, Folorunso DO, Bodunrin MO, Balogun OP. Property evaluation of Igbara-Odo clay for refractories. International Journal of Engineering and Technical Research (IJETR). 2014;2(1):79 – 82.
[43] N'jock MY, Chicot D, Decoopman X, Lesage J, Ndjaka JM, Pertuz A. Mechanical tensile properties by spherical macroindentation using an indentation strain-hardening exponent. International Journal of Mechanical Sciences. 2013;75:257-264. https://doi.org/10.1016/j.ijmecsci.2013.07.008
[44] Arthur EK, Gikunoo E. Property analysis of thermal insulating materials made from Ghanaian anthill clay deposits. Cogent Engineering. 2020;7(1):1-20. https://doi.org/10.1080/23311916.2020.1827493
[45] Shuaib-Babata YL, Yaru SS, Abdulkareem S, Busari YO, Ambali IO, Ajao KS, Mohamme GA. Characterization of Baruten Local Government Area of Kwara State (Nigeria) fireclays as suitable refractory materials. Nigerian Journal of Technology. 2018;37(2):374-386. https://doi.org/10.4314/njt.v37i2.12
[46] Ajala AJ, Badarulzaman NA. Performance assessment of physico-mechanical properties of Aloji fireclay brick. International Journal of Integrated Engineering. 2016;8(2):16-20.
[47] Omidiji1 BV, Owolabi HA, Ogundipe OB. Performance evaluation of refractory bricks produced from Ijero Ekiti Quartz. International Journal of Environmental Science. 2023;8:71-84
[48] Yue C, Liu J, Zhang H, Dai L, Wei B, Chang C. Increasing the hydrophobicity of filter medium particles for oily water treatment using coupling agents. Heliyon. 2018;4(9):1-14. https://doi.org/10.1016/j.heliyon.2018.e00809
[49] Oluwagbenga OP, Majiyebo AE. Development Of Aluminosilicate Refractory Crucibles From The Optimum Mix Of Awo quartz and Ikere Ekiti clays. ATBU Journal of Science, Technology and Education. 2019;7(2):331-340.
[50] Ewais EMM, Bayoumi IMI, El-korashy SA. Magnesia-Calcium Zirconate (M-CZ) composites as clinker of manufacturing refractory bricks of rotary cement kilns (RCK). Ceramics International. 2018;44:2274-2282. https://doi.org/10.1016/j.ceramint.2017.10.188
[51] Acar I. Sintering properties of olivine and its utilization potential as a refractory raw material: mineralogical and microstructural investigations. Ceramics International. 2020;46(18):28025-28034. https://doi.org/10.1016/j.ceramint.2020.07.297

[52] Olaiya K, Rabiu T, Adigun I, Saheed R, Eboreime U. Entrepreneurial approach in production of refractory bricks for foundry furnaces. International Journal of Engineering Research. 2019;6(3):19-25.
[53] ASTM C71. Standard Test Method for Refractory Brick-Transverse Strength. ASTM International. 2018. https://doi.org/10.1520/C0071-18
[54] Gado RA, Hebda M, Łach M, Mikuła J. Alkali activation of waste clay bricks: influence of the silica modulus, SiO2/Na2O, H2O/Na2O molar ratio, and liquid/solid ratio. Materials. 2020;13:1-26. http://dx.doi.org/10.3390/ma13020383
[55] Abd Hamid S, Shahadat M, Ismail S. Development of cost effective bentonite adsorbent coating for the removal of organic pollutant. Applied Clay Science. 2017;149:79-86. https://doi.org/10.1016/j.clayy.2017.07.022
[56] Dhar AK, Himu HA, Bhattacharjee M, Mostufa MG, Parvin F. Insights on applications of bentonite clays for the removal of dyes and heavy metals from wastewater: a review. Environmental Science and Pollution Research. 2023;30(3):5440-5474. https://doi.org/10.1007/s11356-022-24277-x
[57] Ezhkova AM, Yapparov AK, Ezhkov VO, Yapparov IA, Sharonova NL, Degtyareva IA, Khisamutdinov NS, Bikkinina LK. Fabrication of nanoscale bentonite, study of its structure and toxic properties, and determination of safe doses. Nanotechnologies in Russia. 2015;10(1):120-127. https://doi.org/10.1134/S1995078015010061
[58] Mapossa AB, da Silva Júnior AH, de Oliveira CR, Mhike W. Thermal, morphological and mechanical properties of multifunctional composites based on biodegradable polymers/bentonite clay: a review. Polymers. 2023;15(16):3443. https://doi.org/10.3390/polym15163443
[59] Contreras M, Gázquez MJ, Romero M, Bolívar JP. Recycling of industrial wastes for value-added applications in clay-based ceramic products: A global review (2015–19). New Materials in Civil Engineering. 2020:155-219. https://doi.org/10.1016/B978-0-12-818961-0.00005-3

Research on Engineering Structures & Materials
www.jresm.org
MIM Research Group

Research Article

Lightweight SCC with coal bottom ash: Investigating fresh, mechanical, and thermal properties through multifunctional integration

Ibtissam Boulahya*[,a], Abdulkadir Makani[b], Ahmed Tafraoui[c]

Department of Civil Engineering and Hydraulic, TAHRI Mohamed University, EMIA ex LFGM (Laboratory of Eco-Materials: Innovations & Applications), P.O. Box 417 Bechar (08000), Algeria

Article Info

Article History:

Received 22 Feb 2025

Accepted 17 Mar 2025

Keywords:

Coal bottom ash;
Lightweight SCC;
Workability;
mechanical properties;
Thermal properties;
Microstructure

Abstract

Coal bottom ash (CBA), a byproduct of coal-fired power plants, presents a sustainable alternative to natural aggregates in self-compacting concrete (SCC), supporting eco-friendly construction and waste management. This study developed lightweight, thermally insulating SCC (LWSCC) with densities below 2000 kg/m^3, incorporating CBA as a full replacement for coarse aggregates and a partial cement substitute (10%–30%). Results showed that CBA as a saturated coarse aggregate improved workability, increasing slump flow from 727 mm to 800 mm. While CBA powder slightly reduced workability by 5.6%, all mixtures met the SCC standards set by the French Association of Civil Engineering (AFGC). LWSCC mixtures with CBA achieved 90-day compressive strengths of 38–56 MPa. Notably, mixes with 10% CBA powder as a cement replacement exhibited strengths comparable to the reference SCC. The dry density of CBA-based mixtures decreased by up to 15%, remaining within the range for structural lightweight concrete (<2000 kg/m^3). Due to CBA's porous structure, ultrasonic pulse velocity (UPV) decreased by 35%, and water absorption increased by 80% at 30% CBA powder replacement. Additionally, LWSCC with CBA demonstrated enhanced thermal insulation, with thermal conductivity reduced by 52% compared to the reference concrete. Microstructural analysis revealed higher pore volumes and a modest increase in calcium silicate hydrate (C-S-H) gel formation with CBA use. These findings highlight CBA's potential as a sustainable material for lightweight, thermally efficient SCC, balancing structural performance and environmental benefits.

1. Introduction

Self-compacting concrete (SCC) represents a unique type of concrete designed to exhibit self-flowing characteristics under gravity, notably, SCC has a remarkable ability to effectively fill congested reinforcement areas and uniformly occupy formwork, even within densely reinforced structures [1]. Nonetheless, an inherent characteristic of SCC that distinguishes it from conventional concrete is its elevated density, mainly resulting from the increased fine particles content and a moderated proportion of coarse aggregates, comprising approximately 65% to 75% of the concrete volume, aimed at facilitating its flow and passing ability while also resisting segregation [2]. Also, aggregates are pivotal in influencing the properties and characteristics of concrete [3]. A viable solution to this issue involves partially or entirely replacing natural aggregate with lightweight aggregate to create self-compacting lightweight concrete (LWSCC) [4]. This hybrid material blends the features of lightweight concrete (LWC) and self-compacting concrete (SCC), providing benefits such as reduced overall weight, faster construction, and lowered construction

*Corresponding author: boulahya.ibtissam@univ-bechar.dz
[a]orcid.org/0009-0008-2720-6136; [b]orcid.org/0000-0002-4027-9929; [c]orcid.org/0000-0002-0278-935X
DOI: http://dx.doi.org/10.17515/resm2025-704ma0222rs

expenses, removal of noise from vibration equipment, and improved thermal and acoustic insulation due to voids within the lightweight aggregate. [5-7]. In light of the current constraints on aggregate resources and advancements in the concrete sector, discovering novel alternative materials is crucial for sustainability to significantly reduce the utilization of natural resources and the utilization of inexpensive industrial by-products or solid waste in the manufacturing of concrete represents an environmentally-friendly solution. [8]. Moreover, producing cement consumes a considerable number of natural resources and energy, leading to substantial environmental consequences due to the emission of harmful gases. About 600 kg of cement production leads to the release of 400 kg of carbon dioxide [9], underscoring the critical need to find alternative binding materials for ensuring sustainability in the long term.

Coal bottom ash (CBA) is a residual material generated in large volumes during the combustion of coal in power generation plants [10]. In the Bechar region of southwestern Algeria, accumulations of slag heaps have formed over 50 years of coal mining activity which resulted in significant amounts of waste being left in the environment. The CBA by-products have harmful effects on public health and create ecological problems, therefore, utilizing substantial amounts of coal bottom ash (CBA) as building materials specifically as sand and coarse aggregates in different types of concrete mixtures provides a viable solution for managing these wastes efficiently. This industrial residue has the potential to serve as a lightweight coarse aggregate and a partial substitute for cement in the manufacture of lightweight self-compacting concrete. Incorporating CBA into concrete production offers an economically and ecologically viable method of waste disposal. Concurrently, its utilization helps conserve natural resources and advance sustainability [11]. The integration of Lightweight Aggregates (LWA) within concrete sectors, particularly in Self-Compacting Concrete (SCC), is widely acknowledged as a significant advancement. Various types of aggregates, both natural and artificial, have been employed effectively in LWA based SCC. Notably, there is significant potential in utilizing waste materials as LWAs [12-18]. These materials not only enhance sustainability by reusing waste but also cater to the need for lightweight and durable concrete solutions [19].

Similarly, in efforts to mitigate exhaustion of natural resources, minimize environmental footprint of cement manufacturing, and reduce carbon footprints, the use of mineral admixtures derived from by-products has become imperative in contemporary construction [20]. Mineral admixtures having pozzolanic properties such as Fly Ash, ground granulated blast furnace slag [20], silica fume [22], metakaolin [23] and limestone powder [24], are frequently utilized as partial substitutes for ordinary Portland cement (PC) in order to enhance the performance and sustainability of concrete. The utilization of CBA in concrete production has been studied extensively, exploring its potential applications as substitutes for fine and coarse aggregates, as well as cement. As per the findings, replacing sand with CBA was found to lower the workability, dry density, as well as compressive and flexural strengths. [25-26], while Zhang et al [27] stated that concrete incorporating furnace bottom ash (FBA) as a lightweight aggregate can have comparable levels of workability and compressive strength when fully replaced as a fine aggregate. Also, Ojha et al. highlighted that Lightweight Geopolymer Fly Ash Sand (LWGFAS) is versatile and can be utilized in diverse concrete applications, from lightweight to normal-weight concrete, depending on its specific physical and chemical characteristics [28]. According to Kim and lee [29], replacing 100% of normal coarse aggregates with coarse bottom ash slightly reduced the high-strength concrete slump flow dropping from 530 mm to 420 mm, whereas fine bottom ash did not impact the slump flow. Furthermore, both fine and coarse bottom ash aggregates were found to significantly influence flexural strength more than compressive strength. Also, in an investigation reported by Singh et al [30], the results indicate that substituting fine aggregates with CBA at levels of 10%, 15%, 20%, and 25% enhances the compressive strength of concrete. CBA exhibits pozzolanic properties and is classified under ASTM Class F, which makes it suitable for enhancing concrete performance when used as a cement replacement [31]. Cheriaf et al. [32] examined the pozzolanic properties of CBA, and noted a slow initial reaction that gradually accelerated, becoming notably effective after 28 days and particularly after 90 days. They found that combining Ordinary Portland cement with CBA resulted in a 27% increase in the strength activity index. According to Rafieizonooz et al [33], as the curing period increased, concrete incorporating 75% bottom ash and 20% coal fly ash exhibited

significantly more flexural and splitting tensile resistance than the control mix. The initial reduction in flexural strength observed in concrete based coal fly ash-bottom ash at early stages can be explained by the slower hydration and lower pozzolanic activity of Coal Fly Ash (CFA) and Coal Bottom Ash (CBA). However, these mixtures demonstrated enhanced flexural strength after 91 days and 180 days when part or total CBA replaced the fine aggregate. Thus, the inclusion of ground coal bottom ash (CBA) was observed to initially reduce compressive strength during the initial phases of concrete curing. However, over longer periods (more than 28 days), this decrease is less pronounced compared to control concrete mixes. Additionally, the inclusion of cement additives has been proven beneficial in improving compressive strength [11]. Existing literature highlights that there is substantial research indicating the successful application of CBA in both conventional and high-performance concrete [31]. However, there has been limited exploration of CBA's potential as both a lightweight coarse aggregate and a cement replacement in self-compacting concrete. Most studies have focused on its use as fine aggregate [34-37]. When comparing the lifecycle performance of CBA-based self-compacting concrete (SCC) to conventional concrete, key differences highlight its potential as a sustainable alternative. CBA-based SCC utilizes industrial by-products, reducing natural resource demand and lowering carbon emissions during production, unlike conventional concrete, which relies on resource-intensive materials and emits more carbon. Its lower density cuts transportation costs and improves thermal insulation, reducing operational energy use, while conventional concrete is denser and less energy-efficient. CBA-based SCC also offers superior recyclability, minimizing waste, whereas recycling conventional concrete is more energy-intensive. Additionally, CBA provides cost advantages as a low-cost or free by-product, reducing material and processing expenses. Its pozzolanic properties can lower cement usage, further cutting production costs. When sourced and processed efficiently, CBA emerges as an economically competitive and environmentally sustainable alternative, promoting resource conservation and reducing reliance on non-renewable materials [10].

This research offers a novel approach to utilizing Coal Bottom Ash (CBA) as a dual-function material for producing Lightweight Self-Compacting Concrete (LWSCC), addressing both environmental and construction challenges. Unlike previous studies that primarily focused on CBA as a fine aggregate, this study explores its innovative use as a full replacement for coarse aggregates and a partial substitute for cement. By repurposing industrial waste from a defunct coal power plant in Algeria, the research provides an eco-friendly solution to waste management while conserving natural resources. Comprehensive evaluations of LWSCC properties, including fresh-state performance (slump flow, filling ability, and stability) and hardened-state characteristics (compressive strength, dry density, ultrasonic pulse velocity, water absorption, and thermal conductivity), highlight the material's suitability for structural and insulation applications. Advanced microstructural analyses using SEM, TGA, and XRD reveal insights into the internal structure and long-term performance of CBA-based LWSCC. The study also demonstrates significant environmental benefits by reducing the carbon footprint of cement production and showcases the potential for enhanced compressive strength and durability over extended curing periods due to CBA's pozzolanic properties. With densities below 2000 kg/m^3, CBA-based LWSCC effectively combines the self-compacting and lightweight characteristics critical for cost-effective, efficient, and sustainable construction, making it a significant advancement in waste valorization and environmentally conscious concrete technology.

2. Materials and Methods

2.1. Materials

Ordinary Portland cement CEM I 42.5 was used for this experimental work, supplied by an Algerian plant (Bechar southwestern Algeria). It complies with both the Algerian standard NA 442 and the European standard EN 197-1. The chemical composition of the cement is outlined in Table 1, while its physical properties are presented in Table 2.

This study focuses on slag heaps near the Bechar power station (Algeria), formed between 1949 and 1960, which occupy 350,567.11 m^3 (Fig. 1). Composed of coal bottom ash and ashes with varying grain sizes, these heaps result from coal combustion for electricity production. Coal Bottom

Ash (CBA), a byproduct of this process, forms when coarser particles settle at the furnace bottom, constituting 10–20% of coal ash waste. It consists of oxides and metal carbonates, often displaying a dark to reddish color due to iron oxide transformation. Coal ash, produced at around 1,500°C, is categorized into fly ash (75–80%), bottom ash (10–15%), and cinder ash (5%) (Fig. 2)

Table 1. Cement chemical compositions

Composition (%)	SiO_2	Al_2O_3	Fe_2O_3	Cao	MgO	SO_3	Na_2O	K_2O	LOI
Cement	18.91	4.30	4.74	60.33	3.82	2.29	0.17	0.84	<0.5

Table 2. Cement physical properties

Physical properties	Cement
Setting time (min)	≥ 60
Fineness (cm^2/g)	3200
Absolut Density (kg/ m^3)	3050
Heat of hydration (J/g)	270

Coal Bottom Ash (CBA) was manually crushed and further processed using a jaw crusher machine. After sieving, it was classified into coarse aggregates of sizes (3/8) and (8/15), with the finer coal bottom ash powder designated for partial replacement of cement, as depicted in Fig. 3. The Natural fine aggregate (NFA) utilized in this study consisted of river sand obtained from the Bechar region in Algeria, with particles up to 3 mm in size. The coarse aggregate (NCA) was crushed rocks, available in sizes of 3/8 and 8/15. Table 3 details the physical properties of the aggregates used, while Fig. 4 displays their grading curves.

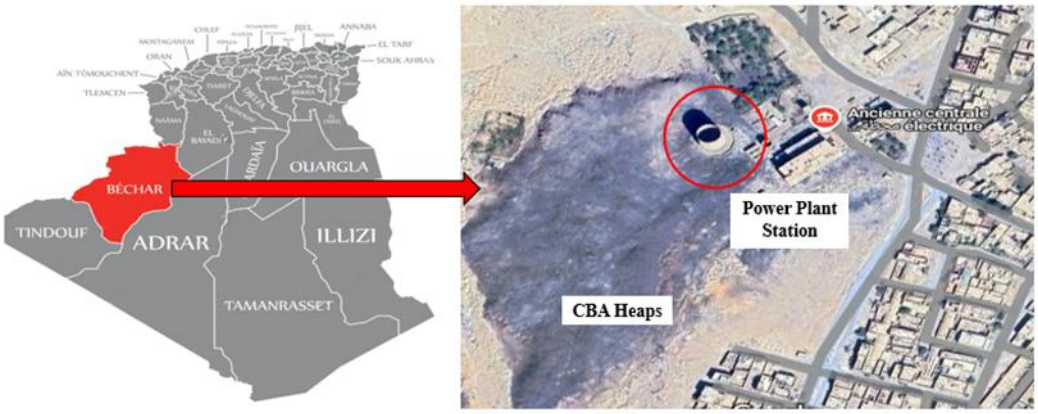

Fig. 1. Satellite image from Google Earth showing the slag heaps of Coal Bottom Ash (CBA) located near the Bechar power station

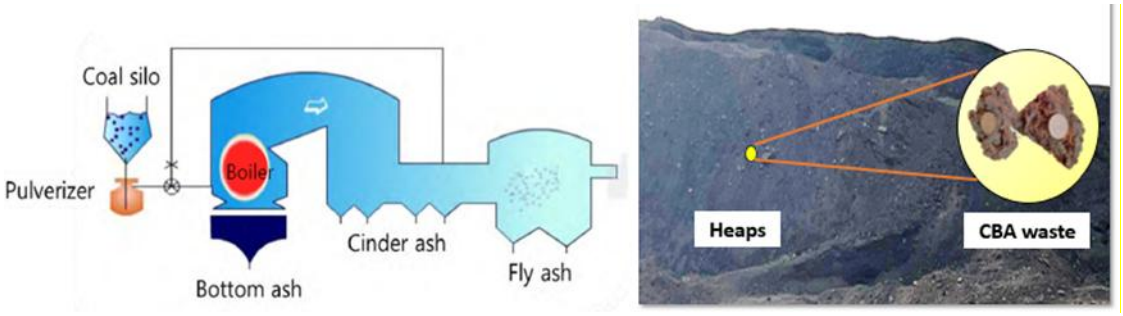

Fig. 2. Process of Coal Bottom Ash (CBA) production in thermal power plants

The grain size distribution of CBAP was analyzed using a specialized device known as the "HELOS/BR optical particle size analyzer". Fig. 5 presents the findings of this analysis, illustrating the CBAP granulometry.

Fig. 3. Preparation procedure CBA aggregate / CBA powder

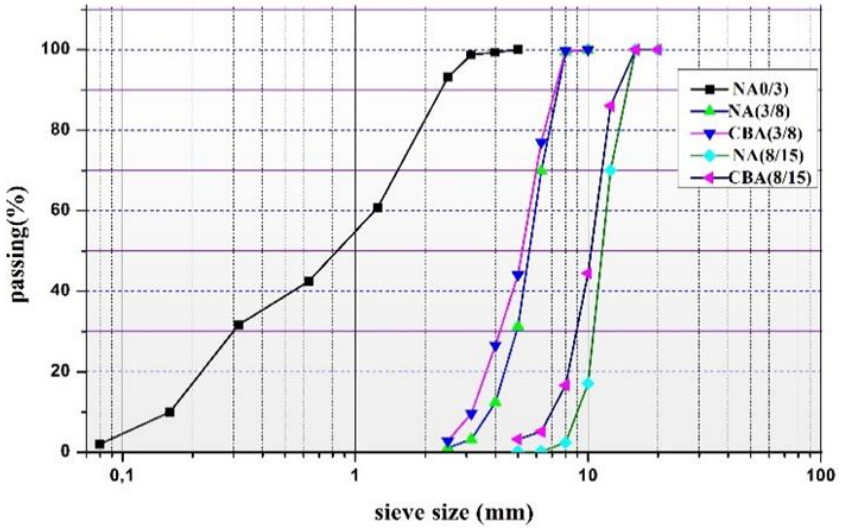

Fig. 4. CBA aggregate gradation curves

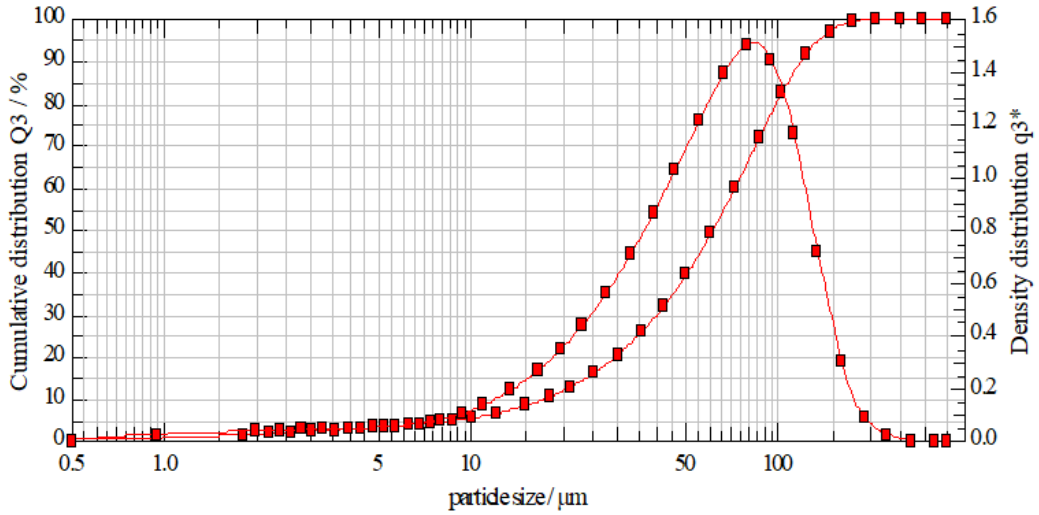

Fig. 5. CBAP laser granulometry

Where, Q3: Cumulative distribution showing the percentage of particles below a certain size. And q*3: Density distribution showing the particle fraction within size intervals.

Table. 3 Aggregate physical properties

Properties	0/3 NFA	3/8 NCA	3/8 CBA	8/15 NCA	8/15 CBA
Bulk density (g/cm^3)	1.6	1.39	0.70	1.40	0.66
Absolute density (g/cm^3)	2.5	2.66	1.93	2.67	1.81
Fineness modulus	2.53	/	/	/	/
Sand equivalent (%)	80.3	/	/	/	/
Water absorption (%)	1.62	0.85	7	0.95	8
Los Angeles cofficient (%)	/	21.56	27.6	20.72	27.9

Chemical composition analysis of CBA using XRF identified silica, iron, and alumina as its main components, along with small quantities of sulfate, magnesium, calcium, and other elements. These findings showed that SiO_2, Al_2O_3, and Fe_2O_3 comprised 83.47% of CBA's composition. Consequently, based on ASTM C 618 standards, CBA qualifies as class “F” pozzolanic material. Table 4 outlines the detailed chemical properties of CBA.

Table 4. CBA chemical compositions

Composition (%)	SiO_2	Al_2O_3	Fe_2O_3	Cao	MgO	SO_3	Na_2O	K_2O	LOI
CBA	44.78	15.79	22.90	2.47	1.43	4.37	0.16	2.38	1.2

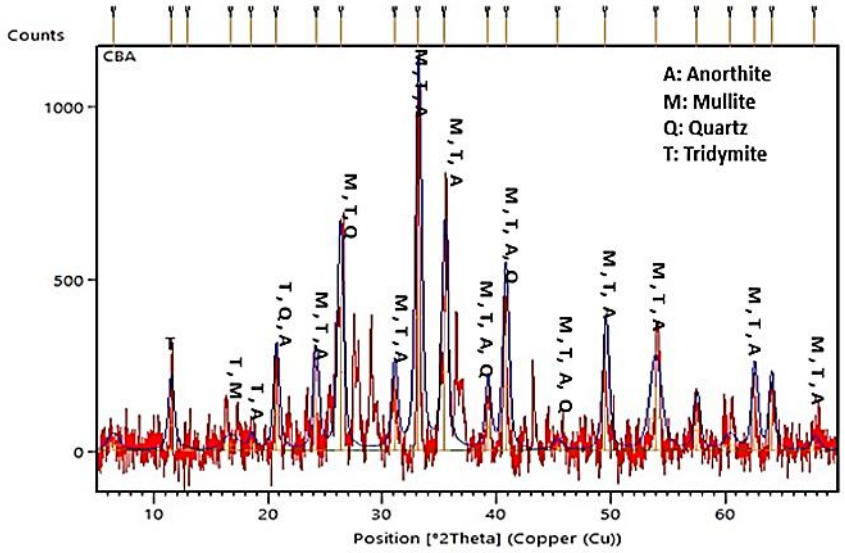

Fig. 6. CBA XRD patterns

X-ray diffraction (XRD) was employed to analyze the CBA crystal structure, depicted in Fig. 6, indicating that quartz, mullite, anorthite, and tridymite are the primary phases in coal bottom ash.

Fig. 7 also provides a scanning electron microscopy (SEM) image of CBA, highlighting its irregularly shaped and porous particles with a complex texture. To ensure optimal workability, a polycarboxylate-based superplasticizer called "MAX SUPERFLOW S180" was employed. This product, produced by the Algerian company "Technachem," adheres to the NF EN 934-2 standards. The mixing process used drinkable water from the laboratory faucet at Bechar University meeting NF EN 1008 quality standards.

Fig. 7. CBA SEM image

2.2. SCC Mixtures

In line with the AFGC guidelines for SCC production, seven LWSCC mixtures were formulated for this study. Initially, a reference mix (RSCC) utilizing 100% natural aggregates without coal bottom ash powder (CBAP) was prepared. Subsequently, six mixtures of Lightweight Self-Compacting Concrete (LWSCC) were formulated, incorporating 100% CBA coarse aggregate (CBASCC), with varying percentages of CBAP (CBASCC-0%, 10%, 15%, 20%, 25%, and 30%). The CBASCC-0% was considered as a reference mix. CBA was preconditioned in a saturated surface-dry (SSD) state before mixing. Table 5 presents the composition of SCC.

Table 5. SCC composition

Composition	RSCC	CBASCC-0%	CBASCC-10%	CBASCC-15%	CBASCC-20%	CBASCC-25%	CBASCC-30%
Cement (kg/m³)	520	520	468	442	416	390	364
CBAP (Kg/m³)		/	52	78	104	130	156
NFA (kg/m³)	900	900	900	900	900	900	900
NCA 3/8 (kg/m³)	150	/	/	/	/	/	/
CCBA3/8 (kg/m³)	/	111.36	111.36	111.36	111.36	111.36	111.36
NCA 8/15 (kg/m³)	580	/	/	/	/	/	/
CCBA (kg/m³)		394.65	394.65	394.65	394.65	394.65	394.65
Water (kg/m³)	256	256	256	260	260	260	260
Superplasticizer (%)	2%	2%	2%	2.1%	2.3%	2.4%	2.4%
W/C	0.48	0.48	0.48	0.50	0.50		0.50

2.3 Fresh State Characterization

Lightweight Self-Consolidating Concrete (LWSCC) must be evaluated to ensure it has the proper filling ability, passing ability, and resistance to segregation, as these are key indicators of its workability. Multiple testing methods are available to assess each of these characteristics, with guidelines provided by resources like the EFNARC [38], AFGC [39] and ACI-237. For filling ability,

tests such as slump flow, T500, V-funnel, O-funnel, and orimet are commonly used. These tests are essential for checking if the LWSCC maintains consistent flow, which is a basic requirement for all types of self-consolidating concrete (SCC), passing ability, on the other hand, is tested using the L-box, U-box, J-ring, and Kajima box [40]. These tests measure the concrete's ability to pass through narrow spaces, which is critical for filling formwork without obstruction. The spacing in these tests represents the minimum gap the LWSCC must navigate smoothly. Lastly, segregation resistance tests help determine how well the concrete mix holds together without separating. This can be assessed through penetration tests, sieve segregation tests, settlement columns, and visual inspections. Segregation is a significant concern, especially when pouring concrete into tall structures, as it can lead to uneven distribution of materials, compromising the quality of LWSCC in structural applications. The concrete fresh properties were assessed following the AFGC specifications. Table 6 provides the main fresh properties of SCC. The slump-flow test, based on EN 12350-8, determined the concrete's spread diameter after free flow. Flowability of LWSCC was measured using L-box tests as per EN 12350-10. Segregation resistance was evaluated using the sieve stability test according to EN 12350-11.

Table 6. SCC fresh state characteristics

	Slump Flow test EN 12350-8	L – box test EN 12350-10	Sieve Stability test EN 12350-11
Limit values	550 - 850 mm	≥ 0.8	≤ 15 %
			

2.4 Hardened State Characterization

The concrete samples' compressive strength was evaluated after curing periods of 7, 28, and 90 days. As per EN 12390-3 using three 70 mm cubic specimens for each mix Fig. 8 (a). The ultrasonic velocity transmitted through the concrete was measured according to the EN 12504-4 code. 58-E4800 UPV Ultrasonic Non-destructive Digital Indicating Tester was used on three dried specimen cubes of 100 mm after 28 days of curing age Fig. 8 (b). The pulse velocity is obtained by dividing the specimen's length by the transit time. The oven dry density of concrete as per EN 12390-7 is assessed after 28 days using three 100 mm cube specimens. This involves measuring their volume and determining the dry mass after being dried at 105 ± 5 °C to a constant mass. The water absorption test was carried out according to ASTM C 642 standards. In this experiment, specimens measuring 100 mm were used after 28 days of curing. Water absorption was evaluated by comparing the weight ratio of samples completely saturated with water to that of samples dried in an oven. The thermal performance of the SCC produced was evaluated using the 'Hot Disk TPS 1500 Thermal Constant Analyzer' following ISO 22007-2 standards. Concrete samples measuring 40 mm × 40 mm × 20 mm were utilized to measure the thermal conductivity of the concrete after 28 days of curing as depict in Fig. 8 (c). Scanning electron microscopy (SEM) was employed to analyze the microstructural properties of the concrete mixtures. Selected samples from various mixes were imaged at 90 days using an Apreo 2 C scanning electron microscope. X-ray diffraction (XRD) was utilized to detect the different phases present in the hardened coal bottom ash lightweight self-compacting concrete (LWSCC) and the control mix. Samples were pulverized after 90 days to observe any alterations in the crystalline phases of the concrete. This analysis was carried out using a Malvern Panalytical XRD device. The pozzolanic reactivity of coal bottom ash was evaluated using a TGA LABSYS evo apparatus to measure the calcium hydroxide (CH) content in various mixes. Small samples were grinded to fine particles and subjected to heating at a 10°C/min rate up to 1000°C in a nitrogen (N2) atmosphere.

(a) (b) (c)

Fig. 8. (a) Compressive strength Test; (b) UPV test; (c) Thermal conductivity test

3. Results and Discussion

3.1 Fresh State Characteristics

Following the AFGC standards, the workability and flow characteristics of each concrete mixture were assessed through tests for slump flow diameter, L-box ratio, and sieve segregation resistance. The findings from these fresh property evaluations, as summarized in Table 7, will be analyzed in detail and discussed in the subsequent section.

Table 7. Fresh properties result of SCC

Mix	Slump-flow (cm)	Class NF EN 206-9	L–box (H2/H1)	Class NF EN 206-9	Sieve Stability (%)	Class NF EN 206-9
RSCC	72.7	SF2	0.94	PL2	9.24	SR2
CBASCC - 0%	80	SF3	0.90	PL2	8.5	SR2
CBASCC-10%	80	SF3	0.88	PL2	7.8	SR2
CBASCC-15%	79.2	SF3	0.85	PL2	7.46	SR2
CBASCC-20%	77	SF3	0.83	PL2	6.24	SR2
CBASCC-25%	76.6	SF3	0.82	PL2	6.12	SR2
CBASCC-30%	75.5	SF2	0.82	PL2	4	SR2

3.1.1 Slump Flow Diameter

As shown in Fig. 9, the slump flow values for all mixtures ranged from 727 to 800 mm, indicating excellent deformability characteristics of the Self-Compacting Concrete (SCC). The incorporation of coal bottom ash (CBA) as coarse aggregate in a saturated surface dry (SSD) condition improved workability compared to the reference mix. However, substituting cement with coal bottom ash powder (CBAP) led to a reduction in the slump flow diameter. Specifically, the mixture containing 10% CBAP exhibited a slump flow value similar to the reference mix, while increasing the CBAP content to 30% resulted in a noticeable decrease in workability. This decline can be attributed to the water-absorptive properties of CBAP, which absorbed additional water during mixing, as well as its relatively low pozzolanic activity, delaying the water-binding process and further impacting workability [41]. The water absorption capacity of CBAP is significantly influenced by its particle size distribution, surface area, and pore structure. Finer particles, characterized by a smaller size,

increase water absorption due to their larger surface area relative to volume, providing more sites for water interaction [42].

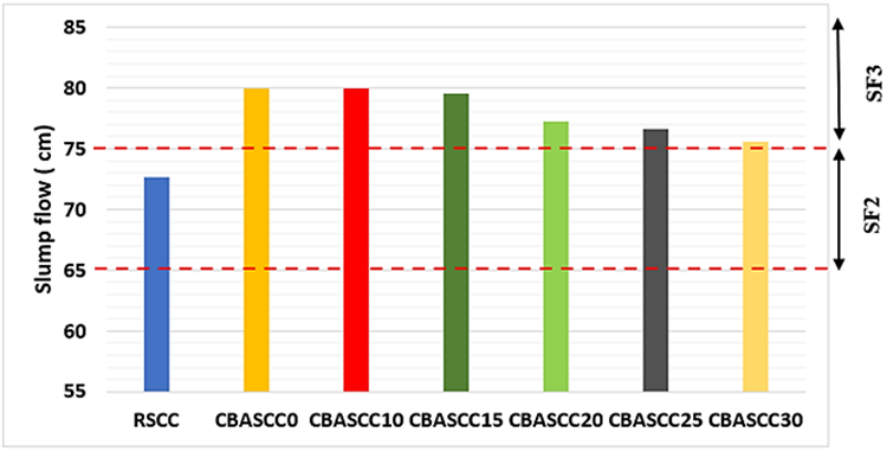

Fig. 9. Effect of CBA on SCC slump flow

Additionally, a higher surface area, often associated with finer or irregularly shaped particles, facilitates greater interaction with water molecules, further enhancing absorption [29]. The pore structure also plays a critical role; open and interconnected pores allow water to penetrate more easily, while micropores increase absorption through capillary action [42], [43]. Also, the irregular surface texture of CBA particles further contributes to the reduced slump flow values. Despite these effects, all mixtures complied with the slump flow diameter requirements of 550–850 mm, corresponding to the SF2 and SF3 consistency classes as specified by the AFGC. These findings align with previous studies [11,34], which also reported similar trends in workability when incorporating CBA and CBAP in concrete mixtures.

3.1.2 Blocking Ratio

Passing ability is evaluated to assess the capacity of fresh LWSCC to flow through restricted spaces, such as areas with dense steel reinforcement, without segregation, blockage, or loss of uniform consistency [12]. The L-box test was used to evaluate the passing ability of Self-Compacting Concrete (SCC). The passing ability ratio H2/H1 (H1 and H2 standing for the concrete height in the vertical and horizontal compartment of the L-box apparatus, respectively showed a slight decline when CBA was used as coarse aggregate, particularly as the proportion of CBAP replacement increased from 0% to 30% (Fig. 10).

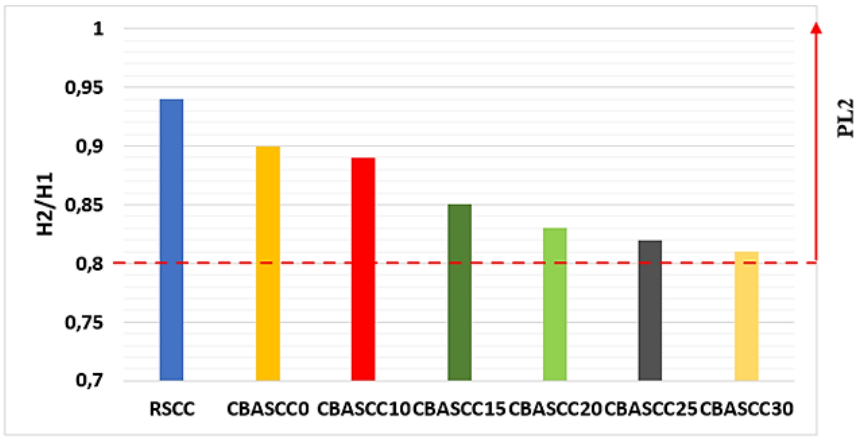

Fig. 10. Effect of CBA on SCC passing ability

The results of the concrete's L-box tests ranged from 0.82 to 0.94, categorizing them under PL2 class as per the guidelines recommended by AFGC. The decrease in the H2/H1 ratio can be linked to the irregular shape and porous nature of CBA particles, along with their highwater absorption.

These characteristics increase friction between particles, hindering the concrete's ability to flow smoothly and reducing its passing ability [36].

3.1.3 Sieve Stability

Segregation resistance is a critical factor in ensuring the homogeneity of lightweight self-compacting concrete (LWSCC), preventing bleeding and the separation of aggregates during placement and transportation [12]. Sieve segregation testing was conducted to evaluate this resistance, with results showing segregation ratios ranging from 4% to 9.24%, as illustrated in the table and Fig. 11. The segregation ratio decreased with the incorporation of coal bottom ash (CBA) as an aggregate and with increasing levels of coal bottom ash powder (CBAP) replacement, indicating improved resistance to segregation. This enhancement can be attributed to the water absorption properties of CBA during the mixing process. Specifically, CBA particles, particularly in their powder form (CBAP), exhibit a high-water absorption capacity due to their fine particle size, large surface area, and porous structure. When CBA absorbs water, it reduces the amount of free water in the mixture, minimizing the risk of bleeding and segregation by preventing excess water from separating from the solid components of the concrete [42]. All concrete mixes achieved a segregation ratio below 15%, indicating that their segregation resistance meets the criteria for SR2 classification. Ting et al [40] reported that adding different types of supplementary materials was found to reduce the passing ability. On the other hand, increasing the binder content improved segregation resistance by making the LWSCC mixture denser. However, higher amounts of water and superplasticizer led to poorer segregation resistance.

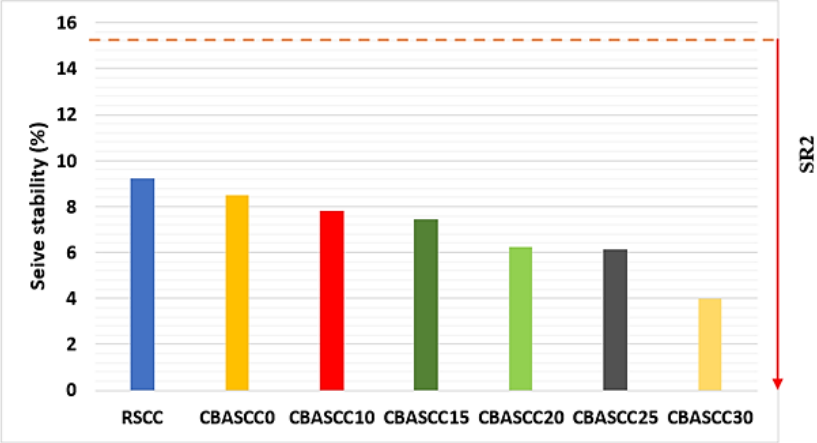

Fig. 11. Effect of CBA on SCC segregation resistance

3.2 Hardened State Results

3.2.1 Compressive Strength

Fig. 12 depicts the results from compressive strength tests conducted at 7, 28, and 90 days. The strength of all specimens increased with longer curing periods up to 90 days, ranging from 38.32 MPa to 56.1 MPa. However, these values were consistently lower than those of SCC containing 100% natural aggregate. The use of coarse CBA aggregate resulted in porous concrete, reducing its compressive strength by approximately 14% at 28 days. Additionally, the compressive strength of Lightweight Self-Compacting Concrete (LWSCC) containing CBA coarse aggregate declined as the amount of coal bottom ash powder (CBAP) in the mixture increased. Notably, at 90 days, CBASCC-10% exhibited a strength about 3% higher than the (CBASCC-0%) mix.

The compressive strength of the concrete containing bottom ash initially declined at replacement levels exceeding 10%. After 90 days of curing, decreases of 3.5%, 15%, 18.7%, and 21% were observed for replacement levels of 15%, 20%, 25%, and 30%, respectively, in comparison to the reference concrete. This decline in strength was linked to the slower initial reactivity of CBAP, contrasting with higher gains observed at 90 days of curing [11]. Kurama et al [44] also observed a comparable trend, indicating an enhancement in compressive strength with a 10% replacement of

cement with CBA. The compressive strength of coal bottom ash lightweight self-compacting concrete exceeded 17.2 MPa, meeting the minimum strength recommended for structural applications by ACI Committee standards.

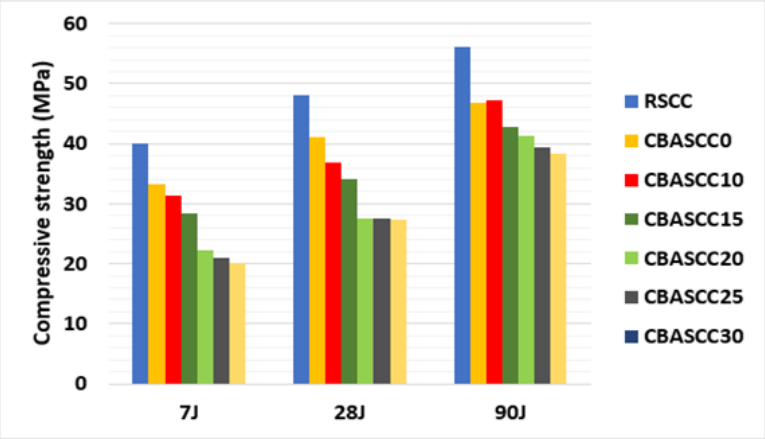

Fig. 12. Effect of CBA on SCC compressive strength

3.2.2 SCC Oven Dry Density

Fig. 13 presents the oven dry density measurements of the concrete after 28 days of curing. Substituting natural coarse aggregate with CBA resulted in a noticeable decrease in density. This decline is attributed to the porous characteristics and reduced unit weight of CBA in contrast to conventional aggregates [10]. Singh et al. noted that the lower density of bottom ash concrete results from the reduced specific gravity of coal bottom ash compared to natural aggregate, replacing river sand with coal bottom ash introduces lighter particles, while the increased void content further decreases the concrete's density [26]. The measured oven dry density values ranged from 1802.7 to 2133.96 kg/m^3. Furthermore, replacing cement with CBAP in the mixture contributed to a reduction in unit weight due to its high internal porosity. Kurt et al.,[41], also observed that replacing cement with pumice powder in concrete mixtures reduced the unit weight.

Additionally, unit weight decreased as the w/ (c + m) ratio and the proportion of mineral additives increased, attributed to the larger void spaces in the concrete and the lower specific gravity of the mineral additives compared to cement, this is due to higher porosity from excess water evaporating during curing and the lower specific gravity of CBAP compared to cement, both of which reduce the concrete's density [41]. Concrete mixes incorporating CBA as coarse aggregates and partial cement replacement showed dry densities below 2000 kg/m^3, meeting the criteria for lightweight aggregate concrete according to EN 206-1 standards.

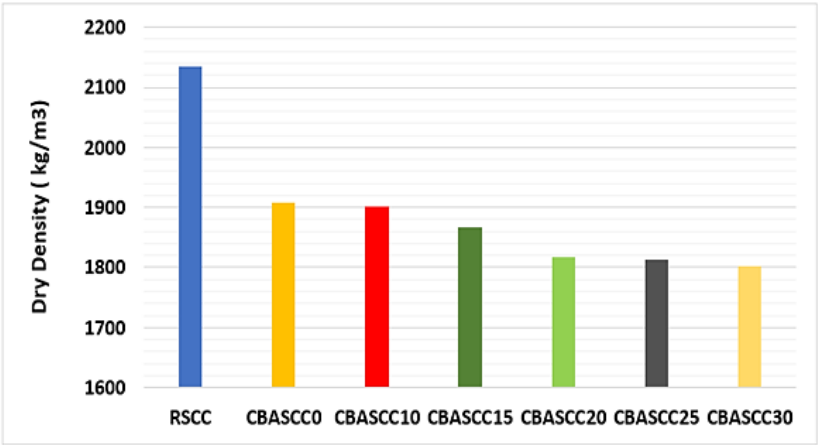

Fig. 13. Effect of CBA on the dry density of SCC

3.2.3 Ultrasonic Pulse Velocity

The ultrasonic pulse velocities (UPV) of the concrete samples ranged from 3 to 4.69 km/s, as depicted in Fig. 14, indicating that the concrete quality meets the criteria specified by ASTM C597. Notably, all experimental concrete mixes showed lower UPV values compared to the control concrete mix (CSCC), attributing this decrease to the incorporation of coal bottom ash (CBA) aggregate. Specifically, the UPV values for concrete mixtures containing CBA aggregate and different proportions of CBAP powder (CBASCC-0%, 10%, 15%, 20%, 25%, and 30%) were reduced by 29%, 26.5%, 33%, 34.6%, 34.8%, and 35.7%, respectively, relative to the control mix CSCC after 28 days of curing. However, CBASCC-10% exhibited a slight increase of 3.4% in UPV in comparison to the reference mix CBASCC-0%. These results from the UPV measurements correlate well with the compressive strength data. Similar findings were previously reported by [45].

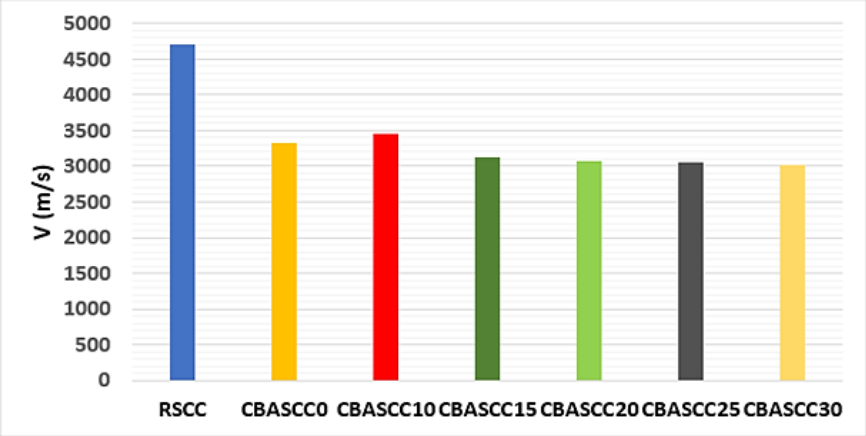

Fig. 14. Effect of CBA on ultrasonic pulse velocity of SCC at 28 days

3.2.4 Water Absorption

Figure 15 shows that the water absorption rate of the reference samples without CBA was 4.2%, which is about 30% lower than the samples with CBA used as a coarse lightweight aggregate. When CBAP was added as a partial replacement for cement, water absorption increased by 15%, 35%, 45%, 50%, and 80% at replacement levels of 10%, 15%, 20%, 25%, and 30%, respectively. This increase was expected because using CBA as a lightweight aggregate and CBAP as a cement substitute increases the amount of void space in the concrete. Similarly, Kurt et al.,[41] found that control samples without mineral additives had lower water absorption compared to samples containing pumice lightweight aggregate and pumice powder. All the CBA based LWSCC exhibits water absorption of less than 8% at all ages indicating good durability [46].

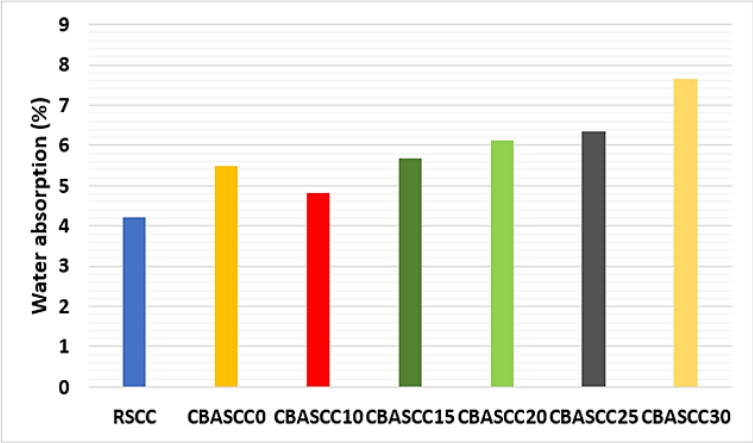

Fig. 15. Effect of CBA on the water absorption of SCC at 28 days

3.2.5 Thermal Conductivity

Thermal conductivity primarily depends on the pore structure of aggregates (whether light, heavy, natural, or recycled), the concrete's density, and the cement matrix [47]. Fig. 16 shows the thermal conductivity coefficients (K) of the SCC tested. Notably, concretes incorporating coal bottom ash (CBA) exhibit improved thermal insulation properties, as evidenced by a significant decrease in thermal conductivity values upon substituting natural aggregate with CBA aggregate. Specifically, the thermal conductivity of concretes decreases from 1.56 to 1.10 W/m.K when natural aggregate is replaced with CBA aggregate and to 0.75 W/m.K when Portland cement is replaced with CBAP compared to the control mix. This represents reductions of 29.4% in thermal conductivity. This is due to the increased void content and lower density of the CBA aggregate relative to normal aggregate. Moreover, the results demonstrate that thermal conductivity decreases further with higher proportions of CBAP incorporation from 1.10 to 0.75 W/m·K when Portland cement is replaced with CBAP compared to the reference mix (CBASCC-0%), this represents reductions of 31.8% in thermal conductivity, attributable to the increased porosity of CBAP. This underscores the significance of material porosity in enhancing thermal insulation performance [48].

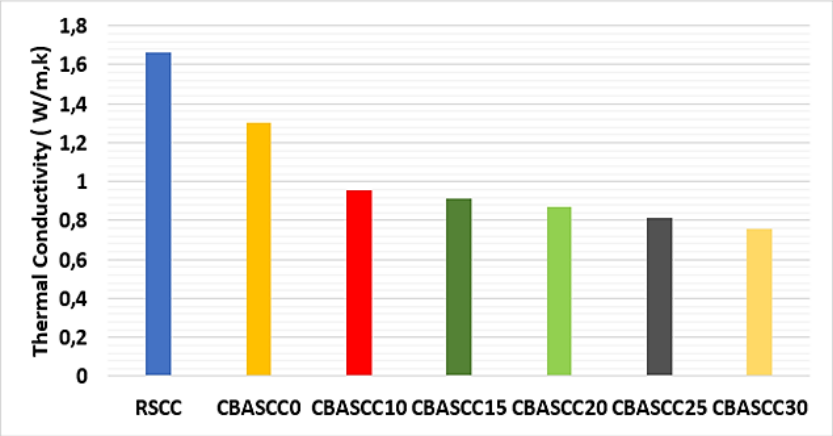

Fig. 16. Effect of CBA on SCC thermal conductivity at 28 days

3.2.6 Correlations

Fig. 17 depicts the relationships between compressive strength, pulse velocity, and thermal conductivity relative to dry density for SCC mixtures following 28 days of curing, evaluated through high R^2 values of 0.93 for compressive strength and 0.96 for pulse velocity. In general, a decrease in the solid structure content of the material results in lower compressive strength [47]. Likewise, compressive strength decreases as dry density decreases Fig. 17 (a), similarly impacting pulse velocity Fig. 17 (b). On the other hand, variations in compressive strength have a corresponding effect on ultrasonic pulse velocity, resulting in a linear decrease as compressive strength decreases, as depicted in Fig. 17 (c) with their respective R^2 values of 0.83. Additionally, the thermal conductivity of concrete is primarily influenced by its density [49].

The reduction in dry density shows a linear correlation with the thermal conductivity coefficient, as indicated by an R^2 value of 0.97 in Fig. 17(d). This relationship highlights dry density as a key factor affecting the thermal properties of concrete. Overall, these findings highlight the interrelationships among material density, mechanical strength, ultrasonic characteristics, and thermal conductivity in SCC mixtures, providing valuable insights into their performance and behavior. Moreover, Similar observations have been reported by several researchers when studying SCC with lightweight aggregates [13, 41, 50].

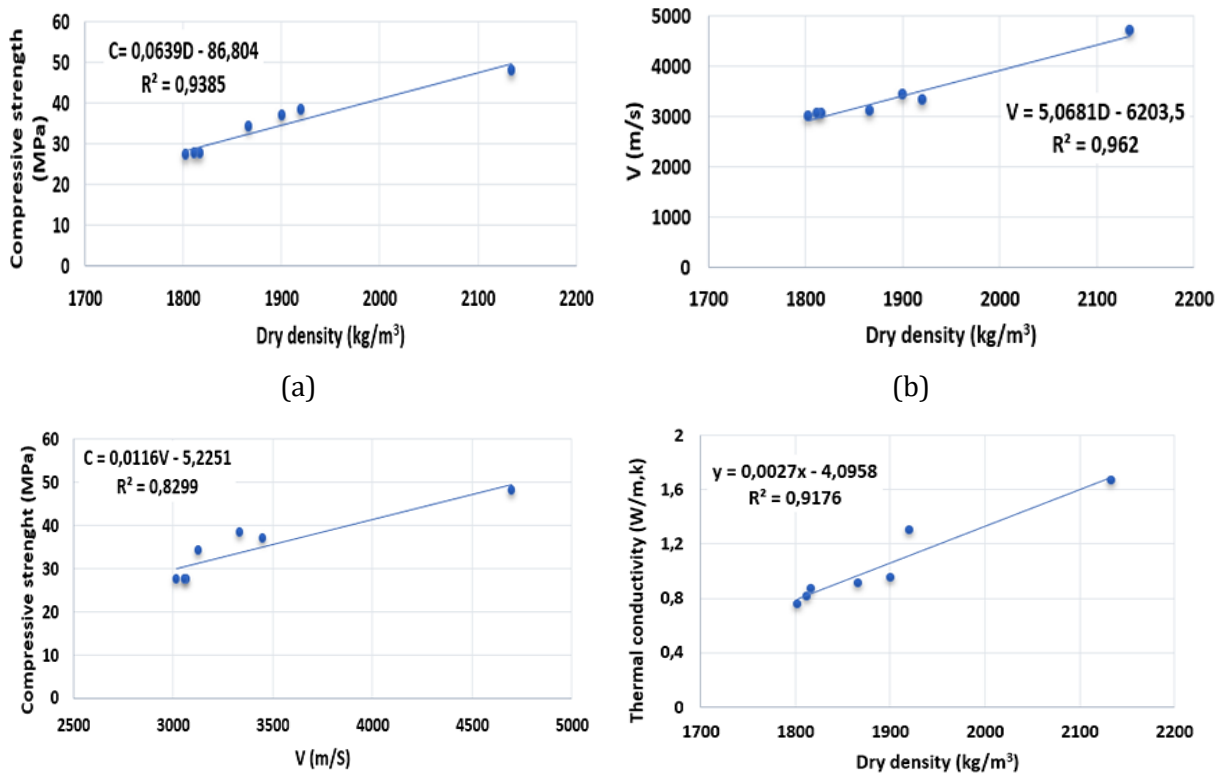

Fig.17. Correlations (a) Compressive strength-dry density; (b) UPV-dry density; (c) Compressive strength-UPV; (d) Thermal conductivity-dry density

3.3 Microstructure Properties

3.3.1 SEM Analysis Results

Concrete microstructure comprises aggregate, interfacial transition zone (ITZ) and hardened paste [11]. In this study, SEM analysis of different concrete mixes CSCC (control), CBASCC-0%, CBASCC-10% and CBASCC-30% after 90 days are presented in Fig. 18. The SEM image of control concrete CSCC, containing 100% natural aggregate Fig. 18 (a), reveals a dense, compact C-S-H gel with large portlandite crystals. In contrast, concrete incorporating coal bottom ash (CBA) aggregate displays noticeable pores and cracks, indicating increased porosity compared to control concrete.

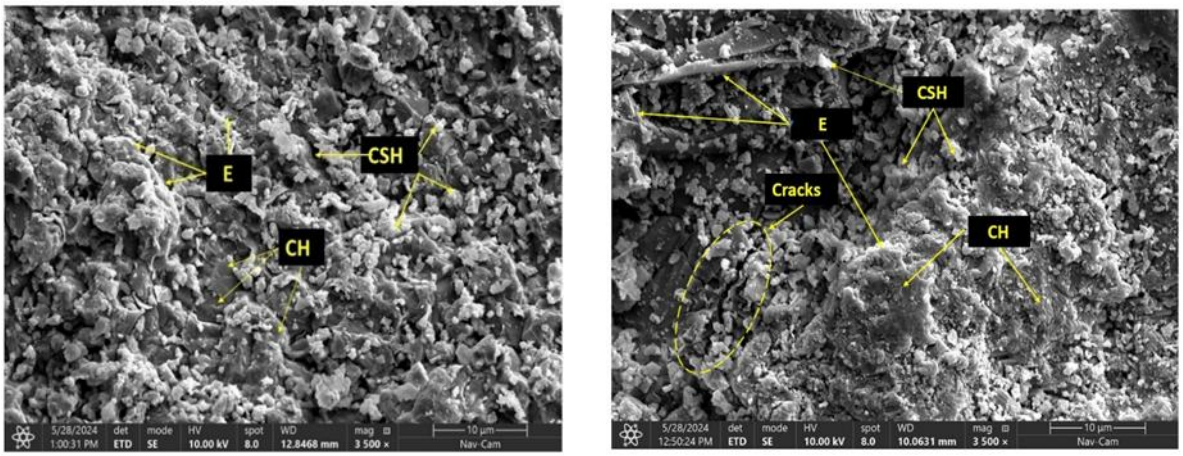

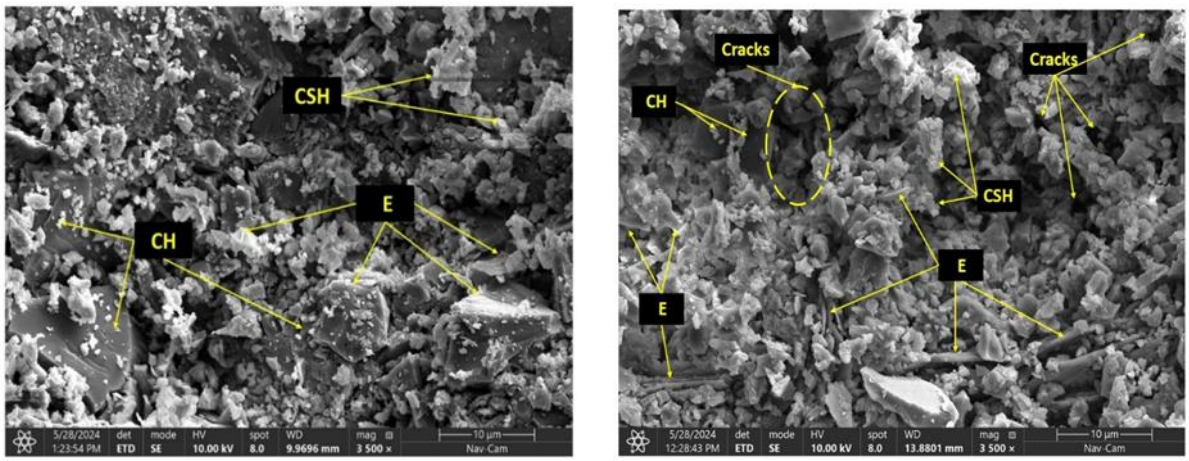

(c) (d)

Fig. 18. SEM image of (a): CSCC, (b): CBASCC-0%, (c): CBASCC-10%, (d): CBASCC-30%

This observation is consistent with findings from water absorption and compressive strength tests. Fig 18. (b-d) show SEM images of CBA concrete mixtures where the C-S-H gel formation appears less distinct and more irregular, often appearing in layered cloud-like formations, with smaller portlandite crystals relative to the control concrete. Both control and CBA concrete mixtures display the presence of C-S-H gel. Notably, when 30% of Portland cement was replaced with CBAP Fig. 18 (d), the formation of ettringite in needle-like structures within voids was observed. Conversely, the concrete with 10% replacement exhibits a more compact structure with smaller pores. This enhancement is credited to the pozzolanic reaction of CBA, which gradually aids in densifying the material and filling pores [51].

3.3.2 XRD Analysis Results

Fig. 19 presents the XRD analysis findings after 90 days of curing, showing quartz from river sand and mullite from CBA aggregate in the diffractograms. Hydration products such as calcium hydroxide (portlandite), calcite, and ettringite are also detected. These diffractograms reveal the presence of quartz from river sand and mullite from CBA aggregate. Hydration products such as calcium hydroxide (portlandite), calcite, and ettringite are also identified. Ettringite peaks are evident in all concrete samples, with slightly higher intensity in CBASCC-30% (Fig. 19d). The presence of calcite (CaCO3) indicates reactions between hydrated phases and atmospheric CO2.

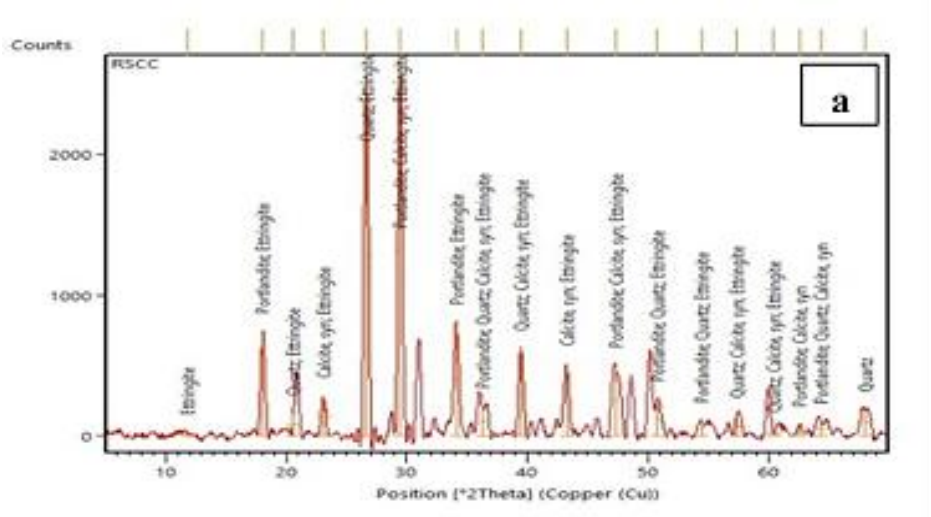

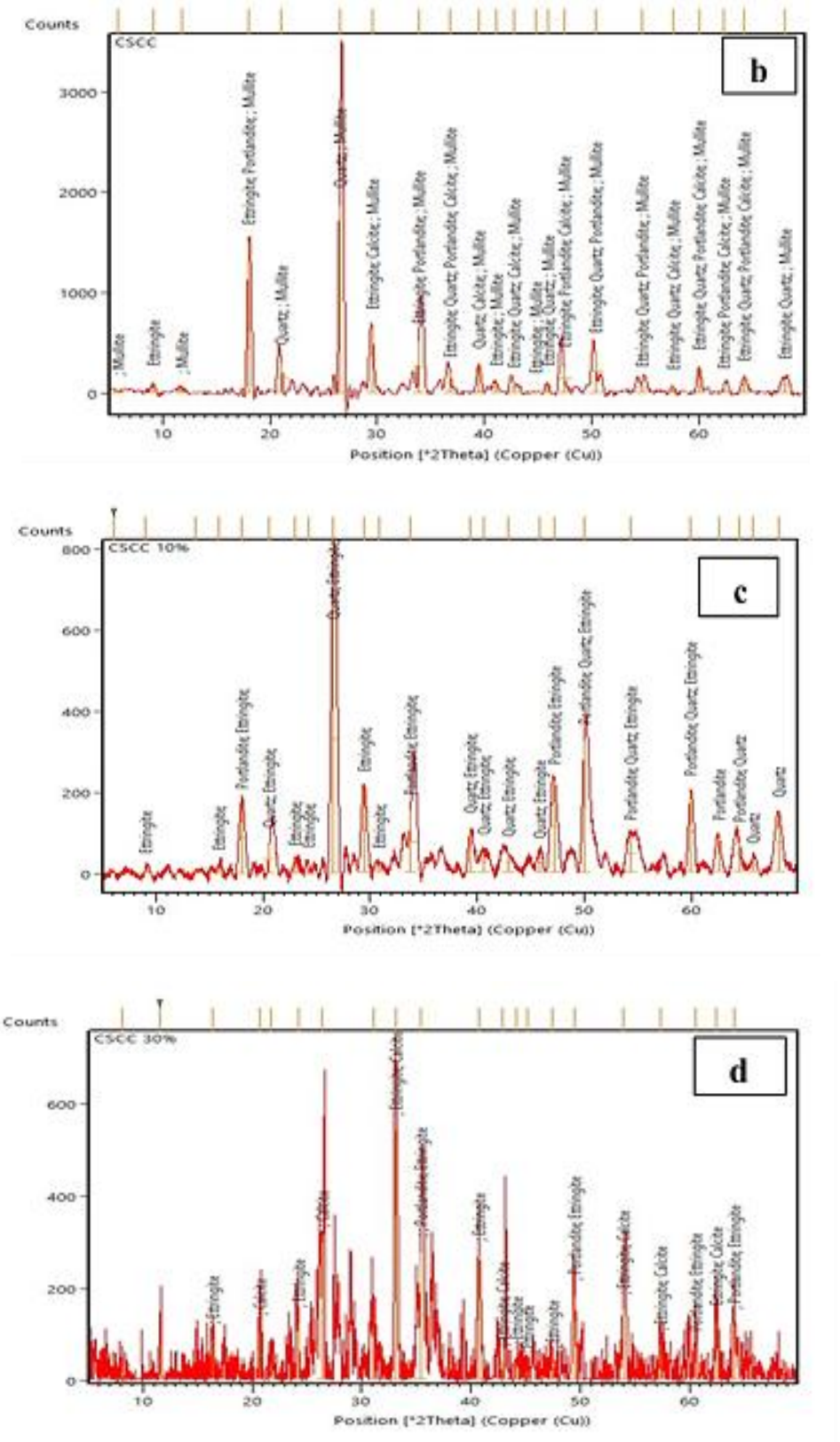

Fig. 19. XRD patterns of (a): CSCC, (b): CBASCC-0%, (c): CBASCC-10%, (d): CBASCC-30%

The portlandite (CH) peak is more pronounced in the Reference and CBASCC-0% mixes (Fig. 19a-b) compared to CBASCC-10% and CBASCC-30% (Fig.19c-d). This decline is attributed to the interaction between CBAP and CH, increasing the creation of both C-S-H and ettringite. The amount of CH consumed in mixtures containing pozzolanic materials is closely linked to the extent of their

pozzolanic reaction [52]. The diffraction peaks typical of C-S-H are often indistinct due to its amorphous nature, often obscured by the more prominent peaks of portlandite. [27]

3.3.3 TGA, DSC Analysis

Fig. 20 displays the results of both differential scanning calorimetry (DSC) and thermogravimetric analysis (TGA) carried out on CBA (coal bottom ash). In the DSC analysis of CBA, an initially endothermic peak was detected at about 100°C, which is attributed to the release of physically associated water and evaporation of moisture [53].

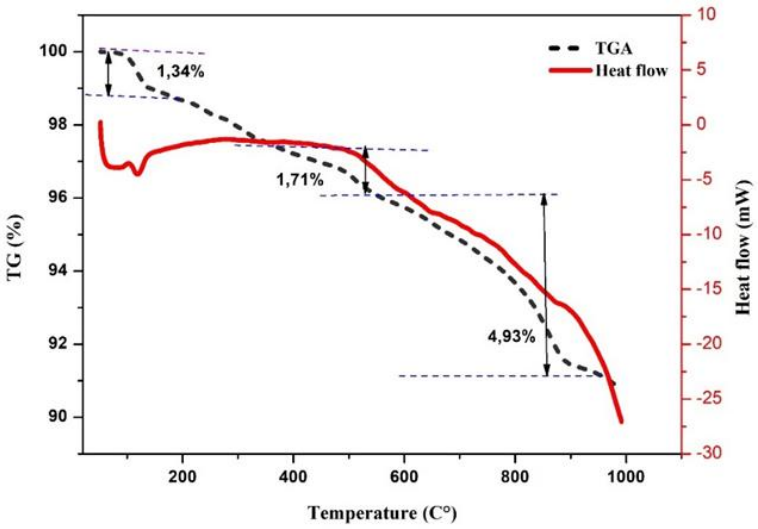

Fig. 20. TGA and DSC analysis of CBA

The TGA curve showed a second mass loss of 1.71% between 370°C and 520°C, attributed to the evaporation of residual carbonaceous materials present in CBA [53]. Additionally, a weight loss of 4.93% above 800°C is proposed to be associated with the dehydroxylation of metallic hydroxides [54]. The most significant mass loss occurred in the temperature range of 600°C to 860°C. Beyond 860°C, CBA exhibited stable thermogravimetric behavior. These findings are consistent with previous studies [55].

TGA and DSC analyses of control concrete CSCC, concrete containing both CBA aggregate and CBAP (CBASCC-10%, 30%) are presented in Fig. 19-20. Four endothermic peaks are observed: at 60°C-170°C, 450°C, 670°C, and 750°C-900°C in the DSC curves Fig. 21. These heat flow peaks primarily correspond to the phase change temperatures of different hydrates present in the cement paste. The first endothermic peak observed at 60°C-170°C is attributed to the release of absorbed water from the formation of specific hydrates such as C-S-H and ettringite. The diffraction peak of ettringite in CBASCC-30% appears to be higher than in CSCC and CBASCC-10%, potentially due to reactions involving active alumina in CBAP. Another notable observation is the diffraction peaks appearing between 450°C and 550°C, corresponding to the decomposition of portlandite into free lime. It is evident from the data that the control mix has higher CH content compared to the mix with 10% CBAP replacement, indicating potential pozzolanic reactions of CBAP. However, the diffraction peak of CH in CBASCC-30% is marginally more prominent than that in CSCC and CBASCC-10%. Excessive CH can lead to an overabundance of free lime, resulting in undesirable effects such as volume expansion and reduced strength, suggesting that incorporating more than 10% CBAP as a cement replacement adversely affects concrete's mechanical properties which can be attributed to delayed hydration and slow pozzolanic activity of CBAP [30]. This result supports the earlier findings regarding the increase in strength with CBA replacement, additionally, Endothermic peaks were detected at approximately 670°C and 750°C. These peaks are associated with the decomposition of C-S-H into a new form of dicalcium silicate (β-C2S) [51] and the decomposition of calcium carbonates ($CaCO_3$), respectively.

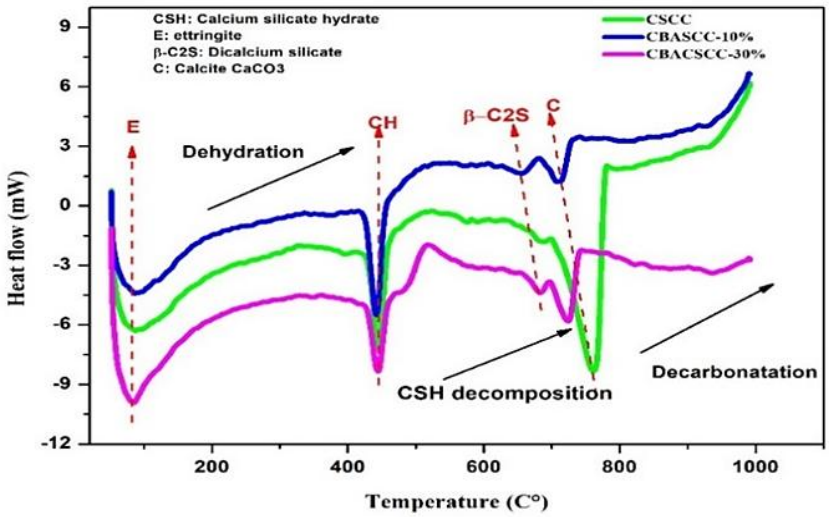

Fig. 21. DSC analysis of concrete

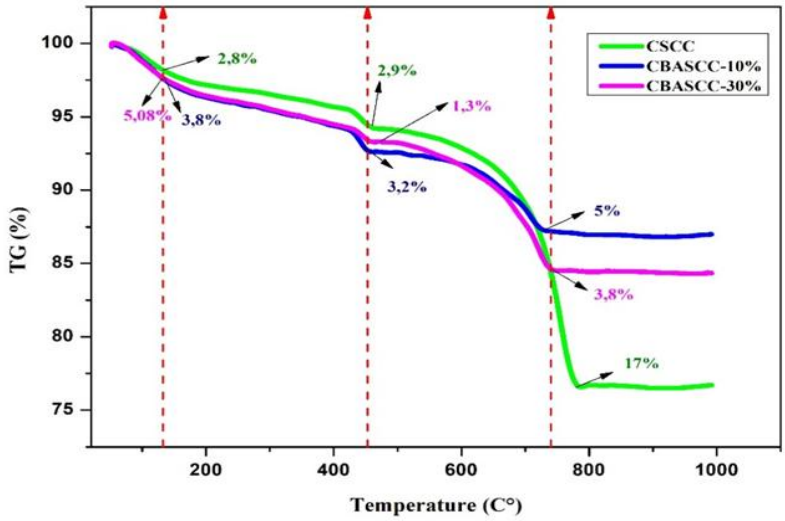

Fig. 22. TGA analysis of concrete

The TGA curves (Fig. 22) of CSCC (control concrete) and CBASCC-10% and CBASCC-30% (concretes with both CBA aggregate and CBAP) display distinct weight loss behaviors. Initially, there is a noticeable weight loss at 200°C, largely due to the evaporation of adsorbed water in the micropores, with values of approximately 2.87%, 3.8%, and 5.08% for CSCC, CBASCC-10%, and CBASCC-30%, respectively. A second phase of weight loss begins around 400°C to 450°C, with corresponding losses of about 2.96%, 3.2%, and 1.36% for CSCC, CBASCC-10%, and CBASCC-30%. This phase is associated with the decomposition of hydrated components such as C-S-H gel and calcium hydroxide (CH), releasing structural water [56]. Further mass losses occur between 700°C and 850°C due to the decomposition of calcite and organic substances. Quantitatively, CSCC, CBASCC-10%, and CBASCC-30% experience weight losses of approximately 17%, 5%, and 3.8%, respectively. Above 850°C, all specimens exhibit a stable mass loss pattern.

4. Conclusions

This study explores the effects of coal bottom ash (CBA) on the fresh properties, mechanical performance, and microstructure of self-compacting concrete (SCC). The experiments replaced natural coarse aggregate with CBA and varied the substitution of Portland cement with CBA powder. The key conclusions drawn from the results are as follows:

- The test results on the fresh concrete properties incorporating coal bottom ash (CBA) reveal that using CBA in SSD state as a coarse aggregate improves the workability of fresh self-compacting concrete (SCC). However, substituting cement with CBA powder decreases workability as the replacement levels increase from 10% to 30%. Despite the reduction in workability, the concretes met the required fresh state properties filling ability (SF3), passing ability (PL2), and segregation resistance (SR2) as per European Guidelines, ensuring adequate workability for SCC applications.
- The oven-dry density of SCC decreased when CBA aggregate was used as lightweight aggregate, dropping from 2133.96 kg/m^3 to 1920 kg/m^3. Similarly, the density decreased with higher levels of CBAP replacement by about 6%, resulting in dry densities below 2000 kg/m^3. This meets the specifications for lightweight self-compacting concrete according to EN 206-1 standards.
- The use of CBA as a lightweight aggregate in SCC resulted in reduced compressive strength and ultrasonic pulse velocity values in the concrete samples after 28 days. These reductions are mainly due to the pore nature of coal bottom ash. On the other hand, substituting 10% CBA powder for Portland cement improved compressive strengths over time, driven by observed pozzolanic activity after 90 days. The compressive strength exceeded 17.2 MPa, meeting the minimum strength requirement for structural applications as specified by ACI Committee standards. Thus, the declines in compressive strength and pulse velocity are linked to the lower unit weight of the concrete.
- The incorporation of coal bottom ash (CBA) reduces the density of the concrete, resulting in lower thermal conductivity and improved thermal insulation. Thermal conductivity values were 52% lower in the CBA-containing concrete compared to the reference mix.
- The CBA concrete had approximately 80% higher water absorption than the reference mix. This increase is due to the larger porosity and void volume caused by the use of CBA both as a lightweight aggregate and as a 30% cement replacement in SCC.
- Microstructural analyses (SEM, XRD, and TGA) reveal that integrating CBA aggregate into SCC results in reduced overall strength, primarily due to increased porosity and other inherent physical weaknesses. However, there is a slight enhancement in the creation of further C-S-H gel, which is attributed to CBA, as confirmed by TGA and XRD findings. Conversely, incorporating 10% CBA powder as a cement replacement produces a denser structure with reduced pore size, highlighting the effective pozzolanic activity of CBAP.

The findings of this study demonstrate that Coal Bottom Ash (CBA)-based self-compacting concrete (SCC) is a sustainable and cost-effective alternative to conventional concrete. By replacing natural aggregates and up to 10% of cement, CBA reduces material costs, lowers carbon emissions, and improves thermal and sound insulation, making it suitable for lightweight structures, green buildings, and precast elements. CBA-based SCC aligns with circular economy principles and reduces the environmental footprint of concrete production.

5. Limitation of Using CBA

The use of Coal Bottom Ash (CBA) in self-compacting concrete (SCC) presents several limitations that must be considered. While CBA improves workability as a coarse aggregate, replacing cement with CBA powder reduces workability at higher replacement levels (10% to 30%). The porous nature of CBA lowers compressive strength, ultrasonic pulse velocity, and density, meeting lightweight concrete standards but potentially limiting structural applications. Increased porosity also leads to higher water absorption, raising concerns about durability under environmental stressors like moisture and freeze-thaw cycles. Although 10% CBA powder replacement enhances pozzolanic activity and densifies the microstructure, higher replacements or aggregate use introduce weaknesses. Additionally, long-term durability data and potential environmental impacts, such as heavy metal leaching, remain unaddressed. These limitations highlight the need for further research to optimize CBA use in SCC.

6. Research Avenues for CBA-Based SCC

To advance the use of Coal Bottom Ash (CBA)-based self-compacting concrete (SCC), further research should focus on optimizing mix designs by refining CBA proportions, particle sizes, and pretreatment methods to enhance workability, strength, and durability. Additionally, studying the long-term durability of CBA-based SCC under environmental stressors like freeze-thaw cycles, chemical exposure, and moisture penetration is critical to ensure its reliability. Research should also evaluate the environmental and health impacts, including leaching potential and lifecycle assessments, to confirm its safety and sustainability. Exploring pretreatment techniques, such as thermal or chemical activation, could improve CBA reactivity and stability. Economic feasibility studies, including cost-benefit analyses and supply chain assessments, are needed to support large-scale implementation. Developing standardized guidelines and promoting CBA-based SCC in building codes and green certifications will facilitate its adoption. Finally, pilot projects in real-world applications can validate its feasibility and benefits, addressing current limitations and positioning CBA-based SCC as a sustainable alternative in modern construction practices.

Acknowledgement

The authors acknowledge the financial backing from the Directorate General for Scientific Research and Technological Development (D.G.R.S.D.T., Algeria) for their research. They also extend their thanks to the members, professors, and students affiliated with the Laboratory of Eco-Materials: Innovations & Applications (EMIA).

References

[1] Okamura H, Ouchi M. Self-compacting concrete. J Adv Concr Technol. 2003;1(1):5-15. https://doi.org/10.3151/jact.1.5
[2] Agha N, Makkani A, Tafraoui A, Zaouai S. Improving the physical and mechanical properties of new concrete containing crushed dune sand and demolition waste as coarse aggregate. J Eng Exact Sci. 2023;9(5):16002-01e. https://doi.org/10.18540/jcecvl9iss5pp16002-01e
[3] Makani A, Vidal T. Relationships between mineralogical and physico-mechanical properties of granitic aggregates. Proc Int Congr Mater Struct Stab. 2013.
[4] Nahhab AH, Ketab AK. Influence of content and maximum size of light expanded clay aggregate on the fresh, strength, and durability properties of self-compacting lightweight concrete reinforced with micro steel fibers. Constr Build Mater. 2020;233:117922. https://doi.org/10.1016/j.conbuildmat.2019.117922
[5] Grabois TM, Cordeiro GC, Toledo Filho RD. Fresh and hardened-state properties of self-compacting lightweight concrete reinforced with steel fibers. Constr Build Mater. 2016;104:284-92. https://doi.org/10.1016/j.conbuildmat.2015.12.060
[6] Kaffetzakis MI, Papanicolaou CG. Bond behavior of reinforcement in lightweight aggregate self-compacting concrete. Constr Build Mater. 2016;113:641-52. https://doi.org/10.1016/j.conbuildmat.2016.03.081
[7] Vakhshouri B, Nejadi S. Mix design of lightweight self-compacting concrete. Case Stud Constr Mater. 2016;4:1-14. https://doi.org/10.1016/j.cscm.2015.10.002
[8] Khan RA, Ganesh A. The effect of coal bottom ash (CBA) on mechanical and durability characteristics of concrete. J Build Mater Struct. 2016;3(1):31-42. https://doi.org/10.34118/jbms.v3i1.22
[9] Mangi SA, Wan Ibrahim MH, Jamaluddin N, Arshad MF, Memon SA, Shahidan S. Effects of grinding process on the properties of the coal bottom ash and cement paste. J Eng Technol Sci. 2019;51(1):1-13. https://doi.org/10.5614/j.eng.technol.sci.2019.51.1.1
[10] Hamada H, Alattar A, Tayeh B, Yahaya F, Adesina A. Sustainable application of coal bottom ash as fine aggregates in concrete: A comprehensive review. Case Stud Constr Mater. 2022;16:e01109. https://doi.org/10.1016/j.cscm.2022.e01109
[11] Singh N, Shehnazdeep, Bhardwaj A. Reviewing the role of coal bottom ash as an alternative of cement. Constr Build Mater. 2020;233:117276. https://doi.org/10.1016/j.conbuildmat.2019.117276
[12] Ting TZH, Rahman ME, Lau HH. Sustainable lightweight self-compacting concrete using oil palm shell and fly ash. Constr Build Mater. 2020;264:120590. https://doi.org/10.1016/j.conbuildmat.2020.120590
[13] Hilal N, Hamah Sor N, Faraj RH. Development of eco-efficient lightweight self-compacting concrete with high volume of recycled EPS waste materials. Environ Sci Pollut Res. 2021;28(36):50028-51. https://doi.org/10.1007/s11356-021-14213-w

[14] Cheboub T, Senhadji Y, Khelafi H, Escadeillas G. Investigation of the engineering properties of environmentally-friendly self-compacting lightweight mortar containing olive kernel shells as aggregate. J Clean Prod. 2020;249:119406. https://doi.org/10.1016/j.jclepro.2019.119406
[15] Zaoiai S, Makani A, Tafraoui A, Benmerioul F. Optimization and mechanical characterization of self-compacting concrete incorporating rubber aggregates. Asian J Civ Eng. 2016;17:817-29.
[16] Poongodi K, Murthi P. Correlation between compressive strength and elastic modulus of lightweight self-compacting concrete using coconut shell as coarse aggregate. Aust J Struct Eng. 2021;22(2):85-95. https://doi.org/10.1080/13287982.2021.1926061
[17] Ahmed FR, Mohammed AS. Chlorine salt influence on durability and strength of additive-free EPS lightweight concrete. Innov Infrastruct Solut. 2024;9:105. https://doi.org/10.1007/s41062-024-01412-w
[18] Djeddou M, Amieur M, Chaid R, Mesbah HA. Development of eco-friendly self-compacting concrete using marble powder, blast furnace slag and glass fibre-reinforced plastic waste: Application of mixture design approach. Res Eng Struct Mater. 2025;11(1):113-38.
[19] Kumar P, Pasla D, Jothi Saravanan T. Self-compacting lightweight aggregate concrete and its properties: A review. Constr Build Mater. 2023;375:130861. https://doi.org/10.1016/j.conbuildmat.2023.130861
[20] Uysal M, Yilmaz K. Effect of mineral admixtures on properties of self-compacting concrete. Cem Concr Compos. 2011;33(7):771-6. https://doi.org/10.1016/j.cemconcomp.2011.04.005
[21] Zrar YJ, Abdulrahman PI, Sherwani AFH, Younis KH, Mohammed AS. Sustainable innovation in self-compacted concrete. Integrating by-products and waste rubber for green construction practices. Struct. 2024;62:106234. https://doi.org/10.1016/j.istruc.2024.106234
[22] Nabighods K, Saradar A, Mohtasham Moein M, Mirgozar Langaroudi MA, Byzyka J, Karakouzian M. Evaluation of self-compacting concrete containing pozzolan (zeolite, metakaolin & silica fume) and polypropylene fiber against sulfate attacks with different pH: An experimental study. Innov Infrastruct Solut. 2024;9(1):1. https://doi.org/10.1007/s41062-023-01309-0
[23] Sadok A, Makani A, Tafraoui A. The use of local metakaolin in the formulation of self-compacting concrete, physico-mechanical characterization. Regul Sci Tobacco. 2024;9(1):4899-4919.
[24] Boubakeur A, Menadi B, Kouider-Djelloul O, Kenai S. Combined effect of ground granulated blast-furnace slag and metakaolin on the performance of recycled self-compacting concrete. MRS Adv. 2023;8(10):596-601. https://doi.org/10.1557/s43580-023-00583-5
[25] Park SB, Jang YI, Lee J, Lee BJ. An experimental study on the hazard assessment and mechanical properties of porous concrete utilizing coal bottom ash coarse aggregate in Korea. J Hazard Mater. 2009;166(1):348-55. https://doi.org/10.1016/j.jhazmat.2008.11.054
[26] Singh M, Siddique R. Strength properties and micro-structural properties of concrete containing coal bottom ash as partial replacement of fine aggregate. Constr Build Mater. 2014;50:246-56. https://doi.org/10.1016/j.conbuildmat.2013.09.026
[27] Zhang B, Poon CS. Use of furnace bottom ash for producing lightweight aggregate concrete with thermal insulation properties. J Clean Prod. 2015;99:94-100. https://doi.org/10.1016/j.jclepro.2015.03.007
[28] Ojha PN, Singh B, Kaura P, Singh A. Lightweight geopolymer fly ash sand: An alternative to fine aggregate for concrete production. Res Eng Struct Mater. 2021;7(3):375-91. https://doi.org/10.17515/resm2021.257ma0205
[29] Kim HK, Lee HK. Use of power plant bottom ash as fine and coarse aggregates in high-strength concrete. Constr Build Mater. 2011;25(2):1115-22. https://doi.org/10.1016/j.conbuildmat.2010.06.065
[30] Singh N, M M, Arya S. Influence of coal bottom ash as fine aggregates replacement on various properties of concretes: A review. Resour Conserv Recycl. 2018;138:257-71. https://doi.org/10.1016/j.resconrec.2018.07.025
[31] Nguyen Thi N, Phi Hong T, Bui Truong S. Utilizing coal bottom ash from thermal power plants in Vietnam as partial replacement of aggregates in concrete pavement. J Eng. 2019;1-11. https://doi.org/10.1155/2019/3903097
[32] Cheriaf M, Rocha JC, Péra J. Pozzolanic properties of pulverized coal combustion bottom ash. Cem Concr Res. 1999;29(9):1387-91. https://doi.org/10.1016/S0008-8846(99)00098-8
[33] Rafieizonooz M, Mirza J, Salim MR, Hussin MW, Khankhaje E. Investigation of coal bottom ash and fly ash in concrete as replacement for sand and cement. Constr Build Mater. 2016;116:15-24. https://doi.org/10.1016/j.conbuildmat.2016.04.080
[34] Zainal Abidin NE, Wan Ibrahim MH, Jamaluddin N, Kamaruddin K, Hamzah AF. The effect of bottom ash on fresh characteristic, compressive strength and water absorption of self-compacting concrete. Appl Mech Mater. 2014;660:145-51. https://doi.org/10.4028/www.scientific.net/AMM.660.145
[35] Ibrahim MHW, Hamzah AF, Jamaluddin N, Ramadhansyah PJ, Fadzil AM. Split tensile strength on self-compacting concrete containing coal bottom ash. Procedia Soc Behav Sci. 2015;195:2280-9. https://doi.org/10.1016/j.sbspro.2015.06.317

[36] Meena A, Singh N, Singh SP. Shear strength and microstructural investigation on high-volume fly ash self-compacting concrete containing recycled concrete aggregates and coal bottom ash. Mater Construcc. 2024;74(353):e333. https://doi.org/10.3989/mc.2024.354623
[37] Raju K, Ramanjaneyulu N, Rao MVS. Strength and durability studies on lightweight self-compacting concrete partially replacing coarse aggregate with sintered fly ash aggregate. CVR J Sci Technol. 2022;23.
[38] EFNARC. The European guidelines for self-compacting concrete: Specification, production, and use. European Federation of National Associations Representing Producers and Applicators of Specialist Building Products for Concrete. 2005.
[39] AFGC. Recommendations for the design, manufacture, and use of self-consolidating concrete. French Association of Civil Engineering. 2008.
[40] Ting TZH, Rahman ME, Lau HH, Ting MZY. Recent development and perspective of lightweight aggregates based self-compacting concrete. Constr Build Mater. 2019;201:763-77. https://doi.org/10.1016/j.conbuildmat.2018.12.128
[41] Kurt M, Gül MS, Gül R, Aydin AC, Kotan T. The effect of pumice powder on the self-compactability of pumice aggregate lightweight concrete. Constr Build Mater. 2016;103:36-46. https://doi.org/10.1016/j.conbuildmat.2015.11.043
[42] Mehdipour I, Khayat KH. Effect of particle-size distribution and specific surface area of different binder systems on packing density and flow characteristics of cement paste. Cem Concr Compos. 2017;78:120-31. https://doi.org/10.1016/j.cemconcomp.2017.01.005
[43] Singh M, Siddique R. Effect of coal bottom ash as partial replacement of sand on properties of concrete. Resour Conserv Recycl. 2016;72:20-32. https://doi.org/10.1016/j.resconrec.2012.12.006
[44] Kurama H, Topçu İB, Karakurt C. Properties of the autoclaved aerated concrete produced from coal bottom ash. J Mater Process Technol. 2009;209(2):767-73. https://doi.org/10.1016/j.jmatprotec.2008.02.044
[45] Torkittikul P, Nochaiya T, Wongkeo W, Chaipanich A. Utilization of coal bottom ash to improve thermal insulation of construction material. J Mater Cycles Waste Manag. 2017;19(1):305-17. https://doi.org/10.1007/s10163-015-0419-2
[46] Kluge RW. Lightweight aggregate concrete. J Proc. 1949;45(5):625-42. https://doi.org/10.14359/12175
[47] Topçu IB, Uygunoğlu T. Effect of aggregate type on properties of hardened self-consolidating lightweight concrete. Constr Build Mater. 2010;24(7):1286-95. https://doi.org/10.1016/j.conbuildmat.2009.12.007
[48] Atyia MM, Mahdy MG, Abd Elrahman M. Production and properties of lightweight concrete incorporating recycled waste crushed clay bricks. Constr Build Mater. 2021;304. https://doi.org/10.1016/j.conbuildmat.2021.124655
[49] Yu QL, Spiesz P, Brouwers HJH. Development of cement-based lightweight composites-Part 1: Mix design methodology and hardened properties. Cem Concr Compos. 2013;44:17-29. https://doi.org/10.1016/j.cemconcomp.2013.03.030
[50] Hashemi SSG, Mahmud HB, Ghuan TC, Chin AB, Kuenzel C, Ranjbar N. Safe disposal of coal bottom ash by solidification and stabilization techniques. Constr Build Mater. 2019;197:705-15. https://doi.org/10.1016/j.conbuildmat.2018.11.123
[51] Wongkeo W, Chaipanich A. Compressive strength, microstructure and thermal analysis of autoclaved and air cured structural lightweight concrete made with coal bottom ash and silica fume. Mater Sci Eng A. 2010;527(16-17):3676-84. https://doi.org/10.1016/j.msea.2010.01.089
[52] Begen D, Calis-Ismetoglu G, Gumus OY, Unal HI. A comparative study of coal fly and bottom ashes as sustainable electroactive vibration damping materials. Environ Eng Res. 2023;29(4):230561. https://doi.org/10.4491/eer.2023.561
[53] Abbas S, Arshad U, Abbass W, Nehdi ML, Ahmed A. Recycling untreated coal bottom ash with added value for mitigating alkali-silica reaction in concrete: A sustainable approach. Sustainability. 2020;12(24):10631. https://doi.org/10.3390/su122410631
[54] Markoš J. Proceedings, Slovak Society of Chemical Engineering. Slovak Society of Chemical Engineering. 2009.
[55] Villain G, Thiery M, Platret G. Measurement methods of carbonation profiles in concrete: Thermogravimetry, chemical analysis and gammadensimetry. Cem Concr Res. 2007;37(8):1182-92. https://doi.org/10.1016/j.cemconres.2007.04.015
[56] Hashemi SSG, Mahmud HB, Djobo JNY, Tan CG, Ang BC, Ranjbar N. Microstructural characterization and mechanical properties of bottom ash mortar. J Clean Prod. 2018;170:797-804. https://doi.org/10.1016/j.jclepro.2017.09.191

Research on Engineering Structures & Materials
www.jresm.org
Research Group

Research Article

Evaluation of the compressive mechanical properties of sulfate-damaged concrete using linear and nonlinear ultrasonic techniques

Teerapath Khumtorn[a], Piya Chotickai[*,b]

Department of Civil Engineering, Faculty of Engineering, Kasetsart University, Bangkok, Thailand

Article Info

Article History:

Received 24 Feb 2025

Accepted 15 Mar 2025

Keywords:

Attenuation;
Concrete;
Evaluation;
Mechanical property;
Sideband peak count;
Sulfate;
Ultrasonic;
Wave energy

Abstract

This paper presents damage evaluation of concrete under external sulfate attack using linear and nonlinear ultrasonic techniques. Concrete specimens with two distinct water-to-cement (W/C) ratios of 0.53 and 0.64 were immersed in a 5% ammonium sulfate solution for 60–240 days before being subjected to a static compression test. The linear (ultrasonic pulse velocity (UPV), wave amplitude, and fundamental frequency amplitude) and nonlinear (characteristic voltage energy (CVE) and sideband-peak-count index) ultrasonic parameters were evaluated for the specimens before and after exposure using narrowband transducers commonly employed for in situ concrete monitoring. The experimental results indicated two distinct phases in the degradation of concrete under sulfate exposure. During the initial phase (0–120 days), the mechanical properties exhibited minimal variation. However, from 120–240 days, a more significant decrease in the elastic modulus and compressive strength was observed in the concrete with a higher W/C ratio. Further, the UPV could not detect changes in mechanical properties without a significant decrease in the elastic modulus. In contrast, other parameters were sensitive to microcrack development during the initial phase. During the rapid deterioration phase, the CVE was the most effective damage indicator for detecting degradation in the mechanical properties of concrete with both W/C ratios.

1. Introduction

During In-service concrete structures can undergo chemical degradation because of their exposure to harsh environmental conditions. Among various degradation processes, sulfate attacks pose a significant threat to concrete structures. Sulfate ions found in groundwater, seawater, industrial environments, and agricultural areas react with cement hydrate products for forming expansive ettringite. This reaction can lead to mass loss, cracking, and degradation of the mechanical properties of concrete [1,2]. The effect of sulfate on concrete is complex and involves various degradation mechanisms that depend on the specific types of cations such as calcium, sodium, magnesium, and ammonium [3]. For example, concrete exposed to ammonium sulfate undergoes a combined acid–sulfate attack. Ammonium ions (NH_4^+) react with portlandite through acid hydrolysis, which results in a decrease in pH and an increase in the porosity of the cement paste, making it more susceptible to the attack and increasing the vulnerability of rebars to corrosion [4]. In addition, the decalcification of calcium-silicate-hydrate (C–S–H) because of its reaction with ammonium sulfate and a corresponding pH reduction leads to a loss of cohesion and disintegration of the cement paste [5]. Deterioration from a sulfate attack can compromise the load-bearing capacity of concrete structures, which creates a demand for a reliable nondestructive testing

*Corresponding author: fengpyc@ku.ac.th
[a]orcid.org/0009-0002-0911-1308; [b]orcid.org/0000-0002-9839-1550
DOI: http://dx.doi.org/10.17515/resm2025-706me0224rs
Res. Eng. Struct. Mat. Vol. 11 Iss. 2 (2025) 843-859

technique that can detect the onset of degradation at an early stage and assess the severity of damage. Several nondestructive testing techniques such as impact echo, resonant frequency, and infrared thermography are commonly used for assessing concrete structures. Among these, ultrasonic measurement is among the most effective methods to evaluate mechanical properties and progression of internal damage in concrete [6].

Various ultrasonic parameters have been used to evaluate concrete properties and damage. These parameters are based on the effect of mechanical properties and distributed microdamage on the characteristics of propagating elastic waves [7]. Numerous studies have been conducted using linear and nonlinear ultrasonic techniques to evaluate load-induced [8-10] and chemical-induced damages in concrete [11-12]. For linear ultrasonic techniques, in which a linear interaction between wave propagation parameters and media is considered, the ultrasonic pulse velocity (UPV), wave amplitude, and fundamental frequency amplitude have been employed [13,14]. The UPV is the most widely used nondestructive testing method for assessing the mechanical properties, integrity, and damage severity of concrete [12,15]. A UPV testing system for concrete typically consists of a pair of piezoelectric transducers (transmitter and receiver) with exciting ultrasonic waves in the range 20–300 kHz [16]. Based on the measurement of the first arrival, the UPV is dependent on the elastic constants of the medium and is insignificantly affected by the effect of scatterers (cracks) on the diversion of the ultrasonic beam, which results in wave amplitude reduction, longer duration, and a downshift in the frequency content [13]. Therefore, a decrease in the effective modulus corresponding to an increase in the microcrack density results in a decrease in the UPV. Despite its insensitivity to the distribution of microcracks, the UPV is effective in detecting the presence of macrocracks. The UPV was reported to significantly decrease in concrete with different water-to-cement (W/C) ratios (0.4–0.75) under compression tests with a degree of damage greater than 60% [17,18]. Based on the wave velocity, an ultrasonic penetration test was used to evaluate the damage layer thickness of concrete subjected to wet–dry cycles in a 10% sodium sulfate solution [19]. After 360 days (24 wet–dry cycles), the wave velocity in the damage layer was reported to decrease by 7.89%, 16.52%, and 16.54% for concrete with water-to-binder ratios of 0.35, 0.45, and 0.55, respectively. Berthaud [8] investigated the effect of acoustic anisotropy due to the porous nature of undamaged concrete and the elastic anisotropy caused by compression damage on the wave velocity and wave amplitude. A noticeable increase in the ultrasonic parameters with stress level was observed in the wave normal to the loading direction in an undamaged state, owing to the closing of existing microcracks. Meanwhile, compression damage was reported to have a greater effect on the reduction in the parameters of waves propagating in the loading direction than those in the normal direction owing to the opening of cracks. The amplitude attenuation of ultrasonic waves with the progression of damage in cylindrical concrete specimens under compression tests has been investigated [20]. This parameter was reported to be insensitive to the initial damage and could detect cracks at approximately 40% of the peak stress.

In nonlinear ultrasonic techniques, the interaction of ultrasonic waves with nonlinear scatterers (such as microcracks) results in changes in the characteristics and shape of the propagating ultrasonic waves [21]. As ultrasonic waves propagate through microcracks, some energy is converted into higher-harmonic components and multiple secondary waves (or sidebands), resulting in wave distortions [17,22]. Several nonlinear ultrasonic parameters, based on wave energy and the generation of harmonic wave components and sidebands, have been utilized to assess the condition of concrete. The reduction in wave energy corresponds to the attenuation of ultrasonic waves owing to scattering and dissipative mechanisms in inhomogeneous materials [11]. Greater attenuation of wave energy is obtained for longer lengths of the wave path and increases in the scatterer (microcrack) intensity [13]. The reductions in the energy of ultrasonic waves in the time domain and the spectral energy density in nonreactive and alkali–silica-reaction-affected concrete slabs during a bending test were investigated using piezoelectric transducers with a 250-kHz central frequency [23]. Both parameters were reported to decrease significantly at the initial structural cracks. However, the attenuation of the wave energy was more effective than that of the spectral energy density for monitoring the stress changes in the slabs. The attenuation of wave energy and UPV obtained from ultrasonic testing using broadband transducers with a

bandwidth centered at 1 MHz was closely correlated with the stiffness evolution and change in the mesoscale elements of mortars under an internal sulfate attack in the presence of different amounts of gypsum ($CaSO_4 \cdot 2H_2O$) during the mixing process [24]. The characteristic voltage energy (CVE) was used to represent the energy of the ultrasonic signals in the time domain. It was evaluated during a compression test of engineered cementitious composite specimens exposed to wet–dry cycles of a sodium sulfate solution [11]. The CVE of transmitted waves from 200-kHz ultrasonic excitation was found to be more sensitive to the damage evolution during the compression test with different degrees of degradation from sulfate attack than primary and secondary wave velocities, where the peak energies were obtained at approximately 60–80% of the compressive strength.

An acoustic nonlinearity parameter as a function of the ratio of the higher-order harmonic amplitude to the square of the fundamental frequency amplitude has been shown to be sensitive to early-stage damage in concrete under compression [17], creep, and cyclic loading [10]. The influences of the degree of damage under compression tests and ultrasonic input power level on the attenuation of the fundamental frequency amplitude and the generation of second harmonic wave components were investigated in concretes with 0.4–0.6 W/C ratios; broadband transducers with central frequencies of 100 kHz and 200 kHz were used for transmitting and receiving waves, respectively [18]. The attenuation of the fundamental frequency amplitude was reported to be significant for degrees of damage exceeding 40%. The attenuation increased with a decrease in the W/C ratio and an increase in the input power level. In addition, the amplitude ratio of the second harmonic wave components to the fundamental frequency increased with the degree of damage and power level.

The sideband peak count (SPC) technique was used to relate the nonlinearity level to the degree of damage by counting the number of peak frequencies above the amplitude threshold [25]. Castellano et al. [26] investigated the variation in the SPC value and UPV on the damage evolution of coarse-grained aggregate concrete under cyclic compression tests using narrowband piezoelectric transducers with a central frequency of 50 kHz. The SPC value was reported to be more sensitive to an early stage of damage than the UPV value and capable of detecting the evolution of subsequent damage. The effectiveness of linear and nonlinear ultrasonic techniques for damage monitoring in a reinforced concrete beam subjected to a bending test was investigated [14]. Nonlinear ultrasonic techniques (SPC and energy distribution indicator) were more sensitive to damage progression than linear ultrasonic techniques (wave velocity and attenuation at the peak frequency). The SPC and energy distribution indicator were the most effective parameters for detecting the initiation of microcrack development at an early stage and the higher damage levels with a large number of cracks appearing on the concrete beam, respectively. The damage index calculated from the difference in the SPC values at the damage and initial stages obtained from ultrasonic measurement using 50-kHz central-frequency transmitters and 100-kHz central frequency receiver transducers was reported to increase with the development of microcracks in cementitious materials subjected to alkali–aggregate reactions [22].

Despite extensive studies on the application of aforementioned ultrasonic techniques to monitor damage in concrete, most focused on detecting the onset and progression of damage in load-induced concrete. Few studies conducted on the effectiveness of these techniques in evaluating the damage to concrete subjected to sulfate attacks, where complex degradation behaviors and non-uniform damage occur across a section, particularly in cases of external sulfate attacks. In addition, most studies have been conducted using relatively high-frequency transducers or a pair of transmitter and receiver transducers with different central frequencies to capture higher harmonic components and/or sidebands for investigating the effect of the nonlinear interaction between damaged concrete and ultrasonic signals. This is not a common ultrasonic testing system used for the in situ monitoring of concrete structures. Therefore, this study focused on the effectiveness of linear and nonlinear ultrasonic techniques to detect the onset of damage and the progression of degradation in the compressive mechanical properties of concrete under sulfate attack using conventional ultrasonic equipment. Concrete specimens with two distinct W/C ratios were immersed in an ammonium sulfate solution for different durations. The variations in the linear (UPV, wave amplitude, and fundamental frequency amplitude) and nonlinear (CVE and SPC)

ultrasonic parameters with exposure duration were determined and compared with the degradation in compressive mechanical properties. The sensitivity and effectiveness of ultrasonic parameters for damage evaluation were presented and discussed.

2. Experimental Program

2.1. Specimen Preparation

Cylindrical concrete specimens with dimensions of 150 mm×300 mm was fabricated using type 1 Portland cement that conforms to ASTM C150 [27], river sand, and crushed limestone gravel. The river sand and crushed limestone gravel had a specific gravity of 2.65 and 2.70 and the maximum particle sizes of 4.75 and 19 mm, respectively. Two W/C ratios of concrete, 0.53 and 0.64, were considered, with corresponding mixture proportions of cement, water, sand, and gravel by weights of 1:0.53:2.39:2.94 and 1:0.64:3.11:3.55, respectively. The specimens were prepared based on ASTM C192 [28]. Fresh concrete was mixed using a mixing machine and cast in cylindrical molds in two layers. Each layer was compacted by tamping 25 times using a rod. The specimens were demolded 24 h after casting and immersed in water for wet curing at 25 °C for 28 days. After the curing period, specimens were immersed in a sulfate solution for different durations. Three concrete specimens were prepared for each concrete mixture and exposure duration.

2.2. Exposure Condition

The specimens were exposed to an ammonium sulfate solution with 5% mass fraction at 25 °C for durations of 0, 60, 120, 180, and 240 days. These exposure durations were selected based on the significant negative effects of sulfate attack in concrete with W/C ratios of 0.47 and 0.57 after 120−180 days of exposure to different concentrations of sodium sulfate solutions [1]. Martins et al. [2] reported a significant decrease in the compressive strength of concrete with a water-to-binder ratio of 0.45 after 63 days of immersion in a 9.3% ammonium sulfate solution, with a strength reduction of 40% after 182 days of immersion. Considering a two-dimensional sulfate attack, paraffin was used to seal the top and bottom surfaces of specimens prior to being subjected to exposure.

2.3. Ultrasonic and Compression Tests

An ultrasonic test was conducted on all specimens under saturated conditions after a 28-day curing period and exposure to the sulfate solution. An ultrasonic test was conducted using a Proceq Pundit Lab+ with a pair of similar narrowband transmitting and receiving transducers. The transducers had a manufacturer-specified central frequency, bandwidth, and diameter of 54 ±5 kHz, less than 10 kHz, and 49.7 mm, respectively. The tests were conducted at a voltage of 500 V. The waveform used for ultrasonic pulses was a sine wave applied in repetitive pulse sequences. Petroleum jelly was used as the acoustic couplant. Ultrasonic waveforms were obtained using a through-transmission method (Fig. 1) measured across a diameter (150 mm) at 50 mm from the top and bottom surfaces and at the mid-height of the specimens. Three repeated readings were obtained at each monitored location for each specimen before and after being subjected to exposure to obtain reliable results. For each reading, both transducers were removed and reattached to the specimen. Ultrasonic signals were recorded at a sampling frequency of 1 MHz within a time window of 1ms. Figure 2a shows the ultrasonic signals obtained from the control specimens. The frequency spectra of ultrasonic signals were analyzed using a fast Fourier transform. The frequency spectra of control specimens with frequency amplitudes normalized to the fundamental frequency amplitude are presented in Fig. 2b. Ultrasonic signals and frequency spectra are used for further analysis to obtain ultrasonic parameters.

A compression test was performed on specimens in a saturated condition after a 28-day curing period for control specimens and after they had been exposed to the sulfate solution for the target durations. Compression tests were conducted using a universal testing machine at a loading rate of 1 mm/min until failure [29]. The load and vertical deformation were monitored during the test to obtain compressive stress−stress characteristics.

Fig. 1. Ultrasonic test

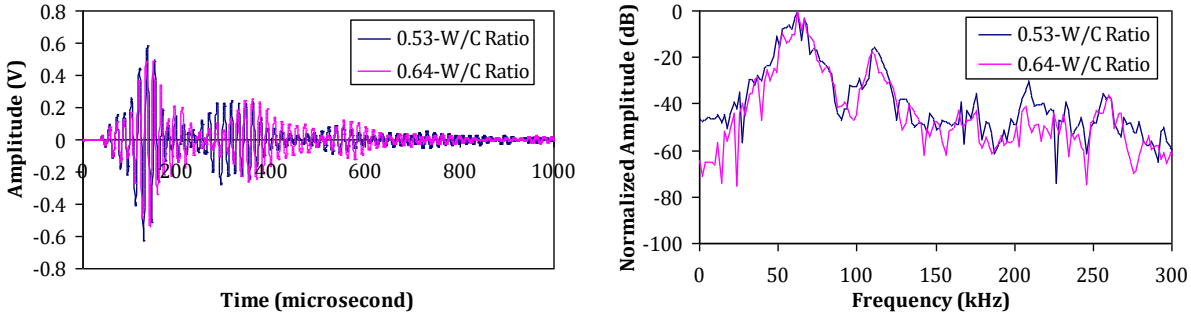

(a) (b)

Fig. 2. Waveforms and frequency spectra of the control specimens (a) Ultrasonic signals in the time domain, (b) Normalized frequency spectra

3. Experimental results

3.1. Compressive Mechanical Properties

The effects of exposure duration on the elastic modulus and compressive strength are presented in Fig. 3. Elastic moduli were determined based on ASTM C469 [30]. Two distinct phases of the degradation of mechanical properties under exposure were observed. An initial phase (0–120 d) with minimal variation, which indicated a transitional period with various mechanisms such as the deposition of ettringite and gypsum and cement hydration, developed in concrete. Subsequently, a significant degradation phase (120–240 days) indicates the onset of rapid deterioration.

For the specimens with the W/C ratio of 0.53, the elastic modulus increased initially and then gradually decreased after 120 d of immersion. This was attributed to an increase in the compactness of the concrete from the deposition of ettringite and gypsum in the initial phase and accumulation of expansive products, which caused microcracks and macrocracks in the later phase [1]. The formation of gypsum and ettringite in concrete exposed to ammonium sulfate can be characterized as [31]

$$Ca(OH)_2 + (NH_4)_2SO_4 \rightarrow CaSO_4 \cdot 2H_2O + 2NH_3 \quad (1)$$

$$xCa \cdot SiO_2 \cdot aq + x(NH_4)_2SO_4 + xH_2O \rightarrow SiO_2 \cdot aq + xCaSO_4 \cdot 2H_2O + 2xNH_3 \quad (2)$$

$$SO_4^{-2} + 2Ca^{+2} + Ca_4Al_2(OH)_{12} \cdot SO_4 \cdot 6H_2O \rightarrow Ca_6Al_2(OH)_{12}(SO_4)_3 \cdot 26H_2O \quad (3)$$

The consumption of portlandite (Eq. 1) decreases the internal concrete pH and increases concrete porosity. The destabilization of C–S–H (Eq. 2) results in the formation of amorphous hydrated silica, gypsum, and gaseous NH_3, which leads to a loss of cohesion and volume swelling [5]. At 240 d, a slight reduction in the elastic modulus of 0.7% was observed for the specimen with the W/C ratio of 0.53. Meanwhile, the elastic modulus of the specimen with the W/C ratio of 0.64 decreased

slightly for an exposure duration of less than 120 d (initial phase) and significantly decreased thereafter. This behavior corresponds to the greater porosity of concrete with a W/C ratio of 0.64, which enables a higher diffusion rate of the external sulfate attack, thereby leading to microcrack development during the initial phase and coalescence of microcracks into macrocracks in the later phase. The development of microcracks has been attributed to the formation of ettringite in small pores, 10–50 nm in size [32]. The transition of degradation phases was in good agreement with that of superficial cracks (Fig. 4) observed in specimens for exposure durations ≥ 120 days, whereas they were not observed in specimens subjected to 60 days of exposure. The difference in the reduction rate of the elastic modulus in specimens with W/C ratios of 0.53 and 0.64 indicated the effect of W/C ratio on the elastic modulus degradation for concrete subjected to a sulfate attack. A similar effect of the W/C ratio on the reduction in the elastic modulus was observed in concrete (W/C ratios of 0.37–0.87) subjected to wet–dry cycles of sodium sulfate solutions [1]. During the 240-day exposure period, the elastic modulus of specimens with a W/C ratio of 0.64 decreased by 82.7%.

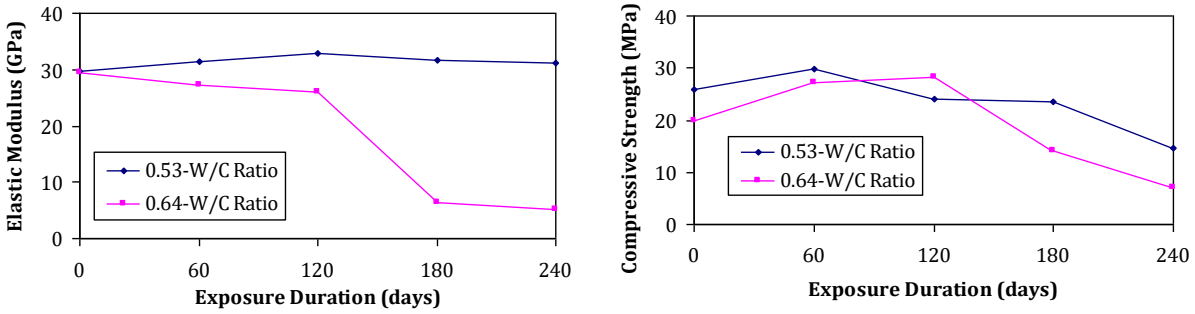

(a) (b)

Fig. 3. Effect of exposure duration on compressive mechanical properties (a) Elastic modulus, (b) Compressive strength

Compressive strengths of specimens with W/C ratios of 0.53 and 0.64 initially increased and then decreased significantly during the latter phase. The initial increase in the compressive strength was attributed to continuous cement hydration and the positive effect of the deposition of chemical products from a sulfate attack on the strength [1]. A similar behavior, characterized by an initial increase followed by a later decrease in compressive strength, was observed in the (0.45-W/C ratio) concrete with a partial replacement of Portland cement with supplementary cementitious materials (silica fume and rice husk ash) immersed in a 9.3% ammonium sulfate solution [2]. Mbessa and Péra [33] reported an increase in the compressive strength of high-strength concrete with different types of ultrafine particles after being subjected to six wet–dry cycles in a 20% ammonium sulfate solution. Specimens with a W/C ratio of 0.64 exhibited a greater loss in the compressive strength over longer exposure durations than that of the specimen with the W/C ratio of 0.53. This was attributed to their higher porosity, which led to a more significant effect of the ammonium sulfate solution on the destabilization of C–S–H, release of calcium ions from a cementitious matrix, and subsequent descaling of the cement matrix [2]. Under a 240-d exposure duration, the compressive strengths of the specimens with W/C ratios of 0.53 and 0.64 decreased by 42.7% and 65.0%, respectively. A significant reduction in the compressive strength was obtained despite the small effect of the sulfate attack on the elastic modulus of specimens with a W/C ratio of 0.53. This was attributed to a variation in the effective cross-section or sound concrete core across the height of the specimens, which results in planes of stress concentration and nonuniform stress distribution [5]. These factors contributed to a significant reduction in compressive strength, and the elastic modulus was significantly affected by local cracks in the specimens. Further, a contradiction between the elastic modulus and compressive strength behavior was observed for specimens with W/C ratios of 0.53 and 0.64 during 60–120 days. For the specimen with a W/C ratio of 0.64, the compressive strength increased, whereas the elastic modulus decreased. In contrast, for the specimen with a W/C ratio of 0.53, the modulus of elasticity increased, whereas the compressive strength decreased. This distinction emphasizes that the elastic modulus and compressive strength are affected by different structural changes.

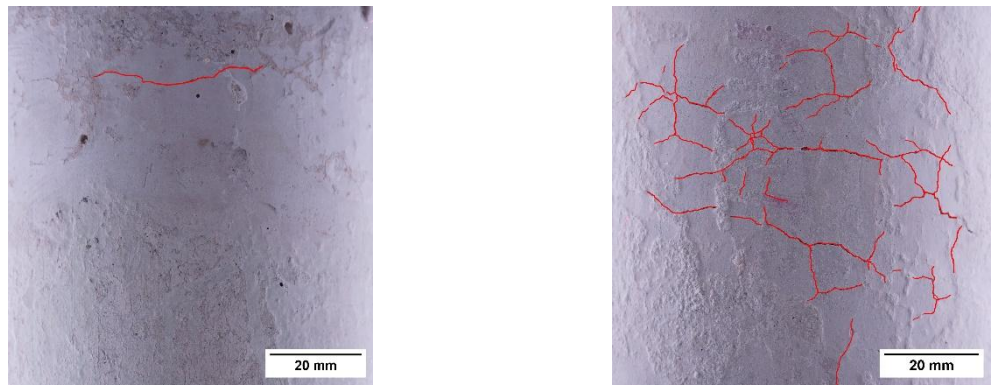

120 days 240 days

(a)

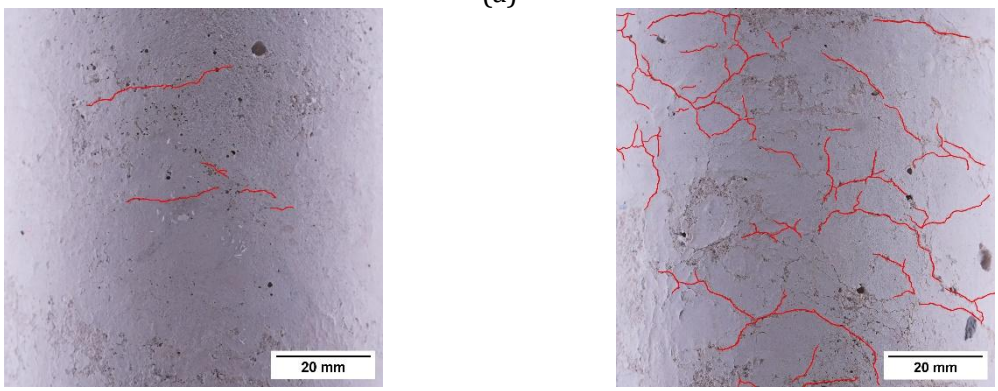

120 days 240 days

(b)

Fig. 4. Cracks on concrete specimens after exposure durations of 120 and 240 days, (a) W/C ratio = 0.53, (b) W/C ratio = 0.64

Average values of the maximum crack width and crack density observed in specimens during the significant degradation phase (120–240 days) are listed in Table 1. The crack density was calculated as the ratio of the total crack length to the cylindrical surface area of specimens (excluding the top and bottom surfaces, which were sealed with paraffin prior to exposure to the sulfate solution).

Table 1. Maximum crack width and crack density

W/C ratio	Exposure duration (days)	Average maximum crack width (mm)	Average crack density (mm^{-1})
0.53	120	0.10	0.0012
	180	0.26	0.0043
	240	0.27	0.0052
0.64	120	0.08	0.0016
	180	0.22	0.0071
	240	0.23	0.0072

A similar method was used by Riener et al. [34] for metal specimens in which the crack density was calculated from the ratio of the crack length to the area of the images of specimens. The average maximum crack widths of specimens with W/C ratios of 0.53 and 0.64 were in the range of 0.08–0.27 mm. Meanwhile, the average crack densities in these specimens increased from 0.0012 to 0.0052 mm^{-1} and 0.0016 to 0.0072 mm^{-1} with an increase in exposure duration from 120 to 240 days, respectively. The greater crack density in specimens with a W/C ratio of 0.64 corresponded to a higher porosity and lower tensile strength in the binder matrix caused by the higher W/C ratio.

3.2. Ultrasonic Pulse Velocity (UPV)

Figure 5 shows the average change in UPV for specimens with different exposure durations. The UPV was calculated as the ratio of the distance between ultrasonic transducers to the time-of-flight. The value of the UPV depends on the mechanical properties of the concrete such as the elastic modulus and density, and it can provide insight into the quality, integrity, and potential damage of the material to the concrete [16]. No significant change in the UPV was observed in specimens with a W/C ratio of 0.53 in the initial (0–120 days) and later (120–240 days) degradation phases, which corresponds to marginal changes in the elastic modulus of the specimens. The UPV was insensitive to variations in the sound concrete section, which significantly affected the reduction in the compressive strength of the specimens in the later phase. Meanwhile, the UPV in specimens with a W/C ratio of 0.64 decreased slightly (~ 1%) at an exposure duration of 120 days and significantly decreased by 47.6 and 52.0% at 180 and 240 days, respectively. The UPV measurements are based on the measurement of the fast-energy component of the ultrasonic beam. The remaining energy arriving at the transmitter and changes in the characteristic shape of the ultrasonic wave were not considered [13]. Consequently, the UPV was not sensitive to microstructural changes during the initial phase. However, the reduction in UPV during the later phase in these specimens was attributed to the degradation of the modulus of elasticity.

The coefficients of variation (COVs) of the UPV in specimens with W/C ratios of 0.53 and 0.64 are listed in Table 2. A relatively low variation in the UPV values (COVs of 2–9%) was observed in specimens subjected to different degradations, which indicates that the UPV provided reliable and stable measurements.

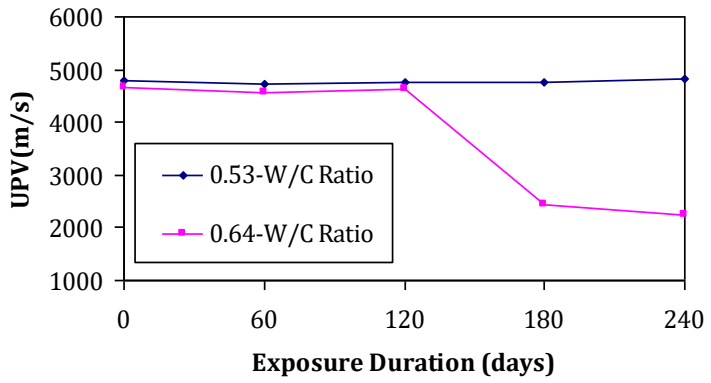

Fig. 5. Change in the UPV

Table 2. Coefficient of variation (COV) (%) of each ultrasonic parameter

W/C ratio	Exposure duration (days)	UPV	Wave amplitude	Fundamental frequency amplitude	CVE	SPC-I
0.53	0	2	17	34	14	8
	60	2	13	30	27	12
	120	1	5	47	19	3
	180	4	32	55	31	5
	240	2	23	59	29	18
0.64	0	4	26	41	21	12
	60	5	11	53	8	13
	120	2	5	30	15	14
	180	9	37	56	53	16
	240	6	51	66	41	16

3.3. Wave Amplitude and Fundamental Frequency Amplitude

The wave and fundamental frequency amplitudes obtained from the ultrasonic measurements of the specimens were evaluated. These amplitudes correspond to the maximum absolute amplitude of the ultrasonic waveforms in the time domain and the amplitude at the fundamental frequency in the frequency domain, respectively. These parameters are affected by the scattering and attenuation mechanisms of ultrasonic waves as they propagate through concrete. Greater attenuation of these parameters occurs with an increase in microcracks, porosity, and degree of damage in the concrete. Transmitted waveforms of the control and specimens exposed for different durations are presented in Fig. 6a. Compared with the control specimen, the ultrasonic signals of damaged specimens exhibited a longer transmission time, lower amplitude, and delay in the maximum peak.

Frequency spectra were obtained from time-domain ultrasonic signals using fast Fourier transform, and they were used for evaluating the attenuation of the amplitude at the fundamental frequency and SPC value associated with the damage induced by exposure. The normalized frequency spectra of specimens with a W/C ratio of 0.64 are presented in Fig. 6b to illustrate the effect of exposure on the frequency components of ultrasonic waves. In this figure, the frequency spectrum of each damaged specimen is normalized with respect to its fundamental frequency amplitude before exposure. The spectral responses of control specimens are noisy because of the inhomogeneity of the concrete resulting from microdefects and microcracks generated during the curing process [35] and effect of aggregates on wave diffraction [22,36]. In addition, the fundamental frequency amplitude decreased with an increasing exposure duration. Despite the low resolution of the narrowband transducer at higher-order frequencies, an increase in the ratio of peak amplitudes of higher-order frequency components (~103–113 kHz) to the fundamental frequency amplitude was observed. An increase in the higher-harmonic wave components was attributed to nonlinear interactions between the ultrasonic wave and damaged concrete, which led to a greater portion of the fundamental frequency being converted to higher-harmonic components [17].

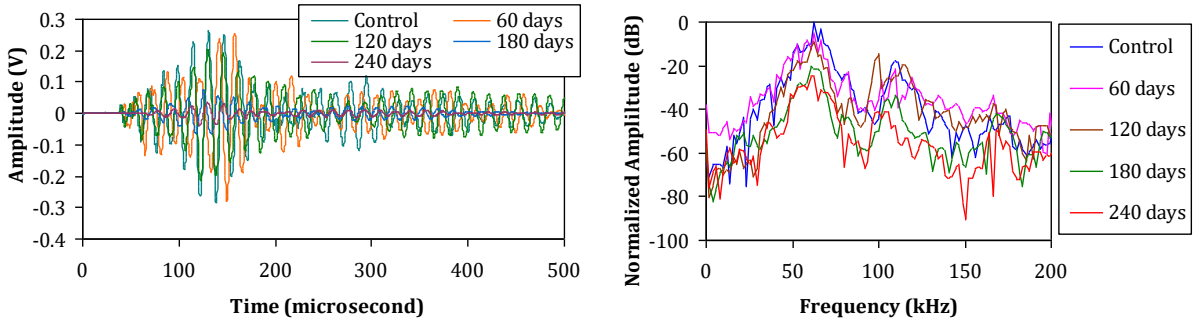

(a) (b)

Fig. 6. Ultrasonic signals of the specimens with a W/C ratio of 0.64 (a) Transmitted waveforms, (b) Normalized frequency spectra

Figure 7 shows the average attenuation of wave amplitudes in specimens exposed for different durations. Significant reductions of 55.3 and 47.1% in the wave amplitude were observed in specimens with W/C ratios of 0.53 and 0.64, respectively, after a 60-d exposure duration. This indicates that the wave amplitude was sensitive to microstructural changes at the initial degradation stage, where a significant reduction in the elastic modulus was not observed in the specimens. With longer exposure durations, the wave amplitude continuously decreased in the specimens with a W/C ratio of 0.64. This indicates that the wave amplitude can detect the damage progression in specimens with a significant increase in porosity from cracking and swelling associated with the sulfate attack, which also resulted in a noticeable decrease in the elastic modulus. Meanwhile, for the specimens with a W/C ratio of 0.53, the wave amplitude gradually decreased with damage progression for exposure durations ≥ 60 days. The transition between the two distinct degradation phases could not be identified from the attenuation of the wave amplitude.

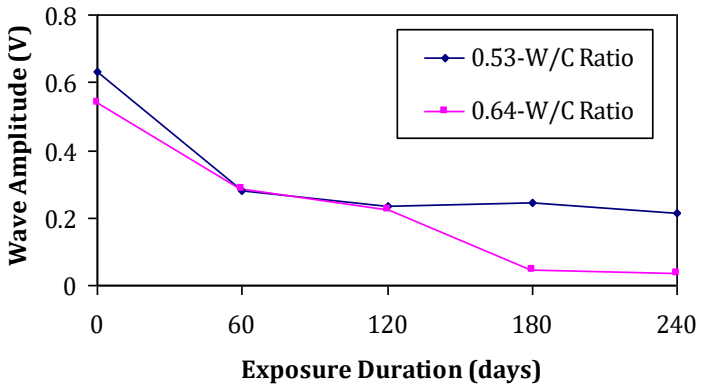

Fig. 7. Change in the wave amplitude

The effect of exposure duration on the average fundamental frequency amplitude is shown in Fig. 8. Similar to the wave amplitude, the fundamental frequency amplitude was sensitive to microstructural changes over the 60-day exposure duration. Significant attenuations in the fundamental frequency amplitudes of 83.6 and 76.1% were obtained for specimens with W/C ratios of 0.53 and 0.64, respectively. These greater attenuations indicate a higher sensitivity of the fundamental frequency amplitude to microcrack development than that of the wave amplitude. For an exposure duration ≥ 60 d, the reduction rate of the fundamental frequency amplitude decreased. A similar finding was reported for reinforced concrete beams subjected to a bending test, wherein a significant reduction in frequency amplitude was observed at the initial damage stage even though no prominent cracks were visible. This reduction becomes less pronounced with an increase in the degree of damage [14].

The COVs of the waves and fundamental frequency amplitudes are listed in Table 2. High COVs were observed for both parameters, which were associated with their relatively low values, inhomogeneous nature of the concrete, and its degradation. Despite higher COV values for wave and fundamental frequency amplitudes compared to those of the UPV, the amplitude attenuation measurements were considerably more sensitive to damage, and therefore, more effective than the UPV for assessing damage conditions in the specimens. In addition, the COVs of the wave and frequency amplitudes increased with a degree of damage and W/C ratio. A similar observation was reported for the damage evaluation parameter, which was calculated from the ratio of the higher-order harmonic amplitude to the square of the fundamental frequency amplitude in concrete subjected to the compression-induced damage [17].

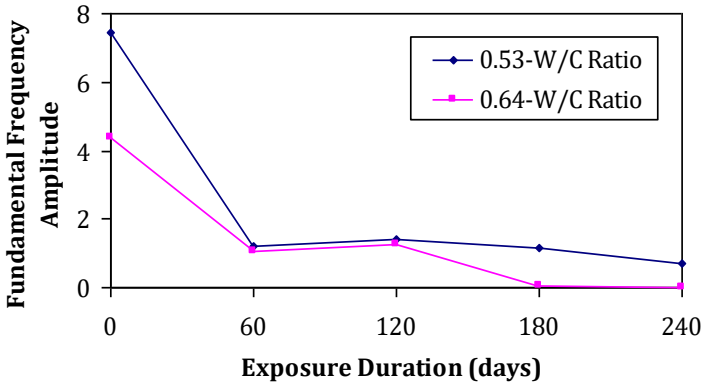

Fig. 8. Change in the fundamental frequency amplitude

3.4. Characteristic Voltage Energy (CVE)

The effect of exposure on the average CVE of specimens is shown in Fig. 9. The CVE is calculated from the area under the rectified signal envelope using the absolute amplitude of the ultrasonic waveform and can be expressed as [11]

$$CVE = \int_0^{t_0} |U_t| dt, \quad (4)$$

where U_t, t, and t_0 represent the voltage amplitude of the ultrasonic waveform in the time domain, wave time in microseconds, and recording time (1 ms) of the specimens, respectively. The change in the CVE with exposure duration in the specimens followed a pattern similar to that of the fundamental frequency amplitude: a significant reduction at 60 days, a relatively constant value between 60 and 120 days, and further reductions with damage progression for exposure durations ≥ 120 days. This behavior was attributed to the significant contribution of the fundamental frequency to the wave energy. Over a 60-d exposure duration, CVE reductions of 58.3 and 49.3% were observed in specimens with W/C ratios of 0.53 and 0.64, respectively. Most of the wave energy loss occurs during the initial damage phase. The CVE exhibited a lower attenuation rate compared to the fundamental frequency amplitude because it considered the entire waveform, which included all frequencies. However, the wave amplitude, fundamental frequency amplitude, and wave energy were strongly correlated because similar narrowband transducers were used for both the transmitter and receiver. Table 2 indicates that CVE exhibits lower COV values than the wave and fundamental frequency amplitudes. In addition, the COVs of the CVE increased with the degree of damage and W/C ratio.

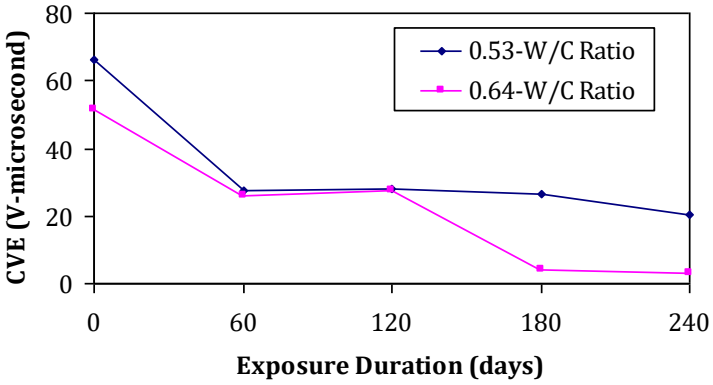

Fig. 9. Change in the CVE

3.5. Sideband Peak Count (SPC)

The SPC value (SPC(th)) was computed from the ratio of the SPC above the moving threshold from 0–100% of the fundamental frequency amplitude and can be expressed as [14]

$$SPC(th) = N_{peak}(th)/N_{total}, \quad (5)$$

where N_{peak} and N_{total} represent the number of sideband peaks above a threshold value and total number of peaks in the frequency spectrum, respectively. At a threshold of 0, the SPC(th) was 1.0.

Figure 10 shows the effect of exposure duration on the average SPC(th) of specimens with a W/C ratio of 0.64. Most sideband peaks in all specimens were observed to be less than 1% of their peak frequency amplitudes, which resulted in a significant reduction in SPC(th) with an increase in the threshold from 0 to 0.01. A similar behavior was observed in specimens with a W/C ratio of 0.53. For clarity, SPC(th) values for thresholds between 0 and 0.01 are not shown in the figure because their scale would obscure the results. The effects of exposure and threshold levels on SPC(th) were observed. For a threshold of less than 0.05, the values of SPC(th) in specimens subjected to exposure were greater than those of the control specimens. This implied an increase in the number of sideband peaks with amplitudes less than 5% of peak amplitudes in these specimens. The SPC(th) varied with exposure duration for thresholds between 0.05 and 0.80; however, it remained relatively constant for thresholds ≥ 0.80. This indicates that the exposure had little effect on the number of sideband peaks with amplitudes greater than 80% of peak amplitudes in these specimens.

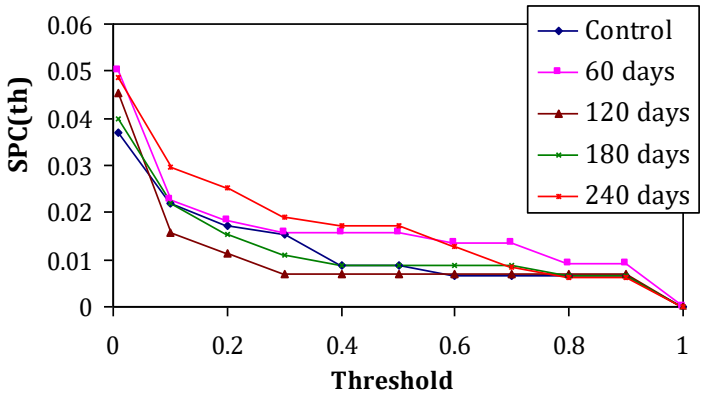

Fig. 10. SPC(th) of the W/C ratio of 0.64

The SPC index (SPC-I) was determined using [26]

$$SPC\text{-}I = (\sum SPC_i)/N(th)_{tot}, \quad (6)$$

where SPC_i and $N(th)_{tot}$ represent the SPC value for a threshold value i and total number of considered thresholds, respectively.

The SPC-I represents the degree of nonlinearity observed in the SPC curve for a single value [37]. The average SPC-I values were computed for different maximum threshold values, i.e., the considered thresholds (TH) of 0–0.3, 0–0.5, 0–0.7, and 0–1.0, as shown in Fig. 11. SPC-I values obtained from different maximum thresholds exhibited similar trends. Owing to the noticeable effect of exposure on the SPC(th) up to a threshold value of 0.80, SPC-I corresponding to a maximum threshold of 1.0, was selected and used for the subsequent sensitivity analysis.

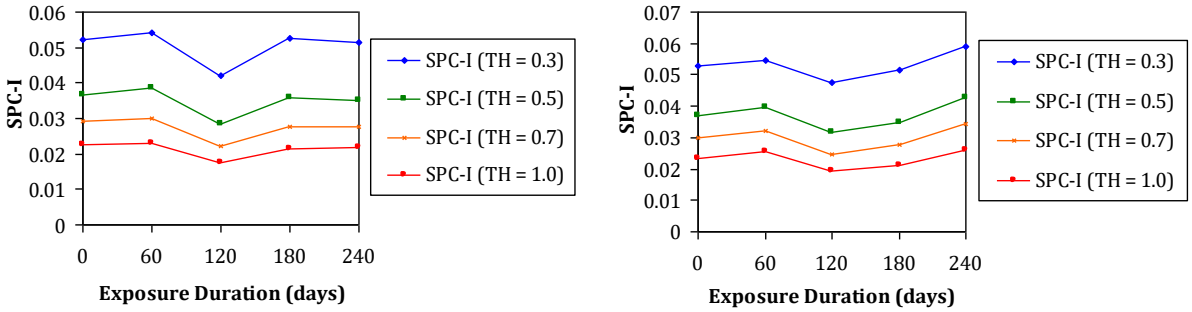

(a) (b)

Fig. 11. Change in the SPC-I (a) W/C ratio of 0.53, (b) W/C ratio of 0.64

The SPC-I in specimens with W/C ratios of 0.53 and 0.64 increased over the 60-d exposure duration. This implies the sensitivity of SPC-I to initial microstructural changes in the specimens. The SPC-I in both W/C ratios decreased at 120 d and increased thereafter. The decrease in SPC-I at 120 days corresponds to a reduction in material nonlinearity from the coalescence of microcracks into macrocracks [26], which is in good agreement with the first superficial cracks observed during this exposure duration (Fig. 4). The increase in SPC-I after ≥ 120 d of exposure corresponds to an increase in nonlinearity in specimens with an increase in microcrack density from the sulfate attack. Despite the relatively low resolution of narrowband transducers at higher-harmonic components, SPC-I was sensitive to microstructural changes in specimens during the initial and significant degradation phases. The phase transition at 120 d is clearly depicted by SPC-I.

3.6. Sensitivity Analysis

Sensitivity analysis was conducted for determining the relative effectiveness of different ultrasonic parameters in detecting the onset and progression of damage in specimens during the initial and significant degradation phases. Average percentage changes in ultrasonic parameters observed in

specimens with W/C ratios of 0.53 and 0.64 before and after exposure during the initial phase (≤ 120 d) are shown in Fig. 12. For the 60-d exposure period, the fundamental frequency amplitude (Freq. Amp.) exhibited the highest percentage reduction in specimens with both W/C ratios, followed by the wave amplitude (Wave Amp.), CVE, SPC-I, and UPV. This implies that the fundamental frequency amplitude was the most sensitive parameter to the initial microstructural changes in the specimens. However, microstructural changes corresponding to the coalescence of microcracks into macrocracks from 60–120 d were effectively detected using SPC-I.

Figures 13 and 14 compare average percentage changes in ultrasonic parameters observed in specimens with W/C ratios of 0.53 and 0.64 before and after exposure during the significant degradation phase (120–240 days), respectively, with average percentage changes in mechanical properties. In addition, correlation coefficients (r) between percentage changes in ultrasonic parameters and mechanical properties are listed in Table 3 and can be expressed as

$$r = \frac{\sum(x_i - \bar{x})(y_i - \bar{y})}{\sqrt{\sum(x_i - \bar{x})^2 \sum(y_i - \bar{y})^2}}, \tag{7}$$

where x_i and $\bar{x}$ represent values and average percentage changes in ultrasonic parameters, respectively, and y_i and $\bar{y}$ represent values and average percentage changes in mechanical properties, respectively. The correlation coefficient (r) is used for measuring a linear relationship between parameters, with values of −1, 1, and 0 indicating perfectly negative, perfectly positive, and no linear relationship, respectively.

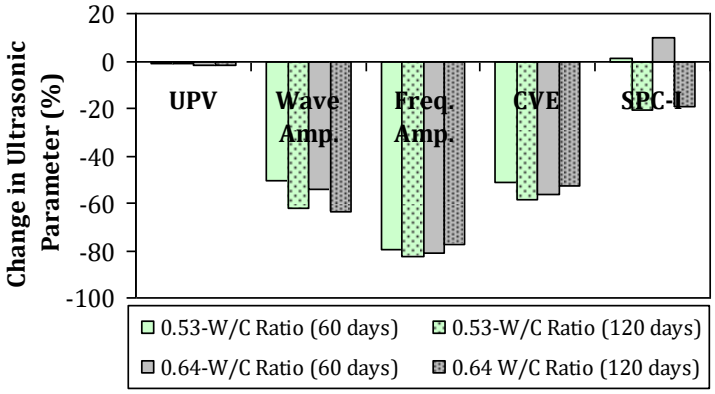

Fig. 12. Percentage change in the ultrasonic parameters during the initial phase

Ultrasonic parameters exhibited different reduction rates with degradation in the mechanical properties with an increase in exposure duration, except for SPC-I, which increased during this phase. Consequently, a negative r value was obtained between SPC-I and mechanical properties, as listed in Table 3. The r value of the UPV for specimens with the W/C ratio of 0.53 is not presented in the table because of its insensitivity to changes in the mechanical properties of the specimens, as shown in Fig. 13. For the specimens with the W/C ratio of 0.64, which showed significant degradations in the mechanical properties during the later phase, relatively high values of r in the range of 0.83–0.97 were obtained from all ultrasonic parameters, except the SPC-I, which exhibited an r value of −0.52. The r values for elastic modulus were greater than those for the compressive strength, suggesting a more direct effect of the modulus on ultrasonic wave characteristics. For the specimens with the W/C ratio of 0.53, the highest r values were obtained from the CVE for the elastic modulus and compressive strength. This implies that the CVE was the most effective parameter to detect the damage progress during the significant degradation phase for specimens with both W/C-ratios.

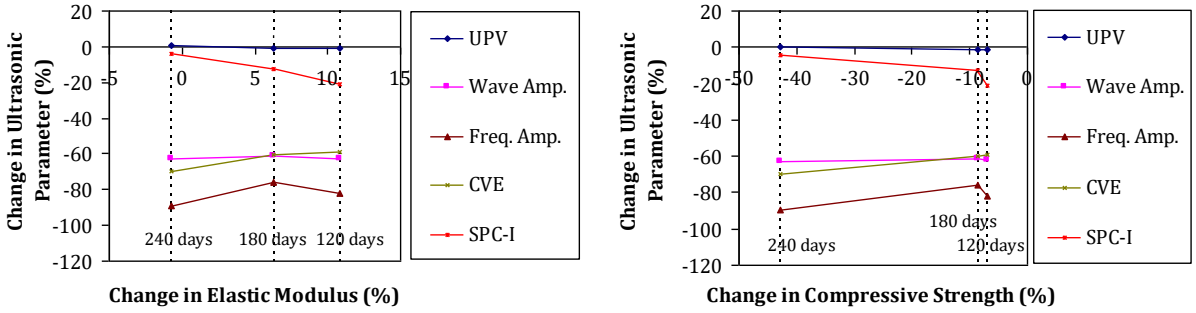

(a) (b)

Fig. 13. Percentage changes in ultrasonic parameters and mechanical properties during the significant degradation phase (120–240 days) for specimens with a W/C ratio of 0.53 (a) Elastic modulus, (b) Compressive strength

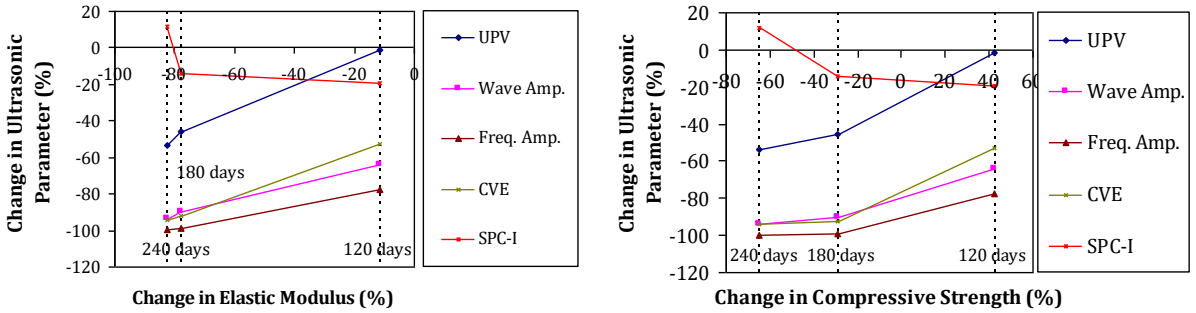

(a) (b)

Fig. 14. Percentage changes in ultrasonic parameters and mechanical properties during the significant degradation phase (120–240 days) for specimens with a W/C ratio of 0.64 (a) Elastic modulus, (b) Compressive strength

Table 3. Coefficient of correlation (r) between percentage changes in the ultrasonic parameters and mechanical properties of concrete during the significant degradation phase.

Ultrasonic parameter	W/C ratio of 0.53		W/C ratio of 0.64	
	Elastic modulus	Compressive strength	Elastic modulus	Compressive strength
UPV	-	-	0.97	0.96
Wave amplitude	0.24	0.57	0.89	0.79
Frequency amplitude	0.32	0.53	0.88	0.83
CVE	0.46	0.62	0.97	0.90
SPC-I	−0.54	−0.48	−0.52	−0.52

4. Conclusions

In this study, ultrasonic measurements were performed on concrete specimens with two distinct W-C ratios immersed in a sulfate solution for different durations. The effects of the sulfate attack on the compressive mechanical properties of concrete specimens and linear and nonlinear ultrasonic parameters were investigated. Based on the experimental and analytical results, the following conclusions were drawn:

- The change in the compressive mechanical properties of concrete specimens under the sulfate attack can be classified into an initial phase (immersion duration of 0–120 d), in which an increase or slight decrease in the mechanical properties was observed depending on the W/C ratio, and a later stage (immersion duration ≥ of 120 d), in which a significant reduction in the mechanical properties occurred.
- The UPV was insensitive to microcrack development during the initial phase. The parameter showed a strong correlation with a degradation in the elastic modulus and compressive

strength in the concrete with a W/C ratio of 0.64 during the significant degradation phase. However, it was incapable of detecting damage progression in the concreate with a W/C ratio of 0.53, where a significant decrease in stiffness was not obtained.

- The attenuation of ultrasonic signal amplitudes, wave energy (CVE), and an increase in sidebands (SPC-I) were sensitive to initial microstructural changes attributed to the sulfate attack, including an increase in concrete porosity caused by the consumption of portlandite and the development of microcracks from the deposition of gypsum and ettringite during the initial phase, with the highest sensitivity observed in the fundamental frequency amplitude. SPC-I was found to be highly sensitive to stage changes (the coalescence of microcracks into macrocracks) during the initial phase and effective in detecting the transition between degradation phases using an ultrasonic testing system commonly employed for monitoring concrete structures. During the significant degradation phase, where the sulfate attack caused considerable destabilization of C–S–H and noticeable progression of superficial cracks, the CVE was the most effective damage indicator for monitoring losses in mechanical properties of concrete at various degradation rates.
- A combination of ultrasonic techniques, which includes the fundamental frequency amplitude, SPC-I, and CVE, can be used for effectively monitoring the microstructural changes and progression of damage in concrete under a sulfate attack.

This study demonstrated the potential of using conventional ultrasonic transducers in structural health monitoring systems for continuous, real-time damage detection in concrete structures exposed to sulfate-rich environments. Although ultrasonic transducers with a higher harmonic resolution (the ability to detect higher-order harmonics) offer enhanced sensitivity to microcracks, they can experience a relatively high attenuation of ultrasonic waves, which may limit their application for in situ monitoring. Compared with traditional evaluation methods such as visual inspection and core sampling, the combination of ultrasonic techniques offers cost and time savings over core sampling and it is more effective than visual inspection in providing detailed information on the onset and progression of damage, thereby facilitating better decision making in the maintenance and assessment of reinforced concrete structures.

Future research should focus on comparing the sensitivity and reliability of ultrasonic techniques with those of other nondestructive methods. In addition, exploring a wider range of W/C ratios or integrating other nondestructive methods for cross-validation could further enhance the accuracy and applicability of ultrasonic monitoring in concrete structures.

Acknowledgement

This study was supported financially by the Master's Degree Education Promotion Program, Plan A, Faculty of Engineering, Kasetsart University.

References

[1] Cheng H, Liu T, Zou D, Zhou A. Compressive strength assessment of sulfate-attacked concrete by using sulfate ions distributions. Construction and Building Materials, 2021;293:123550. https://doi.org/10.1016/j.conbuildmat.2021.123550

[2] Martins MC, Langaro EA, Macioski G, Medeiros MHF, External ammonium sulfate attack in concrete: Analysis of the current methodology. Construction and Building Materials, 2021;277:122252. https://doi.org/10.1016/j.conbuildmat.2021.122252

[3] Hime WG, Mather B, "Sulfate attack," or is it?. Cement and Concrete Research, 1999;29(5):789-791. https://doi.org/10.1016/S0008-8846(99)00068-X

[4] Wang X, Pan Z, Chemical changes and reaction mechanism of hardened cement paste-(NH4)2SO4-H2O system. Construction and Building Materials, 2017;152:434-443. https://doi.org/10.1016/j.conbuildmat.2017.07.018

[5] Bassuoni MT, Nehdi ML. Resistance of self-consolidating concrete to ammonium sulphate attack, Materials and Structures, 2012;45:977-994. https://doi.org/10.1617/s11527-011-9811-0

[6] Kashif Ur Rehman S, Ibrahim Z, Memon SA, Jameel M, Nondestructive test methods for concrete bridges: A review. Construction and Building Materials, 2016;107:58-86. https://doi.org/10.1016/j.conbuildmat.2015.12.011

[7] Kim BC, Kim JY, Characterization of ultrasonic properties of concrete. Mechanics Research Communications, 2009;36(2):207-214. https://doi.org/10.1016/j.mechrescom.2008.07.003
[8] Berthaud Y. Damage measurements in concrete via an ultrasonic technique part II modeling. Cement and Concrete Research, 1991;21(2-3):219-228. https://doi.org/10.1016/0008-8846(91)90002-Y
[9] Antonaci P, Bruno CLE, Gliozzi AS, Scalerandi M, Monitoring evolution of compressive damage in concrete with linear and nonlinear ultrasonic methods. Cement and Concrete Research, 2010;40(7):1106-1113. https://doi.org/10.1016/j.cemconres.2010.02.017
[10] Kim G, Loreto G, Kim JY, Kurtis KE, Wall JJ, Jacobs LJ. In situ nonlinear ultrasonic technique for monitoring microcracking in concrete subjected to creep and cyclic loading. Ultrasonics, 2018;88:64-71. https://doi.org/10.1016/j.ultras.2018.03.006
[11] Wang Z, Liu C, Zuo J, Zhang Z, Han Y, Man S, Monitoring and modeling the damage evolution in engineered cementitious composites subjected to sulfate attack through continuous ultrasonic measurements. Construction and Building Materials, 2020;262:120799. https://doi.org/10.1016/j.conbuildmat.2020.120799
[12] Shafiei S, Mohammadi Y, Effect of AR-glass fibers and natural micronized zeolite on mechanical and permeability properties of concrete exposed to normal, sodium chloride, and magnesium sulfate environments. Construction and Building Materials, 2024;457:139288. https://doi.org/10.1016/j.conbuildmat.2024.139288
[13] Shiotani T, Aggelis DG. Wave propagation in cementitious material containing artificial distributed damage. Materials and Structures, 2009;42:377-384. https://doi.org/10.1617/s11527-008-9388-4
[14] Basu S, Thirumalaiselvi A, Sasmal S, Kundu T, Nonlinear ultrasonics-based technique for monitoring damage progression in reinforced concrete structures. Ultrasonics, 2021;115:106472. https://doi.org/10.1016/j.ultras.2021.106472
[15] Qasrawi HY, Concrete strength by combined nondestructive methods simply and reliably predicted. Cement and Concrete Research, 2000;30(5):739-746. https://doi.org/10.1016/S0008-8846(00)00226-X
[16] Karaiskos G, Deraemaeker A, Aggelis DG, Hemelrijck DV. Monitoring of concrete structures using the ultrasonic pulse velocity method. Smart Materials and Structures, 2015;24(11)1-18. https://doi.org/10.1088/0964-1726/24/11/113001
[17] Stauffer JD, Woodward CB, White KR. Nonlinear ultrasonic testing with resonant and pulse velocity parameters for early damage in concrete. ACI Materials Journal, 2005;102(2):118-121. https://doi.org/10.14359/14305
[18] Shah AA, Hirose S. Nonlinear ultrasonic investigation of concrete damaged under uniaxial compression step loading. Journal of Materials in Civil Engineering, 2010;22(5):476-484. https://doi.org/10.1061/(ASCE)MT.1943-5533.0000050
[19] Jiang L, Niu D, Sun Y, Fei Q. Ultrasonic testing and microscopic analysis on concrete under sulfate attack and cyclic environment. Journal of Central South University, 2014;21:4723-4731. https://doi.org/10.1007/s11771-014-2482-6
[20] Suaris W, Ouyang C, Fernando VM. Damage model for cyclic loading of concrete. Journal of Engineering Mechanics, 1990;116(5):983-1182. https://doi.org/10.1061/(ASCE)0733-9399(1990)116:5(1020)
[21] Shah AA, Ribakov Y, Zhang Ch, Efficiency and sensitivity of linear and non-linear ultrasonics to identifying micro and macro-scale defects in concrete. Materials & Design, 2013;50: 905-916. https://doi.org/10.1016/j.matdes.2013.03.079
[22] Xu Y, Wang Q, Jiang X, Zu H, Wang W, Feng R. Nondestructive assessment of microcracks detection in cementitious materials based on nonlinear ultrasonic modulation technique. Construction and Building Materials, 2021;267:121653. https://doi.org/10.1016/j.conbuildmat.2020.121653
[23] Moradi-Marani F, Rivard P, Lamarche CP, Kodjo SA, Evaluating the damage in reinforced concrete slabs under bending test with the energy of ultrasonic waves. Construction and Building Materials, 2014;73:663-673. https://doi.org/10.1016/j.conbuildmat.2014.09.050
[24] Genovés V, Vargas F, Gosálbez J, Carrión A, Borrachero MV, Payá J. Ultrasonic and impact spectroscopy monitoring on internal sulphate attack of cement-based materials. Materials & Design, 2017;125:46-54. https://doi.org/10.1016/j.matdes.2017.03.068
[25] Liu P, Sohn H, Kundu T, Yang S. Noncontact detection of fatigue cracks by laser nonlinear wave modulation spectroscopy (LNWMS). NDT & E International, 2014; 66:106-116. https://doi.org/10.1016/j.ndteint.2014.06.002
[26] Castellano A, Fraddosio A, Piccioni MD, Kundu T. Linear and nonlinear ultrasonic techniques for monitoring stress-induced damages in concrete. Journal of Nondestructive Evaluation, Diagnostics and Prognostics of Engineering Systems, 2021;4(4):041001. https://doi.org/10.1115/1.4050354
[27] ASTM C150/C150M-20. Standard Specification for Portland Cement, Philadelphia, 2020.
[28] ASTM C192/C192M-19. Standard Practice for Making and Curing Concrete Test Specimens in the Laboratory, Philadelphia, 2020.

[29] ASTM C39/C39M-21. Standard Test Method for Compressive Strength of Cylindrical Concrete Specimens, Philadelphia, 2021.
[30] ASTM C469/C469M-14. Standard Test Method for Static Modulus of Elasticity and Poisson's Ratio of Concrete in Compression, Philadelphia, 2014.
[31] Ibrahim AM, Bassuoni MT, Carroll J, Ghazy A. Evaluation of nanoparticle-enhanced silane and vinyl ester coatings for protecting concrete from ammonium sulfate. Results in Engineering, 2024;(23):102545. https://doi.org/10.1016/j.rineng.2024.102545
[32] Müllauer W, Beddoe RE, Heinz D, Sulfate attack expansion mechanisms. Cement and Concrete Research, 2013;52:208-215. https://doi.org/10.1016/j.cemconres.2013.07.005
[33] Mbessa M, Péra J. Durability of high-strength concrete in ammonium sulfate solution. Cement and Concrete Research, 2001; 31(8): 1227-1231. https://doi.org/10.1016/S0008-8846(01)00553-1
[34] Riener K, Pfalz T, Funcke F, Leichtfried G. Processability of high-strength aluminum 6182 series alloy via laser powder bed fusion (LPBF). The International Journal of Advanced Manufacturing Technology, 2022(119):4963-4977. https://doi.org/10.1007/s00170-022-08673-8
[35] Ammouche A, Breysse D, Hornain H, Didry O, Marchand J. A new image analysis technique for the quantitative assessment of microcracks in cement-based materials. Cement and Concrete Research, 2000;30(1):25-35. https://doi.org/10.1016/S0008-8846(99)00212-4
[36] Anugonda P, Wiehn JS, Turner JA. Diffusion of ultrasound in concrete. Ultrasonics, 2001;39(6):429-435. https://doi.org/10.1016/S0041-624X(01)00077-4
[37] Alnuaimi H, Amjad U, Russo P, Lopresto V, Kundu T. Monitoring damage in composite plates from crack initiation to macro-crack propagation combining linear and nonlinear ultrasonic techniques. Structural Health Monitoring, 2021;20(1):139-150. https://doi.org/10.1177/1475921720922922

Research on Engineering Structures & Materials
www.jresm.org
MIM Research Group

Research Article

Optimizing deep learning architectures for SEM image classification using advanced dimensionality reduction techniques

Cagri Yardimci[*,1,2,a], Mevlut Ersoy[1,b]

[1]*Suleyman Demirel University, Engineering Faculty, Department of Computer Engineering, Türkiye*
[2]*Usak University, Department of Information Technology, Türkiye*

Article Info

Article History:

Received 25 Dec 2024
Accepted 20 Feb 2025

Keywords:

Deep Learning;
Image Processing;
Dimensionality Reduction;
Nanofiber;
SEM

Abstract

Non-negative Matrix Factorization (NMF) and Singular Value Decomposition (SVD) are widely recognized as pivotal dimensionality reduction techniques in the literature, particularly for deep learning applications involving large and high-dimensional datasets like SEM images. This study systematically evaluates the impact of SVD and NMF on the performance, efficiency, and energy consumption of four deep learning architectures: GoogleNet, AlexNet, ResNet, and SqueezeNet. By applying these techniques to reduce dataset dimensions, we observed that SVD excelled in computational efficiency, achieving up to 35% faster processing times compared to raw datasets. NMF, on the other hand, provided superior feature interpretability, which proved beneficial for tasks requiring meaningful pattern extraction. Energy consumption analysis revealed that SVD led to a 28% reduction in computational energy cost on average, making it a practical choice for resource-constrained environments. Among the evaluated models, ResNet consistently delivered the highest classification accuracy after dimensionality reduction, showing an improvement of 4-6% over models trained on non-reduced data. These findings underscore the critical role of dimensionality reduction in enhancing the scalability, energy efficiency, and classification accuracy of deep learning models, offering valuable insights for optimizing high-dimensional data applications in both academic and industrial contexts.

1. Introduction

Deep neural networks have recently demonstrated exceptional accuracy across various domains involving visual, auditory, and textual data (1). Specifically, convolutional neural networks (CNNs) are extensively utilized for tasks such as image recognition (2), object detection (3), speech recognition (4), and neural machine translation (5). Although the training of deep learning models has been significantly accelerated through Graphical Processing Unit (GPU)-based computations (6), deploying these models often occurs on less powerful computing platforms characterized by limited memory, processing capabilities, and battery life (7). The high computational and memory demands of many deep learning architectures pose challenges for deployment on resource-constrained devices, such as mobile phones, or in scenarios requiring low latency (8).

Early CNN models tended to be deeper and heavily overparameterized, whereas recent CNN architectures have adopted compact network design strategies to create lightweight models (9). For instance, the use of 1×1 convolutions has contributed to reducing both computational and memory requirements (10). Pioneering models like GoogleNet avoided fully connected layers, opting instead for global average pooling to process images of varying dimensions (11).

*Corresponding author: cagri.yardimci@usak.edu.tr
[a]orcid.org/0000-0002-0752-0987; [b]orcid.org/0000-0003-2963-7729
DOI: http://dx.doi.org/10.17515/resm2025-592ml1225rs

SqueezeNet, another lightweight architecture, extensively employs convolutions within its boost modules to achieve compactness while maintaining performance (12). In contrast, AlexNet, one of the earliest CNN architectures, does not use depthwise separable convolutions and is not designed as a lightweight model but laid the groundwork for deeper networks (13). ResNet introduced a method called residual learning, which helps train very deep networks. It solves the problem of vanishing gradients by using shortcuts, called skip connections, that allow information to pass through the network more easily (14). In this study, GoogleNet, AlexNet, ResNet, and SqueezeNet are preferred for SEM image classification because they are widely used in varios applications and have different structures. This allows us to compare their efficiency, complexity, and classification performance fairly. Their wide use in the literature also makes them strong benchmark models for deep learning in SEM image analysis.

Despite these innovations, many modern architectures remain overparameterized, highlighting the continued need for effective compression and dimensionality reduction techniques for the data. Datasets characterized by a large number of features are referred to as high-dimensional data and have garnered significant attention in recent years. The rapid acceleration in the growth and update rates of datasets has driven data toward becoming increasingly high-dimensional and unstructured (15). While such voluminous and complex data contains valuable information, it simultaneously complicates the process of efficient utilization. For instance, this large-scale data leading to excessive computational time, storage and energy requirements for data processing (16). Moreover, the abundance of complex information often obscures critical insights, making it challenging to discern the fundamental characteristics of the data. This issue not only demands considerable time and human resources for data processing but also adversely impacts the accuracy of recognition tasks (17). Addressing these challenges necessitates effective methods for analyzing vast quantities of information, extracting meaningful features from high-dimensional data, and mitigating the impact of redundant or correlated factors (18). Dimension reduction offers a solution to these problems. Its core principle involves mapping data samples from a high-dimensional space to a lower-dimensional space, with the primary objective of uncovering and preserving the meaningful low-dimensional structure inherent in high-dimensional observable data (19).

The projection of high-dimensional data onto a lower-dimensional space inevitably results in the loss of some original information. The primary challenge is to derive meaningful reduced data from the high-dimensional dataset that satisfies recognition accuracy and energy requirements while optimally preserving the essential characteristics of the original data (20). Nonetheless, identifying and extracting effective features in practical scenarios is often challenging. As a result, dimensionality reduction has emerged as a critical and complex task in the domains of pattern recognition, data mining, and machine learning (21). This technique has been applied to key tasks such as, image classification, content prediction, and various other industrial applications (22).

Non-negative Matrix Factorization (NMF) is a highly effective dimensionality reduction technique that offers significant advantages over conventional linear methods and other similar approaches (23). Its primary strength lies in its capacity to enforce non-negativity constraints, making it particularly well-suited for datasets characterized by exclusively positive values, such as images, text, and signals (24). This property enables NMF to extract additive and parts-based representations, uncovering fundamental patterns and features embedded within the data. Additionally, the intrinsic sparsity-promoting nature of NMF facilitates the automatic selection of relevant features, thereby reducing dimensionality while retaining essential information (25). Unlike certain linear methods that may face challenges with high-dimensional or complex datasets, NMF exhibits robustness and scalability in handling such complexities (26). Furthermore, the interpretability of NMF adds significant value, as it allows researchers to derive meaningful insights into the latent structure of the data, thereby enhancing data exploration and analysis. In summary, the unique combination of non-negativity, sparsity, interpretability, and scalability positions NMF as a versatile and highly appealing option for dimensionality reduction, offering a compelling alternative to other techniques in this domain (23).

Singular Value Decomposition (SVD) is a widely utilized dimensionality reduction technique that provides robust mathematical foundations and versatility across various applications, as well (27). At its core, SVD decomposes a matrix into three constituent components: two orthonormal matrices containing singular vectors and a diagonal matrix containing singular values. This decomposition provides a compact representation that captures the intrinsic structure of the data (28). This decomposition enables SVD to effectively reduce the dimensionality of complex datasets while preserving essential variance and relationships within the data (29). Moreover, SVD is particularly well-suited for tasks involving noise reduction and data compression, as it isolates dominant patterns and discards less significant components (30). Its mathematical rigor ensures robustness when handling large-scale, high-dimensional datasets, making it a reliable tool in fields such as image processing, text analysis, and recommendation systems. Additionally, SVD provides a geometric interpretation of the data, facilitating improved understanding and visualization of latent structures (31). Overall, the combination of dimensionality reduction, noise filtering, scalability, and interpretability positions SVD as an indispensable technique for exploratory data analysis and machine learning tasks, serving as a cornerstone in modern data science (32).

These methods may exhibit some limitations that can impact their applicability in various scenarios. While dimensionality reduction tries to preserve the most relevant features, some important details may still be lost, which may affect the classification accuracy, especially for complex defect patterns in SEM images. Both techniques reduce the dimensionality of input data. However, their initial calculation can be computationally intensive with NMF requiring recursive optimization especially for large datasets. The effectiveness of both SVD and NMF depends on the optimal selection of parameters, such as the number of retained singular values in SVD or the rank factorization in NMF (33, 34). Low level selections may lead to insufficient image details or extreme feature reduction. While SVD efficiently handles large datasets, it requires matrix decomposition, which may not scale well for extremely high-dimensional data (35). Similarly, NMF is sensitive to local minima during factorization, leading to inconsistent results (36). Both methods operate under linear assumptions, hence they may not effectively capture complex, nonlinear structures in datasets compared to deep learning-based feature extraction techniques (23).

In literature, Hossain et al. explored a novel method for hyperspectral image classification using a 3D CNN with Stochastic Neighbor Embedding (SNE)-based feature extraction. The study utilizes SVD for dimensionality reduction, enhancing the efficiency of the feature extraction process. Additionally, NMF is employed to uncover hidden patterns within the data, further improving the classification accuracy. By combining these techniques with a CNN, the system demonstrates significant improvements in processing hyperspectral data, making it more suitable for complex classification tasks in real-world applications (37). Liu et al. explored the use of dimensionality reduction techniques, including SVD and NMF, to enhance few-shot learning for medical imaging. They highlighted the limitations of SVD in scenarios where the feature space is high-dimensional compared to the dataset size. The authors demonstrated that discriminant analysis outperformed SVD at lower dimensions, while NMF provided a competitive alternative to SVD at intermediate dimensions, particularly improving inference accuracy across multiple medical imaging datasets. This approach addresses the challenges posed by small datasets in medical imaging (38). Saberi-Movahed et al. offered a comprehensive survey on NMF and its application in dimensionality reduction. NMF is highlighted as a robust technique for feature extraction and selection, especially for datasets with non-negative entries. The authors compare NMF with SVD, emphasizing that while SVD is useful for linear dimensionality reduction, NMF provides more interpretable, non-negative representations that are better suited for applications in fields like image and text analysis. The study also discusses recent trends and future research directions in both methods (23). Swaminathan et al. highlighted SVD and NMF for dimensionality reduction and feature extraction in the context of data mining. SVD is used to decompose large datasets into a set of orthogonal components, enhancing the interpretability and reducing computational complexity. On the other hand, NMF is applied to extract latent factors that are inherently non-negative, making it suitable for tasks like topic modeling and clustering. Both techniques help in identifying underlying patterns and structures within the data, improving the overall model performance (39). In their study, Chang and Chen proposed a Basis-Projected Layer (BPL) to improve deep learning

training on sparse datasets, such as GC-MS spectra. They applied SVD to reduce dimensionality and identify the principal components of the dataset. Additionally, NMF was employed to enhance feature extraction, ensuring that only non-negative values were used, which is crucial for interpreting complex datasets. The BPL efficiently transformed sparse data into dense representations, improving model performance, with F1 scores increasing by up to 11.49% (40). Hossain et al. introduced an unsupervised change detection method for Synthetic Aperture Radar (SAR) images, leveraging Deep Semi-Nonnegative Matrix Factorization (Semi-NMF) and SVD networks. Initially, Deep Semi-NMF was employed to extract features and perform pre-classification, identifying pixels with high probabilities of change or no change. Subsequently, image patches centered on these sample pixels were used to train SVD networks, comprising two SVD convolutional layers and a histogram feature generation layer, to capture nonlinear relationships between multi-temporal images. This approach enabled the generation of representative feature expressions with fewer samples, enhancing robustness to speckle noise inherent in SAR imagery. The proposed method demonstrated superior performance in detecting changes across various SAR datasets, highlighting the efficacy of combining Semi-NMF for feature extraction and SVD networks for classification in unsupervised SAR image change detection (41). Du et al. introduced a novel hybrid method combining SVD and NMF for dimensionality reduction in hyperspectral imaging. They applied SVD to decompose the original hyperspectral data matrix, capturing its essential structure, followed by NMF to extract meaningful, non-negative components that enhance interpretability. This hybrid SVD-NMF approach effectively reduced data dimensionality while preserving critical spectral information, improving classification accuracy in hyperspectral images. The method demonstrated superior performance compared to traditional techniques, offering a promising tool for efficient analysis of high-dimensional hyperspectral data (42). Furthermore, Kurra et al. introduced a robust dimensionality reduction technique for hyperspectral blood stain image classification, emphasizing the importance of hyperspectral imaging in forensic science. Their study explored various dimensionality reduction methods, including Factor Analysis (FA), Principal Component Analysis (PCA), and SVD, as preprocessing techniques for deep learning models such as Fast 3D CNN and Hybrid CNN. The results demonstrated that FA outperformed traditional techniques in terms of classification accuracy, particularly in scenarios with high-dimensional hyperspectral data (43).

In this study, the performance of various pre-trained deep learning models is compared to determine their effectiveness on a unique Scanning Electron Microscope (SEM) image dataset, preprocessed using SVD and NMF (44). This research advances the analysis of electrospun PAN nanofibers (45) by focusing on their classification into defective, slightly defective, and non-defective categories (46). By leveraging this unique dataset, the study provides a comprehensive evaluation of prominent pre-trained deep learning models, including GoogleNet, AlexNet, ResNet, and SqueezeNet (47). Furthermore, the impact of SVD and NMF preprocessing on model performance, time management, and energy efficiency is systematically compared against standard image representations. These findings not only enhance the understanding of deep learning applications in nanomaterial classification but also offer valuable insights for improving the accuracy, computational efficiency, and sustainability of future nanofiber classification systems.

2. Materials and Methods

The electrospun PAN nanofiber SEM images, supplied by nanomaterials experts at Usak University, were categorized as slightly defective, defective, or non-defective and utilized for training, validation, and testing of pre-trained deep learning models. All images within these three categories underwent preprocessing using a Bilateral filter. Following this, augmentation techniques, including rotation and random transformations along X and Y axes, were applied to the preprocessed images. Subsequently, SVD and NMF were applied to all the augmented SEM images. The performance, time, and energy consumption metrics of without any dimensionality reduction technique applied (Non), NMF-applied, and SVD-applied images were compared across pre-trained models (Fig. 1). Matlab has been utilized as the project and application development framework. All Matlab runtime executions in this study were performed on a system with an Intel i5-13600K

3.50 GHz CPU, 64GB RAM 5600MHz, an RTX 4060 GPU, and Windows OS, without utilizing parallel computation.

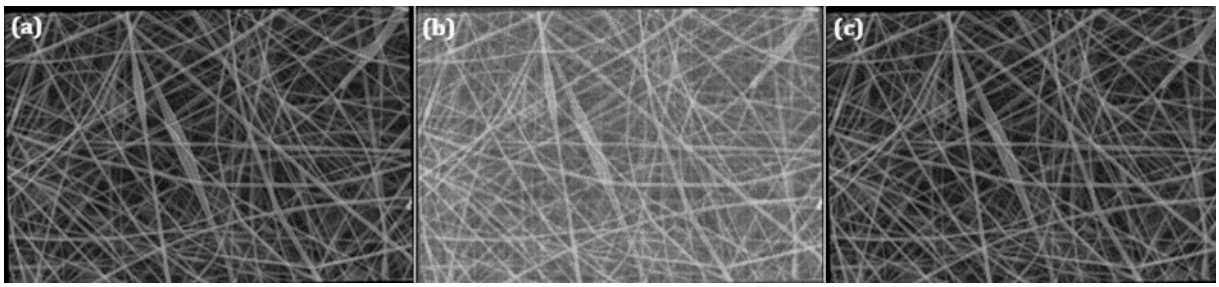

Fig. 1. (a) Non applied SEM image of nanofibers (b) NMF applied SEM image of nanofibers (c) SVD applied SEM image of nanofibers

The augmented training dataset was employed to train pre-trained deep learning architectures, including GoogleNet, AlexNet, ResNet, and SqueezeNet, and subsequently evaluated using the test dataset. Ten percent of the SEM dataset was reserved for testing, while the remaining data was randomly partitioned, allocating 70% for training and 30% for validation. The dataset consists of 53,579 images (16,162 slightly defective, 22,915 defective, and 14,502 non-defective) classified as slightly defective, defective, and non-defective (Table 1). The randomly selected test dataset includes 1,796 slightly defective images, 2,546 defective images, and 1,611 non-defective images. The default input image size was set to 227x227x3 for AlexNet and SqueezeNet, whereas for other models, it was configured as 224x224x3 (48, 49). Consistent and identical training parameters were applied across all models.

Table 1. The dataset segments used in this study

	Slightly Defective	Defective	Non-Defective
Training	16,162	22,915	14,502
Test	1,796	2,546	1,611

3.3 Results and Discussion

This comprehensive analysis highlights the accuracy and efficiency of deep learning models paired with dimensional categorization techniques for nanofiber SEM image categorization. The choice of dimensionality reduction technique plays a critical role in maintaining or enhancing model performance, with SVD emerging as the more favorable option. ResNet and GoogleNet stand out as the most reliable models, capable of delivering near-perfect results under all conditions.

Table 2 illustrates the classification performance of four neural network models (GoogleNet, AlexNet, ResNet, and SqueezeNet) for three categories -slightly defective, defective, and non-defective- with no technique applied (Non). GoogleNet achieved consistently high sensitivity across all categories, with values above 99%, demonstrating its robustness in correctly identifying all classes. The specificity was similarly high, exceeding 99%, indicating its ability to minimize false positives. Accuracy across categories was above 99.8%, underscoring the model's overall strong classification capability. The precision and f1-scores were similarly impressive, showcasing excellent balance between sensitivity and specificity. AlexNet showed competitive performance, particularly in the defective and non-defective categories, where sensitivity reached 100%. Specificity and accuracy were marginally lower than GoogleNet, but still above 99.5%. Precision and f1-scores were also exemplary, reflecting consistent and reliable performance. ResNet emerged as the top performer in the Non condition. Sensitivity and specificity achieved perfect scores (100%) for the non-defective category and slightly defective samples. This indicates an exceptional ability to both identify defective samples and avoid misclassifications. Its precision and F1-scores also aligned with these findings, making it a highly reliable model in this scenario. SqueezeNet, while slightly trailing the other models, still maintained outstanding results, with sensitivity, specificity, and accuracy consistently exceeding 98%. This model was slightly less

sensitive in the non-defective category compared to the others, but its performance was still well within the acceptable range.

Table 2. The performance metrics of models with no dimensionality reduction technique applied

Model Name	Category	Sensitivity (%)	Specificity (%)	Accuracy (%)	Precision (%)	F1-score (%)
GoogleNet	Slightly Defective	99.77	99.18	99.36	98.13	98.95
	Defective	99.88	99.91	99.89	99.88	99.88
	Non-Defective	98.07	99.97	99.46	99.93	98.99
AlexNet	Slightly Defective	99.88	99.83	99.84	99.61	99.75
	Defective	99.88	99.82	99.84	99.76	99.82
	Non-Defective	99.50	100	99.86	100	99.75
ResNet	Slightly Defective	99.94	100	99.98	100	99.97
	Defective	100	99.97	99.98	99.96	99.98
	Non-Defective	100	100	100	100	100
SqueezeNet	Slightly Defective	97.66	99.51	98.95	98.87	98.26
	Defective	99.96	98.88	99.34	98.52	99.24
	Non-Defective	98.75	99.88	99.58	99.68	99.22

Table 3 shows that GoogleNet retained its high performance across all metrics, with sensitivity, specificity, and accuracy close to or exceeding 99.9% in most categories. Notably, the precision and f1-scores remained robust, indicating that dimensionality reduction using NMF did not adversely affect its classification capability. AlexNet showed a slight decline in sensitivity for the non-defective category (96.69%), suggesting a minor trade-off in detecting this class when NMF was applied. Despite this, its specificity and accuracy remained high, indicating an ability to maintain overall performance integrity. ResNet, much like in the Non condition, demonstrated exceptional performance. Its sensitivity for the slightly defective category remained perfect (100%), while other metrics such as specificity and accuracy were slightly reduced but still above 99%. This model appears to be the least affected by NMF, maintaining near-optimal performance across categories. SqueezeNet exhibited the most notable fluctuations with NMF. Sensitivity for the defective and non-defective categories slightly declined, but specificity and accuracy remained consistently high. Precision and f1-scores showed minor reductions, suggesting that while NMF had some impact, the overall classification performance remained strong.

Table 3. The performance metrics of models with NMF applied

Model Name	Category	Sensitivity (%)	Specificity (%)	Accuracy (%)	Precision (%)	F1-score (%)
GoogleNet	Slightly Defective	99.88	99.66	99.73	99.22	99.55
	Defective	99.96	99.97	99.96	99.96	99.96
	Non-Defective	99.19	99.97	99.76	99.93	99.56
AlexNet	Slightly Defective	99.33	99.90	99.73	99.77	99.55
	Defective	100	99.82	99.89	99.76	99.88
	Non-Defective	99.69	99.83	99.79	99.56	99.62
ResNet	Slightly Defective	100	99.78	99.84	99.50	99.75
	Defective	99.68	100	99.86	100	99.84
	Non-Defective	99.93	100	99.98	100	99.96
SqueezeNet	Slightly Defective	98.21	99.51	99.12	98.87	98.54
	Defective	99.52	99.67	99.61	99.56	98.54
	Non-Defective	99.31	99.44	99.41	98.52	98.91

Figure 2 illustrates the classification performance of four distinct deep learning models -GoogleNet, AlexNet, ResNet, and SqueezeNet- applied to SEM images that underwent NMF. The GoogleNet demonstrates exceptional classification accuracy, as evidenced by its confusion matrix. The number of correctly classified images for each category is as follows: 1784 for slightly defective, 2545 for defective, and 1598 for non-defective. Misclassifications are minimal, with only one

slightly defective image misclassified as defective and one as non-defective. Furthermore, 13 non-defective images are misclassified as slightly defective. Notably, there are no instances of defective images being incorrectly labeled. This result indicates that GoogleNet performs remarkably well in distinguishing between the three categories, with negligible confusion, particularly in the Defective category. The AlexNet also exhibits robust performance, though slightly inferior to GoogleNet. It correctly classifies 1784 slightly defective, 2546 defective, and 1696 non-defective images. Misclassifications include five slightly defective images labeled as defective and seven as non-defective. For the non-defective category, four images are misclassified as slightly defective, and one is labeled as defective. This matrix highlights AlexNet's consistent ability to classify defective images accurately but reveals a marginal increase in misclassifications for the slightly defective and non-defective categories compared to GoogleNet. ResNet shows competitive classification accuracy, with 1786 slightly defective, 2538 defective, and 1610 non-defective images correctly identified. slightly defective misclassifications are negligible, with only eight images labeled as defective and none as non-defective. The defective category has minimal misclassification, with eight images incorrectly labeled as slightly defective. For non-defective images, only one instance is misclassified as slightly defective. ResNet demonstrates a high level of accuracy, comparable to GoogleNet, while slightly outperforming AlexNet in certain aspects, particularly in minimizing confusion in the non-defective category. SqueezeNet, while still effective, exhibits a slight decline in classification accuracy compared to the other models. The correct classifications are as follows: 1764 slightly defective, 2534 defective, and 1600 non-defective images. Misclassifications are more pronounced, with nine slightly Defective images labeled as defective and 23 as non-defective. The defective category contains 11 images misclassified as slightly defective and one as non-defective. Similarly, nine non-defective images are mislabeled as slightly defective, and two as defective. While SqueezeNet achieves reasonably good performance, it struggles more with boundary cases between categories, especially for slightly defective and non-defective images, indicating room for improvement.

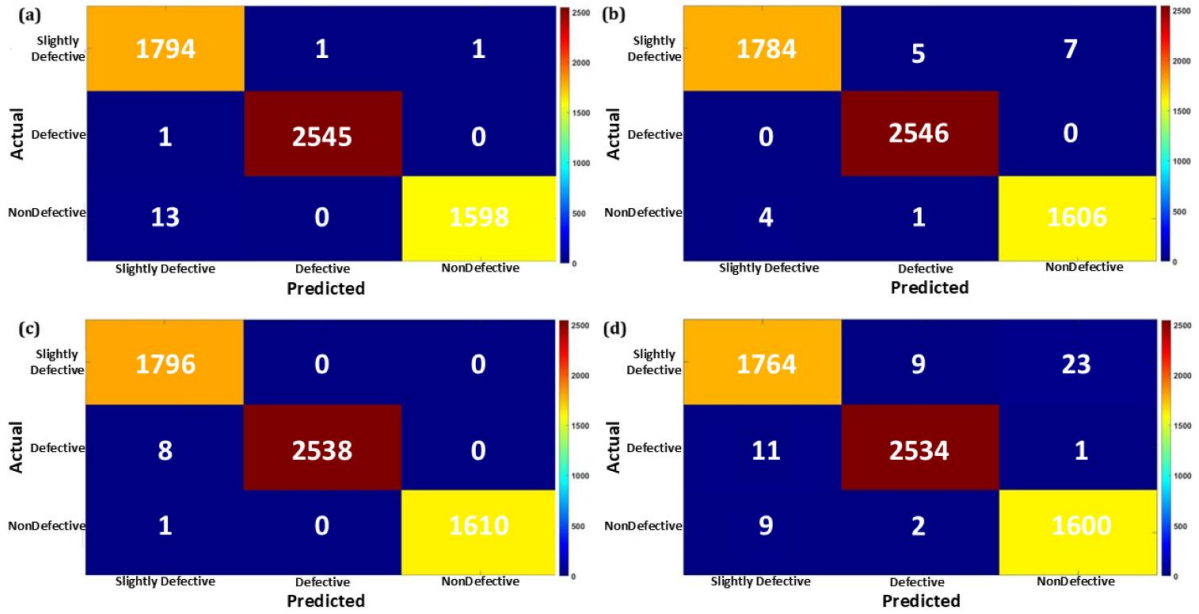

Fig. 2. (a) Confusion matrix of GoogleNet on NMF-processed SEM images (b) Confusion matrix of AlexNet on NMF-processed SEM images (c) Confusion matrix of Resnet on NMF-processed SEM images (d) Confusion matrix of SqueezeNet on NMF-processed SEM images

Table 4 indicates that GoogleNet achieved near-perfect metrics across all categories, with sensitivity, specificity, accuracy, precision, and f1-scores reaching or exceeding 99.9%. This suggests that SVD optimized the feature space for GoogleNet, enabling it to classify nanofiber images with remarkable accuracy. AlexNet benefited notably from SVD, as sensitivity for the slightly defective and non-defective categories rebounded to exceed 99%. The overall metrics improved compared to the NMF condition, showcasing the potential of SVD to mitigate the limitations observed with NMF. ResNet again demonstrated stellar performance. The sensitivity,

specificity, and accuracy reached near-perfect levels, underscoring its reliability and robustness when paired with SVD. Its consistent top performance across all conditions cements its position as the most effective model for this task. SqueezeNet, which exhibited some variability with NMF, showed improved results under SVD. Sensitivity, specificity, and accuracy for all categories exceeded 99%, suggesting that SVD effectively stabilized and enhanced this model's performance.

Table 4. The performance metrics of models with SVD applied

Model Name	Category	Sensitivity (%)	Specificity (%)	Accuracy (%)	Precision (%)	F1-score (%)
GoogleNet	Slightly Defective	99.88	99.80	99.83	99.55	99.72
	Defective	100	99.97	99.98	99.96	99.98
	Non-Defective	99.50	99.97	99.84	99.93	99.72
AlexNet	Slightly Defective	99.27	99.56	99.47	99	99.13
	Defective	99.33	100	99.71	100	99.66
	Non-Defective	99.81	99.65	99.69	99.07	99.44
ResNet	Slightly Defective	100	99.95	99.96	99.88	99.94
	Defective	99.92	100	99.96	100	99.96
	Non-Defective	100	100	100	100	100
SqueezeNet	Slightly Defective	99.83	99.73	99.76	99.39	99.61
	Defective	100	99.94	99.96	99.92	99.96
	Non-Defective	99.31	99.97	99.79	99.93	99.62

Figure 3 illustrates the classification performance of four different deep learning models - GoogleNet, AlexNet, ResNet, and SqueezeNet- applied to SEM images that underwent SVD. GoogleNet demonstrates near-perfect classification accuracy, as evidenced by the confusion matrix. Correct classifications include 1794 slightly defective, 2546 defective, and 1603 non-defective images. Misclassifications are minimal, with one slightly defective image mislabeled as defective and eight non-defective images incorrectly identified as slightly defective. Notably, there are no misclassifications involving defective images being labeled as non-defective or vice versa. This indicates that GoogleNet has an outstanding ability to distinguish between these categories when SVD is applied for feature extraction, with exceptional performance in the defective category. The AlexNet exhibits a strong classification performance, though it is slightly less accurate than GoogleNet. It correctly classifies 1783 slightly defective, 2529 defective, and 1608 non-defective images. Misclassifications include 15 slightly defective images labeled as defective and three non-defective images mislabeled as slightly defective. Two non-defective images are misclassified as defective. These results suggest that while AlexNet performs reliably, it struggles slightly more than GoogleNet, particularly in separating the slightly defective and defective categories. ResNet achieves excellent classification accuracy, with 1796 slightly defective, 2544 Defective, and 1611 non-defective images correctly identified. Misclassifications are limited to two slightly defective images mislabeled as defective. No non-defective images are classified incorrectly. ResNet demonstrates a robust capability in identifying all three categories with high precision, outperforming AlexNet in terms of minimizing errors in the non-defective category and rivaling GoogleNet in overall performance. SqueezeNet, while effective, displays slightly lower classification accuracy compared to the other models. It correctly classifies 1793 slightly defective, 2546 defective, and 1600 non-defective images. Misclassifications include two slightly defective images labeled as defective, one mislabeled as non-defective, and 11 non-defective images misclassified as slightly defective. Although the performance is commendable, the model's tendency to confuse slightly defective and non-defective images is more pronounced than in GoogleNet and ResNet.

In summary, both NMF and SVD demonstrated their utility in maintaining high classification performance while potentially reducing computational complexity. However, SVD appeared to have a more stabilizing effect, particularly for models like SqueezeNet and AlexNet, which showed slight sensitivity drops with NMF. ResNet consistently outperformed other models across all conditions, achieving perfect or near-perfect metrics, particularly in the Non and SVD conditions. This suggests its architecture is well-suited for the classification of nanofiber SEM images. GoogleNet remained highly reliable, with minimal fluctuations across conditions and categories,

reflecting its robustness and adaptability. AlexNet and SqueezeNet showed more pronounced sensitivity to dimensionality reduction techniques, but both achieved strong overall performance, particularly under SVD. The non-defective category consistently exhibited slightly lower sensitivity across models, particularly with NMF. This suggests that distinguishing non-defective samples poses a unique challenge, potentially due to overlapping features with other categories.

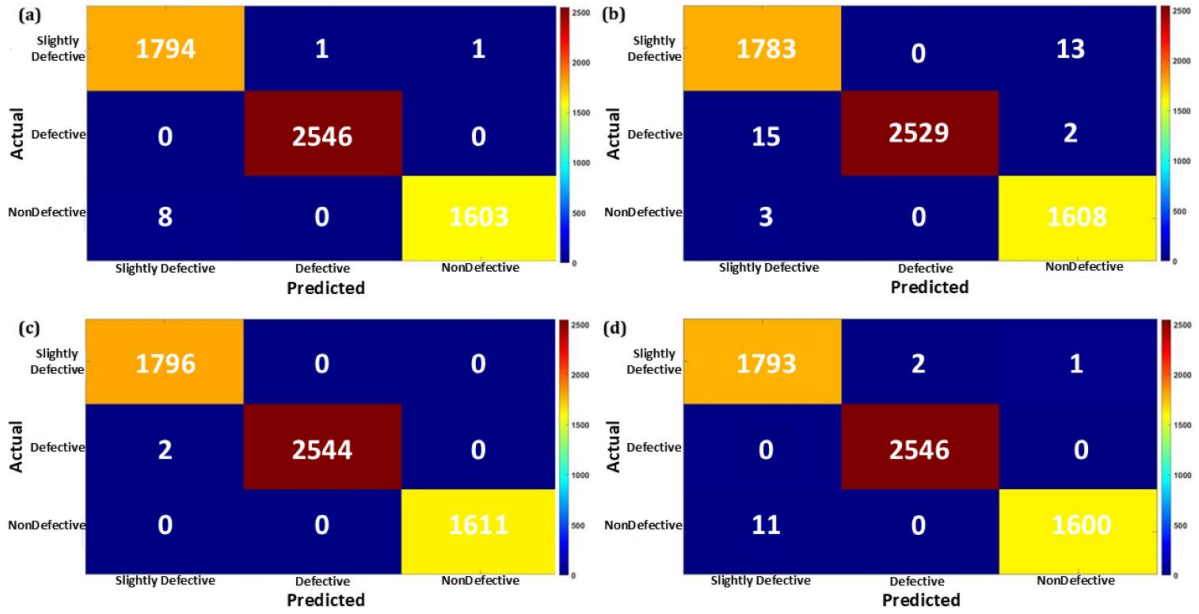

Fig. 3. (a) Confusion matrix of GoogleNet on SVD-processed SEM images (b) Confusion matrix of AlexNet on SVD-processed SEM images (c) Confusion matrix of Resnet on SVD-processed SEM images (d) Confusion matrix of SqueezeNet on SVD-processed SEM images

Table 5 demonstrates that ResNet exhibited the highest total and average processing times (574,955.59 ms and 96.58 ms, respectively). This aligns with its deeper and more complex architecture, which demands significant computational resources. While ResNet achieved superior classification accuracy in previous analyses, this comes at a higher computational cost. GoogleNet and AlexNet had comparable processing times, with AlexNet (88.08 ms average) slightly lagging GoogleNet (89.52 ms average). GoogleNet's relatively low computational demands highlight its efficiency despite achieving high classification performance. SqueezeNet showed the lowest total and average processing times in this condition (439,589.20 ms and 73.84 ms). As a lightweight model, SqueezeNet provides a clear advantage in scenarios where computational efficiency is critical. GoogleNet experienced the most pronounced reduction, with average processing time dropping from 89.52 ms to 51.81 ms. This highlights the effectiveness of NMF in simplifying the feature space, thereby reducing computational demands. AlexNet similarly benefitted from NMF, with a decrease in average processing time from 88.08 ms to 52.30 ms. These results demonstrate that dimensionality reduction via NMF can substantially enhance processing efficiency for models with moderate computational requirements. ResNet and SqueezeNet showed substantial reductions in processing time as well. ResNet's average time dropped to 56.87 ms, while SqueezeNet achieved an average time of 53.62 ms. These improvements make even complex architectures like ResNet more computationally viable in energy-conscious applications. GoogleNet achieved an average processing time of 52.03 ms, slightly higher than its NMF performance but still a significant improvement over the Non condition. This demonstrates SVD's ability to preserve computational efficiency while maintaining model performance. AlexNet displayed similar improvements, achieving the lowest average time of 51.63 ms. These results highlight the potential of SVD for models with moderately complex architectures. Although ResNet remains the most computationally intensive model, its average time was reduced to 57.64 ms under SVD. This reinforces SVD's utility in reducing the computational cost of deep models while preserving their performance advantages. SqueezeNet emerged as the most computationally efficient model under SVD, with an average time of 51.74 ms. This underscores SqueezeNet's suitability for energy-efficient applications, particularly when combined with dimensionality reduction techniques.

Table 5. Processing times of the models based on the reduction technique

Model Name	Technique	Total Processing Time (ms)	Average Processing Time (ms)
GoogleNet	Non	532,931.95	89.52
	NMF	308,422.11	51.81
	SVD	309,749.95	52.03
AlexNet	Non	524,323.83	88.08
	NMF	311,348.93	52.30
	SVD	307,327.59	51.63
ResNet	Non	574,955.59	96.58
	NMF	338,572.12	56.87
	SVD	343,127.07	57.64
SqueezeNet	Non	439,589.20	73.84
	NMF	319,182.19	53.62
	SVD	307,992.35	51.74

This study advances the domain of dimensionality reduction and classification through a robust integration of NMF and SVD techniques, showcasing their complementary strengths for handling high-dimensional datasets such as hyperspectral and electrospun PAN nanofiber SEM images. SVD decomposes data into orthogonal components, preserving key features while eliminating redundancy. These results in faster processing times with a slight increase in classification accuracy. Since NMF enforces non-negativity constraints, it preserves meaningful patterns in the SEM images, which contributes to enhanced interpretability of features. ResNet achieves the highest accuracy due to its deep architecture and residual connections, which prevent vanishing gradients and enable better feature learning, even after dimensionality reduction. GoogleNet shows strong consistency across different reduction techniques due to its Inception modules, which allow multi-scale feature extraction. The architectures of AlexNet and SqueezeNet exhibit slight sensitivity to NMF, which is more affected by feature elimination and requires more preserved information to maintain classification performance. SVD's lower computational complexity results in faster processing times, reducing GPU consumption, leading to the observed 28% decrease in energy costs. ResNet's high processing time is expected due to its deep architecture, but its superior accuracy justifies the trade-off in computational demand. The high-dimensional nature of SEM images with high intra-class similarity makes them ideal candidates for dimensionality reduction, where redundant and correlated features can be removed without significant performance degradation. Unlike Hossain et al. and Du et al., which utilized SVD and NMF independently for feature extraction in hyperspectral imaging, this work demonstrates a hybrid framework that combines the interpretability of NMF with the structural efficiency of SVD, resulting in improved classification accuracy and computational efficiency (37, 42). While Liu et al. focused on enhancing few-shot learning in medical imaging through SVD and discriminant analysis, the present study addresses broader applications by exploring feature-rich datasets and achieving competitive performance across various domains (38). Furthermore, this research builds upon the foundation laid by Swaminathan et al. and Saberi-Movahed et al. by employing sparse representations to reduce computational complexity while preserving essential data characteristics, thus enabling scalability for large-scale classification tasks (23, 39). In particular, (50) aligns with recent research in matrix factorization techniques, as seen in Autoencoder-guided low-rank approximation approaches for dimensionality reduction, where the integration of autoencoders with low-rank decomposition enables efficient feature extraction in cluttered image data. The presented method extends such principles by leveraging the combined strengths of NMF and SVD, enhancing both feature selection and classification performance. Moreover, inspired by the work of Allab et al., who proposed a simultaneous Semi-NMF and PCA approach for clustering, this study similarly emphasizes the benefits of hybrid methods for extracting meaningful low-dimensional representations while mitigating the computational burden associated with high-dimensional datasets (51). Additionally, (52) incorporates the advantages of rank-revealing QR factorization, a method that has demonstrated superior feature selection performance compared to traditional SVD and NMF approaches by improving computational efficiency and reducing redundancy. (53)

combines multi-head attention, CNNs, and wavelet transforms for hyperspectral image classification. These methods capture spatial and spectral patterns well but require high computational power, making them less scalable. In contrast, this study proposes a hybrid framework using matrix factorization, which preserves key features while reducing redundancy more efficiently. Unlike Chang and Chen, who proposed a BPL for sparse datasets, this work emphasizes the dynamic interplay between NMF and SVD in dense and high-dimensional contexts, ensuring both interpretability and precision (40). Furthermore, the integration of Fast Johnson-Lindenstrauss Transform (FJLT) for content-based feature selection, as discussed in recent image hashing techniques, reinforces the computational efficiency of the proposed dimensionality reduction framework (54). Overall, the contributions of this study lie in its ability to unify and extend existing methodologies, offering a versatile and practical solution for dimensionality reduction and classification, with potential applications in diverse fields such as remote sensing, material science, and biomedical imaging.

4. Conclusions

This study has demonstrated the significant potential of dimensionality reduction techniques, particularly NMF and SVD, in optimizing deep learning architectures for the classification of high-dimensional datasets, such as SEM images of electrospun PAN nanofibers. Through comprehensive experimentation with pre-trained models like GoogleNet, AlexNet, ResNet, and SqueezeNet, the findings illustrate that dimensionality reduction can enhance computational efficiency and energy conservation without compromising classification accuracy. SVD emerged as the most effective technique, achieving up to 35% reductions in processing times and an average 28% decrease in energy consumption. Its capacity to preserve the intrinsic structure of data while simplifying computational demands proved particularly advantageous for resource-constrained environments and energy-intensive architectures, such as ResNet. On the other hand, NMF excelled in feature interpretability, enabling more meaningful pattern extraction, which is critical for complex classification tasks. Despite a slight trade-off in computational efficiency compared to SVD, NMF demonstrated its value in enhancing model adaptability to intricate datasets. The results underline the versatility of dimensionality reduction techniques in addressing diverse deployment scenarios. While ResNet consistently achieved the highest classification accuracy, lightweight models such as SqueezeNet, when paired with SVD, offered an optimal balance between performance and resource efficiency, making them particularly suited for real-time and mobile applications. GoogleNet displayed remarkable robustness across conditions, further emphasizing its reliability for nanomaterial classification. In conclusion, this research highlights the importance of integrating dimensionality reduction techniques to strike a balance between accuracy, efficiency, and sustainability in deep learning applications. Future work could investigate hybrid approaches that combine the strengths of SVD and NMF, potentially unlocking further advancements in performance and scalability for industrial and academic applications. These findings provide a foundation for sustainable and effective utilization of deep learning in the classification of high-dimensional datasets. Future work could explore the integration of genetic algorithms to optimize the combination of dimensionality reduction techniques and deep learning architectures, further enhancing the adaptability of models to diverse high-dimensional SEM datasets and improving the overall performance of deep learning models.

References

1] Hussain N, Khan MA, Sharif M, Khan SA, Albesher AA, Saba T, et al. A deep neural network and classical features based scheme for objects recognition: an application for machine inspection. Multimedia Tools and Applications. 2024:1-23.

[2] Absur MN, Nasif KFA, Saha S, Nova SN, editors. Revolutionizing Image Recognition: Next-Generation CNN Architectures for Handwritten Digits and Objects. 2024 IEEE Symposium on Wireless Technology & Applications (ISWTA); 2024: IEEE. https://doi.org/10.1109/ISWTA62130.2024.10651815

[3] Sagar AS, Chen Y, Xie Y, Kim HS. MSA R-CNN: A comprehensive approach to remote sensing object detection and scene understanding. Expert Systems with Applications. 2024;241:122788. https://doi.org/10.1016/j.eswa.2023.122788

[4] Shashidhar R, Shashank M, Sahana B. Enhancing visual speech recognition for deaf individuals: a hybrid LSTM and CNN 3D model for improved accuracy. Arabian Journal for Science and Engineering. 2024;49(9):11925-41. https://doi.org/10.1007/s13369-023-08385-5
[5] Ahammad SH, Kalangi RR, Nagendram S, Inthiyaz S, Priya PP, Faragallah OS, et al. Improved neural machine translation using Natural Language Processing (NLP). Multimedia Tools and Applications. 2024;83(13):39335-48. https://doi.org/10.1007/s11042-023-17207-7
[6] Baloi A, Belean B, Turcu F, Peptenatu D. GPU-based similarity metrics computation and machine learning approaches for string similarity evaluation in large datasets. Soft Computing. 2024;28(4):3465-77. https://doi.org/10.1007/s00500-023-08687-8
[7] Tong A. The Evolution of AI Engineering: Hardware and Software Dynamics, Historical Progression, Innovations, and Impact on Next-Generation AI Systems. Library Progress International. 2024;44(3):19715-37.
[8] Shah A. Resource Optimization Strategies and Optimal Architectural Design for Ultra-Reliable Low-Latency Applications in Multi-Access Edge Computing. 2024.
[9] Chen F, Li S, Han J, Ren F, Yang Z. Review of lightweight deep convolutional neural networks. Archives of Computational Methods in Engineering. 2024;31(4):1915-37. https://doi.org/10.1007/s11831-023-10032-z
[10] Wang A, Chen H, Lin Z, Han J, Ding G, editors. Repvit: Revisiting mobile cnn from vit perspective. Proceedings of the IEEE/CVF Conference on Computer Vision and Pattern Recognition; 2024. https://doi.org/10.1109/CVPR52733.2024.01506
[11] Xie P, Liu Y, Lu Q, Lin X, Yang Y, Hu X. Deep learning-based GoogLeNet-embedded no-pooling dimension fully-connected network for short-term wind power prediction. Systems Science & Control Engineering. 2024;12(1):2399057. https://doi.org/10.1080/21642583.2024.2399057
[12] Hao M, Sun Q, Xuan C, Zhang X, Zhao M. SqueezeNet: An Improved Lightweight Neural Network for Sheep Facial Recognition. Applied Sciences. 2024;14(4):1399. https://doi.org/10.3390/app14041399
[13] Aleti SR, Kurakula K. Evaluation of Lightweight CNN Architectures for Multi-Species Animal Image Classification. 2024.
[14] Vedhamuru N, Malmathanraj R, Palanisamy P. Lightweight deep and cross residual skip connection separable CNN for plant leaf diseases classification. Journal of Electronic Imaging. 2024;33(3):033035. https://doi.org/10.1117/1.JEI.33.3.033035
[15] Łukaszuk T, Krawczuk J. Importance of feature selection stability in the classifier evaluation on high-dimensional genetic data. PeerJ. 2024;12:e18405. https://doi.org/10.7717/peerj.18405
[16] Wang S, Zheng H, Wen X, Fu S. Distributed high-performance computing methods for accelerating deep learning training. Journal of Knowledge Learning and Science Technology ISSN: 2959-6386 (online). 2024;3(3):108-26. https://doi.org/10.60087/jklst.v3.n3.p108-126
[17] Nguyen-Tat B-T, Bui M-Q, Ngo VM. Automating attendance management in human resources: A design science approach using computer vision and facial recognition. International Journal of Information Management Data Insights. 2024;4(2):100253. https://doi.org/10.1016/j.jjimei.2024.100253
[18] Ros F, Riad R. Feature and Dimensionality Reduction for Clustering with Deep Learning: Springer; 2024. https://doi.org/10.1007/978-3-031-48743-9
[19] Luan L, Ravi SK, Bhaduri A, Pandita P, Wang L, Ramachandra N, et al., editors. High-dimensional Surrogate Modeling for Image Data with Nonlinear Dimension Reduction. AIAA SCITECH 2024 Forum; 2024. https://doi.org/10.2514/6.2024-0388
[20] Wu H, Chen Y, Zhu W, Cai Z, Heidari AA, Chen H. Feature selection in high-dimensional data: an enhanced RIME optimization with information entropy pruning and DBSCAN clustering. International Journal of Machine Learning and Cybernetics. 2024:1-44. https://doi.org/10.1007/s13042-024-02143-1
[21] Rajender N, Gopalachari MV. An efficient dimensionality reduction based on adaptive-GSM and transformer assisted classification for high dimensional data. International Journal of Information Technology. 2024;16(1):403-16. https://doi.org/10.1007/s41870-023-01552-9
[22] Suriyan K, Nagarajan R. Recent Trends in Pattern Recognition: Challenges and Opportunities. Machine Learning Techniques and Industry Applications. 2024:201-18. https://doi.org/10.4018/979-8-3693-5271-7.ch010
[23] Saberi-Movahed F, Berahman K, Sheikhpour R, Li Y, Pan S. Nonnegative Matrix Factorization in Dimensionality Reduction: A Survey. arXiv preprint arXiv:240503615. 2024.
[24] Duan J, Xiong J, Li Y, Ding W. Deep learning based multimodal biomedical data fusion: An overview and comparative review. Information Fusion. 2024:102536. https://doi.org/10.1016/j.inffus.2024.102536
[25] Bocchinfuso A, Calvetti D, Somersalo E. Bayesian sparsity and class sparsity priors for dictionary learning and coding. arXiv preprint arXiv:230900999. 2023. https://doi.org/10.1016/j.jcmds.2024.100094
[26] Tang J, Xu X, Wang T, Rezaeipanah A. An efficient network clustering approach using graph-boosting and nonnegative matrix factorization. Artificial Intelligence Review. 2024;57(11):292. https://doi.org/10.1007/s10462-024-10912-1

[27] Zaben M, Hassan MA, Worku MY, Abido MA. Dimension Reduction Techniques for Machine Learning based AC Microgrid Fault Diagnosis: A Systematic Review. IEEE Access. 2024. https://doi.org/10.1109/ACCESS.2024.3486786
[28] Sarkar D, Saha S, Krishnamoorthy J, Bhunia A. Application of singular value decomposition analysis: Insights into the complex mechanisms of amyloidogenesis. Biophysical Chemistry. 2024;306:107157. https://doi.org/10.1016/j.bpc.2023.107157
[29] Nived P, Harikumar S, Anil A. Matrix Factorization For Augmented Deep Learning Model Generation. Procedia Computer Science. 2024;235:628-41. https://doi.org/10.1016/j.procs.2024.04.062
[30] SCHANZE T. Tensor decomposition-based compression and noise reduction of multichannel ECG signals.
[31] Thanh OV. Low-Rank Matrix Factorizations with Volume-based Constraints and Regularizations. arXiv preprint arXiv:241206380. 2024.
[32] Sihare SR. Dimensionality Reduction for Data Analysis With Quantum Feature Learning. Wiley Interdisciplinary Reviews: Data Mining and Knowledge Discovery. 2024:e1568. https://doi.org/10.1002/widm.1568
[33] Cai Y, Gu H, Kenney T. Rank selection for non-negative matrix factorization. Statistics in Medicine. 2023;42(30):5676-93. https://doi.org/10.1002/sim.9934
[34] Falini A. A review on the selection criteria for the truncated SVD in Data Science applications. Journal of Computational Mathematics and Data Science. 2022;5:100064. https://doi.org/10.1016/j.jcmds.2022.100064
[35] Han S, Jung S, Kim K, editors. Robust SVD Made Easy: A fast and reliable algorithm for large-scale data analysis. International Conference on Artificial Intelligence and Statistics; 2024: PMLR.
[36] bin Ismail A. Nonnegative Matrix Factorization: A. 2022.
[37] Hossain MM, Hossain MA, Musa Miah AS, Okuyama Y, Tomioka Y, Shin J. Stochastic neighbor embedding feature-based hyperspectral image classification using 3d convolutional neural network. Electronics. 2023;12(9):2082. https://doi.org/10.3390/electronics12092082
[38] Liu J, Fan K, Cai X, Niranjan M. Few-shot learning for inference in medical imaging with subspace feature representations. PLoS One. 2024;19(11):e0309368. https://doi.org/10.1371/journal.pone.0309368
[39] Swaminathan S, Garg D, Kannan R, Andres F. Sparse low rank factorization for deep neural network compression. Neurocomputing. 2020;398:185-96. https://doi.org/10.1016/j.neucom.2020.02.035
[40] Chang YT, Chen SF. Design of an basis-projected layer for sparse datasets in deep learning training using gc-ms spectra as a case study. arXiv preprint arXiv:240309188. 2024.
[41] Hossain MM, Hossain MA, editors. Feature reduction and classification of hyperspectral image based on multiple kernel PCA and deep learning. 2019 IEEE International Conference on Robotics, Automation, Artificial-intelligence and Internet-of-Things (RAAICON); 2019: IEEE. https://doi.org/10.1109/RAAICON48939.2019.59
[42] Du L, Shang Q, Wang Z, Wang X. Robust image hashing based on multi-view dimension reduction. Journal of Information Security and Applications. 2023;77:103578. https://doi.org/10.1016/j.jisa.2023.103578
[43] Kurra S, Emani PR, Aala S, Chinnadurai S, editors. A Robust Dimension Reduction Technique for Hyperspectral Blood Stain Image Classification. 2024 Second International Conference on Emerging Trends in Information Technology and Engineering (ICETITE); 2024: IEEE. https://doi.org/10.1109/ic-ETITE58242.2024.10493757
[44] Ince Yardimci A. Comparative Study of the Structural, Mechanical and Electrochemical Properties of Polyacrylonitrile (PAN)-Based Polypyrrole (PPy) and Polyvinylidene Fluoride (PVDF) Electrospun Nanofibers. Journal of Macromolecular Science, Part B. 2022;61(9):1103-15. https://doi.org/10.1080/00222348.2022.2127713
[45] Yardimci Aİ, Tanoğlu M, Yilmaz S, Selamet Y. Effect of CNT incorporation on PAN/PPy nanofibers synthesized by electrospinning method. Turkish Journal of Chemistry. 2020;44(4):1002-15. https://doi.org/10.3906/kim-1911-49
[46] Yardimci C, Ersoy M. jabbrv-ltwa-all. ldf jabbrv-ltwa-en. ldf Introducing a Novel Deep Learning Approach for Classification of Defects in Electrospun Polyacrylonitrile (PAN)-Based Nanofibers Using Scanning Electron Microscope (SEM) Imaging. 2024. https://doi.org/10.22541/au.172923149.93559340/v1
[47] Kalaiarasi P, Esther Rani P, editors. A comparative analysis of AlexNet and GoogLeNet with a simple DCNN for face recognition. Advances in Smart System Technologies: Select Proceedings of ICFSST 2019; 2021: Springer. https://doi.org/10.1007/978-981-15-5029-4_54
[48] Abdullah MY. Real time handwriting recognition system using CNN algorithms. Wasit Journal of Computer and Mathematics Science. 2023;2(3):30-8. https://doi.org/10.31185/wjcms.157
[49] Abubakar B, Ali S, Hassan R, Ahmed A, Adamu S, Isa S. Development of a transfer learning based modified VGGNet model with exponential linear unit activation function for maize disease classification. Savannah Journal of Science and Engineering Technology. 2024;2(6):314-21.

[50] Kayacan YE, Erer I, editors. Autoencoder Guided Low-Rank Approximation Approach for Clutter Removal in GPR Images. 2024 47th International Conference on Telecommunications and Signal Processing (TSP); 2024: IEEE. https://doi.org/10.1109/TSP63128.2024.10605982
[51] Allab K, Labiod L, Nadif M, editors. Simultaneous semi-NMF and PCA for clustering. 2015 IEEE International Conference on Data Mining; 2015: IEEE. https://doi.org/10.1109/ICDM.2015.66
[52] Moslemi A, Ahmadian A. Subspace learning for feature selection via rank revealing QR factorization: Fast feature selection. Expert Systems with Applications. 2024;256:124919. https://doi.org/10.1016/j.eswa.2024.124919
[53] Tulapurkar H, Banerjee B, Buddhiraju KM. Multi-head attention with CNN and wavelet for classification of hyperspectral image. Neural Computing and Applications. 2023;35(10):7595-609. https://doi.org/10.1007/s00521-022-08056-w
[54] Lv X, Wang Z. An extended image hashing concept: content-based fingerprinting using FJLT. EURASIP Journal on Information Security. 2009;2009:1-16. https://doi.org/10.1155/2009/859859

Research on Engineering Structures & Materials
www.jresm.org
Research Group

Research Article

Influence of hydroxyethyl cellulose on the stability of foamed concrete

Shuping Sun[1,a], Ronggui Liu[*,2,b], Hongmei Chen[3,c], Shu Sun[4,d]

[1]*School of Architecture and Environmental Engineering, Silicon Lake College, Jiangsu, China*
[2]*School of Civil Engineering and Mechanics, Jiangsu University, Jiangsu, China*
[3]*Nantong Polytechnic Institute, Jiangsu, China*
[4]*Taizhou Vocational and Technical College, Jiangsu, China*

Article Info

Article History:

Received 17 Oct 2024
Accepted 06 Jan 2025

Keywords:

Foamed concrete;
Hydroxyethyl cellulose;
Foam stability;
Compressive strength;
Pore Structure

Abstract

As a lightweight material, foamed concrete has been widely used in construction because of its excellent lightweight properties, heat preservation and sound absorption. However, due to its low strength, its further application is limited. Hydroxyethyl cellulose (HEC) was employed in this study to modify the sodium dodecyl sulfate (SDS) based foaming agent to enhance the stability and performance of foamed concrete. The effects of HEC content on foam stability, bleeding, fluidity, strength, water absorption and internal pore structure were systematically investigated. The results indicate that as the HEC content increases, the foam stability improves, while the fluidity and water absorption of the foamed concrete slurry decrease. Compared with the control group (without HEC), the content of 0.15% HEC increased the 28-day compressive strength by 33.66%, reaching 2.75 MPa. Furthermore, HEC optimized the pore structure, significantly reducing the average pore diameter. When the HEC content reached 2%, the proportion of small pores was approximately 99%. These findings suggest that HEC effectively improves the overall performance of foamed concrete, offering a theoretical foundation for its broader application in engineering.

1. Introduction

Foamed concrete has gained wide applications in subgrade backfill, building insulation, and lightweight structural components due to its lightweight nature, strong fluidity, excellent thermal insulation, energy efficiency, and environmental benefits [1-3]. However, despite its advantages, foamed concrete faces significant challenges such as low strength, high water absorption, and poor stability, which limit its engineering applications, especially in scenarios that require high strength and long-term stability [4].

Recent studies have shown that the pore structure of foamed concrete plays a crucial role in its mechanical properties and stability. The formation and retention of foam, as well as the stability during mixing and curing processes, are key factors determining its final performance [5, 6]. Many studies have demonstrated that adding various chemical additives can significantly improve foam stability and mechanical properties. For instance, Chao Liu et al. [7] investigated the effects of hydroxypropyl methylcellulose (HPMC) and silica flour (SF) on the stability, rheology, and printability of foamed concrete. The results showed that HPMC significantly increased the yield stress and plastic viscosity of the concrete. Dong and Zhang [8] explored the combinations of common foaming agents (such as LAS, SDS, and magnesite) with HPMC and found that adding

*Corresponding author: liurg@ujs.edu.cn
[a]orcid.org/0009-0008-1680-6697; [b]orcid.org/0009-0009-9213-0526; [c]orcid.org/0009-0002-7517-4649; [d]orcid.org/0009-0009-8877-1654
DOI: http://dx.doi.org/10.17515/resm2025-488st1017rs

HPMC could effectively reduce the foam bleeding rate. Ailar Hajimohammadi et al. [9] studied the effects of xanthan gum on the viscosity of foaming liquids and foam stability, demonstrating that it significantly increased the liquid viscosity and reduced foam bleeding rate. Han Zhu et al. [10] showed that when the xanthan gum concentration reached 0.5%, the surface tension and foam multiplication of the foaming solution were 28.68×10^{-3} N/m and 21 times, respectively. To further improve foam stability in foamed concrete, researchers have also tested the addition of CO_2 [11], WLP [12], UEO [13], Ca $(OH)_2$ [14], H-SNP [15] and other foam stabilizers [16-18] to enhance foam stability and improve the overall performance of foamed concrete.

While many studies focus on individual additives, research on the synergistic effects of multiple additives on the long-term stability and mechanical properties of foamed concrete is limited. Zhang et al. [19] modified sodium dodecyl sulfate (SDS)-based foaming agents with amphiphilic nano-silica (ANS) and found that ANS significantly improved the microstructure of the foamed concrete. Specifically, the addition of ANS increased the proportion of small pores (less than 500 μm) to about 99%, creating a more uniform pore distribution. This change enhanced both the strength and stability of the foamed concrete. The authors attributed these improvements to the synergistic effect between SDS and ANS, where ANS stabilized the foam structure and prevented pore coalescence during curing. These findings highlight the need for further exploration of additive combinations to optimize foamed concrete's properties for high-performance engineering applications like building insulation and road construction.

In addition to research on additives, the type and selection of foaming agents also play a crucial role in the quality of foamed concrete [20-22]. Li Hou et al. [23] investigated the effects of four types of surfactants (anionic, cationic, nonionic, and amphoteric) as foaming agents on the properties of foamed concrete. They found that SDS exhibited the best stability as a foaming agent. Chao Sun et al. [24] compared synthetic surfactants (SS) with plant-based surfactants (PS) and animal glue/blood-based surfactants (AS), revealing that synthetic surfactants outperformed the others in terms of foam stability and strength. L. Korat and V. Ducman [25] assessed the combination of SDS with hydrogen peroxide (H2O2) as a foaming agent, showing that an appropriate amount of SDS and H2O2 significantly improved the foam stability and durability. However, despite these advancements in the performance of foaming agents and stabilizers, there remains a lack of comprehensive research on the combined effects and interactions of different additives, particularly on the synergistic mechanisms between stabilizers and foaming agents.

Hydroxyethyl cellulose (HEC), a water-soluble polymer, has been widely applied in cement-based materials because it significantly improves their rheological properties and stability. Research has shown that HEC enhances the workability and stability of concrete, promotes uniform pore distribution, and prevents segregation during curing, thereby further improving the material's mechanical properties [26]. However, despite the extensive studies on the use of HEC in cement-based materials, its role in foamed concrete, particularly its synergistic effects with other additives, has not been fully explored.

This study aims to address this gap by systematically investigating the synergistic effects of HEC as a stabilizer and SDS as a foaming agent. Specifically, the study has two main objectives: (1) to examine the impact of different HEC content on foam stability, slurry fluidity, compressive strength, and water absorption in foamed concrete; and (2) to use scanning electron microscopy (SEM) to analyze the pore morphology and size distribution of foamed concrete, revealing the mechanism through which HEC enhances foam stability. By optimizing the HEC content, this study aims to improve the overall performance of foamed concrete, facilitating its broader application in high-rise building insulation, lightweight partition walls, and road construction.

2. Materials and Methods

2.1. Materials

In this study, Ordinary Portland cement (P.O. 42.5) produced by Nanjing Cement Co., LTD was used. The cement's main physical properties and chemical compositions are detailed in Table 1 and Table 2, respectively. Additionally, we employed a commercially available composite foaming agent,

primarily composed of sodium dodecyl sulfate (SDS). The foam stabilizer used was hydroxyethyl cellulose (HEC) with a viscosity of 100,000, and its physical indexes are presented in Table 3. In this paper, H0, H1, H2, H3 and H4 were used to represent the HEC content of 0%, 0.05%, 0.1%, 0.15% and 0.2%, respectively. The percentage range of HEC was determined based on preliminary testing and the recommended range provided in reference [19].

Table 1. Physical properties of cement

Cement Type	Density (kg/m^3)	Specific Surface Area (m^2/kg)	Standard Consistency (%)	Setting Time (min)		Comp. Strength (MPa)		Flexural Strength (MPa)		Stability
				Initial	Final	3d	28d	3d	28d	
P.O 42.5	3100	358	28.3	193	277	30.1	59.6	5.0	8.7	Qualified

Table 2. Chemical composition of cement

Component	CaO	SiO_2	Al_2O_3	Fe_2O_3	MgO	SO_3	Insoluble Residue	Loss on Ignition
Content (%)	64.63	21.96	4.73	3.68	2.59	0.3	0.63	2.89

Table 3. Physical properties of HEC

Code	Molar substitution (M.S.)	Moisture (%)	Water-insoluble substances (%)	Heavy metals (μg/g)	PH	Ash content (%)	Lead (%)
Content	1.8-2.0	≤10	≤0.5	≤20	6.0-8.5	≤5	≤0.001

2.2. Specimen Preparation

In this experiment, the foam was prepared using the pre-foaming method. Firstly, clean water was added to the container according to the prescribed quantity, and hydroxyethyl cellulose (HEC) was added under low-speed stirring. After stirring until all the materials were completely dissolved, the foaming agent was slowly poured into the water according to the quantity to obtain the foaming liquid. Then, the foaming liquid is transported to the foaming machine through the catheter, and the foam is prepared by air compression.

Table 4. Proportions of FC (per m^3)

Group	Wet density (kg/m^3)	Cement (kg)	Water (kg)	Foam (kg)	HEC (g)
H0	700	464	208.8	27.3	0
H1	700	464	208.8	27.3	5.27
H2	700	464	208.8	27.3	10.53
H3	700	464	208.8	27.3	15.8
H4	700	464	208.8	27.3	21.06

In this study, the mix ratio of foamed concrete was designed by controlling the wet density of the slurry, with a water-cement ratio of 0.45, as detailed in Table 4. The preparation process is illustrated in Fig. 1. After mixing the cement slurry, prepared foam was added, and the mixture was stirred to ensure uniformity before being poured into molds for curing. As depicted in the figure, the water and cement were first poured into the mixing bucket sequentially, and the mixture was stirred using a handheld mixer at high speed (600 r/min) for 60 seconds until the cement slurry

was thoroughly blended. Afterward, the prepared foam was added, and the mixture was stirred at low speed (300 r/min) for an additional 90 seconds to ensure uniformity. The preparation was conducted at room temperature (20 ± 2°C). The prepared slurry was then weighed, and once the wet density of the slurry was within 3% of the target wet density, the foamed concrete slurry was poured into prepared molds. The surface of the molds was covered with plastic film to prevent moisture loss. After being placed in a standard curing environment for 48 hours, the specimens were demolded and continued curing until the specified curing period was reached.

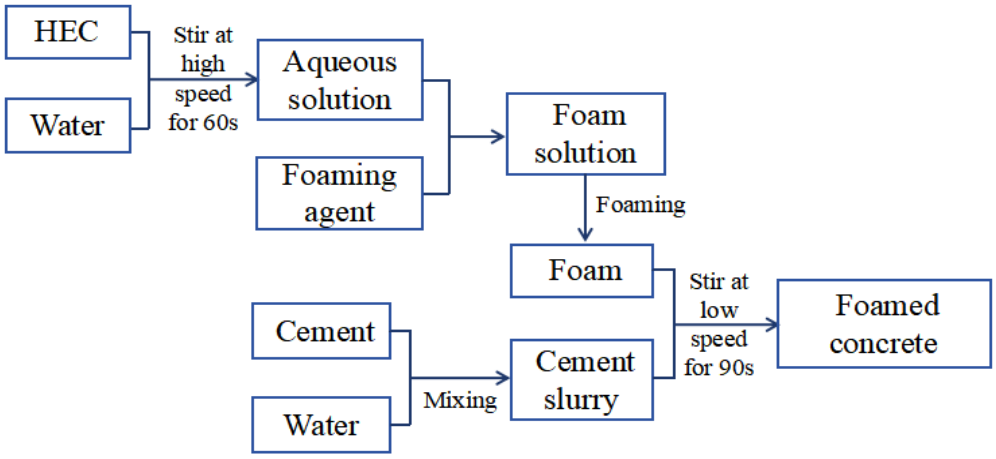

Fig. 1. Preparation process of foamed concrete

2.3. Test Method

2.3.1. Foam Stability Test

Foam stability is a critical factor in ensuring the successful casting of foamed concrete and is primarily evaluated by measuring the water bleeding rate and settlement distance. The testing method is as follows: First, the prepared foam is placed into a 1L container, and the surface is leveled with a spatula. A square piece of paper with a 2cm side length is then placed on top of the foam, and the timer is started. As the foam breaks down, water gradually bleeds out. The exuded water is collected and weighed to calculate the water bleeding rate, which is the ratio of the mass of the exuded water to the original foam mass. Simultaneously, the settlement distance of the foam over 1h is recorded. Each test is repeated three times for different amounts of foam stabilizer added to the foaming agent, and the results' arithmetic average is taken as the final value.

2.3.2. Flowability Test

The freshly mixed foamed concrete is poured into a hollow cylindrical mold (inner diameter of 80 mm, height of 80 mm) placed vertically on a smooth glass plate. After the mold is filled, it is lifted vertically, allowing the foamed concrete to spread naturally on the glass surface. After standing for 1 minute, the maximum horizontal diameter of the spread sample is measured using a vernier caliper, which is taken as the flowability of the material.

2.3.3. Compressive Strength

The 100mm × 100mm × 100mm cube specimen maintained to the specified age is placed in the center of the lower pressure plate of the universal testing machine to ensure that the bearing surface of the specimen is perpendicular to the top surface. A universal testing machine with a measuring range of 50 kN and an accuracy of 0.5% is used to apply pressure at a constant loading rate of 0.2 kN/s to record the maximum pressure value when the specimen is broken. The arithmetic average of the peak strength from three parallel specimens in each group was calculated to determine the unconfined compressive strength of the group.

2.3.4. Water Absorption

The water absorption of foamed concrete was determined according to GB/T 11969-2020 [27]. After 28 days of curing, the specimens were dried in an oven at 105 ℃ until a constant mass was reached, and the dry weight (m_1) was recorded. The specimens were then immersed in water for 1, 3, 5, 7, 12, 24, 36, 48, and 72 hours. After each interval, they were removed, surface water was wiped off, and the specimens were reweighed to obtain the wet weight (m_2). The water absorption of the foamed concrete was calculated as the percentage increase in weight due to water uptake using the following formula (1). The average water absorption value was reported based on at least three specimens.

$$Water\ absorption\ (\%) = \frac{m_2 - m_1}{m_1} \times 100 \quad (1)$$

Where, m_1 is the dry weight of the specimen; m_2 is the wet weight of the specimen after immersion.

3. Results and Discussion

3.1. Foam Stability

Foam stability is a crucial factor influencing the mechanical properties of foamed concrete. The foam stability results, shown in Fig. 2, illustrate the positive effect of increasing HEC content on foam persistence. Foam stability improves with higher HEC content, with the foam lasting nearly intact at higher content (H3 and H4). In contrast, without HEC (H0), most foam dissipates within 1 hour. This suggests that the inclusion of HEC has a substantial positive effect on the long-term stability of the foam.

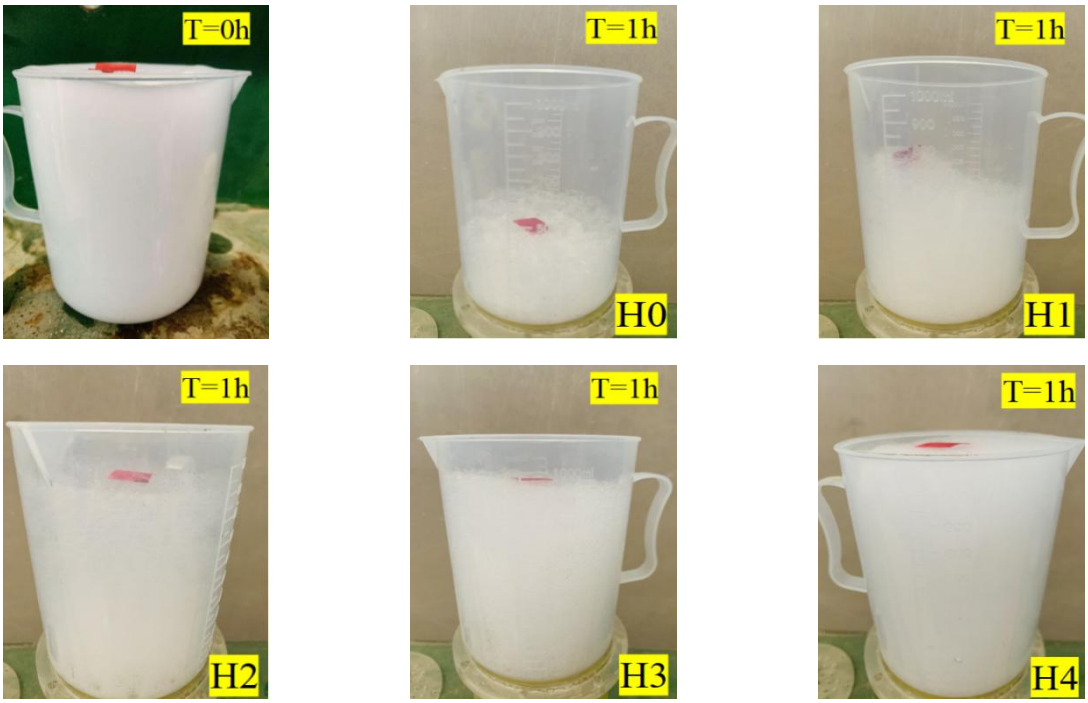

Fig. 2. The stability of foam with different HEC content in air

Fig. 3(a) shows the cumulative bleeding rate of foam with different HEC content in the air. As observed from the figure, the cumulative bleeding rate of foam without HEC (H0) increases significantly over time, exceeding 30% at 240 minutes. In contrast, when the HEC content exceeds 0.15% (H3), the cumulative bleeding rate continues to rise but gradually stabilizes after 60 minutes. Fig. 3(b) shows the cumulative bleeding rate of different groups at 60 minutes. It is evident that the bleeding rate for the control group without HEC (H0) reached 29.7%. However, the content of HEC as a stabilizer reduced the bleeding rates to 15.1%, 5.2%, 2.9%, and 1.4% for H1 through H4, respectively. Fig. 3(b) further illustrates the stabilizing effect of HEC decreases when the

concentration exceeds 0.15% (H3), suggesting an optimal range for HEC content to maximize foam stability.

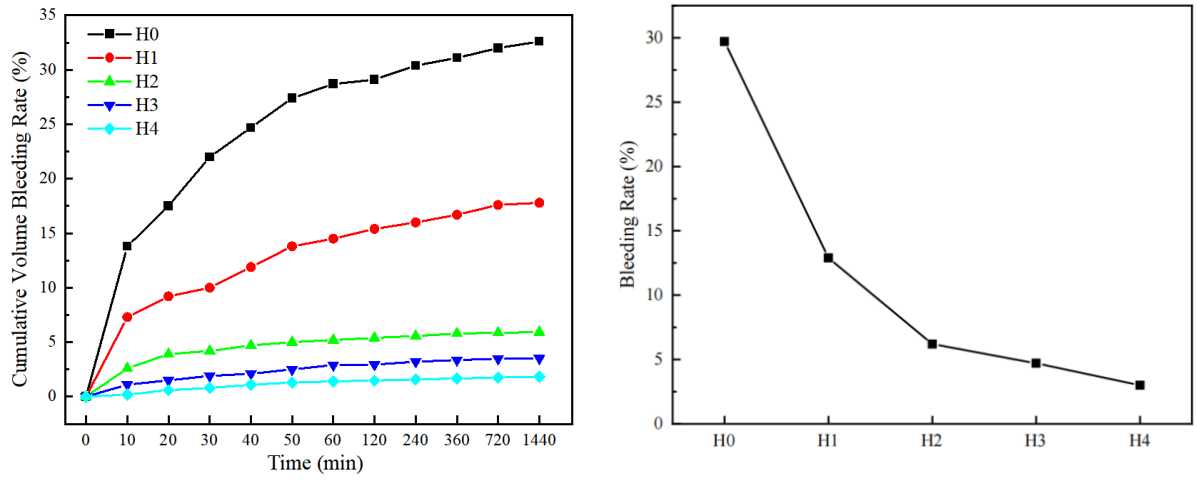

Fig. 3. Change of volume bleeding rate of foamed concrete with time

Experimental results show that incorporating HEC significantly enhances foam stability and reduces foam rupture. This improvement is primarily due to its unique physical and chemical properties, which affect the foam system in several ways. Firstly, HEC is a nonionic, water-soluble polymer with excellent thickening properties. When dissolved in cement paste, HEC forms a high-viscosity solution. This increased viscosity makes the paste more resistant to flow, which slows the rising speed of air bubbles within it. As the bubbles rise more slowly, the chances of bubble collision and coalescence are reduced, helping to maintain foam uniformity and stability. Furthermore, the higher viscosity prevents the rapid rupture of bubbles after their formation, effectively extending the foam's lifespan. Secondly, HEC molecules have hydrophilic hydroxyethyl groups and a hydrophobic cellulose backbone. This unique molecular structure allows HEC to adsorb at the gas-liquid interface of bubbles, forming a protective film around them. This film plays a crucial role in preventing bubble coalescence and rupture, thereby enhancing foam stability [28]. It also helps reduce the effects of surface tension differences, which can cause bubble instability and rupture. Emil D. Manev [29] similarly proposed that a thicker, more uniform film provides greater resistance to external forces, further reducing the likelihood of bubble collapse. Our results support Manev's hypothesis, as higher HEC content led to the formation of more robust protective films around the bubbles.

In addition to HEC's direct stabilizing effects, its synergistic interaction with SDS significantly improves foam performance. Sodium dodecyl sulfate (SDS), an anionic surfactant, reduces surface tension at the air-liquid interface, promoting the formation of smaller, more uniform bubbles. When combined with HEC, SDS molecules adsorb onto the bubble surface, creating a stable interface that prevents bubble rupture. This dual mechanism produces a dynamic stabilization effect, where SDS provides surface-level stability, and HEC reinforces the bulk properties of the foam, collectively enhancing foam preservation.

3.2. Flowability

In practical applications, foamed concrete is typically poured in situ. If the slurry fluidity is too low, it can cause difficulties during mixing and pouring, reducing construction efficiency. Conversely, if the slurry fluidity is too high, it may result in insufficient foam stability, weakening the structure and compromising performance. Therefore, optimizing the balance between fluidity and foam stability is crucial when preparing foamed concrete.

Fig. 4. shows the slurry fluidity of freshly mixed foamed concrete with different HEC contents, while Fig. 5 displays the corresponding flow values. As shown in Fig. 5, it can be seen that the flow values for H0, H1, H2, H3, and H4 are 185 mm, 163 mm, 157 mm, 149 mm, and 128 mm, respectively.

These results demonstrate a clear decrease in slurry fluidity as the HEC content increases. This trend aligns with the findings of Dong and Zhang [8], who reported that stabilizers like HEC increase the viscosity of the cement slurry, leading to reduced flowability. However, unlike other stabilizers such as HPMC, HEC exhibits a stronger ability to balance fluidity and foam stability, making it particularly advantageous for high-performance applications. HEC is a nonionic water-soluble polymer, when dissolved in water, its long-chain molecules unfold to form a three-dimensional network structure. This network interacts with water molecules, significantly increasing the viscosity of the solution. As the HEC content increases, the concentration of HEC molecules in the solution also rises, resulting in a denser network structure.

Fig. 4. Fresh foamed concrete slurry with different HEC content

Furthermore, the high viscosity of HEC enhances the adhesion between solid particles in the slurry, promoting the formation of flocculation structures. These structures further increase the slurry's viscosity and yield stress, making the slurry more viscous and reducing its fluidity. While HEC content reduces fluidity by increasing slurry viscosity, it simultaneously improves foam stability. HEC molecules adsorb onto the surface of air bubbles, forming a viscoelastic film that thickens and strengthens the bubble walls, preventing rupture and coalescence.

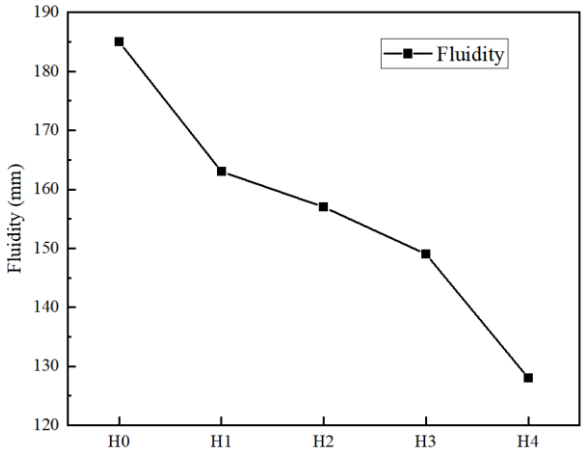

Fig. 5. Fluidity of fresh foamed concrete with different HEC content

The increased viscosity of the slurry also slows the drainage of liquid from the bubble film, reducing the likelihood of thinning and rupture of the foam. From the above, it can be concluded that while HEC has a positive effect on foam stability, this comes at the expense of slurry fluidity. In practical applications, achieving a balance between fluidity and foam stability is crucial. Excessive HEC content can cause the slurry overly viscous, complicating construction operations. Conversely, insufficient HEC content may not adequately stabilize the foam. This can lead to uneven pore structure distribution within the specimen, ultimately resulting in poor mechanical properties of the material. Therefore, optimizing the HEC content is critical to achieving both good workability and desirable physical and mechanical properties in foamed concrete.

3.3. Compressive Strength

The relationship between different HEC contents and the 7-day and 28-day compressive strength of the specimens is shown in Fig. 6. As can be seen from the figure, at 0.15% HEC content (H3), the compressive strength reaches its peak, with 7-day and 28-day compressive strengths of 1.52 MPa and 2.75 MPa, respectively. These values represent increases of 49.02% and 36.14% compared to the control group without HEC (H0). However, when the HEC content increases further to 0.2% (H4), the compressive strength shows a slight decrease. Nonetheless, the 28-day compressive strength remains 33.66% higher than that of the H0 group. This indicates that selecting the optimal HEC content (0.1%-0.15%) is critical to balancing foam stability and mechanical performance. Excessive HEC content, while enhancing foam stability, may lead to over-thickened slurry and uneven pore structure, which negatively impacts load-bearing capacity.

This significant increase aligns with the findings by Zhang et al. [19], who reported that using nano-silica as a stabilizer resulted in a more rounded and uniform pore structure, enhancing the strength of foamed concrete. Similarly, HEC improves the microstructure of foamed concrete by refining pore distribution and enhancing foam stability. Additionally, this study demonstrates that HEC also improves the elasticity and strength of the bubble films, further enhancing the mechanical properties of foamed concrete.

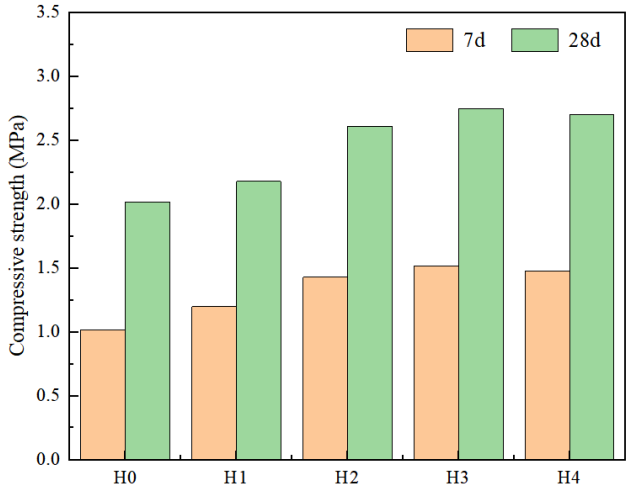

Fig. 6. The compressive strength of foamed concrete with different HEC content

The mechanism underlying these improvements is attributed to the ability of HEC to enhance the strength and elasticity of bubble films. As a result, bubbles are stably encapsulated within the concrete slurry, forming a small and evenly distributed pore structure. This structure helps distribute external stresses uniformly, thereby enhancing the material's overall load-bearing capacity [30]. Similarly, Wei She [31] observed that strengthening the bubble film reduces internal gas diffusion and increases the bubbles' resistance to external disturbances. These findings align with our results, demonstrating that HEC not only reinforces bubble films but also reduces gas escape, which collectively contributes to the improved compressive strength of the foamed concrete. Additionally, as the HEC content increases, the consistency of the solution improves

significantly. This leads to more even distribution of water within the cement paste. As a result, the cement in the material becomes fully hydrated, which further enhances the material's strength.

However, as the HEC content continues to increase, foam stability improves, but bubble size and distribution have already reached stability. This limits any further contribution to compressive strength. Excessive HEC can adsorb and bind moisture from the mixture, inhibiting the cement hydration reaction and reducing the density of the cement paste. Moreover, the stabilizer forms a film at the bubble interface, weakening the bond between the cement particles and the bubbles, which lowers the strength of the interfacial transition zone. Ji and Sun [32] also observed that excessive stabilizer content overly stabilizes the bubbles, preventing their necessary rupture. This leads to excessive porosity, which undermines the compressive strength of the material. In practical applications, maintaining HEC within the range of 0.1%-0.15% achieves the best balance between foam stability, workability, and mechanical performance.

Fig. 7. Failure pattern of specimen

Fig. 7 shows the damage condition of the foamed concrete sample after the compressive strength test. The figure reveals longitudinal cracks and local spalling are present on the surface of the specimen, indicating a typical brittle failure mode. The cracks may be caused by weak interfaces within the foamed concrete, which cannot withstand stress effectively during the loading process and gradually fracture. The propagation path of the cracks is closely related to the material's pore distribution and foam stability. Although HEC was used as a stabilizer in this study to improve foam stability, the interfacial strength may still be insufficient under higher loads, resulting in brittle failure. This phenomenon indicates that the mechanical properties of foamed concrete depend on more than just the material's intrinsic strength. Factors such as pore structure distribution and interfacial bond strength also play a significant role. Therefore, in follow-up studies, the effect of different stabilizer contents on pore structure will be further analyzed to optimize the mechanical performance of foamed concrete.

3.4. Water Absorption

In this study, the immersion test was conducted over a period of 72 hours to evaluate the initial water absorption rate of the specimens. The results provide deeper insights into the long-term performance of the foamed concrete. Fig. 8 shows that foamed concrete exhibited a high-water absorption rate during the initial stage. With the extension of soaking time, the water absorption rate of foamed concrete gradually tended to be stable and showed a gradual decline with the increase of HEC content. After 12h, the water absorption rate of the material gradually slowed down. After 24h immersion, the mass water absorption of 5 groups reached 31.2%, 28.7%, 26%, 19.6% and 16.2%, respectively.

The decline in water absorption with higher HEC content can be attributed to several factors. First, as a thickening agent, HEC increases the viscosity of the cement paste, which helps to evenly disperse air bubbles and prevent them from coalescing and rising. Secondly, the addition of SDS further stabilizes the bubble structure by reducing surface tension. The combination of HEC and

SDS reduces the connectivity of voids within the cement matrix, creating a denser microstructure that limits water penetration. These observations align with the findings of Li et al. [12], who reported that stabilizers improve the homogeneity of pore structures, reducing water pathways and enhancing durability. They also highlighted that stabilizer minimize the formation of micro-cracks, contributing to the long-term durability of cement-based materials. Similarly, this study found that higher HEC content results in a denser cement matrix with fewer micro-cracks, further improving water resistance and overall durability.

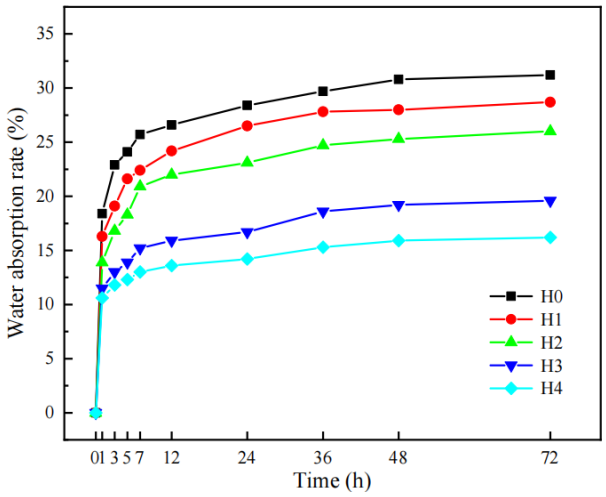

Fig. 8. Water absorption of foamed concrete with different HEC content

3.5. Pore Structure

Numerous studies have demonstrated that the pore structure of foamed concrete plays a crucial role in determining its overall performance. Fig. 9 displays scanning electron microscope (SEM) images reveal the internal pore structure of samples with varying HEC content. Fig. 10 illustrates the pore size distribution calculated using Image-J software. From Fig. 9, it is evident that the internal pore structure undergoes significant changes as the HEC content increases. When no HEC is added, the pores are interconnected and unevenly distributed. At 1% HEC content, pore connectivity decreases, and the number of small pores increases. At 2% HEC content, the pore distribution becomes more uniform, with smaller pore sizes throughout the specimen. As the HEC content increases, the pores become more uniform, the pore walls thinner, and the number of small pores increases. These changes in pore structure have a direct impact on the engineering properties of the material. For instance, in lightweight partition walls and insulation layers, a stable and uniform pore structure reduces thermal conductivity while maintaining structural integrity under load.

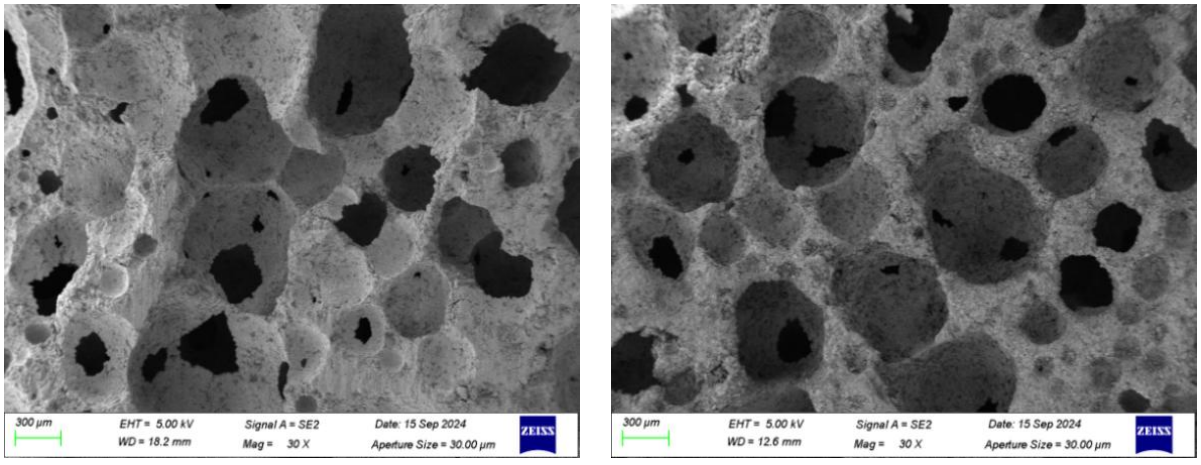

(a) (b)

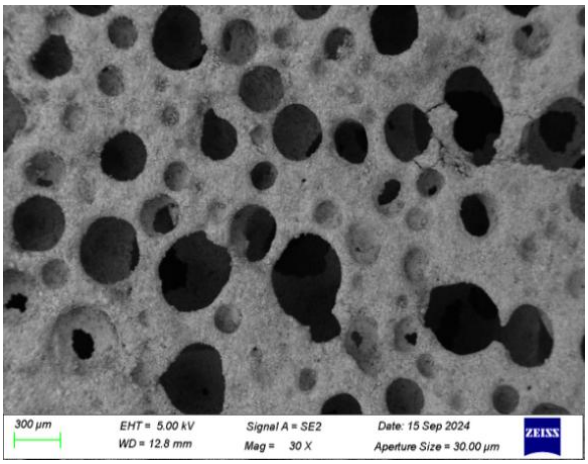

(c)

Fig. 9. SEM scanning images of specimens with different HEC content. (a) HEC=0%; (b) HEC=1%; (c) HEC=2%

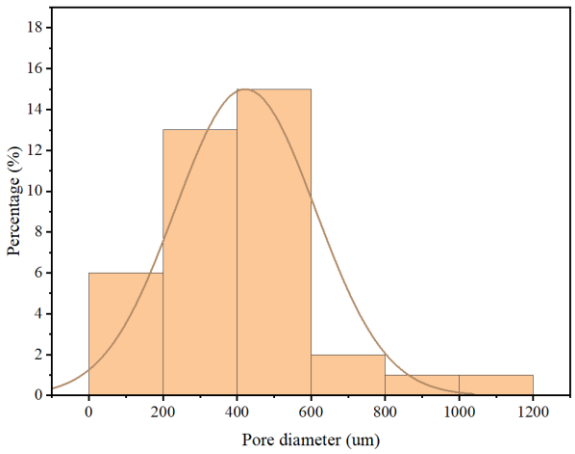

(a)

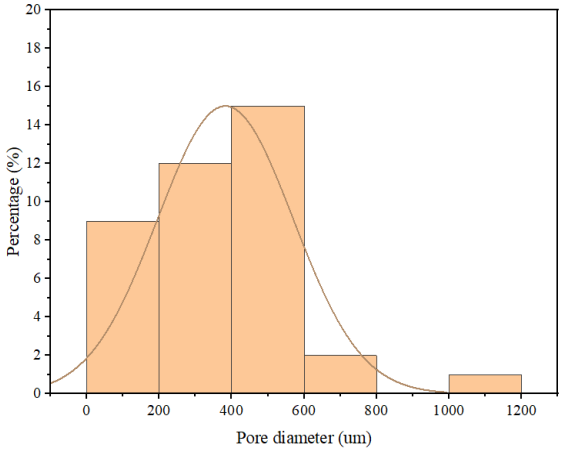

(b)

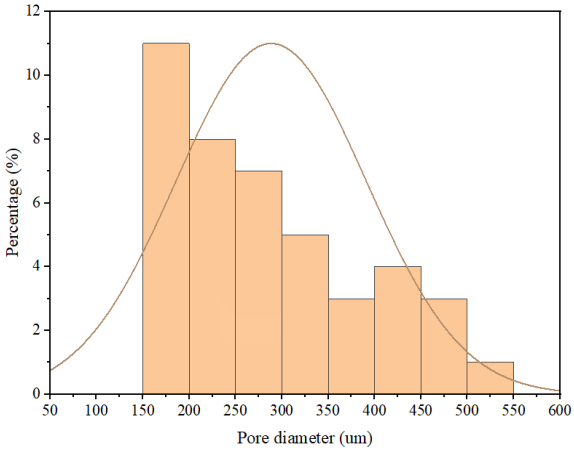

(c)

Fig. 10. Diagrams of the pore size distribution. (a) HEC=0%; (b) HEC=1%; (c) HEC=2%

Furthermore, minimizing the number of large pores significantly decreases water absorption, enhancing the material's long-term durability, particularly in moisture-prone environments. Fig. 10 illustrates the pore size distribution within the specimens with different HEC contents. As shown in Fig. 10, when the HEC content was 0%, 1%, and 2%, the average pore size was 422.18 µm, 382.76 µm, and 288.39 µm, respectively. According to the classification in reference [19], pores

with diameters larger than 500 μm were defined as large-diameter pores, while those smaller than 500 μm were classified as small-diameter pores. In the H0 group, the proportion of small pores was 95.7%, while in the groups with 1% and 2% HEC content, the proportion of small pores increased to 97.2% and 99%, respectively. These changes align with findings by Qiu et al. [21] who reported that the particle size distribution of bubbles gradually Narrows as the stabilizer concentration increases. The analysis of the micro-pore structure reveals that the incorporation of HEC significantly influences the pore size and distribution within foamed concrete. HEC not only reduces the average pore size but also creates a more uniform pore distribution, optimizing the material's microstructure. This regulation of pore size and distribution is crucial for enhancing the material's properties, making it more suitable for engineering applications. Microstructural analysis confirms that HEC plays a critical role in improving the quality and performance of foamed concrete.

4. Conclusions

This study explores the impact of Hydroxyethyl Cellulose (HEC) on the stability, mechanical properties, and pore structure of foamed concrete. A series of experiments were conducted to analyze the effects of varying HEC content on foam stability, slurry fluidity, compressive strength, water absorption, and internal pore structure. The goal was to determine the optimal HEC dosage to improve the overall performance of foamed concrete without compromising its workability. The mechanism of HEC was revealed. The main conclusions reached by this paper are as follows:

- The content of Hydroxyethyl Cellulose (HEC) significantly enhances the stability of foam in foamed concrete. By forming high-viscosity solutions and protective films around bubbles, HEC reduces bubble rupture and coalescence. When the HEC content is 0.15%, the cumulative bleeding rate of the foam decreased from 29.7% without HEC to only 1.4%.
- The use of HEC decreases water absorption in foamed concrete. As the HEC content increases, the material absorbs less water, with the highest HEC group showing only 16.2% water absorption after 24 hours of immersion.
- HEC also improves the compressive strength of foamed concrete. At the HEC content of 0.15%, the 28-day compressive strength increases by 33.66%, reaching 2.75 MPa. The study shows that the optimal HEC content for strength improvement lies between 0.1% and 0.15%.
- While HEC improves stability and strength, excessive content increases viscosity and reduces fluidity, affecting construction workability. Therefore, maintaining an optimal HEC dosage is essential to achieve the desired balance between stability, strength, and fluidity.
- The content of HEC significantly improved the pore structure of foamed concrete. At the HEC content of 2%, the average pore diameter decreased to 288.39 μm, compared to 422.18 μm without HEC, representing a reduction of approximately 31.6%. Additionally, the proportion of small pores increased to 99%, indicating a more uniform pore distribution and a denser overall structure.

This study highlights the significant potential of HEC as a stabilizer for enhancing the stability, strength, and durability of foamed concrete. Future research should focus on evaluating its long-term performance under environmental conditions such as freeze-thaw cycles, wet-dry cycles, and chemical exposure, which are critical for ensuring material durability in practical applications. From a practical standpoint, HEC-enhanced foamed concrete offers a cost-effective and sustainable solution for lightweight, durable, and moisture-resistant construction materials. Its ability to refine pore structure, reduce water absorption, and improve compressive strength makes it ideal for energy-efficient buildings, thermal insulation systems, and lightweight partition walls.

References

[1] Liu M, Wang J, Wang C, et al. Stress-Solid Materials-Voids interaction of foamed concrete in isotropic compression [J]. Construction and Building Materials, 2022, 358. https://doi.org/10.1016/j.conbuildmat.2022.129468

[2] Zhang H, Wang J, Liu Z, et al. Strength characteristics of foamed concrete under coupling effect of constant compressive loading and freeze-thaw cycles [J]. Construction and Building Materials, 2024, 411. https://doi.org/10.1016/j.conbuildmat.2023.134565

[3] Zhang H, Wang J, Wang C, et al. Using Foamed Concrete Layer to Optimize the Design of Pavement and Subgrade Structures: from the Perspectives Economy and Durability [J]. Arabian Journal for Science and Engineering, 2023, 48(10): 12859-74. https://doi.org/10.1007/s13369-023-07606-1
[4] Awang H, Azree M, Mydin O, et al. Effects of Fibre on Drying Shrinkage, Compressive and Flexural Strength of Lightweight Foamed Concrete [J]. Advanced Materials Research, 2012, 587: 144-9. https://doi.org/10.4028/www.scientific.net/AMR.587.144
[5] Nguyen T T, Bui H H, Ngo T D, et al. Experimental and numerical investigation of influence of air-voids on the compressive behaviour of foamed concrete [J]. Materials & Design, 2017, 130: 103-19. https://doi.org/10.1016/j.matdes.2017.05.054
[6] Nambiar E K K, Ramamurthy K. Air-void characterisation of foam concrete [J]. Cement and Concrete Research, 2007, 37(2): 221-30. https://doi.org/10.1016/j.cemconres.2006.10.009
[7] Liu C, Wang X, Chen Y, et al. Influence of hydroxypropyl methylcellulose and silica fume on stability, rheological properties, and printability of 3D printing foam concrete [J]. Cement and Concrete Composites, 2021, 122. https://doi.org/10.1016/j.cemconcomp.2021.104158
[8] Dong S F, Zhang W. Study on Foaming Agent Foam Ability and Stability for Foam Concrete [Z]. Aarchitecture, building materials and engineering management, PTS 1-4. 2013: 1304-7. https://doi.org/10.4028/www.scientific.net/AMM.357-360.1304
[9] Hajimohammadi A, Ngo T, Kashani A. Sustainable one-part geopolymer foams with glass fines versus sand as aggregates [J]. Construction and Building Materials, 2018, 171: 223-31. https://doi.org/10.1016/j.conbuildmat.2018.03.120
[10] Zhu H, Chen L, Xu J, et al. Experimental study on performance improvement of anionic surfactant foaming agent by xanthan gum [J]. Construction and Building Materials, 2020, 230. https://doi.org/10.1016/j.conbuildmat.2019.116993
[11] Zhang Y M, Jiang Y, Ling T C. Use of CO2 as a controlled foam stabilizer to enhance pore structure and properties of foamed concrete [J]. Cement and Concrete Composites, 2024, 145. https://doi.org/10.1016/j.cemconcomp.2023.105356
[12] Li G Y, Tan H B, He X Y, et al. Research on the properties of wet-ground waste limestone powder as foam stabilizer in foamed concrete [J]. Construction and Building Materials, 2022, 329. https://doi.org/10.1016/j.conbuildmat.2022.127203
[13] Chen H G, Liang K K, Chow C L, et al. Enhancing the engineering performance of lightweight limestone calcined clay cement concrete using used engine oil as a foam stabilizer [J]. Journal of Building Engineering, 2024, 95. https://doi.org/10.1016/j.jobe.2024.110187
[14] Xiong Y L, Li B L, Chen C, et al. Properties of foamed concrete with Ca(OH)₂ as foam stabilizer [J]. Cement and Concrete Composites, 2021, 118. https://doi.org/10.1016/j.cemconcomp.2021.103985
[15] Song N, Li Z H, Yi W M, et al. Properties of foam concrete with hydrophobic starch nanoparticles as foam stabilizer [J]. Journal of Building Engineering, 2022, 56. https://doi.org/10.1016/j.jobe.2022.104811
[16] Fan C, Wu R, Huang X, et al. Preparation and characterization of the lightweight concrete produced by H_2O_2 chemical foaming in situ [J]. Journal of Functional Materials, 2016, 47(5): 5129-32.
[17] Zhang X Z, Yang Q, Li Q F, et al. Effect of Phenolic Particles on Mechanical and Thermal Conductivity of Foamed Sulphoaluminate Cement-Based Materials [J]. Materials 2019, 12(21). https://doi.org/10.3390/ma12213596
[18] Jiang S, Wang L, Feng K. Compound modified experiment of protein-concrete foaming agent [J]. Journal of Functional Materials, 2015, 46(9): 09056-61.
[19] Zhang C, Fan D, Lu J-X, et al. Ultra-stable foam enabled by nano silica engineering for foam concrete improvement [J]. Cement and Concrete Composites, 2024, 150: 105575. https://doi.org/10.1016/j.cemconcomp.2024.105575
[20] Hou L, Li J, Lu Z Y, et al. Influence of foaming agent on cement and foam concrete [J]. Construction and Building Materials, 2021, 280. https://doi.org/10.1016/j.conbuildmat.2021.122399
[21] Qiu Y Q, Zhang L J, Chen Y S, et al. Experimental Study on Application Performance of Foamed Concrete Prepared Based on a New Composite Foaming Agent [J]. Advances in materials science and engineering, 2022, 2022. https://doi.org/10.1155/2022/7217479
[22] Panesar D K. Cellular concrete properties and the effect of synthetic and protein foaming agents [J]. Construction and Building Materials, 2013, 44: 575-84. https://doi.org/10.1016/j.conbuildmat.2013.03.024
[23] Hou L, Li J, Lu Z, et al. Influence of foaming agent on cement and foam concrete [J]. Construction and Building Materials, 2021, 280: 122399. https://doi.org/10.1016/j.conbuildmat.2021.122399
[24] Sun C, Zhu Y, Guo J, et al. Effects of foaming agent type on the workability, drying shrinkage, frost resistance and pore distribution of foamed concrete [J]. Construction and Building Materials, 2018, 186: 833-9. https://doi.org/10.1016/j.conbuildmat.2018.08.019

[25] Ducman V, Korat L. Characterization of geopolymer fly-ash based foams obtained with the addition of Al powder or H2O2 as foaming agents [J]. Materials Characterization, 2016, 113: 207-13. https://doi.org/10.1016/j.matchar.2016.01.019
[26] Wang H, Wei X, Du Y, et al. Effect of water-soluble polymers on the performance of dust-suppression foams: Wettability, surface viscosity and stability [J]. Colloids and Surfaces A: Physicochemical and Engineering Aspects, 2019, 568: 92-8. https://doi.org/10.1016/j.colsurfa.2019.01.062
[27] Foaming agents for foamed concrete: [S]. Ministry of Industry and Information Technology, People's Republic of China, 2013:
[28] Fameau A-L, Salonen A. Effect of particles and aggregated structures on the foam stability and aging [J]. Comptes Rendus Physique, 2014, 15(8): 748-60. https://doi.org/10.1016/j.crhy.2014.09.009
[29] Manev E D, Nguyen A V. Critical thickness of microscopic thin liquid films [J]. Advances in Colloid and Interface Science, 2005, 114-115: 133-46. https://doi.org/10.1016/j.cis.2004.07.013
[30] Yekeen N, Idris A K, Manan M A, et al. Bulk and bubble-scale experimental studies of influence of nanoparticles on foam stability [J]. Chinese Journal of Chemical Engineering, 2017, 25(3): 347-57. https://doi.org/10.1016/j.cjche.2016.08.012
[31] She W, Du Y, Miao C, et al. Application of organic- and nanoparticle-modified foams in foamed concrete: Reinforcement and stabilization mechanisms [J]. Cement and Concrete Research, 2018, 106: 12-22. https://doi.org/10.1016/j.cemconres.2018.01.020
[32] Ji Y C, Sun Q J. The Stabilizing Effect of Carboxymethyl Cellulose on Foamed Concrete [J]. International Journal Of Molecular Sciences, 2022, 23(24). https://doi.org/10.3390/ijms232415473

Research on Engineering Structures & Materials
www.jresm.org
MIM Research Group

Research Article

The effect of multi-component composite foam stabilizers on the performance of foam concrete

Qunyu Chen*[,a], Qihao Wang[b]

School of Chemical Engineering, Xuzhou College of Industrial Technology, Xuzhou, 221140, China

Article Info

Article History:

Received 21 Dec 2024

Accepted 08 Mar 2025

Keywords:

Multi-component composite stabilizer;
Foam concrete;
Porosity structure;
Performance enhancement

Abstract

Foam concrete, as a lightweight and environmentally friendly building material, has broad applications in construction, insulation, and other fields. However, issues such as uneven pore structure and insufficient mechanical properties limit its performance and wider adoption. To solve these problems, this study investigates the effects of three foam stabilizers (HPMC, XG, PAM) on foam stability, compressive strength, and dry density of foam concrete through single-factor and orthogonal experiments. A composite stabilizer formulation (HPMC 0.1%, XG 0.06%, PAM 0.03%) is proposed, significantly enhancing the pore structure, stability, compressive strength, and cost-efficiency of foam concrete. The optimized formulation achieves a 28-day compressive strength of 4.45 MPa, representing a 35.26% improvement compared to single stabilizers, while reducing the overall stabilizer amount. Water absorption and SEM pore size analyses confirm the optimized pore structure, with pore sizes mainly concentrated in the 0-400 μm range, effectively reducing large pores. These findings provide critical insights into enhancing the mechanical properties and durability of foam concrete, offering a practical approach to developing more efficient, cost-effective, and sustainable building materials with broad engineering application potential in construction and thermal insulation systems. For future applications, the proposed composite stabilizer formulation could be adapted for use in high-strength foam concrete and specialized construction areas, such as fire-resistant building materials, to optimize performance and reduce costs.

1. Introduction

During Foam concrete is a lightweight, energy-efficient, and environmentally friendly building material that has gained widespread use in construction, thermal insulation, soundproofing, and seismic applications in recent years [1, 2]. However, its broader adoption is hindered by several limiting factors, such as low strength, high water absorption, and poor durability [3, 4]. Research has shown that the performance of foam concrete is largely dependent on its internal pore structure, particularly factors such as foam stability, pore uniformity, and pore size distribution [5, 6]. Therefore, producing a sufficient amount of foam that remains stable for an extended period is crucial for improving the performance of foam concrete. Foam stabilizers are essential additives in foam concrete production. They can effectively prevent the breakage or coalescence of foam bubbles during mixing, transportation, and curing by reducing the surface tension of the bubbles and enhancing the stability of the foam film. Commonly used foam stabilizers include polymer-based stabilizers [7], surfactant-based stabilizers [8-10], particulate stabilizers [11, 12], and composite stabilizers [13, 14]. Among these, surfactants are particularly favored in foam concrete preparation due to their excellent wettability and interfacial activity.

*Corresponding author: cqy@mail.xzcit.cn
[a]orcid.org/0009-0009-0828-2827; [b]orcid.org/0009-0006-9988-9509
DOI: http://dx.doi.org/10.17515/resm2025-585ma1221rs

Numerous studies have investigated the effects of single foam stabilizers on foam stability and concrete performance. For example, Ailar Hajimohammadi et al. [15] found that adding xanthan gum, a thickening agent, increased the compressive strength of mechanically foamed samples by 34% and chemically foamed samples by approximately 20%. Yuanliang Xiong's research [16] showed that the carboxyl group (-COOH) in formic acid enhances foam drainage by absorbing water, though excessive amounts reduce foam stability. Similarly, S. S. Sahu [17] observed that incorporating 0.2% carboxymethyl cellulose (CMC) into a sodium lauryl sulfate (SLS) solution increased viscosity by 134%, reduced bubble size, and improved the compressive strength by approximately 20%. Shizhao Yang et al. [18] reported that adding 0.2% hydroxypropyl methylcellulose (HPMC) to low-density foam concrete increased compressive strength by 27.22%. Dongyu Chen [19] used waste cooking oil to produce sodium oleate (SO), improving the pore structure and mechanical properties of foam concrete. While these studies demonstrate that single foam stabilizers can enhance foam concrete performance, challenges such as high dosage requirements, high costs, and limited applicability remain [20].

To address the limitations of single foam stabilizers, researchers have increasingly developed multi-component composite foam stabilizers, leveraging the synergistic effects of various components to enhance foam stability and uniformity. Juan He et al. [21] combined α-olefin sulfonate (AOS), sodium dodecyl sulfate (K12), fatty alcohol polyoxyethylene ether sulfate (AES), and silicone resin polyether emulsion FM-500 (MPS) to prepare foam stabilizers, identifying AOS as the component providing the best foam stability. Yuanliang Xiong [22] proposed a strategy to modify foam using nano-alumina (NA), and experiments indicated that NA significantly reduced the drainage of foam and improved foam stability. Furthermore, Juan He et al. [23] developed a highly effective multi-component composite foaming agent (CFA) that produced foam with no settling or liquid exudation within one hour, while also optimizing the pore structure and mechanical properties of the foam concrete. Although significant progress has been made in the development of multi-component composite foam stabilizers, many challenges remain unresolved. For instance, optimizing the composition and application methods of composite foam stabilizers to comprehensively enhance the overall performance of foam concrete is still a pressing issue.

In this study, a novel composite foam stabilizer was developed by combining an anionic surfactant (AOS) with hydroxypropyl methylcellulose (HPMC), xanthan gum (XG), and polyacrylamide (PAM) under the premise of economic and environmental sustainability. The research investigates the effects of different foam stabilizers on foam stability and foam concrete performance, aiming to clarify their mechanisms in optimizing pore structure, improving mechanical properties, and ensuring long-term stability. By screening various functional components and employing orthogonal experimental design, the study systematically analyzes the regulatory effects of composite foam stabilizers on the mechanical strength and pore size distribution of the specimens. The optimal formulation is determined to provide theoretical guidance and technical support for improving the performance of foam concrete and advancing the practical application of foam stabilizers in engineering.

2. Materials and methods

2.1. Materials

The cement used in this experiment is ordinary Portland cement (OPC) with a grade of 42.5, produced by Anhui Conch Cement Company Limited. Its physical properties are shown in Table 1. To reduce production costs and support the recycling of industrial waste, 40% of the cement was replaced with fly ash as the binder material. Preliminary trials showed that this proportion effectively balanced cost reduction, improved material properties, and ensured sufficient workability. The main technical parameters of the fly ash are presented in Table 2. The foaming agent used in the experiment is a commercially available anionic surfactant, with sodium α-alkyl sulfonate (AOS) as the primary component. The key technical specifications of the foaming agent are provided in Table 3.

Three types of foam stabilizers were used in this study: Hydroxypropyl methylcellulose (HPMC), a white fibrous or granular powder with a viscosity of 100,000 mPa·s and a density of 1.39 g/m^3;

Xanthan gum (XG) is a high molecular weight polysaccharide polymer produced through pure culture fermentation of microorganisms, using starch as the main raw material. It appears as an off-white or light-yellow powder; and Polyacrylamide (PAM), a water-soluble polymer compound in the form of white granules or powder at room temperature.

Table 1. Physical properties of cement

Cement Type	Density (kg/m³)	Specific Surface Area (m²/kg)	Standard Consistency (%)	Setting Time (min)		Compressive Strength (MPa)		Flexural Strength (MPa)		Stability
				Initial	Final	3d	28d	3d	28d	
P.O 42.5	3100	358	28.3	193	277	30.1	59.6	5.0	8.7	Standard

Table 2. Main technical parameters of fly ash

LOI (%)	Water Demand Ratio (%)	Activity Index (%)	CaO (%)	SiO_2 (%)	Al2O3 (%)	MgO (%)	SO_3 (%)	Fe_2O_3 (%)
4.67	95	70	2.60	48.54	34.68	0.459	1.12	5.23

Table 3. Main technical indicators of foaming agent

Total Solids Content (%)	Activity Content (%)	Unsulfated Matter (%)	Sulfate (%)	Free Alkali	pH
95	91-94	≤5.5	≤5.5	≤0.9	8.5-11.5

2.2. Test Scheme

2.2.1. Single Factor Test

Based on previous research and existing literature [15, 18], this study utilized three foam stabilizers (HPMC, XG, and PAM) at different dosages. First, a single-factor experiment was conducted to examine the effects of various stabilizer dosages on foam stability and mechanical strength, with the experimental conditions outlined in Table 4. Building on these results, an orthogonal experiment was then performed to evaluate the synergistic effects of combining multiple stabilizers, focusing on their impact on mechanical strength and pore size distribution. Finally, the optimal composite formulation was determined, achieving the best balance between foam performance, material properties, and cost-effectiveness.

Table 4. Single factor test scheme

Series	Foam stabilizer	Concentration (wt %)
Ref	-	-
A	HPMC	0.1, 0.2, 0.3, 0.4
B	XG	0.05, 0.1, 0.15, 0.2
C	PAM	0.02, 0.04, 0.06, 0.08

2.2.2. Orthogonal Test

Based on the results of the preliminary single-factor experiments, a three-factor, three-level L9(3^3) orthogonal experiment was conducted to optimize the formulation of foam stabilizers. The concentrations of HPMC, XG, and PAM were selected as the experimental factors, with their levels

refined based on the single-factor results. The 28-day compressive strength was used as the primary evaluation index, and the optimal combination of the three foam stabilizers was determined.

2.3. Sample Preparation

The foam was produced using the pre-foaming method. First, the foaming agent was dissolved in water at a dilution ratio of 1:80, which was selected based on preliminary trials to achieve optimal foam stability and workability. Then, the foam stabilizers were added in the specified proportions and thoroughly mixed using a magnetic stirrer at a speed of 120-150 r/min. After stirring, the mixture was allowed to stand for 10 minutes to form the foaming solution. The foaming solution was then injected into the foaming machine, where foam was generated by air compression.

Water, cement, and fly ash were sequentially added into the mixing container, with a water-to-binder ratio of 0.45. A handheld mixer was used to stir at 120 r/min for 120s, followed by stirring at 300 r/min for 90s to form a uniform cement-based slurry. The prepared foam was then introduced into the slurry, and the mixture was stirred at 120 r/min for 60s to obtain a homogeneous foam concrete slurry.

The slurry was poured into the mold up to about half of its height, and the sides of the mold were gently tapped. The slurry was then poured further until it slightly exceeded the top surface of the mold. After gently vibrating the mold again, the surface was leveled with a spatula. The top of the mold was covered with plastic wrap, and labels were affixed. Finally, the mold was placed in a standard curing room (20 ± 2°C, RH ≥ 95%) for curing for 28 days. The specific preparation process for the specimens is shown in Fig. 1.

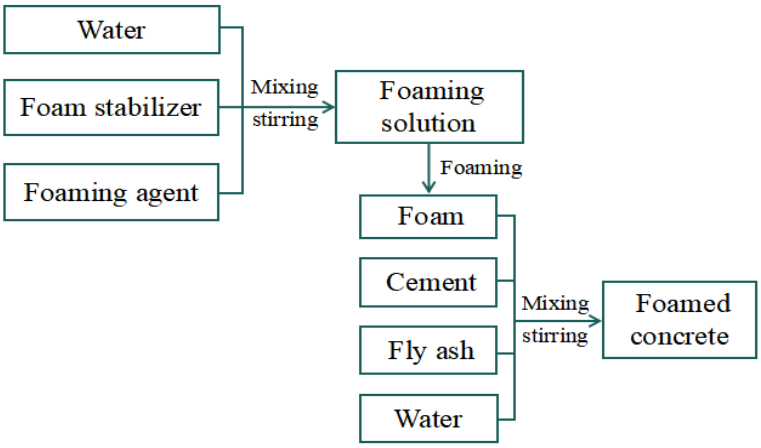

Fig. 1. Flowchart of sample preparation process

2.4. Test Methods

2.4.1. Foam Stability

Foam stability is a critical factor affecting the performance of foam concrete. In this study, the 1-hour water bleeding rate and settlement distance were used as evaluation indicators. The testing method was based on the standard "Foaming Agents for foamed concrete" (JCT 2199-2013) [24]. The prepared foam was placed into a 1L glass beaker and left to stand at room temperature for 1 hour. After this period, the water separated from the foam was collected and weighed. The water bleeding rate was calculated as the ratio of the water volume to the initial mass of the foam. The settlement distance was measured as the height difference between the foam's initial position and its descent within 1 hour, indicating how far the foam dropped. Each group of tests was repeated three times, and the average value was calculated to ensure data accuracy and repeatability.

2.4.2. Compressive Strength

Unconfined compressive strength is the most important indicator for evaluating the mechanical properties of foam concrete. For the compressive strength test, cubic specimens of 100mm ×

100mm × 100mm, cured to the specified age, were taken out and visually inspected. The surface of each specimen must be smooth, free from cracks or significant defects. The specimen was then placed at the center of the lower platen of the material testing machine, and loading was applied at a rate of 1mm/min until failure occurred. The maximum load at failure was recorded, and the unconfined compressive strength for the group of specimens was calculated as the arithmetic average of three parallel tests.

2.4.3. Dry Density

For each group, three foam concrete specimens are selected and removed from the curing environment. The specimens are then placed in a forced-air drying oven and dried at 60 ± 5°C for 24h. After that, the temperature is raised to 105 ± 5°C, and drying continues until a constant mass m_0 is achieved (when the difference between two consecutive weight measurements is less than 0.1g). Next, the length, width, and height of the specimens are measured using a vernier caliper with an accuracy of 0.01mm, and the volume V of the specimens is calculated. Finally, the dry density of the foam concrete is determined using Equation (1).

$$\rho_0 = \frac{m_0}{V} \tag{1}$$

where: ρ_0 is dry density of the foam concrete specimen (kg/m^3); m_0 is dried mass of specimen (kg); V is volume of specimen (m^3).

2.4.4. Water Absorption

Water absorption tests were conducted by immersing the foam concrete samples in water and measuring their weight gain over time. The specimens were dried to a constant weight before immersion, then periodically removed from water, surface-dried, and weighed at designated time intervals (1, 3, 5, 7, 12, 24, and 48 hours). The water absorption rate was calculated as the percentage increase in weight relative to the initial dry weight.

2.4.5. Pore Structure

The pore structure parameters were tested using small specimens with a side length of 10 mm and a thickness of 3 mm. After cutting, the samples were placed in a drying oven and dried at low temperature until they reached a constant weight. The cross-sectional surfaces of the samples were then lightly polished to obtain a clear surface. After gold sputtering, the specimens were vacuumed and placed under a scanning electron microscope (SEM) for imaging. Pore analysis was performed on the acquired images using Image-J software.

3. Results and discussions

3.1 Foam Stability of Single-Component Foam Stabilizer

Fig. 2 illustrates the influence of three different foam stabilizers on foam stability. The results indicate that as the concentration of the stabilizers increases, both the foam accumulated bleeding rate and settlement distance decrease significantly. As shown in Fig. 2(a), HPMC notably improves foam stability and maintains its excellent stabilizing effect even at higher concentrations. When the HPMC dosage reaches 0.3%, the foam accumulated bleeding rate decreases to 3.69%, and the settlement distance reduces to 1.56 mm, representing a 93.46% improvement in foam stability compared to the case without stabilizers. This phenomenon can be attributed to the unique properties of HPMC, a non-ionic polymer material. Its molecular structure is rich in hydroxyl (-OH) and methoxy (-OCH_3) groups. These groups can form hydrogen bonds with water molecules, which significantly increases the viscosity of the slurry and reduces the accumulated bleeding rate. Additionally, the dense protective film formed by HPMC on the bubble surface effectively prevents bubble rupture and coalescence, further enhancing foam stability.

As shown in Fig. 2(b), with the increase in XG concentration, foam stability first decreases significantly and then stabilizes. When the XG concentration rises from 0% to 0.15%, the foam drainage rate decreases by 15.9%, and the settlement distance reduces by 7.72 mm. XG, as a thickening agent, primarily enhances foam stability by increasing the viscosity of the slurry, which

reduces water migration. However, as foam viscosity continues to rise, the effect of inhibiting bubble rupture and water migration reaches a saturation point, leading to stabilization of the foam structure [25]. Consequently, the improvement in foam stability becomes less pronounced. When the XG concentration increases further to 0.2%, the foam accumulated bleeding rate and settlement distance decrease by only 0.68% and 0.7 mm, respectively.

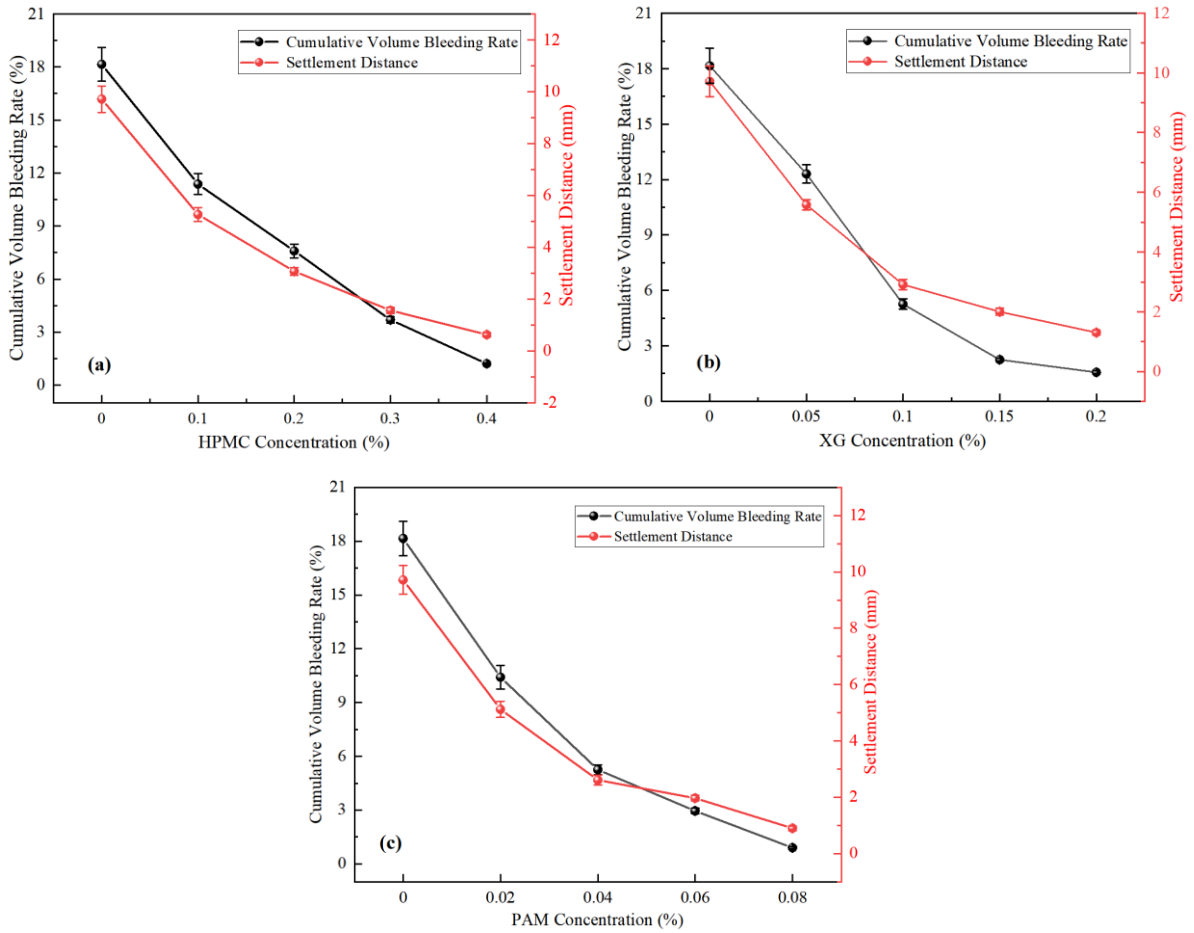

Fig. 2. Effect of foam stabilizer on the foam property (a) HPMC; (b) XG; (c) PAM

As shown in Fig. 2(c), with the increase in PAM concentration, foam stability improves significantly. Even at lower concentrations, foam performance is notably enhanced, resulting in a more uniform and finer foam. At a PAM concentration of just 0.04%, the foam accumulated bleeding rate and settlement distance decrease by 71.07% and 73.14%, respectively, compared to when no foam stabilizer is used. This improvement is primarily due to the amide groups (-$CONH_2$) in the PAM molecules, which form hydrogen bonds with water molecules. This significantly enhances the water retention capacity of the slurry, reducing water migration and minimizing the drainage phenomenon. Additionally, the long-chain molecular structure of PAM forms a protective film on the bubble surface, effectively preventing bubble rupture and enhancing the structural integrity of the foam. As the PAM concentration increases further, foam stability continues to improve. However, excessively high concentrations may lead to over-thickening of the slurry, which inhibits foam formation and affects overall foam quality.

Although each of the three foam stabilizers offers distinct advantages, they also have limitations when used individually. For instance, while HPMC significantly enhances foam stability, it is costly and requires large quantities. XG's stabilizing effect is limited and diminishes as its concentration increases. PAM is effective at low concentrations, but excessive use can lead to over-thickening, which negatively affects foam quality. To overcome these limitations and reduce costs, this study employs an orthogonal experiment. The goal is to systematically explore the synergistic effects and optimal ratios of the three stabilizers, ultimately achieving a comprehensive improvement in foam stability.

3.2. Mechanical Property of Foam Concrete

The effect of foam stabilizer concentration on the mechanical strength of foam concrete is shown in Fig. 3. Over time, the compressive strength of all samples increased to varying degrees. As seen in Fig. 3(a), with the increase of HPMC concentration, the compressive strength of the foam concrete at both 7 and 28 days showed a significant upward trend. When the HPMC concentration reached 0.3%, the 7d and 28d compressive strengths increased by 42.59% and 36.23%, respectively, compared to the 0% concentration. However, when the HPMC concentration continues to increase, the improvement of compressive strength gradually flattens out. This may be due to the thickening effect of high HPMC concentrations, which raises the viscosity of the slurry and interferes with the cement hydration process, thereby limiting further strength enhancement. Literature [18] also indicates that under the same water-to-cement ratio, excessive addition of HPMC increases the viscosity of the slurry, making mixing more difficult and potentially reducing the strength of the specimens.

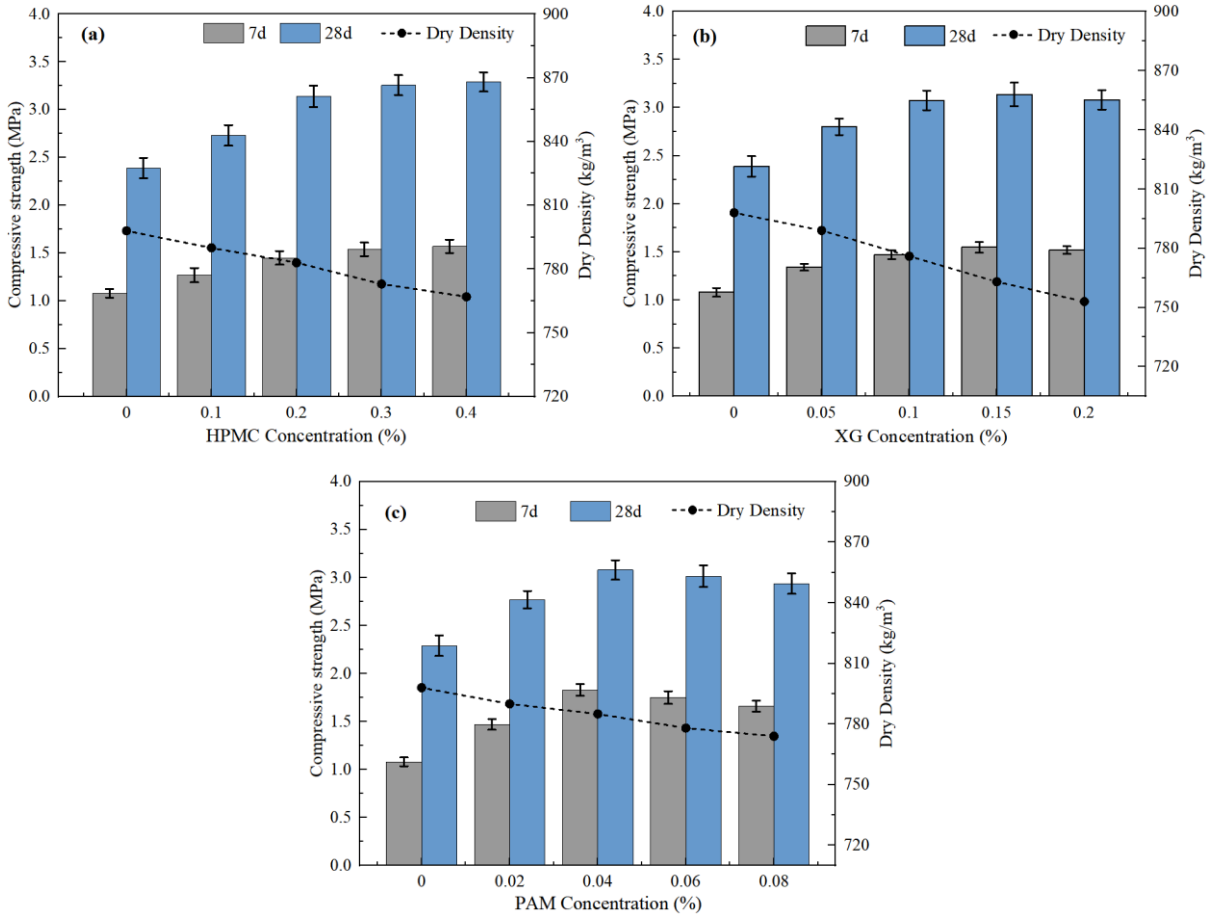

Fig. 3. Effect of foam stabilizers on the foam property (a) HPMC; (b) XG; (c) PAM

Additionally, as shown in Fig. 3(b), increasing the XG concentration also contributes to enhancing the compressive strength of foam concrete. When the XG concentration increased from 0% to 0.15%, the 28d compressive strength increased from 2.39 MPa to 3.14 MPa, and the 7d compressive strength rose from 1.08 MPa to 1.55 MPa, showing a noticeable improvement. However, as the XG concentration continued to increase, there was a slight decrease in strength, indicating that the thickening effect of XG reaches a saturation point. This is because XG, as a water-soluble polymer, enhances the slurry's encapsulating ability and the stability of bubbles through its thickening effect. This results in a more uniform and finer foam structure, which in turn improves material strength. However, excessive XG can reduce slurry flowability, leading to uneven bubble distribution and the formation of large pores and interconnected voids. This ultimately lowers the compressive strength of the material.

In Fig. 3(c), the effect of PAM concentration on the compressive strength of foam concrete also follows a certain trend. As the PAM concentration increases, the compressive strength of foam concrete gradually improves, especially at lower concentrations, where the foam performance is significantly enhanced. When the PAM concentration reaches 0.04%, the 7d and 28d compressive strengths reach their maximum values, increasing by 69.44% and 34.93%, respectively, compared to samples without stabilizer. This enhancement is due to PAM's long-chain structure and amide groups, which form hydrogen bonds with water molecules. This improves the slurry's water retention and viscosity, stabilizing the foam and creating a more uniform pore structure. At the optimal concentration, PAM effectively balances foam stability and slurry workability. However, when the PAM concentration is too high, the slurry becomes excessively viscous, potentially inhibiting foam formation and negatively affecting the final strength of the foam concrete. The compressive strength is improved by reducing large pores and interconnected voids.

As seen in Fig. 3, with the increase in the concentration of foam stabilizers concentration, the apparent dry density of the specimens shows a decreasing trend. This indicates that the thickening and stabilizing effects of the foam stabilizers delay bubble rupture and collapse, leading to a higher number of uniformly distributed bubbles in the slurry, which in turn reduces the dry density of the material. This finding is consistent with the conclusions of other researchers who have controlled the apparent dry density of foam concrete by adjusting the foam content [26-28]. In contrast, due to the relatively weak thickening effect of PAM, its impact on reducing dry density is less pronounced compared to XG and HPMC. However, the weaker thickening effect of PAM actually benefits the flowability and uniform distribution of the slurry. Additionally, at lower concentrations, PAM can still effectively reduce the risk of bubble rupture and collapse, demonstrating good economic feasibility and applicability.

The concentration of foam stabilizers has an optimal range for improving the mechanical strength of foam concrete. Both excessively high and low concentrations can reduce strength enhancement. Therefore, selecting the right stabilizer concentration is key to optimizing foam concrete performance. In addition to the laboratory findings, foam stabilizers are crucial for improving the strength, stability, and fire resistance of foam concrete. They are suitable for construction applications such as lightweight insulation, fireproof panels, and soundproofing solutions. Foam stabilizers also provide cost-effective benefits by improving material performance and reducing cementitious materials. This not only enhances properties but also makes foam concrete a more economical and competitive choice in the construction industry.

3.3. Orthogonal Experiment

Based on the results of preliminary single-factor studies, it was found that HPMC, XG, and PAM all demonstrate effective foam stabilization, significantly extending the foam's lifespan and reducing breakage. However, some studies have indicated that excessively high concentrations of a single foam stabilizer can inhibit the foaming ability of the solution, restricting bubble formation and expansion [29, 30]. Therefore, to achieve better performance and reduce costs, it is worth exploring the combination of multiple foam stabilizers to achieve a synergistic effect. This approach could further enhance the stability and mechanical properties of foam concrete, offering a more scientifically grounded and comprehensive strategy for formulation optimization in practical engineering applications. Building on the findings from the preliminary single-factor experiments, the levels of each factor were further refined and optimized. Using the 28-day compressive strength as the main test criterion, a three-factor, three-level L9(3^3) orthogonal experiment was designed and conducted. The specific experimental design and results are shown in Table 5.

According to the results of the orthogonal experiment, the optimized composite foam stabilizer formulation significantly improved the compressive strength of foam concrete. Under various concentration combinations of HPMC, XG, and PAM, the 28-day compressive strength of the samples showed a significant increase compared to the use of a single stabilizer. Through range analysis and variance analysis of the experimental data, as shown in Tables 6-7, the results indicate that all three foam stabilizers have a significant effect on the compressive strength of the material, with the influence ranked as follows: PAM > XG > HPMC. The optimal foam stabilizer combination for achieving the highest compressive strength is HPMC 0.1%, XG 0.06%, and PAM 0.03%. Under

this combination, the compressive strength of the foam concrete reaches 4.45 MPa, which is 35.26% higher than the maximum compressive strength achieved with 0.4% HPMC alone (3.29 MPa), while significantly reducing the number of stabilizers used.

Table 5. Orthogonal test schemes

No.	Factor			Index
	HPMC /%	XG /%	PAM /%	Compressive strength /MPa
1	0.05	0.03	0.01	3.19
2	0.05	0.06	0.03	4.23
3	0.05	0.09	0.02	3.86
4	0.1	0.03	0.03	4.17
5	0.1	0.06	0.02	4.24
6	0.1	0.09	0.01	3.93
7	0.15	0.03	0.02	3.46
8	0.15	0.06	0.01	3.75
9	0.15	0.09	0.03	4.31

Table 6. Range analysis of compressive strength

	Factors		
	HPMC	XG	PAM
K_1	11.28	10.82	10.87
K_2	12.34	12.22	11.56
K_3	11.52	12.1	12.71
K_4	3.760	3.607	3.623
k_1	4.113	4.073	3.853
k_2	3.840	4.033	4.237
k_3	11.28	10.82	10.87
k_4	12.34	12.22	11.56
R	0.353	0.467	0.613

Table 7. ANOVA of compressive strength

Factor	SS	DF	MS	F-value	P
HPMC	0.206	2	0.103	44.558	*
XG	0.401	2	0.201	86.846	*
PAM	0.576	2	0.288	124.62	**
Error	0.005	2	0.002		
Total	138.39	9			
		* P<0.05, ** P<0.01			

In the optimized formulation, the composite foaming agent (CS) fully utilized the synergistic effects of its components, significantly enhancing the compressive strength of foam concrete. HPMC increased the viscosity of the slurry through its thickening effect, reducing the loss of foam liquid; XG formed a protective layer on the foam surface, effectively preventing foam rupture; PAM improved the water retention and optimized the distribution of bubbles, further enhancing the uniformity of the foam structure. Compared to single foaming agents, the synergistic effect of the composite foaming agent effectively improved the compressive strength of the material and significantly reduced the amount of foaming agents used, achieving a dual optimization of both performance and cost.

3.4. Water Absorption

To investigate the effect of a foam stabilizer on the durability and pore structure of foam concrete, water absorption tests were conducted on two groups of specimens: one without the stabilizer

(Ref) and one with the stabilizer (CS). The results are shown in Fig.4. The Ref group exhibited a high-water absorption rate in the early stage of immersion (1 h), reaching 19.97%. The absorption continued to increase over time and reached 35.09% after 48 h. During the first 24 h, the absorption rate increased rapidly and then slowed down, indicating a high proportion of interconnected pores that allowed water to penetrate and spread quickly. In contrast, the CS group showed a significantly lower water absorption rate throughout the test. At 1 h, the absorption was only 12.45%, and after 48 h, it increased to 20.1%, which was much lower than that of the Ref group. This result suggests that the foam stabilizer effectively reduced water penetration. The trend of the absorption curve also indicates that the CS group had a more stable and gradual increase in absorption. This suggests that the internal pore structure became more uniform, with fewer interconnected pores, reducing the pathways for water migration.

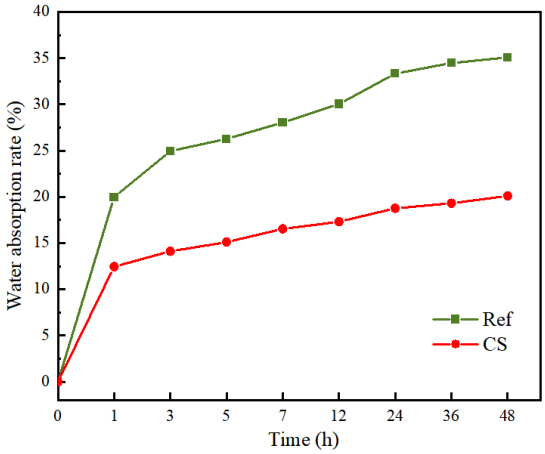

Fig. 4. Water absorption behavior of foam concrete

The introduction of the foam stabilizer not only reduced the water absorption of foam concrete but also improved its pore structure. The pores became more closed and less connected, reducing capillary water transport. This improvement may result from the stabilizer's role in the hydration process, which enhanced bubble stability and produced more uniform pore walls. As a result, large voids were reduced, and the overall density of the material increased. The optimized pore structure directly enhanced the water resistance and durability of the concrete, reducing the risk of water-induced degradation in long-term applications. Therefore, foam concrete with a foam stabilizer performs better in high-humidity or submerged environments. It can effectively slow down the deterioration caused by water penetration, making it a more reliable material for use in buildings, underground structures, and marine applications.

3.5. Pore structure of Foam Concrete

Fig. 5 illustrates the differences in pore structure between the control group sample (Ref), which had no stabilizer, and the sample with the optimized composite stabilizer (CS) under scanning electron microscopy. As shown in the figure, the Ref group displays a relatively loose pore structure, with irregular bubbles and low roundness, resulting in significant pore heterogeneity. This structural characteristic contributes to poor stability and mechanical properties of the foam concrete. In contrast, the CS group with the composite stabilizer shows a more uniform and finer pore structure, with significantly improved bubble roundness and more regular shapes. The observations further indicate that the addition of stabilizers not only enhances the stability of the foam but also optimizes the uniformity of the pores, thereby improving the overall performance of the foam concrete. The incorporation of the composite stabilizer creates a more uniform and refined pore network. This small, uniform pore structure helps to better disperse external pressure, enhancing the compressive strength of the material and reducing structural damage during use.

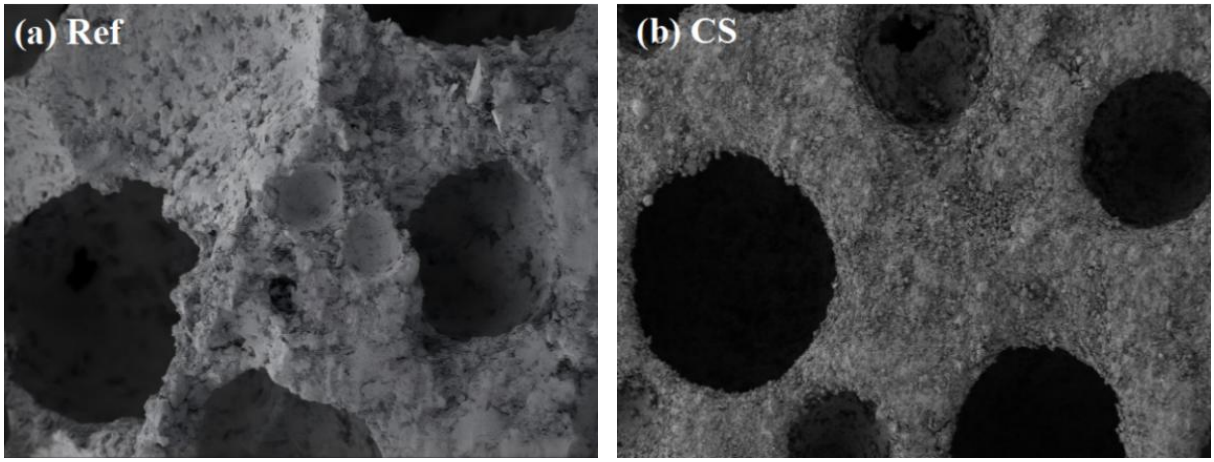

Fig. 5. Pore structures of foam concrete (a) Ref; (b) CS

To further quantify the differences in pore size distribution, this study performed a detailed analysis of the pore structure of the samples, as shown in Fig.6. The analysis results reveal that in the samples with the composite stabilizing agent (CS), the majority of the pores are concentrated in the 0-400 μm range, indicating smaller and more uniform pore sizes. In contrast, the pores of the control sample (Ref) are primarily distributed in the 600-1400 μm range, with larger and more widely distributed pores. Notably, in the 700-900 μm range, the sample with CS stabilizer shows significantly lower pore frequency compared to the control sample, and no pores larger than 900 μm are observed. This phenomenon highlights the unique advantage of the CS stabilizer in regulating pore size distribution. It effectively reduces the formation of large pores, optimizing the pore structure of the foam concrete and improving its stability and mechanical properties. These findings provide valuable guidance for the formulation design and production process of foam concrete, especially in applications that require high stability and strength.

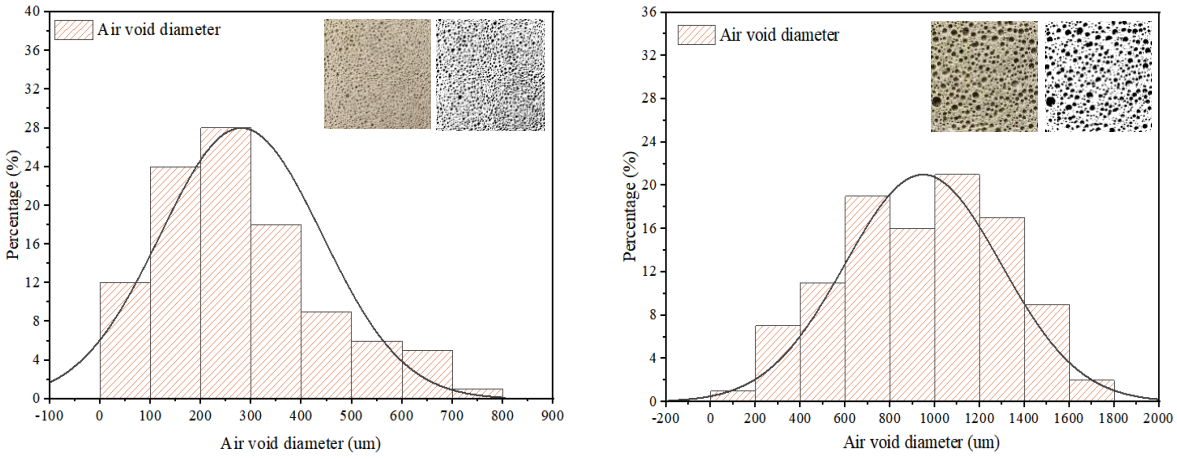

(a) (b)

Fig. 6. Pore diameter of foam concrete (a)CS and (b)Ref

4. Conclusion

This study systematically examined the effects of three stabilizing agents—HPMC, XG, and PAM—on the stability and mechanical properties of foam concrete. Through orthogonal experiments, the optimal composite ratio was identified, and a stabilizing agent combination with significant synergistic effects was proposed. The main conclusions are as follows:

- HPMC, XG, and PAM all significantly improve foam stability, but their mechanisms of action differ. HPMC provides the most significant improvement in stability at higher concentrations, while PAM is more effective at lower concentrations.

- The concentration of foam stabilizers greatly influences the compressive strength of foam concrete. Adding an appropriate amount of HPMC, XG, and PAM can effectively improve the compressive strength. However, excessively high concentrations can lead to over-thickening of the slurry, which may hinder the cement hydration process and limit further strength development.
- The results of the orthogonal experiment indicate that the optimal ratio of the three foam stabilizers is HPMC 0.1%, XG 0.06%, and PAM 0.03%. Under this formulation, the 28-day compressive strength of the foam concrete reaches 4.45 MPa, which represents a 35.26% increase in strength compared to the use of a single stabilizer, while significantly reducing the number of stabilizers required.
- The water absorption test and SEM pore size analysis show that after incorporating the composite foam stabilizer (CS), the internal pores become more uniform and finer, with most pore sizes concentrated in the 0–400 μm range. Compared to the control group, the pore size is significantly reduced, with no large pores exceeding 900 μm. This improvement in pore structure enhances the material's overall stability and compressive strength.

This study primarily investigated the effects of single and composite stabilizers on the properties of foam concrete. However, there are still limitations, such as the lack of evaluation of high-strength foam concrete, the long-term synergistic effects of composite stabilizers, and the durability of foam concrete in complex environments. Future studies will examine the effectiveness of the proposed stabilizer formulation in high-strength foam concrete, investigate its performance at high temperatures, and assess its applicability in real-world engineering conditions. This will provide more comprehensive theoretical and practical support for the broader application of foam concrete.

Acknowledgement

The author would like to express their sincere gratitude to the Jiangsu Province Industry University Research Cooperation Project (No. BY20230789) for its financial support and valuable resources, which have greatly contributed to the successful completion of this research.

References

[1] Zhang H, Wang J, Wang C, et al. Using Foamed Concrete Layer to Optimize the Design of Pavement and Subgrade Structures: from the Perspectives Economy and Durability [J]. Arabian Journal for Science and Engineering, 2023, 48(10): 12859-74. https://doi.org/10.1007/s13369-023-07606-1

[2] Zhang H, Wang J, Liu Z, et al. Strength characteristics of foamed concrete under coupling effect of constant compressive loading and freeze-thaw cycles [J]. Construction and Building Materials, 2024, 411. https://doi.org/10.1016/j.conbuildmat.2023.134565

[3] Liu M, Wang J, Wang C, et al. Stress-Solid Materials-Voids interaction of foamed concrete in isotropic compression [J]. Construction and Building Materials, 2022, 358. https://doi.org/10.1016/j.conbuildmat.2022.129468

[4] Zhao X, Lim S-K, Tan C-S, et al. Properties of Foamed Mortar Prepared with Granulated Blast-Furnace Slag [J/OL] 2015, 8(2):462-73. https://doi.org/10.3390/ma8020462

[5] Jiang S, Wang L, Feng K. Compound modified experiment of protein-concrete foaming agent [J]. Journal of Functional Materials, 2015, 46(9): 09056-61.

[6] Hamad, Ali J. Materials, Production, Properties and Application of Aerated Lightweight Concrete: Review [J]. International Journal of Materials Science and Engineering, 2014. https://doi.org/10.12720/ijmse.2.2.152-157

[7] Chen H G, Liang K K, Chow C L, et al. Enhancing the engineering performance of lightweight limestone calcined clay cement concrete using used engine oil as a foam stabilizer [J]. Journal Of Building Engineering, 2024, 95. https://doi.org/10.1016/j.jobe.2024.110187

[8] Gonzenbach U T, Studart A R, Tervoort E, et al. Ultrastable particle-stabilized foams [J]. Angewandte Chemie - International Edition, 2006, 45(21): 3526-30. https://doi.org/10.1002/anie.200503676

[9] Drenckhan W, Langevin D. Monodisperse foams in one to three dimensions [J]. Current Opinion in Colloid & Interface Science, 2010, 15(5): 341-58. https://doi.org/10.1016/j.cocis.2010.06.002

[10] Fan C, Wu R, Chen H, et al. Influence of HPMC on the Properties of Lightweight Aggregate Concrete by Chemical Foaming in situ [J]. The Chinese Journal of Process Engineering, 2016, 16(4): 679-83.

[11] Zhang Y M, Jiang Y, Ling T C. Use of CO2 as a controlled foam stabilizer to enhance pore structure and properties of foamed concrete [J]. Cement & Concrete Composites, 2024, 145. https://doi.org/10.1016/j.cemconcomp.2023.105356
[12] Krämer C, Azubike O M, Trettin R H F. Reinforced and hardened three-phase-foams [J]. Cement and Concrete Composites, 2016, 73: 174-84. https://doi.org/10.1016/j.cemconcomp.2016.07.012
[13] She W, Du Y, Miao C, et al. Application of organic- and nanoparticle-modified foams in foamed concrete: Reinforcement and stabilization mechanisms [J]. Cement and Concrete Research, 2018, 106: 12-22. https://doi.org/10.1016/j.cemconres.2018.01.020
[14] Qiu Y Q, Zhang L J, Chen Y S, et al. Experimental Study on Application Performance of Foamed Concrete Prepared Based on a New Composite Foaming Agent [J]. Advances In Materials Science And Engineering, 2022, 2022. https://doi.org/10.1155/2022/7217479
[15] Hajimohammadi A, Ngo T, Mendis P. Enhancing the strength of pre-made foams for foam concrete applications [J]. Cement and Concrete Composites, 2018, 87: 164-71. https://doi.org/10.1016/j.cemconcomp.2017.12.014
[16] Xiong Y, Hu Z, Jia Z, et al. Effect of formic acid as an accelerator on foam-stability, compressive strength, and pore size distribution of foam concrete [J]. Journal of Building Engineering, 2023, 66. https://doi.org/10.1016/j.jobe.2023.105923
[17] Sahu S S, Ranjani Gandhi I S, Kumar A, et al. Evaluation of Suitability of Carboxymethyl Cellulose in Performance Improvement of Sodium Lauryl Sulfate Foam and Compressive Strength of Foam Concrete [J]. Advances in Civil Engineering Materials, 2021, 10(1): 74-92. https://doi.org/10.1520/ACEM20200083
[18] Yang S, Yao X, Li J, et al. Preparation and properties of ready-to-use low-density foamed concrete derived from industrial solid wastes [J]. Construction and Building Materials, 2021, 287. https://doi.org/10.1016/j.conbuildmat.2021.122946
[19] Chen D, Chen M, Zhou X, et al. Effects of waste cooking oil derivatives as a foam stabilizer on properties of foam and foamed geopolymer concrete [J]. Construction and Building Materials, 2024, 450. https://doi.org/10.1016/j.conbuildmat.2024.138675
[20] Krämer C, Kowald T L, Butters V, et al. Carbon nanotube-stabilized three-phase-foams [J]. Journal of Materials Science, 2016, 51(8): 3715-23. https://doi.org/10.1007/s10853-015-9689-2
[21] He J, Gao Q, Song X, et al. Effect of foaming agent on physical and mechanical properties of alkali-activated slag foamed concrete [J]. Construction and Building Materials, 2019, 226: 280-7. https://doi.org/10.1016/j.conbuildmat.2019.07.302
[22] Xiong Y, Zhu Y, Chen C, et al. Effect of nano-alumina modified foaming agents on properties of foamed concrete [J]. Construction and Building Materials, 2021, 267. https://doi.org/10.1016/j.conbuildmat.2020.121045
[23] He J, Liu G, Sang G, et al. Investigation on foam stability of multi-component composite foaming agent [J]. Construction and Building Materials, 2023, 391. https://doi.org/10.1016/j.conbuildmat.2023.131799
[24] Foaming agents for foamed concrete: [S]. Ministry of Industry and Information Technology, People's Republic of China, 2013:
[25] Wagh C D, Gandhi I S R. Investigations on the performance of xanthan gum as a foam stabilizer and assessment of economic and environmental impacts of foam concrete production [J]. Journal of Building Engineering, 2024, 82: 108286. https://doi.org/10.1016/j.jobe.2023.108286
[26] Zhong M, Meng J, Ning B, et al. Effects of foam stabilizers on the properties and microstructure of autoclaved aerated concrete from iron tailings [J]. Journal of Materials Science, 2024, 59(39): 18395-411. https://doi.org/10.1007/s10853-024-10299-y
[27] Yang C, Wang L, Tian Y, et al. Fundamental Characteristics of Alkali Activated Slag Cement Foam Concrete [J]. Bulletin of the Chinese Ceramic Society, 2016, 35(2): 555-60.
[28] Amran Y H M, Farzadnia N, Abang Ali A A. Properties and applications of foamed concrete; a review [J]. Construction and Building Materials, 2015, 101: 990-1005. https://doi.org/10.1016/j.conbuildmat.2015.10.112
[29] Zhang H, Wang Z, Zhang T, et al. Foam Stabilization Process for Nano-Al2O3 and Its Effect on Mechanical Properties of Foamed Concrete [J/OL] 2024, 14(18):10.3390/nano14181516 https://doi.org/10.3390/nano14181516
[30] Guo R, Xue C, Guo W, et al. Preparation of foam concrete from solid wastes: Physical properties and foam stability [J]. Construction and Building Materials, 2023, 408: 133733. https://doi.org/10.1016/j.conbuildmat.2023.133733

Research on Engineering Structures & Materials
www.jresm.org
Research Group

Research Article

Experimental study on the compression characteristics of sandy soil under impact loading

Shu Sun [1,a], Dong Zhu [*, 2, b], Zehui Zhang [3,c]

[1]*School of Architecture and Eng., Taizhou Polytechnic College, Taizhou, 225300, Jiangsu, China*
[2]*The 3rd Geological Brigade of Zhejiang Province, Jinhua, Zhejiang, China, 321000*
[3]*China Design Testing Technology Co., Ltd, Nanjing 210000, China*

Article Info

Article History:

Received 23 Dec 2024
Accepted 23 Mar 2025

Keywords:

Sandy soil;
Split Hopkinson pressure bar;
Strain rate effect;
Moisture content;
Repeated impacts

Abstract

Sandy granular materials, as complex non-equilibrium energy-dissipative filling materials, are widely used in the energy-dissipating layers of protective structures. To investigate the effects of strain rate and energy absorption characteristics of sandy soils, a dynamic compression test using a split Hopkinson pressure bar (SHPB) was designed and conducted on unsaturated sandy soil under passive confining conditions. The influences of strain rate, moisture content, and the number of impacts on the dynamic response of sandy soils were analyzed. The test results indicate significant strain rate effects on the dynamic elastic modulus and peak stress of the specimens. When the applied strain rate is within the range of 255–578 s^{-1}, an increase in strain rate enhances both the dynamic elastic modulus and peak stress of the specimens, although variations in moisture content alter the magnitude of this effect. Moreover, as the strain rate increases, the energy density of the specimens grows exponentially, with a significantly enhanced rate of increase in the higher strain rate range; in comparison, moisture content has a smaller effect on energy density. Under repeated impact conditions, moisture content significantly influences the dynamic elastic modulus more than it does peak stress. The cumulative effect of repeated impacts can significantly improve the soil's resistance to deformation; however, as the specimen compaction increases, the energy density gradually stabilizes. Therefore, appropriately reducing the compaction of the energy-dissipating layers can enhance energy absorption performance. These findings offer technical insights that can guide the design of protective structures for both military and civil applications.

1. Introduction

During Sandy granular materials consist of numerous solid particles and are characterized by high porosity and significant compressibility [1]. These materials are widely distributed, readily accessible, and exhibit substantial dispersion and attenuation of stress waves generated by impacts and explosions. Consequently, they are widely used as impact-resistant materials in protective engineering structures [2], including wave-dissipation layers in military engineering [3,4], cushion layers in rockfall-resistant sheds, and pile-plate retaining walls in mountainous regions [5–7]. Therefore, investigating the dynamic mechanical behavior of sandy soils under impact loading is of considerable theoretical importance and practical value for damage evaluation and the design of protective structures.

Investigating the dynamic response of sandy soils can be achieved using weighted hammer systems [8], excitation tubes [9], pendulums [10], and explosive modeling tests [11]. However, drop

*Corresponding author: xcb@hrbeu.edu.cn
[a]orcid.org/0009-0009-8877-1654; [b]orcid.org/0009-0007-8662-3813; [c]orcid.org/0000-0002-0882-689X
[d]orcid.org/0000-00xx-xxxx-xxxx
DOI: http://dx.doi.org/10.17515/resm2025-586me1223rs

hammer and pendulum devices often struggle to capture accurate mechanical responses under medium to high strain rates. Additionally, explosive modeling tests typically rely on embedded manometers for stress measurements, which can introduce issues such as transmission stresses exceeding incident stresses, calibration difficulties due to significant wave impedance differences, and interference with stress waves. Alternatively, the SHPB test, which operates at medium to high strain rates (10^{2}–10^{4} s^{-1}), is widely employed for impact loading studies. This method effectively characterizes the dynamic responses of various materials, including metals [12], concrete [13], rocks [14], ceramics [15], foams [16], and granular media [17].

Over recent decades, research on the dynamic response of granular materials has primarily focused on the propagation characteristics of stress waves and the development of dynamic constitutive models. Yu et al. [18, 19] employed SHPB tests to investigate the attenuation of compression waves in coral and silica sands. Their results demonstrated that coral sand exhibited 30% higher attenuation of compression waves compared to silica sand. Ross et al. [20] examined the propagation characteristics of stress waves in sandy soil specimens of varying lengths under lateral confinement. Shukla and Damania [21] found that stress wave propagation in granular materials depends not only on the physical and mechanical properties of the particles, interparticle filling materials, and porosity, but is also significantly influenced by the topological structure of the granular assembly and the local interactions between particles. Lv et al. [22] compared the variation of peak stress waves in silica sand and calcareous sand at identical lengths, using this comparison to characterize the wave dissipation capacity of different media. Regarding the dynamic stress-strain relationship of soils, Bragov et al. [23] conducted SHPB experiments as early as 1996 to reveal the strain rate effect on cohesive soils, noting that higher strain rates lead to increased dynamic peak strength. Felice et al. [24] experimentally demonstrated that saturated sandy soils exhibit significant strain rate effects. However, these studies primarily focused on key factors influencing the dynamic mechanical behavior of granular materials, such as particle morphology, grain size distribution, moisture content, and relative density. To quantify the dynamic response characteristics of soils under dynamic loading and their evolution, and to develop accurate constitutive models that reflect particle-level effects, Bragov et al. [25] proposed a generalized dynamic compressible constitutive model for quartz sand based on improved SHPB experiments. Ma et al. [26] developed a constitutive model for frozen clay that comprehensively incorporates confining pressure, strain rate, and freezing temperature, using an original component assembly approach. Fu et al. [27], based on damage and fracture mechanics, proposed a constitutive model to predict the stress-strain behavior of frozen soils.

It has been established that the compressive properties of granular media are influenced not only by porosity and the physical and mechanical properties of the particles [28, 29], but also by the local interactions between particles [30]. Figure 1 illustrates the surface morphology of the sandy soil used in this study, along with typical calcareous sand (coral sand) and quartz sand [31]. The pore characteristics, particle size, and surface roughness of these three types of granular particles differ considerably. Calcareous sand, which has a more developed internal pore structure, exhibits a greater capacity for compressive deformation and energy absorption under dynamic loading. In contrast, quartz sand, with its angular particle surfaces and stronger interlocking between particles, demonstrates higher initial strength and shear resistance. Unlike sand particles, sandy soils contain a larger proportion of unbreakable particles smaller than 0.074 mm [32]. These variations in particle morphology and internal structure suggest that the dynamic characteristics of the sandy soil studied here under dynamic loading may differ significantly from those of typical sand particles.

In summary, significant advancements have been made in understanding the dynamic mechanical responses of sand particles. However, research on the impact characteristics of soils remains in its early stages, with several key issues still requiring further investigation. These include the strain rate sensitivity of sand particles, as well as the influence of moisture content on the stress-strain relationship of the material. Furthermore, the differences in the dynamic mechanical behavior of soils under continuous and repeated impact loads, as opposed to single impact responses, are not yet well understood. To address these gaps, this study introduces an enhanced SHPB impact experiment, incorporating a precise rigid sleeve apparatus designed to control the length and

compaction of granular material specimens. The objective is to analyze and quantify the effects of moisture content and the number of impacts on the dynamic mechanical and energy characteristics of sandy soils.

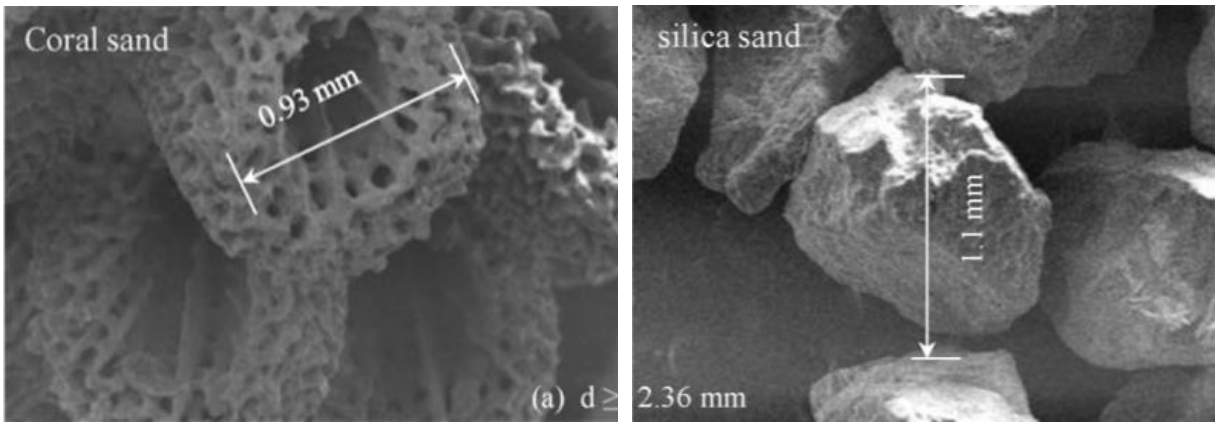

(a)

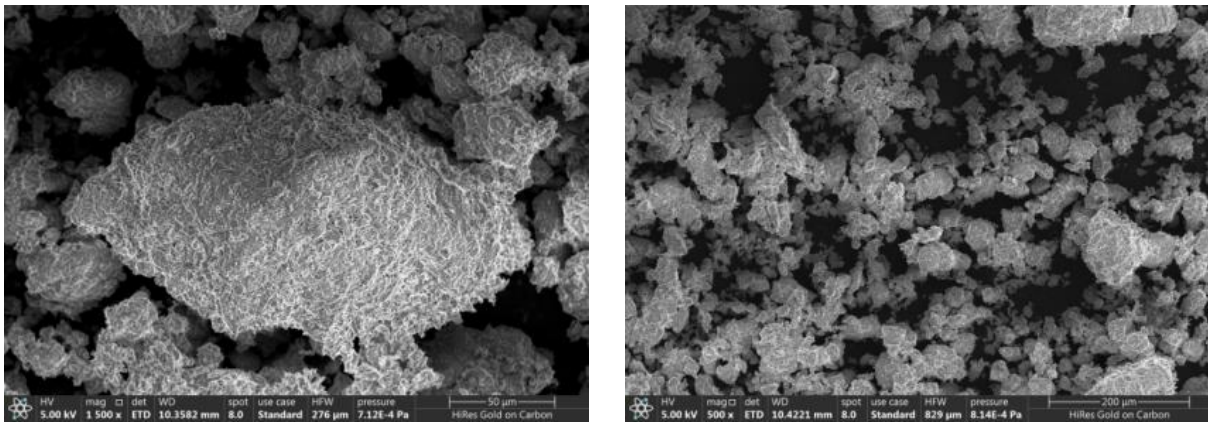

(b)

Fig. 1. Surface morphological structure of typical particles (a) Calcareous and siliceous sands [31] (b) Sandy soils used in this paper

2. Test Materials and SHPB Setup

2.1 Test Materials

The sandy soil used was collected from Shandong Province through an excavation process. The sampling depth was 1.00 m, and the soil appeared yellowish-brown in color. To determine the particle size distribution of the test soil, a sufficient amount of soil was first dried in a constant-temperature oven at 105°C for 36 hours. The dried soil then underwent sieve analysis using standard sieves. During the sieving process, larger gravel particles were selectively removed to ensure uniformity of the test samples. Based on the particle size proportions retained on each sieve, a particle size distribution curve was plotted (Fig. 2). From this curve, the average particle size of the original sand sample was determined to be 0.18 mm, the coefficient of uniformity was 2.009, and the coefficient of curvature was 81.08. The content of particles with a diameter greater than 2 mm did not exceed 50% of the total weight, while particles with a diameter greater than 0.075 mm constituted more than 50% of the total weight, classifying the material as typical sandy soil [33]. A field-emission scanning electron microscope (FE-SEM) was used to capture the surface morphology of the soil particles (Fig. 1b). The results revealed that the particles were irregular in shape, with some exhibiting aggregation and forming agglomerate structures. These structures may result from electrostatic forces or weak bonding forces between the particles. The elemental composition of the soil was analyzed using energy dispersive spectroscopy (EDS) (Fig. 3). Silicon

(Si) and oxygen (O) were found to be the most abundant elements, with Si content at 30.02% and O content at 38.88%. Other elements included aluminum (Al) at 9.82%, potassium (K) at 2.35%, calcium (Ca) at 1.55%, and iron (Fe) at 7.56%.

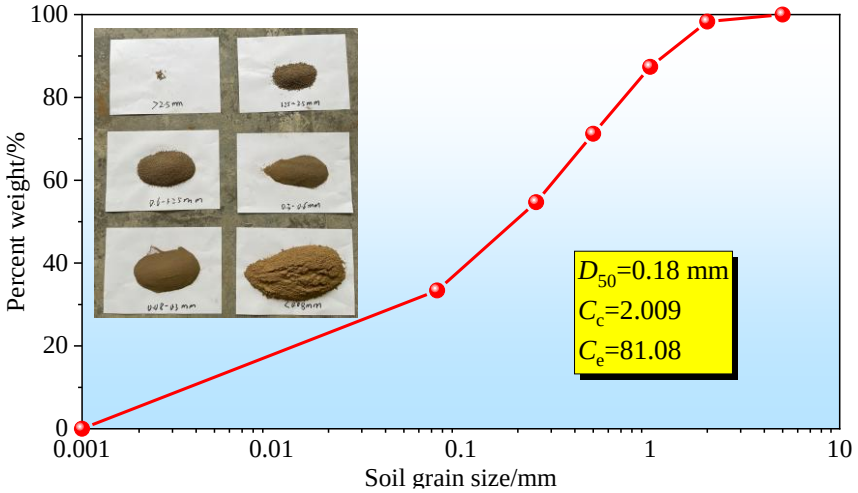

Fig. 2. Particle size distribution

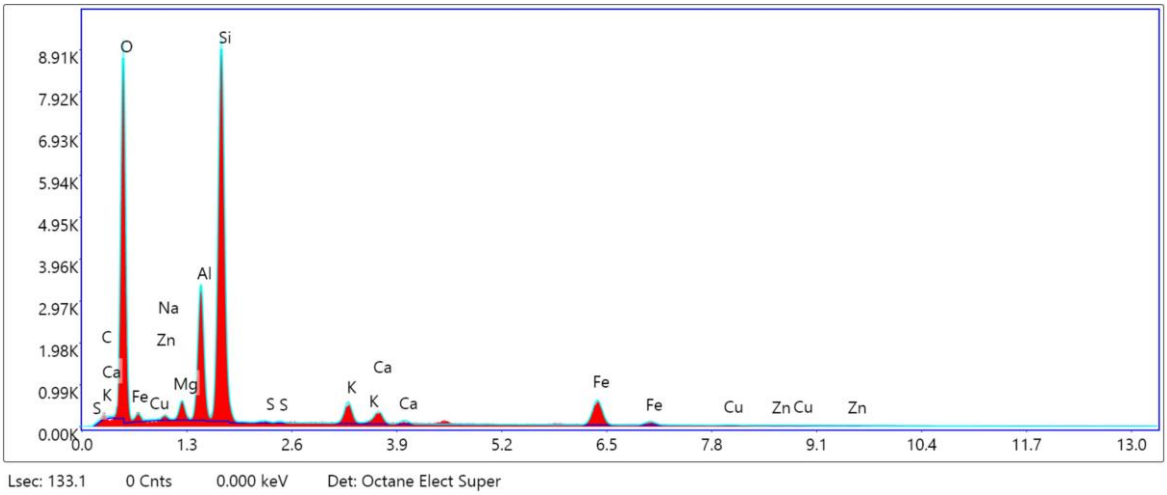

Fig. 3. EDS spectra of specimens

2.2 SHPB for Dynamic Experiments

A SHPB apparatus with a bar diameter of Φ40 mm was used for the experiments (Fig. 4). The SHPB setup primarily consists of a loading system, pressure bars, and a data acquisition module. The loading system utilizes compressed nitrogen gas to drive a projectile that impacts the incident bar, with the projectile velocity controlled by adjusting the gas pressure. The SHPB apparatus includes an incident bar and a transmission bar, measuring 2400 mm and 2000 mm in length, respectively. Both bars are made of 7075 aluminum alloy, with an elastic modulus of 71 GPa and an elastic wave propagation velocity of 5000 m/s within the bars. Due to the low and variable wave impedance of the granular materials tested in this study, high-sensitivity semiconductor strain gauges were employed. These strain gauges have a resistance value of 120 Ω and a gain factor of 1000. The strain gauges were positioned 850 mm from both ends of the specimen to accurately measure strain during impact testing.

Sandy soil, being a granular material, must be contained within a sleeve for dynamic loading tests. An improved loading sleeve has been designed specifically for granular materials. This sleeve consists primarily of an outer sleeve, an inner sleeve, and three sets of plates to control the specimen length. The outer sleeve is made of high-strength steel, measuring 400.0 mm in length, with an inner diameter of 40.1 mm and a wall thickness of 2.0 mm. It provides lateral confinement

to the granular material while allowing the incident bar to slide and rotate within the sleeve. The inner sleeve, constructed from the same material as the outer sleeve, has an inner diameter of 25.0 mm and a wall thickness of 1.0 mm. The set of plates includes a front-end plate, a rear end plate, and a supporting plate. Both the front and rear end plates are made from the same material as the SHPB bars, with a diameter of 40.0 mm and a thickness of 15.0 mm. The supporting plate, made of the same material as the sleeve, is positioned beneath the rear end plate to prevent deformation during the pre-compression of the specimen, thereby ensuring experimental accuracy. Precise control of the specimen length is achieved through various combinations of the inner sleeve, outer sleeve, and plates, with the error in specimen length maintained within 2.0%.

Sandy soil is a loose, porous material characterized by low strength and low wave impedance. Under loading, it undergoes significant deformation, which substantially attenuates the amplitude of transmitted waves. In SHPB tests, to satisfy the assumption of uniform deformation, the specimen's cross-sectional area must not exceed that of the bars during loading. As a result, a specimen diameter of 40 mm is selected. Furthermore, an excessively thick specimen makes it challenging to achieve stress equilibrium, while an overly thin specimen significantly increases frictional forces, leading to considerable experimental errors. According to studies by Gray [34] and Li et al. [35], the optimal length-to-diameter ratio (L/D) for specimens falls within the range of 0.5 to 1.0.

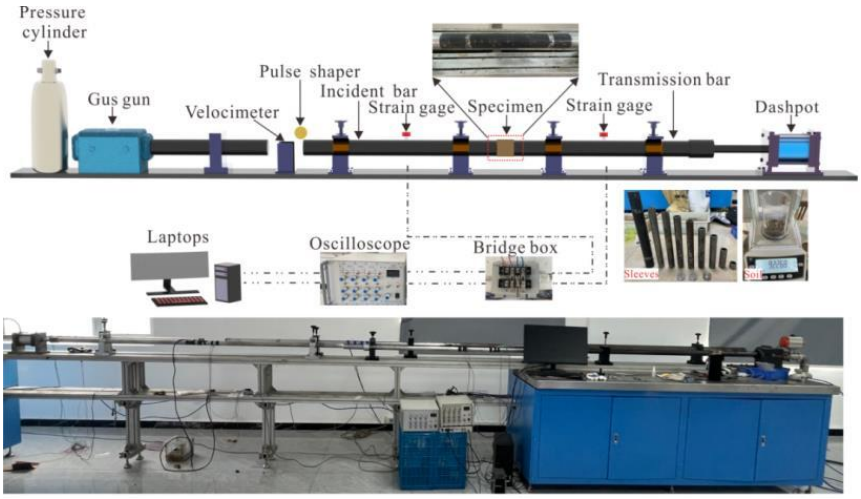

Fig. 4. Improved SHPB

2.3 Specimen Preparation and Impact Conditions

Specimens with dimensions of Φ40 mm × 30 mm and moisture contents of 34%, 40%, 45%, and 48% were prepared as follows: A precise mass of 2.0 kg of dry loess was weighed, and the corresponding amount of distilled water was calculated to achieve the desired moisture content. The soil and water were thoroughly mixed, sealed in plastic wrap, and allowed to stand for 24 hours to ensure uniform moisture distribution. With a known dry density of 1.70 g/cm^3, the required mass of the soil-water mixture was then determined for each specimen. The mixture was subsequently placed into a cylindrical mold and compressed using a static loading device to form the specimens. This preparation procedure ensures the consistent formation of remolded soil specimens with the targeted moisture contents for experimental testing.

The specific steps for each impact test are as shown in Fig. 5: (1) Position the support plate on a flat, horizontal surface, then stack the rear end plate on top of the support plate. Secure the sleeve and rear end plate in place using bolts; (2) Evenly pour the pre-weighed sand sample into the sleeve, gently pressing and leveling it. Subsequently, slowly slide the front end plate onto the top of the sample to ensure that air is expelled from the sleeve; (3) Place the appropriately sized inner sleeve onto the front end plate, position a steel plate at the top end of the inner sleeve, and gently press the sample until the ends of both the inner and outer sleeves are aligned and flush; (4) Remove the inner sleeve and secure the front end plate with bolts to prevent any alterations to the

sample's physical state during handling; (5) Place the assembled specimen between the incident and transmission bars, ensuring that the sleeve is level and that the end face of the incident bar makes full contact with the end face of the front end plate. To minimize friction, apply lubricant to the contact surfaces between the incident bar and the front-end plate, as well as between the transmission bar and the rear end plate.

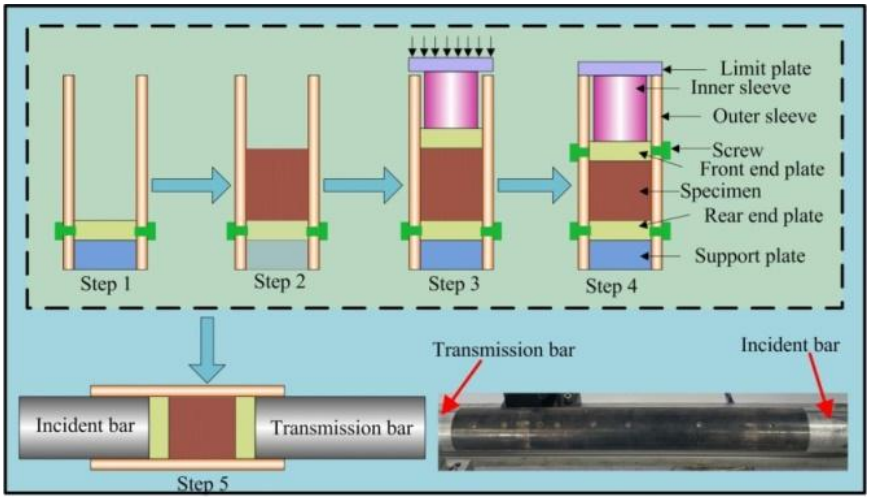

Fig. 5. Experimental steps

To investigate the influence of moisture content and continuous repeated impacts on the mechanical properties of soil specimens, the experiments were conducted under three distinct loading conditions: (1) Specimens with identical moisture content were subjected to impact tests at varying air pressure levels to achieve different strain rates; (2) Under a constant air pressure, remolded soil specimens with moisture contents of 34%, 40%, 45%, and 48% were tested to analyze the impact of moisture content on their dynamic behavior; (3) With consistent moisture content and air pressure, the same specimen was subjected to multiple continuous repeated impacts to assess the effects of repeated loading on its mechanical response.

2.4 Data Acquisition and Calculation Methods

During the experiment, the bullet is propelled from the gun barrel by air pressure, striking the incident bar at a specific velocity and generating an elastic compressive wave (incident wave) within the bar. Upon reaching the front surface of the specimen, the substantial difference in wave impedance between the specimen and the bar results in partial reflection of the incident wave back into the incident bar (reflected wave), while the remaining portion of the wave is transmitted through the specimen into the transmission bar (transmitted wave) and absorbed by the damper. The bullet's impact velocity is regulated by the air pressure system, enabling the generation of different strain rates during loading. The stress and strain time-history curves of the specimen are recorded using semiconductor strain gauges mounted on the incident and transmission bars. The resulting voltage signals are then converted into strain signals using the following equation:

$$\varepsilon = \frac{4U_{in}(V)}{KU_{WB}(V)nA_u} \tag{1}$$

where U_{in} represents the voltage measured by the semiconductor strain gauge, K is the gauge's sensitivity coefficient (valued at 2.08), and n is the number of arms in the Wheatstone bridge, with a half-bridge configuration used in this experiment. The gain coefficient Au was determined to be 1000 through preliminary tests, and the bridge voltage U_{WB} was set at 4 V.

Assuming one-dimensional stress and homogeneity conditions, and for specimens that satisfy stress equilibrium, the two-wave method can be applied to calculate the dynamic stress $\sigma(t)$, strain $\varepsilon(t)$, and strain rate $\dot{\varepsilon}(t)$ of the material under various strain rate conditions. This approach allows for the determination of the stress-strain relationships of the test material at different strain rates [36]:

$$\sigma(t) = \frac{A_b}{A_s} E_0 \varepsilon_t(t) \quad (1)$$

$$\varepsilon(t) = \frac{2C_0}{L_s} \int_0^t \varepsilon_r(t) dt \quad (1)$$

$$\dot{\varepsilon}(t) = \frac{2C_0}{L_s} \varepsilon_r(t) \quad (1)$$

where $\sigma(t)$, $\varepsilon(t)$ and $\dot{\varepsilon}(t)$ represent stress, strain, and strain rate, respectively. L_s and A_s denote the specimen's length and cross–sectional area, respectively. C_0, E_0, and A_b are the stress wave velocity, elastic modulus, and cross-sectional area of the pressure bar, respectively. $\varepsilon_r(t)$ and $\varepsilon_t(t)$ are the reflected and transmitted strains measured by the strain gauges on the incident and transmission bars, respectively. t represents time.

3. Experimental Results and Analysis

3.1 Validation of Data Reliability

Pulse shapers can modify waveforms and help achieve stress equilibrium [37]. Commonly used shaper materials include brass, rubber, and resin. In this study, annealed brass was utilized for pulse-shaping tests. To reduce high-frequency oscillations and dispersion effects, a brass shaper with a thickness of 1.0 mm and a diameter of 10 mm was attached to the end of the incident bar. Figure 6 shows the error calibration waveform during the unloaded test with the pulse shaper. The results indicate that the pulse shaper effectively filters out high-frequency waves generated at the moment of impact. The use of the shaper significantly mitigates the dispersion effect of the incident wave, resulting in a smoother waveform. Additionally, compared to tests without a pulse shaper, the application of the pulse shaper increased the pulse duration by 60%, greatly enhancing the reliability of the experiment. Figure 7 illustrates the relationship between strain rate and time after applying the pulse shaper.

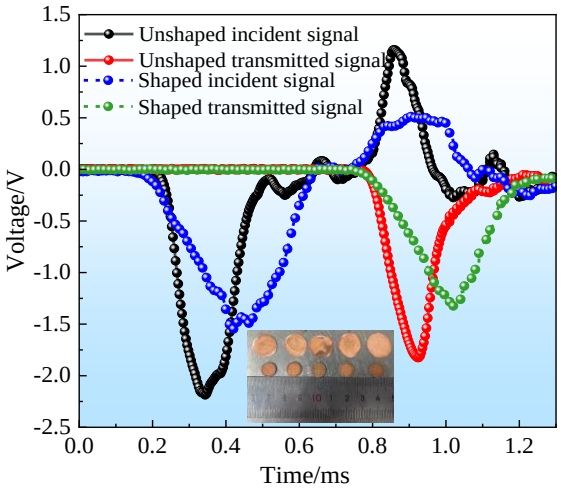

Fig. 6. Effect of pulse shaper on results

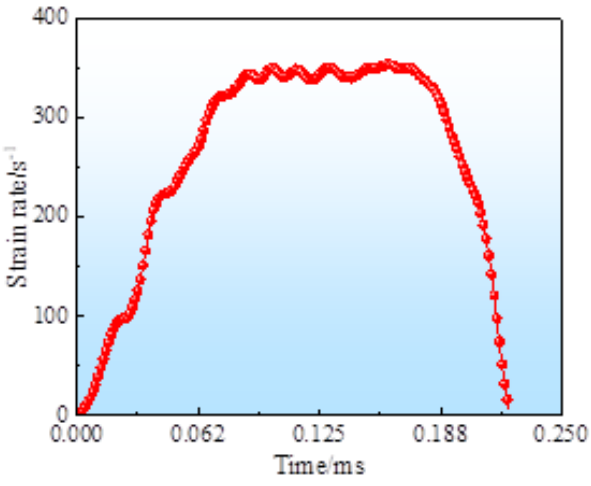

Fig. 7. Strain rate analysis

In the initial phase, the strain rate gradually increases, indicating a progressively rising loading rate. During the stabilization phase, the strain rate reaches its peak and remains elevated, achieving a relatively stable dynamic loading process. This also demonstrates that the SHPB test can achieve constant strain rate loading. Figure 8(a) shows a typical three-wave voltage signal, indicating that the waveform is smooth and continuous, without noticeable jumps or oscillations, thereby confirming the absence of wave superposition effects within the specimen. The stress-time histories at both ends of the specimen, calculated using the wave front alignment method, are presented in Fig. 8(b). The results indicate that the sum of the incident and reflected voltage signals at one end of the specimen is approximately equal to the transmitted voltage signal at the other

end, satisfying the stress equilibrium condition. Furthermore, as depicted in Fig. 8c, the results of the three experiments under identical conditions exhibit high consistency, with minimal data dispersion. In summary, the test method is reliable and the test results are valid.

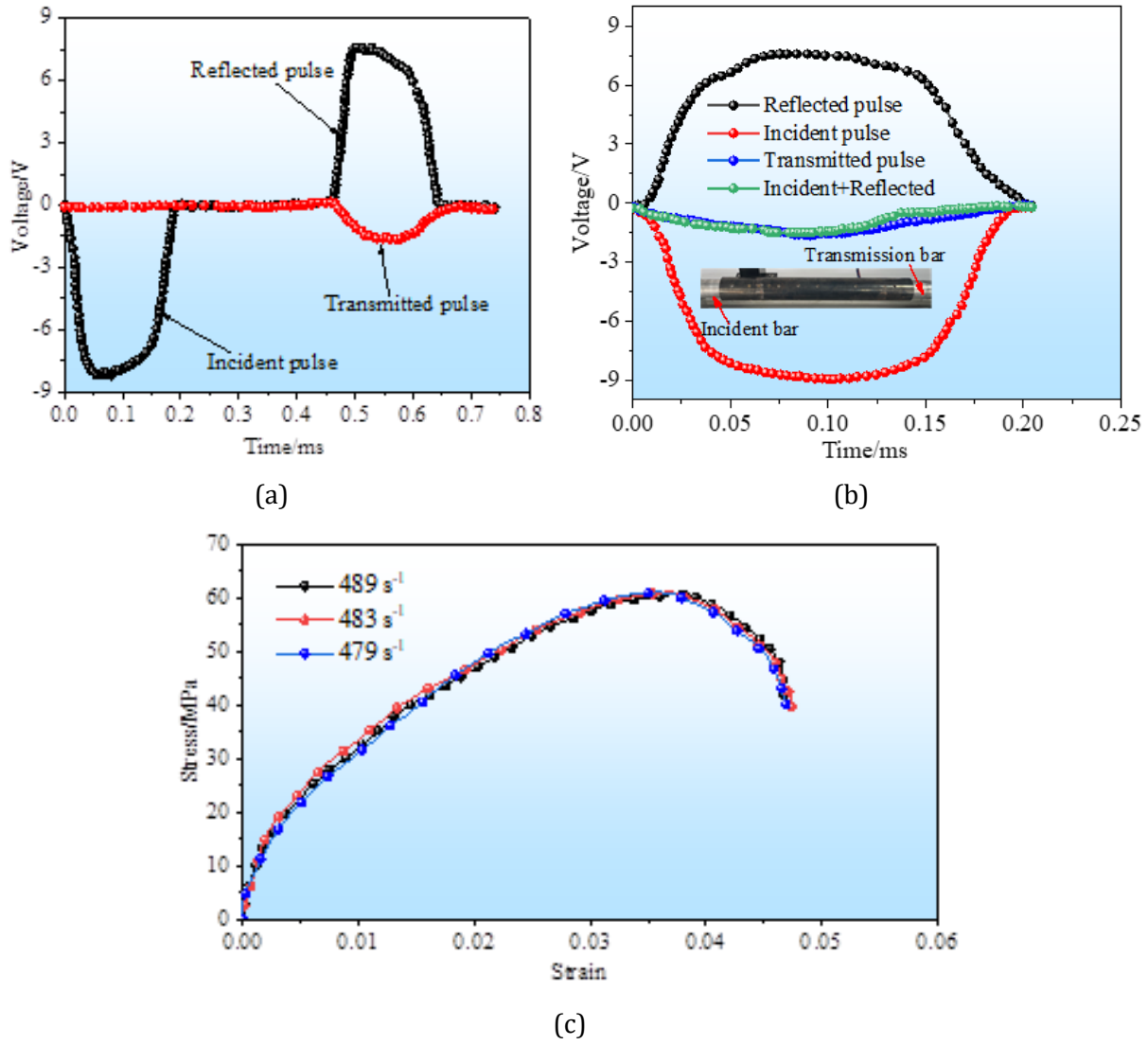

Fig. 8. Effectiveness analysis (a) raw waveform(b) stress equilibrium (c) repeatability verification

3.2 Effect of Strain Rate on Dynamic Stress-Strain Behavior

Figure 9 presents a generalized dynamic stress-strain curve for the test specimens, highlighting the dynamic compression process, which can be divided into three distinct stages: the elastic stage (AB), the yield stage (BC), and the unloading stage (CD).

- Elastic Stage (AB): During this phase, as strain increases, stress increases approximately linearly. The stress remains below the elastic limit of the soil skeleton, and the material exhibits reversible deformation. The soil structure remains largely intact, indicating no permanent change in the particle arrangement.
- Plastic Stage (BC): This stage, also referred to as the compaction stage, is characterized by the rearrangement of soil particles, which gradually fills the voids between grains. The soil becomes more compact, and particle movement is significantly restricted. This results in irreversible plastic deformation, with stress continuing to rise until it reaches the peak value. The peak stress corresponds to the maximum compressive strength of the sample.
- Unloading Stage (CD): Subsequently, the specimen enters the unloading phase, where the stress decreases rapidly, and the test ends.

Figure 10a illustrates the dynamic stress-strain relationships of specimens with 35% moisture content under varying loading strain rates. The results reveal that as the strain rate increases from 258–572 s^{-1}, the compressive strength of the material significantly rises, with the peak stress increasing from 20 MPa to 70 MPa. This demonstrates a pronounced strain rate effect in the tested sandy soil. Additionally, when the strain rate is below 413 s^{-1}, the specimens exhibit a significant strain rate dependence, with the peak stress increasing as the loading strain rate rises. However, when the strain rate exceeds 486 s^{-1}, the peak stress gradually stabilizes, and the rate sensitivity diminishes. This trend is even more apparent in the semi-logarithmic plot shown in Figure 10b.

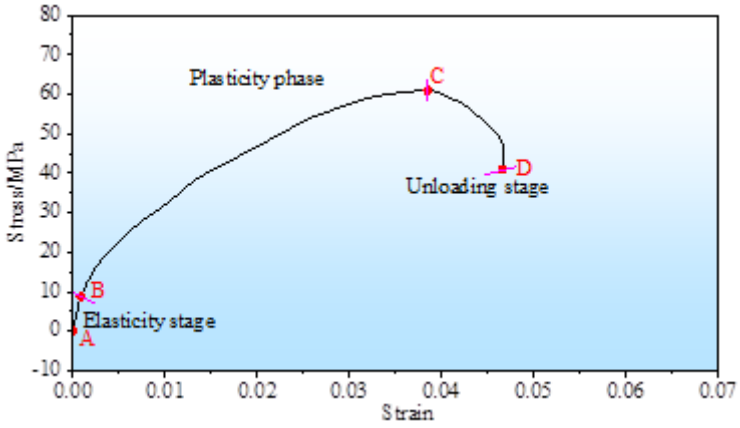

Fig. 9. Typical stress-strain curve

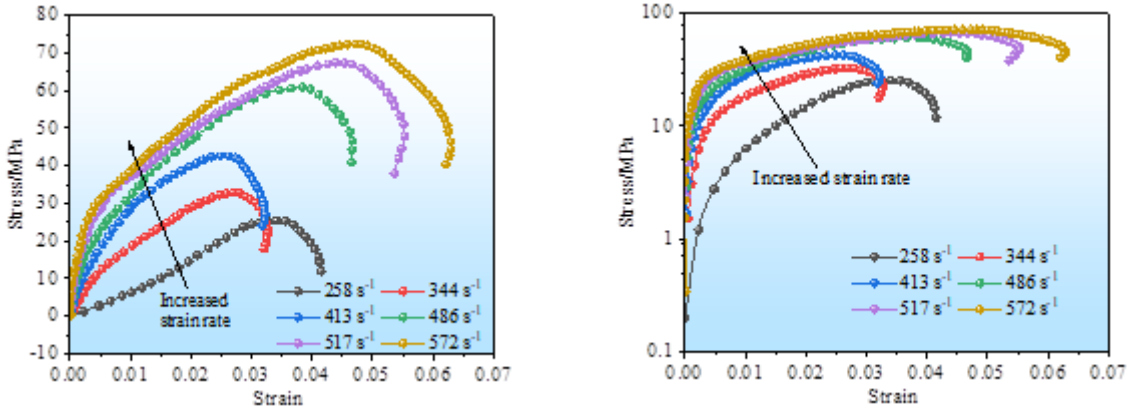

(a) (b)

Fig. 10. Effect of loading strain rate on dynamic stress-strain (a) linear scale (b) semi-logarithmic scale

3.3 Effect of Moisture Content on Compressive Characteristics

To investigate the effect of moisture content on the dynamic response of the specimens, Figure 11 presents the stress-strain relationships of specimens at a strain rate of 570 s^{-1}. The results show that the stress-strain curves of the specimens exhibit three distinct stages. Higher moisture content results in a smoother transition from the elastic phase to the plastic phase, with a broader strain range at lower stress levels. As the moisture content increases from 34% to 48%, the specimens exhibit pronounced strain rate sensitivity. As the strain rate increases, the peak stress rises from 65.73 MPa to 71.18 MPa, reflecting an 8.3% increase. Furthermore, the higher the moisture content, the smaller the strain corresponding to the peak stress. This phenomenon can be attributed to the reduction in pore volume within the soil with increasing moisture content. Since water within the pores is incompressible, the axial compression of the soil under impact loading decreases with increasing moisture content.

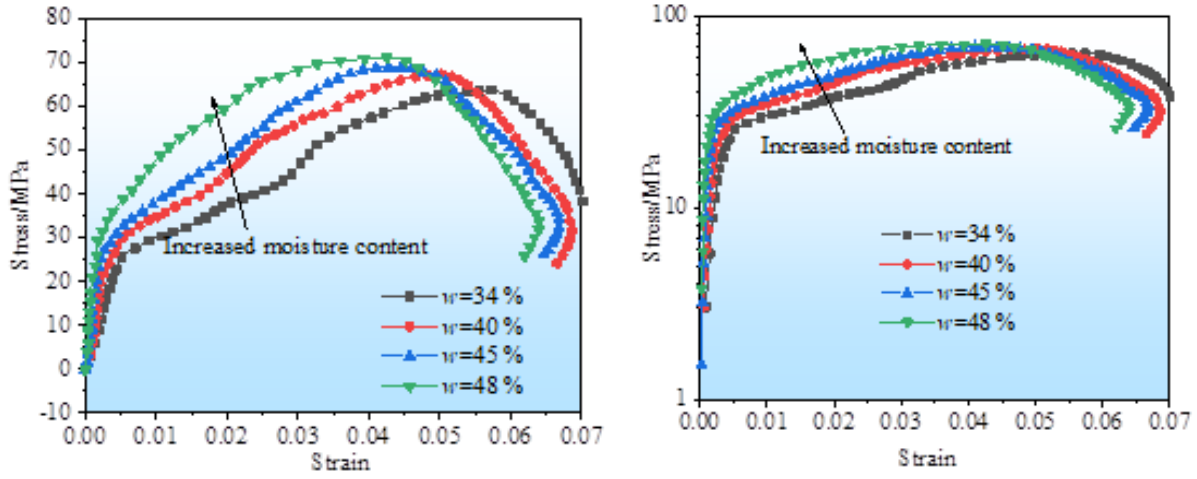

Fig. 11. Effect of moisture content on stress-strain (a) linear scale (b) semi-logarithmic scale

To further investigate the relationship between the dynamic response parameters of sandy soil during the elastic deformation phase and the strain rate, the dynamic elastic modulus is defined as the slope of the tangent to the stress-strain curve:

$$E_d = \frac{\sigma_d}{\varepsilon_d} \tag{5}$$

where σ_d represents the maximum stress in the elastic phase of the stress-strain curve, and ε_d corresponds to the strain at the maximum stress during the elastic phase.

Figures 12 present the fitting relationships between the dynamic elastic modulus and strain rate for samples with varying moisture contents. The fitting results show that both the dynamic elastic modulus and peak stress exhibit a linear increase with increasing strain rate across all moisture content conditions. The fitting accuracy for all curves exceeds 90%, indicating a strong correlation. In the linear fitting functions, the slope represents the rate at which the dynamic response parameters increase with strain rate under identical conditions.

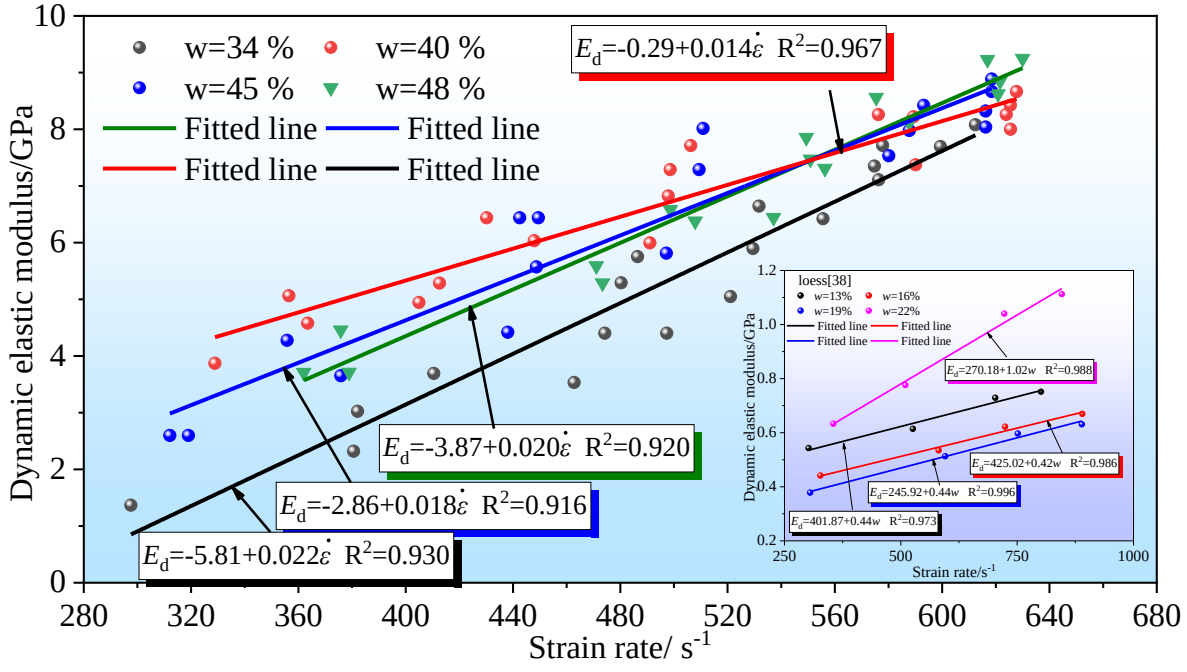

Fig. 12. Effect of strain rate on dynamic elastic modulus in sandy soil and loess

Based on the slopes in Fig. 12, the corresponding values for samples with moisture contents of 34%, 40%, 45%, and 48% are 0.022, 0.014, 0.018, and 0.020, respectively. This indicates that the influence of moisture content on the dynamic elastic modulus initially decreases and then increases. Figure 12 further illustrates the relationship between dynamic elastic modulus and strain rate for loess specimens with varying moisture contents under impact loading [38]. The results demonstrate a strong linear correlation between dynamic elastic modulus and strain rate within the 300–900 s^{-1} range, which is consistent with the findings of this study.

Similar trends are observed in the effect of moisture content on the peak stress of the samples, as shown in Fig. 13. For moisture contents of 34%, 40%, 45%, and 48%, the corresponding slopes of the fitted lines are 0.169, 0.106, 0.147, and 0.118, respectively. Furthermore, a study on the dynamic mechanical response of compacted clay [39] reported a similar pattern to that presented in Fig. 13. These results suggest that under dynamic loading conditions, an increase in strain rate generally enhances the contact stiffness between soil particles, leading to an improvement in the dynamic elastic modulus.

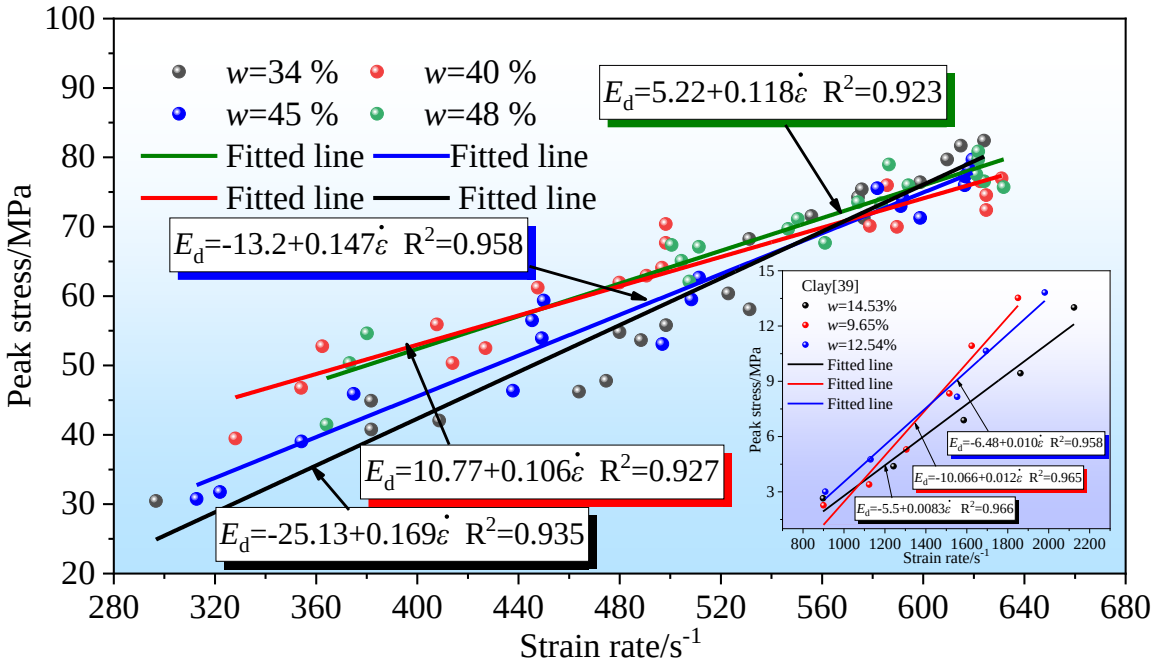

Fig. 13. Effect of strain rate on peak stresses in sandy soil and clays

The area under the stress-strain curve represents the energy absorbed per unit volume by the material during deformation, commonly referred to as energy density [40]. The specific expression is as follows:

$$\eta = \int_0^{\varepsilon} \sigma d\varepsilon \tag{6}$$

Figure 14 illustrates the effect of loading strain rate on the energy density of the specimens. The results demonstrate that as the strain rate increases, the energy density follows an exponential growth trend, with the rate of increase becoming more pronounced at higher strain rates. Specifically, as the loading strain rate increases from 258–572 s^{-1}, the energy density rises from 0.474 MJ/m^3 to 2.698 MJ/m^3, representing a 469.2% increase. This indicates that with an increase in loading strain rate, the specimen's compactness improves, leading to enhanced contact forces and friction between particles, which results in a significant rise in energy density. In addition, the variation of energy density with strain rate exhibits similar characteristics in sandy soils compared to compacted clay soils.

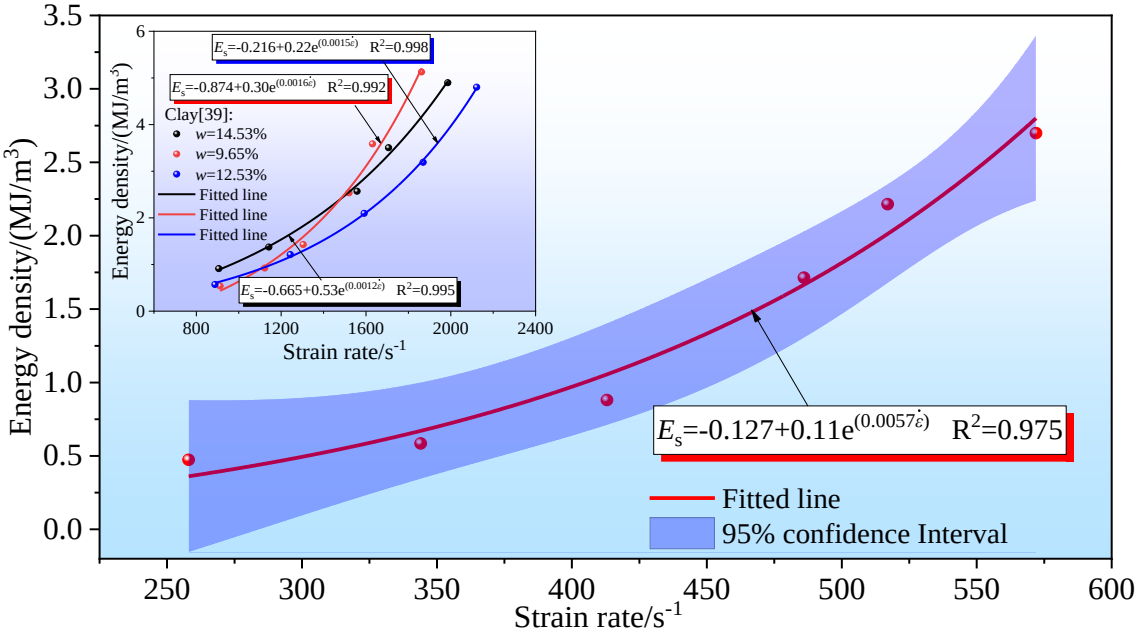

Fig. 14. Effect of strain rate on the energy density

Figure 15 illustrates the impact of moisture content on the energy density of the specimens. The results show that, under consistent loading strain rate conditions, energy density decreases linearly as moisture content increases. Specifically, when moisture content rises from 34% to 48%, energy density declines from 2.54 MJ/m^3 to 2.2 MJ/m^3, reflecting a reduction of 13.4%. This trend can be attributed to the fact that increasing moisture content adds a thin water film around soil particles, which reduces inter-particle bonding and frictional resistance, thereby lowering energy density. However, compared to the impact of loading strain rate on energy density, the effect of moisture content on the specimen's energy density is relatively minor. This finding aligns with the characteristics of silica sand discussed in [41].

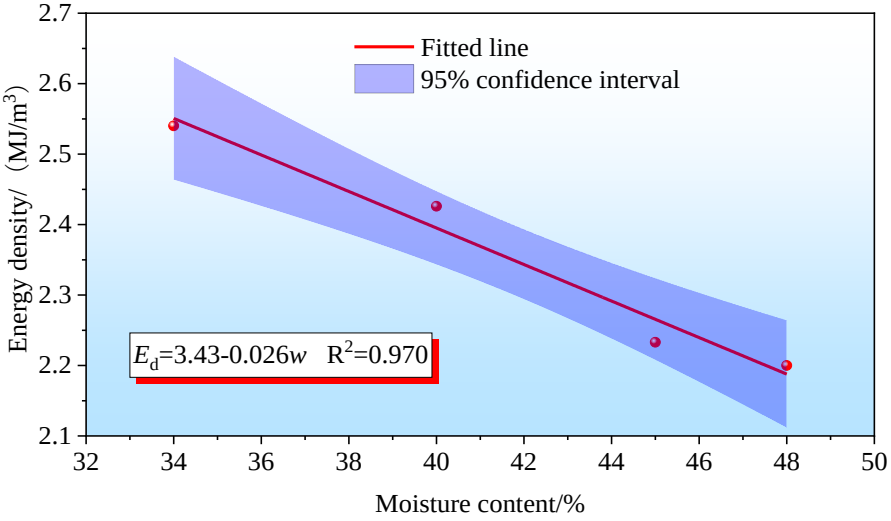

Fig. 15. Effect of moisture content on energy density

3.4 Effect of Repeated Impacts

In practical engineering, single-impact conditions are the most common. However, sandy soil may also experience repeated impacts. Therefore, it is essential to study the compression characteristics of soil under repeated impact loading.

Figure 16 illustrates the dynamic stress-strain characteristics of the specimen under single, triple, and quintuple impact conditions with an impact pressure of 0.05 MPa. The results indicate that as

the number of impacts increases, the internal pores of the specimen compress, resulting in enhanced soil compactness. Concurrently, soil particles may fracture and rearrange, which improves inter-particle bonding and friction, leading to a gradual increase in peak stress. Specifically, under a single impact load, the peak stress is 25.49 MPa. After five repeated impacts, the peak stress increases to 33.83 MPa, reflecting a 32.7% rise. Moreover, the stress-strain patterns observed for calcareous sand [42] under single, triple, seven, and ten impact conditions closely resemble those shown in this study (Fig. 16).

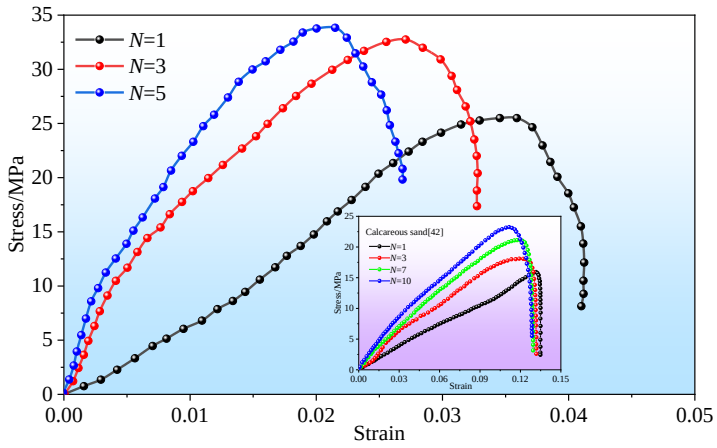

Fig. 16. Effect of number of impacts on stress-strain in sandy and calcareous sands

Figures 17 and 18 illustrate the effects of varying impact pressures on the dynamic elastic modulus and peak stress of the specimen. The results demonstrate that both peak stress and dynamic elastic modulus exhibit an exponential increase with successive impact repetitions. The dynamic elastic modulus reflects the soil's resistance to deformation under dynamic loading. Under the influence of impact loads, the soil's pore structure undergoes significant changes due to compression and particle rearrangement, resulting in increased soil stiffness, as indicated by the rapid rise in the dynamic elastic modulus. As the number of impacts increases, the available space for further compaction of the soil pores decreases, leading to a gradual reduction in the rate of increase, with the curves eventually leveling off.

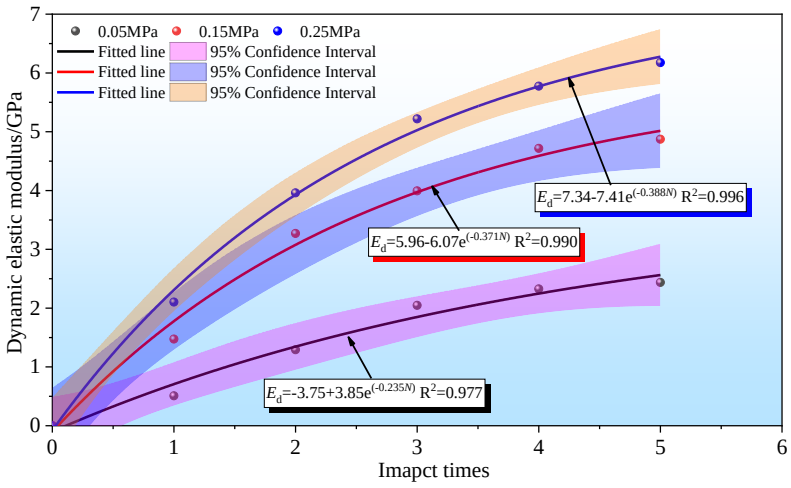

Fig. 17. Effect of impact number on dynamic elastic modulus of elasticity

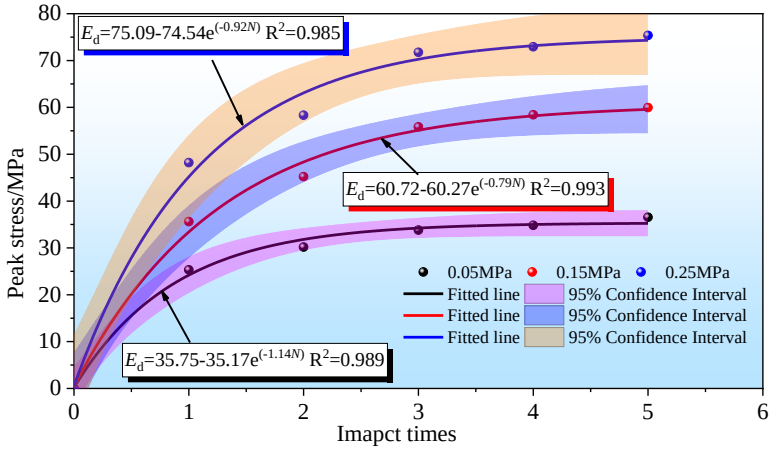

Fig. 18. Effect of impact number on dynamic peak stress

Figures 19 and 20 illustrate the variations in dynamic elastic modulus and peak stress with the number of impacts for specimens with different moisture contents. The results show that both dynamic elastic modulus and peak stress follow a similar exponential function relationship with increasing impact repetitions. Specifically, as the moisture content increases from 34% to 48%, the dynamic elastic modulus rises from 4.95 GPa to 6.98 GPa, while the peak stress increases from 59.72 MPa to 67.95 MPa, corresponding to increments of 41.0% and 13.8%, respectively. Overall, the effect of moisture content on the dynamic elastic modulus is more significant than its impact on peak stress. According to Yang et al study [43], the increase in moisture content promotes the formation of capillary bridges between particles, which alters their contact states. This microscopic interaction enhances the contact stiffness between particles and improves the overall structural stability, leading to a significant increase in the dynamic elastic modulus. In contrast, peak stress is influenced by not only moisture content but also factors such as sandy soil density, particle gradation, and loading rate. As a result, the effect of moisture content on peak stress is relatively less pronounced and exhibits a more dispersed influence.

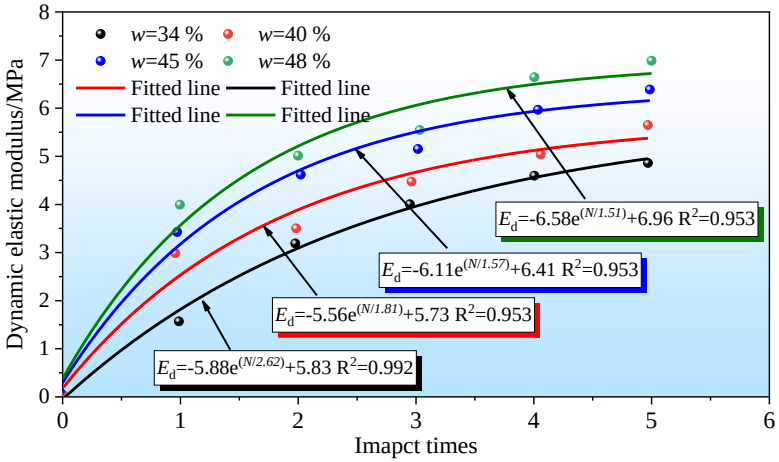

Fig. 19. Effect of the number of impacts on dynamic elastic modulus

Figure 21 compares the effects of repeated impacts on the energy density of sandy soil and calcareous sand [42]. The results indicate that the energy density of both materials increases with the number of impacts, reaches a peak, and then gradually decreases. This behavior is primarily attributed to energy dissipation mechanisms, such as internal friction and micro-crack propagation within the granular materials. As the number of impacts increases, the microstructure of the materials degrades, leading to reduced energy dissipation efficiency and a subsequent decline in energy density after reaching its peak [44]. Therefore, engineered protective structures can be designed to attenuate impact loads by reducing the density of the energy-dissipating layers.

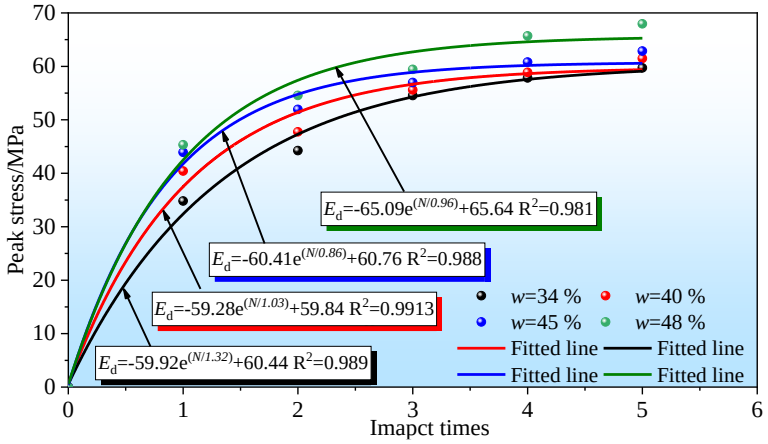

Fig. 20. Effect of the number of impacts on peak stress

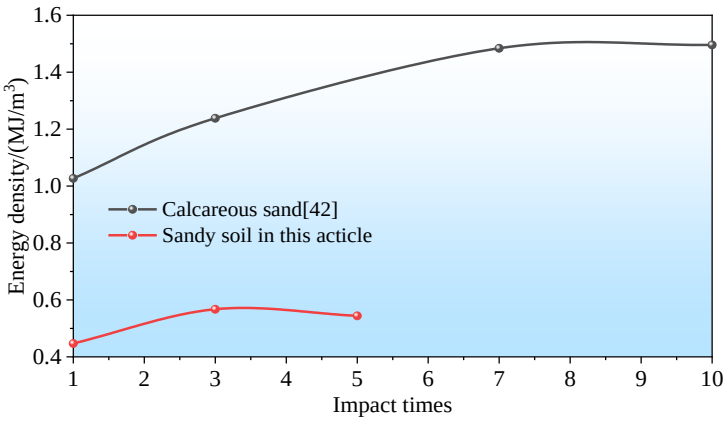

Fig. 21. Effect of the number of impacts on the energy density of sandy soils and calcareous sands

4. Conclusions

Based on dynamic compression tests conducted on sandy soil under passive confining pressure using the SHPB system, this study investigates the effects of loading strain rate, sample moisture content, and impact repetition on the dynamic compression characteristics of the soil. Quantitative relationships between the dynamic response parameters and their influencing factors have been established. The main conclusions are as follows:

- The dynamic stress-strain curve of the samples displayed three distinct stages: elastic, plastic, and unloading. Both the dynamic elastic modulus and peak stress increased linearly with the strain rate. Moreover, the strain rate effect was observed across all moisture content conditions.
- As moisture content increased, the stress-strain relationship showed a reduction in total strain, while both the dynamic elastic modulus and peak stress increased. Notably, at a moisture content of 34%, the strain rate sensitivity of the dynamic elastic modulus and peak stress was most pronounced. In contrast, at 40% moisture content, the sensitivity of the dynamic response parameters to strain rate was the least.
- With an increasing number of impacts, both the dynamic elastic modulus and peak stress of the soil exhibited an exponential growth trend. Higher impact air pressure resulted in more pronounced variations in the dynamic response parameters. Additionally, as the moisture content increased from 34% to 48%, the dynamic elastic modulus increased from 4.95 GPa to 6.98 GPa, and the peak stress rose from 59.72 MPa to 67.95 MPa, corresponding to increases of 41.0% and 13.8%, respectively.

- Currently, research on the dynamic mechanical properties and energy dissipation behavior of sandy soils under impact loading remains limited. This study significantly advances the understanding of these properties, contributing to the development of more accurate constitutive models for sandy soils. Moreover, the test results offer robust technical support for the buffering and shock-absorbing capabilities of sandy soils under impact loads, serving as a valuable reference for the design and construction of protective structures involving sandy soils.

Acknowledgement

The authors acknowledge that this study is supported by 2024 Jiangsu Universities Qinglan Project, China.

References

[1] Wang S, Shen L, Maggi F, Zein AE, Nguyen, GD, Zheng Y. Influence of dry density and confinement environment on the high strain rate response of partially saturated sand. International Journal of Impact Engineering. 2018; 116: 65–78. https:// doi.org/10.1016/j.ijimpeng.2018.02.006
[2] Li JC, Ma GW. Experimental study of stress wave propagation across a filled rock joint. International Journal of Rock Mechanics and Mining Sciences. 2009; 46(3):471–478.https:// doi.org/10.1016/j.ijrmms.2008.11.006
[3] Zhou H, Ren HQ, WU XY. A review of sacrificial claddings in multilayer protective structure. Explosion and Shock Waves. 2022; 42(11):3–28.
[4] Guruprasad S, Mukherjee A. Layered sacrificial claddings under blast loading. Part II: experimental studies. International Journal of Impact Engineering. 2000; 24(9): 975–984. https:// doi. 10.1016/S0734-743X(00)00005-1
[5] Zhao DB, Yi WJ, Kunnath SK. Numerical simulation and shear resistance of reinforced concrete beams under impact. Engineering Structures. 2018; 166: 387–401. https:// doi.org/10.1016/j.engstruct.2018.03.072
[6] Prisco CD, Vecchiotti M. Design charts for evaluating impact forces on dissipative granular soil cushions. Journal of Geotechnical and Geoenvironmental Engineering. 2010; 136(11): 1529–1541.https:// doi.org/10.1061/(ASCE)GT.1943-5606.0000363
[7] Bhatti AQ, Kishi N. Impact response of RC rock-shed girder with sand cushion under falling load. Nuclear Engineering and Design. 2010; 240(10):2626–2632. https:// doi.org/10.1016/j.nucengdes.2010.07.029
[8] Wu JL, Hu XW, Mei XF, Xu ZP, Luo G. Dynamic response of RC slab with cushion layer composed ofsandy soil to rockfall impact. Hydrogeology and Engineering Geology. 2021; 48(1): 78–87.https:// doi.org/10.16030/j.cnki.issn.1000-3665.202004029
[9] Lv H, Wang ZQ. Experimental study of shock attenuation by dense packed sand wall. China Safety Science Journal. 2016; 26(10):64-69.https:// doi.10.16265/j.cnki.issn1003-3033.2016.10.012
[10] Cai GP, Guo JS, Xia LY. Particle Size Distribution Characteristics of Bond Impact Based on Weibull Distribution. Metal Mine. 2016; (04):118-121.https:// doi.CNKI:SUN:JSKS.0.2016-04-026
[11] Pan YH, Zong ZH, Qian HM, et al. Experiment study on blast wave propagation in calcareous sand. Explosion and Shock Waves, 2023; 43(05): 1–15.https:// doi.10.11883/bzycj-2022-0117
[12] Gara N, Verma R, Velmurugan R. Impact behaviour of Al 2014 wrought alloy using Split-Hopkinson pressure bar (SHPB): Its influence on mechanical and microstructural properties. Materials Characterization. 2024; 43(05): 113860.https:// doi.org/10.1016/j.matchar.2024.113860
[13] Zhang M, Wu H J, Li QM, Huang FL. Further investigation on the dynamic compressive strength enhancement of concrete-like materials based on split Hopkinson pressure bar tests. Part I: Experiments .International Journal of Impact Engineering. 2009; 36(12):1327–1334.https:// doi.org/10.1016/j.ijimpeng.2009.04.009
[14] Ai D, Zhao Y, Wang Q ,Wang Q, Li CW. Experimental and numerical investigation of crack propagation and dynamic properties of rock in SHPB indirect tension test. International Journal of Impact Engineering. 2019; 126:135–146.https:// doi.org/10.1016/j.ijimpeng.2019.01.001
[15] Wei Y, Lu Z, Hu K, Li XY, Li PJ. Dynamic response of ceramic shell for titanium investment casting under high strain-rate SHPB compression load. Ceramics International. 2018; 44:11702-11710.https://doi.org/10.1016/j.ceramint.2018.03.247
[16] Xu PB, Yu Y, Li K, Wu XT. SHPB experiment research on dynamic property of expanded polystyrene foam. Polymer Testing. 2018; 69:431–436. https:// doi.org/10.1016/j.polymertesting.2018.06.004
[17] Lv YR, Li X, Wang, Y. Particle breakage of calcareous sand at high strain rates. Powder Technology. 2020; 336: 776–786. https://doi.org/10.1016/j.powtec.2020.02.062

[18] Yu X, Ren W, Zhou B,Chen L, Xu X, Ren G. Experimental study on the mechanical behavior and energy absorption capacity of coral sand at high strain rates. Ocean Engineering. 2024; 291:1–13. http:// doi. org/10.1016/j.oceaneng.2023.116343
[19] Yu X, Chen L, Fang Q, Zhang JH, Guo D, Hou XF. Determination of attenuation effects of coral sand on the propagation of impact-induced stress wave. International Journal of Impact Engineering. 2019; 125:63–82.http:// doi. org/10.1016/j.ijimpeng.2018.11.004
[20] Ross CA, Thompson PY, CHARLIE WA, Doehring DO. Transmission of pressure waves in partially saturated soils. Experimental Mechanics. 1989; 29(1):80–83.http:// doi. org/10.1007/BF02327786
[21] Shukla A, Damania C. Experimental investigation of wave velocity and dynamic contact stresses in an assembly of disks. Experimental Mechanics. 1987; 27(3):268–281.
[22] Lv Y, Ng C W W, Wang Y. Evaluation of Wave Dissipation in Sand under Impact Loading. Journal of Geotechnical and Geoenvironmental Engineering. 2019; 145(9):06019007.http:// doi.10.1061/(ASCE)GT.1943-5606.0002104.
[23] Bragov AM, Grushevsky GM, Lomunov AK. Use of the Kolsky method for confined tests of soft soils. Experimental Mechanics. 1996; 36(3): 237–242. http:// doi. org/10.1007/BF02318093
[24] Felice CW, Gaffney ES, Brown JA. Extended split-hopkinson bar analysis for attenuating materials. Journal of Engineering Mechanics. 1991; 117(5): 1119–1135. https:// doi. org/10.1061/(ASCE)0733-9399(1991)117:5(111)
[25] Brogov AM, Lomunov AK, Sergeichev IV, Tsembelis K, Proud WG. Determination of physic mechanical properties of soft soils from medium to high strain rates. International Journal of Impact Engineering. 2008; 35(9):967–976.http:// doi. org/10.1016/j.ijimpeng.2007.07.004
[26] Ma DD, Ma QY, Yuan P. SHPB tests and dynamic constitutive model of artificial frozen sandy clay under confining pressure and temperature state. Cold Regions Science and Technology. 2017; 136: 37–43. http:// doi.org/10.1016/j.coldregions.2017.01.004
[27] Fu T, Zhu Z, Cao C. Simulating the dynamic behavior and energy consumption characteristics of frozen sandy soil under impact loading. Cold regions science and technology. 2019; 166: 1–15. http:// doi.org/10.1016/j.coldregions.2019.102821
[28] Martin BE, Chen W, Song B, Akers SA. Moisture effects on the high strain-rate behavior of sand . Mechanics of Materials. 2009; 41(6):786–798. http:// doi. org/10.1016/j.mechmat.2009.01.014
[29] Dwivedu SK, Pei L, Teeter R. Two-dimensional mesoscale simulations of shock response of dry sand. Journal of Applied Physics. 2015; 117(8):083502. http://doi:10.1063/1.4913479
[30] Waymel RF, Wang EH, Awasthi A, Geubelle PH, Lambros J. Propagation and dissipation of elasto-plastic stress waves in two dimensional ordered granular media. Journal of the Mechanics and Physics of Solids. 2017; 120:117–131. https:// doi.org/10.1016/j.jmps.2017.11.007
[31] Lv Y, Li F, Liu Y, Fan P, Wang M. Comparative study of coral sand and silica sand in creep under general stress states. Canadian Geotechnical Journal. 2017; 54(11): 1601–1611. https:// doi.org/10.1139/cgj-2016-0295
[32] Hardin B.O. Crushing of soil particles. Canadian Geotechnical Journal. 1985;111(10): 1177–1192. https:// doi.org/10.1061/(ASCE)0733-9410(1985)111:10(1177)
[33] Ministry of Housing and Urban Rural Development of the People's Republic of China. Standard for geotechnical testing method: GB/T 50123–2019. Beijing: China Planning Press, 2019.
[34] Gray G T. Classic split-Hopkinson pressure bar testing: ASM Handbook (Vol. 8): mechanical testing and evaluation. 10th ed. Ohio: Materials Park of ASM International, 2000.
[35] Li SL, Liu DS, Li XL, et al. Experimental study on the length effect of ϕ75 mm split Hopkinson compression bar. Journal of China University of Mining and Technology. 2010; 39(1): 93–97.
[36] Chen XD, Asce AM, Ge LM, Zhou,JK, Wu SX. Experimental Study on Split Hopkinson Pressure Bar Pulse-Shaping Techniques for Concrete. Journal of Materials in Civil Engineering. 2015: 04015196. https:// doi.org/10.1061/(ASCE)MT.1943-5533.0001494
[37] Bragov AM, Lomunov AK, Lamzin DA, Konstantinov AY. Dispersion correction in split-Hopkinson pressure bar: theoretical and experimental analysis. Continuum Mechanics and Thermodynamics. 2022; 34: 895–907.https:// doi.10.1007/s00161-019-00776-0
[38] Tong CX, Xing DP, Hao ZB, et al. Study on Dynamic mechanical behavior of loess under impact loading. Chinese Journal of Highways. 2025; 38(01):73–82. https:// doi.10.19721/j.cnki.1001-7372.2025.01.004
[39] Liu JX, Chen ZF, Xu WF, et al. Experimental study on dynamic mechanical properties of compacted clay under different compaction degrees and water contents. Rock and Soil Mechanics. 2012; 33(6):1631–1639.https:// doi.10.16285/j.rsm.2012.06.017
[40] Ramesh KT. High rates and impact experiments. Springer Handbook of Experimental Solid Mechanics. Berlin: Springer, 2008. https:// doi. org/10.1007/978-0-387-30877-7_33
[41] Barr A, Clarke S, Petkovski, M. et al. Effects of strain rate and moisture content on the behaviour of sand under one-dimensional compression. Experimental Mechanics. 2016; 56(9):1–15. https://doi. org/10.1007/s11340-016-0200-z

[42] OuYang HR, Dai GL, Qin W, Zhang CF, Gong WM. Dynamic behaviors of calcareous sand under repeated one-dimensional impacts. Soil Dynamics and Earthquake Engineering. 2021;150: 106891. https://doi.org/10.1016/j.soildyn.2021.106891
[43] Yang CH, Wang YY, Li JG, et al. Testing study about the effect of different water content on rock creep law. Journal of China Coal Society. 2007; 32(7): 695–699.
[44] Ding YY, Zheng ZJ, Wang SL, et al. The dependence of energy absorption behavior of cellular materials on relative density and impact velocity. Chinese Journal of Solid Mechanics. 2018; 39(6): 578–586. https:// doi. 10.19636/j.cnki.cjsm42-1250/o3.2018.030

Research on Engineering Structures & Materials
www.jresm.org
MIM Research Group

Research Article

Influence of quartz replacement by Iraqi porcelanite and silica fume on the properties of porcelain products

Marwa Marza Salman[1,a], Hussein Talab Nhabih[*,2,b]

[1]*Faculty of Engineering, Babylon University, Babylon, Iraq*
[2]*Department of Civil Engineering, Faculty of Engineering, Babylon University, Babylon, Iraq*

Article Info

Article History:

Received 02 Nov 2024
Accepted 06 Feb 2025

Keywords:

Silica fume;
Porcelanite;
Quartz;
Porcelain;
Mullite

Abstract

In this work, Iraqi porcelanite and silica fume were used as a silica source with replacement of quartz in the manufacture of porcelain products to investigate their influence on properties of these products. The specimens were prepared with composition (50: 30: 20) % as kaolin, silica source and feldspar respectively. Then, they dried at (383 K) temperature for 3 hrs. and sintered at (1473 K) temperature by soaking time for 2hrs. The fracture strength, hardness, apparent porosity, bulk density, linear shrinkage, and XRD, SEM and EDS analyses of the specimens were examined. The test results indicated that replacement of quartz by these sources improves the densification behavior and mechanical strength due to form of more amount from the glassy phase and interlocked crystals from mullite phase within the microstructure. Also, this replacement gives an economic interest for the energy saving and reduction of the material consumption, in addition to produce porcelain products with the best mechanical properties.

1. Introduction

Porcelain products are ceramic materials. Ceramic material can outperform its metal and polymer contestants in various applications due to its chemical inertness, low density relatively, that means lightweight, structural and thermal stability in high temperature, resistance of corrosion, involving hot corrosive gases or liquids [1-3]. Porcelain products are high-vitrified ceramic material manufactured from mixtures formulated from feldspar, quartz and kaolin. The feldspars [(K, Na)2O. Al2O3. 6H2O], that serve as fluxes; quartz or flint (SiO2), which retains the formed article shape through sintering; and kaolin [Al2Si2O5 (OH)4], which provides plasticity for the ceramic mixtures [4-6]. These three components put porcelain with the phases systems [(K, Na)2O-Al2O3-SiO2] by term of the oxides components, therefore it is named the triaxial porcelain ceramic [7]. The microstructure for the porcelain body constitutes from main phases which are needle shaped mullite crystals, a heterogeneous glassy matrix, irregular-shaped closed pores and some quartz particles. Mullite crystals, which form by the solid-state decomposition for feldspar with kaolin, donate the excellent chemical, thermal and mechanical properties. Porcelain composition consider from the most-complex ceramic systems because of the processing paths, the complex interaction among raw materials and the firing process kinetics [8, 9].

The increase of mechanical strength and the reduction of the production costs represent the quest over the period of time. In most attempts for increasing the strength, importance was concentrated for decreasing the quartz content within the formula of porcelain due to the phase transformation for β to α quartz that takes place during cooling at temperature (846 K). The phase transformation results into reduction of the volume for the quartz grain and may lead to crack in the ceramic body [10]. Therefore, there are researches to improve the mechanical properties via minimization of the

*Corresponding author: eng.hussein.t@uobabylon.edu.iq
[a]orcid.org/0000-0002-3100-1124; [b]orcid.org/0000-0003-3071-4998
DOI: http://dx.doi.org/10.17515/resm2025-514ma1102rs

quartz use. These involve substitutions of quartz by kyanite [11], Al2O3 [5, 12, 13], rice husk ash [8, 14-16], sillimanite sand [17], fly ash [18], partial substitution of quartz and feldspar with blast furnace slag and fly ash [19, 20], by a blend of silica fume and rice husk ash [21]. Also, there is an effort to part of quartz by fired porcelain that produces a negative result of the bending strength [22]. All these investigators observed a remarkable enhancement of the mechanical properties of porcelain bodies by use the substitution of quartz. In this work, the silica sources used for a substitution of quartz in porcelain bodies are Iraqi porcelanite and silica fume. Silica fume SF, which too defined as micro silica, produces into the metallurgical manufacturing as a waste product which arises from a manufacture of silicon alloys, ferrosilicon or metallic silicon. It involves of microscope sphere-shaped grains that approximately has 0.1 μm diameter and 20 m2/g surface area [23, 24]. It is described with flabby nature which makes it behaves such as a smoke or fume when spread in air, spherical shape, high surface area, and glassy nature [25-27]. In code ACI 116R, silica fume can be defined "very fine non-crystalline silica formed by the electrical arc furnace as a byproduct for the silicon element or by the production of alloys containing silicon" [28, 29]. While, Iraqi porcelanite is a term utilized for identification siliceous rocks by Iraqi geologist, and which is similar to diatomite. This rock is existent in diverse sites from Iraq. Iraqi porcelanite rock composed of Opal-CT (cristobalite-tridymite crystals deposits) derivative of biogenic amorphous opal silica (mainly of diatoms). Diatomite stratification present at several diverse countries and differs with its purity, quality, and utilization between the countries [30-32]. From the important physical properties of Iraqi porcelanite rocks are: porosity, fineness of pores, sorption capacity, light weight and low heat conductivity [32]. Table 1 displays the chemical composition for Iraqi kaolin clay [2], the Iraqi porcelanite rocks [31], and silica fume [21]. This work aims to study the influence of utilization of Iraqi porcelanite and silica fume as a silica source with replacement of quartz in the manufacture of porcelain products on the physical, mechanical and microstructural properties for these products.

Table 1. The chemical composition (% wt.) for some raw materials [2, 21, 31]

Constituents	SiO_2	Al_2O_3	Fe_2O_3	MgO	CaO	Na_2O	K_2O	P_2O_5	Cl	TiO_2	SO_4	LOI
Iraqi porcelanite rocks	70.36	2.6	1.0	5.4	6.1	0.73	0.14	1.42	1.08	-	0.37	10.8
Iraqi kaolin clay	47.4	38.5	0.5	0.3	0.3	0.3	0.6	-	-	0.1	-	12.0
Silica fume	96.05	1.53	0.39	0.60	-	0.34	-	-	-	-	-	0.90

LOI: loss on ignition.

2. Materials and Methods

In this study, Iraqi porcelanite and silica fume were used as a total replacement for quartz in porcelain manufacture. The specimens were prepared by a blend of raw materials with composition (50: 30: 20) % as kaolin, silica source and feldspar respectively. The mixing percentage for raw materials in the specimens is shown in Table 2.

Table 2. Composition of raw material (% wt.) for the specimens.

Raw material	Sample's symbol		
	A	B	C
Kaolin clay [$Al_2Si_2O_5(OH)_4$]	50	50	50
Sodium feldspar [$Na_2O.Al_2O_3.6H_2O$]	20	20	20
Quartz [SiO_2]	30	0	0
Silica fume [SiO_2]	0	30	0
Iraqi porcelanite [$SiO_2.CaO.MgO.Al_2O_3.(OH)_4$]	0	0	30

The powders of materials were mixed in an electrical mixer for 4 hrs in order to homogenize the mixture. The particle size averages of powders of kaolin clay and Iraqi porcelanite were tested by Bettersize 2000 laser particle size analyzer and that were 32.6 μm and 10.2 μm respectively. Table 3 shows the physical properties of Iraqi kaolin clay [2] and silica fume [6]. While, the bulk density and porosity are considered the main physical properties of Iraqi porcelanite rocks, which are (1.1) g/cm^3 and (38.5) % respectively [31].

Table 3. Physical properties of Iraqi kaolin clay and silica fume [2, 6]

Iraqi kaolin clay		Silica fume	
Property	Value	Property	Value
Color	Gray	Color	Grey
Density (g/cm^3)	1.8-2.6	Specific gravity	2.2
Melting point (k)	2043	Diameter (μm)	<1μm
Water solubility	Insoluble	Surface area (m^2/g)	15-30

Hydraulic pressing machine, 13 mm diameter of a steel die and 80 MPa pressure of pressing were used to form the porcelain samples. Polyvinyl alcohol PVA was employed as a plasticizer to bond particles of the materials powders with technique of a semi-dry pressing. Then, a drying furnace with (383 K) temperature was used for drying of the specimens from the moisture. After that, an electrical furnace with (1473 K) temperature, 278 K/min heating rate and 2 hrs soaking period was utilized for sintering of the specimens. Fig. 1 displays the specimens formed in this work.

(a) (b) (c)

Fig. 1. The specimens formed in this work: A (specimens with silica fume), B (specimens with Iraqi porcelanite), C (specimens with quartz)

After that, the samples properties were tested and these tests were included the physical properties (density, porosity and linear shrinkage), mechanical properties (fracture strength and hardness), XRD analysis and SEM of microstructure. They were made as the following:

Archimedes procedure was applied to calculate the porosity and density for porcelain specimens, which were tested depending on ASTM C373-88 standard, and Eqs. (1) and (2) were employed to calculate the density (D, g/cm^3) and porosity (P_o, %) for porcelain specimens respectively [33].

$$D = \frac{M_D * D_{water}}{M_S - M_P} \quad (1)$$

$$P_o\ \% = \frac{M_S - M_D}{M_S - M_P} .100 \quad (2)$$

where, D_{water} symbolizes the density of water (g/cm^3); M_D symbolizes a dry mass for the specimen (g); M_P symbolizes the suspended mass for sample (g); M_S symbolizes the water-saturated mass for sample (g). A linear shrinkage on firing (LS, %) for the sintered specimens was calculated depending on ASTM C1407 standard with usage Eq. (3) below.

$$LS = \frac{D_b - D_f}{D_b}.100 \quad (3)$$

where, D_b and D_f symbolize the diameters of sample before and after firing process respectively. Then, the mechanical testing machine was used to test the fracture strength of specimens ($б_f$, MPa) depending on ASTM standard C773-88 by use Eq. (4) below [34].

$$\sigma_f = \frac{R}{C_A} \quad (4)$$

where, R symbolize an applied force until fracture (N), and C_A symbolize the specimens' cross-section area (mm^2). The microhardness for specimens (HV, MPa) was tested by Vickers hardness test. 90 N indentation load applied for 10 s on the surface of the specimen and Eq. (5) were employed to measure Vickers hardness values depending on ASTM standard C1327- 90 [6, 35].

$$HV = 1.854.\ \frac{L}{n^2} \quad (5)$$

where, L symbolize indentation load (N), while n symbolize indentation diagonal on the sample surface (mm). After that, the powders of specimens were analyzed by XRD diffraction analysis for identification the crystalline phases developed in the specimens. The specimens were ground to take the fine powders that were utilized for XRD diffraction analysis. XRD pattern was gotten by employ SHIMADZU XRD – 6000 devices. This test was achieved by use the continuous scan mode with θ-2θ range as 20 °-70 °, 7 °/min scan speed and 2θ =0.02 ° the step size. Also, the microstructures and chemical composition of specimens were analyzed with scanning electron microscopy SEM and energy dispersive spectroscopy EDS to observe the surface morphology, structure and chemical composition for the specimens.

3. Results and Discussion

Different sources of silica were used as a substitution for quartz in porcelain specimens. These sources are Iraqi porcelanite and silica fume, and the content of silica in them was 70.36 % and 96.05 % respectively as shown in Table 1. These sources contain other chemical constituents. The chemical composition of these sources effected on the properties of porcelain specimens as explained below.

In Figs. 2, 3 and 4, the effect of silica source on the linear shrinkage on firing, apparent porosity and bulk density for the sintered samples is respectively shown. Where, the firing shrinkage and bulk density for specimen with Iraqi porcelanite C were the highest, and those for specimen with quartz A were the lowest among the porcelain specimens. The object in contrast with the porosity. Where, the apparent porosity for specimen with quartz A was the highest, and that for specimen with Iraqi porcelanite C was the lowest among the porcelain specimens. That because of the higher vitrification which happens in the specimens produced with Iraqi porcelanite and silica fume, due to form the glassy phase with more quality in these specimens, as a result to present the alkalis in the chemical composition of Iraqi porcelanite and silica fume which is shown in Table 1. In addition, it can be shown from Table 1 that the quality and quantity of alkalis in the chemical composition of Iraqi porcelanite are more than that of silica fume. Also, other authors emphasized that the sintering occurs in an existence of the liquid phase in many states. Particularly as various phases are existent, this sintering is named a liquid-phase sintering [4, 36, 37]. The liquid phase makes on the approach of particles under an effect of the forces of surface energy generated from tiny pores in specimens. Therefore, open porosity reduces with increasing the glassy phase formation in the specimen. Also, the firing shrinkage and bulk density for specimens increase with increasing of the sintering ability. That means an improving of the densification behavior for the porcelain specimens with replacement of quartz by Iraqi porcelanite or silica fume. This improved densification behavior for the porcelain specimens with presence of different silica sources was associated by the material reactivity, which means the higher surface area in comparison with the quartz powder. Similar results were observed by other works when quartz was replaced with different silica sources [14, 38, 39]. Also, the flabby nature of silica fume particles increased the

firing shrinkage of specimen B [21]. It can be benefited from the results of this work in industrial environments, particularly that produced large amounts of porcelain products. Where, use of silica source contained considerable number of fluxes can be reduced or eliminated the use of fluxes in porcelain manufacture and gave product with good properties. So, the economic interest in comparison with use of quartz from side of the material consumption, and the energy saving because of a presence of the flux's materials in a composition of these silica sources (Iraqi porcelanite and silica fume).

While Figs. 5 and 6 display the influence of silica source on the fracture strength and hardness for the porcelain specimens in that order. It can be shown that the fracture strength for specimen with silica fume B was the highest, and that for specimen with quartz A was the lowest among the porcelain specimens. While, the hardness for specimen with Iraqi porcelanite C was the highest, and that for specimen with quartz A was the lowest among the porcelain specimens. These results obtained because of the pores reduction and the bond process between the grains of specimens, due to form the glassy phase in the porcelain specimens, which means a higher vitrification for specimens. So, more rigid network formed in the specimens, that led to an enhancement in the mechanical properties. In addition, the results of XRD patterns and SEM images identify a presence of higher mullite phase in specimen B and C due to the existence of excess content from alumina in the composition of Iraqi porcelanite and silica fume, as shown in Table 1, that may be contributed in improving of the strength. Similar results were observed by other works [21, 38]. Improving of mechanical properties for products is an important point in the development of industry. Therefore, use of these silica sources (Iraqi porcelanite and silica fume) can be contributed in the development of porcelain industry.

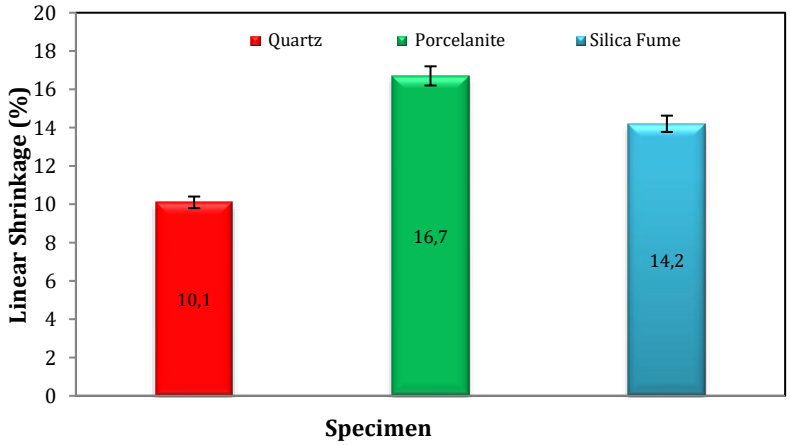

Fig. 2. Silica source effect on the firing shrinkage of porcelain specimens

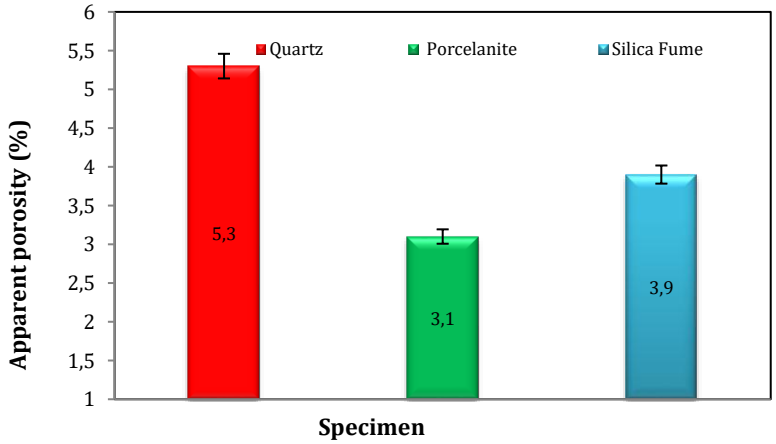

Fig. 3. Silica source effect on the apparent porosity of porcelain specimens

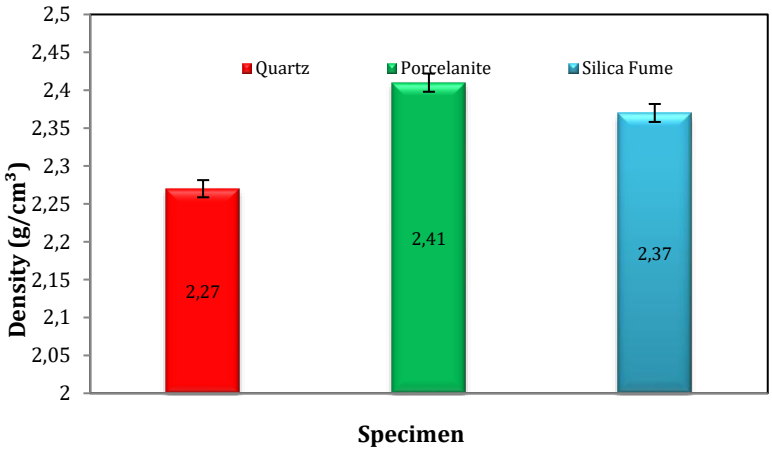

Fig. 4. Silica source effect on the bulk density of porcelain specimens

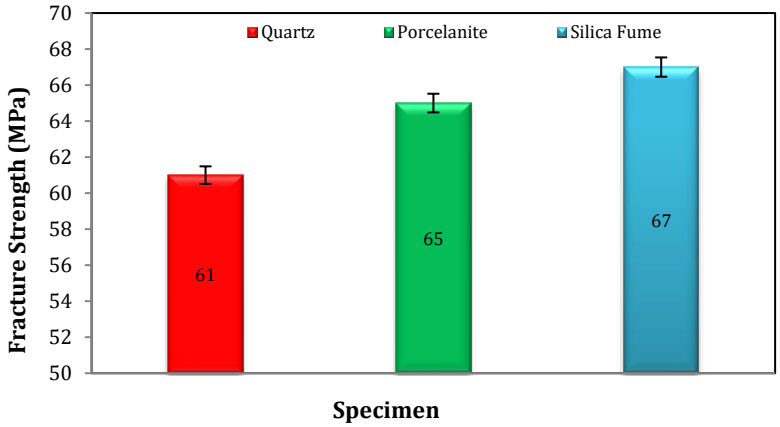

Fig. 5. Silica source effect on the fracture strength of porcelain specimens

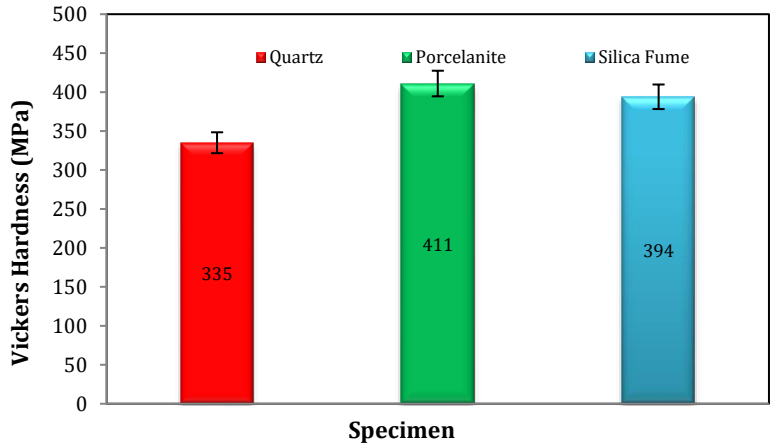

Fig. 6. Silica source effect on the hardness of porcelain specimens

The XRD patterns for the samples A, B and C, that are shown in Fig. 7, display the existence of two main crystalline phases that are, mullite (ICDD 074-4143) and quartz (ICDD 046-1045) in all the samples. It can be observed that the peaks of mullite phase increased and the peak intensity of quartz reduced considerably. XRD patterns showed that use of Iraqi porcelanite and silica fume significantly reduced an amount of the free quartz for the samples B and C, and increased the mullite phase due to the existence of excess content from alumina in their composition as shown in Table 1. Similar results were observed by other works [4, 15, 38].

While SEM images and EDS spectra for the specimens A, B and C are shown in Fig. 8 (a, c and e) SEM images and (b, d and f) EDS spectra for the specimens respectively. SEM images display the existence of a large quantity of remained undissolved free quartz in the microstructure for specimen A, and the reduction in content and size of the quartz crystals and the pores and also the increase in content of the needle-shaped, interlocked mullite crystals embedded with the glassy phase in the microstructure for B and C specimens due to replace the quartz with Iraqi porcelanite and silica fume. This replacement can be possible to remove a large amount from the inherent defects in the porcelain microstructure and to improve the mechanical properties for it. Similar results were observed by other works [21, 38, 40]. From EDS analysis results for the specimens, it can be shown that the Figs. 8 (b), (d) and (f) for the specimens A, B and C respectively are mainly composed of Si, Al and O elements with fewer amounts of Na, Mg, K, Ca and Fe elements in different percentages for all specimens. Where, Si element percentage in Fig. 8 (b) EDS spectra for the specimen A formed with quartz was higher in comparison with that in Fig. 8 (d) EDS spectra for the specimen B formed with silica fume and Fig. 8 (f) EDS spectra for the specimen C formed with Iraqi porcelanite. While, Al element percentage increases with respect to Si element percentage in Figs. 8 (d) and (f) due to the existence of excess content from alumina in composition of these specimens as shown in Table 1. In addition to existence of P and Cl elements in Fig. 8 (f) EDS spectra for the specimen C formed with Iraqi porcelanite due to presence of P_2O_5 and Cl in Iraqi porcelanite composition. These results corresponding with results of XRD analysis for the same specimens.

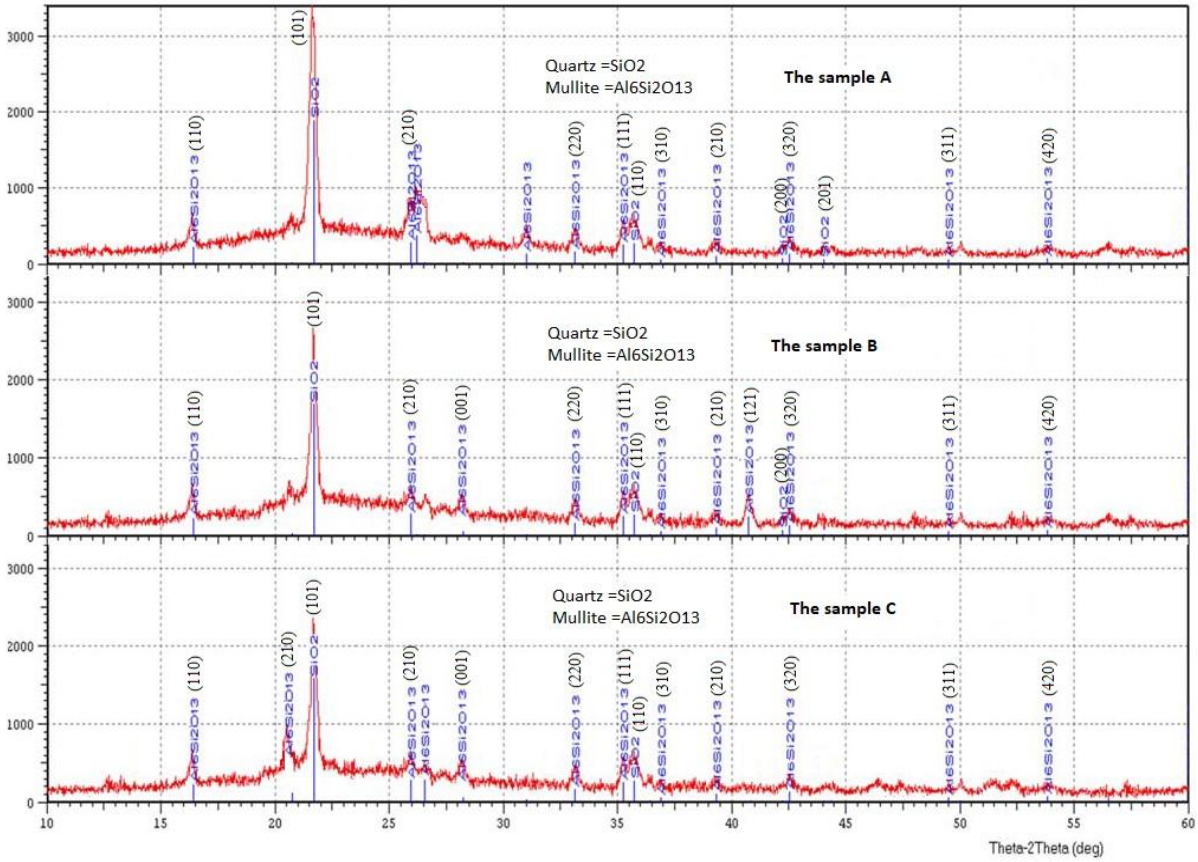

Fig. 7. XRD patterns of the sample A (with quartz), sample B (with silica fume) and sample C (with Iraqi porcelanite)

In comparison this work with researches utilizing alternative silica sources (such as references 4 and 21), these researches employ two alternative silica sources together in the same sample by partial and total substitution of quartz. While, this work employs the total substitution of quartz by one alternative silica source for each sample. Also, it employs Iraqi porcelanite (as alternative silica source) which has a rich chemical composition with the alkalis and an excess content from alumina in his composition. The alkalis are considered fluxes in the ceramic manufacture while alumina can

be contributed in formation a large amount of mullite phase. Thus, it can be obtained the best mechanical properties and densification behavior by use such this source.

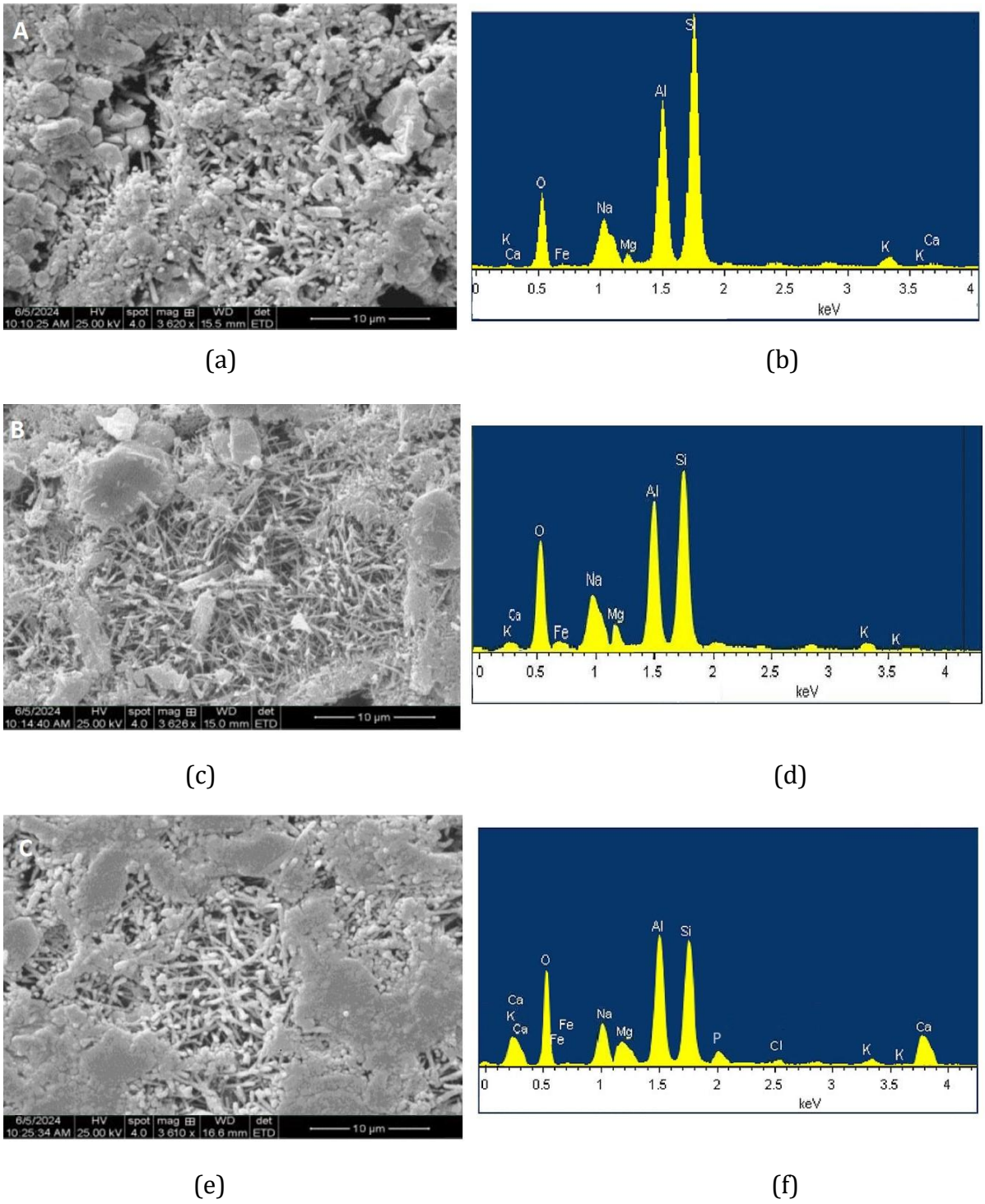

Fig. 8. (a) SEM image and (b) EDS spectra for the sample A (with quartz), (c) SEM image and (d) EDS spectra for the sample B (with silica fume), and (e) SEM image and (f) EDS spectra for the sample C (with Iraqi porcelanite)

4. Conclusions

In this work, Iraqi porcelanite and silica fume were used as a silica source with replacement of quartz in the manufacture of porcelain products to investigate their influence on properties of these products. The fracture strength, hardness, apparent porosity, bulk density, linear shrinkage, and

XRD, SEM and EDS analyses of the specimens were examined. From the results for these tests, it can be concluded that:

- The densification behaviour improves for the porcelain specimens with replacement of quartz by Iraqi porcelanite or silica fume due to form of more amount of the glassy phase in specimen B and C due to existence of considerable amount of the alkalis in their chemical composition.
- The mechanical strength for these specimens improves because of a formation of more quantity from well-interlocked mullite crystals, and a reduction of the content and size for both the quartz crystals and the pores in the microstructure of the specimen B and C.
- XRD patterns for the porcelain specimens show that use of Iraqi porcelanite and silica fume significantly reduce an amount of the free quartz for the samples B and C, and increase the mullite phase due to the existence of excess content from alumina in their composition.
- SEM and EDS analyses display that usage of Iraqi porcelanite and silica fume considerably reduce an amount of the free quartz for the samples B and C, and increase the mullite phase due to the presence of excess content from alumina in their composition.
- The replacement of quartz by Iraqi porcelanite or silica fume in the manufacture of porcelain products improves the physical, mechanical and microstructural properties for these products.
- The replacement of quartz by Iraqi porcelanite or silica fume in the manufacture of porcelain products gives the economic interest in comparison with use of quartz from side of the material consumption, and the energy saving because of a presence of the fluxes materials in a composition of these sources.

Acknowledgement

The authors would like to acknowledge and express their thankfulness to all those who have helped to bring this modest effort to fruition in its present form.

References

[1] Antunes MLP, Botignon de Sá A, Oliveira PS, Range EC. Utilization of gypsum from construction and demolition waste in Portland cement mortar. Cerâmica, 2019; 65(Suppl.1): 1-8. https://doi.org/10.1590/0366-6913201965s12588

[2] Salman MM, Radhi NS, Sabr OH, Nhabih HT. Utilization of diverse cheap materials as pore generating agent to manufacture low-cost porous ceramic. Cerâmica, 2020; 66: 179- 185. https://doi.org/10.1590/0366-69132020663782873

[3] Scheffler M, Colombo P. Cellular ceramics: structure, manufacturing, properties and applications. Wiley-VCH, Weinheim. 2005; 356-360. https://doi.org/10.1002/3527606696

[4] Jamo HU, Umar ID, Abdu S, Tambalo ZA, Abdulkarim S, Salisu IT, Liman AM, Abdullahi MB, Izzudden M. Improvement of porcelain physical properties through the substitution of quartz element with rice husk ash and palm oil fuel ash. Sci. Wo. J., 2022; 17 (1): 38-44.

[5] Das SK, Dana K. Differences in densification behaviour of K-and Na-feldspar-containing porcelain bodies. Thermochim. Act.a., 2003; 406 (1): 199-206. https://doi.org/10.1016/S0040-6031(03)00257-0

[6] Salman MM, Nhabih HT. Assessment of the partial and total replacement of feldspar by waste glass on porcelain properties. J. Ceram. Proc. Rese., 2020; 21 (3): 371-377.

[7] Buchanan WT, Svare CW, Turner KA. The effect of repeated firings and strength on marginal distortion in two ceramometal systems. J. Prost. Dent., 1991; 45 (5): 502-506. https://doi.org/10.1016/0022-3913(81)90035-4

[8] Jamo HU, Noh MZ, Ahmad ZA. Effect of Mould Pressure and Substitution of Quartz by Rice Husk Ash on the Bulk Density and Compressive Strength of Porcelain Body. In Mater. Sci. For., 2015; 819: 212-217. https://doi.org/10.4028/www.scientific.net/MSF.819.134

[9] Edwards HG. Porcelain Analysis and Its Role in the Forensic Attribution of Ceramic Specimens. Cham, Switzerland: Springer. 2022. https://doi.org/10.1007/978-3-030-80952-2

[10] Olorunyolemi OC, Ogunsanya OA, Akinwande AA, Balogun OA, Kumar MS. Influence of SiO2 form the rice husk ash and coal fly ash particles on the mechanical behaviour and grain characteristics of the stir-casted hybrid composites. J. Jpn. Inst. Energy., 2022; 101: 132-137. https://doi.org/10.21203/rs.3.rs-1269445/v1

[11] Schroeder JE. Inexpensive high-strength electrical porcelain. AMERIC. CERAM. SOCI. BULL., 1978; 57(5): 526-531.
[12] Kobayashi Y, Ohira O, Satoh T, Kato E. Effect of quartz on the sintering and bending strength of the porcelain bodies in quartz-feldspar-kaolin system. J. Ceram. Soc. Jpn., 1994; 102: 99-104. https://doi.org/10.2109/jcersj.102.99
[13] Nayak SK, Satapathy A, Mantry S. Use of waste marble and granite dust in structural applications: A review", J. Build. Engine., 2022; 46: 103742-103747. https://doi.org/10.1016/j.jobe.2021.103742
[14] Prasad CS, Maiti KN, Venugopal R. Effect of rice husk ash in whiteware compositions", Ceram. Inter., 2001; 27(6): 629-635. https://doi.org/10.1016/S0272-8842(01)00010-4
[15] Jamo HU, Noh MZ, Ahmad ZA. Influence of Temperature on the Substitution of Quartz by Rice Husk Ash (RHA) in Porcelain Composition. In Appl. Mech. and Mater., 2014; 465: 1297-1303. https://doi.org/10.4028/www.scientific.net/AMM.465-466.1297
[16] Noh MZ, Jamo HU, Ahmad ZA. The Hardness Properties of Porcelain with Substitution of Quartz by Rice Husk Ash at Different Soaking Time. In Mater. Sci. For., 2016; 840: 39-43. https://doi.org/10.4028/www.scientific.net/MSF.840.39
[17] Maiti KN, Kumar S. Effect of substitution of quartz by beach sand sillimanite on the properties of conventional porcelain. Br. Ceram. Trans. J., 1990; 89(1): 24-27.
[18] Dana K, Das SK. Evolution of microstructure in flyash-containing porcelain body on heating at different temperatures. Bull. Mater. Sci., 2004; 27 (2): 183- 188. https://doi.org/10.1007/BF02708503
[19] Dana K, Dey J, Das SK. Synergistic effect of fly ash and blast furnace slag on the mechanical strength of traditional porcelain tiles. Ceram. Inter., 2005; 31(1): 147-152. https://doi.org/10.1016/j.ceramint.2004.04.008
[20] Nhabih HT, Hussein AM, Salman MM. Study a Structural Behavior of Eccentrically Loaded GFRP Reinforced Columns Made of Geopolymer Concrete. Civil Eng. J., 2020; 6 (3): 653-575. https://doi.org/10.28991/cej-2020-03091492
[21] Prasad CS, Maiti KN, Venugopal R. Effect of substitution of quartz by rice husk ash and silica fume on the properties of whiteware compositions. Ceram. Inter., 2003; 29: 907-914. https://doi.org/10.1016/S0272-8842(03)00035-X
[22] Stathis G, Ekonomakou A, Stournaras CJ, Ftikos C. Effect of firing conditions, filler grain size and quartz content on bending strength and physical properties of sanitaryware porcelain. J. Eur. Ceram. Soc., 2004;24(8): 2357-2366. https://doi.org/10.1016/j.jeurceramsoc.2003.07.003
[23] Ghavami S, Farahani B, Jahanbakhsh H, Moghadas Nejad F. Effects of Silica Fume and Nano-silica on the Engineering Properties of Kaolinite Clay. AUT J. Civil Eng., 2018; 2 (2): 135-142.
[24] Nhabih HT, Al-Badkubi MRKM, El-barbary AA, Salman MM. Recycling harmful plastic waste to produce a fiber equivalent to carbon fiber reinforced polymer for reinforcement and rehabilitation of structural members. Curved and Layered Structures, 2024; 11: 20240003. https://doi.org/10.1515/cls-2024-0003
[25] Chatterjee M, Ganguli D. Powder preparation for advanced ceramic, in: S. Kumar (Ed.), Hand Book of Ceramics, Vol. I, Kumar & Associates, Calcutta, India, 1994.
[26] Nhabih HT, Hashim AM, Salman MM. Effect of Delay Curing Start on Durability and Mechanical Properties of High and Normal Strength Concrete. Journal of Engineering and Applied Sciences, 2018; 13(10): 8216-8223.
[27] Hussein AM, Nhabih HT, Jabbar DN. Environmental impact of fuel stations on some heavy metal concentrations in nearby surface crust soils in urban areas: A case study of soil heavy metal contamination. IOP Conf. Series: Materials Science and Engineering, 2020; 745: 012164. https://doi.org/10.1088/1757-899X/745/1/012164
[28] ACI COMMITTEE 116, Cement and Concrete Terminology (ACI 116R-00), American Concrete Institute, New York, America. 2000.
[29] Hashim AM, Nhabih HT. Influence of CaCO3 with Nanoparticles on the Mechanical Characteristics and Concrete Microstructure. International Journal of Civil Engineering and Technology, 2018; 9(10):799-808.
[30] Jaffar RA. Removal of Azure Dyes Using Iraqi Porcelanite Rocks and Novel PMF Polymer, MSc. thesis, College of Science, University of Karbala, Karbala, Iraq, 2014.
[31] Jabboory WM. Mining geology of the porcelanite deposits in wadi Al-Jandali- western desert, Iraq, MSc. thesis, College of Science, University of Baghdad, Baghdad, Iraq, 1999.
[32] Al-Aagily MM. Manufacturing and characterization of porcelanite ceramic filter by slip casting technique, MSc. thesis, College of Engineering, University of Babylon, Babylon, Iraq, 2010.
[33] ASTM C373, Standard test method for water absorption, bulk density, apparent porosity, and apparent specific gravity of fired whiteware products, ASTM Int., West Conshohocken. 1988.
[34] ASTM C773, Standard test method for compressive (crushing) strength of fired whiteware materials, ASTM Int., West Conshohocken. 1988.

[35] Roy M. Mullite development on firing in porcelain stoneware bodies. M.Sc. thesis, The University of British Columbia, Columbia. 2010.
[36] Martín-Márquez J, Rincón JM, Romero M. Mullite development on firing in porcelain stoneware bodies. Journal of the European Ceramic Society, 2010; 30(7): 1599-1607. https://doi.org/10.1016/j.jeurceramsoc.2010.01.002
[37] Romero M, Martín-Márquez J, Rincón JM. Kinetic of mullite formation from a porcelain stoneware body for tiles production. Journal of the European Ceramic Society, 2006; 26(9): 1647-1652. https://doi.org/10.1016/j.jeurceramsoc.2005.03.235
[38] Sarkar R, Ghosh S, Das SK. Waste Silica from Aluminum Fluoride Industries Used for Ceramic Whitewares. American Ceramic Society Bulletin, 2007; 86(10): 9201- 9208.
[39] Dana K, Das SK. Effect of Substitution of Fly Ash for Quartz in Triaxial Kaolin-Quartz-Feldspar System. J. Eur. Ceram. Soc., 2004;24: 3169-3175. https://doi.org/10.1016/j.jeurceramsoc.2003.10.008
[40] Maiti KN, Kumar S. Effect of glass-ceramics and sillimanite sand additions on microstructure and properties of porcelain. Ceram. Int., 1992;18 (6): 403-412. https://doi.org/10.1016/0272-8842(92)90073-M

Research on Engineering Structures & Materials
www.jresm.org
Research Group

Research Article

Laboratory improvement of clay mineralogical and swelling properties using hydraulic binder treatment

Mehdi Mebarki [*1,2,a], Sabah Benyahia [3,4,b], Saci Dahmani [1,5,c]

[1]*Department of Science and Technology, Tamanghasset University, Tamanghasset, Algeria*
[2]*Civil Engineering Laboratory, Risks and Structures in Interaction (LGC - ROI), University of Mostefa Ben Boulaid Batna 2, Batna, Algeria*
[3]*Department of Geology, University of Mostefa Ben Boulaid Batna 2, Batna, Algeria*
[4]*Hazards and Territory Planning Laboratory (LRNAT), University of Mostefa Ben Boulaid Batna 2, Batna, Algeria*
[5]*Laboratory of Exploiting and Valorization of Natural Resources in arid zones, University of Ouergla, Algeria*

Article Info

Article History:

Received 13 Mar 2025
Accepted 21 Apr 2025

Keywords:

Clay soil;
Hydraulic binders;
Treatment;
Swelling potential;
Mineralogy;
Microstructure

Abstract

This article outlines the findings from experimental research to improve the mechanical characteristics, notably the swelling potential of a clay sourced from the Boumagueur area in eastern Algeria. In a first part, oedometer tests conducted according to ASTM 4546-03, revealed that increasing binder content significantly reduced swelling properties. From the natural state (without hydraulic binder) to 9% binder content, swelling pressure decreased by 72% for samples treated with lime, 58% for cement, and 62% for the lime-cement mixture. Similarly, swelling potential was notably reduced, with lime treated samples showing an 87% decrease, compared to 57% for cement and 73% for the lime-cement mixture. In the second part of this work, X-ray diffraction analysis confirmed that the reduction in swelling was due to the formation of a cementitious phase, such as hydrated calcium silicate (CSH). Overall, the addition of hydraulic binders effectively improved the swelling behavior of the soil.

1. Introduction

The swelling phenomenon of clay soils is one of the significant problems in geotechnics, referring to the volume increase that occurs when these soils absorb water. This behavior primarily due to the mineralogical composition and structural characteristics of clay particles, which allow strong interactions with water molecules triggering hydration phenomena, resulting in an increase in volume. Clay minerals, such as montmorillonite or smectite, which have a layered structure consisting of alumina (Al_2O_3) and silica (SiO_2), are characterized by weak bonding, allowing water to easily penetrate the interlayer spaces. Consequently, this further weakens the bonds between the layers, causing their separation and leading to significant volumetric swelling [1].

The swelling of certain clay soils, particularly in arid or semi-arid area, causes damage and disorder mainly affecting structures built on the surface and underground [2, 3]. Losses in different types of construction attributed to this phenomenon are very costly. Barbosa et al. [4] reported that the volumetric variation of expansive soils in the state of Acre (Brazil) caused significant financial losses. Similarly, Jones and Jefferson [5] have referred to swelling clays as being the most damaging geohazard in Britain, costing the insurance industry significant financial losses per year. Other

*Corresponding author: meb_mehdi@hotmail.com
[a]orcid.org/0009-0008-1727-2009; [b]orcid.org/0009-0007-6949-8678; [c]orcid.org/0009-0007-6836-9225
DOI: http://dx.doi.org/10.17515/resm2025-752ma0313rs

similar studies of the swelling soils have been made in China [6], Africa [7] and Australia [8]. To clarify the mechanisms at the origin of this phenomenon and to reduce its effect by proposing effective mitigation measures, this phenomenon was widely studied using various techniques by numerous researchers [9, 10]. Meanwhile, many studies have focused on soil stabilization using additives, owing to their ability to improve the geotechnical properties of clay soils [11, 12]. Several and different materials were used as additives to stabilize clay soils and reduce their swelling, such as the incorporation of sand [13, 14], fly ash [15, 16], milk of lime [17, 18], cement [19, 20], lime [21, 22].

The inclusion of lime and/or cement to treat clay soils therefore incentivizes engineers to opt for these stabilizers owing to its beneficial impacts on improving various geotechnical properties of these soils. Many studies have illustrated that treatment with these hydraulic binders, can ameliorate the properties of soils exhibiting subpar physical and mechanical characteristics, such as high plasticity, high swelling, low permeability, and weak mechanical strength, along with susceptibility to water-induced effects. The addition of lime and/or cement into clay soil was observed to diminish its plasticity and compressibility, while augmenting its permeability and mechanical strength, due to hydraulic binder ability to induce soil particle flocculation [23, 24, 29, 26, 27]

Por et al. [28] conducted tests on Na-montmorillonite bentonite. The experimental program involved unconfined compression, vertical free swelling strain, and confined swelling pressure tests. The experimental results show that the cement addition led to marked decreases in the vertical free swelling strain and to the obvious improvement of strength and stiffness of soils. In addition, it was noted that the cement had a greater effect in reducing vertical swelling pressure than the lateral swelling pressure of the soils during one-dimensional swelling. Al-Gharbawi et al. [29], found that the expansive soil treated with cement, has a reduction in free swelling and swelling pressure of about 65 and 76% respectively, compared to untreated soil. In addition to these results, it was also observed in many studies that adding cement reduces the plasticity index and compressibility, while augmenting the mechanical strength of swelling soils [30, 31, 32]. Kemissa et al. [33] present a series of laboratory test results of physical and mechanical characterization obtained on an over consolidated expansive clay treated with lime. They noted an important reduction of its plasticity, which becomes less sensitive to water, resulting in an appreciable mitigation of its potential of swelling. They concluded also that the best performances were obtained for a treatment dosage of 8% lime, which led to a significant improvement of bearing capacity and drained and undrained shear strength of studied soil. Similar results have also demonstrated the effectiveness of adding lime to improve the physical and mechanical properties of swelling soils [34, 35, 36, 37, 38].

For its use in the road works as roadway foundation, Khemissa and Mahamedi [39] investigated a highly plastic swelling clay. The test results demonstrated a significant improvement in the mechanical properties of this swelling clay when treated with varying proportions of a cement-lime mixture and compacted under optimal Proctor conditions. They observed a reduction in the plasticity index and noted that the clay became non-expansive and more compactable. This was accompanied by an increase in CBR values, allowing this fact of increasing the bearing pressure of clay. Additionally, the shear strength of the clay improved, further increasing its bearing capacity. Notably, the best performance was achieved with a combined treatment of 8% cement and 4% lime. Wang and Korkiala [40] conducted incremental loading oedometer tests on soft clay and found that increasing the cement-lime dosage and curing time led to a reduction in the initial void ratio and an increase in the clay dry mass. Their results also revealed a significant increase in the compression index at low cement-lime dosages until a peak value around 3% cement-lime, followed by a significant decrease with higher cement-lime dosage. The most evident effect of chemical treatment was the increase in the elastic limit. The addition of hydraulic binders (lime and/or cement) to soil in the presence of water, initially trigger the flocculation of soil particles, and subsequently, induce a pozzolanic reaction. Calcium cations released from hydraulic binders react with silica ($SiO2$) and/or alumina ($Al2O3$) to form cementing agents such as calcium silicate hydrate (CSH), calcium aluminate hydrate (CAH), and calcium aluminosilicate hydrates (CASH) [41,

42, 43, 44, 45]. These compounds interact with clay minerals, altering the soil structure and improve its physical and mechanical properties [46, 47, 48, 49].

This study investigates the effectiveness of lime and cement in stabilizing swelling clay soils, particularly in the Boumagueur – Batna region of eastern Algeria, which is significantly affected by this geotechnical issue. This phenomenon causes differential soil movements, leading to significant damage such as deformations of the roadways; cracks mainly affecting the different elements of the structures (foundations, engineering structures, masonry, etc.) built at shallow depth and without particular precautions. The research evaluates how used hydraulic binders alter the soil mineralogical composition, reduce compressibility, and mitigate swelling effects. By addressing these regional challenges, the study contributes to the literature on soil stabilization, providing practical solutions for similar geotechnical issues in areas prone to swelling soils.

2. Studied Soil and Used Materials

2.1. Studied Soil

The soil under study originates from the urban vicinity of Boumagueur, situated approximately 85 kilometers southwest of the Batna province -Algeria- (see Fig. 1). Several disorders caused by the swelling phenomenon were observed in studied area (see Fig. 2). Generally, these disorders affect light constructions with a single ground floor, which is the most widespread type of construction in this region, and manifest themselves in the form of: detachment of the parts attached to the main parts, detachment and deformation of the exterior slabs as well as various structural cracks with variable openings.

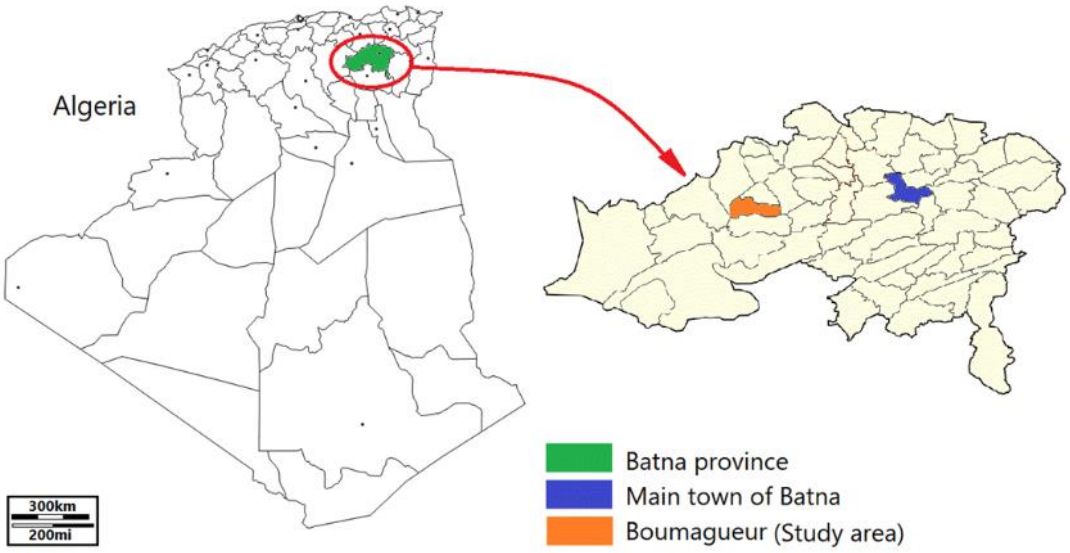

Fig. 1. Geographic location of the Boumagueur region

Geological scrutiny, relying on cartographic data in Fig.3 (1/50 000 geological maps, [50]) and on-site examinations, reveals that the Boumagueur area predominantly features geological formations from the Tertiary and Quaternary periods. These formations consist of:

- Quaternary sedimentary deposits comprising limestone, sand, silt, sandy clay, conglomerates, and gravel.

Tertiary formations include marls, clays, clay marls, and conglomerate limestones. Some marls may exhibit sandy characteristics and contain notable gypsum content.

To provide soil samples for this study, core drilling was conducted in the study area. Tests were carried out on samples taken at a starting depth of 2.5 m. The outcomes of the physical and chemical characterization tests performed on the swelling soil in question are outlined in Table 1 and 2, respectively.

Based on the USCS/LPC classification system, the studied soil is categorized as CH, which refers to a highly plastic clay with low organic matter.

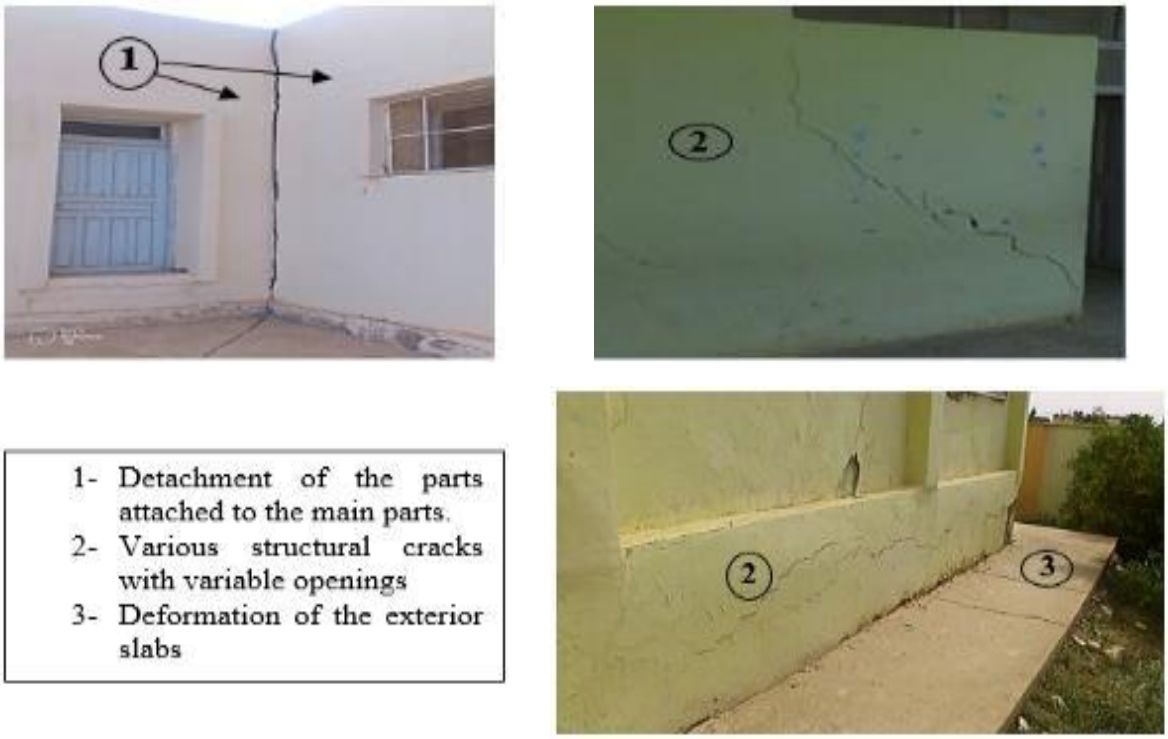

Fig. 2. Some pathological cases observed in the study region

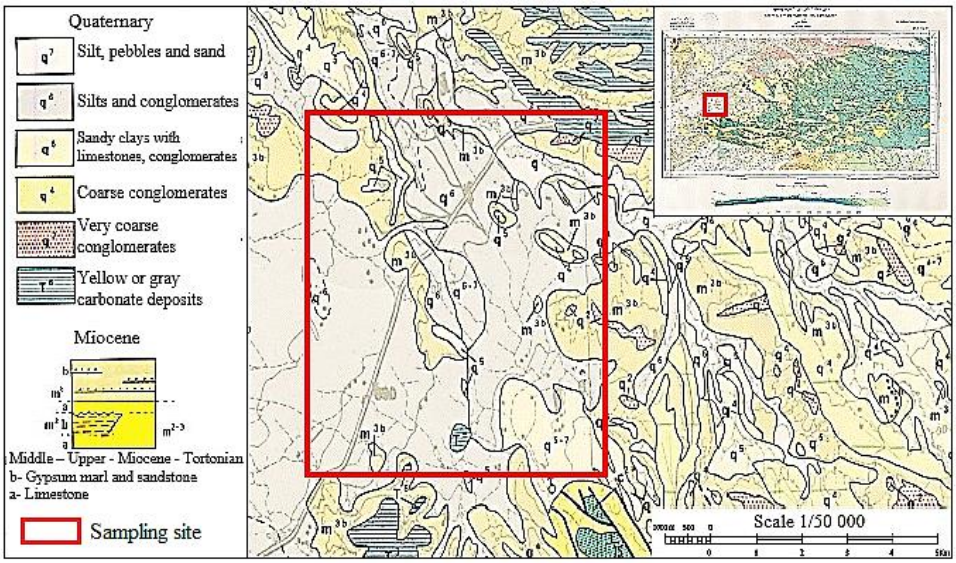

Fig. 3. Extract from the geological map of N'Gaous (1/50000; Source: National Institute of Cartography - Algiers)

Table 1. Physical characteristics of the studied material

Particle size		Atterberg limit			Shrinkage limite	Density of solid grains
Clay		LL	PL	PI	SL	gs
(% < 2 µm)	(% < 80 µm)	(%)	(%)	(%)	(%)	(kN/m3)
60	98	59	28	31	10	26.5

Table 2. Chemical properties of the studied material

Value of methylene blue	Specific surface area	CaCO3 Content	Organic matter	Clay activity
7.2	(m2/g) 150.7	(%) 46	(%) 8.5	0.51

The mineralogical composition of the soil under examination was identified through X-ray diffraction analysis (see Fig. 4). The soil consists of 63% clay minerals, comprising 5% illite, 15% kaolinite and 43% smectite. The latter presents a significant variation in volume (swelling) during interaction with water [1]. A detailed percentage distribution of each mineral component is provided in Table 3.

Table 3. Mineralogical composition of the studied soil

Quartz	Calcite	Gypsum	Dolomite	Feldspar	Smectite	Illite	Kaolinite
19%	16%	0.1%	0.5%	1.4%	43%	5%	15%

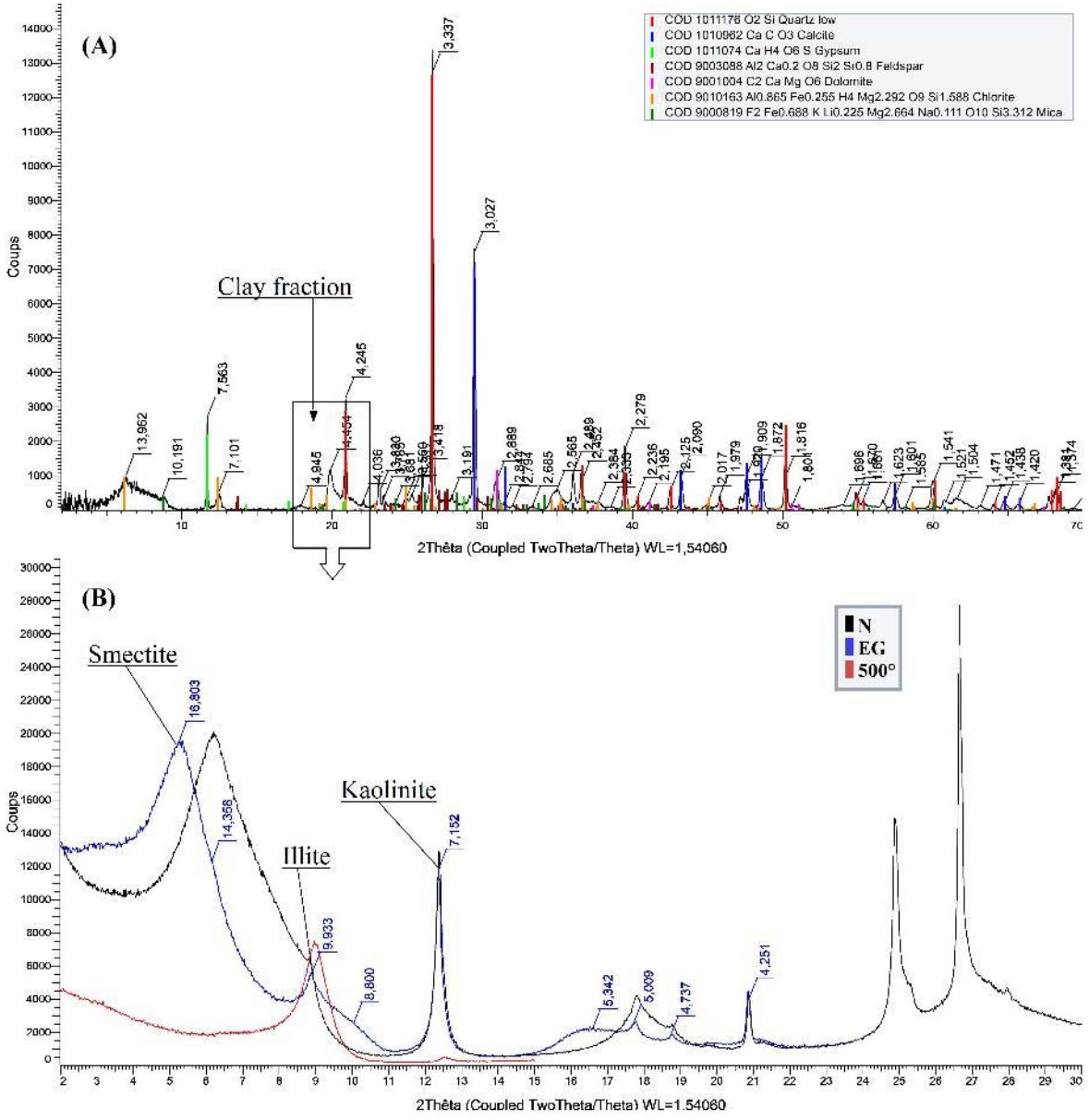

Fig. 4. X-ray diffraction of studied soil: (A) total clay of sample; (B) clay fraction

2.2. Hydraulic Binders Used

2.2.1 Lime

The lime used in this study is a commercial quicklime sourced from a local Algerian production facility. Its composition is predominantly calcium oxide (CaO) at a minimum of 85%, with traces of other impurities, as confirmed by X-ray diffraction analysis (see Fig. 5).

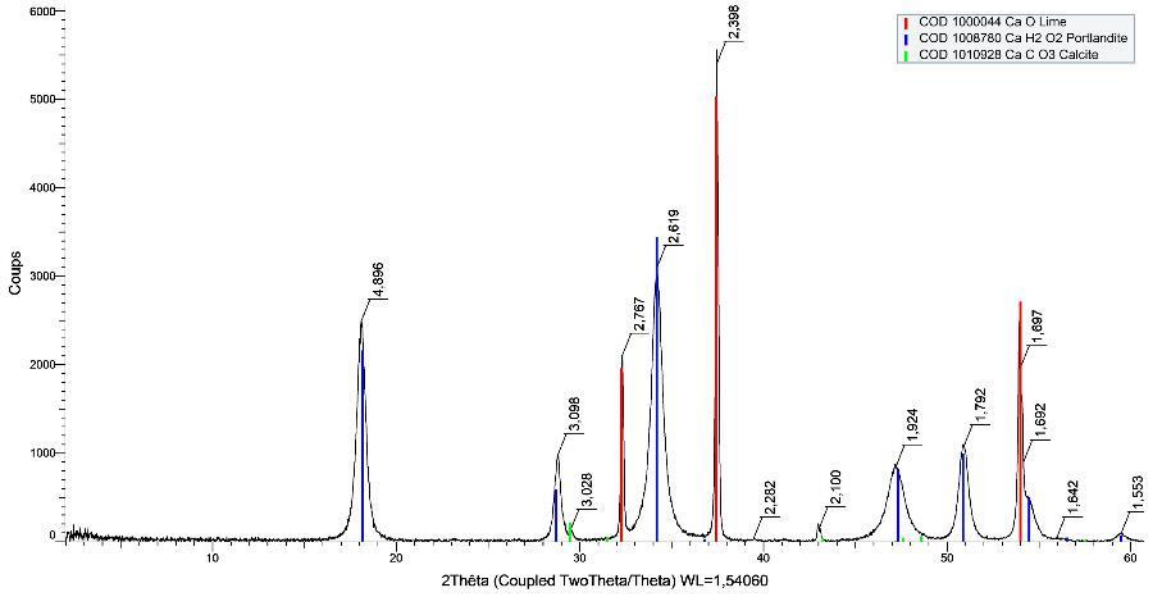

Fig. 5. X-ray diffraction of the used lime

2.2.2 Cement

The employed cement is a Portland cement (CPJ - CEMII / A 42.5 with a minimum of 65% clinker), made at the Ain-Touta cement plant in Batna, and readily available on the market. Its compressive strength at day 28 is between 42.5 and 62.5 N/mm^2. X-ray diffraction tests on the used cement are presented in Fig. 6.

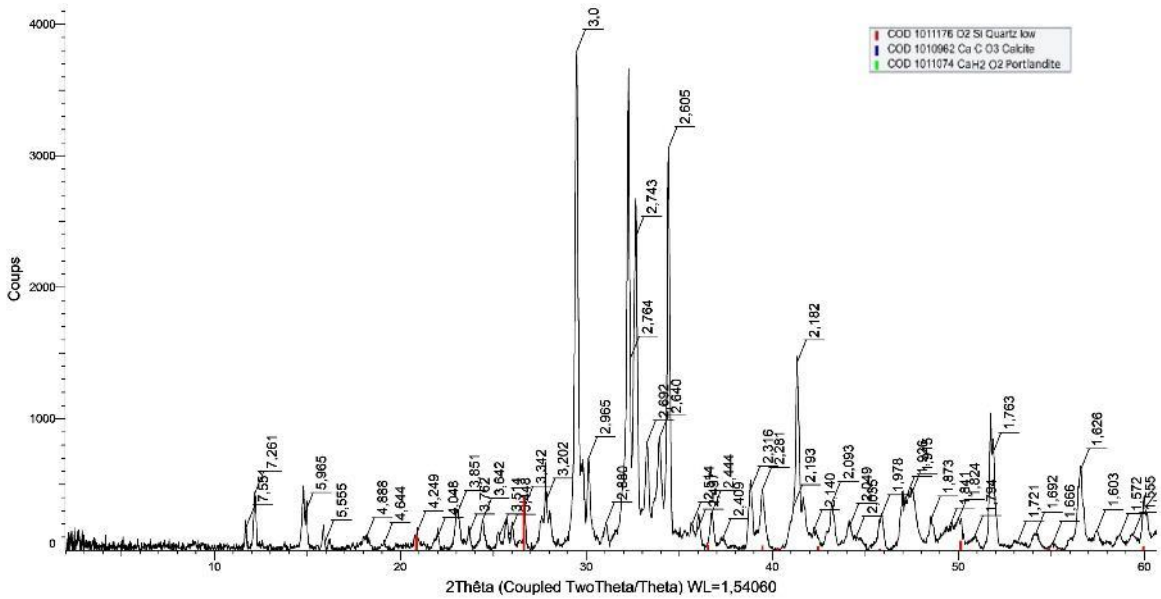

Fig. 6. X-ray diffraction of the used cement

The cement chemical characteristics given by the supplier are summarized in Table 4.

Table 4. Chemical composition of the used cement

SiO_2	Al_2O_3	Fe_2O_3	CaO	MgO	K_2O	Na_2O	SO_3	CaO_{Free}	LOI*
23.50%	5%	4.20%	56.50%	1.80%	0.96%	0.80%	2.60%	0.94%	3.70%

(*) LOI : loss on ignition.

2.2.3 Cement-Lime Mixture

Lime can offer an advantage by reducing the plasticity index (PI) of highly plastic soils (swelling soils), while cement has the advantage of improving mechanical strength in addition to reducing the PI [51]. In this study, a mixture of the same cement and lime was used for treatment of studied soil to investigate and compare its effect on clay soils swelling with the effect of each hydraulic binder alone (lime and cement). The percentages used to prepare the cement-lime mixture are summarized in Table 5.

Table 5. Used percentages to prepare the cement-lime mixture

Binder	Lime	Cement	Lime	Cement	Lime	Cement	Lime	Cement
Binder addition	1 %	2 %	3 %	2 %	5 %	2 %	7 %	2 %
Mixture	3 %		5 %		7 %		9 %	

2.3. The Soil-Hydraulic Binder Mixture

In an oven and at a temperature of at 50°C, the soil studied was first dried, then ground into fine powder after being sieved through a 2 mm mesh. The studied soil and the hydraulic binder used for treatment were mixed using a mechanical mixer at 5 to 10 min until homogenized (NF P94-100 Standard). Following this, distilled water was added to the mixture, with the water content adjusted to match the natural moisture level of the soil (Initial water content w_i = 20%). The mixture obtained from the soil, hydraulic binder and water, was statically compacted in a CBR press by a compaction pressure of 50 kN and at a slow speed of 2 mm/min into rigid steel molds (70 mm in diameter and 20 mm in height). Immediately after preparation, the samples were carefully packed in film paper and sealed with paraffin to minimize moisture loss, then stored at a controlled temperature of 20°C for 28 days.

For each used hydraulic binder (Lime, Cement, Lime + Cement), four hydraulic binder contents (3%, 5%, 7% and 9%) were used in this study. The hydraulic binder contents used in the treatment of the studied soil is calculated using the following expression:

$$Hydraulic\ binder\ contents\ (\%) = \frac{Hydraulic\ binder\ mass}{Hydraulic\ binder\ masse + Dry\ soil\ masse} \quad (1)$$

3. Experimental Methods

3.1. Oedometric Tests

Oedometric tests, following the free swelling method (standard ASTM 4546-03, Method A), were performed on untreated and as well as on treated soil with hydraulic binders to determine the effect of the latter on the studied soil swelling. In these tests, a soil sample measuring 7 cm in diameter and 2 cm in height was placed in a classical oedometer cell with a moving ring. The sample was subjected to a piston load of 1.5 kPa, and finally saturated by immersion.

Vertical strain was recorded using an LVDT type strain sensor, and the swelling potential (ΔH/H) was calculated as the ratio of the maximum deformation after sample saturation to the initial height. Subsequently, the sample was progressively loaded, and the vertical pressure required to restore the sample to its original height was determined as the swelling pressure. The loading mode used in these tests is successive step mechanical loading. The transition from one loading to another takes place when the strains stabilize.

3.2. Mineralogical Analysis

To assess the reactivity of minerals (both clay and non-clay) with the hydraulic binders, the mineralogical composition of the studied material (disoriented powder) and its clay fraction (clay slides <2μm) were analyzed using X-ray diffraction. The diffractometer used is a Bruker D8 Advance diffractometer, operates at a voltage of 40 kV and an intensity of 25 mA, using Cu-Kα1 radiation (λ = 1.5406 Å). The diffraction speed used is 0.6 s/step, rotation speed 2° 2θ/min, covering an angular range "2θ" from 2° to 45°.

3.2.1 Powder Diffractogram

The powder diffractogram method, is used to identify all the minerals present in the sample, including quartz, feldspars, calcite, gypsum, and phyllosilicates. To prepare and analyze the total disoriented powder, the sample was first dried in an oven at 40 °C, then manually ground and sieved at 250 μm. The powdered material was placed on a PVC sample holder, lightly compacted, and the supports were closed to avoid any influence on preferential orientation of the mineral particles. The samples were subsequently subjected to X-ray radiation scanning over an angular range of 2° to 45° 2Θ for the determination of the total mineralogical composition.

3.2.2 Clay Fraction Slide Diffractogram

The clay slides (oriented samples) are prepared by directly depositing a diluted suspension of particles less than 2 μm on a ground glass slide, followed by air drying. The clay suspension used for X-ray diffraction was previously decalcified, and the clay fraction (< 2 μm) was extracted after a decantation process through a sedimentation process based on Stokes law. The first centimeter of the suspension was applied to a glass slide, and dried overnight at room temperature [52]. The type of clay minerals is determined by analyzing three slides subjected to different preparation protocols: air drying (natural state), solvation with ethylene glycol (EG) for 24 hours (to highlight swelling clays), and heating at 500 °C for 4 hours (to induce the destruction of kaolinite).

3.2.3 Qualitative Identification

Qualitative identification was performed by referring to the intermediate spacing values [53] and the intensity of the main reflections observed in the three X-ray diffractograms of each mineral. Semi-quantitative estimates were based on the measurement of the intensities of the characteristic peaks from the X-ray patterns. The semi-quantitative analysis was estimated using correction factors proposed by Cook et al. [54] and Boski et al. [55] for total disoriented powder and those of Fagel et al. [56] for clay minerals.

4. Results and Discussions

4.1. Free Swelling Oedometric Tests

Atterberg limit tests conducted on the studied soil reveal its high plasticity (PI = 31%). Additionally, X-ray diffractograms indicate a significant presence of smectite (43%) in the soil composition. In general, the more clay in a soil, the higher the plasticity, the greater the potential swell, the higher the compressibility [57].

Table 6. Values of the swelling pressure and swelling potential of the different oedometric tests

Hydraulic binder content (%)	Hydraulic binder used					
	Lime		Cement		Lime-Cement mixture	
	Ps (kPa)	ΔH/H (%)	Ps (kPa)	ΔH/H (%)	Ps (kPa)	ΔH/H (%)
0	190	16.60	190	16.60	190	16.60
3	120	4.50	125	12.24	127	8.40
5	94	3	100	10.73	110	6.40
7	71	2.60	95	9.20	90	5
9	54	2.20	80	7.15	72	4.50

This is due to the fact that certain families of clay minerals, particularly smectite, exhibit particularly weak bonds between their constituent layers, to the extent that the amount of water likely to be adsorbed within the clay particles themselves can be substantial, leading to significant volume changes [1].To monitor the changes in the swelling parameters of the studied soil according to the hydraulic binders used for the treatment, oedometric tests were conducted on both untreated and treated samples (different hydraulic binders' contents), at room temperature. The results of these tests, including the swelling pressure and swelling potential, are summarized in Table 6. Fig. 7, 8 and 9 show the variation of the void ratio as a function of the total vertical stresses of all conducted oedometric tests.

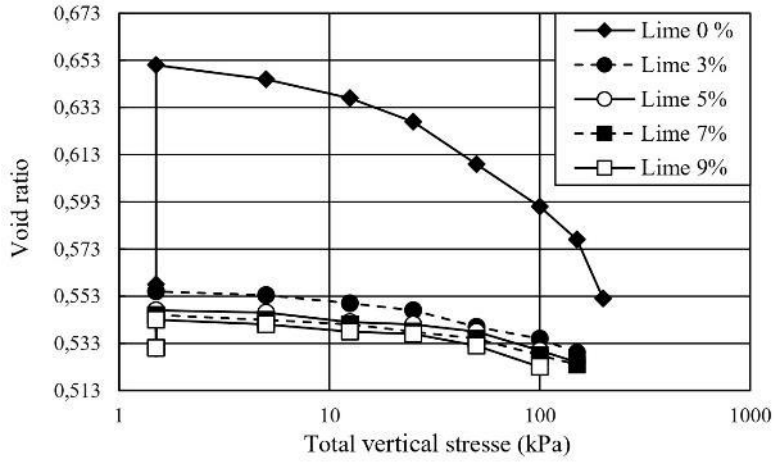

Fig. 7. Oedometric tests curves of treated soil with different lime contents

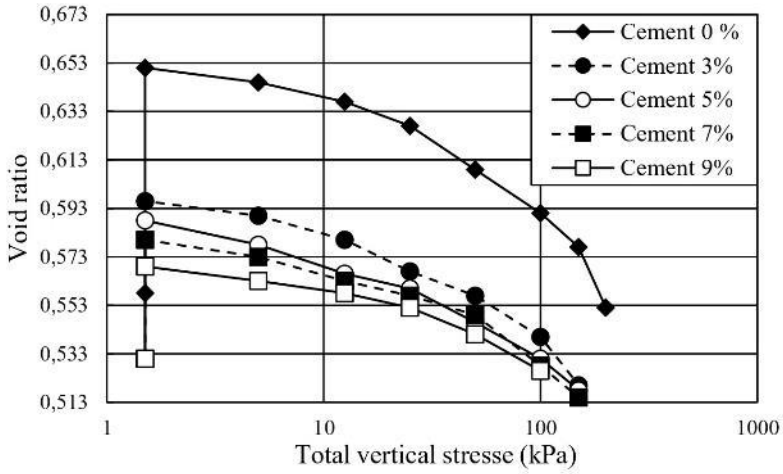

Fig. 8. Oedometric tests curves of treated soil with different cement contents

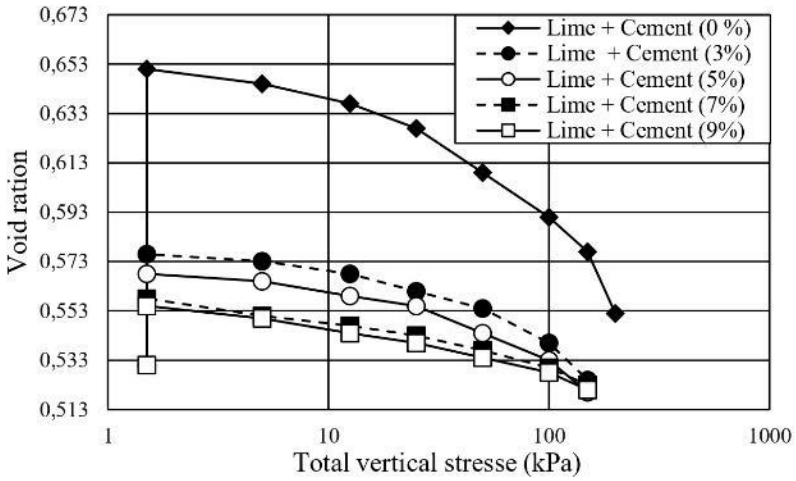

Fig. 9. Oedometric tests curves of treated soil with different mixture (lime-cement) contents

The variations in swelling pressure as a function of hydraulic binder content were plotted in Fig. 10. We note that the untreated sample exhibits a swelling pressure of around 190 kPa. We note also a decrease in the swelling pressure with hydraulic binder content increasing. Concerning the lime treatment, the results show that the effect of lime is greater than that of other binders (cement and the Lime-Cement mixture). The samples treated with lime showed a reduction in swelling pressure of around 72%, for a binder content of 9%. Fig. 11 represents the variations in the swelling potential as a function of the hydraulic binder content. It is also noted that the swelling potential is significantly influenced by variation in hydraulic binder content, so that an increase in the latter is accompanied by a decrease in the swelling potential. From the natural state (without hydraulic binder) to a binder content of 9%, the samples treated with lime showed a reduction in swelling potential of around 86%. For samples treated with cement and with Lime-Cement Mixture, the decrease in swelling potential is 57% and 73%, respectively.

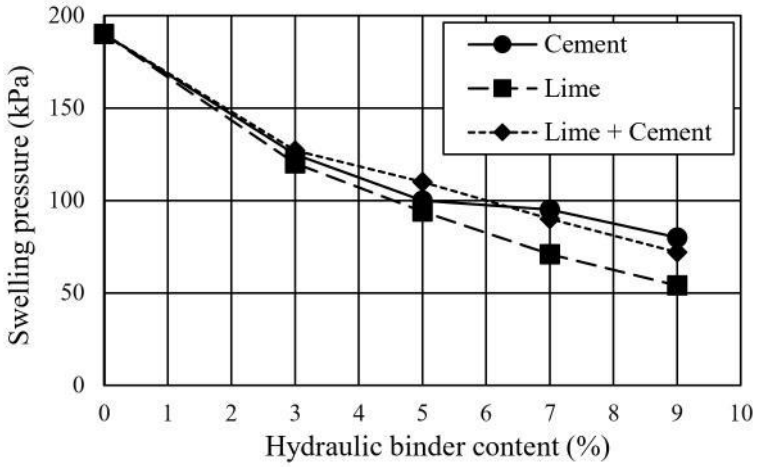

Fig. 10. Variations of swelling pressure as a function of used hydraulic binder content

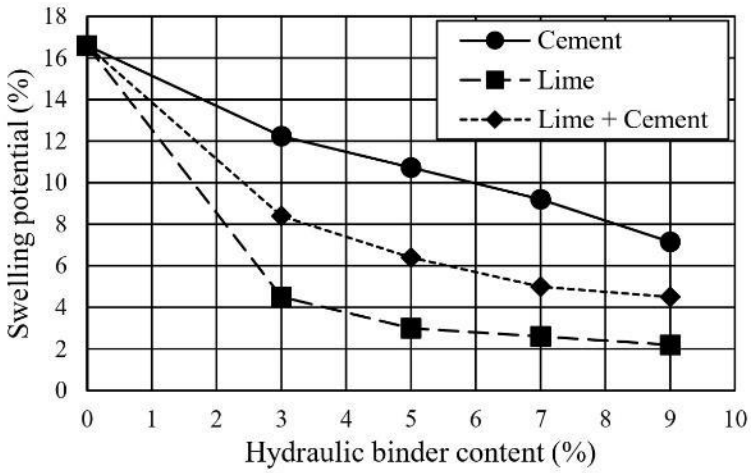

Fig. 11. Variations of swelling potential as a function of used hydraulic binder content

From the obtained results, we note that the swelling soils compressibility decreases with the hydraulic binder content increasing (lime and/or cement). The use of hydraulic binders such as lime or cement has proven effective in the treatment of clays. Abdalla et al. [58] demonstrated that the addition of a hydraulic binder such as lime induces flocculation of clay particles, reducing and limiting swelling. In addition, pozzolanic reactions generated by hydraulic binders produce cementitious compounds such as calcium silicate hydrates (CSH), which stiffen the soil structure and improve its mechanical properties [59]. These transformations also help reduce the swelling of clay soils to minimize disorders associated with volumetric variations.

4.2. Impact of Hydraulic Binders on the Mineralogical Characteristics of the Studied Material

The studied samples, untreated and treated at different values of hydraulic binder content, are characterized mineralogically in order to evaluate the reactivity of minerals (clay and non-clay) with hydraulic binders and the formation of cement phases. The evolution of chemo-mineralogical properties during treatment was studied using X-ray diffraction, to highlight crystallized phases such as portlandite and CAH, CASH and CSH type phases.

4.2.1 Treatment Effect on The Entire Studied Material

Fig. 12, 13 and 14 show the different results of the X-ray diffraction analysis of the untreated and treated samples with the different used hydraulic binders. The results shows that the samples were subjected to a mineralogical change and the formation of new minerals after treatment with hydraulic binders. The comparison of the diffractograms of the untreated and treated samples with the different used hydraulic binders (lime, cement and lime-cement mixture) at different hydraulic binder contents (3% and 5%) reveals the emergence of new peaks, indicating the formation of pozzolanic products (CSH) in the treated samples. We also note in the diffragtograms of the different treated samples, a reduction in the clay fraction intensity with the increase of hydraulic binder content. This reduction in the clay fraction is attributed to the formation of pozzolanic type reaction products (CSH) during curing time. These products result from the reaction between silicon released by clay minerals and hydraulic binders (lime, cement, and lime-cement mixture) [60, 61]. The formation of this cementitious compound (CSH) binds clay particles tightly, leading to improved mechanical properties and enhanced stability against swelling [62, 63].

Conversely, the other cementitious compounds (CAH) and (CASH) were not detected in the treated samples, this absence can be attributed to the fact that the progression of pozzolanic activity is strongly influenced by the mineralogy of the clays [64]. The lack of these compounds (CAH and CASH) may be linked to the mineralogical composition of the clay minerals, particularly the presence of smectite, which supplies silica for the formation of (CSH) compounds. Similar results were obtained by De Windt et al [65], who showed that the ongoing dissolution of smectite during pozzolanic reactions serves as a source of silica, facilitating the formation of (CSH) compounds. In Fig. 12 and for sample treated with a lime content of 5%, the presence of portlandite ($Ca(OH)_2$), resulting from the hydration of lime, is observed with a very low intensity. When lime (CaO) introduced into the soil, an exothermic reaction occurs within the first few hours, involving the hydration of lime to form calcium hydroxide ($Ca(OH)_2$).

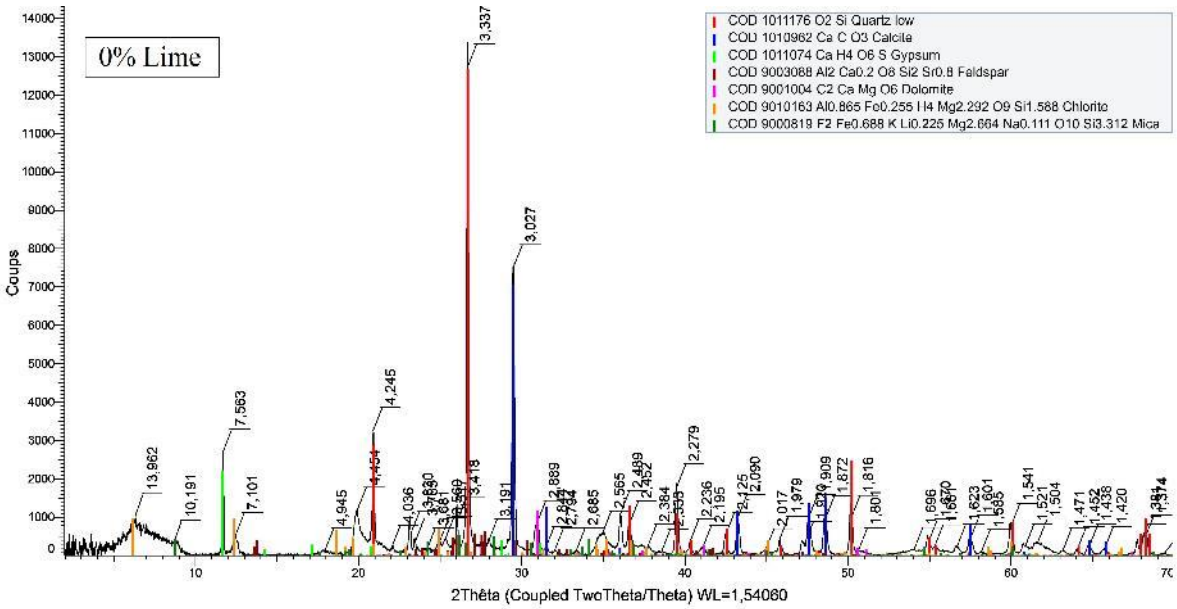

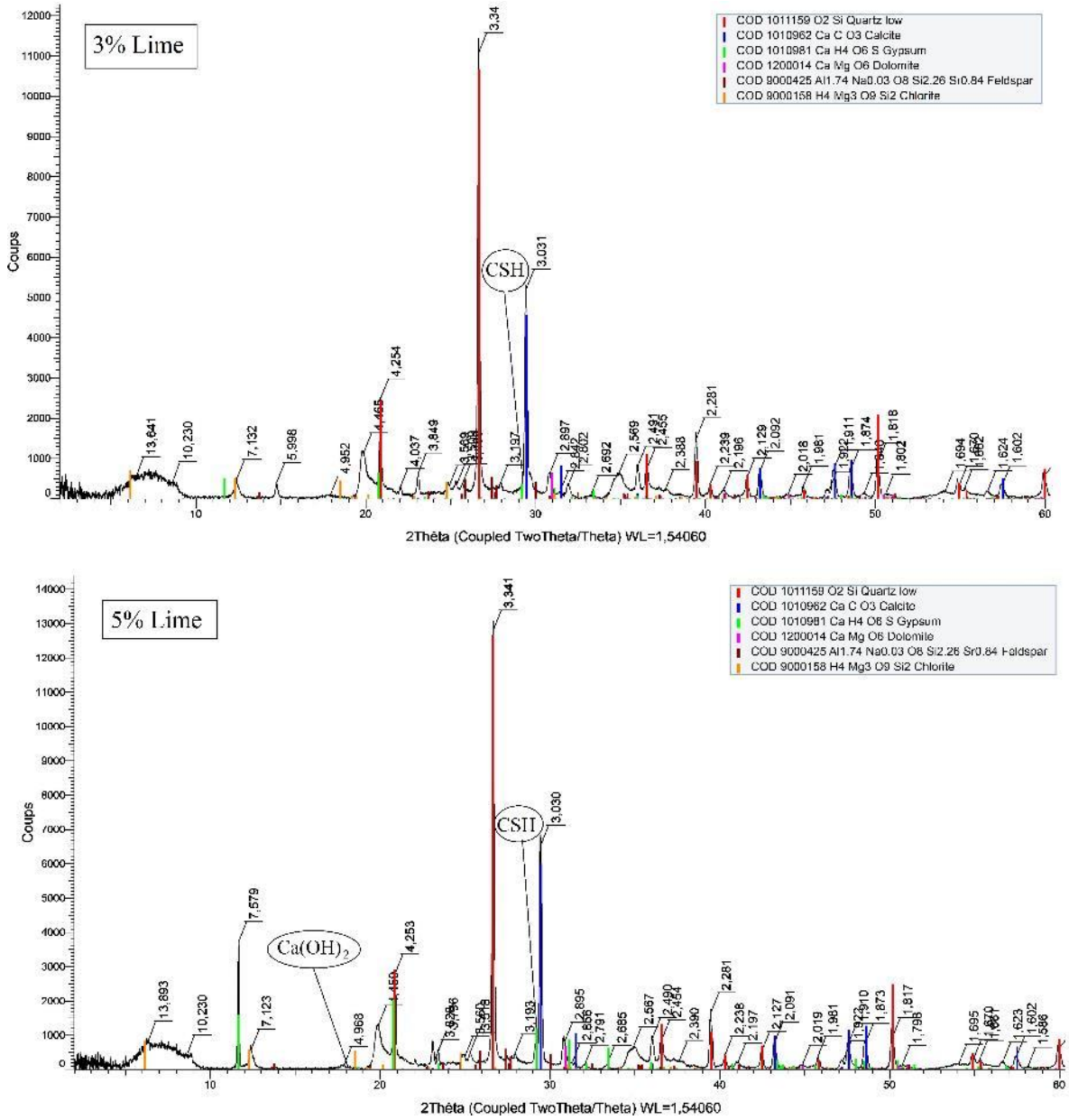

Fig. 12. X-ray diffractograms of total untreated and treated clay with lim

The very low intensity of portlandite is explained by the fact that, at higher lime doses, the amount of interstitial water is insufficient to fully hydrate all the added lime. For samples treated with a lime content of 3%, the absence of portlandite is noted, which is attributed to the complete consumption of the added lime through reactions after 28 days of hardening [66]. Regarding the intensity and relative abundance of other non-clay minerals (Quartz, Calcite and Gypsum), no reduction was observed during treatment with the various hydraulic binders. This indicates that these minerals remained unaffected by the binders used.

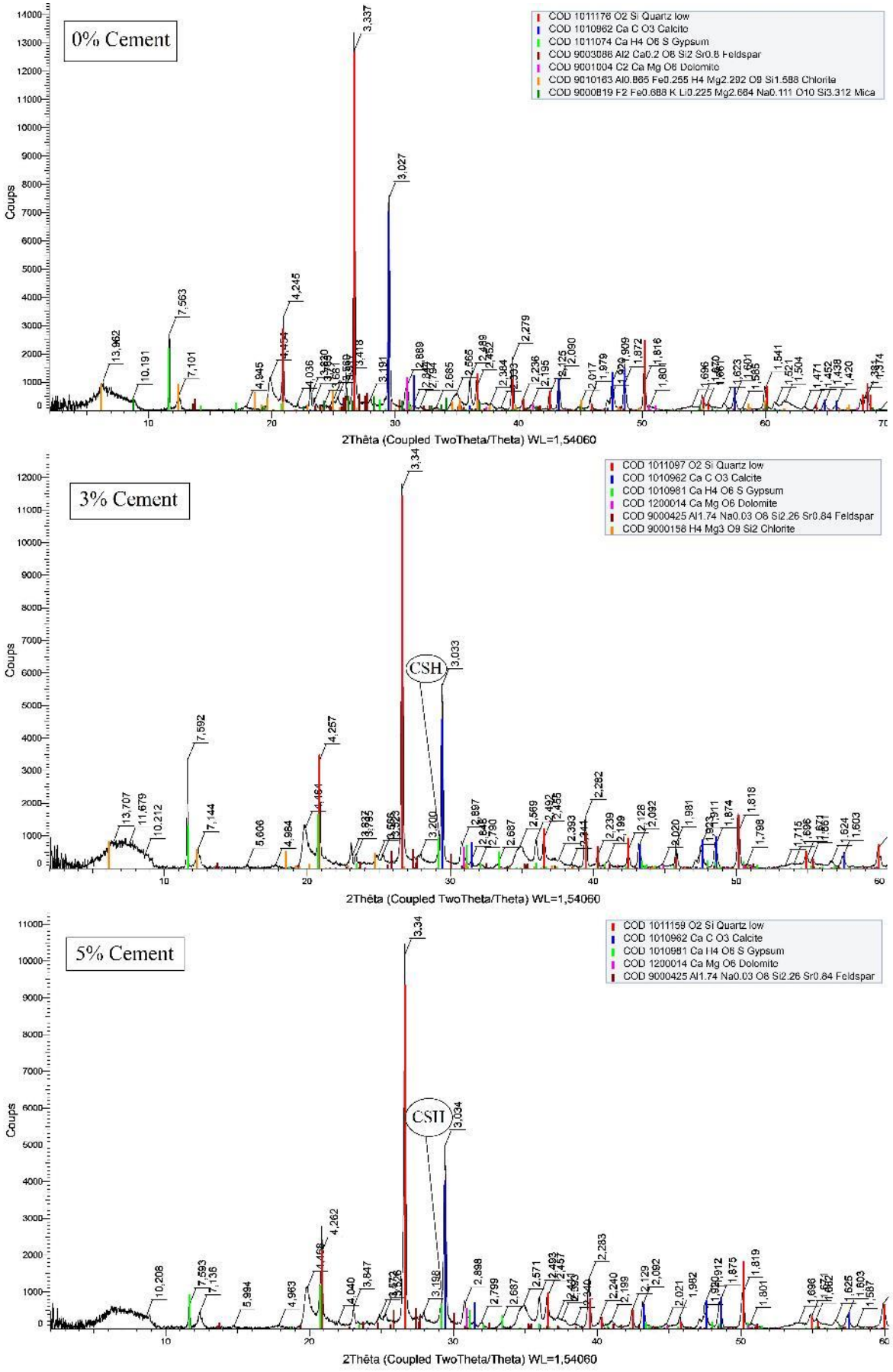

Fig. 13. X-ray diffractograms of total untreated and treated clay with cement

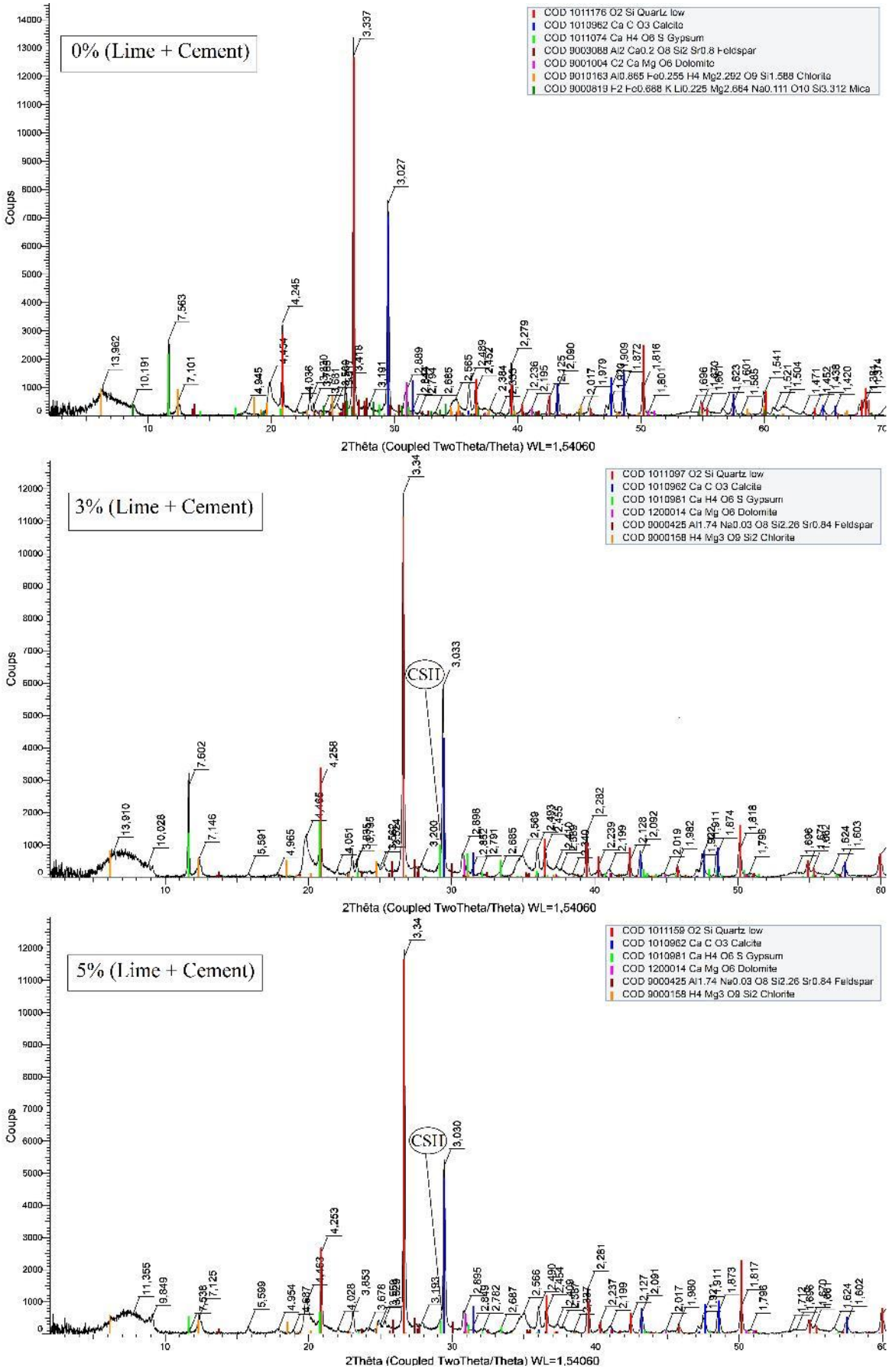

Fig. 14. X-ray diffractograms of total untreated and treated clay with lime-cement mixture

4.2.2 Treatment effect on the clay fraction

The changes in the intensity of clay minerals in the analyzed soil, depending on the content of the applied hydraulic binder, are illustrated in Figures 15, 16, and 17. The results reveal significant variations in the soil mineralogical composition, particularly regarding clay minerals. Initially, the soil exhibits a high clay content (63%), of which 43% consists of smectite, a highly swelling mineral.

The addition of lime results in a reduction in the proportion of smectite, decreasing from 43% to 13.3% with 3% lime, and then to 12.28% with 5% lime. Illite also shows a slight decrease of 4.5% at a lime content of 3%, and a more pronounced decrease to 2.85% at 5% lime. In contrast, kaolinite remains relatively stable, maintaining a constant proportion of 15% at a lime content of 3%, and a slight decrease of 13.53% at 5% of lime. Consequently, the total percentage of clay minerals decreases significantly, from 63% to approximately 29-33%, depending on the lime dosage (see Figure 15). Similarly, the addition of cement induces a gradual reduction in smectite (see Fig. 16), although less pronounced than that observed with lime: with 3% cement, the proportion of smectite decreases to 28.66%, and further to 16.38% with 5% cement.

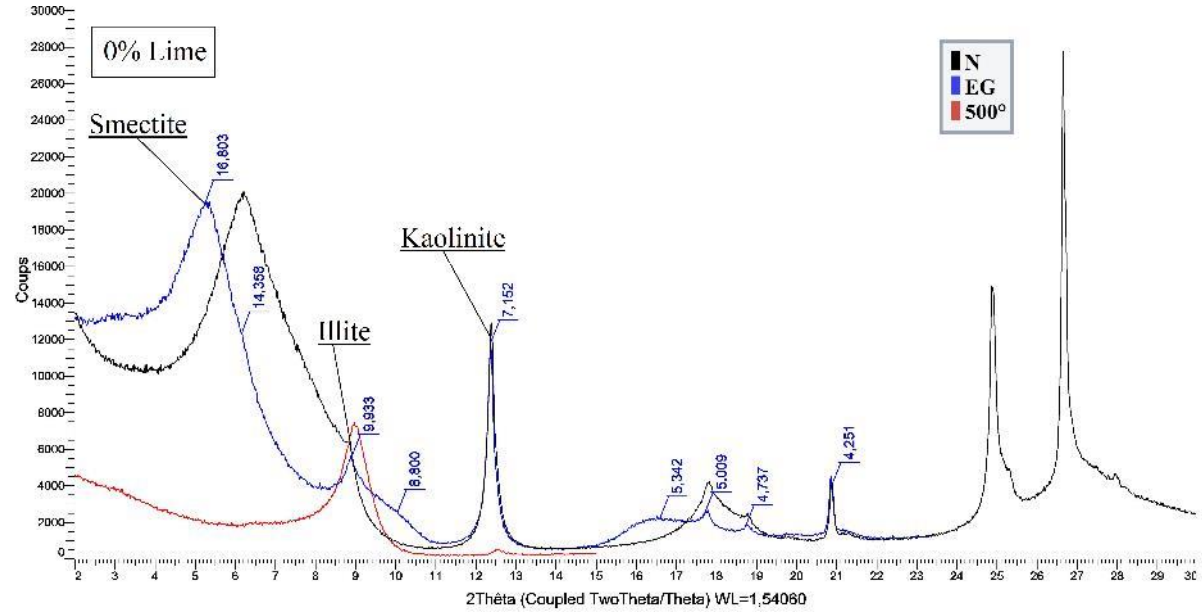

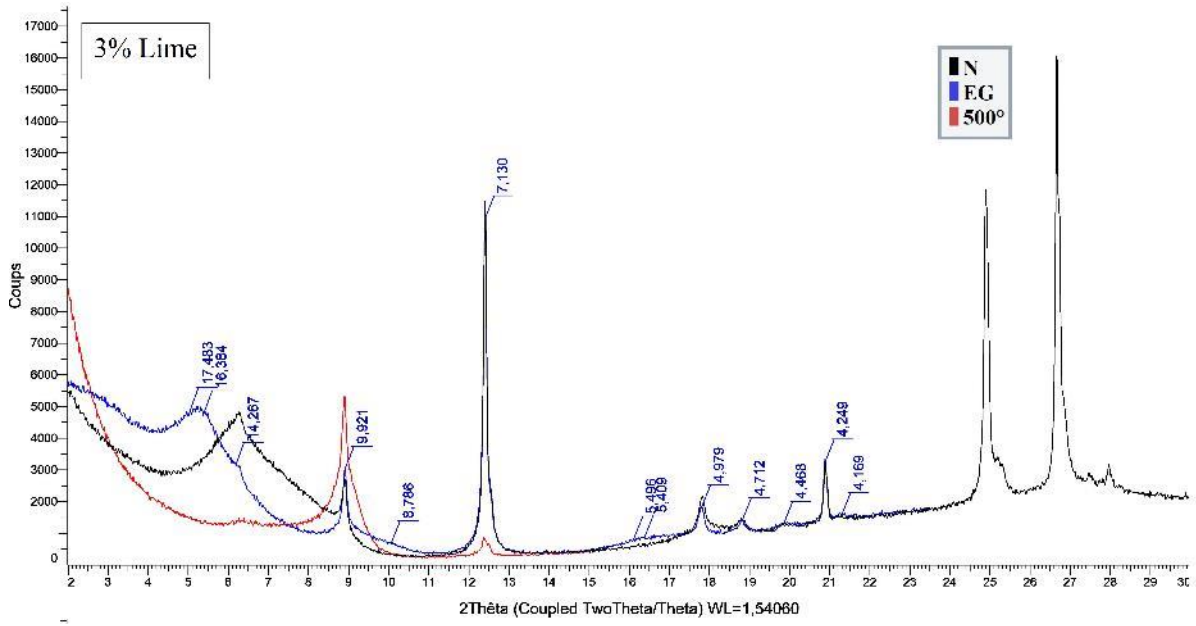

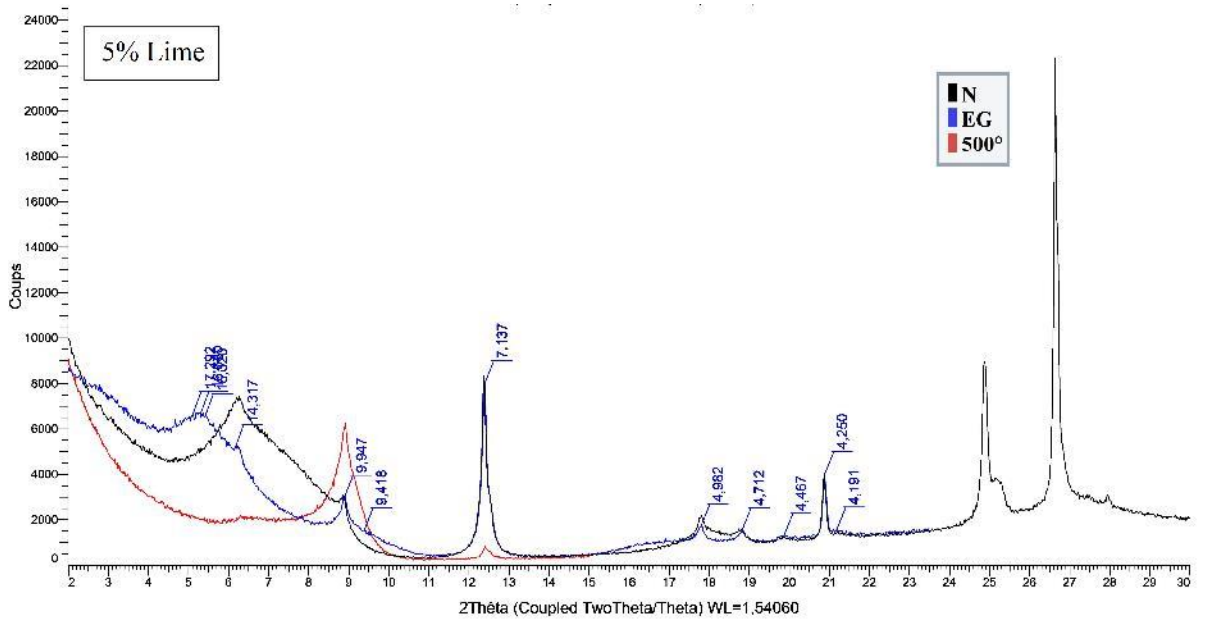

Fig. 15. X-ray diffractograms of clay fraction of untreated and treated studied soil with lime

This effect is primarily attributed to pozzolanic reactions between the cement and clay minerals, which transform the particle structure and stiffen the soil. With the addition of 3% cement, the proportion of illite slightly decreases to 4.16%, and further declines to 2.90% with 5% cement, while the kaolinite peak remains stable. However, the total percentage of clay minerals remains slightly higher than with lime alone, ranging around 34–48%.

The effect of the lime - cement mixture (Fig. 17) reveals a particularly interesting synergy. At 3%, the mixture does not bring any notable improvement: the 43% of smectite and 5% of illite remain high at 40.95% and 4.57%, respectively, while the kaolinite remains stable at 15% for the both mixture content (3% and 5%), suggesting this dosage is insufficient to trigger effective chemical reactions. However, at 5%, the mixture proves to be highly efficient, reducing the same fraction of smectite and illite to 14.20% and 3.33%, respectively, and consequently, a reduction of the clay fraction of about 33%.

The obtained results show that the used hydraulic binders (lime and/or cement) in this study, have a significant effect on the mineralogy of the studied soil. During the treatment, the significant reduction in the intensity of smectite and illite is due to the high reactivity of these two minerals with the used hydraulic binders (lime and/or cement). This high reactivity leads to the formation of pozzolanic reaction products (CSH) during the hardening process. These products are formed through the reaction between the hydraulic binders and the silica released from smectite and illite.

Concerning the intensity of kaolinite, which did not exhibit a clear reduction during the treatment, this indicates that the reactivity of this mineral with the hydraulic binders used is limited. Therefore, it can be concluded that kaolinite was not significantly affected by this type of hydraulic binder during the treatment.

In summary, lime is highly effective even at low dosages, especially on the most active clay minerals. Cement requires a higher dosage to achieve comparable effectiveness. The contents of 5% of lime-cement mixture or of lime offers the best solution, allowing for a significant reduction in clay mineral content. It should be noted that the 15% of kaolinite fraction remains constant in nearly all cases, suggesting that this category is less reactive to the applied treatments. Variations in the 5% fraction are moderate but still confirm the treatment's effectiveness, particularly with the high concentration of lime (5%), which represents the best performance observed.

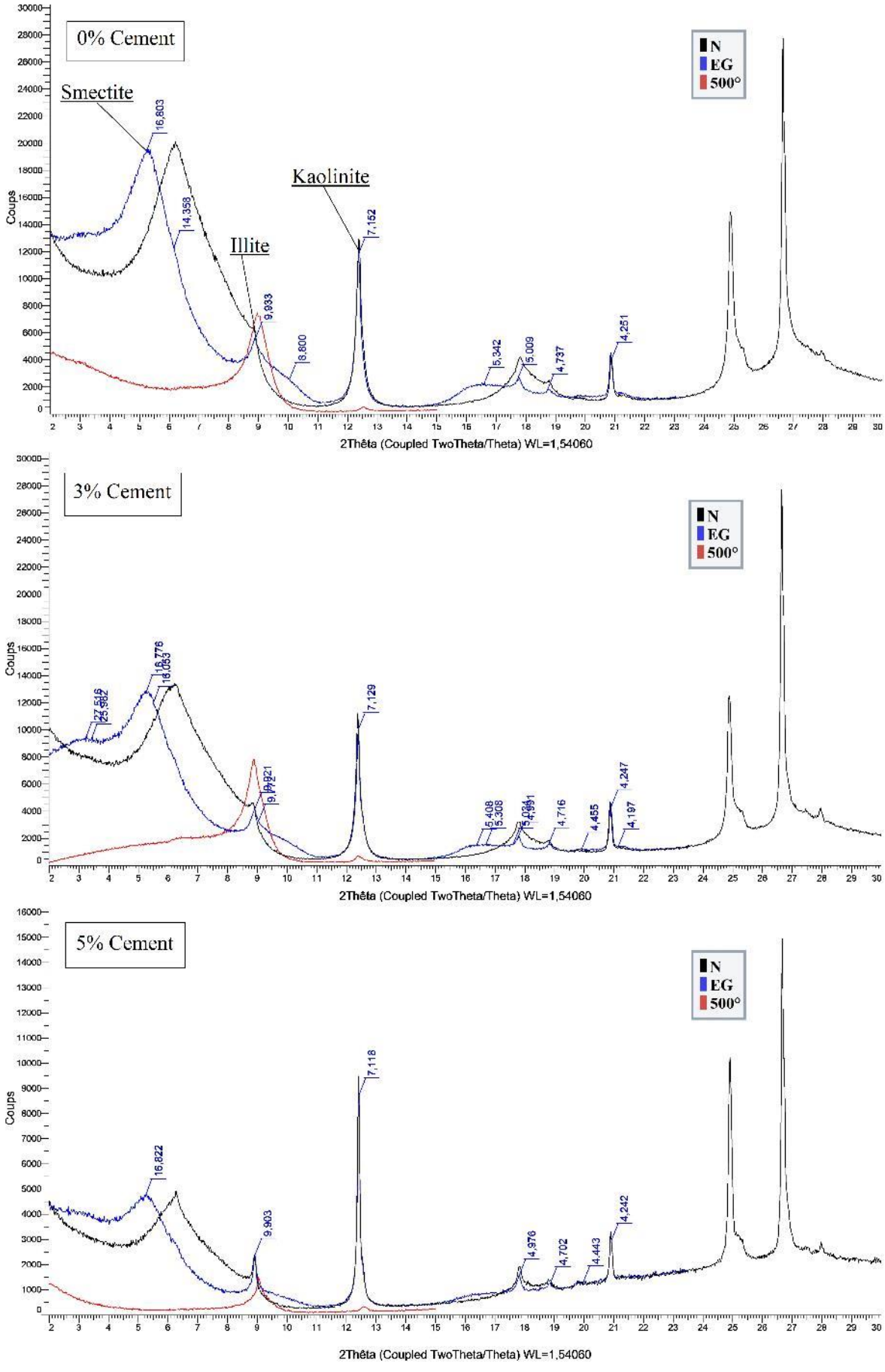

Fig. 16. X-ray diffractograms of clay fraction of untreated and treated studied soil with cement

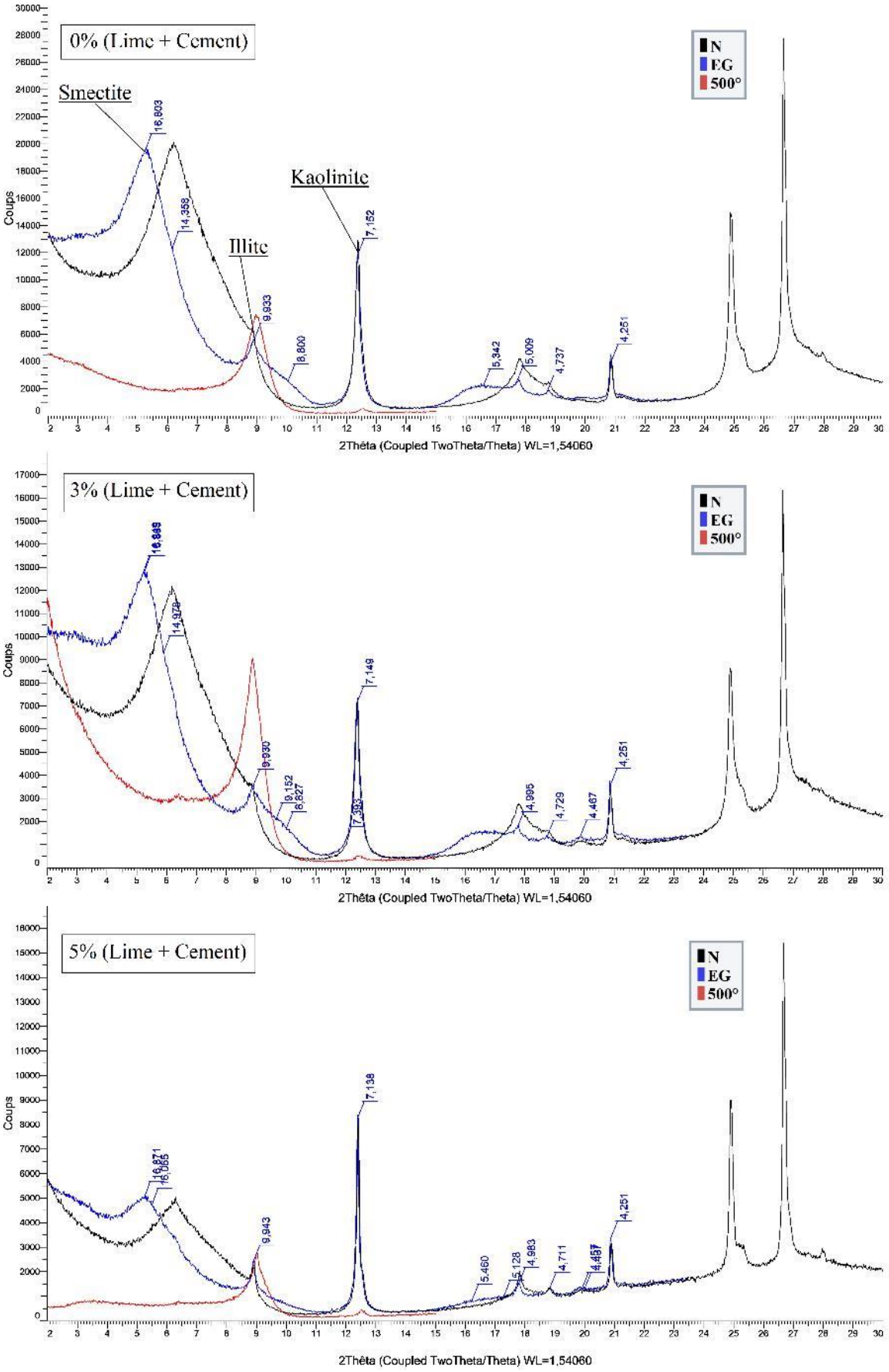

Fig. 17. X-ray diffractograms of clay fraction of untreated and treated studied soil with lime-cement mixture

5. Conclusions

The swelling behavior and mineralogical characteristics of clay soils were investigated during treatment with hydraulic binders, including lime, cement, and a lime-cement mixture. The study aimed to evaluate the impact of these additives on the soil sensitivity to water and its swelling potential. The results highlight how the addition of these binders influences the soil mineralogical composition and its interaction with water, ultimately affecting its swelling properties.

The soil in the study area of Boumagueur is predominantly clayey, exhibiting high plasticity and a significant potential for swelling. This sensitivity to swelling has resulted in numerous damages and deteriorations in various building elements such as foundations, structures, and masonry. The grain size distribution analysis of the soil reveals a substantial percentage of fines, approximately 60%, while oedometric tests confirm its high swelling potential. Additionally, the mineralogical composition of the soil, determined through X-ray diffraction, indicates a clay mineral content of 63%, with smectite constituting 43% of this composition.

The oedometric tests results of the treated soil illustrate the influence of different types and percentages of hydraulic binders on the swelling behavior of a clayey soil (swelling potential and swelling pressure). Without any binder hydraulic (0%), the soil exhibits a high swelling potential of 16.6% and a pressure of 190 kPa, indicating a swelling nature. The addition of lime, even at a low dosage (3%), significantly reduces the swelling: the potential drops to 4.5% and the pressure to 120 kPa. This improvement continues with increasing dosage, reaching a minimum swelling potential of 2.2% and a pressure of 54 kPa at 9%.

Cement, on the other hand, shows less efficiency compared to lime. At 3%, it reduces the swelling potential to 12.24% and the pressure to 125 kPa. At 9%, these values decrease to 7.15% for the potential and 80 kPa for the pressure. The lime-cement mixture yields approximately similar results to those of cement regarding the swelling pressure values. At 3%, the mixture reduces the swelling potential to 8.4% and the pressure to 127 kPa, at 9%, values reach 4.5% for swelling potential and 72 kPa for swelling pressure.

The X-ray diffraction analysis reveals a mineralogical transformation in the samples and the emergence of new minerals following treatment with hydraulic binders.

A comparison of the diffractograms between untreated and treated samples with various hydraulic binders (lime, cement, and lime-cement blend) reveals the emergence of new peaks, indicating the formation of pozzolanic products, such as calcium silicate hydrates (CSH), in the treated samples.

Furthermore, the diffractograms of the treated samples exhibit a decrease in the intensity of the clay fraction as the content of hydraulic binder increases. This reduction in the clay fraction stems from the formation of pozzolanic reaction products (CSH) during the hardening process. These products result from the reaction between hydraulic binders and silicon released by clay minerals.

For samples treated with a lime content of 5%, the presence of portlandite ($Ca(OH)_2$) is observed with very low intensity. This phenomenon can be attributed to the high lime dosage, where the quantity of pore water is insufficient to fully hydrate the added lime.

The addition of hydraulic binders to swelling soils serves to decrease their sensitivity to water and fosters the formation of strong bonds between particles, mitigating the swelling phenomenon. As a result, treatments involving hydraulic binders such as lime, cement, and lime-cement mixture prove to be effective in stabilizing of this type of clayey soils and improving their geotechnical properties.

In conclusion, the study clearly demonstrates the effectiveness of lime in altering the clay mineral composition of the soil. It offers the best performance in reducing active clay minerals, with smectite content decreasing sharply from 43% to 13.3% with 3% lime, and further to 12.28% at 5%. Overall, lime reduces the total clay fraction from 63% to as low as 29%. The persistence of kaolinite around 15% across all treatments confirms its limited reactivity.

Based on the results of this study, several practical recommendations can be proposed for the effective application of hydraulic binders in stabilizing clay soils, particularly in the Boumagueur region:

- The performance of lime, especially at moderate dosages (3–5%), suggests its preferential use in road subgrades, foundation platforms, and earthworks where control of swelling is essential. Its effectiveness in reducing active clay minerals like smectite and minimizing swelling potential makes it a reliable stabilizer with economic efficiency.
- Before large-scale application, it is essential to carry out tests to assess field performance; moisture sensitivity tests to simulate local hydrological conditions as well as shrinkage and cracking assessments, especially for surface layers.
- Lime stabilization, due to its cost-effectiveness and local availability, may offer a better return on investment for large-area applications.

References

[1] Mitchell JK, Soga K. Fundamentals of soil behavior. New York: John Wiley & Sons, 2005; 3: 558.
[2] Medjnoun A, Khiatine M, Bahar R. Caractérisation minéralogique et géotechnique des argiles marneuses gonflantes de la région de Médéa, Algérie. Bull Eng Geol Environ, 2014; 73(4):1259-1272. https://doi.org/10.1007/s10064-014-0582-z
[3] Bahar R, Kenai S. Désordres dus à l'infiltration des eaux : cas de la ville d'El-Affroun. Revue Française de Géotechnique, 2002; 101:91–103. https://doi.org/10.1051/geotech/2002101091
[4] Barbosa VHR, Marques MES, Guimarães ACR. Predicting Soil Swelling Potential Using Soil Classification Properties. Geotechnical and Geological Engineering, 2023; 41:4445–4457. https://doi.org/10.1007/s10706-023-02525-2
[5] Jones LD, Jefferson I. Expansive soils, Chapter 5. ICE Publishing, 2012 ; 413-441.
[6] Miao L, Wang F, Cui Y, Shi SB. Hydraulic characteristics, strength of cyclic wetting-drying and constitutive model of expansive soils. Proceedings of the 4th international conference on problematic soils, China, 2012; 21-23.
[7] Gaspar TAV, Jacobsz SW, Heymann G, Toll DG, Gens A, Osman AS. The mechanical properties of a high plasticity expansive clay. Engineering Geology, 2022; 303:1-11. https://doi.org/10.1016/j.enggeo.2022.106647
[8] Li J, Cameron D, Ren G. Case study and back analysis of a residential building damaged by expansive soils. Computers and Geotechnics, 2014; 56:89-99. https://doi.org/10.1016/j.compgeo.2013.11.005
[9] Ighil Ameur L. Analysis of climate change impacts on the shrinkage-swelling phenomenon of clayey soils to adapt infrastructures. 8th International Conference on Unsaturated Soils (UNSAT 2023), 2023; 382:1-6. https://doi.org/10.1051/e3sconf/202338201003
[10] Faye K, Samb F, Faye PS, Berthaud Y. Factors Predisposing and Triggering the Phenomenon of Shrinkage-Swelling of Clay Soils in the Urban Center of Diamniadio. Geomaterials, 2023; 13(2):23-34. Doi:10.4236/gm.2023.132002
[11] Mavroulidou M, Zhang X, Gunn MJ, Cabarkapa Z. Water Retention and Compressibility of a Lime-Treated, High Plasticity Clay. Geotechnical and Geological Engineering, 2013; 31:1171–1185. https://doi.org/10.1007/s10706-013-9642-6
[12] Saadeldin R, Siddiqua S. Geotechnical characterization of a clay–cement mix. Bull Eng Geol Environ, 2013; 72:601–608. https://doi.org/10.1007/s10064-013-0531-2
[13] Amri S, Akchiche M, Bennabi A, Hamzaoui R. Geotechnical and mineralogical properties of treated clayey soil with dune sand. Journal of African Earth Sciences, 2019; 152:140–150. https://doi.org/10.1016/j.jafrearsci.2019.01.010
[14] Bhardwaj A, Sharma RK, Sharma A. Stabilization of Clayey Soil Using Waste Foundry Sand and Molasses. Sustainable Development Through Engineering Innovations: Select Proceedings of SDEI, Springer Singapore, 2021; 113:641–649. https://doi.org/10.1007/978-981-15-9554-7_57
[15] Aslan Topcuoglu Y, Gurocak Z. Changes in the Strength of High-Plasticity Clays After Stabilization: an Experimental Study. Iranian Journal of Science and Technology, Transactions of Civil Engineering, 2023; 47(2):1109-1123. https://doi.org/10.1007/s40996-022-00991-x
[16] Tuleun LZ, Wasiu J. Mechanical behavior of silty-clayey lateritic soil stabilized with recycled municipal solid waste ash. Research on Engineering Structures & Materials. 2024. http://dx.doi.org/10.17515/resm2024.204me0303rs
[17] Belabbaci Z, Berrabah AT, Bouri DE. Experimental and finite element analysis of slope stability treated by lime milk (case of El Amir Abdelkader embankment). Mechanics and Mechanical Engineering, 2021; 25 (1):77–83.

[18] Zeyneb B, Sidi Mohamed AM, Abdelmalek. The Impact of Mineral Salts and Milk of Lime on Physicochemical Parameters and Swelling :(Case of Clays of Tlemcen Algeria). Journal of Civil Engineering Research, 2012; 2012 2(5):25-30. https://doi.org/10.5923/j.jce.20120205.01
[19] Kamel GM, Idriss G, Benchaa B. Effet de chaux, ciment et sel sur le potentiel de gonflement des argiles gonflantes des régions arides en Algérie. European Journal of Environmental and Civil Engineering, 2013; 17(5):315–328. https://doi.org/10.1080/19648189.2013.785722
[20] Quang ND, Chai JC. Permeability of lime- and cement-treated clayey soils. Canadian Geotechnical Journal, 2015; 52 (9):1221–1227. https://doi.org/10.1139/cgj-2014-0134
[21] Jahandari S, Saberian M, Zivari F, Li J, Ghasemi M, Vali R. Experimental study of the effects of curing time on geotechnical properties of stabilized clay with lime and geogrid. International Journal of Geotechnical Engineering, 2017; 13(2):172-183. https://doi.org/10.1080/19386362.2017.1329259
[22] Malkanthia SN, Balthazaara N, Perera AADAJ. Lime stabilization for compressed stabilized earth blocks with reduced clay and silt. Case Studies in Construction Materials journal, 2020; 12:1-8. https://doi.org/10.1016/j.cscm.2019.e00326
[23] Badv K, Hoseinpour Lonbar J. Treatment of Urmia Peat by Cement Kiln Dust. Iranian Journal of Science and Technology, Transactions of Civil Engineering, 2018; 42:451–459. https://doi.org/10.1007/s40996-018-0112-5
[24] Vitale E, Deneele D, Paris M, Russo G. Multi-scale analysis and time evolution of pozzolanic activity of lime treated clays. Applied Clay Science, 2017; 141:36–45. https://doi.org/10.1016/j.clay.2017.02.013
[25] Cuisinier O, Jean-Claude A, Le Borgne T, Deneele D. Microstructure and hydraulic conductivity of a compacted lime-treated soil. Engineering Geology, 2011; 123(3):187–193. https://doi.org/10.1016/j.enggeo.2011.07.010
[26] Ghanizadeh AR, Yarmahmoudi A, Abbaslou H. Mechanical Properties of Low Plasticity Clay Soil Stabilized with Iron Ore Mine Tailing and Portland Cement. Journal of Mining and Environment, 2020; 11(3):837-853. https://doi.org/10.22044/jme.2020.9304.1860
[27] Federico A, Vitone C, Murianni A. On the mechanical behaviour of dredged submarine, clayey sediments stabilized with lime or cement. Canadian Geotechnical Journal, 2015; 52(12):2030-2040. https://doi.org/10.1139/cgj-2015-0086
[28] Por S, Nishimura S, Likitlersuang S. Deformation characteristics and stress responses of cement-treated expansive clay under confined one-dimensional swelling. Appl. Clay Sci, 2017; 146:316–324. https://doi.org/10.1016/j.clay.2017.06.022
[29] Al-Gharbawi ASA, Najemalden AM, Fattah MY. Expansive Soil Stabilization with Lime, Cement, and Silica Fume. Applied Sciences, 2023; 13(1):436. https://doi.org/10.3390/app13010436
[30] Al-Rawas AA, Hago AW, Al-Sarmi H. Effect of lime, cement and Sarooj (artificial pozzolan) on the swelling potential of an expansive soil from Oman. Building and Environment, 2005; 40(5):681-687. https://doi.org/10.1016/j.buildenv.2004.08.028
[31] Lemos SGP, Almeida MDSS, Consoli NC, Nascimento TZ, Polido UF. Field and laboratory investigation of highly organic clay stabilized with portland cement. Journal of Materials in Civil Engineering, 2020; 32(4):1-10. https://doi.org/10.1061/(ASCE)MT.1943-5533.0003111
[32] Pakbaz MS, Alipour R. Influence of cement addition on the geotechnical properties of an Iranian clay. Applied Clay Science, 2012; 67–68:1-4. https://doi.org/10.1016/j.clay.2012.07.006.
[33] Khemissa M, Mahamedi A, Mekki L. Laboratory investigation of the treatment effects by hydraulic binders on the physical and mechanical properties of an over consolidated expansive clay. International Journal of Geotechnical Engineering, 2017; 13(6):594-607. https://doi.org/10.1080/19386362.2017.1376816
[34] Rao SM, Shivananda P. Compressibility behaviour of lime-stabilized clay. Geotech Geol Engv 2005; 23:309–319. https://doi.org/10.1007/s10706-004-1608-2
[35] Nalbantoglu Z, Tuncer ER. Compressibility and hydraulic conductivity of a chemically treated expansive clay. Canadian Geotechnical Journal, 2001; 38(1):154-160. https://doi.org/10.1139/t00-076
[36] Al-Kiki IMA, Al-Juari KAK, Khattab AA. Strength, durability, and hydraulic properties of clayey soil stabilized with lime and industrial waste lime. Al-Rafidain Engineering Journal (AREJ), 2008; 16(1):102-116. https://doi.org/10.33899/rengj.2008.44026
[37] Le Runigo B, Cuisinier O, Cui YJ, Ferber V, Deneele D. Impact of initial state on the fabric and permeability of a lime treated silt under long-term leaching. Canadian Geotechnical Journal, 2009; 46(11):1243–1257. https://doi.org/10.1139/T09-06
[38] De Brito Galvão TC, Elsharief A, Simões GF. Effects of lime on permeability and compressibility of two tropical residual soils. Journal of environmental engineering, 2004; 130(8):881-885. https://doi.org/10.1061/(asce)0733-9372(2004)130:8(881)
[39] Khemissa M, Mahamedi A. Cement and lime mixture stabilization of an expansive overconsolidated clay. Applied Clay Science, 2014; 95:104-110. https://doi.org/10.1016/j.clay.2014.03.017

[40] Wang D, Korkiala-Tanttu L. 1-D compressibility behaviour of cement-lime stabilized soft clays. European Journal of Environmental and Civil Engineering, 2018; 24(7):1013-1031. https://doi.org/10.1080/19648189.2018.1440633
[41] Bouras F, Tapsoba N, Martin M, Sabio S, Jacquet A., Beck K, Belayachi N, Bouasker M, Al-Mukhtar M. Effect of hydrated lime and cement on the engineering behavior of highly expansive clay. Athens Journal of Technology and Engineering, 2020; 7(1):1-14. https://doi.org/10.30958/ajte.7-1-1
[42] Eades JL, Grim RE. Reaction of hydrated lime with pure clay minerals in soil stabilization. Highway Research Board Bulletin, 1960; 262:51-63. http://onlinepubs.trb.org/Onlinepubs/hrbbulletin/262/262-004.pdf
[43] Eisazadeh A, Kassim KA, Nur H. Solid-state NMR and FTIR studies of lime stabilized montmorillonitic and lateritic clays. Applied Clay Science, 2012; 67:5-10. https://doi.org/10.1016/j.clay.2012.05.006
[44] Mahedi M, Cetin B, White DJ. Performance evaluation of cement and slag stabilized expansive soils. Transportation Research Record, 2018; 2672(52):164-173. https://doi.org/10.1177/0361198118757439
[45] Mutaz E, Dafalla MA. Chemical analysis and X-ray diffraction assessment of stabilized expansive soils. Bulletin of Engineering Geology and the Environment, 2014; 73:1063-1072. https://doi.org/10.1007/s10064-014-0587-7
[46] Aldaood A, Bouasker M, Al-Mukhtar M. Effect of water during freeze-thaw cycles on the performance and durability of lime-treated gypseous soil. Cold Regions Science and Technology, 2016; 123:155-163. http://dx.doi.org/10.1016/j.coldregions.2015.12.008
[47] Khattab SAA, Al-Mukhtar M, Fleureau JM. Long-term stability characteristics of a lime-treated plastic soil. Journal of materials in civil engineering, 2007; 19(4):358-366. https://doi.org/10.1061/(ASCE)0899-1561(2007)19:4(35)
[48] Petry TM, Little DN. Review of stabilization of clays and expansive soils in pavements and lightly loaded structures-history, practice, and future. Journal of materials in civil engineering, 2002; 14(6):447-460. https://doi.org/10.1061/(ASCE)0899-1561(2002)14:6(447)
[49] Richardson IG. The calcium silicate hydrates. Cement and concrete research, 2008; 38(2):137-158. https://doi.org/10.1016/j.cemconres.2007.11.005
[50] Bellion Y, Balais J. Explanatory Notice of the Scale Geological Map of N'gaous 1/50000. 1976.
[51] Bhattacharja SANKAR, Bhatty JI, Todres HA. Stabilization of clay soils by Portland cement or lime–a critical review of literature. PCA R&D Serial, 2003; 60(1): 124-133.
[52] Moore DM, Reynolds RC. X-Ray Diffraction and the Identification and Analysis of Clay Minerals. Oxford University Press, New York, 1989; 332.
[53] Brown G, Brindley GW. X-ray diffraction procedures for clay mineral identification. In: Brindley, G.W., Brown, G. (Eds.), Crystal Structures of Clay Minerals and their X-ray Identification. Mineral. Soc. Monog, 1980; 5, 305–359.
[54] Cook HE, Johnson PD, Matti JC, Zemmels I. Methods of sample preparation and X-ray diffraction analysis, X-ray mineralogy laboratory, Deep Sea Drilling Project, University of California, Riverside. Initial reports of the deep-sea drilling project, 25, 999-1007.
[55] Boski T, Pessoa J, Pedro P, Thorez J, Dias JMA, Hall I.R. Factors governing abundance of hydrolyzable amino acids in the sediments from the N.W. European Continental Margin. Prog. Oceanogr, 1998; (42): 145‑164. https://doi.org/10.1016/S0079-6611(98)00032-9
[56] Fagel N, Thamó-Bózsó E, Heim B. Mineralogical signatures of Lake Baikal sediments: source of sediment supplies through Late Quaternary. Sedimentary Geology, 2007; (194), 37–59. https://doi.org/10.1016/j.sedgeo.2006.04.006
[57] Mitchell JK, Kenichi S. Fundamentals of soil behavior. New York: John Wiley & Sons, 2005.
[58] Abdalla TA, Salih NB. Hydrated Lime Effects on Geotechnical Properties of Clayey Soil. Journal of Engineering, 2020; 26(11):150-169. Doi:10.31026/j.eng.2020.11.10
[59] Yong RN, Ouhadi VR. Experimental study on instability of bases on natural and lime/cement-stabilized clayey soils. Applied clay science, 2007; 35(3-4):238-249. https://doi.org/10.1016/j.clay.2006.08.009
[60] Barman D, Dash SK. Stabilization of expansive soils using chemical additives: A review. Journal of Rock Mechanics and Geotechnical Engineering, 2022; 14(4):1319-1342. https://doi.org/10.1016/j.jrmge.2022.02.011
[61] Mengue E, Mroueh H, Lancelot L, Medjo Eko R. Physicochemical and consolidation properties of compacted lateritic soil treated with cement. Soil and Foundation, 2017; 57(1):60-79. http://dx.doi.org/10.1016/j.sandf.2017.01.005.
[62] Al-Mukhtar M, Lasledj A, Alcover JF. Behaviour and mineralogy changes in lime-treated expansive soil at 20 C. Applied clay science, 2010; 50(2):191-198. https://doi.org/10.1016/j.clay.2010.07.023

[63] Rosone M, Celauro C, Ferrari A. Microstructure and shear strength evolution of a lime-treated clay for use in road construction. International Journal of Pavement Engineering, 2020; 21(9):1147-1158. https://doi.org/10.1080/10298436.2018.1524144

[64] Maubec N, Deneele D, Ouvrard G. Influence of the clay type on the strength evolution of lime treated material. Applied Clay Science, 2017; 137:107-114. https://doi.org/10.1016/j.clay.2016.11.033

[65] De Windt L, Deneele D, Maubec N. Kinetics of lime/bentonite pozzolanic reactions at 20 and 50 °C: batch tests and modelling. Cement and Concrete Research, 2014; 59:34–42. https://doi.org/10.1016/j.cemconres.2014.01.024

[66] Benyahia S, Boumezbeur A, Lamouri B, Fagel N. Swelling properties and lime stabilization of N'Gaous expansive marls, NE Algeria. Journal of African Earth Sciences, 2020; 170:103895. https://doi.org/10.1016/j.jafrearsci.2020.103895

Research on Engineering Structures & Materials
www.jresm.org

Research Article

Experimental investigation and modelling of the layered concrete with different proportions of steel fibers

B. Jagadish Chakravarti [*,a], K. Rajasekhar [b]

Department of Civil Engineering, Andhra University, Visakhapatnam, India

Article Info

Article History:

Received 16 Mar 2025

Accepted 24 Apr 2025

Keywords:

Layered concrete;
Steel fibers;
Aspect ratio;
ANSYS

Abstract

This study examines the effect of steel fibers (SF) in concrete with different dosages ranging from 0 to 1.5%. Hooked end steel fibers of length 35mm and diameter 0.55mm with an aspect ratio of 63.64 were used. A total of 90 specimens were cast to evaluate the mechanical properties such as compression, split and flexural strength at 7 and 28 days. At steel fiber dosage of 1.5% layered concrete specimens were cast. Layered concrete is one of the best breakthroughs because of its strength and crack resistance. The Specimens were divided into three equal portions of depth d/3 each, such as bottom layer, middle layer and top layer respectively, wherein steel fiber reinforced concrete (SFRC) was cast in the bottom layer followed by middle layer consisting of conventional concrete and above its top layer comprising of SFRC. Experimental results indicate that compressive, split tensile and flexural strengths of layered concrete compared to conventional concrete were increased by 19.14%, 100.90% and 127.25% respectively. Results obtained experimentally and analytically using ANSYS software were validated and both values have strongly correlated.

1. Introduction

Concrete, a predominant building material, accounts for half of building structures and materials for roads and bridges due to its strength, plasticity, and affordability. To improve mechanical properties of concrete, Steel Fibers (SF) are induced in the concrete, termed as Steel Fiber Reinforced Concrete (SFRC), SF have become crucial in enhancing the characteristics of concrete, including, energy absorption, toughness and strength. SF used are short, discontinuous, and randomly distributed all over concrete and they enhance tensile, flexural and shear strength, toughness, resistance to impact, fracture and frost damage. Using SF in concrete increases mechanical properties, self-weight, and unit weight of concrete [1]. SFRC is also utilized to construct machine foundations and other components subjected to dynamic loads [2]. SFRC is frequently employed in industrial sector to construct tunnel linings [3] and road pavements [4]. Micro cracks formed due to shrinkage caused by evaporation of water or applied loading intersect with SF which are randomly distributed in concrete mixture thereby limiting propagation of cracks and enhance tensile strength of concrete. Volume of fibers (V_f) and aspect ratio influence the workability and strength improvement of SFRC. SF used should be clean and free from rust. Fiber content in normal weight concrete ranges from 30 to 157 kg/m^3 with an aspect ratio of 30 to 100 and quantity of fibers that can be used without compromising strength depends on placing of steel reinforcement, fiber shapes, aspect ratio and amount of water reducing admixtures used [5]. Concrete performance is improved by fiber dosage and aspect ratio to enhance fiber matrix bond, but higher aspect ratio influences uniform distribution of fibers and also dosage of fibers of length 12 to 60 mm in addition to superplasticizer is limited to 2% by volume of concrete beyond which

*Corresponding author: chakrime16@gmail.com
[a]orcid.org/0000-0002-4287-1491; [b]orcid.org/0000-0002-4263-9270
DOI: http://dx.doi.org/10.17515/resm2025-764me0316rs

fiber balling occurs [5-6]. Compressive strength increases from minimal to 23% with 2% by volume of steel fiber and with an aspect ratio of 100 [7]. Fibers show little effect on compressive strength, increasing from 0 to 25% with fiber content less than 2% [8-12]. Higher fiber content (>2%) does not enhance compressive strength and reduces workability from achieving full compaction of concrete. A significant benefit of embedding fibers into concrete is that they enhance its tensile and flexural strength after cracking when subjected to both static and impact loads [13-15]. SF are commonly employed in Fiber reinforced concrete (FRC) as they act as a bridge at the fracture interface, leading to ductile behavior after cracking [16]. Incorporating fibers into the matrix resulted in an enhancement of the pullout characteristics, including average and identical bond strengths, as well as pullout energy, which were enhanced as fiber volume fraction, increased up to a maximum of 2%, however pullout parameters were worsened with fiber volume fraction above 2% [17]. Varying proportions of SF from 0.5%,1.0%,1.5% and 2.0% increase mechanical properties of concrete thereby concluded that feasible range of SF to be 1-1.5% [18]. Smooth SF do not develop proper bond in concrete mix [6]. Fiber distribution throughout whole volume of concrete beam renders it an economically inefficient material for beams [19]. Combination of small quantity of V_f in top layer and large quantity of V_f in bottom layer enhances performance regarding flexural load and flexural energy [20]. Fibers re-arranged in the double layer UHPFRC beams Compared to single layer (uniform distribution) UHPFRC beams gives better performance with same quantity of fibers [20]. A single-layered concrete slab exhibits three-dimensional orientation of placing of fibers, while a multi-layered concrete slab demonstrates a planar orientation of fibers; hence, the multi-layered concrete performs superiorly compared to the single-layered variant [21]. The upper layer mixture was poured into the mould after 45 minutes [20]. During the casting of the upper layer, the lower layer has sufficient strength to support upper layer matrix, thereby preventing deformation at the layer interface; concurrently, the initial setting of lower layer matrix had not yet occurred [20], leading to a robust interfacial bond. Two layered concrete beams were cast using high strength concrete and normal strength concrete which were placed in compression and tension zones respectively, to improve ductility of compression zone, fibers were introduced in this zone thereby reducing high fiber utilization and control shear failure [22]. Performance of layered beams, comprising normal concrete in upper layer and fiber-reinforced lightweight concrete in lower layer, does not affect bond between the layers [23]. A finite element analysis (FEA) model was created to predict the behavior of normal and SFRC infilled composite circular columns under axial compressive load using ANSYS software. Stress-strain relationship data was obtained by conducting compression tests on cylinders for conventional concrete and SFRC, and this is taken as input for modelling in ANSYS software and for circular steel tube, a typical stress–strain relation was simulated by an elastic-perfectly plastic model [24]**.** Finite element modelling of conventional concrete and SFRC beams were carried out using ANSYS software. Modelling results and experimental results were strongly correlated [25]. Drucker and Prager yield surface parameters were used to model the beams and simulate using ANSYS [26]. Extensive research on SF with different aspect ratios and V_f when distributed homogenously in the entire cross section is being carried out to investigate the effect of SF in the mechanical properties of concrete rather than in layered concrete.

The aim of this study is to compare the behavior of SF when placed randomly in conventional concrete for dosages ranging from 0-1.5% and in layered concrete at optimum dosage of 1.5%. The specimens in layered concrete were divided into three equal depths of d/3 each viz., top, middle and bottom layers respectively. Top and bottom layers were cast with SFRC and middle layer was cast with conventional concrete.

2. Experimental Program

2.1 Materials

An ordinary Portland cement of 53 grade conforming to IS 269-2015 [27] of brand KCP was used. River sand with a fineness modulus of 2.56 and conforming to zone-III as per IS 383-2016 [28] having specific gravity of 2.63. Crushed stone of sizes 20mm and 10mm as per IS 383-2016 [28] with a percentage of 60% and 40% having combined specific gravity of 2.88 was used. The physical and chemical properties of cement were given in tables. Hooked end steel fibers of length 35mm

and diameter 0.55mm with an aspect ratio of 63.64, super plasticizer of conplast 430 conforming to IS 9103-1999 obtained from FOSROC chemicals having specific gravity of 1.18 was used in this study.

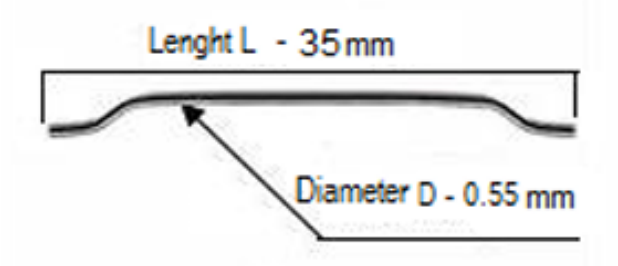

Fig. 1. Hooked-end steel fiber

Table 1. Physical properties of cement

S. No	Properties		OPC 53 grade	Requirements as per IS 269:2015
1	Fineness (m2/kg)		299	Min.225
2	Specific gravity		3.13	------
3	Normal Consistency (%)		29.5	-------
4	Setting time (Minutes)		165	Min.30
5	Soundness (mm)		0.5	Max.10
6	Compressive strength	7 days	49	
		28 days	60	

Table 2. Chemical properties of cement

S. No	Properties	OPC 53 grade	Requirements as per IS 269:2015
1	Lime Saturation Factor	0.92	0.8-1.02
2	Ratio of percentage of Alumina to that of Iron Oxide	1.24	Min. 0.66
3	Insoluble Residue (% by mass)	0.47	Max. 5.0
4	Magnesia (% by mass)	1.10	Max. 6.0
5	Sulphuric Anhydride (% by mass)	1.74	Max. 3.5
6	Total loss of ignition (%)	1.24	Max. 4.0
7	Chlorides (%)	0.002	Max. 0.1

Table 3. Quantities per cubic meter of concrete

S. No	Mix Notation	Cement (kgs)	Sand (kgs)	Coarse Aggregate (kgs)	Steel fiber dosage (kgs)	Water/Cement ratio	Super Plasticizer (Liters)
1	M30SF0.0	394	714	1213	0	0.42	3.94
2	M30SF0.5	394	714	1213	39.25	0.42	3.94
3	M30SF1.0	394	714	1213	78.5	0.42	3.94
4	M30SF1.5	394	714	1213	117.75	0.42	3.94
5	M30SF1.5-L*	394	714	1213	117.75	0.42	3.94

M30SF0-M-Mix;30-Compressive strength of concrete; SF0-Steel fibers of dosage 0%; SF1.5-Steel fibers of dosage 1.5%; L*- Layered concrete;

2.2 Preparation of Samples

The concrete Mixes were prepared using Indian standard codes of IS 456-2000 [29] and 10262-2019 [30]. A total of 30 Cubes of dimensions 150x150x150mm, 30 cylinders of dimensions 150x300mm and 30 prisms of dimensions 100x100x500mm were cast. Conventional concrete was prepared using constituent materials i.e. cement, sand, aggregates, water, and super plasticizer. SFRC was prepared using above mentioned materials in addition to steel fiber dosages ranging from 0-1.5%. The SF were added in small amounts to avoid fiber balling and improve workability of concrete.

The layered concrete has three equal layers, viz., top, middle, and bottom layers, each having of uniform depth. Initially the bottom layer was cast using SFRC for a depth of d/3 measured with a ruler and left undisturbed for 45 minutes, not more than its initial setting time. The bottom layer was laid upon middle layer of depth d/3, measured using a ruler, was cast, comprising conventional concrete. After 45 minutes, the top layer was cast with SFRC following the aforementioned process.

3. Numerical Analysis

Finite Element Analysis (FEA), utilized in structural engineering, assesses the overall behavior of a structure by partitioning it into numerous elements, each possessing clearly defined mechanical and physical properties. Modelling the intricate behavior of reinforced concrete, characterized by its non-homogeneity and anisotropy, is a significant difficulty in the finite element analysis of civil engineering constructions. A competent modelling of concrete on a finite element (FE) platform necessitates the utilization of an acceptable element type, sufficient mesh size, suitable boundary conditions, a realistic loading environment, and proper time stepping, alongside the provision of relevant concrete properties.

3.1 Finite Element Formulation

Numerical method such as finite element method was used for the complex problem, in this study prism specimens were modelled using ANSYS 2024R2 for the validation of the experimental results. The prisms of size 100x100x500mm were modelled in ANSYS using CPT 215 element to get ultimate load and deflection.

3.2 Element Description

CPT215 is a 3-D eight-node coupled physics solid element capable of modelling coupled physics phenomena such as structural-pore-fluid-diffusion-thermal analysis and prevents volumetric mesh locking in nearly incompressible cases. Furthermore, the CPT215 element, when coupled with damage-plastic micro plane models, helps to reduce numerical instability and mesh sensitivity for strain-softening materials. The element is defined by eight nodes as shown in Fig. 15 and can have UX, UY, UZ, Pressure and Temperature degrees of freedom at each node.

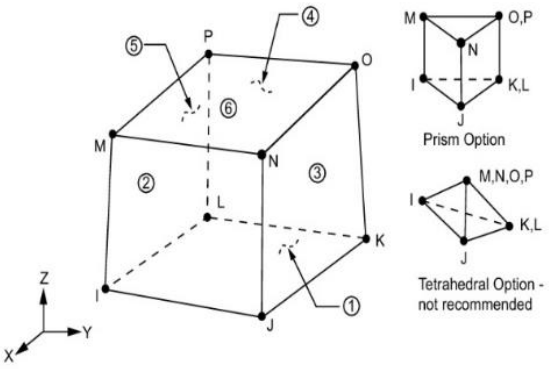

Fig. 15. Structural solid geometry

3.3 Material properties for the prism model

The prisms were modelled in ANSYS and for the analysis of the prisms the following material properties were considered as shown in Table 4.

Table 4. Parameters for various types of concretes

Parameters	Symbol	Mix Notation				
		M30SF0.0	M30SF0.5	M30SF1.0	M30SF1.5	M30SF1.5-L*
Modulus of elasticity (MPa)	E	27920	28720	30530	31700	31800
Poisson's ratio (Unit less)	μ	0.20	0.21	0.22	0.22	0.22
Uniaxial compressive strength (MPa)	f_{uc}	40.59	43.11	46.52	47.85	48.36
Bi-Axial Compressive Strength (MPa)	f_{bc}	46.68	49.57	53.49	55.02	55.61
Tensile strength (MPa)	f_t	3.32	4.05	5.02	5.95	6.67
Tension cap hardening constant (unit less)	R_t	1	1	1	1	1
Compressive hardening constant (MPa^2)	D	20000	30000	60000	90000	110000
Intersection points between the compression cap and the Drucker–Prager yield function (unit less)	σ_v^C	-31.11	-33.04	-35.66	-36.68	-37.07
Compression cap ratio constant (unit less)	R_C	2	2	2	2	2
Tensile damage threshold (unit less)	Γt	0	0	0	0	0
Compressive damage threshold (unit less)	Γc	2e-5	2e-5	2e-5	2e-5	2e-5
Compression damage evolution (unit less)	βc	4000	2000	2000	2000	2000
Tension damage evolution (unit less)	βt	6000	3000	3000	3000	3000
Nonlocal range parameter (mm^2)	c	900	1225	1225	1225	1225
Over-nonlocal parameter (unit less)	m	2.5	2	2	2	2

4. Results and Discussions

4.1 Workability of Concrete

Slump cone of dimensions 100x200x300mm was used to measure the concrete workability. The slump value is decreased with increasing fiber volume fractions, aspect ratio and decreasing fiber diameter [31]. The M30SF0.0 means conventional concrete of grade 30MPa without SF obtained a slump of 160mm, for M30SF0.5, M30SF1.0 and M30SF1.5 with varying steel fiber dosages of 0.5%,1.0% and 1.5% the slump values were recorded as 145mm,125mm and 90mm respectively as shown in Fig. 2. The steel fiber quantity ranging from 0.5% to 1.5% gradually reduces the workability beyond which it leads to less compaction and create more pores in the concrete.

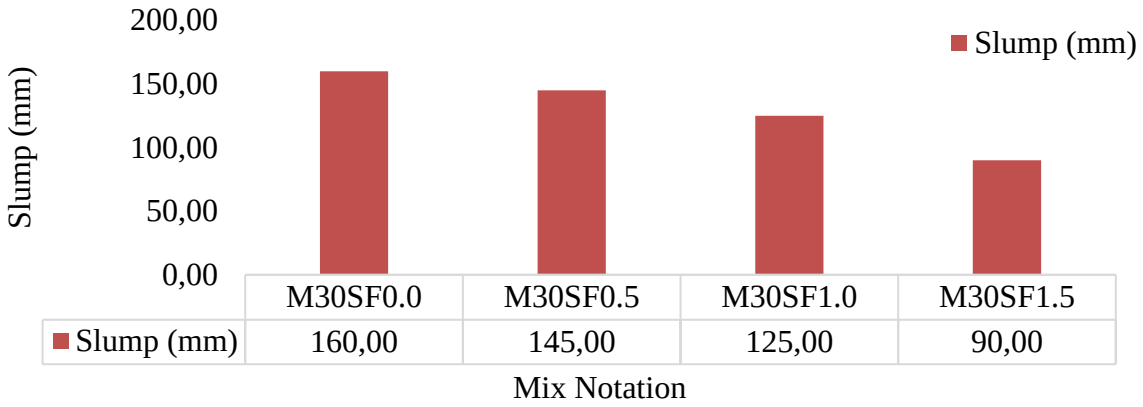

Fig. 2. Slump values of various mixes

4.2 Compressive Strength

The compressive strength values of specimens were determined using 300 Ton Compression testing machine (CTM) as shown in Fig. 3. The inclusion of SF of length 35mm, diameter 0.55mm with an aspect ratio of 63.64, enhance the compressive strength from 6.21% to 17.89% with fiber dosage varying from 0.5% to 1.5%. The ultimate strength of concrete was improved by arresting the crack growth which depends on the bond strength of steel fiber and matrix.

Fig. 3. Testing of cube

Fig. 4. Casting of layered cubes

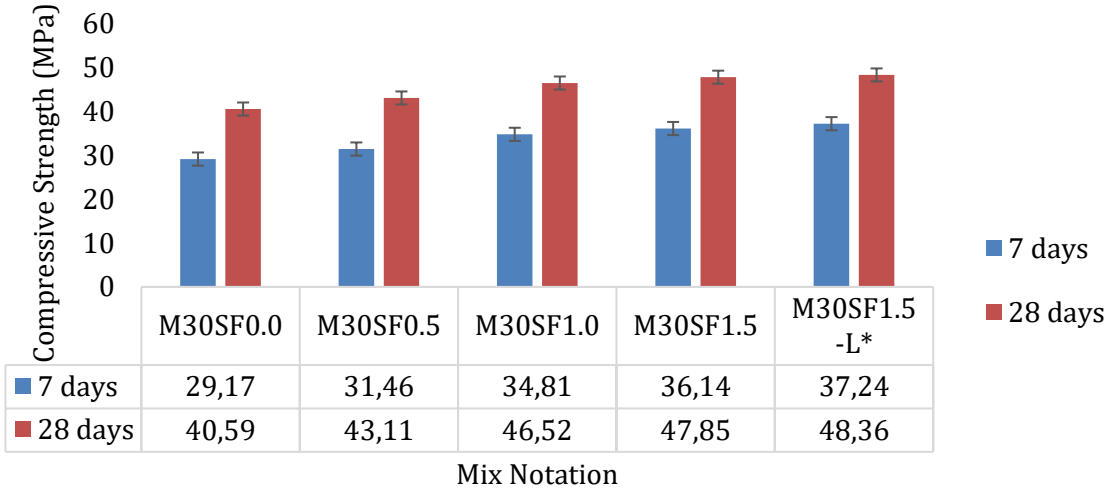

Fig. 5. Compressive strength values of various mixes

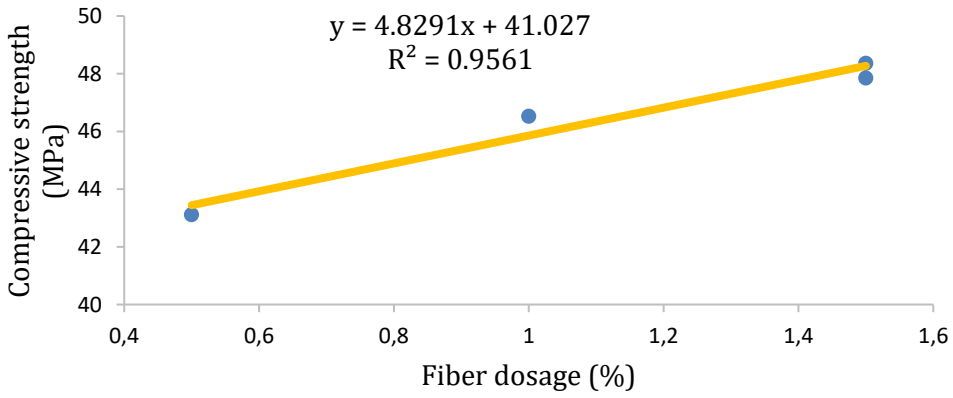

Fig. 6. Relationship between compressive strength vs Fiber percentage

The fiber dosage of 1.5% gives maximum strength which was considered as optimum dosage with which layered concrete cubes were prepared. The cube of depth 150mm was divided into three equal layers of 50mm each. The cubes were cast from the bottom layer with SFRC and each layer was left undisturbed for a duration of 45min [20] before casting the consequent layer. The above procedure was followed for the middle layer with conventional concrete and the top layer with SFRC and the depths were measured using a Ruler as shown in Fig. 4. The strengths of the cube specimens were 37.24 MPa and 48.36 MPa at 7 and 28days respectively as shown in Fig. 5. The illustration depicts the correlation between fiber dosage and compressive strength. The R^2 value of 0.9561 as shown in Fig. 6. Signifies the prediction of compressive strength and fiber dosage of the SFRC.

4.3 Split Tensile Strength

The split tensile strength values of conventional concrete without SF and SFRC were measured using a 300 Ton CTM, as depicted in the Fig. 7. The split tensile strength of conventional concrete without SF was measured at 2.29 MPa and 3.32 MPa for specified time periods. When SF were added at varying dosages of 0.5% to 1.5%, the strength values improved from 21.98% to 79.52% at 28 days. At 1.5% steel fiber dosage, the cylinders of depth 300mm were cast and partitioned into three levels, each measuring 100mm. The cylinders were fabricated using a three-layer approach, starting with a bottom layer of SFRC, followed by a middle layer of conventional concrete, and then topped with another layer of SFRC and each layer was left undisturbed for a duration of 45min before casting the consequent layer and not more than the initial setting time [20] and the depth was measured using a ruler as shown in Fig. 8. The split tensile strengths of layered concrete were measured to be 5.06 MPa and 6.67 MPa at 7 and 28 days, respectively as shown in Fig. 9.

Fig. 7. Testing of cylinder

Fig. 8. Casting of layered cylinder

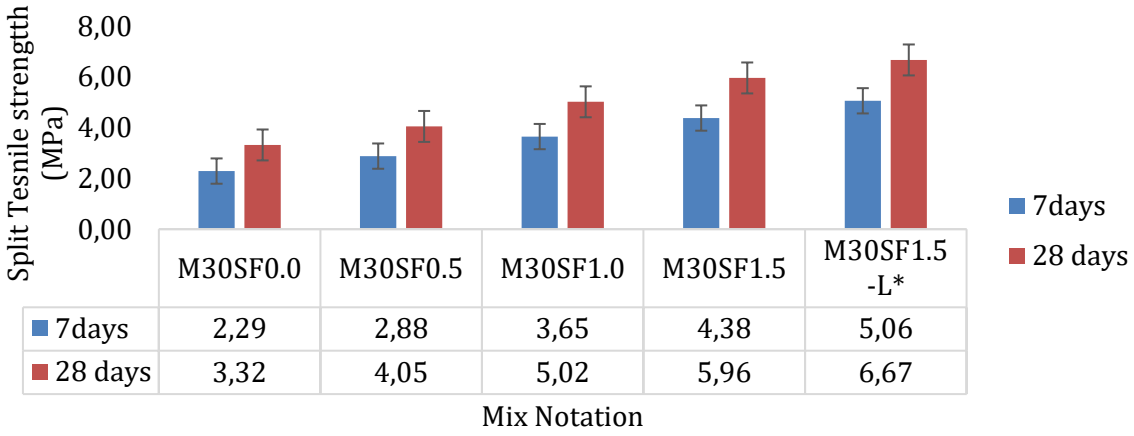

	M30SF0.0	M30SF0.5	M30SF1.0	M30SF1.5	M30SF1.5 -L*
7days	2,29	2,88	3,65	4,38	5,06
28 days	3,32	4,05	5,02	5,96	6,67

Fig. 9. Split tensile strength of various mixes

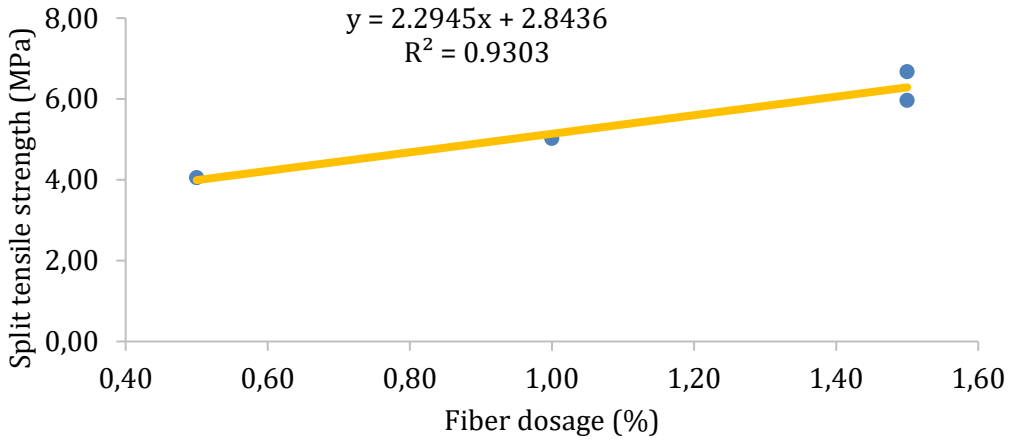

Fig. 10. Relationship between Split tensile strength vs Fiber percentage

The Fig10. shows the relationship between fiber dosage and split tensile strength. The R^2 value of 0.9303 as shown in Fig. 10. indicates a better prediction of split tensile strength and fiber dosage of the SFRC.

4.4 Flexural Strength

The flexural strength values of conventional concrete and SFRC were using a 100 Ton Universal Testing Machine, as depicted in the and Fig. 11. The flexural strength of conventional concrete without SF was found to be 3.96MPa and 5.21MPa for 7 and 28 days respectively. The inclusion of SF at different dosages of 0.5%, 1.0% and 1.5% resulted in a rise in flexural strength with a percentage of 33.97% to 102.88% at 28 days. The optimum dosage for prisms made with layered concrete is 1.5%, which leads to the highest flexural strength at 7 and 28 days. The prism, which had a depth of 100mm, was divided into three levels, with each level measuring 33.33mm. The prism was constructed utilizing a layered method, beginning with a bottom layer with SFRC, followed by a middle layer with conventional concrete, and then top layer with SFRC and each layer was left undisturbed for a duration of 45min before casting the consequent layer [20] and the depth was measured using a ruler as shown in Fig. 12. The flexural strengths of layered concrete were determined to be 9.32 MPa and 11.84 MPa after 7 and 28 days, respectively as shown in Fig. 13. The Fig14. shows the relation between fiber dosage and flexural strength. The R^2 value of 0.9359 indicates a better prediction for the flexural strength and fiber dosage of the SFRC.

Fig. 11. Testing of Prism

Fig. 12. Casting of layered Prism

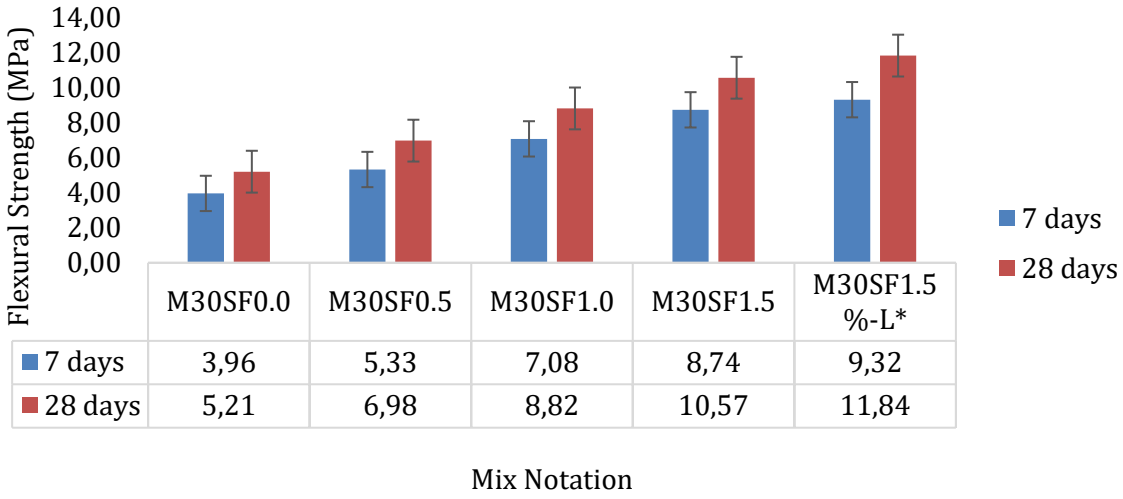

	M30SF0.0	M30SF0.5	M30SF1.0	M30SF1.5	M30SF1.5 %-L*
7 days	3,96	5,33	7,08	8,74	9,32
28 days	5,21	6,98	8,82	10,57	11,84

Fig. 13. Flexural strength of various mixes

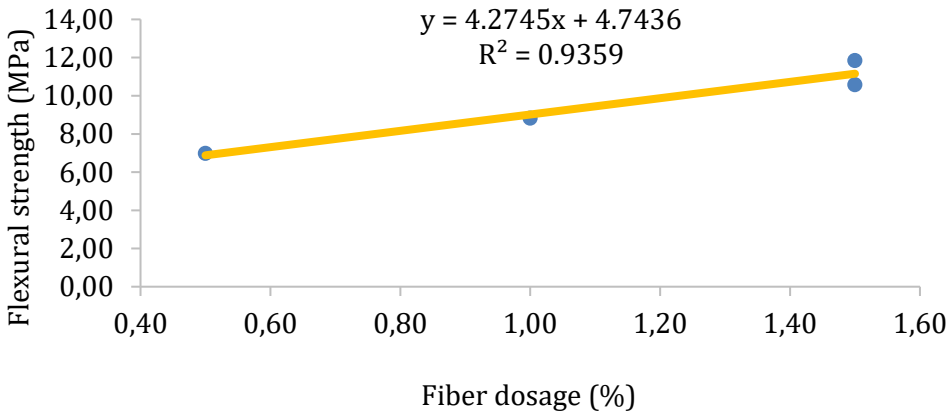

Fig. 14. Relationship between flexural strength vs fiber percentage

4.5 Numerical Validation

FRC is considered as a quasi-homogeneous material which means the fibers are not arranged homogeneously in reality during filling the construction form work, fibers added to concrete mix obtain non-homogeneous distribution. In spite of randomly mixing of fibers, to facilitate modelling it was assumed that the fibers were mixed homogeneously [25].

For the linear analysis of concrete, the modulus of elasticity and Poisson's ratio of the materials are sufficient. However, for the non-linear analysis, the two elastic constants are insufficient; hence,

the Drucker-Prager yield parameters are extremely useful for understanding the non-linear behavior of the concrete. The researcher [26] proposed a damage-plasticity micro plane model for analyzing concrete's non-linear behavior, which uses the Drucker-Prager yield parameters listed in the table and includes formulas to calculate these parameters.

Table 5. Load-Deflection values of different types of concretes

S. No	Mix Notation	ANSYS			EXPERIMENTAL	
		Ultimate Load (N)	Deflection (mm)	stiffness	Ultimate Load (N)	Deflection (mm)
1	M30SF0.0	13040	0.31	42420	13025	0.30
2	M30SF0.5	17461	0.41	42944	17445	0.40
3	M30SF1.0	22062	0.48	45630	22051	0.48
4	M30SF1.5	26446	0.56	47343	26425	0.56
5	M30SF1.5-L*	29630	0.61	48733	29600	0.60

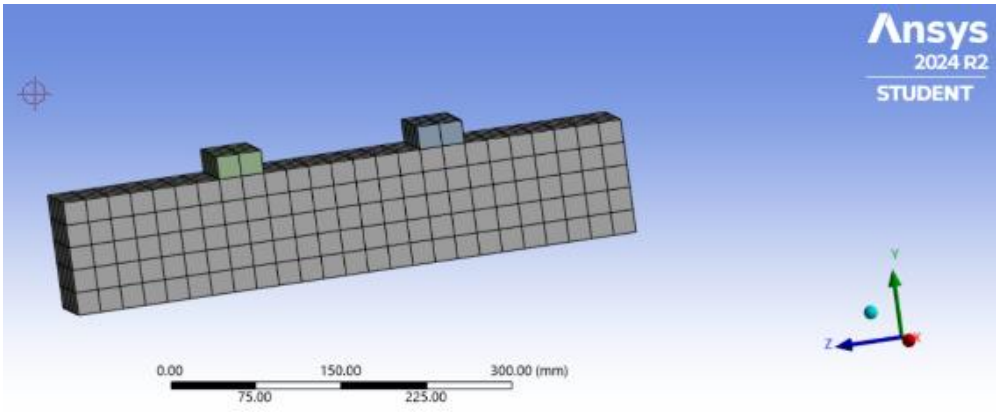

Fig. 16. Meshing of the Prism M30SF0.0

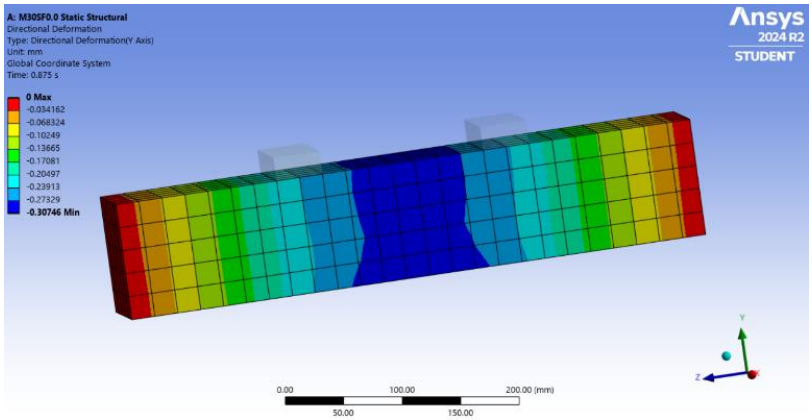

Fig. 17. Deformation of the Prism M30SF0.0

Prisms were tested under four-point loading. The Boundary conditions of the prisms were simply supported, the meshing was done perfectly, all the elements in the meshing are an 8-noded hexahedral elements, and no other element shapes are involved in the meshing. The element metrics reach 1.0 and consist of 1008 nodes and 645 elements as shown in Fig. 16. This analysis is static, and the time step is required to be completed in 1 second.

The M30SF0.0 prisms tested under four-point loading achieves maximum load recorded was 13040 N at a time step of 0.875 s, and the corresponding deflection at that point was 0.31 mm as shown in Fig. 17. Similarly, for M30SF0.5, M30SF1.0, M30SF1.5, and M30SF1.5-L*, the maximum loads were 17461 N, 22062 N, 26446 N and 29630 N at time steps of 0.91 s, 0.915 s, 0.92 s, and 0.98 s and the corresponding deflections were 0.41 mm,0.48 mm,0.56 mm and 0.61 mm respectively as

shown in Table 5. The deformation of M30SF0.0 is illustrated in Fig. 17. The boundary conditions were simply supported, exhibiting zero deformation at the supports and maximum deformation was observed near the center of the beam.

5. Conclusions

The mechanical characteristics of conventional concrete without SF were greatly improved by the inclusion of SF in various dosages. The experimental study yielded the following conclusions

- The double-hooked end steel fibers, varying from 0.5% to 1.5% slightly improved the compressive strength upto 17.89% for 28 days.
- The split tensile strength of SFRC was enhanced from 21.98% to 79.52% for fiber dosage ranging from 0.5% to 1.5% compared to conventional concrete
- The flexural strength of concrete was improved by 33.97%, 69.29% and 102.88% for varying percentages of SF. The maximum strength was attained at 1.5%.
- Layered concrete containing SFRC at top and bottom layers respectively and conventional concrete in the middle layer has a compressive strength of 48.36 MPa, split tensile strength of 6.67 MPa and flexural strength of 11.84 MPa at 28days.
- The compressive, split and flexural strengths of layered concrete were enhanced by 19.14%,100.90% and 127.25% to that of conventional concrete.
- Layered concrete subjected to load containing SFRC at bottom layer utilises to repair connections between the transition zone of the aggregate and matrix contact, hence preventing the formation of microcracks at that portion only.
- Linear relation was observed between fiber dosage and compressive strength, split tensile strength and flexural strength with R^2 values of 0.9561,0.9303 and 0.9359 respectively.
- The flexural strength values of prisms were compared both experimentally and numerically. The modelling results have aligned with that of the experimental values in terms of load and deflection.

References

[1] Yazıcı Ş, İnan G, Tabak V. Effect of aspect ratio and volume fraction of steel fiber on the mechanical properties of SFRC. Construction and Building Materials. 2007 Jun 1;21(6):1250-3. https://doi.org/10.1016/j.conbuildmat.2006.05.025

[2] Błaszczyński T, Przybylska-Fałek M. Steel fiber reinforced concrete as a structural material. Procedia Engineering. 2015 Jan 1;122:282-9. https://doi.org/10.1016/j.proeng.2015.10.037

[3] Buratti N, Ferracuti B, Savoia M. Concrete crack reduction in tunnel linings by steel fiber-reinforced concretes. Construction and Building Materials. 2013 Jul 1;44:249-59. https://doi.org/10.1016/j.conbuildmat.2013.02.063

[4] Madhkhan M, Azizkhani R, Harchegani MT. Effects of pozzolans together with steel and polypropylene fibers on mechanical properties of RCC pavements. Construction and Building materials. 2012 Jan 1;26(1):102-12. https://doi.org/10.1016/j.conbuildmat.2011.05.009

[5] ACI Committee 544.3R-93. Guide for specifying, proportioning, mixing, placing and finishing steel fiber reinforced concrete, American Concrete Institute, Farmington Hills, Michigan, 1993.

[6] Bentur A, Mindess S. Fiber reinforced cementitious composites. CRC press; 2006 Nov 16

[7] Williamson GR. The effect of steel fibers on the compressive strength of concrete. Special Publication. 1974 Jan 1;44:195-208. https://www.concrete.org/publications/internationalconcreteabstractsportal/m/details/id/17894

[8] Morris AD, Garrett GG. A comparative study of the static and fatigue behaviour of plain and steel fiber reinforced mortar in compression and direct tension. International Journal of Cement Composites and Lightweight Concrete. 1981 May;3(2). https://doi.org/10.1016/0262-5075(81)90002-6

[9] Mangat PS, Azari MM. Influence of steel fiber reinforcement on the fracture behaviour of concrete in compression. International Journal of Cement Composites and Lightweight Concrete. 1984 Nov 1;6(4):219-32. https://doi.org/10.1016/0262-5075(84)90017-4

[10] Fanella DA, Naaman AE. Stress-strain properties of fiber reinforced mortar in compression. InJournal Proceedings 1985 Jul 1 (Vol. 82, No. 4, pp. 475-483). https://doi.org/10.14359/10359

[11] Faisal FW, Ashour SA. Mechanical properties of high-strength fiber reinforced concrete. ACI Material Journal. 1992 Sep;89(5):449-455. https://doi.org/10.14359/2390

[12] Reinhardt HH. Third international RILEM workshop on high performance fiber-reinforced cement composites: HPFRCC3. Materials and Structures. 1999 May 16;32:622-623. https://doi.org/10.1007/bf02480499
[13] Gopalaratnam VS, Shah SP. Properties of steel fiber reinforced concrete subjected to impact loading. InJournal Proceedings 1986 Jan 1 (Vol. 83, No. 1, pp. 117-126). https://doi.org/10.14359/1750
[14] Schrader EK. Impact resistance and test procedure for concrete. InJournal Proceedings 1981 Mar 1 (Vol. 78, No. 2, pp. 141-146). https://doi.org/10.14359/6932
[15] Dey V, Bonakdar A, Mobasher B. Low-velocity flexural impact response of fiber-reinforced aerated concrete. Cement and Concrete Composites. 2014 May 1;49:100-10. https://doi.org/10.1016/j.cemconcomp.2013.12.006
[16] Choi SW, Choi J, Lee SC. Probabilistic analysis for strain-hardening behavior of high-performance fiber-reinforced concrete. Materials. 2019 Jul 27;12(15):2399. https://doi.org/10.3390/ma12152399
[17] Yoo DY, Lee JH, Yoon YS. Effect of fiber content on mechanical and fracture properties of ultra high performance fiber reinforced cementitious composites. Composite structures. 2013 Dec 1;106:742-53. https://doi.org/10.1016/j.compstruct.2013.07.033
[18] Wang HT, Wang LC. Experimental study on static and dynamic mechanical properties of steel fiber reinforced lightweight aggregate concrete. Construction and Building Materials. 2013 Jan 1;38:1146-51. doi.org/10.1016/j.conbuildmat.2012.09.016
[19] Alberti MG, Enfedaque A, Gálvez JC. On the prediction of the orientation factor and fiber distribution of steel and macro-synthetic fibers for fiber-reinforced concrete. Cement and Concrete Composites. 2017 Mar 1;77:29-48. https://doi.org/10.1016/j.cemconcomp.2016.11.008
[20] Cao YY, Li PP, Brouwers HJ, Sluijsmans M, Yu QL. Enhancing flexural performance of ultra-high performance concrete by an optimized layered-structure concept. Composites Part B: Engineering. 2019 Aug 15;171:154-65. https://doi.org/10.1016/j.compositesb.2019.04.021
[21] Mastali M, Naghibdehi MG, Naghipour M, Rabiee SM. Experimental assessment of functionally graded reinforced concrete (FGRC) slabs under drop weight and projectile impacts. Construction and Building Materials. 2015 Oct 1;95:296-311.
[22] Iskhakov I, Ribakov Y. A design method for two-layer beams consisting of normal and fibered high strength concrete. Materials & Design. 2007 Jan 1;28(5):1672-7. https://doi.org/10.1016/j.matdes.2006.03.017
[23] Nes LG, Øverli JA. Structural behaviour of layered beams with fiber-reinforced LWAC and normal density concrete. Materials and Structures. 2016 Jan;49:689-703. https://doi.org/10.1617/s11527-015-0530-9
[24] Eltobgy HH. Structural design of steel fiber reinforced concrete in-filled steel circular columns. Steel and Composite Structures. 2013 Mar 1;14(3):267-82. https://doi.org/10.12989/scs.2013.14.3.267
[25] Bleive LL, Lusis V. Experimental study and numerical modelling for flexural capacity of FRC structural elements. InENVIRONMENT. TECHNOLOGIES. RESOURCES. Proceedings of the International Scientific and Practical Conference 2021 Jun 16 (Vol. 3, pp. 30-35). https://doi.org/10.17770/etr2021vol3.6661.
[26] Zreid I, Kaliske M. A gradient enhanced plasticity–damage microplane model for concrete. Computational Mechanics. 2018 Nov;62(5):1239-57. https://doi.org/10.1007/s00466-018-1561-1
[27] IS 269:2015 ordinary portland cement specifications (sixth revision)
[28] IS 383:2016 coarse and fine aggregate for concrete-specification (Third Revision)
[29] IS 456:2000 plain and reinforced concrete-code of practice (Fourth Revision)
[30] IS 10262:2019 concrete mix proportioning-guidelines (second revision)
[31] Hughes BP, Fattuhi NI. The workability of steel-fiber-reinforced concrete. Magazine of concrete research. 1976 Sep;28(96):157-161.https://doi.org/10.1680/macr.1976.28.96.157

Research on Engineering Structures & Materials
www.jresm.org
MIM Research Group

Research Article

Experimental study on friction characteristics between stainless steel and saturated dense coral sand

Duc Tiep Pham[1,a], Thi Lua Hoang[*2,b], Viet Chinh Mai[1,c], Kim Thanh Tong[1,d], Duc Phong Pham[1,e], Minh Ngoc Do[3,f]

[1]*Institute of Techniques for Special Engineering, Le Quy Don Technical University, Hanoi, Vietnam*
[2]*Faculty of Civil Engineering, Thuyloi University, Hanoi, Vietnam*
[3]*Faculty of Civil Engineering, University of Transport Technology, Hanoi, Vietnam*

Article Info

Article History:

Received 10 Jan 2025
Accepted 13 Mar 2025

Keywords:

Coral sand;
Stainless steel;
Soil-Structural interaction;
Shear strength;
Interface friction angle;
Load repetition

Abstract

Coral sand is one of the typical subsoils for construction projects on coastal and island regions in Southeast Asia, including Vietnam's islands. In these regions, many structures are made from stainless steel to withstand the marine environment. Due to the load characteristics, these structures often face stability challenges, such as excessive settlement and horizontal displacement. Although these stability issues are closely related to the interaction behavior between the soil and the structure, the interfacial friction resistance between the coral sand and the steel has not been fully clarified. Therefore, in this paper, the friction characteristics between coral sand and stainless steel will be investigated through experiments. A series of direct shear tests using a modified shear box were conducted, considering the influence of magnitude of normal loads, the repetition of load, and the shear rate. The experimental results show that, the magnitude of loads affects the level of particle interlock and particle breakage, thereby affecting the interaction friction strength. Under a low number of load repetition cycles (<10 times), the soil particles become more densely packed, resulting in higher friction strength, however, at a higher number of cycles, grain breakage increased causing the decrease in friction strength. For the effect of shearing rate, no significant effect was observed.

1. Introduction

Coral sand is one of the typical subsoils utilized as foundation soil for many construction projects on coastal and island regions in Southeast Asia, including Vietnam's islands on the East sea. In these regions, stainless steel structures are usually used for the foundations instead of conventional concrete structures, to protect the structures from the damages caused by the marine environment. Figure 1 shows stainless steel pile foundations for Pillars on coral sand ground on offshore island in Vietnam's East sea. Due to special properties of the loads acting on offshore structures, these structural foundations often face many stability issues which closely relate to the interfacial frictional resistance between the soil and the structures such as excessive settlement or horizontal displacement. Therefore, when designing the structures on coral sand ground, it is necessary to understand the frictional characteristics between the soil and the structures.

Soil-structure interaction friction is governed by both soil and structure properties and has been well studied on both sandy and clayey soil. In term of soil properties, from early studies, Uesugi and Kishida [1] investigated the influence of particle shape on friction between granular soil and steel, and they found that the angularity of particles has great effects on the pipe–soil interface shear

*Corresponding author: hoangthilua@tlu.edu.vn
[a]orcid.org/0000-0002-1799-8191; [b]orcid.org/0000-0001-7124-0181; [c]orcid.org/0000-0001-7601-3391; [d]orcid.org/0009-0006-4892-4001; [e]orcid.org/0000-0002-9182-9441; [f]orcid.org/0009-0007-8198-0985
DOI: http://dx.doi.org/10.17515/resm2025-617ma0110rs

strength because the angular particles interlock more strongly, compared to rounded particles. Tiwari and AI-Adhadh [2] studied the influence of relative density and moisture content of well graded sand and showed that the difference in soil-structure frictional resistances depends on soil types, void ratio and water content. Canakci et al. [3] indicated that for the sandy-organic soil mixtures, the interfacial friction resistance was also affected by the water content and the percentages of granular in the mixed soil, however, it is interesting that the shape of the granular particles in the mixtuers had no noticeable effects. Raad et al. [4] carried out 64 direct shear tests to study friction angles between a poorly-graded sand and four types of structural materials; they found that, differing from the previous reports on well graded sand, the soil relative density has no effect on the shear strength of the soil, and the interface frictional strength were lower than internal frictional strength due to the interlock of the particles.

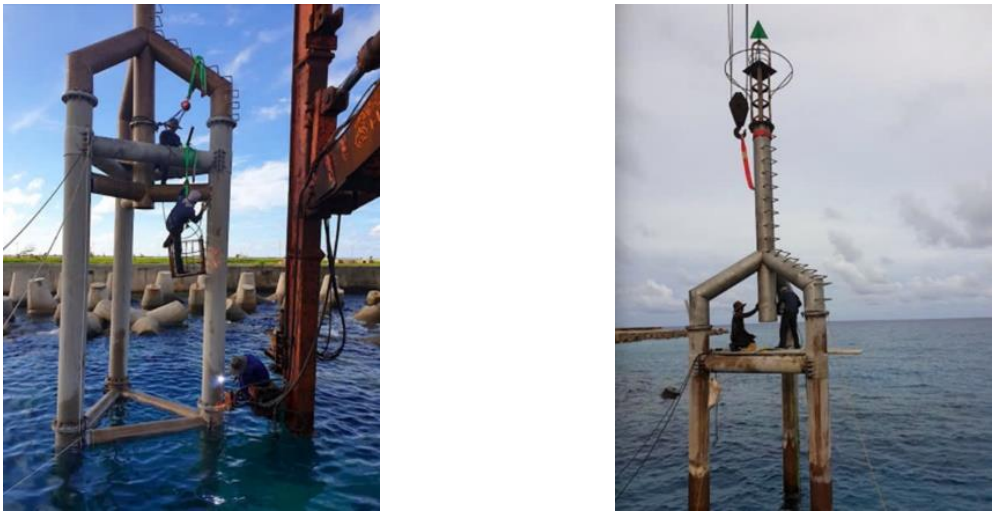

Fig. 1. Stainless steel pile foundations for Pillars on coral sand ground on offshore island in Vietnam's East sea

Regarding the influences of structural materials, Tsubakihara and Kishida [5] conducted research on the interface shear behavior between normal consolidated Kawasaki clay and steel, and they indicated that the increment in surface roughness led to the increased shearing resistance until reaching the critical steel roughness. Hu and Pu [6] conducted a series of direct shear tests to study sand-steel interface with different roughness of steel, the particle movement during experiments at the interface were recorded; and they found that when the ratio of surface roughness to the mean diameter of sand particles was greater than 0.01, the thickness of the shear band was 5D50 at the interface. Gireesha and Muthukkumaran [7], Tiwari el al. [2] and Raad et al. [4] studied the differences in behaviors between three structural materials with pure sand, they found that the friction angle between sand-concrete was the highest, compared to those between sand-wood or sand-steel. Han et al. [8] performed a comprehensive study on the interfacial friction between steel and silica sand, considering both steel roughness, particle geometry and gradation of the sand via direct shear and direct interface shear tests; the experimental results showed that steel surface roughness plays an important role in the interface shear strength. The critical shear strength between lightly rusted steel and sand is higher than that between smooth steel and sand, up to 13% for the case of graded sands and about 50% for the case of uniform sands; these values were higher for the cases of rusted steel surfaces and continued to increase for the cases of heavily rusted steel surfaces. Guo et al. [9] investigate the effect of groove feature on steel-sand interface shear behavior based on direct shear tests results; and they concluded that the interface friction angle increases with the intersection angle between the groove direction and shear direction, and also increases with increasing the groove width.

Besides the above major influence factors, many other studies have been done to investigate more deeply and detailly about various factors affecting the frictional behavior between soils and structures such as: particle size, grain gradation, bonding and slipping of the particles, and soil moisture [10, 8, 11, 12, 13]; the thickness of interfacial shearing layer, shearing rate, and loading

properties [14, 15, 16, 17, 18, 19, 20] ; structural material and structural configuration [21, 22]; the roughness of the structural surface [23, 24, 13]; and temperature variations [25].

From the literature survey, there is limited information on the frictional behavior between coral sand and stainless steel available for practicing engineers. The coral sand usually contains a large part of the materials derived from coral and marine life, so it has unique properties such as being easily crushed and having uneven edges. Because the interfacial behavior depends deeply on the soil properties, with soils having such unique properties, further research is needed.

In this study, the interface frictional characteristics between coral sand and stainless steel will be investigated using experimental methods. A series of direct shear tests were conducted using an automated device with modified lower shear box apparatus. The main focuses are placed on the characteristics of the applied loads such as loading rate, load magnitude, and load repetition, these are the common characteristics of the loads acting on offshore structures. The sand is in saturated state during the experimental process, similar to its working condition on construction site.

In the next sections, the details of this study are organized as follows: Section 2 provides information on the studied coral sand, the testing machine and the modifications of the shear box, and the experimental procedures. Section 3 presents the experimental results and discussion on the internal shear strength parameters and the effects of loading properties on the interface friction characteristic between coral sand and steel, the main findings of this study are drawn. Section 4 is the conclusion of the study, where the main findings are summarized and remarked.

2. Description of the Experiments

2.1. Physical Characteristics of Coral Sand

The coral sand utilized in this study was sourced from an offshore island located in the East Sea of Vietnam, as shown in Fig. 2. The properties of the sand were investigated through a series of laboratory soil tests, including grain size analysis and direct shear tests (DSTs). Table 1 shows the summary of physical properties of the studied sand. It is noted that, for direct shear tests, the samples were prepared with the relative density D_r of 70%, the soil was in saturated condition during the tests, and the results of the direct shear tests will be presented and analyzed in the next section for comparison purposes.

Fig. 2. Coral sand mixture collected from an offshore island of Vietnam

Figure 3 shows the grading curve for the sand. Based on the results of the grading curve analysis, the coefficient of uniformity (Cu) is determined to be 5.74, and the coefficient of curvature (Cc) is calculated as 1.23. In accordance with the TCVN 5747:1993 standard [26] (as well as in

accordance with the Unified Soil Classification System USCS), the coral sand is classified as SW-type sand, signifying that it is clean and well-graded.

Table 1. Physical properties of coral sand

Parameter	Value
Density of soil particle, ρ_s (g/cm^3)	2.671
Maximum void ratio, e_{max}	1.188
Minimum void ratio, e_{min}	0.643
Coefficient of uniformity, C_u	5.74
Coefficient of curvature, C_c	1.23

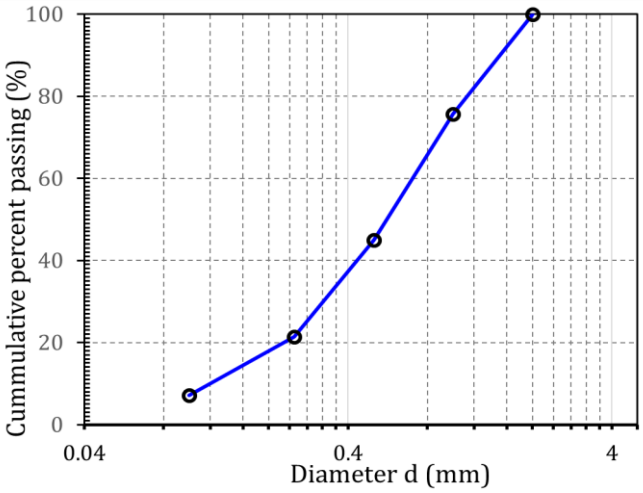

Fig. 3. Grading curve of the coral sand

2.2. Shear Testing Machine and Modified Shear Box

To investigate the mechanical behavior of the contact surface between coral sand and stainless steel, the ShearMatic automatic shear testing machine (Fig. 4) is employed with an improved lower shear box design, as illustrated in Fig. 5. The lower shear box was specifically designed and manufactured to enable its assembly with the upper shear box and to securely hold the steel plate in the experiments. In this study, 316L stainless steel is used because this steel is commonly utilized for pile foundations on Vietnam offshore islands due to its excellent corrosion resistance in marine environments.

Fig. 4. The ShearMatic automatic shear testing machine

The manufacturing process for the lower shear box is detailed as follows:

- The lower shear box is fabricated from steel to ensure compatibility with the existing upper shear box and to securely hold the experimental stainless-steel plate (Fig. 6);
- The 316L stainless steel plate is processed and manufactured from a steel block. The surface roughness of the plate is measured as R_a=4.576μm (Fig. 7). The average roughness R_a is defined as thearithmetic mean deviation of the roughness profile.
- The stainless steel plate is placed onto the lower shear box (Fig. 8). The experimental setup is then used to measure the frictional behavior between the stainless steel and coral sand, as depicted in Fig. 9.

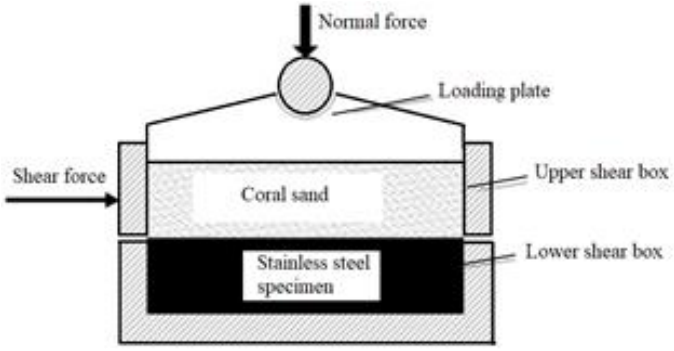

Fig. 5. Shear box model used to determine the interfacial friction angle between stainless steel and coral sand

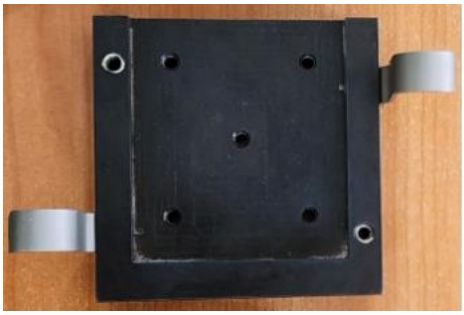

Fig. 6. Fabrication of the lower shear box for securing the 316L stainless steel plate

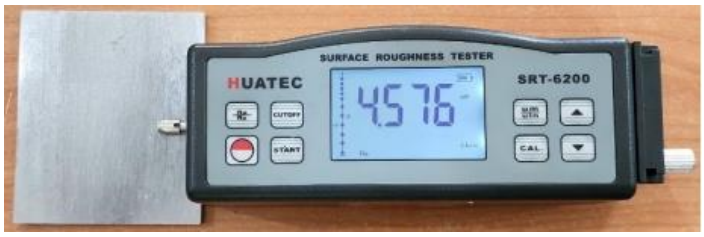

Fig. 7. Measurement of the surface roughness of the 316L stainless steel plate

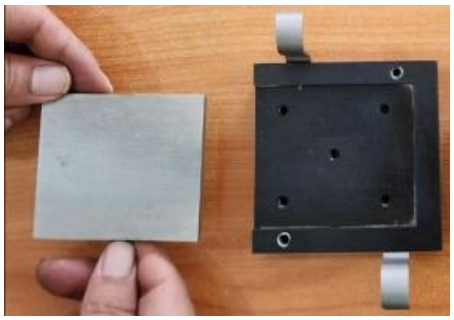

Fig. 8. Placement of the stainless steel plate on the lower shear box

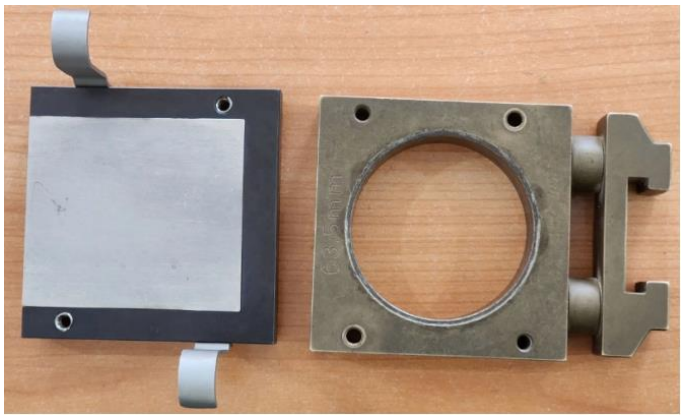

Fig. 9. Fully assembled improved lower and upper shear box

2.3. Procedure of the Experiments to Determine the Friction Between Stainless Steel and Coral Sand

Observations of the geological column in the study area reveal that the coral sand layer within the borehole has an average Standard Penetration Test (SPT) hammer number of N=40. According to the TCVN 9351:2022 standard [27], this hammer number corresponds to a dense state with a

relative density (D_r) of 70%. To examine the friction characteristics between stainless steel and coral sand in this study, the authors prepares samples with a relative density matching the field conditions (D_r=70%).

The friction between stainless steel and coral sand is determined using the ShearMatic automatic shear testing machine equipped by an improved lower shear box, following the nine-step procedure outlined below:

- Step 1: Calculate Sample Mass :

Based on the target relative density (D_r) and the known parameters (Table 1), the required mass of dry coral sand to prepare the sample is calculated.

- Step 2: Prepare The Sample

The sample is prepared in the shear box apparatus with fixed dimensions (diameter D = 6.35cm, height h_m=12.5mm). The pre-calculated mass of dry coral sand is poured into the shear box, and compaction is performed as shown in Fig. 11. The compaction process is done until the predetermined height (h_m) is achieved, ensuring the desired density.

- Step 3: Install The Shear Box

The shear box containing the prepared sample is placed into the ShearMatic automatic shear testing machine.

- Step 4: Set initial parameters

Before starting the experiment, the initial parameters are set. These include the sample size, input parameters for the consolidation stage (vertical load σ_v, consolidation speed, and data recording speed), and input parameters for the direct shear stage (shear rate SR, maximum horizontal displacement, and data recording speed).

- Step 5: Saturate the Sample

The sample is placed in a tray filled with water and soaked for approximately 15 minutes to achieve saturation, as shown in Fig. 12.

- Step 6: Perform the Consolidation Stage

The sample undergoes a consolidation stage under the normal stress to replicate in-situ conditions.

- Step 7: Apply Horizontal Force

Horizontal force is incrementally applied to simulate the shear process. The pins that lock the upper shear box and lower shear box are removed before applying the horizontal force.

- Step 8: Record Measurements And Complete The Test

Measurements are recorded throughout the test process, which is concluded when the horizontal displacement reaches the specified limit.

The present study addresses three key issues related to load properties to investigate the factors influencing the frictional resistance between the stainless steel and coral sand, as outlined below:

- Problem 1: Investigating the effect of shear rate (SR).
- Problem 2: Examining the effect of magnitude of the normal pressure applied to the sample (ML).
- Problem 3: Analyzing the effect of the number of static load repetition cycles (LR).

The American Petroleum Institute proposed the API curve of sand skin friction load transfer (American petroleum institute [28]). Analysis of this curve indicates that when the displacement between the structure's surface and the sand δ reaches [δ] = 0.1inch (2.54 mm), the friction intensity between the sand and the steel surface reaches its limiting value. Accordingly, this study adopts a displacement value of [δ] = 2.54mm to determine the critical friction value between the coral sand and the surface of the stainless-steel plate.

Fig. 10. Weighing the coral sand for sample preparation

Fig. 11. Compacting the coral sand within the shear box

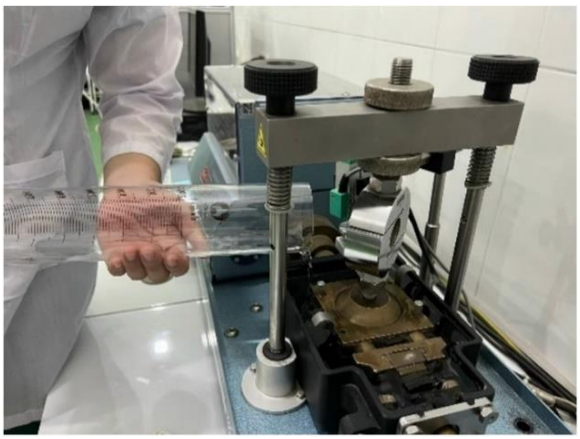

Fig. 12. Saturating the coral sand sample by introducing water into the shear box

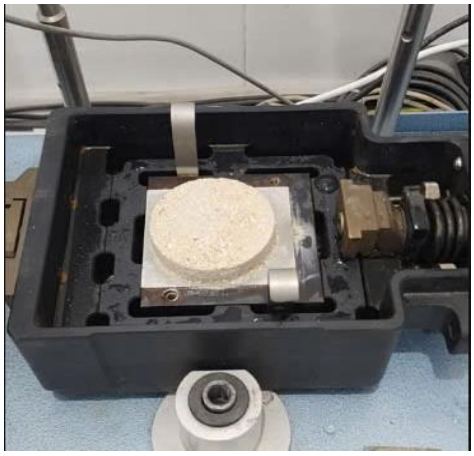

Fig. 13. Coral sand sample after completion of the shear test

3. Experimental Results and Discussion

3.1. Internal Shear Strength Parameters of the Coral Sand

Prior to conducting the tests to investigate the interfacial frictional behavior between coral sand and stainless steel, the internal shear strength characteristics of the sand were determined through a series of direct shear tests using the same ShearMatic automatic shear testing machine. Fig. 14 presents the friction force–horizontal displacement curves obtained from these tests for three samples subjected to different levels of normal stress. The results indicate that the shear strength of all samples initially increased with horizontal displacement (δ), reaching peak strength at δ = 3.5–4.5 mm. Furthermore, higher applied normal stress resulted in peak shear strength occurring at a greater horizontal displacement. Beyond this peak, the coral sand exhibited post-peak softening behavior, which is consistent with materials governed by the Hypoplastic model.

From the friction force - horizontal displacement as shown in Fig. 14, the peak shear strength corresponding for each level of the normal applied load was obtained. Figure 15 shows the relations between the normal stress and the shear strength for the three samples. The least squares method was used to create the fitting line to determine the shear strength parameters of the sand. From the fitting line on Fig. 15, the internal friction angle φ of the sand is determined by the angle of inclination of this line (tan φ = 1.278 corresponds to φ = 52^o), while the apparent cohesion c of the sand is the ordinate of the intersection of the line with the vertical y-axis (c = 53.578 kPa). It can be seen from the results that the coral sand using in this study has a high internal friction angle φ of 52^o, and a high internal apparent cohesion c of 53.578 kPa. The rough structure of coral grains is the reason for the high internal friction angle. The apparent cohesion of the sand herein is due to the mutual clogging of the particles, which is different from the cohesion of clayey soils. For coral sand, sand particles especially have uneven edges and irregular shapes, which lead to the high

apparent cohesion. This result is also consistent with the results conducted from previous studies on the mechanical properties of coral sand [29, 30].

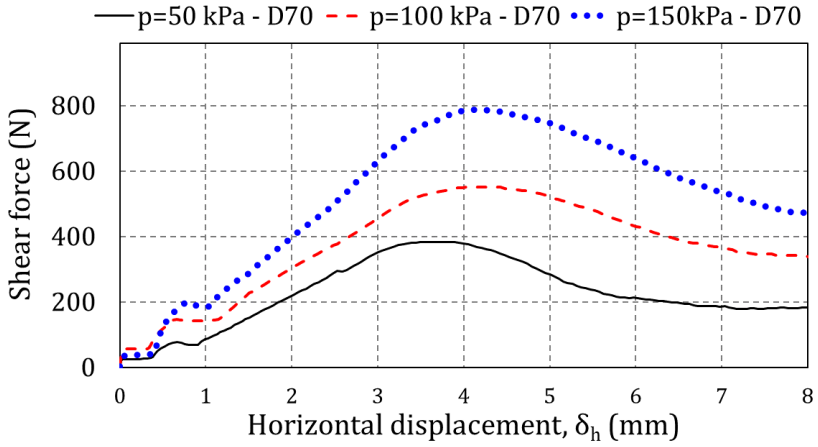

Fig. 14. Horizontal displacement – Shear force relations of the coral sand

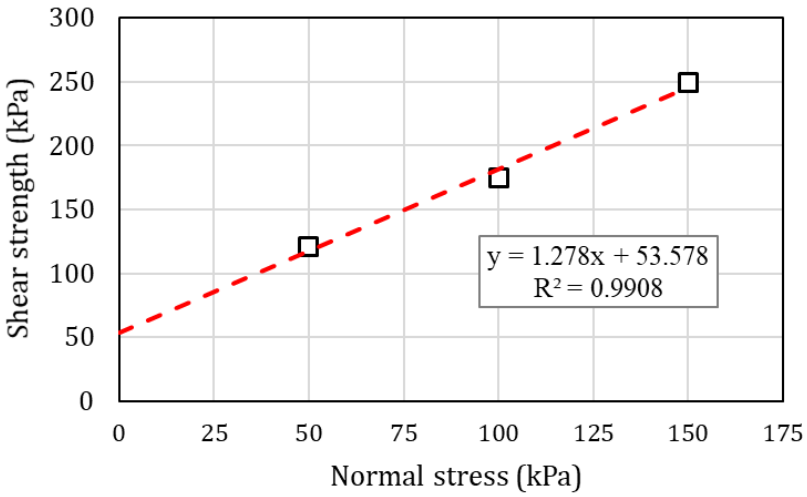

Fig. 15. Normal stress – Internal shear strength relations of the coral sand

3.2. Effect of Shear Rate on Interface Friction between Stainless Steel Plate and Coral Sand

In this parametric study, samples are tested at seven different shear rates. The samples are prepared with the same relative density of 70% and subjected to the same normal pressure of 100 kPa. The applied shear rates vary across the following levels: 0.1mm/min; 0.25mm/min; 0.75mm/min; 1.0mm/min; 2.0mm/min; 3.0mm/min; and 4.0mm/min.

The relationships between friction force and horizontal displacement obtained from the tests are presented in Fig. 16. The analysis of the curves in Fig. 16 reveals that none of the curves corresponding to different shear rates display peak values. Moreover, the shear rate has a minimal impact on the frictional behavior between coral sand and stainless steel, with differences in friction force across the shear rates being only approximately 5 percent of average friction force of all 7 tests. This is attributed to the random distribution of grain sizes on the contact surface between the stainless-steel plate and the coral sand sample, which occurs during the sample preparation process. Comparing to the test results conducted by Al-Mhaidib [14] for a local poor-graded sand, the shear rate reported by Al-Mhaidib had more clear effects on the interface shear stress as the interface friction angle increased noticeably with increasing shear rate. In contrary, Rahman et al. [31] investigated the interfacial friction angle between steel and a coarse sand having C_u of 3.89 and C_c of 1.21, considering the wide range of shearing rate from 0.05mm/min to 2.5mm/min; and they found that the interface friction angle decreased with increasing shearing rate. Looking back

to previous studies, there is limited studies dealing with the effects of shear rate on the interface shear strength between sand and steel for comparison, however, it can be seen that the behavior of coral sand in this case is quite different from above mentioned sands.

Figure 16 shows that the critical friction force is attained at a horizontal displacement ranging from approximately δ=0.5m÷1.0mm. In comparison to the study conducted by Al-Mhaidib [14], which utilized a steel plate with a surface roughness of R_a=1.06 μm and white silica sand with a relative density of 64%, they reported from their test results that a larger displacement range of 2.0 mm to 3.0 mm at maximum friction force. Furthermore, the friction force - horizontal displacement curves in the test of Al-Mhaidib [14] also did not display peak values.

Within the shear rate range of 0.1mm/min to 4mm/min, the friction intensity between the stainless steel surface and coral sand is observed to vary between 44.56 kPa and 48.96 kPa. Consequently, the interfacial friction angle between the stainless steel surface and coral sand changes from 24.02 degrees to 26.08 degrees. A relative comparison with silica sand, based on the finding of Al-Mhaidib [14], reveals that coral sand, due to its rough and angular grain structure, gernerates greater interfacial friction resistance at the steel surface.

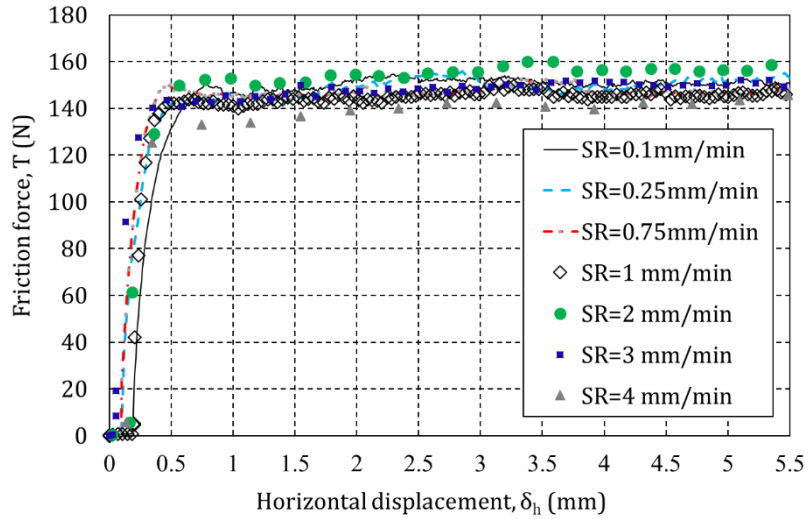

Fig. 16. Friction force versus horizontal displacement for coral sand and stainless-steel surface under normal stress of 100 kPa

3.3. Effect of Normal Pressure on the Interface Friction Angle between Stainless Steel Plate and Coral Sand

In this study, eight tests are performed to investigate influence of normal pressure on the interface friction angle. The samples are prepared with the relative density of D_r=70%, the shear rate of SR=1.0mm/min, and the normal pressures σ_v applied at varying levels: 12.5kPa; 25kPa; 35kPa; 50kPa; 100kPa; 200kPa; 300kPa; 400kPa. It is noted that the selected range of normal pressures encompasses the typical range of normal loads encountered in real structural applications.

3.3.1. Relation Between the Interface Shear Force and The Relative Lateral Displacement for Different Normal Pressures

Figure 17 shows the relations between the interface shear forces and the relative lateral displacements with different magnitudes of the applied normal stress. The results reveal that, at first, as the horizontal displacement between the two surfaces increases, the friction force at the interface between the stainless steel and coral sand increases, and then it eventually stabilizes. This behavior closely resembles that of the ideal elastic-plastic model. Additionally, the friction force between the stainless steel and coral sand increases with increasing the magnitude of the applied normal pressure.

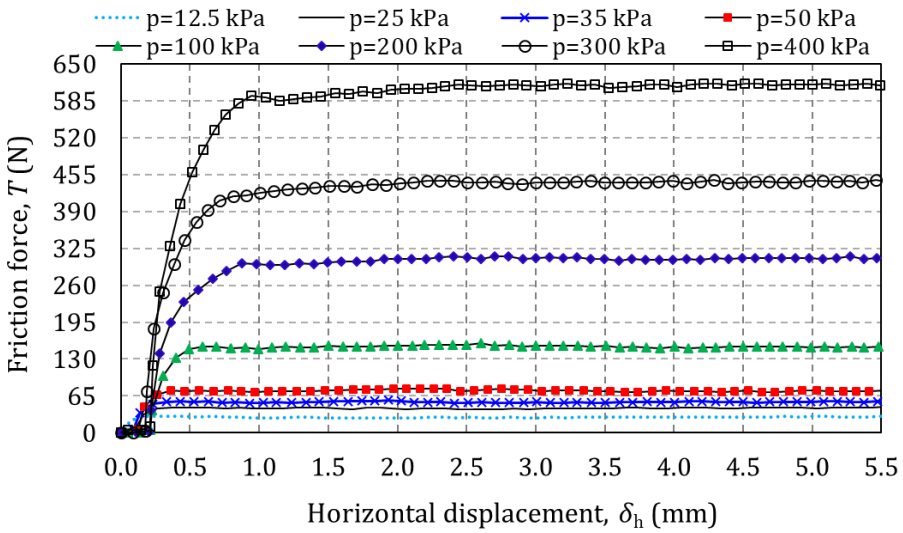

Fig. 17. Relation of friction force - horizontal displacement under varying normal pressures

3.3.2. Determine Interface Shear Strength Parameters from Relations Between Friction Force and Horizontal Displacement

The Mohr-Coulomb model is commonly used to simulate the strength characteristics of the contact surface between a structure and soil. The strength parameters of the contact surface are generally comparable to those of the surrounding soil but are adjusted using the interface reduction coefficient R_{inter}. For the coral sand, the strength of the contact surface between the structure and the sand is often characterized by a single parameter, the interface friction angle [24]. However, Li et al. [32] suggests that this strength includes two components: the interface friction angle and the cohesion.

If the contact surface between stainless steel and coral sand is assumed to be governed solely by the interface friction angle (δ), then this parameter can be determined by each individual experiment using the following equation:

$$\delta = arctan(\frac{\tau}{\sigma_v}) \quad (1)$$

Where τ is shear stress, σ_v is the normal stress applying on the coral sand sample.

The interface friction angle (δ) of the samples at various compressive pressures is computed using formula (1), and the results displayed in Table 2 and Fig. 18. The regression method is applied to establish the correlation function between the interface friction angle and the normal pressure, as follows:

$$\delta = 6893.15 \times \sigma^{-2.64} + 25.57 \quad (2)$$

Figure 18 exhibits that within the low range of normal pressure ($\sigma_v \leq 35$ kPa), a decrease in applied pressure causes an increase in the interface friction angle. In contrast, the surface friction angle stabilizes at approximately 25.57 degrees when the normal pressure surpasses 35 kPa.

If the characteristics of the stainless steel-coral sand interface shear strength are considered to comprise two components, including interface friction angle and cohesion, the correlation between the normal pressure and the interface shear strength is presented in Fig. 19.

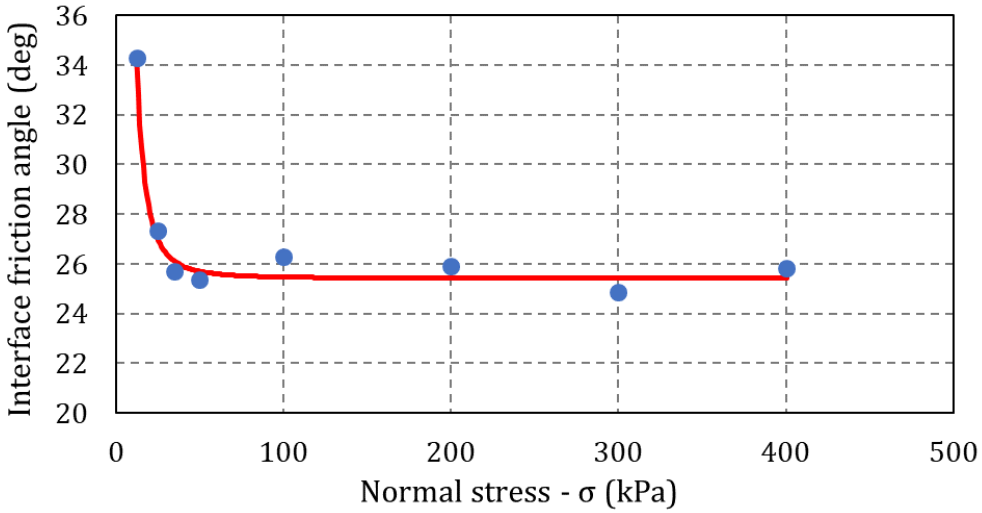

Fig. 18. Relation between normal pressure and interface friction angle between stainless steel and coral sand governed solely by the interface friction angle, based on equation (1) and (2).

Table 2. Analysis results of normal pressure - external friction angle of the interface of stainless steel and coral sand

Normal pressure σ (kPa)	Friction force corresponding to horizontal displacement of 2.54mm (N)	Interface shear strength τ (kPa)	Without cohesion	With cohesion		Note
			Interface friction angle, δ=atan (τ/σ) (Deg)	Cohesion c (kPa)	Interface friction angle δ (Deg)	
12.5	27.01	8.53	34.30	3.85	20.24	Low normal stress
25.0	40.93	12.92	27.34			
35.0	53.34	16.84	25.70			
50.0	75.12	23.72	25.38	0.49	25.48	High normal stress
100.0	156.29	49.35	26.27			
200.0	307.93	97.23	25.93			
300.0	440.50	139.09	24.87			
400.0	612.67	193.46	25.81			

For low normal pressure ($\sigma_v \leq 35$ kPa), based on three experimental data, a first-degree equation is established based on three experimental data points. The equation contains two unknowns: the tangent of the interface friction angle (tanδ) and cohesive strength (c), treated as constant. By applying the least squares method, the interface friction angle is determined to be 20.24^o while the cohesive strength is calculated as 3.85 kPa.

In the same way, for higher normal pressure (exceeding 35 KPa), an analysis of five experimental data using the least squares method yields an interface friction angle of 25.48 ^{o} and a cohesion of 0.49 kPa.

The mass of the experimental sample is relatively small (less than 100 gr), making it prone to considerable error if the grain composition of the sample are re-determined after loading. Furthermore, the sample mass does not meet the requirements for grain composition analysis as stipulated by the relevant standard (TCVN 4198:2014 [33]). Consequently, this analysis is not conducted in this study. However, the particle breakage property of coral sand under the affect of the applied load is the difference between coral sand and silica sand, this property has been confirmed in many recent studies [34, 35, 36].

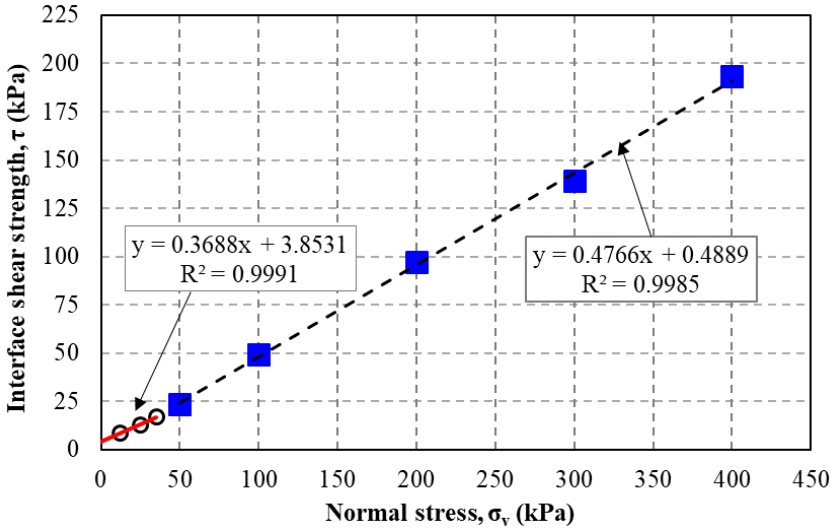

Fig. 19. Relation between normal pressure and ~~surface~~ interface shear strength between stainless steel and coral sand governed by both interface friction angle and cohesion

3.3.3. Discussion on Influence of Normal Pressure on Interface Shear Strength

Compare the interface shear strength parameters between the cases of low normal pressure and the cases of higher normal pressure, it can be seen that the interfacial friction angle is significantly higher for the cases of the higher pressures, meanwhile the interfacial cohesion is higher for the cases of the lower pressures. According to the research, under the low normal pressure, the rough and the angular grains of coral sand exhibit minimal breakage and are capable of interlocking with the rough grooves on the steel surface. This phenomenon results in a higher value in the cohesive strength to 3.85 kPa. Conversely, under higher normal pressures, the grains are more prone to breakage and rearrangement, resulting in the increase of relative density. Consequently, the interface friction angle increase. Here, the interaction behavior between the steel surface and coral sand is similar to that of the silica sand, and the interface friction angle is considered as the primary component contributing to the interface shear strength.

Compare to the internal shear strength parameters, both the interface friction angle and interface cohesion are significant smaller. The interface friction angle is only 38%-48% of the internal friction angle, and the interface cohesion is only under 8% of the internal cohesion. In current design, many engineers use an empirical coefficients between interfacial and internal resistances R_{inter} = 0.6 ÷ 0.7 (this means that the interfacial shear strength parameters are about 60% ÷ 70% of the values of the internal shear strength paramters). However, the use of a common R_{inter} value may not be appropiate in this case. Considering steel piles - a common structures on coral sand ground, the load-bearing capacity of these piles is closely related to the pile-soil interaction. Currently, pile shaft resistance are usually calculated using empirical formulas related to soil properties. Fig. 20. compares the interface friction resistances measured from the experiments with the resistances calculated by three different formulas for the coral sand in this study. Three calculation schemes include: (1) using the equation founded by Meyerhof based on N-SPT value (N= 40) of the ground [37]; (2) Using empirical resistance values according to the depth of soil layer and dense state of the soil [38,39]; (3) Using the equation recommended by API for offshore structures [28], based on effective overburden pressure and soil relative density.

It is seen from Fig. 20. that scheme (1) indicates a constant shear strength while the measured shear strength increases with normal pressure. The scheme (2) presents higher values when the normal pressures are less than 120 kPa but lower values when the normal pressures surpass 120 kPa, compared to measured values. The scheme (3) shows that the trend is quite similar to the trend of experimental results, however, at large normal pressures, calculated values were noticeable maller than the measured values.

In general, the differences between the experimental results and calculated results of this study emphasizes that, when designing a steel structure on coral sand ground, it is necessary to understand the frictional behavior between the structure and the soil.

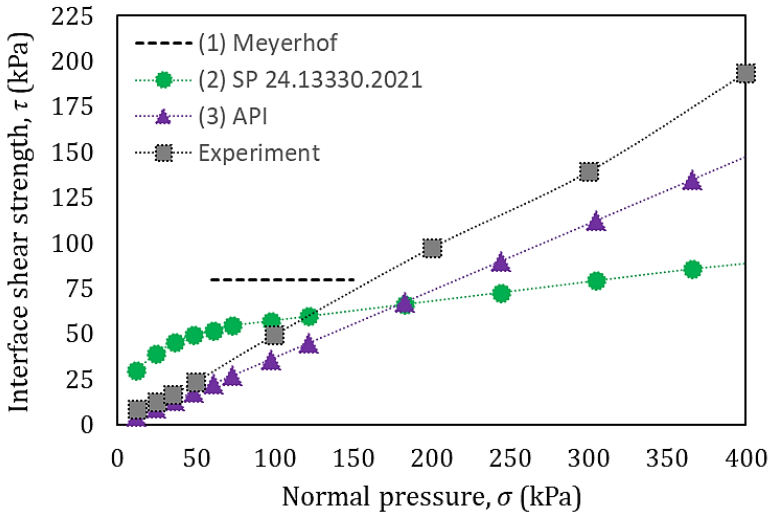

Fig. 20. Relation between normal pressure and interface shear strength from experiment and calculations.

3.4. Effect of Repeated Loading on the Interface Friction Angle between Stainless Steel Plate and Coral Sand

The offshore structures built on coral sand ground is often subjected to repeated loads from sea waves. Current study investigates the impact of the number cycles of repeated load on the friction force between the stainless steel and the coral sand. Five experimental samples are tested. All sample are prepared with the same relative density of D_r=70% and the same shear rate of SR=1.0mm/min, as described in the previous sections. The samples are subjected to varying numbers of repeated horizontal load cycles (5, 10, 20, 30, and 40 cycles) before being horizontally loaded to failure. Parameters for the movement of lower shear box in each cycle as follows:

- Maximum amplitude: A ≤ 0.5mm
- Forward travel velocity: SR_1=1mm/min
- Reverse travel velocity: SR_2=1mm/min

The horizontal travel of the lower shear box over five cycles is shown in Fig. 21. The results reveal that the forward and reverse travel amplitudes of the lower plate are not identical, with the actual travel amplitude measured at 0.214 mm.

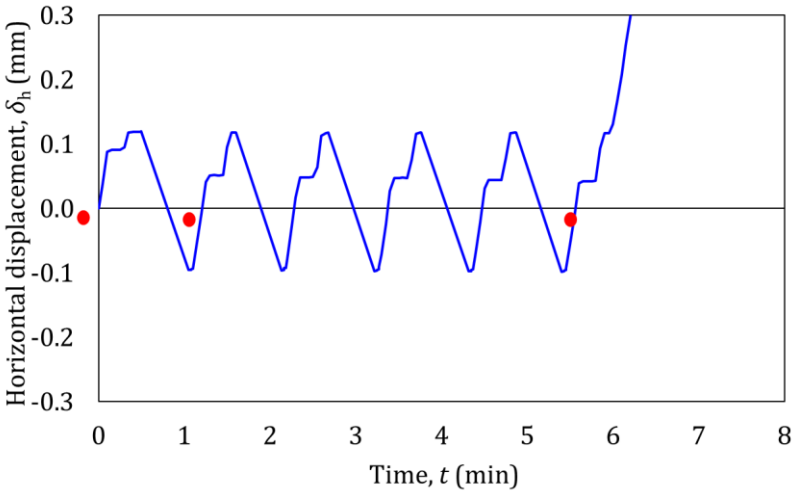

Fig. 21. Horizontal displacement of the lower shear box over time across five loading cycles

Figure 22 depicts the travel of the lower shear box and the interface friction force during both the repeated loading phase and the subsequent loading phase until specimen failure. The results indicate that for a small number of cycles (10 cycles or fewer), the interface friction forces are higher, in comparison with those of larger number of load cycles. This phenomenon can be explained that the repeated loading process compacts the particles, leading tighter packing and an increase in surface friction force. However, as the number of cycles increases (larger than 10 cycles), the repeated loading process leads to the breakage of larger particles and increasing the surface wear. This results in a restructure and rearrangement of particles with an increased proportion of fine particles, causing a gradual decline in interfacial friction force. When the number of cycles reaches 40, the interfacial friction force is nearly equivalent to that of the sample that have not been subjected to repeated loading.

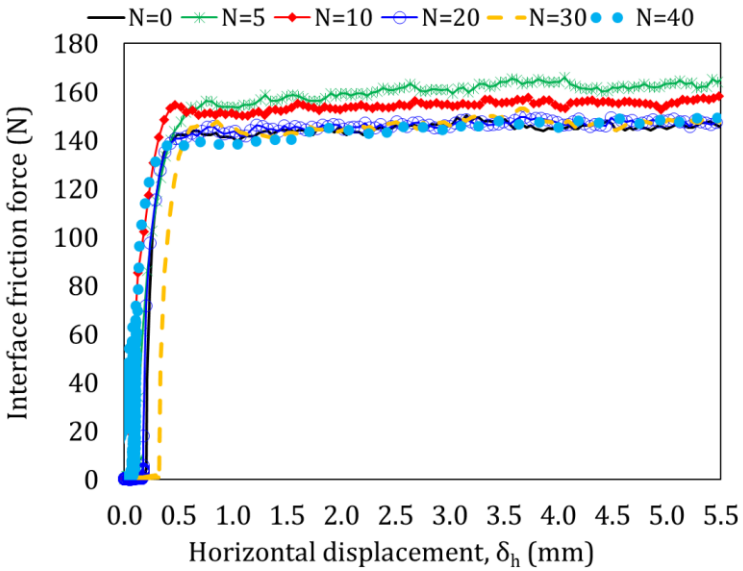

Fig. 22. Relationships between interfacial friction force and horizontal displacement for varying numbers of cycles

4. Conclusions

In this study, the interface friction characteristics between 316L stainless steel and saturated dense coral sand were investigated using a Shearmatic automatic shear testing machine with a modified lower shear box. The key findings can be summarized as follows:

- The relationship between horizontal displacement and interface friction force does not exhibit a peak value. The shear rate has an insignificant impact on interface friction, with friction force variations remaining within 5% across different shear rates.
- The horizontal displacement required for the interface friction force of coral sand reaches its critical value is lower, compared to corresponding displacement value of white silica sand. Compared to silica sand with the equivalent density, coral sand demonstrates a higher interfacial frictional strength due to its rough and angular grain structure.
- Under low normal pressure, coral sand exhibits minimal grain breakage, allowing the rough, angular particles to interlock with the grooves on steel surface, leading to an increase in unit cohesion. In contrast, at higher normal pressures, increased particle breakage results in a smoother particle structure, reducing unit cohesion and shifting the dominant interaction mechanism to frictional resistance.
- Load repetition significantly influences interface friction behavior. At fewer than 10 load cycles, particle compaction enhances higher frictional strength. However, at more than 10 cycles, grain breakage and particle rearrangement reduce interface friction strength. Under larger number of load cycles, the interfacial friction strength is reduced to approximately the interface friction strength of the case of not being subjected to repeated loading.

- The interface friction angle and cohesion are significantly lower than the internal shear strength parameters. The interface friction angle is only 38%-48% of the internal friction angle, while the interface cohesion is less than 8% of the internal cohesion. These findings highlight the necessity of considering actual interface shear behavior rather than relying on empirical reduction factors when designing steel structures on coral sand foundations.

References

[1] Uesugi M, Kishida H. Influential factors of friction between steel and dry sands. Soils and Foundations, 1986; 26(2):33-46. https://doi.org/10.3208/sandf1972.26.2_33

[2] Tiwari B, Al-Adhadh AR. Influence of relative density on static soil-structure frictional resistance of dry and saturated sand. Geotechnical and Geological Engineering, 2014; 32(2):411-427. https://doi.org/10.1007/s10706-013-9723-6

[3] Canakci H, Hamed M, Celik F, Sidik W, Eviz F. Friction characteristics of organic soil with construction materials. Soil and Foundation, 2016; 56(6):965-972. https://doi.org/10.1016/j.sandf.2016.11.002

[4] Raad A, Abbas BJ, Al. Khuzaie HMA. Behavior of sand soil due to interaction between soil and structural materials. International journal of civil engineering and technology, 2018; 9(9):194-214.

[5] Tsubakihara Y, Kishida H. Frictional Behaviour between Normally Consolidated Clay and Steel by Two Direct Shear Type Apparatuses. Soils and Foundations, 1993; 33:1-13. https://doi.org/10.3208/sandf1972.33.2_1

[6] Hu LM, Pu JL. Experimental study on mechanical characteristics of soil-structure interface. Chinese Journal of Geotechnical Engineering, 2001; 23(4):431-435.

[7] Gireesha NT, Muthukkumaran K. Study on soil structure interface strength property. International Journal of Earth Sciences and Engineering, 2011; 4(6): 89-93.

[8] Han F, Ganju E, Salgado R, Prezzi M. Effects of interface roughness, particle geometry, and gradation on the sand-steel interface friction angle. Journal of geotechnical and geoenvironmental engineering, 2018; 144(12):04018096. https://doi.org/10.1061/(ASCE)GT.1943-5606.0001990

[9] Guo J, Wang X, Lei S, Wang R, Kou H, Wei D. Effects of groove feature on shear behavior of steel-sand interface. Advances in civil engineering, 2020; 9593187. https://doi.org/10.1155/2020/9593187

[10] Aksoy HS, Gor M, Inal E. Determination of friction angles between soil and steel - FRP piles. Turkish journal of science and technology, 2017; 13(1):19-23.

[11] Liang Y, Lu X, Wang J, Liu M. Experimental study of shear behavior of interfaces between crushed sandstone-mudstone particle mixture and smooth steel plate. Soil mechanics and foundation engineering, 2016; 53(3):158-165. https://doi.org/10.1007/s11204-016-9380-x

[12] Miura K, Maeda K, Furukawa M, Toki S. Mechanical Characteristics of Sands with Different Primary Properties. Soils and Foundations, 1998; 38:159-172. https://doi.org/10.3208/sandf.38.4_159

[13] Vangla P, Latha Gali M. Effect of particle size of sand and surface asperities of reinforcement on their interface shear behavior. Geotextiles and Geomembranes, 2016; 44(3):254-268. https://doi.org/10.1016/j.geotexmem.2015.11.002

[14] Al-Mhaidib AI. Shearing rate effect on interfacial friction between sand and steel. Proceedings of the fifteenth International offshore and polar engineering conference, 2005; 633-640.

[15] Boulon M, Nova R. Modelling of soil-structure interface behaviour a comparison between elastoplastic and rate type laws. Computers and Geotechnics, 1990; 9:21-46. https://doi.org/10.1016/0266-352X(90)90027-S

[16] Fakharian K, Evgin E. Cyclic simple-shear behavior of sand-steel interfaces under constant normal stiffness condition. Journal of Geotechnical and Geoenvironmental Engi neering, 1997; 123(12):1096-1105. https://doi.org/10.1061/(ASCE)1090-0241(1997)123:12(1096)

[17] Khemissa M, Tallah N, Bencheikh B. Experimental and numerical modeling of the sand-steel interface behavior under monotonic loading. Innovative Infrastructure Solutions, 2018; 3(1):25. https://doi.org/10.1007/s41062-018-0130-y

[18] Liu FY, Wang P, Geng X, Wang J, Lin X. Cyclic and post-cyclic behaviour from sand-geogrid interface large-scale direct shear tests. Geosynthetics International, 2015; 23(2):1-11. https://doi.org/10.1680/jgein.15.00037

[19] Mortara G, Ferrara D, Fotia G. Simple model for the cyclic behavior of smooth sand-steel interfaces. Journal of Geotechnical and Geoenvironmental Engineering, 2010; 136(7):1004-1009. https://doi.org/10.1061/(ASCE)GT.1943-5606.0000315

[20] Zaman MM, Desai CS, Drumm EC. Interface model for dynamic soil-structure interaction. Journal of Geotechnical Engineering, 1984; 110(9):1257-1273. https://doi.org/10.1061/(ASCE)0733-9410(1984)110:9(1257)

[21] Garbellini C, Laloui L. Soil-structure interaction of surface footings. Computers and Geotechnics, 2021; 134:104103. https://doi.org/10.1016/j.compgeo.2021.104103

[22] Potyondy JG. Skin friction between various soils and construction materials. G' eotechnique, 1961; 11(4):339-353. https://doi.org/10.1680/geot.1961.11.4.339
[23] Clough GW, Duncan JM. Finite element analyses of retaining wall behavior. Journal of Soil Mechanics and Foundation Division, 1971; 97(12):1657-1673. https://doi.org/10.1061/JSFEAQ.0001713
[24] Feng ZK, Xu WJ, Meng QS. Mechanical behaviors of interaction between coral sand and structure surface. Journal of Central South University, 2020; 27(11):3436-3449. https://doi.org/10.1007/s11771-020-4557-x
[25] Di Donna A, Ferrari A, Laloui L. Experimental investigations of the soil-concrete interface: physical mechanisms, cyclic mobilization, and behaviour at different temperatures. Canadian Geotechnical Journal, 2016; 53(4):659-672. https://doi.org/10.1139/cgj-2015-0294
[26] TCVN 5747:1993 - Vietnamese National Standard. Soil - Classification for civil engineering, 1993.
[27] TCVN 9351:2022 - Vietnamese National Standard. Soils - Field testing method - Standard penetration test, 2022.
[28] American Petroleum Institute. API Recommended Practice 2A-WSD - Planning, Designing, and Constructing Fixed Offshore Platforms - Working Stress Design. 21st ed, 2002.
[29] Wu Y, Wang X, Shen JH, Cui J, Zhu CQ, Wang XZ. Experimental study on the impact of water content on the strength parameters of coral gravelly sand. Journal of Marine Science and Engineering, 2020; 8(9):634. https://doi.org/10.3390/jmse8090634
[30] Chen X, Shen J, Wang X, Yao T, Xu D. Effect of saturation on shear behavior and particle breakage of coral sand. Journal of Marine Science and Engineering, 2022; 10(9):1280. https://doi.org/10.3390/jmse10091280
[31] Rahman SMS, Raju MR, Haque MF, Sajib SR, Kabir MH. Assessment of interfacial friction angles of sand-structural materials. Discover Geoscience, 2024, 2:39. https://doi.org/10.1007/s44288-024-00048-8
[32] Li X, Zhang R, Yang Z, Chen P, Ji F, Wen B. Mechanical behavior analysis and bearing capacity calculation of CFG pile composite foundation on coral sand site. Frontiers in Earth Science, 2023; 11:1204989. https://doi.org/10.3389/feart.2023.1204989
[33] TCVN 4198:2014 - Vietnamese National Standard. Soils - Laboratory methods for particle - size analysis, 2014.
[34] Gao R, Ye J. Mechanical behaviors of coral sand and relationship between particle breakage and plastic work. Engineering Geology, 2023; 316:107063. https://doi.org/10.1016/j.enggeo.2023.107063
[35] Yu FW. Particle breakage in triaxial shear of a coral sand. Soils and Foundations, 2018b; 58(4):866-80. https://doi.org/10.1016/j.sandf.2018.04.001
[36] Yu FW. The behavior of coral sands incorporating particle breakage in triaxial tests. International Journal of Geomechanics, 2019.
[37] Das, Braja M., and Sivakugan, Nagaratnam (2018) Principles of Foundation Engineering. Cengage Learning, Boston, MA, USA.
[38] SP 24.13330.2021. Pile Foundations. Russian Ministry of Construction: Moscow, Russia, 2021.
[39] TCVN 10304:2014 - Vietnamese National Standard. Pile Foundation - Design Standard, 2014.

www.jresm.org

Research on Engineering Structures and Materials

Compendex on Engineering Village

Scopus®

DRJI

TÜBİTAK ULAKBİM

ProQuest

crossref

Google Scholar

Universal Impact Factor
Scientifically derived Journal Impact Factor

SIS Scientific Indexing Services

Journal Seeker Research Bible

CiteFactor
Academic Scientific Journals

EZB Elektronische Zeitschriftenbibliothek

Open Academic Journals Index

GIF GLOBAL IMPACT FACTOR

ASOS indeks

Cosmos

Publication Forum

INFOBASE INDEX

ROOTINDEXING
JOURNAL ABSTRACTING AND INDEXING SERVICE

Scope Database
Journal Indexing & Citation Analysis

Research Group

https://mimrg.net/